RELATIONSHIP BETWEEN ERODIBILITY AND PROPERTIES OF SOILS

A Dissertation

by

IMAN SHAFII

Submitted to the Office of Graduate and Professional Studies of
Texas A&M University
in partial fulfillment of the requirements for the degree of

DOCTOR OF PHILOSOPHY

Chair of Committee,	Jean-Louis Briaud
Committee Members,	Zenon Medina-Cetina
	Hamn-Ching Chen
	Mary Jo Richardson
Head of Department,	Robin Autenrieth

December 2018

Major Subject: Civil Engineering

ABSTRACT

The objective of this study was to develop equations correlating the erosion resistance of a soil to its geotechnical properties. Existing erosion tests and erosion correlations are documented. Around 200 erosion tests, and more than 200 geotechnical index property tests were conducted at Texas A&M University. A spreadsheet called TAMU-Erosion was developed. It consists of nearly 1000 erosion test results along with the major geotechnical properties including the 200 tests performed at Texas A&M University and many other tests collected from world-wide sources. The erosion tests' raw data are embedded in TAMU-Erosion, along with an inquiry operation manual which allows the user to search the database in TAMU-Erosion. Numerical simulations were performed to compare different erosion tests. The erosion chart is populated with the Unified Soil Classification System (USCS) categories based on all the tests performed and collected; this chart helps to obtain the basic erosion parameters. Two statistical approaches were implemented to generate the best fit models linking the erodibility parameters to the geotechnical properties. These approaches were the deterministic frequentists' regression, and the probabilistic Bayesian inference. This study aimed at finding a balance between the accuracy required for highway projects and the simplicity of the recommended models.

DEDICATION

I dedicate this dissertation to my parents, and my beloved wife, Rashno. I am greatly indebted to you. Thank you for your constant support and unconditional love. I love you all dearly.

ACKNOWLEDGEMENTS

I would like to express my sincere gratitude to my dissertation advisor, Dr. Jean-Louis Briaud for his endless support during my PhD studies. I will always remember my PhD work under his supervision as one of the most tremendous opportunities of my entire life. I greatly appreciate all his contributions of time, ideas, and funding to make my PhD experience as fruitful and sensational as it is now to me. Dr. Briaud is a class act. On academic level, he taught me fundamentals of conducting scientific research in the field of geotechnical engineering and allowed me to grow as a research scientist. Under his supervision, I learned how to define a research problem, study and find the solutions for it, and finally move in the right direction to solve it. I learned that the most important mission of a scientist is to always push the envelope of knowledge for the good of human beings. On a personal level, he inspired me every day by his hardworking and enthusiastic attitude. He taught me to be responsible, diligent, and pragmatic–while understanding the fundamental phenomena to accomplish any dream. He has been a tremendous mentor, and I am forever grateful to him.

I would also like to thank my other advisory committee members (Dr. Zenon Medina-Cetina, Dr. Hamn-Ching Chen, and Dr. Mary Jo Richardson) for their contributions, valuable advice, excellent feedbacks, and insightful questions. I am grateful to Dr. Medina-Cetina for his crucial support, guidance, and contributions in the final stage of my PhD dissertation. I am also grateful to Dr. Chen for his time and valuable advice in parts of my PhD project. I also express gratitude to Dr. Richardson for serving on my advisory committee and dedicating her time to overseeing my research and providing valuable advice. I am also appreciative of Dr. Marcelo

Sanchez of the Civil Engineering Department to attend my final defense on such a short notice as a substitute for Dr. Medina-Cetina who was not able to attend.

I wish to thank many people for their input and cooperation. They include Dr. Stephane Bonelli from the University of Grenoble, France, Dr. Anna Shidlovskaya from the University of Mines, Russia, and Mr. Tony Wahl from the US Bureau of Reclamation. Also, I would like to acknowledge Mr. Mostafa Bahmani and Mr. Yichuan Zhu, PhD students of Department of Civil Engineering at Texas A&M University for their contributions to Sections 6.2 and 7.4, respectively. I would also like to acknowledge the Houston office of Fugro USA Land, as well as the College Station and Conroe offices of Terracon Consultants for providing help in many key moments during this PhD research. Finally, I would like to thank the staff and lab coordinators in the geotechnical engineering program at Texas A&M University who helped during this project thereby making this study possible.

Last but not least, I am greatly indebted to my family and my beloved wife, Rashno. To my extraordinary parents: I deeply appreciate you for spiritually and financially supporting me in all the time of my education, and for encouraging me to pursue my interests and become the person who I am today. To my caring and beautiful wife: words cannot express how grateful I am for your support, dedication, and unconditional love through my good and bad times. You always cheer me up, thank you.

CONTRIBUTORS AND FUNDING SOURCES

Contributors

The dissertation herein was supported by a dissertation committee consisting of Professor Jean-Louis Briaud of the Department of Civil Engineering, Professors Zenon Medina-Cetina and Hamn-Ching Chen of Department of Civil Engineering; and Professor Mary Jo Richardson of the Department of Oceanography at Texas A&M University.

The numerical analyses depicted in Sections 6.1 and 6.2 were conducted in part by Professor Chen and Mr. Mostafa Bahmani of the Department of Civil Engineering, respectively. The data analyses depicted in Section 7.4 was conducted in large by Professor Medina-Cetina.

All other word conducted for the dissertation was completed by the student independently.

Funding Sources

This dissertation herein was funded by National Cooperative Highway Research Program (NCHRP) under NCHRP Project 24-43.

TABLE OF CONTENTS

Page

Page

Page

Page

Page

LIST OF FIGURES

Page

Page

Page

Page

Page

Page

Page

Page

Page

Page

Page

Page

Page

Page

Page

LIST OF TABLES

Page

Page

Page

Page

Page

1. INTRODUCTION

1.1. Erosion Definition

The phenomenon of erosion is the result of interaction between three main components including the erodible material, the eroding fluid (in most cases water), and the geometry of the obstacle impacting the flow. In this process the fluid generates the "load", the erodible material provides the resistance while the obstacle induces the disturbance. Briaud (2008) divided the erodible materials into three categories:

- Soil: those earth elements which can be classified by the Unified Soil Classification System (USCS).
- Rock: those earth elements that have an unconfined compressive strength of the intact rock core of more than 500 kPa with joint spacing of at least 0.1 m.
- Intermediate geomaterials: any earth material intermediate between rock and soils.

Erodibility can be defined as the behavior of the eroding material when subjected to the flow of the eroding fluid. The eroding water is quantified by its velocity, and the obstacle geometry is characterized by its dimensions. Figure 1 shows the forces acting on a soil particle at the interface surface between the water and the soil.

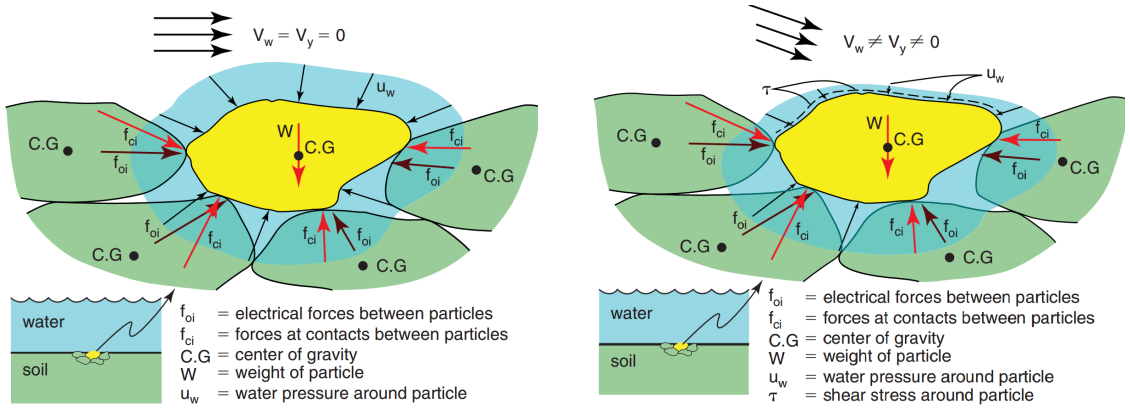

a) No-flow condition b) With the water flow

Figure 1. Free body diagram of a soil particle or rock block in two different stages a) no-flow condition, b) with the water flow (Briaud, 2008)

Given to its application in the nature, erosion phenomenon can be divided into two different groups:

1) Internal erosion which is important for seepage through embankment dams, levees, canal sides embankments
2) Surface erosion which is important for bridge scour, overtopping of levees, dams, highway embankments, meander migration.

1.1.1. *Internal Erosion*

The type of erosion in which the soil particles are transported within the body of an earth structure such as an embankment dam from the upstream source to the downstream by the eroding fluid is known as internal erosion (Wan and Fell, 2002). Due to the process in which the eroded particles are carried from an embankment dam or its foundation, internal erosion is subdivided into two different types: piping and suffusion.

The first type is piping. This phenomenon is mainly the result of a backward erosion due to the high exit gradient at the downstream part of embankments or the boundaries between the coarse downstream of a rockfill dam and its core. Basically, this high exit gradient detaches the particles and initiates the internal erosion. This erosion process leads to the formation of a continuous tunnel in the embankment which is known as a pipe. It is also worth mentioning that other factors such as hydraulic fracturing or poor compaction of the soil might cause some potential crack through the core of the dam which can result in piping. Similar to the definition made by Terzaghi and Peck (1948), the phenomenon of heave in dams can be named as a special case of piping, which happens when the effective stress of the soil at the toe is decreased due to high seepage gradient.

The other type of internal erosion is suffusion. This internal instability mostly happens in those soils whose grain size distribution does not meet the requirements of self-filtering conditions such as poorly graded soils (Wan and Fell, 2002). Suffusion is the result of replacement and erosion of very fine soils existing in the matrix of coarser particles by the eroding flow. CFGB (1997) reports several dam failures in France caused mainly by suffusion.

Von Thun (1996), described seepage and piping failures as the No. 1 dam safety problem in the western USA. Indeed, a study on the relative risk of failure of dams in the USA revealed that 60% of all failures of embankment dams higher than 15.2m (50 feet) in the western USA were due to piping.

1.1.2. *Surface Erosion*

Surface erosion occurs on the surface of the soil such as in river beds, during overtopping flow of levee and embankments, and bridge scours. Similar to the erosion shown in Figure 1, the surface erosion happens in three main stages:

1) A drag force and the resulting shear stress are developed on the surface at the interface between the soil particles/ rock block and the eroding fluid.

2) The eroding fluid causes a decrease in the normal stress induced on the surface of the soil particle/ rock block. In other words, as the velocity of the eroding fluid increases in the space surrounding the soil particles, given to the rule of conservation of energy and Bernoulli's principle, the normal pressure induced by the eroding fluid decreases to maintain the flow.

3) Due to the turbulence in the water, the normal stress and the induced shear stress on the hydraulic interface between the eroding fluid and soil fluctuate. At high velocities, these fluctuations create cyclic loading of the soil particle which makes erosion easier to occur (Croad, 1981; Hofland et al., 2005).

The combination of the drag shear force, the uplift normal force, and their fluctuations act together to remove the soil particle/rock block and initiate the surface erosion process.

As mentioned earlier, surface erosion is the key element in bridge scour. Scour around b ridge supports is the most common cause of bridge failure (Arneson et al., 2012). More than 80 percent of all bridges in the United States (approximately 500,000 bridges) are located over water which highlights the significance of studying surface erosion. Studies have shown that in 60 percent of the cases where bridge collapse has happened, the failure was due to the bridge scour (Briaud et al., 1999). Bridge scour is a serious and costly problem for the environment and leads to severe disasters such as the one reported in 159 counties of Georgia in 1994 (CDC, 1994).

1.2. Soil Erodibility and Constitutive Models

This project deals with the first category of erodible materials defined by Briaud (2008): soils. It is well understood that knowledge of erodibility of soil is the key step to probe and control the serious environmental hazards caused by erosion such as bridge scour, embankment and floodwall overtopping erosion, dam spillway erosion and stream stability.

Despite the large number of contributions to soil erosion and despite developing several testing methods both in the field and laboratories, no unified method for estimating the erodibility characteristics of soils has been achieved so far. One of the complexities in trying to unify erodibility measurement methods is that some researchers have tested human-made soils to impose specific condition, or have reproduced the field conditions in the lab, while others have tested samples collected from the field.

The only way to come up with a common reliable model to estimate the erodibility characteristics of each soil is to first identify the major parameters involved in the erosion process, which not only does exist in all different types of tests, but also does not depend on the test condition and soil type.

The erodibility of the soil can be defined as the relationship between the erosion rate of soil/ rock $\dot{z}$ and the velocity (v) of eroding fluid at the interface between soil/rock and water.

$$\dot{z} = f(v) \tag{1}$$

Where, $\dot{z}$ is the erosion rate (depth/time), and v is the velocity of eroding fluid (length/time).

Eq. 1, however, is not satisfactory enough; because, the velocity varies in direction and intensity in the flow field (Briaud 2008). Indeed, the water velocity profile reaches a value of zero

at the interface between the water and the soil. A more fundamental definition is the relationship between the erosion rate and the shear stress at the water-soil interface.

$$\dot{z} = f(\tau) \tag{2}$$

Where, $\dot{z}$ is the erosion rate (depth/time), and τ is the hydraulic shear stress at the interface (force/length square).

However, the velocity is often used because it is easier to get a feel for velocity than for shear stress. In an effort to normalize Eq. 1, the erodibility of a soil can be defined as the relationship between the erosion rate $\dot{z}$ and the mean depth velocity v of the water in excess of the critical velocity v_c (Figure 2). The following equation has been proposed:

$$\dot{z}/v_c = \alpha((v - v_c)/v_c)^m \tag{3}$$

Where, α and m are unit-less coefficients depending on the properties of the soil. Also, a normalized version of Eq. 2 has been proposed (Figure 2).

$$\dot{z}/v_c = \alpha'((\tau - \tau_c)/\tau_c)^{m'} \tag{4}$$

Where, α' and m' are unit less coefficients depending on the properties of the soil. The erosion function described by Eq. 4 represents the constitutive law of the soil for erosion problems much like a stress strain curve would represent the constitutive law of the soil for a settlement problem. While a shear stress-based definition is an improved definition over a velocity-based definition, it is still not completely satisfactory as the shear stress is not the only stress which contributes to the erosion rate. Indeed, the fluctuations in normal stress and shear stress due to turbulence intensity apply pulsations which can suck the soil particle or cluster of soil particles out of position and then entrained it in the flow through the drag force. A more complete description of the erosion function is given by Eq. 5:

$$\frac{\dot{z}}{v} = \alpha\left(\frac{\tau-\tau_c}{\rho v^2}\right)^m + \beta\left(\frac{\Delta\tau}{\rho v^2}\right)^n + \gamma\left(\frac{\Delta\sigma}{\rho v^2}\right)^p \tag{5}$$

Where $\dot{z}$ is the erosion rate (mm/hr), v the water velocity (m/s), τ the hydraulic shear stress (N/m^2), τ_c the threshold or critical shear stress (N/m^2) below which no erosion occurs, ρ the mass density of water (kg/m^3), $\Delta\tau$ the turbulent fluctuation of the hydraulic shear stress (N/m^2), and $\Delta\sigma$ the turbulent fluctuation of the net uplift normal stress (N/m^2). All other quantities are parameters characterizing the soil being eroded. While this model is quite thorough, it is rather impractical at this time to determine all the parameters needed in Eq. 5 on a site specific and routine basis. Today Eq. 3 and 4 are broadly accepted and will form the basis of this project (Shafii et al., 2016). After investigating and measuring the hydrodynamic forces on gravel particles using a video analysis technique, Shafii et al. (2018) have recently introduced a more practical erosion model (Eq. 6).

$$\frac{\dot{z}}{0.1} = \left(\frac{\tau}{\tau_c}\right)^{\alpha} \times \left(\frac{\sigma}{\sigma_c}\right)^{\beta} \tag{6}$$

Where, $\dot{z}$ is the erosion rate (mm/hr), τ_c (Pa) and σ_c (Pa) are the critical shear stress and critical normal stress associated with 0.1 mm/hr erosion rate, and α and β are the unit-less erosion model parameters. Eq. 6 is expected to capture the influence of both shear and normal stresses during erosion.

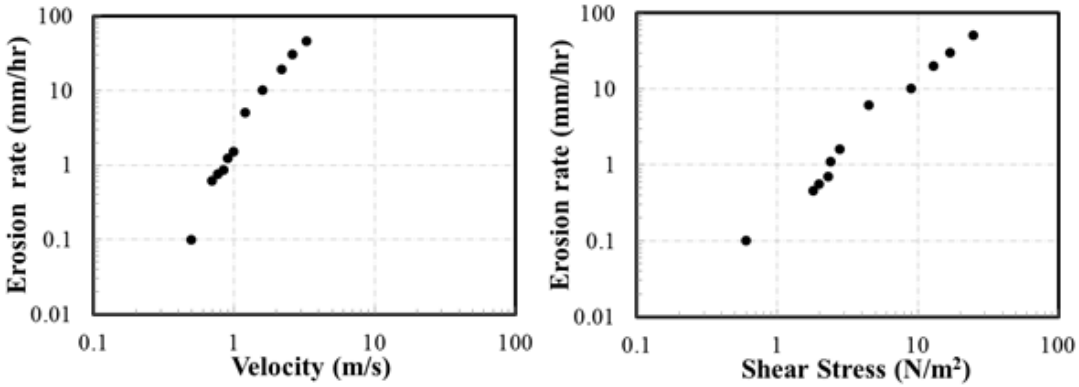

Figure 2. Examples of erosion function (Briaud, 2013)

1.3. Erodibility Parameters

One of the important goals of this study is to organize and analyze many different erosion test results while using one single mathematical model; in this way the data will become comparable. The following erodibility parameters have been selected because they are widely accepted among hydraulic and geotechnical engineers and have a simple and easily understood definition.

1.3.1. *Erosion Rate*

The erosion rate of a soil can be identified in many different ways, depending on the erosion testing method. This rate can be generally expressed in three main forms:

1) Rate of change in depth of a soil surface under a specific hydraulic shear stress induced by the eroding fluid flow (i.e. Erosion Function Apparatus, Jet Erosion Test, etc.).

2) Rate of change in the soil volume during a specific time period while the soil is subjected to a hydraulic shear stress induced by the eroding fluid flow.

3) Rate of change in the eroded soil mass sometimes also presented as the rate of mass removal per unit area (i.e. Hole Erosion Test).

1.3.2. *Slope of Erosion Function*

Another important erodibility parameter is the normalized erosion rate against the flow velocity or the hydraulic shear stress. As shown in Figure 2, the result of an erosion test can be presented in two different forms: erosion rate versus velocity, and erosion rate versus hydraulic shear stress. There are different methods to determine the slope of erosion function. In this study, the slope of the erosion rate versus velocity curve will be designated as E_v, and the slope of erosion

rate versus shear stress will be designated as E_τ. In Chapter 5, the procedure for determining E_v and E_τ is detailed for each test result.

1.3.3. *Critical Velocity/ Shear Stress*

These values of the critical velocity/ shear stress refer to the initiation of the erosion process. Basically, the critical velocity (v_c) in an erosion test refers to the maximum velocity that the soil can resist without getting eroded. In terms of the hydraulic shear stress, this value is known as critical shear stress (τ_c). Depending on the type of erosion test, researchers have used different definitions and different techniques to identify the critical velocities and critical shear stress. In this study, the critical velocity and critical shear stress will be determined using the same procedure independent of the type of erosion test. This procedure will be discussed in Chapter 5.

1.3.4. *Erosion Category*

Briaud (2008) and Hanson and Simon (2001) have developed category charts to make it easier to identify the erodibility of soils. Figure 3 shows the erosion categories developed by Briaud (2008) in his 2007 Ralph B. Peck Lecture. In that chart, the erosion categories are bound by lines in the $\dot{z}$ versus v and the $\dot{z}$ versus τ plots. These charts were based on many years erosion testing at Texas A&M University. The lines giving the boundaries between categories originate at the critical velocity and critical shear stress. Table 1 shows the critical values for the velocity and the shear stress for each erosion category in Figure 3.

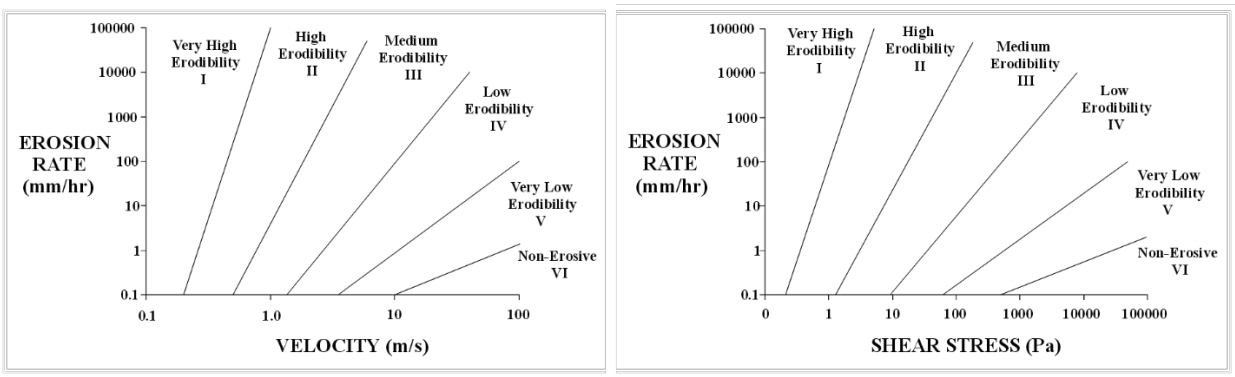

Figure 3. Erosion category for soils and rocks based on velocity and shear stress proposed by Briaud (2008) – Areas I to VI in the graphs refer to the erodibility category of sediments

Table 1. Threshold velocities and shear stress associated with each erosion category

Category No.	Erosion Category Description	v_c (m/s)	τ_c (Pa)
I	Very high erodibility geomaterials	0.1	0.1
II	High erodibility geomaterials	0.2	0.2
III	Medium erodibility geomaterials	0.5	1.3
IV	Low erodibility geomaterials	1.35	9.3
V	Very low erodibility geomaterials	3.5	62.0
VI	Non-erosive materials	10	500

1.4. Research Approach and Project Tasks

The goal of this project is to develop equations quantifying the erodibility of soils based on soil properties. Different soils exhibit different erodibility (sand, clay); therefore, erodibility is tied to soil properties. On the other hand, many researchers have attempted to develop such equations without much success. One problem is that erodibility is not a single number but a relationship between the erosion rate and the water velocity or the hydraulic shear stress. This erosion function is a curve and it is difficult to correlate a curve to soil properties. Another problem that needs to be solved is associated with the availability of several erosion testing devices. In the laboratory, they include many erosion tests such as the pinhole test, the hole erosion test, the jet

erosion test, the rotating cylinder test, the erosion function apparatus test. In the field, they include the jet erosion test, the NC State in situ scour evaluation probe test, the TAMU borehole erosion test and pocket erodometer test, and etc. All these tests measure the soil erodibility but give different results. It is important to give the DOT engineers options so that she or he can choose one test or another. Therefore, it would be helpful if all these tests could give the same answer. Indeed, the soil does not know the difference and the erosion function is a fundamental property of the soil. Experimental and numerical efforts were made to advance in this direction.

The tasks are as follows:

PHASE I

Task 1: Identification of current knowledge on soil erosion and soil properties

Task 2: Identification of current soil erodibility data and correlations

Task 3: Assessment of current and promising erosion tests

Task 4: Interim Report and work plan for Phase II

PHASE II

Task 5: Perform erosion tests with different devices using the same prepared soils

Task 6: Perform erosion tests using many different soils to develop the erodibility equations

Task 7: Development of regression equations and validation

Task 8: Verification, synthesis and analysis of all data to propose best solution

The major objective of this study was to develop equations which optimize the balance between reliability and simplicity. The reliability must take into account the accuracy required for highway projects while the simplicity must consider the economic aspects of highway projects. The summary of the findings for each chapter is discussed below.

1.4.1. *Task 1: Identification of current knowledge on erosion and soil properties*

Erodibility definition was the first step. The soil erodibility is not a single number but a relationship between the hydraulic load (water velocity or shear stress) and the soil resistance (erosion rate). The equation sought to connect the soil properties to soil erodibility links the elements of the erosion function (critical velocity, critical shear stress, initial slope of the erosion rate versus velocity or shear stress curve) to various soil properties.

In the identification of current geotechnical property practices, the focus was to the most commonly used soil properties in the regression equations. Among those soil properties are the mean grain size, the plasticity index, the water content, the percent passing sieve #200, the unit weight, the undrained shear strength, etc. In the identification of the current erosion testing practices, the objective was to learn about all of the available erosion testing devices, and next to place a focus on the most commonly used erosion tests both in the laboratory and in the field. This knowledge is documented in the Chapter 2 of this report.

1.4.2. *Task 2: Identification of current soil erodibility data correlations*

In the identification of current erodibility data, all the data on soil erodibility parameters (namely critical velocity, critical shear stress, initial slope of the erosion rate vs. velocity or shear stress curve) and common soil properties were collected. The existing correlations are documented in the Chapter 3 of this report. Additionally, a huge spreadsheet is developed as part of this study and presented in the Chapter 5 of this report.

1.4.3. *Task 3: Assessment of current and promising erosion tests*

The most commonly available erosion tests both laboratory tests and in situ tests are reviewed in Chapter 2. Each one of those tests has advantages and limitations. These tests are also

assessed with respect to issues such as “range of soil types that can be tested”, “cost of the test”, “cost of the device”, “best applications”, etc. These comparisons help the DOT engineer select the best tests to be chosen for a given situation. The assessment is documented at the end of Chapter 2. One of the critical issues associated with these different devices and tests is that they do not give the same erosion parameters; they do not lead to the same type of results. To solve this problem, numerical simulations are used. These simulations would then lead to a common data reduction process of erosion tests, a common output of all erosion tests, bring uniformity in erosion studies, and keep all soil erosion testing options open for the scour and erosion engineer. Information on the numerical simulations is documented in the Chapter 6 of this report.

1.4.4. *Task 5: Perform erosion tests with different devices using the same soils*

This task was dedicated to testing the same soil with different erosion testing devices. The soils to be tested were man-made soils because it is the only way to be sure that identical and reproducible samples can be prepared and tested. These soils included as a minimum a gravel, a compacted sand, a compacted silt, and a compacted high plasticity clay. All soil properties tests, all pocket erodometer tests, and all EFA tests, JET tests, and HET tests were performed at the Erosion Laboratory at Texas A&M University. For the in situ tests, the borehole erosion test and the pocket erodometer test were conducted at the RELLIS Sand and Clay sites at Texas A&M University. The results of this task are documented in the Chapter 4 of this report.

1.4.5. *Task 6: Perform erosion tests to develop the erodibility equations*

This task was dedicated to testing the different soil samples with different erosion testing devices at Texas A&M University. The data obtained during this task alongside with all collected

data during other tasks are used to develop the erodibility equations. Chapter 4 of this report as well as the Appendixes 1 and 2 extensively document the results of the work done on Task 6.

1.4.6. *Task 7: Development of regression equations and validation*

This task was dedicated to developing the regressions equations correlating the erodibility parameters and the geotechnical properties of soils. Two major statistical methods were used to accomplish this task: 1) A frequentists' approach with the plots of "probability of over-predicting" and "probability of under-predicting" for the selected models. As part of this approach, first and second order statistical analyses were conducted. This was followed by the regression and optimization techniques (i.e. cross-validation). 2) A probabilistic approach using the Bayesian inference. The main benefit of the use of the Bayesian inference is the definition of a metric of confidence on the model predictions. The results of the both statistical approaches are extensively documented in the Chapter 7 of this report, as well as in the Appendices C to E.

1.4.7. *Task 8: Verification, synthesis and analysis of all data to propose best solution*

Once all the testing has been conducted and once the statistical/correlation analysis has been conducted, all aspects of the project are synthesized and analyzed to present a complete solution package to address the main objective of this research. Also, the classification charts presented in Figure 3 which link the likely soil erosion function to the soil classification as a first step in any soil erosion problem are updated. The results of this task are documented in the Chapter 8 of this report.

2. EXISTING EROSION TESTS

This chapter describes some of the most common tests developed over the years to quantify soil erodibility. The drawbacks and advantages of the most important testing methods are evaluated and identified. Generally, erosion testing is divided into the two following groups:

1) Laboratory erosion testing
2) Field erosion testing

The erosion tests presented in this chapter are divided into two sections based on their application whether in the laboratory or in the field. It must be noted that some of the erosion tests have applications in both the laboratory and the field; however, they are discussed only once in either section 2.1 or 2.2.

2.1. Laboratory Erosion Testing

2.1.1. *Erosion Function Apparatus (EFA)*

In the early 1990s, the idea of the Erosion Function Apparatus (EFA) was first developed, established, and patented by Briaud at Texas A&M University (Briaud et al., 1999, 2001a, 2001b). Today the EFA is being manufactured by Humboldt, Inc. and used widely by many engineering organizations. This test was originally developed to evaluate the erodibility of a wide range of both cohesive and non-cohesive soils from gravels to clay and silt. Figure 4 shows a schematic diagram as well as a photograph of the EFA device.

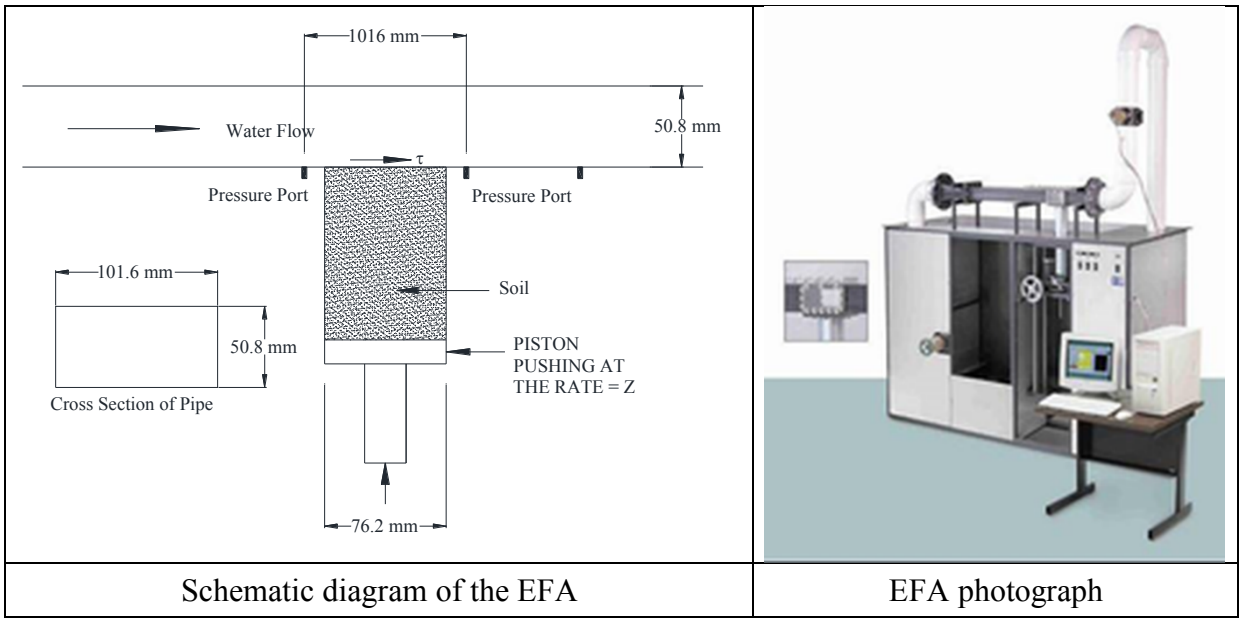

Schematic diagram of the EFA | EFA photograph

Figure 4. Schematic diagram of the Erosion Function Apparatus and a photograph of the testing apparatus (Texas A&M University).

Soil samples are taken using ASTM standard Shelby tubes with an outside diameter of 76.2 mm (ASTM D1587). Similarly, for soft rocks, a rock core sample can be extracted and placed into a Shelby tube for rock erosion testing. Water, as the eroding fluid, is driven using a pump into a 1.2 m long rectangular cross section 101.6 × 50.8 mm as shown in Figure 4. The water flow can be adjusted using a valve, and the average water velocity is measured by a flowmeter in line with the flow. One end of the Shelby tube is placed on the bottom of a circular plate which is connected to a piston. The piston is designed to push the sample up into the flow when necessary. The sample is pushed upward until it becomes flush with the bottom of the rectangular cross section pipe.

The test procedure is as follows (Briaud et al., 2001):

1) Place one end of the Shelby tube on the circular plate piston, push it up until it becomes flush with the bottom surface of the rectangular cross section pipe.
2) Fill the rectangular pipe with water and wait for one hour

3) Initiate the flow with a small flow velocity, typically 0.2 m/s.
4) Start recording time. Hold the sample surface flush with the bottom of the rectangular pipe during the induced flow velocity. The test operator needs to make sure that the soil surface is kept flush all the time by pushing the soil with the piston as it is eroded by the water and maintain a level interface. Continue this until 50 mm of the soil is eroded or 30 mins have passed. Read the protrusion height by observing the change in the height of the bottom of the piston.
5) Redo step 3 and 4 for a new and higher flow velocity (i.e. 0.2 m/s, 0.6 m/s, 1 m/s, 1.5 m/s, 2 m/s, 3 m/s, 4.5 m/s, and 6 m/s).

The scour rate versus flow velocity is plotted. Figure 2 shows an example of EFA test results as both erosion rate versus velocity and erosion rate versus shear stress. The shear stress on the eroded surface of the soil is calculated by using Moody chart (Moody, 1944).

$$\tau = \frac{1}{8} f \rho v^2 \quad (7)$$

Where, τ refers to the shear stress (pa), ρ is the density of water (1000 kg/m^3), and v is the flow velocity (m/s). f is the friction factor obtained using Moody chart.

2.1.1.1. Advantages

1) Minimize the sample disturbance effect, as it takes the sample directly from the field using Shelby tubes.
2) Can be used for natural samples as well as human made samples
3) Gives the critical velocity and the critical shear stress. Can give the erosion function directly.
4) EFA test results are directly used as input to the TAMU-SCOUR method for bridge scour depth predictions (Chapter 6 of HEC-18).

5) EFA can test the erodibility of the soil at any depth as long as a sample can be recovered.
6) While the EFA test is a surface erosion test, it can be used to evaluate internal erosion as well because the EFA erosion function represents the erodibility of the soil at the element level.
7) Can test very soft to very hard soils. Very broad applications.

2.1.1.2. Drawbacks

1) Shear stress is indirectly measured from velocity using Moody charts which might not be accurate. Also, the average flow velocity is used in the calculations instead of the actual velocity profile.
2) In some cases that field samples are required, obtaining samples is difficult and costly. The test needs to be done on the sample before the sample is affected by long periods of storage.
3) Particles larger than 40 mm in size cannot be tested with confidence as the diameter of the sampling tube is 75 mm.
4) The EFA is a fairly expensive device (around $50k).

Several other organizations copied the idea of the EFA and developed similar devices such as the SERF and the ESTD which are also presented in this chapter.

2.1.2. *Sediment Erosion Rate Flume (SERF)*

This apparatus was developed by Sheppard and his colleagues at the University of Florida to measure the erodibility of cohesive and non-cohesive sediments (Trammel, 2004). Figure 5 shows a photograph of the SERF.

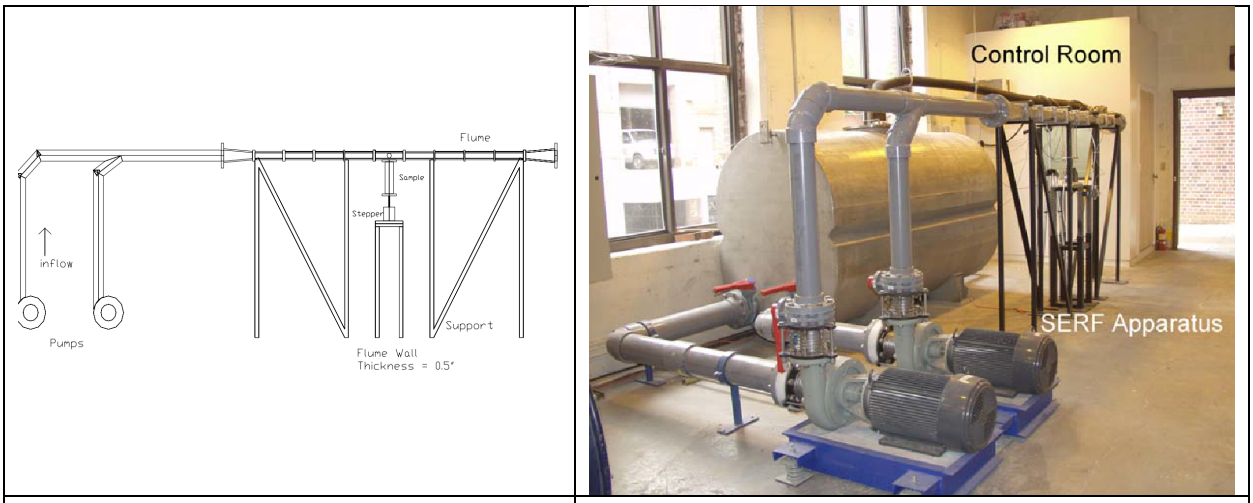

Schematic diagram of the SERF	SERF photograph

Figure 5. SERF apparatus at University of Florida (Trammel, 2004)

SERF has a 9 ft. long rectangular channel with dimensions of 5.08 cm × 20.32 cm elevated at 5.5 ft. which is fed by two 500 gpm parallel pumps from a large 1100-gallon water tank. The flow channel is designed to have a 1 ft. straightener in the beginning in order to reduce the turbulence of the water discharge. The specimen cross section is placed in the center of the rectangular channel. Flow is driven through 3 ft. long, and right after, reaches the specimen's cross section which is 1 ft. long. It then proceeds another 4 ft. of the channel and is directed to the reservoir tank. The reason that two pumps are used is to account for harder soil samples, where both pumps can be running. Also, erosion of the Shelby tube size sample is continuously monitored by the control computer using an attached video camera next to the test section. An array of sonic SeaTek Transponders is attached at the top of the flume right above the test section; these transponders give the mean elevation of the sample surface which is used to prompt the computer to advance of the piston and keep the sample surface flush with the bottom of the flue. Basically, SERF is controlled and monitored automatically by a computer software. The summation of

upward movements recorded and steps by the motor for a specific flow velocity (shear stress) divided by that particular time period reflects the erosion rate.

SERF includes pressure ports in 2 ft. distance from the center of the test section at both sides which calculates the pressure drops happened in the flume using the following equation.

$$\tau = \frac{(\Delta p \times \text{Area})}{(2w+2h)\times L} \quad (8)$$

Where, τ refers to the hydraulic shear stress (Pa), Δp is the recorder pressure drop (Pa), A is the cross-section area of the rectangular channel, L is the distance between pressure ports (which is 4 ft.), and (2w+2h) refer to the hydraulic radius in the channel.

In addition to similar advantages mentioned for EFA, SERF is independent from the operator and runs with an automated system.

2.1.2.1. Drawbacks

1) The device is expensive and requires a bulky setup.
2) The automation of the process requires the use of very expensive instruments which also require significant expertise when they break down or need to be adjusted.
3) The samples have to be prepared in the cylinder of the test device. This limits the use of SERF to disturbed or human made samples.

2.1.3. *Ex-Situ Scour Testing Device (ESTD)*

The Ex-Situ Scour Test Device (ESTD) was developed by Kerenyi and his colleagues at the FHWA Turner Fairbanks research center (Shan et al., 2015). The purpose was to simulate the velocity profile for open channel conditions. Figure 6 shows a schematic diagram along with a photograph of this test device.

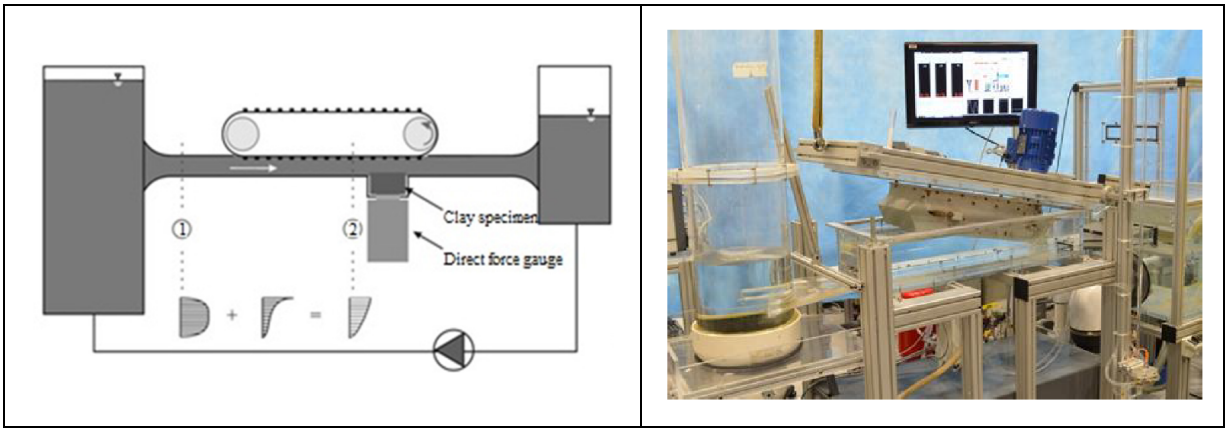

Schematic diagram of the ESTD	ESTD photograph

Figure 6. Schematic diagram and photograph of Ex-situ Scour Testing Device

A cylindrical soil specimen with the diameter of 63.5 mm and height of 15 mm is placed on the top of a direct force gauge. A 580 mm rectangular channel with a dimension of 12 cm × 2 cm connects the inlet tank to the outlet tank. Similar to EFA, a flowmeter is attached to the device to measure the flow velocity in the channel. A moving belt, as shown in Figure 6, is used to entrain the water and reproduce the expected log-law velocity profile in the field. Also, the roughness of the channel is controlled by attaching a wide range of sand papers to the bottom of the channel surface. Instead of calculating the hydraulic shear stress at the interface of the eroding fluid and the soil indirectly from velocity or pressure drop, a direct force gauge is used to instantaneously capture both normal forces and shear stress induced on the soil surface. The samples for the ESTD are prepared in the lab typically using a Pugger Mixer which prevents existence of air bubbles in the specimen. Also, the samples are left in water to slake before performing the ESTD test. The advantages and drawbacks of the ESTD are.

2.1.3.1.Advantages

1) ESTD is automated

2) ESTD is designed to reproduce the open channel flow condition.

3) Existence of sensors to measure the vertical force and shear stress directly, are very helpful. Effect of turbulence can be more precisely studied using the results of the vertical force on the interface.

2.1.3.2.Drawbacks

1) The ESTD is not well suited to practical use for site specific problems. The set-up is time consuming.

2) It cannot reflect the actual field conditions, as the soil specimens are all hand-made in the lab.

2.1.4. *Sediment Erosion at Depth Flume (Sedflume)*

This apparatus was originally developed at University of Santa Barbara for the purpose of measuring the sediment erosion at high shear stress and with depth (McNeil et al., 1996). Sedflume has been used by researchers for coastal applications and by the US Army Corps of Engineers. The primary application of this device is in studying sediment transport and suspension rate during high stress floods. Figure 7 shows a schematic diagram of Sedflume along with a photograph of the testing device.

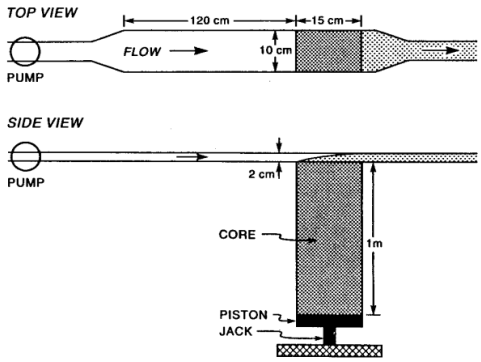

Schematic diagram of the Sedflume (McNeil, 1996)	Sedflume photograph (USACE)

Figure 7. Schematic diagram of Sedflume with a Sedflume photograph

The channel of the flume is 120 cm long and the rectangular cross section is 10 cm × 2 cm as shown in Figure 7. The Sedflume also exists as a portable lab which can be moved to a site. At the ned of the straight channel is a 15 cm long section where the top of the soil sample comes through. The rectangular soil sample is 1 m long and has cross section dimensions of 15 cm × 10 cm. Test samples are collected in two ways: directly from the site or recreated in the lab using a sediment slurry. In deeper waters, divers might be needed to put the coring tube and extract sample from the site. In soft soils, the sampler can be pushed into the soil while in stiffer soils, a Vibracoring head can be used. The test sample is then placed on a piston with a hydraulic jack which is used to adjust the height of the sample. As in the EFA, the operator needs to keep the sample flush with the flume surface. The flow also is adjusted by a valve, and a flowmeter is attached to the flume to measure the flow rate of the eroding fluid. Water powered by a pump flows into the flume and testing proceeds in the following steps (McNeil et al., 1996):

1) Place one end of the rectangular coring tube on piston located at the bottom of the test section.

2) Use the piston to extrude the sample upward until it becomes flush with the bottom of flume surface.
3) Make sure that as the soil surface erodes, you maintain a level interface between the sample and the bottom of flume surface.
4) Record the amount of eroded sediments by recording the upward movement of piston.
5) Repeat the steps 2 to 4 for higher flow velocities and thus higher shear stress values.

As for the EFA, the shear stress is calculated using Eq. 7. Advantages and drawbacks of the Sedflume are presented below:

2.1.4.1. Advantages

1) The field version helps minimize the sample disturbance effect. Also, with the field version, the actual water from the field can be used in the test.
2) Directly measures the erosion rate versus shear stress curve from the field, and determines the critical shear stress

2.1.4.2. Drawbacks

1) As for the EFA, the shear stress calculation is based on the mean flow velocity and the use of Moody chart instead of direct measurements.
2) The lab apparatus is very bulky and costly. The sample preparation is time consuming and the test setup in the field is also time consuming.
3) Only disturbed or reconstructed samples can be tested.
4) There are several limitations in sample collection especially for deep water conditions.

Roberts et al. (2003) developed a similar device to the Sedflume called the Adjustable Shear Stress Erosion and Transport (ASSET) Flume. ASSET Flume was designed to be larger than Sedflume to overcome the channel wall effects on the flow. The other difference was that the

eroded sediments were collected and then dried to obtain the bed-load and suspended fractions in the flume.

2.1.5. *Some other flume tests*

In addition to the EFA and similar tests, several researchers have performed flume tests to study the erodibility potential of different soils. Gibbs (1962) conducted some flume tests in the laboratory on intact soil samples (mostly CL and ML) from canal banks. The purpose of his tests was to investigate the influence of different plasticity properties and in-situ density of the soils on the erosion resistance of these soils. His findings will be summarized in the next chapter of this report.

A few years later, Lyle and Smerdon (1965), from Texas A&M University, constructed a laboratory flume test to study the effect of soil properties (especially compaction) on erosion resistance of soils. Lyle and Smerdon (1965) conducted erosion tests on seven Texas soils in a 22 m long hydraulic flume with a 76 cm × 40 cm. The slope of the flume was also 0.2%. The 55 m long sample soil was placed in the center cross section of the flume. The velocity of the water flow was measured using six pitot tubes installed in 6 different points of the flow. The depth of flow was also measured accurately during the flow using 17 piezometers along the flow channel. The shear stress induced on the eroded surface was calculated as the product of hydraulic gradient (s) and water unit weight. Lyle and Smerdon then defined the critical shear stress as the shear stress which initiates the erosion of the soil. The samples that were replicated using the suspended samplers during each increase in the flow were tested in the lab and the plasticity index and void ratio (compaction) were recorded. The critical shear stress was then plotted against the compaction

and plasticity properties of the soil. The findings of Lyle and Smerdon (1965) will further be discussed in the next chapter of the report.

Kandiah and Arulanandan (1974) also used flume tests to study the erodibility of Yolo lam clay. The main purpose of their research was to compare the erodibility results obtained from the flume test and the rotating cylinder test. Also, effect of compaction and water content on the critical shear stress was investigated. Some of their findings will be discussed in the next chapter of this report.

Arulanandan and Perry (1983) studied the erodibility potential of core materials used for better representing the common dam filter design method which was being practiced during that time. In order to quantify the critical shear stress imparted on the cracks within the core of the dam, Arulanandan and Perry used both flume tests and rotating cylinder tests.

The research on evaluating the soil properties were continued and different researchers used different approaches to find the erodibility parameters. Shaikh et al. (1988) performed flume tests to evaluate the influence of clay material and compaction of soil on the erosion resistance of soils. To do so, they constructed a 250 cm long rectangular channel with a 15.5 cm × 11 cm cross-section (see Figure 8). The slope of the flume was adjustable. As shown in Figure 8, three samples which were 15.2 cm long with a 10.5 cm × 2.25 cm cross section, could be tested at the same time with the same slope. The flow depth could be adjusted between 80 cm and 210 cm. The flow velocity was also measured using a pitot tube as shown in Figure 8.

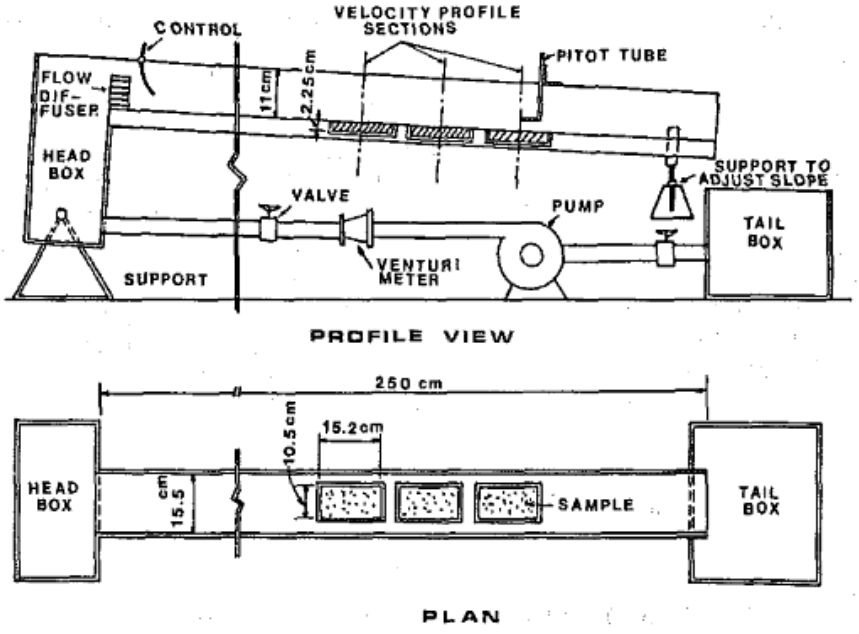

Figure 8. A schematic diagram of the flume test used by Shaikh et al. (1988)

Chow (1959) calculated the shear stress induced on the surface of the sample by using the smooth channel flow equation:

$$\frac{\mathrm{V}}{\mathrm{V}^*} = 5.5 + 5.75 \log\left(\frac{V^* \times y}{\nu}\right) \tag{9}$$

Where, V^* is a parameter called the shear velocity ($\frac{\tau}{\rho_w}$), V refers to the velocity of flow at a depth y in the turbulent zone, ρ_w is the water density, and ν is the viscosity of water. Shaikh et al. (1988) defined the erosion rate as the rate of weight removal in a given time. Then, they could plot the erosion rate ($N/m^2/min$) versus hydraulic shear stress (Pa).

Six years later, Ghebreiyessus et al., (1994) developed a new enclosed flume test to study the soil resistance to erosion as well as the influence of geotechnical parameters in soil erodibility. For this purpose, a 250 cm long rectangular flume with a 20.3 cm × 2.5 cm cross section was

constructed (Figure 9). The flume dimensions were selected to generate a steady flow condition according to Chow (1959) equations.

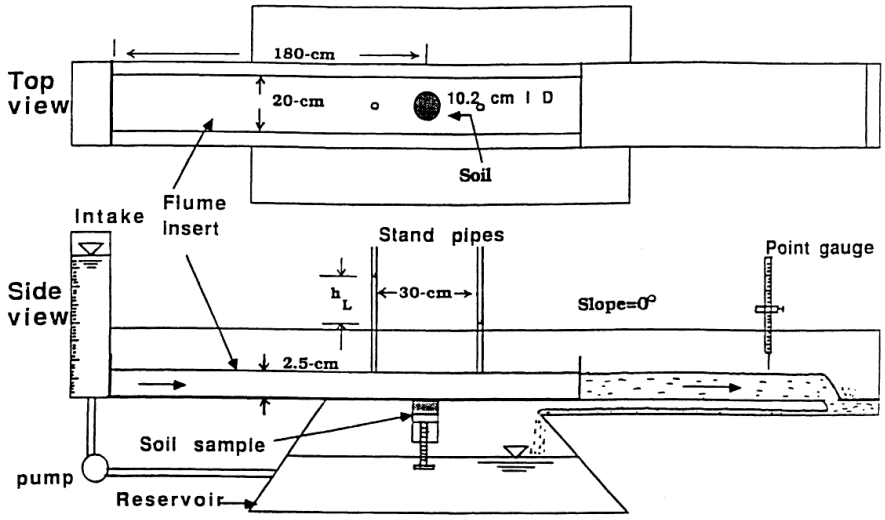

Figure 9. A schematic diagram of the constructed enclosed flume (Ghebreiyessus et al., 1994)

The test samples were cylindrical with a 10.2 cm inner diameter and were mounted on a mechanical piston to maintain a level interface with the bottom surface of the flume. Erosion rates were calculated as the rate of dried mass removal in a given time. The shear stress on the soil sample was predicted as.

$$\tau = \frac{\gamma \times h_L \times R}{L} \tag{10}$$

Where, τ (Pa) is the hydraulic shear stress on the soil surface, h_L (m) refers to the head loss measured using two stand pipes at both sides of the sample, R (m) is the hydraulic radius of the flume, L (m) is the length of flume, and γ_w (N/m^3) refers to the unit weight of water.

Several other attempts were also made to develop a flume erosion testing apparatus. Some examples are the attempts made by Navaroo (2004), Hobson (2008), and Wang (2008) all at Georgia Tech University to modify the EFA method.

2.1.6. *Jet Erosion Test (JET)*

The JET is an erosion test which can be credited to Hanson and developed at the USDA-ARS (Hanson, 1990). Hanson (1990) first developed this testing device for the purpose of measuring the soil erodibility in situ. The JET test was standardized as ASTM D5852 in 1995 and includes both the in-situ and the lab version of the JET test. It included a nozzle with a diameter of 13 mm, which was held 22 cm away from the center of soil surface. Figure 10 shows a schematic diagram of the in-situ version of the JET apparatus. To read the change in the depth of the hole made in the soil by the jet, a pin profiler is used after each jet sequence (Hanson, 1990).

The JET test has been modified since its inception. Hanson and Hunt (2007) developed a new laboratory version of the JET apparatus. The circular jet submergence tank in this version has a diameter of 305 mm, and its height is 305 mm. The scour readings are made using a point gauge which is aligned with the orifice and measures the scour in the center of the specimen. The soil specimen is compacted in a 4" standard compaction mold which is centered in the jet submergence tank and placed below the jet nozzle. The distance between the nozzle and the soil surface in the standard compaction mold is 33 mm. JET is currently used by some DOTs and engineering firms.

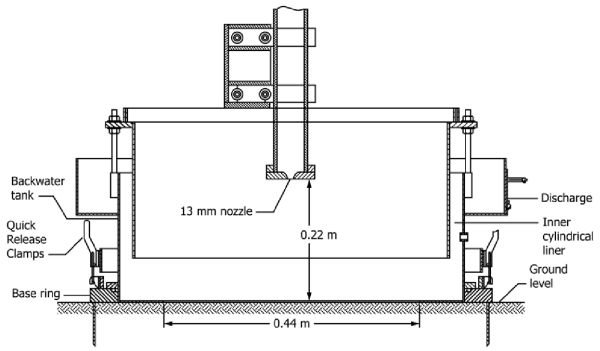

Schematic diagram of the JET (ASTM D5852-95)

JET photographs of lab version (Hanson & Hunt, 2007), In-situ (Hanson & Cook, 2004)

Figure 10. Schematic diagram of submerged JET apparatus for field testing (ASTM D5852-95) along with the photographs of lab version and in-situ version of JET (Hanson and Hunt, 2007)

The step by step procedure of a JET test in the laboratory is (Hanson and Hunt, 2007):

1) Compact the sample in the 4" standard compaction mold and trim the top surface.
2) Center the specimen in the submergence tank right below the jet orifice. Fill the tank with water.
3) Adjust the pressure head at the jet orifice to be 775 mm.
4) Direct the water jet at a given velocity perpendicularly to the soil surface and record the depth of the hole made by the jet as a function of time (not more than 2 hours), while holding the jet in a stationary position.

The last version of the JET test is a miniature of the original JET apparatus, called the mini JET. It was first used in the field by Simon et al. (2010) at 35 sites in Oregon (Al-Madhhachi et al., 2013). Compared to the previous versions, it is easily portable, and can be used both in the field and the lab on the 4" standard compaction mold sample. The submergence tank in the mini

JET has a dimension of 101.6 mm, and height of 70 mm. The adjustable mini JET nozzle is 3.18 mm in diameter, and the head pressure at the nozzle is typically 450 to 610 mm.

Figure 11 shows the stress distribution at the soil surface proposed by Hanson and Cook (2004). The erosion rate is calculated as the slope of the curve linking the depth of the hole to the time of jetting. The shear stress associated with the jetting process is calculated as a function of the maximum stress due to the jet velocity at the nozzle using the following equation:

$$\tau = C_f \times \rho \times U_0^2 \times \left(\frac{J_p}{J_i}\right)^2 \quad (11)$$

Where, C_f is the coefficient of friction (typically 0.00416), U_0 is the velocity of the jet at the origin ($\sqrt{2gh}$), ρ is the fluid density, J_i is the initial jet orifice height from the soil surface, and J_p is called the potential core length (6.3 × nozzle diameter). The critical shear stress, τ_c, is defined as the stress which exists when the hole is deep enough that the jet is no longer adequate to cause additional downward erosion (Hanson and Cook, 2004). To describe the relationship between the JET erosion rate and the jet velocity or calculated shear stress (erosion function), Hanson used a linear relationship and called the slope of the line the erosion coefficient K_D (Hanson, 1991 and 1992; Hanson and Cook, 2004):

$$\dot{z} = K_D(\tau - \tau_c) \quad (12)$$

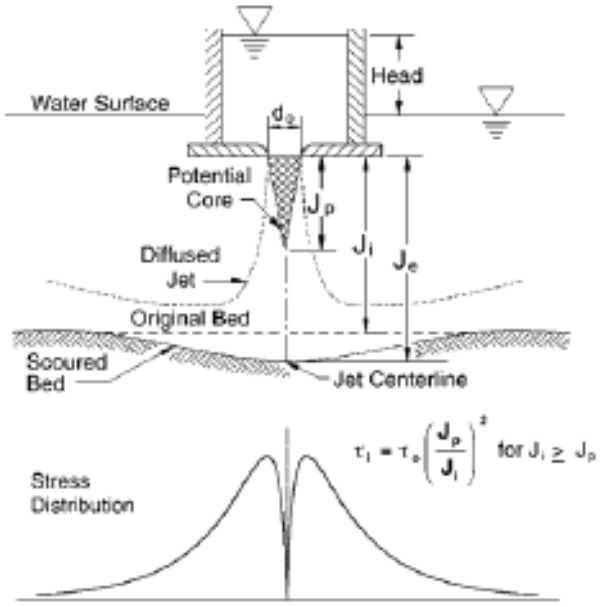

Figure 11. Stress distribution at the soil surface in Jet Erosion Test (Hanson, 1990)

Based on many JETs performed over time, Hanson classified the erodibility of soils according to their K_D value as shown in Figure 12.

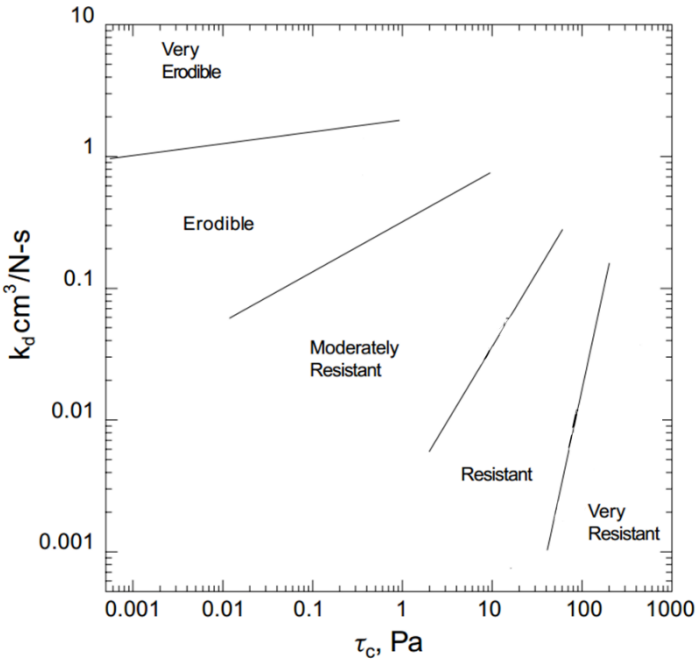

Figure 12. Jet Erosion Test: Hanson's classification according to the erosion coefficient (Hanson and Simon, 2001; Chedid et al., 2018))

2.1.6.1.Advantages

1) The JET can be run both in the field and in the lab.
2) The JET is simple, quick, and inexpensive compared to other types of erosion test.
3) The JET can be performed on any surface vertical, horizontal, and inclined (Hanson et al., 2002).

2.1.6.2.Drawbacks

1) For cohesive soils with a large coarse grain fraction, the JET might not be appropriate, as the submerged JET typically is not strong enough to move the coarse particles out of the eroded hole.
2) The JET is limited to testing the soil at the ground surface and cannot measure the erosion properties of the soil at depth.

3) The flow within the eroded hole and at the soil boundary is complex and difficult to analyze

Prior to Hansen (1990), a few scholars had conducted some studies on erodibility of soils by shooting jet into the surface of the soil. Here is summary of some of that work.

2.1.7. *Jet apparatus to measure the tractive resistance of cohesive channel beds*

Dunn (1959) used a Jet test to calculate the critical shear stress of cohesive channel beds. This test contained a vertical submerged impinging jet perpendicular to the soil surface. Dunn observed that the location of the maximum shear stress is the same for different pressure heads at the nozzle.

In order to measure the induced shear stress, Dunn used a device including a steel plate which was almost fully covered with soil particles, except for a one square inch area at the location of maximum shear stress that was not covered with any soil. Dunn also measured the vane shear strength of the tested samples. Using this approach, he was able to observe the change in maximum shear stress with change in vane shear strength for each soil sample. Dunn found that the vane shear strength was proportional to the maximum shear stress at the start of the erosion process. Dunn proposed that the most important soil properties affecting resistance to erosion were the percent of clay and silt, the soil plasticity and the grain size distribution. A summary of his findings in correlating erodibility parameters to soil properties is presented in next chapter.

2.1.8. *Submerged jet test at the University of Texas*

Moore and Masch (1962) also developed a submerged jet test at the University of Texas. In the proposed test, the change in the scour depth of the sample was obtained for different jet velocities but the hydraulic shear stress at the soil surface was not calculated. Moore and Masch

used a cylindrical sample with a diameter of 127 mm (5 inches) and height of 101.6 mm (4 inches). The jet velocity was kept constant for more than one hour; meanwhile, the eroded weight of the sample was recorded every 10 minutes. Using the volume of the soil removed, the change in depth of the hole was calculated. The same procedure was repeated for higher velocities, and data were compared.

It was inferred that the depth of the hole in the sample can be affected by the following parameters: velocity of submerged jet, diameter of the impinging jet, head pressure at the jet nozzle, eroding fluid's viscosity, and the "scour resistance of the sediments". Figure 13 shows a schematic diagram of the vertical jet scour test.

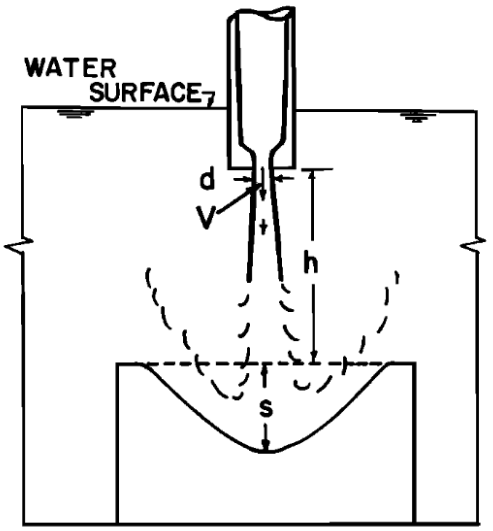

Figure 13. Schematic diagram of the vertical jet scour test developed by Moore and Masch (1962)

Moore and Masch defined a variable called the Scour Rate Index, K_s. This parameter was the slope in the $\left(\frac{S_{ave}}{h_0}\right) versus \left(\frac{t\mu}{\rho d^2}\right)$, where S_{ave} was the depth of the scour hole for a specific jet velocity, h_0 was the distance from the jet orifice to the soil surface, t was the time of scour for a

specific velocity, μ refers to the viscosity of the eroding fluid, ρ is the eroding fluid density, and d is the nozzle diameter. Moore and Masch could observe that measured K_s was linearly correlated with the Reynolds No. The work of Moore and Masch was studied and used by Hanson for his JET analysis.

Moore and Masch conclusions were challenged by a clay mineralogist, named Martian (1962). Martian believed that kinematic viscosity of an eroding fluid such as water is not an appropriate parameter, since it is highly sensitive with even minor changes in the clay percentage or pH of the water.

2.1.9. *Rotating cylinder apparatus developed in University of Texas*

In addition to trying a submerged jet test, Moore and Masch (1962) developed a new scour testing apparatus which worked by subjecting the sample to a rotating flow around the side of the cylinder. The main purpose to implement this device, was that by that time, other available tests for predicting the erodibility of soil (i.e. jet apparatus developed by Dunn (1959)) could not accurately measure the hydraulic shear stress on the surface of the soil.

A 76.2 mm (3 inches) diameter cylinder of cohesive soil with a length of 76.2 mm (3 inches) was used as the test specimen. The testing apparatus included a larger translucent cylinder which had the option to rotate around the vertical axis. The maximum rotation speed that the apparatus could handle was 2500 rpm. The test specimen was then placed into the cylinder coaxially, and the residual space between the sample and translucent cylinder was filled with the eroding fluid. The fluid rotation would apply the shear stress onto the soil surface. Figure 14 shows a schematic diagram of the rotating cylinder testing device.

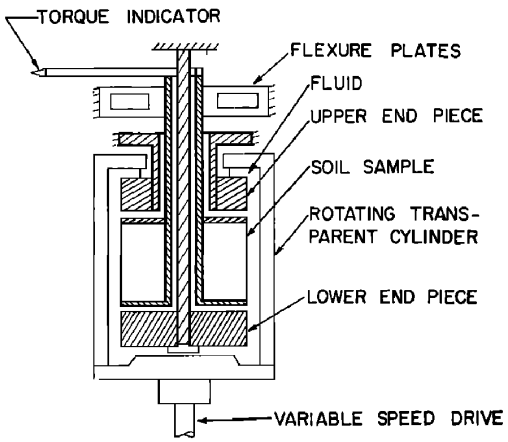

Figure 14. Schematic diagram of the rotating cylinder test developed by Moore and Masch (1962)

As shown in Figure 14, the soil sample was constructed around a flexure pivot, which could help calculate the torque directly applied to the sides of the sample. The induced torque on the sample was then calculated and thus, the shear stress could be back calculated. One of the challenges that Moore and Masch had, was to choose the right liquid as the shear transmitter in the annular space of the cylinder. They found that the use of some liquids such as glycerin would form a resistive layer on the soil surface. Finally, they decided to use water in the annular space to transmit the shear stress onto the side surface of the sample. The test procedure is explained below:

1) Place the cylindrical 76.2 mm diameter sample in the apparatus.
2) Fill the empty space by water.
3) Increase the rotating speed, until you could observe that the surface scour is happening.
4) Record the reading of the torque. Using the calculated torque, measure the shear stress.

It is worth mentioning that in order to calibrate the test, the operator needed to use a dummy sample, and induce a known torque on the sample. Then the rpm required to rotate the sample was recorded. This way, a plot of different rpms and different torques would be obtained. Moore and

Masch recommended to choose the rate of mass removal during a particular time period as the erosion rate. The rotating cylinder test apparatus was later used and modified by some researchers. Masch et al., (1965) worked more on the recommendations made by Moore and Masch (1962) and developed the original guideline for the rotating cylinder test. Arulanandan et al. (1973) slightly modified the previous version of the rotating cylinder and studied the effect of clay mineralogy on the erodibility of the soils by conducting some tests on Yolo loam. Kandiah and Arulanandan also used the rotating cylinder test and compared their results with the results of a flume test on the Yolo loam clay. Arulanandan et al., (1975) used the modified rotating cylinder with the purpose of studying the effect of pore fuid composition and also the concentration of salt in the eroding fluid. The soil samples they used were remolded saturated soils. A summary of their results will be presented in the next sections of this report.

Some of the advantages and drawbacks of the early version of the rotating cylinder test are:

2.1.9.1. Advantages

1) Contrary to most erosion tests, a very small amount of water is needed.
2) The shear stress can be directly estimated using the induced torque on the side surface of the specimen.
3) Can generate very high shear stresses. Very good for intact rock erosion.
4) The influence of the physico-chemical properties of the eroding fluid (i.e. pH, salinity) on erosion rate can be easily studied.

2.1.9.2. Drawbacks

1) Due to the existence of the shaft within the soil sample in the apparatus, the test can only be conducted on remolded samples.

2) The samples need to be cohesive and strong enough to stand under its own weight therefore testing of coarse grain soils and soft clays and silts in not possible.
3) There is no direct measurement of torque, as the induced torque are calibrated based on the results on dummy samples.
4) Expensive test.

2.1.10. *Improved rotating cylinder test*

Chapius and Gatian (1986) used the same principles of the rotating cylinder apparatus developed by Moore and Masch (1962) and improved the testing technique in order to be able to test not only remolded samples but also intact samples in the test. Before this, the rotating cylinder test could only run erodibility test on reconstructed clays and recreated mixtures in the lab. As mentioned earlier, the clay samples were reconstructed around a center shaft which made it possible to measure the torque on the sample. In the apparatus developed by Chapius and Gatian (1986) no flexure pivot was in the middle of the sample; therefore, the intact sample could be placed between the upper and bottom end of the device. Figure 15 shows a photograph of the testing apparatus.

The other advantage of this version of the rotating cylinder compared to earlier versions was that it could directly measure the torque through a pulley weight system. The weight system included masses ranging from 0 to 40 grams and had a precision of 0.1 g. The device could also produce a maximum 1750 rpm rotational speed. It was observed that the roughness of the side surface of the soil was constantly changing during a test, and therefore was affecting the shear stress measurements.

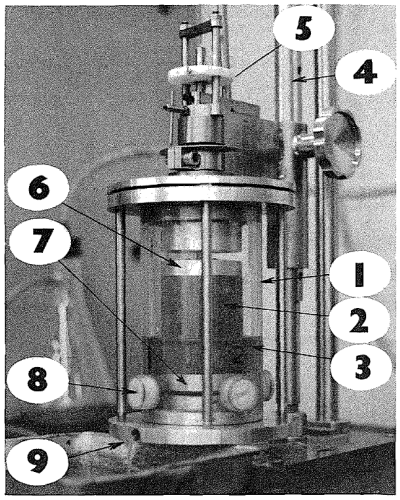

Figure 15. A photograph of the improved rotating cylinder test (Chapuis and Gatian, 1986)

The step by step procedure of the improved rotating cylinder test was (Chapuis and Gatian, 1986):

1) Place the 75 mm diameter clay sample with a height of 89 mm into the apparatus cylindrical cell.
2) Depending on the purpose of the test, fill the annular space around the sample with the eroding liquid (it can be water, or other chemical liquids).
3) Induce a stationary torque to the sample using the pulley weight system.
4) On the same rpm, record the induced shear stress for stages of 10 to 30 minutes.
5) After each stage, collect the eroded samples, oven dry and record the eroded mass for that particular time under that particular shear stress.

2.1.11. *Rotating Erosion Test Apparatus (RETA)*

Kerr (2001) and Sheppard et al. (2006) followed the similar concept and modified the previous versions of the rotating cylinder test. The modified version which is called, Rotating

Erosion Test Apparatus (RETA) was constructed at University of Florida. Currently five RETA units are being used by FDOT (Sheppard et al. 2006). This test was modified to be used only for stiff clays and hard rocks such as sandstone and limestone. It basically holds the same constraint which also exists in previous versions: using a self-supporting sample. RETA can handle the test up to several days, which, in some cases such as hard rocks, is needed to evaluate the erosion rate for a particular shear stress. The samples tested with RETA can be both 61 mm (2.4) inches and 101.6 mm (6 inches) with a height of 101.6 mm (4 inches).

The test apparatus is equipped with a torque transducer at its base and a load cell to record the weight of the sample. It is also equipped with water cooling system to reduce the temperature for long tests (more than 72 hrs for rocks). The central shaft still exists; therefore, intact samples are not usable unless a center hole can be drilled through them. After drilling the hole, the sample is oven dried, and placed in the device to saturate. During the saturation, the device applies a very small torque to the sample for at least a day. This way, the loose material is peeled away. Sheppard et al. (2006) believed that the results of shear stress would be unexpectedly large without removing the loose material before doing the test. After the sample is saturated, it will be inserted into a sleeve and placed in the RETA cylinder for the test. Figure 16 shows a photograph of the testing machine.

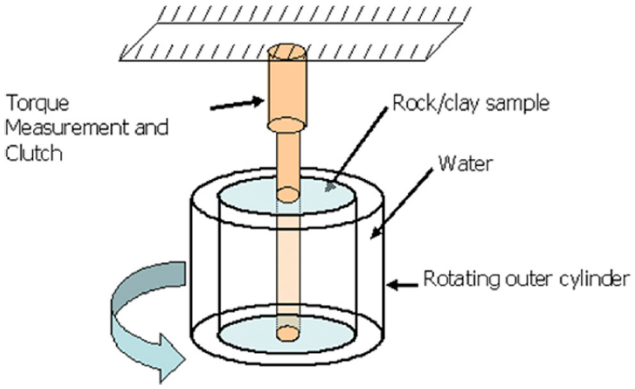

Schematic diagram of the RETA

RETA photographs

Figure 16. A schematic and a photograph of the Rotating Erosion Testing Apparatus (RETA) at University of Florida (Bloomquist et al., 2012)

2.1.12. *Pinhole Erosion Test*

Sherard et al. (1976) developed a laboratory test to measure qualitatively the erodibility of fine-grained soils. In this test, distilled water was passed through a drilled hole under a pressure head of 51 mm in the center of the sample, and the erosion resistance of the soil was observed. The punched hole in the center of the sample has a diameter of 1 mm. The test was particularly designed to study and simulate the leakage effect in both dispersive and non-dispersive fine-grained soils, which was the case in most earth embankments. The pinhole test was later standardized as ASTM D4647. The test consists compacting a 38 mm long soil sample in a 33 mm inside diameter plastic cylinder. A truncated jet nozzle with a diameter of 1.5 mm directs the water through the punched 1 mm dimeter hole in the center of cylindrical specimen. Figure 17 depicts a schematic diagram of the test apparatus.

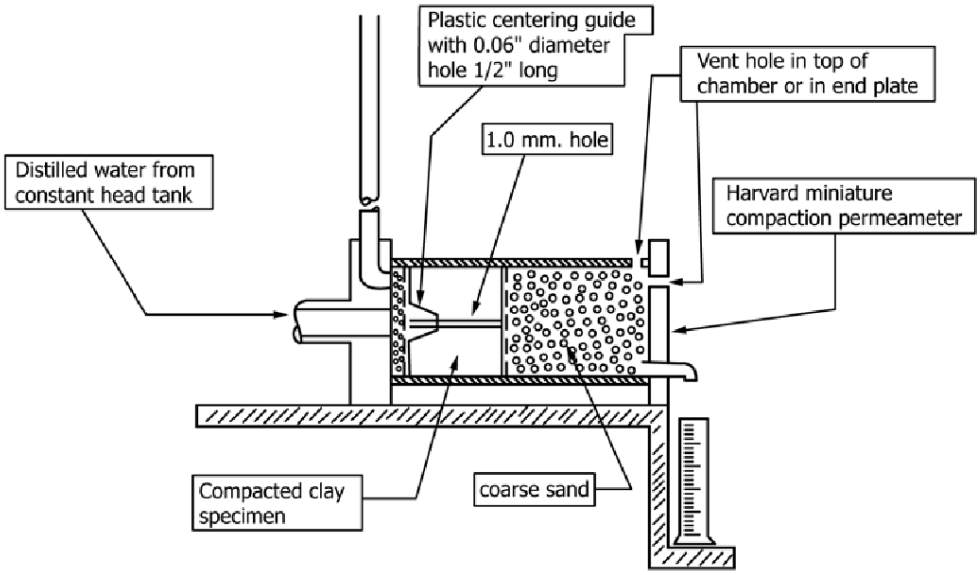

Figure 17. A schematic diagram of the Pinhole Erosion Test apparatus (ASTM D4647)

Sherard et al. (1976) noticed considerable differences in the behavior of dispersive and non-dispersive clays when subjected to water flow by observing the appearance of the flowing water and final size of the hole in the tested sample. With some limitations, the test could be done on intact filed samples. The procedure for this test is:

1) Create a 38 mm long sample by compacting the soil in the test cylinder above the coarse sand space which is covered by a wire screen (Figure 17).
2) Make sure that the soil specimen is representative of the field conditions in terms of moisture content and dry unit weight.
3) Push the truncated cone jet nozzle into the center of the cylindrical sample.
4) Punch a 1 mm diameter hole in the center of the sample, using the test wire punch.
5) After removing the wire punch and placing a wire screen on the top of sample, fill the remaining space with coarse sand.
6) Start the test by shooting the jet into the hole with a pressure head of 51 mm.

7) Continue the test up to 5 minutes. Depending on the effluent cloudiness and the measured flow rate decide to continue the test or not for higher pressure heads as described in the ASTM standard.

The results of the pinhole erosion test is then interpreted using Table 2. Based on the criteria defined in Table 2, the erosion resistance of soil is classified in one of the 9 defined categories.

Table 2. Interpretation the results of the pinhole test (ASTM D4647)

Dispersive Classification	Head, mm	Test time for given head, min.	Final flow rate through specimen, mL/s	Cloudiness of flow at end of test		Hole size after test, mm
				from side	from top	
D1	50	5	1.0–1.4	dark	very dark	≥2.0
D2	50	10	1.0–1.4	moderately dark	dark	>1.5
ND4	50	10	0.8–1.0	slightly dark	moderately dark	≤1.5
ND3	180	5	1.4–2.7	barely visible	slightly dark	≥1.5
	380	5	1.8–3.2			
ND2	1020	5	>3.0	clear	barely	<1.5
ND1	1020	5	≤3.0	perfectly clear	perfectly clear	1.0
Method B						
D	50	10	...	slightly dark to dark	very dark to moderately dark	≥1.5
SD	180–380	5	...	barely visible	slightly dark	≥1.5
ND	380	5	...	clear	barely visible to clear	<1.5

2.1.13. *Drill Hole Test*

Lefebvre et al. (1985) developed a new technique to predict the internal erosion resistance of natural clays. The concern was the erodibility of the natural clays in the Eastern part of Canada. The test was inspired by the earlier version of the pinhole test. The testing apparatus uses a 10 cm long cylindrical sample with a diameter if 35.5 mm. At the center of the sample, a 6.35 mm hole is drilled. Schematic diagrams of the test are shown in Figure 18. The test is conducted by circulating water through the bored hole into the sample. The pressure drop through the sample is measured using a differential manometer connected to both sides of the sample. A tank is used to produce a 143 cm pressure head and thereafter direct the flow through the sample. The flow is adjusted using a valve and measured by a flowmeter.

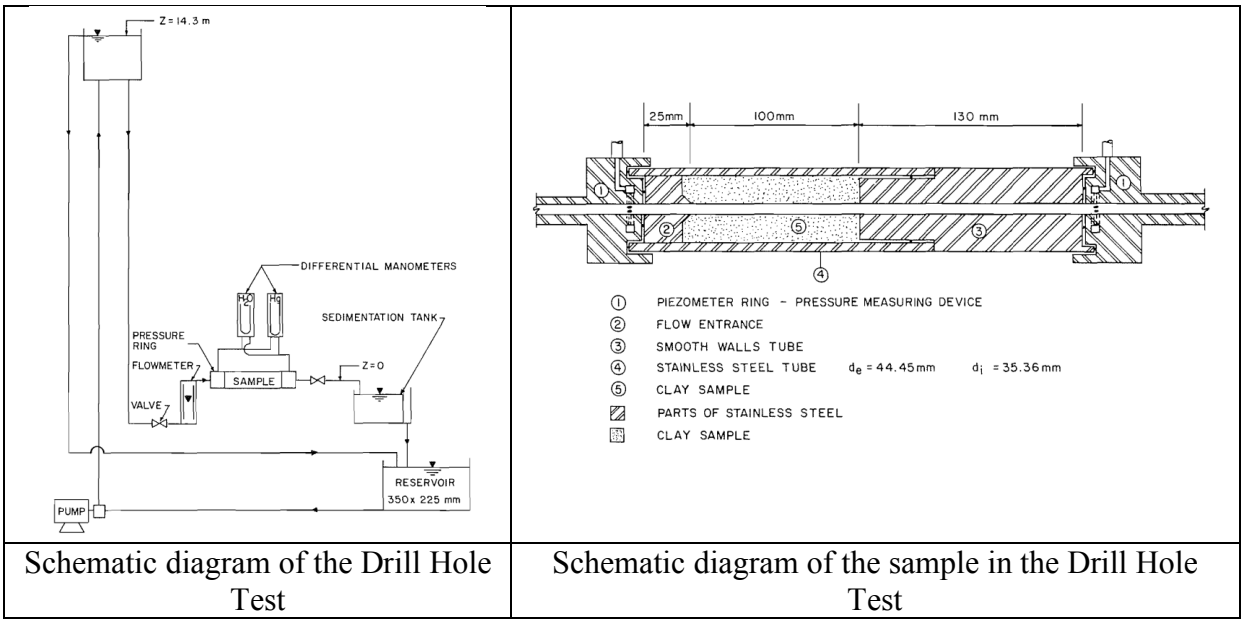

Schematic diagram of the Drill Hole Test	Schematic diagram of the sample in the Drill Hole Test

Figure 18. Schematic diagrams of the whole Drill Hole Test assembly along with the sample setup (Lefebvre et al., 1985)

Using the adjusting valve, the flow velocity is increased by 0.5 m/s every 15 minutes. The deposited sediment in the reservoir tank is dried and weighted to measure the mass removal rate for that particular velocity. The average diameter of the hole is recorded after each step. The shear stress is calculated using the pressure drop measured by the manometers. The results are reported as removed mass versus velocity or shear stress.

Lefebvre et al. (1985) also observed that the change in roughness of the hole during the test can be interpreted using Moody diagram (Moody, 1944), knowing the friction factor and the Reynolds number. Erosion at the clay particle level is accompanied with an increase in the hole smoothness (decrease in relative roughness), while erosion of lumps of clay particles lead to an increase in hole roughness.

2.1.14. *Hole Erosion Test (HET)*

The HET is a laboratory erosion tests which evolved from the older Pin Hole test and can be credited to Robin Fell in Australia (Wan and Fell, 2002; Wahl, 2009; Benahmed and Bonelli, 2012). The test (Figure 19) consists of drilling a 6 mm diameter hole through a soil sample and forcing water to flow through the hole at a chosen velocity while recording the rate of mass removal per unit area as a function of time to obtain an erosion rate (kg/s/m^2). The soil is compacted in a 100 mm (4 in.) diameter standard compaction mold. Similar to drill hole test, the sample is connected to a tank which can maintain a variable head ranging from 50 to 800 mm. The flow is also controlled through a valve.

The rate of mass removal per unit area is calculated as $\frac{\rho_d}{2} \times \frac{d\phi}{dt}$, where $d\phi$ is the change in diameter of the hole, and ρ_d is the dry unit weight of the sample. Since the diameter of the hole cannot be monitored during the test, this value is indirectly predicted using the measured flow rate, the hydraulic gradient, and Eqs. 13 and 14. Eq. 13 refers to laminar flow conditions, while Eq. 14 refers to turbulent flow. Turbulent flow is associated with a Reynold's number higher than 5000.

$$\phi_t = \left(\frac{16 \times Q_t \times f_{Laminar,t}}{\pi \rho_w g s_t}\right)^{\frac{1}{3}} \quad (13)$$

$$\phi_t = \left(\frac{64 \times Q_t^2 \times f_{Turbulant,,t}}{\pi^2 \rho_w g s_t}\right)^{\frac{1}{5}} \quad (14)$$

Where, Q_t is the flow rate at time t, $f_{Laminar,t}$ and $f_{Turbulant,t}$ are the estimated friction factors at time t, ρ_w is the water unit weight, g is the ground gravity acceleration, and s_t is the hydraulic gradient obtained from the manometers at both ends of the sample. In these equations, the friction factors are estimated using the recorded hole diameter before and after the test.

The test results link the rate of mass removal per unit area to the net shear stress above critical; the shear stress on the wall of the hole is estimated using Eq. 15. This equation is obtained

after considering force equilibrium on the body of the eroding fluid along the pre-formed hole at a particular time, t.

$$\tau = \rho_w \times g \times s_t \times \frac{\phi}{4} \tag{15}$$

Where, ρ_w is the density of water, s_t is the hydraulic gradient across the hole, and ϕ is the diameter at time t. The equation used for the erosion function is linear

$$\dot{m} = C_e\left(\tau - \tau_c\right) \tag{16}$$

The parameter C_e is called the erosion coefficient. The erosion rate index is then defined as

$$I_{HET} = -\log_{10}\left(C_e(s/m)\right) \tag{17}$$

Wan and Fell went on to propose some erosion categories based on I_{HET} (Table 3).

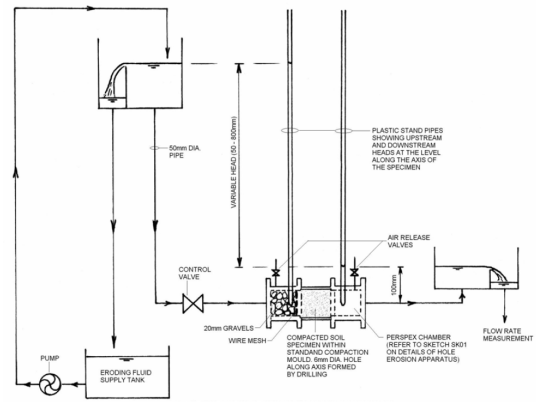

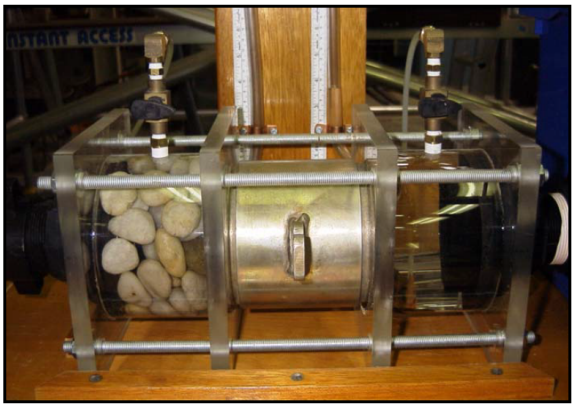

Schematic diagram of the HET	Photograph of the HET sample setup

Figure 19. A schematic diagram of the HET and a photograph of the sample setup

Table 3. Hole Erosion Test – Fell's classification according to the erosion index (Wan and Fell, 2002)

Group Number	Erosion Rate Index, I_{HET}	Description
1	< 2	Extremely rapid
2	2 – 3	Very rapid
3	3 – 4	Moderately rapid
4	4 – 5	Moderately slow
5	5 – 6	Very slow
6	> 6	Extremely slow

2.1.14.1. Advantages

1) Direct similitude with piping erosion in earth dams
2) Can apply a wide range of pressure heads and therefore wide range of hydraulic shear stress at the soil-water interface.

2.1.14.2. Drawbacks

1) The sample needs to be cohesive and strong enough to stand under its own weight. Therefore, the test cannot be run on cohesion-less samples.
2) Very difficult to run on intact samples in Shelby tubes from field. Better for remolded samples in the lab.
3) Difficult and time-consuming preparation of the test
4) No direct monitoring of the erosion process. The erosion rate needs to be extrapolated and inferred.
5) The hydraulic shear stress is inferred, and not directly measured.
6) The data reduction process is very subjective.
7) The flow within the eroded hole and at the soil boundary is complex and difficult to analyze.

2.1.15. *Slot Erosion Test (SET)*

Slot Erosion Test was also developed by Wan and Fell (2002) in Australia. The concept of SET is very similar to what was explained for the HET, except that the sample is different in this test. The test (Figure 20) consists of drilling a 2.2 mm wide, 10 mm deep at the surface of a 1 m long rectangular soil sample and having water within the slot at a chosen velocity while recording the rate of mass removal per unit area as a function of time to obtain an erosion rate (kg/s/m^2).

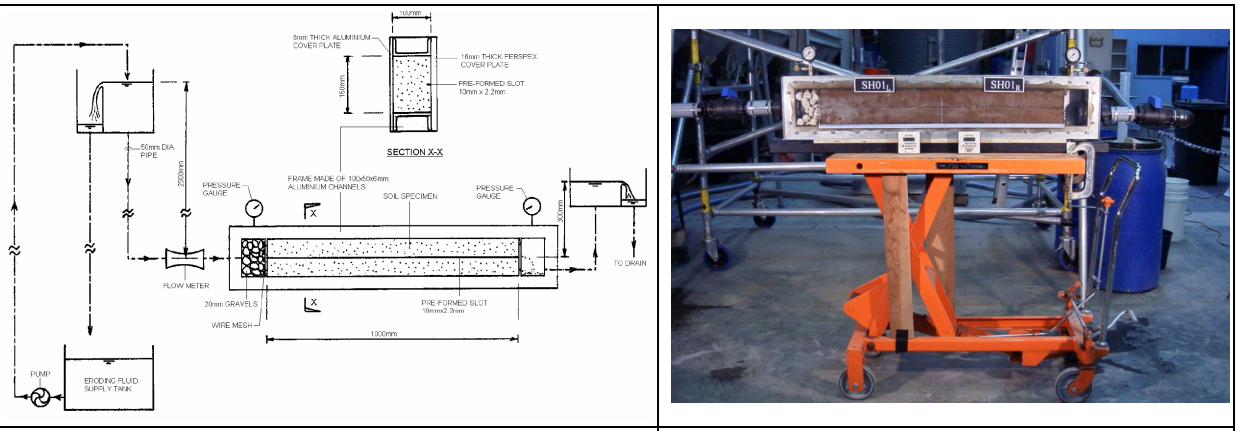

Schematic diagram of the SET	Photograph of the SET sample setup

Figure 20. A schematic diagram of the HET and a photograph of the sample setup (Wan and Fell, 2002)

As in the HET, the shear stress is calculated using Eq. 18. In the SET, the hydraulic diameter ($\frac{A_{slot}}{P_w}$) is used instead of $\frac{\phi}{4}$ in Eq. 18. A_{slot} refers to the cross-sectional area of the pre-formed slot and, P_w is the wetted perimeter. I_{SET} is also calculated with the same procedure explained for calculating I_{HET} (Eq. 17).

All the tests described to study internal erosion require that the soil be a self-supporting (cohesive) soils. Cohesion-less soils cannot preserve an open hole or slot; therefore, HET, SET,

drill hole, or pin hole tests, for cases where non-cohesive soils form a high stress portion of the embankment, cannot appropriately simulate the actual field conditions. For that reason, new internal erosion test devices are being developed. Some of these devices are described below.

2.1.16. *Stress-Controlled Erosion Apparatus*

Chang and Zhang (2011) developed a new test for studying the internal erosion in soils at Hong Kong University. They ran some tests on a handmade cohesion-less soil. A schematic diagram of this test is shown in Figure 21. The test consists a triaxial system which is fed by a water supply system and controlled by a computer. The porous stone used in this apparatus is modified to accommodate the high permeability of the tested soil in this experiment. The soil sample is 10 cm in diameter, 10 cm high and is mounted on a hollow base with a 10 mm thick 95 mm diameter perforated plate. Water flow seeps through the hollow base and the perforated plate and the soil sample.

Before the internal erosion testing starts, a 10 kPa confining pressure is applied to the sample. Then, de-aired water is injected slowly into the specimen from the bottom base to saturate the sample. During the erosion test, the vertical deformation of the sample is measured using an Linear Variable Differential Transformer (LVDT), and the radial deformations can be measured using a video camera. The test is controlled by adjusting the hydraulic gradient of the seepage water through the sample. A soil collection system is placed at the bottom of the triaxial system. Each hydraulic gradient is maintained for a 10-minute period and the eroded mass of soil is collected, dried, and weighted.

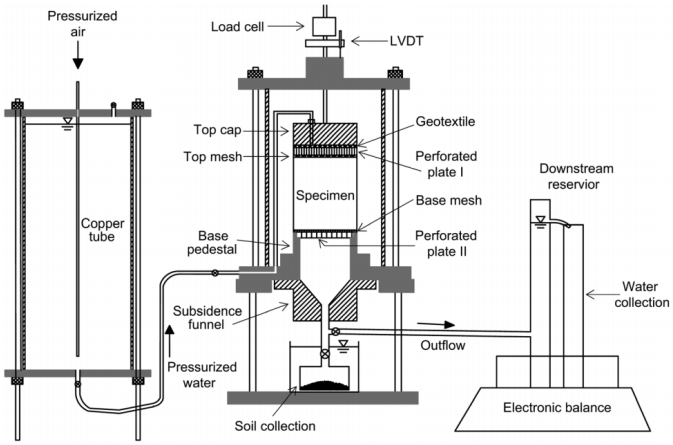

Schematic diagram of the stress-controlled apparatus

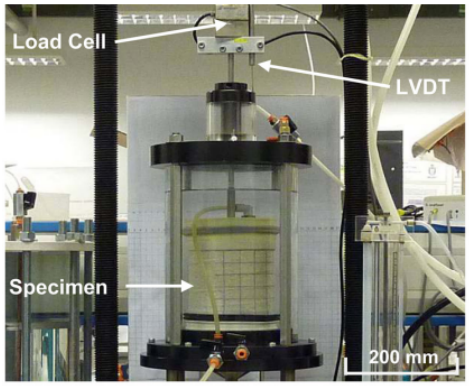

Photograph of the stress-controlled apparatus

Figure 21. A schematic diagram of the stress-controlled erosion apparatus (Chang and Zhang, 2011)

2.1.17. *True Triaxial Piping Test Apparatus (TTPTA)*

Richards and Reddy (2010) developed a True Triaxial Piping Test Apparatus (TTPTA) at the University of Illinois at Chicago to study the internal erosion in both cohesive and cohesion-less soils. The test consists of applying a wide range of confining pressures, with measurements of pore pressure and hydraulic gradient in a true triaxial cell (Figure 22). The results of this test give the critical hydraulic gradient as well as the critical velocity.

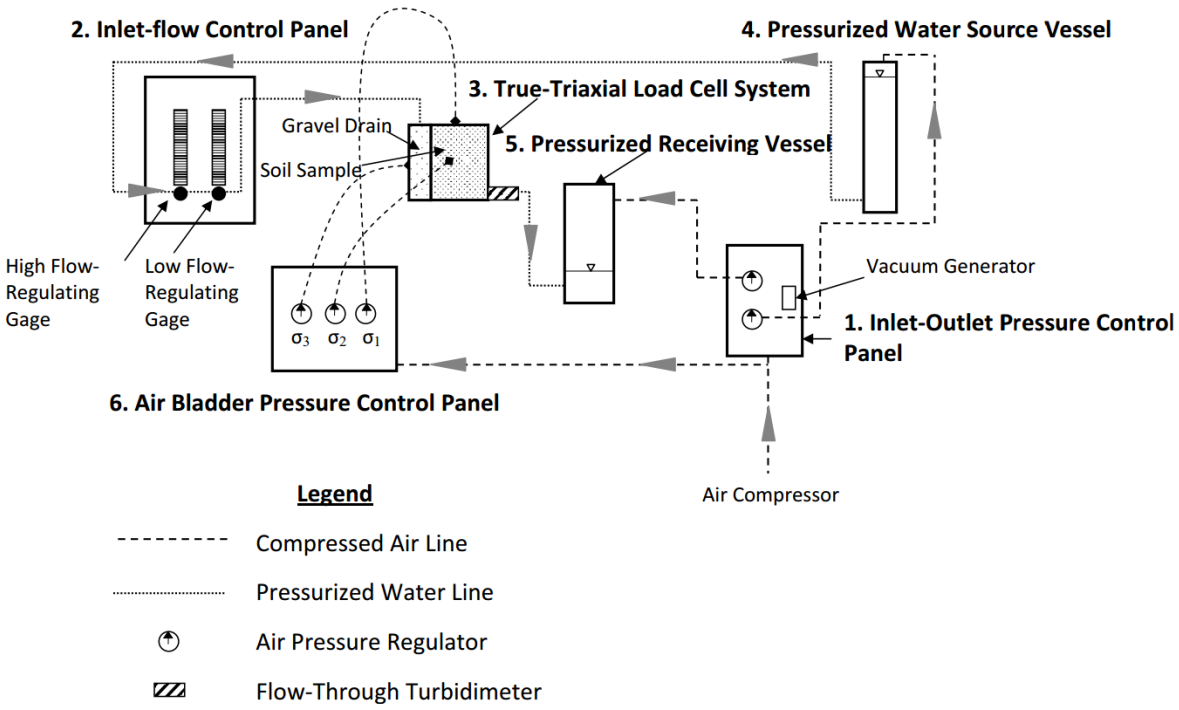

Figure 22. A schematic diagram of the TTPTA (Richards and Reddy, 2010)

2.1.18. *Constant Gradient Piping Test Apparatus*

Fleshman and Rice (2013) developed a new test apparatus to evaluate the hydraulic conditions required for starting the piping erosion. The testing apparatus is shown in Figure 23. The sample is held in a sample holder, while a constant hydraulic gradient is imposed throughout the sample. During the test, the differential head alongside the sampler is increased, and the pore pressure as well as the soil behavior are monitored. The testing device was tested on various sandy soils with different grain size distribution, specific gravity, and gradation and the critical hydraulic condition (i.e. critical gradient) in which the piping erosion is initiated was recorded. It was observed that the initiation of the erosion occurs in four stages: 1) the first observable movement of particles, 2) progression of heave, 3) boil formation, and 4) final or total heave.

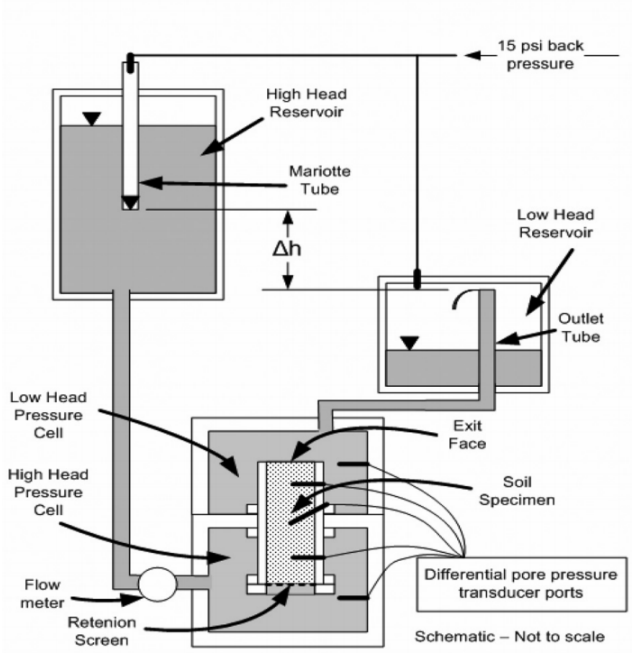

Figure 23. A schematic presentation of the constant gradient piping test apparatus (Fleshman and Rice, 2013)

2.2. Field Erosion Testing

2.2.1. *Pocket Erodometer Test (PET)*

The Pocket Erodometer Test (PET) was developed by Briaud et al. (2012) at Texas A&M University. The Pocket Erodometer is a regulated mini jet impulse generating device. The jet is aimed horizontally at the vertical face of the sample. The jet velocity is calibrated to be always 8 m/s and the nozzle is kept 50 mm form the soil surface. The depth of the hole in the surface of the sample created by 20 impulses of water is recorded. The eroded depth is compared to an erosion chart to determine the erosion category of the soil which helps the geotechnical engineer with preliminary design of erosion projects.

Many different options were considered during the development of the Pocket Erodometer including the most appropriate device, velocity range, direction of application, distance from the

face of the sample, and repeatability from one person to another. Figure 24 shows the schematic diagram of the PET, along with a photograph from the test (Briaud et al., 2012). The original device selected for the Pocket Erodometer is 105 mm × 77 mm × 18 mm. The diameter of the nozzle is about 0.5 mm (see Figure 24). The jet velocity of 8 m/s was chosen because it eroded most tested specimens.

The Pocket Erodometer needs to be calibrated before the test to reproduce the velocity of 8 m/s at the nozzle. The following equation is used to calibrate the velocity of the impinging jet at the nozzle:

$$v = \frac{x}{\left(\frac{2H}{g}\right)^{0.5}} \tag{18}$$

Where, x and H are shown in the schematic diagram of PET depicted in Figure 24, and v is the initial horizontal velocity right at the nozzle.

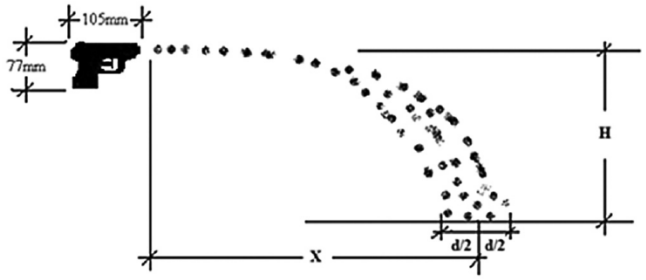

Schematic diagram of the PET (Briaud et al., 2012)

PET photographs (Briaud et al., 2012)

Figure 24. Schematic diagram of Pocket Erodometer Test and a photograph of the test device

The height of the erodometer (shown as H in Figure 24) must be kept constant during the calibration process. Also, external forces such as wind should be avoided. The PET can be done

with any type of apparatus which can meet the requirements of this test and reproduce 8 m/s velocity at nozzle with ± 0.5 m/s with impulse time period of near 0.15 sec. Briaud et al. (2012) then conducted PET on many samples from different levees and compared the results with the EFA results obtained. The comparisons resulted in an erosion category chart based on the PET depth ranges (See Figure 25). The step by step process of PET is explained below (Briaud et al., 2012):

1) Place the sample horizontally either on a flat surface or by holding it in your hand. Note: The test must not be run with the jet pointed vertically.
2) Smooth the surface to remove any uneven soil. You want to begin with a smooth and vertical surface, so that it is easy to measure the erosion depth
3) Hold the Pocket Erodometer (PE) pointed at the smooth end of the sample, 50 mm away from the face.
4) Keeping the jet of water from the PET aimed horizontally at a constant location, squeeze the trigger 20 times at a rate of 1 squeeze per second, forming an indentation in the surface of the sample. Each squeeze should fully compress the trigger and then the trigger should be fully released before it is re-compressed.
5) Using the end of a digital caliper or an appropriate measuring tool, measure the depth of the hole created.
6) The test should be repeated at least 3 times in different locations across the face of the sample and an average should be used to ensure a good estimate.
7) Determine the erosion category using Figure 25.

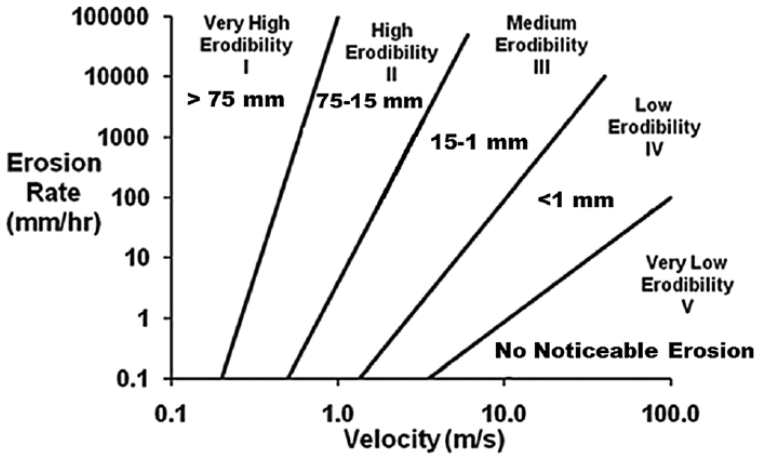

Figure 25. Erosion depth ranges of Pocket Erodometer Test (PET), depicted on the erosion categories proposed by EFA

2.2.1.1. Advantages

1) Very low price.
2) Very handy and simple to operate both in the field and in the laboratory.
3) Gives a quick and crude estimate of soil erodibility.

2.2.1.2. Drawbacks

1) Very small scale.
2) Only gives the erosion category and no measurement of critical shear stress or critical velocity.
3) Only useful for preliminary field evaluation, and not good for design purposes

2.2.2. *In-situ Erosion Evaluation Probe (ISEEP)*

Gabr et al. (2013) developed an erosion testing device, called the In-situ Erosion Evaluation Probe (ISEEP) at North Carolina State University. The test is conducted by advancing a vertical jet probe into the subsurface soil and measuring the rate of advancement.

As discussed earlier, all other in-situ tests were limited to evaluate the scour potential of the soil only on the ground surface (i.e. JET, Sedflume, etc.), and EFA was the only test that could evaluate the erodibility of the natural soil associated with a particular depth. The ISEEP flow velocities are normally much less than the imparted velocities in the EFA. ISEEP can investigate the erodibility of any soil at any depth provided the probe can penetrate by erosion.

The results of ISEEP are reported based on the concept of "Stream Power" which was first presented by Annandale and Parkhill (1995) who believed that this concept would better represent the erodibility potential of an eroding fluid compared to velocity or shear stress. Annandale (2006) defined the stream power, P, using Eq. 19 and 20.

$$P = \gamma_w q H \tag{19}$$

$$P = \tau U_0 \tag{20}$$

Where, P is the stream power (Watts per unit area), γ_w is the water unit weight, q refers to the flow discharge in unit area, H is the energy head, τ is the shear stress, and U_0 is the velocity. Eq. 20 shows that the stream power is a function of both the shear stress and the velocity. Figure 26 shows a photograph of the ISEEP device which was tested at the NCSU lab before being used in the field.

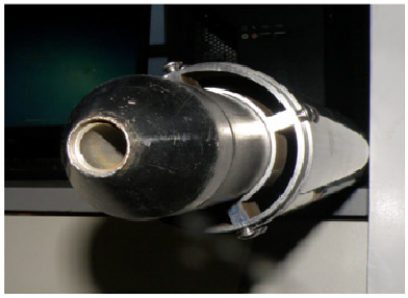

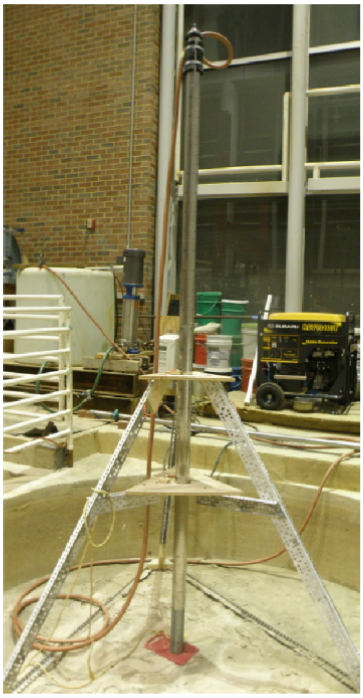

Truncated cone probe	ISEEP prototype

Figure 26. ISEEP apparatus prototype at NCSU (Gabr et al., 2013)

The jet nozzle is a truncated cone probe which is guided into the soil as the soil is being eroded by the impinging jet. The eroded material moves up through the annulus space between the probe and the wall of the hole created by erosion. The water velocity at the nozzle is controlled digitally by a variable speed pump on the ground surface. The rate of advancement into the soil subsurface is measured and represents the erosion rate. The body of the probe is divided into sections so that the length can be adjusted for deep locations in the field. The orifice of the jet nozzle is 19 mm (0.75 inches) long and the nozzle velocity can go up to 12 m/s. During penetration, the advancement is recorded using a video camera.

The results of this test are reported as the rate of advancement (penetration) versus the stream power value, P. The bed shear stress is obtained from Eq. 21 based on Julien (1995) study:

$$\tau = C\rho_w U^2 \quad (21)$$

Where, τ is the bed shear stress, U is the jet velocity, ρ_w is the water density, and C is a diffusion coefficient which varies depending on flow condition. Some advantages of the ISEEP are mentioned below:

2.2.2.1. Advantages

1) It can evaluate the erodibility of any soil at any depth with a wide range of jet velocity.
2) There is no need for sample extraction and procurement.

2.2.2.2. Drawbacks

1) The penetration may be limited if the probe fails to erode the soil. Better to be used in sandy soils.
2) The use of the stream power makes it difficult to compare this device with other erosion devices.
3) Fairly expensive test, and difficult to interpret.

2.2.3. *Borehole Erosion Test (BET)*

The Borehole Erosion Test (BET) is an in-situ test developed by Briaud at Texas A&M University (Briaud et al., 2016). The purpose of this test is to quantify the erodibility of the soil layers as a function depth as follows. Figure 27 shows the schematic diagram of the BET, and field work photographs.

1) Drill a hole into the ground, say 100 mm in diameter, 10 m deep.
2) Remove the rods and measure the initial diameter of the borehole with a borehole caliper.
3) Re-insert the rods to the bottom of the hole and circulate water down the rod and up the outside annulus of the hole for a given time, say 15 minutes.

4) Remove the rods and measure the diameter of the hole with the borehole caliper.

5) The increase in diameter of the borehole at a certain depth given by the calipers divided by the flow time is the erosion rate of the soil at that depth for the flow velocity applied during the test.

6) Profiles of erosion rate for different velocities can be prepared in that fashion.

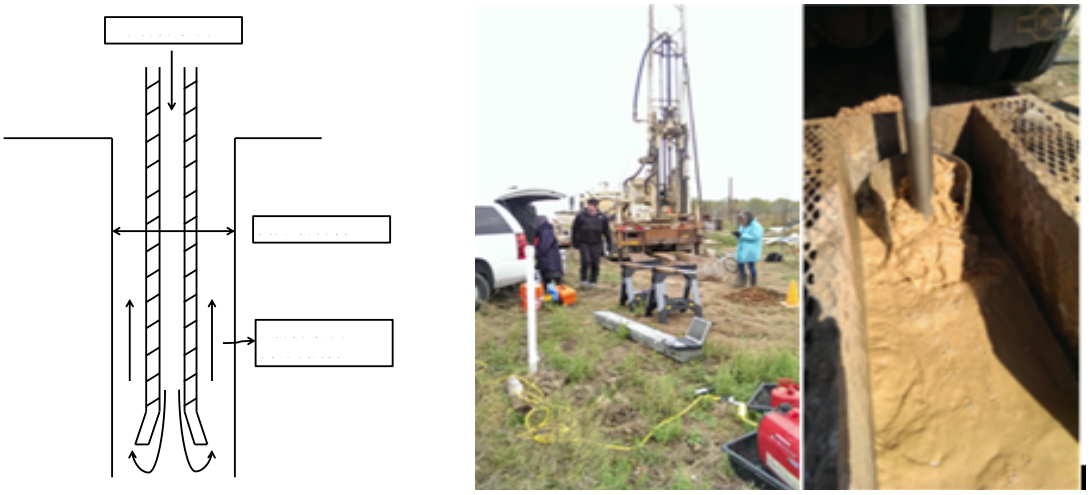

Schematic diagram of BET Photographs from BET in the field

Figure 27. A schematic diagram of Borehole Erosion (BET) test and photographs of the test at the Riverside campus at Texas A&M University (Briaud et al., 2016)

The advantages and drawbacks for this test are below.

2.2.3.1. Advantages

1) Only typically available field equipment (common drilling rig for wet rotary boring, flow meter in line with the drilling rig pump, and borehole caliper) is used to perform a BET test. Therefore, the BET can be performed by many.

2) Each test gives the erosion function for all layers traversed since a complete borehole diameter profile is obtained from the caliper. This would require many tests on many samples if laboratory tests were to be conducted.
3) It has two component tests: the lateral erosion test associated with the increase in diameter of the borehole and the bottom erosion test associated with the increase in depth below the bottom of the drilling rods during the flow. The later one is much like an in-situ jet erosion test.
4) Can be used in any soil or rock where a hole can be drilled.

2.2.3.2. Drawbacks

1) The shear stress is obtained from Moody chart.
2) Limited by pump flow available on the drill rig.
3) Fairly expensive setup.
4) In sand boreholes, the addition of Bentonite during drilling needs to be controlled in order not to impact the erosion resistance.

2.2.4. *In-situ Scour Testing Device (ISTD)*

In-situ Scour Testing Device (ISTD) is the most recent field erosion test device that is currently under development by the U.S. Federal Highway Administration (FHWA). Zinner et al. (2016) presented the concept behind the ISTD and its application in pier scour studies. This device has a cylindrical shape and can be used in a boring test rig and fit into the steel casing of hollow stem augers to evaluate the erodibility of soil at any depth. The ISTD generates a horizontal flow at the bottom of the borehole. Figure 28 shows a diagram of the cylindrical ISTD concept. So far,

the ISTD is applicable only for soils below the ground water table, and with a maximum N-value of 30. The development is on-going by the FHWA.

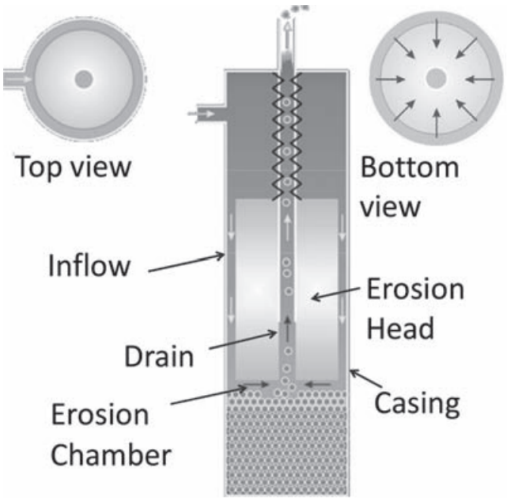

Figure 28. A schematic diagram of the cylindrical ISTD concept (Zinner et al., 2016)

A summary of all the erosion tests reviewed is presented in Table 4 in terms of their application in the field or the lab. Table 5 shows some of the most practical erosion tests with information regarding their ability to measure shear stress, with the soil type that can be tested, and the cost associated with them.

Table 4. Summary of all types of erosion tests in terms of their application

LABORATORY EROSION TESTS	IN SITU EROSION TESTS
❖ Lab Jet Erosion Test (JET) ❖ Hole Erosion Test (HET) ❖ Pinhole Erosion Test ❖ Drill hole Erosion Test ❖ Slot Erosion Test (SET) ❖ Rotating Cylinder Test (RCT) and improved versions ❖ Rotating Erosion Testing Apparatus (RETA) ❖ EFA and similar versions of it (e.g.: Sedflume, SERF, ESTD) ❖ Stress-controlled Erosion Apparatus ❖ True Triaxial Piping Test Apparatus (TTPTA) ❖ Constant Gradient Piping Test Apparatus	❖ Field Jet Erosion Test (JET) ❖ In Situ Scour Evaluation Probe from North Carolina State University (ISEEP) ❖ Borehole Erosion Test (BET) ❖ Pocket Erodometer Test (PET) ❖ ASSET ❖ In-Situ Scour Testing Device (ISTD) ❖ Field Flume Tests

Table 5. Some of erosion tests with information about their application

Erosion Tests	Range of soil can be test	Range of stress that applied	Cost o Test	Cost o Devic	Reliabi Resul
Lab JET	Sands to c	lays < 100 Pa	Low	Low	Good
In-situ JET	Sands to c	lays < 500 Pa	Mediu	Mediu	Good
EFA	Sands to c	lays < 165 Pa	Low	High	Good
HET	Clayey soil	Up tp 800 P	Maediu	High	Good
SET	Clayey soil	Up to 400 P	Maediu	High	Mediu
RETA	Clayey soil	s < 100 Pa	High	High	Mediu
PET	Sands to c	lays < 20 Pa	Low	Low	Mediu
ISEEP	Sands to c	lays < 650 Pa	High	High	Good
BET	Sands to c	lays < 600 Pa	Mediu	Mediu	Good

3. EXISTING CORRELATIONS BETWEEN SOIL ERODIBILITY AND PROPERTIES

It is well accepted that different soils have different critical velocities and different erosion rates beyond the critical threshold. Therefore, soil erodibility depends on the soil properties. At the same time, a reliable and broadly accepted relationship between soil erodibility and soil properties has not been found. However, a number of attempts have been made on the basis of erosion tests databases which are more or less populated. Some of these attempts are reviewed next.

3.1. Existing Correlations

Dunn (1959) carried out submerged JET tests on remolded samples of sand and of fine grain soils such as silty clay. Dunn proposed a relationship between the critical shear stress obtained using a 1 in^2 steel plate in the location of maximum observed scour, and two basic soil properties that he believed were the most influential parameters. This relationship was proposed for the soils with PI ranging from 5 to 16.

$$\tau_c = 0.001 \times (S_v + 180) \times \tan(30 + 1.73 \times PI) \quad (22)$$

Where, S_v refers to the shear strength of the soil (psi) which were measure using a rotating vane, τ_c is the critical hydraulic shear stress (psi), PI is the plasticity index (%), and the unit of the angle in the tangent is degrees.

Gibbs (1962) conducted flume tests on undisturbed samples (mostly CL and ML) from 45 case studies to assess the influence of field density on erosion resistance of the soil. Gibbs plotted

his results versus field density and liquid limit. Recorded critical shear stresses ranged from 0.7 Pa to 2.87 Pa. Gibbs observed that clays are more resistant to erosion compared to coarser material. Also, the highly plastic samples generally showed more resistance to erosion in comparison with low plasticity soils. Gibbs observed that gradation of a soil is an important parameter in the erosion resistance of coarser soils while for finer samples, plasticity seems to be more effective. Although there was no good relation found between dry density and the critical shear stress, liquid limit generally seemed to be proportional to the critical shear stress for several cases. Consequently, Gibbs (1962) recommended four categories based on the results of flume tests on the tested samples (right plot in Figure 29).

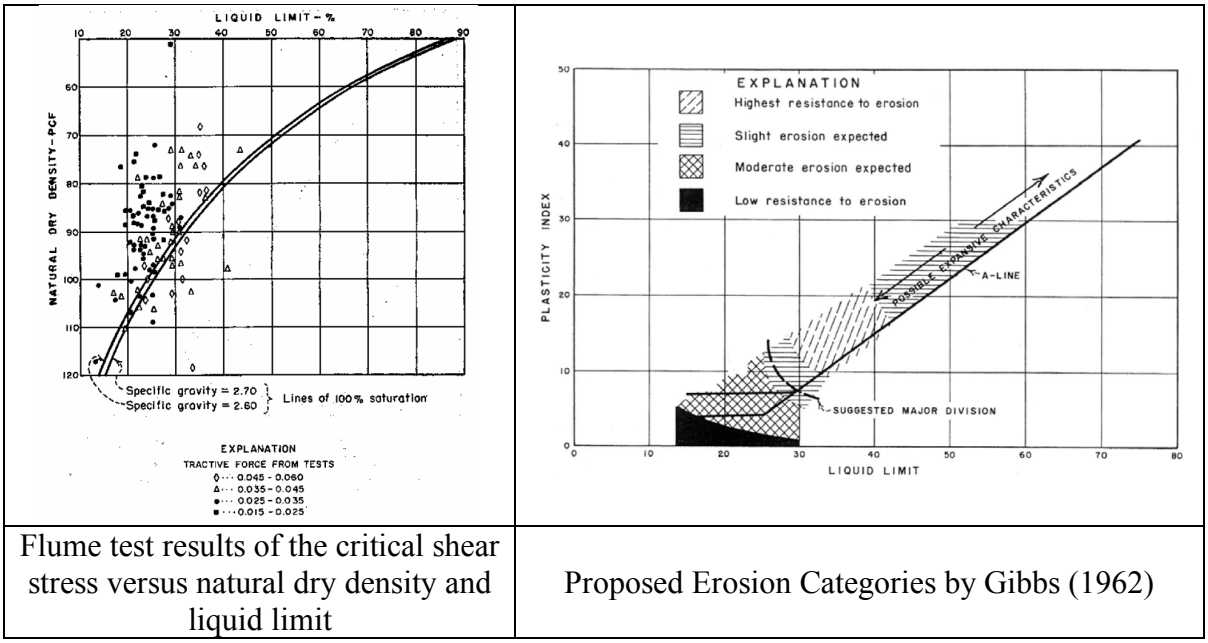

Flume test results of the critical shear stress versus natural dry density and liquid limit	Proposed Erosion Categories by Gibbs (1962)

Figure 29. Flume test results of the critical shear stress versus natural dry density and liquid limit and the proposed erosion categories (Gibbs, 1962)

A few years after Gibbs (1962), Lyle and Smerdon (1965) performed some flume tests on seven Texas soils. Lyle and Smerdon studied both the individual and combined influence of

different engineering properties such as degree of compaction ad PI on the erosion resistance. The soils tested in their study consisted of two non-plastic soils (Amarillo fine sandy loam and Lufkin fine sandy loam), and five plastic soils (Reagan silty clay loam, San Saba clay, Houston black clay, Lake Charles clay, and Lufkin Clay).

For each soil tested, the average particle size, the percent clay, the dispersion ratio, the vane shear strength, and the PI were measured. In addition to the physical engineering properties, the percent organic matter, the Ca-Na ratio, and the cation exchange potential were obtained for each soil. Lyle and Smerdon (1965) first studied the effect of compaction (void ratio), and linearly correlated the void ratio and the critical shear stress. Table 6 shows the results of these linear regressions.

Table 6. Results of linear regression study on correlations between critical shear stress and void ratio (Lyle and Smerdon, 1965).

Test Series No.	Regression Equation	t value	Significance level
1	$\tau_c(psf) = 0.0255 - 0.00714 \times e$	12.93	0.05
2	$\tau_c(psf) = 0.0279 - 0.00316 \times e$	-	0.01
3	$\tau_c(psf) = 0.0271 - 0.00577 \times e$	11.5	0.1
4	$\tau_c(psf) = 0.036 - 0.01778 \times e$	13.45	0.05
5	$\tau_c(psf) = 0.07387 - 0.0338 \times e$	2.53	0.4
6	$\tau_c(psf) = 0.0323 - 0.00653 \times e$	21.3	0.05
7	$\tau_c(psf) = 0.0640 - 0.00959 \times e$	0.604	0.7

After examining the test results, Lyle and Smerdon (1965) concluded that in addition to the void ratio, other influential parameters are in order of decreasing impact plasticity index, dispersion ratio, percent organic matter, vane shear strength, cation exchange potential, average particle size (D_{50}), Ca-Na ratio, and clay percentage. Thereafter, Lyle and Smerdon (1965) proposed linear regressions for each of these parameters combined with the void ratio. Table 7

shows the results of these linear regressions. The R-square values or any other parameter representing the significance level of the proposed equations were not reported along with the results. After these equations were established, further efforts were made to involve more parameters; some link was observed between the Ca-Na ratio and the slope of the critical shear stress-void ratio plot.

Table 7. Proposed regression equations linking the critical shear stress with soil properties with having void ratio included in all (Lyle and Smerdon, 1965)

Soil property	General equation
Plasticity index, I_w	$\tau_c = 0.00771 + 0.0233(1.2 - e) + [0.00079 + 0.00035(e - 1.2)]I_w$
Dispersion ratio, D_r	$\tau_c = [0.0322 + 0.0086(1.2 - e)](10) - (n)D_r$ $where\ n = 0.00452(10)^{0.32(e-1.2)}$
Percent organic matter, P_{om}	$\tau_c = [0.0105 + 0.0124(1.2 - e)]P_{om}(n)$ $where\ n = 0.765(10)^{-0.42(1.2-e)}$
Vane shear strength, S_v	$\tau_c = [0.0140 + 0.00192(1.2 - e)](\frac{S_v}{10})(n)$ $where\ n = 0.205(10)^{-0.61(1.2-e)}$
Cation exchange capacity, CEC	$\tau_c = [0.00429 + 0.0136(1.2 - e)] + [0.0140 + 0.00116(e - 1.2)]\log(CEC)$
Mean particle size, M	$\tau_c = [0.01199 + 0.0101(1.2 - e)] - [0.00589 + 0.0009(e - 1.2)]\log(M)$
Calcium-sodium ratio, R_{cn}	$\tau_c = [0.02024 + 0.0235(1.2 - e)] + [0.00264 + 0.00812(e - 1.2)]\log(R_{cn})$
Percent clay, P_c	$\tau_c = [0.0141 + 0.0075(1.2 - e)](10)^{0.00621P_c}$

Smerdon and Beasley (1961) performed flume tests on 11 cohesive Missouri soils to investigate the relationships between main engineering properties of soils and critical shear stress measured in the flume tests. The proposed empirical equations were:

$$\tau_c = 0.0034(I_w)^{0.84} \quad (23)$$

$$\tau_c = 10.2(D_r)^{-0.63} \quad (24)$$

$$\tau_c = 3.54 * 10^{-28.1 D_{50}} \quad (25)$$

$$\tau_c = 0.493 * 10^{0.0182 P_c} \quad (26)$$

τ_c = critical shear stress (Pa)

I_w = plasticity index

D_r = dispersion ratio

D_{50} = mean particle size (m)

P_c = percent clay by weight (%)

Partheniades (1965) proposed the following model to link the erosion rate to the shear stress of fine-grained soils. This model was used later on by Hanson (Hanson and Cook, 2004) with an exponent "a" equal to 1 and by Briaud (2001) with an exponent a different from 1.

$$\dot{z} = k_d \left(\tau_a - \tau_c\right)^a \quad (27)$$

$\dot{z}$ = erosion rate (m/sec)

k_d = erodibility coefficient (m^3/N*sec)

α = exponent typically assumed to be 1

τ_α = applied shear stress on the soil boundary (Pa)

τ_c = critical shear stress (Pa)

Neil (1967) proposed an equation to predict the critical velocity of coarse grain soils based on experimental data on six sizes of graded gravels, two sizes of uniform glass balls, and cellulose acetate balls ranging in diameter from 6 to 30 mm. In the equation proposed by Neil (1967), the depth of flow is included; this would indicate that the critical shear stress is not merely a soil property (Clark and Wynn, 2007).

$$\frac{\rho V_{mc}^2}{\gamma_s D_g} = 2.50\left(\frac{D_g}{d}\right)^{-0.20} \tag{28}$$

V_{mc} = competent mean velocity for first displacement of bed material

D_g = effective diameter of bed grains

d = depth of flow

$\gamma_s = g(\rho_s-\rho)$

g = acceleration due to gravity

ρ = fluid mass density

ρ_s = bed-material mass density

Kandiah and Arulanandan (1974) also performed both flume tests and rotating cylinder tests on saturated and unsaturated Yolo lam clay. The influence of the Sodium Adsorption Ratio (SAR) as well as the salt concentration of the sample on soil erodibility was investigated. SAR is defined in Eq. 29.

$$\text{SAR} = [\text{Na}]/\sqrt{0.5[(Ca^{++}) + (Mg^{++})]} \tag{29}$$

Kandiah and Arulanandan also studied the influence of the water content of the compacted samples on flaking. They concluded that an increase in salt concentration leads to a decrease in the critical shear stress; while, an increase in SAR would raise the critical shear stress. They also found that the water content of the sample in the saturated state, does not have a significant impact on erodibility. However, for unsaturated compacted sample, it was observed that an increase in moisture content leas to an increase in the critical shear stress.

Sargunan (1976) also used the rotating cylinder test to study the impact of mineralogy, soil pore fluid, and the eroding fluid chemistry on the erodibility of cohesive soils. However, this study did not end up with proposed regression equations. Sargunan tried Na instead of Ca or Mg and

observed that the critical shear stress typically decreases when the SAR increases. Also, it was found that an increase in salt concentration, at a given SAR, led to an increase in critical shear stress. However, Sargunan indicated that the influence of mineralogy is more significant when the SAR was relatively high.

Arulanandan and Perry (1983) challenged the contemporary filter design method, in which dam engineers of the time were using widely-graded sand-gravel combinations as filter for the core materials without taking erosion into account. Arulanandan and Perry concluded that using the classification plot based on plasticity proposed by Gibbs (1962) (Figure 29), is not sufficient to categorize erodibility, since some dam failures were observed in the "high resistance to erosion" zone of Gibbs (1962) proposed plot. Using flume tests and rotating cylinder tests, Arulanandan and Perry studied 29 dams which consisted of both dispersive and nondispersive core materials and performed erodibility tests on them. As a result, three general categories were proposed for the erodibility of core materials in dams:

1) Erodible soils: which have a critical shear stress less than 0.4 Pa. Filter tests are highly recommended to ensure the success of a filter to resist erosion.
2) Moderately erodible soils: critical shear stress is between 0.4 and 0.9 Pa. Similar testing as in category 1 is needed to certify the filter material.
3) Resistant soils: regular filter design procedure can be implemented in these cases.

The other findings of Arulanandan and Perry (1983) was that a non-dispersive clay does not necessarily refer to an erosion resistant clay, due to many factors such as clay type, composition of eroding fluid as well as pore fluid, pH, organic matter, temperature, and structure of the soil. This was also shown by Acciardi (1984) where some soils which were classified as "dispersive clay" using a pinhole test, were categorized in the third category (erosion resistant soils) of

Arulanandan and Perry category chart. Arulanandan and Perry proposed plots for saturated remolded soils to relate the critical shear stress and eroding fluid concentration. Figure 30 shows two of the proposed plots relating the eroding fluid concentration with the erosion rate and critical shear stress.

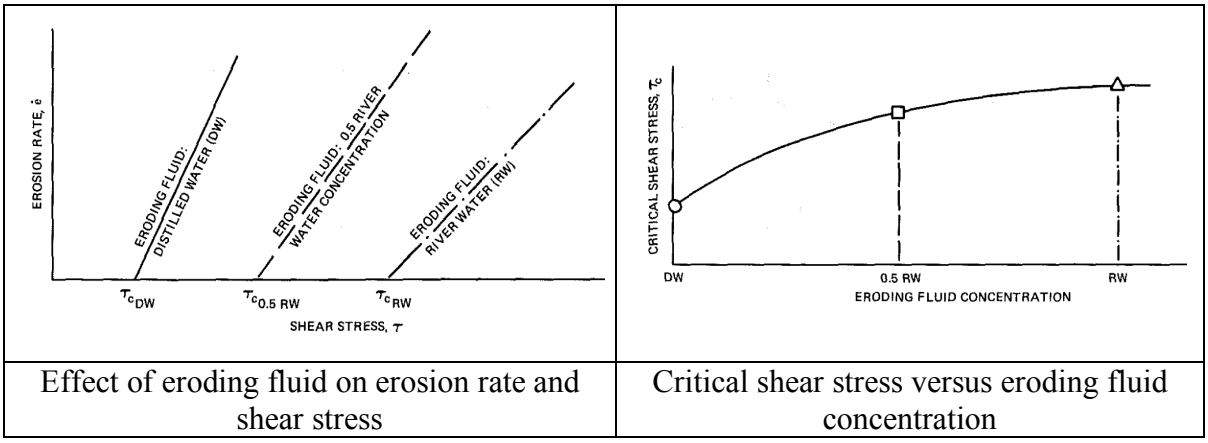

Effect of eroding fluid on erosion rate and shear stress	Critical shear stress versus eroding fluid concentration

Figure 30. Proposed charts by Arulanandan and Perry (1983) for relating erosion rate, critical shear stress, and eroding fluid concentration

Chen and Anderson (1987) investigated the damages due to overtopping in 21 embankments in 5 states of the US. They proposed equations for the critical shear stress τ_c and the erosion rate E as shown below:

- Non-cohesive material for a shear Reynolds number greater than 70:

$$\tau_c = 0.05(\gamma_s - \gamma)D_{50} \tag{30}$$

Where,

$$\gamma_s = unit\ weight\ of\ soil, \qquad \gamma = unit\ weight\ of\ water,$$

$$D_{50} = median\ particle\ size\ of\ soil$$

- Cohesive material (un-compacted, ranging from a silty loam soil to a highly cohesive clay soil) with PI being the plasticity index

$$\tau_c = 0.0034(PI)^{0.84} \quad (31)$$

- Cohesive material (normally compacted)

$$\tau_c = 0.019(PI)^{0.58} \quad (32)$$

- Highly cohesive soil such as clay ($PI \geq 10$)

$$E = 0.000086(\tau - \tau_c)^{0.91} \quad (33)$$

- Low-cohesive soil such as sandy clay ($PI \leq 5$)

$$E = 0.00022(PI)^{0.43} \quad (34)$$

- Non-cohesive sand/gravel soil

$$E = 0.00324(PI)^{1.3} \quad (35)$$

Where E is the erosion rate in cubic feet per second-foot, τ and τ_c are the shear stress and the critical shear stress in pounds per square foot, γ_s and γ are the soil and the water unit weights in pounds per cubic foot, PI is the plasticity Index in percent, and D_{50} is the mean grain size in feet. Chen and Anderson later created monographs using Eq. 30 to 35 in order to predict the damages to embankments caused by flood overtopping.

Shaikh et al. (1988) used a flume system to study the erodibility of unsaturated compacted clay soils. Various mixtures of materials (Na-montmorillonite + silica) were used to prepare four samples with different clay percentages (100%, 70%, 40%, and 10%). According to their tests on the four clayey samples, Shaikh et al. proposed empirical correlations for linking the erosion rate of the compacted clayey samples to the clay percentage and critical shear stress for the range of moisture content and saturation tested. They also found out that the compacted moisture content of the samples does not have a significant effect on erosion rates. The reason was that because the

same compaction method was implemented, the orientation of particles was similar for all the samples. They first defined the erosion function as a linear equation shown below (Shaikh et al., 1988):

$$\dot{\epsilon} = C\tau \tag{36}$$

Where, $\dot{\epsilon}$ is the erosion rate (N/m^2/min), τ is the hydraulic shear stress, and C is defined as the erosion-rate coefficient (1/min). Shaikh et al. proposed the following relationships between C, percent clay (PC), and torvane shear stress (S_t).

$$C = 4.14 \times (PC)^{-0.91} \tag{37}$$

$$C = 0.157 \times (S_t)^{-1.338} \tag{38}$$

Where, PC is the percent clay and S_t is the torvane shear strength (MPa), and C is the erosion rate coefficient (1/min).

Shaikh et al. (1988b) tested Ca-montmorillonite (which is a non-dispersive clay) and Na-montmorillonite (which is a dispersive clay) using a flume system to study the relationships between dispersivity and erodibility of the soil. The dispersivity of the soils was measured according to Sherard et al. (1976). Again, the effect of the compacted moisture content was believed to be minimal. Shaikh et al. (1988b) proposed the following equation for relating erodibility to the chemistry of the pore water (using Sodium Adsorption Ratio).

$$C = 4.41 \times (SAR)^{-1.34} \tag{39}$$

Where, SAR is the sodium adsorption ratio (meq/L)$^{0.5}$, and C is the erosion-rate coefficient (1/min).

Hanson (1992) and Hanson and Robinson (1994) used submerged jet tests in the laboratory to investigate the impact of compaction and associated moisture content on the erosion resistance of soils. The soils tested were clays and silty clays with a plasticity index ranging from 7 to 12%.

29 samples were prepared at different moisture contents and compaction efforts using both static and dynamic compaction methods. Hanson and Robinson plotted the dry density and moisture content versus the unitless Jet Index (J_i) which was defined earlier by Hanson (1991):

$$\frac{D_s}{t} = J_i U_0 \left(\frac{t}{t1}\right)^{-0.931} \quad (40)$$

Where, D_s refers to the maximum scour depth, t is the time of erosion, J_i is the jet index (unitless), U_0 is the jet velocity at the nozzle, and $t1$ refers to time unit equivalent of 1 second. Hanson (1991) showed that $J_i \leq 0.02$ refers to high erodible materials, while $J_i > 0.002$ associates with very low erodible geomaterials.

Comparison between the J_i values and the moisture content and dry unit weight indicated that J_i decreases (erosion resistance increases) when the dry density increases at a constant moisture content. Also, it was concluded that for a given dry unit weight, an increase in moisture content would decrease J_i (or increases the erosion resistance of the soil) for unsaturated soil samples. For saturated samples, however, an increase in moisture content increases the J_i value. Hanson and Robinson also compared the test results with the open channel tests conducted by Robinson (1990) on the same samples and found it in agreement with their findings.

Ghebreiyessus et al. (1994) also performed flume tests on Mexico silty loamy soils to study the effect of vane shear strength and bulk density on the soil erodibility parameters. Table 8 shows the results of their regression analyses. The erosion or detachment rate is defined here as the rate of mass removal per unit area (g m^{-2} s-).

Table 8. Predicted regression models for relationships between erosion rate, shear stress, bulk density, and vane shear strength (Ghebreiyessus et al., 1994)

❖ Y = detachment rate (g m^{-2} s^{-1}); ρ_b = bulk density (Mg/m^3); τ = shear stress (Pa); VE = vane shear strength (kPa)

Briaud et al. (2001) and Briaud (2008) proposed a set of equations to predict the critical velocity and critical shear stress of coarse grain soils based on many EFA erosion tests performed at Texas A&M University.

$$v_c(m/s) = 0.35\left(D_{50}(mm)\right)^{0.45} \tag{41}$$

$$\tau_c(Pa) = D_{50}(mm) \tag{42}$$

Briaud (2008) concluded that for fine grained soils there is no direct relationship between critical velocity/shear stress and the mean particle size. However, Briaud (2008) bracketed the data with an upper bound and a lower bound equation as follows.

$$\text{Upper bound} \quad v_c(\text{m/s}) = 0.03\left(D_{50}(mm)\right)^{-1} \tag{43}$$

$$\text{Lower bound} \quad v_c(\text{m/s}) = 0.1\left(D_{50}(mm)\right)^{-0.2} \tag{44}$$

$$\text{Upper bound} \quad \tau_c(\text{Pa}) = 0.006\left(D_{50}(mm)\right)^{-2} \tag{45}$$

$$\text{Lower bound} \quad \tau_c(\text{m/s}) = 0.05\left(D_{50}(mm)\right)^{-0.4} \tag{46}$$

Figure 31 shows the scattered data for fine grain soils with the defined upper and lower bound, as well as for the coarse grain soils.

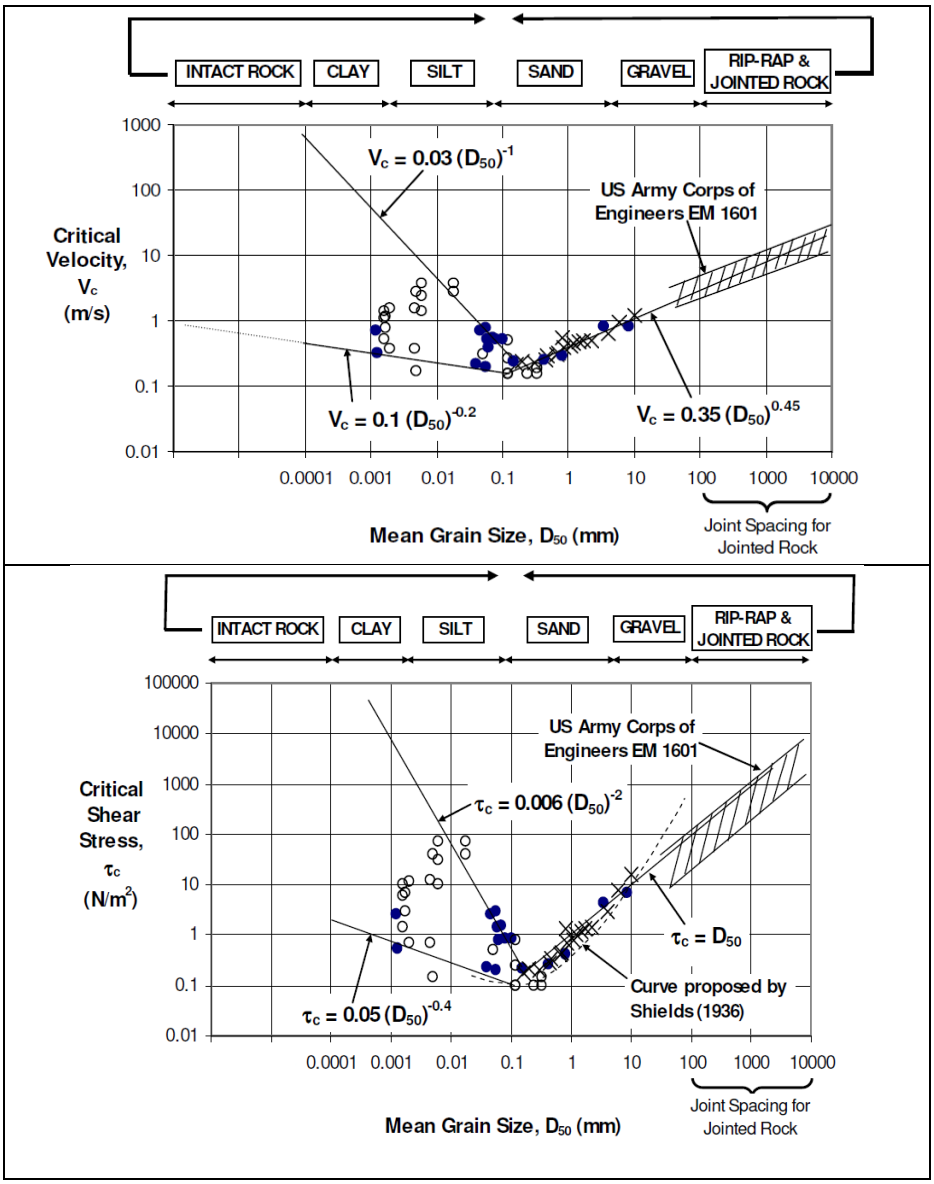

Figure 31. Plots of critical velocity and shear stress versus the mean particle size (Briaud, 2008)

Hanson and Simon (2001) for soils with 50 to 80% silt size material proposed a relationship between the critical shear stress and the erodibility coefficient. The results were based on eighty-three submerged jet tests in the Midwestern US.

$$k_d = 0.2\tau_c^{-0.5} \tag{47}$$

Where, k_d = erodibility coefficient ($\frac{cm}{N-sec}$) and τ_c = critical shear stress (Pa).

Wynn et al. (2004) investigated the influences of vegetation on stream bank erosion for twenty-five (25) sites in Virginia. Wynn et al. used Hanson's submerged jet test to measure the critical shear stress and erodibility of soils. Measured critical shear stresses ranged from 0 to 22 Pa. They concluded that bulk density is the most influential parameter in soil erodibility. Depending on the soil texture, other influencing parameters were inferred to be moisture content, root density, pore and stream water chemistry, and freeze-thaw cycling. They categorized the data into three groups. Groups 1 and 2 included plastic soils, while group 3 was comprised of non-plastic soils. Group 1 included plastic soils with higher bulk densities, lower PI, and lower organic content than the soils in Group 2. Table 9 shows the results of regression analyses on the critical shear stress and some engineering properties.

Table 9. Regression equations for soil critical shear stress in southwest VA (Wynn et al., 2004)

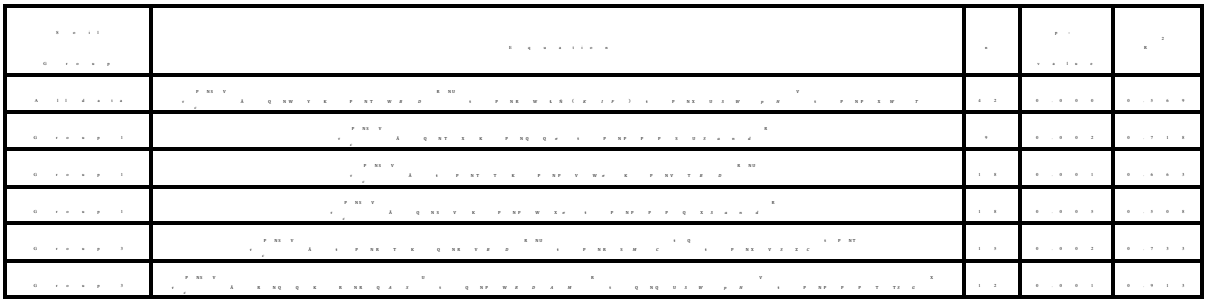

- KIF is the potassium intensity factor, WT refers to temperature of water (°C), BD is the bulk density (g/cm^3), σ is the standard deviation of the particle size distribution, Sand refers to sand percentage, MC refers to moisture content, SWpH is the ratio of pore water to river water pH, AS is the aggregate stability, SG is the soil specific gravity, and RDAM is related to the difference between median and average periods frozen.

Amos et al. (2004) studied the stability of the seabed in the Venice Lagoon using two benthic, annular flumes and soils from 24 sites. Water temperature, salinity, organic content, and bulk densities were controlled under different conditions. Amos et al. proposed an equation for natural lacustrine, estuarine, and marine muds which could link the critical shear stress and the wet sediment bulk density:

$$\tau_{cr} = 5.44\times10^{-4}\left(\rho_b\right) - 0.28 \tag{48}$$

Where, τ_{cr} is the critical shear stress (Pa), and ρ_b is the sediment wet bulk density (kg/m^3). Eq. 48 is based on 73 sets of data, and the R-square value for Eq. 48 is 0.46.

Thoman and Niezgoda (2008) studied the stability of 25 channel sites in Wyoming. To do so, they conducted several in-situ JET tests and measured the erodibility parameters; the geotechnical properties were obtained from parallel laboratory tests. They found that most influential parameters are activity, organic content, cation exchange capacity, soil pH, and dispersion ratio. No linear correlation was found between the critical shear stress and each one of the aforementioned geotechnical parameters; however, combining all five parameters, Thoman and Niezgoda (2008) proposed the following equation:

$$\tau_c = 77.28 + 2.20\left(Act\right) + 0.26\left(DR\right) - 13.49\left(SG\right) - 6.40\left(pH\right) + 0.12\left(w\right) \tag{49}$$

Where τ_c is the critical shear stress in Pascals, Act is the soil activity (ratio of $\frac{PI}{\%\ of\ Clay}$), DR is the dispersion ratio, SG is the specific weight, pH is the chemical index for acidity, and w

is the water content (%). The reliability of the proposed model can be seen in Figure 32. The dashed lines show the one standard deviation range.

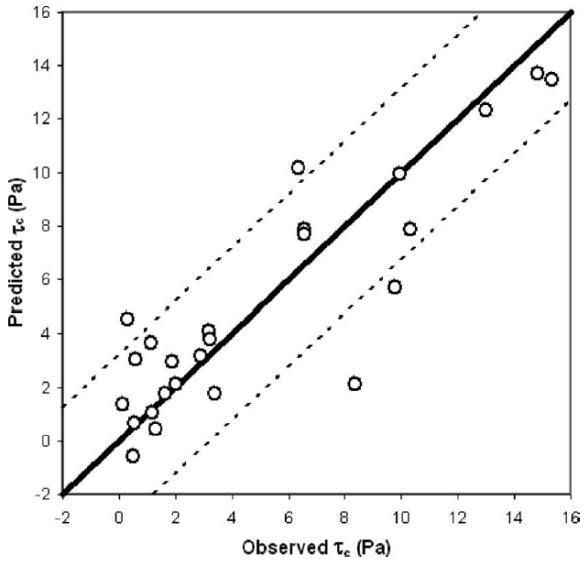

Figure 32. Estimated versus actual critical shear stress from the Wyoming channels (Thoman and Niezgoda, 2008)

Winterwerp and van Kesteren (2004) presented a theoretical derivation of an erosion rate parameter M:

$$M = \frac{c_v \varphi_{s,0} \rho_{dry}}{10 D_{50} c_u} = \frac{c_v \left(\frac{1}{1 + \left(W_0 \varphi_s / \varphi_w \right)} \right) \rho_{dry}}{10 D_{50} c_u} \tag{50}$$

Where, c_v is a vertical consolidation coefficient, $\varphi_{s,0}$ is the volumetric concentration, W_0 is the water content, φ_s is the density of the primary sediment particles, φ_w is the density of the water, φ_{dry} is the dry bulk density, D_{50} is the mean particle size, and c_u is the undrained shear strength.

Julian and Torres (2006) developed an equation linking the critical shear stress in Pa to the silt and clay content in percent (SC).

$$\tau_c = 0.1 + 0.1779(SC) + 0.0028(SC)^2 - 0.0000234(SC)^3 \quad (51)$$

Mostafa et al. (2008) developed a relationship between a non-dimensional shear stress of mass erosion and a non-dimensional soil parameter.

$$\tau_p^* = -23.67\chi + 17.28 \quad (52)$$

$$\tau_m^* = -107.56\chi + 79.59 \quad (53)$$

With: $\chi = \frac{LI}{S_G - 1}$

$\tau_p^* = \text{Non} - \text{dimensional erosion resistance for particle erosion}$

$\tau_m^* = \text{Non} - \text{dimensional erosion resistance for mass erosion}$

$\chi = \text{Non} - \text{dimensional soil parameter}$

$LI = \text{Liquidity index} = \frac{\omega - \omega_{\text{PL}}}{PI}$

$S_G = \text{Specific gravity based on moist bulk density}$

$\tau^* = Non - dimensional\ erosion\ resistance = \frac{\tau}{\rho(S_G - 1)gD_{50}}$

$\tau = Erosion\ resistance$

$\rho = \text{Density of clear water}$

$g = \text{Gravitational acceleration}$

$D_{50} = \text{Mean sediment size}$

Fleshman and Rice (2013) developed a piping erosion test device called the constant gradient piping test apparatus and performed multiple tests on sandy soils to investigate the effect of grain size, gradation, and specific gravity on the critical hydraulic gradient required for piping

to start. Although no practical correlation equation was proposed, Fleshman and Rice (2013) showed that in general the angular sandy soils have a relatively more piping resistance. Also, greater piping resistance was observed when the sandy samples were graded. The specific gravity was also shown to be directly proportional to the piping resistance.

Singh and Thmopson (2015) used the Cohesive Strength Meter (CSM) in different soil moisture contents, and measured the in-situ critical shear stress in field and grassed waterway. The study showed that the critical shear stress varies with moisture content and is not constant for a soil. Also, it was observed that the critical shear stress is proportional to the soil moisture until it is below the plastic limit. Singh and Thompson (2015) proposed the following equation for the case in which the soil moisture content is less than the plastic limit in grassed waterways. The R^2 associated with Eq. 54 is 0.68.

$$\tau_c = 0.70 \times e^{0.06 \times (moisture\ content,\%)} \tag{54}$$

Karim and Tucker-Kulesza (2018) evaluated the erosion resistance of 15 selected bridge sites in Kansas using the EFA and Electrical Resistivity Tomography (ERT). It was observed that the erodibility of a soil change with the in-situ electrical resistivity (ER) of the soil. Therefore, ERT could be used as an alternative quick tool to predict the erodibility of a site instead of performing different erosion tests such as the EFA. By comparing the results of the EFA with ERT for high erodible sites, Karim and Tucker-Kulesza (2018) indicated that when the ER exceeds 50 Ωm, there will be 93% chance that the tested soil is categorized as high erodibility. ERT was introduced as a crude tool to identify the critical locations prone to erosion in a site. The selected critical locations then need further investigation to evaluate the erodibility.

It is very important to evaluate the reliability of these equations as the scatter in the data may be significant. In the next section of this chapter, the influence of each soil properties is discussed in qualitative terms.

3.2. Influence Factors on Erosion

The erodibility of soils varies significantly from soil to soil; therefore, in general, erodibility depends on engineering soil properties. Some of the broad geological properties likely to influence erodibility include:

- Soil micro- and macro structure;
- Lithification;
- Strength of structural (cohesion) forces between particles and between water molecules and particles;
- Lithology and anisotropy of soil at the different scales (laboratory and in situ);
- Grain size distribution;
- Mineral and chemical composition of soil;
- Geotechnical properties;
- Presence of fissures in a given soil massive that impact at a full-scale field behaviour of clay.

It is clear that many factors can influence the erosion behaviour of a soil. Based on the literature review conducted for this report, a list of typical parameters which affect the erosion resistance of soils is shown in Table 10. This table is divided into two categories: the more easily obtained parameters and the less easily obtained parameters. As mentioned earlier, the main goal of this study is to find a practical and promising tool to link the soil erodibility parameters and common geotechnical parameters.

3.2.1. *Effects of Less Typically Obtained Parameters*

The fact that the following parameters are not easily obtained does not mean that they are not important when it comes to predicting erosion.

Table 10. Influencing soil and water properties in erosion resistance of soils

More typically obtained properties:	**Less typically obtained properties:**
• Plasticity index • Liquidity Index • Unit weight • Water content • Undrained shear strength • Percent passing sieve #200 • Percent clay particles • Percent silt particles • Mean grain size • Coefficient of uniformity • Percent compaction (for man-made soils only) • Soil swell potential • Soil void ratio	• Specific gravity of solids • Soil dispersion ratio • pH (flowing water and pore water) • Salinity of eroding fluid • Organic content • Soil cation exchange cap • Soil clay minerals • Soil sodium adsorption ratio • Soil activity • Soil temperature • Density of cracks

3.2.1.1. Mineralogy and particle size distribution

One of the very important parameters that needs to be carefully studied is the effect of mineralogy and of particle size distribution on the erosion resistance of soils. In terms of grain size distribution, there are four major fractions (i.e. gravel, sand, silt, clay) which affect erosion resistance of soil under different flow conditions.

Gravel fraction (2-20 mm): The erosion behavior of the gravel fraction depends mostly on the correlation between the weight of the particle and the hydrodynamic force applied to the particle. The mineral composition of gravel is an issue as well, and becomes important when the particle is formed by carbonate minerals ($CaCO_3$). Leaching of carbonate minerals is likely to

occur in the presence of aggressive carbon dioxide in aqueous form (CO_2). The following reaction between carbonate minerals and water takes place:

$$CaCO_3+H_2O+CO_2\,(\text{aqueous}) \rightarrow Ca\,(HCO_3)_2 \quad (55)$$

As a result of this reaction, lightly soluble calcium bicarbonate will form which goes to an aqueous phase, and thereafter calcium carbonate is gradually destroyed. As a result, the content of hydro carbonate-ion (HCO_3) in the water increases as well as the content of calcium-ion (Ca^{2+}). The erosion behavior of the gravel fraction in soil can be important for glacial (moraine) clayey soil containing these fractions.

Sand fraction (0.075-2 mm): The influence of the sand particles on soil erosion is similar to that of the gravel particles as the most important factor that affects erodibility of sand is the particle's weight and its mineral composition.

Silt fraction (0.002-0.07 mm): The silt fraction is the least erosion resistant and soaking resistant of all the fractions. The presence of silt particles in soil may cause the collapse of the structure during wetting. For example, loess is less water resistant because it is made primarily of silts size particles (more than 70%). Some clayey soils in semi-arid zones such as Texas contain a great amount of silt particles and could erode rapidly.

Clay fraction (<0.002 mm): In clayey soils, the individual clay particles can form micro-aggregates (from single to dozens of micrometers) and macro-aggregates (from dozens to thousands of micrometers) (Osipov et al., 1989). The microstructure of clayey soil can be identified using the light and electronic microscope. The erosion behavior of clayey soils depends on the presence of these micro- and macro- aggregates in the matrix, on the ability of the particles to coagulate, on the size and shape of the particles, and on the clay ability to resist desagreggation when submerged in water. The most active aggregate formation is associated with the smectite

group (montmorillonite, nontronite, bentonite etc.). In this case, the erodibility of the clay containing smectites depends on the strength between the clay aggregates. After the bonds between clay aggregates collapse, the erosion resistance depends on the force between individual clay particles and the strength of those forces.

The clay fraction swells when it interacts with water. The swell potential typically increases with a decrease in water flow velocity. The presence of clay particles in sand creates a cohesion between sand particles which can significantly increase the resistance to erosion. The three major groups of clay minerals are kaolinite, illite, and montmorillonite. These minerals have very different types of structure including bonding between layers. Figure 33 shows four general different clay mineral microstructures.

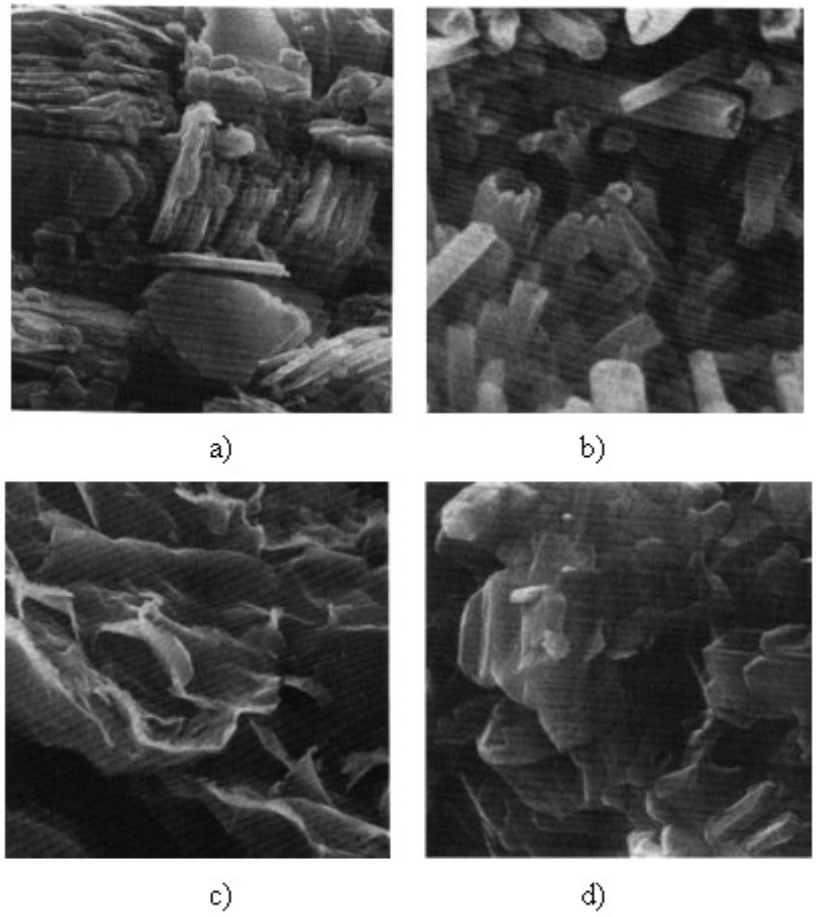

Figure 33. Clay mineral microstructure (Mitchell, 1993 after Tovey, 1971) a- kaolinite, b- halloysite, c- montmorillonite, d- illite.

Many studies have been conducted to find out potential relationships between erodibility and particle size. Particle size should be a factor taken into account only for coarse-grain soil. For fine-grain soils, particle size by itself without considering the electrostatic and electromagnetic forces is not an adequate representative.

Maslov (1968) and Justin (1923) working separately obtained very similar results when studying the relationship between critical velocity and size of particles. Table 11 and Figure 34 show that the critical velocity decreases as the diameter of the particle decreases. It was also observed that the erosion resistance increases with an increase in amount of particles with diameter of less than 0.05 and 0.001 mm.

Table 11. Critical velocity of water flow (V_{cr}) depending on the diameter of the particles (after Maslov, 1968 and Justin 1923)

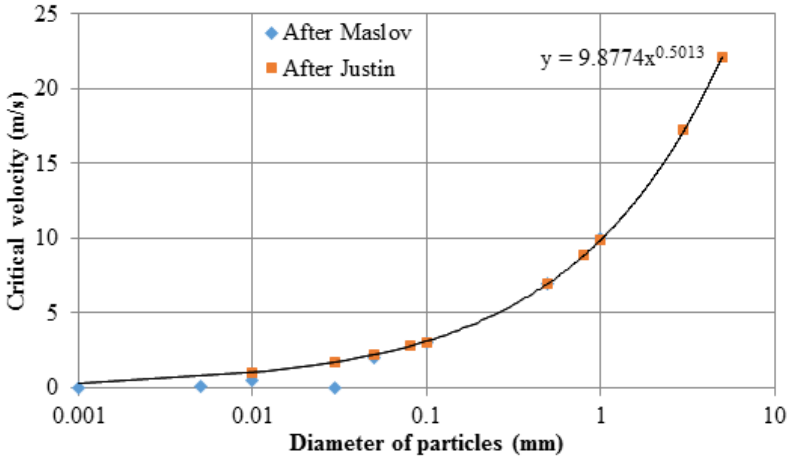

Figure 34. Critical velocity of water flow in different soils (Maslov, 1968; Justin 1923)

3.2.1.2.Structural or Cohesion Forces

The nature and the magnitude of the structural or cohesion forces play a very important role in understanding the erodibility of clayey soils. The strength of the structural forces can vary significantly and depends on their nature and on the soil properties. The forces are held by forces which may be ion-electrostatic, molecular, magnetic, and chemical in nature.

One of the strongest forces is the chemical force which exists in igneous rocks as well as in clay if the natural water content (WC) of clay is below the plastic limit (PL) (Table 12). The nature of this force is electrical interaction between atoms. Once this chemical force fails, it cannot be recovered.

Molecular and ion-electrostatic (Coulomb) forces exist mostly in soft clays when the water content (WC) reaches the liquid limit (LL). Molecular forces or Van der Waal's forces are weaker than the chemical forces. The strength of the molecular force depends on the water content of the clay as well as on the dispersion ratio. With an increase in dispersion, the magnitude of the molecular forces increases. The maximum strength of the molecular forces is found in dry clay. With an increase in water content of clay, the strength of the molecular force decreases. If the clay becomes wet, the diffusion layer of ions between and around particles causes the formation of the molecular-ion-electronic force. This force is very likely to be destroyed by water flow.

Table 12. Type of cohesion forces in fine grain soils (clayey soils) (Osipov et al., 1989)

Mirzhulava (1967) obtained a relationship between the critical velocity and the cohesion of saturated soils (Figure 35) indicating that the critical velocity of saturated soils increases with an increase in soil cohesion. Working with unsaturated soils, Shidlovskaya et al. (2016). The results of this study also show that the critical velocity increases with an increase in the untrained shear strength of clay (Figure 36).

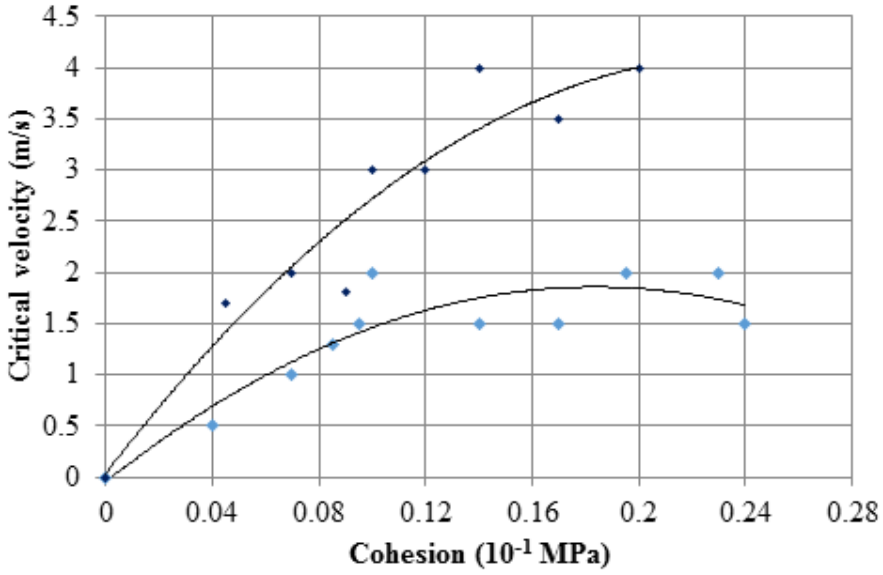

Figure 35. Critical velocity vs. cohesion for saturated soil (Mirzhulava, 1967)

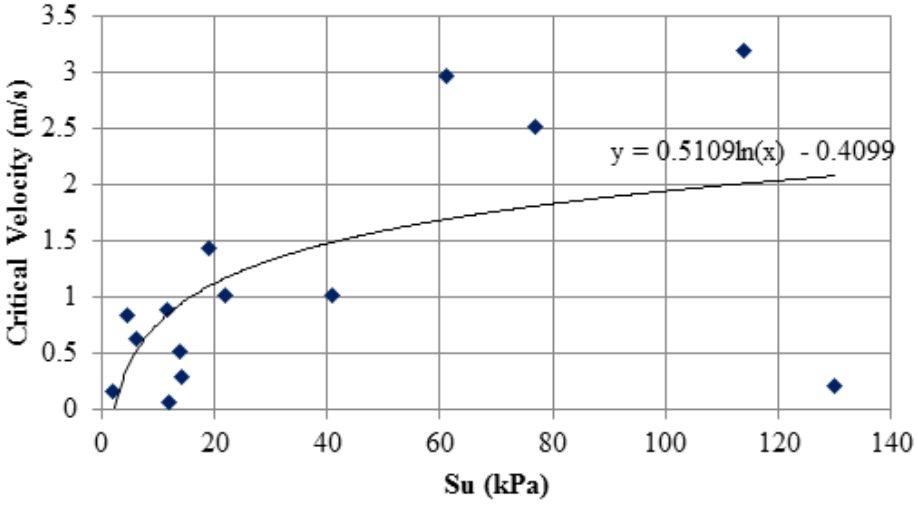

Figure 36. Relationship between the critical velocity and the undrained shear strength for clays

3.2.1.3.Disturbance of the Soil Structure

Disturbance of the soil structure also has an impact on erosion resistance. Gordaniaya (1957) studied the influence of disturbance on erodibility of carbonated lean clay (Table 13). This

table clearly shows that disturbing the soil structure decreases significantly the critical velocity. The critical velocity of the same carbonated lean clay at a given water content decreases by a factor of 3 to 5 times when going from the undisturbed to the disturbed state. Carbonate soils are proned to have strong cementation but are not very resistant to chemical processes such as dissolution and leaching.

Table 13. Critical velocity of water flow for carbonated lean clay (Gordaniaya, 1957)

3.2.1.4.Chemical Composition of Soil

The chemistry of soil has an impact on both fine-grain and coarse-grain soil erodibility. Erosion, especially suffusion, is likely to occur in sandy and clayey soil containing soluble salts. This type of erosion corresponds to a dissolution of salt and to a collapse of the corresponding bonds in the soil. The more soluble cases would be those with chloride and sulfate in the soils. The presence of these salts in the chemical composition of the soil accelerates the erosion process, due to the co-occurrence of mechanical and chemical erosion. Table 14 shows the solubility of different salts in water.

Table 14. Solubility of different salts in water

3.2.1.5.Organic Content of Soil

Another influencing factor in erosion is the presence of biogenic (microorganisms) and abiogenic (organic matter in colloidal form) in soil. Organic colloids with a size of less than 0.0001 mm can clog the pore space and decrease the permeability of the soil. This is more important in coarse-grain soil (sand). The presence of organic colloids in the pore space can create some particle-particle cohesion as well as organic colloid-particle cohesion. This would lead to a decrease in water permeability and increase the resistance to erosion. The adhesion of micro-organisms cells on soil particles result in the formation of biofilms which are extracellular substances glued to particles. This bond between the biofilm and the particle can help resist against erosion.

Microbial enzyme is a product of microbial activity and works to stabilize active clay particles. It has a hydrophobic effect on the clay. Strengthening clayey soils using enzyme technology is one of the soil improvement methods applied to decrease hydrophilicity of clays and

to protect them from erosion. However, in water erosion, the flow velocity at which the organic matter could be washed away may not be very high.

3.2.1.6.Presence of Cracks and Fissures (Micro- and Macro-Scale)

In a fractured rock or fissured soil mass, the water discharges through the existing cracks and fissures. An increase in water discharge through the fissured soil mass provides an increase in opening of the fissures by erosion. Table 15 shows the critical velocity of rocks depending on the opening of the cracks in the rock mass. Note that the erosion rate would change as the opening of the cracks increases.

Table 15. Critical velocity for rocks depending on opening of cracks (Bogdanov et al., 1972)

3.2.1.7.Wet-Dry Cycles

The wet-dry cycles are due to the weather and associated moisture migration in the soil profile by a thermal gradient during the year. These cycles have an impact on the soil erodibility. For example, the formation of shrinkage cracks and then water flowing through the cracks can erode a soil significantly. The density and size of the shrinkage cracks depends on the initial water content of the clay and on its plasticity index. This is particularly important at shallower depths

with problems such as overtopping of levees during hurricanes or floods, river banks erosion, surface erosion of highway embankments and so on.

As mentioned earlier, this study will focus on the influences of the most common geotechnical parameters (See Table 10).

4. EROSION EXPERIMENTS

This chapter presents the results of all the erosion experiments performed as part of this NCHRP project. Section 4.1 of this chapter is dedicated to the Soil Erosion Laboratory at Texas A&M University, and the testing devices that were built as part of this project. The design plans as well as photographs of each device that was built is presented in this section. Section 4.2 presents the erosion test plan matrix according to Tasks 5 and 6 of this project, and Section 4.3 presents the results of erosion experiments (i.e. Mini-JET, EFA, HET, PET, and BET). Finally, Section 4.4 presents the comprehensive information on the geotechnical properties of all tested samples. Appendix A and Appendix B of this report, include all detailed erosion test results, and the geotechnical properties spreadsheets for each sample, respectively. Also, from each sample that was tested in any erosion device, many photographs and videos were taken before, during, and after the tests. The photographs and videos are collected in a file and held by the authors.

4.1. TAMU Erosion Lab and Testing Devices

The very primary step to perform Tasks 5 and 6 of the project was to furnish the erosion lab with all necessary testing equipment and work condition at Texas A&M University. Therefore, a Hole Erosion Test (HET) and a Jet Erosion Testing device were constructed in the lab. Also, the two Erosion Function Apparatus (EFA) machines at Texas A&M University were re-furnished and armored into proper condition. Following is the summary of the work done on the construction of each aforementioned device, and the refurbishment of the Soil Erosion Laboratory at Texas A&M University.

4.1.1. *Construction of the Hole Erosion Test (HET) Apparatus*

The HET apparatus was constructed at Texas A&M University in accordance with the work done by Wan and Fell (2002) at the University of New South Wales in Australia. A schematic diagram of this device, along with the design drawings are included in Figure 37 to Figure 41. A couple of dummy tests were also conducted to make sure that the constructed apparatus is ready for the testing schedule. Figure 42 shows a final version of the HET apparatus in the soil erosion lab at Texas A&M University, with labels describing each piece.

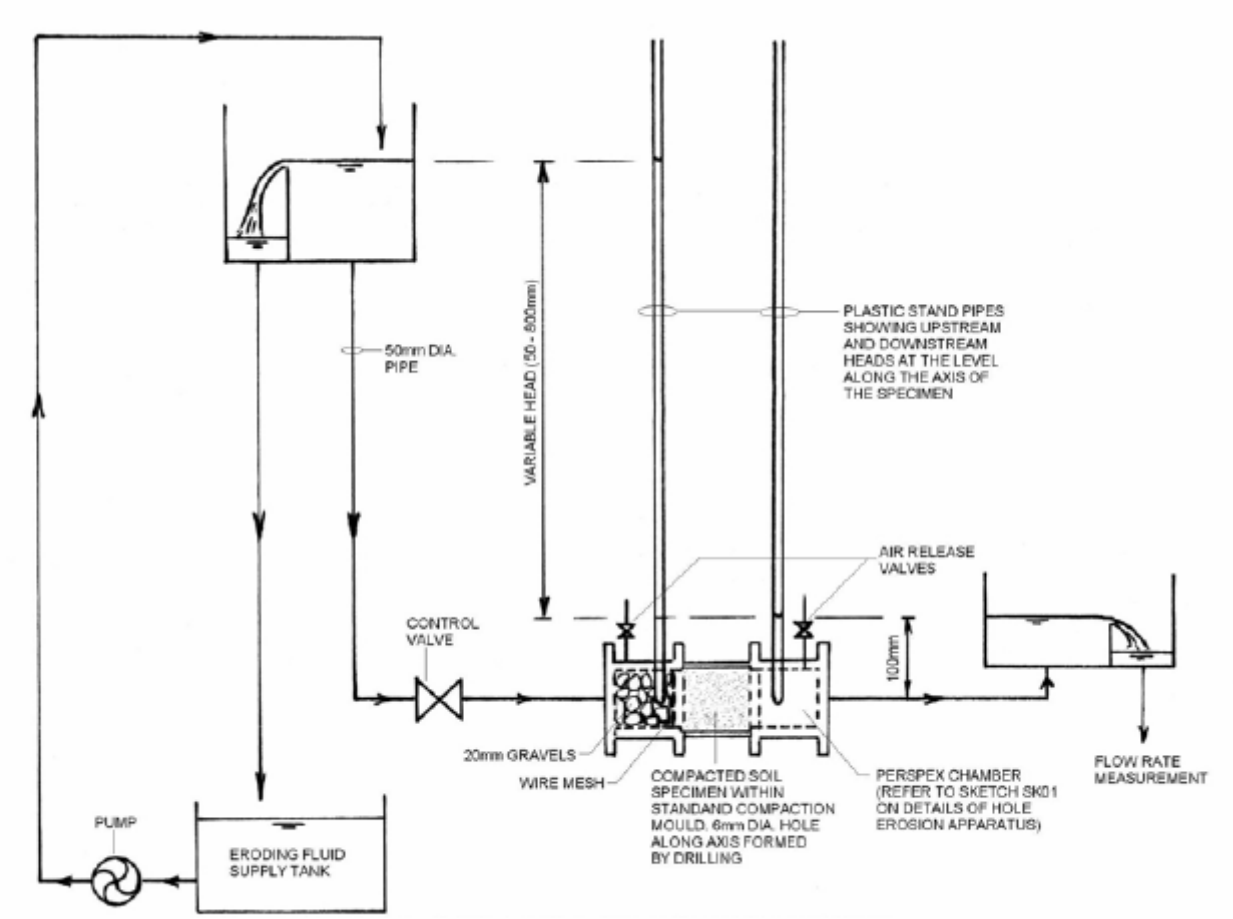

Figure 37. Schematic of the Hole Erosion Test assembly (Wan and Fell, 2002)

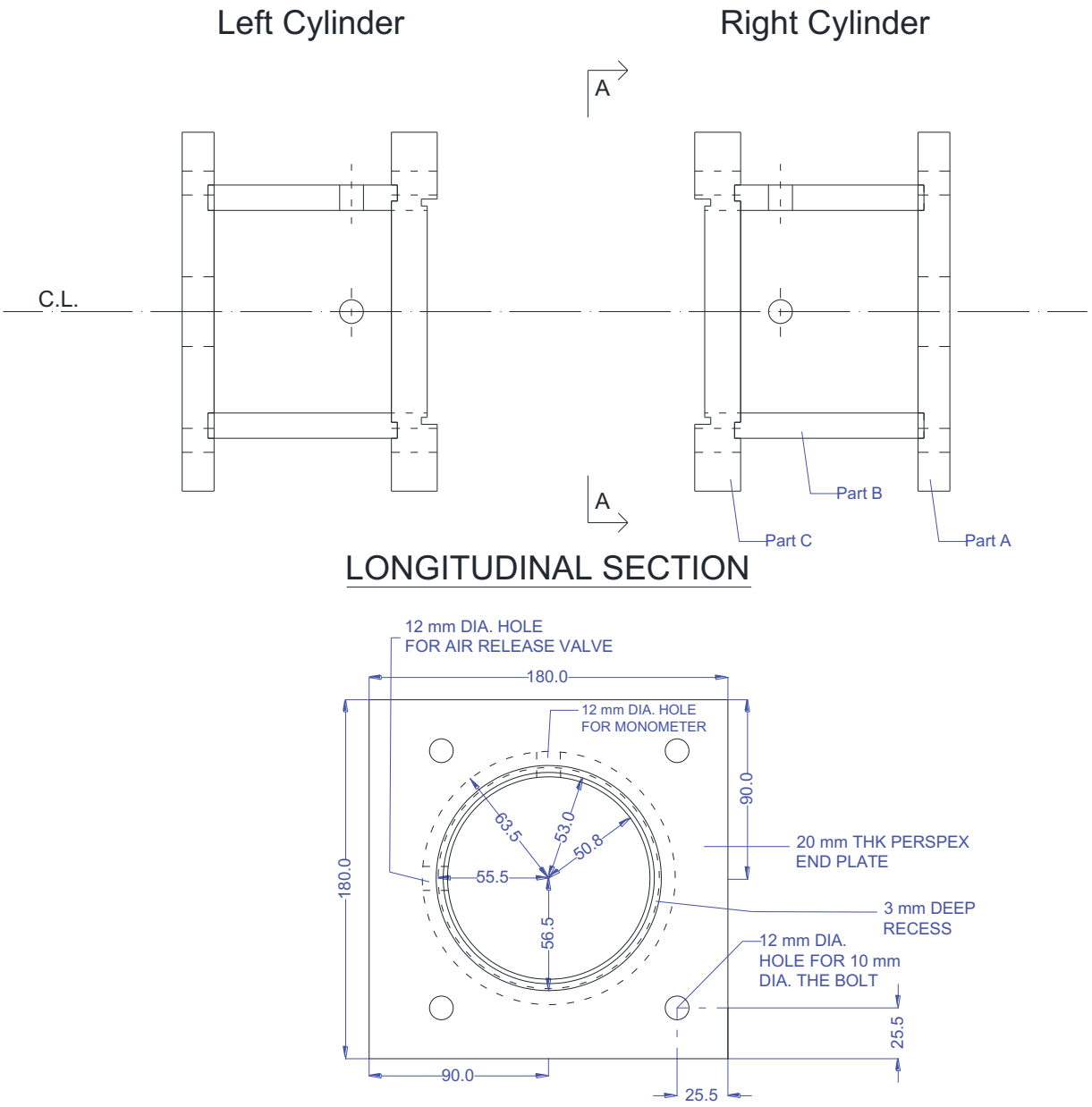

Figure 38. Drawing of the whole assembly in one glance (all dimensions are in mm)

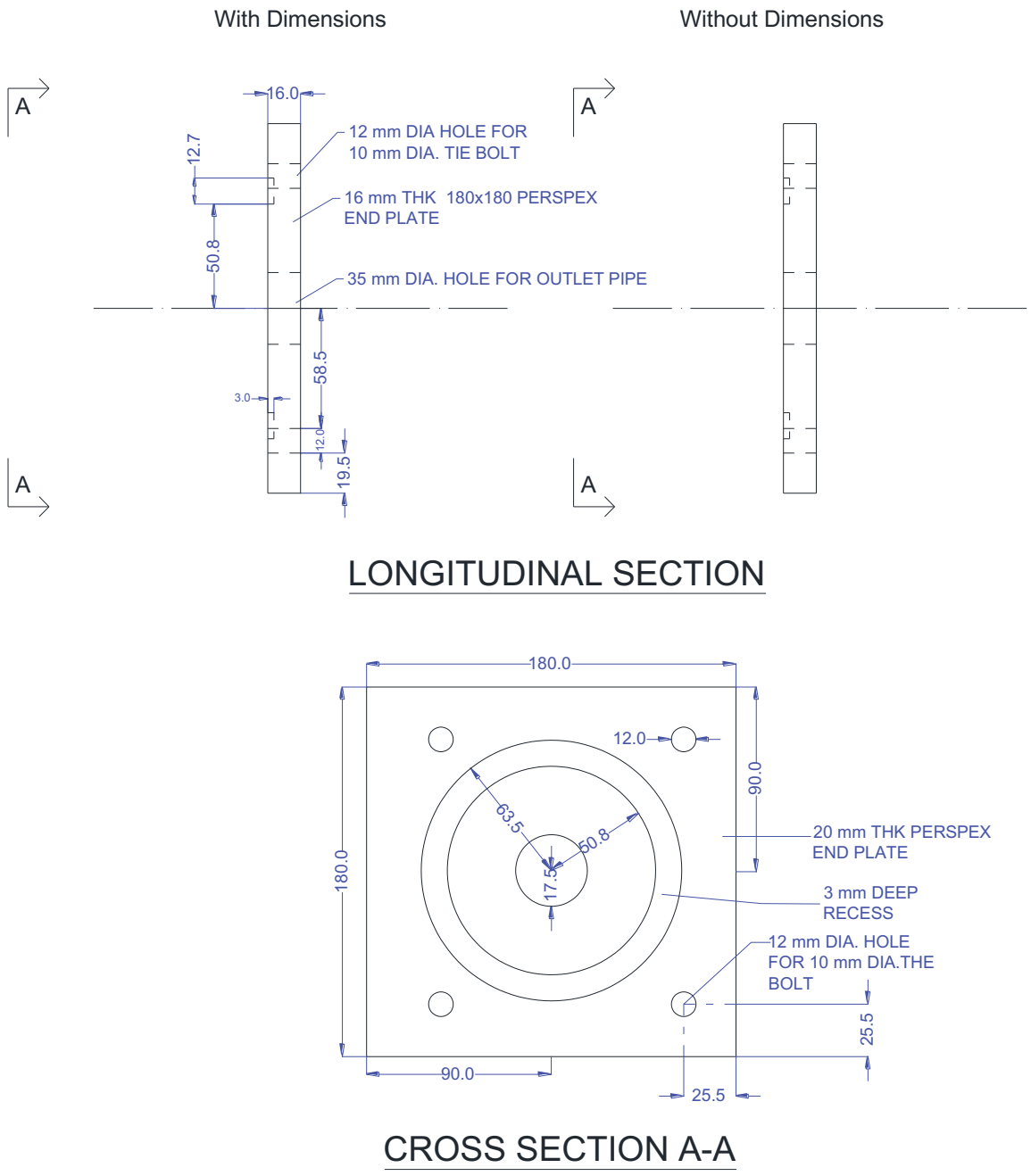

Figure 39. Drawings associated with the "Part A: End Plate" (all dimensions are in mm)

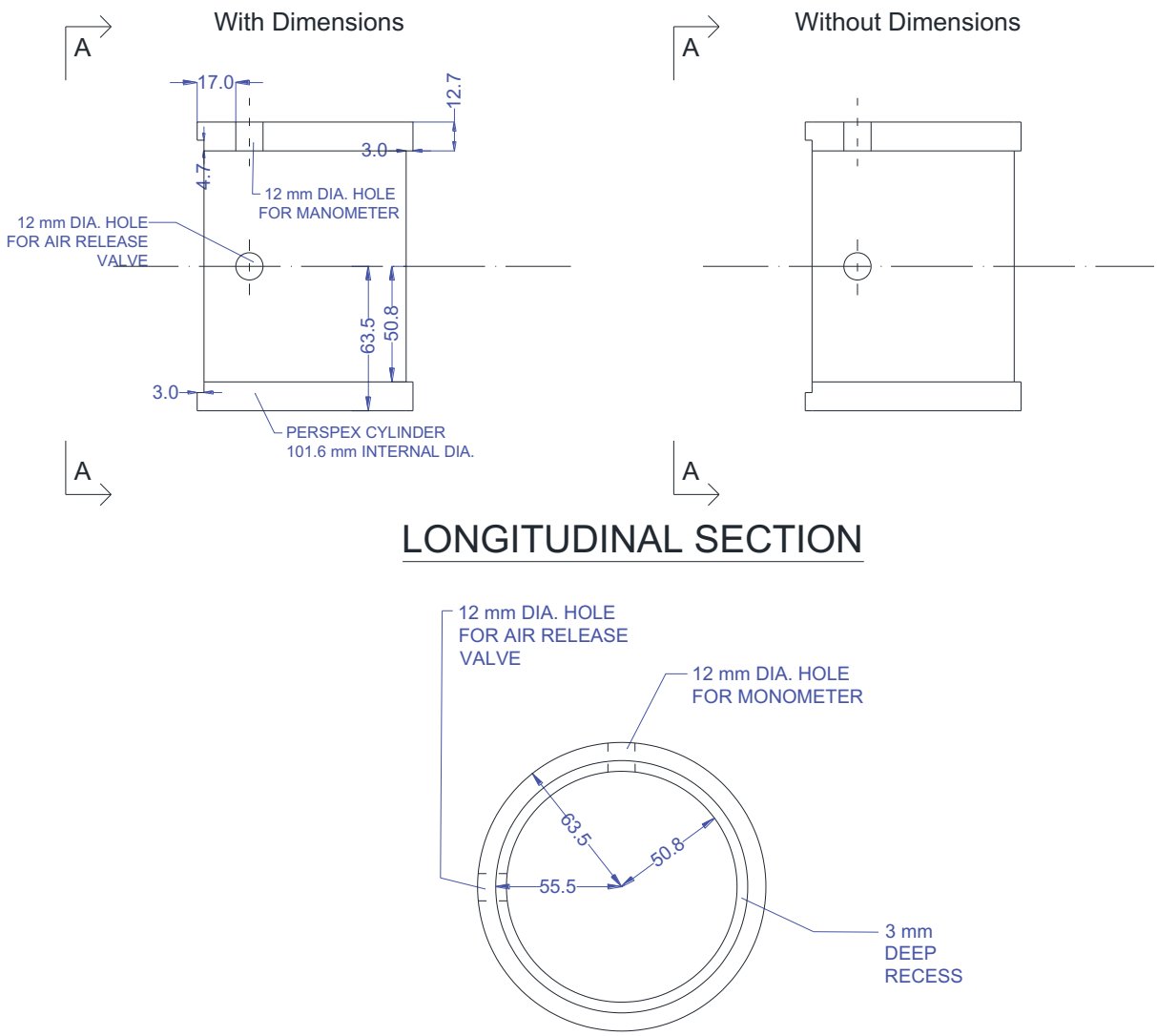

Figure 40. Drawings associated with the "Part B: Middle Cylinder" (all dimensions are in mm)

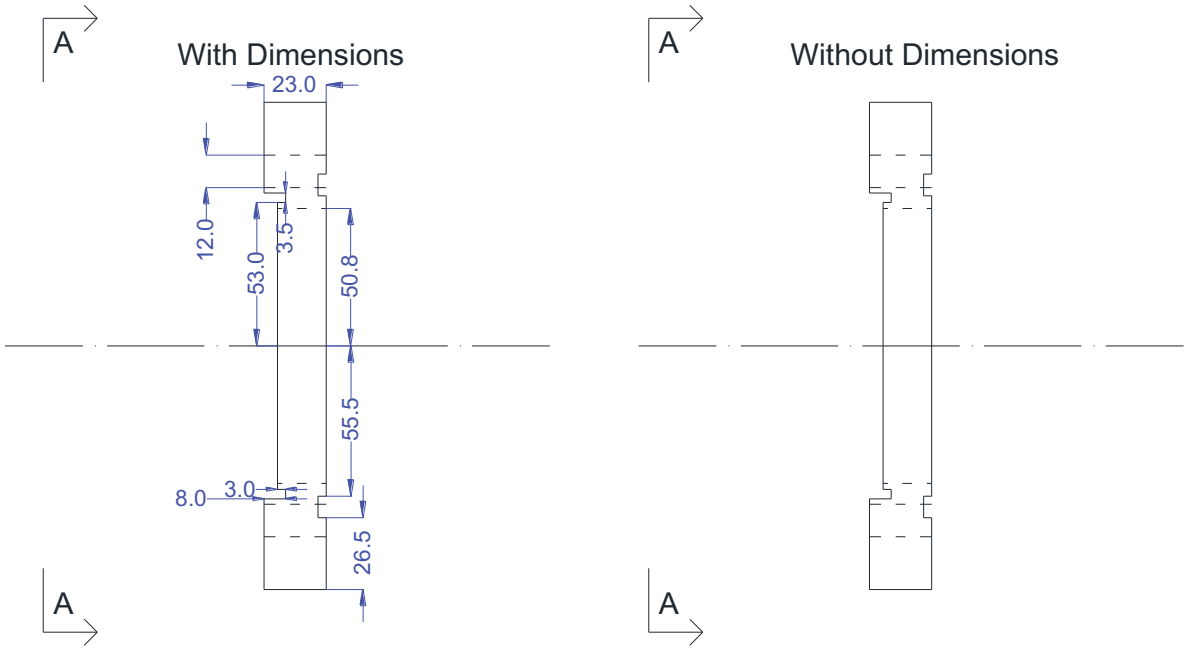

LONGITUDINAL SECTION

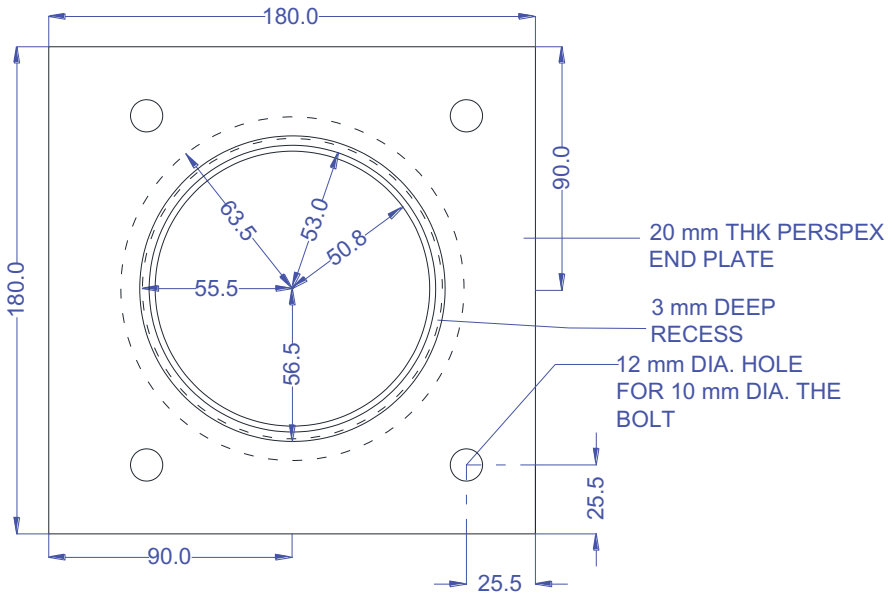

CROSS SECTION A-A

Figure 41. Drawings associated with the "Part C: Inlet Plate" (all dimensions are in mm)

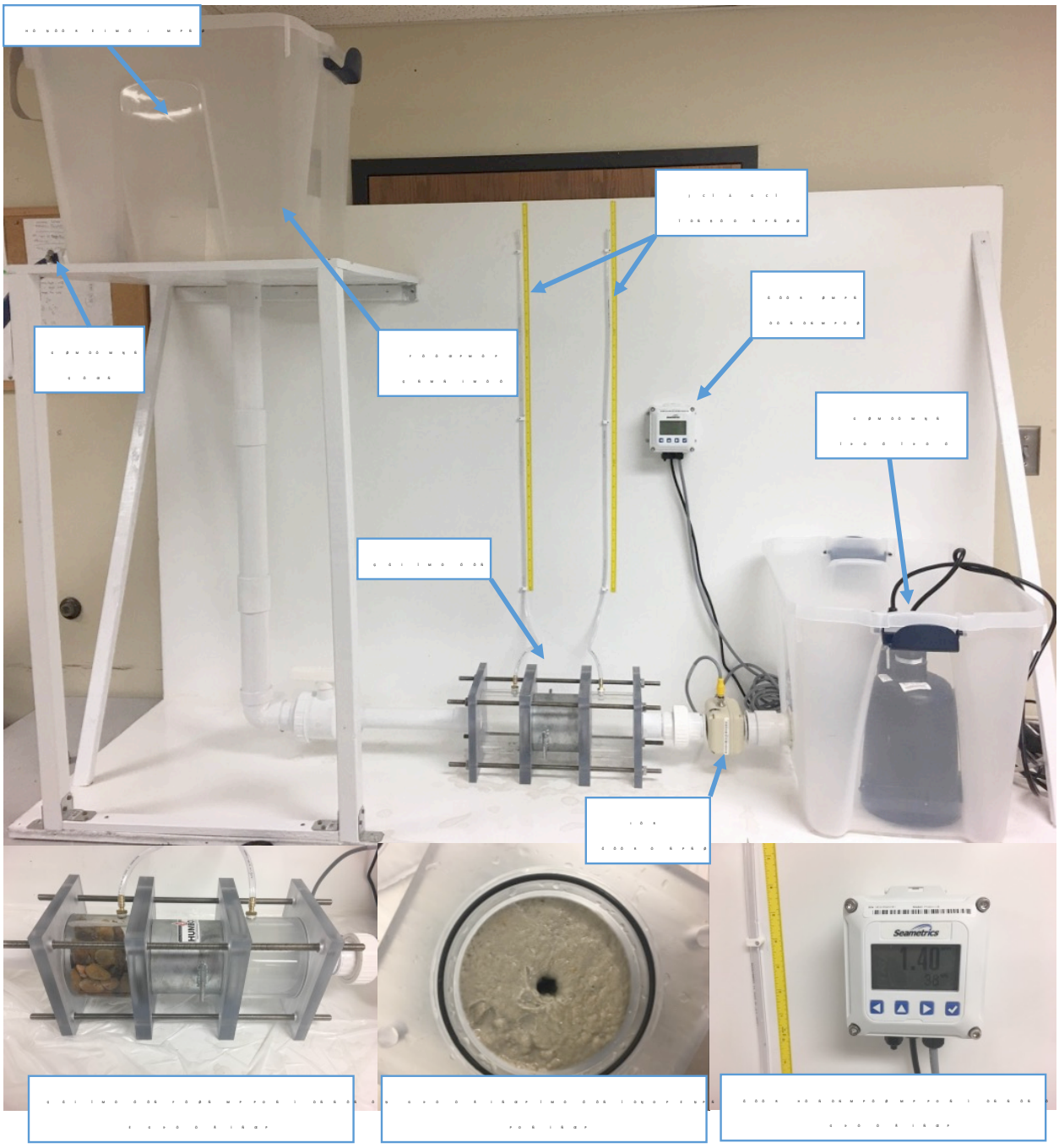

Figure 42. Photos taken from the HET assembly at Texas A&M University

4.1.2. *Construction of the Mini-JET Apparatus*

The core part of the mini JET device was obtained from Dr. Garey Fox, professor in the Biosystems and Agricultural Engineering Department at Oklahoma State University. The JET test

assembly was then constructed in the erosion lab at Texas A&M University (Figure 43). A couple of dummy tests were also conducted to ensure that there is no considerable leakage and hindrance with the testing process. Figure 43 shows some photos taken from the JET assembly with labels describing each piece.

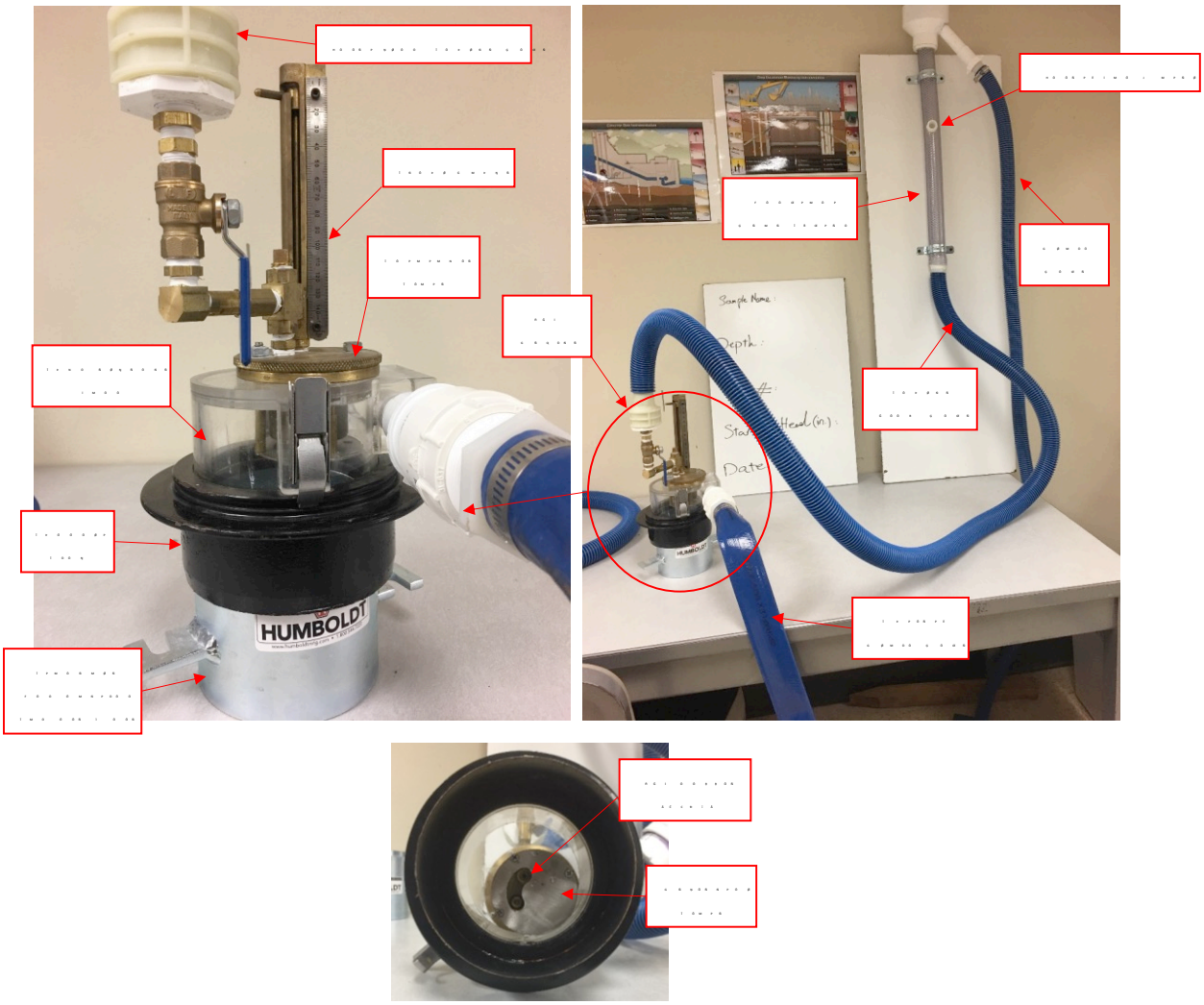

Figure 43. Photos taken from the JET assembly at Texas A&M University

4.1.3. *Refurbishment of the EFA machines and the TAMU Erosion Lab*

There are two EFAs in the TAMU Soil Erosion Laboratory. Both machines were repaired and upgraded for the second phase of the project. Figure 44 shows some photos of the erosion laboratory, the control desk, and the two EFAs. The difference between the two EFAs is the way the sample extrusion is controlled. In the EFA #1 shown in Figure 44, the test operator needs to extrude the sample from the tube manually by pushing the button on the control board of the EFA, while in the EFA #2 the extrusion is controlled through the desktop on the control desk; however, one of the operators still need to stand by the EFA to monitor if there is any scour on the sample. Figure 44 shows the general view of the erosion lab as well as the two EFA machines.

Figure 44. Erosion laboratory at Texas A&M University, showing the two EFAs and the control desk

4.2. Test Plan Matrix

As discussed earlier in Chapter 1, the Tasks 5 and 6 of this project are dedicated to the testing of different soil samples using various erosion testing devices. The majority of these erosion tests consists of laboratory tests using the devices developed in the soil erosion laboratory at Texas A&M University. The remaining are associated with the field tests which were conducted on the clay and sand sites located at the RELLIS Campus at Texas A&M University. A total 168 new erosion tests were planned to be performed during this project. Table 16 shows the experimental plan proposed for this project. A testing matrix was proposed in order to perform all erosion tests in accordance with the progress schedule timeline of the project. Table 17 shows the proposed testing matrix for this project.

Table 16. Experimental test plan proposed for this project

Table 17. Proposed testing matrix for this project

NCHRP Proj	24-43						
Research Ag	Texas A&M University System						
Laboratory L	Iman SHAFII						
FY	TIME FR	TASK	#	TARGET	Week 1 (9/29	Week 2 (10/7	Week 3 (10/14	Week 4 (10/22
201	September October	5		Perform erosion different device same prepare	1 EFA, 1 JET, 1 w/ soil prop Celnty	1 EFA, 1 JET, 1 w/ soil prop Celtt	1 EFA, 1 JET, 1 w/ soil prop Semtl	1 EFA, 1 JET, 1 w/ soil prop Semtie
				Percent complet	100	100	100	100
	TIME FR	TASK	#	TARGET	Week 1 (10/29	Week 2 (11/7	Week 3 (11/14	Week 4 (11/22
	October 3 November	5		Check repeatabi	1 EFA, 1 JET, 1 on same a Slaty	1 EFA, 1 JET, 1 on same a Silab	1 EFA, 1 JET, 1 on same a Sandb	1 EFA, 1 JET, 1 on same a Gravo
				Percent complet	100	100	100	100
	TIME FR	TASK	#	TARGET	Week 1 (11/29	Week 2 (12/7	Week 3 (12/14	Week 4 (12/22
	November Decembe	5		Organize field e demonstraation a	1 PET, (possibl on clay site in REL w/ associated so	1 PET, (possibl on sand site in RU Campus	1 BET, (possib on clay site in REL w/ associated so	1 BET, (possib on sand site in RU Campus
				Percent complet	100	100	100	100
FY	TIME FR	TASK	#	TARGET	Week 1 (12/2	Week 2 (1/5 t	Week 3 (1/14	Week 4 (1/22
	December January	6		Erosion tests to equations (14 clay sam	*Holidays (Chris*	1 EFA, 1 JET, 1 w/ soil prop Celntyie	1 EFA, 1 JET, 1 w/ soil prop Celtyie	1 EFA, 1 JET, 1 w/ soil prop Celntyie
				Percent complet	100	100	100	100
	TIME FR	TASK	#	TARGET	Week 1 (1/29	Week 2 (2/7 t	Week 3 (2/14	Week 4 (2/22
	January 3 February	6		Erosion tests to equations (14 clay sam	1 EFA, 1 JET, 1 w/ soil prop Celntyie	1 EFA, 1 JET, 1 w/ soil prop Celtyie	1 EFA, 1 JET, 1 w/ soil prop Celntyie	1 EFA, 1 JET, 1 w/ soil prop Celntyie
				Percent complet	100	100	100	100
	TIME FR	TASK	#	TARGET	Week 1 (2/29	Week 2 (3/7 t	Week 3 (3/13	Week 4 (3/19
	February March 3	6		Erosion tests to equations (14 clay sam	1 EFA, 1 JET, 1 w/ soil prop Celntyie	1 EFA, 1 JET, 1 w/ soil prop Celntyie	*Holidays (Spri*	1 EFA, 1 JET, 1 w/ soil prop Celtyie
				Percent complet	100	100	100	100
	TIME FR	TASK	#	TARGET	Week 1 (3/29	Week 2 (4/7 t	Week 3 (4/14	Week 4 (4/22
	March 30 April 30	6		Erosion tests to equations (14 clay sam	1 EFA, 1 JET, 1 w/ soil prop Celntyie	1 EFA, 1 JET, 1 w/ soil prop Celntyie	1 EFA, 1 JET, 1 w/ soil prop Celntyie	1 EFA, 1 JET, 1 w/ soil prop Celntyie
				Percent complet	100	100	100	100
	TIME FR	TASK	#	TARGET	Week 1 (4/29	Week 2 (5/7 t	Week 3 (5/14	Week 4 (5/22
201	April 30t May 30t	6		Erosion tests to equations (8 silt sampl	1 EFA, 1 JET, 1 w/ soil prop Siltie	1 EFA, 1 JET, 1 w/ soil prop Siltie	1 EFA, 1 JET, 1 w/ soil prop Siltie	1 EFA, 1 JET, 1 w/ soil prop Siltie
				Percent complet	100	100	100	100
	TIME FR	TASK	#	TARGET	Week 1 (5/29	Week 2 (6/7 t	Week 3 (6/14	Week 4 (6/22
	May 30th June 30	6		Erosion tests to equations (8 silt sampl	1 EFA, 1 JET, 1 w/ soil prop Siltie	1 EFA, 1 JET, 1 w/ soil prop Siltie	1 EFA, 1 JET, 1 w/ soil prop Siltie	1 EFA, 1 JET, 1 w/ soil prop Siltie
				Percent complet	100	100	100	100
	TIME FR	TASK	#	TARGET	Week 1 (6/29	Week 2 (7/7 t	Week 3 (7/14	Week 4 (7/22
	June 30t July 30t	6		Erosion tests to equations (6 sand samp	1 EFA, 1 JET, 1 w/ soil prop Semtie	1 EFA, 1 JET, 1 w/ soil prop Semtie	1 EFA, 1 JET, 1 w/ soil prop Semtie	1 EFA, 1 JET, 1 w/ soil prop Semtie
				Percent complet	100	100	100	100
	TIME FR	TASK	#	TARGET	Week 1 (7/29	Week 2 (8/7 t	Week 3 (8/14	Week 4 (8/22
	July 30th August 3	6		Erosion tests to equations (finish 6 sands, s	1 EFA, 1 JET, 1 w/ soil prop Semtie	1 EFA, 1 JET, 1 w/ soil prop Semtie	1 EFA, 1 JET, 1 w/ soil prop Gtiee	1 EFA, 1 JET, 1 w/ soil prop Gtiee
				Percent complet	100	100	100	100
	TIME FR	TASK	#	TARGET	Week 1 (8/29	Week 2 (9/7 t		
	July 30th August 3	6		Erosion tests to equations (4 gravel sam	1 EFA, 1 JET, 1 w/ soil prop Gtiee	1 EFA, 1 JET, 1 w/ soil prop Gtiee		
				Percent complet	100	100		

4.3. Results of Erosion Tests

This section presents the results of all the erosion tests performed during Tasks 5 and 6 of this project. As discussed in the previous section, the used erosion test devices include EFA, JET, HET, PET, and BET. Also, the detailed information on the geotechnical properties of all tested samples are presented in Section 4.4.

4.3.1. *Erosion Tests Performed During Task 5*

As discussed in Chapter 1, Task 5 was dedicated to accomplishing two major missions:

1) Testing the same soil with different erosion testing devices (i.e. EFA, JET, HET, PET) to evaluate the repeatability of the results for each erosion test.
2) Organizing field demonstration tests including the PET, and the BET.

For the purpose of ensuring the repeatability of the erosion tests, all four types of soils (i.e. gravel, sand, silt, clay) are prepared and tested using EFA, JET, HET, and PET. Table 18 shows the primary description of the soils during Task 5. Thirty-two samples (Table 18) were tested. The first letter in the sample name refers to the first letter of the soil type. The second letter refers to the first letter of each apparatus type. The number at the end of the sample name is "1" if the sample is tested for the first time, and "2" if it is tested for the second time to ensure repeatability. For example, CJ-2 means that the sample is a clay which is tested by JET for the second time to evaluate the repeatability of this device.

Table 18. Description of the soils used during Task 5

Soil Type	Description	Erosion Test	Sample Name	Target Water Content (%)	Target Wet Unit Weight (kN/m^3)
Gravel	Pea Gravel from *Lowes*	HET JET EFA PET	GH-1 & GH-2 GJ-1 & GJ-2 GE-1 & GE-2 GP-1 & GP-2	10%	20
Sand	Mixture of (20% Bentonite+ 80% Silica Sand 60-80) from *Armadillo Clay & Supplies Co.* in Austin	HET JET EFA PET	SH-1 & SH-2 SJ-1 & SJ-2 SE-1 & SE-2 SP-1 & SP-2	10%	19
Silt	Porcelain Grolleg Kaolin from *Armadillo Clay & Supplies Co.* in Austin	HET JET EFA PET	MH-1 & MH-2 MJ-1 & MJ-2 ME-1 & ME-2 MP-1 & MP-2	18%	16
Clay	Mixture of (60% Porcelain Grolleg Kaolin + 40% Bentonite) from *Armadillo Clay & Supplies Co.* in Austin	HET JET EFA PET	CH-1 & CH-2 CJ-1 & CJ-2 CE-1 & CE-2 CP-1 & CP-2	15%	14

The results of the work done to check the repeatability of erosion tests for each sample is described in the following sections:

1. Ensuring repeatability of the Erosion Function Apparatus (EFA)
    1.1. Ensuring the repeatability of EFA for the clay sample
    1.2. Ensuring the repeatability of EFA for the silt sample
    1.3. Ensuring the repeatability of EFA for the sand sample
    1.4. Ensuring the repeatability of EFA for the gravel sample
2. Ensuring repeatability of the Pocket Erodometer Test (PET)
    2.1. Ensuring the repeatability of PET for the clay sample
    2.2. Ensuring the repeatability of PET for the silt sample
    2.3. Ensuring the repeatability of PET for the sand sample

2.4. Ensuring the repeatability of PET for the gravel sample

3. Ensuring repeatability of the Jet Erosion Test (JET)

3.1. Ensuring the repeatability of JET for the clay sample

3.2. Ensuring the repeatability of JET for the silt sample

3.3. Ensuring the repeatability of JET for the sand sample

3.4. Ensuring the repeatability of JET for the gravel sample

4. Ensuring repeatability of the Hole Erosion Test (HET)

4.1. Ensuring the repeatability of HET for the clay sample

4.2. Ensuring the repeatability of HET for the silt sample

4.3. Ensuring the repeatability of HET for the sand sample

4.4. Ensuring the repeatability of HET for the gravel sample

4.3.1.1. Ensuring the repeatability of the EFA

Clay Samples (CE-1 & CE-2)

The prepared clay samples were a mixture of 60% Porcelain Grolleg Kaolin plus 40% Bentonite purchased from Armadillo Clay & Supplies Co. in Austin. Both samples were remolded and compacted to re-produce the target condition in Table 18. Results of the EFA tests on CE-1 and CE-2 are presented in Figure 45 and Figure 46 against velocity and shear stress, respectively. Both samples can be categorized as Medium Erodibility Category (III). The critical velocities for CE-1 and CE-2 are 1.18 and 1.04 m/s, respectively. The critical shear stress values are also measured as 7.59 and 5.93 Pa for CE-1 and CE-2, respectively. The results of each EFA test is also presented in the format of an "EFA result spreadsheet" in Appendix A. Figure 47 shows an example of the EFA result spreadsheet for the sample CE-1.

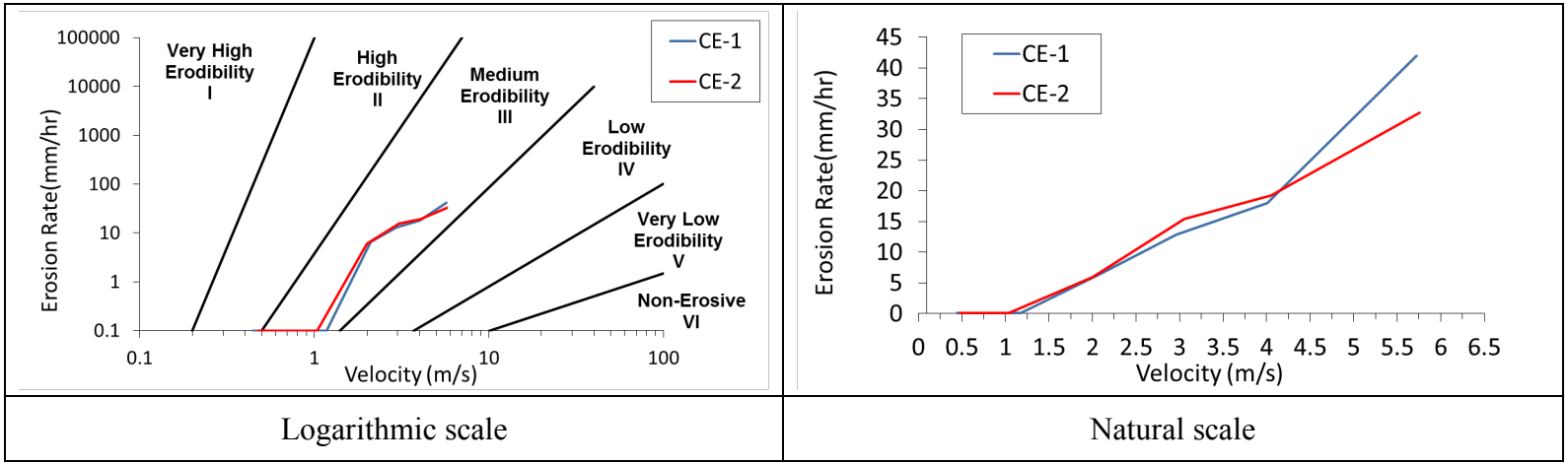

Figure 45. EFA test results based on velocity for ensuring the repeatability of the EFA on clay samples

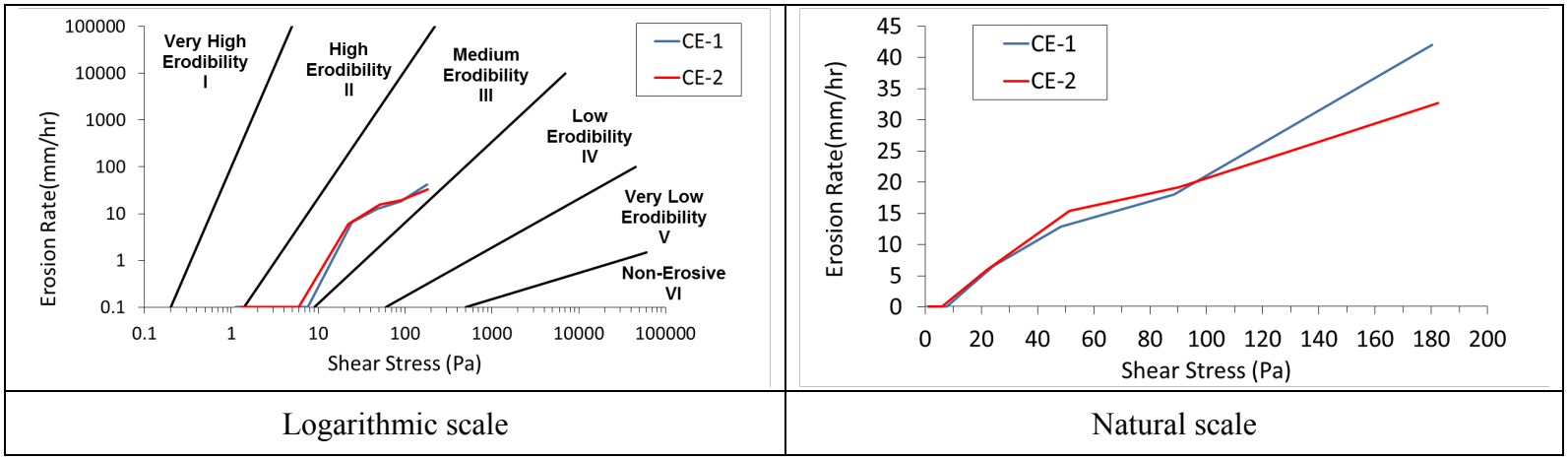

Figure 46. EFA test results based on shear stress for ensuring the repeatability of the EFA on clay samples

Silt Samples (ME-1 & ME-2)

Silt samples were 100% Porcelain Grolleg Kaolin purchased from Armadillo Clay & Supplies Co. in Austin. Both samples were remolded and compacted to re-produce the target condition described in Table 18. Results of the EFA tests on ME-1 and ME-2 are presented in Figure 48 and Figure 49 against velocity and shear stress, respectively. Both samples can be categorized as in the High to Medium Erodibility Category (II to III). The critical velocities for ME-1 and ME-2 are 0.1 m/s. The critical shear stress values are also measured as 0.1 Pa.

Velocity	Equivalent Roughness	Reynolds Number	Friction Factor	Shear Stress	Erosion Reading	Test Time	Erosion Rate
m/sec	mm	R_e	Moody chart	P_a	mm	sec	mm/hr
0.445	1.000	27011	0.045	1.113	0	570	0.000
1.175	1.000	71359	0.044	7.598	0	840	0.000
2.102	1.000	127626	0.044	24.303	1	550.002	6.545
2.962	1.000	179859	0.044	48.266	2	559.98	12.858
4.011	1.000	243503	0.044	88.469	3	600	18.000
5.724	1.000	347528	0.044	180.202	7	600	42.000

Velocity(m/sec)	0.445	1.175	2.102	2.962	4.011	5.724
Shear stress(P_a)	1.113	7.598	24.303	48.266	88.469	180.202
Erosion Rate(mm/hr)	0.100	0.100	6.545	12.858	18.000	42.000

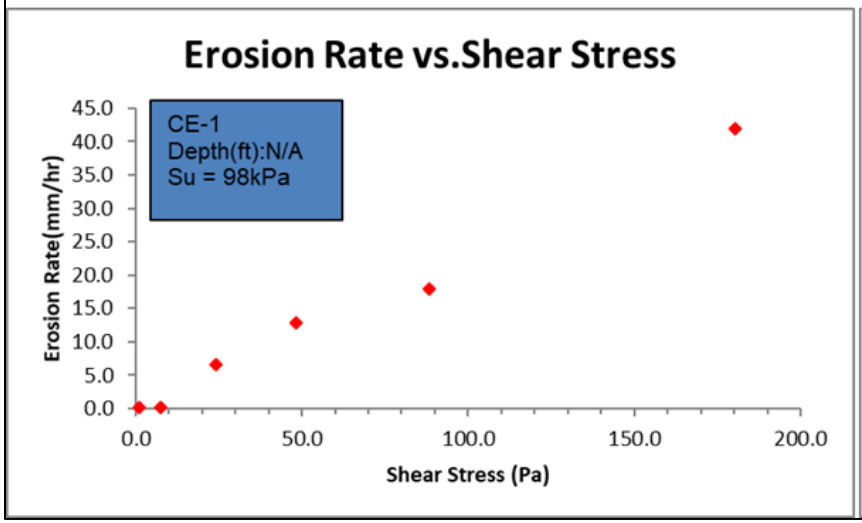

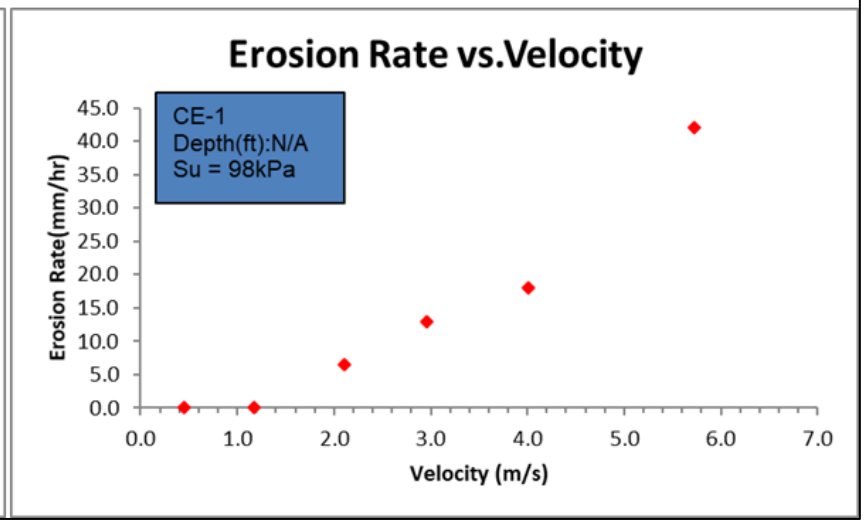

Figure 47. EFA result spreadsheet for CE-1

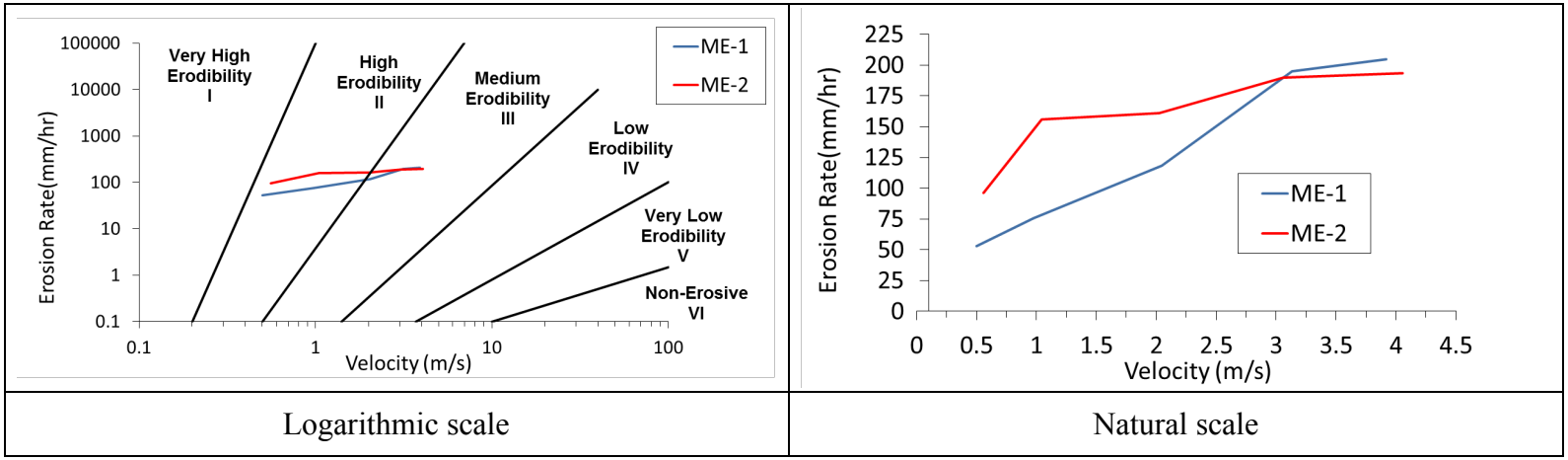

Figure 48. EFA test results based on velocity for ensuring the repeatability of the EFA on silt samples

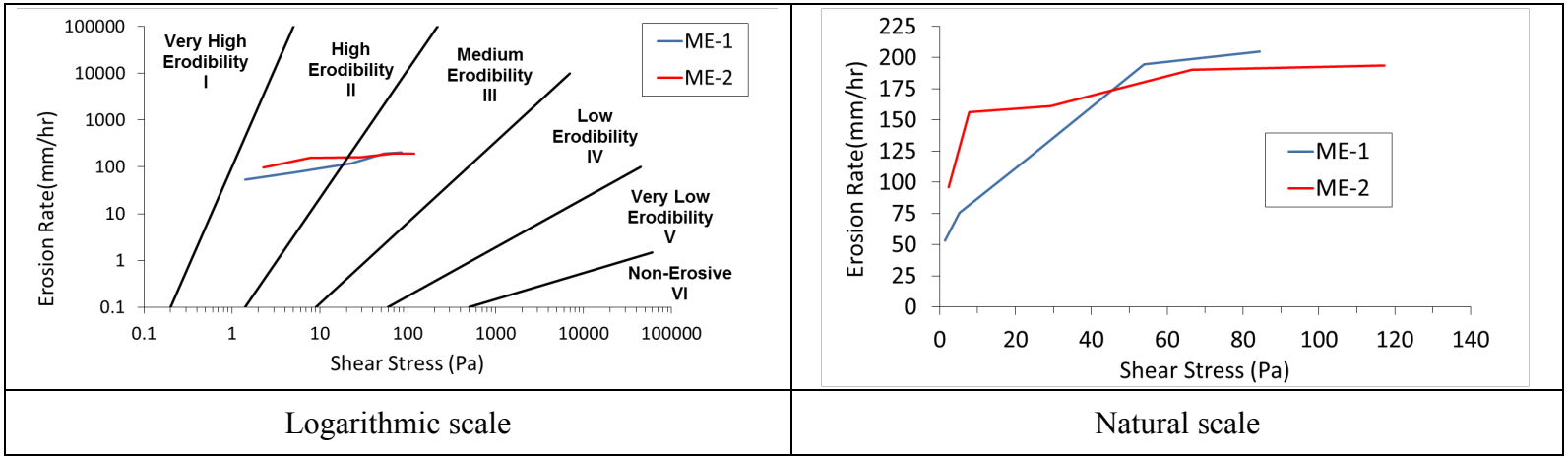

Figure 49. EFA test results based on shear stress for ensuring the repeatability of the EFA on clay samples

Sand Samples

Sand samples were a mixture of (20% Bentonite+ 80% Silica Sand 60-80) both purchased from Armadillo Clay & Supplies Co. in Austin. Both samples were remolded and compacted to re-produce the target condition described in Table 18. Results of the EFA tests on SE-1 and SE-2 are presented in Figure 50 and Figure 51 against velocity and shear stress, respectively. Both samples can be categorized as Medium Erodibility Category (III).

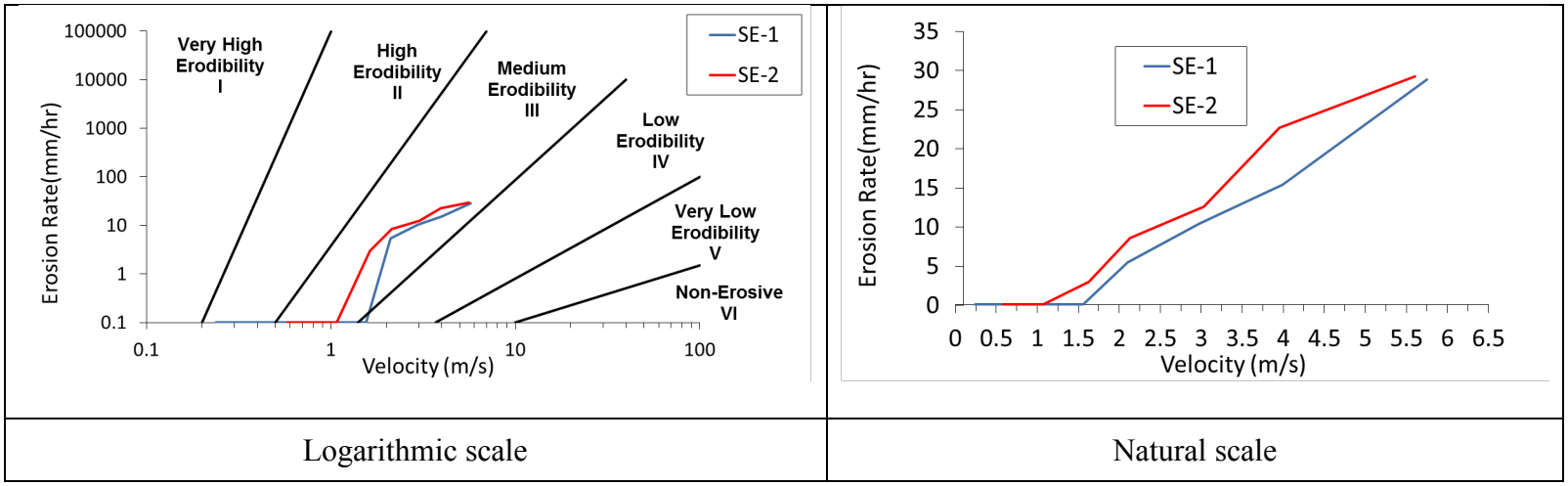

Logarithmic scale | Natural scale

Figure 50. EFA test results based on velocity for ensuring the repeatability of the EFA on sand samples

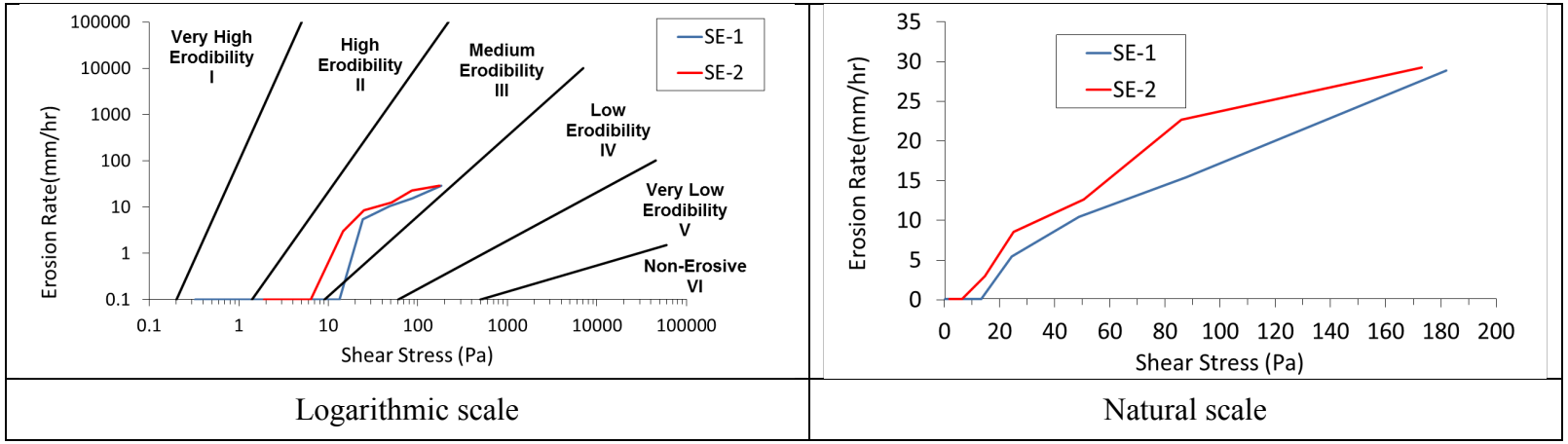

Figure 51. EFA test results based on shear stress for ensuring the repeatability of the EFA on sand samples

Gravel Samples

Gravel samples were Pea Gravel purchased from Lowes in College Station. Both samples were remolded and compacted to reproduce the target condition described in Table 18. Results of the EFA tests on GE-1 and GE-2 are presented in Figure 52 and Figure 53 against velocity and shear stress, respectively. Both samples can be categorized as in the Medium to low Erodibility Category (III to IV). The critical velocities for GE-1 and GE-2 are 1.44 and 1.5 m/s. The critical shear stress values are also measured as 17.63 and 19.13 Pa.

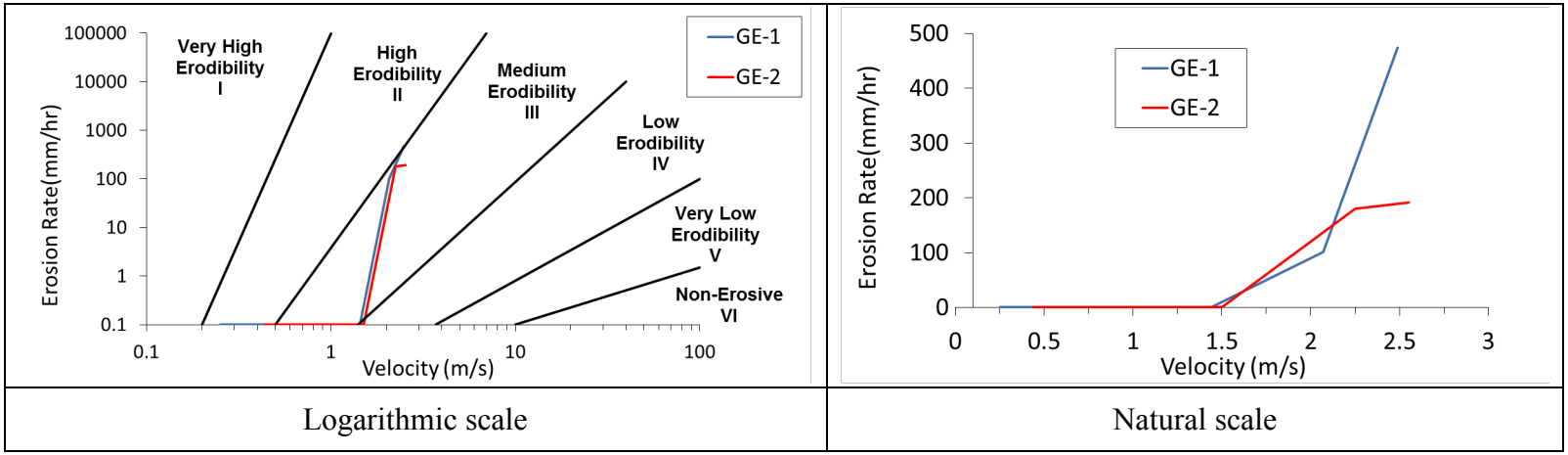

Figure 52. EFA test results based on velocity for ensuring the repeatability of the EFA on gravel samples

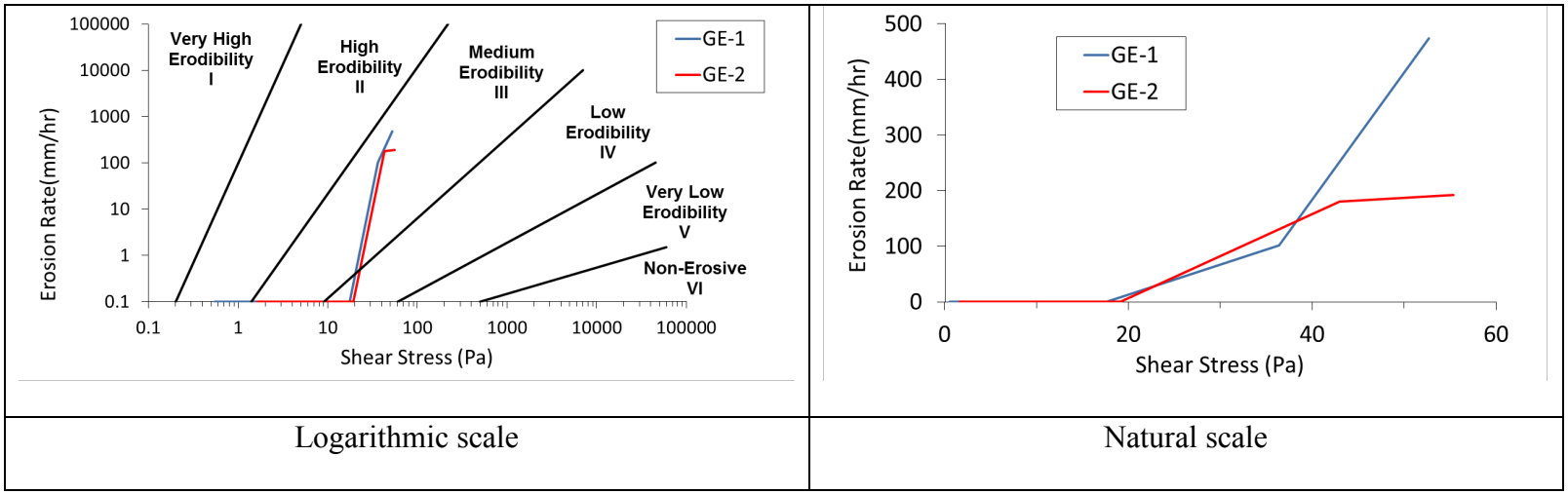

Figure 53. EFA test results based on shear stress for ensuring the repeatability of the EFA on gravel samples

4.3.1.2.Ensuring the repeatability of the PET

The pocket erodometer test (PET) was performed on the top surface of each sample prior to each EFA test. As discussed earlier in Chapter 2, the PET consists of applying 20 times a jet of water at 8 m/s by squeezing the trigger of a water pistol positioned 50 mm from the sample face. The jet hits the sample surface at the same location at one end of the sample. The depth of the hole formed on the sample surface is then measured and entered in the PET erosion categories chart. The PET was conducted two times at different location on the top end of each sample. Results of the PET test are shown in Table 19. Results show a reasonable repeatability for each soil type. It is worth noting that performing the PET on gravel samples is not feasible.

Table 19. Results of the Pocket Erodometer Test (PET) on each sample

Clay Samples		**Silt Samples**		**Sand Samples**		**Gravel Samples**	
CP-1	CP-2	MP-1	MP-2	SP-1	SP-2	GP-1	GP-2
2.11 mm	3.0 mm	5.33 mm	5.3 mm	5.4 mm	4.22 mm	Not Applicable	

As discussed in Chapter 2, Results of the PET can be associated with the erosion category chart (Figure 54). All the points fall the Medium Erodibility (III) category on this chart. Comparing this result with the results of EFA test shows a compliance between the two tests.

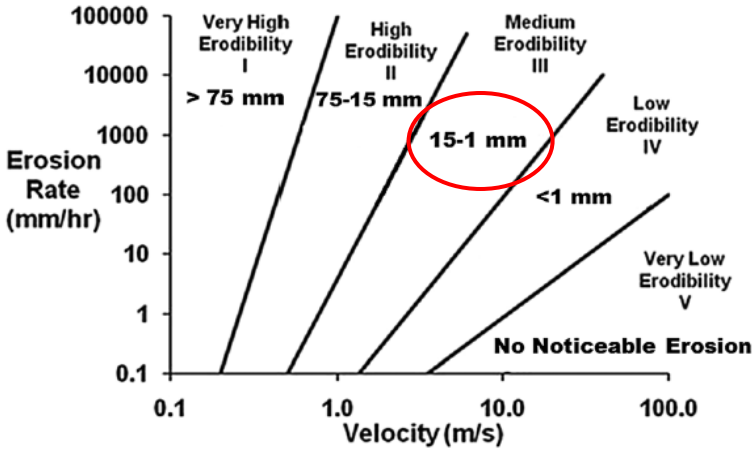

Figure 54. Erosion categories for the tested samples according to the PET Category Chart

4.3.1.3.Ensuring the repeatability of the HET

Clay Samples (CH-1 & CH-2)

As said earlier, clay samples were a mixture of 60% Porcelain Grolleg Kaolin plus 40% Bentonite purchased from Armadillo Clay & Supplies Co. in Austin. Results of the HETs on CH-1 and CH-2 are presented in Figure 55 and Figure 56, respectively. Please note that the HET results are plotted as erosion rate (mm/hr) against hydraulic shear stress. HET plots include several fluctuations due to the errors associated with the constant head system both upstream and downstream. Note that Wan and Fell (2002) had the same type of curves and fitted a best line on each plot and estimated the critical shear stress in that fashion. The critical shear stress values are also measured as 70 and 67 Pa for CH-1 and CH-2, respectively. As explained in Chapter 2, HET results start with a decrease in erosion rate with an increase in shear stress; thereafter, both erosion rate and shear stress start increasing. The first part of the curve is typically attributed to the thickness of the disturbed zone due to drilling the 6 mm hole in the center of the sample. The second part of the curve corresponds to the erosion of the undisturbed soil. The erosion part of the

CH-1 and CH-2 test result curves were plotted in the erosion category chart. It can be concluded that both samples place in the Low Erodibility category (IV) (Figure 57). The main reason that the curves are in two different shear stress ranges is that the initial head condition for CH-1 and CH-2 were different (815 mm and 360 mm, respectively); however, tracking the erosion part of the curves both cross the horizontal axis at a critical shear stress of 70 Pa. The results of all HET tests are also presented in the format of an "HET result spreadsheet" in Appendix A. Figure 58 shows an example of the HET result spreadsheet for the sample CH-1.

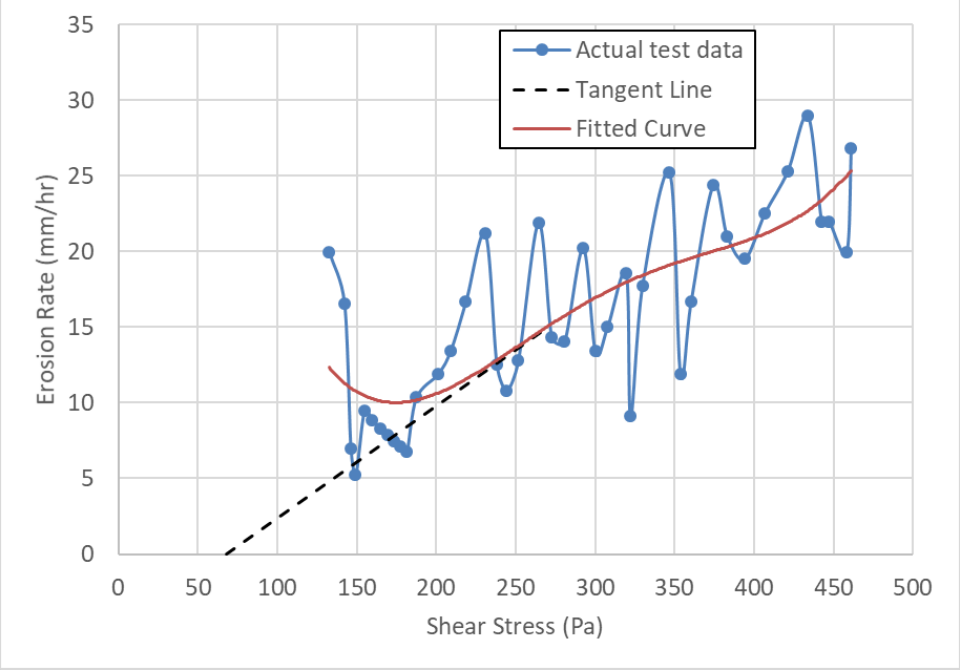

Figure 55. HET data for CH-1

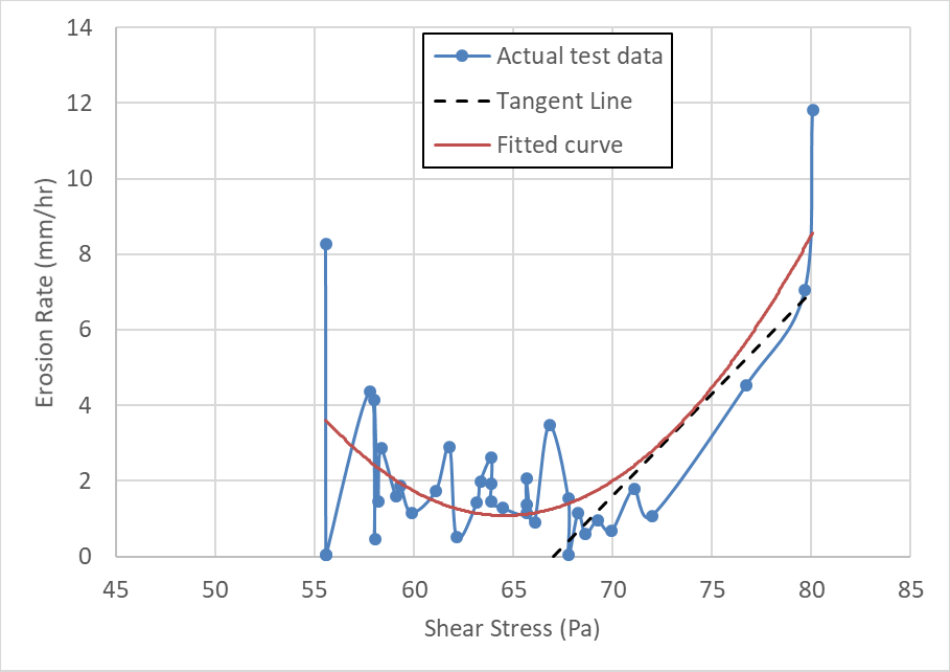

Figure 56. HET data for CH-2

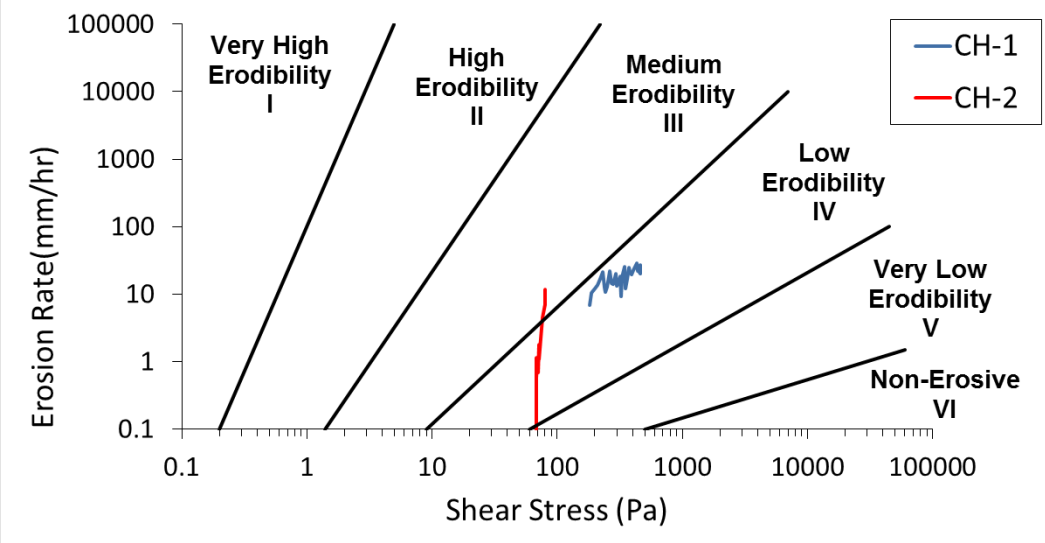

Figure 57. Erosion part of the clay HET curves plotted on the Erosion Category Chart

Silt Samples (MH-1 & MH-2)

As said earlier, silt samples were 100% Porcelain Grolleg Kaolin purchased from Armadillo Clay & Supplies Co. in Austin. Results of the HETs on MH-1 and MH-2 are presented in Figure 59 and Figure 60, respectively. The critical shear stress values are also measured as 50 and 46 Pa for CH-1 and CH-2, respectively. The erosion functions of MH-1 and MH-2 were plotted in the erosion category chart. It can be seen that erosion curves fall in the Medium Erodibility category (III) (Figure 61). The initial head was 330 and 321 mm for MH-1 and MH-2, respectively.

Time	Time	Flowrate		U/S Tube	D/S Tube	Pressure Differential	
(mins)	(s)	(gpm)	(l/min)	in	in	(in)	(mm)
0.00	0	0.54	2.04	32.0	0.00	32.0	813
1.00	60	0.54	2.04	32.0	0.00	32.0	813
2.00	120	0.55	2.08	32.0	0.00	32.0	813
3.00	180	0.55	2.08	32.0	0.00	32.0	813
4.00	240	0.55	2.08	32.0	0.00	32.0	813
5.00	300	0.55	2.08	32.0	0.00	32.0	813
6.00	360	0.55	2.08	32.0	0.00	32.0	813
7.00	420	0.55	2.08	32.0	0.00	32.0	813
8.00	480	0.55	2.08	32.0	0.00	32.0	813
9.00	540	0.55	2.08	32.0	0.00	32.0	813
10.00	600	0.55	2.08	32.0	0.00	32.0	813
11.00	660	0.55	2.08	32.0	0.00	32.0	813
12.00	720	0.57	2.16	32.0	0.00	32.0	813
14.00	840	0.63	2.38	32.0	0.00	32.0	813
15.00	900	0.67	2.54	32.0	0.00	32.0	813
16.00	960	0.73	2.76	32.0	0.00	32.0	813
17.00	1020	0.82	3.10	32.0	0.00	32.0	813
18.00	1080	0.86	3.26	32.0	0.00	32.0	813
19.00	1140	0.89	3.37	32.0	0.00	32.0	813
20.00	1200	0.95	3.60	32.0	0.00	32.0	813
21.00	1260	1.05	3.97	32.0	0.00	32.0	813
22.00	1320	1.11	4.20	32.0	0.00	32.0	813
23.00	1380	1.17	4.43	32.0	0.00	32.0	813
24.00	1440	1.27	4.81	32.0	0.00	32.0	813
25.00	1500	1.33	5.03	32.0	0.00	32.0	813
26.00	1560	1.4	5.30	31.9	0.00	31.9	810
27.00	1620	1.5	5.68	32.0	0.00	32.0	813
28.00	1680	1.53	5.79	31.8	0.00	31.8	806
29.00	1740	1.62	6.13	31.5	0.00	31.5	800
30.00	1800	1.78	6.74	31.8	0.00	31.8	806
31.00	1860	1.84	6.97	31.8	0.00	31.8	806
32.00	1920	1.93	7.31	31.5	0.00	31.5	800
33.00	1980	2.09	7.91	31.5	0.00	31.5	800
34.00	2040	2.22	8.40	31.3	0.00	31.3	794
35.00	2100	2.35	8.90	31.3	0.00	31.3	794
36.00	2160	2.51	9.50	31.3	0.00	31.3	794
37.00	2220	2.7	10.22	31.3	0.00	31.3	794
38.00	2280	2.92	11.05	31.0	0.00	31.0	787
39.00	2340	3.08	11.66	31.0	0.25	30.8	781
40.00	2400	3.23	12.23	30.8	0.50	30.3	768
41.00	2460	3.39	12.83	30.8	0.50	30.3	768
42.00	2520	3.58	13.55	30.5	1.00	29.5	749

Sample length	Gradient	Flow rate	Friction Factor		Hole diameter (m)		Reynold's No.		Diameter
			If Laminar	If Turbulent	If Laminar	If Turbulent	If Laminar	If Turbulent	
L (mm)	S	Q (m3/s)	f	f	D	D	Re(l)	Re(t)	D (m)
115	7.067826087	3.4069E-05	136.7985	154.5297	0.0070000	0.0070000	6005.940	6005.940	0.007
115	7.067826087	3.4069E-05	1.6541E+02	2.4342E+02	0.0074575	0.0076659	5637.470	5484.198	0.007665949
115	7.067826087	3.4700E-05	1.9403E+02	3.3230E+02	0.0079132	0.0082185	5411.261	5210.237	0.008218461
115	7.067826087	3.4700E-05	2.2264E+02	4.2119E+02	0.0082845	0.0086175	5168.727	4968.996	0.008450962
115	7.067826087	3.4700E-05	2.5126E+02	5.1008E+02	0.0086252	0.0089539	4964.550	4782.303	0.008625178
115	7.067826087	3.4700E-05	2.7987E+02	5.9897E+02	0.0089409	0.0092462	4789.235	4631.100	0.008940912
115	7.067826087	3.4700E-05	3.0849E+02	6.8785E+02	0.0092358	0.0095057	4636.323	4504.695	0.009235795
115	7.067826087	3.4700E-05	3.3711E+02	7.7674E+02	0.0095130	0.0097395	4501.240	4396.523	0.009512962
115	7.067826087	3.4700E-05	3.6572E+02	8.6563E+02	0.0097749	0.0099529	4380.640	4302.276	0.009774856
115	7.067826087	3.4700E-05	3.9434E+02	9.5452E+02	0.0100234	0.0101494	4272.007	4218.985	0.010023421
115	7.067826087	3.4700E-05	4.2295E+02	1.0434E+03	0.0102602	0.0103317	4173.407	4144.519	0.010260234
115	7.067826087	3.4700E-05	4.5157E+02	1.1323E+03	0.0104866	0.0105021	4083.321	4077.303	0.010486593
115	7.067826087	3.5961E-05	4.8018E+02	1.2212E+03	0.0108318	0.0108154	4096.947	4103.138	0.010831779
115	7.067826087	3.9747E-05	5.3741E+02	1.3990E+03	0.0116276	0.0115674	4218.294	4240.243	0.011627571
115	7.067826087	4.2270E-05	5.6603E+02	1.4878E+03	0.0120756	0.0120027	4319.661	4345.909	0.012075647
115	7.067826087	4.6056E-05	5.9464E+02	1.5767E+03	0.0126318	0.0125666	4499.271	4522.613	0.012631821
115	7.067826087	5.1734E-05	6.2326E+02	1.6656E+03	0.0133383	0.0133100	4786.289	4796.455	0.013338291
115	7.067826087	5.4258E-05	6.5187E+02	1.7545E+03	0.0137560	0.0137078	4867.324	4884.446	0.013756042
115	7.067826087	5.6150E-05	6.8049E+02	1.8434E+03	0.0141149	0.0140352	4909.064	4936.937	0.01411486
115	7.067826087	5.9936E-05	7.0910E+02	1.9323E+03	0.0146246	0.0145426	5057.371	5085.894	0.014542584
115	7.067826087	6.6245E-05	7.3772E+02	2.0212E+03	0.0153214	0.0152734	5335.497	5352.298	0.015273351
115	7.067826087	7.0030E-05	7.6633E+02	2.1101E+03	0.0158071	0.0157517	5467.073	5486.333	0.015751651
115	7.067826087	7.3815E-05	7.9495E+02	2.1989E+03	0.0162848	0.0162202	5593.578	5615.855	0.016220165
115	7.067826087	8.0125E-05	8.2356E+02	2.2878E+03	0.0169345	0.0168945	5838.691	5852.543	0.016894462
115	7.067826087	8.3910E-05	8.5218E+02	2.3767E+03	0.0173940	0.0173410	5953.005	5971.214	0.017341007
115	7.04573913	8.8326E-05	8.8080E+02	2.4656E+03	0.0179085	0.0178421	6086.294	6108.962	0.017842098
115	7.067826087	9.4635E-05	9.0941E+02	2.5545E+03	0.0185022	0.0184602	6311.799	6326.171	0.018460165
115	7.012608696	9.6528E-05	9.3803E+02	2.6434E+03	0.0188673	0.0187641	6313.443	6348.174	0.018764106
115	6.957391304	1.0221E-04	9.6664E+02	2.7323E+03	0.0194751	0.0193560	6476.207	6516.038	0.019356047
115	7.012608696	1.1230E-04	9.9526E+02	2.8212E+03	0.0202392	0.0201963	6847.182	6861.712	0.020196345
115	7.012608696	1.1609E-04	1.0239E+03	2.9100E+03	0.0206584	0.0205933	6934.369	6956.274	0.020593321
115	6.957391304	1.2176E-04	1.0525E+03	2.9989E+03	0.0212395	0.0211506	7074.544	7104.285	0.021150577
115	6.957391304	1.3186E-04	1.0811E+03	3.0878E+03	0.0220068	0.0219632	7393.915	7408.609	0.021963162
115	6.902173913	1.4006E-04	1.1097E+03	3.1767E+03	0.0227106	0.0226639	7610.447	7626.118	0.022663903
115	6.902173913	1.4826E-04	1.1383E+03	3.2656E+03	0.0233427	0.0233140	7837.926	7847.575	0.023314048
115	6.902173913	1.5836E-04	1.1669E+03	3.3545E+03	0.0240592	0.0240654	8122.274	8120.192	0.024065377
115	6.902173913	1.7034E-04	1.1956E+03	3.4434E+03	0.0248514	0.0249081	8458.577	8439.345	0.024908084
115	6.846956522	1.8422E-04	1.2242E+03	3.5323E+03	0.0257797	0.0258737	8818.401	8786.355	0.025873748
115	6.79173913	1.9432E-04	1.2528E+03	3.6211E+03	0.0265166	0.0266065	9043.113	9012.545	0.026606548
115	6.681304348	2.0378E-04	1.2814E+03	3.7100E+03	0.0272926	0.0273388	9213.894	9198.314	0.027338807
115	6.681304348	2.1388E-04	1.3100E+03	3.7989E+03	0.0279409	0.0280050	9445.917	9424.321	0.028004957
115	6.515652174	2.2586E-04	1.3386E+03	3.8878E+03	0.0289000	0.0289000	9644.294	9644.294	0.0289

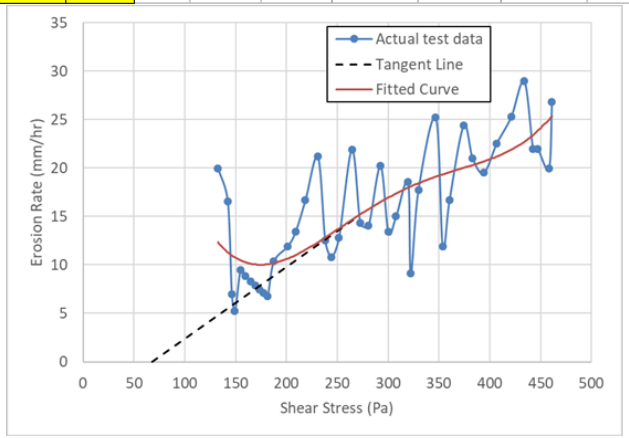

Figure 58. HET result spreadsheet for the sample CH-1

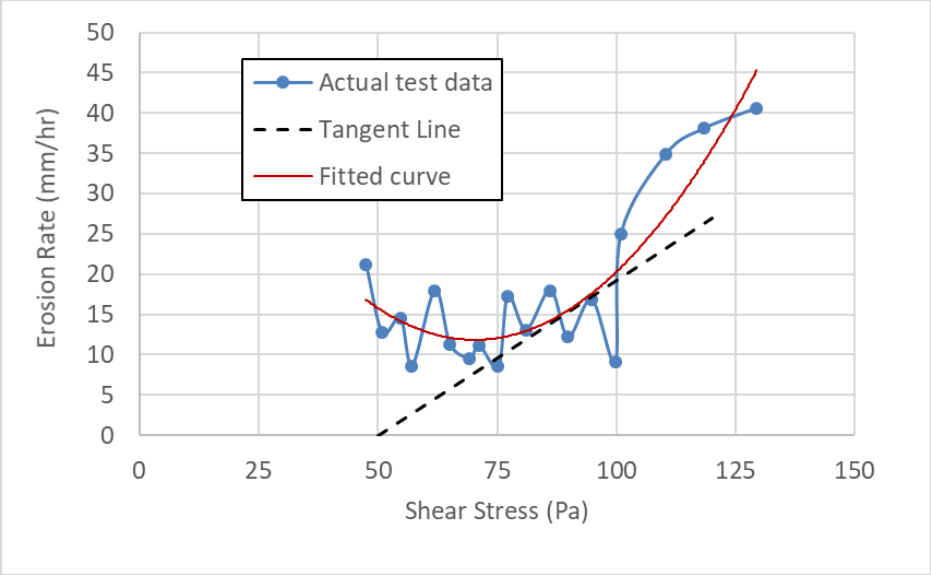

Figure 59. HET data for MH-1

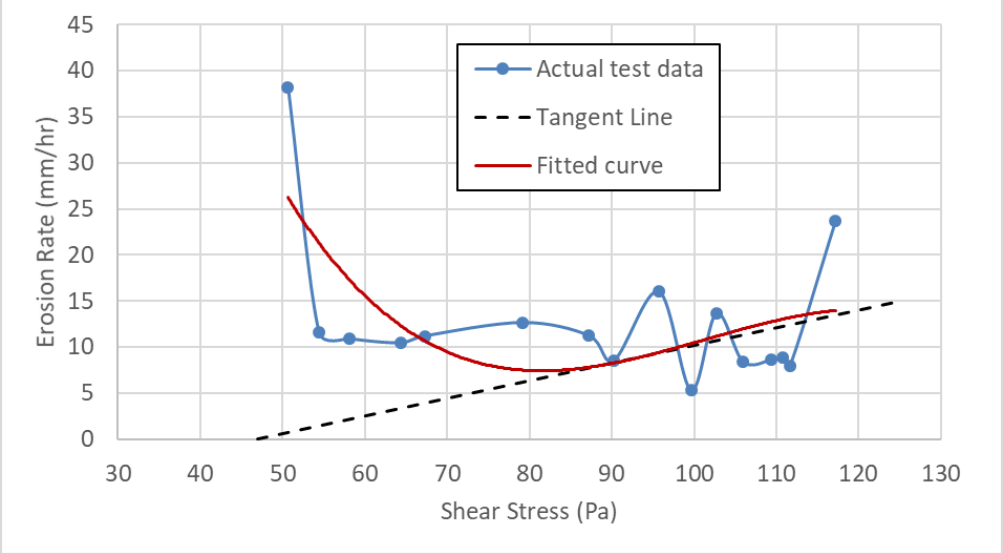

Figure 60. HET data for MH-2

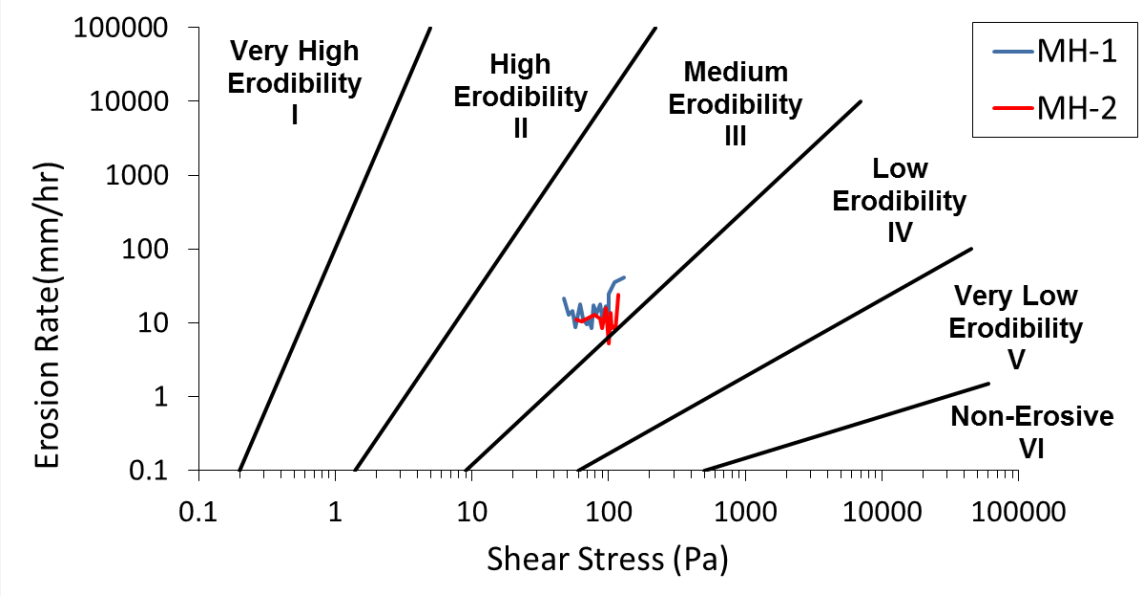

Figure 61. Erosion part of the silt HET curves plotted on the Erosion Category Chart

Sand Samples (SH-1 & SH-2)

As said earlier, the sand samples were a mixture of 20% Bentonite plus 80% Silica Sand 60-80 both purchased from Armadillo Clay & Supplies Co. in Austin. The results of the HETs on SH-1 and SH-2 are presented in Figure 62 and Figure 63, respectively. The critical shear stress values are also measured as 111 and 108 Pa for CH-1 and CH-2, respectively. For the purpose of comparison and populating the TAMU-Erosion Spread Sheet, the erosion part of the SH-1 and SH-2 test result curves were plotted in the erosion category chart. It can be seen that both erosion curves fall at the boundary between the Medium and Low Erodibility category (III & IV) (Figure 64). The initial head was 514 and 508 mm for SH-1 and SH-2, respectively.

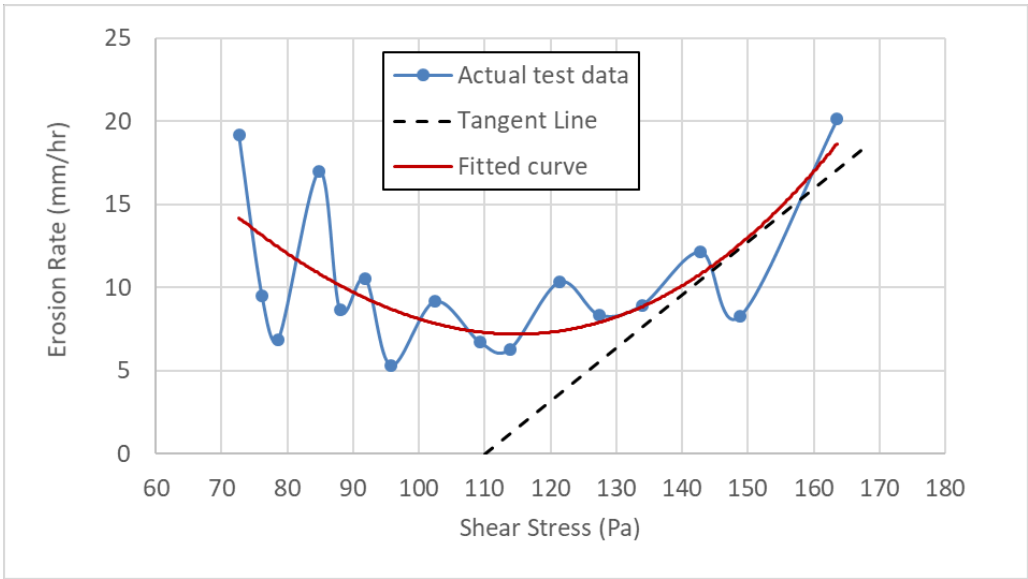

Figure 62. HET result for SH-1

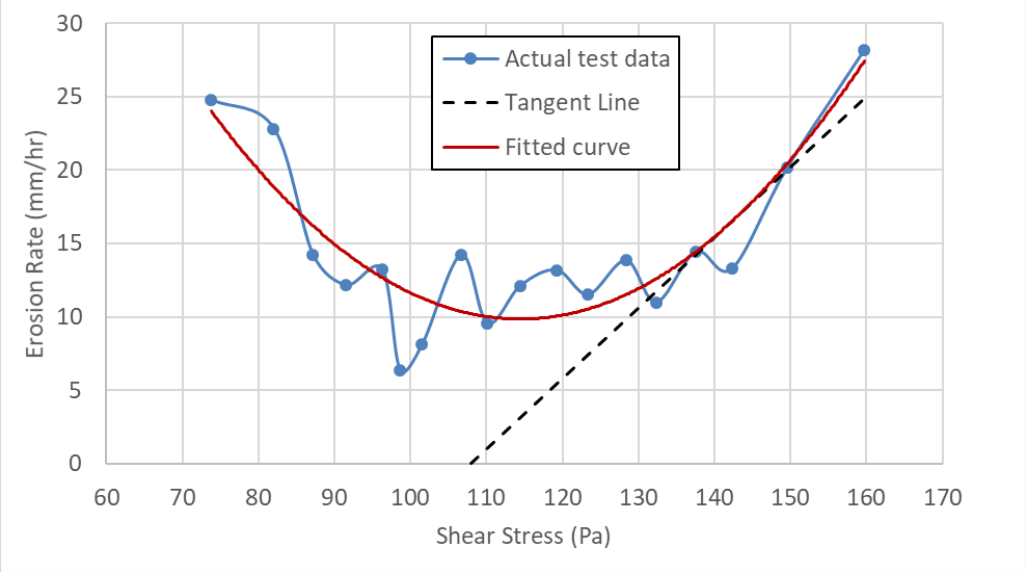

Figure 63. HET result for SH-2

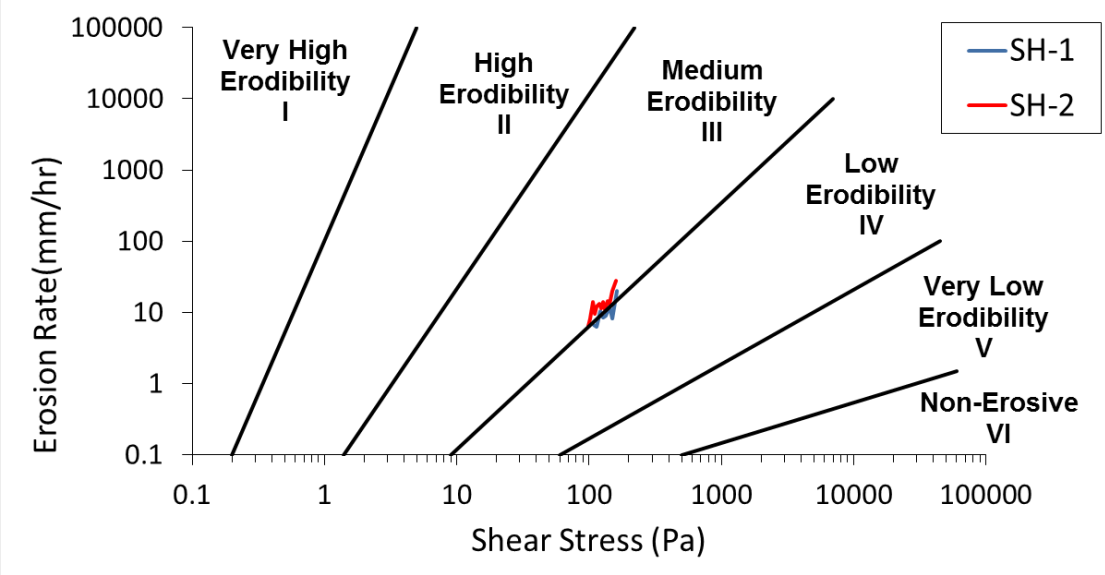

Figure 64. Erosion part of the sand HET curves plotted on the Erosion Category Chart

Gravel Samples (GH-1 & GH-2)

The HET can only be performed in soils where a horizontal hole can hold up and be self-supporting (i.e. fine-grained soils). Therefore, no HET could be conducted for the gravel samples.

4.3.1.4.Ensuring the repeatability of the JET

As discussed earlier in Chapter 2, for every Jet Erosion Test (JET) the operator collects the depth of the hole being created at the center of the sample as a function of time under a constant head condition. The collected data are then back analyzed to estimate two main erodibility parameters (critical shear stress and rate of erosion). There are three techniques to interpret the JET results: 1) Blaisdell solution, 2) Scour Depth solution, 3) Iterative solution. Figure 65 shows an example of the reading inputs during a JET, and final results of a sample JET spread sheet, respectively. Each method gives a different set of erodibility parameters: critical shear stress (τ_c), and detachment coefficient (k_d).

It is the test operator's duty to find the best solution for interpreting the jet test results. In addition, since one of the goals of this research project is to establish relationships between soil erodibility and engineering properties, it is very important to understand each solution well, and choose a consistent method of data interpretation for all jet test results. Here is a summary of the differences between each interpretation technique:

The most established solution in the literature is the Blaisdell solution which was developed and used by Hanson and Cook (1997, 2004). This technique was created based on a hyperbolic function (Blaisdell et al., 1981) to model the development of the scour hole. This report does not intend to go through the details of this hyperbolic function; however, it is worth mentioning that this function employs the real-time depth of the scour hole, and water jet velocity at the jet nozzle to predict the maximum depth of erosion, where the hole stops being eroded. Thereafter, the estimated equilibrium depth is used to measure the critical shear stress (Eq. 56):

$$\tau_c = \tau_0 \times \left[\frac{J_p}{J_e}\right]^2 \tag{56}$$

Where J_e is the equilibrium depth, and J_p is the potential core length (nozzle diameter x 6.2). τ_0 is the maximum shear stress at the water-soil boundary. Value of k_d is then determined using the least squared derivation between the real time and predicted time. Further information is provided in Section 2.1.6. It was found in the literature that this technique highly under predicts the values of τ_c and k_d. After running many JETs and letting the sample erode until it reaches the equilibrium depth, it was observed that the equilibrium depth estimated using the Blaisdell solution is typically lower than the actual equilibrium depth. This consequently leads to under prediction of the critical shear stress, and subsequently detachment coefficient (k_d). The other issue with the Blaisdell solution was the high variability of the critical shear stress (Simon et al., 2010; Cossette et al., 2012).

In an effort to improve the Blaisdell solution and reduce the scatter in τ_c vs. k_d, Simon et al., (2010) developed the Iterative solution. In this technique, the results of τ_c and k_d from Blaisdell solution are used for the next iteration to minimize the root mean square deviation between the real time and predicted time; however, many examples have shown that the same variation in results were often observed.

The other technique is the Scour Depth solution firstly developed by Daly et al. (2013). The big difference with the other two techniques, is that it solves for k_d and τ_c at the same time. As shown in Figure 65, the plot of scour depth versus time is better predicted using the scour depth solution. In this method, JET should be run until the sample stops eroding in the center (reaches the equilibrium depth).

So far, JET results are often reported using the Blaisdell solution technique. However, new studies by Daly et al. (2015) and Khanal et al. (2016) have reported the JET results in form of all three solution techniques. Khanal et al. (2016) have investigated the influence of the operator-dependent variables such as reading intervals, ending time, and pressure head setting on the JET results interpreted through all three solutions. It has been partially concluded that Scour Depth solution gives the most accurate results in terms of scour depth versus time. This solution also makes less assumptions (such as assuming the final equilibrium depth (J_e), or predicted time) compared to Blaisdell and Iterative solutions. Due to the fact that it makes less assumptions than the Blaisdell and Iterative solution, the JET results obtained from the scour depth solution was selected and compared to the erosion results obtained from HET or EFA. One of the disadvantages of the scour depth solution however occurs in the case where the soil is very resistant to erosion. In this case, it is rarely possible to end with the equilibrium depth; therefore, the iterative solution

is a better solution to predict the subtle changes in scour depth and obtain the equilibrium depth and consequently the erodibility parameters.

For this project, the JET results are reported according to all three solutions discussed above. For the regression analyses which are presented in the next chapters, the scour depth solution will be used as the primary solution, unless there is a special case in which the iterative solution or Blaisdell solution are more appropriate to use.

Scour Depth Readings						Head Setting	
Time (min)	Diff Time (min)	Pt Gage Reading (mm)	Depth (ft)	Pt Gage Reading (ft)	Maximum Depth of Scour (ft)	Time (min)	Head (in)
0	0	32	0.105	0.895	0.000	0	45.00
0.25	0.25	34	0.112	0.888	0.007	0.25	45.00
0.5	0.25	36	0.118	0.882	0.013	0.5	45.00
0.75	0.25	38.5	0.126	0.874	0.021	0.75	45.00
1	0.25	40.5	0.133	0.867	0.028	1	45.00
1.5	0.5	41	0.135	0.865	0.030	1.5	45.00
2	0.5	43	0.141	0.859	0.036	2	45.00
2.5	0.5	46	0.151	0.849	0.046	2.5	45.00
3	0.5	48	0.157	0.843	0.052	3	45.00
3.5	0.5	49.5	0.162	0.838	0.057	3.5	45.00
4	0.5	51	0.167	0.833	0.062	4	45.00
4.5	0.5	51.5	0.169	0.831	0.064	4.5	45.00
5	0.5	52	0.171	0.829	0.066	5	45.00
6	1	53	0.174	0.826	0.069	6	45.00
7	1	54	0.177	0.823	0.072	7	45.00
8	1	55.5	0.182	0.818	0.077	8	45.00
9	1	57	0.187	0.813	0.082	9	45.00
10	1	58.5	0.192	0.808	0.087	10	45.00
11	1	59	0.194	0.806	0.089	11	45.00

a) JET input readings (orange cells are recorded by the operator)

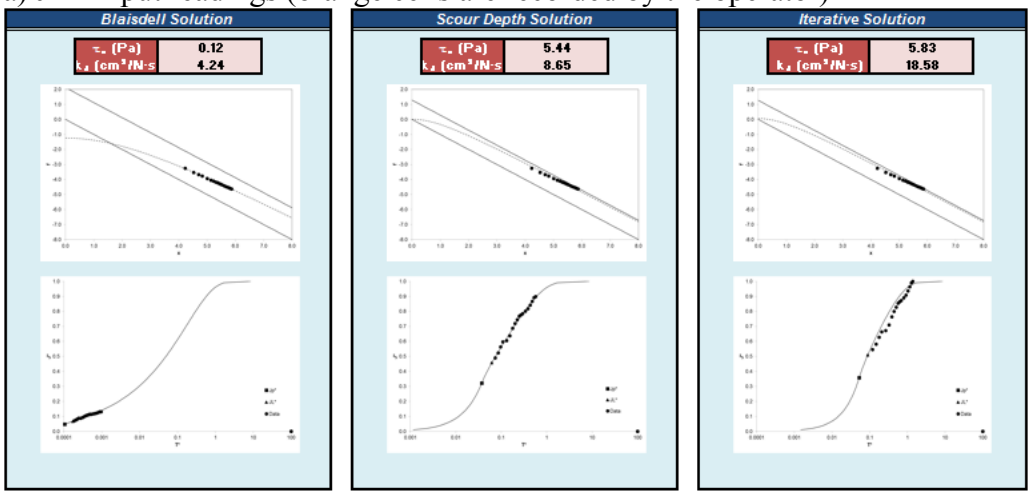

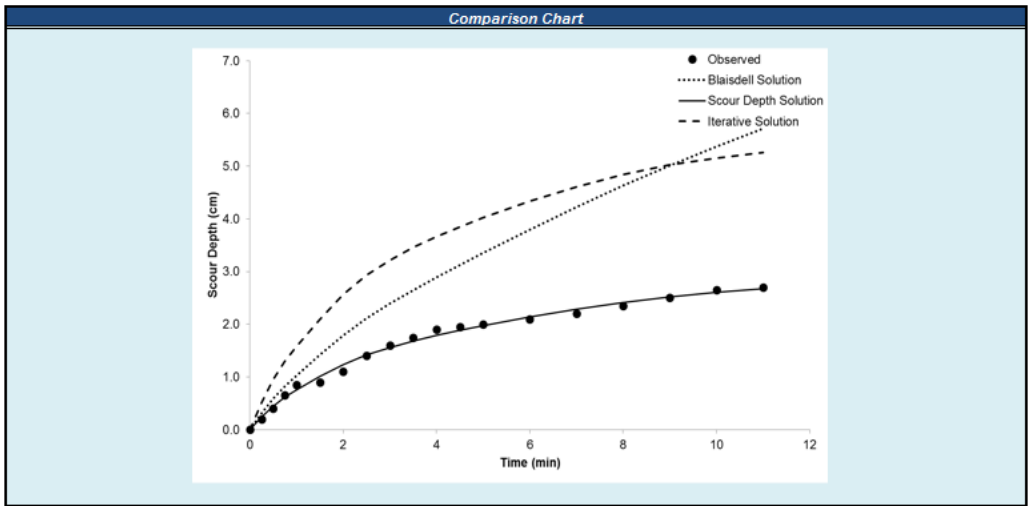

b) JET final results

Figure 65. Example of the (a) reading inputs during a JET, (b) final results of a sample JET spread sheet

Clay Samples (CJ-1 & CJ-2)

As discussed above JET test data can be reduced using three different techniques: 1) Blaisdell Solution (Hanson and Cook, 2004), 2) Scour Depth Solution (Daly et al. 2013), 3) Iterative Solution (Simon et al. 2010). All three techniques lead to the critical shear stress (τ_c) and erodibility or detachment coefficient (k_d) which is the linear slope of the early part of the erosion curve in the erosion rate-shear stress plot. Table 20 shows the results of the three solutions for CJ-1 and CJ-2. A reasonable repeatability is observed for all three techniques. The results of all JET tests are also presented in the format of a "JET result spreadsheet" in Appendix A. Figure 66 shows an example of the JET result spreadsheet for the sample CJ-1.

Table 20. JET results for the samples CJ-1 and CJ-2

Sample	Blaisdell Solution		Scour Depth Solution		Iterative Solution	
	τ_c (Pa)	k_d (cm^3/N.s)	τ_c (Pa)	k_d (cm^3/N.s)	τ_c (Pa)	k_d (cm^3/N.s)
CJ-1	5.79	0.59	8.80	2.56	5.80	3.82
CJ-2	4.81	0.53	6.74	1.19	4.92	3.76

Site:	
Date:	12/15/2016
Test #:	CJ-1
JET #:	1
Operator:	Iman
Test Location:	A&M Erosion Lab

Pt Gage Reading at Nozzle (mm):	4
Ref. Pt Gage Reading at Nozzle (ft):	0.9869
Nozzle Diameter (in):	0.125
Nozzle Height (ft):	0.1378

Initial guess* for τ_c (Pa):	1
Initial guess* for k_d ($cm^3/N{\cdot}s$):	1

Scour Depth Readings						Head Setting	
Time (min)	Diff Time (min)	Pt Gage Reading (mm)	Depth (ft)	Pt Gage Reading (ft)	Maximum Depth of Scour (ft)	Time (min)	Head (in)
0	0	46	0.151	0.849	0.000	0	45.00
0.25	0.25	47	0.154	0.846	0.003	0.25	45.00
0.75	0.5	47	0.154	0.846	0.003	0.75	45.00
1.5	0.75	47.5	0.156	0.844	0.005	1.5	45.00
2	0.5	47.5	0.156	0.844	0.005	2	45.00
3	1	48	0.157	0.843	0.007	3	45.00
4	1	48	0.157	0.843	0.007	4	45.00
6	2	48.5	0.159	0.841	0.008	6	45.00
9	3	49	0.161	0.839	0.010	9	45.00
12	3	49	0.161	0.839	0.010	12	45.00
15	3	49	0.161	0.839	0.010	15	45.00
18	3	49.5	0.162	0.838	0.011	18	45.00
23	5	50	0.164	0.836	0.013	23	45.00
28	5	51	0.167	0.833	0.016	28	45.00
33	5	51	0.167	0.833	0.016	33	45.00
38	5	51.5	0.169	0.831	0.018	38	45.00
43	5	52	0.171	0.829	0.020	43	45.00
48	5	52	0.171	0.829	0.020	48	45.00
53	5	52	0.171	0.829	0.020	53	45.00

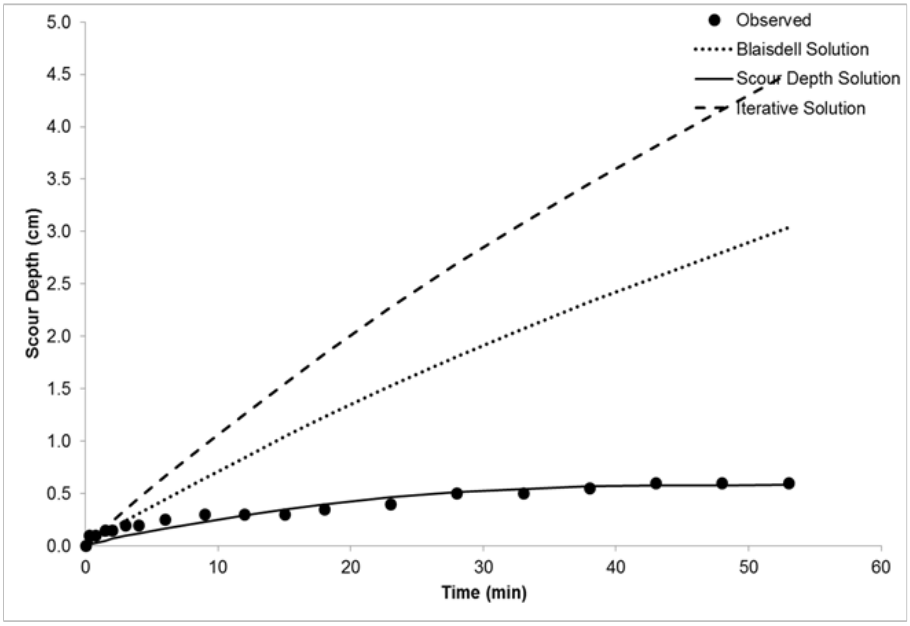

Figure 66. JET result spreadsheet for CJ-1

Silt Samples (MJ-1 & MJ-2)

Table 21 shows the JET results obtained for the samples MJ-1 and MJ-2. A reasonable repeatability is observed for all three techniques.

Table 21. JET results for the samples MJ-1 and MJ-2

Sample	Blaisdell Solution		Scour Depth Solution		Iterative Solution	
	τ_c (Pa)	k_d (cm^3/N.s)	τ_c (Pa)	k_d (cm^3/N.s)	τ_c (Pa)	k_d (cm^3/N.s)
MJ-1	1.9	1.45	1.74	1.4	4.74	5.22
MJ-2	1.37	1.02	3.89	2.12	3.63	5.2

Sand Samples (SJ-1 & SJ-2)

Table 22 shows the JET results obtained for the samples SJ-1 and SJ-2. Except for the iterative solution, a reasonable repeatability is observed for the other techniques, especially for the critical shear stress values.

Table 22. JET results for the samples SJ-1 and SJ-2

Sample	Blaisdell Solution		Scour Depth Solution		Iterative Solution	
	τ_c (Pa)	k_d (cm^3/N.s)	τ_c (Pa)	k_d (cm^3/N.s)	τ_c (Pa)	k_d (cm^3/N.s)
SJ-1	4.10	1.34	8.30	5.56	5.15	10.54
SJ-2	4.06	0.73	8.03	3.59	3.96	5.48

Gravel Samples (GJ-1 & GJ-2)

Similar to the HET, the JET can only be performed in fine grained soils. Therefore, no HET could be conducted for the gravel samples.

4.3.1.5.Field Erosion Device Demonstration

As shown in Table 17, the last part of Task 5 consists of organizing field demonstration tests including the BET device, the PET, and possibly the ISEEP of NC-State and the ISTD of the FHWA. Invitation letters were sent to Dr. Gabr of North Carolina State University for bringing their erosion testing device (ISEEP), as well as to Dr. Kerenyi for bringing the FHWA in-situ testing device to add to the measurements made as part of this study. Dr. Gabr of the NC-State did not have the funds necessary to bring his equipment to College Station. Dr. Kereneyi of the FHWA, mentioned that they are still working on improving their device and need more time, thus are not ready to contribute to this project.

It was decided to perform feasible available field tests at the National Geotechnical Experimentation Site at RELLIS Campus of Texas A&M University. These tests include the BET and the PET on both sand and clay sites. Terracon Consultants, Inc. in Conroe, TX provided necessary equipment to perform the Field Demonstration for this project. This section presents the results of the BET in clay and sand sites. The following BET procedure was undertaken in both sites:

1. Sampling from 2 to 5 ft, from 6 to 9 ft, and from 10 to 13 ft in a 14 ft deep borehole with 3” diameter Shelby Tubes. Three 3 ft long Shelby Tube samples every 4 ft. Use 3 inch drill bit if necessary.
2. Insert mechanical caliper (Figure 67) and measure diameter vs. depth.
3. Circulate the drilling fluid (Figure 68) for one minute in order to flush the borehole.
4. Insert mechanical caliper and measure diameter vs. depth.
5. Withdraw mechanical caliper.

6. Insert drilling rods down to 6” above the bottom of the hole, circulate drilling fluid for 15 minutes at maximum pump velocity.
7. Withdraw NW drilling rods.
8. Insert mechanical caliper and measure diameter vs. depth.
9. Withdraw mechanical caliper.
10. Insert drilling rods 6” above the bottom of the hole, circulate drilling fluid for 15 minutes at half the previous rate.
11. Withdraw NW drilling rods.
12. Insert mechanical caliper and measure diameter vs. depth.
13. Withdraw mechanical caliper.
14. Insert drilling rods 6” above the bottom of the hole, circulate drilling fluid for 15 minutes at a flow rate to be decided in the field.
15. Withdraw NW drilling rods.
16. Insert mechanical caliper and measure diameter vs. depth.
17. Withdraw mechanical caliper.
18. Plot the data and adjust the procedure.

A photograph from the pump and the flowmeter assembly on the drill rig is shown in Figure 69. One borehole in the sand site and one borehole in the clay site were drilled using 3 in diameter hollow stem augers. The drilling rods used to circulate the drilling fluid was 2.75 in diameter. This leaves an almost quarter inch empty space between the drilling rods and the borehole wall. During the test, the flow rate is constantly monitored using the in-line flowmeter shown in Figure 69; therefore, the velocity of the fluid in the borehole can be obtained by dividing the flow rate by the

annular space between the drilling rods and the borehole wall. Results of the BET for clay and sand are discussed in the following.

Figure 67. Photographs taken from the mechanical caliper (3 arms) in closed-arm and opened-arm conditions

Figure 68. Circulating the drilling fluid in the borehole in order to flush

Figure 69. Photograph of the pump and the in-line flowmeter assembly on the drill rig

BET at Clay Site

One borehole was drilled down to the depth of 14 ft. The borehole was located at the coordinates: N 30°.38.104', W 096°.29.348'. Soil was classified as CH throughout the borehole. As described earlier in the BET procedure, the zero reading was measured after 1 minute of flushing at 36 gpm (0.002271 m^3/s) flow. After that, three different flows of 35 gpm (0.002208 m^3/s), 21 gpm (0.001325 m^3/s), and 33 gpm (0.002082 m^3/s) were generated in the borehole and maintained for 10 minutes each. The diameter profile was obtained after each flow using the mechanical caliper shown in Figure 67. Figure 70 shows the caliper readings in five different stages:

1) Before flushing: right after the borehole was drilled and before doing the 1-minute flushing
2) After flushing: readings were made after 1-minute flushing
3) Reading 1: the borehole diameter profile was obtained after 10 minutes of 35 gpm flow
4) Reading 2: the borehole diameter profile after 10 minutes of 21 gpm flow
5) Reading 3: the borehole diameter profile after 10 minutes of 33 gpm flow

It should be noted that the caliper readings at each of the aforementioned stages were obtained in two runs in order to make sure that the readings are repeatable. For all the cases, an acceptable overlay was observed, and the repeatability of caliper readings were confirmed. The borehole diameter profiles shown in Figure 70 portray the averaged diameter profile between the first and second runs at each stage. Before doing any calculations of the erosion rate, Figure 70 clearly shows that there is a weak sand fissure at the proximity of the depth of 7.5 to 8.5 ft which has caused much higher diameter enlargement. This observation, indeed, is an example of one of the most important advantages of the BET compared to many other erosion tests in catching a continuous erodibility profile in a site prior to construction of bridges, levees, dams, etc.

While Figure 70 shows the borehole diameter profile at different stages during the test, it must be noted that the erosion function curve (i.e. "average erosion rate vs. the fluid velocity" plots) were constructed for each 2 ft intervals (i.e. 2-4 ft, 4-6 ft., 6-8 ft., 8-10 ft., 10-12 ft.) separately. Table 23 gives the flow rates, velocities, and time of application of each velocity for the BET at clay site. Figure 71 shows the erosion function curves for each of the 2 ft intervals.

As discussed in Section 2.2.3, the BET has two component tests: the lateral erosion test associated with the increase in diameter of the borehole (also called as the LBET), and the bottom erosion test associated with the increase in depth below the bottom of the drilling rods during the flow (also called as the BBET). The first one is very similar in concept to the HET but with a larger hole and a vertical flow direction. The latter one is much like an in-situ jet erosion test.

The depth increase at the bottom of the borehole was monitored after each stage (BBET); however, these measurements did not lead to a reasonable erosion rate at the bottom of the hole. The main reason was that as the wall of the borehole was being eroded, some eroded materials would settle and remain at the bottom of the borehole, and therefore, the measurements of the bottom depth did not necessarily represent the actual erodibility of the soil at that depth. This issue, however, was not confronted during the BET at the sand site. The following section presents the results of the LBET and the BBET in the sand site.

Table 23. Flow, velocity, and time for the BET at clay site

Depth	Flow (m^3/s)	Velocity (m/s)	Duration (min)	Change in profile (Figure 70)
2 ft – 4 ft	0.002271	1.967	1	before flushing to after flushing
	0.002208	1.308	10	After flushing to reading 1
	0.001325	0.773	10	Reading 1 to reading 2
	0.002082	1.063	10	Reading 2 to reading 3
4 ft – 6 ft	0.002271	2.639	1	before flushing to after flushing
	0.002208	1.444	10	After flushing to reading 1
	0.001325	0.967	10	Reading 1 to reading 2
	0.002082	1.431	10	Reading 2 to reading 3
6 ft – 8 ft	0.002271	2.450	1	before flushing to after flushing
	0.002208	1.280	10	After flushing to reading 1
	0.001325	0.669	10	Reading 1 to reading 2
	0.002082	0.687	10	Reading 2 to reading 3
8 ft – 10 ft	0.002271	N/A	1	before flushing to after flushing
	0.002208	0.596	10	After flushing to reading 1
	0.001325	0.418	10	Reading 1 to reading 2
	0.002082	0.433	10	Reading 2 to reading 3
10 ft – 12 ft	0.002271	2.242	1	before flushing to after flushing
	0.002208	1.188	10	After flushing to reading 1
	0.001325	0.621	10	Reading 1 to reading 2
	0.002082	0.712	10	Reading 2 to reading 3

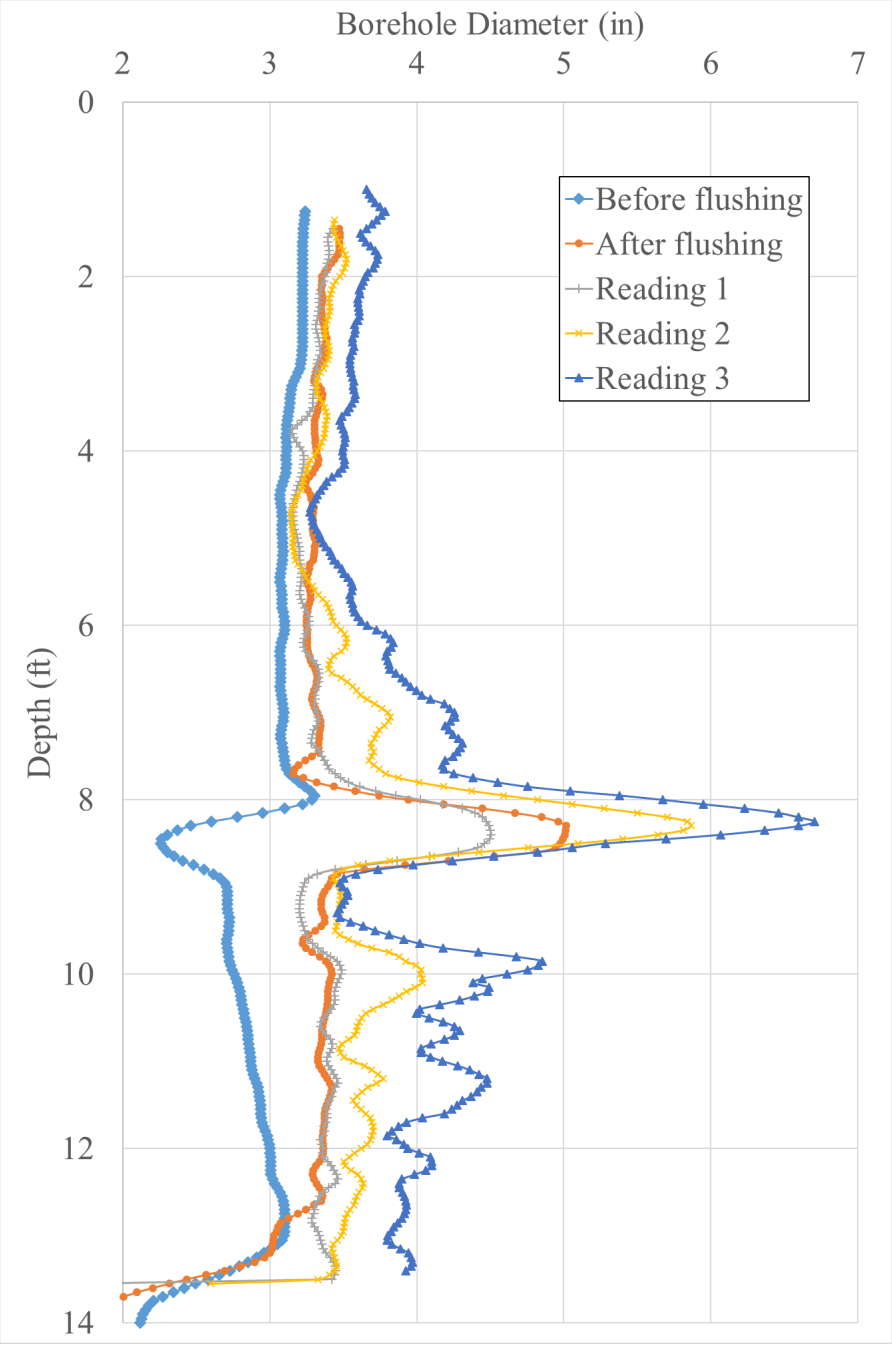

Figure 70. Clay borehole diameter profile at different stages during the BET

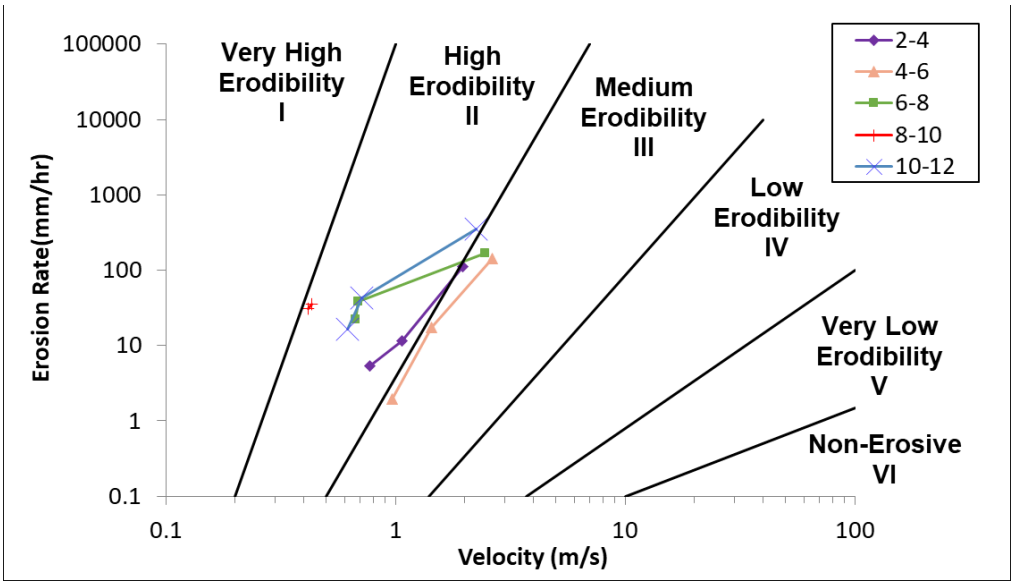

Figure 71. LBET Results - erosion function curves for each of the 2 ft. intervals in the clay site

Figure 72 shows the results of some earlier EFA tests performed on samples taken from the same depths in the clay site. Clearly, there is a gap between the results of the two tests; however, in both tests, most erosion is observed in the soil layers deeper than 6 ft. Existence of a weak sand fissure at the proximity of 8 ft makes a big difference in the erosion resistance of the borehole in the clay site.

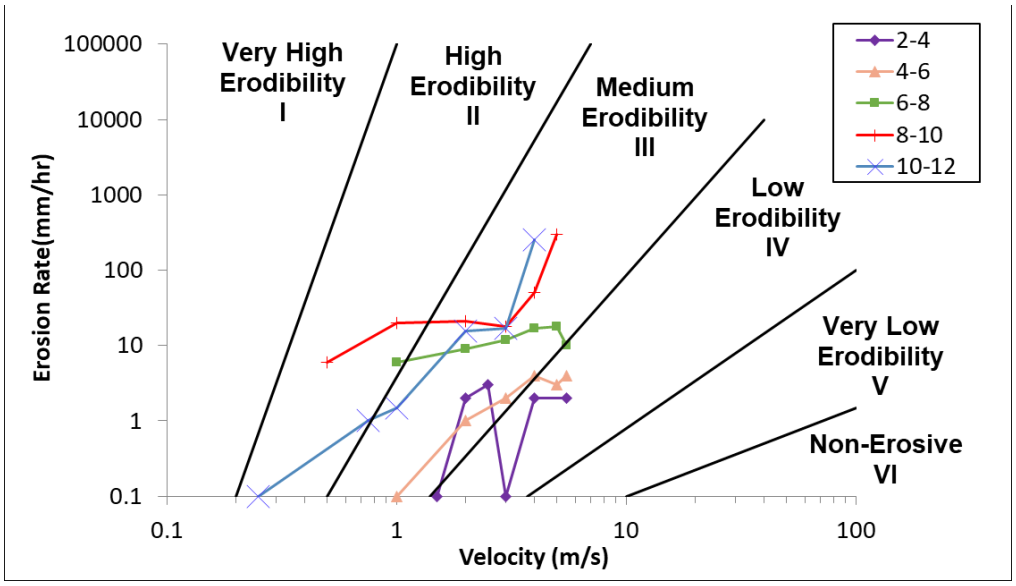

Figure 72. EFA Results - erosion function curves for each of the 2 ft. intervals in the clay site

BET at Sand Site

One borehole was drilled down to the depth of 12 ft. The borehole was located at the coordinates: N 30°.38.301', W 096°.27.606'. Soil was classified as SC throughout the borehole. Similar to what described earlier in the BET procedure, the borehole was flushed for almost 30 seconds at 37 gpm (0.002334 m^3/s) flow. After that, two different flows of 34 gpm (0.002145 m^3/s) and 38 gpm (0.002397 m^3/s) were generated in the borehole and maintained for 7 minutes each. The borehole diameter profile was obtained after each flow using the mechanical caliper shown in Figure 67. Figure 73 shows the caliper readings in four different stages during the test:

1) Before flushing: right after the borehole was drilled and before doing the 30-seconds flushing

2) After flushing: readings were made after 30 seconds flushing

3) Reading 1: the borehole diameter profile after 7 minutes of 34 gpm flow

4) Reading 2: the borehole diameter profile after 7 minutes of 38 gpm flow

Similar to the BET at the clay site, the caliper readings at each of the aforementioned stages were obtained in two runs in order to make sure that the readings are repeatable. For all the cases, an acceptable overlay was observed, and the repeatability of caliper readings were confirmed with maximum 2% error. The borehole diameter profiles shown in Figure 73 portray the averaged diameter profile between the first and second runs at each stage. It is clearly shown that the diameter enlargement at depths closer to the ground surface (0-3 ft) was significantly higher than other depths. While Figure 73 shows the borehole diameter profile at different stages during the BET, it must be noted that the erosion function curve (i.e. "average erosion rate vs. the fluid velocity" plots) were constructed for each 2 ft intervals (i.e. 1-3 ft, 3-5 ft., 5-7 ft., 7-9 ft., 9-11 ft.) separately. Table 24 gives the flow rates, velocities, and time of application of each velocity for the BET at sand site. Figure 74 shows the erosion function curves for each of the 2 ft intervals.

Figure 75 shows the results of some earlier EFA tests performed on the sand site samples. The sand samples tested in the EFA were mixed from different depths, and constructed in the laboratory to represent a similar condition in the field. The EFA results are in an acceptable consistency with the BET results specifically for the soil deeper than 5 ft. As mentioned earlier, the first five feet showed a significant erosion during the BET. One of the reasons for a much higher erosion in depths closer to the ground surface was that as the test was being performed, the cohesion-less sand wall on top of the borehole became weaker and started eroding more compared to deeper layers. However, in deeper layers, more reasonable erosion was observed.

The BET results discussed above are all associated with the increase in the diameter of the borehole (LBET). For the sand borehole, the depth increase at the bottom of the borehole was also monitored (BBET). The erosion function curve for the bottom of the sand borehole is shown in Figure 76. Briaud et al. (2016) showed that the flow velocity of the jet eroding the borehole is

almost equal to the average velocity of the flow in the annular space between the drilling rods and the borehole wall at depths close to the jet nozzle. For this purpose, the average velocities of the flow for the depth 9'-11' is chosen to represent the velocities of the jet at the bottom of the borehole. The BBET result presented in Figure 76 shows a higher erosion rate compared to the LBET result for the depth 9-11 ft in Figure 74.

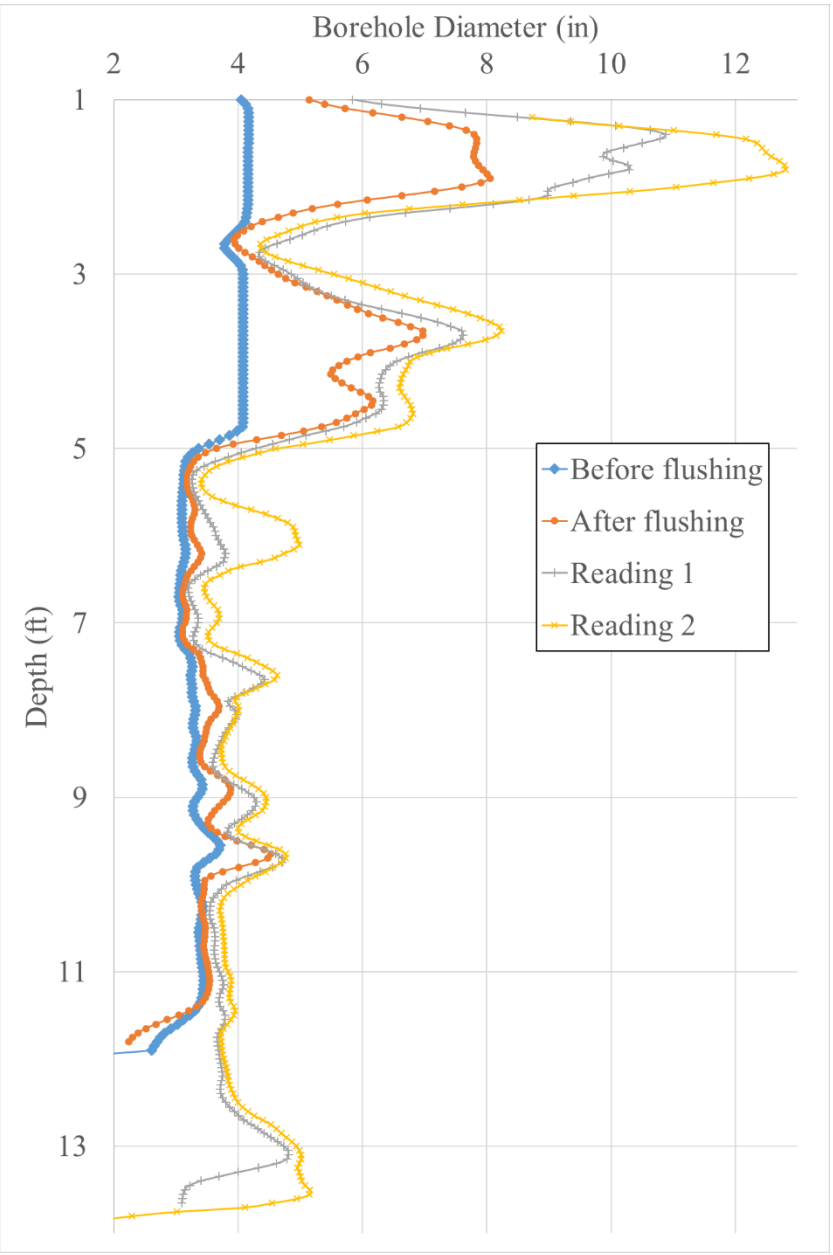

Figure 73. Sand borehole diameter profile at different stages during the BET

Table 24. Flow, velocity, and time for the BET at sand site

Depth	Flow (m^3/s)	Velocity (m/s)	Duration (min)	Change in profile (Figure 73)
1 ft – 3 ft	0.002334	0.518	0.5	before flushing to after flushing
	0.002145	0.147	7	After flushing to reading 1
	0.002397	0.102	7	Reading 1 to reading 2
3 ft – 5 ft	0.002334	0.548	0.5	before flushing to after flushing
	0.002145	0.179	7	After flushing to reading 1
	0.002397	0.162	7	Reading 1 to reading 2
5 ft – 7 ft	0.002334	2.453	0.5	before flushing to after flushing
	0.002145	1.555	7	After flushing to reading 1
	0.002397	1.191	7	Reading 1 to reading 2
7 ft – 9 ft	0.002334	1.652	0.5	before flushing to after flushing
	0.002145	0.988	7	After flushing to reading 1
	0.002397	0.721	7	Reading 1 to reading 2
9 ft – 11 ft	0.002334	1.207	0.5	before flushing to after flushing
	0.002145	0.769	7	After flushing to reading 1
	0.002397	0.647	7	Reading 1 to reading 2

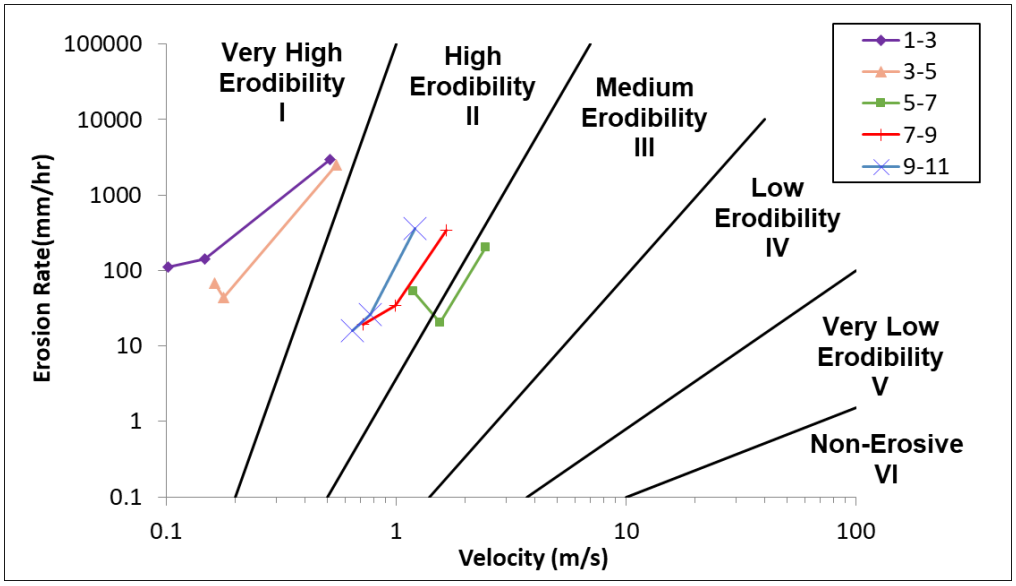

Figure 74. LBET Results - erosion function curves for each of the 2 ft intervals in the sand site

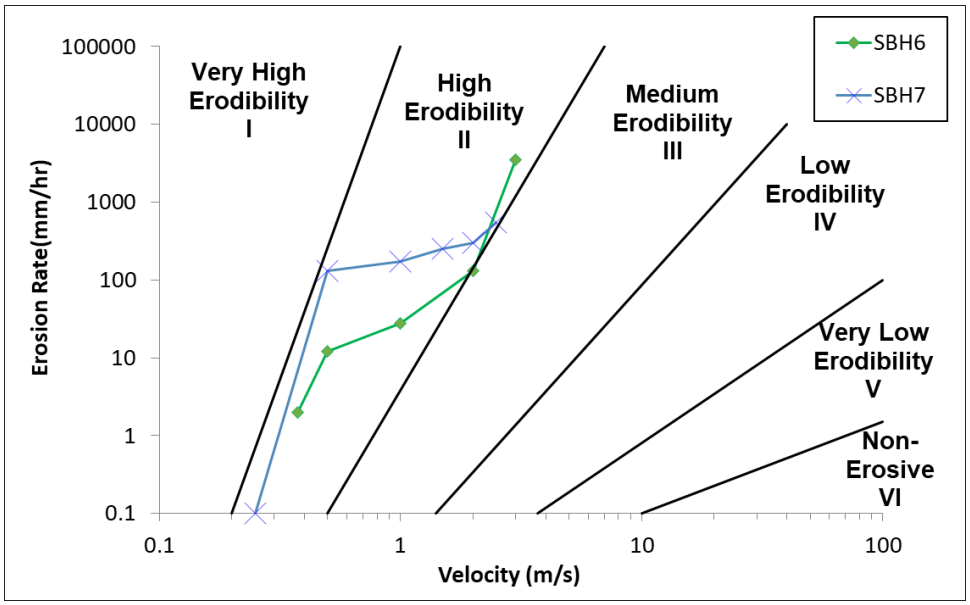

Figure 75. EFA Results - erosion function curves for each of the 2 ft intervals in the sand site

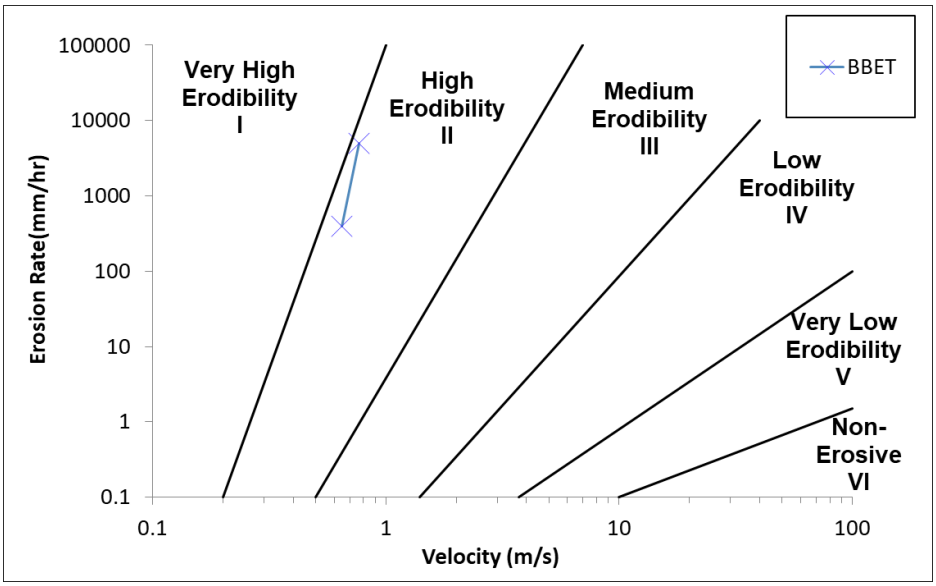

Figure 76. BBET Results - erosion function associated with the bottom of the sand borehole

4.3.2. *Erosion Tests Performed During Task 6*

As discussed in Chapter 1, Task 6 was dedicated to run different erosion tests on many natural samples. More than 128 erosion tests (32 EFA, 32 JET, 32 HET, and 32 PET) on 14 natural

clay, 8 silt, 6 sand, and 4 gravel samples were performed. Many of these tests were performed on the natural samples taken from Terracon office in Houston. Some were collected from the Alcona Dam near Oscoda, Michigan, as well as Tittabawassee River in Midland, Michigan, Crane Creek in California, and Freeport and Lissie in Texas. After Hurricane Harvey, Iman Shafii (Lead Engineer working on this NCHRP Project) joined the Geotechnical Extreme Events Reconnaissance (GEER) team supported by National Science Foundation (NSF). During this major effort, 15 samples from different locations were obtained and brought to the soil erosion laboratory for erosion testing (primarily for the EFA testing).

A few challenges confronted the investigating team during the erosion testing phase in Task 6, due to the limitations with each erosion testing device. Following revisions were made to the testing plan:

1. On HET testing on clay and silt samples: HET was primarily conducted on remolded samples instead of natural samples, following the advice of the panel.

2. On HET testing on sand and gravel (6 tests on sand, and 4 tests on gravel): The HET tests could not be properly conducted on sand and gravel samples due to the limitations associated with its setup. The drilled hole in all cases collapsed for sand samples. For gravel samples, clearly, this test was not feasible. Therefore, it was decided to increase the number of erosion tests on any other sample (mostly coarse-grained samples) using other erosion tests (i.e. EFA and PET) to make up for the number of erosion tests promised in the proposed testing matrix.

3. On JET testing on gravel (4 tests on gravel): The JET test also is not designed for gravel samples. Therefore, no JET was reported for gravel samples.

A summary of the samples tested during the Task 6 of this project is shown in Table 25. Majority of Table 25 is incorporated with intact samples; however, some cohesion-less samples were remolded in the laboratory to follow the testing matrix shown in Table 17. Erosion result spreadsheets as described in earlier sections were prepared for each tested sample separately. Appendix A shows the results of EFA, JET, and HET for all samples tested in this project. The total number of tests performed during Task 6 turned out to be more than 168 erosion tests promised in the proposed testing matrix.

Table 25. Summary list of the tested samples during Task 6

Test	Samples Name	Collected from	Date Collected	Site
Intact Samples				
EFA and PET	B-1 (23'-25')	G2 Consulting Group, LLC	Dec 2016	Tittabawassee River, Midland, MI
	B-7 (22'-24')			
	B-9A (25'-27')			
	B-9A (29'-31')			
	B-7-16 @ 8.5'	Barr Engineering Co.	Nov 2016	Alcona Dam, Oscoda, MI
	B-7-16 @ 11.6'			
	B-7-16 @ 13.5'			
	B-7-16 @ 15.3'			
	B-9-16 @ 16.1'			
	B-9-16 @ 17.3'			
	B-11-16 @18'			
	B-11-16 @ 20.5'			
	B-12-16 @ 18.1'			
	B-12-16 @ 18.9'			
	B-12-16 @ 20.5'			
	B-13-16 @ 19'			
	B-13-16 @ 20.5'			
	B-13-16 @ 23.5'			
	B-2 (13'-15')	Terracon, Houston	Oct 2016	Beaumont Formation, TX
	B-6 (0'-2')			
	B-1 (4'-6')			
	B-1 (28'-30')			
	B-8 (2'-4') 5694			
	B-1 (12.5'-14.5')	American Geotechnics	Apr 2017	Crane Creek, CA

Table 25 (Continued). Summary list of the tested samples during Task 6

Test	Samples Name	Collected from	Date Collected	Site
Intact Samples				
EFA and PET	GEER Sample #1	Geotechnical Extreme Events Reconnaissance (GEER)	Sept 2017	Port Aransas bridge, TX
	GEER Sample #2			Bay City Bridge, TX
	GEER Sample #3			
	GEER Sample #4			
	GEER Sample #5			
	GEER Sample #6			San Louis Pass, TX
	GEER Sample #7			
	GEER Sample #8			Levee at Brazos River, TX
	GEER Sample #9			Rosenberg Culvert Bridge, TX
	GEER Sample #10			
JET and PET	B-1 (2'-4')	Terracon, Houston	Oct 2016	Beaumont Formation, TX
	B-1 (4'-6')			
	B-1 (8'-10')			
	B-1 (10'-12')			
	B-1 (13'-15')			
	B-1 (18'-20')			
	B-1 (28'-30')			
	B-2 (2'-4')			
	B-2 (8'-10')			
	B-2 (13'-15')			
	B-3 (8'-10')			
	B-4 (8'-10')			
	B-5 (4'-6')			
	B-5 (6'-8')			
	B-6 (0'-2')			
	B-2 (8'-10')	Terracon, Houston	Winter 2016	Lissie Formation TX
	B-3 (10'-12')			
	B-8 (2'-4')	Terracon, Houston	Winter 2016	Alluvium, Freeport TX
	B-13 @ 20'			
	B-13 @ 18'			
	B-9A @ 26'	G2 Consulting Group, LLC	Dec 2016	Tittabawassee Midland, MI
	B-9A @ 27'			
	B-1 (23'-25')			
	B-7 (22'-24')			
	GEER Sample #2	GEER	Sept 2017	Bay City Bridge, TX

Table 25 (Continued). Summary list of the tested samples during Task 6

Test	Samples Name	Collected from	Date Collected	Site
Remolded Samples				
EFA and PET	Teton Dam 1	N/A	N/A	N/A
	Teton Dam 2			
	Teton Dam 3			
	Sample 2 (FHWA)			
	S-0-0-0			
	Sand #1			
	Sand #2			
	Gravel #1			
	Gravel #2			
	Gravel #3			
	Gravel #4			
JET and PET	Teton Dam Core			
	S-0-0-0			
	Sand #1			
	Sand #2			
	Sample 2 (FHWA)			
HET and PET	Clay #1	N/A	N/A	N/A
	Clay #2			
	Clay #3			
	Clay #4			
	Clay #5			
	Clay #6			
	Clay #7			
	Clay #8			
	Clay #9			
	Clay #10			
	Clay #11			
	Clay #12			
	Clay #13			
	Clay #14			
	Silt 1			
	Silt 2			
	Silt 3			
	Silt 4			
	Silt 5			
	Silt 6			
	Silt 7			
	Teton Dam Core			

4.4. Soil Geotechnical Properties

Soil index tests were conducted for all the samples tested by any erosion testing device. The geotechnical tests include: unit weight (ASTM D7263-09), moisture content (ASTM D2216-10), Atterberg limits (ASTM D4318-17), mini vane shear test (ASTM D4648), pocket penetrometer, sieve analysis (ASTM D422), hydrometer analysis (ASTM D7928-17), USCS (ASTM D2487-17), AASHTO classification, and specific gravity test (ASTM D854-14). Existing relevant geologic information such as latitude and longitude location, origin, water table data of the samples, etc. are also recorded for each sample when possible. All this information are compiled in a comprehensive two-page "soil properties spread sheet" for each sample. As an illustration, Figure 77 and Figure 78 show the two pages of the completed soil properties spread sheet for the sample B-7-16 (13'-15.5'). Such spread sheets were developed for all the soil samples that were tested in different erosion testing devices. Appendix B documents all the soil properties spreadsheets developed for this project.

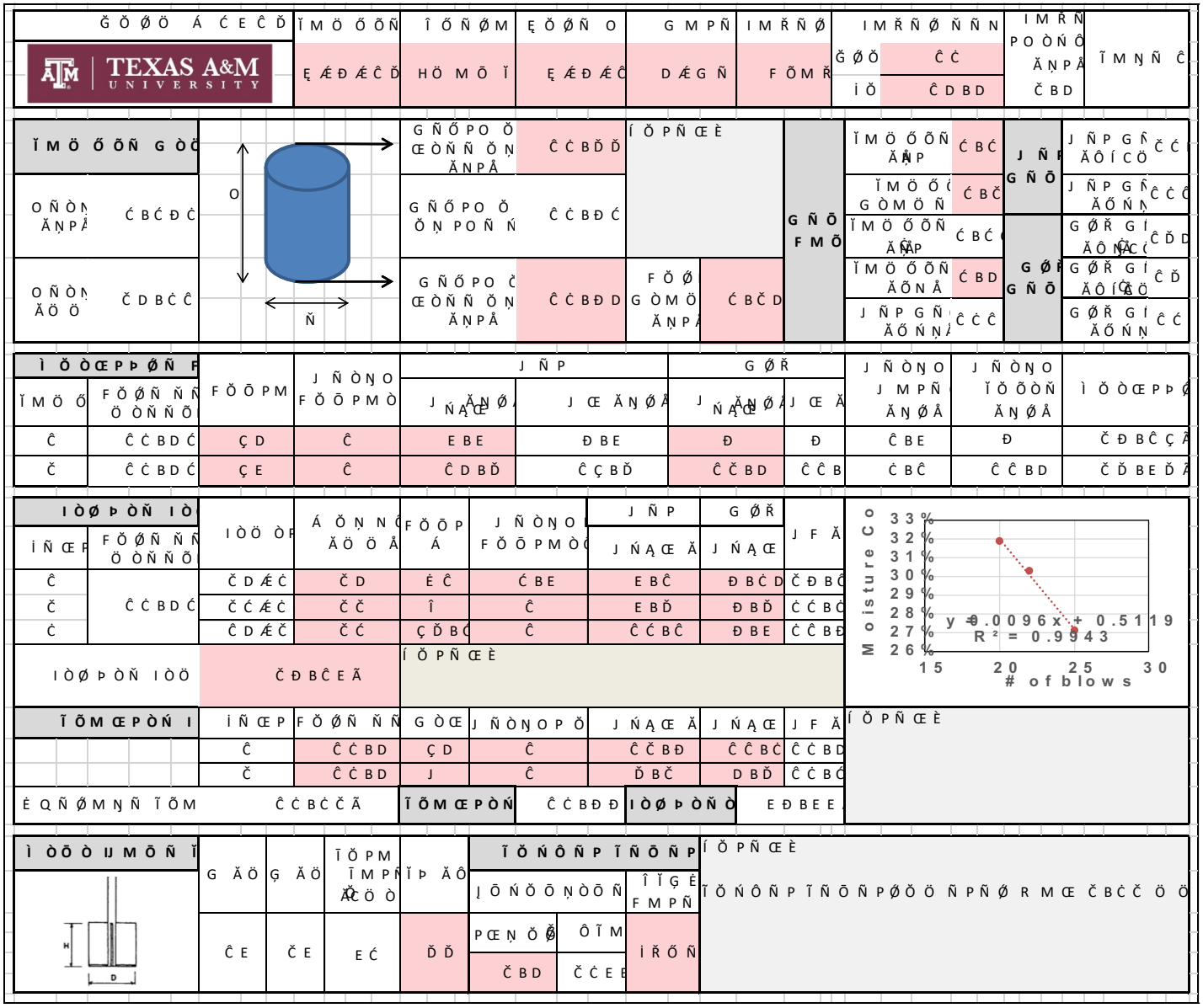

Figure 77. Page 1 of the "soil properties spread sheet" for B-7-16 (13'-15.5')

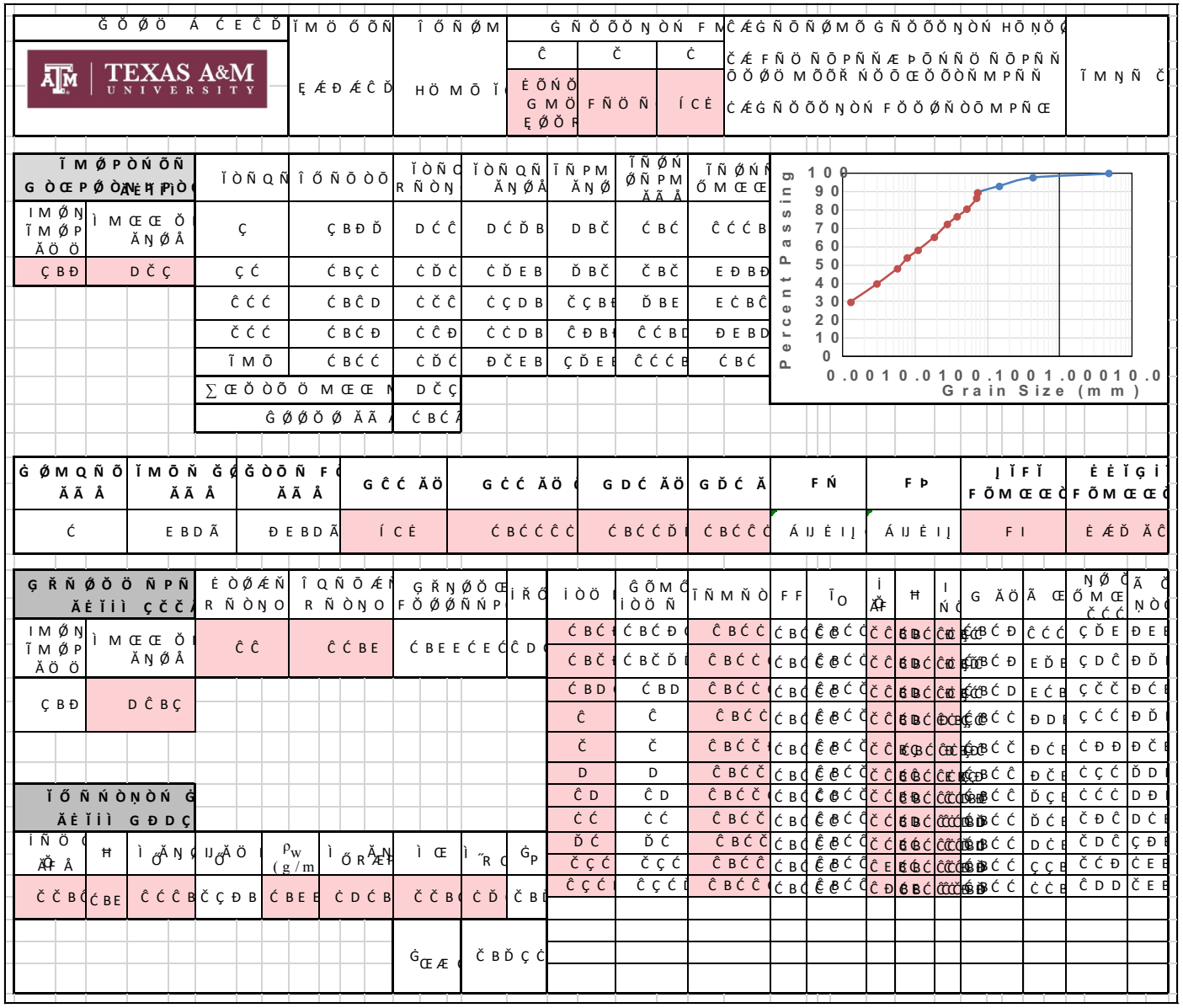

Figure 78. Page 2 of the "soil properties spread sheet" for B-7-16 (13'-15.5')

5. ORGANIZATION AND INTERPRETATION OF THE DATA

One of the major problems with analyzing erodibility parameters is that these parameters are derived from different test types and are not consistent with one another. While bringing some uniformity between tests results is important and is addressed through the literature review and will be more discussed in numerical simulations in Chapter 6, it is equally important to collect existing erodibility data obtained from each test. The first step in collecting such data was to come up with an acceptable and consistent fashion to organize the erosion data collected. To achieve this goal, a global erosion spread sheet called TAMU-Erosion Spread Sheet was developed. The entire TAMU-Erosion Spreadsheet in .xlsm format is available on the NCHRP website. Section 5.1 presents how the TAMU-Erosion was organized and developed. Section 5.2 introduces the entries of each column in the TAMU-Erosion. Section 5.3 provides the reader with a manual on how to probe and use the TAMU-Erosion.

5.1. Development and Organization of the TAMU-Erosion

As part of the Task 2 of this project, 750 erosion tests were collected from the literature review as well as by contacting researchers and organizations working on erosion around the world. Table 26 shows the 34 organizations and people contacted in the first phase of this project. Erosion data were extracted from technical reports, lab test results, field test results, and well-known journal/conference papers. In parallel with the erosion tests, the geotechnical properties of each tested sample, alongside with any information on the latitude and longitude location or origin of them were compiled.

The data collected includes the results of commercially used erosion tests such as the Erosion Function Apparatus test (EFA), the Jet Erosion Test (JET), the Hole Erosion Test (HET), the Slot Erosion Test (SET), the Ex-situ Scour Test Device (ESTD), the Borehole Erosion Test (BET), the Rotating Erosion Testing Apparatus (RETA), the Sediment Erosion Rate Flume (SERF), the In-situ Scour Profile (ISEEP), and some large scaled flume tests.

In addition to the aforementioned erosion tests, according to Chapter 4, around 250 erosion tests were performed during this project. These tests include the EFA, the JET, the HET, the PET, and the BET. Alongside with the erosion testing, all major geotechnical properties tests were conducted on each sample that was tested in any erosion device (Section 4.4 and Appendix B), and soil properties spreadsheets were generated for each sample.

Collected erosion tests during Task 2 and performed tests during Tasks 5 and 6 formed a global spreadsheet that consists of 975 erosion tests. This spreadsheet is called the TAMU-Erosion Spreadsheet. Table 27 shows a summary of the number of test results obtained to date for each erosion device. Figure 79 shows a summary chart of data compilation for the TAMU-Erosion Spreadsheet since the start of the project.

Table 26. A selected list of contact people and organizations around the world

	Contact Person	Organization		Contact Person	Organization
1	Stephane Bonelli	IRSTEA, France	18	J Beard	NCDOT, USA
2	Sherry Hunt	USDA, USA	19	M Haeri	NCDOT, USA
3	Wibowo, Johannes L ERDC-GSL-MS	USACE, USA	20	Kaye Brubaker	U of Maryland, USA
4	Axel Montalvo	USACE, USA	21	Timothy Straub	USGS, USA
5	Anna Shidlovskaya	U of Mines, Russia	22	Tom Over, USGS	USGS, USA
6	Tony Wahl	USBR, USA	23	Derrick Dasenbrock	MnDOT, USA
7	Morvant, Maurice FCL	Fugro, USA	24	Abdelkrim	ESTP, France
8	John Delphia	TxDOT, USA	25	Marie-Jo GOEDERT	ESTP, France
9	Jeff Locke & Devin Leonard	Fugro, USA	26	Heibaum, Michael	BAW, Germany
10	M. A. Gabr	NCSU, USA	27	Chenzuyu (Tsinghua)	Beijing, China
11	Beatrice Hunt	AECOM, USA	28	Gijs Hoffmans	Deltares, Netherlands
12	Richard Whitehouse	HRWallingFord, UK	29	Stephen Benedict	USGS, USA
13	Kiseok Kwak	KICT, Korea	30	Christophe Chevalier	IFSTAR, France
14	Brian Anderson	Auburn, USA	31	Garey Fox	Oklahoma State University, USA
15	Robbin Fell	UNSW, Australia	32	Peter Allen	Baylor University, USA
16	Kornel Kerenyi	FHWA, USA	33	Lin Wang	China Institute of Water Resources
17	D Henderson	NCDOT, USA	34	Mike C. Lin & Scott Shewbridge	USACE, USA

Table 27. A summary of the erosion test data in the TAMU-Erosion Spread Sheet

Erosion test type	Number of collected test result data
EFA	346
HET	233
SET	84
ESTD	17
ISEEP	6
SERF	13
JET	147
BET	17
RETA	14
PET	95
Large-scaled widening test	3
TOTAL	975

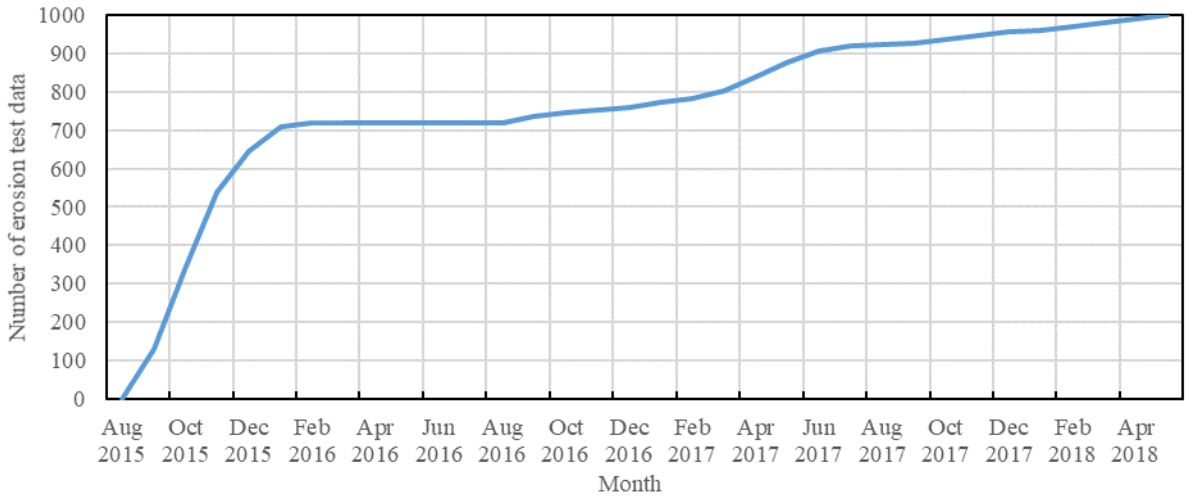

Figure 79. Summary chart of data compilation for the TAMU-Erosion Spreadsheet since the start of the project

The important characteristic of the TAMU-Erosion is its ability to bring a wide range of erodibility parameters together and compare them in a consistent fashion as proposed by Briaud (2008). The erodibility parameters which were selected to represent the erosion characteristics of a soil are the critical shear stress τ_c, the critical velocity v_c,the initial slope $E_v$of the $\dot{z}$ versus v

curve, and the initial slope E_τ of the $\dot{z}$ versus τ curve. In addition, the erosion function category (EC) in the Briaud erosion chart (2013) is considered as an additional parameter to describe erosion characteristics of a soil and is added as a parameter for the erosion correlations study. Figure 3 shows the erosion categories based on both velocity and shear stress, respectively.

In TAMU-Erosion, all the erosion data are analyzed according to the procedures described below for the five erodibility parameters: τ_c, v_c, E_v, E_τ, and EC.

1) *Critical velocity,* v_c: all the data points of the velocity erosion curve are plotted on the erosion chart (Figure 3). This plot is on log scale for both the x and the y axes. The "zero" on the y axis (log scale) is set at an arbitrarily low erosion rate of 0.1 mm/hour. If the erosion curve intercepts the horizontal axis at any point, that point is the critical velocity. If there is no data point on that axis, the line between the first two points of the erosion curve, is extrapolated linearly and the point at which this extrapolated line crosses the horizontal axis is selected as the critical velocity value.
2) *Critical shear stress,* τ_c: all the data points of the shear stress erosion curve are plotted on the erosion chart (Figure 3). This plot is on log scale for both the x and the y axes. The "zero" on the y axis (log scale) is set at an arbitrarily low erosion rate of 0.1 mm/hour. If the erosion curve intercepts the horizontal axis at any point, that point is the critical shear stress. If there is no data point on that axis, the line between the first two points of the erosion curve, is extrapolated linearly and the point at which this extrapolated line crosses the horizontal axis is selected as the critical shear stress value. Figure 80 shows an example of how the critical shear stress is calculated for a case where the line has to be extended to cross the horizontal axis.

3) The *initial slope* E_v of the $\dot{z}$ versus v plot is obtained by fitting a straight line through the initial points of the curve.

4) The *initial slope* E_τ of the $\dot{z}$ versus τ plot is obtained by fitting a straight line through the initial points of the curve.

5) For the *erosion function category (EC)*, the median point in the erosion curve is considered as the representative point for EC. Therefore, EC depends on the location of the median point on the erosion curve. The number of points on the erosion function can therefore impact the choice of EC; it is recommended that many points be obtained to define the erosion function. Figure 81 shows an example of how EC is determined. EC for this particular example is obtained as 2.25. Note that the dash lines on Figure 81 represent the EC values corresponding to 1.25, 1.75, 2.25, 2.75, and so on.

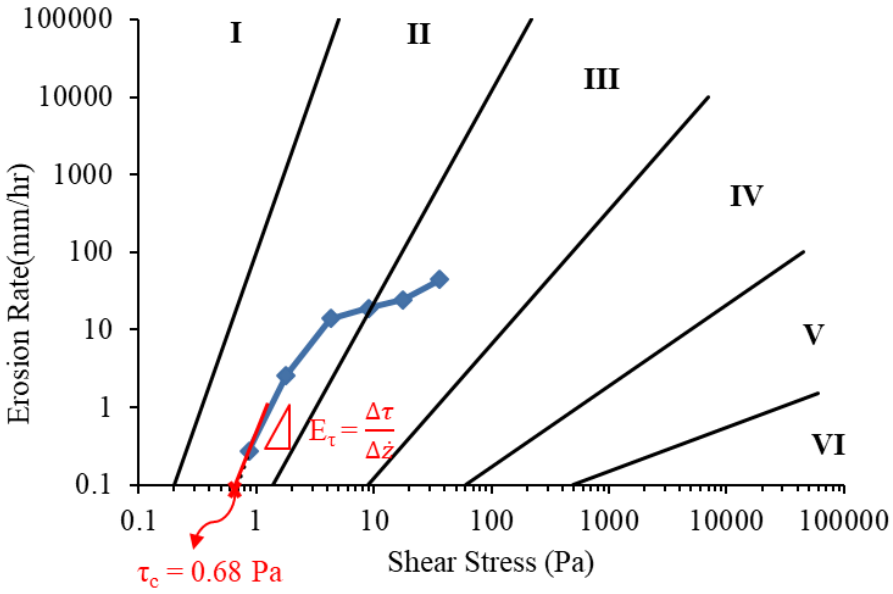

Figure 80. An example showing how critical shear stress is obtained when erosion curve itself does not cross the horizontal axis

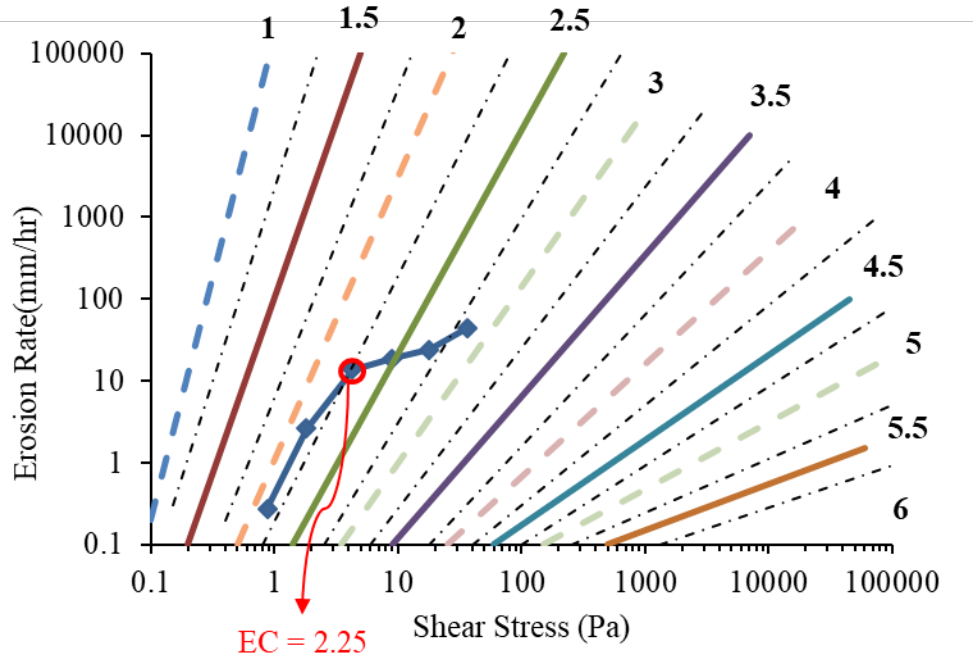

Figure 81. An example showing how EC is obtained for a sample erosion curve – EC for this example is 2.25

5.2. Column Contents in the TAMU-Erosion

As discussed in the previous section, TAMU-Erosion includes 975 erosion tests, or in other words 975 rows. Each row in the TAMU-Erosion consists of 50 columns. The entries for the columns are listed in Table 28 from left to right.

All test results are presented in the same format of erosion rate versus velocity and/or versus shear stress. Furthermore, they are all plotted on the erosion categories proposed by Briaud (2013). In several cases, the data collected had to be digitized. Now, all plots of erosion functions in the erosion function column have embedded spread sheets of their own. That way the user can click on the plot and obtain the point by point data. A manual on how to use the TAMU-Erosion is presented in the Section 5.3. A comments column for each erosion test as gives pertinent details

about any special treatment or condition during the erosion test, or in interpretation of the results. Also, a column for general comments about the sample provide related special information about the sample, if applicable. Figure 82 shows a general view of TAMU-Erosion, including the three parts: Part 1) Record Information, Part 2) Erosion Information, and Part 3) Soil Properties Information which itself is divided into two sections. Section 1 refers to the most common geotechnical soil properties while Section 2 refers to less common properties. The entries of each aforementioned part are described in the following sections. It is very important to note that obviously many cells in the TAMU-Erosion are empty, due to the lack of information for each sample.

5.2.1. *Part 1 – Record Information*

This part of the TAMU-Erosion presents the general record information of the soil sample. Figure 83 shows a zoomed-in picture of the "Part 1 – Record Information" of one sample from the TAMU-Erosion as an illustration. The column "Record Number" shows the row number associated with the sample in the TAMU-Erosion. Second column "Contact/Credit" provides information about the person or entity that owns the data associated with this sample. The third column "Date conducted/ Sampled" shows when the test was conducted or sometimes as in the case of natural samples, when the sample is obtained from the field. The fourth column "Project Title/ Sponsor" presents the title of the project or the sponsor, when applicable, that led to the measurement of this sample's test results. The fifth column "Sample Name" shows the name associated with the sample. The sixth column "Sample Depth" provides the depth of the sample in the case of natural samples. The unit of depth is either meter or feet, depending on the original data. The sample is classified according to the USCS and AASHTO classification methods in the

seventh and eighth columns, respectively. Finally, the last column in Part 1 identifies whether the sample is remolded (manmade) or natural (intact).

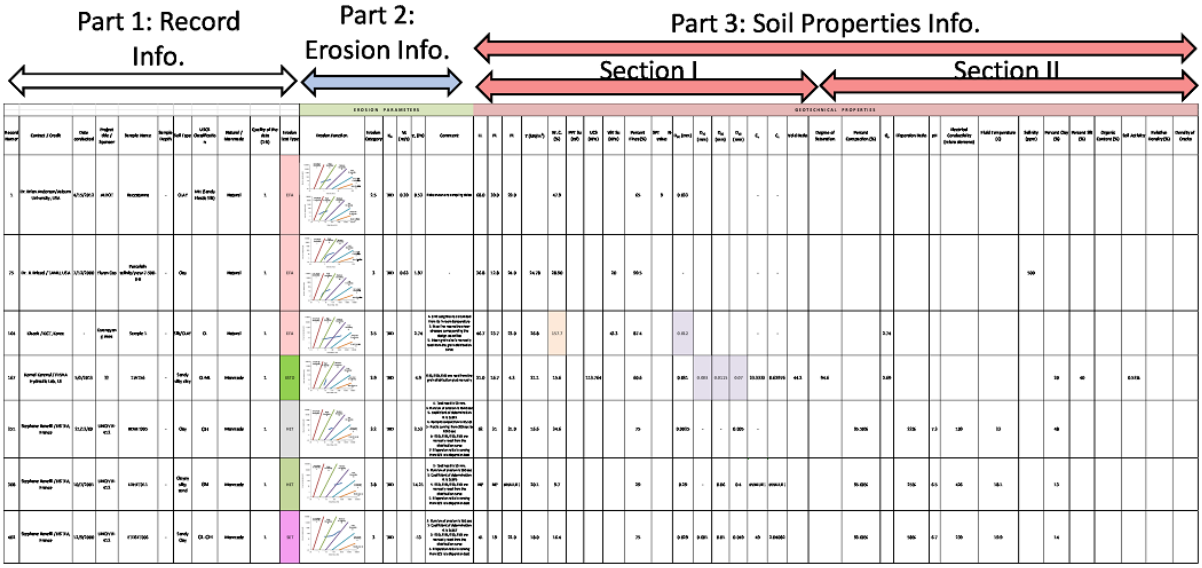

Figure 82. General view of the TAMU-Erosion Spread Sheet

Table 28. A list of entries in the TAMU-Erosion Spread Sheet

1. Record Number	27. Tensile strength (kPa)
2. Contact / Credit	28. UCS (kPa)
3. Data Conducted / Sampled	29. Vane shear strength, S_u (kPa)
4. Project Title / Sponsor	30. Percent fines (%)
5. Sample Name	31. SPT N-value
6. Sample Depth	32. D_{50} (mm)
7. Soil Type	33. D_{10} (mm)
8. USCS Classification	34. D_{30} (mm)
9. AASHTO Classification	35. D_{60} (mm)
10. Natural / Manmade	36. C_u
11. Quality of Data (1-3)	37. C_c
12. Erosion Test Type	38. Void ratio (e)
13. Erosion Function Curve	39. Degree of saturation (S_r)
14. Erosion Category	40. Relative compaction
15. Slope of velocity curve (E_v)	41. Specific Gravity (G_s)
16. Slope of shear stress curve (E_τ)	42. Dispersion ratio
17. Critical Velocity (V_c)	43. pH
18. Critical Shear Stress (τ_c)	44. Electrical Conductivity (micro-siemens)
19. Remarks on erosion test	45. Fluid Temperature (C)
20. General comments	46. Salinity (ppm)
21. Liquid limit (LL)	47. Percent Clay (%)
22. Plastic limit (PL)	48. Percent Silt (%)
23. Plasticity index (PI)	49. Organic Content (%)
24. Wet unit weight, γ ($\frac{kN}{m^3}$)	50. Soil Activity
25. Water content (%)	
26. Pocket penetrometer strength (kPa)	

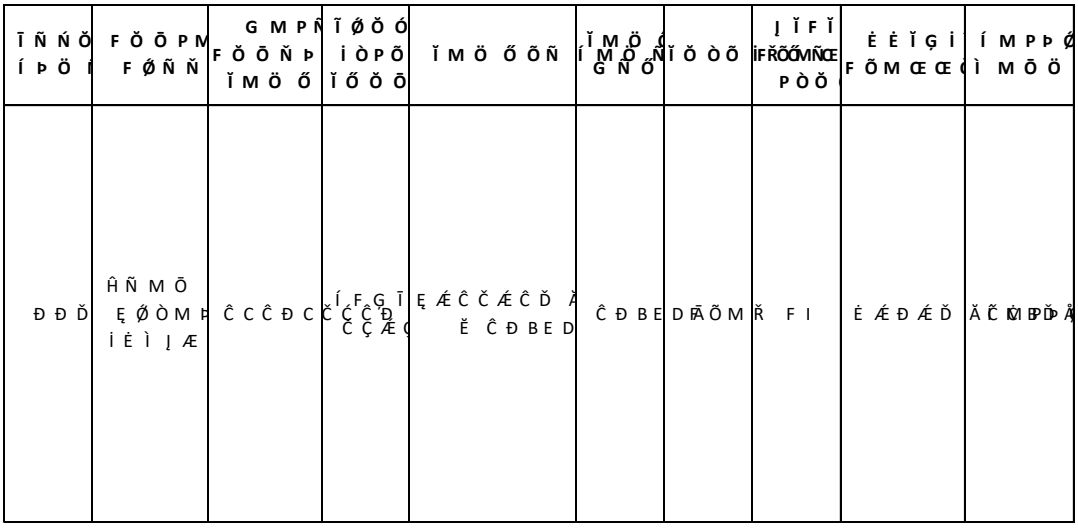

Figure 83. Record information (Part 1) of the TAMU-Erosion

5.2.2. *Part 2 – Erosion Information*

This part of the TAMU-Erosion presents the erosion test results of the sample. Figure 84 shows a zoomed-in picture of the "Part 2 – Erosion Information" of the same sample that was described in the previous section, as an illustration. The first column "Erosion Test Type" identifies the type of the erosion test that was conducted on the sample. In this example, the sample was tested in the EFA. Each erosion test type is designated with a specific color in the TAMU-Erosion. A list of the colors used to designate each erosion test in the TAMU-Erosion is shown in Table 29. These colors help the user identify each test more easily in a big-picture view of the spreadsheet.

Table 29. List of colors used to designate each erosion test in the TAMU-Erosion

Erosion Test Type	Associated Color
EFA	Pink
JET	Light Blue
HET	Gray
PET	Orange
SET	Lavender
SERF	Yellow
ESTD	Green
ISEEP	Dark Blue
BET	Dark Orange
RETA	Red
Large-scaled Flume	White

The second column "Erosion Function" plots the erosion test results on the erosion category chart which was proposed by Briaud (2008). As mentioned earlier, all plots of erosion functions in the erosion function column have embedded spread sheets of their own. That way the user can click on the plot and obtain the point by point data. A manual on how to use the TAMU-Erosion is presented later in Section 5.3. The next five columns (i.e. "Erosion Category", "E_v",

"E_τ", "V_c", and "τ_c") present the five erodibility parameters obtained after each erosion test. It should be noted that not all erosion tests can produce all five erodibility parameters. For instance, the JET and the HET can only report three out of five of these erodibility parameters (i.e. Erosion Category, E_τ, and τ_c), while the EFA can generate all five parameters. Finally the last column on Figure 84, "Remarks on Erosion Test", presents any special treatment or necessary comment regarding the erosion test.

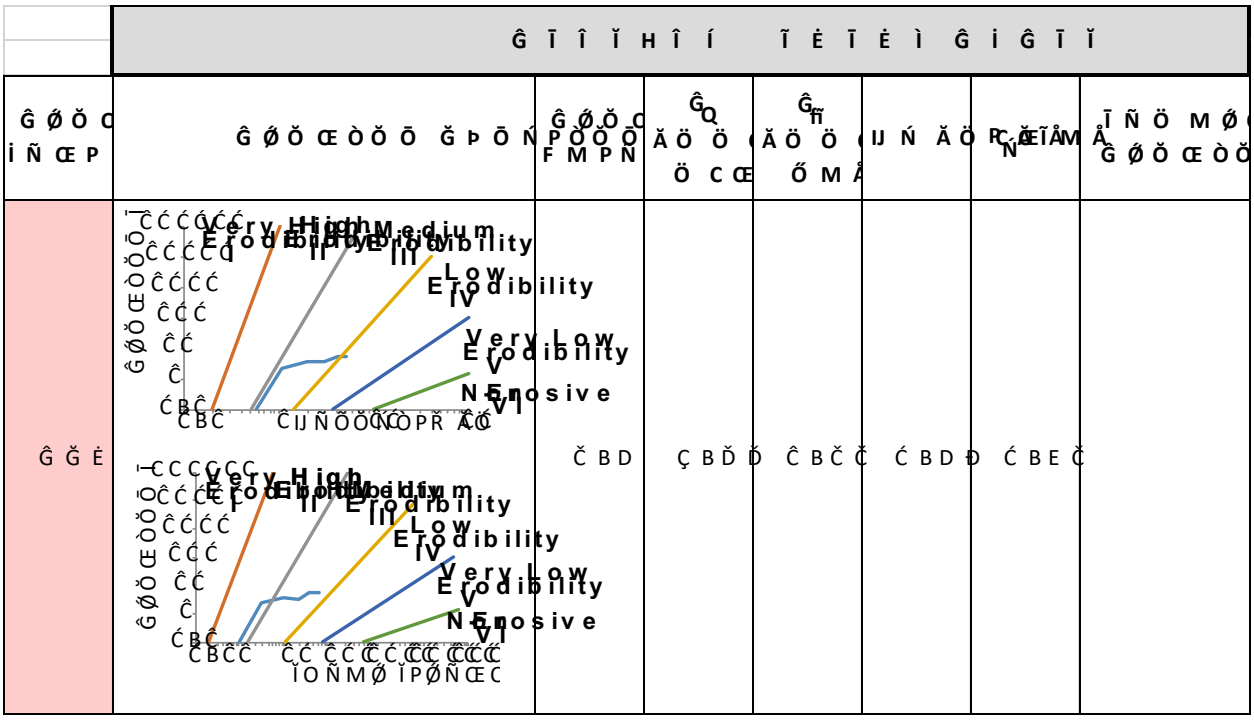

Figure 84. Erosion information (Part 2) of the TAMU-Erosion Spread Sheet

5.2.3. *Part 3 – Soil Properties Information*

Section 1 – More typically obtained geotechnical properties

This part of the TAMU-Erosion presents the geotechnical index properties of the sample that are more typically obtained by the DOT engineers. Figure 85 shows a zoomed-in picture of

the Section 1 of the "Part 2 – Erosion Information" for the same sample that was described in the previous section, as an illustration. The first column provides some general information about the location of the sample, longitude/latitude coordinates, color, and any special treatment of the sample, where applicable. The other columns as shown in Figure 85 include mostly the more typically obtained geotechnical properties.

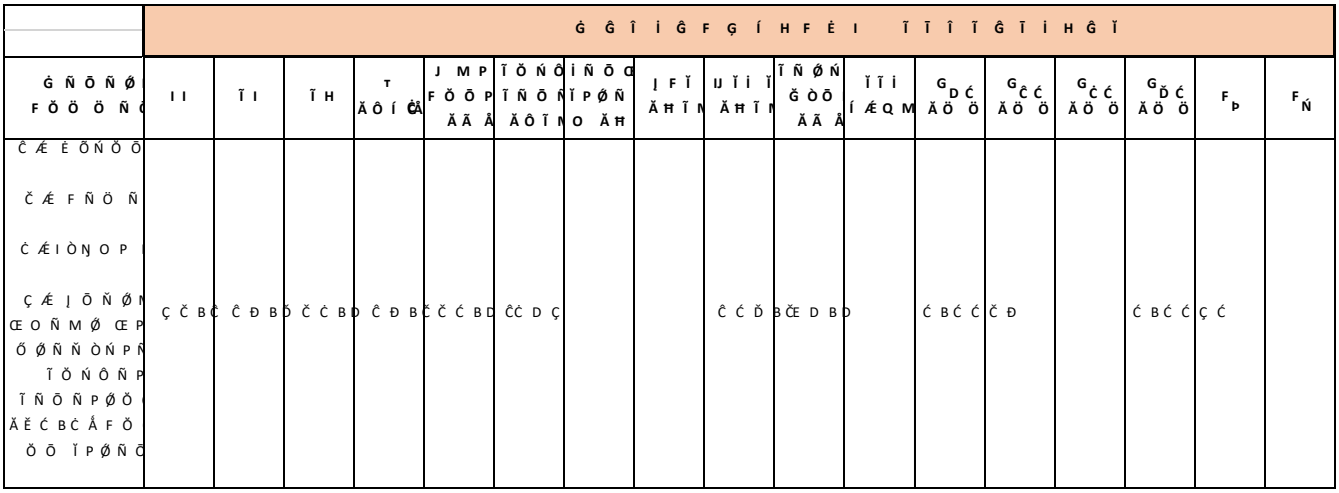

Figure 85. Geotechnical Properties (Part 3-Section 1) of the TAMU-Erosion

Section 2 – Less typically obtained geotechnical properties

This part of the TAMU-Erosion presents the geotechnical index properties of the sample that are less typically obtained by the DOT engineers. Figure 86 shows a zoomed-in picture of the Section 2 of the "Part 2 – Erosion Information" for the same sample that was described in the previous section, as an illustration. The columns that represent the less typically obtained geotechnical properties are shown in Figure 85.

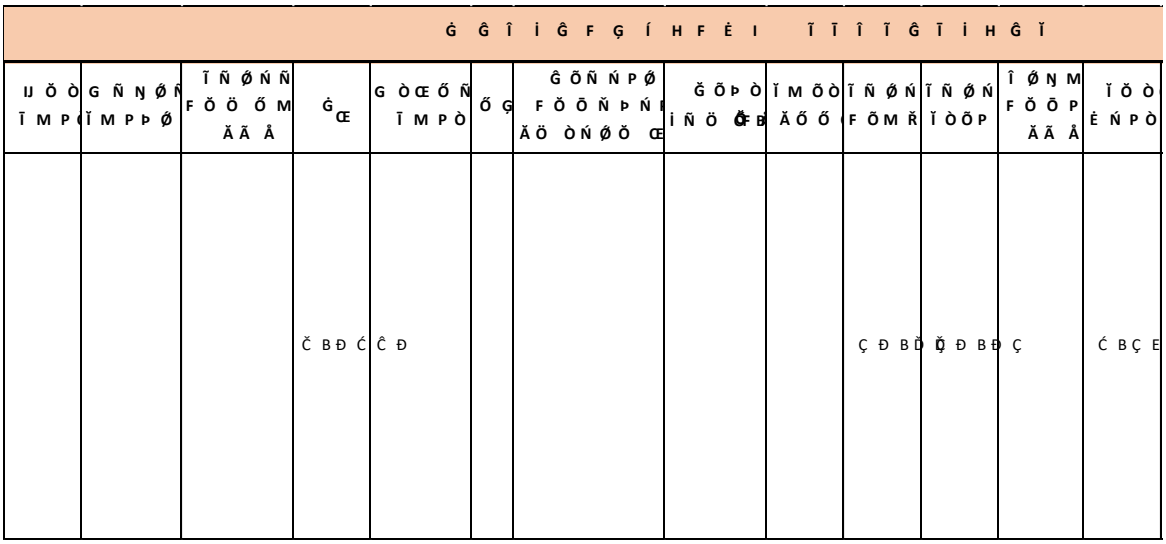

Figure 86. Geotechnical Properties (Part 3-Section 2) of the TAMU-Erosion

5.3. TAMU-Erosion Manual

One of the most important features of TAMU-Erosion is its ability to be filtered with regard to any column-entry. In other words, TAMU-Erosion is a relational spreadsheet which allows the user to perform multi-conditional inquiries. Table 28 shows a list of all 50 entries for one test record in TAMU-Erosion. In the following, the description of the embedded sheets in TAMU-Erosion is provided. Also, the manual for sample inquiry operation in the Windows version of the Microsoft Excel (2016) is presented.

5.3.1. *Description of Embedded Sheets in TAMU-Erosion*

The first sheet in TAMU-Erosion is called "About". This sheet provides all the information about the spreadsheet including: what it is called, when it is developed, who the authors are, what organization has performed the research, and for whom organization the spreadsheet is developed. This sheet also includes the responses to the three basic questions: 1) what is the TAMU-Erosion?,

2) what does TAMU-Erosion incorporate?, and 3) what does TAMU-Erosion do?. Figure 87 shows the picture of the first sheet named as “About” in TAMU-Erosion.

The second sheet, named as “Inquiry Operation Manual” provides the instruction on how to filter and search within TAMU-Erosion. The instructions presented within this sheet are according to the Microsoft Excel (2016) for Windows. The macOS version of the Microsoft Excel might be slightly different in appearance, however, it is similar to the Windows version in terms of the procedure. The instructions provided in the “Inquiry Operation Manual” are also presented in following Section 5.3.2.

The third sheet embodies the entire TAMU-Erosion spreadsheet, which is explained in the previous sections 5.1 and 5.2. The fourth sheet to the end incorporate the original test data used to plot the erosion functions for each erosion test. In fact, each sheet is named in the format of a three-word title: “abbreviated or summarized project name-contact organization-erosion test type”. For instance, the embedded sheet named as “ALDOT-Auburn-EFA Data” provides the EFA test data corresponding to an Alabama Department of Transportation project, and the contact organization is the Auburn University. It should be noted that the detailed information on the title of the project and person to contact are stated in the corresponding row in TAMU-Erosion. It should be also noted that the name of some embedded sheets are in the format of a two-word title: “contact organization-erosion test type”. Figure 88 shows the image of a small part of TAMU-Erosion, focusing on the embedded sheets.

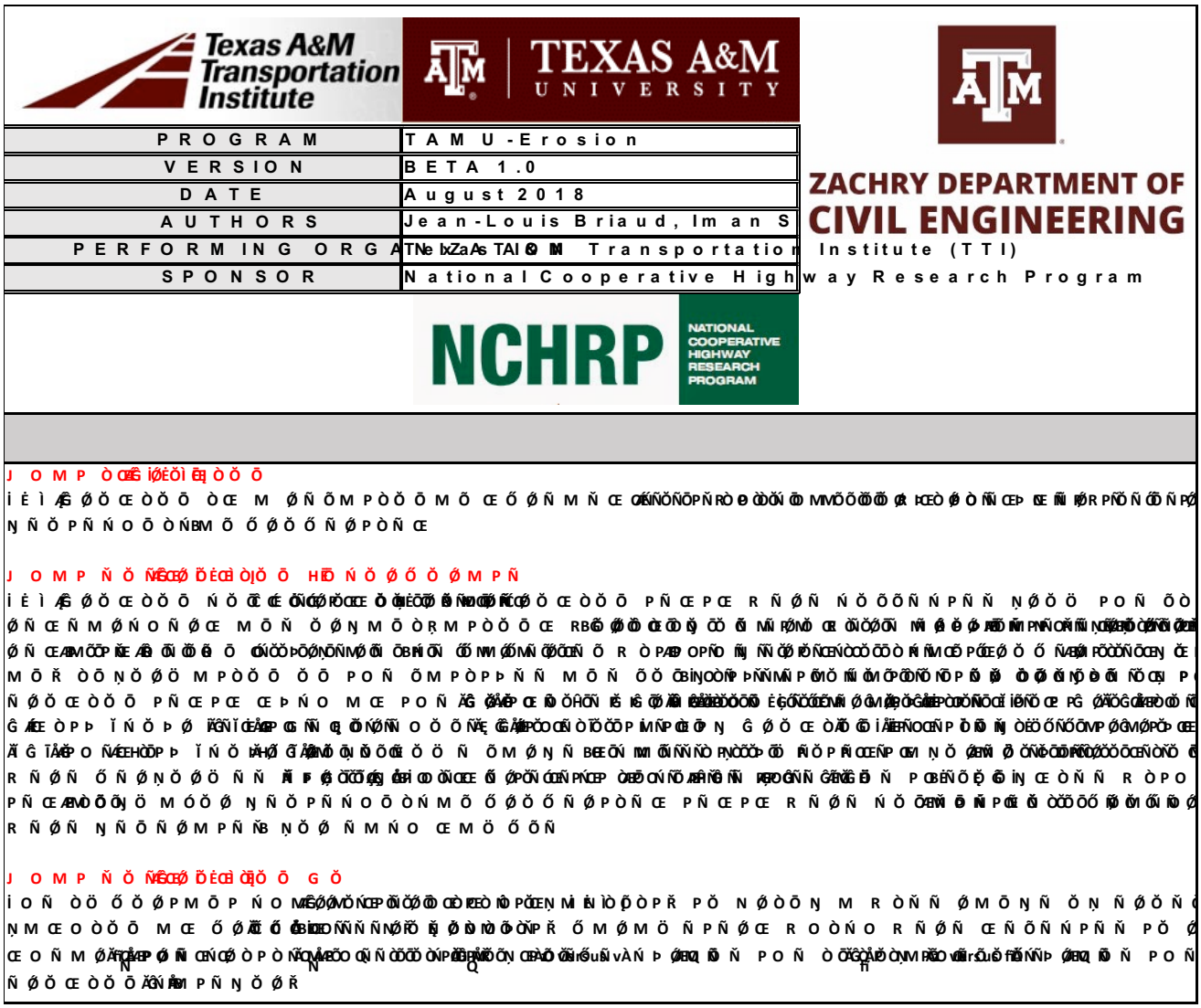

Figure 87. An image of the first sheet named as "About" in TAMU-Erosion

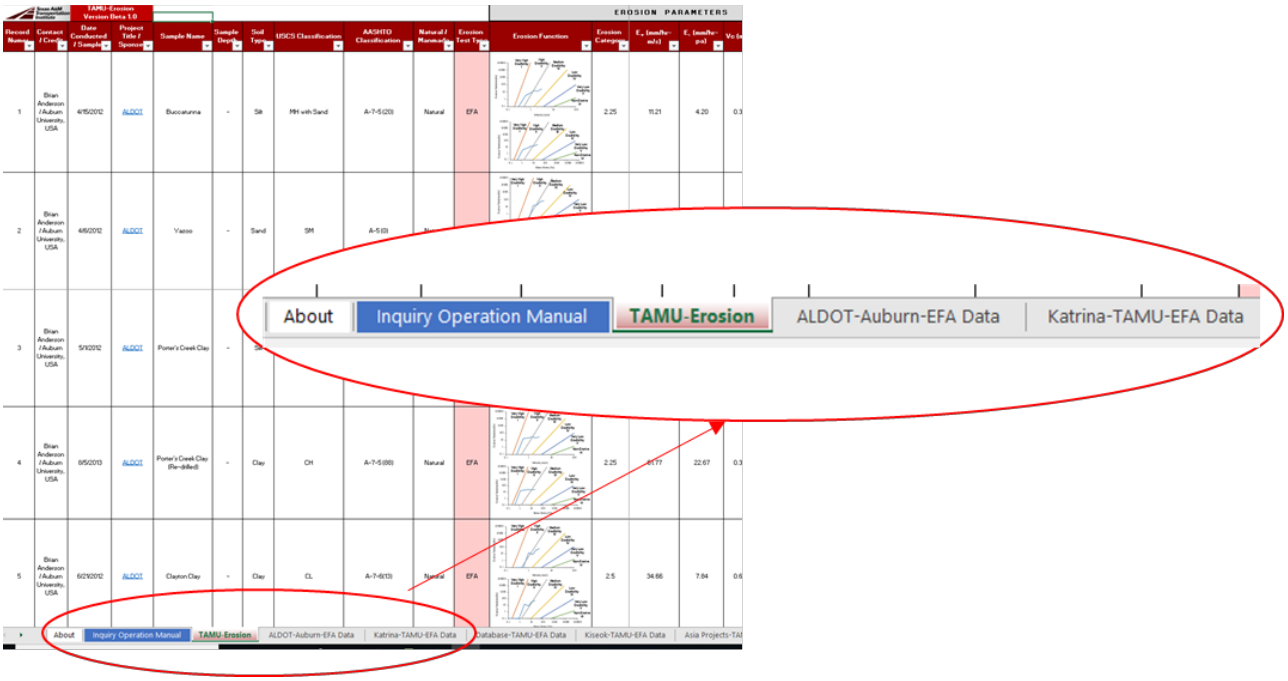

Figure 88.The image of a small part of TAMU-Erosion focusing on the embedded sheets

5.3.2. *Inquiry Operation Manual*

The operation manual in this section is presented using an example inquiry within the TAMU-Erosion. The procedure explained below can be used in any other application regardless of the number of the filters that the user desires to incorporate to search into the spreadsheet. The list of the choices that the user can opt from to filter each column-entry are also described within this example inquiry.

As shown in Figure 89, the bottom-left corner of each column's header shows a small arrow which can be expanded by clicking it. After clicking on the arrow, the list of choices that the user can select from is shown. Depending on the column entry, the list can include the names of the contact people, project titles, sample names, soil type, USCS, etc. For example, Figure 89 shows the list of the contact people/organizations that have contributed to the TAMU-Erosion. The user has the option to filter the TAMU-Erosion data to the data associated with only one, two, or a few

of the contact people by only checking the box near the desired contact person/organization and unchecking all other choices. In this example inquiry, the entire data are filtered down to only show the erosion test data from "Jean-Louis Briaud / TAMU, USA". As shown in Figure 89, the user also has the option to write down any name in the small search box instead of scrolling down within all the choices to find the desired person.

In this example inquiry, the next goal is to filter down the Briaud data to show only the data for "clay" samples. Figure 90 shows the list of choices to select from in the "soil type" column. Similarly, all the boxes should must be unchecked except for the box near the clay choice. As shown in Figure 90, user has the options: cemented sand, clay, gatarock, gravel, limestone, sand, silt, and silt-clay to select from. Also, some data do not have any entries in the "soil type" column; they are shown with a dash, -, in the choices.

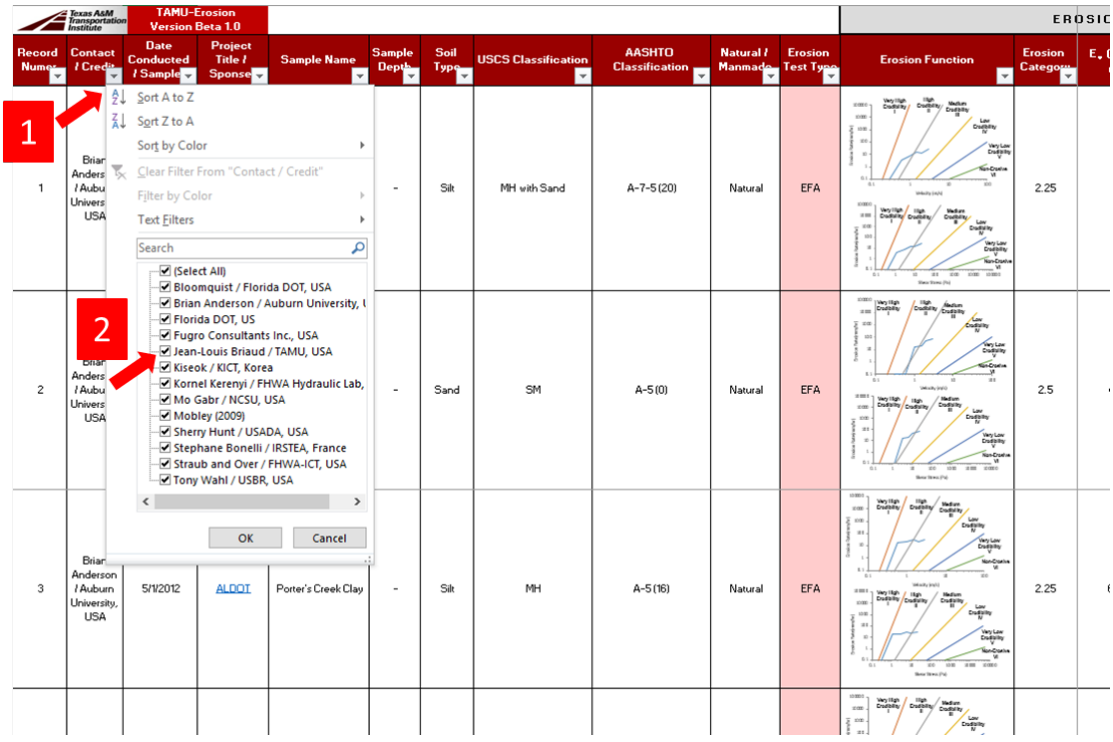

Figure 89. Filtering the data with regard to the contact person/organization – In this example inquiry: Steps 1 and 2 show how to filter data to show only the data from Jean-Louis Briaud

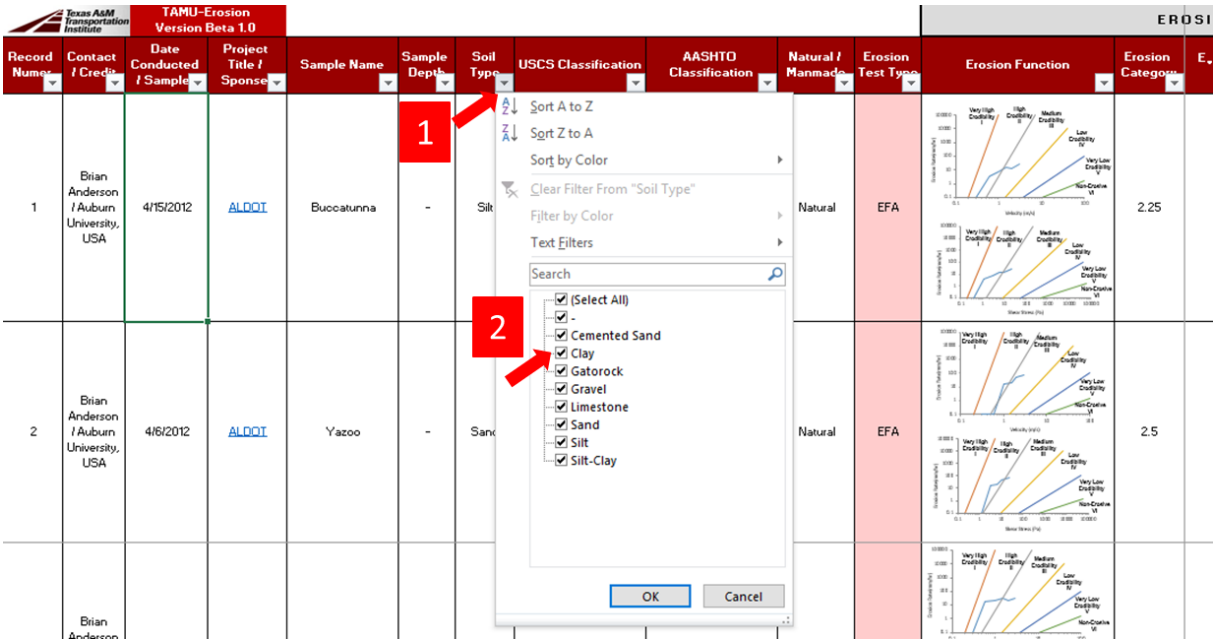

Figure 90. Filtering the data with regard to the soil type

In this example inquiry, the next goal is to further filter the clay data into only low plastic clays (CL) soils. Figure 91 shows the list of USCS that the user can select from. Similar top previous columns, the entries might be missing for some columns; they are shown with a dash, -. The user has the option to select from either “USCS classification” or “AASHTO classification” or even both columns. It is very important to mention that Figure 91 shows all possible choices for the USCS entry, while if the user selects only “clay”, as in the example inquiry, the USCS choices are limited to only the clay symbols (See Figure 92). As shown in Figure 92, after filtering the data into only clay soils, the USCS options are also narrowed down to a list of high plasticity clay (CH), CH with sand, low plasticity clay (CL), CL / CH, CL with sand, CL with sand / SC, and high plasticity organic clay (OH).

It should be noted that at each step, the user can clear the filter by selecting the "Data" from the Tabs toolbar in Microsoft Excel, and then clicking on the "clear" Command on the Command Toolbar. (i.e. Select: Data → Clear). Figure 93 shows this process.

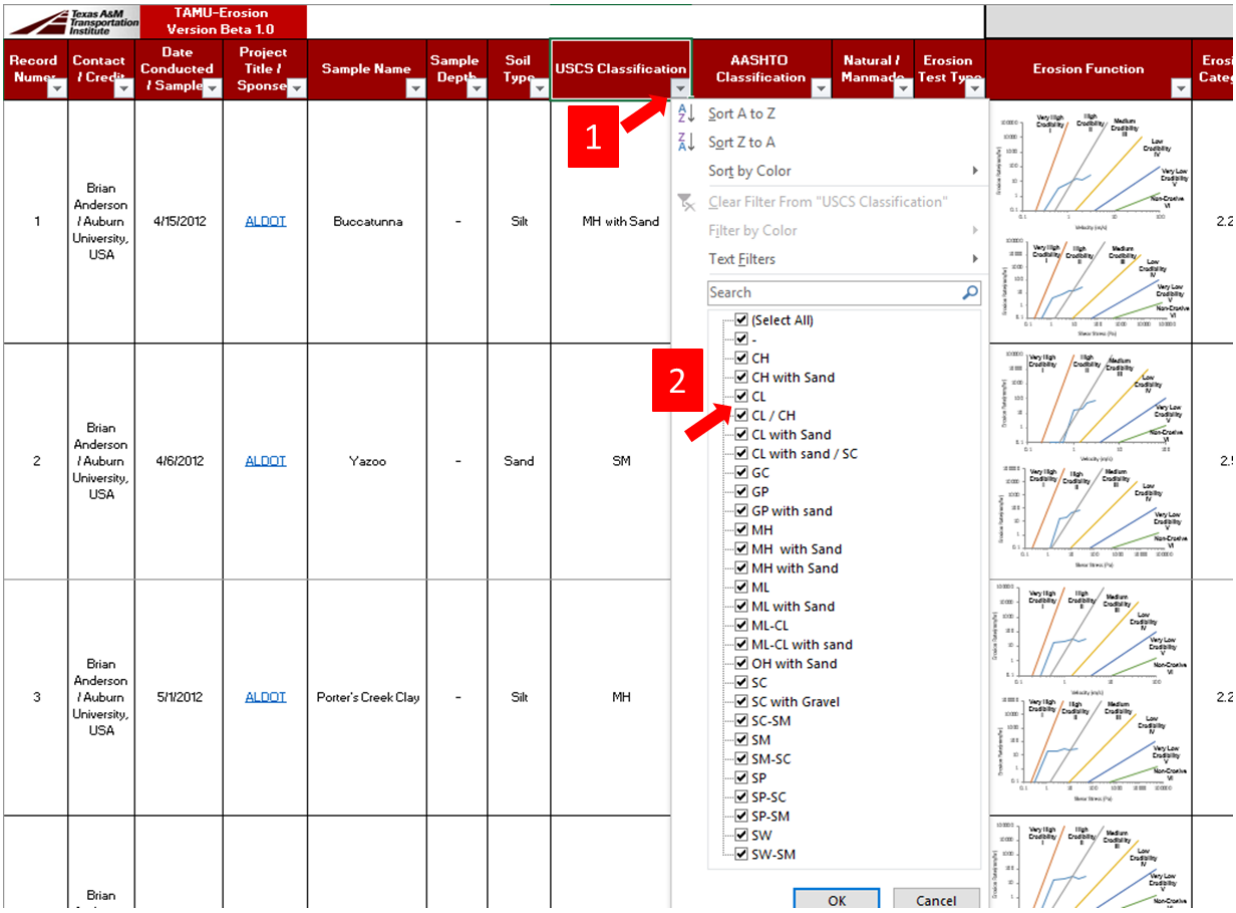

Figure 91. Filtering the data with regard to the USCS

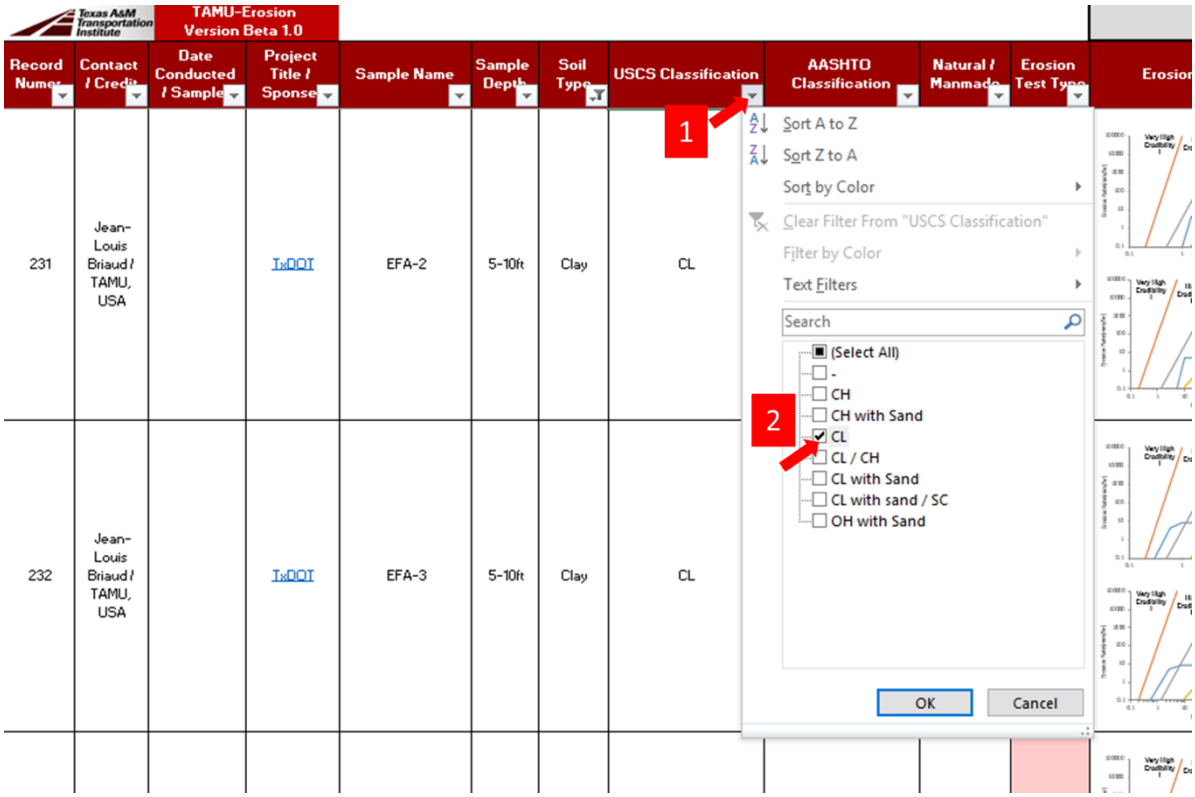

Figure 92. Filtering the data with regard to the USCS – In this example inquiry: Steps 1 and 2 show how to filter data to show only the low plastic clay (CL) soils out of all clay data

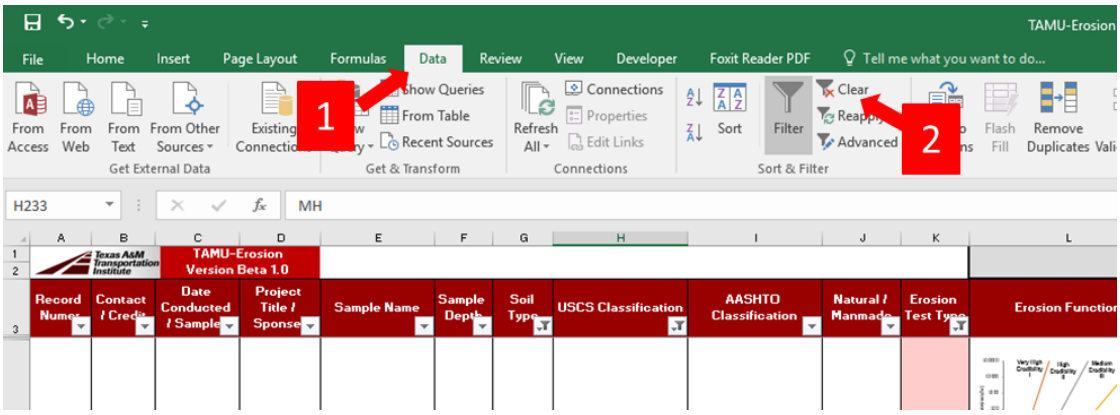

Figure 93. Clearing the filters

The next step in this example inquiry is to filter the selected data further into only the EFA test data. Figure 94 shows the process of checking the box near the EFA and unchecking all other

choices. As shown in Figure 94, the choices adjust themselves and update, as the prior filters are applied to the search. In this example, the choices are narrowed down to the list of BET, EFA, ESTD, HET, JET, widening test, PET, and SET.

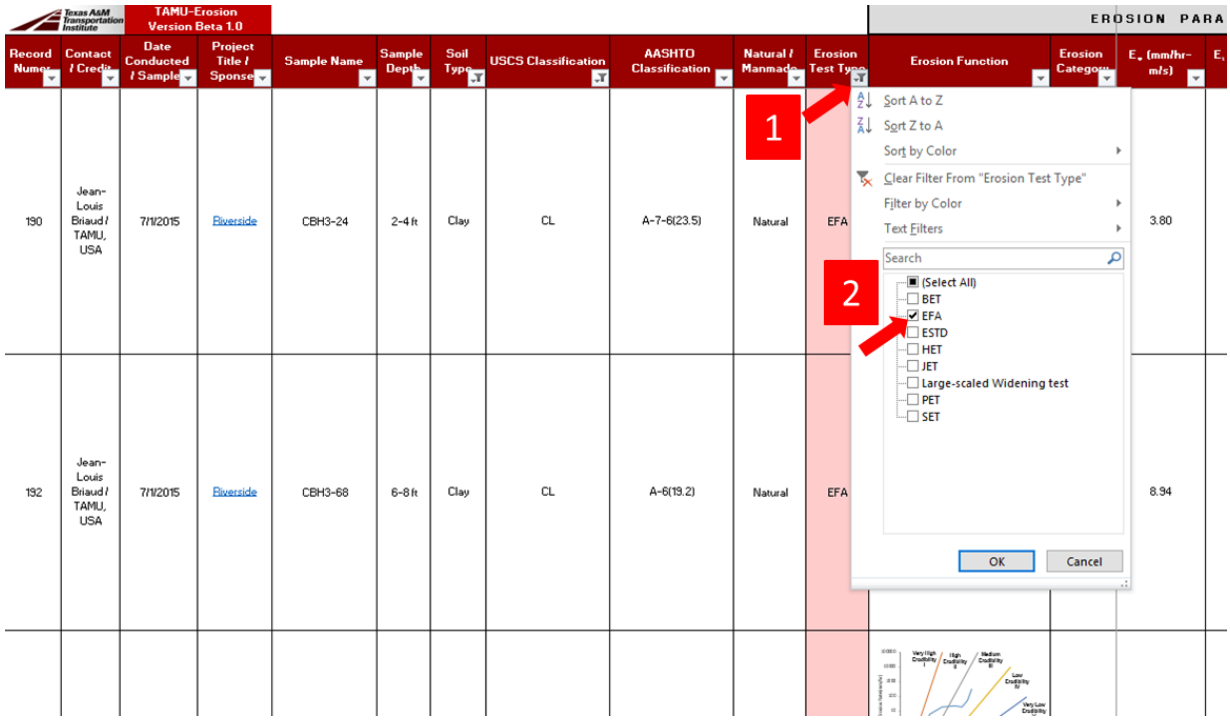

Figure 94. Filtering the data with regard to the erosion test type - In this example inquiry: Steps 1 and 2 show how to filter data to show only the EFA data

The next step in this example inquiry is to filter the data further into the data that have liquid limit (LL) between 5% and 30%. Figure 95 shows how the selected data can be filtered with regard to the LL. Please note that more filters on each column entry can be applied and added to the search criteria. In this example inquiry, only the filter process with regard to LL is shown. The same procedure can be applied to all other column entries.

As shown in Figure 95, Microsoft Excel itself has some pre-defined boundaries such as "Greater Than …" or "Between", etc. which can be selected. However, the custom filter allows

the user to choose any arbitrary boundary for filtering the data. After selecting "Custom Filter …" as shown in Figure 95, the custom AutoFilter window pops up (Figure 96). This window allows the user to select within a wide range of choices to define a custom boundary to filter the data. As described earlier, the example inquiry in this section narrows the data to those that have a liquid limit between 5% and 30%. Figure 96 shows how this range is define in the custom AutoFilter window in the Microsoft Excel (2016).

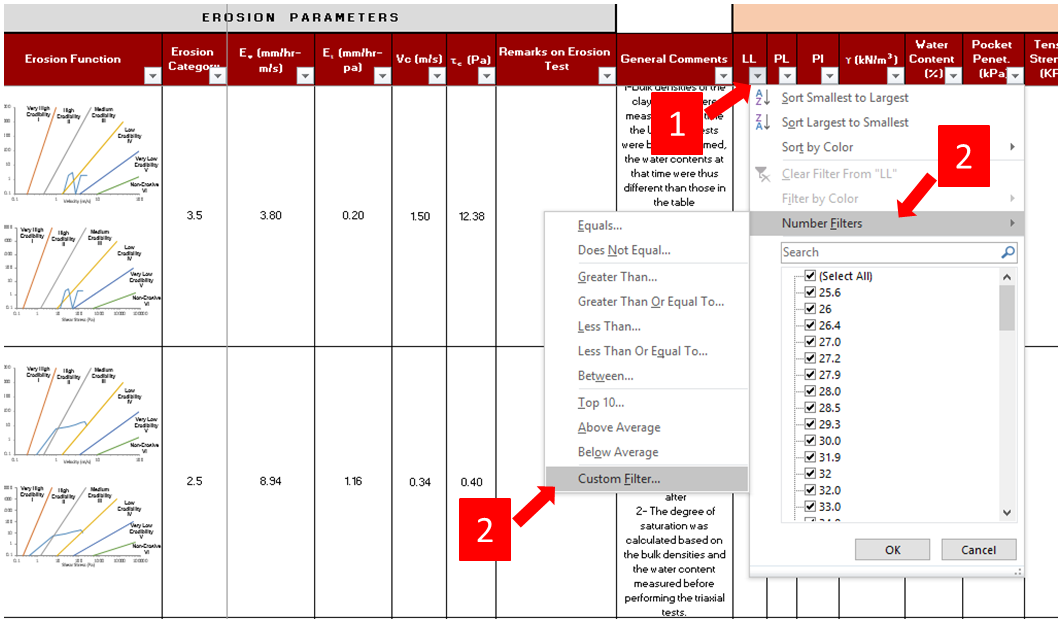

Figure 95. Filtering data with regard to the liquid limit

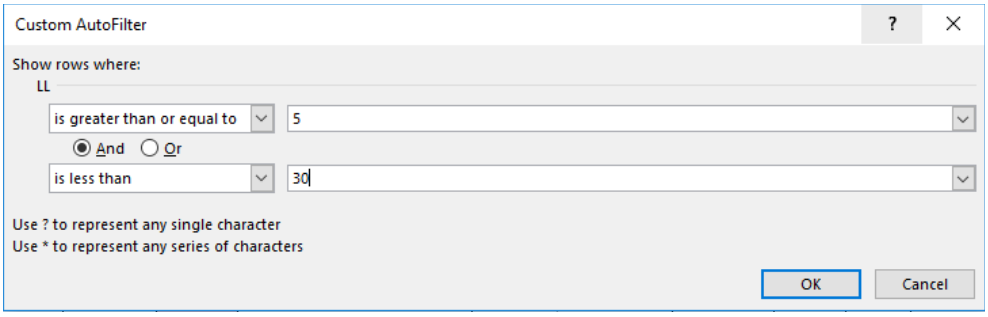

Figure 96. Custom AutoFilter window in the Microsoft Excel - In this example inquiry: The data is filtered to show only the liquid limit between 5% and 30%

6. COMPARISON OF SOIL EROSION TESTS BY NUMERICAL SIMULATIONS

As discussed in Chapters 1 and 2, one of the critical issues associated with all different erosion test devices is that they do not give the same erosion parameters; they do not lead to the same type of results. To overcome this issue, all tests need to be studied in the same fashion. In Chapter 2, all available erosion tests, their applications, test results, as well as their physical specifications are discussed in detail. Table 4 shows all different types of erosion tests explained in this report. Performing numerical studies for all tests would be cost prohibitive; therefore, we decided to study a selected number of tests among the most common ones: Erosion Function Apparatus (EFA), Jet Erosion Test (JET), Hole Erosion Test (HET), and Borehole Erosion Test (BET).

The numerical simulations presented in this chapter are divided into two separate sections: 1) evolution of the hydraulic shear stress at the soil-water interface in non-erodible soils, and 2) monitoring the variation in shear stress at the soil-water interface including the erosion process. Section 6.1 presents the results of numerical simulations for the JET, EFA, HET, and BET prior to erosion. Section 6.2 presents a novel technique using numerical simulations to compare the results of the EFA with JET, BET, and HET, including the erosion process.

6.1. Results of Numerical Simulation on Non-Erodible Soils

6.1.1. *CHEN4D Code*

For this task, computational fluid dynamics (CFD) is used together with a code called CHEN4D. The goal is to simulate each test and develop data reduction techniques which will give

the same soil erosion information from these erosion tests without changing the test. CHEN4D (Computational Hydraulic Engineering in 4 Dimensions) was developed by H.C. Chen. It is used to perform CFD simulations of the JET test, the HET test, the BET test and back calculate the erosion function which leads to proper matching of these test results with the erosion function from the EFA. These simulations are expected to lead to a common data reduction process of erosion tests, a common output of all erosion tests, bring uniformity in erosion studies, and keep all soil erosion testing options open for the scour and erosion engineer.

The CHEN4D code solves unsteady 3D Navier-Stokes equations together with advanced near-wall turbulence closure and sediment transport models for fluid-structure interaction problems around complex configurations. A moving overset (chimera) grid approach is implemented to accommodate time-domain simulation of arbitrary body motions and grid deformations such as those encountered in multiple-ship and floating pier interactions, greenwater and slamming impact of ships in random waves, vortex-induced motion of offshore platforms, pier-scour, abutment scour, and bridge scour including overtopping. Both the soil roughness and bed load transport models have been incorporated in CHEN4D for the simulation of erosion and accretion of deformable soils. The industry standard CFD models such as FLUENT and STAR-CCM+ have limited capability dealing with arbitrary multiple-body motions or large grid deformations.

6.1.2. *JET Simulations*

In this part of the interim report, results of numerical simulations on the JET are discussed. The simulations are based on the large laboratory JET device developed by Hanson and Hunt (2007) (Figure 97). The goal for this phase of the work was to simulate the submerged jet test

through CHEN4D code to obtain the hydraulic shear stress distribution on the surface of the sample prior to any erosion of the soil. Therefore, the soil is assumed to be non-erodible, and the distribution of jet flow velocity and shear stress on the surface of the soil is obtained. Two cases are assumed for the surface of the soil: 1) smooth surface which can represent a clayey soil, and 2) 5% roughness which can represent a coarse sand and gravel. Figure 98 shows the distribution of shear stress versus the distance away from the center line of the soil surface for the smooth case (clayey soils). The shear stress distributions in different time steps, as well as the time-averaged shear stress are depicted in Figure 98. The time-averaged shear stress distribution for the smooth and 5% roughness surfaces are shown in Figure 99. The results are in general agreement with the shape of Hanson's shear stress distribution shown in Figure 11. The shear stress on the point of impingement is zero, while the maximum shear stress occurs at a short distance from the center. Figure 99 shows that for a smooth surface soil (clayey soils), the maximum is less compared to the case where the soil surface is rough. Also, it is observed that the maximum shear stress happens farther from the center for the smooth soil surface than for the rough one.

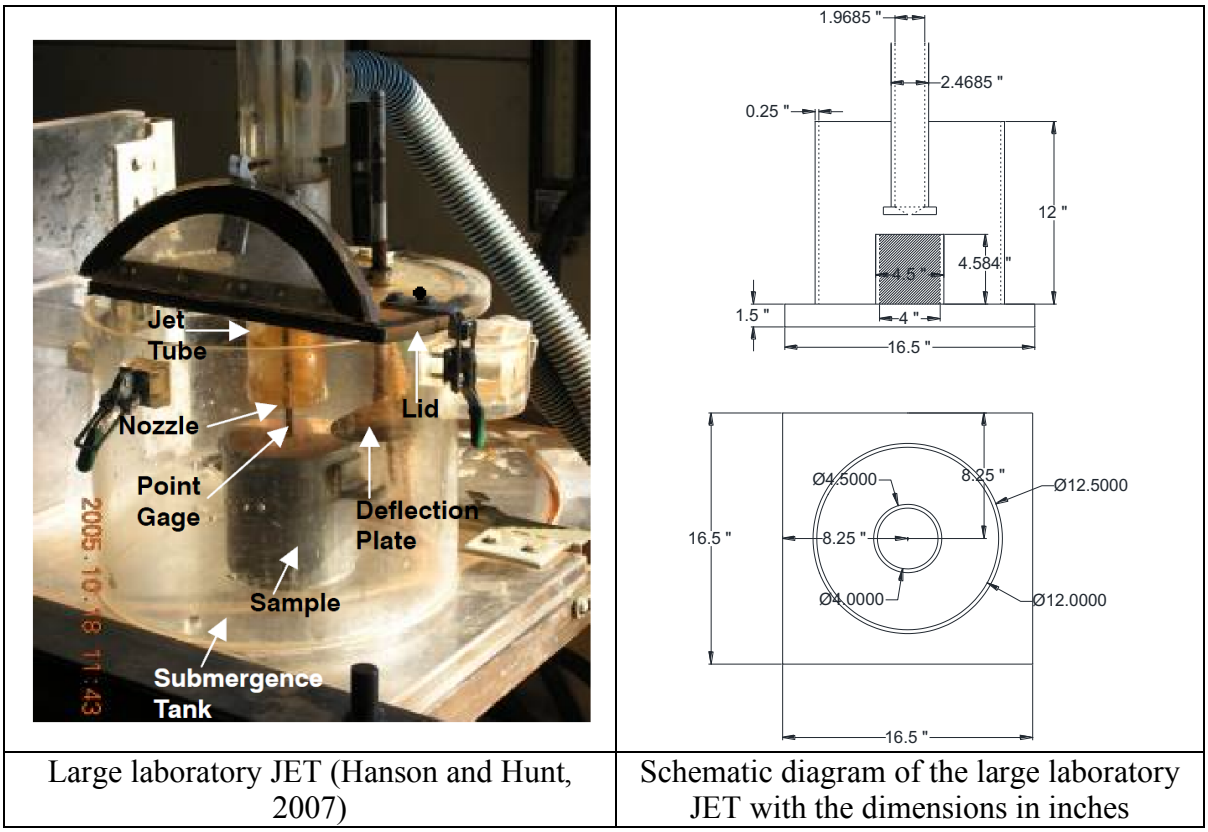

Large laboratory JET (Hanson and Hunt, 2007)	Schematic diagram of the large laboratory JET with the dimensions in inches

Figure 97. Photograph of large laboratory JET device used in the numerical simulations, along with a schematic diagram of that with dimensions

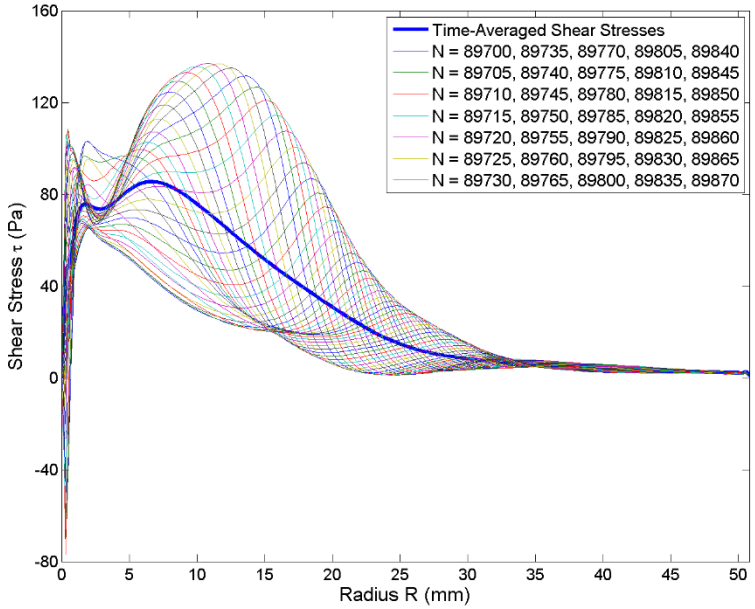

Figure 98. Shear stress distribution on the soil surface from the center of the surface to the sides in different time steps

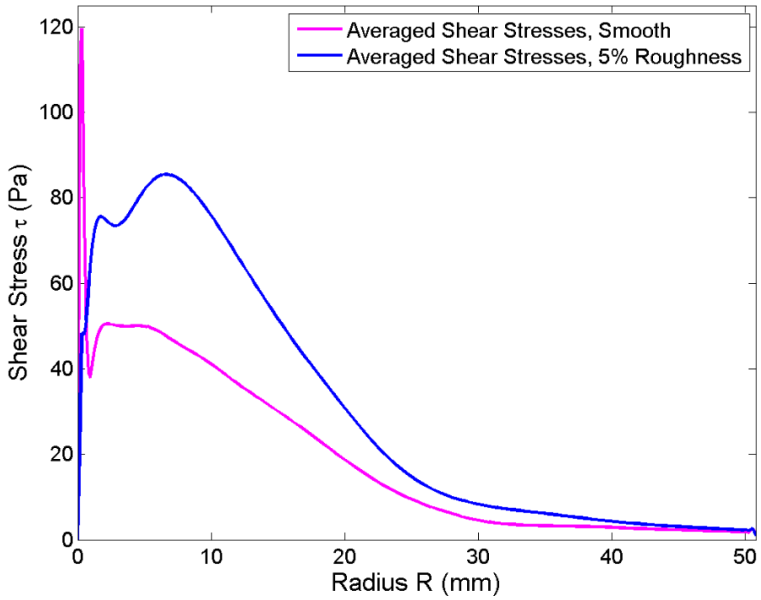

Figure 99. Average-time shear stress distribution for smooth and with 5% roughness surfaces

Figure 100 shows the evolution of the jet on the smooth surface as the steady state jet condition develops. Figure 101 shows the evolution of the jet on the rough surface as the steady state jet condition develops. The next step will be to replace the soil (white block) with an erodible surface to obtain the erodibility parameters of different soils for different hydraulic conditions.

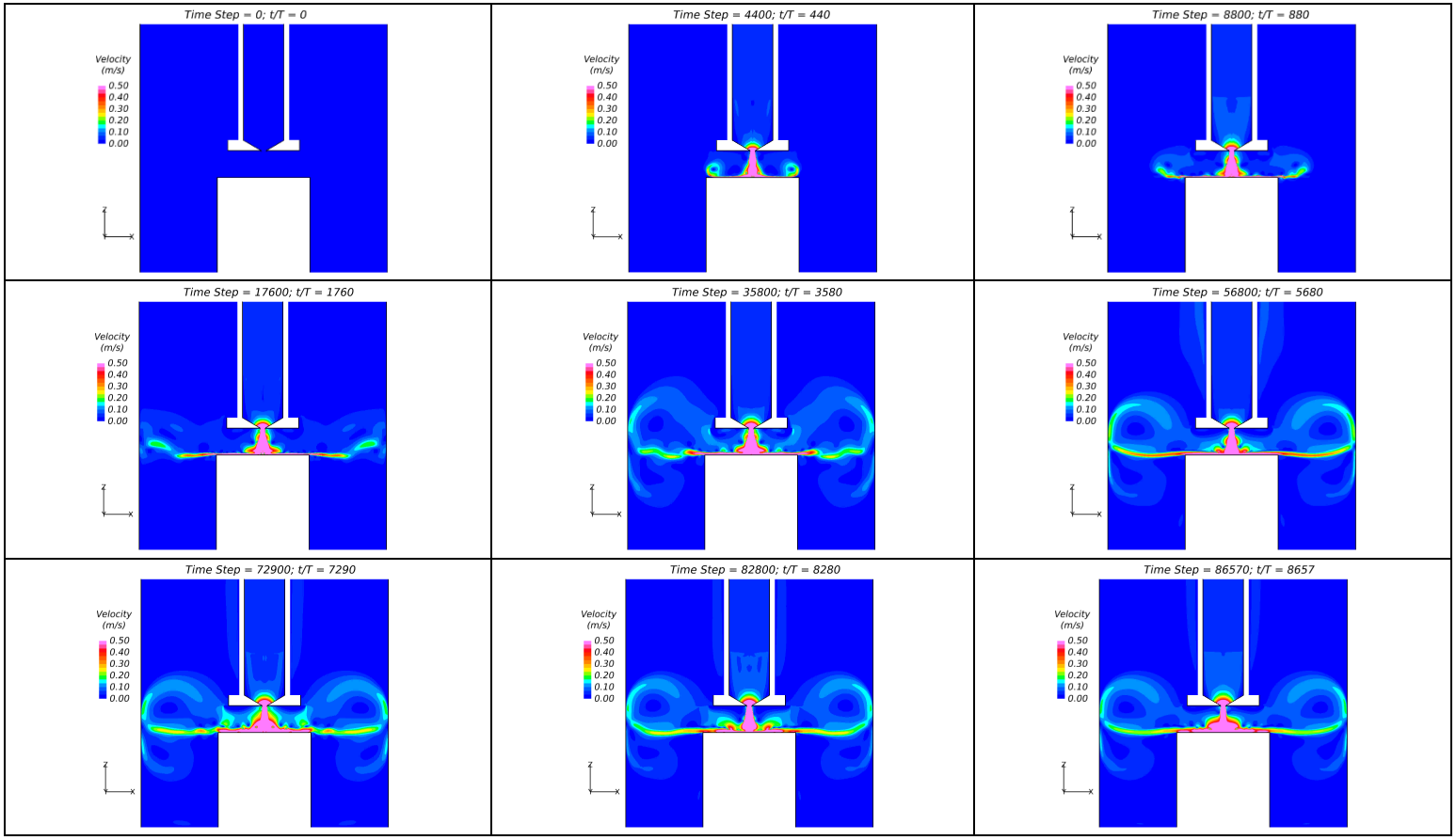

Figure 100. Velocity results of submerged jet evolution in different time steps for the smooth surface (starting from top left to bottom right)

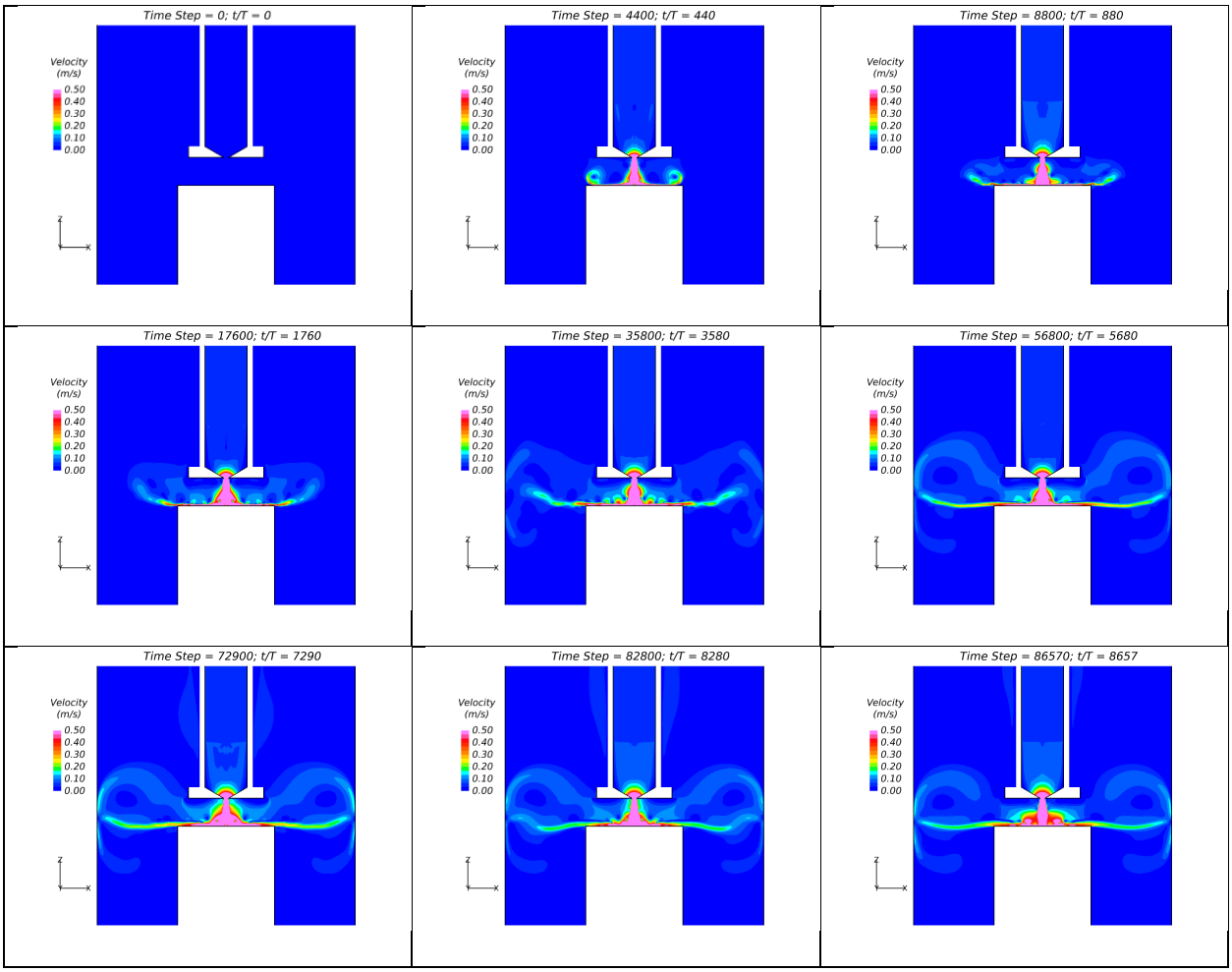

Figure 101. Velocity results of submerged jet evolution in different time steps for the rough surface (starting from top left to bottom right)

6.1.3. *HET Simulations*

CFD Numerical simulations were performed for the Wan and Fell (2002) HET. Figure 102 shows the geometry of the HET used in the numerical simulations. For more details about the HET, please refer to Chapter 2 of this report.

As in the case of the JET simulations, it is assumed that the soil is non-erodible. The water flow velocity and shear stress distributions through the HET hole are obtained. The initial stresses were evaluated for the 6 mm diameter hole in the center of the sample at an average velocity (in the hole) of 2.5 m/s. For the HET simulations, the same two cases as the JET are considered: 1)

smooth soil which represents clayey soils, and 2) surface with 5% roughness which implies sandy soils. It is worth mentioning that in the HET, the soil is compacted in a 4 inches (101.6 mm) inner diameter compaction mold, and a 6 mm hole is drilled in the center of the sample. The time-averaged shear stress distributions through the 6 mm hole along the 101.6 mm length of the sample was obtained. Figure 103 shows that the shear stress along the hole is approximately 30 Pa for coarser surface (sandy soils). As expected, the shear stress is less when the surface is smooth (clayey soils).

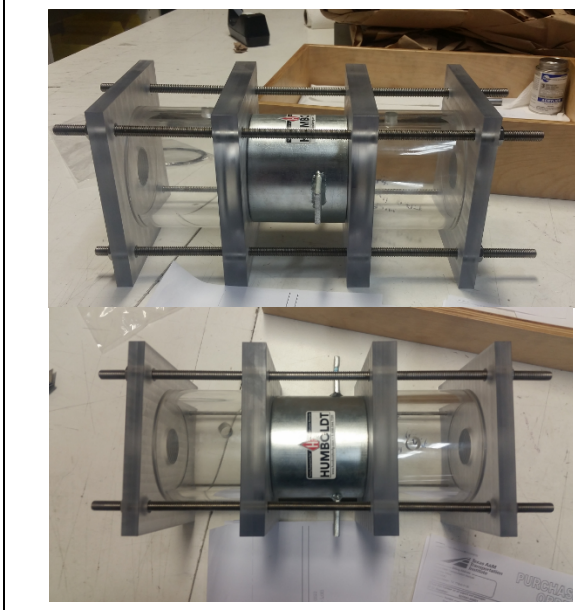

Two photographs of HET at Texas A&M University

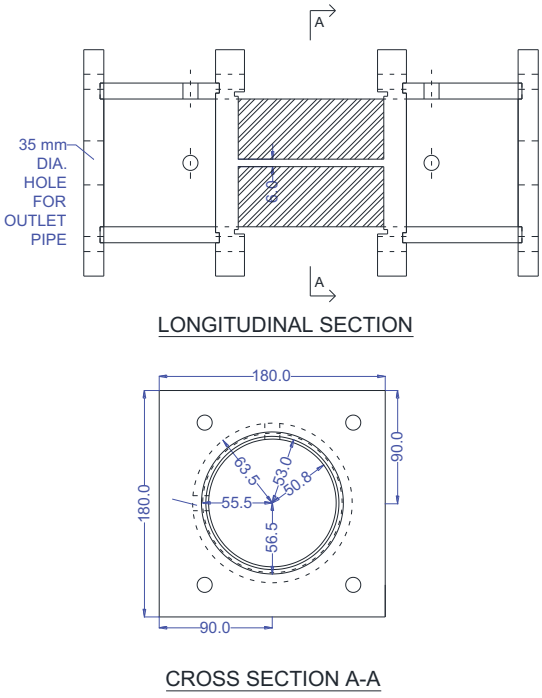

Schematic diagram of the HET with the dimensions in mm

Figure 102. Photograph and diagram of the HET used in numerical simulations

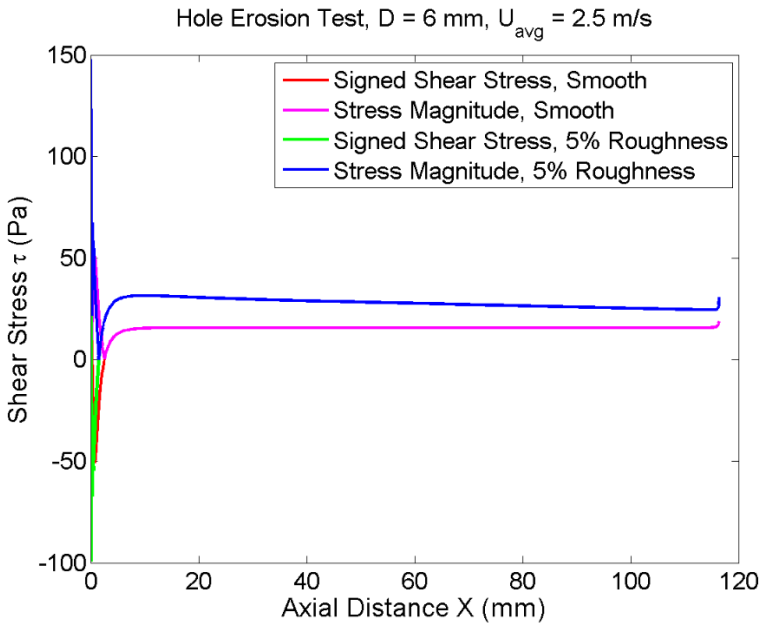

Figure 103. Shear stress distribution through the drilled hole along the length of the sample for both smooth and 5% rough surfaces, considering an average velocity of 2.5 m/s in the hole

The flow condition at the beginning of the hole is not constant. The existence of negative shear stress at the beginning is due to a small region of recirculation right where flow impinges into the hole. Due to this separate region, contraction happens, and consequently flow starts recirculating to get into the hole.

The shear stress along the drilled hole can also be estimated using Moody charts (Figure 104). Assuming a flow velocity of 2.5 m/s and diameter of 6 mm, the discharge is $7.1 \times 10^{-5}\ m^3/s$. Reynolds Number (Re) is calculated to be 14670 using Eq. 57.

$$Re = \frac{\rho_w v D}{\mu} \tag{57}$$

Where, ρ_w (kg/m^3) is density of water, v (m/s) is the flow velocity, D (m) is the diameter of flow channel, and μ is viscosity of water (1.027×10^{-3} kg/m/s). Knowing that the surface roughness is 5%, the friction factor is obtained approximately 0.075 from the Moody diagram.

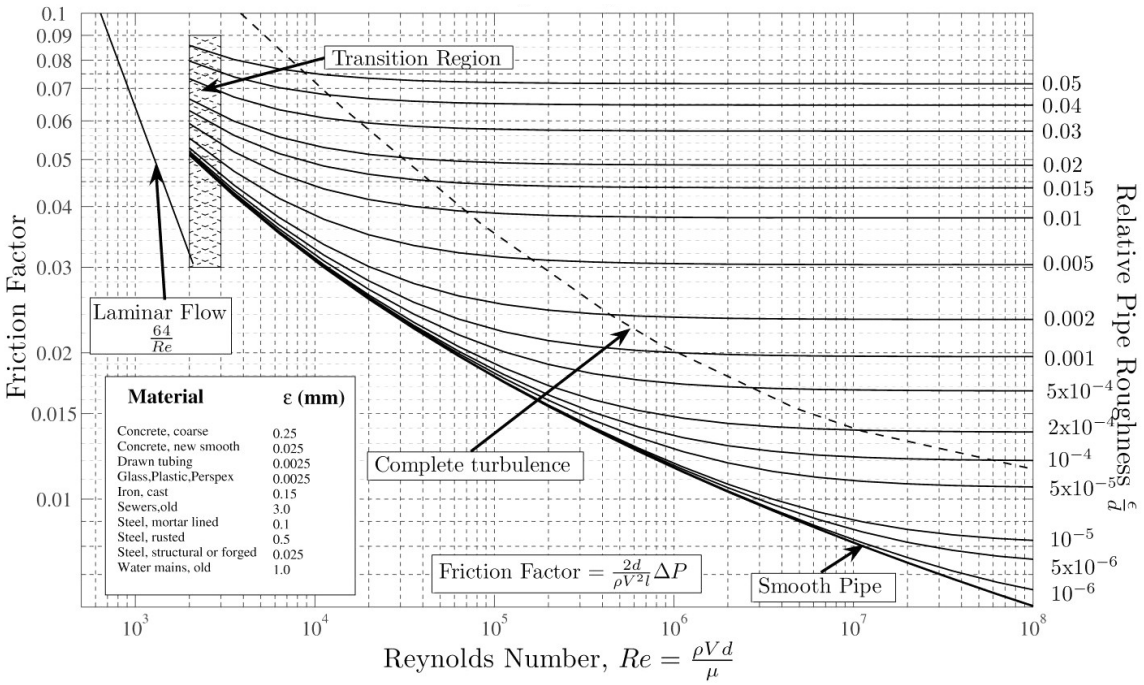

Figure 104. Moody diagram (Moody, 1944)

Using Eq. 7, the shear stress is calculated to be 50 Pa which is larger than the 25 Pa obtained through the numerical analyses' results shown in Figure 103. The difference shows that there is a discrepancy between the Moody chart predictions and the numerical simulations and that Moody charts overestimate the shear stress by 100% in this case. For the case of a smooth pipe, knowing that the Reynolds Number (Re) is 14670, the friction factor is 0.028 from the Moody Diagram (See Figure 104). Using Eq. 7, the shear stress is calculated as 21.875 Pa which is larger than the 10 Pa obtained through the numerical simulation shown in Figure 103. Again, the Moody Diagram gives higher values. The evolution of the velocity for the smooth case is shown in Figure 105, as an illustration.

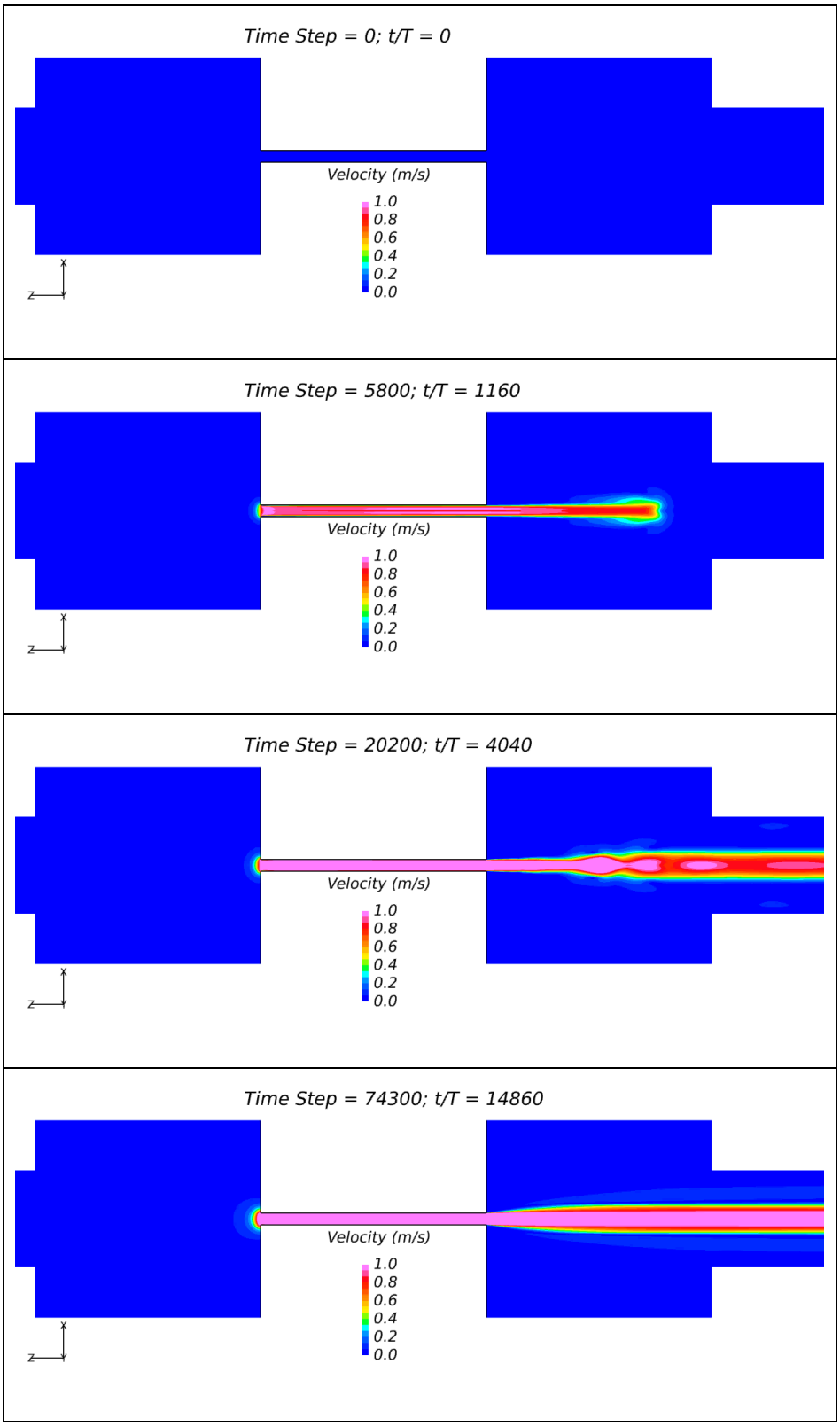

Figure 105. Velocity evolution for the smooth case

6.1.4. *EFA Simulations*

The EFA geometry used in the simulations is as described in Chapter 2. As mentioned earlier, EFA comprises of a rectangular channel which is approximately 1.24 m long. On the bottom surface, Shelby tube size sample with an outer diameter of 76.2 mm is extruded. The surface of the conduit is assumed to be smooth. Three target velocities (U = 1 m/s, 3 m/s, and 6 m/s) are considered in the results. The channel height is used as the characteristic length instead of the channel hydraulic diameter (D_h = 67.33 mm) in the simulations. The roughness of the soil surface is 5% (of the channel height) in all the cases.

Figure 106 to Figure 108 show the shear stress distribution on both top and bottom surface of the channel for U = 1 m/s, 3 m/s, and 6 m/s, respectively. In these figures, both the smooth (upper half) and rough (lower half) results on the same figure are plotted to facilitate a direct comparison of the effect of surface roughness.

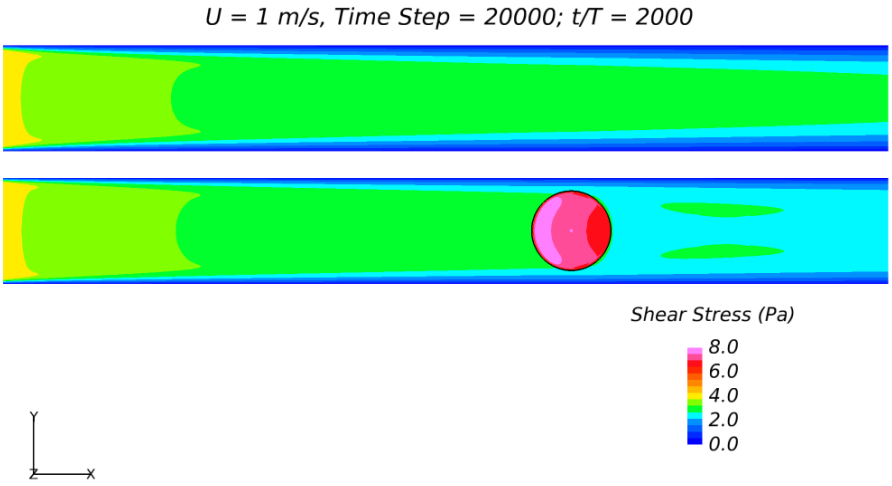

Figure 106. Shear stress distribution on both top surface (which is smooth) and bottom surface (which encompasses the rough soil surface) for the U = 1 m/s

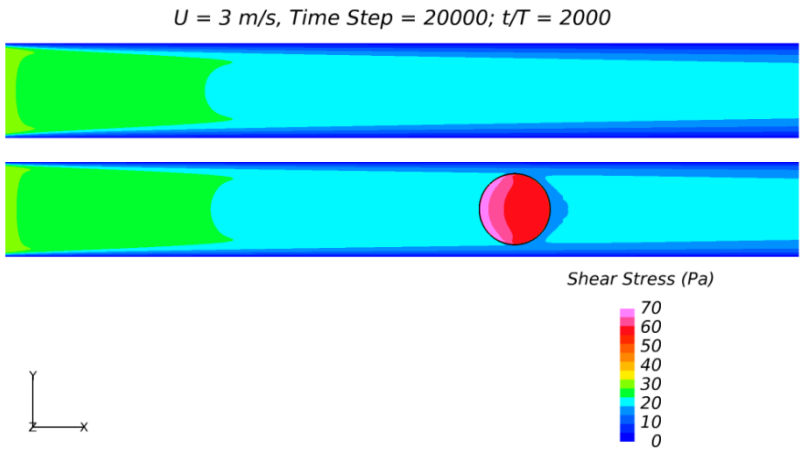

Figure 107. Shear stress distribution on both top surface (which is smooth) and bottom surface (which encompasses the rough soil surface) for the U = 3 m/s

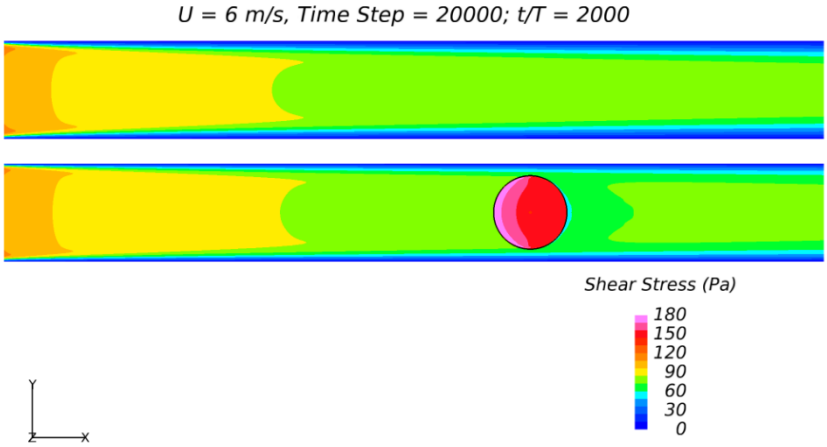

Figure 108. Shear stress distribution on both top surface (which is smooth) and bottom surface (which encompasses the rough soil surface) for the U = 6 m/s

The shear stresses are also calculated using Moody chart (Figure 104). Reynolds number can be calculated using ρ_w=1000 kg/m^3, D = 0.00508 m, and $\mu_w = 1.027 \times 10^{-3}$ kg/m/s. The friction factors for the case of 5% roughness are then obtained as 0.079, 0.075, and 0.073 for U = 1 m/s, 3 m/s, and 6 m/s, respectively. Eq. 7 is then used to measure the shear stresses for each velocity. The resulting shear stresses from Moody chart are 9.875 Pa, 84.375 Pa, and 324 Pa for U

= 1 m/s, 3 m/s, and 6 m/s, respectively. Comparing the shear stress results obtained from the numerical simulations with Moody chart shows that as in the case of the HET results, Moody chart overestimate the shear stress values by about 25%.

Figure 109 to Figure 111 shows the shear stress evolution when the velocity is 1 m/s, 3 m/s, and 6 m/s, respectively. The soil surface roughness is 5% in all the cases.

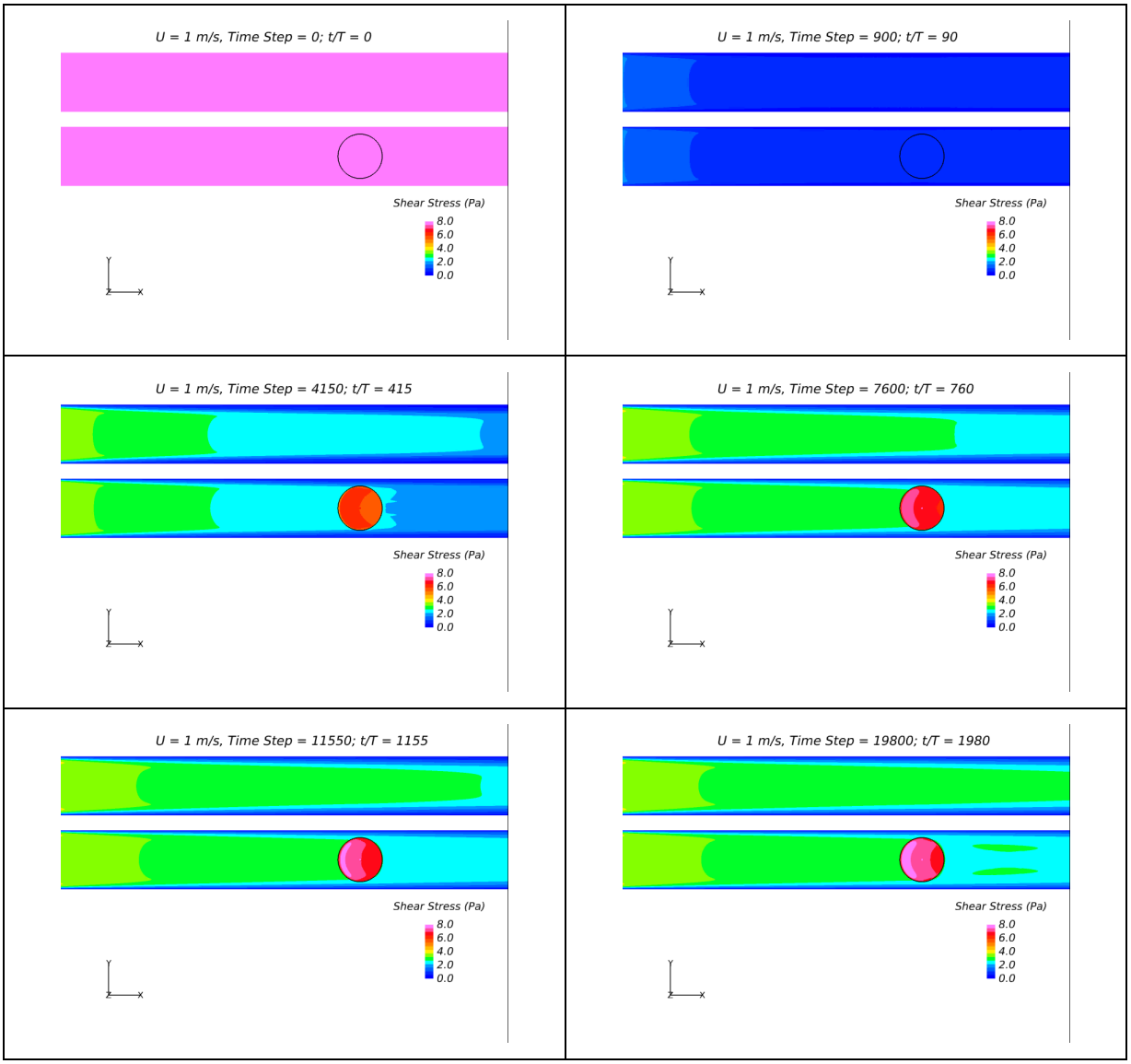

Figure 109. Shear stress evolution captured in six time steps, when the flow velocity in the conduit is 1 m/s (starting from top left to bottom right)

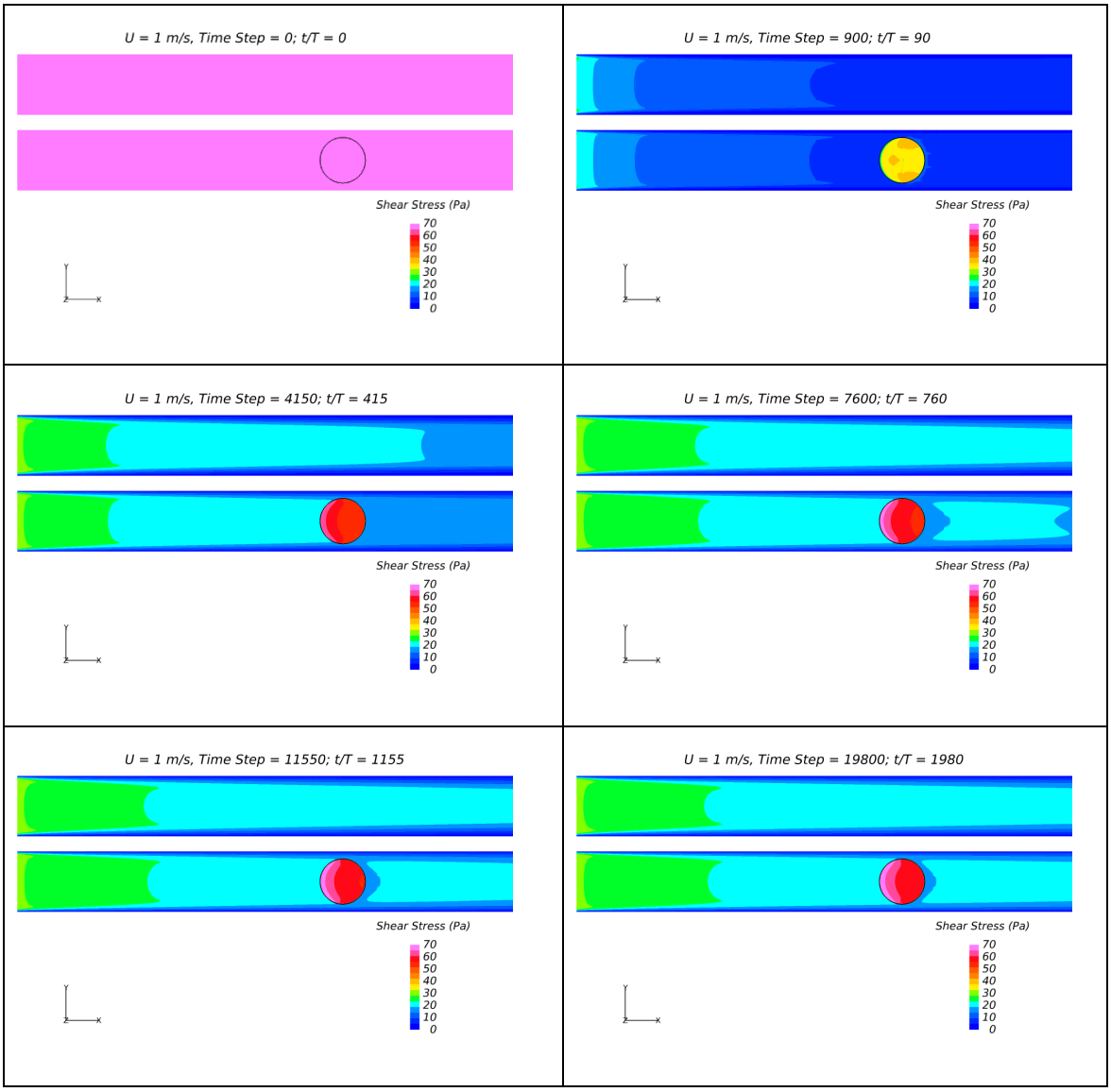

Figure 110. Shear stress evolution captured in six time steps, when the flow velocity in the conduit is 3 m/s (starting from top left to bottom right)

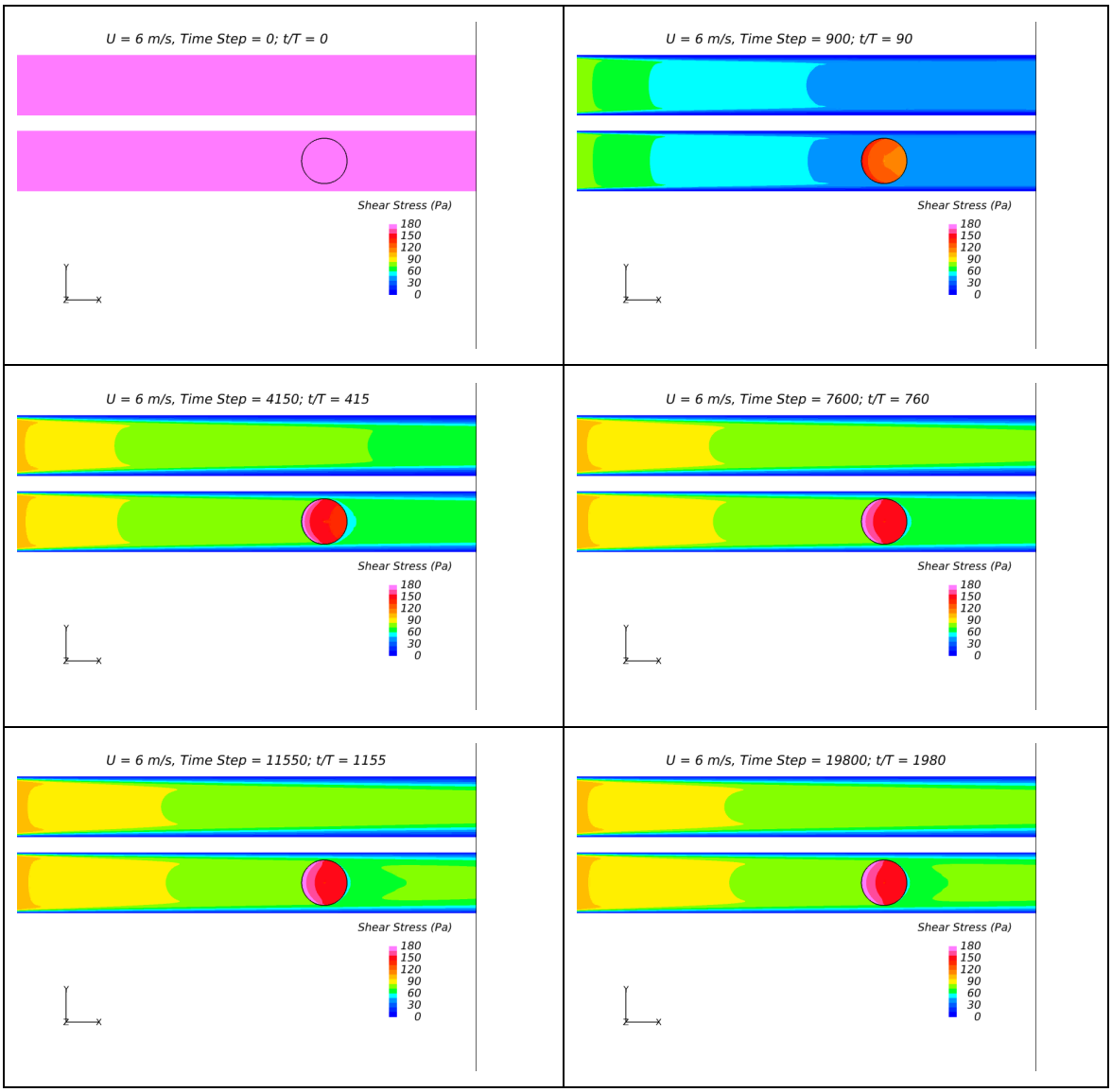

Figure 111. Shear stress evolution captured in six time steps, when the flow velocity in the conduit is 6 m/s (starting from top left to bottom right)

6.1.5. *BET Simulations*

Numerical simulations were also performed for the Borehole Erosion Test (BET), assuming a non-erodible soil with the purpose of obtaining the shear stress distribution at the soil surface. The geometry of the BET is described in Chapter 2. For the following simulations, two flow rates (23 gpm and 90 gpm) are considered. Also, three distances between the jet orifice and

the bottom surface of the borehole are considered (1 inch, 3 inches, and 6 inches). Figure 27 shows the schematic diagram of the BET. As shown in Figure 27, the jet is inducing shear stress both at the circular bottom surface, and along the side walls in the z-direction. Shear stress results for both regions are presented for the two aforementioned flow rates.

Figure 112 shows the shear stress distribution along the radius of the circular bottom surface of the borehole, when the flow rate is 90 gpm. Obviously, when the gap between the jet orifice and the bottom surface is smaller, the maximum induced shear stress will be larger and farther from the jet impingement point.

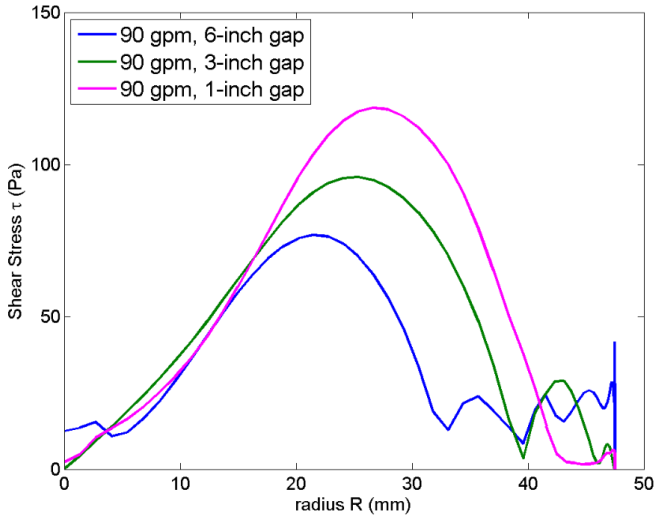

Figure 112. Shear stress distribution within the circular bottom surface of the drilled hole with 1 inch, 3-inch, and 6-inch gap between the jet orifice and borehole bottom surface, when the flow rate is 90 gpm

Figure 113 also shows the shear stress distribution along the side wall of the drilled hole for the same three gap intervals, when the flow rate is 90 gpm. It is observed that the maximum shear stress is largest when the gap between the discharge orifice and the bottom surface is 3 inches.

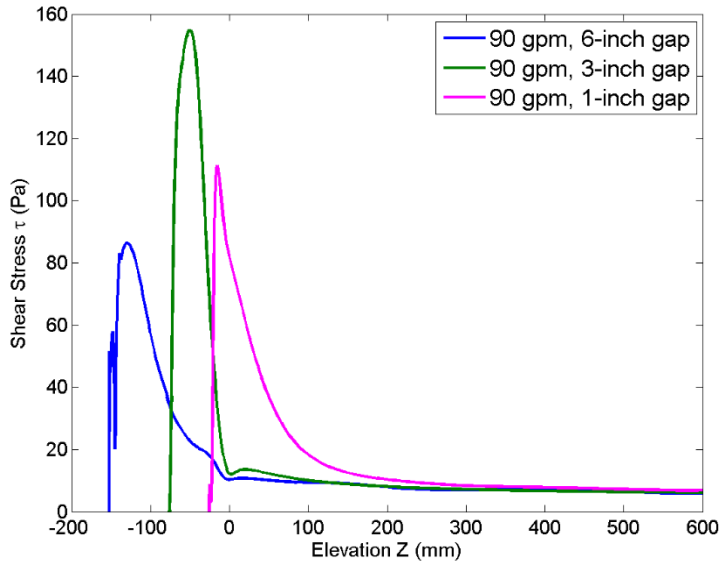

Figure 113. Shear stress distribution along the side wall surface of the drilled hole with 1 inch, 3-inch, and 6-inch gap between the jet orifice and borehole bottom surface, when the flow rate is 90 gpm

The same approach was used for a flow rate of 23 gpm. Figure 114 and Figure 115 show the results for the shear stress on the circular bottom surface and on the side wall, respectively. In these figures, the effect of a 2% roughness is shown only when the gap between the discharge orifice and the bottom surface is 1 inch.

Figure 114 shows that the shear stress is higher when the gap is small (1 inch), and decreases when the gap increases. Also, the shear stress distribution is slightly different when a 2% roughness is considered for the bottom surface (coarser soils). Comparison between Figure 114 and Figure 112 shows that the shear stress distribution is smoother at higher flow rates.

Figure 115 shows the measured shear stress along the side wall of the borehole. The maximum shear stress, similar to the case that flow rate was 90 gpm, happens when the gap between the jet orifice and bottom of the borehole is 3 inches. Also, it is observed that 2% roughness on sides will result in a slightly higher shear stress values compared to the smooth side.

It also shows that after about 0.5 m above the bottom discharge the shear stress on the borehole wall has become constant.

Figure 116 shows an example of the numerical simulations in four different time steps. In this example, the gap between discharge orifice and the bottom of the borehole is 1 inch, and the flow rate is 23 gpm. Velocities range from 0 to 6 m/s at the bottom of the borehole, and 0 to 2 m/s on the sides.

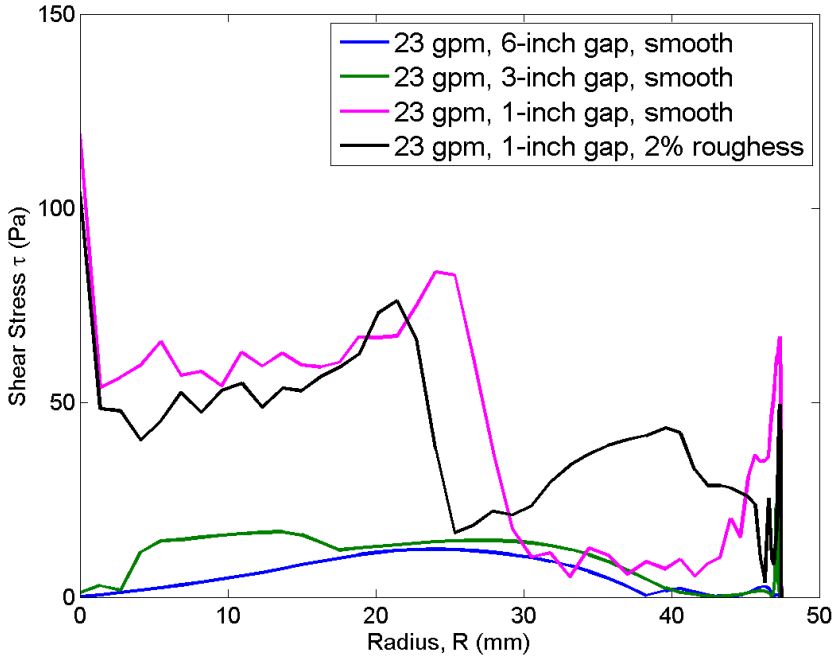

Figure 114. Shear stress distribution within the circular bottom surface of the drilled hole with 1 inch, 3-inch, and 6-inch gap between the jet orifice and borehole bottom surface, when the flow rate is 23 gpm

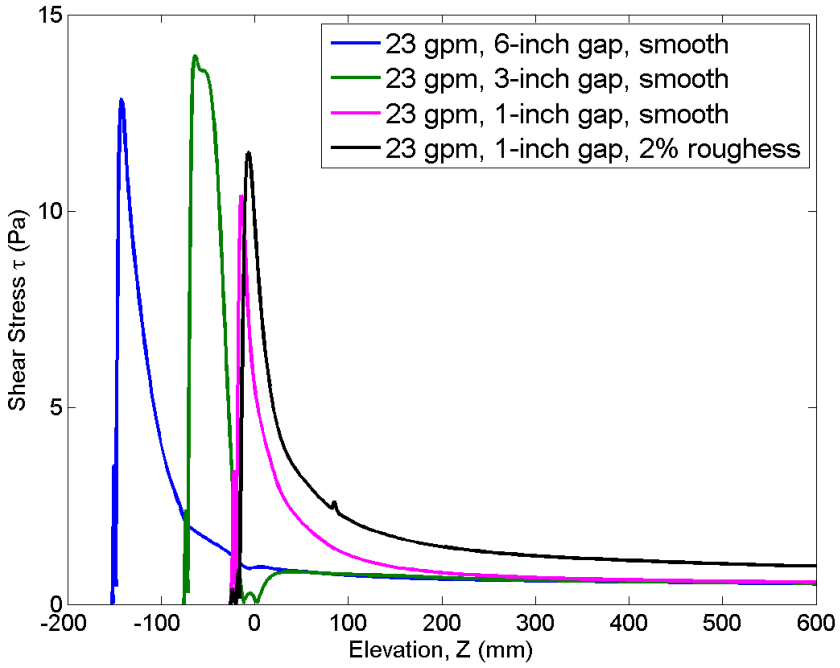

Figure 115. Shear stress distribution along the side wall surface of the drilled hole with 1 inch, 3-inch, and 6-inch gap between the jet orifice and borehole bottom surface, when the flow rate is 23 gpm

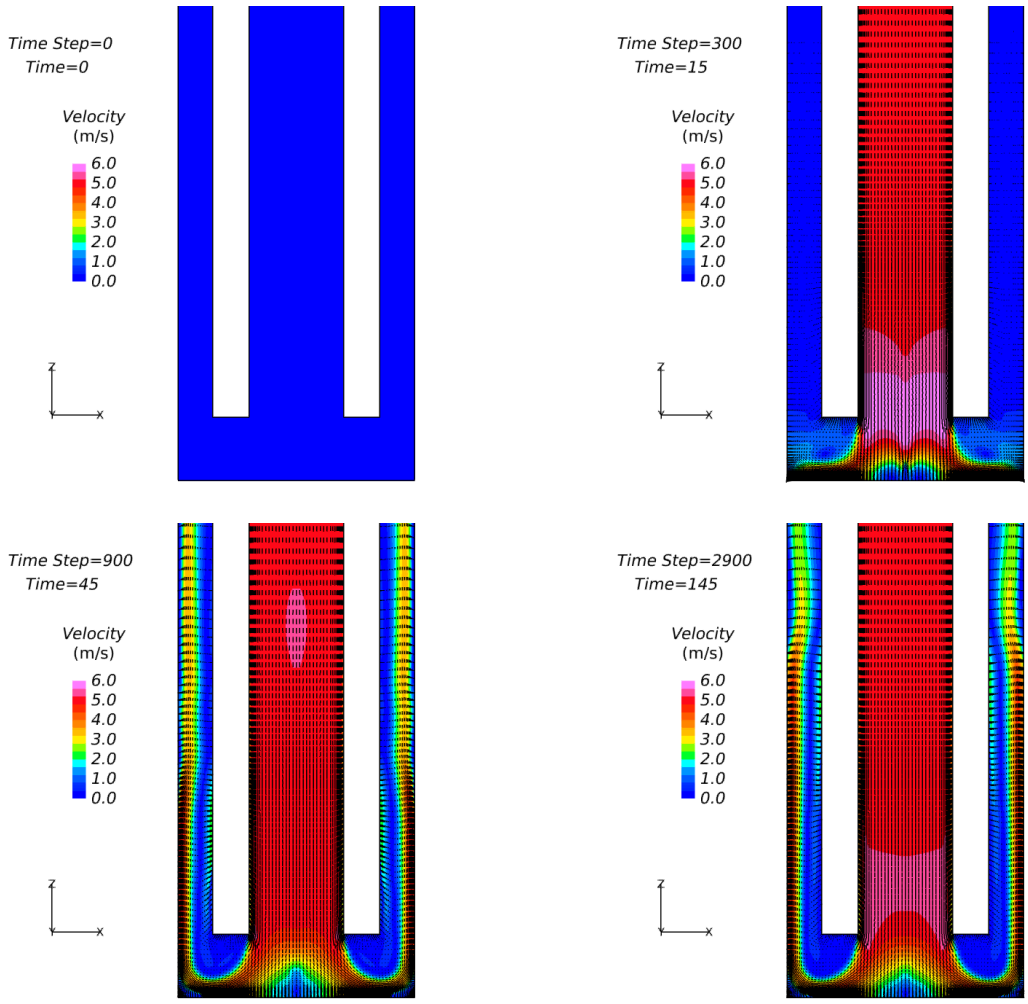

Figure 116. An example of velocity results of jet evolution in different time steps for the rough when the gap between orifice and bottom surface is 1 inch (starting from top left to bottom right)

6.2. Results of Numerical Simulation Including Erosion

6.2.1. *Methodology*

In the previous section, the development of shear stress on the soil-water interface was simulated and discussed for the EFA, JET, HET, and BET, with an assumption that the soil is not erodible. This section presents the results of the numerical simulations including the erosion

process. The software used for this purpose is CD-adapco's Star Computational Continuum Mechanics (Star CCM+) (2014). Star CCM+ can generate the computational fluid dynamics (CFD) in soil-fluid interaction problems such as the erosion process.

The primary goal of using numerical simulations was to compare the results of the four aforementioned erosion testing methods (i.e. EFA, HET, JET, and BET) in similar soil samples. As discussed in Chapter 1, the results of each erosion test can be translated into a relationship between the shear stress/velocity and the erosion rate. In fact, the erosion rate ($\dot{z}$) is a function of shear stress/velocity (See Eqs. 1 and 2). The relationship between the erosion rate and the shear stress (or velocity) is called the "Erosion Function".

The numerical simulations are concentrated on finding out that how the JET, the HET, and the BET would react to the erosion function obtained from the EFA on one common soil sample. The results of the numerical simulations are compared with the actual test results obtained through experiments. The soil surface in the JET, the HET, and the BET is defined as a moving boundary. The erosion process is simulated using the movement of these boundaries. This movement develops according to the erosion function equation that is obtained from the EFA test performed on the same soil sample. Figure 117 shows a flowchart describing the procedure for each numerical simulation.

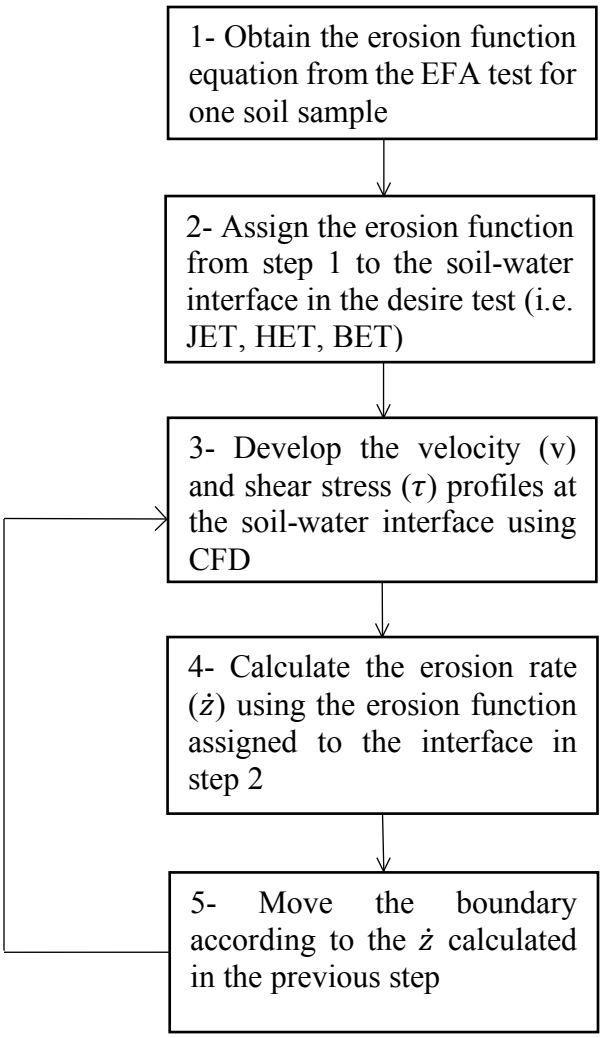

Figure 117. The procedure of the numerical simulations conducted to compare the results of the EFA with the results of the HET, the JET, and the BET

The numerical simulations according to the procedure shown in Figure 117 are presented in the three following forms:

1) EFA's Erosion Function on the JET
2) EFA's Erosion Function on the HET
3) EFA's Erosion Function on the BET

Before discussing the results of these comparisons, the details of the mesh created for the JET, the HET, and the BET in Star CCM+ are presented below.

6.2.2. *Mesh Geometry and Soil-Water Interface*

For all the three erosion tests (JET, HET, and BET), two-dimensional axisymmetric models were created. The mesh used in these models is quadrilateral. The detailed information on the mesh used for each erosion test is presented in Table 30 below. Also, Figure 118, Figure 119, and Figure 120 show the axisymmetric models created for the JET, the HET, and the BET, respectively. It should be noted that the dimensions used for the models are in accordance with the dimension of these testing devices in the Erosion Laboratory at Texas A&M University. For detailed information on dimensions of each test device, please refer to the Section 4.1 of this report.

Table 30. Detailed information on the created mesh for each erosion test

Erosion Test	*Type of Mesh*	*Number of Cells*	*Number of Faces*	*Number of Vertices*
JET	Quadrilateral	8809	17501	9115
HET	Quadrilateral	22918	45151	23673
BET	Quadrilateral	31765	62244	33054

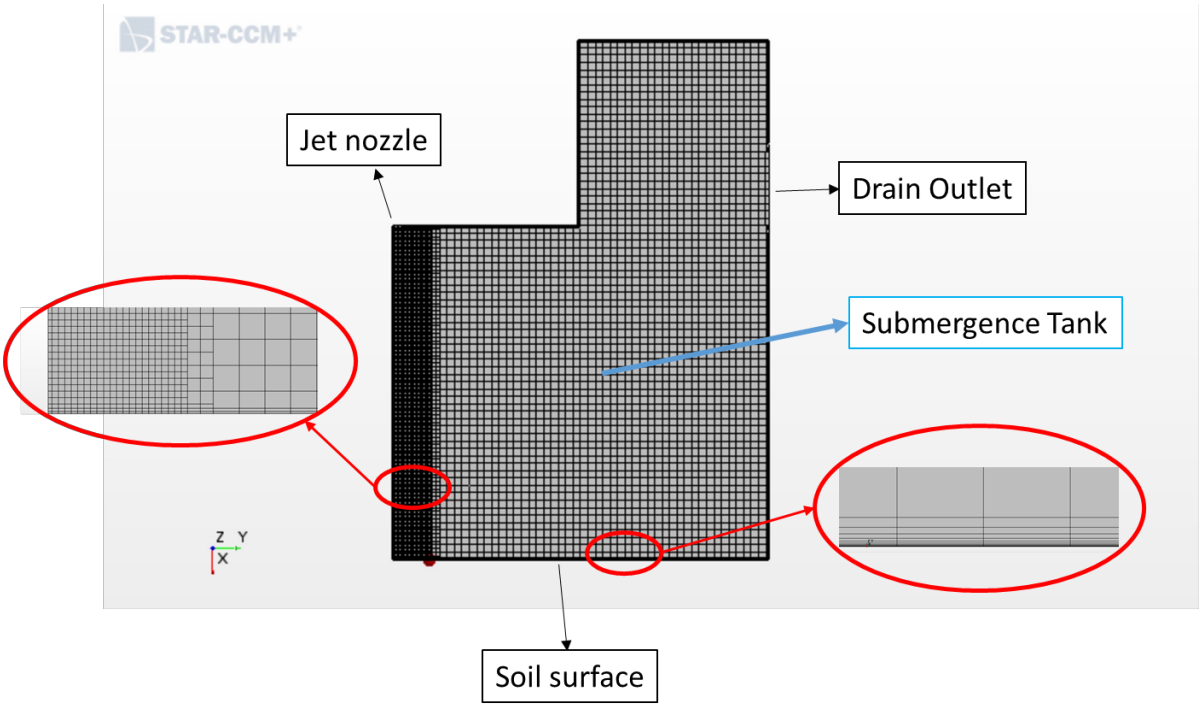

Figure 118. The axisymmetric model for the JET

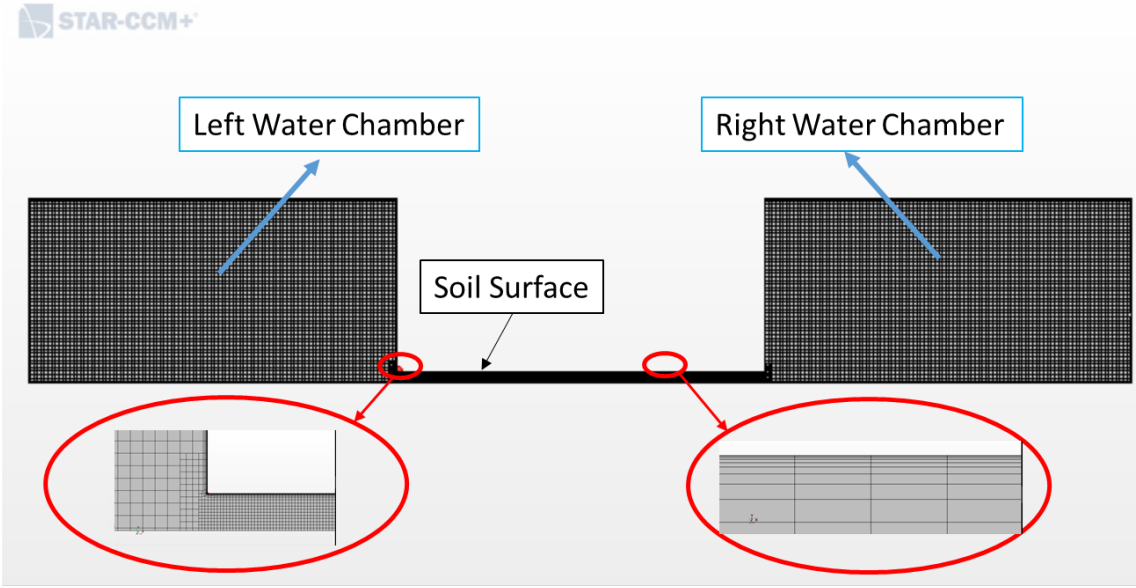

Figure 119. The axisymmetric model for the HET

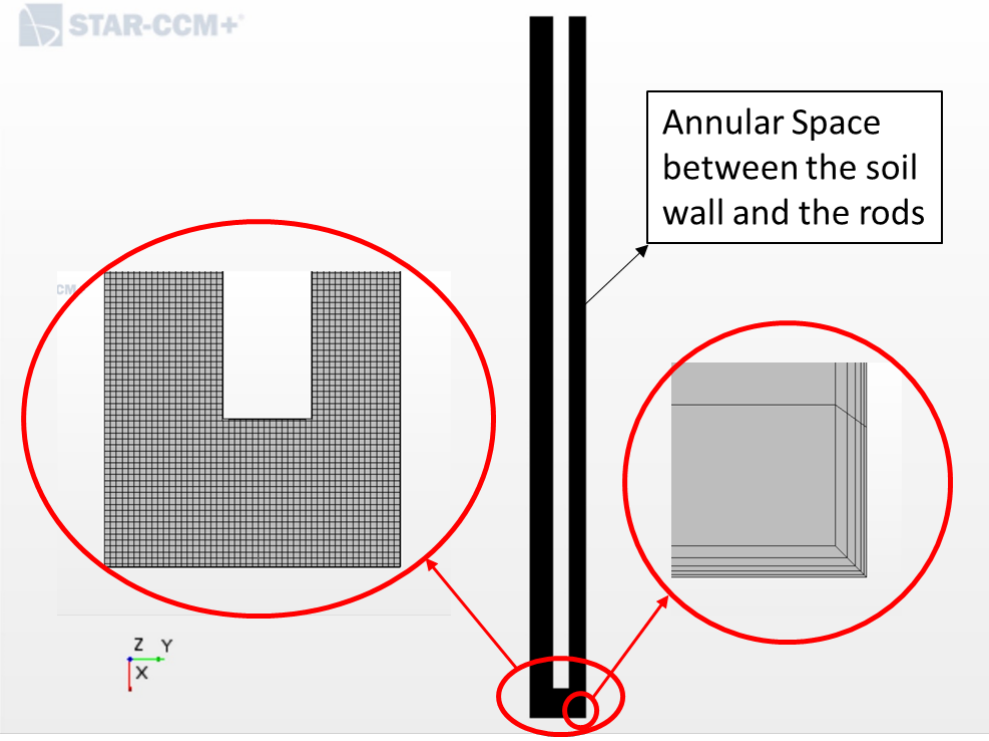

Figure 120. The axisymmetric model for the BET

One of the important laws in the fluid dynamics is the law of the "wall". This law states that in turbulent flow, the mean velocity at a specific point and the logarithm of the distance between that point and the fluid region boundary (or the "wall") are proportional. The effect of this law is very significant especially for those parts of the flow that are closer than 20% of the flow height to the wall. The general formulation of the law of the wall (Eq. 58) solves for the average velocity parallel to the wall in turbulent flows (high Reynold's numbers).

$$u^+ = \frac{1}{\kappa}\ln y^+ + C^+ \tag{58}$$

Where u^+ is a dimension-less velocity parameter and equals u (average velocity parallel to the wall) divided by the u_T (friction velocity); y^+ refers to the dimension-less wall coordinate, and is obtained using Eq. 59. The parameters κ and C^+ are two constants that are equal to 0.41 and 0.5, respectively, for a smooth wall according to Schlichting and Gersten (2000).

$$y^+ = \frac{y \times u_T}{\nu} \quad (59)$$

Where ν is the local kinematic viscosity of the fluid; u_T is mentioned earlier is the friction velocity at the closest fluid region boundary, and y is the distance of the point to the nearest wall. y^+ is one of the most important parameters in defining the law of the wall and conducting the fluid mechanics numerical simulations. For this study, the value of y^+ is designed to be less than 1 to achieve very small cell distance between the wall and the point of flow ($y < 10^{-6}\ m$).

6.2.3. *Model Development*

Numerical simulations were performed for the JET, HET, and BET as explained in the previous sections (Figure 117). The results of comparisons between the EFA Test with other erosion tests are presented separately in the following sections.

6.2.3.1. EFA's Erosion Function on the JET

As discussed in Section 6.2.1, the erosion rate can be written as a function of shear stress. For the purpose of comparing the EFA test results with the JET results, a procedure as described in Figure 117 was followed for four different samples (2 sand, 1 silt, and 1 clay). The names of these samples are: Sand #1 & Sand #2 (sand samples), FHWA Sample 2 (silt sample), and B-1 (4'-6') Beaumont (clay sample).

As presented in Figure 117, the first step was to obtain the relationship between the erosion rate ($\dot{z}$) and the shear stress for each sample in the EFA. This relationship, also called the erosion function, is obtained after testing each of the four samples in the EFA, and then assigned to the soil-water interface in the JET simulation which is defined in the form of a moving boundary. Once the shear stress is developed on the soil-water interface, the erosion rate at the boundary is calculated using the assigned erosion function, and the boundary moves accordingly. This process

repeats itself and the boundary keeps moving until the developed shear stress on the interface becomes equal or less than the critical shear stress for the tested soil.

In order to distinguish between smooth clay and rough sand surface, the Roughness Height (RH) is defined in Star CCM+. RH is the height of the roughness of the soil particles (equivalent to Ɛ defined in Moody diagram shown in Figure 104). In this study, for each simulation whether the sample is clay, silt, or sand, four RH values were considered: 1) RH = 0 mm or smooth surface, 2) RH = 0.5 mm, 3) RH = 1 mm, and 4) RH = 3 mm.

Figure 121 shows the results of the numerical simulations for the sample Sand #1 when the erosion function obtained from the EFA test on the exact same sample is used at the soil-water interface in the JET model. It is shown that the observed JET results (black circles) are slightly over-estimated through Star CCM+ when their erosion function obtained from the EFA is assigned to the soil-water interface. This over-estimation is less pronounced when the roughness height is close to 0 mm (smooth surface). The actual average roughness height ($D_{50}/2$) for SE-1 is about 0.14 mm, therefore, smooth surface results would be a relatively reasonable assumption.

Figure 122 shows an example of the numerical simulations in four different time steps for the Sand #1 sample. In this example, the soil-water interface is defined as a moving boundary. Also, the velocity profile of the flow is shown for each time step. Velocity for this example ranges between 0 to 3.2 m/s. The highest amount of velocity is of course at the jet nozzle and when the water reaches the soil surface, its velocity becomes less. This process continues until the shear stress induced on the boundary (soil-water interface) becomes less than the measured critical shear stress from the EFA's erosion function.

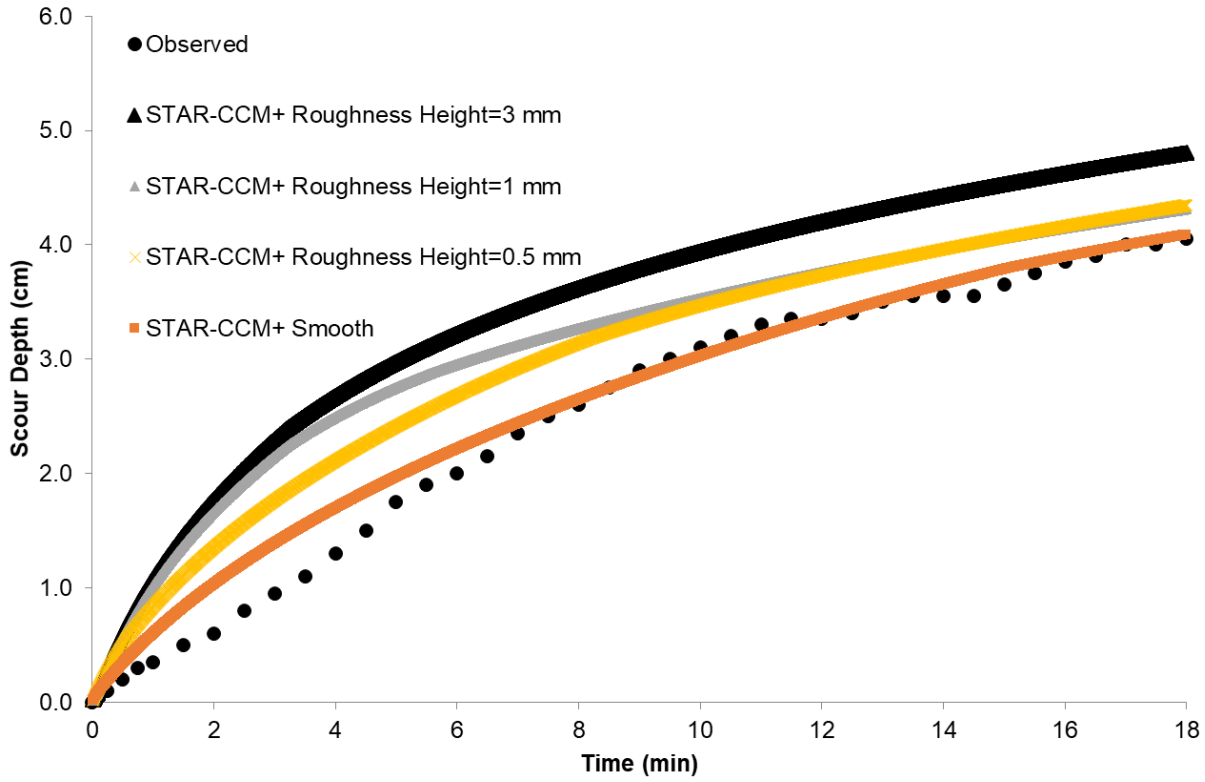

Figure 121. The scour depth versus time for observed JET & simulated JET for Sand #1

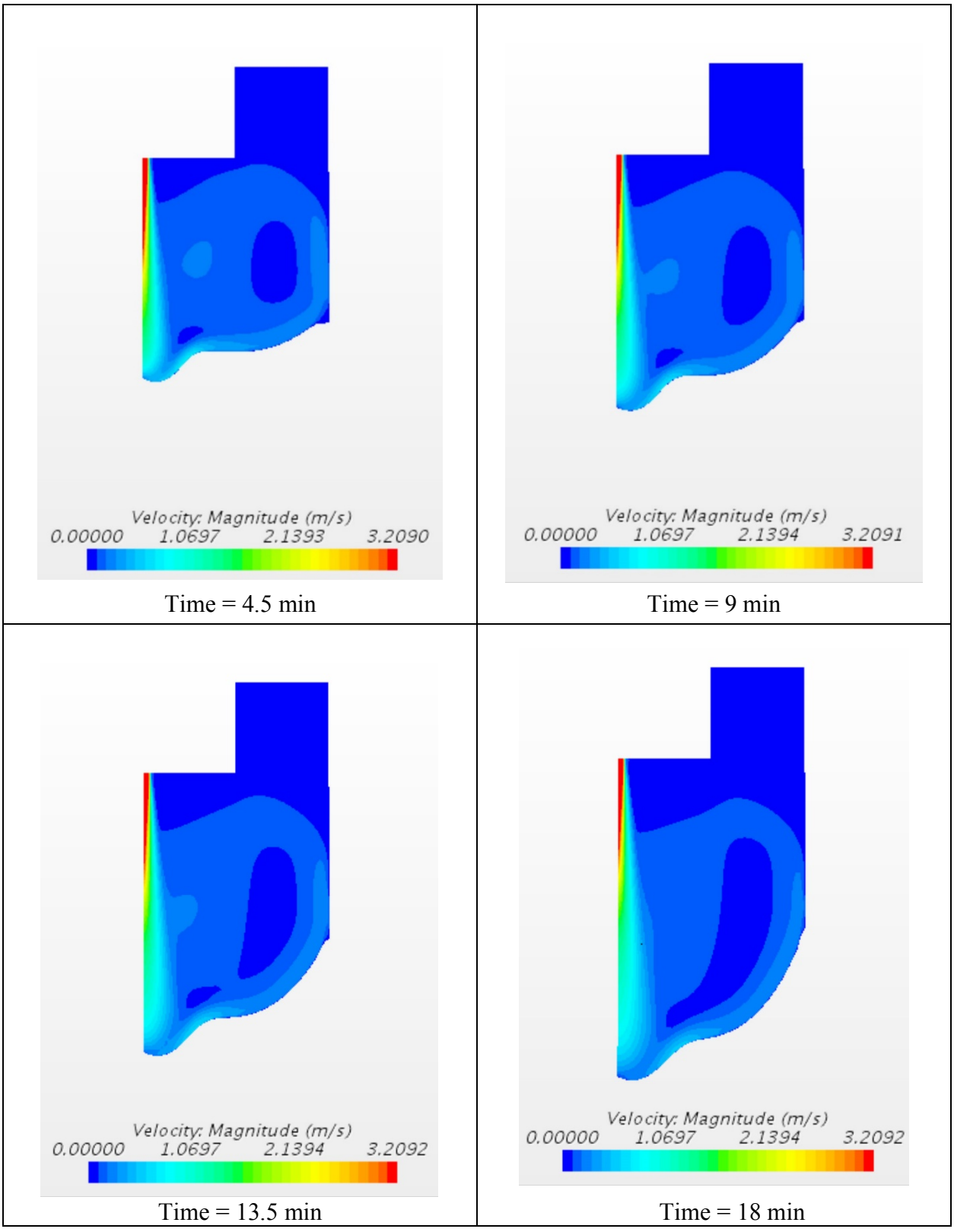

Figure 122. An example of the moving boundary for Sand #1 with RH = 0.5 mm.

Figure 123 shows the results of the numerical simulations for the sample Sand #2 when the erosion function obtained from the EFA test on the exact same sample is used at the soil-water interface in the JET model. It is shown that the observed JET results (black circles) are slightly under-estimated through Star CCM+ when their erosion function obtained from the EFA is assigned to the soil-water interface. This under-estimation is more pronounced when the roughness height is close to 0 mm (smooth surface). The actual average roughness height ($D_{50}/2$) for SE-2 is about 0.122 mm. At the end of the 40 minutes JET, the observed scour hole was 2.2 cm, while the Star CCM+ simulations (using the EFA erosion function assigned to the soil-water interface) resulted in almost 1.4 cm scour hole in the smooth surface case. Figure 123 also shows that in higher roughness heights (near 3 mm), results of the numerical simulations tend to be closer to the observation for the sample SE-2.

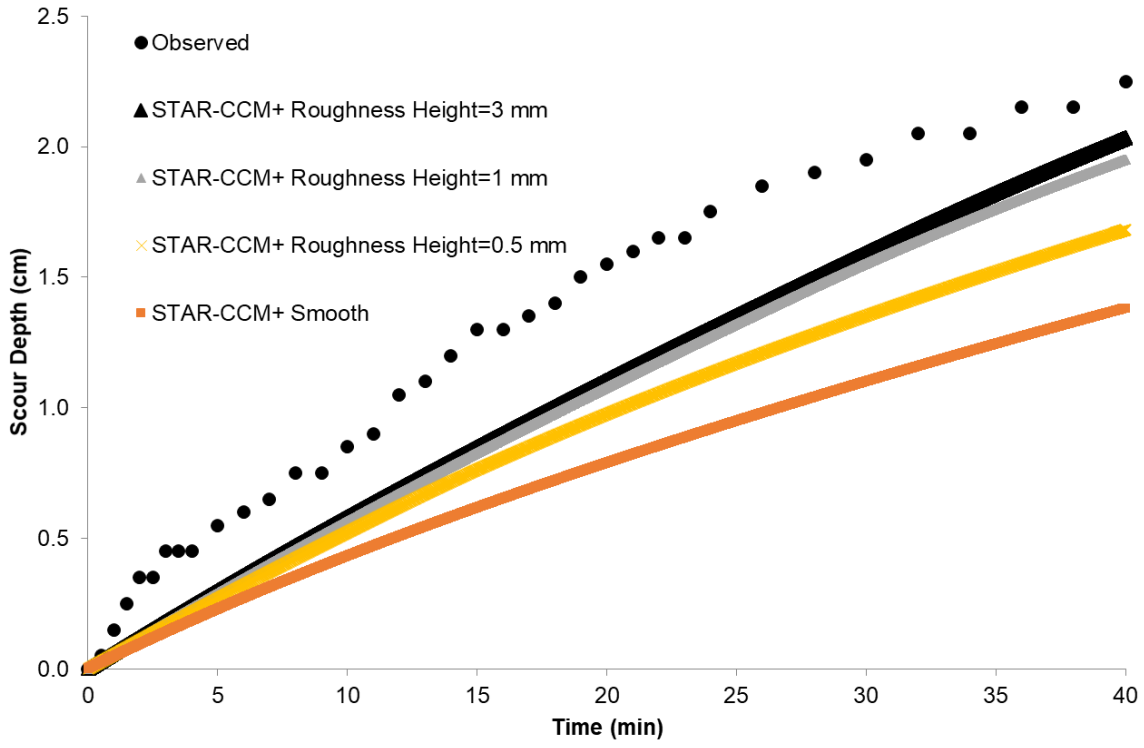

Figure 123. The scour depth versus time for observed JET & simulated JET for Sand #2

Figure 124 shows the results of the numerical simulations for the sample B-1 (4'-6') when the erosion function obtained from the EFA test on the exact same sample is used at the soil-water interface in the JET model. It is shown that the observed JET results (black circles) are slightly over-estimated through Star CCM+ when their erosion function obtained from the EFA is assigned to the soil-water interface. This over-estimation is more pronounced when the roughness height is greater. The actual average roughness height ($D_{50}/2$) for B-1 (4'-6') is about 0.0024 mm. At the end of the 40 minutes JET, the observed scour hole was 0.62 cm, while the Star CCM+ simulations (using the EFA erosion function assigned to the soil-water interface) resulted in almost 1.0 cm scour hole in the smooth surface case.

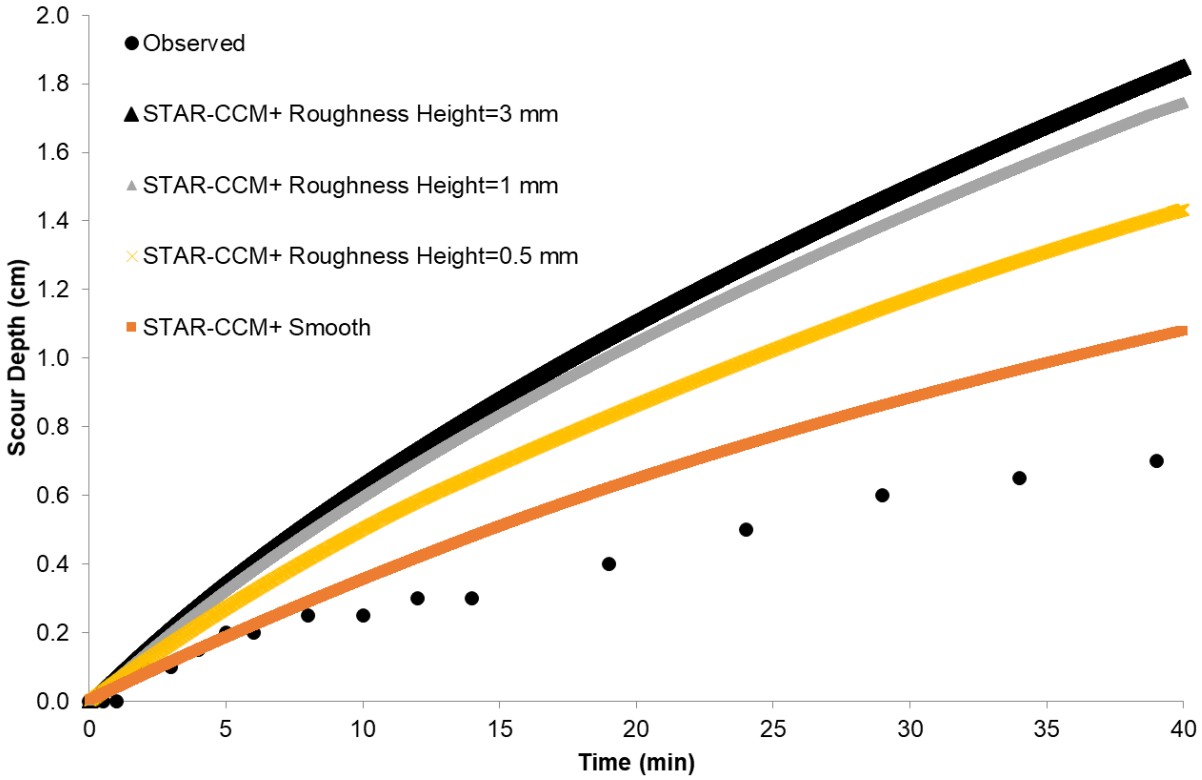

Figure 124. The scour depth versus time for observed JET & simulated JET for B-1 (4'-6')

Figure 125 shows the results of the numerical simulations for FHWA Sample 2 when the erosion function obtained from the EFA test on the exact same sample is used at the soil-water interface in the JET model. It is shown that the observed JET results (black circles) are slightly under-estimated through Star CCM+ when their erosion function obtained from the EFA is assigned to the soil-water interface. This under-estimation is less observed when the roughness height is greater. The actual average roughness height ($D_{50}/2$) for FHWA Sample 2 is about 0.0031 mm. At the end of the 40 minutes JET, the observed scour hole was 1.6 cm, while the Star CCM+ simulations (using the EFA erosion function assigned to the soil-water interface) resulted in almost 0.8 cm scour hole in the case of smooth surface.

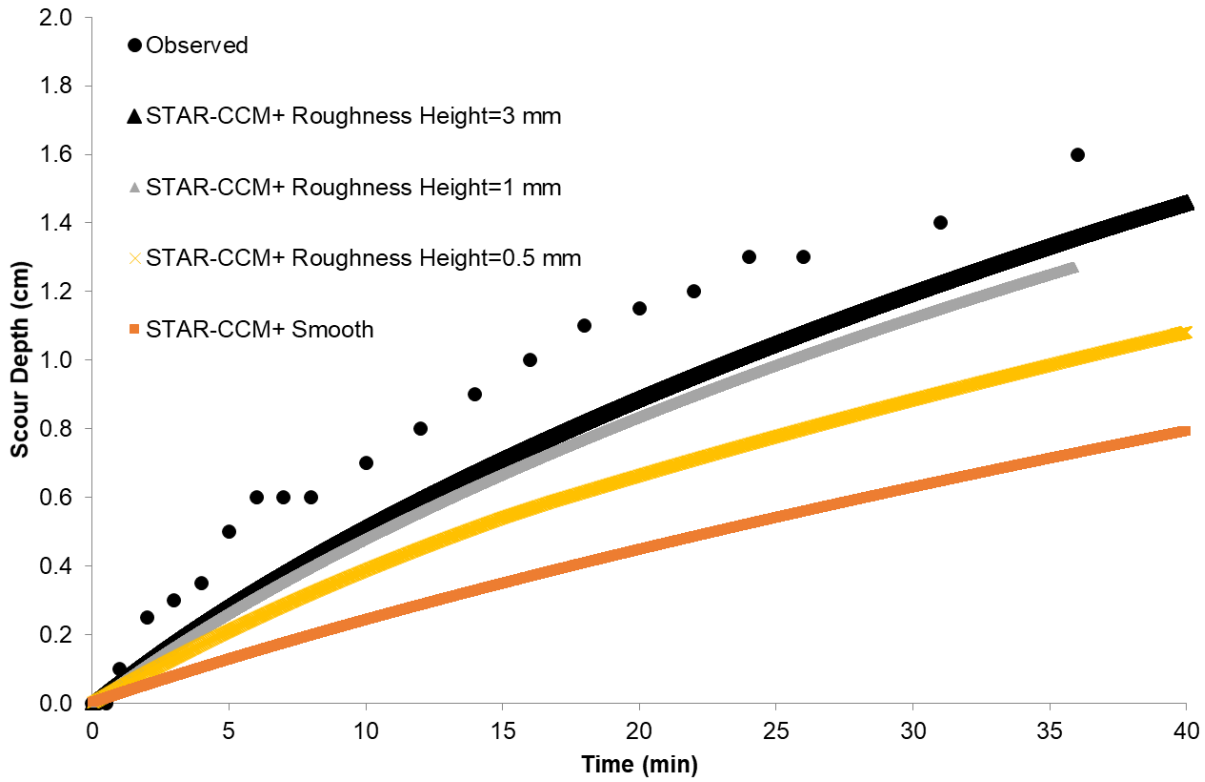

Figure 125. The scour depth versus time for observed JET & simulated JET for FHWA Sample 2

6.2.3.2.EFA's Erosion Function on the HET

Similar approach, as outlined in Figure 117, was taken to compare the results of the EFA with the HET on same soil samples. The erosion process for two different samples (1 silt and 1 clayey sand) was simulated using Star CCM+ after assigning the EFA erosion function to the soil-water interface in the HET model. The name of these samples are: SH-1 (sand samples) and Teton Sample (silt sample). The results of the numerical simulations were compared with the observations of the hole diameter enlargement during the HET for the same samples. Similar to the case of EFA-JET comparison, four different roughness heights (RH) were considered: smooth, 0.5 mm, 1 mm, and 3 mm for each simulation.

Figure 126 shows the results of the numerical simulations for SH-1 when the erosion function obtained from the EFA test on the exact same sample is used at the soil-water interface in the HET model. It is shown that the observed average hole diameter evolution during the HET would lie between the results of the Star CCM+ numerical simulations for the cases of smooth to 0.5 mm RH surface. The actual average roughness height ($D_{50}/2$) for SH-1 is about 0.1 mm. At the end of the 1500 seconds (25 minutes) HET, the average diameter of the initial hole has become around 13 mm. The Star CCM+ simulations (using the EFA erosion function assigned to the soil-water interface) also resulted in almost an average 13 mm hole diameter in the case of 0.5 mm roughness height. It is worth mentioning that in the beginning of the test where the hole longitudinal wall is smoother, the observed evolution of hole diameter tends to be more matching with the results of numerical simulations for the case of smooth surface.

Figure 127 shows an example of the numerical simulations in three different time steps for SH-1. In this example, the soil-water interface is defined as a moving boundary. Also, the velocity

profile of the flow is shown for each time step. Velocity for this example ranges between 0 to 3.75 m/s.

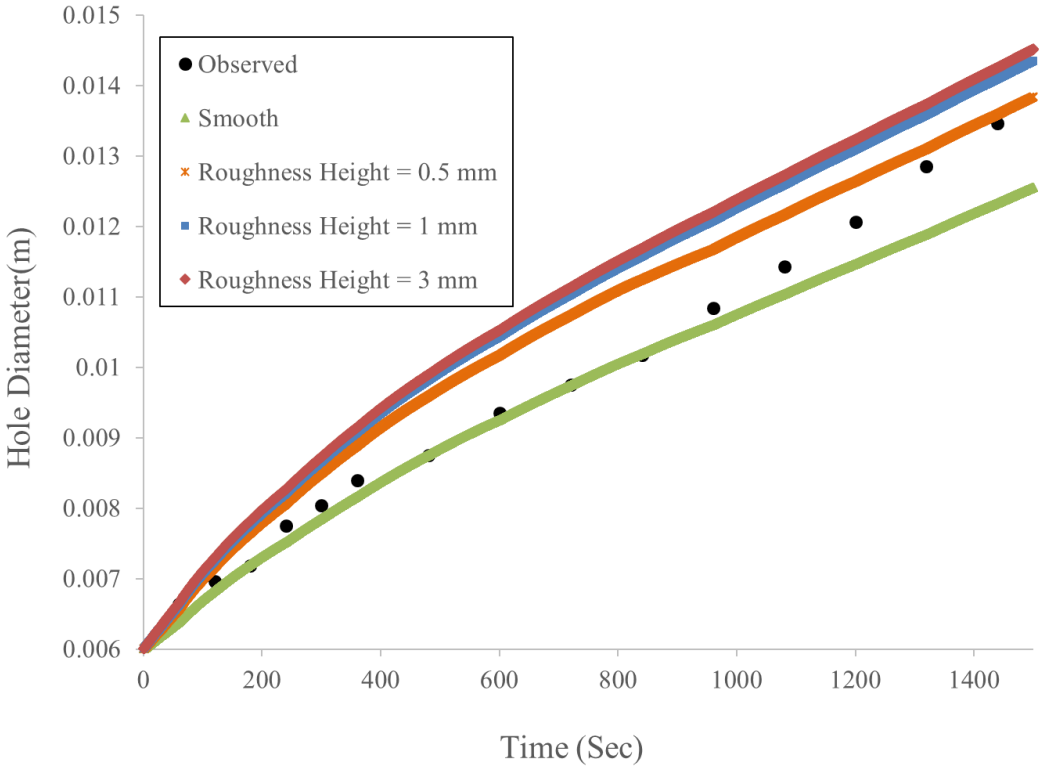

Figure 126. The average hole diameter versus time for observed HET & simulated HET for SH-1

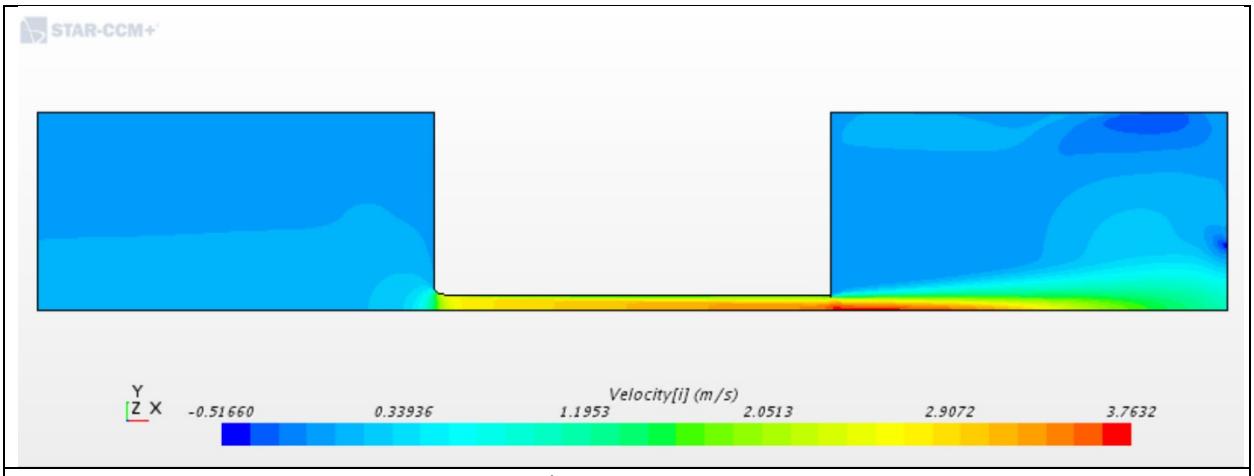

Time = 350 sec

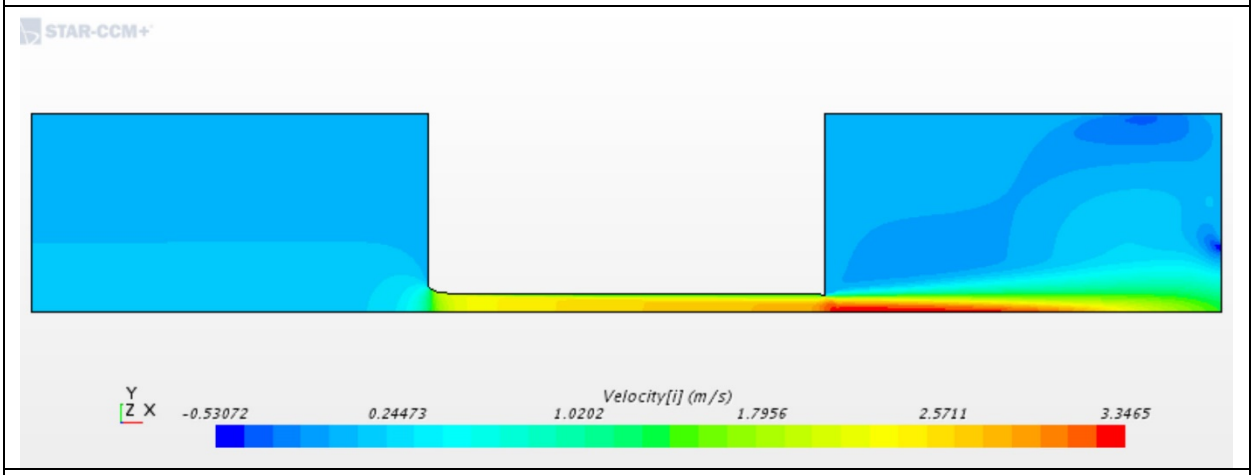

Time = 700 sec

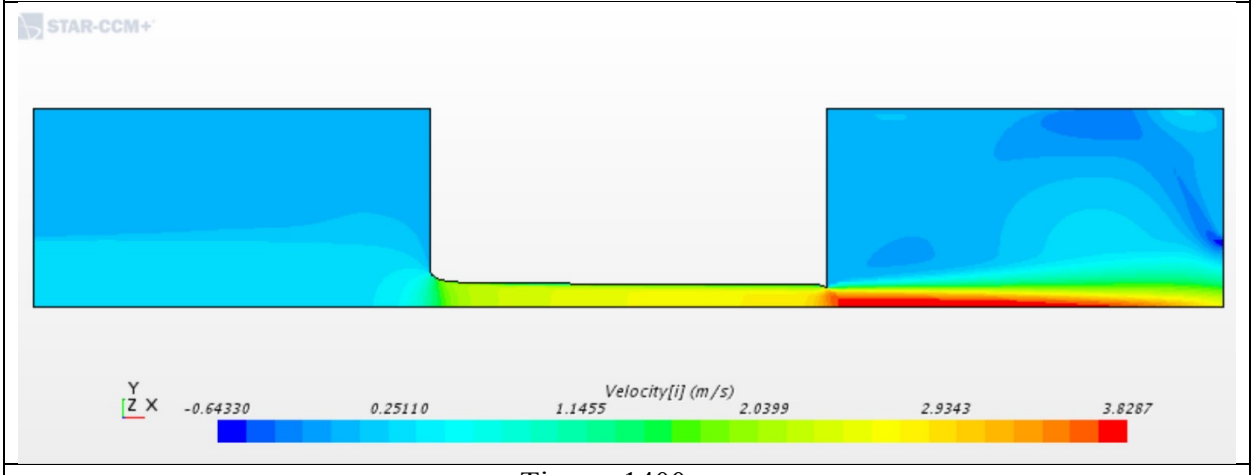

Time = 1400 sec

Figure 127. An example of the moving boundary for SH-1 with RH = 0.5 mm

Figure 128 shows the results of the numerical simulations for Teton Sample when the erosion function obtained from the EFA test on the exact same sample is used at the soil-water interface in the HET model. It is shown that the observed HET results (black circles) are under-estimated through Star CCM+ when their erosion function obtained from the EFA is assigned to the soil-water interface. This under-estimation is even more pronounced when the surface is smoother. The actual average roughness height ($D_{50}/2$) for SH-1 is about 0.015 mm. At the end of the 175 seconds (almost 3 minutes) HET, the diameter of the initial hole has become around 32 mm. However, the Star CCM+ simulations (using the EFA erosion function assigned to the soil-water interface) resulted in almost half of the enlargement in the hole diameter for the case of smooth surface.

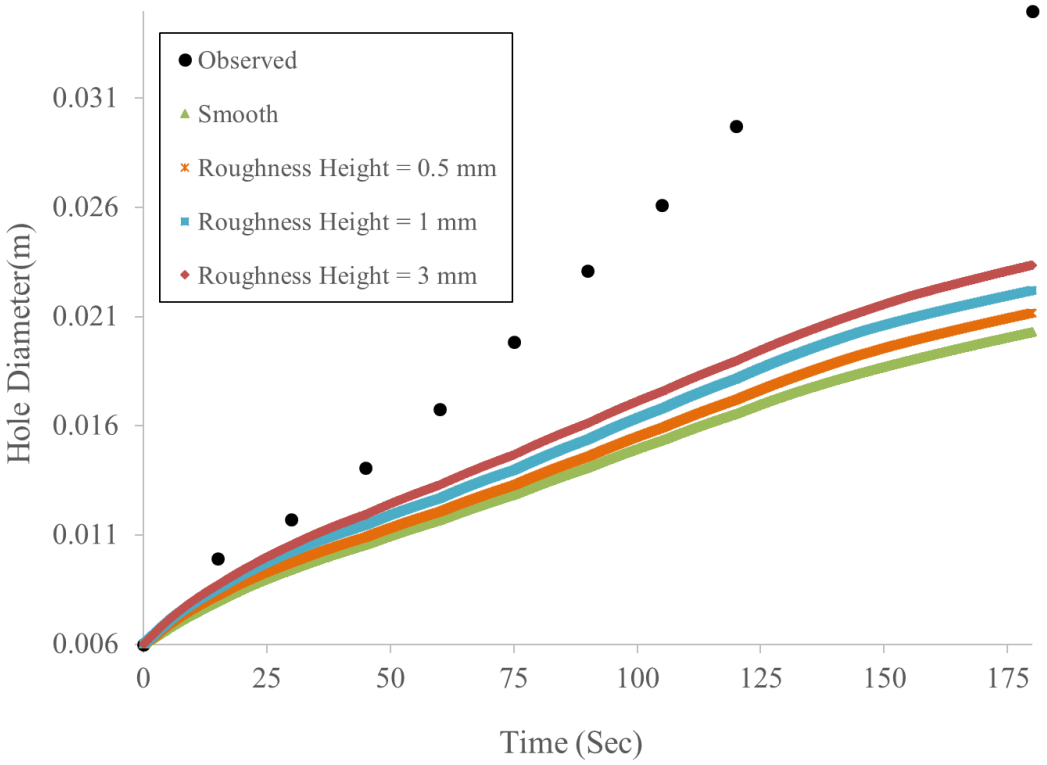

Figure 128. The average hole diameter versus time for observed HET & simulated HET for Teton Sample

6.2.3.3.EFA's Erosion Function on the BET

Similar approach, as outlined in Figure 117, was taken to compare the results of the EFA with the BET on same soil samples. The erosion process for one clay sample (CBH3) was simulated using Star CCM+ after assigning the EFA erosion function to the soil-water interface in the BET model. The results of the numerical simulations were compared with the observations of the borehole diameter enlargement at depth 8 to 10 ft during the BET for the same samples. Three different roughness heights (RH) were considered: smooth, 0.5 mm, 1 mm for each simulation.

Figure 129 shows the results of the numerical simulations for CBH3 when the erosion function obtained from the EFA test on the exact same sample is used at the soil-water interface. It was observed that change in the RH did not make a noticeable difference in the diameter enlargement profile, therefore, only one line represents the scour profile in the three cases. Also, it must be noted that in the numerical simulations, the initial borehole profile had to be considered as a straight vertical line (dashed line in Figure 129), whereas in reality the borehole profile was very irregular in comparison. The difference between the initial borehole profiles in the numerical simulations and the actual BET field measurement resulted in different scour profiles after 20 minutes of test; however, both results confirmed two common observations: 1) The maximum scour happens close to the bottom of the borehole (z = 9.8 ft), and 2) the maximum diameter enlargement is close to 2 cm.

Figure 130 shows an example of the numerical simulations in three different time steps for SH-1. In this example, the soil-water interface is defined as a moving boundary. Also the velocity profile of the flow is shown for each time step. Velocity for this example ranges between 0 to 3.75 m/s.

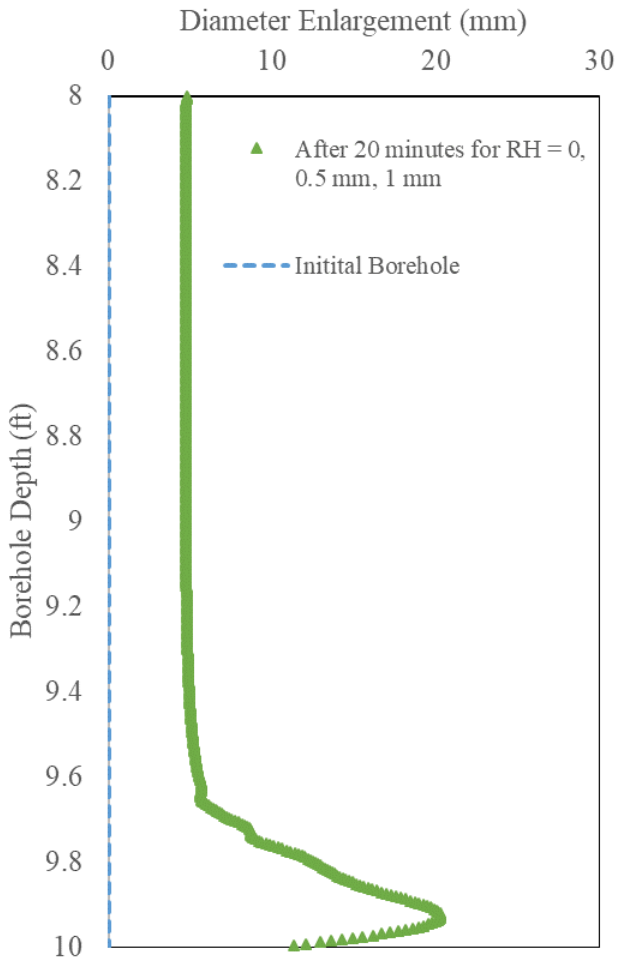

Figure 129. Results of the BET numerical simulation after 20 minutes using the EFA's erosion function

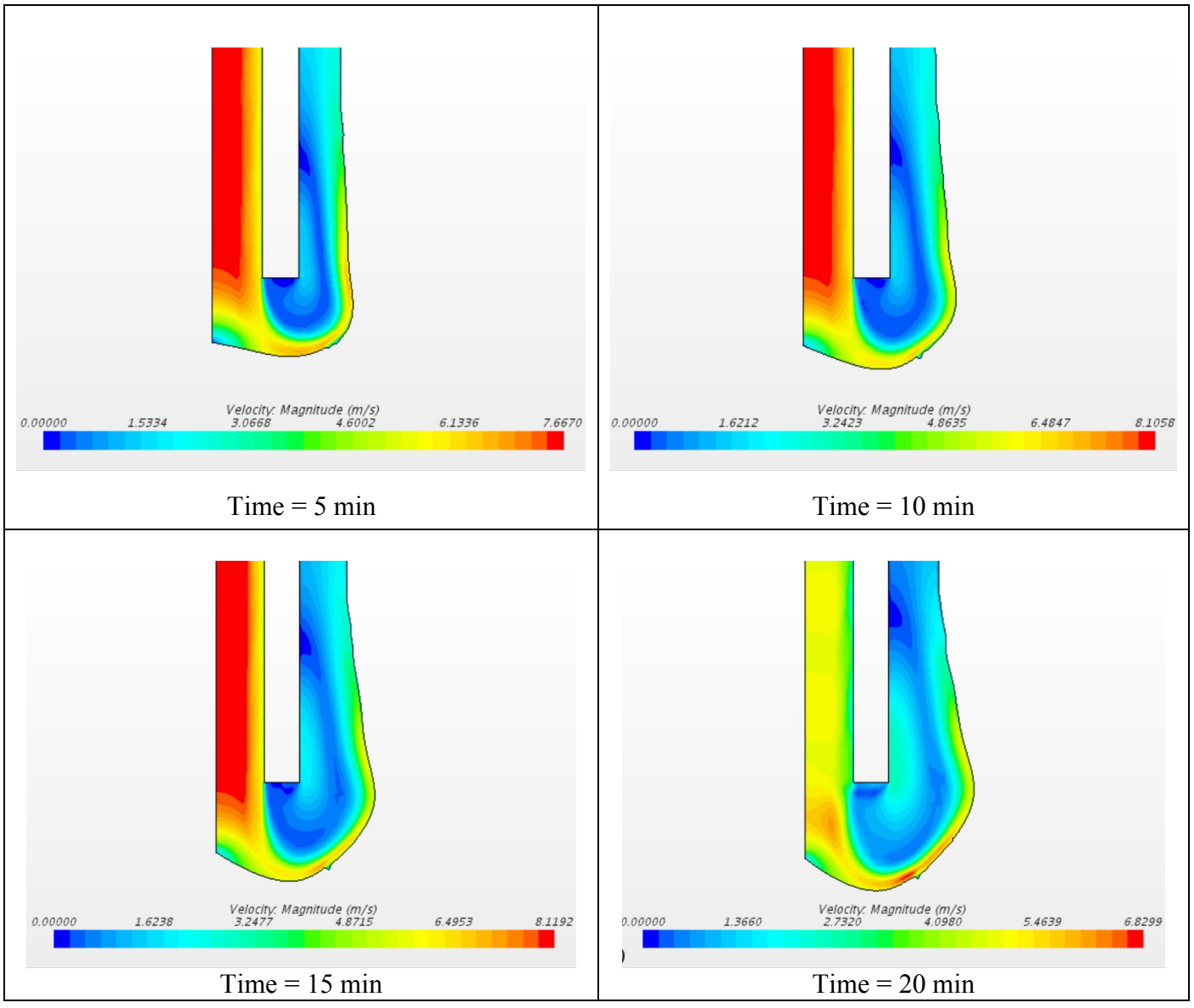

Figure 130. An example of the moving boundary for the Riverside Sample with RH = 0.5 mm

6.2.4. *Comparison and Uniformity*

The results of the numerical simulations on the JET, HET, and BET were presented in the previous section. The goal, as discussed earlier, was to investigate how the JET, the HET, and the BET would react if the erosion function equation obtained from the EFA test on the same soil, is assigned to the soil-water interface. Consequently, the results of numerical simulations were

compared with the actual observations for each test. In this section, a summary of the findings is presented.

Table 31 shows a summary of the numerical simulation results as discussed in the Section 6.2 of this report. The findings show that the erosion function obtained from the EFA test for each sample can be reasonably used to produce a similar "scour versus time" plot to what the JET, the HET, and the BET experiments would result. However, the variety of interpretation techniques that are used for each test to obtain the shear stress in the soil-water interface leads to different erosion functions. Therefore, one must be aware of the interpretation techniques that each test uses to obtain the erosion function (erosion rate versus shear stress). It is also worth noting that for the case of the HET results, the scour values actually refer to the average diameter of the drilled hole in the center of the sample.

Table 31. Summary of the numerical simulation results

	Sample Name	Roughness Height (mm)	Final observed scour (mm)	Final Calculated Scour using the EFA Erosion Function (mm)				Figure
				RH = 0 mm	RH = 0.5 mm	RH = 1 mm	RH = 3 mm	
JET	Sand #1	0.14	40	40.8	43.5	43.1	48	Figure 121
	Sand #2	0.122	23	13.8	16.8	20	20.3	Figure 123
	B-1 (4-6)	0.0024	7	10.8	14.3	17.5	18.5	Figure 124
	FHWA S2	0.0031	17	8	10.8	12.8	14.6	Figure 125
HET	SH-1	0.1	13.4	12.5	13.5	14	14.2	Figure 126
	Teton	0.015	35	19	20	21	22.5	Figure 128
BET	Riverside	0.00038	20[1]	20.31	20.35	20.40	-	Figure 129

[1] The scour values shown for the BET are in fact the maximum diameter enlargements in 8'-10' depth of the borehole

7. CORRELATION EQUATIONS DEVELOPMENT

The main goal of this research was to develop equations correlating soil erosion parameters defined in previous chapters (i.e. EC, E_v, E_τ, v_c, and E_τ) to the common soil engineering properties. Since the majority of the erosion test data compiled in the TAMU-Erosion were comprised of the data obtained from the EFA, the JET, and the HET, and given the fact that these tests are the main erosion tests, the regression analyses were focused on these three tests.

Section 7.1 of this chapter presents the quickest method to estimate the erosion resistance of a soil using the Unified Soil Classification System (USCS). In section 7.2, the plots of critical shear stress/velocity versus mean particle size (Figure 31) are populated with the hundreds of the EFA test data compiled in the TAMU-Erosion spreadsheet, and new equations are developed. Tasks 7 and 8 of this project consist of performing two parallel statistical approaches: 1) Deterministic frequentists' regression analysis, and 2) Probabilistic (Bayesian) analysis. The goal is to reach the best potential fits between erodibility parameters and geotechnical properties of soils. The experimental design, optimization, model selection, and final results of the deterministic frequentists' regression approach is comprehensively presented in Section 7.3. The results of the probabilistic (Bayesian) approach is presented in Section 7.4.

7.1. Determining the Erosion Resistance Using the USCS

As discussed in Chapter 1, the Erosion Function Charts are charts that show erosion categories in the Ż–v and Ż–τ space (Figure 3). These charts were conceptually designed to eliminate the need for site-specific erosion testing in the case of preliminary investigations and first order erosion analyses. It was first developed on the basis of EFA tests performed at Texas

A&M University, after the Hurricane Katrina in 2005. The categories in the charts are zoned according to boundaries that originate at the critical velocity of the corresponding erosion category. Table 1 shows the values of τ_c and v_c according to the erosion categories.

One of the goals of this NCHRP project was to introduce zones on the erosion charts that best represent different soil types and to characterize these zones by using the USCS classification. For coarse-grained soils, the erodibility is influenced mostly by gravity forces and therefore by the grain size. Since the USCS soil classification for coarse-grained soils is based primarily on grain size distribution, it is thought to have good potential for distinguishing between erosion categories of coarse-grained soils. For fine-grained soils, parameters such as soil structure, orientation of clay particles and aging may be important in characterizing erodibility (Lefebvre et al., 1986; Partheniades, 2009). It was also observed that the plasticity, clay content, and soil activity play the most dominant roles in erosion resistance of fine-grained soils. Plasticity parameters form the basis of the USCS classification for fine-grained soils and it is reasonable to think that, as such, the USCS category has good potential for distinguishing between erosion categories for fine-grained soils as well.

As discussed earlier in the previous chapters, about 330 EFA test results compiled in the TAMU-Erosion Spreadsheet were divided into different USCS classification groups. Table 32 below shows the USCS classification groups along with the number of EFA tests in each group.

Table 32. List of the USCS classifications associated with the 330 samples

USCS Classification	Number of samples
CH	63
CL	131
GP	7
GC	1
MH	14
ML	24
ML-CL	14
SC	28
SC-SM	8
SM	17
SP	16
SP-SC	3
SP-SM	2
SW-SM	1

Figure 131 through Figure 144 show the erosion functions of the samples plotted according to their USCS category in velocity space. The highlighted zones and the dashed red lines on each figure are proposed, after considering the two following criteria: 1) The highlighted zone contains nearly 90% of the EFA test data for that specific USCS category, 2) The zone is adjusted (especially in the cases that the EFA data are not many to make an inclusive conclusion) so it is in a reasonable consistence with the previously proposed version of this chart by Briaud et al. (2008). It is observed that the erosion functions for soils with a given USCS category do not generally fall distinctly into a single erosion category but rather seem to plot approximately across two categories. Figure 145 summarizes all results into the two erosion category charts shown in Figure 3.

Figure 145 can be used as a preliminary step to estimate the erodibility of any sample, using the USCS. The width of each box, that is associated with a USCS category, represents the

zone in which 90% of the EFA results performed on such samples would fall in the Erosion Category Chart. For instance, if the soil type of a location in an arbitrary geotechnical site is classified as SM (silty sand) according to the USCS, it would most likely (with close to 90% confidence based on the EFA results compiled in the TAMU-Erosion) fall into the Category II (high erodibility) on Figure 145. Similarly, a soil classified as CH (fat clay) would most likely fall into the Category III (medium erodibility), and a SP (poorly graded sand) would fall within the Categories I and II (very high to high erodibility). Evidently, the wider the box is for a USCS category, the more the variability of the erodibility is for that particular soil type.

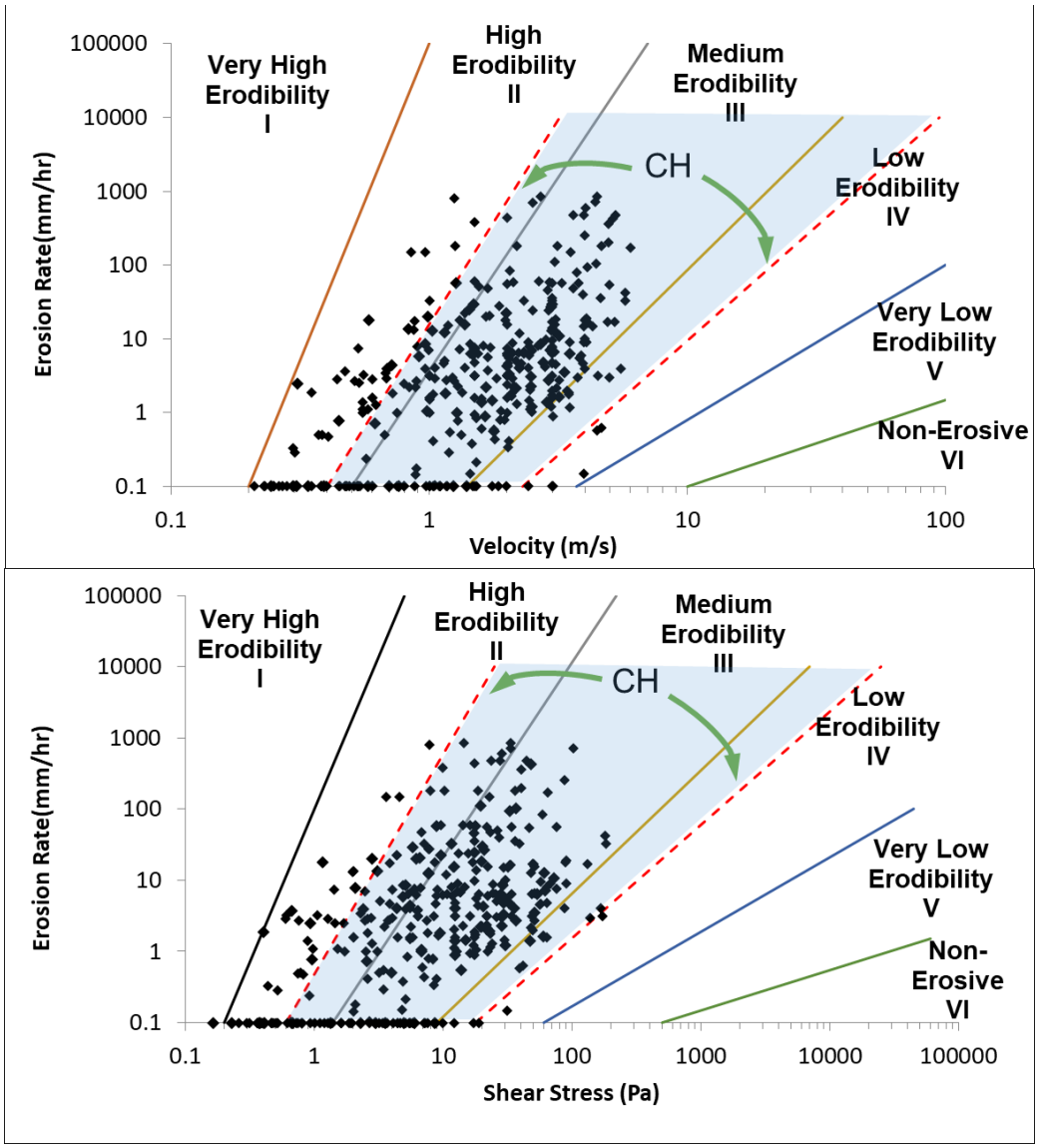

Figure 131. Velocity-Erosion Rate and Shear Stress-Erosion Rate Plots for CH soils

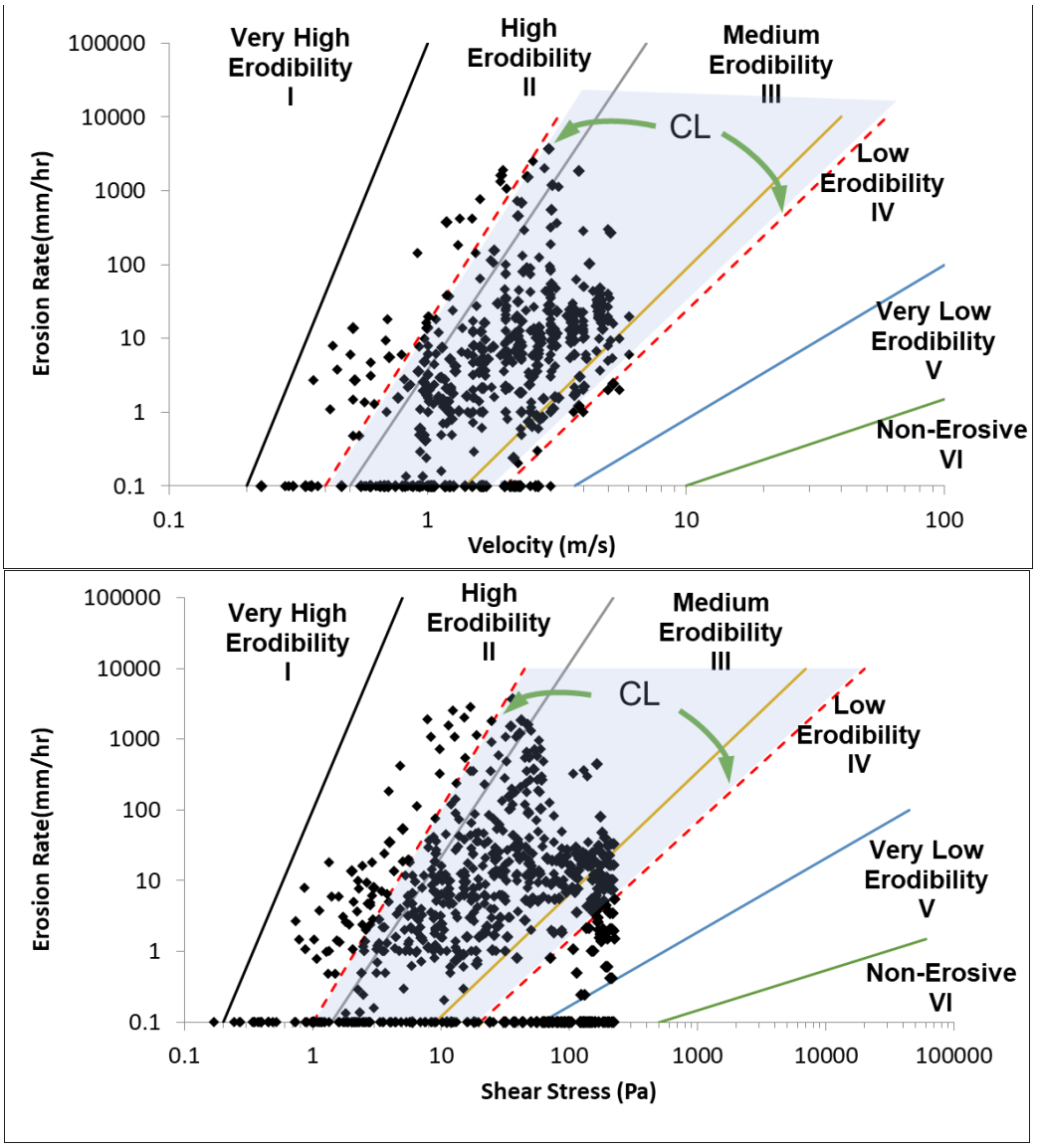

Figure 132. Velocity-Erosion Rate and Shear Stress-Erosion Rate Plots for CL soils

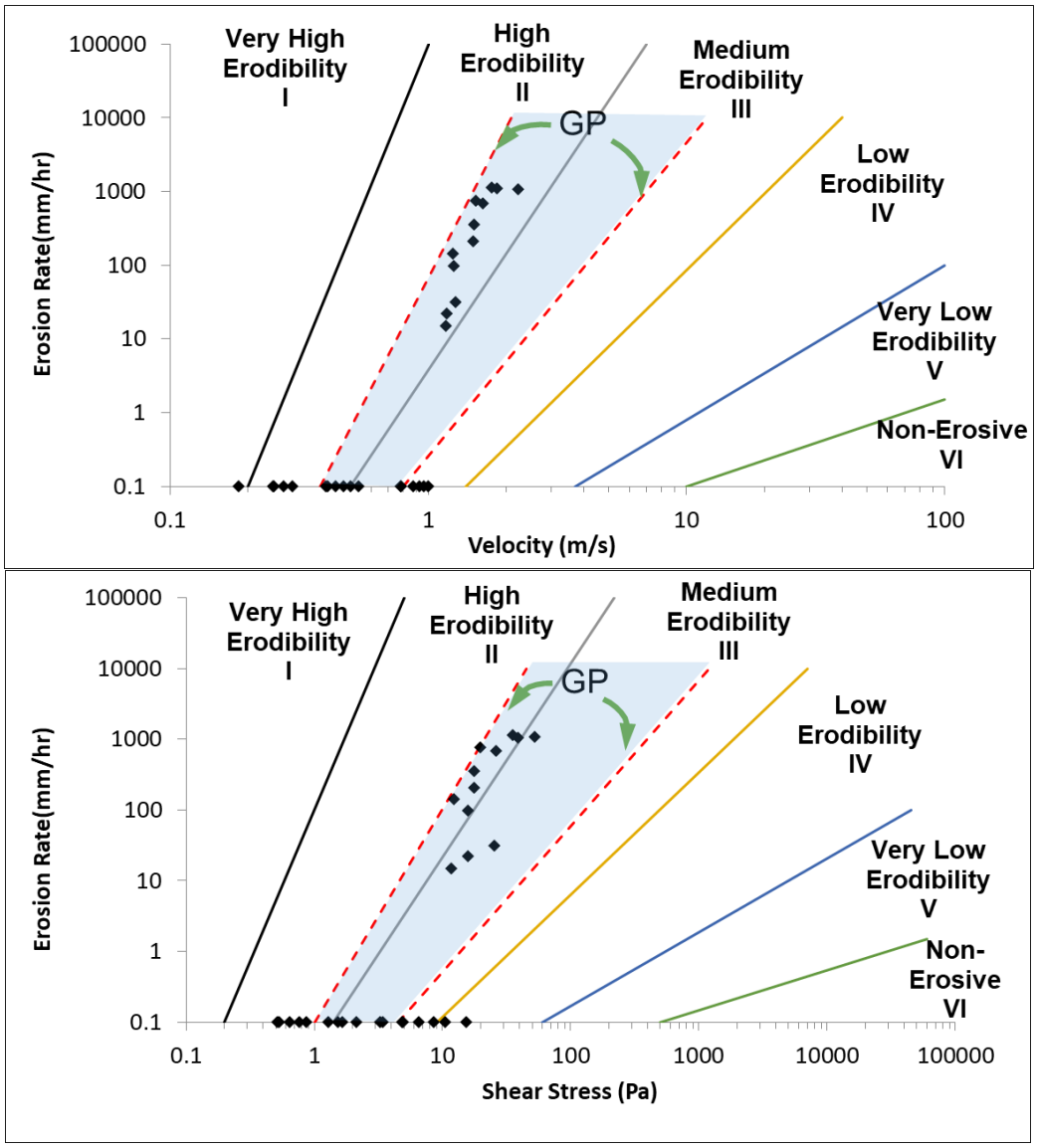

Figure 133. Velocity-Erosion Rate and Shear Stress-Erosion Rate Plots for GP soils

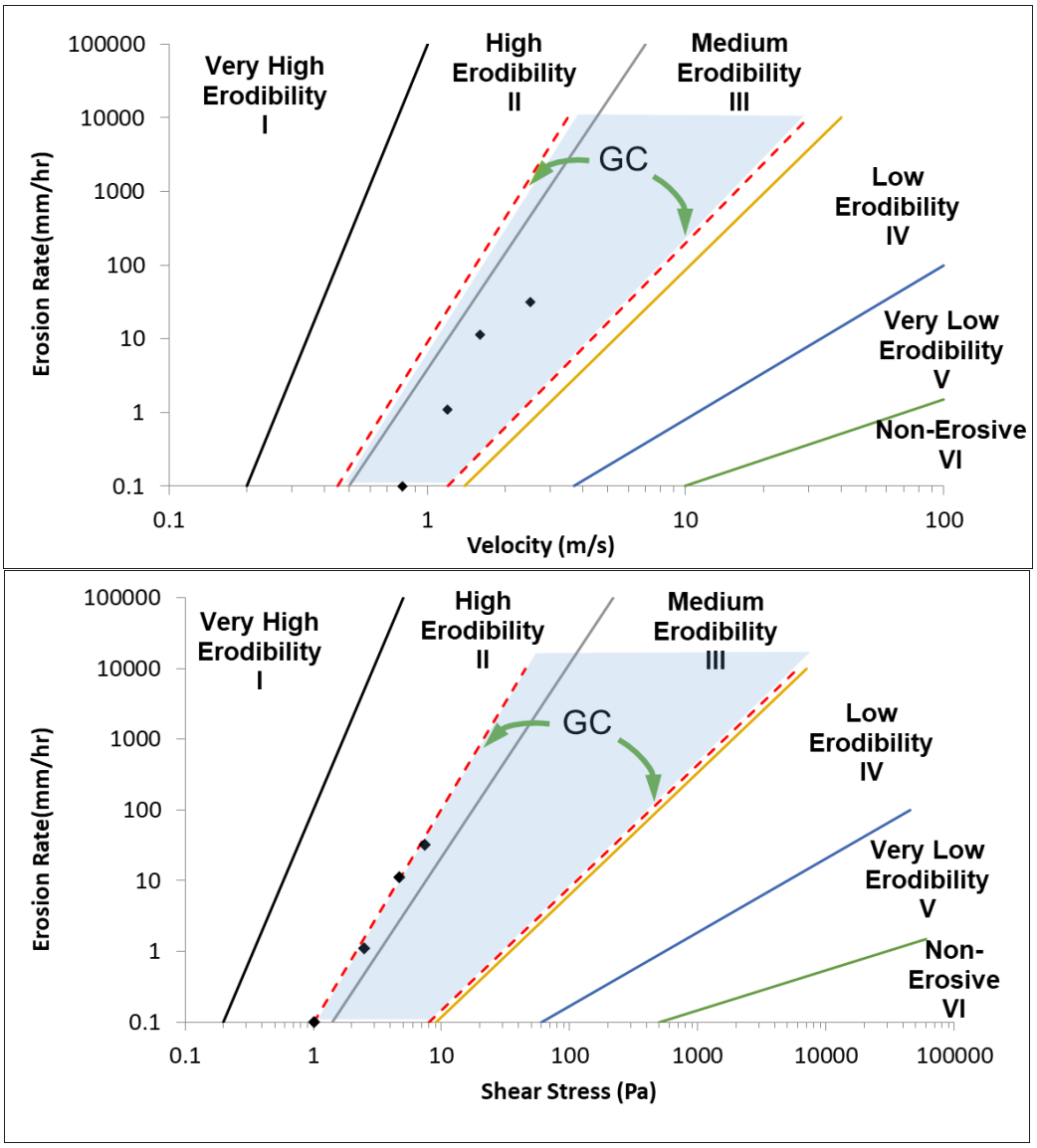

Figure 134. Velocity-Erosion Rate and Shear Stress-Erosion Rate Plots for GC soils

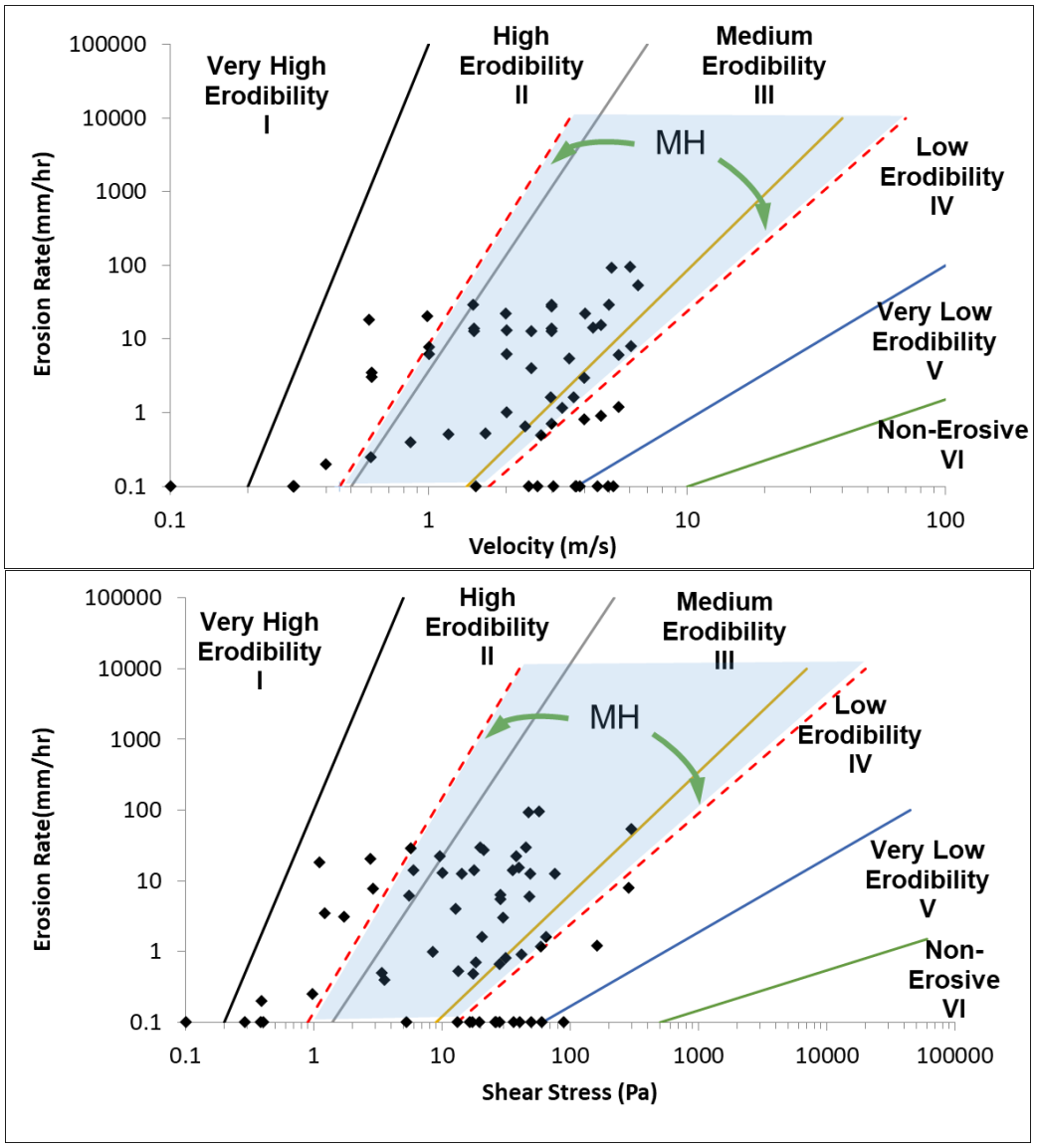

Figure 135. Velocity-Erosion Rate and Shear Stress-Erosion Rate Plots for MH soils

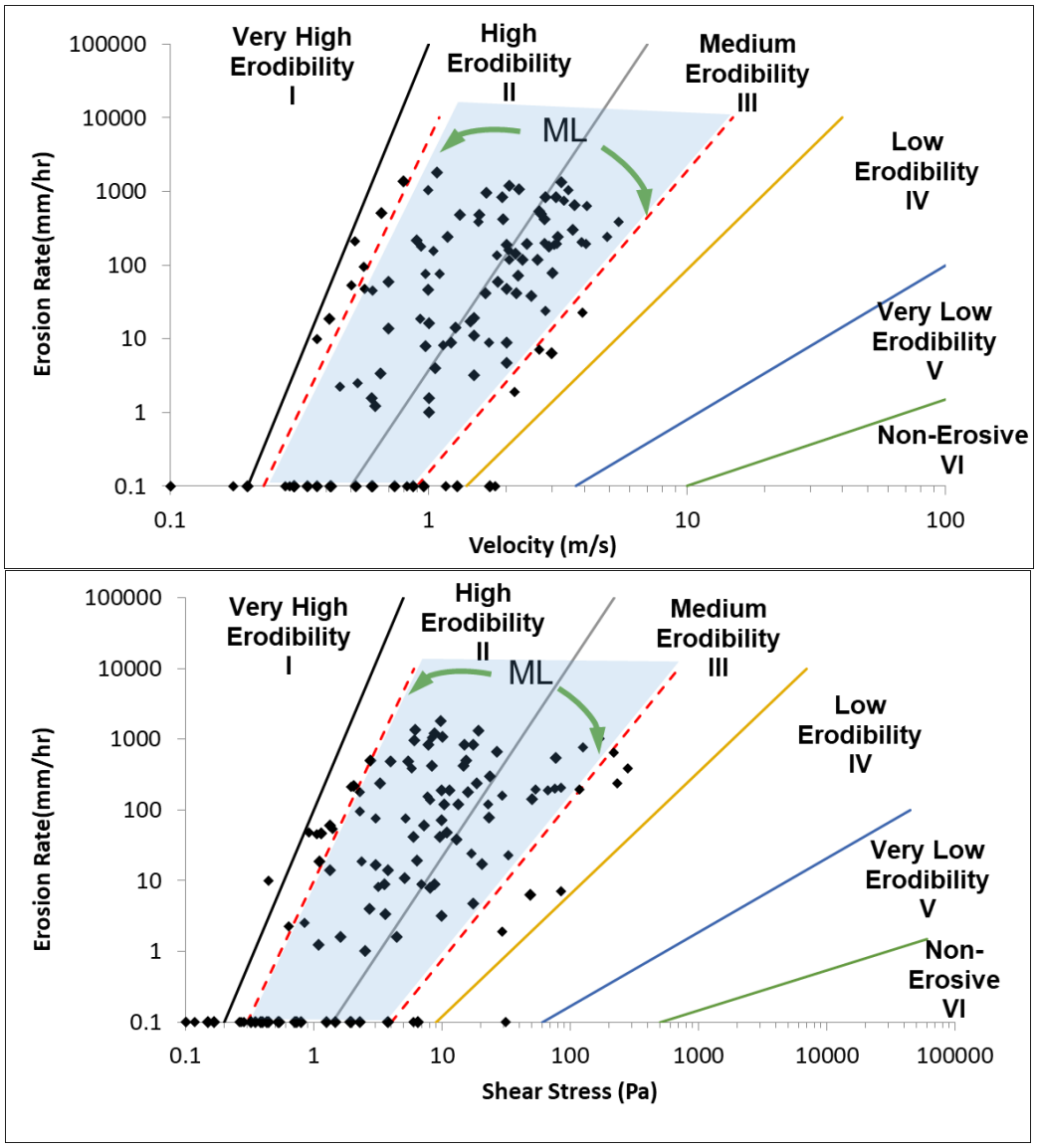

Figure 136. Velocity-Erosion Rate and Shear Stress-Erosion Rate Plots for ML soils

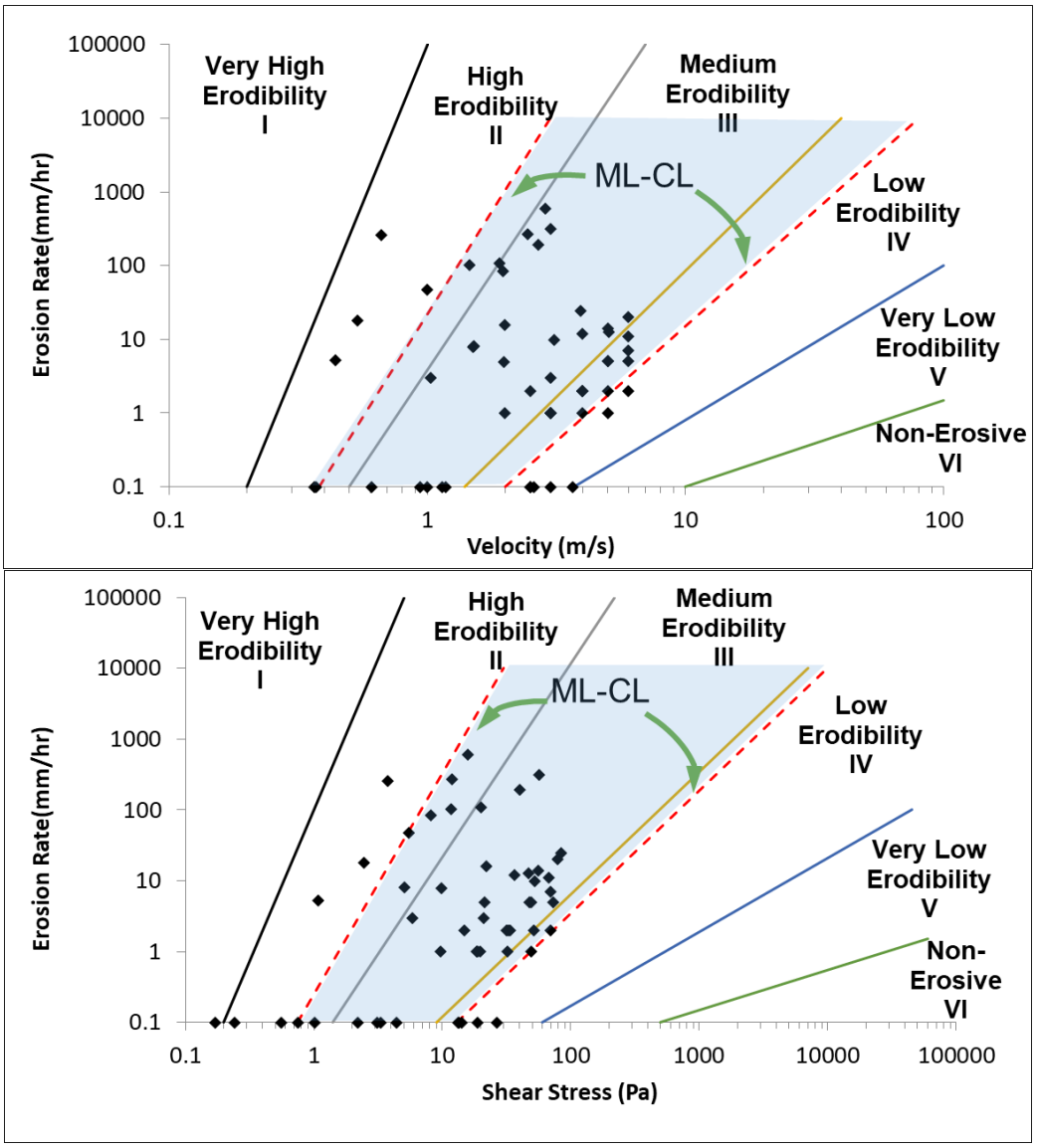

Figure 137. Velocity-Erosion Rate and Shear Stress-Erosion Rate Plots for ML-CL soils

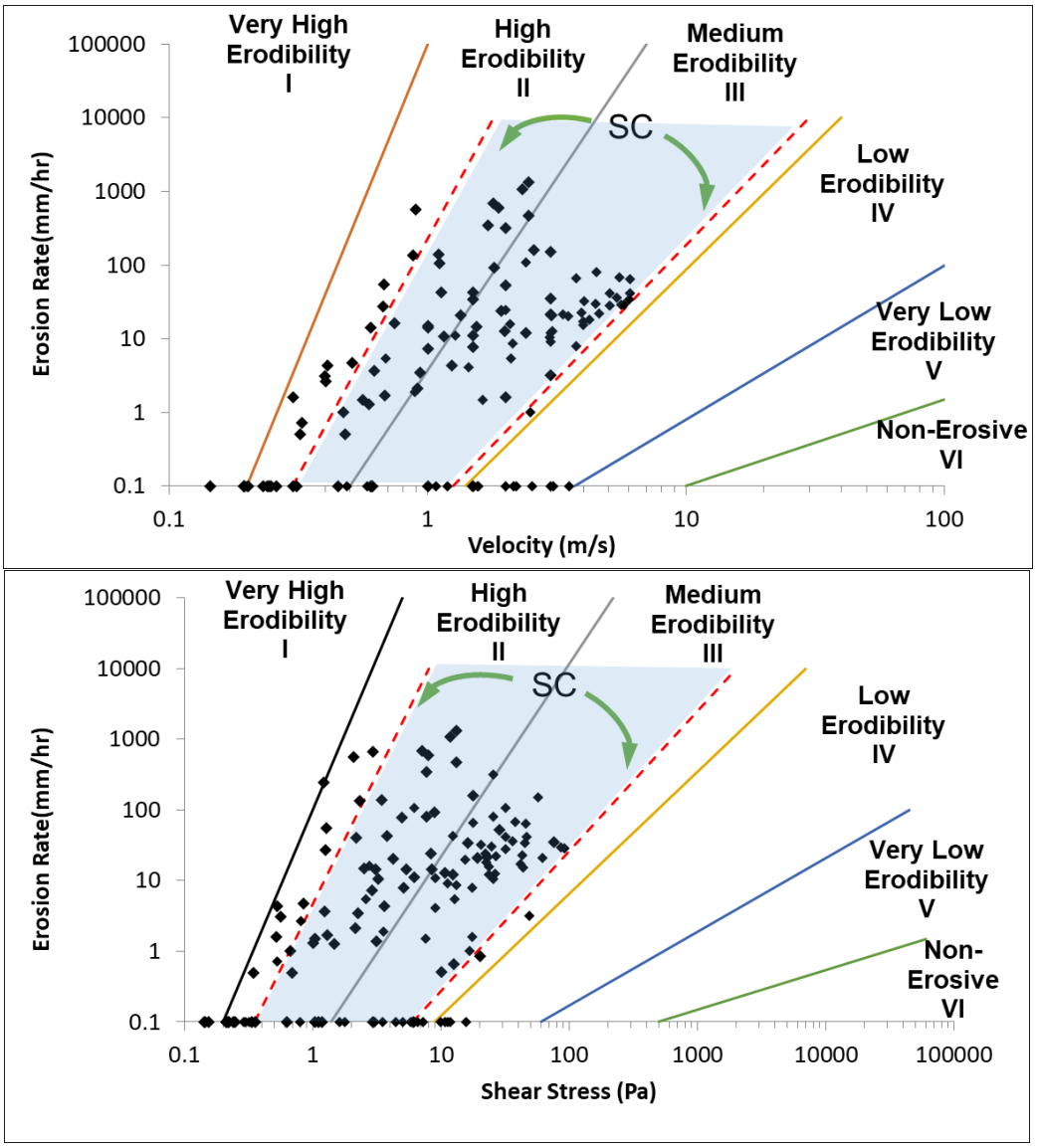

Figure 138. Velocity-Erosion Rate and Shear Stress-Erosion Rate Plots for SC soils

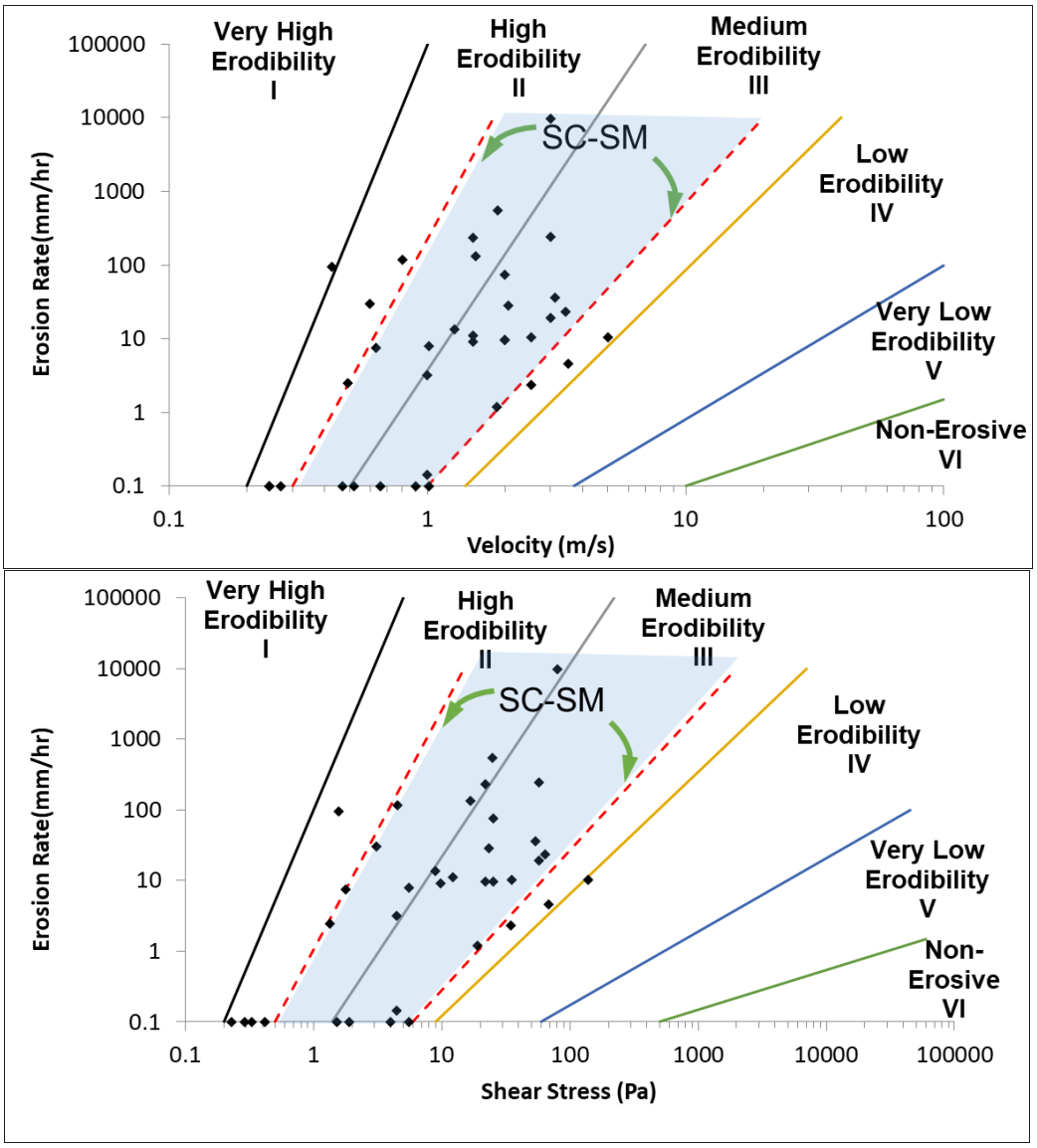

Figure 139. Velocity-Erosion Rate and Shear Stress-Erosion Rate Plots for SC-SM soils

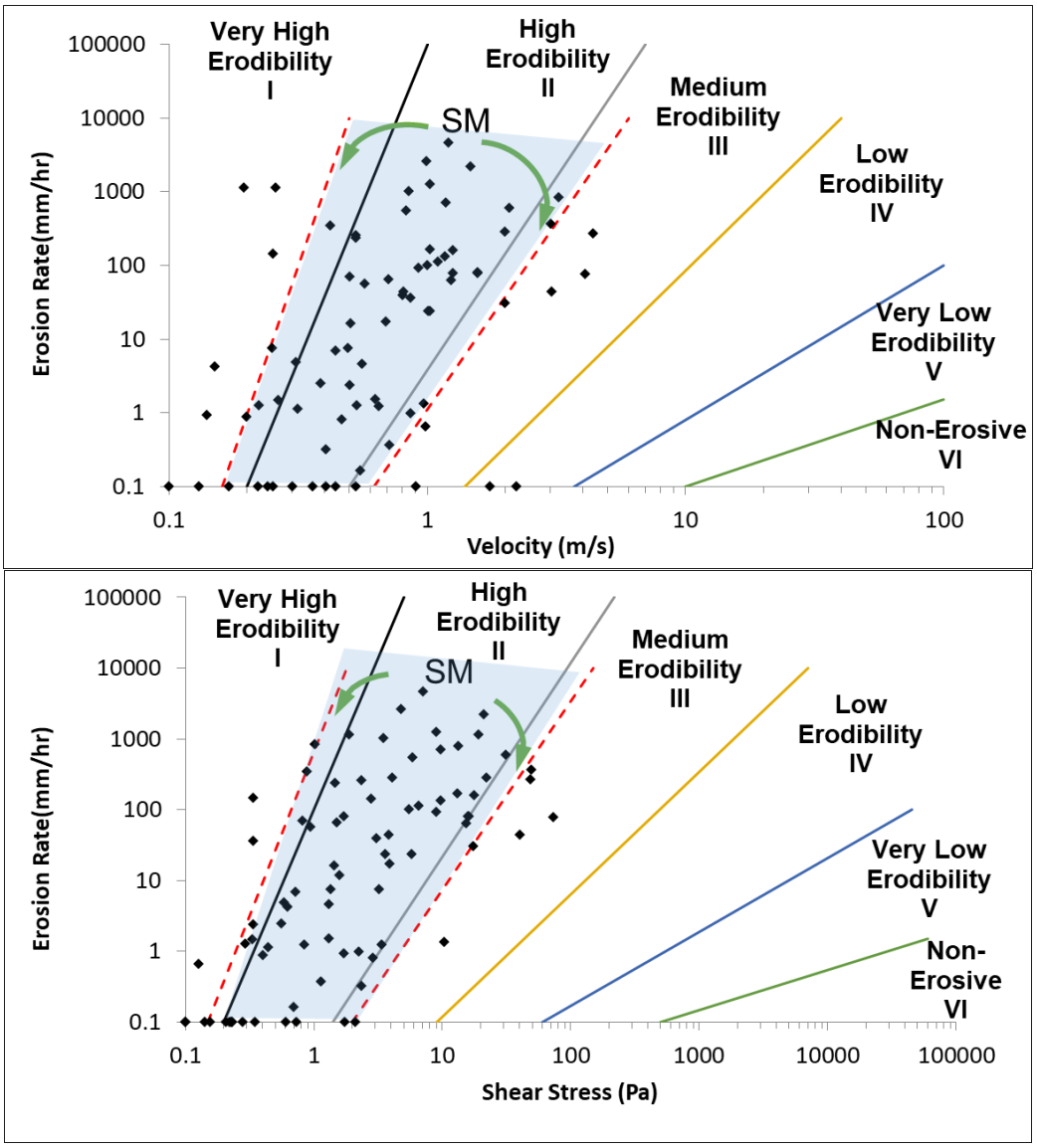

Figure 140. Velocity-Erosion Rate and Shear Stress-Erosion Rate Plots for SM soils

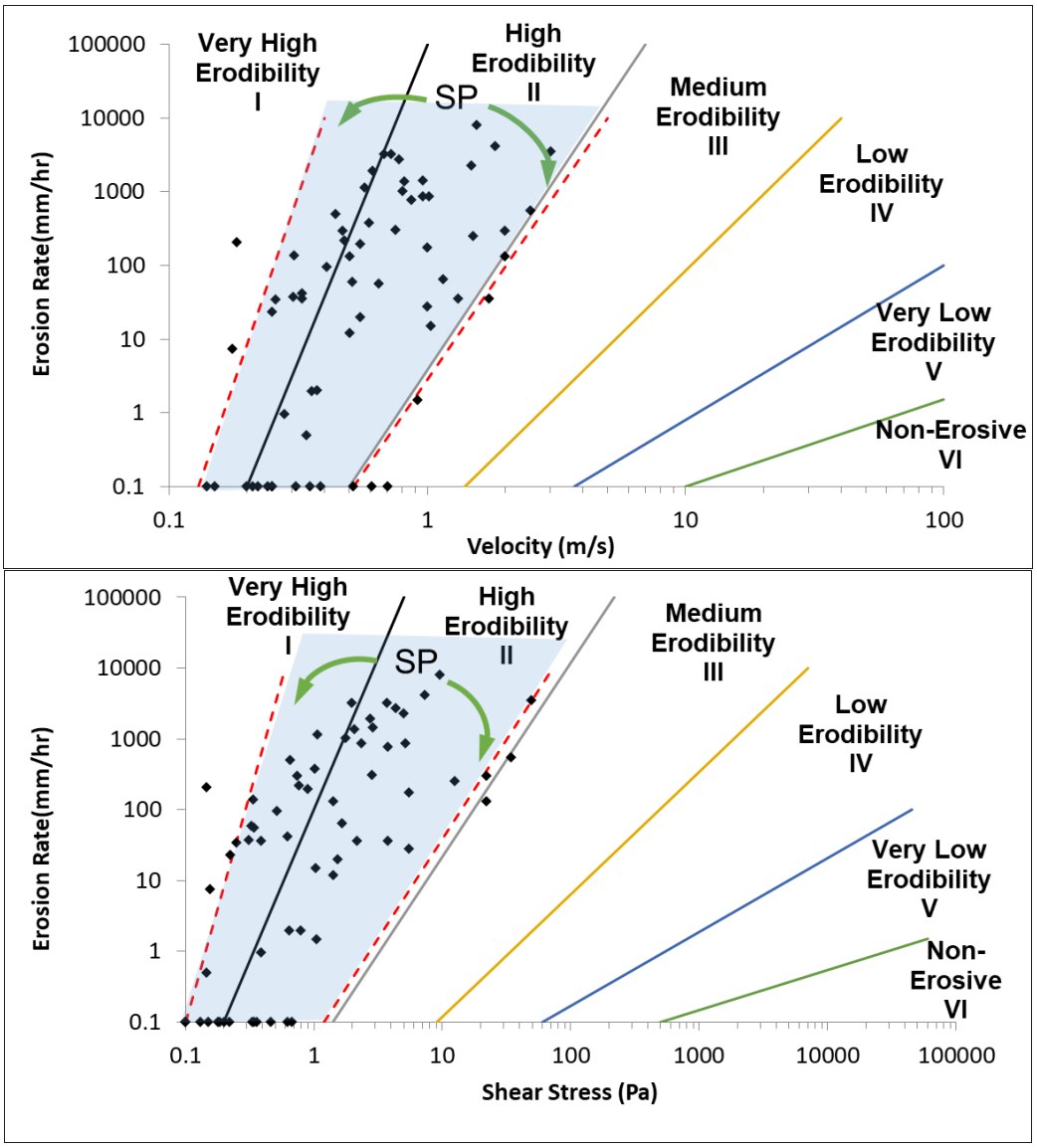

Figure 141. Velocity-Erosion Rate and Shear Stress-Erosion Rate Plots for SP soils

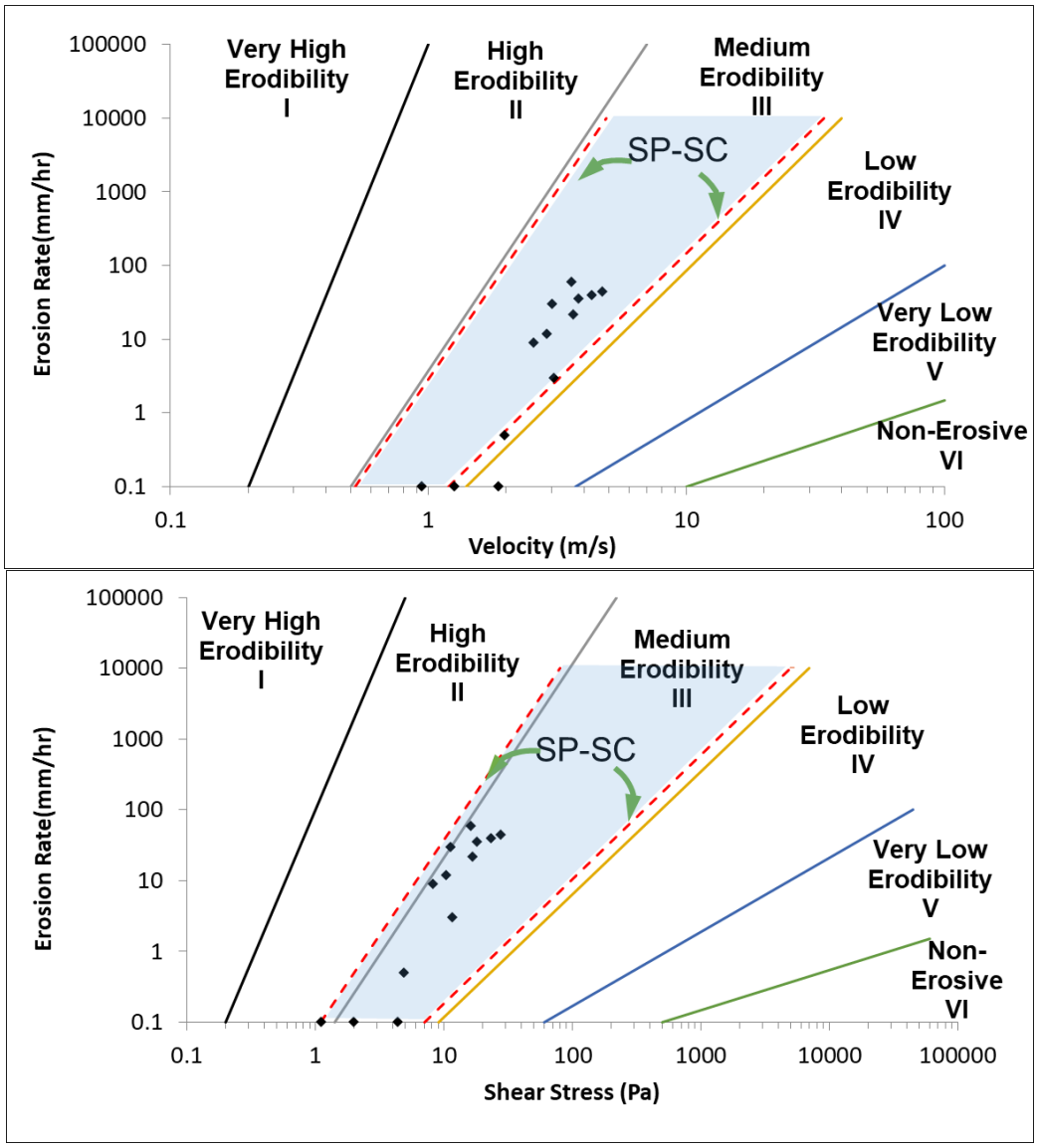

Figure 142. Velocity-Erosion Rate and Shear Stress-Erosion Rate Plots for SP-SC soils

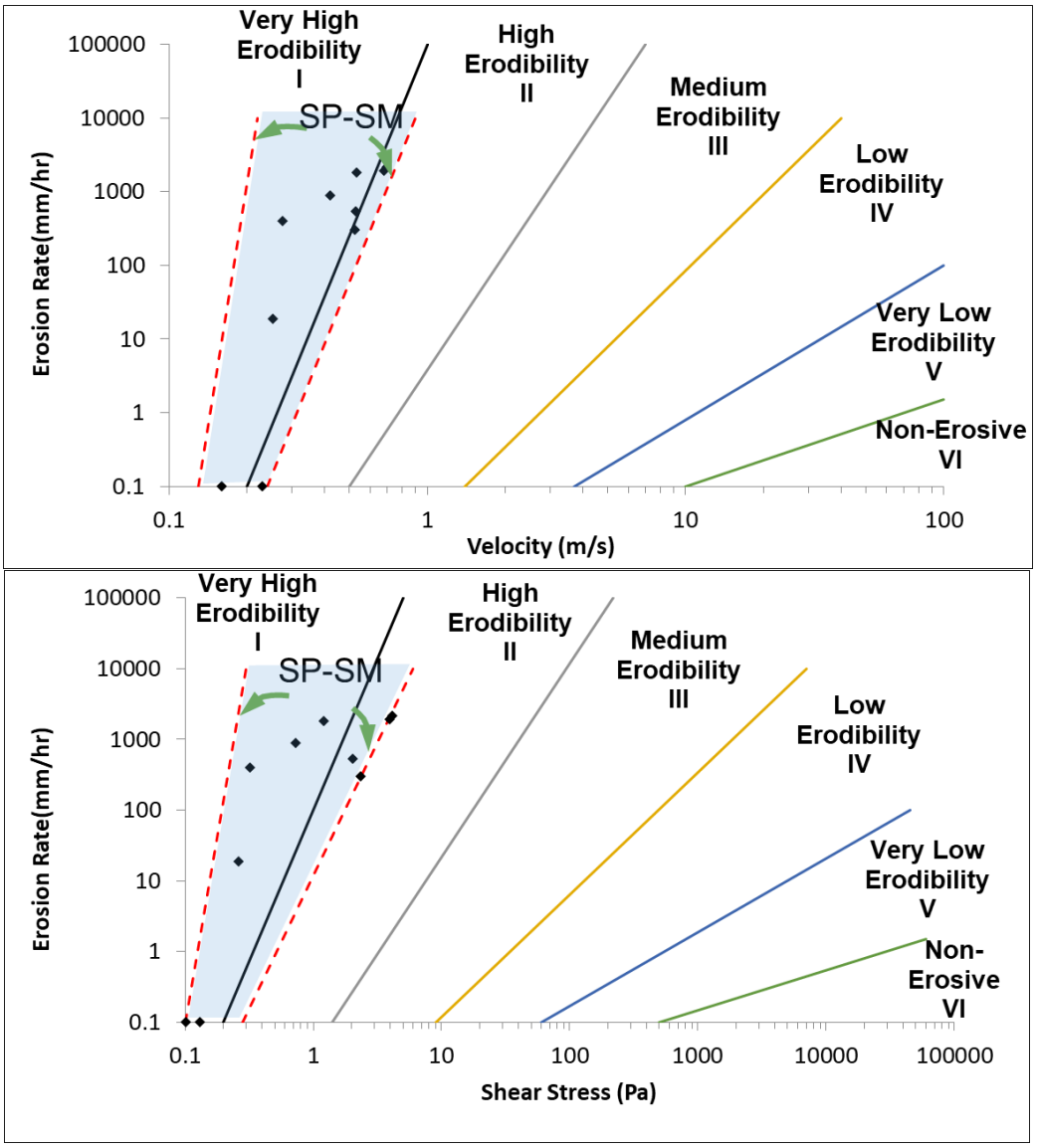

Figure 143. Velocity-Erosion Rate and Shear Stress-Erosion Rate Plots for SP-SM soils

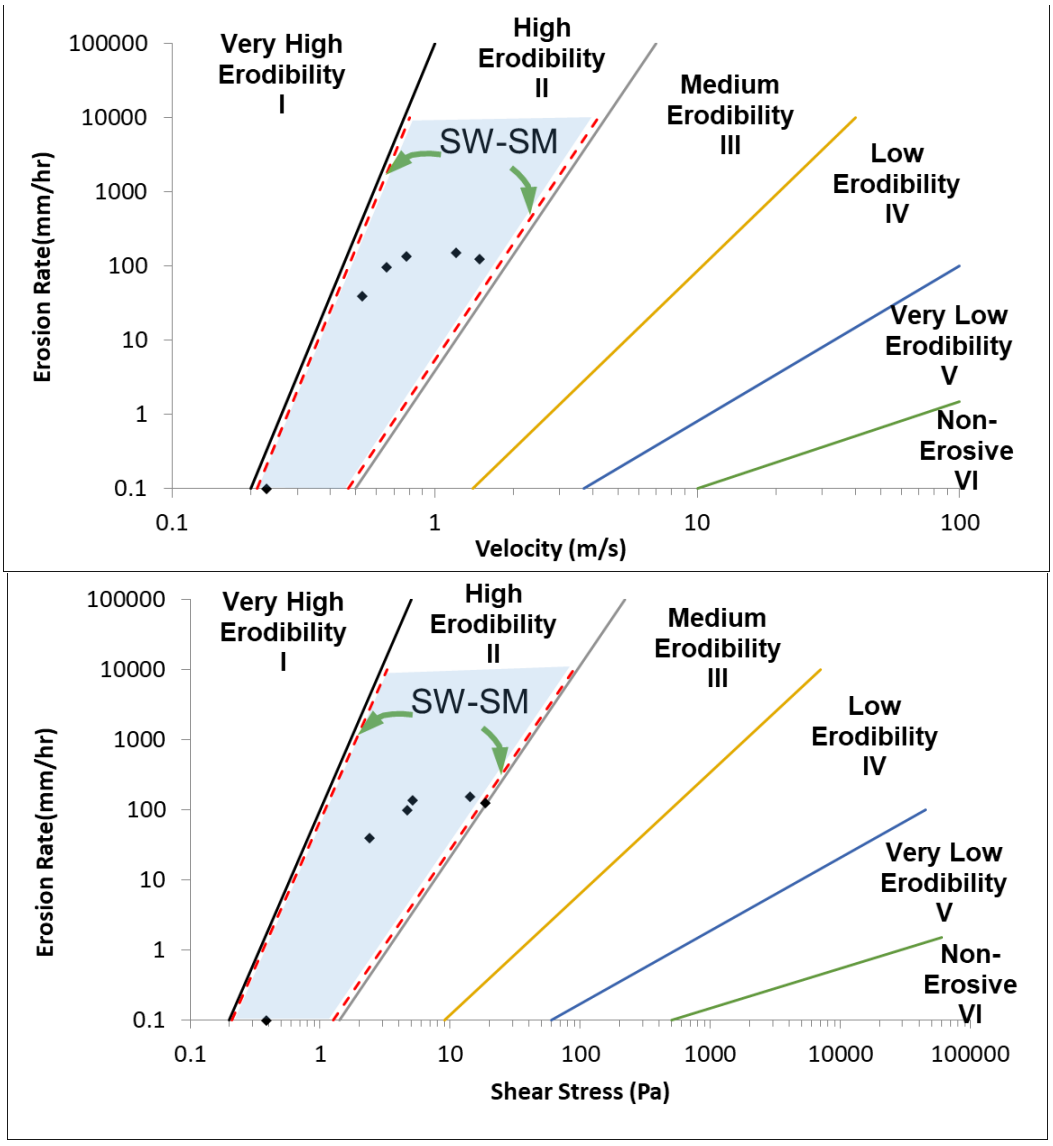

Figure 144. Velocity-Erosion Rate and Shear Stress-Erosion Rate Plots for SW-SM soils

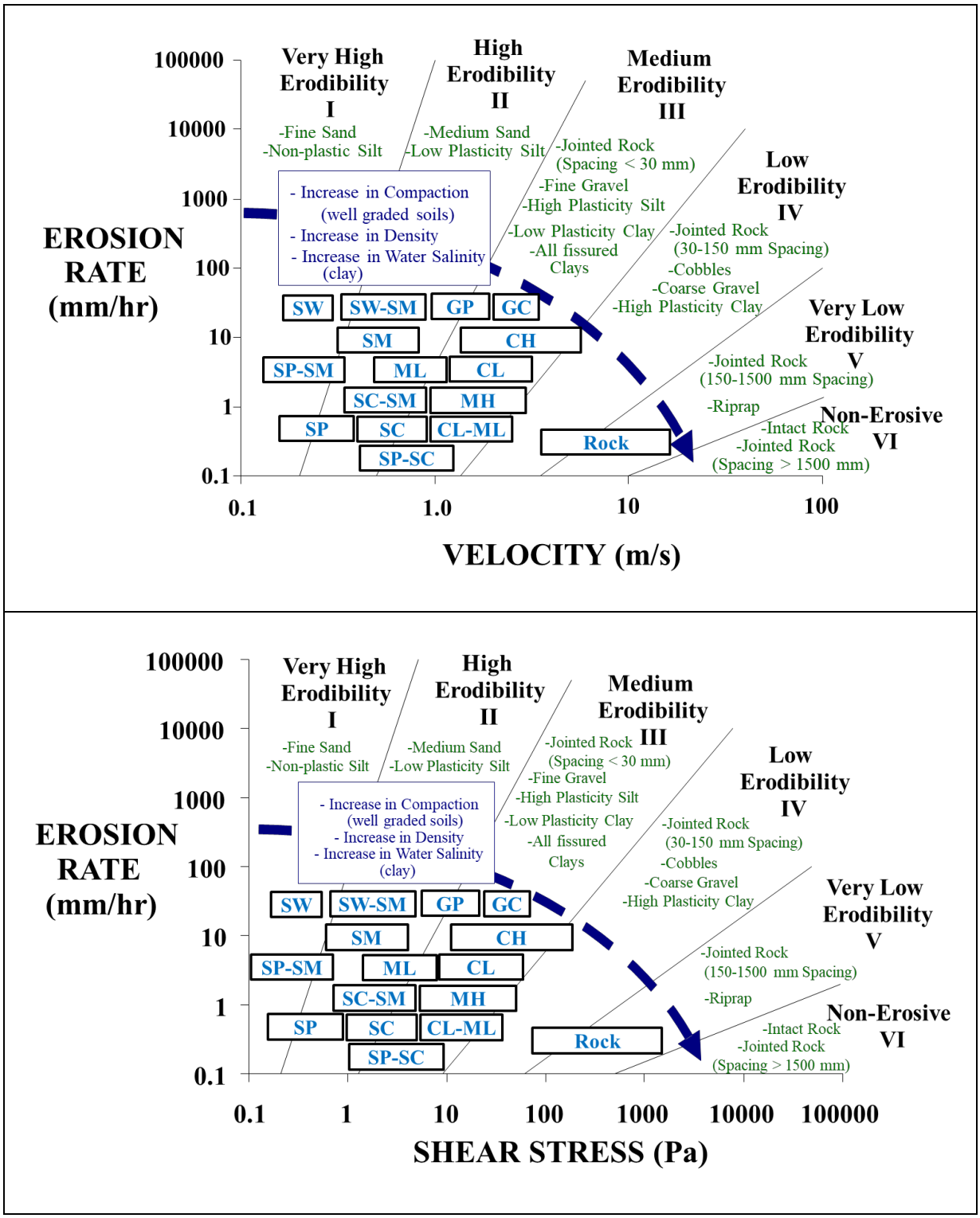

Figure 145. Erosion Category Charts with the USCS Symbols

7.2. Plots of Critical Velocity and Shear Stress versus Mean Particle Size

Briaud et al. (2001) and Briaud et al. (2017) proposed a set of equations to predict the critical velocity and critical shear stress of coarse-grained soils based on many EFA erosion tests performed at Texas A&M University. The number of data points used to generate the equations and corresponding plots were limited to few erosion test results. One of the goals of this NCHRP project was to update and possibly modify the older plots and equations using hundreds of new test results compiled in the TAMU-Erosion Spreadsheet.

It was observed that for soils with mean particle size larger than 0.3 mm, following relationships exist between the critical velocity/shear stress and mean particle size (Eqs. 60 and 61).

$$v_c(m/s) = 0.315\left(D_{50}(mm)\right)^{0.5} \tag{60}$$

$$\tau_c(Pa) = D_{50}(mm) \tag{61}$$

It was also concluded that for fine-grained soils there is no direct relationship between critical velocity/shear stress and the mean particle size. However, the data can be bracketed with an upper bound and a lower bound equation as follows (Eqs. 62 to 65).

$$\text{Upper bound} \quad v_c(\text{m/s}) = 0.07\left(D_{50}(mm)\right)^{-1.45} \tag{62}$$

$$\text{Lower bound} \quad v_c(\text{m/s}) = 0.1\left(D_{50}(mm)\right)^{-0.12} \tag{63}$$

$$\text{Upper bound} \quad \tau_c(\text{Pa}) = 0.06\left(D_{50}(mm)\right)^{-2.3} \tag{64}$$

$$\text{Lower bound} \quad \tau_c(\text{m/s}) = 0.05\left(D_{50}(mm)\right)^{-0.25} \tag{65}$$

One major difference of the updated plots with earlier versions (Figure 31) is that the boundary in which Eqs. 60 and 61 are valid is shifted to D_{50} = 0.3 mm. In earlier versions of these

plots, there was this wrong notion that for soils that are categorized as coarse-grained soils according to USCS classification system (D_{50} > 0.074 mm), direct relationships between critical velocity/shear stress and D_{50} exist.

Figure 146 and Figure 147 show the scattered data for fine-grained soils with the defined upper and lower bound, as well as for the coarse-grained soils. These figures show clearly that mean particle size is not a sufficient parameter for soils that have a D_{50} smaller than 0.3 mm. Therefore, more parameters that specifically involve the plasticity behavior of fine-grained soils affect the critical velocity and critical shear stress of the soils. On the other hand, it is evident that once the soil has a relatively larger mean particle size (D_{50} > 0.3 mm), the mean particle size becomes the predominant parameter in showing the erosion resistance. Eqs. 60 and 61 are strong equations for predicting the values of the critical shear stress and the critical velocity for coarse sand to very large gravels.

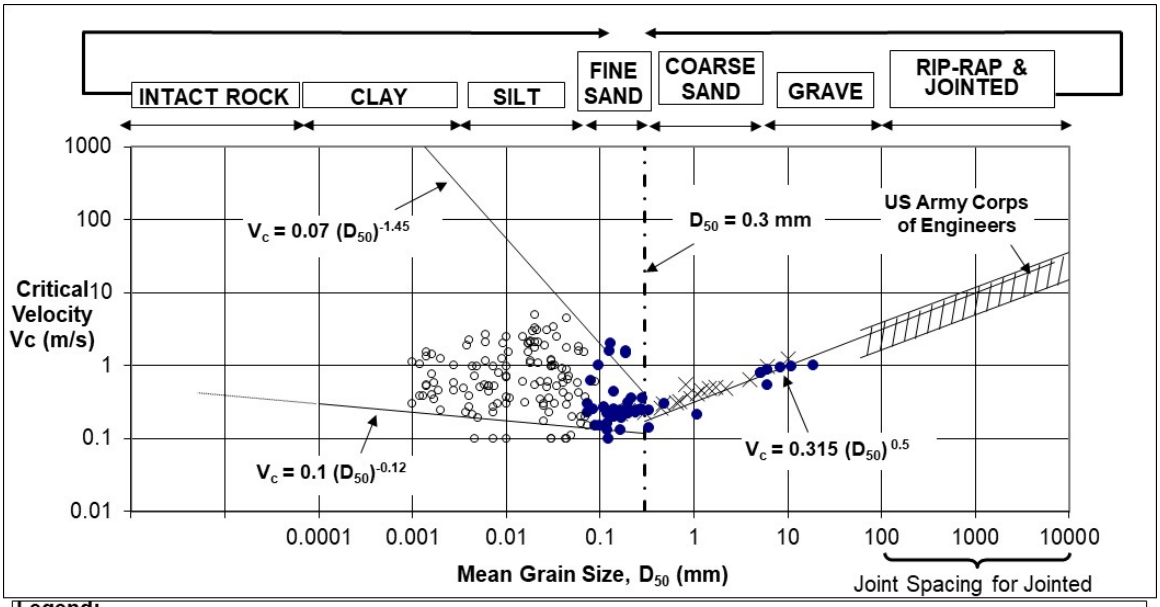

Figure 146. Mean particle size vs. critical velocity

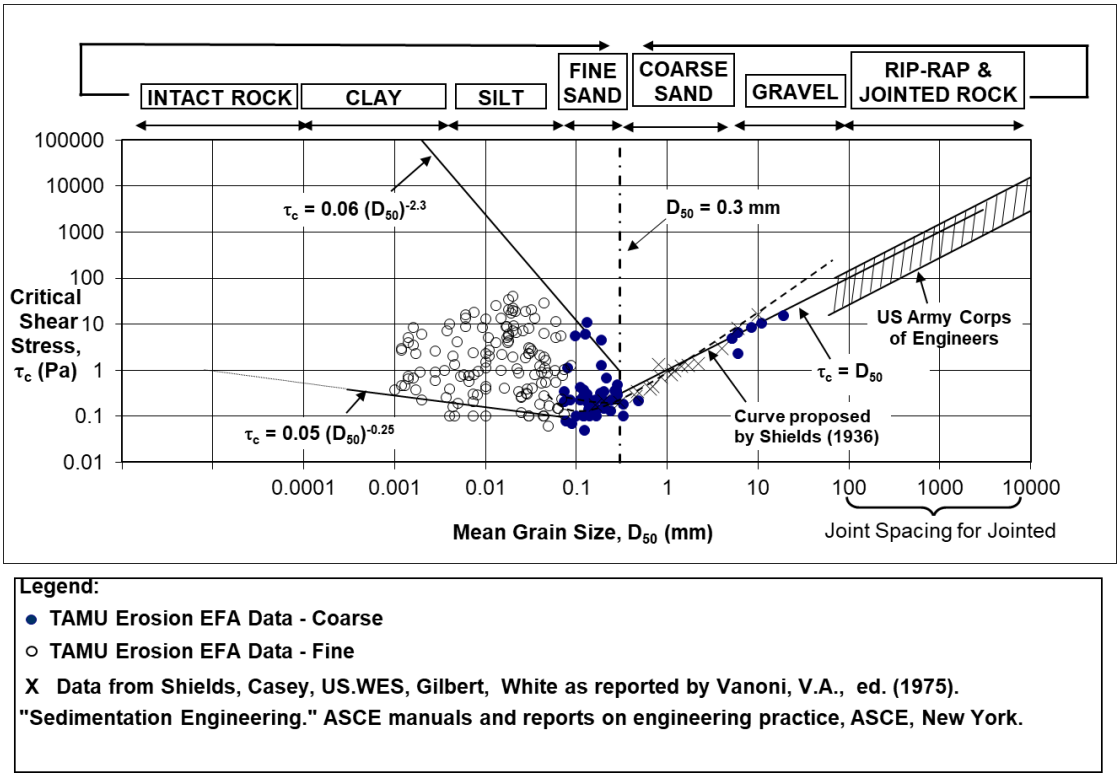

Figure 147. Mean particle size vs. critical shear stress

7.3. Deterministic (Frequentists) Regression Analysis

As discussed in Chapter 1, Tasks 7 and 8 of this project consist of performing two parallel statistical approaches (i.e. “Frequentists’ Regression” and “Bayesian Inference”) with the goal of reaching the best potential fits between erodibility parameters and geotechnical properties of soils. This section is dedicated to the step by step process of Frequentists’ Regression. This approach was implemented in three major steps:

1. First Order Statistical Analysis
2. Second Order Statistical Analysis
3. Regression, Optimization, and Model Selection

7.3.1. *First Order Statistical Analysis*

The first step was to develop the "first order statistical features". This step in Statistics is known as a very crucial step to learn about all the details and complexities within the raw data themselves, before making any effort to generate relationships among them. The programming language of Python is used as the primary tool for this project and the software "Stata" and "SPSS" are used as alternative tools for overseeing the results. This step consisted of obtaining the primary statistical measures of our database (i.e. number of data, range, quartiles, mean, median, mode, standard deviation, histograms, probability density functions, empirical cumulative density functions, etc.). As discussed earlier in Chapter 5, overall, there are 5 erodibility parameters (function variables). These parameters are the critical shear stress τ_c, the critical velocity v_c, the initial slope E_v of the $\dot{z}$ versus v curve, the initial slope E_τ of the $\dot{z}$ versus τ curve and the erosion function category (EC) in the Briaud erosion chart (2013). Up to 16 geotechnical engineering parameters (model variables) are also collected for each sample. These parameters include LL, PL, PI, Water Content (WC), S_u, γ, D_{10}, D_{30}, D_{50}, D_{60}, C_c, C_u, Percent Fine (PF), G_s, Percent Clay (PC), and Soil Activity (A). Nearly 1000 erosion tests compiled in the TAMU-Erosion were studied in different groups. Chapter 5 showed that TAMU-Erosion incorporates more than ten different erosion tests; however, the three major erosion tests (i.e. EFA, HET, and JET) were chosen to further investigate the potential relationships.

The study of the "first order statistical features" was started with the global dataset (including all different tests and all soil types all together). Next, the data was divided based on their erosion test type, and the "first order statistical features" for each sub-group was developed. Next, the data for each sub-group was again divided with regard to their soil type (coarse/fine) according to the USCS. The aforementioned groups are labeled as: 1)TAMU/Global Dataset, 2)

TAMU/Fine Dataset, 3) TAMU/Coarse Dataset, 4) EFA/Global Dataset, 5) EFA/Fine Dataset, 6) EFA/Coarse Dataset, 7) JET/Global Dataset, 8) JET/Fine Dataset, 9) JET/Coarse Dataset, 10) HET/Global Dataset, 11) HET/Fine Dataset, 12) HET/Coarse Dataset

A flowchart diagram of the grouping procedure is shown in Figure 148 below.

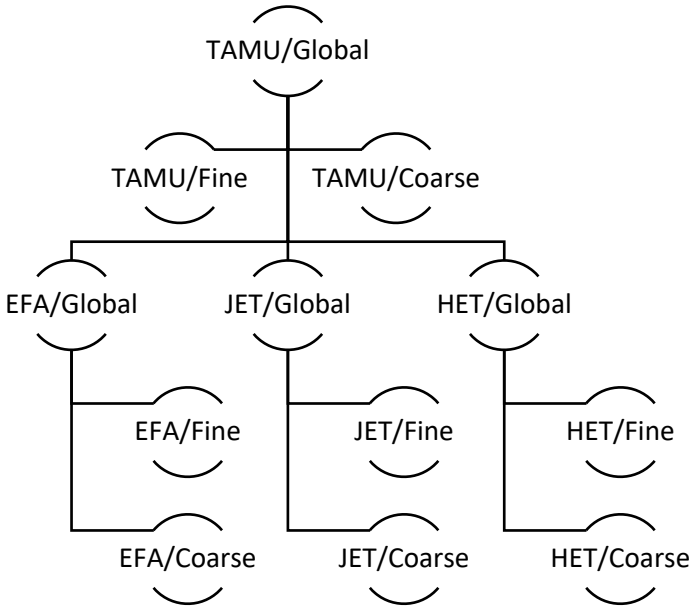

Figure 148. Flowchart diagram of the grouping procedure

As shown in Figure 148, twelve datasets were obtained, and the first order statistics analyses were performed on each dataset separately. The "first order statistical features" of all function and model variables are obtained for the aforementioned groups. Table 33 to Table 44 show these results.

Table 33. First order statistics results for the TAMU Spreadsheet – TAMU/Global Dataset

	EC	E_v (mm-s/m-hr)	E_τ (mm/hr-Pa)	V_c (m/s)	τ_c (Pa)	LL (%)	PL (%)	PI (%)	γ (kN/m^3)	WC (%)	S_u (kPa)	PF (%)	D_{50} (mm)	C_u	C_c	PC (%)
count	831	314	810	319	807	675	674	676	729	729	244	683	483	172	172	584
mean	2.86	129.07	88.18	0.90	64.33	43.14	19.93	23.17	19.17	22.15	51.97	66.24	0.21	64.85	4.07	26.58
std	0.78	565.28	522.91	0.87	153.28	22.48	7.46	19.41	2.13	17.87	39.65	26.72	1.18	102.68	8.85	19.50
min	0.75	0.07	0	0.1	0.0001	14.5	6.3	1.5	11.4	1.02	2	0	0.0009	1.29	0.11	0
25%	2.5	3.2875	0.3425	0.29	0.56	30	15	11.8	18.1	14.2	20	42.95	0.0058	4.7949	1.0641	13
50%	3	8.885	1.425	0.6	5.7	37.6	19	21.9	19.2	18.5	38	75	0.0302	30	1.95541	20
75%	3.25	29.27	7.2275	1.065	32.255	48.2	23	30	20.3	26.88	76.05	87.165	0.13	49	3.4087	39.925
max	5.5	6300	6690.26	5.2	1158	264.1	77	238.8	25.13	286.7	150.7	100	19	850	82	96.39

Table 34. First order statistics results for the TAMU Spreadsheet – TAMU/Fine Dataset

	EC	E_v (mm-s/m-hr)	E_τ (mm/hr-Pa)	V_c (m/s)	τ_c (Pa)	LL (%)	PL (%)	PI (%)	γ (kN/m^3)	WC (%)	S_u (kPa)	PF (%)	D_{50} (mm)	C_u	C_c	PC (%)
count	612	239	595	243	594	570	570	572	537	556	211	502	328	91	91	421
mean	3.03	29.86	16.64	0.95	81.25	44.53	19.91	24.61	19.08	24.83	53.34	80.23	0.02	38.27	3.30	32.58
std	0.74	87.38	105.43	0.87	173.24	23.28	7.48	20.19	2.15	19.06	40.12	13.25	0.02	90.46	8.64	19.66
min	0.75	0.07	0	0.1	0.01	15.2	6.3	1.5	11.4	7.51	3.3	48	0.0009	1.29	0.28	0
25%	2.5	2.775	0.22	0.34	0.9225	30	15	13	17.9	16.625	20	75	0.0025	5.41026	0.96	18.3
50%	3	6.56	0.79	0.7	6.125	39	18.8	22	19	20.75	39.2	81	0.016	30	1.57035	29.7
75%	3.5	16.915	3.005	1.155	64.8225	51	23	31	20.2	29.215	77.5	90.075	0.031	49	2.04082	48
max	5.5	761.8	1718.02	5.2	1158	264.1	77	238.8	25.13	286.7	150.7	100	0.075	850	82	96.39

Table 35. First order statistics results for the TAMU Spreadsheet – TAMU/Coarse Dataset

	EC	E_v (mm-s/m-hr)	E_τ (mm/hr-Pa)	V_c (m/s)	τ_c (Pa)	LL (%)	PL (%)	PI (%)	γ (kN/m^3)	WC (%)	S_u (kPa)	PF (%)	D_{50} (mm)	C_u	C_c	PC (%)
count	219	75	215	76	213	105	104	104	192	173	33	181	155	81	81	163
mean	2.37	445.21	286.18	0.73	17.16	35.55	20.07	15.28	19.42	13.52	43.22	27.44	0.62	94.72	4.93	11.09
std	0.67	1092.66	974.27	0.85	48.34	15.49	7.42	11.69	2.05	9.06	35.84	12.54	2.03	107.80	9.05	5.69
min	1	0.35	0.05	0.1	0.0001	14.5	7.7	2	12.3	1.02	2	0	0.074	1.42857	0.11	0
25%	2	8.13	2.46	0.23	0.23	24.5	16	5.7	18.63	9.7	22	22	0.13	3.88235	1.125	7
50%	2.5	30.79	9	0.325	3.46	36	19	15.05	19.6	11.6	32	29	0.22	38	3.4087	13
75%	2.75	296.67	109.05	0.9075	13.8	39	22.975	21.25	20.5	15.8	45.49	35.14	0.29	230	6.94901	15
max	4.25	6300	6690.26	4	513	90.6	43	56.8	24.29	82	132	65	19	500	57.12	29

Table 36. First order statistics results for the TAMU Spreadsheet – EFA/Global Dataset

	EC	E_v (mm-s/m-hr)	E_τ (mm/hr-Pa)	V_c (m/s)	τ_c (Pa)	LL (%)	PL (%)	PI (%)	γ (kN/m^3)	WC (%)	S_u (kPa)	PF (%)	D_{50} (mm)	C_u	C_c	PC (%)
count	333	307	330	312	331	275	274	274	256	267	190	274	193	66	66	145
mean	2.60	105.67	46.45	0.92	4.25	47.70	20.82	26.85	19.20	27.01	46.24	69.48	0.38	44.42	3.65	21.15
std	0.70	476.80	285.49	0.87	7.92	27.67	9.34	24.62	2.77	14.41	37.20	31.72	1.85	125.83	12.20	19.74
min	0.75	0.07	0.01	0.1	0.05	14.5	6.3	1.5	12.3	1.02	2	0	0.001	1.32	0.11	0
25%	2.25	3.205	0.44	0.3	0.335	32.1	14.3	13	17.55	17.945	19	46.55	0.0082	3.2867	0.86595	5
50%	2.5	8.02	1.615	0.615	1.6	40.9	18.5	22.9	18.91	25.25	32.6	84.3	0.029	5.66536	1.11743	18.06
75%	3	26.725	5.74	1.0925	5.045	58.9	24.4	34.3	20.425	31.2	63.125	95.23	0.088	15	1.47322	28.88
max	5.5	6300	4470.97	5.2	88.35	264.1	77	238.8	25.13	88.1	143.5	100	19	850	82	96.39

Table 37. First order statistics results for the TAMU Spreadsheet – EFA/Fine Dataset

	EC	E_v (mm-s/m-hr)	E_τ (mm/hr-Pa)	V_c (m/s)	τ_c (Pa)	LL (%)	PL (%)	PI (%)	γ (kN/m^3)	WC (%)	S_u (kPa)	PF (%)	D_{50} (mm)	C_u	C_c	PC (%)
count	256	235	253	239	254	232	231	231	192	213	161	203	140	35	35	104
mean	2.71	30.21	11.18	0.97	4.73	48.89	20.70	28.16	19.47	29.66	47.42	86.24	0.02	36.54	3.49	26.02
std	0.65	88.10	46.26	0.87	8.68	28.56	9.14	25.80	2.81	13.36	37.73	13.78	0.02	143.54	13.67	20.92
min	0.75	0.07	0.01	0.1	0.06	15.2	6.3	1.5	13.87	9.8	3.3	48	0.001	1.32	0.44462	0
25%	2.5	2.665	0.36	0.34	0.435	34.225	14.4	15.35	17.6975	21.7	19	78.9	0.00567	3.97077	0.89663	7.5
50%	2.75	6.17	1.15	0.7	1.89	41	18.2	23.2	19.1	27.75	33.8	90.5	0.0172	5.71429	1.06786	21.98
75%	3	16.915	3.7	1.165	5.1075	59.25	24.2	35	20.625	32.9	67	97.3	0.03155	8.06818	1.35425	33.775
max	5.5	761.8	478	5.2	88.35	264.1	77	238.8	25.13	88.1	143.5	100	0.088	850	82	96.39

Table 38. First order statistics results for the TAMU Spreadsheet – EFA/Coarse Dataset

	EC	E_v (mm-s/m-hr)	E_τ (mm/hr-Pa)	V_c (m/s)	τ_c (Pa)	LL (%)	PL (%)	PI (%)	γ (kN/m^3)	WC (%)	S_u (kPa)	PF (%)	D_{50} (mm)	C_u	C_c	PC (%)
count	77	72	77	73	77	43	43	43	64	54	29	71	53	31	31	41
mean	2.22	351.95	162.34	0.75	2.69	41.29	21.49	19.81	18.39	16.54	39.72	21.58	1.32	53.32	3.83	8.77
std	0.75	934.81	572.69	0.86	4.32	21.40	10.45	15.34	2.50	13.72	34.00	15.31	3.37	103.93	10.51	7.57
min	1	0.35	0.08	0.1	0.05	14.5	7.7	2	12.3	1.02	2	0	0.074	1.63	0.11	0
25%	1.75	7.155	1.81	0.23	0.21	24.5	13	6.1	16.67	9.6775	15.7	8.5	0.12	2.455	0.85932	1
50%	2	24.455	4.8	0.34	0.34	38	19.3	15.1	18.63	15.6	31.4	20	0.17	4.87805	1.125	8.5
75%	2.5	247.048	20.97	0.93	4.4	54.6	28.5	32.45	20.2	19.75	45.49	35.07	0.28	57.725	1.64528	15
max	4	6300	4470.97	4	20.03	90.6	43	56.8	23.3	82	132	50.36	19	500	57.12	25

Table 39. First order statistics results for the TAMU Spreadsheet – HET/Global Dataset

	EC	E_v (mm-s/m-hr)	E_τ (mm/hr-Pa)	V_c (m/s)	τ_c (Pa)	LL (%)	PL (%)	PI (%)	γ (kN/m^3)	WC (%)	S_u (kPa)	PF (%)	D_{50} (mm)	C_u	C_c	PC (%)
count	232	0	231	0	231	185	185	185	233	233	21	221	154	53	53	221
mean	3.40	n/a	28.49	n/a	194.50	41.58	19.59	21.99	19.14	18.43	61.10	63.18	0.10	91.86	4.25	28.41
std	0.70	n/a	132.72	n/a	237.10	18.41	6.00	15.17	1.56	8.32	38.76	21.99	0.11	92.71	2.33	18.91
min	1	n/a	0	n/a	0.1	20	11	2.9	13.9	7.5	4.3	22	0.001	1.29	0.48	2
25%	3	n/a	0.13	n/a	15.305	30	15	15	18.3	12.56	43.1	42	0.0025	30	2.04082	13
50%	3.5	n/a	0.64	n/a	89.75	36	19	20	19.3	16.2	57.4	73.4	0.038	38	3.4087	24.84
75%	4	n/a	3.31	n/a	314.98	42	22	24	20.1	21.2	71.8	80.06	0.22	230	6.80272	44.75
max	4.75	n/a	1684.04	n/a	1158	148.1	33	125.8	22.9	44	143.5	100	0.29	230	7.74	77

Table 40. First order statistics results for the TAMU Spreadsheet – HET/Fine Dataset

	EC	E_v (mm-s/m-hr)	E_τ (mm/hr-Pa)	V_c (m/s)	τ_c (Pa)	LL (%)	PL (%)	PI (%)	γ (kN/m^3)	WC (%)	S_u (kPa)	PF (%)	D_{50} (mm)	C_u	C_c	PC (%)
count	169	0	168	0	168	169	169	169	170	170	21	158	92	25	25	158
mean	3.68	n/a	2.10	n/a	254.35	42.12	19.64	22.48	18.73	20.91	61.10	75.44	0.02	29.30	3.49	34.76
std	0.58	n/a	7.81	n/a	248.77	19.18	6.27	15.79	1.46	8.28	38.76	11.24	0.02	19.33	2.66	18.84
min	1	n/a	0	n/a	4.65	20	11	2.9	13.9	7.51	4.3	51	0.001	1.29	0.48	2
25%	3.25	n/a	0.0775	n/a	57.795	30	15	12	18	15.085	43.1	68.8	0.002	2.9	1.14	18.9
50%	3.75	n/a	0.29	n/a	192.93	36	19	22	18.87	18.5	57.4	79	0.0111	30	2.04082	30.9
75%	4	n/a	0.96	n/a	379.525	44	22	24	19.8	23.3235	71.8	84	0.0312	49	6.80272	49.5
max	4.75	n/a	70.81	n/a	1158	148.1	33	125.8	21.8	44	143.5	100	0.075	49	7.74	77

Table 41. First order statistics results for the TAMU Spreadsheet – HET/Coarse Dataset

	EC	E_v (mm-s/m-hr)	E_τ (mm/hr-Pa)	V_c (m/s)	τ_c (Pa)	LL (%)	PL (%)	PI (%)	γ (kN/m^3)	WC (%)	S_u (kPa)	PF (%)	D_{50} (mm)	C_u	C_c	PC (%)
count	63	0	63	0	63	16	16	16	63	63	0	63	62	28	28	63
mean	2.67	n/a	98.85	n/a	34.92	35.94	19.06	16.88	20.24	11.72	n/a	32.44	0.22	147.71	4.93	12.51
std	0.41	n/a	241.37	n/a	79.15	0.25	0.25	0.50	1.27	3.07	n/a	7.22	0.06	96.76	1.78	3.10
min	2	n/a	0.05	n/a	0.1	35	19	15	17.8	7.5	n/a	22	0.13	38	3.4087	7
25%	2.25	n/a	2.895	n/a	8.73	36	19	17	19.35	9.6	n/a	29	0.1525	38	3.4087	13
50%	2.75	n/a	12.82	n/a	13.35	36	19	17	19.9	10.8	n/a	34	0.23	230	3.4087	13
75%	3	n/a	85.355	n/a	23.815	36	19	17	21.3	14	n/a	42	0.29	230	6.94901	14
max	4.25	n/a	1684.04	n/a	513	36	20	17	22.9	18.9	n/a	46.5	0.29	230	6.94901	23.9

Table 42. First order statistics results for the TAMU Spreadsheet – JET/Global Dataset

	EC	E_v (mm-s/m-hr)	E_τ (mm/hr-Pa)	V_c (m/s)	τ_c (Pa)	LL (%)	PL (%)	PI (%)	γ (kN/m^3)	WC (%)	S_u (kPa)	PF (%)	D_{50} (mm)	C_u	C_c	PC (%)
count	145	0	145	0	144	122	122	123	118	108	28	76	29	6	6	108
mean	2.47	n/a	272.67	n/a	5.35	36.09	17.65	18.43	19.43	20.11	88.45	63.89	0.05	83.71	14.94	21.36
std	0.67	n/a	1082.02	n/a	9.44	12.63	4.90	12.17	1.86	36.46	39.37	25.31	0.07	77.59	21.88	12.54
min	1.25	n/a	0.03	n/a	0.0001	14.5	7.7	2.9	11.4	7.16526	22.2	17.12	0.0009	7.14	0.98	1.5
25%	2	n/a	1.29	n/a	0.18	27.725	14.3	6	18.7	11.8145	52.375	41.125	0.0053	43.3625	1.87	11.1575
50%	2.5	n/a	4.92	n/a	1.12	36	16.55	19.1	19.45	14.4	79.6	68.8	0.0165	69.64	4.805	20
75%	3	n/a	29.53	n/a	7.2675	42	21.975	24	20.4	17.385	129.2	84	0.0625	85.83	16.995	29.7
max	3.75	n/a	6690.26	n/a	60.72	79.5	34.1	50.3	24.29	286.7	150.7	100	0.28	230	57.12	64.66

Table 43. First order statistics results for the TAMU Spreadsheet – JET/Fine Dataset

	EC	E_v (mm-s/m-hr)	E_τ (mm/hr-Pa)	V_c (m/s)	τ_c (Pa)	LL (%)	PL (%)	PI (%)	γ (kN/m^3)	WC (%)	S_u (kPa)	PF (%)	D_{50} (mm)	C_u	C_c	PC (%)
count	97	0	97	0	96	85	85	86	80	80	24	56	25	3	3	73
mean	2.63	n/a	58.39	n/a	6.38	39.38	17.14	22.18	19.43	23.18	91.77	77.29	0.02	70.55	3.83	26.38
std	0.63	n/a	238.47	n/a	10.40	13.10	4.83	11.99	1.89	41.98	38.55	13.04	0.03	26.46	3.39	11.42
min	1.25	n/a	0.03	n/a	0.01	15.2	9.9	2.9	11.4	7.55	22.2	51.5	0.0009	40	1.87	5.3
25%	2.25	n/a	0.86	n/a	0.31	29	13	11.325	18.8225	13.6925	55.375	68.8	0.0049	62.915	1.87	18.9
50%	2.75	n/a	2.92	n/a	1.78	36.7	16	22.2	19.64	15.935	83.15	79.8	0.0082	85.83	1.87	28
75%	3.25	n/a	11.59	n/a	8.32	47	21	31	20.35	18.68	129.4	87.3025	0.0461	85.83	4.805	30
max	3.75	n/a	1718.02	n/a	60.72	79.5	34.1	50.3	23.05	286.7	150.7	100	0.0733	85.83	7.74	64.66

Table 44. First order statistics results for the TAMU Spreadsheet – JET/Coarse Dataset

	EC	E_v (mm-s/m-hr)	E_τ (mm/hr-Pa)	V_c (m/s)	τ_c (Pa)	LL (%)	PL (%)	PI (%)	γ (kN/m^3)	WC (%)	S_u (kPa)	PF (%)	D_{50} (mm)	C_u	C_c	PC (%)
count	48	0	48	0	48	37	37	37	38	28	4	20	4	3	3	35
mean	2.13	n/a	705.68	n/a	3.29	28.52	18.84	9.69	19.43	11.33	68.55	26.38	0.21	96.86	26.06	10.87
std	0.63	n/a	1784.55	n/a	6.78	7.20	4.94	7.08	1.81	2.37	44.03	5.14	0.07	117.60	28.54	7.15
min	1.25	n/a	0.41	n/a	0.0001	14.5	7.7	3.9	15.8	7.16526	30.1	17.12	0.1351	7.14	0.98	1.5
25%	1.6875	n/a	4.0325	n/a	0.115	22	16	5	18.475	10	39.85	25.1	0.15603	30.295	10.53	6.83
50%	2	n/a	20.875	n/a	0.45	30	17	6	19.4	11.2	57.45	25.1	0.204	53.45	20.08	8
75%	2.5625	n/a	208.705	n/a	2.8025	30	25	14	20.4	11.9804	86.15	25.1	0.25375	141.725	38.6	20
max	3.5	n/a	6690.26	n/a	28.92	39	25	22	24.29	17.8787	129.2	42.5	0.28	230	57.12	29

As part of the first order statistical analyses of the parameters, and in order to learn about the statistical traits of each parameter, the histograms, probability density functions (PDF) and empirical cumulative density functions (ECDF) were plotted for each parameter. After that, multiple statistical distribution models were fitted to the actual data with the goal of finding the best representative distribution for each parameter in each group. Figure 149 shows an example of a histogram, PDF, and ECDF plots for the critical velocities of the TAMU/Global group in the TAMU-Erosion Spreadsheet, which are fitted with many statistical distribution models (i.e. Normal, Log-Normal, Exponential, Rayleigh, Alpha, Gamma, and Beta). Figure 150 and Figure 151 show the same set of plots for the TAMU/Coarse and TAMU/Fine, respectively.

Results show that the critical velocity (v_c) can be well represented by Exponential distribution. Same approach was taken for all erodibility parameters (i.e. v_c, τ_c, E_v, E_τ, and EC) as well as all 12 major geotechnical properties (i.e. LL, PL, PI, γ, WC, Su, PF, D50, Cu, Cc, PC, and Activity). The goal was to identify the best statistical distribution models that can best represent each parameter. The findings of this effort are not only very important in understanding of each erodibility parameter as well as geotechnical properties, but also a vital tool to perform Frequentist Regression and Bayesian Inference.

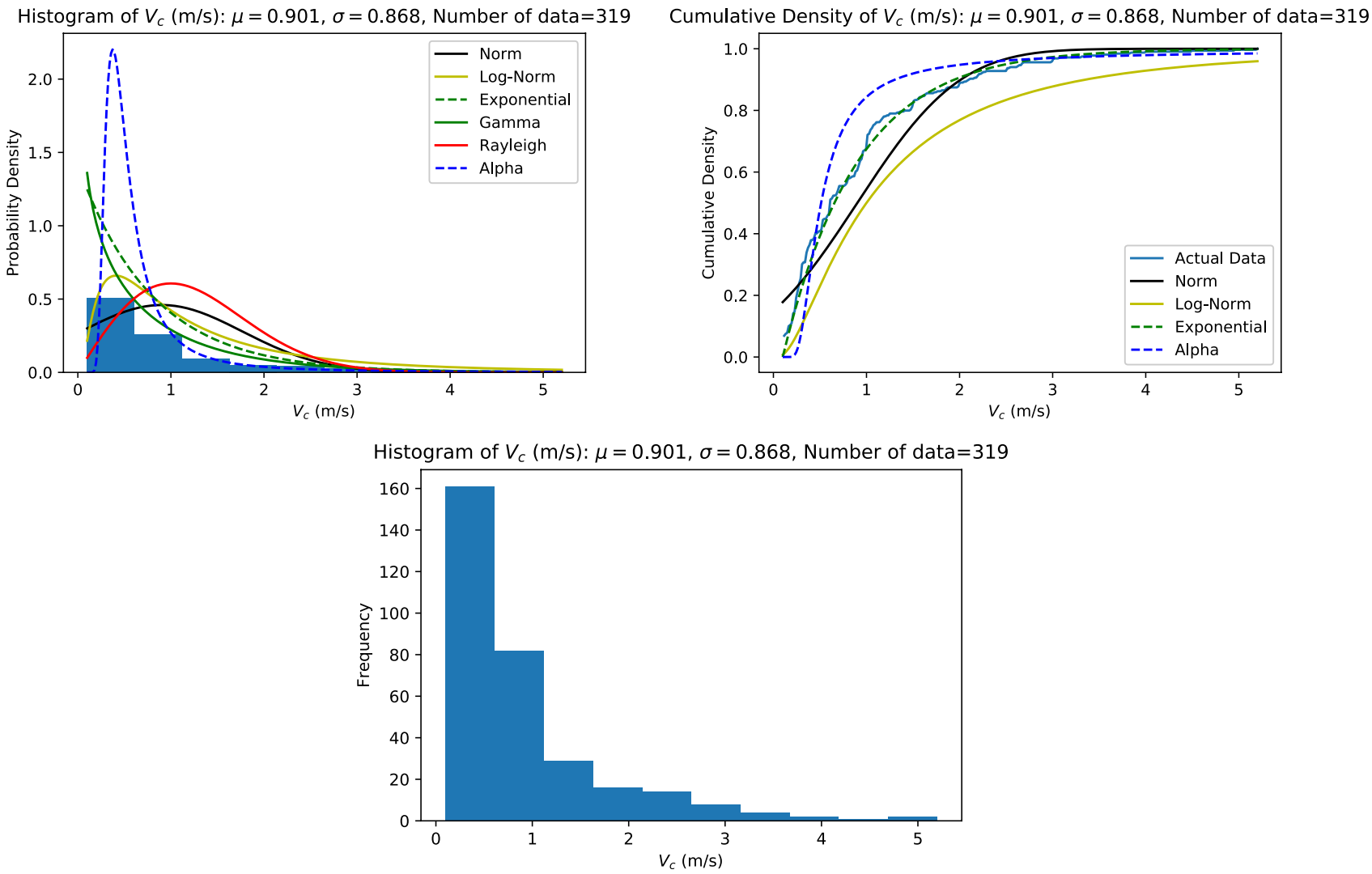

Figure 149. PDF, ECDF, and Histogram Plots for Critical Velocity in the TAMU/Global Dataset

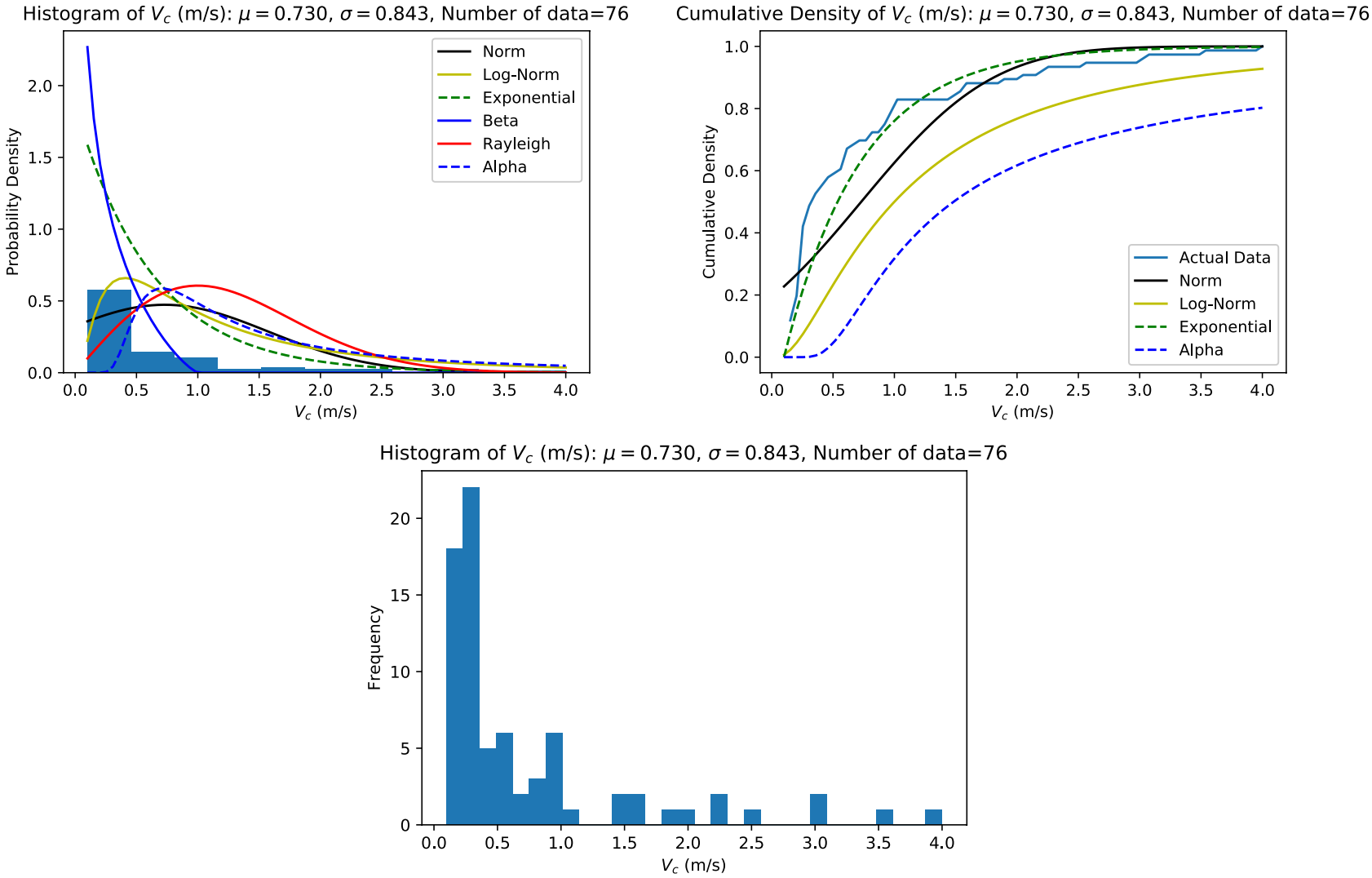

Figure 150. PDF, ECDF, and Histogram Plots for Critical Velocity in the TAMU/Coarse Dataset

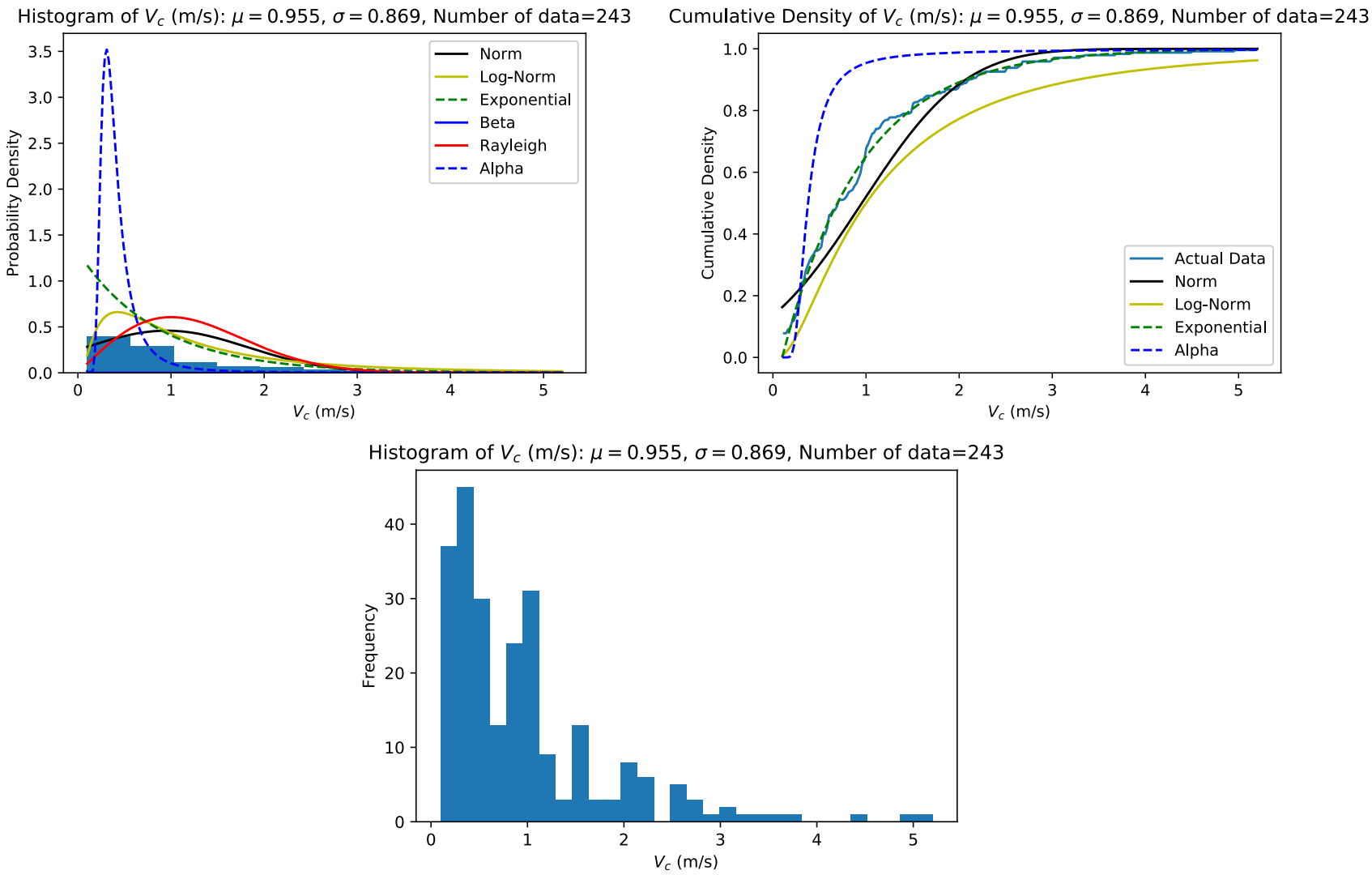

Figure 151. PDF, ECDF, and Histogram Plots for Critical Velocity in the TAMU/Fine Dataset

Similar figures are included in the Appendix C for all five erodibility parameters as well as 12 major geotechnical properties for each subgroup (see Figure 148). The results of the best simplest statistical model for each parameter and in each subgroup are obtained and shown in Table 45 and Table 46. Table 45 shows the best models to represent each erodibility parameter (v_c, τ_c, E_v, E_τ, and EC) in each subgroup. Table 46 shows the best models to represent each major geotechnical property (i.e. LL, PL, PI, γ, WC, S_u, PF, D_{50}, C_u, C_c, and PC) in each subgroup.

Table 45. Best simplest models to represent the erodibility parameters

		Best Simplest Statistical Model to Represent Each Parameter				
Number	Subgroups	EC	E_v	E_τ	V_c	τ_c
1	TAMU/Global	Normal	Exponential	Log-Normal	Exponential	Exponential
2	TAMU/Fine	Normal	Exponential	Log-Normal	Exponential	Exponential
3	TAMU/Coarse	Normal	Exponential	Exponential	Exponential	Log-Normal
4	EFA/Global	Normal	Exponential	Log-Normal	Exponential	Exponential
5	EFA/Fine	Normal	Exponential	Log-Normal	Exponential	Exponential
6	EFA/Coarse	Normal	Exponential	Exponential	Exponential	Log-Normal
7	JET/Global	Normal	-	Log-Normal	-	Log-Normal
8	JET/Fine	Normal	-	Log-Normal	-	Log-Normal
9	JET/Coarse	Normal	-	Log-Normal	-	Alpha
10	HET/Global	Normal	-	Log-Normal	-	Normal
11	HET/Fine	Normal	-	Exponential	-	Normal
12	HET/Coarse	Normal	-	Normal	-	Log-Normal

Table 46. Best simplest models to represent the geotechnical properties

		Best Simplest Statistical Model to Represent Each Parameter										
Number	Subgroups	LL	PL	PI	γ	WC	S_u	PF	D_{50}	C_u	C_c	PC
1	TAMU/Global	Normal	Normal	Normal	Normal	Normal	Exponential	Normal	Gamma	Exponential	Exponential	Normal
2	TAMU/Fine	Normal	Normal	Normal	Normal	Normal	Exponential	Normal	Normal	Exponential	Exponential	Normal
3	TAMU/Coarse	Normal	Normal	Normal	Normal	Normal	Exponential	Normal	Gamma	Normal	Exponential	Normal
4	EFA/Global	Normal	Normal	Normal	Normal	Normal	Exponential	Normal	Gamma	Exponential	Log-Normal	Exponential
5	EFA/Fine	Normal	Normal	Normal	Normal	Normal	Exponential	Normal	Exponential	Exponential	Log-Normal	Normal
6	EFA/Coarse	Normal	Exponential	Exponential	Normal	Normal	Exponential	Normal	Log-Normal	Exponential	Log-Normal	Normal
7	JET/Global	Normal	Normal	Normal	Normal	Normal	Normal	Normal	Gamma	Normal	Normal	Normal
8	JET/Fine	Normal	Normal	Normal	Normal	Exponential	Normal	Normal	Normal	Normal	Normal	Normal
9	JET/Coarse	-	-	-	Normal	Normal	-	Normal	-	-	-	Normal
10	HET/Global	Normal	Normal	Normal	Normal	Normal	Normal	Normal	Normal	Normal	Normal	Normal
11	HET/Fine	Normal	Normal	Normal	Normal	Normal	Normal	Normal	Normal	Alpha	Normal	Normal
12	HET/Coarse	Normal	Normal	Normal	Normal	Normal	-	Normal	Normal	Alpha	Normal	Normal

In order to compare the erodibility parameters obtained through EFA, HET, and JET, the box plots related to τ_c, E_τ, and EC are also presented in Figure 152. The outlier points are removed from the plots. Results show that the critical shear stress in the HET were much larger than other tests. Also, EC was slightly higher in the HET, while EC range is very similar in EFA and JET. The E_τ range was also higher in JET compared to EFA and HET.

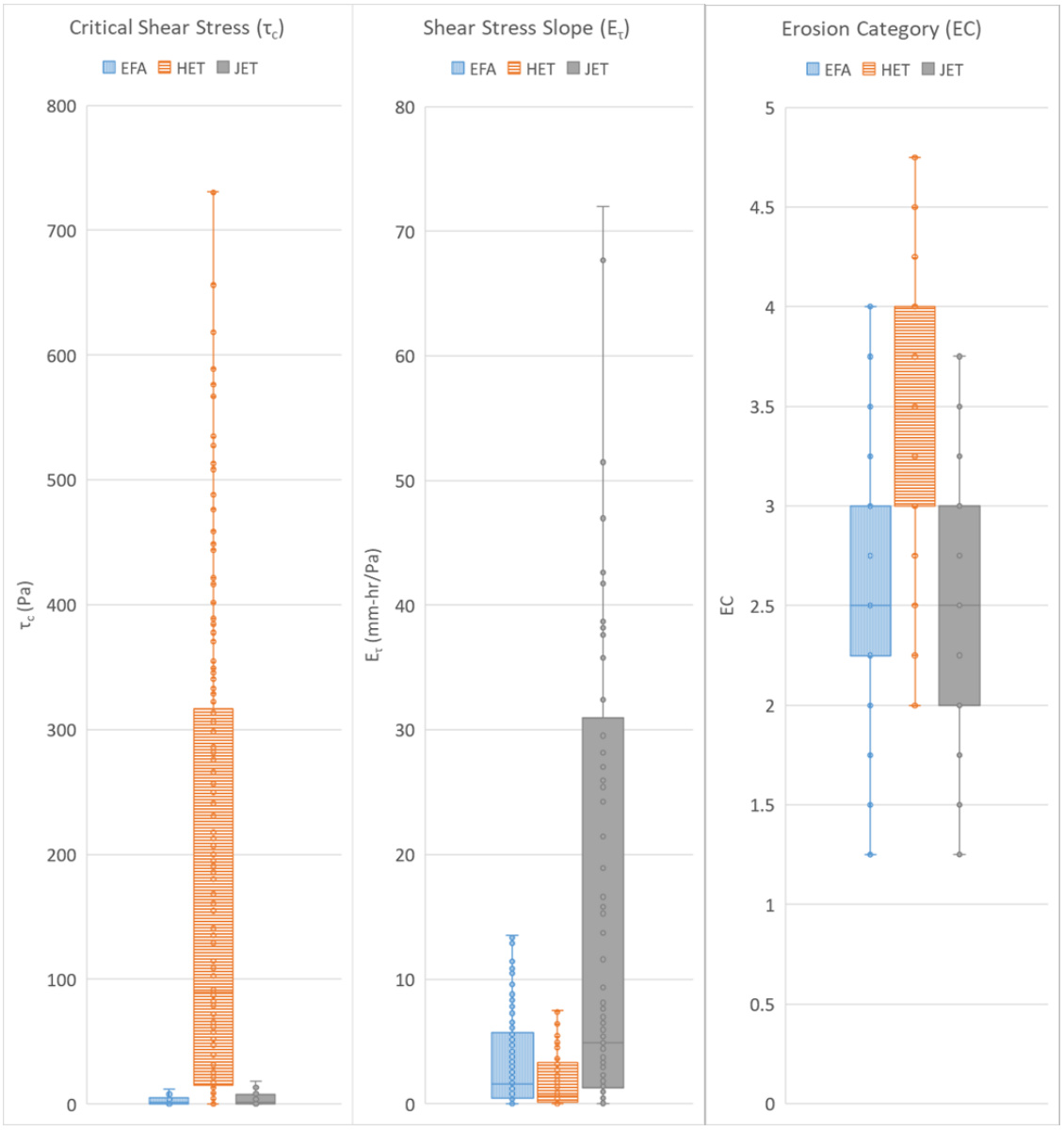

Figure 152. Box plots related to τ_c, E_τ, and EC in EFA, HET, and JET

According to the erosion experiments described in Chapter 4, a few repetitive samples were tested in the EFA, the HET, and the JET to see how each erosion test would perform on an identical sample. The number of repetitive samples that were tested in both EFA and JET was 9. The number of repetitive samples that were tested in both EFA and HET was 3. Results of comparisons are shown in Figure 153.

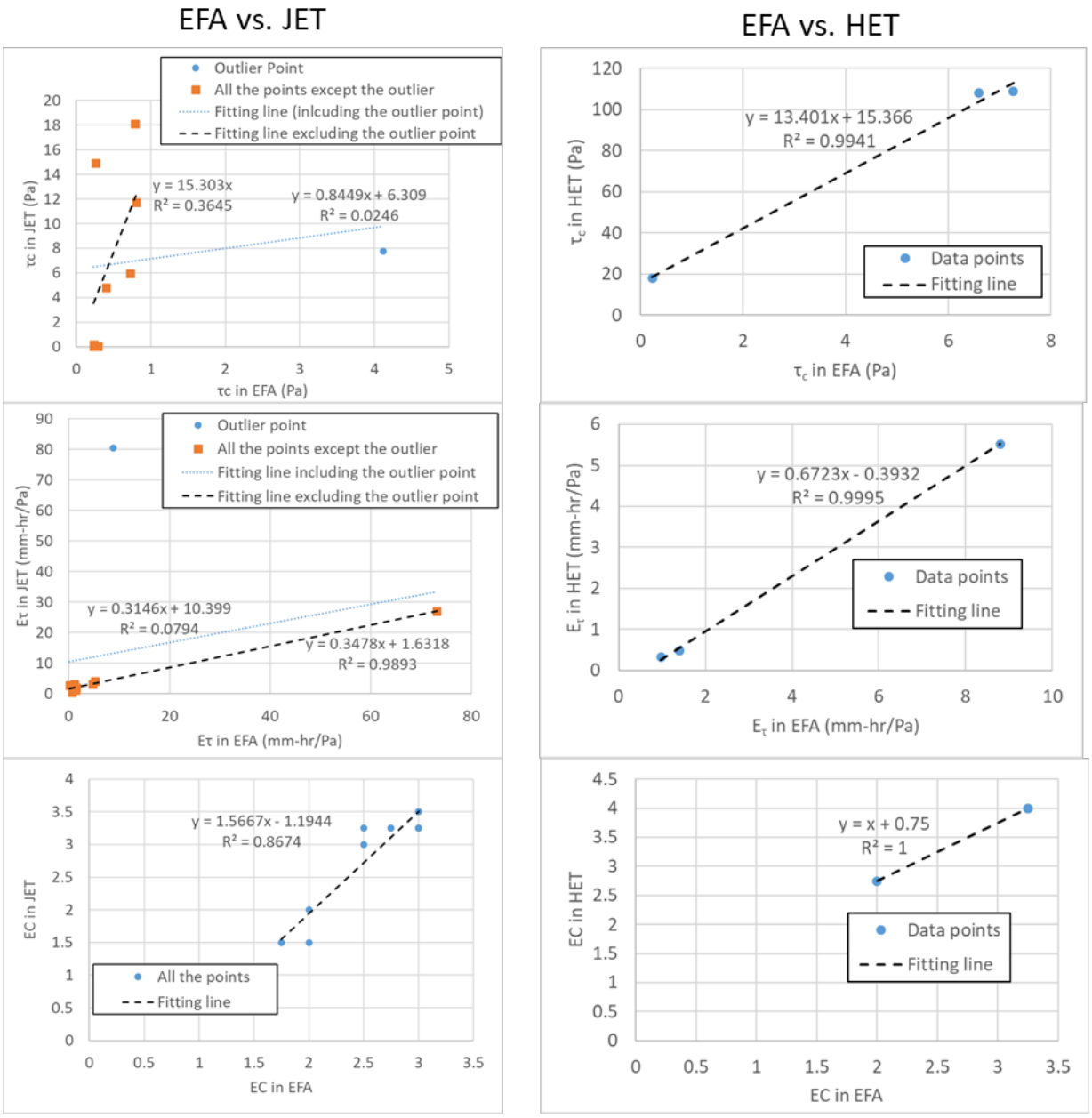

Figure 153. Comparison of EFA vs. JET and EFA vs. JET on repetitive samples

7.3.2. *Second Order Statistical Analysis*

This step dealt with constructing the correlation matrices for the different parameters defined in each group and discussed in the previous step. Before generating the regression relationships, it was needed to learn about any potential inter-parameter's relationships between the model variables (geotechnical parameters) and the function variables (erosion parameters). In order to do that, the correlation matrices were formed between the parameters and the Pearson's Correlation Coefficient (PCC) was obtained for each matrix. PCC is defined as the covariance of the two variables divided by the product of their standard deviations. It ranges from -1 to +1, and reflects the linear dependency between two variables, with +1 showing a strong positive relationship, -1 indicating a solid negative relationship, and 0 referring to no relationship at all. Figure 154 shows an example of the results after the "second order statistical analysis" for EFA-Fine data. Such plots were created for all aforementioned groups explained in Figure 148 and compiled in the Appendix C. The knowledge developed after the second order statistical analysis is very important for implementing the "Bayesian Inference" approach.

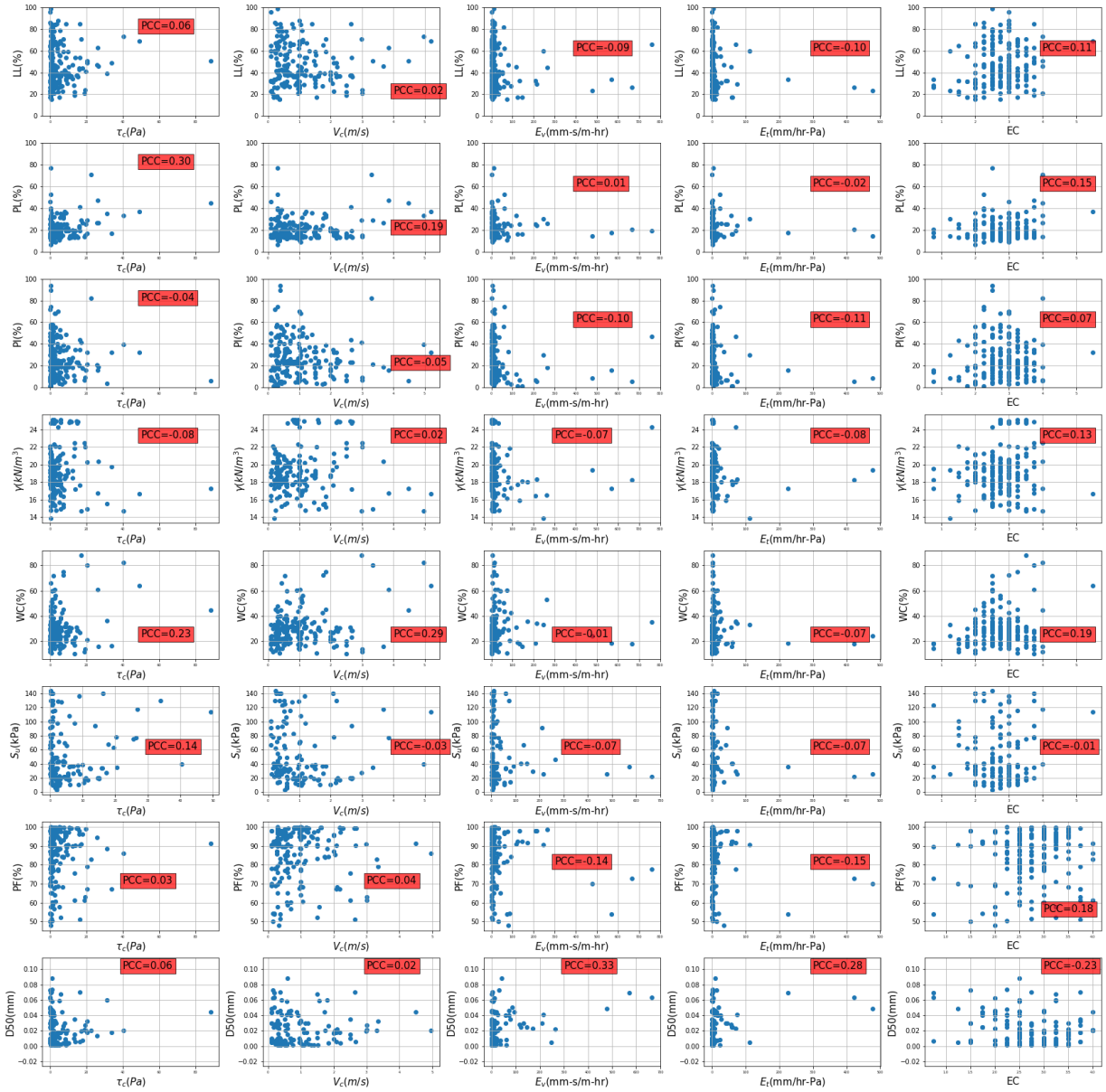

Figure 154. Correlation Matrix for EFA-Fine Data

7.3.3. *Experimental Design*

7.3.3.1. Model Expression

After learning about each parameter, this step dealt with generating the relationship equations between the erosion parameters and the geotechnical engineering parameters.

Two models were used in this research which are called the "Linear Model" and the "Power Model". The Power Model for this research project is the multiple nonlinear model shown in Eq. 66.

$$Y = A \times (P_1)^{\alpha_1} \times (P_2)^{\alpha_2} \times (P_3)^{\alpha_3} \times (P_4)^{\alpha_4} \times \dots \quad (66)$$

Where, Y refers to the dependent variable which in this case includes: τ_c, v_c, E_v, E_τ, and EC; P_i s are the soil geotechnical properties which are used in the regressions; A and α_i are the constant parameters defined in the model expression.

The Linear Model on the other hand was the simple first-degree linear model as described in Eq. 67.

$$Y = [\alpha_1 \times (P_1) + \alpha_2 \times (P_2) + \alpha_3 \times (P_3) + \cdots] + \beta \quad (67)$$

Where, Y refers to the dependent variable which in this case includes: τ_c, v_c, E_v, E_τ, and EC; P_i s are the soil geotechnical properties which are used in the regressions; α_i and β are the constant parameters defined in the model expression.

Several combinations between a function variable, say, τ_c, and model variables (i.e. LL, PL, PI, Water Content, Unit weight, …) can be selected to generate regression equations. In order to obtain the best fits, it was decided to study nearly all possible combinations and evaluate the goodness of each fit. Therefore, 135 regression combination groups are constructed for each function variable in each aforementioned subgroup (as shown in Figure 148). In addition to that, two model expressions (Eqs. 66 and 67) are used to develop the equations. In other words, the total number of regression equations is 2x5x135 (2 model expressions x 5 function parameters x 135 combination group) = 1350 regression equations for each subgroup (as shown in Figure 148).

7.3.3.2.Measures of Statistical Significance

Best models are selected after passing through a four-filter process:

1) R^2
2) Mean Square Error (MSE)
3) $\frac{F\ value}{F\ statistic}$
4) Cross-Validation Score

Each generated model is checked with filters 1 to 4, one after another. Each model that does not qualify the requirements of one specific filter, is not going to be further studied in the following filters and is thus eliminated from the best model sets.

R-squared or R^2 also called coefficient of determination is one of the most well-known statistical measures of fit. It represents how far the actual data stands from the fitted regression model. The mathematical definition of R-squared is shown below:

$$R^2 = 1 - \frac{\Sigma(y_i - f_i)^2}{\Sigma(y_i - \bar{y})^2} \tag{68}$$

Where, y_i are the data, $\bar{y}$ is the mean value of the data set, and f_i are the predicted values using the fitted regression model. In this study, R-squared values for each regression are reported. R-squared ranges from 1.0 being an absolute fit, to 0 being not any relationship. R squared can also sometimes be negative. Generally speaking, R-squared values more than 0.6 can be considered as potential correlations in many engineering applications. However, in many sources, R-squared values even more than 0.4 are accepted by researchers.

The Mean Squared Error (MSE) is another statistical measure to evaluate the quality of a predicting model. MSE is also sometimes called the mean squared deviation. It always gets a non-negative value, and reflects the average of the squared difference between the predicted value and the actual value. The mathematical definition of MSE is shown below:

$$MSE = \frac{1}{n}\Sigma\left(Y_i - \hat{Y}_i\right)^2 \quad (69)$$

Where, Y_i are the data, $\hat{Y}_i$ refer to the predicted value using the estimator, and n is number of the predicted data points.

The main concern with R^2 and MSE is that they cannot completely represent the statistical significance of an estimator; therefore, an additional statistical measure is used in this study. The main problem with R-squared is that it is highly dependent on the number of variables involved in the regression model. For example, when you have only one parameter to predict, and our data set includes only one data, any regression model can lead to an R-squared of 1.

In order to reject the null hypothesis in a regression model, the F-value can be used. The F-value is obtained from Eq. 70:

$$F_{value} = \frac{SSE\ (reg)}{SSE\ (res)} \times \left(\frac{D}{V} - 1\right) \quad (70)$$

Where SSE(reg) is the sum of square errors for the regression values, SSE(res) is the sum of square errors for the residual values, D is the number of data points, and V is the number of variables. As can be seen from the equations, if the regression model has a lot of error (SSE(res) is large) then F will be small. Also, if the number of data points is close to the number of variables, then F will be small again. The goal is to maximize the value of F and in any case to make it higher than F statistic, a target value given in statistic tables.

Note that the R-squared and MSE values represent the goodness of a fit evaluation, while the F test (comparing the F-value with the F-statistic) indicates whether there is enough data or not to propose the equation. The probability level for the F-test in this study is chosen as 5%.

After the first three filters (R^2, MSE, $\frac{F\ value}{F\ statistic}$) are passed successfully, cross-validation score of the selected models would be examined. Over-fitting is a common problem in many similar statistical analyses conducted in different fields of engineering. Over-fitting may happen

when the equation is generated based on all the data points available in the dataset. In this case, the proposed model is not necessarily designed for yet-unseen data. As a result, adding a few data points to the existing dataset, or removing some data from it can sometimes dramatically change the goodness of fit of the model. One approach to evaluate if this is a problem is to divide the dataset into two random subsets and call them training and testing subsets (i.e. 85% and 15% of the data, respectively). After that the model is trained using the training subset, and validated through the testing subset. One issue with this approach is that our analysis is very dependent on the random "train" and "test" subsets that we chose in the beginning.

Cross-validation is a technique used to assess the estimator performance by folding the dataset into 'k' random folds. The model is trained using the 'k-1' fold, and then validated using the remaining folds. The final score of the cross-validation is the average of all scores for each time that the model is trained and validated (the average of k scores). Cross-validation was used to further sieve the best models, and end up with the most robust equations.

This four-filter model selection process was performed for each subgroup as shown in Figure 1. This process incorporates studying of thousands of generated models in the first step, narrowing down to smaller number of models after passing each filter. By the end of the fourth filter, the best models to correlate erodibility parameters to geotechnical properties were supposed to be achieved.

For the "Coarse" datasets (subgroups of TAMU/Coarse, EFA/Coarse, HET/Coarse, and JET/Coarse) 105 soil parameter combination groups were chosen for each function variable; however, for "Global" and "Fine" datasets (subgroups of TAMU/Global, TAMU/Fine, EFA/Global, EFA/Fine, HET/Global, HET/Fine, JET/Global, JET/Fine), 135 soil parameter

combination groups were selected for each function variable. Units of the parameters used in regression analyses as well as list of these combination groups are presented in Appendix D.

After the requirements of all four filters are met successfully, the best fitting models are selected. If more than one fitting model meet the filter requirements, the authors' engineering judgement helps narrow down the choices into one or at most two equations. More regarding the selected models is discussed in Chapter 8.

7.3.3.3. Probability of Over/Under-Predicting (POO/POU)

The best correlation equations that can estimate each erodibility parameter (i.e. τ_c, v_c, E_τ, E_v, and EC) are selected according to the four-filter process discussed in the previous section. These equations are obtained through a deterministic statistical analysis, meaning that they reflect the predicted value as a single number, with no quantification of the possible error associated with predicting the future event.

One of the major goals of this study is to provide the scour engineer with a reliability-based approach to also assess whether the predicted values are conservative enough for engineering design purposes. This approach is called the "Probability of Over/Under-Predicting (POU/POO)" approach. As an instance, the scour engineer needs to know the probability that the predicted τ_c is smaller than the actual τ_c, in order to be on the safe side in the design problem. Similarly, critical velocity (v_c) and erosion category (EC) are among those erodibility parameters that require the probability of under-predicting (POU). On the other hand, the scour engineer needs to know the probability that the predicted E_τ (or E_v) is larger than the actual E_τ (or E_v), in order to be on the safe side in the design problem. Therefore, in such cases, the probability of over-predicting (POO) is presented.

Eq. 71 shows the probabilistic model which consists of the selected deterministic predicted erodibility parameter and a correction factor, θ.

$$Z_{new} = \theta \times Z_{det} \tag{71}$$

Where Z_{new} refers to the new value for the erodibility parameter, θ refers to the correction factor, and Z_{det} is the deterministically predicted erodibility parameter. θ can also be inferred as the ratio of the "Z_{new}" over "Z_{det}".

Depending on the erodibility parameter, the "POU vs. θ" or "POO vs. θ" plots are developed for the best selected equations in the next section. These plots help the engineers find the best correction factors associated with a confidence level in design problems. Figure 155 gives an example of how POU is calculated for a function parameter such as EC. POU refers to the probability that the predicted values (Z_p) are smaller than the measured values (Z_m). The black solid line in Figure 155 represents the case in which Z_m = Z_p. In this example, two different correction factors ($\theta = 0.6$ and $\theta = 1.0$) are considered. The data points associated with '$\theta = 1.0$' are shown with black 'o' markers, and the data points associated with the '$\theta = 0.6$' are shown with red '+' markers. The POU is then calculated by counting the number of data points above the black solid line (the data points in which $Z_m > Z_p$) and dividing that by the total number of data points.

In this report, these plots are often accompanied with an offset value. As an example, the POO is calculated as the probability of "$Z_m - Z_p < offset\ value$" instead of the probability of "$Z_m - Z_p < 0$". The "offset values" are small compared to the standard deviation of the parameter, and can often be neglected; however, due to the fact that the R^2 for selected equations were very high and the parameter values were very small in many cases, the lack of an offset value could lead to unrealistic POU or POO values.

The following section presents the process in which the best equations are selected for each erodibility parameter. The "POU vs. Correction Factor" or "POO vs. Correction Factor" plots are also presented for the selected equations.

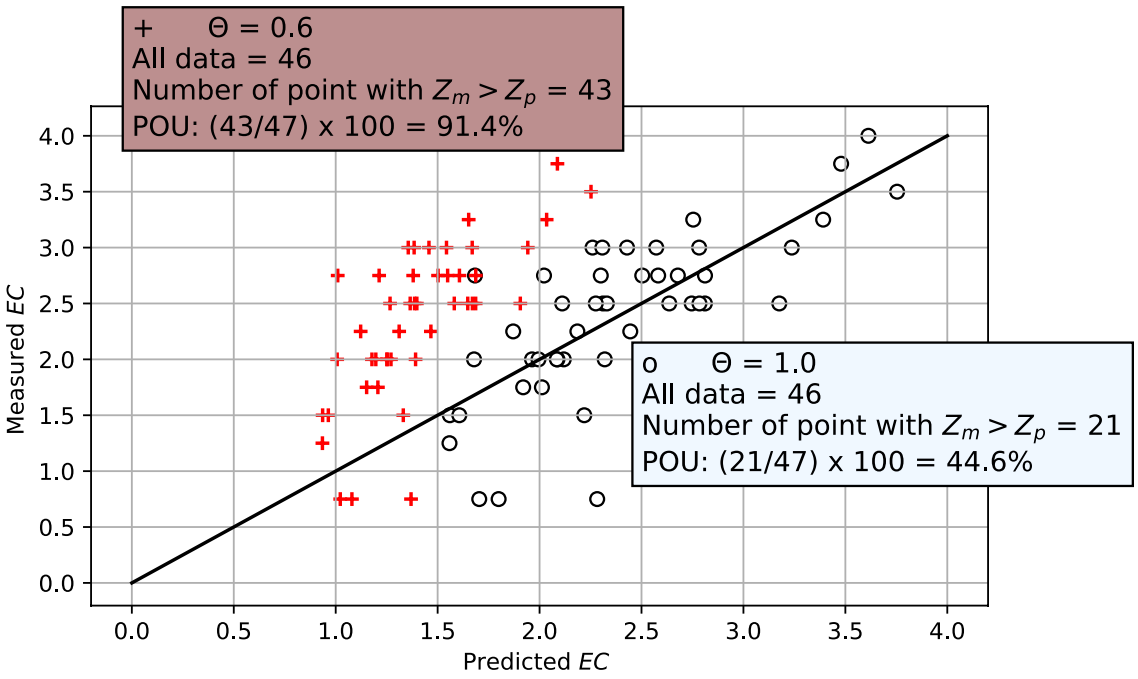

Figure 155. An example of how POU is obtained for two different correction factors

7.3.4. *Regression, Optimization, and Model Selection*

The step-by-step procedure discussed in Section 7.3.3 to select the best fitting models is implemented for each erodibility parameter (i.e. τ_c, v_c, E_τ, E_v, EC) in the followings. The selected correlation equations in this section are repeated in the next Chapter, and recommendations on how they should be used are provided. The units and description of all the parameters used in the following equations in this section are listed in Table 47, as well as in the Appendix D of the appendices report.

Table 47. Units and descriptions of the parameters used in regression analyses

Parameter	Description	Unit
τ_c	Critical Shear Stress	Pa
C_c	Coefficient of Curvature	-
C_u	Coefficient of Uniformity	-
D50	Mean Particle Size	mm
EC	Erosion Category	-
E_v	Slope of Velocity-Erosion Rate	mm-s/m-hr
E_τ	Slope of Shear-Erosion Rate	Mm/hr-Pa
LL	Liquid Limit	%
PC	Clay Percentage (<0.002 mm)	%
PF	Percent Finer than Sieve #200	%
PI	Plasticity Index	%
PL	Plastic Limit	%
PP	Pocket Penetrometer Strength	kPa
S_u	Undrained Shear Strength	kPa
V_c	Critical Velcoity	m/s
VST	Vane Shear Strength	kPa
WC	Water Content	%
γ	Unit weight	kN/m^3

7.3.4.1. Critical Shear Stress (τ_c)

First filter is R^2. The study started from the very top subgroup in Figure 148, TAMU/Global. This database includes all existing data, regardless of test type or fine/coarse nature of the samples. Figure 156 shows the number of data in each of the 135 soil parameter combination groups. Figure 157 and Figure 158 show the results of R2 for these 135 soil parameter combination groups with the "Linear Model" (Eq. 67) and "Power Model" (Eq. 66), respectively.

Figure 157 and Figure 158 show very poor R^2 values (< 0.2) for the critical shear stress in the TAMU/Global dataset. Obviously, following through filters 2 to 4 are not reasonable for this dataset. The same poor results were observed when the dataset was changed to TAMU/Fine, TAMU/Coarse. These observations prove that the regression analyses needed to be narrowed down to each test separately, and consecutively coarse or fine nature of the soils. Therefore, the

subgroups of EFA/Global, EFA/Fine, EFA/Coarse, JET/Global, JET/Fine, JET/Coarse, HET/Global, HET/Fine, and HET/Coarse were used to implement the regression analyses, as described below.

EFA Dataset

It was observed that dividing the EFA/Global dataset into EFA/Fine and EFA/Coarse leads to better results. Figure 159 shows the number of data points in each of all the 135 combination groups in the EFA/Fine dataset. Also, Figure 160 and Figure 161 show the results of R^2 for each combination group, for the "Linear Model" and "Power Model", respectively.

R^2 values of groups 108 to 135 are generally higher than the rest for both "Linear" and "Power" models; however, a quick glance shows that the "Power" model is a better fit for the existing data in the case of critical shear stress in EFA/Fine dataset.

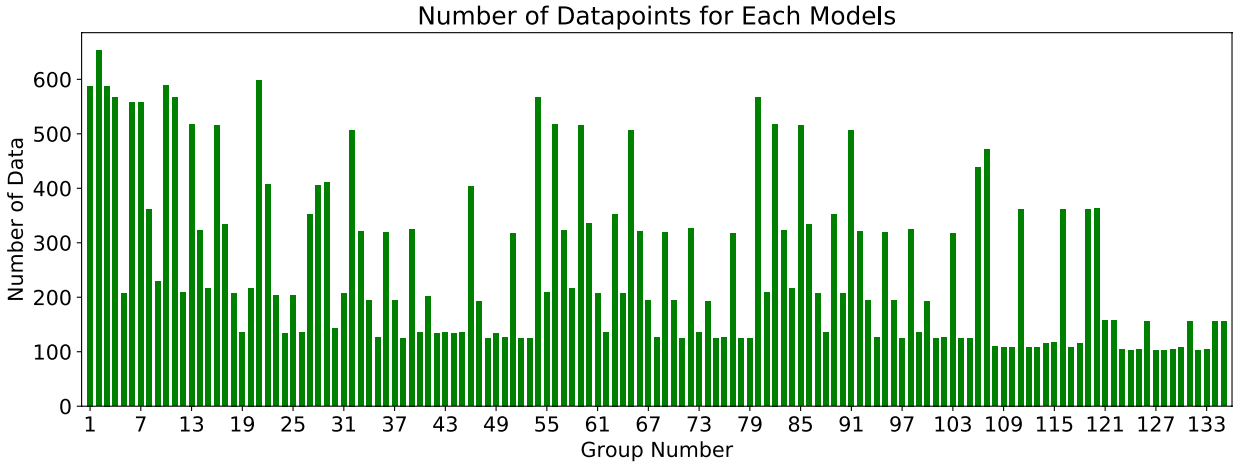

Figure 156. Number of data in each 135 soil parameter combination groups for the TAMU/Global dataset – Critical Shear Stress

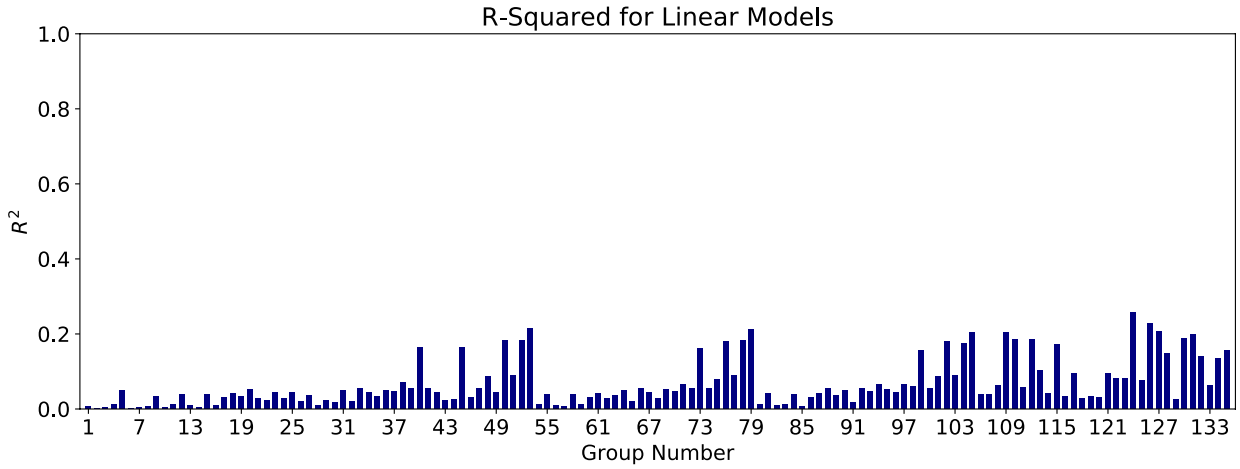

Figure 157. R^2 results for the "Linear Models" in TAMU/Global dataset – Critical Shear Stress

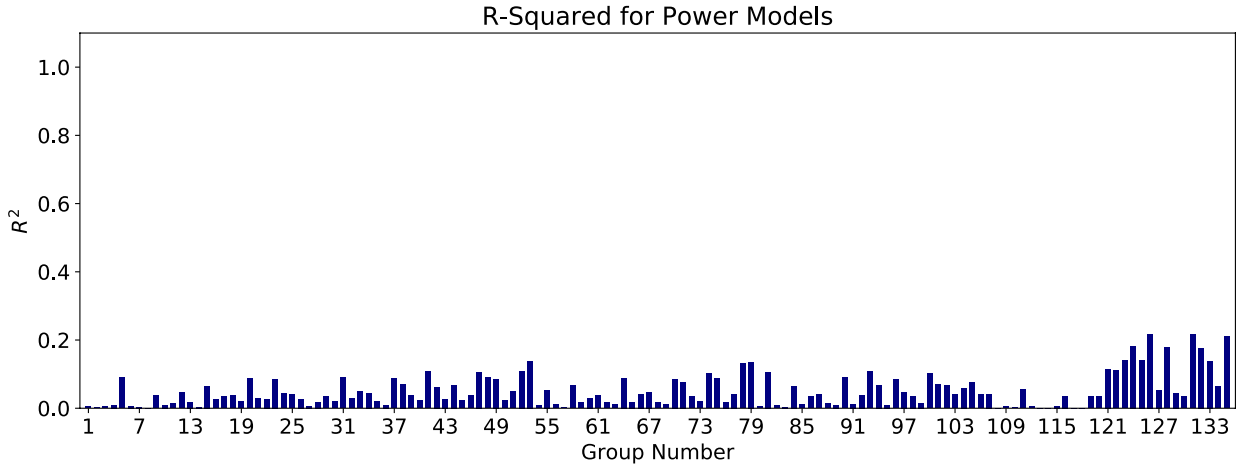

Figure 158. R^2 results for the "Power Models" in TAMU/Global dataset – Critical Shear Stress

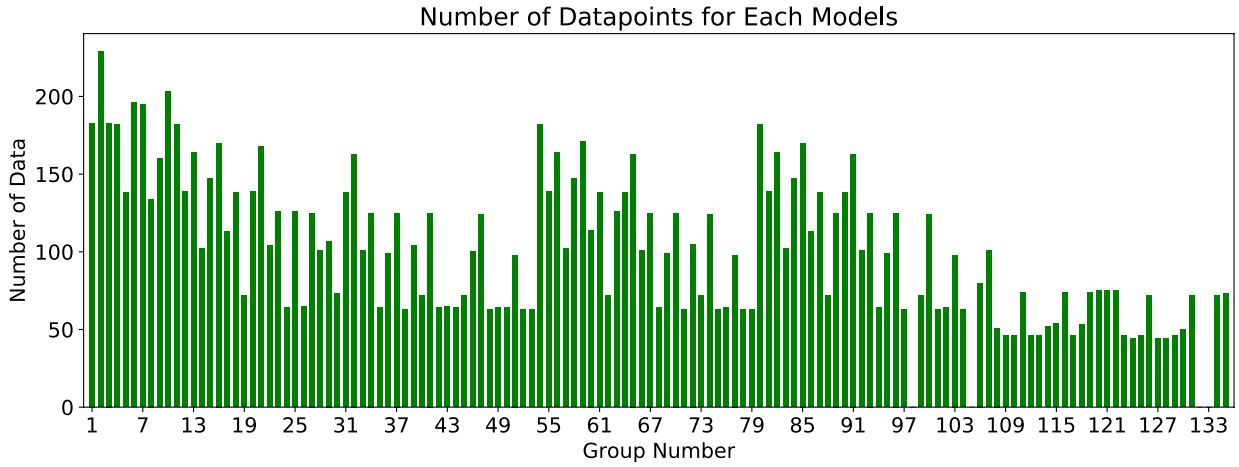

Figure 159. Number of data in each 135 combination groups for the EFA/Fine dataset – Critical Shear Stress

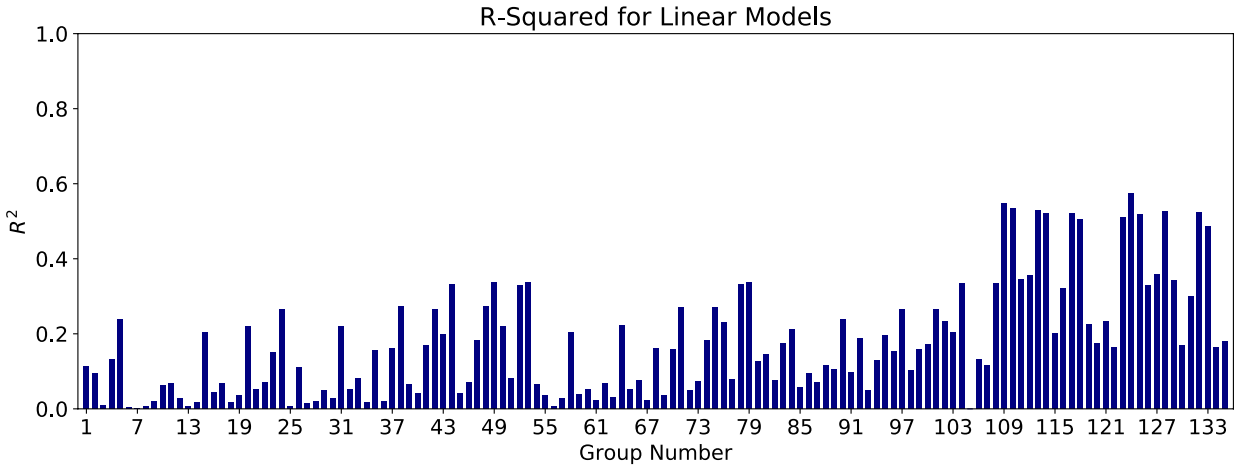

Figure 160. R^2 results for the "Linear Models" in EFA/Fine dataset – Critical Shear Stress

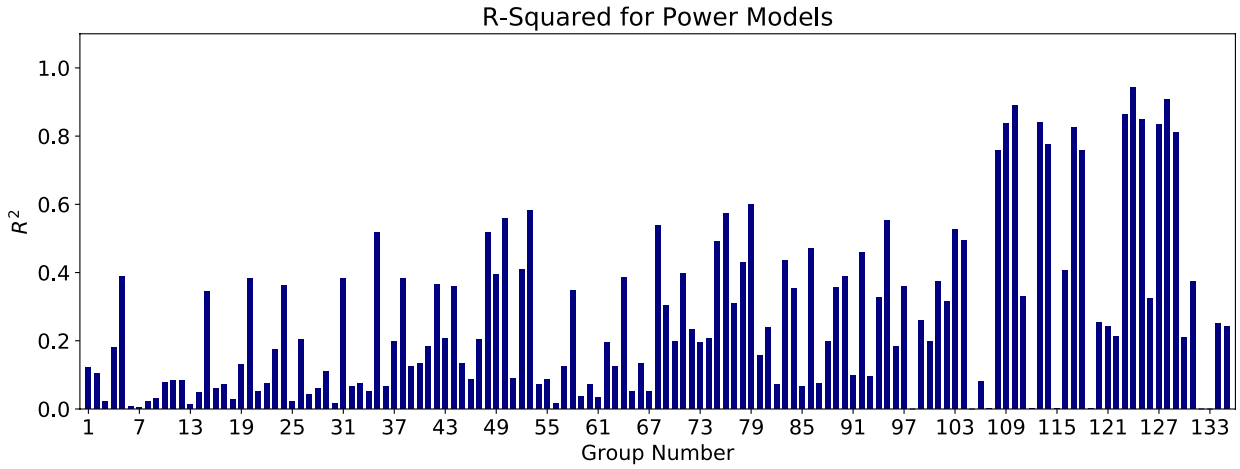

Figure 161. R^2 results for the "Power Models" in EFA/Fine dataset – Critical Shear Stress

Next step was to select the best R^2 values, and move forward with Filter 2 (Mean Square Error). Figure 162 and Figure 163 show the values of MSE for the "Linear" and "Power" models, respectively. As expected, the MSE values are generally lower for same group numbers (108 to 135) in both figures.

After passing through filters 1 and 2 (R^2 and MSE), "Power" models associated with groups 109, 110, 113, 123, 124, 125, and 128 were selected for further analysis. Filter 3, F-value/F-stat, was determined for each group. In cases that F-value/F-stat is lower than 1, the model needs to be removed from the selection list. Otherwise, the model remains in the list. Table 48 shows the results of the selected models after meeting the requirements of the first three filters (R2, MSE, and F-value/F-stat).

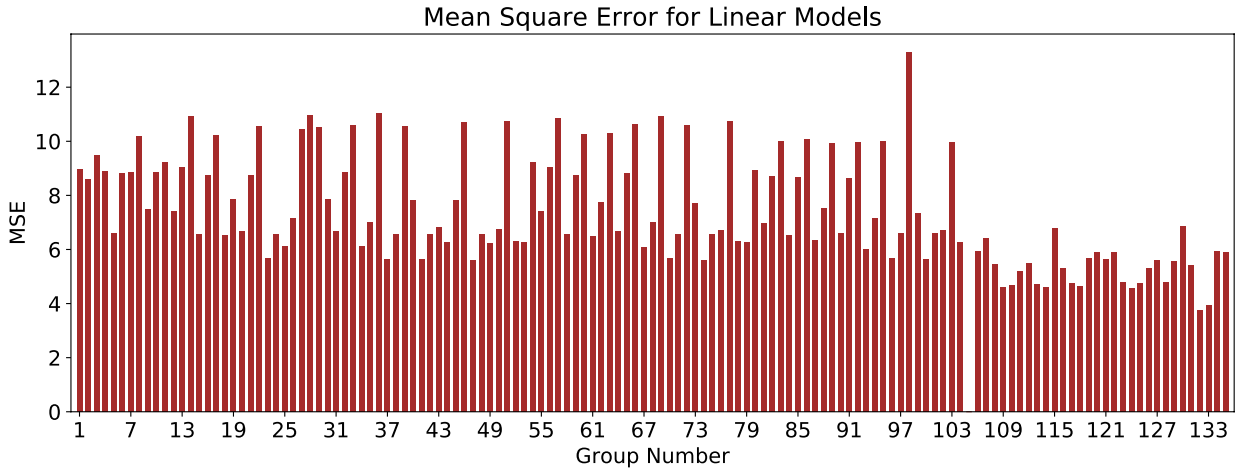

Figure 162. MSE results for "Linear Models" in EFA/Fine dataset – Critical Shear Stress

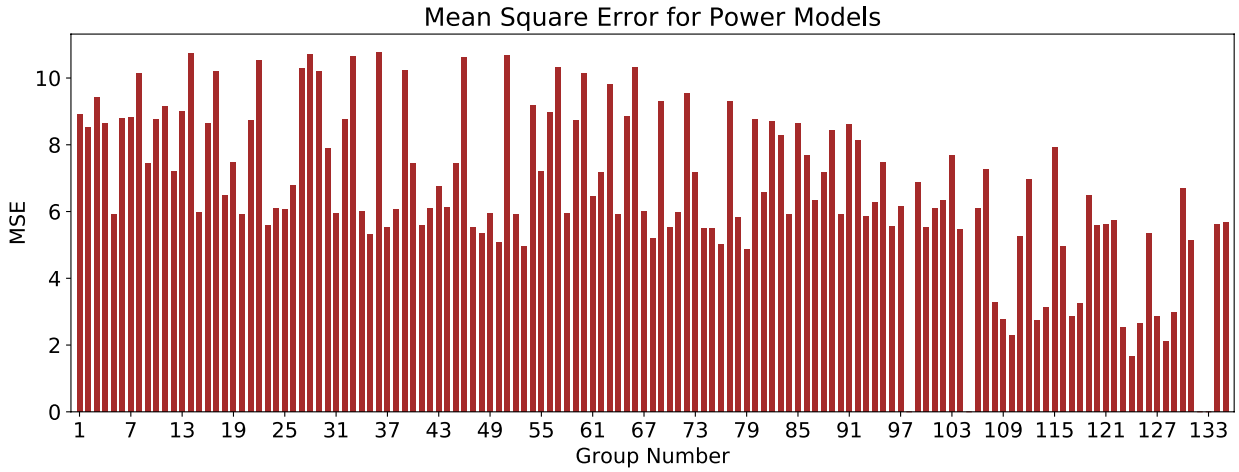

Figure 163. MSE results for "Power Models" in EFA/Fine dataset – Critical Shear Stress

Table 48. Selected "Power" models for critical shear stress in the EFA/Fine dataset

Group No.	Independent Variables	Model Expression	R^2	MSE	F-value/F-stat	Cross-Validation Score
109	PC, γ, WC, S_u, PF, D50	$\tau_c = (5.5 \times 10^{-9}) \times \gamma^{-1.03} \times WC^{4.03} \times S_u^{1.57} \times PF^{-0.22} \times D50^{-0.68} \times PC^{9.6\times10^{-8}}$	0.84	2.76	3.5	0.66
110	PC, WC, S_u, PF, D50	$\tau_c = (1.5 \times 10^{-5}) \times WC^{4.37} \times S_u^{1.49} \times PF^{-3.25} \times D50^{-1.1} \times PC^{6.1\times10^{-8}}$	0.86	2.50	4.7	0.83
113	PC, γ, WC, S_u, D50	$\tau_c = (7.9 \times 10^{-7}) \times \gamma^{-2.74} \times WC^{3.74} \times S_u^{1.59} \times D50^{-0.64} \times PC^{1.4\times10^{-7}}$	0.84	2.73	4.9	0.65
123	A, PL, γ, WC, S_u	$\tau_c = (3.56 \times 10^{12}) \times A^{0.77} \times PL^{1.02} \times \gamma^{-16.05} \times WC^{1.04} \times S_u^{2.27}$	0.87	2.53	7.1	0.18
124	γ, A, WC, S_u, PF, D50	$\tau_c = (158.06) \times \gamma^{5} \times A^{-0.46} \times WC^{10.03} \times S_u^{1.83} \times PF^{-18.28} \times D50^{-4.21}$	0.94	1.67	3.9	0.66
125	γ, WC, S_u, PF, A	$\tau_c = (3.25 \times 10^{12}) \times \gamma^{-14.93} \times WC^{1.18} \times S_u^{2.34} \times PF^{-0.17} \times A^{1.05}$	0.85	2.67	5.1	0.25
128	D50, γ, WC, S_u, A	$\tau_c = (2.2 \times 10^{12}) \times D50^{-0.74} \times \gamma^{-18.99} \times WC^{3.57} \times S_u^{2.43} \times A^{-0.72}$	0.91	2.11	2.9	-0.08

Table 48 shows the selected models which meet the requirements of the first three filters; however, not all of them perform satisfactorily in the cross-validation test. As mentioned earlier, cross-validation is a technique used to assess the estimator performance by folding the dataset into 'k' random folds. The model is trained using the 'k-1' fold, and then validated using the remaining folds. The final score of the cross-validation is the average of all scores for each time that the model is trained and validated (the average of k scores). Out of the 7 selected groups in Table 48, groups 110 and to some extent group 124 (highlighted in blue) are the ones that pass all four filters successfully.

Section 7.3.3.3 and Eq. 67 discussed the reliability-based approach called the POU approach. The plots of "POU vs. θ" are shown in Figure 164 and Figure 165 for groups 110 and 124, respectively. The vertical axes in these plots represent the probability that the predicted τ_c using the selected model is smaller than the actual τ_c, in percentage (with ± 0.5 Pa precision). The horizontal axes represent the correction factor (θ) that can multiply to the predicted value to reach a certain POU level (See Eq. 67). For instance, Figure 164 shows that by using the Group 110

correlation equation (see Table 48), there is near 73% chance that the predicted τ_c is smaller than the actual τ_c (with ± 0.5 Pa precision). However, if the scour engineer desires a higher confidence level, say, near 90%, then he/she needs to multiply the predicted value by 0.6. Figure 165, on the other hand, shows that by using the Group 124 correlation equation (see Table 48), there is almost 90% chance that the predicted value is smaller than the actual τ_c (with 0.5 Pa offset). These plots give the engineers flexibility in choosing the desired correction factors according to the design application.

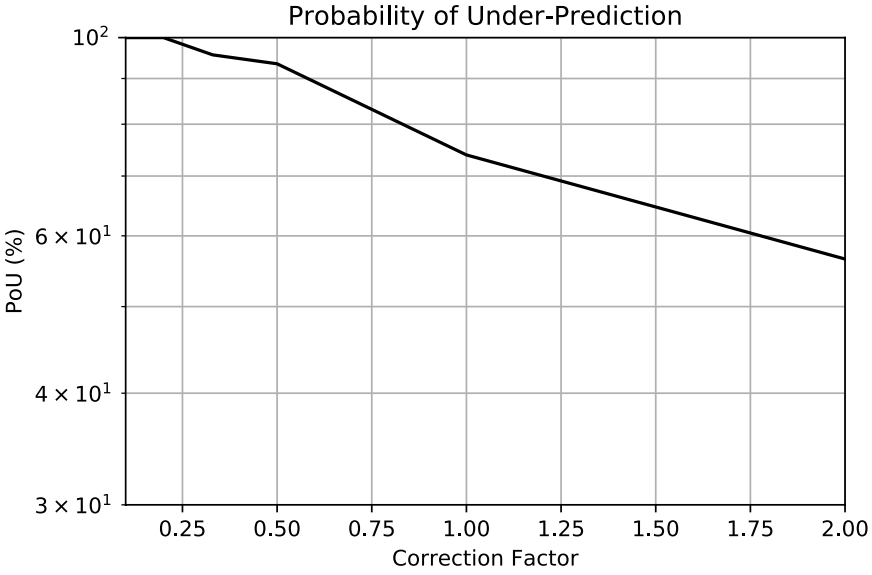

Figure 164. Plot of POU vs. correction factor for the Group 110 (Power) - τ_c in the EFA/Fine dataset

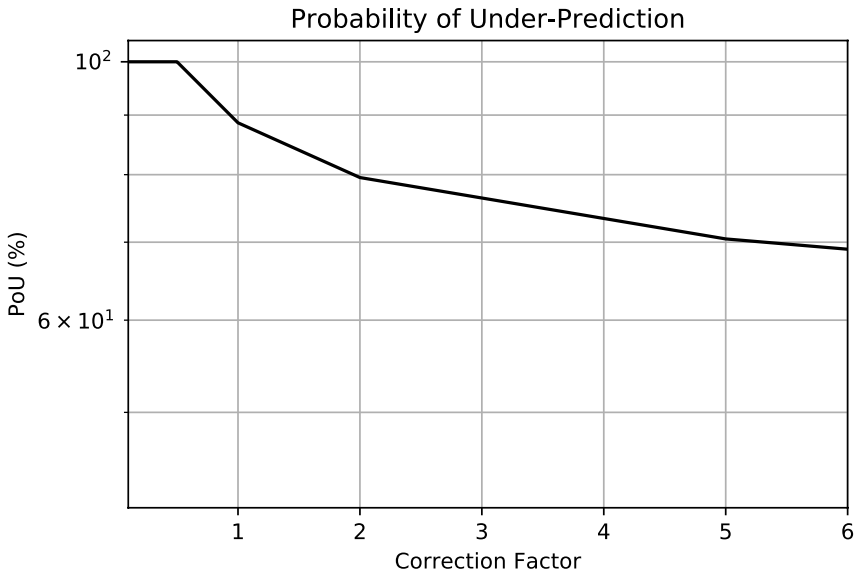

Figure 165. Plot of POU vs. correction factor for the Group 124 (Power) - τ_c in the EFA/Fine dataset

The same exact procedure was conducted in the EFA/Coarse dataset, and the best models are selected. Figure 166 shows the number of data points in each of all the 105 combination groups in the EFA/Coarse dataset. Also, Figure 167 and Figure 168 show the results of R^2 for each combination group, for the "Linear Model" and "Power Model", respectively.

In contrary to the EFA/Fine dataset, both "Linear" and "Power" models show a few good groups in terms of R^2 values; however, as shown in Figure 166, the number of data points in most groups are very lower compared to the EFA/Fine dataset. In other words, many regression groups might meet the requirements of the first two filters, R^2 and MSE; however, they only might marginally pass through the F-test. Figure 169 and Figure 170 show the values of MSE for the "Linear" and "Power" models, respectively.

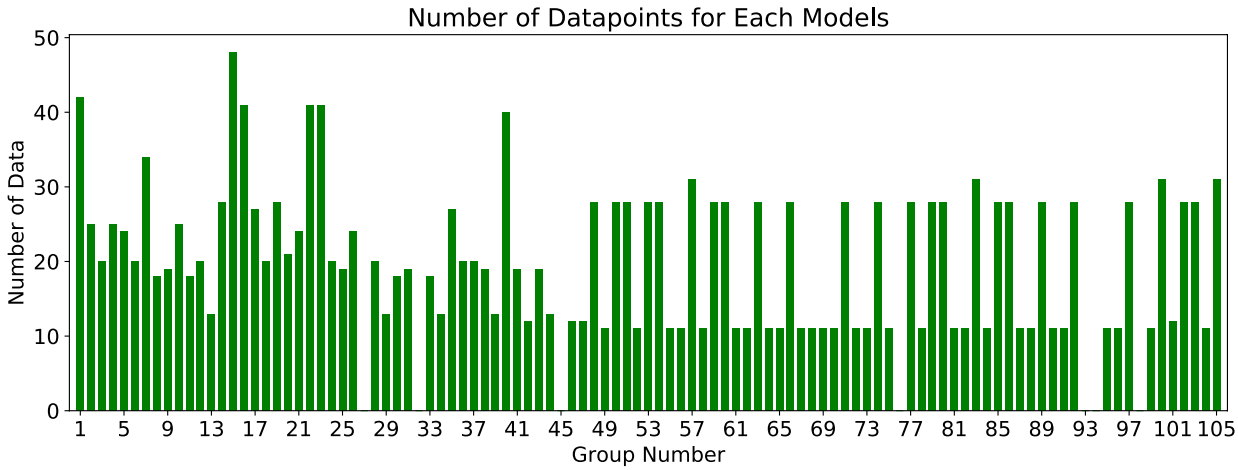

Figure 166. Number of data in each 105 combination groups for the EFA/Coarse dataset – Critical Shear Stress

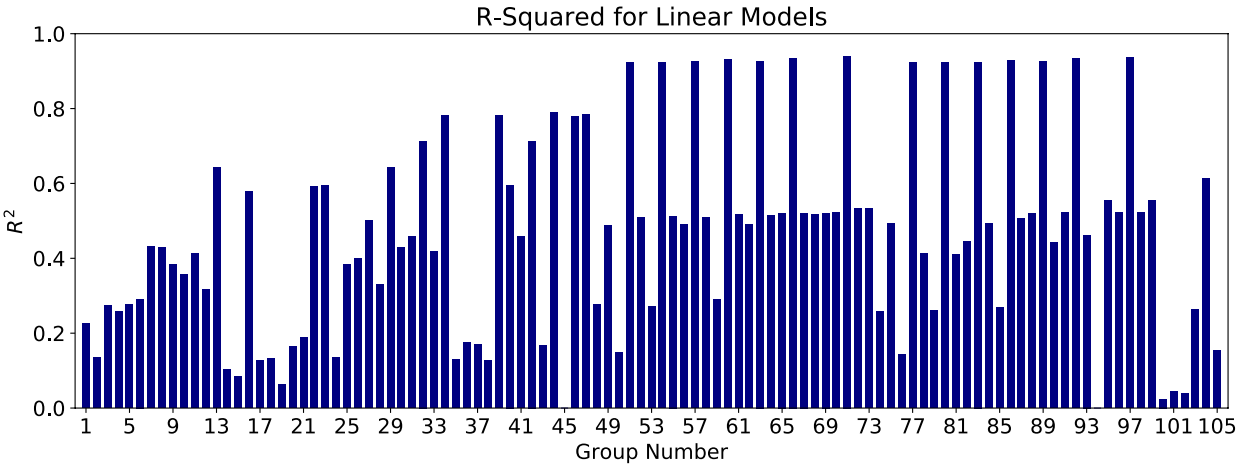

Figure 167. R^2 results for the "Linear Models" in EFA/Coarse dataset – Critical Shear Stress

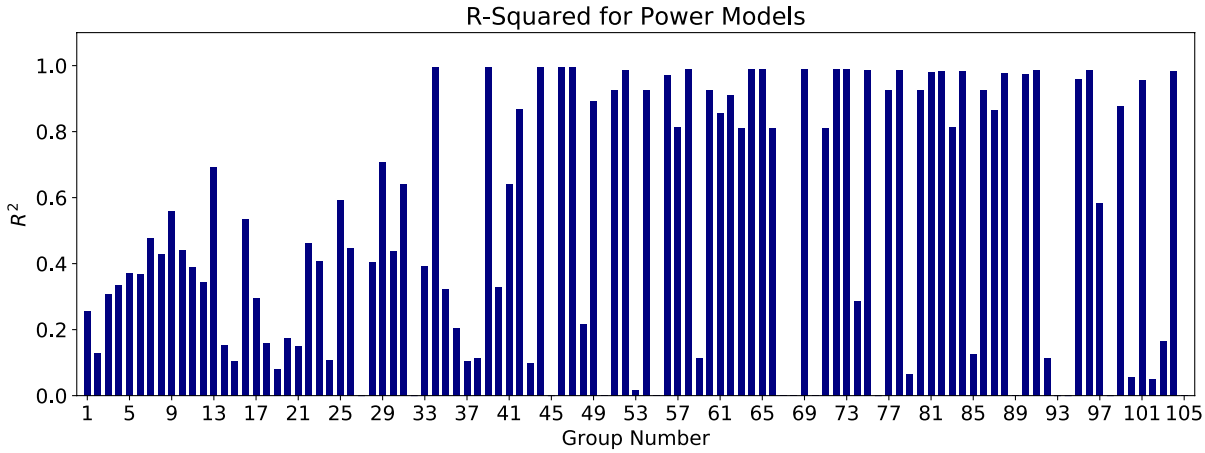

Figure 168. R^2 results for the "Power Models" in EFA/Coarse dataset – Critical Shear Stress

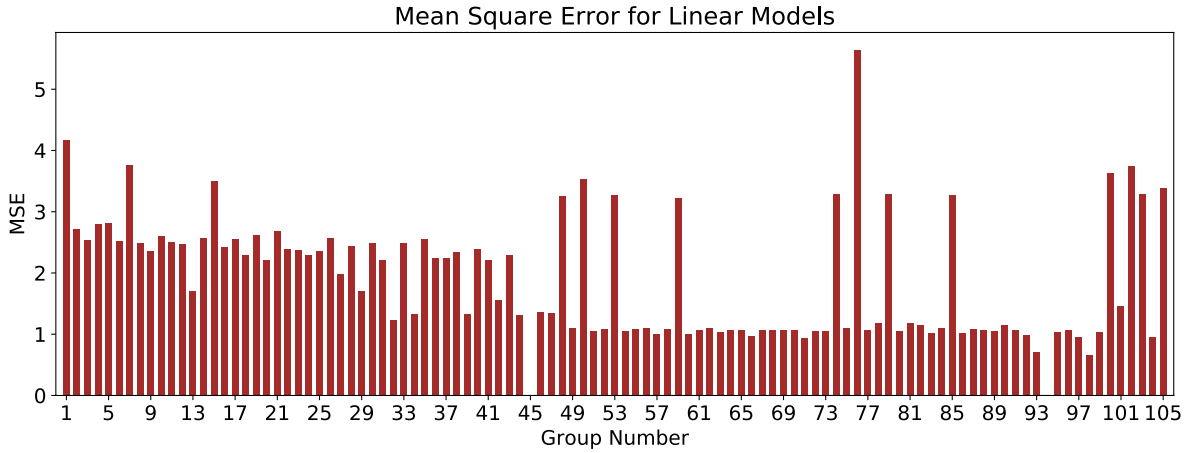

Figure 169. MSE results for "Linear Models" in EFA/Coarse dataset – Critical Shear Stress

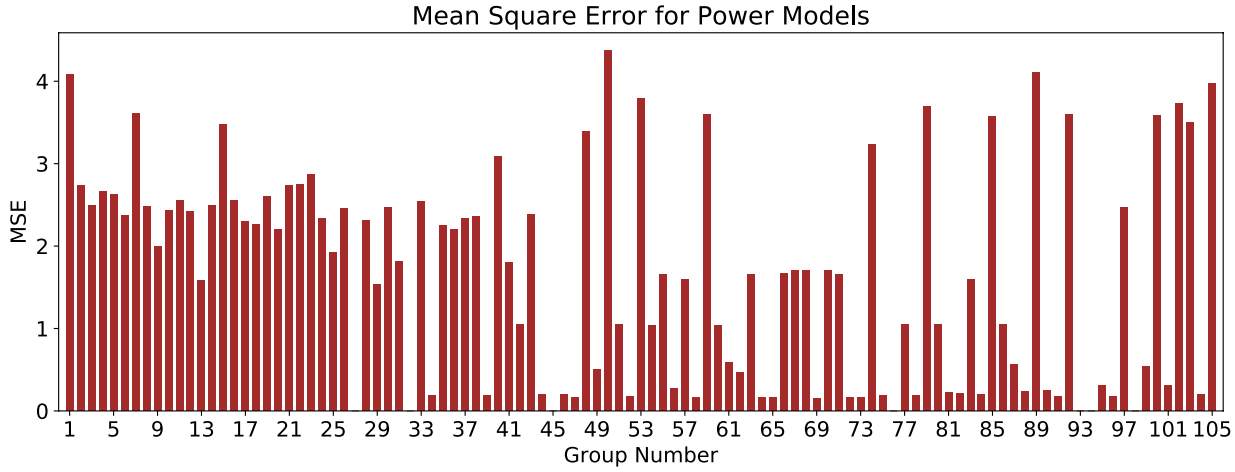

Figure 170. MSE results for "Power Models" in EFA/Coarse dataset – Critical Shear Stress

After passing through filters 1 and 2 (R^2 and MSE), "Linear" models associated with groups 51, 54, 57, 60, 63, 66, 71, 77, 80, 83, 86, 89, 92, and 97 were selected for further analyses. Also "Power" models associated with groups 34, 44, 46, 47, 51, 54, 56, 57, 58, 60, 64, 65, 66, 71, 77, 80, 83, 84, 86, 95, and 101 were selected for further analyses.

Filter 3, F-value/F-stat, was determined for each group mentioned above. Table 49 shows the results of the selected "Linear" models after meeting the requirements of the first three filters (R2, MSE, and F-value/F-stat). As shown in Table 49, all selected models perform satisfactorily in the cross-validation test. Table 50 also shows the results of the selected "Power" models after meeting the requirements of the first three filters. The best models that also have a good cross-validation score are highlighted in blue in both "Linear" and "Power" forms. Out of all the highlited correlation equations in Table 49 and Table 50, the Group 77 correlation equation in "Power" form was selected as the most promising equation. Figure 171 shows the plot of "POU vs. θ" for this model. The vertical axis in Figure 171 represent the probability that the predicted τ_c using the selected model is smaller than the actual τ_c, in percentage (with 0.3 Pa offset). In order to reach a 90% confidence that the predicted τ_c is smaller than the actual τ_c, the predicted value should be multiplied by 0.82.

Table 49. Selected "Linear" models for critical shear stress in the EFA/Coarse dataset

Group No.	Independent Variables	Model Expression	R^2	MSE	F-value/F-stat	Cross-Validation Score
51	C_c, γ, D50	$\tau_c = -0.016 \times C_c + 0.09 \times \gamma + 0.86 \times D50 - 1.12$	0.92	1.05	5.1	0.89
54	C_c, WC, D50	$\tau_c = -0.009 \times C_c - 0.03 \times WC + 0.82 \times D50 + 0.83$	0.92	1.06	5.1	0.89
57	PF, C_c, D50	$\tau_c = 0.015 \times PF - 0.01 \times C_c + 0.88 \times D50 + 0.05$	0.93	1.01	5.4	0.88
60	C_c, γ, WC, PF	$\tau_c - 0.023 \times C_c + 0.16 \times \gamma - 0.06 \times WC + 0.82 \times D50 - 1.6$	0.93	1.00	2.6	0.89
63	C_c, γ, PF, D50	$\tau_c = -0.015 \times C_c + 0.06 \times \gamma + 0.01 \times PF + 0.88 \times D50 - 0.89$	0.93	1.03	2.9	0.87
66	C_c, WC, PF, D50	$\tau_c = -0.01349 \times C_c - 0.06 \times WC + 0.03 \times PF + 0.85 \times D50 + 0.62$	0.93	0.98	2.9	0.88
71	C_c, γ, WC, PF, D50	$\tau_c = -0.024 \times C_c + 0.13 \times \gamma - 0.08 \times WC + 0.03 \times PF + 0.84 \times D50 - 1.38$	0.94	0.93	2.1	0.88
77	C_u, γ, D50	$\tau_c = 0.001 \times C_u + 0.06 \times \gamma + 0.86 \times D50 - 0.71$	0.92	1.06	5.1	0.9
80	C_u, WC, D50	$\tau_c = 0.001 \times C_u - 0.03 \times WC + 0.83 \times D50 + 0.72$	0.92	1.05	5.1	0.88
83	PF, C_u, D50	$\tau_c = 0.015 \times PF + 0.0007 \times C_u + 0.88 \times D50 + 0.02$	0.92	1.01	5.3	0.88
86	C_u, γ, WC, D50	$\tau_c = 0.001 \times C_u + 0.11 \times \gamma - 0.05 \times WC + 0.83 \times D50 - 1.03$	0.93	1.02	3.3	0.89
89	C_u, γ, PF, D50	$\tau_c = 0.00025 \times C_u + 0.04 \times \gamma + 0.01 \times PF + 0.88 \times D50 - 0.55$	0.93	1.05	3.3	0.86
92	C_u, WC, PF, D50	$\tau_c = -0.00037 \times C_u - 0.06 \times WC + 0.03 \times PF + 0.85 \times D50 + 0.56$	0.93	0.99	3.3	0.87
97	C_u, γ, WC, PF, D50	$\tau_c = -0.001 \times C_u + 0.09 \times \gamma - 0.07 \times WC + 0.03 \times PF + 0.85 \times D50 - 0.88$	0.94	0.96	2.4	0.86

Table 50. Selected "Power" models for critical shear stress in the EFA/Coarse dataset

Group No.	Independent Variables	Model Expression	R^2	MSE	F-value/F-stat	Cross-Validation Score
34	PI, VST, PF, D50	$(32400.5) \times PI^{-0.27} \times VST^{6.28} \times PF^{-19.79} \times D50^{-15.93}$	0.99	0.191	140	-15.44
44	PI, γ, VST, PF, D50	$(7.8 \times 10^{-5}) \times PI^{1.41} \times \gamma^{0.82} \times VST^{4.91} \times PF^{-15.57} \times D50^{-18.06}$	0.99	0.198	88	-1.4
46	PI, WC, VST, PF, D50	$(267267.2) \times PI^{-0.36} \times \gamma^{-0.21} \times VST^{6.24} \times PF^{-20.26} \times D50^{-16.14}$	0.99	0.197	70.5	0.08
47	PI, γ, WC, VST, PF, D50	$(35.65) \times PI^{-0.19} \times \gamma^{7.82} \times WC^{-2.91} \times VST^{2.36} \times PF^{-16.46} \times D50^{-14.05}$	0.99	0.169	56.1	0.09
51	C_c, γ, D50	$(2.32) \times C_c^{0.04} \times \gamma^{-0.13} \times D50^{0.77}$	0.93	1.045	36	0.98
52	C_c, WC, VST	$(1228385.72) \times C_c^{-0.31} \times WC^{-11.03} \times VST^{2.35}$	0.98	0.178	38.6	0.1
54	C_c, WC, D50	$(1.67) \times C_c^{0.05} \times WC^{-0.04} \times D50^{0.76}$	0.93	1.043	36.2	0.98
58	C_c, γ, WC, VST	$(0.22) \times C_c^{-0.55} \times \gamma^{5.95} \times WC^{-10.42} \times VST^{1.6}$	0.99	0.168	24.3	-0.5
60	C_c, γ, WC, D50	$(1.517) \times C_c^{0.06} \times \gamma^{0.04} \times WC^{-0.04} \times D50^{0.76}$	0.93	1.043	29.1	0.97
64	C_c, WC, VST, PF	$(1.09 \times 10^{-5}) \times C_c^{5.12} \times WC^{-20.76} \times VST^{-12.04} \times PF^{29.64}$	0.98	0.164	25.8	-1.5
77	C_u, γ, D50	$(1.58) \times C_u^{-0.04} \times \gamma^{0.02} \times D50^{0.77}$	0.93	1.044	36.1	0.99
78	C_u, WC, VST	$(257.02) \times C_u^{-1.73} \times WC^{-8.77} \times VST^{4.76}$	0.98	0.183	33.1	0.04
80	C_u, WC, D50	$(1.66) \times C_u^{-0.04} \times WC^{-0.01} \times D50^{0.78}$	0.93	1.044	36.1	0.98
86	C_u, γ, WC, D50	$(1.378) \times C_u^{-0.04} \times \gamma^{0.07} \times WC^{-0.01} \times D50^{0.78}$	0.93	1.044	29.1	0.96
88	C_u, γ, VST, D50	$(5.845 \times 10^{11}) \times C_u^{-3.07} \times \gamma^{-19.6} \times VST^{10.74} \times D50^{1.62}$	0.97	0.236	21	0.03
95	C_u, γ, WC, VST, D50	$(2.24 \times 10^{11}) \times C_u^{-2.31} \times \gamma^{-16.85} \times WC^{-0.48} \times VST^{8.48} \times D50^{1.18}$	0.96	0.307	19	-11.3
101	C_c, C_u, PI	$(2.555 \times 10^{13}) \times C_c^{-4.19} \times C_u^{22.94} \times PI^{-80.26}$	0.95	0.313	26.7	-0.44
104	C_c, C_u, VST	$(5.87 \times 10^{-13}) \times C_c^{-0.503} \times C_u^{-2.32} \times VST^{8.47}$	0.98	0.204	25.5	0.01

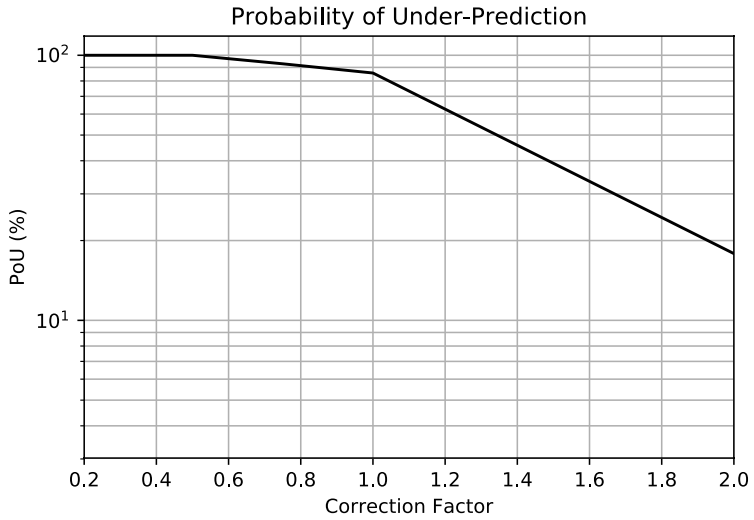

Figure 171. Plot of POU vs. correction factor for the Group 77 (Power) - τ_c in the EFA/Coarse dataset

JET Dataset

Similar approach was taken to select the best correlating equation for critical shear stress in the JET database. However, there are two important notes to notice about the JET database:

1) The JET was primarily performed on the finer soils (D_{50} < 0.3 mm), and therefore, the number of data points in the JET/Coarse dataset are substantially low compared to the JET/Fine dataset. Figure 133 and Figure 134 show the number of data points in each of all the 135 combination groups in the JET/Global dataset and each of the 105 combination groups in the JET/Coarse dataset, respectively.
2) The R^2 values for the JET/Global dataset (D50 < 0.3 mm), although low themselves, are still better than the R^2 values for the JET/Fine dataset. Therefore, the regression results for the JET/Global dataset are presented as the best models.

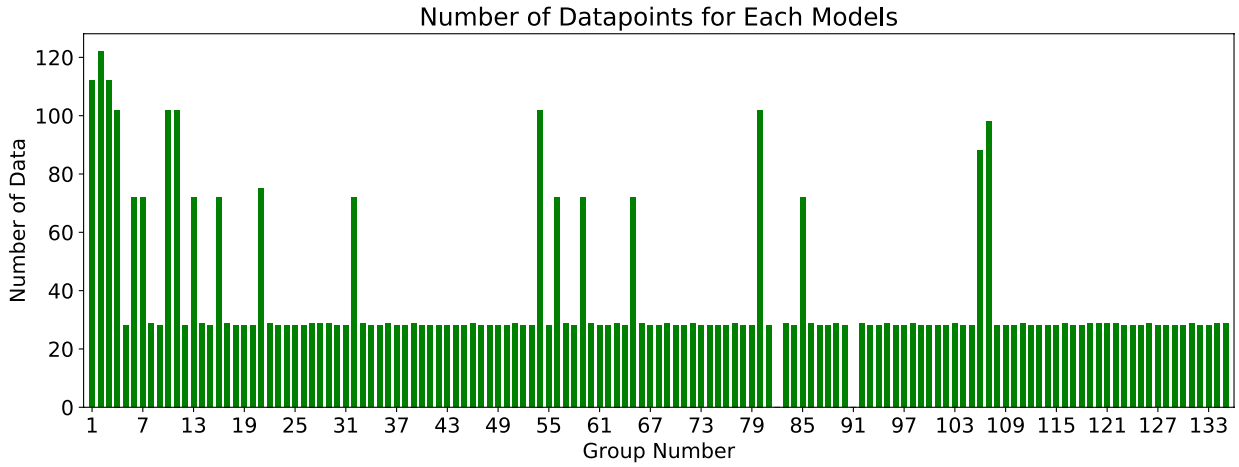

Figure 172. Number of data in each 135 combination groups for the JET/Global dataset – Critical Shear Stress

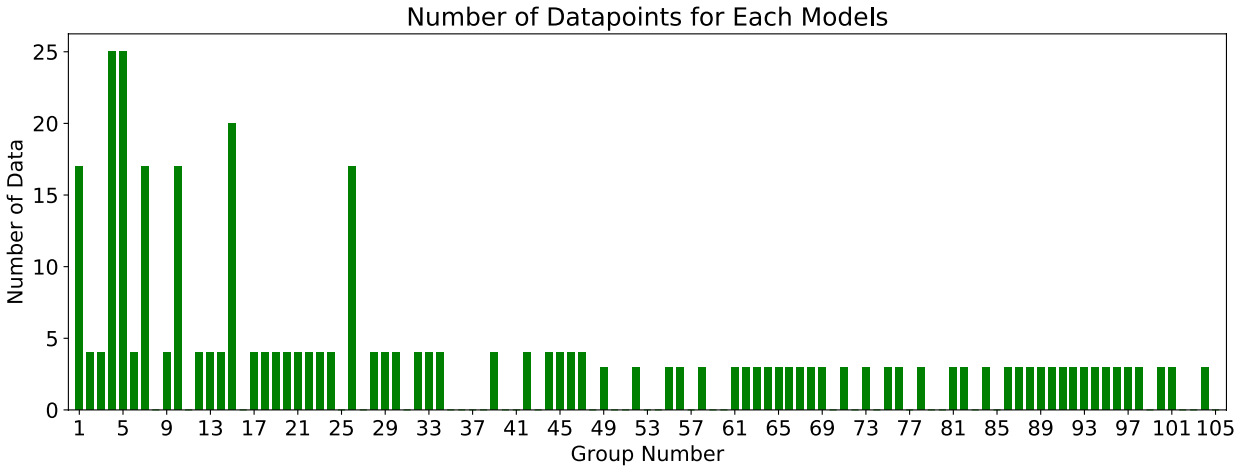

Figure 173. Number of data in each 105 combination groups for the JET/Coarse dataset – Critical Shear Stress

Figure 174 and Figure 175 show the results of R^2 for each combination group in the JET/Global dataset, for the "Linear Model" and "Power Model", respectively. Both plots show relatively poor R^2 for the JET/Global dataset. One of the major reasons behind the poor relationships for critical shear stress in the JET database is the variety of methods to interpret the raw data and obtain the critical shear stress. Section 4.3.1.4 of this report discussed these different methods. More on the JET issues is discussed in Chapter 8.

Figure 176 and Figure 177 show the values of MSE for the "Linear" and "Power" models, respectively.

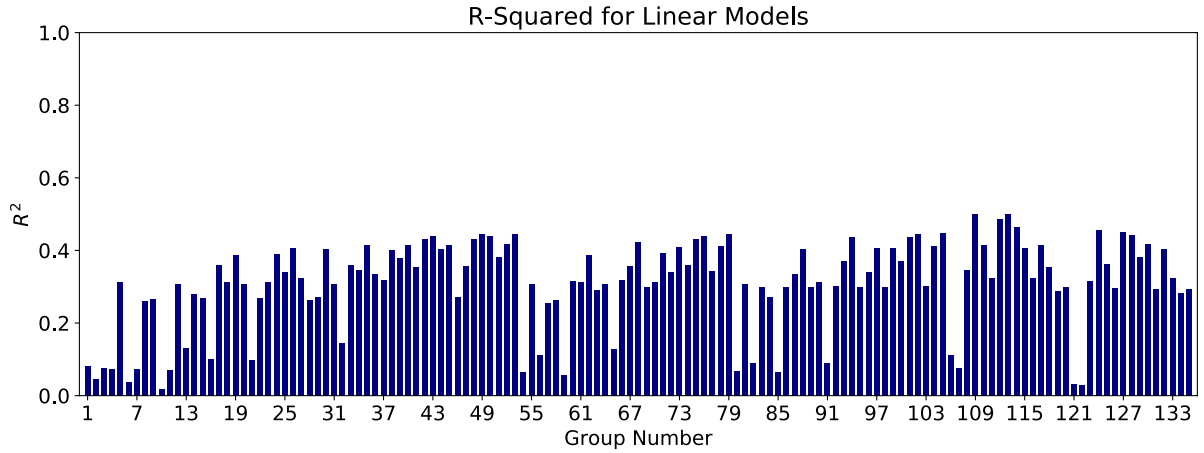

Figure 174. R^2 results for the "Linear Models" in JET/Global dataset – Critical Shear Stress

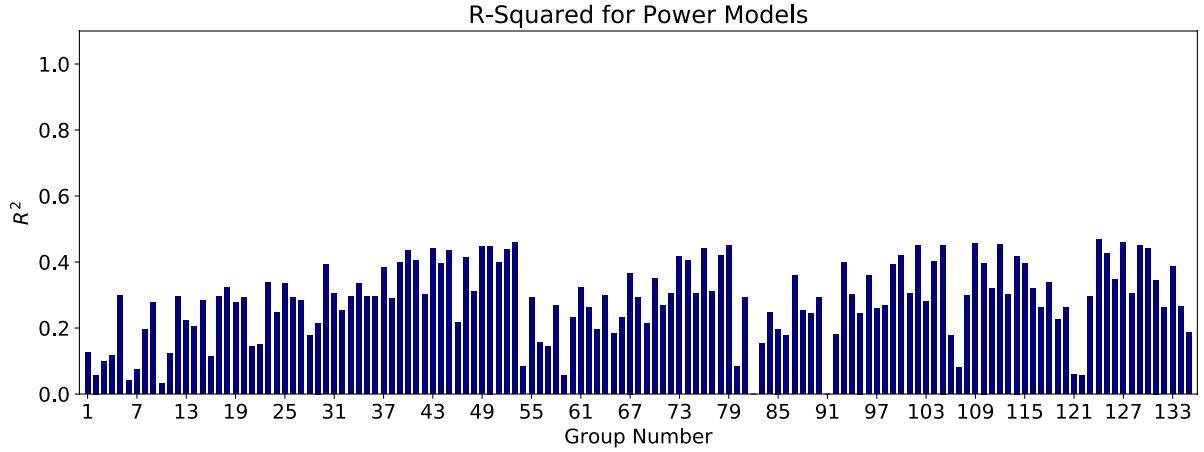

Figure 175. R^2 results for the "Power Models" in EFA/Coarse dataset – Critical Shear Stress

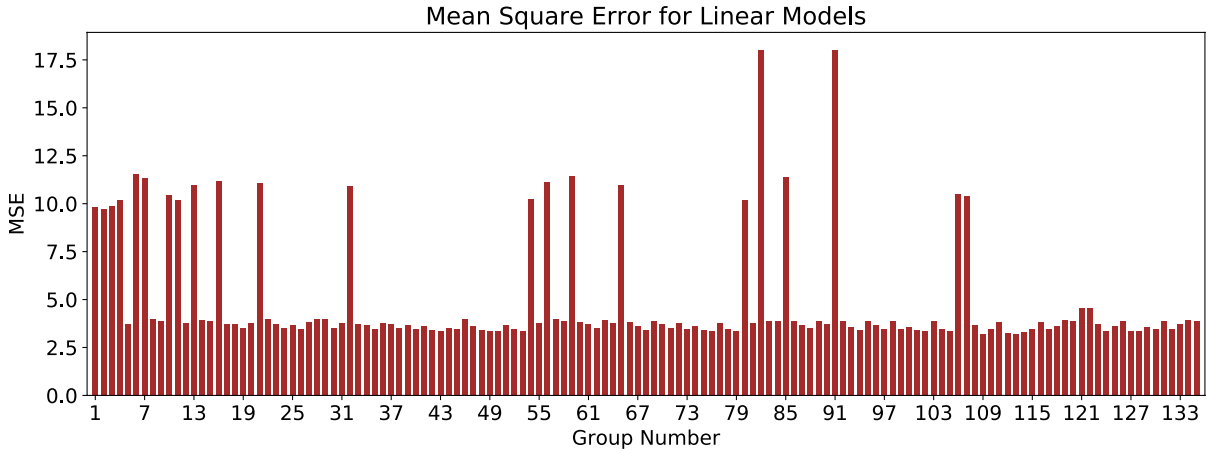

Figure 176. MSE results for "Linear Models" in JET/Global dataset – Critical Shear Stress

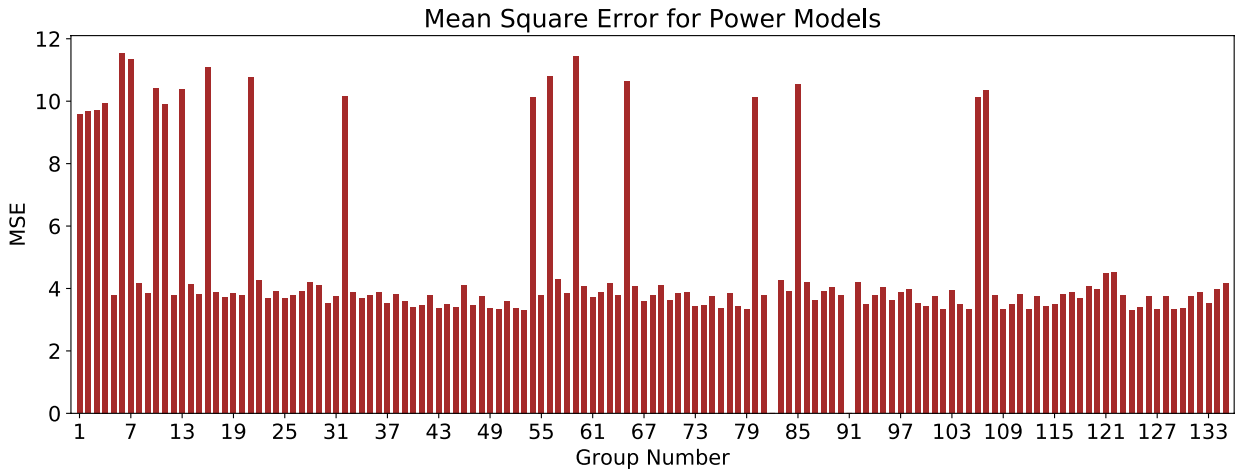

Figure 177. MSE results for "Power Models" in JET/Global dataset – Critical Shear Stress

After passing through filters 1 and 2 (R^2 and MSE), "Linear" models associated with groups 49, 76, 109, 112, and 113 in the JET/Global dataset were selected for further analyses. Also "Power" models associated with groups 53, 79, 109, and 124 in the JET/Global dataset were selected for further analyses.

Filter 3, F-value/F-stat, was determined for each group mentioned above. Table 51 shows the results of the selected "Linear" models after meeting the requirements of the first three filters (R2, MSE, and F-value/F-stat). As shown in Table 51, almost none of the selected models perform well in the cross-validation test. Table 52 also shows the results of the selected "Power" models after meeting the requirements of the first three filters. The best models that also have a good cross-validation score are highlighted in blue in both "Linear" and "Power" forms. Out of all the correlation equations in Table 51 and Table 52, the Group 113 correlation equation in "Linear" form was selected as the most promising equation. Figure 178 shows the plot of "POU vs. θ" for this model. The vertical axis in Figure 178 represent the probability that the predicted τ_c using the selected model is smaller than the actual τ_c, in percentage (with 1 Pa offset). In order to reach a

90% confidence that the predicted τ_c is smaller than the actual τ_c, the predicted value should be multiplied by 0.6.

Table 51. Selected "Linear" models for critical shear stress in the JET/Global dataset

Group No.	Independent Variables	Model Expression	R^2	MSE	F-value/F-stat	Cross-Validation Score
49	γ, WC, S_u, PF, D50	$\tau_c = -0.769 \times \gamma - 0.08 \times WC + 0.04 \times S_u - 0.07 \times PF - 46.05 \times D50 + 28.36$ $for\ D50 < 0.3\ mm$	0.44	3.36	1.318	0.05
76	LL, γ, S_u, PF, D50	$\tau_c = -0.011 \times LL - 0.71 \times \gamma + 0.04 \times S_u - 0.08 \times PF - 46.8 \times D50 + 26.56$ $for\ D50 < 0.3\ mm$	0.44	3.38	1.299	0.04
109	PC, γ, WC, S_u, PF, D50	$\tau_c = -0.272 \times PC - 1.28 \times \gamma + 0.22 \times WC + 0.07 \times S_u + 0.03 \times PF - 31.65 \times D50 + 31.03$ $for\ D50 < 0.3\ mm$	0.50	3.20	1.365	-0.02
112	PC, γ, S_u, PF, D50	$\tau_c = -0.176 \times PC - 1.24 \times \gamma + 0.06 \times S_u + 0.02 \times PF - 34.03 \times D50 + 33.38$ $for\ D50 < 0.3\ mm$	0.49	3.24	1.563	0.08
113	PC, γ, WC, S_u, D50	$\tau_c = -0.248 \times PC - 1.23 \times \gamma + 0.21 \times WC + 0.07 \times S_u - 36.89 \times D50 + 31.82$ $for\ D50 < 0.3\ mm$	0.50	3.20	1.647	0.1

Table 52. Selected "Power" models for critical shear stress in the JET/Global dataset

Group No.	Independent Variables	Model Expression	R^2	MSE	F-value/F-stat	Cross-Validation Score
53	PI, γ, WC, S_u, PF, D50	$\tau_c = (2.697) \times PI^{0.13} \times \gamma^{2.02} \times WC^{-0.43} \times S_u^{0.43} \times PF^{1.69} \times D50^{.27}$ $for\ D50 < 0.3\ mm$	0.46	3.32	7.155	-1.5
79	LL, γ, WC, S_u, PF, D50	$\tau_c = (7.412) \times LL^{0.14} \times \gamma^{-2.43} \times WC^{-0.38} \times S_u^{0.47} \times PF^{1.64} \times D50^{0.27}$ $for\ D50 < 0.3\ mm$	0.45	3.35	7.005	-0.69
109	PC, γ, WC, S_u, PF, D50	$\tau_c = (76.49) \times PC^{-0.26} \times \gamma^{-3.17} \times WC^{-0.2} \times S_u^{0.56} \times PF^{1.68} \times D50^{0.23}$ $for\ D50 < 0.3\ mm$	0.46	3.33	7.089	-1.62
124	γ, A, WC, S_u, PF, D50	$\tau_c = (3.86) \times \gamma^{2.1} \times A^{0.19} \times WC^{-0.41} \times S_u^{0.44} \times PF^{1.73} \times D50^{1.26}$ $for\ D50 < 0.3\ mm$	0.47	3.30	6.891	-0.77

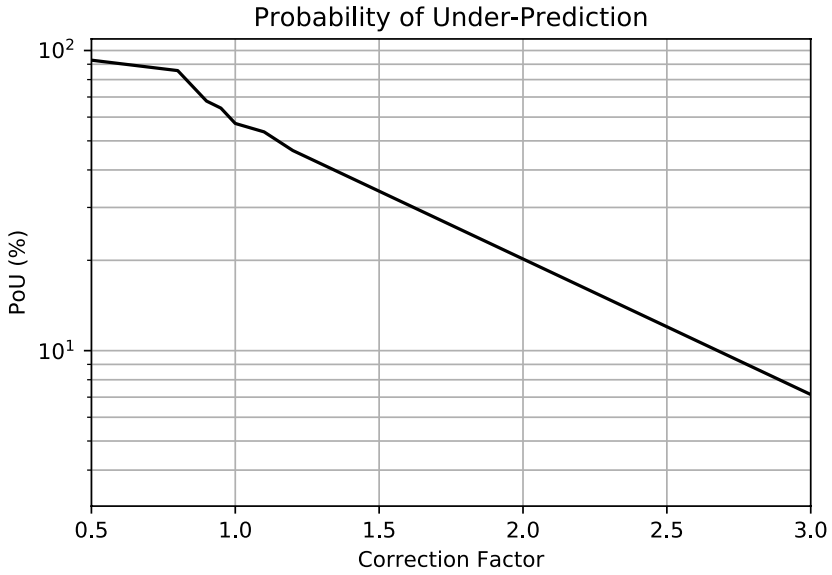

Figure 178. Plot of POU vs. correction factor for the Group 113 (Linear) - τ_c in the JET/Global dataset

HET Dataset

Similar approach was taken to select the best correlating equation for critical shear stress in the HET database. On the HET database, there are also two important observations to notice:

1) The HET was primarily performed on the finer soils (D_{50} < 0.3 mm), and therefore, the number of data points in the HET/Coarse dataset are substantially low compared to the

JET/Fine dataset. In fact, many combination groups on the HET/Coarse database have zero data points. Figure 179 and Figure 180 show the number of data points in each of all the 135 combination groups in the HET/Global dataset and each of the 105 combination groups in the HET/Coarse dataset, respectively.

2) The R^2 values for the HET/Global dataset (D50 < 0.3 mm) are significantly better than the R^2 values for the HET/Coarse and HET/Fine dataset. Therefore, the regression results for the HET/Global dataset are presented as the best models.

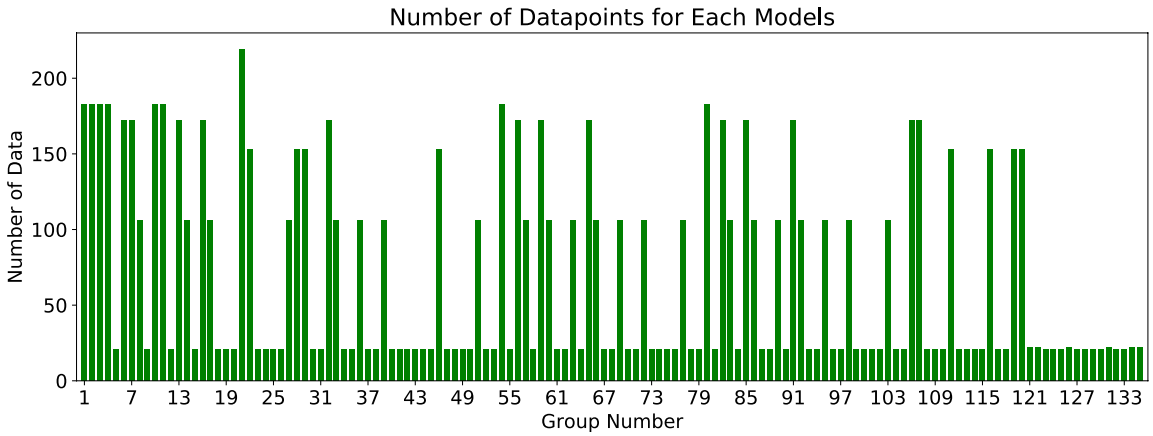

Figure 179. Number of data in each 135 combination groups for the HET/Global dataset – Critical Shear Stress

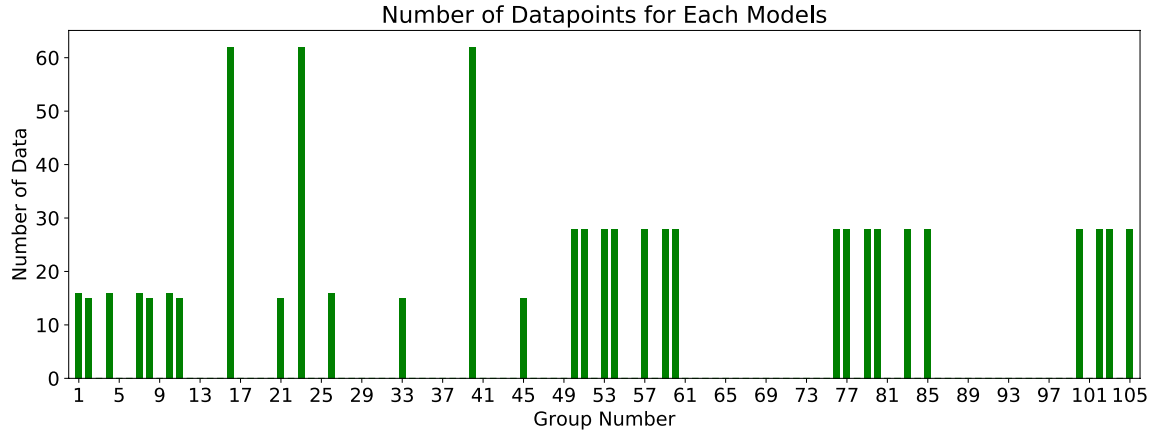

Figure 180. Number of data in each 105 combination groups for the HET/Coarse dataset – Critical Shear Stress

Figure 181 and Figure 182 show the results of R^2 for each combination group in the HET/Global dataset, for the "Linear Model" and "Power Model", respectively. Both plots show that the best R^2 for the HET/Global dataset are around 0.60 to 0.65. One of the major reasons behind the poor relationships for critical shear stress in the JET database is that the method used to calculate the erodibility parameters in the HET includes many crude judgements. More on the HET issues is discussed in Chapter 8. Figure 183 and Figure 184 show the values of MSE for the "Linear" and "Power" models, respectively.

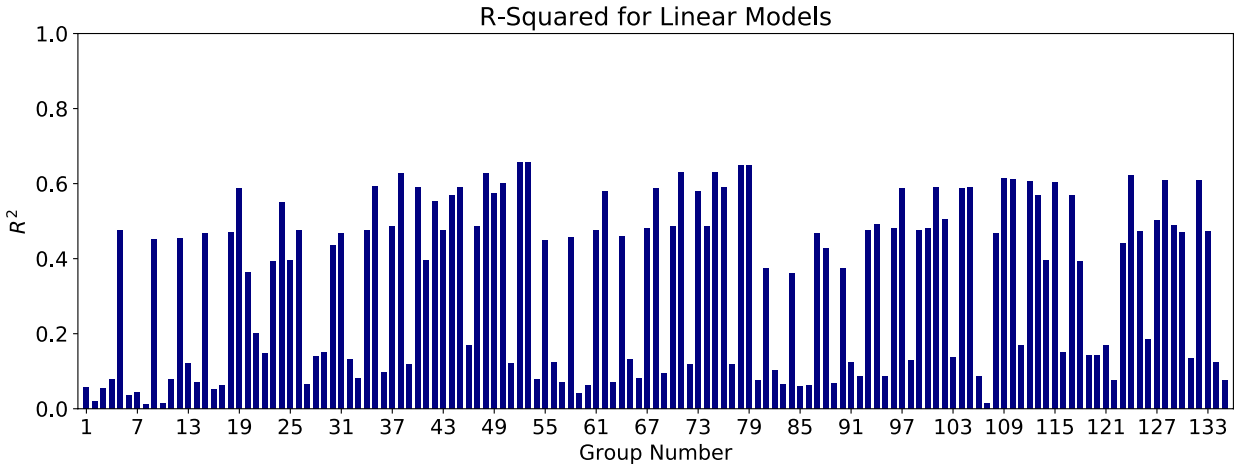

Figure 181. R^2 results for the "Linear Models" in HET/Global dataset – Critical Shear Stress

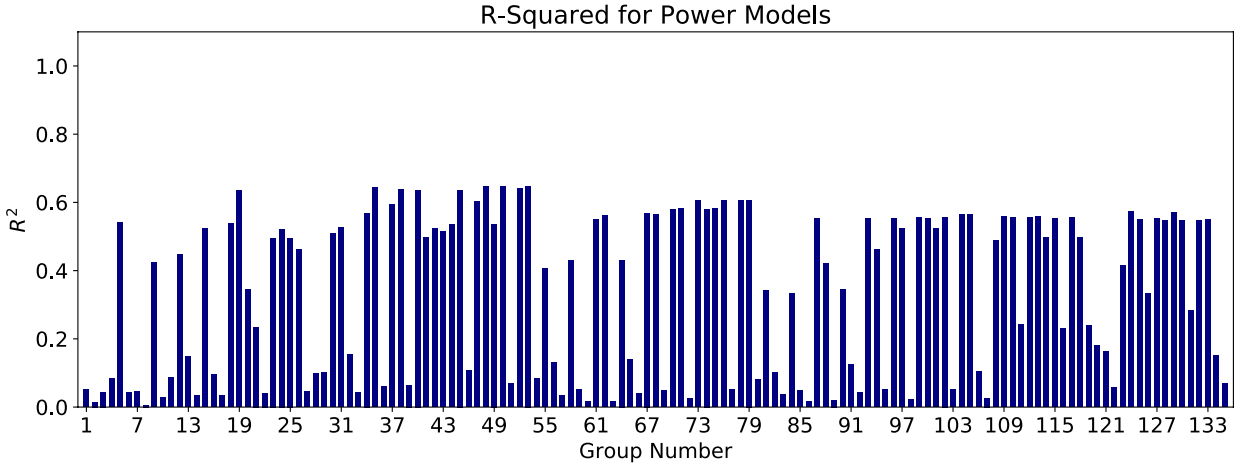

Figure 182. R^2 results for the "Power Models" in HET/Global dataset – Critical Shear Stress

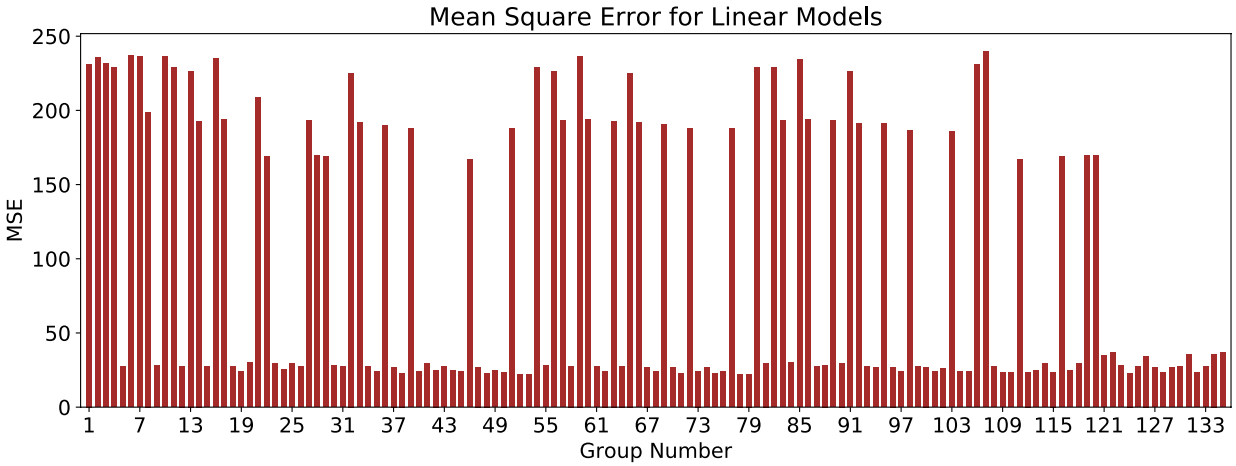

Figure 183. MSE results for "Linear Models" in HET/Global dataset – Critical Shear Stress

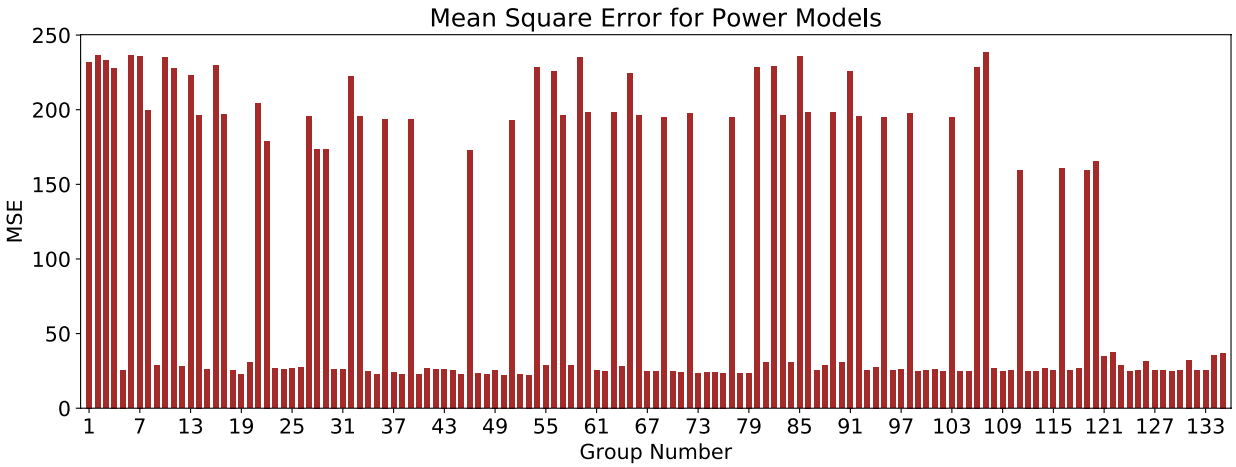

Figure 184. MSE results for "Power Models" in HET/Global dataset – Critical Shear Stress

After passing through filters 1 and 2 (R^2 and MSE), "Linear" models associated with groups 38, 48, 49, 52, 53, 71, 78, 79, 124, and 128 in the HET/Global dataset were selected for further analyses. Also "Power" models associated with groups 19, 35, 38, 40, 48, 50, and 52 in the HET/Global dataset were selected for further analyses.

Filter 3, F-value/F-stat, was determined for each group mentioned above. Table 53 shows the results of the selected "Linear" models after meeting the requirements of the first three filters (R^2, MSE, and F-value/F-stat). As shown in Table 53, almost none of the selected models perform

well in the cross-validation test. Table 54 also shows the results of the selected "Power" models after meeting the requirements of the first three filters. The best models that also have a good cross-validation score are highlighted in blue in both "Linear" and "Power" forms. Out of all the correlation equations in Table 53 and Table 54, the Group 19 correlation equation in "Power" form was selected as the most promising equation. Figure 185 shows the plot of "POU vs. θ" for this model. The vertical axis in Figure 185 represent the probability that the predicted τ_c using the selected model is smaller than the actual τ_c, in percentage (with 0.4 Pa offset). In order to reach a 90% confidence that the predicted τ_c is smaller than the actual τ_c, the predicted value should be multiplied by 0.6.

Table 53. Selected "Linear" models for critical shear stress in the HET/Global dataset

Group No.	Independent Variables	Model Expression	R^2	MSE	F-value/F-stat	Cross-Validation Score
38	PI, WC, S_u, D50	$\tau_c = 0.446 \times +3.48 \times WC + 0.82 \times S_u + 2153.5 \times D50 - 98.12$	0.63	23.0	1.945	0.01
48	PI, γ, WC, S_u, D50	$\tau_c = 0.45 \times PI - 0.61 \times \gamma + 3.6 \times WC + 0.83 \times S_u + 2161.4 \times D50 - 89.22$	0.63	23.0	1.741	-0.09
49	γ, WC, S_u, PF, D50	$\tau_c = 3.66 \times \gamma + 6.55 \times WC + 0.98 \times S_u + 0.61 \times PF + 3053.2 \times D50 - 281.53$	0.58	24.5	1.397	-0.05
52	PI, WC, S_u, PF, D50	$\tau_c = 0.49 \times PI + 5.26 \times WC + 0.92 \times S_u + 0.7 \times PF + 2958 \times D50 - 201.85$	0.66	22.0	1.977	0.1
53	PI, γ, WC, S_u, PF, D50	$\tau_c = 0.479 \times PI + 1.43 \times \gamma + 5.1 \times WC + 0.91 \times S_u + 0.73 \times PF + 2979.7 \times D50 - 227.85$	0.66	22.0	1.574	-0.13
71	LL, WC, S_u, D50	$\tau_c = 0.416 \times LL + 3.86 \times WC + 0.85 \times S_u + 2216.6 \times D50 - 113$	0.63	22.9	2.257	0.11
78	LL, WC, S_u, PF, D50	$\tau_c = 0.423 \times LL + 5.4 \times WC + 0.93 \times S_u + 0.55 \times PF + 2870.5 \times D50 - 198$	0.65	22.3	1.905	0.07
79	LL, γ, WC, S_u, PF, D50	$\tau_c = 0.414 \times LL + 1.63 \times \gamma + 5.19 \times WC + 0.91 \times S_u + 0.6 \times PF + 2897.1 \times D50 - 227.7$	0.65	22.3	1.519	0.01
124	γ, A, WC, S_u, PF, D50	$\tau_c = 2.1 \times \gamma + 8.71 \times A + 7.3 \times WC + 1.03 \times S_u + 0.48 \times PF + 2808.5 \times D50 - 265$	0.63	23.1	1.353	-0.6
128	D50, γ, WC, S_u, A	$\tau_c = 2257.2 \times D50 + 0.57 \times \gamma + 6.34 \times WC + 0.99 \times S_u + 9.34 \times A - 171.52$	0.61	23.5	1.616	0.06

Table 54. Selected "Power" models for critical shear stress in the HET/Global dataset

Group No.	Independent Variables	Model Expression	R^2	MSE	F-value/F-stat	Cross-Validation Score
19	PI, S_u, D50	$\tau_c = (25.07) \times PI^{0.27} \times S_u^{0.55} \times D50^{0.5}$	0.64	22.7	16.049	0.43
35	PI, γ, S_u, D50	$\tau_c = (495.9) \times PI^{0.32} \times \gamma^{-1.1} \times S_u^{0.57} \times D50^{0.49}$	0.65	22.4	12.907	-0.47
38	PI, WC, S_u, D50	$\tau_c = (54.04) \times PI^{0.31} \times WC^{-0.28} \times S_u^{0.5} \times D50^{0.47}$	0.64	22.6	12.650	-0.1
40	PI, S_u, PF, D50	$\tau_c = (38.24) \times PI^{0.26} \times S_u^{0.55} \times PF^{-0.11} \times D50^{0.48}$	0.64	22.7	12.580	-0.19
48	PI, γ, WC, S_u, D50	$\tau_c = (562.6) \times PI^{0.33} \times \gamma^{-1.01} \times WC^{-0.13} \times S_u^{0.54} \times D50^{0.47}$	0.65	22.4	10.322	-0.14
50	PI, γ, S_u, PF, D50	$\tau_c = (1430.36) \times PI^{0.3} \times \gamma^{-1.2} \times S_u^{0.56} \times PF^{-0.21} \times D50^{0.44}$	0.65	22.4	10.366	-0.48
52	PI, WC, S_u, PF, D50	$\tau_c = (209.5) \times PI^{0.3} \times WC^{-0.41} \times S_u^{0.46} \times PF^{-0.26} \times D50^{0.41}$	0.64	22.6	10.176	-0.41
53	PI, γ, WC, S_u, PF, D50	$\tau_c = (2491.8) \times PI^{0.32} \times \gamma^{-1.04} \times WC^{-0.26} \times S_u^{0.5} \times PF^{-0.28} \times D50^{0.4}$	0.65	22.3	8.410	-0.47

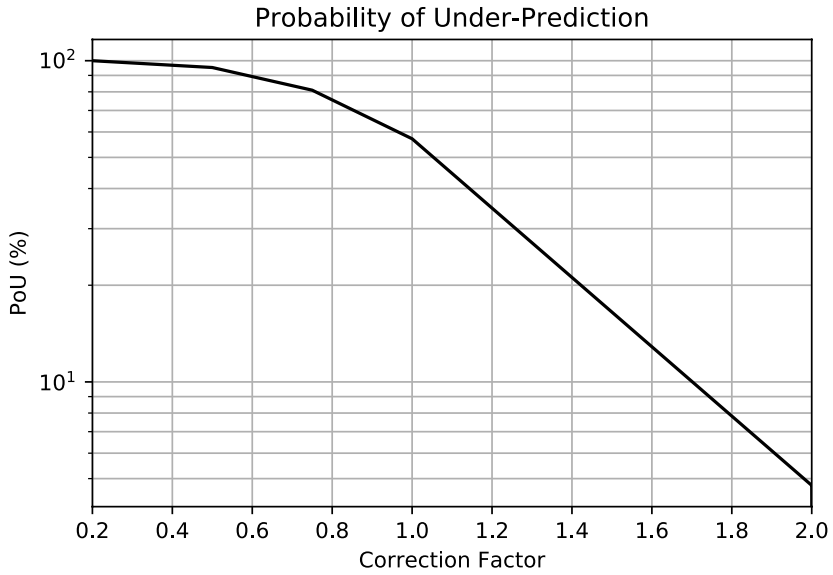

Figure 185. Plot of POU vs. correction factor for the Group 19 (Power) - τ_c in the HET/Global dataset

7.3.4.2.Critical Velocity (v_c)

The same four-filter process discussed in Section 7.3.3 is implemented in this section to obtain the best models for critical velocity. First observation was that among the three erosion tests studied in this Chapter (EFA, JET, HET), only the EFA test has v_c or critical velocity as one of its

outputs. In other words, results of JET and HET consist of only three erodibility parameters (i.e. τ_c, E_τ, and EC) in contrary with the EFA results which include all five erodibility parameters (i.e. τ_c, v_c, E_τ, E_v, and EC). Therefore, the study of regression analysis for critical velocity is limited to only the EFA dataset.

EFA Dataset

Similar to the case of critical shear stress, it was observed that dividing the EFA/Global dataset into the EFA/Fine and the EFA/Coarse datasets would significantly improve the regression results. Figure 186 shows the number of data points in each of all the 135 combination groups in the EFA/Fine dataset. Also, Figure 187 and Figure 188 show the results of R^2 for each combination group, for the "Linear Model" and "Power Model", respectively.

R^2 values of groups 109 to 135 are generally higher than the rest for both "Linear" and "Power" models. Figure 189 and Figure 190 also show the results of the MSE for each of the 135 combination groups in the EFA/Fine dataset, for "Linear" and "Power" models, respectively.

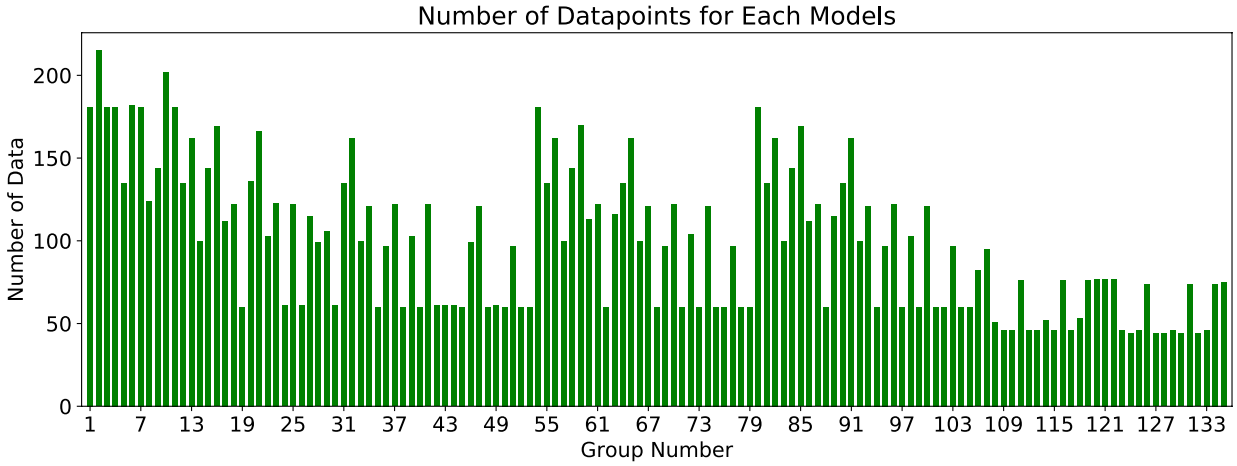

Figure 186. Number of data in each 135 combination groups for the EFA/Fine dataset – Critical Velocity

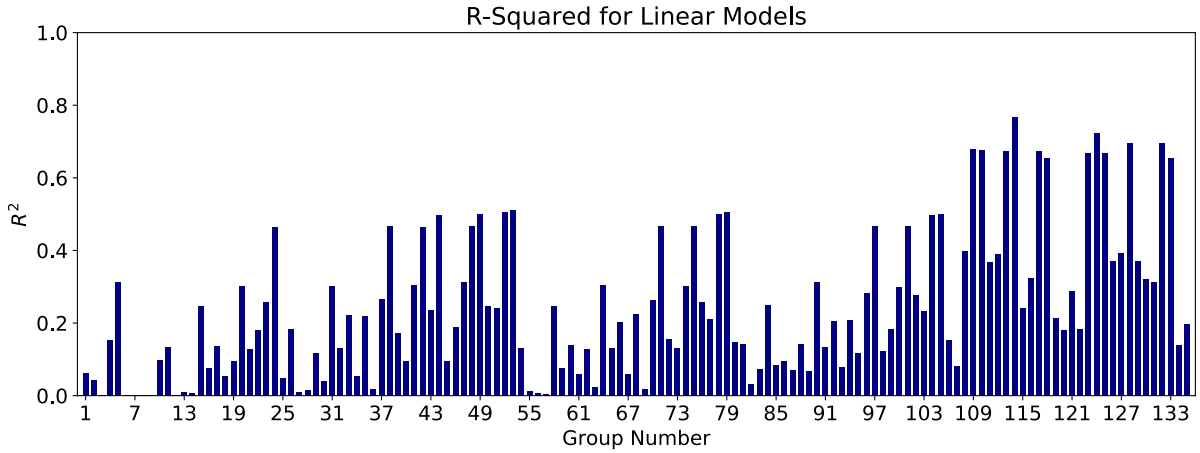

Figure 187. R^2 results for the "Linear Models" in EFA/Fine dataset – Critical Velocity

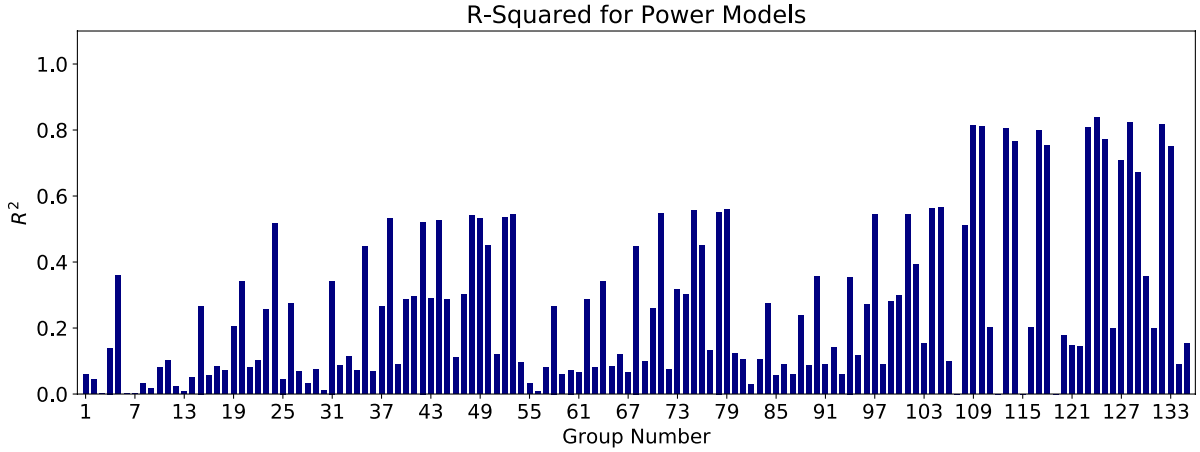

Figure 188. R^2 results for the "Power Models" in EFA/Fine dataset – Critical Velocity

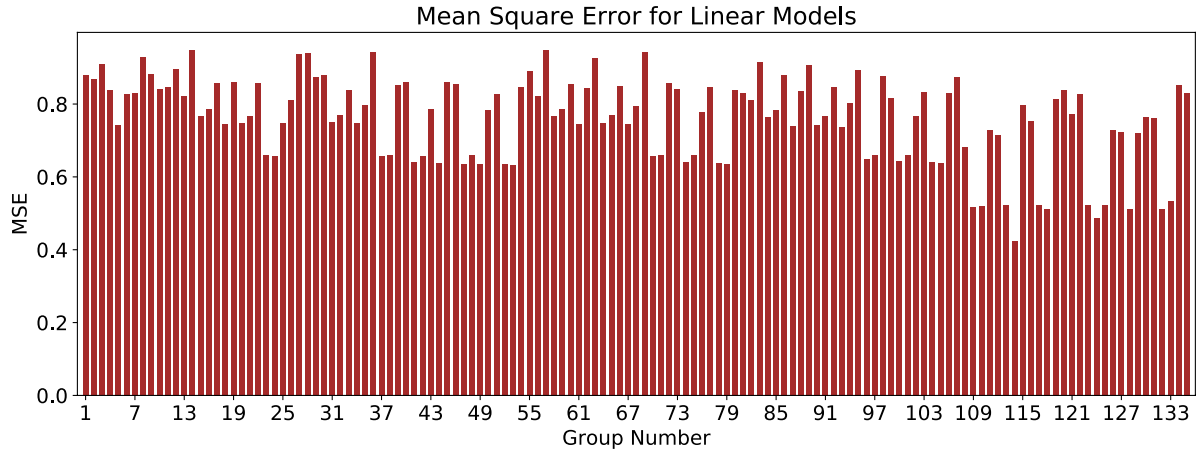

Figure 189. MSE results for "Linear Models" in EFA/Fine dataset – Critical Velocity

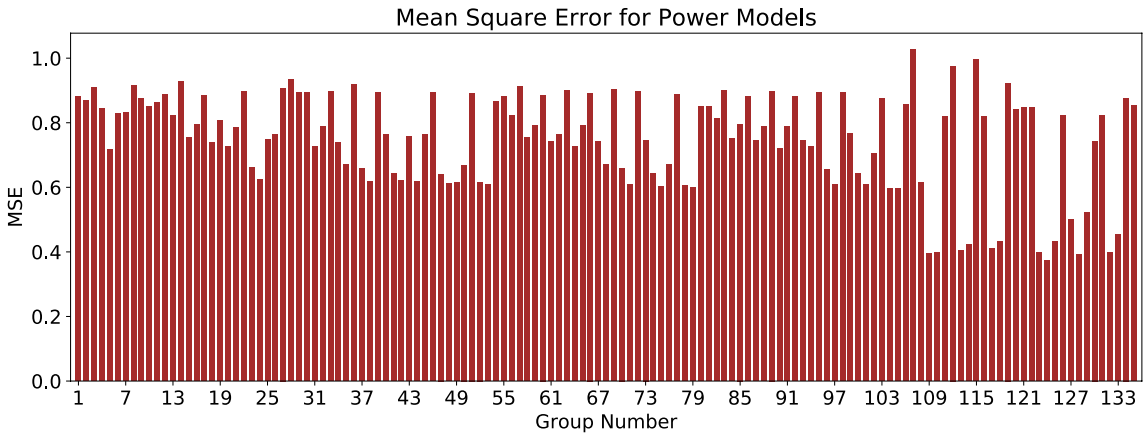

Figure 190. MSE results for "Power Models" in EFA/Fine dataset – Critical Velocity

After passing through filters 1 and 2 (R^2 and MSE), "Linear" models associated with groups 114, 124, 128, and 132 in the EFA/Fine dataset were selected for further analyses. Also "Power" models associated with groups 109, 110, 113, 114, 117, 118, 123, 124, 125, 128, 132, and 133 in the EFA/Fine dataset were selected for further analyses.

Filter 3, F-value/F-stat, was determined for each group mentioned above. Table 55 shows the results of the selected "Linear" models after meeting the requirements of the first three filters (R^2, MSE, and F-value/F-stat). As shown in Table 55, all four selected models perform acceptably in the cross-validation test. Table 56 also shows the results of the selected "Power" models after meeting the requirements of the first three filters. The best models that also have the best cross-validation scores are highlighted in blue in both "Linear" and "Power" forms. Out of all the correlation equations in Table 55 and Table 56, the Group 117 correlation equation in "Power" form was selected as the most promising equation. Figure 191 shows the plot of "POU vs. θ" for this model. The vertical axis in Figure 191 represent the probability that the predicted v_c using the selected model is smaller than the actual v_c, in percentage (with 0.2 m/s offset). In order to reach a 90% confidence that the predicted v_c is smaller than the actual v_c, the predicted value should be multiplied by 0.8.

Table 55. Selected "Linear" models for critical velocity in the EFA/Fine dataset

Group No.	Independent Variables	Model Expression	R^2	MSE	F-value/F-stat	Cross-Validation Score
114	PC, γ, WC, S_u, PF	$v_c = 0.012 \times PC - 0.038 \times \gamma + 0.041 \times WC \pm 0.0042 \times S_u - 0.008 \times PF + 0.328$	0.77	0.42	21.5	0.58
124	γ, A, WC, S_u, PF, D50	$v_c = -0.075 \times \gamma - (0.171 \times A + 0.05 \times WC + 0.0042 \times S_u - 0.02 \times PF - 11.33 \times D50 + 2.41$	0.72	0.49	16.6	0.64
128	D50, γ, WC, S_u, A	$v_c = -2.561 \times D50 - 0.022 \times \gamma + 0.051 \times WC + 0.005 \times S_u - 0.146 \times A - 0.384$	0.69	0.51	14.9	0.62
132	A, WC, S_u, D50	$v_c = -0.142 \times A + 0.051 \times WC + 0.004 \times S_u - 2.674 \times D50 - 0.784$	0.69	0.51	15.07	0.62

Table 56. Selected "Power" models for critical velocity in the EFA/Fine dataset

Group No.	Independent Variables	Model Expression	R^2	MSE	F-value/F-stat	Cross-Validation Score
109	PC, γ, WC, S_u, PF, D50	$v_c = (40.218) \times PC^{0.12} \times \gamma^{-2.23} \times WC^{1.66} \times S_u^{0.48} \times PF^{-1.57} \times D50^{-0.33}$	0.81	0.39	21.16	0.87
110	PC, WC, S_u, PF, D50	$v_c = (0.013) \times PC^{0.13} \times WC^{2.13} \times S_u^{0.51} \times PF^{-1.62} \times D50^{-0.36}$	0.81	0.4	23.74	0.87
113	PC, γ, WC, S_u, D50	$v_c = (0.1085) \times PC^{0.19} \times \gamma^{-2.3} \times WC^{1.6} \times S_u^{0.49} \times D50^{-0.12}$	0.8	0.41	22.92	0.81
114	PC, γ, WC, S_u, PF	$v_c = (2.699) \times PC^{0.39} \times \gamma^{-2.4} \times WC^{1.54} \times S_u^{0.4} \times PF^{-0.51}$	0.77	0.42	23.23	0.83
117	PC, WC, S_u, D50	$v_c = (2.518 \times 10^{-5}) \times PC^{0.2} \times WC^{2.06} \times S_u^{0.51} \times D50^{-0.13}$	0.80	0.41	26.05	0.80
118	PC, WC, S_u, PF	$v_c = (1.8 \times 10^{-4}) \times PC^{0.4} \times WC^{2.01} \times S_u^{0.45} \times PF^{-0.31}$	0.75	0.43	25.80	0.77
123	A, PL, γ, WC, S_u	$v_c = (0.00875) \times A^{-0.24} \times PL^{1.11} \times \gamma^{-2.07} \times WC^{1.38} \times S_u^{0.58}$	0.81	0.40	21.56	0.78
124	γ, A, WC, S_u, PF, D50	$v_c = (7.299) \times \gamma^{-2.02} \times A^{-0.41} \times WC^{2.25} \times S_u^{0.39} \times PF^{-1.68} \times D50^{-0.41}$	0.84	0.37	18.09	0.74
125	γ, WC, S_u, PF, A	$v_c = (57.994) \times \gamma^{-3.76} \times WC^{1.48} \times S_u^{0.54} \times PF^{-0.18} \times A^{-0.23}$	0.77	0.43	19.1	0.68
128	D50, γ, WC, S_u, A	$v_c = (0.00728) \times D50^{-0.26} \times \gamma^{-2.05} \times WC^{2.21} \times S_u^{0.46} \times A^{-0.39}$	0.82	0.39	22.9	0.50
132	A, WC, S_u, D50	$v_c = (3.92 \times 10^{-6}) \times A^{-0.41} \times WC^{2.65} \times S_u^{0.46} \times D50^{-0.28}$	0.82	0.40	26.11	0.69
133	A, WC, S_u, PF	$v_c = (7 \times 10^{-5}) \times A^{-0.28} \times WC^{2.23} \times S_u^{0.54} \times PF^{-0.12}$	0.75	0.45	23.71	0.67

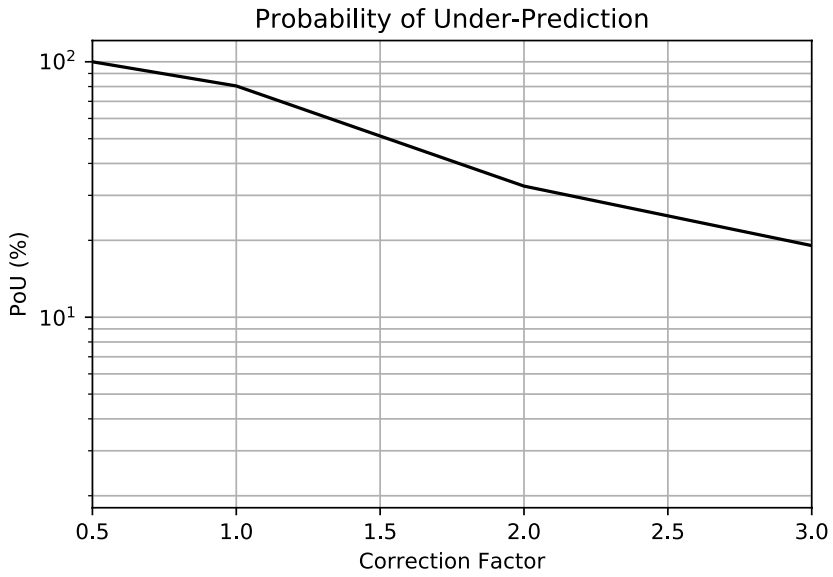

Figure 191. Plot of POU vs. correction factor for the Group 117 (Power) - v_c in the EFA/Fine dataset

The same procedure was conducted in the EFA/Coarse dataset, and the best models are selected for critical velocity. Figure 192 shows the number of data points in each of all the 105 combination groups in the EFA/Coarse dataset. Also, Figure 193 and Figure 194 show the results of R^2 for each combination group, for the "Linear" and "Power" models, respectively.

Both "Linear" and "Power" models show a few good groups in terms of R^2 values; however, as shown in Figure 192, the number of data points in most groups are lower compared to the EFA/Fine dataset. Figure 195 and Figure 196 show the values of MSE for the "Linear" and "Power" models, respectively.

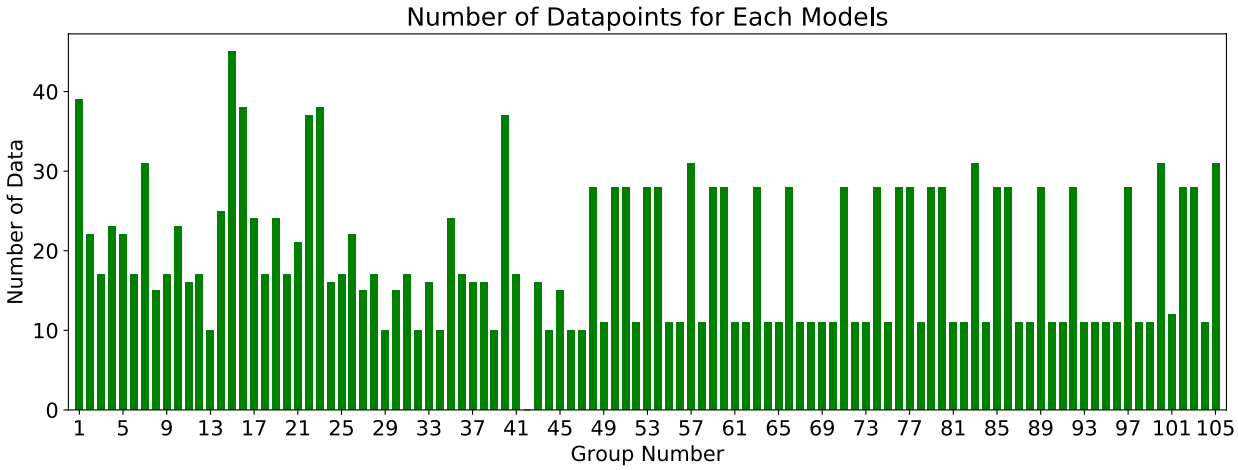

Figure 192. Number of data in each 105 combination groups for the EFA/Coarse dataset – Critical Velocity

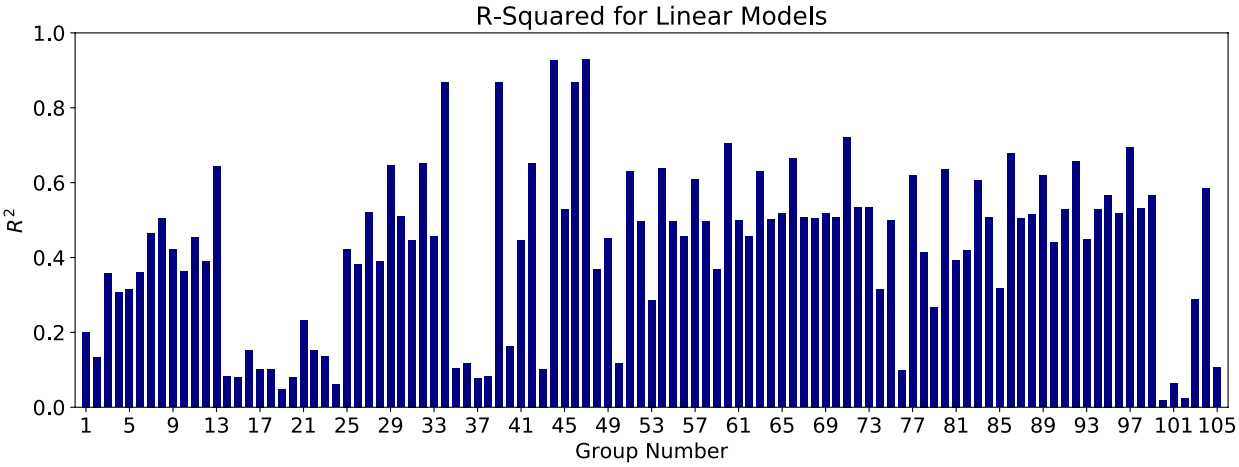

Figure 193. R^2 results for the "Linear Models" in EFA/Coarse dataset – Critical Velocity

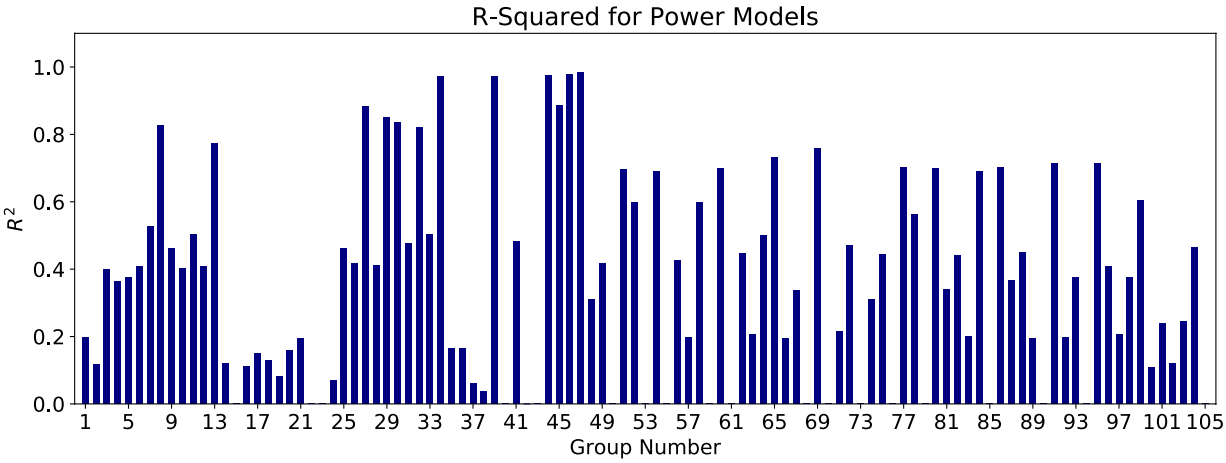

Figure 194. R^2 results for the "Power Models" in EFA/Coarse dataset – Critical Velocity

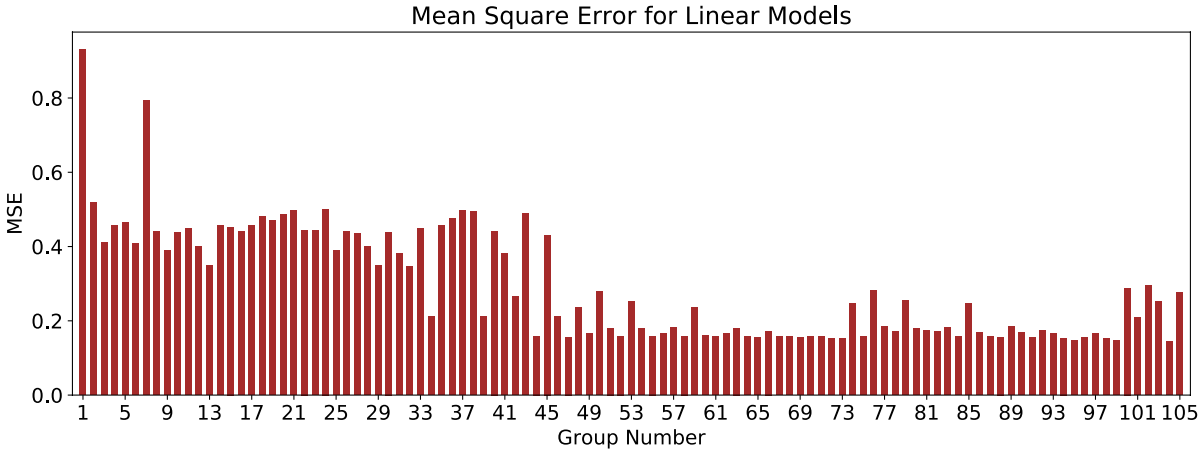

Figure 195. MSE results for "Linear Models" in EFA/Coarse dataset – Critical Velocity

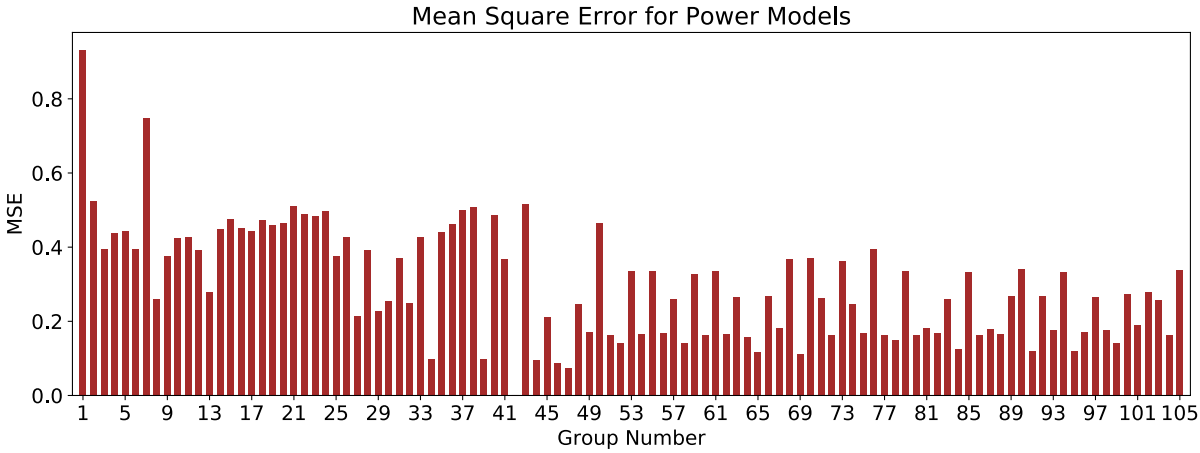

Figure 196. MSE results for "Power Models" in EFA/Coarse dataset – Critical Velocity

After passing through filters 1 and 2 (R^2 and MSE), "Linear" models associated with groups 44 and 47 were selected for further analyses. Also "Power" models associated with groups 8, 27, 30, 44, 45, 46, and 47 were selected for further analyses.

Filter 3, F-value/F-stat, was determined for each group mentioned above. Table 57 shows the results of the selected "Linear" models after meeting the requirements of the first three filters (R2, MSE, and F-value/F-stat). As shown in Table 57, only one selected model performs satisfactorily in the cross-validation test. Table 58 also shows the results of the selected "Power" models after meeting the requirements of the first three filters. The best models that also have a good cross-validation score are highlighted in blue in both "Linear" and "Power" forms. Out of all the highlighted correlation equations in Table 57 and Table 58, the Group 27 correlation equations in "Power" form was selected as the most promising equation. Figure 197 shows the plot of "POU vs. θ" for this model. The vertical axis in Figure 197 represent the probability that the predicted v_c using the selected model is smaller than the actual v_c, in percentage (with 0.1 m/s offset). In order to reach a 90% confidence that the predicted v_c is smaller than the actual v_c, the predicted value should be multiplied by 0.7.

Table 57. Selected "Linear" models for critical velocity in the EFA/Coarse dataset

Group No.	Independent Variables	Model Expression	R^2	MSE	F-value/F-stat	Cross-Validation Score
44	PI, γ, VST, PF, D50	$v_c = 0.002 \times PI - 0.1 \times \gamma + 0.01 \times VST - 0.09 \times PF - 13.6 \times D50 + 7.21$ $for\ 0.074 < D50 < 0.3$	0.93	0.16	2.43	0.67
47	PI, γ, WC, VST, PF, D50	$v_c = 0.002 \times PI - 0.11 \times \gamma - 0.007 \times WC + 0.009 \times VST - 0.092 \times PF - 13.846 \times D50 + 7.46$	0.93	0.16	0.75	-0.75

Table 58. Selected "Power" models for critical velocity in the EFA/Coarse dataset

Group No.	Independent Variables	Model Expression	R^2	MSE	F-value/F-stat	Cross-Validation Score
8	PI, γ, D50	$v_c = (3 \times 10^{-15}) \times PI^{1.27} \times \gamma^{8.35} \times D50^{-2.75}$ $for\ 0.074 < D50 < 0.3$	0.83	0.26	9.56	0.74
27	PI, γ, WC, D50	$v_c = (3 \times 10^{-15}) \times PI^{1.24} \times \gamma^{8.11} \times WC^{0.54} \times D50^{-2.35}$ $for\ 0.074 < D50 < 0.3$	0.88	0.22	10.73	0.72
30	PI, γ, PF, D50	$v_c = (4 \times 10^{-15}) \times PI^{1.33} \times \gamma^{7.81} \times PF^{0.55} \times D50^{-2.34}$ $for\ 0.074 < D50 < 0.3$	0.84	0.25	7.09	0.62
44	PI, γ, VST, PF, D50	$v_c = (0.027) \times PI^{0.18} \times \gamma^{2.31} \times VST^{1.37} \times PF^{-5.89} \times D50^{-5.22}$ $for\ 0.074 < D50 < 0.3$	0.97	0.09	7.10	0.91
45	PI, γ, WC, PF, D50	$v_c = (4 \times 10^{-15}) \times PI^{1.27} \times \gamma^{7.87} \times WC^{0.51} \times PF^{0.23} \times D50^{-2.24}$ $for\ 0.074 < D50 < 0.3$	0.88	0.21	7.97	0.28
46	PI, WC, VST, PF, D50	$v_c = (7162.39) \times PI^{-0.12} \times WC^{-0.66} \times VST^{1.33} \times PF^{-7.27} \times D50^{-6.05}$ $for\ 0.074 < D50 < 0.3$	0.98	0.09	7.86	0.94
47	PI, γ, WC, VST, PF, D50	$v_c = (2.055) \times PI^{0.03} \times \gamma^{3.11} \times WC^{-0.92} \times VST^{1} \times PF^{-7.24} \times D50^{-6.32}$ $for\ 0.074 < D50 < 0.3$	0.98	0.08	4.97	0.90

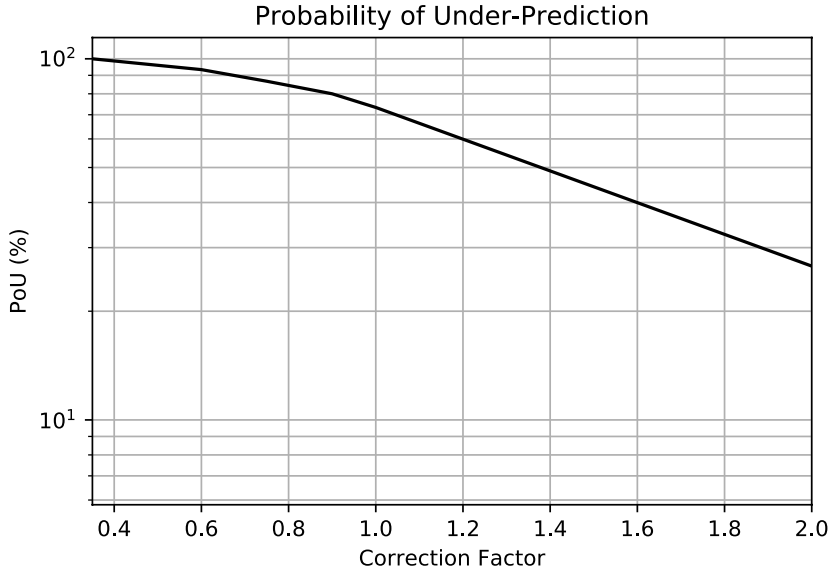

Figure 197. Plot of POU vs. correction factor for the Group 27 (Power) - v_c in the EFA/Coarse dataset

7.3.4.3. Initial Slope of Erosion Rate-Shear Stress (E_τ)

The same four-filter process discussed in Section 7.3.3 is implemented in this section to obtain the best models for the initial slope of the erosion rate-shear stress curve (E_τ). The study of regression analysis for E_τ is performed in three different sections for the EFA, HET, and JET separately.

EFA Database

Similar to the cases of critical shear stress and critical velocity, it was observed that dividing the EFA/Global dataset into the EFA/Fine and the EFA/Coarse datasets would significantly improve the regression results. Figure 198 shows the number of data points in each of all the 135 combination groups in the EFA/Fine dataset. Also, Figure 199 and Figure 200 show the results of R^2 for each combination group, for the "Linear" and "Power" models, respectively.

R^2 values of "Power" models are generally higher than the "Linear" models. Also, it can be observed that the R^2 values are considerably higher for groups 123 to 135 in Figure 200. Figure 201 shows the results of the MSE for each of the 135 combination groups in the EFA/Fine dataset, for "Power" models.

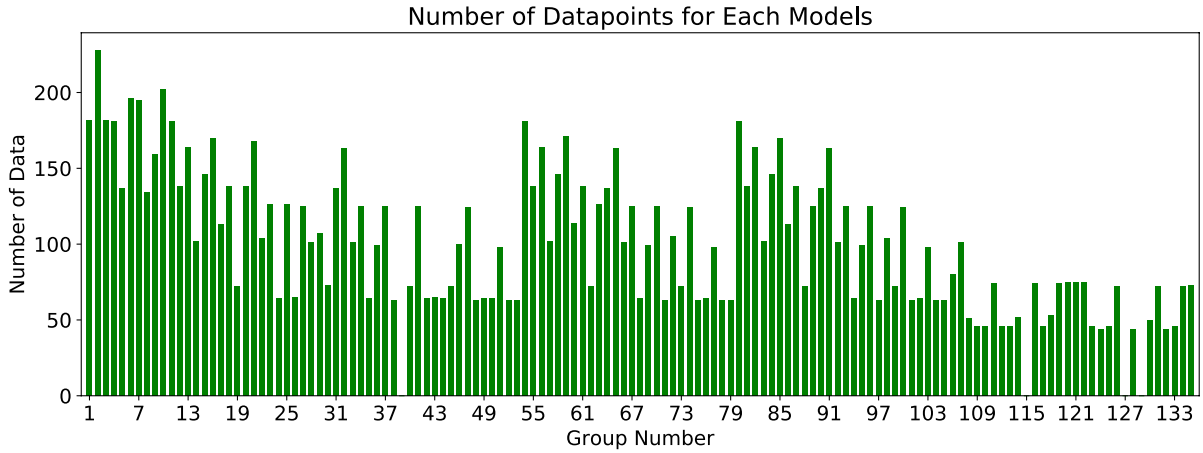

Figure 198. Number of data in each 135 combination groups for the EFA/Fine dataset – E_τ

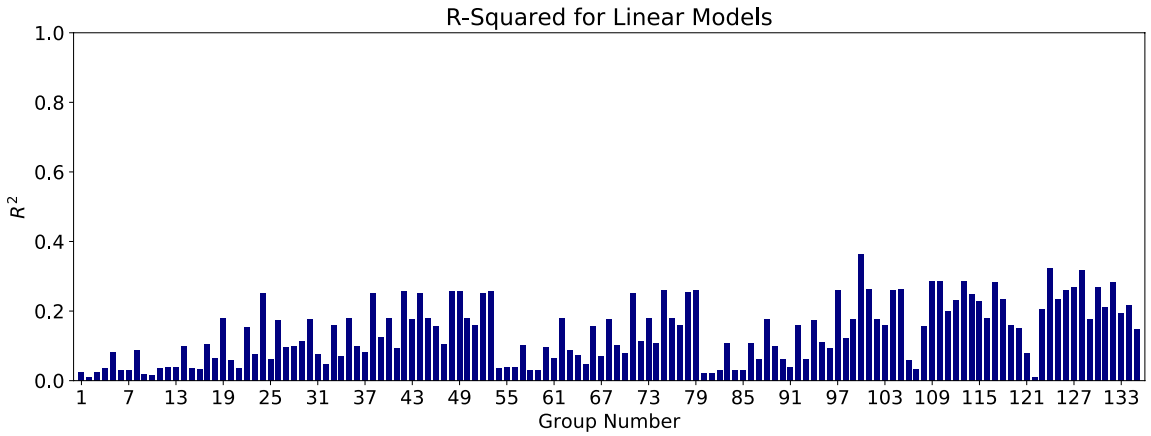

Figure 199. R^2 results for the "Linear Models" in EFA/Fine dataset – E_τ

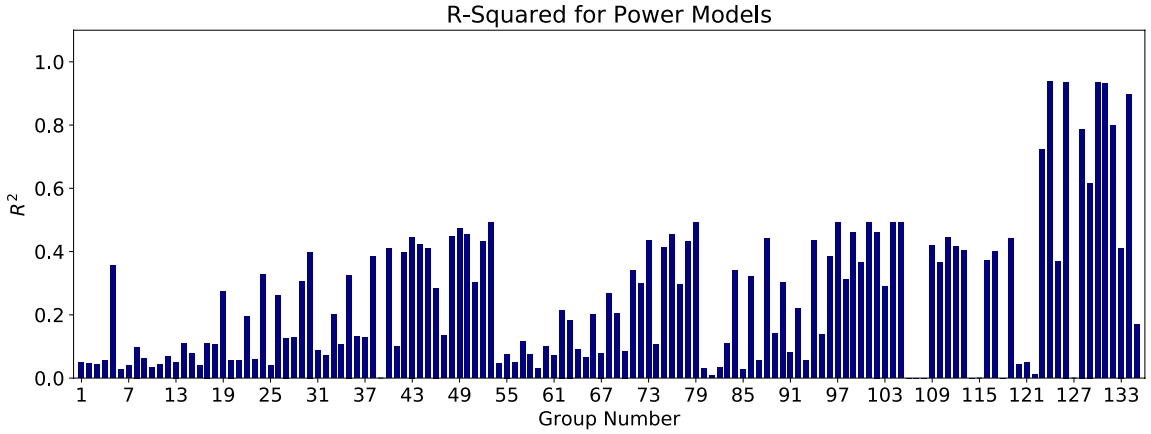

Figure 200. R^2 results for the "Power Models" in EFA/Fine dataset – E_τ

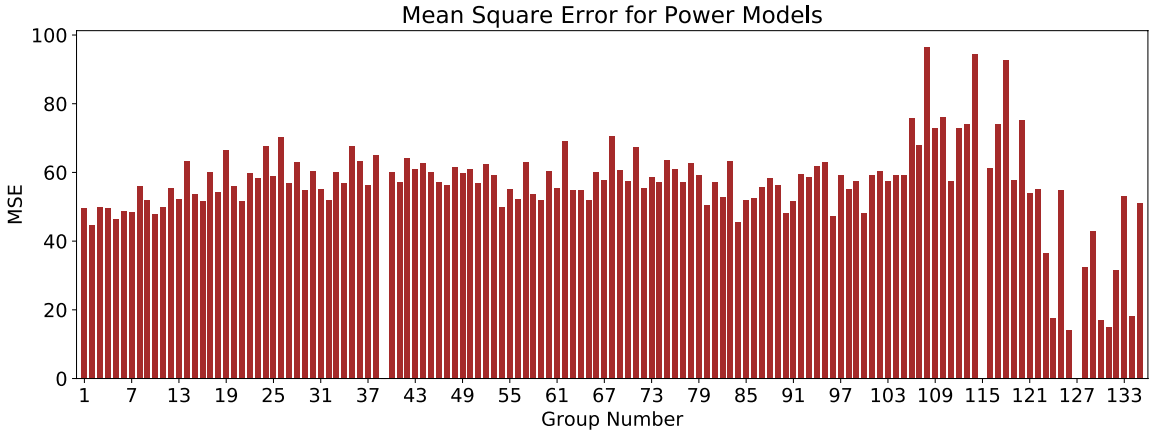

Figure 201. MSE results for the "Power Models" in EFA/Fine dataset – E_τ

After passing through filters 1 and 2 (R^2 and MSE), "Power" models associated with groups 124, 126, 128, 130, 131, 132, and 134 were selected for further analyses.

Filter 3, F-value/F-stat, was determined for each group mentioned above. Table 59 shows the results of the selected "Power" models after meeting the requirements of the first three filters (R2, MSE, and F-value/F-stat). The best models that also have a good cross-validation score are highlighted in blue. The Group 134 correlation equations in "Power" form was selected as the most promising equation. Figure 202 shows the plot of "POO vs. θ" for this model. The vertical axis in Figure 202 represents the probability that the predicted E_τ using the selected model is greater than the actual E_τ, in percentage (with 4 mm/hr-Pa offset). In order to reach a 87% confidence that the predicted E_τ is greater than the actual E_τ, the predicted value should be multiplied by 2.

Table 59. Selected "Power" models for E_τ in the EFA/Fine dataset

Group No.	Independent Variables	Model Expression	R^2	MSE	F-value/F-stat	Cross-Validation Score
124	γ, A, WC, S_u, PF, D50	$E_\tau = (1.043059638 \times 10^{13}) \times \gamma^{-8.58} \times A^{-0.01} \times WC^{-1.69} \times S_u^{-0.36} \times PF^{5.29} \times D50^{5.69}$	0.94	17.7	9.6	0.04
126	D50, γ, WC, PF, A	$E_\tau = (1.208024 \times 10^{13}) \times D50^{7.36} \times \gamma^{-10.09} \times WC^{-1.58} \times PF^{7.04} \times A^{0.05}$	0.94	14.26	21.3	0.51
128	D50, γ, WC, S_u, A	$E_\tau = (2.3983097 \times 10^{13}) \times D50^{2} \times \gamma^{-3.07} \times WC^{-1.99} \times S_u^{-1.57} \times A^{-0.09}$	0.79	32.56	6.6	0.09
130	D50, S_u, PF, A	$E_\tau = (789314.3) \times D50^{21.14} \times S_u^{-1.13} \times PF^{13.17} \times A^{1.98}$	0.93	17.2	11.7	-0.63
131	D50, WC, PF, A	$E_\tau = (86.707) \times D50^{31} \times WC^{0.1} \times PF^{21} \times A^{2.89}$	0.93	14.9	24.1	-0.21
132	A, WC, S_u, D50	$E_\tau = (2.63681129 \times 10^{13}) \times A^{0.31} \times WC^{-3.85} \times S_u^{-2.57} \times D50^{2.02}$	0.80	31.7	10.3	0.06
134	A, γ, PF, D50	$E_\tau = (1.429078 \times 10^{13}) \times A^{-0.47} \times \gamma^{-10.43} \times PF^{6.14} \times D50^{7.52}$	0.90	18.2	22.9	0.53

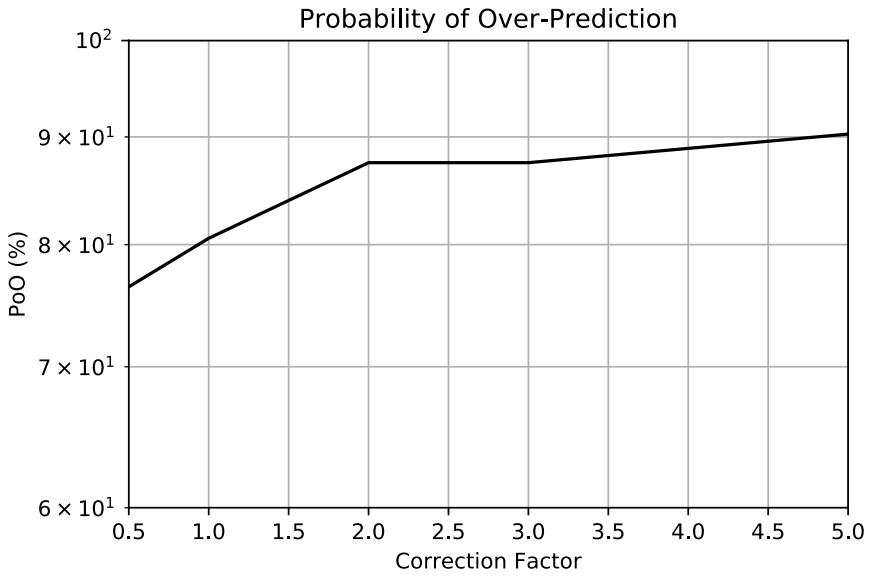

Figure 202. Plot of POO vs. correction factor for the Group 134 (Power) - E_τ in the EFA/Fine dataset

The same procedure was conducted in the EFA/Coarse dataset, and the best models are selected for E_τ. Figure 203 shows the number of data points in each of all the 105 combination groups in the EFA/Coarse dataset. Also, Figure 204 and Figure 205 show the results of R^2 for each combination group, for the "Linear" and "Power" models, respectively.

Both "Linear" and "Power" models show a few good groups in terms of R^2 values; however, as shown in Figure 192, the number of data points in most groups are lower compared to the EFA/Fine dataset. Figure 195 and Figure 196 show the values of MSE for the "Linear" and "Power" models, respectively.

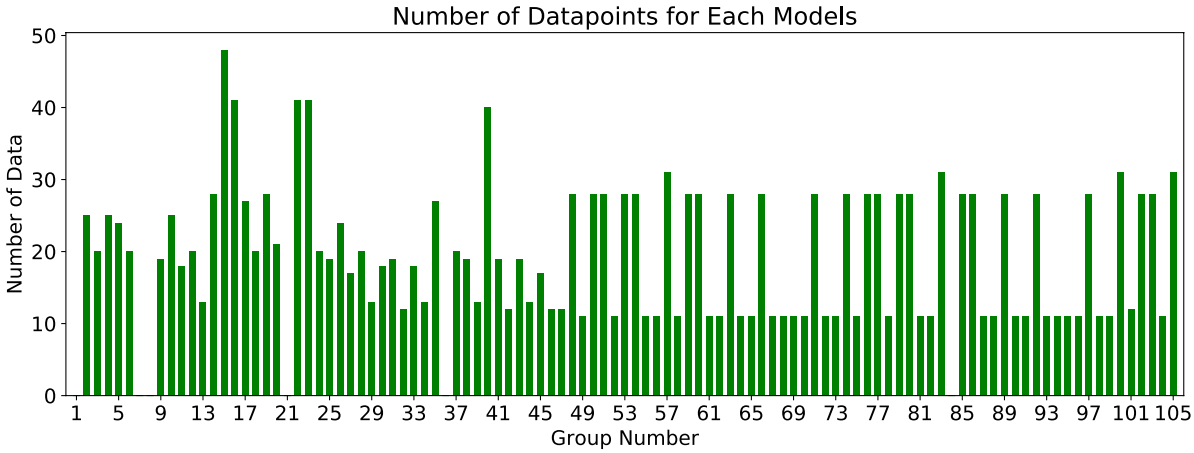

Figure 203. Number of data in each 105 combination groups for the EFA/Coarse dataset – E_τ

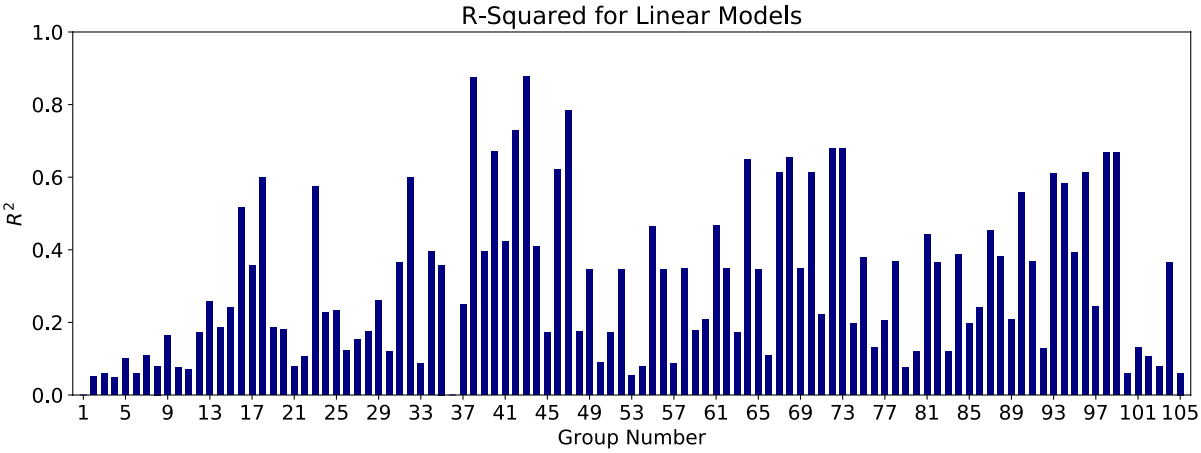

Figure 204. R^2 results for the "Linear Models" in EFA/Coarse dataset – E_τ

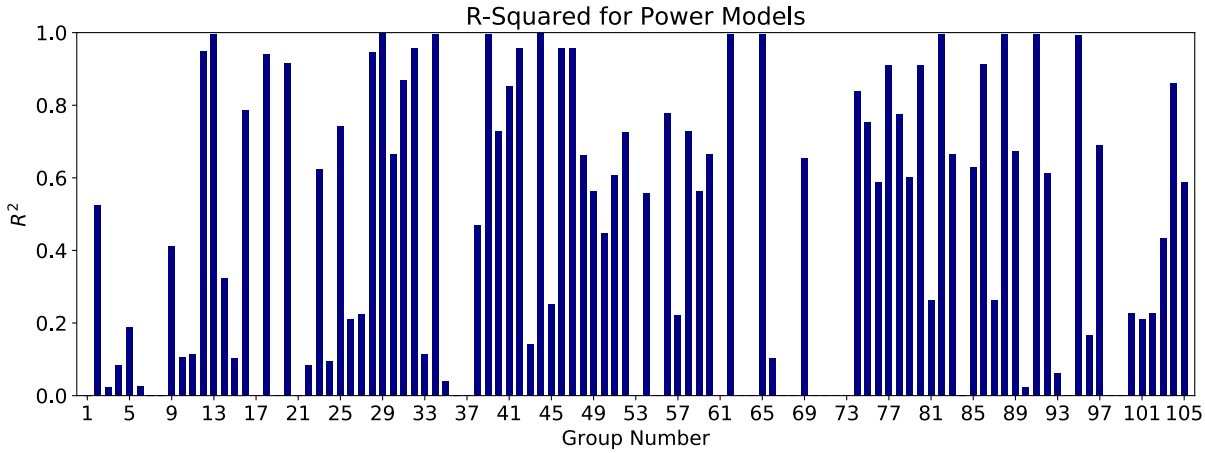

Figure 205. R^2 results for the "Power Models" in EFA/Coarse dataset – E_τ

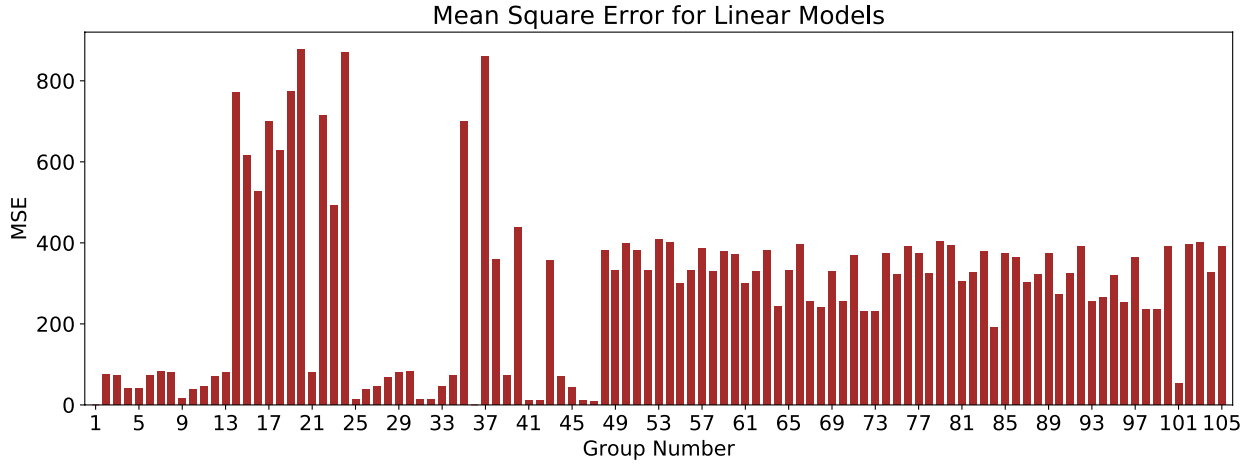

Figure 206. MSE results for the "Linear Models" in EFA/Coarse dataset – E_τ

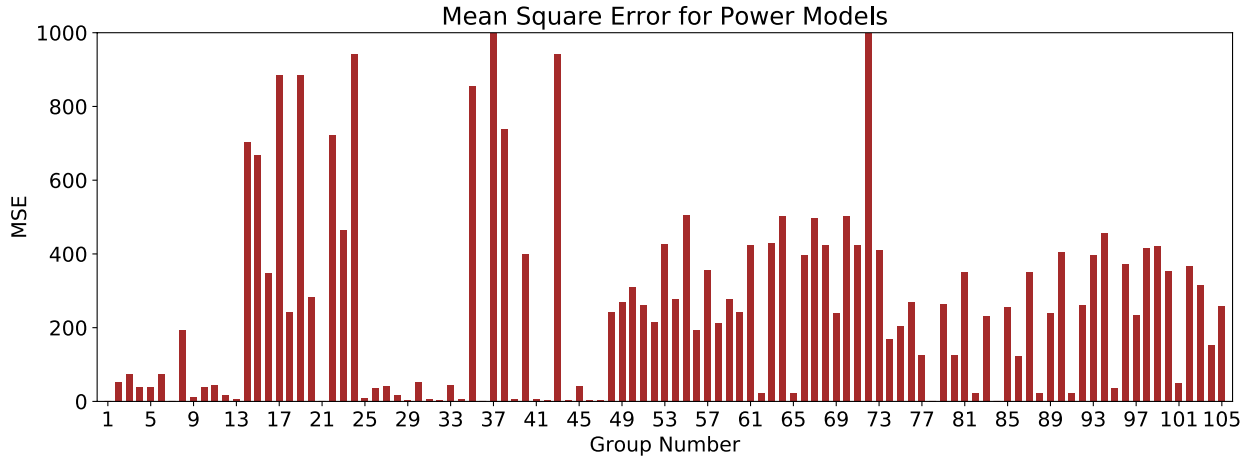

Figure 207. MSE results for the "Power Models" in EFA/Coarse dataset – E_τ

After passing through filters 1 and 2 (R^2 and MSE), "Linear" models associated with groups 38, 42, 43, and 47 were selected for further analyses. Also "Power" models associated with groups 12, 13, 16, 18, 20, 28, 31, 34, 39, 40, 41, 42, 44, 74, 77, 80, 82, 86, 91, and 95 were selected for further analyses.

Filter 3, F-value/F-stat, was determined for each group mentioned above. Table 60 shows the results of the selected "Linear" models after meeting the requirements of the first three filters (R^2, MSE, and F-value/F-stat). As shown in Table 60, none of the selected models perform satisfactorily in the cross-validation test. Table 61 also shows the results of the selected "Power" models after meeting the requirements of the first three filters. The Group 77 correlation equations in "Power" form was selected as the most promising equation. Figure 208 shows the plot of "POO vs. θ" for this model. The vertical axis in Figure 208 represent the probability that the predicted E_τ using the selected model is greater than the actual E_τ, in percentage (with 15 mm/hr-Pa offset). In order to reach a 80% confidence that the predicted E_τ is greater than the actual E_τ, the predicted value should be multiplied by 2.5.

Table 60. Selected "Linear" models for E_τ in the EFA/Coarse dataset

Group No.	Independent Variables	Model Expression	R^2	MSE	F-value/F-stat	Cross-Validation Score
38	WC, VST, PF, D50	$E_\tau = 79.308 \times WC + 7.52 \times VST - 38.22 \times PF + 20.35 \times D50 - 374.67$	0.88	359.3	7.71	-8.5
42	PI, γ, WC, VST, 50	$E_\tau = -0.669 \times PI - 5.06 \times \gamma - 1.89 \times WC - 0.31 \times VST + 112.8 \times D50 + 149.23$	0.73	10.3	0.64	-0.35
43	γ, WC, VST, PF, D50	$E_\tau = -31.207 \times \gamma + 78.76 \times WC + 7.86 \times VST - 36.82 \times PF + 39.92 \times D50 + 180.81$	0.88	356	5.98	-7.4
47	PI, γ, WC, VST, PF, D50	$E_\tau = -0.897 \times PI - 5.82 \times \gamma - 1.5 \times WC - 0.2 \times VST - 1.01 \times PF + 46.15 \times D50 + 198.61$	0.78	9.19	0.49	-1.5

Table 61. Selected "Power" models for E_τ in the EFA/Coarse dataset

Group No.	Independent Variables	Model Expression	R^2	MSE	F-value/F-stat	Cross-Validation Score
12	PI, VST, PF	$E_\tau = (0.00009) \times PI^{0.33} \times VST^{-10.86} \times PF^{12.46}$	0.95	17.39	26.4	-0.97
13	PI, VST, D50	$E_\tau = (1.096668 \times 10^{13}) \times PI^{1.69} \times VST^{-8.13} \times D50^{1.05}$	0.99	5.41	22.2	-0.35
16	γ, WC, D50	$E_\tau = (93090257.5) \times \gamma^{-7.02} \times WC^{2.04} \times D50^{-0.72}$	0.79	349.1	19.6	-0.14
18	WC, VST, D50	$E_\tau = (4112.67) \times WC^{0.01} \times VST^{-2.95} \times D50^{-3.2}$	0.94	243.5	23.9	-4.5
20	VST, γ, D50	$E_\tau = (604968.99) \times VST^{-3.74} \times \gamma^{-1.52} \times D50^{-3.77}$	0.92	281.8	18.1	-9.01
28	PI, γ, VST, PF	$E_\tau = (4630.2794 \times 10^{8}) \times PI^{2.45} \times \gamma^{-20.92} \times VST^{-4.78} \times PF^{12.80}$	0.95	17.58	19.9	-2.5
31	PI, WC, VST, PF	$E_\tau = (2.59644111 \times 10^{13}) \times PI^{-0.87} \times WC^{-5.19} \times VST^{-0.72} \times PF^{-3.65}$	0.87	5.9	18.1	-0.33
34	PI, VST, PF, D50	$E_\tau = (7.1386087 \times 10^{12}) \times PI^{1.6} \times VST^{-8.56} \times PF^{1.17} \times D50^{2.04}$	0.99	4.99	9.1	-1.53
39	PI, VST, PF, D50	$E_\tau = (7.13860971 \times 10^{12}) \times WC^{1.6} \times VST^{-8.56} \times PF^{1.17} \times D50^{2.04}$	0.99	4.99	8.8	-0.03
40	γ, WC, PF, D50	$E_\tau = (2.881) \times \gamma^{-1.44} \times WC^{3.32} \times PF^{0.00000002} \times D50^{0.91}$	0.73	398.4	41.1	-0.53
41	PI, γ, WC, VST, PF	$E_\tau = (2.99273 \times 10^{13}) \times PI^{-1.06} \times \gamma^{-4.34} \times WC^{-2.08} \times VST^{-0.28} \times PF^{-2.23}$	0.85	6.23	13.3	-0.11rr
42	PI, γ, WC, VST, D50	$E_\tau = (1591199925) \times PI^{-1.69} \times \gamma^{-2.09} \times WC^{0.79} \times VST^{-1.39} \times D50^{3.68}$	0.96	4.05	8.3	-7.09
44	PI, γ, VST, PF, D50	$E_\tau = (127160023) \times PI^{1.75} \times \gamma^{6.82} \times VST^{-10.86} \times PF^{1.11} \times D50^{2.88}$	0.99	4.15	9.6	-0.37
74	C_u, γ, WC	$E_\tau = (3785948678096) \times C_u^{-1.86} \times \gamma^{-10.09} \times WC^{3.01}$	0.84	167.8	16.7	0.58
77	C_u, γ, D50	$E_\tau = (3228.7) \times C_u^{-2.8} \times \gamma^{-1.58} \times D50^{-2.91}$	0.91	126.3	28.02	0.64
80	C_u, WC, D50	$E_\tau = (34.62) \times C_u^{-3.6} \times WC^{-0.52} \times D50^{-3.99}$	0.91	124.6	28.9	0.62
82	C_u, VST, D50	$E_\tau = (12.22) \times C_u^{-16.14} \times VST^{-23.44} \times D50^{-43.92}$	0.99	22.6	10.04	-3.76
86	C_u, γ, WC, D50	$E_\tau = (0.148) \times C_u^{-4.71} \times \gamma^{1.83} \times WC^{-1.11} \times D50^{-5.42}$	0.91	124.3	23.4	-3.96
91	C_u, WC, VST, D50	$E_\tau = (45.82) \times C_u^{-13.48} \times WC^{0.67} \times VST^{-22.78} \times D50^{-40.08}$	0.99	22.6	9.5	-10.54
95	C_u, γ, WC, VST, D50	$E_\tau = (9.2 \times 10^{-15}) \times C_u^{-2.13} \times \gamma^{15.56} \times WC^{-2.7} \times VST^{-7.67} \times D50^{-12.99}$	0.99	37.13	11.1	-10.35

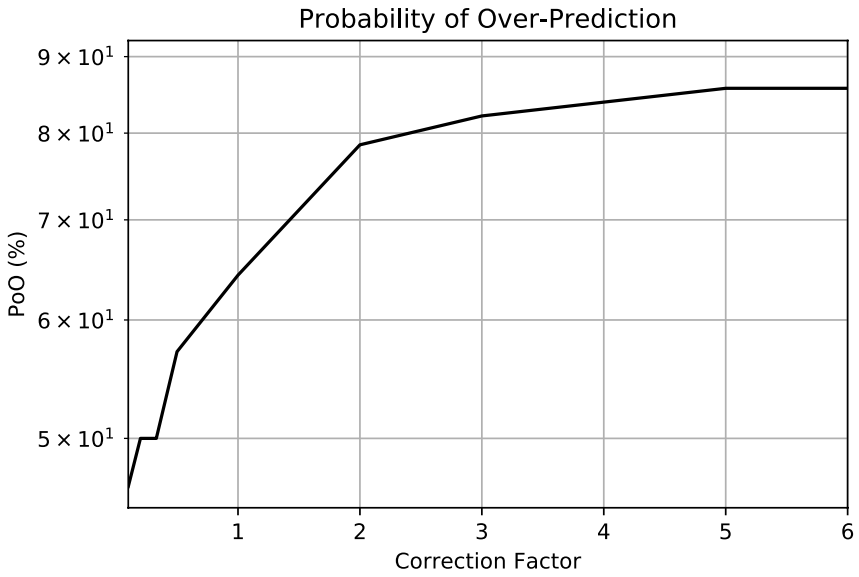

Figure 208. Plot of POO vs. correction factor for the Group 77 (Power) - E_τ in the EFA/Coarse dataset

JET Database

Similar to the case of the EFA database, it was observed that dividing the JET/Global dataset into the JET/Fine and the JET/Coarse datasets would significantly improve the regression results. Figure 209 shows the number of data points in each of all the 135 combination groups in the JET/Fine dataset. Figure 210 and Figure 211 show the results of R^2 for each combination group, for the "Linear" and "Power" models, respectively.

R^2 values of "Power" models are generally higher than the "Linear" models. Figure 212 and Figure 213 show the results of the MSE for each of the 135 combination groups in the EFA/Fine dataset for "Power" and "Linear" models, respectively.

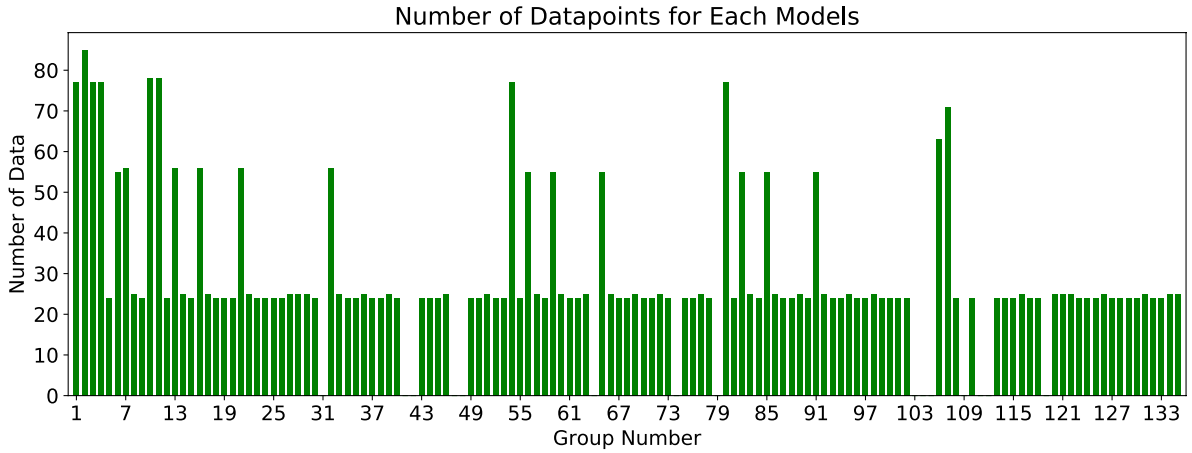

Figure 209. Number of data in each 135 combination groups for the JET/Fine dataset – E_τ

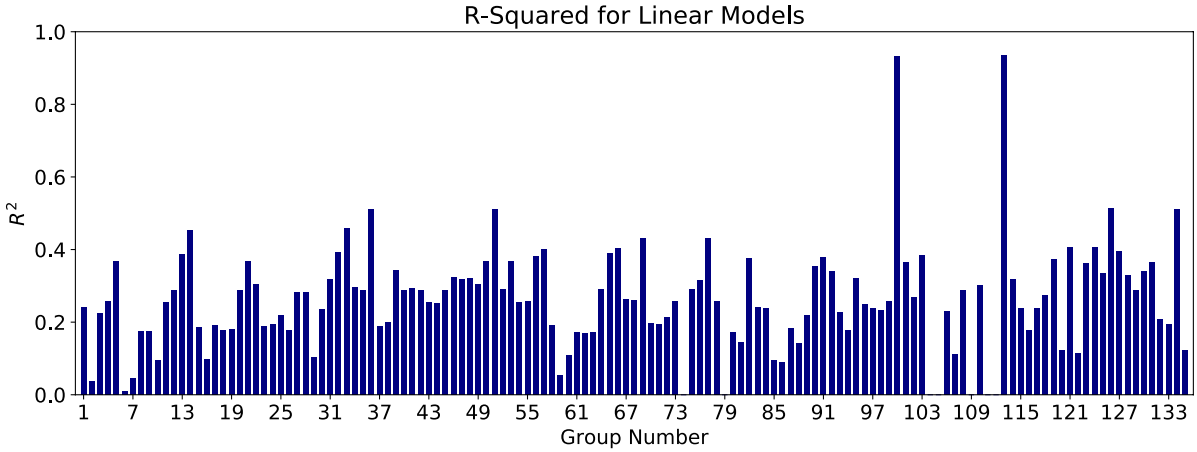

Figure 210. R^2 results for the "Linear Models" in JET/Fine dataset – E_τ

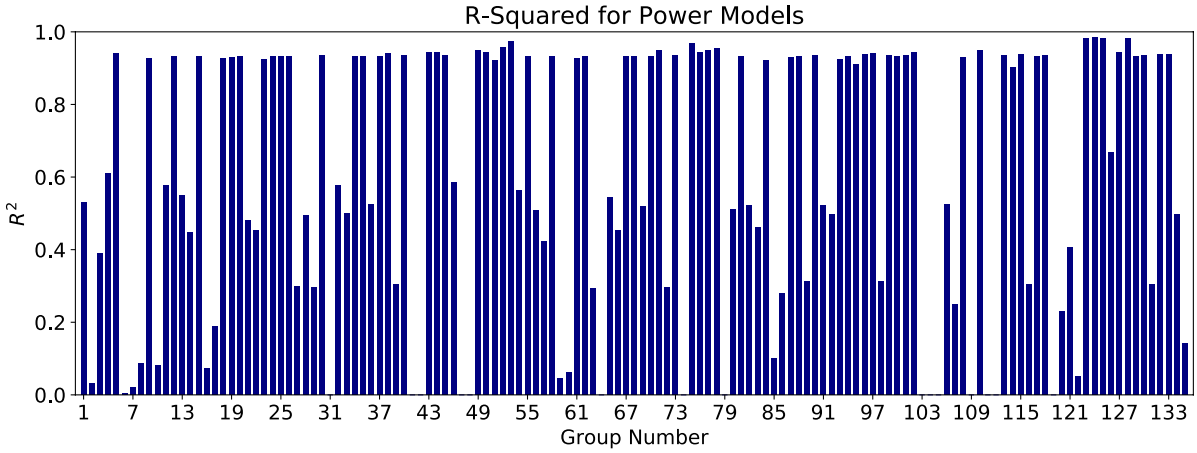

Figure 211. R^2 results for the "Power Models" in JET/Fine dataset – E_τ

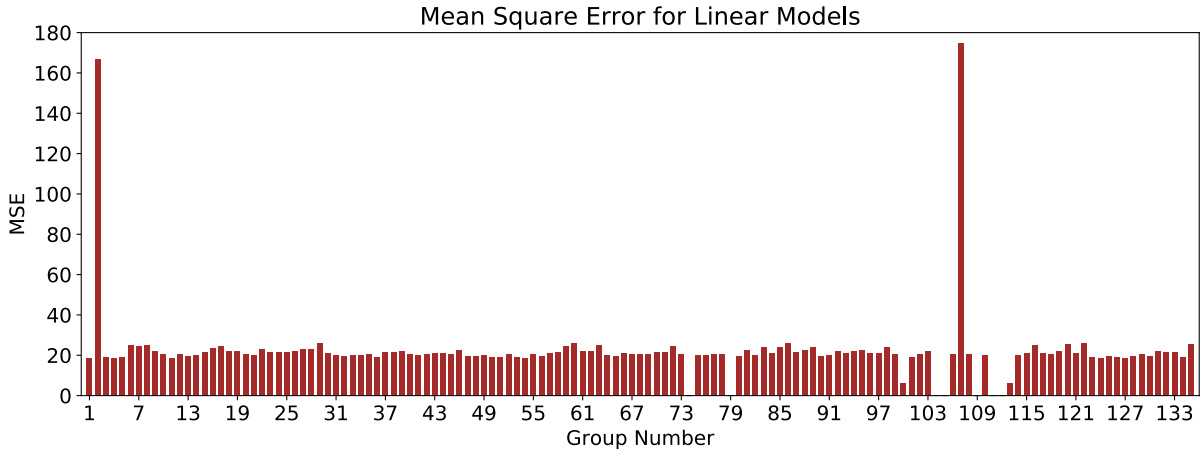

Figure 212. MSE results for the "Linear Models" in JET/Fine dataset – E_τ

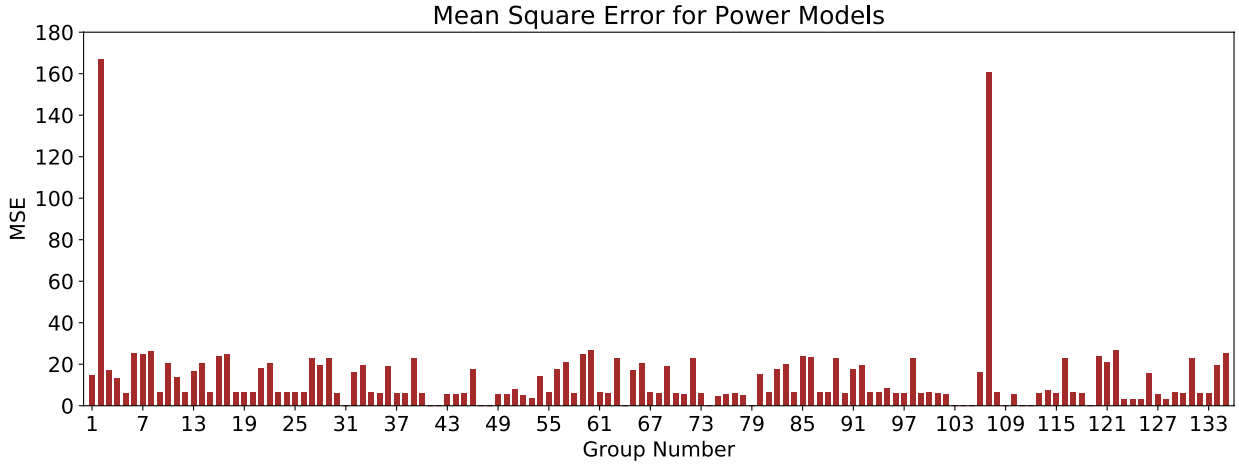

Figure 213. MSE results for the "Power Models" in JET/Fine dataset – E_τ

After passing through filters 1 and 2 (R^2 and MSE), "Linear" models associated with groups 100 and 113 were selected for further analyses. Also "Power" models associated with groups 5, 12, 15, 20, 24, 38, 43, 71, 75, 78, 97, 123, 125, 128 were selected for further analyses.

Filter 3, F-value/F-stat, was determined for each group mentioned above. Table 62 shows the results of the selected "Linear" models after meeting the requirements of the first three filters (R^2, MSE, and F-value/F-stat). As shown in Table 62, none of the selected models perform satisfactorily in the cross-validation test. Table 63 also shows the results of the selected "Power"

models after meeting the requirements of the first three filters. The Group 15 correlation equations in "Power" form was selected as the most promising equation. Figure 214 shows the plot of "POO vs. θ" for this model. The vertical axis in Figure 214 represent the probability that the predicted E_τ using the selected model is greater than the actual E_τ, in percentage (with 6 mm/hr-Pa offset). In order to reach a 88% confidence that the predicted E_τ is greater than the actual E_τ, the predicted value should be multiplied by 2.

Table 62. Selected "Linear" models for E_τ in the JET/Fine dataset

Group No.	Independent Variables	Model Expression	R^2	MSE	F-value/F-stat	Cross-Validation Score
100	PL, γ, WC, S_u, PF	$E_\tau = 2.468 \times PL - 9.40 \times \gamma - 3.30 \times WC - 0.38 \times S_u - 0.39 \times PF + 287.11$	0.93	6.29	2.31	-0.59
113	PC, γ, WC, S_u, D50	$E_\tau = 0.707 \times PC - 7.10 \times \gamma - 2.89 \times WC - 0.39 \times S_u + 162.63 \times D50 + 218.4$	0.94	6.14	2.54	-0.64

Table 63. Selected "Power" models for E_τ in the JET/Fine dataset

Group No.	Independent Variables	Model Expression	R^2	MSE	F-value/F-stat	Cross-Validation Score
5	LL, PL, γ, WC, S_u	$E_\tau = (35913.13) \times LL^{-9.69} \times PL^{17.77} \times \gamma^{-5.74} \times WC^{5.46} \times S_u^{-7.08}$	0.94	5.94	6.98	-0.79
12	PI, γ, S_u	$E_\tau = (0.085) \times PI^{-0.62} \times \gamma^{8.57} \times S_u^{-5.24}$	0.93	6.29	8.63	-0.95
15	PI, WC, S_u	$E_\tau = (396599.6) \times PI^{-2.54} \times WC^{4.58} \times S_u^{-4.91}$	0.93	6.30	9.11	0.23
20	γ, WC, S_u	$E_\tau = (4.363 \times 10^{-4}) \times \gamma^{12.07} \times WC^{-1.96} \times S_u^{-5.48}$	0.93	6.27	8.74	-0.52
24	WC, S_u, D50	$E_\tau = (1986216) \times WC^{2.74} \times S_u^{-4.32} \times D50^{1.22}$	0.93	6.29	10.01	-2.08
38	PI, WC, S_u, D50	$E_\tau = (13854336090024) \times PI^{2.48} \times WC^{-4.79} \times S_u^{-3.95} \times D50^{1.47}$	0.94	5.89	8.21	-1.46
43	γ, S_u, PF, D50	$E_\tau = (1.7 \times 10^{-9}) \times \gamma^{-13.49} \times S_u^{-1.21} \times PF^{20.76} \times D50^{5.49}$	0.94	5.74	7.33	-8.18
71	LL, WC, S_u, D50	$E_\tau = (21641385785) \times LL^{4.5} \times WC^{-5.05} \times S_u^{-3.92} \times D50^{1.93}$	0.95	5.40	8.14	-1.43
75	LL, γ, WC, S_u, D50	$E_\tau = (5.3 \times 10^{-15}) \times LL^{9.24} \times \gamma^{27.26} \times WC^{-14.86} \times S_u^{-8.38} \times D50^{1.49}$	0.97	4.35	7.99	-330
78	LL, WC, S_u, PF, D50	$E_\tau = (5.22 \times 10^{-7}) \times LL^{2.07} \times WC^{-4.74} \times S_u^{-3.15} \times PF^{11.19} \times D50^{3.13}$	0.95	5.15	8.1	-2.95

Table 63 (Continued). Selected "Power" models for E_τ in the JET/Fine dataset

Group No.	Independent Variables	Model Expression	R^2	MSE	F-value/F-stat	Cross-Validation Score
97	PL, WC, S_u, D50	$E_\tau = (11377689319) \times PL^{4.36} \times WC^{-5.78} \times S_u^{-3.61} \times D50^{0.61}$	0.94	5.89	7.88	-76.1
123	A, PL, γ, WC, S_u	$E_\tau = (5.8 \times 10^{-9}) \times A^{5.32} \times PL^{1.00} \times \gamma^{31.35} \times WC^{-12.88} \times S_u^{-9.08}$	0.98	3.27	8.90	-7.25
125	γ, WC, S_u, PF, A	$E_\tau = (1.341 \times 10^{-7}) \times \gamma^{32.96} \times WC^{-12.31} \times S_u^{-9.47} \times PF^{-1.21} \times A^{5.72}$	0.98	3.27	8.66	-2.5
128	D50, γ, WC, S_u, A	$E_\tau = (1.898 \times 10^{-5}) \times D50^{0.58} \times \gamma^{28.59} \times WC^{-11.37} \times S_u^{-8.88} \times A^{5.55}$	0.98	3.23	8.59	-2.28

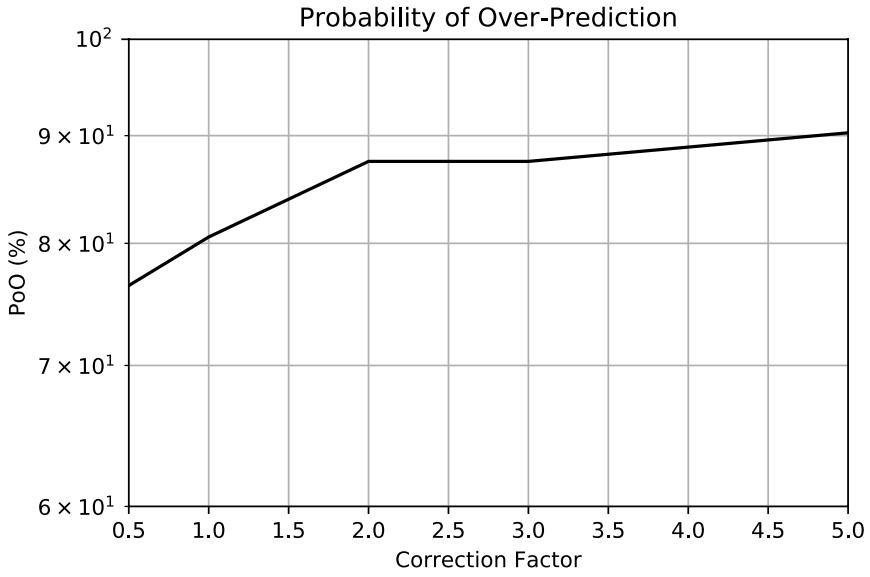

Figure 214. Plot of POO vs. correction factor for the Group 15 (Power) - E_τ in the JET/Fine dataset

The same procedure was conducted in the JET/Coarse dataset, and the best models are selected for E_τ. Figure 215 shows the number of data points in each of all the 105 combination groups in the EFA/Coarse dataset. Also, Figure 204 and Figure 205 show the results of R^2 for each combination group, for the "Linear" and "Power" models, respectively.

Both "Linear" and "Power" models show many good groups in terms of R^2 values; however, as shown in Figure 215, the number of data points in most groups are extremely low. Only a few combination groups consist of sufficient amount of data for regression analyses.

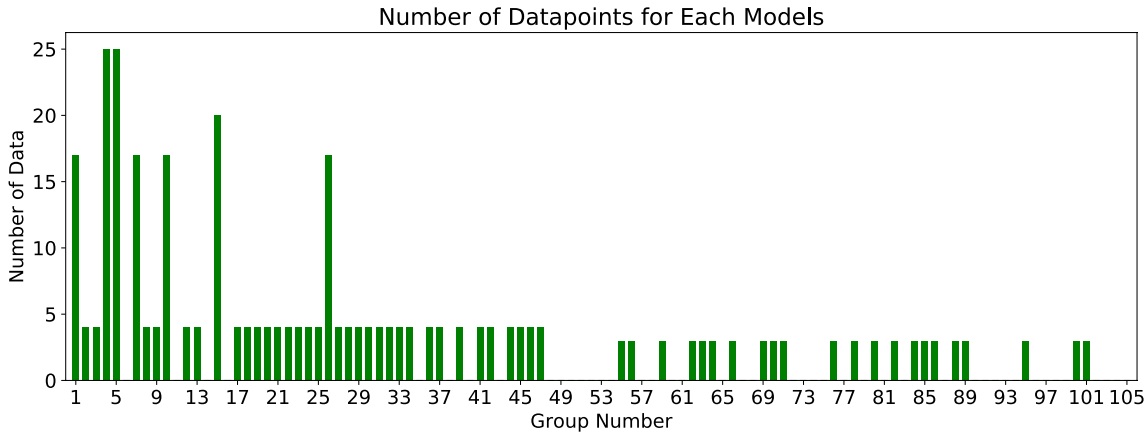

Figure 215. Number of data in each 105 combination groups for the JET/Coarse dataset – E_τ

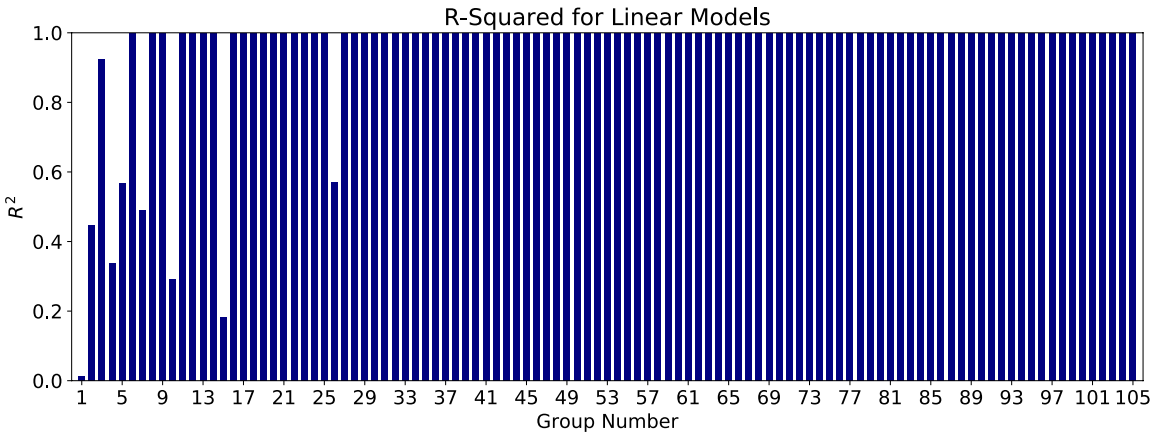

Figure 216. R^2 results for the "Linear Models" in JET/Coarse dataset – E_τ

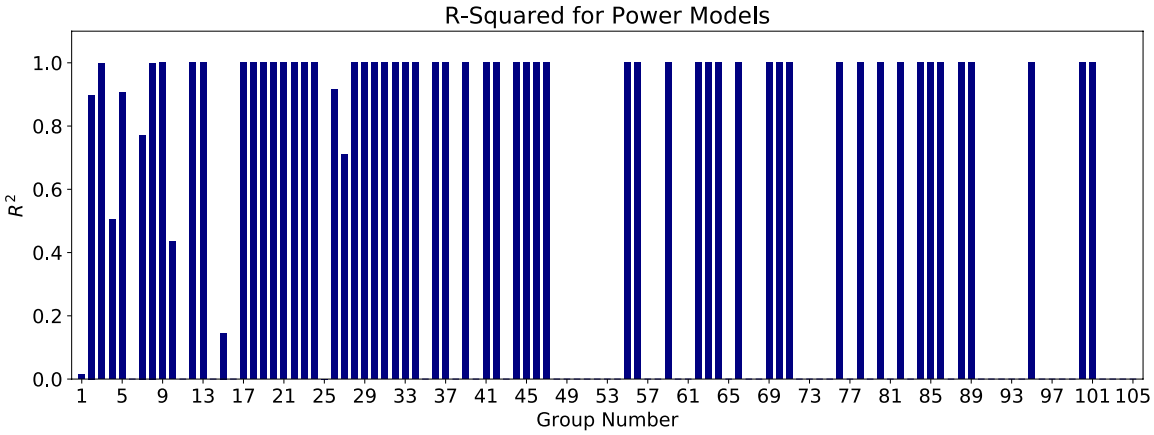

Figure 217. R^2 results for the "Power Models" in JET/Coarse dataset – E_τ

After passing through filters 1 and 2 (R^2 and MSE), "Linear" models associated with groups 5 and 26 were selected for further analyses. Also "Power" models associated with groups 5, 7, and 26 were selected for further analyses.

Filter 3, F-value/F-stat, was determined for each group mentioned above. Table 64 shows the results of the selected "Linear" models after meeting the requirements of the first three filters (R^2, MSE, and F-value/F-stat). As shown in Table 64, none of the selected models perform satisfactorily in the cross-validation test. Table 65 also shows the results of the selected "Power" models after meeting the requirements of the first three filters. The Group 5 correlation equations in "Power" form was selected as the most promising equation. Figure 218 shows the plot of "POO vs. θ" for this model. The probability that the predicted E_τ using the selected model is greater than the actual E_τ, in percentage (with 5 mm/hr-Pa offset). In order to reach a 90% confidence that the predicted E_τ is greater than the actual E_τ, the predicted value should be multiplied by 1.4.

Table 64. Selected "Linear" models for E_τ in the JET/Coarse dataset

Group No.	Independent Variables	Model Expression	R^2	MSE	F-value/F-stat	Cross-Validation Score
5	PI, γ, WC	$E_\tau = -1.827 \times PI - 28.85 \times \gamma - 13.87 \times WC + 797.2$	0.57	63.2	2.99	0.06
26	PI, γ, WC, PF	$E_\tau = -7 \times PI - 30.85 \times \gamma - 13.85 \times WC + 5.6 \times PF + 722.2$	0.57	70.5	1.22	-86.9

Table 65. Selected "Power" models for E_τ in the JET/Coarse dataset

Group No.	Independent Variables	Model Expression	R^2	MSE	F-value/F-stat	Cross-Validation Score
5	PI, γ, WC	$E_\tau = (55637006351614) \times PI^{-0.19} \times \gamma^{-6.39} \times WC^{-3.67}$	0.90	29.6	8.13	0.67
7	PI, γ, PF	$E_\tau = (14284687933437) \times PI^{-1.53} \times \gamma^{-12.16} \times PF^{3.62}$	0.77	51.42	6.56	-0.53
26	PI, γ, WC, PF	$E_\tau = (17383934656478) \times PI^{-0.05} \times \gamma^{-7.97} \times WC^{-4.03} \times PF^{1.9}$	0.92	31.3	4.35	0.26

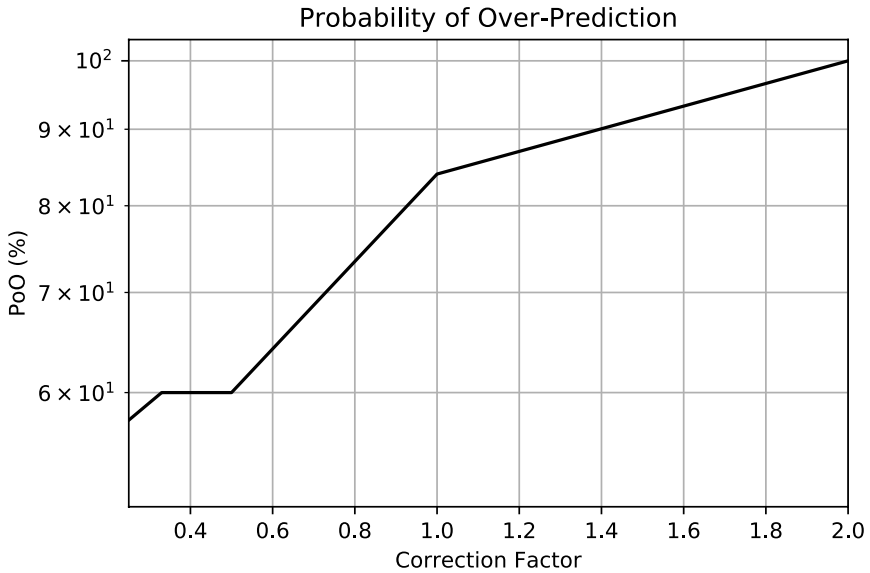

Figure 218. Plot of POO vs. correction factor for the Group 5 (Power) - E_τ in the JET/Coarse dataset

HET Database

It was observed that dividing the HET/Global dataset into the HET/Fine and the HET/Coarse datasets would not significantly improve the regression results; however, the HET/Coarse database included a few combination groups with acceptable R^2 values. Figure 219 shows the number of data points in each of all the 105 combination groups in the HET/Coarse dataset. Many combination groups as shown in Figure 219, do not include any data points. Figure 220 and Figure 221 show the results of R^2 for each combination group, for the "Linear" and "Power" models, respectively. It is noteworthy that as the HET is limited to finer grained soils, the HET/Coarse database corresponds to soils with D50 ranging from 0.074 mm to 0.3 mm.

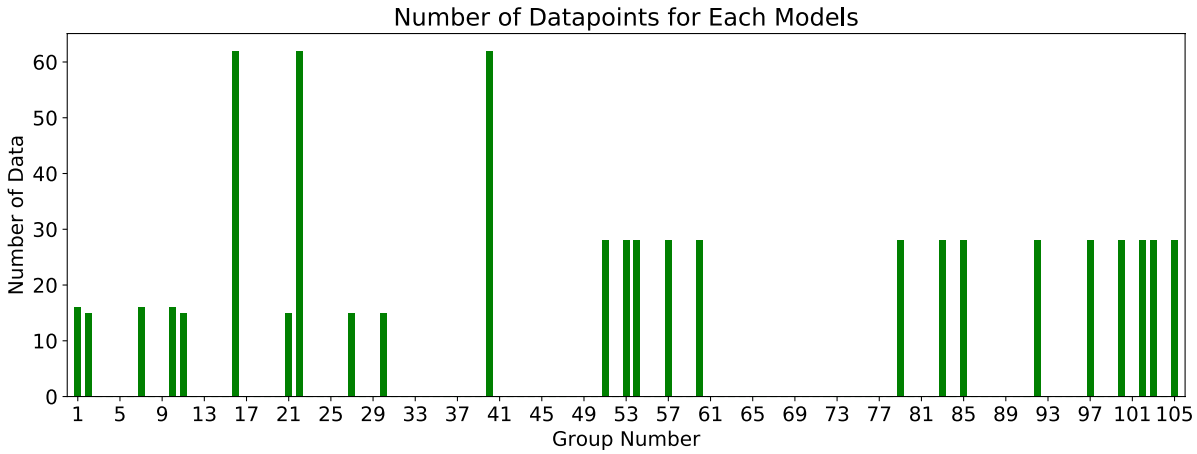

Figure 219. Number of data in each 105 combination groups for the HET/Coarse dataset – E_τ

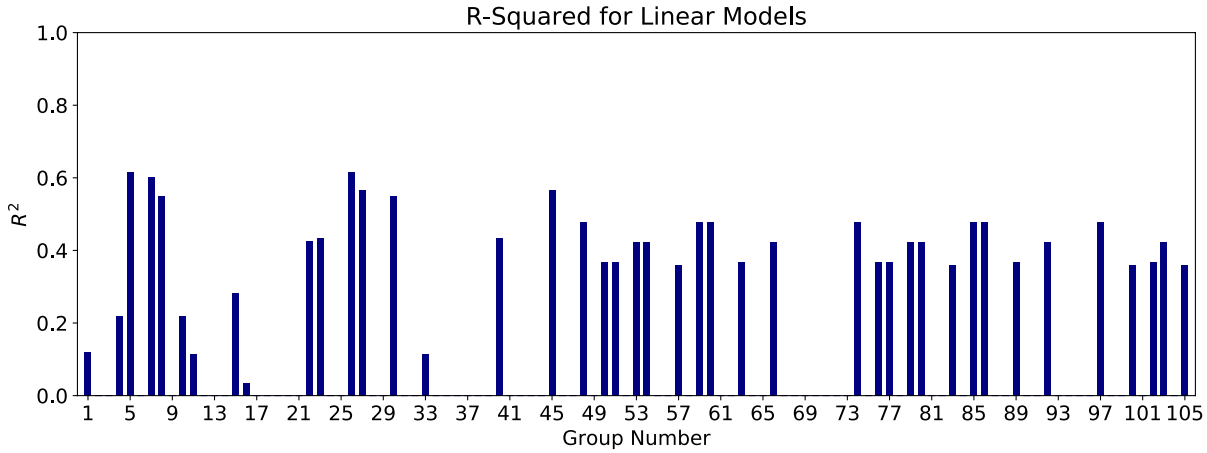

Figure 220. R^2 results for the "Linear Models" in HET/Coarse dataset – E_τ

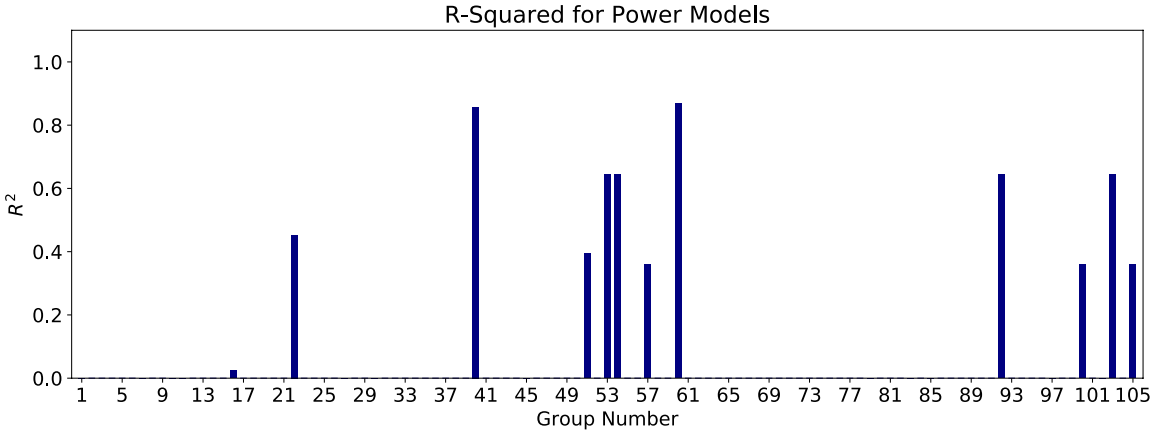

Figure 221. R^2 results for the "Power Models" in HET/Coarse dataset – E_τ

After passing through filters 1 and 2 (R^2 and MSE), "Power" models associated with groups 40 and 60 were selected for further analyses. "Linear" models did not lead to any better R^2 values; therefore, the study of best fitting models was limited to "Power" models.

Filter 3, F-value/F-stat, was determined for each group mentioned above. Table 66 shows the results of the selected "Power" models after meeting the requirements of the first three filters (R^2, MSE, and F-value/F-stat). The Group 40 correlation equations in "Power" form was selected as the most promising equation. Figure 222 shows the plot of "POO vs. θ" for this model. The

probability that the predicted E_τ using the selected model is greater than the actual E_τ, in percentage (with 10 mm/hr-Pa offset). In order to reach a 80% confidence that the predicted E_τ is greater than the actual E_τ, the predicted value should be multiplied by 2. As mentioned earlier, it is important to note that the equation associated with the Group 40 should be used for coarse-grained soils with D_{50} ranging between 0.074 mm and 0.3 mm.

Table 66. Selected "Power" models for E_τ in the HET/Coarse dataset

Group No.	Independent Variables	Model Expression	R^2	MSE	F-value/F-stat	Cross-Validation Score
40	γ, WC, PF, D50	$E_\tau = (2.951) \times \gamma^{26.08} \times WC^{-7.48} \times PF^{-19.96} \times D50^{-5.32}$	0.86	91.04	34.67	0.55
60	C_c, γ, WC, D50	$E_\tau = (4.4 \times 10^{-9}) \times C_c^{-3.11} \times \gamma^{26.08} \times WC^{-7.52} \times D50^{19.36}$	0.87	121.8	15.56	0.20

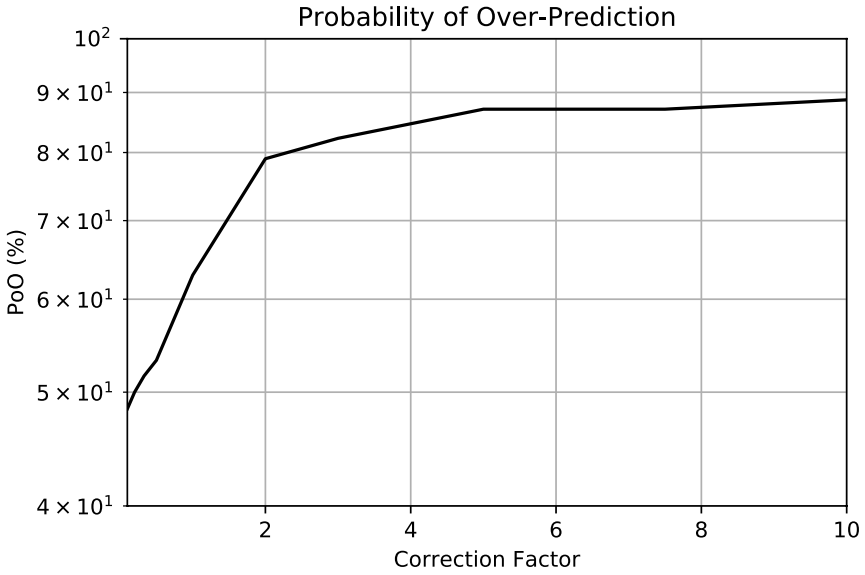

Figure 222. Plot of POO vs. correction factor for the Group 40 (Power) - E_τ in the HET/Coarse dataset

The same procedure was conducted in the HET/Global dataset (soils with D_{50} < 0.3 mm), and the best models are selected for E_τ. Figure 223 shows the number of data points in each of all the 135 combination groups in the HET/Global dataset. Also, Figure 224 and Figure 225 show the results of R^2 for each combination group, for the "Linear" and "Power" models, respectively. Figure 226 and Figure 227 show the results of the MSE for each of the 135 combination groups in the EFA/Fine dataset for "Power" and "Linear" models, respectively. As expected, the combination groups with better R^2 values possess a lower MSE value as well.

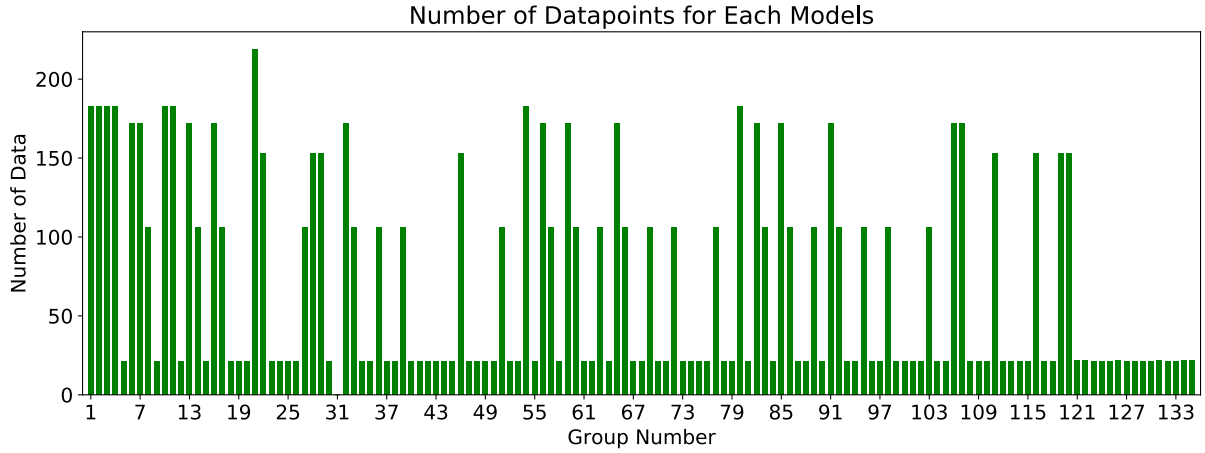

Figure 223. Number of data in each 135 combination groups for the HET/Global dataset – E_τ

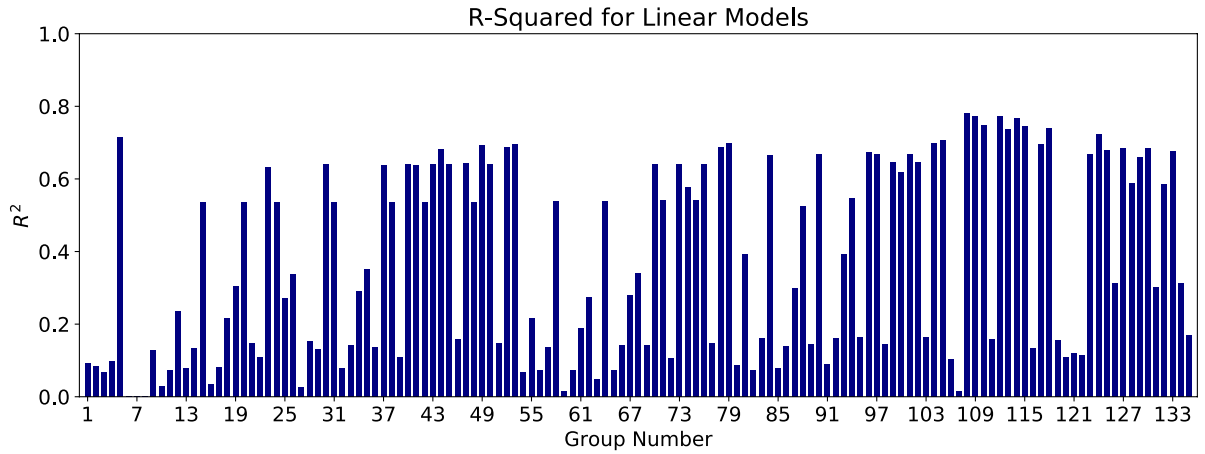

Figure 224. R^2 results for the "Linear Models" in HET/Global dataset – E_τ

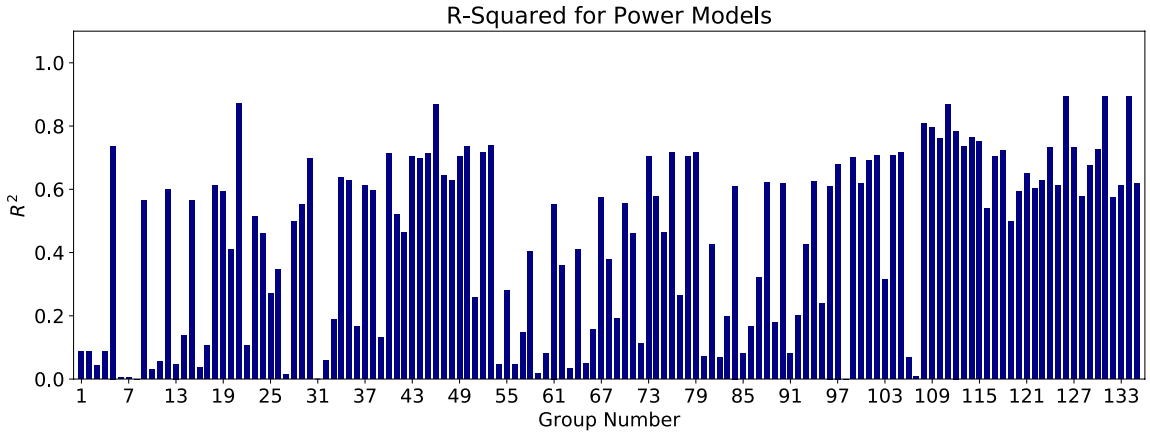

Figure 225. R^2 results for the "Power Models" in HET/Global dataset – E_τ

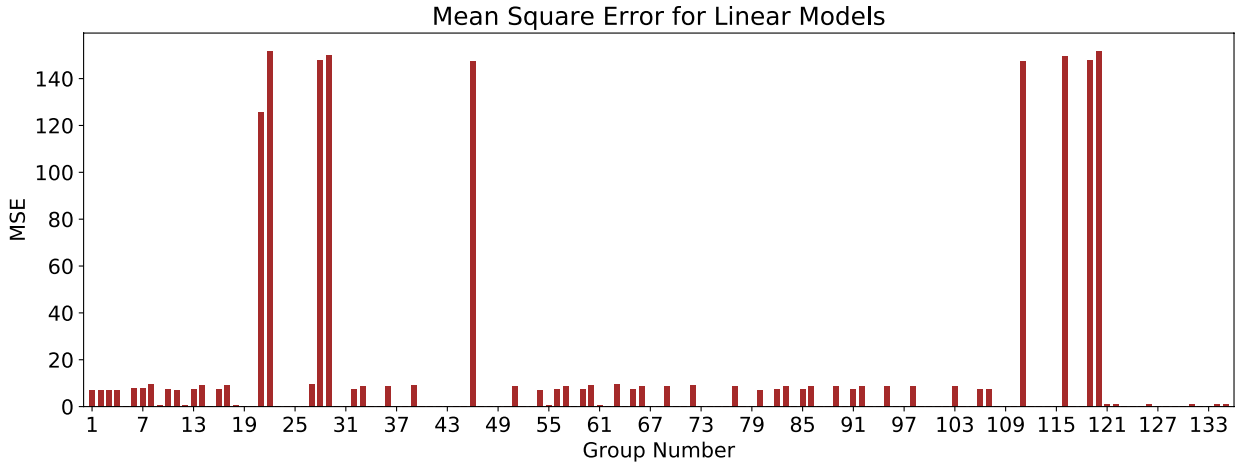

Figure 226. MSE results for the "Linear Models" in HET/Global dataset – E_τ

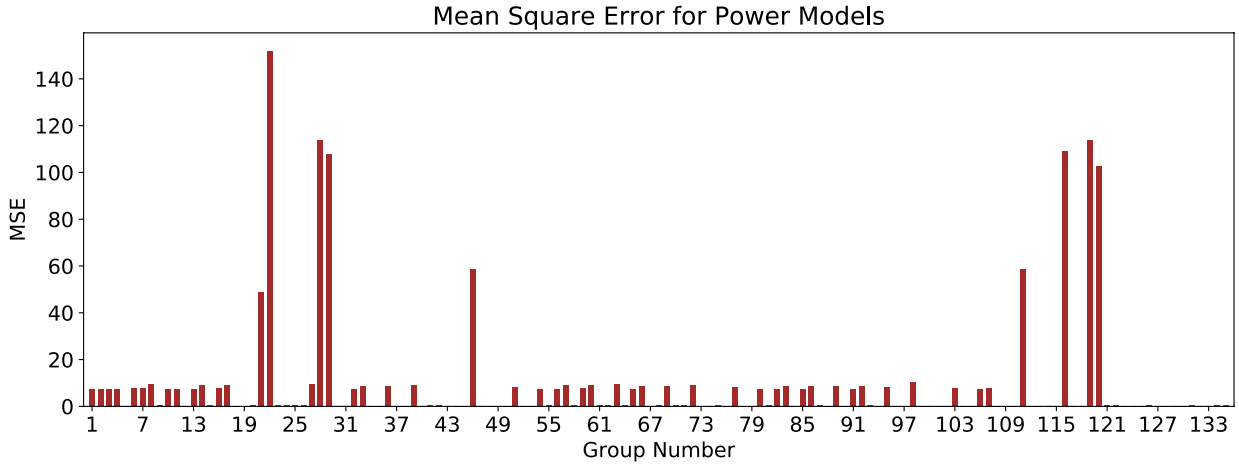

Figure 227. MSE results for the "Power Models" in HET/Global dataset – E_τ

After passing through filters 1 and 2 (R^2 and MSE), "Linear" models associated with groups 5, 49, 53, 78, 79, 104, 105, 108, 109, 110, 112, 113, 114, 115, 118, and 124 were selected for further analyses. Also "Power" models associated with groups 5, 49, 53, 79, 105, 108, 109, 110, 112, 114, 115, and 118 were selected for further analyses.

Filter 3, F-value/F-stat, was determined for each group mentioned above. Table 67 shows the results of the selected "Linear" models after meeting the requirements of the first three filters (R^2, MSE, and F-value/F-stat). As shown in Table 67, many of the selected models perform satisfactorily in the cross-validation test. Table 68 also shows the results of the selected "Power" models after meeting the requirements of the first three filters. The best models that also have a good cross-validation score are highlighted in blue in both "Linear" and "Power" forms. Out of all the highlighted correlation equations, the Group 108 equation in "Power" form was selected as the most promising equation. Figure 228 shows the plot of "POO vs. θ" for this model. The vertical axis in Figure 228 represent the probability that the predicted E_τ using the selected model is greater than the actual E_τ, in percentage (with 0 mm/hr-Pa offset). In order to reach a 90% confidence that the predicted E_τ is greater than the actual E_τ, the predicted value should be multiplied by 1.45. It is noteworthy that the equation associated with the combination group 108 in "Power" form is best to be used for finer-grained soils with D_{50} smaller than 0.3 mm.

Table 67. Selected "Linear" models for E_τ in the HET/Global dataset

Group No.	Independent Variables	Model Expression	R^2	MSE	F-value/F-stat	Cross-Validation Score
5	LL, PL, γ, WC, S_u	$E_\tau = -0.01 \times LL + 0.07 \times PL + 0.07 \times \gamma - 0.08 \times WC - 0.0045 \times S_u - 0.16$	0.71	0.26	2.581	0.37
49	γ, WC, S_u, PF, D50	$E_\tau = 0.061 \times \gamma - 0.06 \times WC - 0.004 \times S_u + 0.02 \times PF + 21.73 \times D50 - 1.33$	0.69	0.27	2.316	0.32
53	PI, γ, WC, S_u, PF, D50	$E_\tau = 0.001 \times PI + 0.05 \times \gamma - 0.07 \times WC - 0.004 \times S_u + 0.02 \times PF + 21.58 \times D50 - 1.18$	0.70	0.27	1.879	0.31
78	LL, WC, S_u, PF, D50	$E_\tau = 0.002 \times LL - 0.06 \times WC - 0.0036 \times S_u + 0.02 \times PF + 20.42 \times D50 - 0.17$	0.69	0.27	2.287	0.35
79	LL, γ, WC, S_u, PF, D50	$E_\tau = 0.001 \times LL + 0.054 \times \gamma - 0.07 \times WC - 0.004 \times S_u + 0.02 \times PF + 21.3 \times D50 - 1.16$	0.70	0.27	1.886	0.31
104	PL, WC, S_u, PF, D50	$E_\tau = 0.024 \times PL - 0.06 \times WC - 0.0035 \times S_u + 0.01 \times PF + 15.67 \times D50 + 0.09$	0.70	0.27	2.386	0.31
105	PL, γ, WC, S_u, PF, D50	$E_\tau = 0.023 \times PL + 0.054 \times \gamma - 0.07 \times WC - 0.004 \times S_u + 0.02 \times PF + 16.84 \times D50 - 0.91$	0.71	0.26	1.971	0.29
108	LL, PL, γ, PC, S_u	$E_\tau = -0.005 \times LL + 0.06 \times PL + 0.1 \times \gamma - 0.02 \times PC - 0.0001 \times S_u - 1.47$	0.78	0.23	3.697	0.52
109	PC, γ, WC, S_u, PF, D50	$E_\tau = -0.03 \times PC + 0.094 \times \gamma + 0.01 \times WC + 0.0003 \times S_u + 0.02 \times PF + 8.86 \times D50 - 2$	0.77	0.23	2.791	0.46
110	PC, WC, S_u, PF, D50	$E_\tau = -0.027 \times PC + 0.02 \times WC + 0.0008 \times S_u + 0.01 \times PF + 8.95 \times D50 - 0.32$	0.75	0.25	3.068	0.45
112	PC, γ, S_u, PF, D50	$E_\tau = -0.028 \times PC + 0.1 \times \gamma - 0.0003 \times S_u + 0.02 \times PF + 8.31 \times D50 - 1.86$	0.77	0.23	3.134	0.51
113	PC, γ, WC, S_u, D50	$E_\tau = -0.04 \times PC + 0.07 \times \gamma + 0.01 \times WC + 0.0004 \times S_u - 10.12 \times D50 + 0.26$	0.74	0.25	2.689	0.48
114	PC, γ, WC, S_u, PF	$E_\tau = -0.034 \times PC + 0.09 \times \gamma + 0.0045 \times WC - 0.00003 \times S_u + 0.01 \times PF - 1.35$	0.77	0.24	3.716	0.63
115	PC, S_u, PF, D50	$E_\tau = -0.023 \times PC - 0.0002 \times S_u + 0.01 \times PF + 8.08 \times D50 - 0.03$	0.75	0.25	3.679	0.51
118	PC, WC, S_u, PF	$E_\tau = -0.031 \times PC + 0.01 \times WC + 0.0004 \times S_u + 0.01 \times PF + 0.36$	0.74	0.25	3.608	0.62
124	γ, A, WC, S_u, PF, D50	$E_\tau = 0.045 \times \gamma + 0.09 \times A - 0.05 \times WC - 0.003 \times S_u + 0.02 \times PF + 19.41 \times D50 - 1.16$	0.72	0.26	3.009	0.27

Table 68. Selected "Power" models for E_τ in the HET/Global dataset

Group No.	Independent Variables	Model Expression	R^2	MSE	F-value/F-stat	Cross-Validation Score
5	LL, PL, γ, WC, S_u	$E_\tau = (3.96 \times 10^{-5}) \times LL^{-1.62} \times PL^{2.71} \times \gamma^{3.17} \times WC^{-0.42} \times S_u^{-0.15}$	0.74	0.25	8.578	0.21
49	γ, WC, S_u, PF, D50	$E_\tau = (4.1 \times 10^{-5}) \times \gamma^{1.19} \times WC^{-0.25} \times S_u^{-0.02} \times PF^{2.67} \times D50^{1.21}$	0.71	0.27	7.968	0.08
53	PI, γ, WC, S_u, PF, D50	$E_\tau = (10^{-5}) \times PI^{-0.4} \times \gamma^{2.11} \times WC^{0.16} \times S_u^{0.03} \times PF^{2.12} \times D50^{1.01}$	0.74	0.25	8.012	-1.53
79	LL, γ, WC, S_u, PF, D50	$E_\tau = (1.7 \times 10^{-5}) \times LL^{-0.61} \times \gamma^{1.52} \times WC^{0.11} \times S_u^{0.03} \times PF^{2.85} \times D50^{1.20}$	0.72	0.26	5.568	-0.16
105	PL, γ, WC, S_u, PF, D50	$E_\tau = (3.16 \times 10^{-4}) \times PL^{0.82} \times \gamma^{1.41} \times WC^{-0.58} \times S_u^{-0.08} \times PF^{1.63} \times D50^{1.04}$	0.72	0.26	5.960	-2.92
108	LL, PL, γ, PC, S_u	$E_\tau = (9 \times 10^{-6}) \times LL^{-0.35} \times PL^{1.59} \times \gamma^{3.3} \times PC^{-0.48} \times S_u^{-0.19}$	0.81	0.21	9.238	0.51
109	PC, γ, WC, S_u, PF, D50	$E_\tau = (4 \times 10^{-6}) \times PC^{-0.48} \times \gamma^{2.34} \times WC^{-.71} \times S_u^{0.08} \times PF^{1.52} \times D50^{0.71}$	0.80	0.22	5.466	0.32
110	PC, WC, S_u, PF, D50	$E_\tau = (0.006) \times PC^{-0.38} \times WC^{0.57} \times S_u^{0.15} \times PF^{1.40} \times D50^{0.7}$	0.76	0.24	8.259	0.48
112	PC, γ, S_u, PF, D50	$E_\tau = (8.5 \times 10^{-5}) \times PC^{-0.39} \times \gamma^{2.1} \times S_u^{-0.04} \times PF^{1.43} \times D50^{0.64}$	0.78	0.23	9.017	0.48
114	PC, γ, WC, S_u, PF	$E_\tau = (2 \times 10^{-5}) \times PC^{-0.66} \times \gamma^{2.28} \times WC^{0.43} \times S_u^{-0.06} \times PF^{0.97}$	0.76	0.24	8.881	-2.16
115	PC, S_u, PF, D50	$E_\tau = (0.031) \times PC^{-0.3} \times S_u^{0.02} \times PF^{1.41} \times D50^{0.67}$	0.75	0.24	6.363	0.34
118	PC, WC, S_u, PF	$E_\tau = (0.016) \times PC^{-0.56} \times WC^{0.37} \times S_u^{0.04} \times PF^{0.86}$	0.72	0.26	7.113	0.48
124	γ, A, WC, S_u, PF, D50	$E_\tau = (1.84 \times 10^{-4}) \times \gamma^{1.06} \times A^{0.26} \times WC^{-0.12} \times S_u^{-0.02} \times PF^{2.28} \times D50^{1.18}$	0.73	0.25	5.349	-0.24

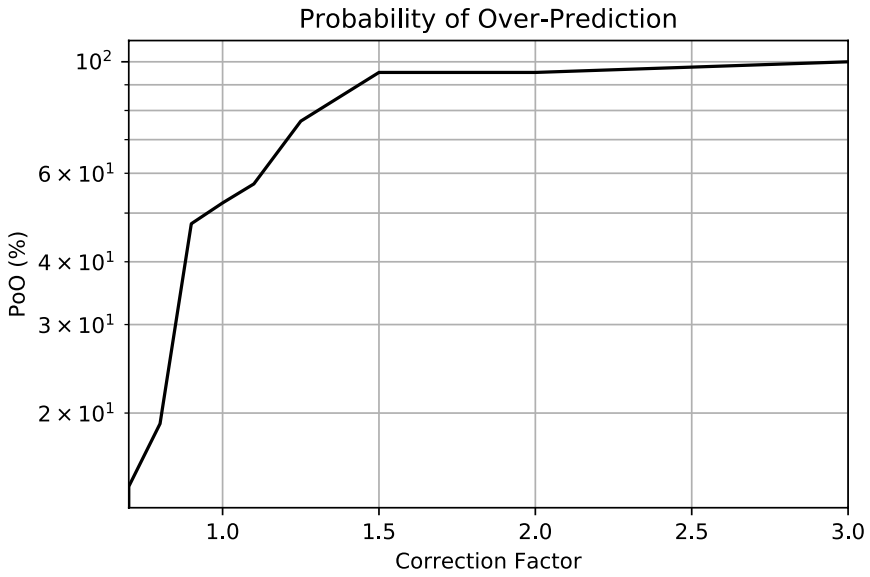

Figure 228. Plot of POO vs. correction factor for the Group 108 (Power) - E_τ in the HET/Global dataset

7.3.4.4.Initial Slope of Erosion Rate-Velocity (E_v)

The same four-filter process discussed in Section 7.3.3 is implemented in this section to obtain the best models for E_v. Similar to the case of critical velocity (v_c), among the three erosion tests studied in this Chapter (EFA, JET, HET), only the EFA test can reflect E_v as one of its outputs. In other words, results of JET and HET consist of only three erodibility parameters (i.e. τ_c, E_τ, and EC) in contrary with the EFA results which include all five erodibility parameters (i.e. τ_c, v_c, E_τ, E_v, and EC). Therefore, the study of regression analysis for E_v is limited to only the EFA dataset.

EFA Dataset

Similar to the case of E_τ, it was observed that dividing the EFA/Global dataset into the EFA/Fine and the EFA/Coarse datasets would significantly improve the regression results for E_v. Figure 229 shows the number of data points in each of all the 135 combination groups in the

EFA/Fine dataset. Figure 230 and Figure 231 show the results of R^2 for each combination group, for the "Linear Model" and "Power Model", respectively.

Results show that "Power" models in general perform better than the "Linear" models. Also, R^2 values of groups 109 to 135 are generally higher than the rest for both "Power" models. Figure 232 and Figure 233 show the results of the MSE for each of the 135 combination groups in the EFA/Fine dataset, for "Linear" and "Power" models, respectively.

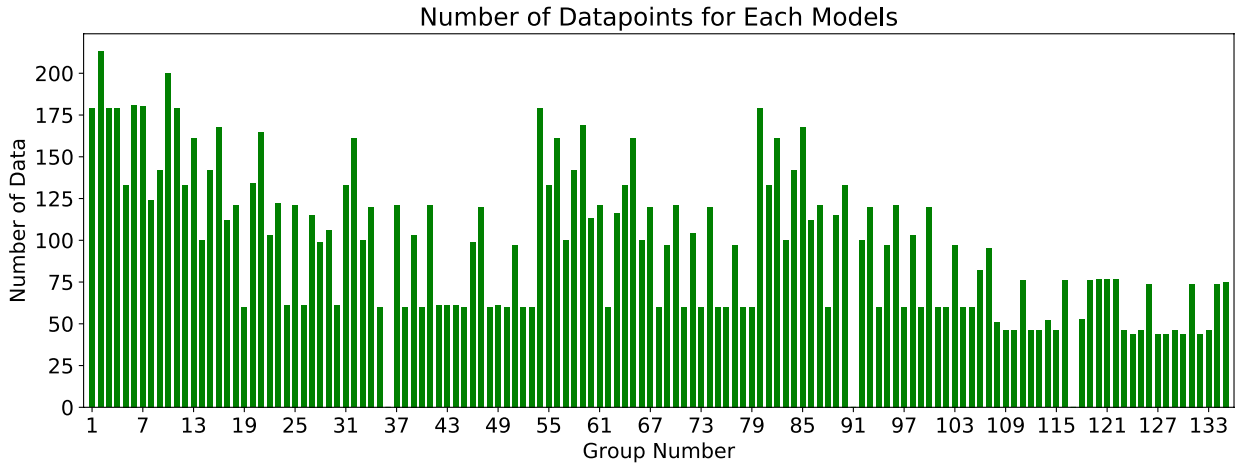

Figure 229. Number of data in each 135 combination groups for the EFA/Fine dataset – E_v

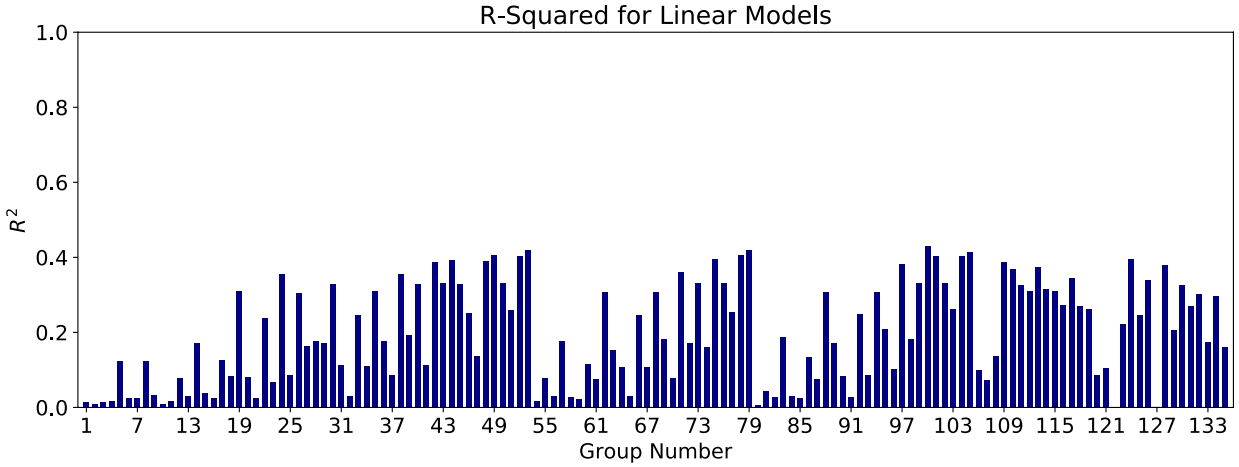

Figure 230. R^2 results for the "Linear Models" in EFA/Fine dataset – E_v

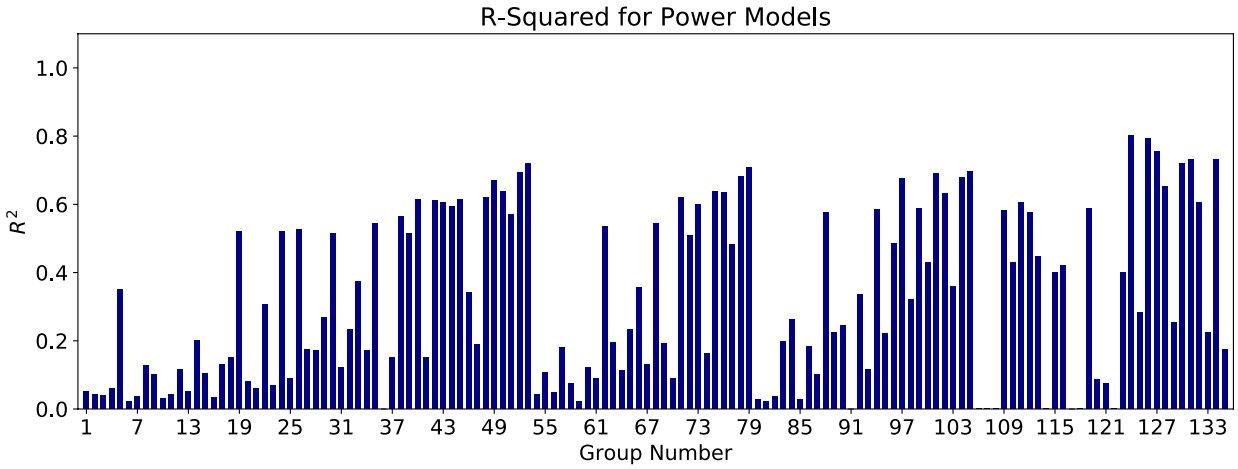

Figure 231. R^2 results for the "Power Models" in EFA/Fine dataset – E_v

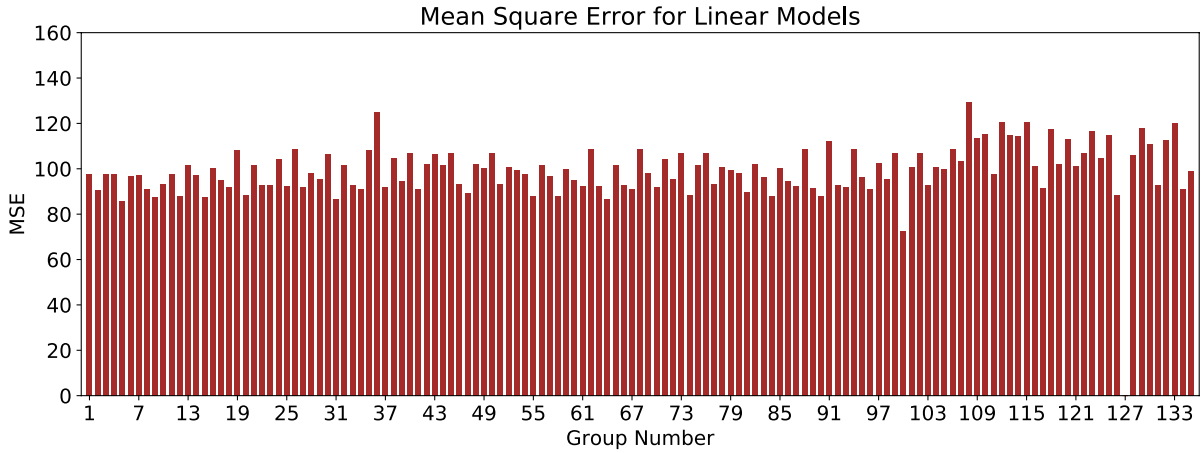

Figure 232. MSE results for the "Linear Models" in EFA/Fine dataset – E_v

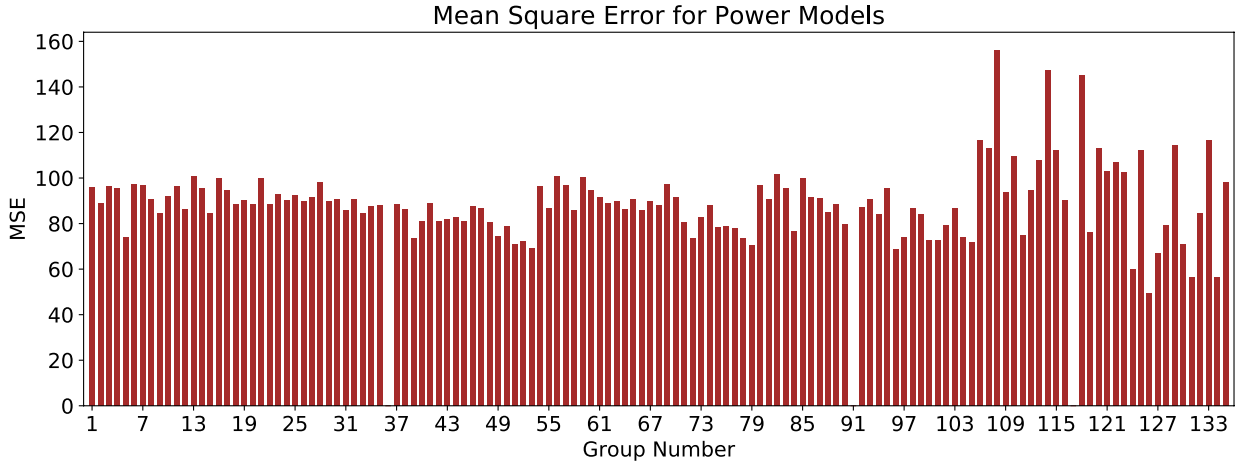

Figure 233. MSE results for the "Power Models" in EFA/Fine dataset – E_v

After passing through filters 1 and 2 (R^2 and MSE), "Power" models associated with groups 53, 79, 101, 105, 124, 126, 127, 131, and 134 were selected for further analyses. "Linear" models did not lead to any better R^2 values; therefore, the study of best fitting models was limited to "Power" models.

Filter 3, F-value/F-stat, was determined for each group mentioned above. Table 69 shows the results of the selected "Power" models after meeting the requirements of the first three filters (R^2, MSE, and F-value/F-stat). The Group 126 equations in "Power" form was selected as the most promising equation. Figure 234 shows the plot of "POO vs. θ" for this model. The probability that the predicted E_v using the selected model is greater than the actual E_v, in percentage (with 10 mm-s/m-hr offset). In order to reach a 80% confidence that the predicted E_v is greater than the actual E_v, the predicted value should be multiplied by 2.

Table 69. Selected "Power" models for E_v in the EFA/Fine dataset

Group No.	Independent Variables	Model Expression	R^2	MSE	F-value/F-stat	Cross-Validation Score
53	PI, γ, WC, S_u, PF, D50	$E_v = (9785577.4) \times PI^{0.61} \times \gamma^{-4.16} \times WC^{-1.62} \times S_u^{-0.54} \times PF^{4.04} \times D50^{3.45}$	0.72	69.2	324.6	-5.9
79	LL, γ, WC, S_u, PF, D50	$E_v = (142233608) \times LL^{0.92} \times \gamma^{-4.48} \times WC^{-1.42} \times S_u^{-0.38} \times PF^{2.83} \times D50^{3.30}$	0.71	70.6	320.1	-0.55
101	PL, γ, WC, S_u, D50	$E_v = (662947356) \times PL^{2.07} \times \gamma^{-2.93} \times WC^{-1.58} \times S_u^{-0.35} \times D50^{2.14}$	0.70	72.6	318.5	-0.43
105	PL, γ, WC, S_u, PF, D50	$E_v = (3.12869 \times 10^{10}) \times PL^{1} \times \gamma^{-5.09} \times WC^{-1.26} \times S_u^{-0.29} \times PF^{1.63} \times D50^{3.04}$	0.70	71.8	316.3	-0.05
124	γ, A, WC, S_u, PF, D50	$E_v = (1.4227 \times 10^{13}) \times \gamma^{-8.45} \times A^{0.04} \times WC^{-1.18} \times S_u^{-0.06} \times PF^{4.12} \times D50^{4.81}$	0.80	60.1	221.2	-2.33
126	D50, γ, WC, PF, A	$E_v = (1.682339 \times 10^{13}) \times D50^{5.10} \times \gamma^{-9.20} \times WC^{-1.13} \times PF^{4.69} \times A^{-0.01}$	0.79	49.5	384.3	0.52
127	D50, γ, S_u, PF, A	$E_v = (1.429 \times 10^{13}) \times D50^{6.09} \times \gamma^{-10.23} \times S_u^{0.58} \times PF^{4.79} \times A^{-0.4}$	0.75	66.8	361.5	0.4
131	D50, WC, PF, A	$E_v = (4610.15) \times D50^{28.67} \times WC^{0.52} \times PF^{18.36} \times A^{2.76}$	0.73	56.4	355.6	-0.98
134	A, γ, PF, D50	$E_v = (2.0788 \times 10^{13}) \times A^{-0.3} \times \gamma^{-9.71} \times PF^{4.48} \times D50^{5.61}$	0.73	56.3	329.9	0.05

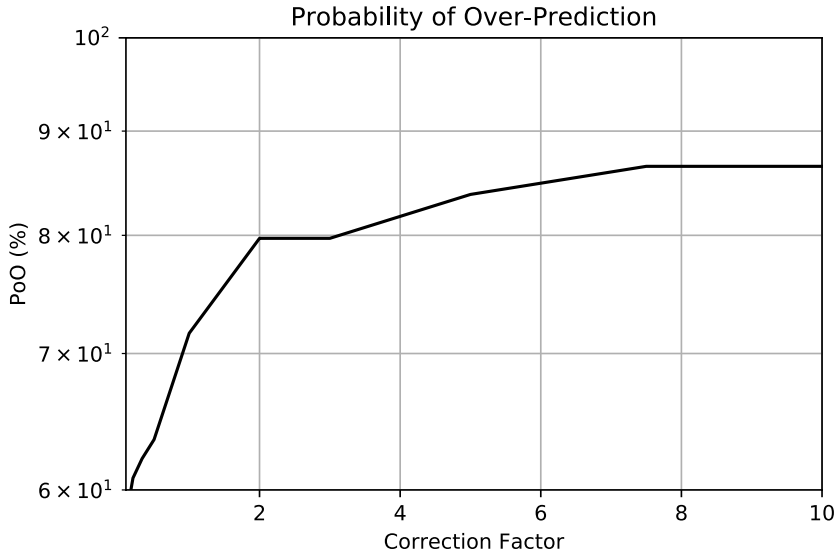

Figure 234. Plot of POO vs. correction factor for the Group 126 (Power) - E_v in the EFA/Fine dataset

The same procedure was conducted in the EFA/Coarse dataset, and the best models are selected for E_v. Figure 235 shows the number of data points in each of all the 105 combination groups in the EFA/Coarse dataset. Figure 236 and Figure 237 show the results of R^2 for each combination group, for the "Linear" and "Power" models, respectively.

Both "Linear" and "Power" models show some good groups in terms of R^2 values; however, as shown in Figure 235, the number of data points in most groups are very low.

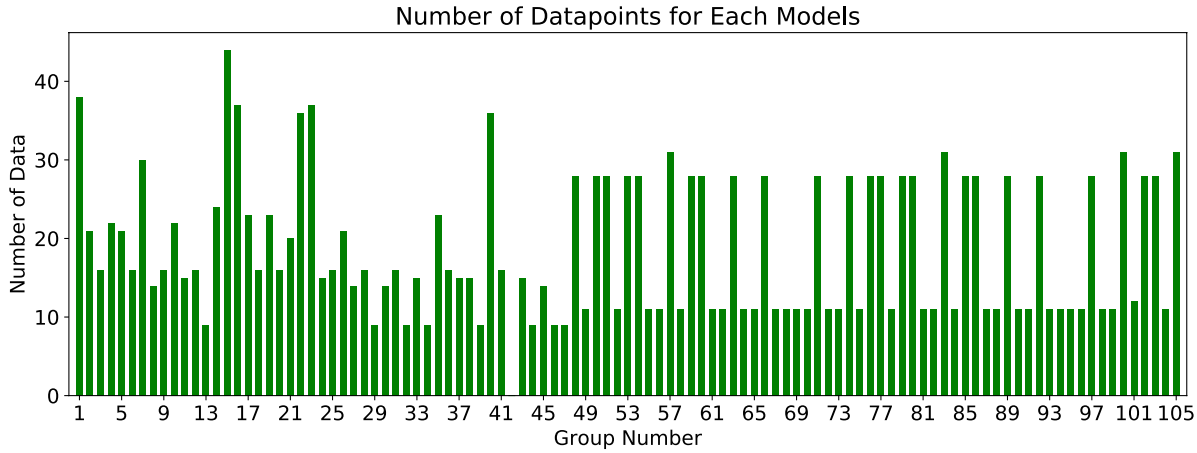

Figure 235. Number of data in each 105 combination groups for the EFA/Coarse dataset – E_v

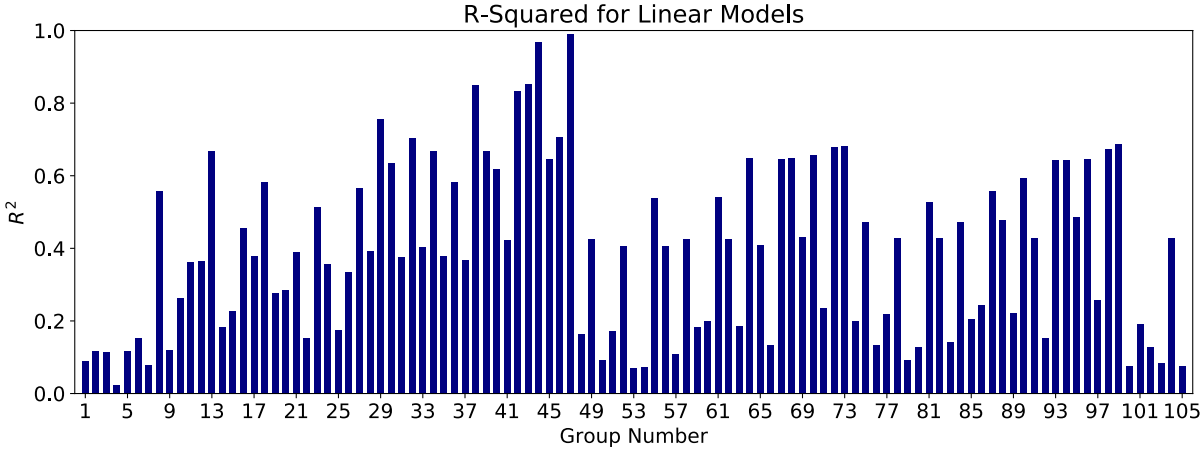

Figure 236. R^2 results for the "Linear Models" in EFA/Coarse dataset – E_v

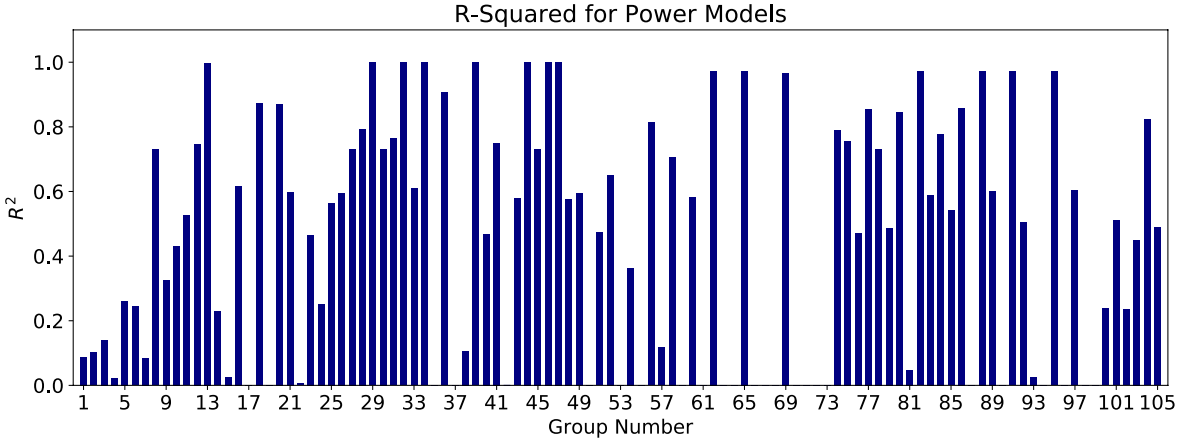

Figure 237. R^2 results for the "Power Models" in EFA/Coarse dataset – E_v

After passing through filters 1 and 2 (R^2 and MSE), "Linear" models associated with groups 38,42, 43, and 45 were selected for further analyses. Also "Power" models associated with groups 18, 20, 28, 34, 36, 44, 46, 56, 65, 74, 77, 80, 82, 86, and 88 were selected for further analyses.

Filter 3, F-value/F-stat, was determined for each group mentioned above. Table 70 shows the results of the selected "Linear" models after meeting the requirements of the first three filters (R^2, MSE, and F-value/F-stat). As shown in Table 70, none of the selected models perform satisfactorily in the cross-validation test. Table 71 also shows the results of the selected "Power" models after meeting the requirements of the first three filters. The Group 86 correlation equations in "Power" form was selected as the most promising equation. Figure 238 shows the plot of "POO vs. θ" for this model. The probability that the predicted E_v using the selected model is greater than the actual E_v, in percentage (with 10 mm-s/m-hr offset). In order to reach a 80% confidence that the predicted E_v is greater than the actual E_v, the predicted value should be multiplied by 5.

Table 70. Selected "Linear" models for E_v in the EFA/Coarse dataset

Group No.	Independent Variables	Model Expression	R^2	MSE	F-value/F-stat	Cross-Validation Score
38	WC, VST, PF, D50	$E_v = 101.665 \times WC + 4.65 \times VST - 55.46 \times PF - 85.9 \times D50 + 355.9$	0.85	643.1	5.46	-2.3
42	PI, γ, WC, VST, 50	$E_v = -4.543 \times PI - 35.21 \times \gamma - 9.16 \times WC - 2.03 \times VST + 1277.9 \times D50 + 901.4$	0.83	49.23	5.11	-4.6
43	γ, WC, VST, PF, D50	$E_v = -59.184 \times \gamma + 101.11 \times WC + 5.77 \times VST - 54.22 \times PF - 45 \times D50 + 1391$	0.85	635.7	2.09	-22.4
45	PI, γ, WC, PF, D50	$E_v = -6.62 \times PI - 48.82 \times \gamma - 2.92 \times WC - 10.46 \times PF + 216.18 \times D50 + 1497$	0.65	88.3	0.96	-0.03

Table 71. Selected "Power" models for E_v in the EFA/Coarse dataset

Group No.	Independent Variables	Model Expression	R^2	MSE	F-value/F-stat	Cross-Validation Score
18	WC, VST, D50	$E_v = (9280.99) \times WC^{-0.13} \times VST^{-2.35} \times D50^{-2.58}$	0.87	570	8.62	-2.8
20	VST, γ, D50	$E_v = (1481.13) \times VST^{-2.18} \times \gamma^{0.5} \times D50^{-2.36}$	0.87	577	8.40	-0.58
28	PI, γ, VST, PF	$E_v = (2.991 \times 10^{13}) \times PI^{-1.03} \times \gamma^{-5} \times VST^{0.48} \times PF^{-3.56}$	0.79	58.0	4.9	-0.7
34	PI, VST, PF, D50	$E_v = (805281.14 \times 10^{7}) \times PI^{-1.52} \times VST^{-0.42} \times PF^{-8.05} \times D50^{-2.93}$	0.99	4.85	0.93	-0.57
36	γ, WC, VST, D50	$E_v = (2 \times 10^{-5}) \times \gamma^{8.94} \times WC^{-1.11} \times VST^{-5.3} \times D50^{-5.08}$	0.91	491	8.8	-5.02
44	PI, γ, VST, PF, D50	$E_v = (820969.5 \times 10^{6}) \times PI^{-1.06} \times \gamma^{-3.54} \times VST^{-1.6} \times PF^{-2.2} \times D50^{1.15}$	0.99	2.02	0.89	0.82
46	PI, WC, VST, PF, D50	$E_v = (84388620) \times PI^{-0.73} \times WC^{1.28} \times VST^{-1.6} \times PF^{-1.63} \times D50^{2.76}$	0.99	3.21	0.91	-0.51
56	C_c, VST, D50	$E_v = (5401.92) \times C_c^{-1.54} \times VST^{-3.54} \times D50^{-4.73}$	0.81	399	2.98	-0.25
65	C_c, WC, VST, D50	$E_v = (10199544.5) \times C_c^{-5.65} \times WC^{4.51} \times VST^{-31.3} \times D50^{-35.32}$	0.97	155.6	13.4	-1.98
74	C_u, γ, WC	$E_v = (23300967450) \times C_u^{-1.32} \times \gamma^{-7.26} \times WC^{2.04}$	0.79	389.2	9.9	0.29
77	C_u, γ, D50	$E_v = (4489.56) \times C_u^{-2.97} \times \gamma^{-1.18} \times D50^{-2.25}$	0.86	323.5	19.2	0.37
80	C_u, WC, D50	$E_v = (152.16) \times C_u^{-2.53} \times WC^{-0.32} \times D50^{-2.92}$	0.85	324	17.9	0.01
82	C_u, VST, D50	$E_v = (95.18) \times C_u^{-13.21} \times VST^{-20.14} \times D50^{-37.13}$	0.97	155.9	21.7	0.03
86	C_u, γ, WC, D50	$E_v = (88969.4) \times C_u^{-1.77} \times \gamma^{-2.26} \times WC^{0.34} \times D50^{-1.69}$	0.86	319.4	15.9	0.64
88	C_u, γ, VST, D50	$E_v = (7.6 \times 10^{-5}) \times C_u^{-3.28} \times \gamma^{7.23} \times VST^{-14.04} \times D50^{-20.09}$	0.97	155.6	13.43	-1.28

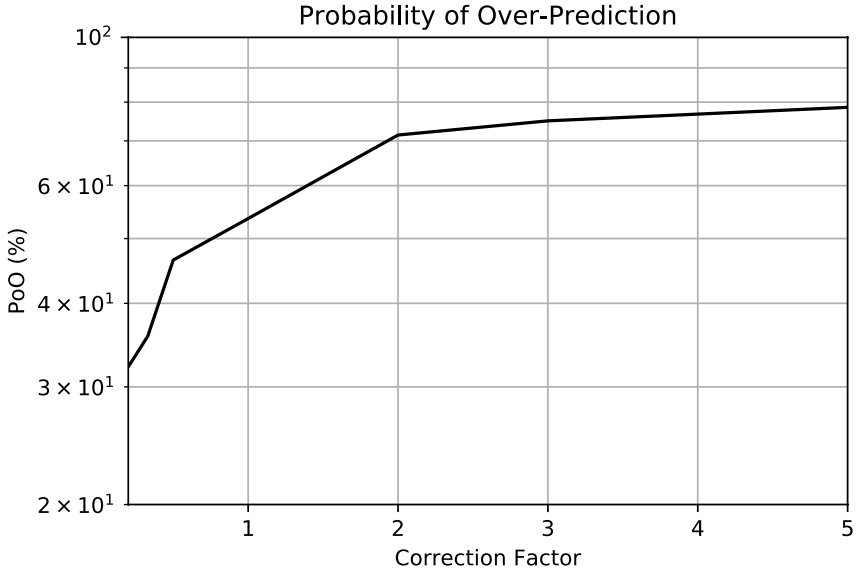

Figure 238. Plot of POO vs. correction factor for the Group 86 (Power) - E_v in the EFA/Coarse dataset

7.3.4.5.Erosion Category (EC)

The same four-filter process discussed in Section 7.3.3 is implemented in this section to obtain the best models for erosion category (EC). The study of regression analysis for EC is performed in three different sections for the EFA, HET, and JET separately.

EFA Database

It was observed that dividing the EFA/Global dataset into the EFA/Fine and the EFA/Coarse datasets would improve the regression results. Figure 239 shows the number of data points in each of all the 135 combination groups in the EFA/Fine dataset. Figure 240 and Figure 241 show the results of R^2 for each combination group, for the "Linear" and "Power" models, respectively.

R^2 values for both "Linear" and "Power" models are not very high (up to 0.6). Also, it can be observed that the better R^2 values are observed in the combination groups 109 to 135. Figure 242 and Figure 243 show the results of the MSE for each of the 135 combination groups in the EFA/Fine dataset, for "Linear" and "Power" models, respectively. It is observed that in general, "Power" and "Linear" models are not noticeably different.

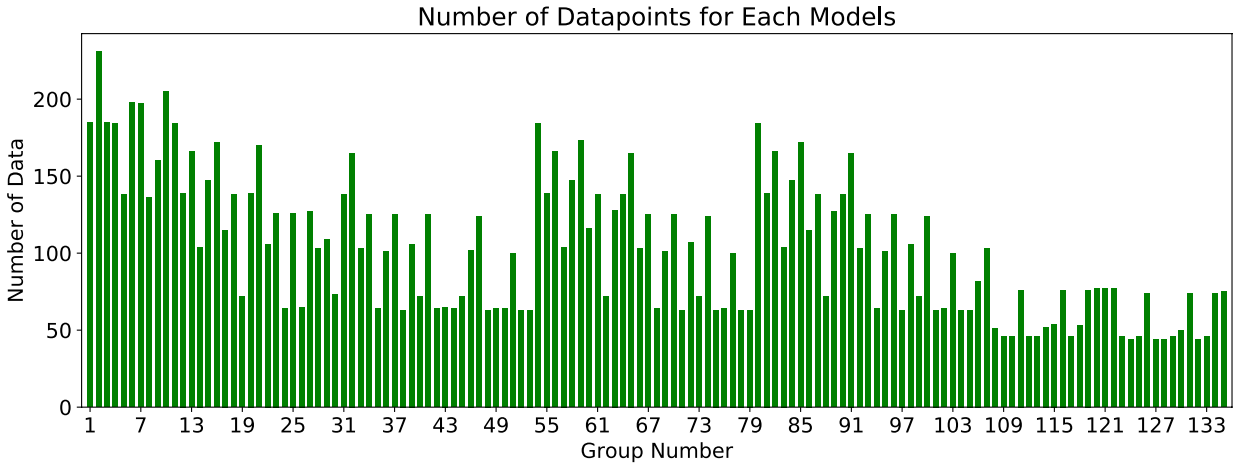

Figure 239. Number of data in each 135 combination groups for the EFA/Fine dataset – EC

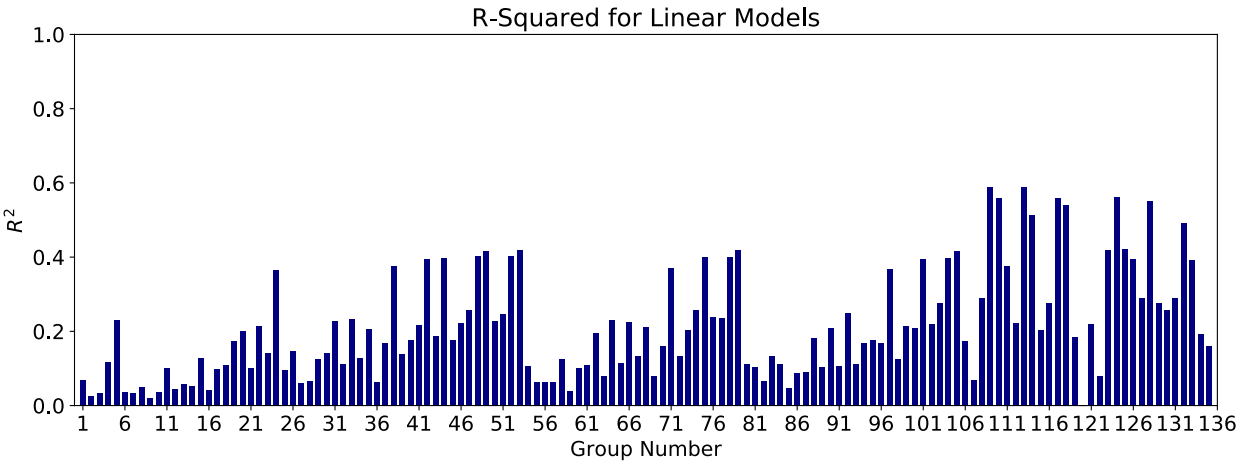

Figure 240. R^2 results for the "Linear Models" in EFA/Fine dataset – EC

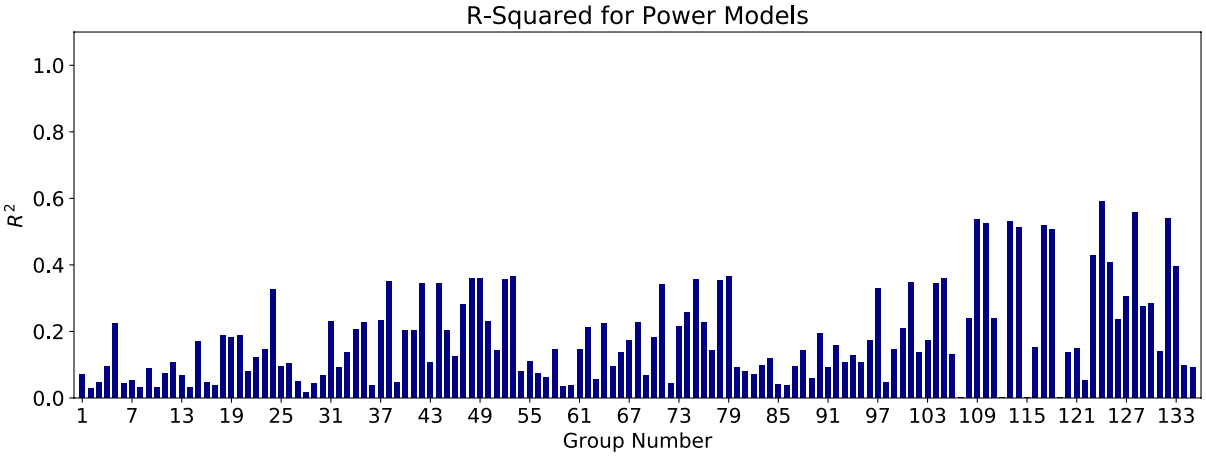

Figure 241. R^2 results for the "Power Models" in EFA/Fine dataset – EC

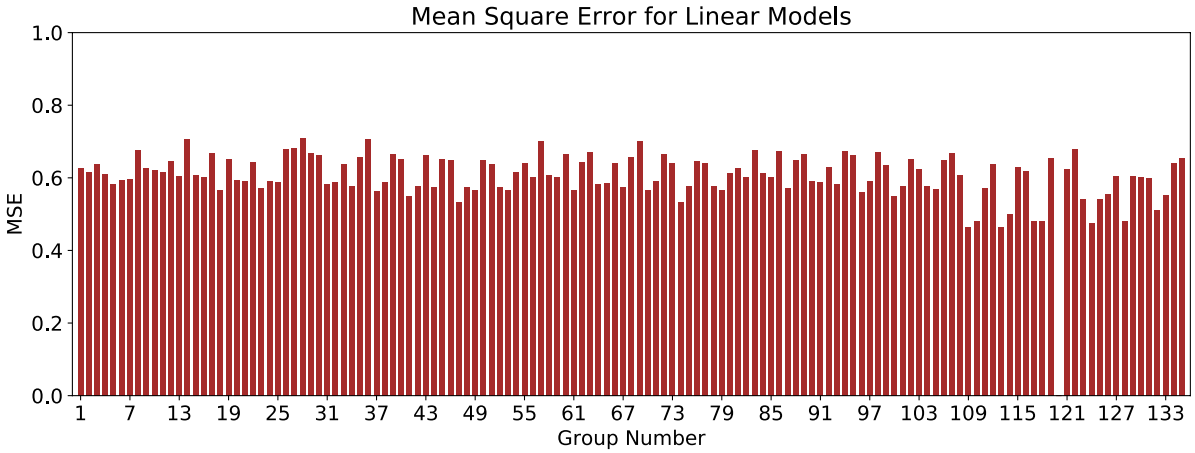

Figure 242. MSE results for the "Linear Models" in EFA/Fine dataset – EC

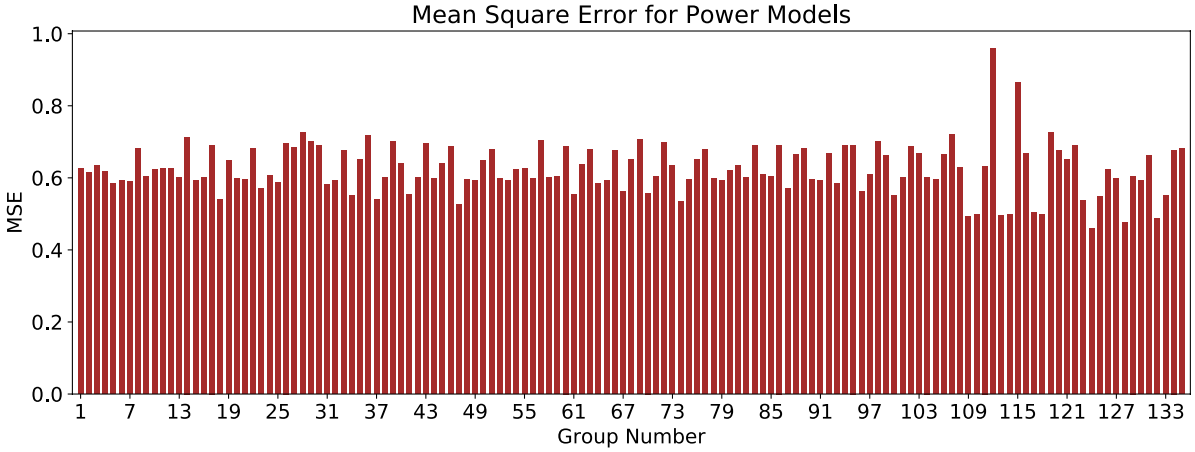

Figure 243. MSE results for the "Power Models" in EFA/Fine dataset – EC

After passing through filters 1 and 2 (R^2 and MSE), "Linear" models associated with groups 109, 110, 113, 117, and 124 were selected for further analyses. Also "Power" models associated with groups 124, 128, and 132 were selected for further analyses.

Filter 3, F-value/F-stat, was determined for each group mentioned above. Table 72 shows the results of the selected "Linear" models after meeting the requirements of the first three filters (R^2, MSE, and F-value/F-stat). As shown in Table 72, most of the selected models perform satisfactorily in the cross-validation test. Table 73 also shows the results of the selected "Power"

models after meeting the requirements of the first three filters. The Group 132 correlation equations in "Power" form was selected as the most promising equation. Figure 244 shows the plot of "POU vs. θ" for this model. The probability that the predicted EC using the selected model is smaller than the actual EC, in percentage. In order to reach a 90% confidence that the predicted EC is smaller than the actual EC, the predicted value should be multiplied by 0.75.

Table 72. Selected "Linear" models for EC in the EFA/Fine dataset

Group No.	Independent Variables	Model Expression	R^2	MSE	F-value/F-stat	Cross-Validation Score
109	PC, γ, WC, S_u, PF, D50	$EC = 0.02 \times PC + 0.112 \times \gamma + 0.04 \times WC + 0.0005 \times S_u + 0.0012 \times PF - 3.09 \times D50 - 1.27$	0.59	0.47	3.96	0.33
110	PC, WC, S_u, PF, D50	$EC = 0.022 \times PC + 0.03 \times WC + 0.0016 \times S_u - 0.0029 \times PF - 3.85 \times D50 + 1.2$	0.56	0.48	4.13	0.35
113	PC, γ, WC, S_u, D50	$EC = 0.02 \times PC + 0.11 \times \gamma + 0.04 \times WC + 0.0005 \times S_u - 3.853 \times D50 - 1.088$	0.59	0.46	4.64	0.43
117	PC, WC, S_u, D50	$EC = 0.023 \times PC + 0.03 \times WC + 0.0017 \times S_u - 1.845 \times D50 + 0.8566$	0.56	0.48	4.97	0.43
124	γ, A, WC, S_u, PF, D50	$EC = 0.125 \times \gamma - 0.072 \times A + 0.04 \times WC + 0.0001 \times S_u - 0.0086 \times PF - 16.12 \times D50 + 0.259$	0.56	0.47	3.34	0.33

Table 73. Selected "Power" models for EC in the EFA/Fine dataset

Group No.	Independent Variables	Model Expression	R^2	MSE	F-value/F-stat	Cross-Validation Score
124	γ, A, WC, S_u, PF, D50	$EC = (0.193) \times \gamma^{0.53} \times A^{-0.07} \times WC^{0.64} \times S_u^{0.08} \times PF^{-0.47} \times D50^{-0.16}$	0.59	0.46	6.09	0.58
128	D50, γ, WC, S_u, A	$EC = (0.0237) \times D50^{-0.11} \times \gamma^{0.65} \times WC^{0.59} \times S_u^{0.08} \times A^{-0.06}$	0.56	0.48	8.23	0.53
132	A, WC, S_u, D50	$EC = (0.1933) \times A^{-0.06} \times WC^{0.51} \times S_u^{0.09} \times D50^{-0.12}$	0.55	0.49	7.99	0.53

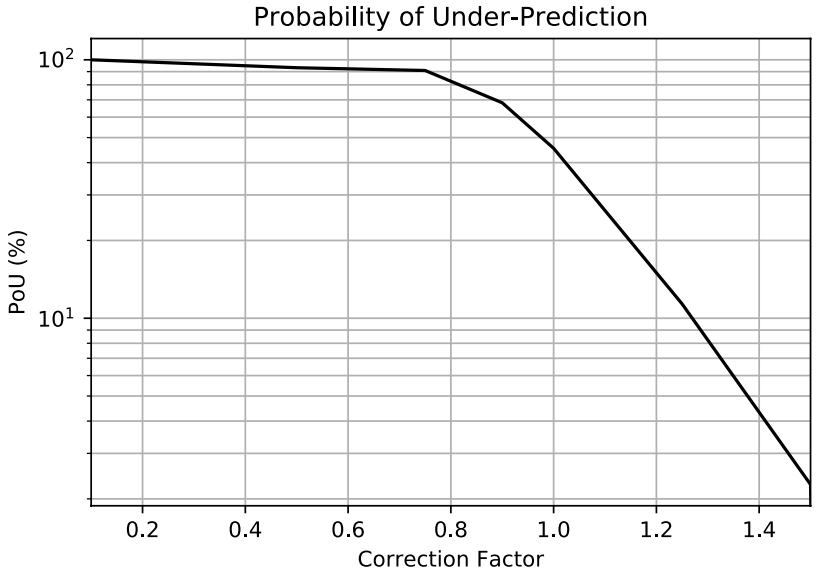

Figure 244. Plot of POU vs. correction factor for the Group 132 (Power) - EC in the EFA/Fine dataset

The same procedure was conducted in the EFA/Coarse dataset, and the best models are selected for EC. Figure 245 shows the number of data points in each of all the 105 combination groups in the EFA/Coarse dataset. Figure 246 and Figure 247 show the results of R^2 for each combination group, for the "Linear" and "Power" models, respectively. Both "Linear" and "Power" models show some good groups in terms of R^2 values; however, as shown in Figure 245, the number of data points are very low in many combination groups.

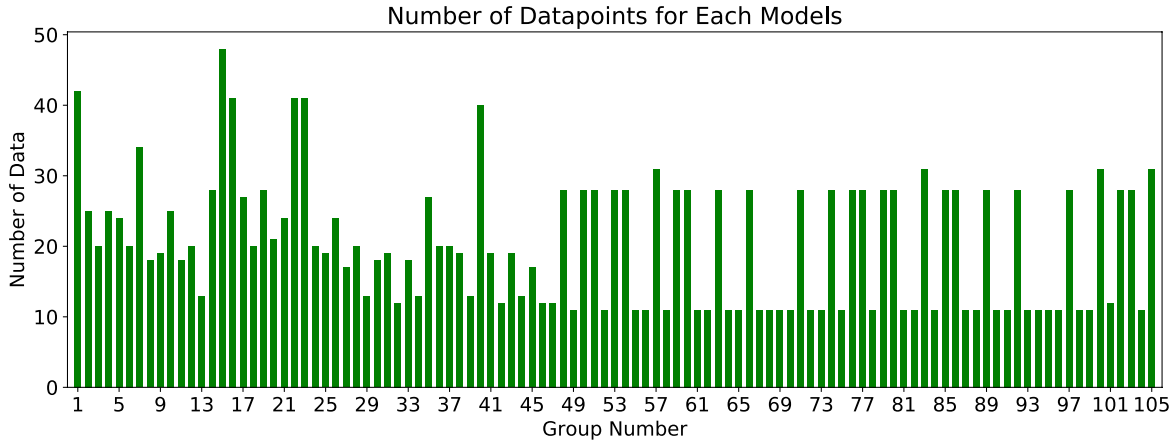

Figure 245. Number of data in each 105 combination groups for the EFA/Coarse dataset – EC

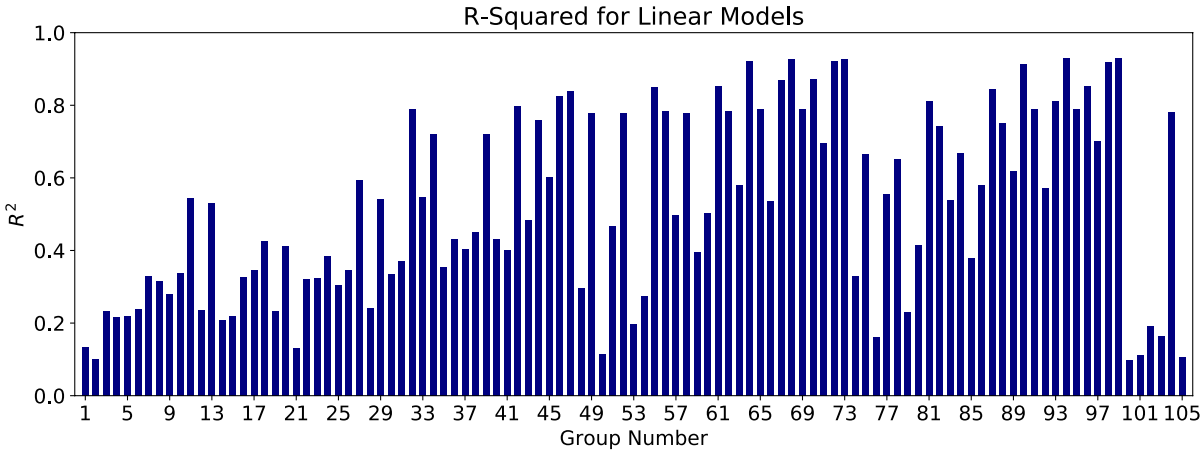

Figure 246. R^2 results for the "Linear Models" in EFA/Coarse dataset – EC

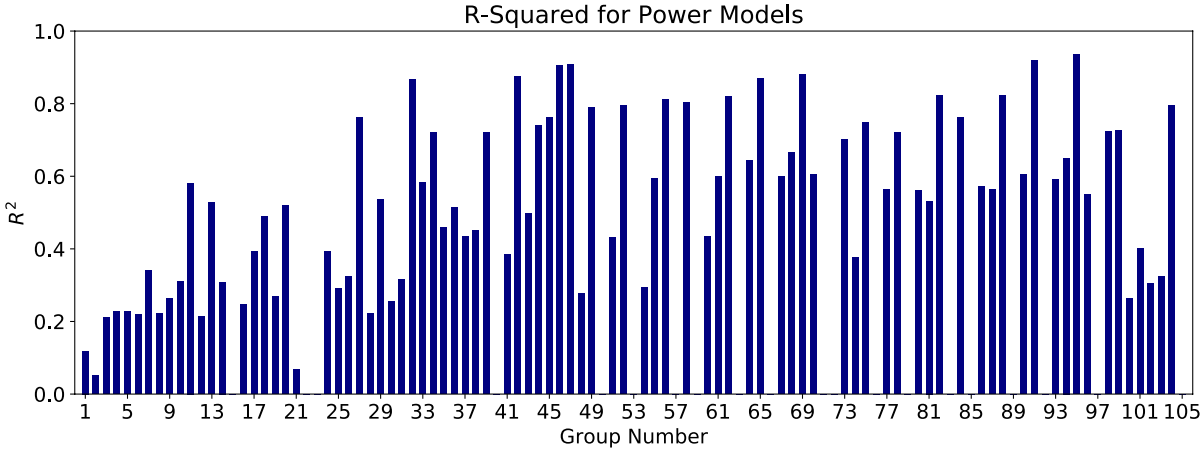

Figure 247. R^2 results for the "Power Models" in EFA/Coarse dataset – EC

After passing through filters 1 and 2 (R^2 and MSE), "Linear" models associated with groups 42, 46, 47, 55, 61, 64, 67, 68, 70, 72, 73, 87, 90, 94, 98, and 99 were selected for further analyses. Also "Power" models associated with groups 32, 42, 46, 47, 65, 69, 91, and 95 were selected for further analyses.

Filter 3, F-value/F-stat, was determined for each group mentioned above. Table 74 shows the results of the selected "Linear" models after meeting the requirements of the first three filters (R^2, MSE, and F-value/F-stat). Table 75 also shows the results of the selected "Power" models after meeting the requirements of the first three filters. The Group 91 correlation equations in "Power" form was selected as the most promising equation. Figure 248 shows the plot of "POU vs. θ" for this model. The probability that the predicted EC using the selected model is smaller than the actual EC, in percentage. In order to reach a 90% confidence that the predicted EC is smaller than the actual EC, the predicted value should be multiplied by 0.84. It is also noteworthy that the equation associated with the Group 91 combination group is best to be used for soils with D_{50} ranging between 0.074 and 0.3 mm.

Table 74. Selected "Linear" models for EC in the EFA/Coarse dataset

Group No.	Independent Variables	Model Expression	R^2	MSE	F-value/F-stat	Cross-Validation Score
42	PI, γ, WC, VST, D50	$EC = 0.02 \times PI - 0.03 \times \gamma - 0.02 \times WC + 0.0027 \times VST - 5.586 \times D50 + 3.917$	0.80	0.27	0.93	0.08
46	PI, WC, VST, PF, D50	$EC = 0.017 \times PI - 0.01 \times WC + 0.0049 \times VST - 0.023 \times PF - 7.27 \times D50 + 4.01$	0.82	0.25	1.11	-0.5
47	PI, γ, WC, VST, PF, D50	$EC = 0.014 \times PI - 0.05 \times \gamma - 0.01 \times WC + 0.006 \times VST - 0.027 \times PF - 7.36 \times D50 + 5.231$	0.84	0.24	0.70	-2.12
55	C_c, VST, PF	$EC = -0.01 \times C_c + 0.0094 \times VST + 0.0137 \times PF + 1.105$	0.85	0.24	2.78	0.33
61	C_c, γ, VST, PF	$EC = -0.009 \times C_c - 0.02 \times \gamma + 0.0095 \times VST + 0.0145 \times PF + 1.458$	0.85	0.24	1.68	0.01
64	C_c, γ, PF, D50	$EC = -0.0047 \times C_c - 0.03 \times WC + 0.0031 \times VST + 0.028 \times PF + 1.524$	0.92	0.18	1.59	0.55
67	C_c, VST, PF, D50	$EC = -0.015 \times C_c + 0.0092 \times VST + 0.02 \times PF + 2.69 \times D50 + 0.534$	0.87	0.23	1.94	-0.16
68	C_c, γ, WC, VST, PF	$EC = -0.003 \times C_c - 0.03 \times \gamma - 0.03 \times WC + 0.0032 \times VST + 0.03 \times PF + 1.995$	0.93	0.17	2.00	0.61
70	C_c, γ, VST, PF, D50	$Ec = -0.014 \times C_c - 0.01 \times \gamma + 0.0092 \times VST + 0.021 \times PF + 2.578 \times D50 + 0.75$	0.87	0.22	1.07	-0.5
72	C_c, WC, VST, PF, D50	$EC = -0.0041 \times C_c - 0.04 \times WC + 0.003 \times VST + 0.028 \times PF - 0.23 \times D50 + 1.58$	0.92	0.18	1.85	-0.13
73	C_c, γ, WC, VST, PF, D50	$EC = -0.0009 \times C_c - 0.03 \times \gamma - 0.04 \times WC + 0.0027 \times VST + 0.029 \times PF - 0.74 \times D50 + 2.24$	0.93	0.17	0.94	0.14
87	C_u, γ, VST, PF	$EC = -0.001 \times C_u - 0.07 \times \gamma + 0.01 \times VST + 0.02 \times PF + 2.2$	0.84	0.25	1.56	-0.76
90	C_u, WC, VST, PF	$EC = -0.0001 \times C_u - 0.04 \times WC + 0.0015 \times VST + 0.032 \times PF + 1.55$	0.91	0.18	3.04	0.27
94	C_u, γ, WC, VST, PF	$Ec = -0.0005 \times C_u - 0.047 \times \gamma - 0.036 \times WC + 0.004 \times VST + 0.032 \times PF + 2.338$	0.93	0.17	2.10	0.35
98	C_u, WC, VST, PF, D50	$EC = 0.00006 \times C_u - 0.04 \times WC + 0.002 \times VST + 0.029 \times PF - 1.2 \times D50 + 1.85$	0.92	0.18	1.79	0.14
99	C_u, γ, WC, VST, PF, D50	$EC = -0.0004 \times C_u - 0.044 \times \gamma - 0.036 \times WC + 0.003 \times VST + 0.031 \times PF - 0.32 \times D50 + 2.37$	0.93	0.17	0.98	-1.55

Table 75. Selected "Power" models for EC in the EFA/Coarse dataset

Group No.	Independent Variables	Model Expression	R^2	MSE	F-value/F-stat	Cross-Validation Score
32	PI, WC, VST, D50	$EC = (0.722) \times PI^{0.21} \times WC^{-0.16} \times VST^{0.05} \times D50^{-0.5}$ $for\ 0.074 < D50 < 0.3$	0.87	0.22	40.8	0.49
42	PI, γ, WC, VST, D50	$EC = (0.1685) \times PI^{0.24} \times \gamma^{0.42} \times WC^{-0.13} \times VST^{0.05} \times D50^{-0.53}$ $for\ 0.074 < D50 < 0.3$	0.87	0.21	27.5	0.54
46	PI, WC, VST, PF, D50	$EC = (1.055) \times PI^{0.15} \times WC^{-0.04} \times VST^{0.17} \times PF^{-0.36} \times D50^{-0.61}$ $for\ 0.074 < D50 < 0.3$	0.90	0.19	36.2	0.22
47	PI, γ, WC, VST, PF, D50	$EC = (0.44) \times PI^{0.17} \times \gamma^{0.26} \times WC^{-0.04} \times VST^{0.16} \times PF^{-0.34} \times D50^{-0.62}$ $for\ 0.074 < D50 < 0.3$	0.91	0.18	21.8	-0.16
65	C_c, WC, VST, D50	$EC = (0.7423) \times C_c^{0.03} \times WC^{-0.25} \times VST^{0.21} \times D50^{-0.41}$ $for\ 0.074 < D50 < 0.3$	0.87	0.23	18.1	0.65
69	C_c, γ, WC, VST, D50	$EC = (2.22) \times C_c^{0.04} \times \gamma^{-0.41} \times WC^{-0.24} \times VST^{0.24} \times D50^{-0.4}$	0.88	0.22	11.3	-0.08
91	C_u, WC, VST, D50	$EC = (1.12) \times C_u^{0.1} \times WC^{-0.28} \times VST^{0.02} \times D50^{-0.44}$ $for\ 0.074 < D50 < 0.3$	0.92	0.18	29.9	0.80
95	C_u, γ, WC, VST, D50	$EC = (0.222) \times C_u^{0.17} \times \gamma^{0.72} \times WC^{-0.36} \times VST^{-0.17} \times D50^{-0.54}$ $for\ 0.074 < D50 < 0.3$	0.94	0.16	21.2	0.79

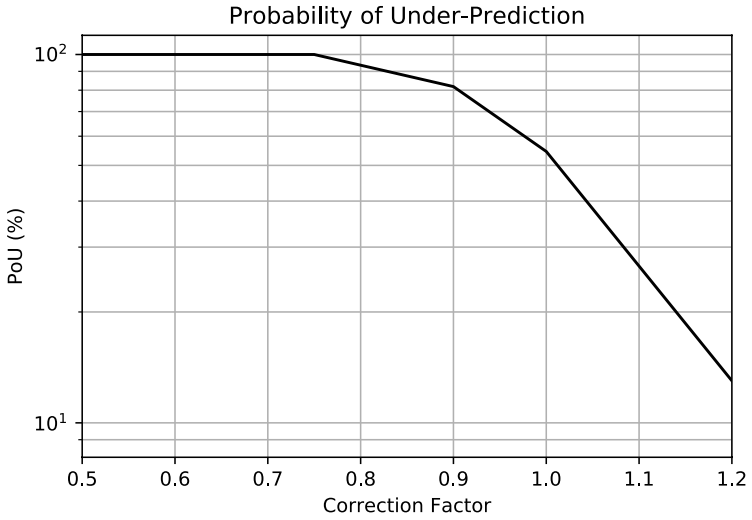

Figure 248. Plot of POU vs. correction factor for the Group 91 (Power) - EC in the EFA/Coarse dataset

JET Dataset

Similar approach was taken to select the best correlating equation for EC in the JET database. On the JET database, there are two important observations to notice:

1) The JET was primarily performed on the finer soils (D_{50} < 0.3 mm), and therefore, the number of data points in the JET/Coarse dataset are substantially low compared to the JET/Fine dataset. In fact, many combination groups on the JET/Coarse database have zero data points.
2) The R^2 values for the JET/Global dataset (D50 < 0.3 mm) are significantly better than the R^2 values for the JET/Coarse and JET/Fine dataset. Therefore, the regression results for the JET/Global dataset are presented as the best models.

Figure 249 shows the number of data points in each of all the 135 combination groups in the JET/Global dataset. Figure 250 and Figure 251 show the results of R^2 for each combination group, for the "Linear" and "Power" models, respectively. Both "Linear" and "Power" models show some reasonable groups in terms of R^2 values.

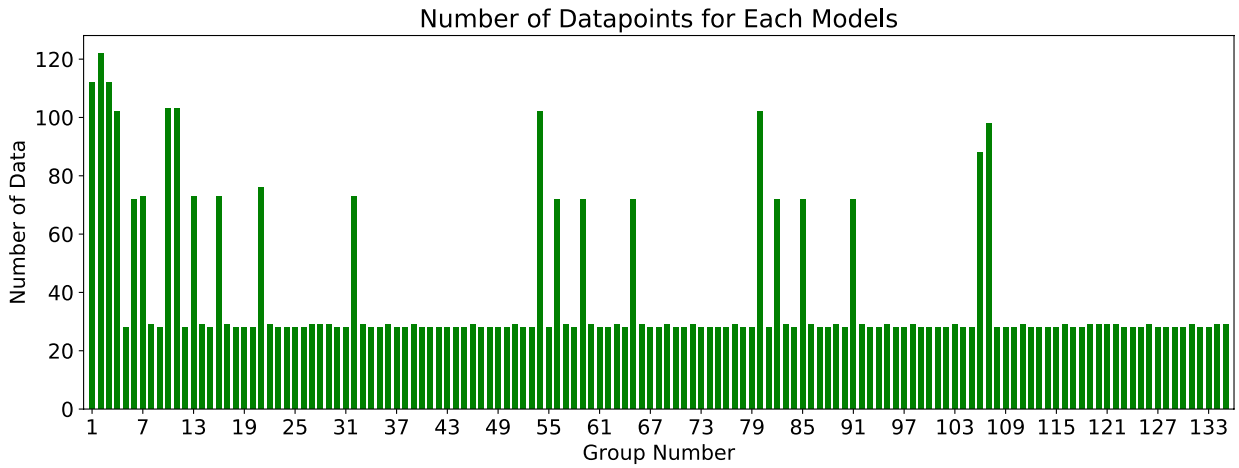

Figure 249. Number of data in each 135 combination groups for the JET/Global dataset – EC

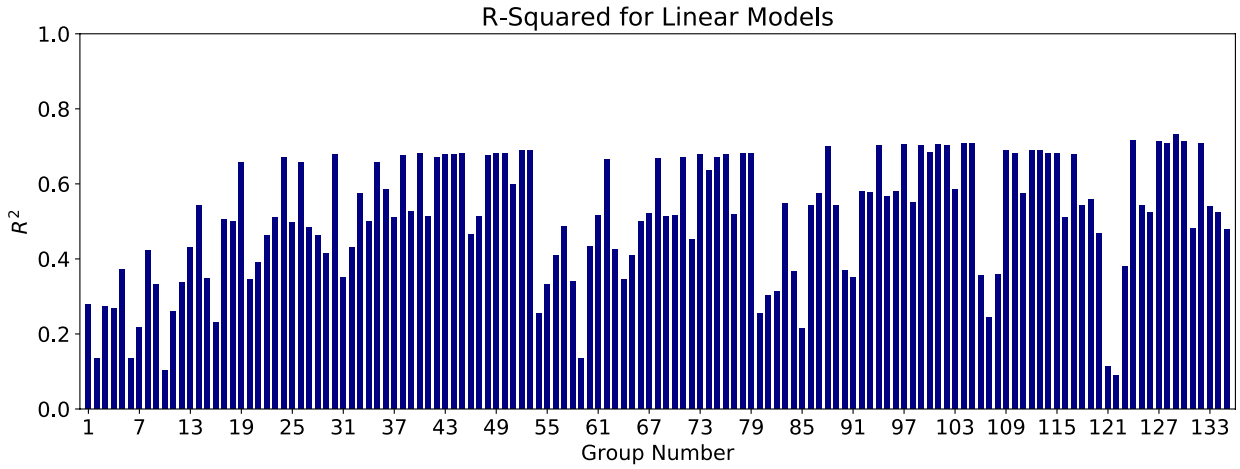

Figure 250. R^2 results for the "Linear Models" in JET/Global dataset – EC

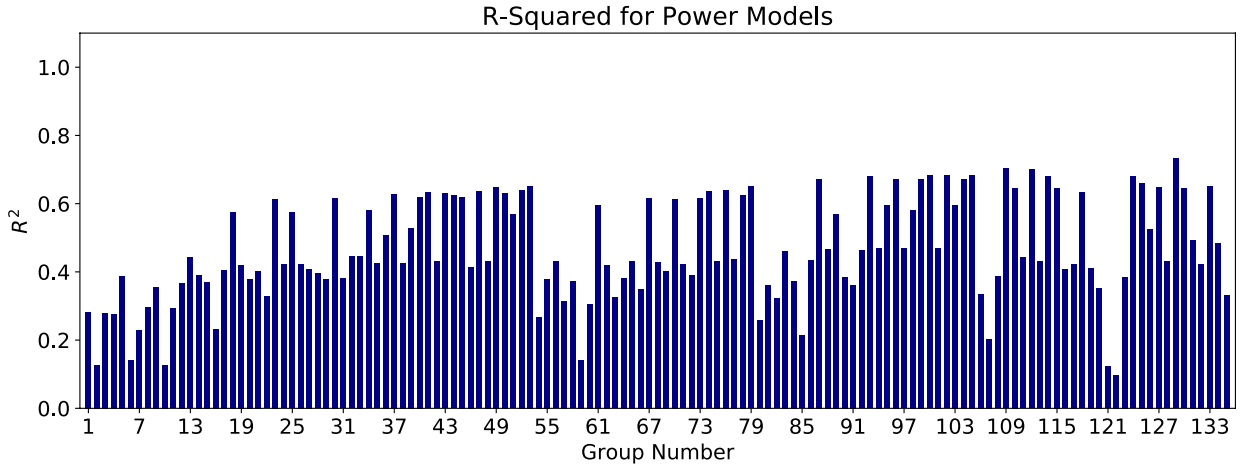

Figure 251. R^2 results for the "Power Models" in JET/Global dataset – EC

After passing through filters 1 and 2 (R^2 and MSE), "Linear" models associated with groups 30, 40, 49, 50, 52, 53, 88, 94, 97, 104, 124, and 129 were selected for further analyses. Also "Power" models associated with groups 87, 93, 100, 102, 109, 112, and 129 were selected for further analyses.

Filter 3, F-value/F-stat, was determined for each group mentioned above. Table 76 shows the results of the selected "Linear" models after meeting the requirements of the first three filters (R2, MSE, and F-value/F-stat). As shown in Table 76, almost all of the selected models perform

satisfactorily in the cross-validation test. Table 77 also shows the results of the selected "Power" models after meeting the requirements of the first three filters. The best models that also have a good cross-validation score are highlighted in blue in both "Linear" and "Power" forms. Out of all of the highlighted correlation equations in Table 76 and Table 77, the Group 88 correlation equation in "Linear" form was selected as the most promising equation. Figure 252 shows the plot of "POU vs. θ" for this model. The vertical axis in Figure 252 represent the probability that the predicted EC using the selected model is smaller than the actual EC, in percentage. In order to reach a 90% confidence that the predicted EC is smaller than the actual EC, the predicted value should be multiplied by 0.85. It should be noted that the proposed equations is best for soils with D_{50} smaller than 0.3 mm.

Table 76. Selected "Linear" models for EC in the JET/Global dataset

Group No.	Independent Variables	Model Expression	R^2	MSE	F-value/F-stat	Cross-Validation Score
30	PF, S_u, D50	$EC = -0.007 \times PF + 0.003 \times S_u - 6.48 \times D50 + 3.5$	0.68	0.26	5.58	0.58
40	PI, S_u, PF, D50	$EC = 0.003 \times PI + 0.0029 \times S_u - 0.009 \times PF - 6.73 \times D50 + 3.6$	0.68	0.26	4.39	0.58
49	γ, WC, S_u, PF, D50	$EC = -0.019 \times \gamma - 0.01 \times WC + 0.003 \times S_u - 0.006 \times PF - 6.37 \times D50 + 3.95$	0.68	0.26	3.52	0.28
50	PI, γ, S_u, PF, D50	$EC = 0.003 \times PI - 0.0004 \times \gamma + 0.003 \times S_u - 0.009 \times S_u - 6.73 \times D50 + 3.61$	0.68	0.26	3.54	0.47
52	PI, WC, S_u, PF, D50	$EC = 0.006 \times PI - 0.013 \times WC + 0.002 \times S_u - 0.007 \times PF - 6.65 \times D50 + 3.72$	0.69	0.25	3.55	0.52
53	PI, γ, WC, S_u, PF, D50	$EC = 0.006 \times PI - 0.01 \times \gamma - 0.013 \times WC + 0.002 \times S_u - 0.007 \times PF - 6.37 \times D50 + 3.83$	0.69	0.25	3.00	0.42
88	PL, S_u, D50	$EC = -0.022 \times PL + 0.0031 \times S_u - 5.5 \times D50 + 3.34$	0.70	0.25	6.23	0.58
94	PL, γ, S_u, D50	$EC = -0.023 \times PL - 0.01 \times \gamma + 0.003 \times S_u - 5.4 \times D50 + 3.64$	0.70	0.25	4.96	0.33
97	PL, WC, S_u, D50	$EC = -0.029 \times PL + 0.009 \times WC + 0.0037 \times S_u - 5.25 \times D50 + 3.23$	0.71	0.25	5.11	0.58
104	PL, WC, S_u, PF, D50	$EC = -0.027 \times PL + 0.011 \times WC + 0.0038 \times S_u - 0.002 \times PF - 5.74 \times D50 + 3.35$	0.71	0.24	5.13	0.24

Table 76 (Continued). Selected "Linear" models for EC in the JET/Global dataset

Group No.	Independent Variables	Model Expression	R^2	MSE	F-value/F-stat	Cross-Validation Score
124	γ, A, WC, S_u, PF, D50	$EC = -0.017 \times \gamma + 0.2 \times A - 0.008 \times WC + 0.003 \times S_u - 0.005 \times PF - 6.54 \times D50 + 3.75$	0.72	0.24	3.96	0.47
129	LL, γ, A, S_u, PF	$EC = -0.013 \times LL - 0.05 \times \gamma + 0.31 \times A + 0.0054 \times S_u + 0.018 \times PF + 2.6$	0.73	0.23	5.03	0.20

Table 77. Selected "Power" models for EC in the JET/Global dataset

Group No.	Independent Variables	Model Expression	R^2	MSE	F-value/F-stat	Cross-Validation Score
87	PL, S_u, PF	$EC = (0.8) \times PL^{-0.25} \times S_u^{0.09} \times PF^{0.38}$	0.67	0.26	286.6	0.40
93	PL, γ, S_u, PF	$EC = (1.639) \times PL^{-0.26} \times \gamma^{-0.22} \times S_u^{0.1} \times PF^{0.37}$	0.68	0.26	235.2	0.05
100	PL, γ, WC, S_u, PF	$EC = (2.33) \times PL^{-0.23} \times \gamma^{-0.32} \times WC^{-0.06} \times S_u^{0.09} \times PF^{0.38}$	0.68	0.26	195.7	0.10
102	PL, γ, S_u, PF, D50	$EC = (1.644) \times PL^{-0.23} \times \gamma^{-0.29} \times S_u^{0.11} \times PF^{0.4} \times D50^{0.02}$	0.68	0.26	196.3	0.05
109	PC, γ, WC, S_u, PF, D50	$EC = (4.345) \times PC^{-0.13} \times \gamma^{-0.79} \times WC^{-0.05} \times S_u^{0.13} \times PF^{0.52} \times D50^{0.04}$	0.70	0.25	163.8	0.14
112	PC, γ, S_u, PF, D50	$EC = (3.282) \times PC^{-0.14} \times \gamma^{-0.75} \times S_u^{0.14} \times PF^{0.52} \times D50^{0.05}$	0.70	0.25	165.7	0.17
129	LL, γ, A, S_u, PF	$EC = (4.35) \times LL^{-0.34} \times \gamma^{-0.61} \times A^{0.14} \times S_u^{0.13} \times PF^{0.51}$	0.73	0.23	190.4	0.25

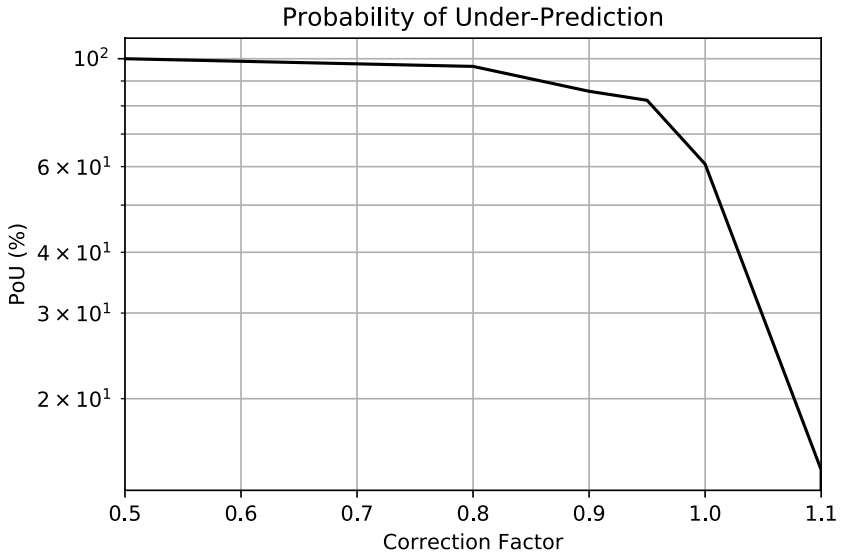

Figure 252. Plot of POU vs. correction factor for the Group 88 (Linear) - EC in the JET/Global dataset

HET Database

Although the number of data points in the HET/Coarse combination groups are very low in most cases, it was observed that dividing the HET/Global dataset into the HET/Fine and the HET/Coarse datasets would improve the regression results. Figure 253 shows the number of data points in each of all the 135 combination groups in the HET/Fine dataset. Figure 254 and Figure 255 show the results of R^2 for each combination group, for the "Linear" and "Power" models, respectively.

R^2 values for both "Linear" and "Power" models are not very high (up to 0.7). Figure 256 and Figure 257 show the results of the MSE for each of the 135 combination groups in the HET/Fine dataset, for "Linear" and "Power" models, respectively. It is observed that in general, "Power" and "Linear" models are not noticeably different.

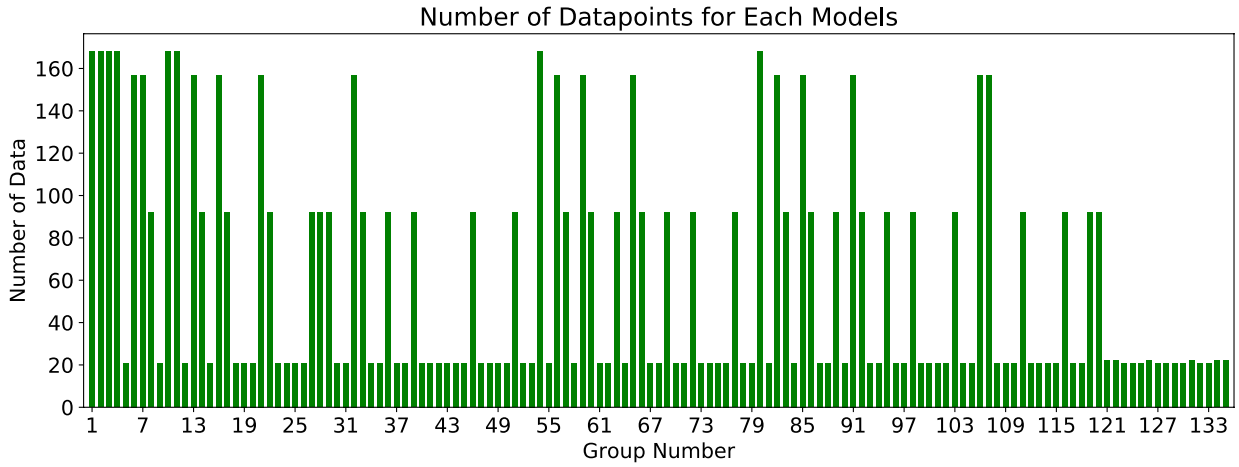

Figure 253. Number of data in each 135 combination groups for the HET/Fine dataset – EC

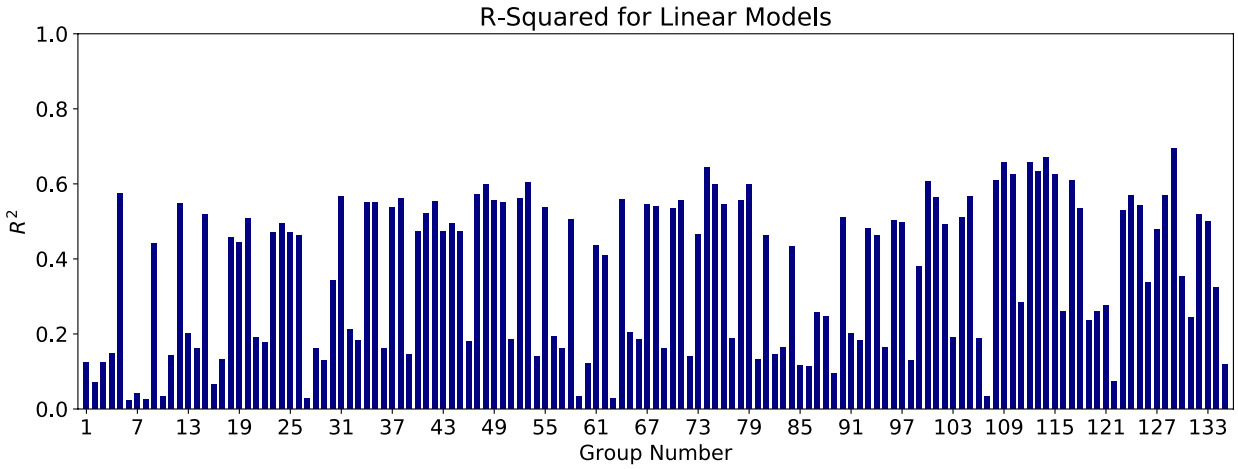

Figure 254. R^2 results for the "Linear Models" in HET/Fine dataset – EC

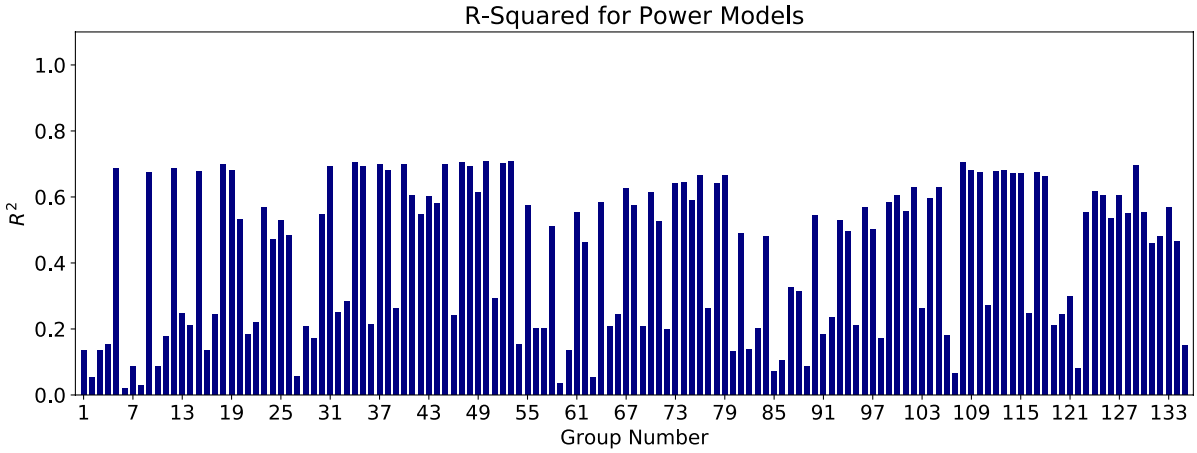

Figure 255. R^2 results for the "Power Models" in HET/Fine dataset – EC

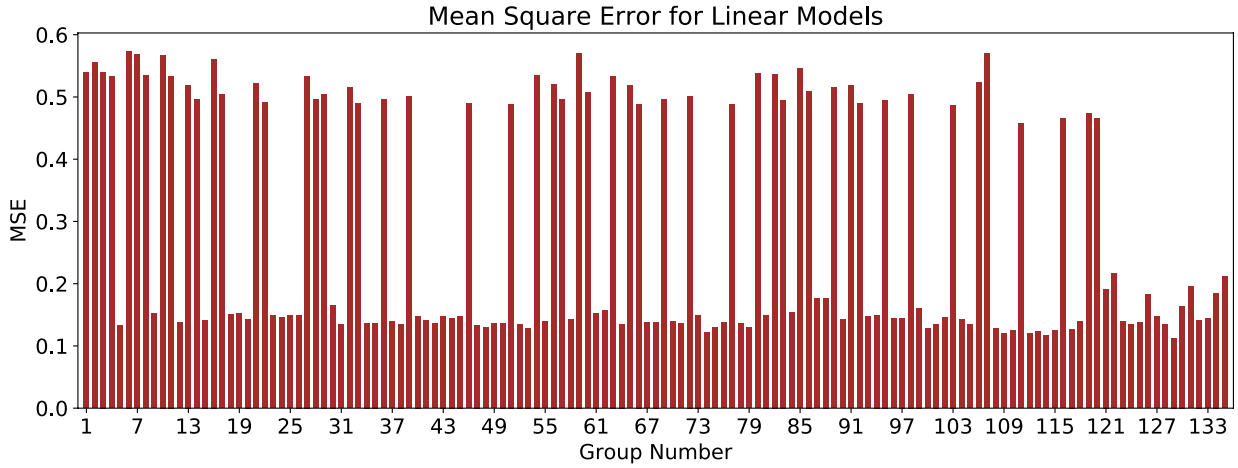

Figure 256. MSE results for the "Linear Models" in HET/Fine dataset – EC

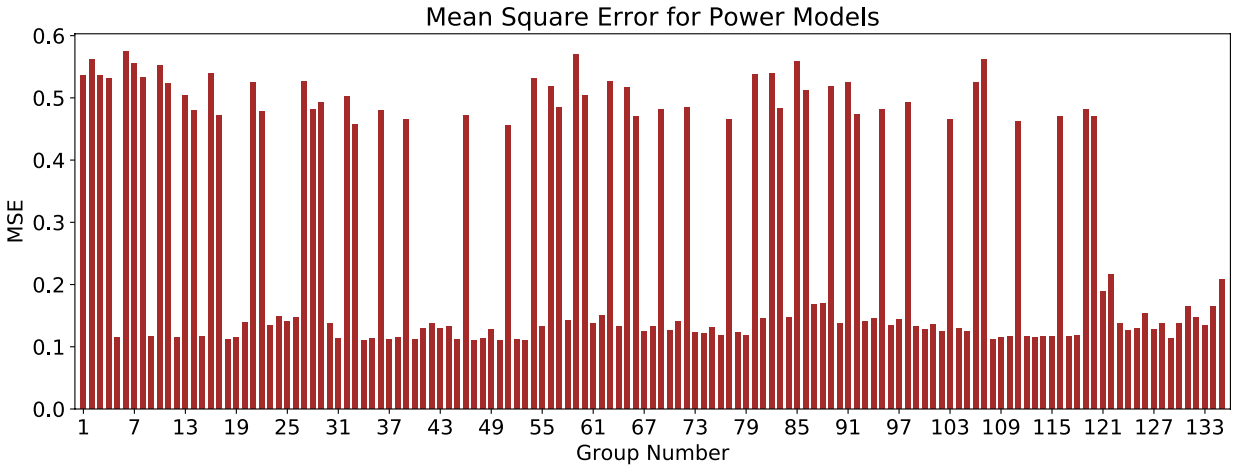

Figure 257. MSE results for the "Power Models" in HET/Fine dataset – EC

After passing through filters 1 and 2 (R^2 and MSE), "Linear" models associated with groups 48, 53, 74, 79, 100, 109, 112, 114, and 129 were selected for further analyses. Also "Power" models associated with groups 5, 12, 18, 19, 31, 34, 35, 37, 40, 47, 50, 52, 53, 108, 109, 112, 113, and 129 were selected for further analyses.

Filter 3, F-value/F-stat, was determined for each group mentioned above. Table 78 shows the results of the selected "Linear" models after meeting the requirements of the first three filters (R2, MSE, and F-value/F-stat). Table 79 also shows the results of the selected "Power" models after meeting the requirements of the first three filters. The best models that also have a good cross-validation score are highlighted in blue in both "Linear" and "Power" forms. The Group 12 correlation equation in "Power" form was selected as the most promising equation. Figure 258 shows the plot of "POU vs. θ" for this model. The vertical axis in Figure 258 represent the probability that the predicted EC using the selected model is smaller than the actual EC, in percentage. In order to reach a 100% confidence that the predicted EC is smaller than the actual EC, the predicted value should be multiplied by 0.95.

Table 78. Selected "Linear" models for critical shear stress in the HET/Fine dataset

Group No.	Independent Variables	Model Expression	R^2	MSE	F-value/F-stat	Cross-Validation Score
48	PI, γ, WC, S_u, D50	$EC = 0.002 \times PI + 0.05 \times \gamma + 0.02 \times WC + 0.004 \times S_u + 5.43 \times D50 + 1.59$	0.60	0.13	1.548	-0.18
53	PI, γ, WC, S_u, PF, D50	$EC = 0.002 \times PI + 0.05 \times \gamma + 0.03 \times WC + 0.0037 \times S_u + 0.001 \times PF + 6.82 \times D50 + 1.36$	0.60	0.13	1.242	-0.39
74	LL, γ, WC, S_u, PF	$EC = 0.002 \times LL + 0.05 \times \gamma + 0.01 \times WC + 0.0029 \times S_u - 0.002 \times PF + 2.05$	0.64	0.12	2.097	-0.50
79	LL, γ, WC, S_u, PF, D50	$EC = 0.002 \times LL + 0.051 \times \gamma + 0.03 \times WC + 0.0037 \times S_u + 0.0007 \times PF + 6.48 \times D50 + 1.36$	0.60	0.13	1.220	-0.52
100	PL, γ, WC, S_u, PF	$EC = 0.012 \times PL + 0.05 \times \gamma + 0.02 \times WC + 0.0033 \times S_u - 0.0045 \times PF + 1.82$	0.61	0.13	1.929	0.12
109	PC, γ, WC, S_u, PF, D50	$EC = 0.014 \times PC + 0.044 \times \gamma - 0.0015 \times WC + 0.002 \times S_u + 0.0038 \times PF + 13.1 \times D50 + 1.46$	0.66	0.12	2.416	0.25
112	PC, γ, S_u, PF, D50	$EC = 0.014 \times PC + 0.04 \times \gamma + 0.0021 \times S_u + 0.0038 \times PF + 13.17 \times D50 + 1.44$	0.66	0.12	3.018	0.32
114	PC, γ, WC, S_u, PF	$EC = 0.008 \times PC + 0.04 \times \gamma - 0.01 \times WC + 0.0015 \times S_u - 0.0016 \times PF + 2.44$	0.67	0.12	2.052	0.09
129	LL, γ, A, S_u, PF	$EC = 0.003 \times LL + 0.05 \times \gamma - 0.04 \times A + 0.0021 \times S_u - 0.0014 \times PF + 2.17$	0.69	0.11	1.623	-0.42

Table 79. Selected "Power" models for critical shear stress in the HET/Fine dataset

Group No.	Independent Variables	Model Expression	R^2	MSE	F-value/F-stat	Cross-Validation Score
5	LL, PL, γ, WC, S_u	$EC = (1.87) \times LL^{0.08} \times PL^{-0.12} \times \gamma^{0.16} \times WC^{-0.005} \times S_u^{0.03}$	0.69	0.12	796.3	0.26
12	PI, γ, S_u	$EC = (1.67) \times PI^{0.04} \times \gamma^{0.15} \times S_u^{0.03}$	0.70	0.11	1172.2	0.54
18	PI, S_u, PF	$EC = (3.23) \times PI^{0.05} \times S_u^{0.03} \times PF^{-0.06}$	0.70	0.11	1172.3	0.57
19	PI, S_u, D50	$EC = (2.57) \times PI^{0.05} \times S_u^{0.03} \times D50^{0.01}$	0.68	0.12	917.4	0.54
31	PI, γ, WC, S_u	$EC = (1.74) \times PI^{0.05} \times \gamma^{0.17} \times WC^{-0.03} \times S_u^{0.03}$	0.69	0.11	911.5	0.38
34	PI, γ, S_u, PF	$EC = (2.221) \times PI^{0.04} \times \gamma^{0.13} \times S_u^{0.03} \times PF^{-0.06}$	0.71	0.11	968.3	0.40
35	PI, γ, S_u, D50	$EC = (1.68) \times PI^{0.05} \times \gamma^{0.15} \times S_u^{0.03} \times D50^{0.01}$	0.69	0.11	968.6	0.24
37	PI, WC, S_u, PF	$EC = (3.221) \times PI^{0.05} \times WC^{0.0016} \times S_u^{0.035} \times PF^{-0.06}$	0.70	0.11	963.5	0.39
40	PI, S_u, PF, D50	$EC = (3.47) \times PI^{0.04} \times S_u^{0.03} \times PF^{-0.08} \times D50^{-0.01}$	0.70	0.11	963.5	0.33
47	PI, γ, WC, S_u, PF	$EC = (2.211) \times PI^{0.04} \times \gamma^{0.13} \times WC^{-0.01} \times S_u^{0.03} \times PF^{-0.05}$	0.71	0.11	781.6	0.24

Table 79 (Continued). Selected "Power" models for critical shear stress in the HET/Fine dataset

Group No.	Independent Variables	Model Expression	R^2	MSE	F-value/F-stat	Cross-Validation Score
50	PI, γ, S_u, PF, D50	$EC = (2.4) \times PI^{0.04} \times \gamma^{0.12} \times S_u^{0.03} \times PF^{-0.07} \times D50^{-0.01}$	0.71	0.11	780.2	0.15
52	PI, WC, S_u, PF, D50	$EC = (3.708) \times PI^{0.04} \times WC^{-0.02} \times S_u^{0.03} \times PF^{-0.09} \times D50^{-0.01}$	0.70	0.11	771.9	-0.26
53	PI, γ, WC, S_u, PF, D50	$Ec = (2.547) \times PI^{0.04} \times \gamma^{0.13} \times WC^{-0.03} \times S_u^{0.03} \times PF^{-0.08} \times D50^{-0.01}$	0.71	0.11	638.6	-0.11
108	LL, PL, γ, PC, S_u	$EC = (2.064) \times LL^{0.06} \times PL^{-0.06} \times \gamma^{0.09} \times PC^{0.02} \times S_u^{0.03}$	0.70	0.11	622.9	0.32
109	PC, γ, WC, S_u, PF, D50	$EC = (1.861) \times PC^{0.04} \times \gamma^{0.12} \times WC^{0.02} \times S_u^{0.04} \times PF^{-0.0011} \times D50^{0.02}$	0.68	0.12	608.8	0.39
112	PC, γ, S_u, PF, D50	$Ec = (1.919) \times PC^{0.04} \times \gamma^{0.13} \times S_u^{0.04} \times PF^{-0.005} \times D50^{0.02}$	0.68	0.12	778.3	0.51
113	PC, γ, WC, S_u, D50	$EC = (1.854) \times PC^{0.04} \times \gamma^{0.12} \times WC^{0.02} \times S_u^{0.04} \times D50^{0.02}$	0.68	0.12	778.1	0.44
129	LL, γ, A, S_u, PF	$EC = (2.123) \times LL^{0.07} \times \gamma^{0.15} \times A^{-0.03} \times S_u^{0.04} \times PF^{-0.09}$	0.69	0.11	779.6	0.19

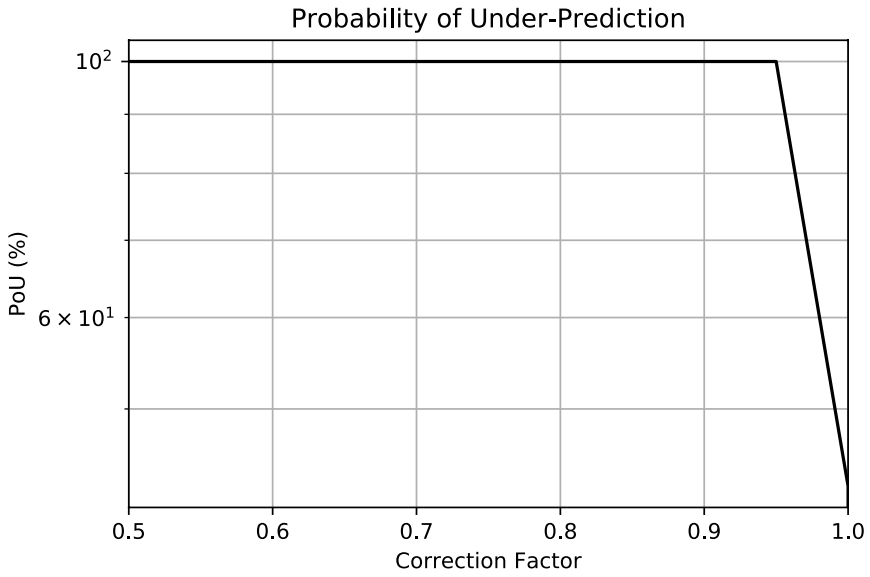

Figure 258. Plot of POU vs. correction factor for the Group 12 (Power) - EC in the HET/Fine dataset

The same procedure was conducted in the HET/Coarse dataset, and the best models are selected for EC. Figure 259 shows the number of data points in each of all the 105 combination groups in the EFA/Coarse dataset. Figure 260 and Figure 261 show the results of R^2 for each combination group, for the "Linear" and "Power" models, respectively.

Both "Linear" and "Power" models show some good groups in terms of R^2 values; however, as shown in Figure 259, the number of data points are very low in most combination groups. In fact, close to half of the combination groups do not have any data points.

After passing through filters 1 and 2 (R^2 and MSE), "Linear" models associated with groups 4, 5, 7, 10, 15, 26, 48, 50, 51, 53, 54, 57, 59, 60, 63, 66, 71, 74, 76, 79, 85, 100, 102, and 103 were selected for further analyses. Also "Power" models associated with groups 4, 5, 7, 15, 26, 48, 50, 51, 57, 59, 60, 71, 74, 76, 77, 79, 83, 85, 86, 97, 102, 103, and 105 were selected for further analyses.

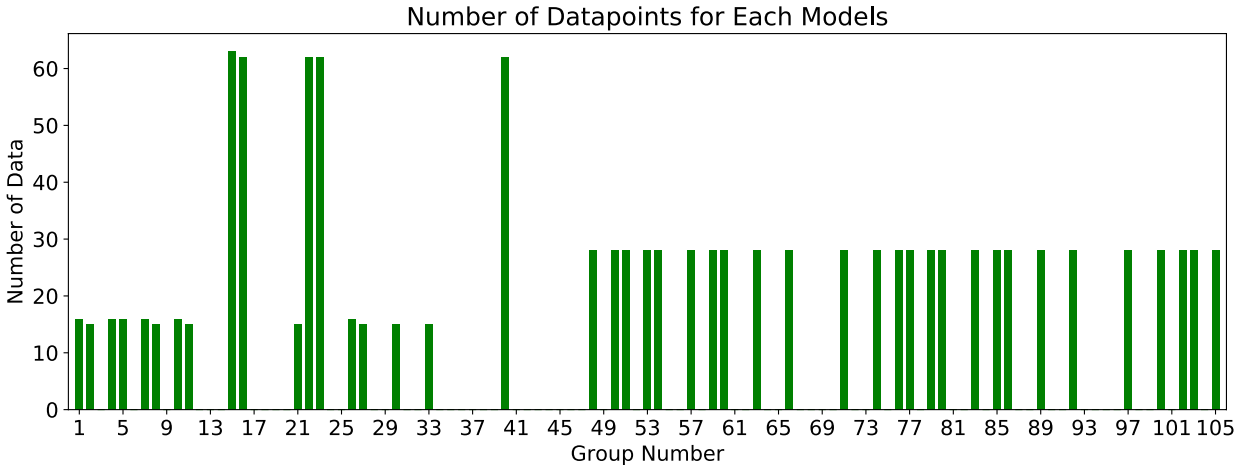

Figure 259. Number of data in each 105 combination groups for the HET/Coarse dataset – EC

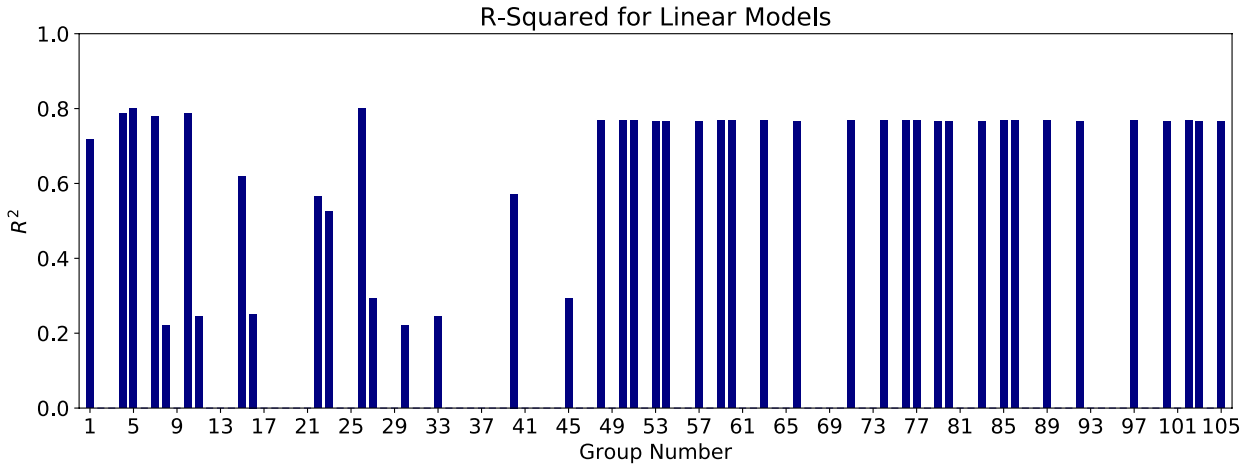

Figure 260. R^2 results for the "Linear Models" in HET/Coarse dataset – EC

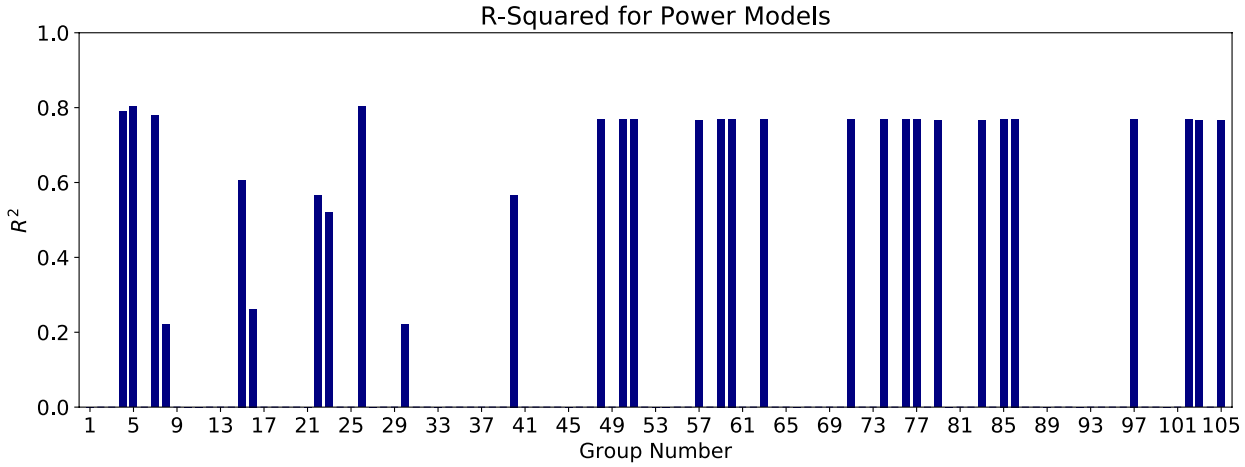

Figure 261. R^2 results for the "Power Models" in HET/Coarse dataset – EC

Filter 3, F-value/F-stat, was determined for each group mentioned above. Table 80 shows the results of the selected "Linear" models after meeting the requirements of the first three filters (R2, MSE, and F-value/F-stat). Table 81 also shows the results of the selected "Power" models after meeting the requirements of the first three filters. The best models that also have a good cross-validation score are highlighted in blue in both "Linear" and "Power" forms. The Group 48 correlation equation in "Power" form was selected as the most promising equation. Figure 262 shows the plot of "POU vs. θ" for this model. The vertical axis in Figure 262 represent the

probability that the predicted EC using the selected model is smaller than the actual EC, in percentage. In order to reach a 90% confidence that the predicted EC is smaller than the actual EC, the predicted value should be multiplied by 0.85. It is very important to note that the proposed equation associated with the Group 48 should be used for soils with D_{50} ranging from 0.074 to 0.3 mm.

Table 80. Selected "Linear" models for critical shear stress in the HET/Coarse dataset

Group No.	Independent Variables	Model Expression	R^2	MSE	F-value/F-stat	Cross-Validation Score
4	PI, WC	$EC = -0.569 \times PI + 0.07 \times WC + 11.94$	0.79	0.17	6.29	0.04
5	PI, γ, WC	$EC = -0.557 \times PI + 0.12 \times \gamma + 0.05 \times WC + 9.41$	0.80	0.16	4.58	0.11
7	PI, γ, PF	$EC = -0.014 \times PI + 0.21 \times \gamma + 0.09 \times PF - 3.6$	0.78	0.17	6.29	0.13
10	PI, WC, PF	$EC = -0.015 \times PI + 0.07 \times WC + 0.09 \times PF - 1.1$	0.79	0.17	4.6	0.04
15	γ, WC, PF	$EC = -0.128 \times \gamma + 0.02 \times WC + 0.05 \times PF + 3.38$	0.62	0.25	4.59	0.55
26	PI, γ, WC, PF	$EC = -0.014 \times PI + 0.12 \times \gamma + 0.05 \times WC + 0.09 \times PF - 2.78$	0.80	0.16	3.11	0.10
48	C_c, γ, WC	$EC = -0.138 \times C_c + 0.05 \times \gamma - 0.0037 \times WC + 2.35$	0.77	0.17	4.58	0.70
50	C_c, γ, PF	$EC = -0.004 \times C_c + 0.04 \times \gamma + 0.02 \times PF + 0.92$	0.77	0.17	4.59	0.73
51	C_c, γ, D50	$EC = -0.145 \times C_c + 0.04 \times \gamma - 0.0045 \times D50 + 2.5$	0.77	0.17	4.59	0.73
53	C_c, WC, PF	$EC = -0.005 \times C_c + 0.004 \times WC + 0.04 \times PF + 1.55$	0.77	0.17	4.56	0.71
54	C_c, WC, D50	$EC = -0.177 \times C_c + 0.004 \times WC - 0.0055 \times D50 + 3.41$	0.77	0.17	4.57	0.71
57	PF, C_c, D50	$EC = 0.03 \times PF - 0.01 \times C_c - 0.0002 \times D50 + 1.61$	0.77	0.17	4.59	0.74
59	C_c, γ, WC, PF	$EC = -0.004 \times C_c + 0.05 \times \gamma - 0.0037 \times WC + 0.02 \times PF + 0.89$	0.77	0.17	3.13	0.69
60	C_c, γ, WC, D50	$EC = -0.138 \times C_c + 0.05 \times \gamma - 0.0037 \times WC - 0.0043 \times D50 + 2.35$	0.78	0.16	3.08	0.69
63	C_c, γ, PF, D50	$EC = -0.0044 \times C_c + 0.04 \times \gamma + 0.02 \times PF - 0.0001 \times D50 + 0.92$	0.77	0.16	3.11	0.73
66	C_c, WC, PF, D50	$EC = -0.0054 \times C_c + 0.004 \times WC + 0.03 \times PF - 0.0002 \times D50 + 1.55$	0.76	0.17	3.06	0.71
71	C_c, γ, WC, PF, D50	$EC = -0.004 \times C_c + 0.05 \times \gamma - 0.0037 \times WC + 0.024 \times PF - 0.0001 \times D50 + 0.9$	0.77	0.17	2.84	0.69
74	C_u, γ, WC	$EC = 0.003 \times C_u + 0.05 \times \gamma - 0.0037 \times WC + 1.3$	0.77	0.17	4.58	0.64
76	C_u, γ, PF	$EC = 0.003 \times C_u + 0.04 \times \gamma \times 0.0003 \times PF + 1.33$	0.77	0.17	4.59	0.73
79	C_u, WC, PF	$EC = 0.003 \times C_u + 0.004 \times WC + 0.0003 \times PF + 2.1$	0.77	0.17	4.56	0.71
85	C_u, γ, WC, PF	$EC = 0.003 \times C_u + 0.05 \times \gamma - 0.0037 \times WC + 0.0003 \times PF + 1.28$	0.77	0.16	3.10	0.64
100	C_c, C_u	$EC = -0.00006 \times C_c + 0.003 \times C_u + 2.11$	0.76	0.16	6.3	0.68
102	C_c, C_u, γ	$EC = -0.00005 \times C_c + 0.003 \times C_u + 0.04 \times \gamma + 1.34$	0.77	0.16	4.45	0.67
103	C_c, C_u, WC	$EC = -0.0006 \times C_c + 0.003 \times C_u + 0.004 \times WC + 2.1$	0.76	0.17	4.40	0.66

Table 81. Selected "Power" models for critical shear stress in the HET/Coarse dataset

Group No.	Independent Variables	Model Expression	R^2	MSE	F-value/F-stat	Cross-Validation Score
4	PI, WC	$EC = (1675.1) \times PI^{-2.62} \times WC^{0.4}$	0.79	0.17	419.5	0.51
5	PI, γ, WC	$EC = (151.5) \times PI^{-2.42} \times \gamma^{0.74} \times WC^{0.27}$	0.80	0.16	329.3	-0.10
7	PI, γ, PF	$EC = (7.31) \times PI^{-1.92} \times \gamma^{1.32} \times PF^{0.19}$	0.78	0.17	330.1	-0.20
15	γ, WC, PF	$EC = (3.47) \times \gamma^{-0.84} \times WC^{0.07} \times PF^{0.61}$	0.61	0.26	321.8	0.51
26	PI, γ, WC, PF	$EC = (1.848) \times PI^{-1.39} \times \gamma^{0.74} \times WC^{0.27} \times PF^{0.42}$	0.80	0.16	294.5	-1.19
48	C_c, γ, WC	$EC = (1.045) \times C_c^{-0.25} \times \gamma^{0.45} \times WC^{-0.04}$	0.77	0.17	328.6	0.78
50	C_c, γ, PF	$EC = (27.15) \times C_c^{-0.84} \times \gamma^{0.34} \times PF^{-0.61}$	0.77	0.17	328.6	0.75
51	C_c, γ, D50	$EC = (1.23) \times C_c^{-0.25} \times \gamma^{0.34} \times D50^{-0.04}$	0.77	0.17	328.8	-22.7
57	PF, C_c, D50	$EC = (0.272) \times PF^{0.65} \times C_c^{0.14} \times D50^{0.13}$	0.76	0.17	323.5	0.65
59	C_c, γ, WC, PF	$EC = (5.834) \times C_c^{-0.57} \times \gamma^{0.45} \times WC^{-0.04} \times PF^{-0.35}$	0.77	0.16	291.5	0.67
60	C_c, γ, WC, D50	$EC = (1.16) \times LL^{-0.28} \times \gamma^{0.45} \times WC^{-0.04} \times D50^{0.03}$	0.77	0.17	292.6	-18.62
71	C_c, γ, WC, PF, D50	$EC = (0.06) \times C_c^{0.09} \times \gamma^{0.45} \times WC^{-0.04} \times PF^{1.01} \times D50^{0.67}$	0.77	0.17	266.4	0.12
74	C_u, γ, WC	$EC = (0.45) \times C_u^{0.1} \times \gamma^{0.45} \times WC^{-0.04}$	0.77	0.17	329.5	0.66
76	C_u, γ, PF	$EC = (0.98) \times C_u^{0.23} \times \gamma^{0.34} \times PF^{-0.33}$	0.77	0.17	328.3	0.55
77	C_u, γ, D50	$Ec = (0.02) \times C_u^{-6.07} \times \gamma^{0.34} \times D50^{-18.16}$	0.77	0.17	330.1	0.62
79	C_u, WC, PF	$EC = (34.54) \times C_u^{0.78} \times WC^{-0.004} \times PF^{-1.8}$	0.76	0.17	330.1	0.54
83	PF, C_u, D50	$Ec = (0.21) \times PF^{1.87} \times C_u^{2.11} \times D50^{7.77}$	0.76	0.17	326.6	-8.3
85	C_u, γ, WC, PF	$EC = (9.902) \times C_u^{0.72} \times \gamma^{0.45} \times WC^{-0.04} \times PF^{-1.73}$	0.77	0.17	329.5	0.65
86	C_u, γ, WC, D50	$EC = (3.97) \times C_u^{4.03} \times \gamma^{0.45} \times WC^{-0.04} \times D50^{11.56}$	0.77	0.16	295.6	0.55
97	C_u, γ, WC, PF, D50	$EC = (0.19) \times C_u^{0.67} \times \gamma^{0.45} \times WC^{-0.04} \times PF^{0.74} \times D50^{2.44}$	0.77	0.17	258.1	0.55
102	C_c, C_u, γ	$EC = (0.006) \times C_c^{1.35} \times C_u^{0.65} \times \gamma^{0.34}$	0.77	0.17	328.9	0.53
103	C_c, C_u, WC	$EC = (3.42) \times C_c^{-0.27} \times C_u^{0.03} \times WC^{-0.004}$	0.76	0.17	329.5	0.57
105	C_c, C_u, PF	$EC = (0.0032) \times C_c^{1.57} \times C_u^{0.6} \times PF^{0.43}$	0.76	0.17	329.5	-9.5

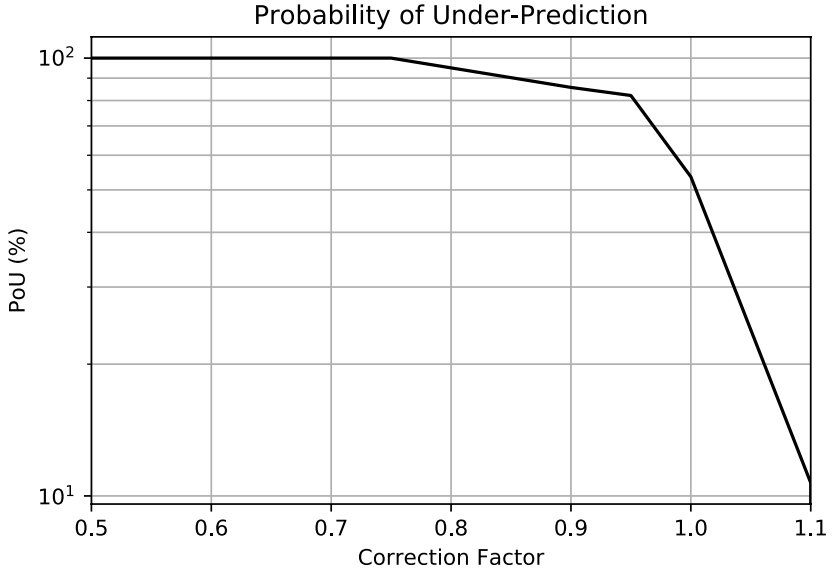

Figure 262. Plot of POU vs. correction factor for the Group 48 (Power) - EC in the HET/Coarse dataset

7.4. Probabilistic (Bayesian) Analysis

The preceding section focused on selecting the 'optimal' vector of model parameters that maximize the likelihood of fitting experimental observations. This section introduces a series of Bayesian probabilistic calibrations carried out on a set of regression (empirical) models proposed as 'optimal' to capture only the model's first order statistics (expected or mean behavior). The Bayesian regression analysis introduces a methodology to fully assess both first and second order statistics (expected or mean, and variance and covariance respectively) when presented to physical evidence generated by the same erosion tests presented in the deterministic regression analysis discussed in the previous section. That is, Bayesian regression allows to quantify varying uncertainty scenarios resulting from different sources of evidence (i.e. varying experimental observations, varying model complexity and varying expert's judgment), providing further inferences to better understand the performance of a given regression model. This is achieved by providing a full characterization of all possible solutions of the model parameters and their relative probabilities while simultaneously providing a systematic and transparent approach to assess the performance of the proposed regression model.

The major difference between the Bayesian analysis and deterministic frequentists' regression approach is in how each one of them interprets the observed data and model parameters. Frequentists' regression assumes that the model parameters are in fact fixed unknown parameters, and the observed data are random repeatable samples. On the other hand, the Bayesian inference approach assumes that the observed data are fixed values, while the model parameters are random parameters. Therefore, a frequentists' regression approach results in fixed values attributed to the model parameters, whereas the Bayesian approach would result in posterior probability distributions for each model parameter rather than a fixed value.

The main benefit of the use of the Bayesian inference approach is the definition of a metric of confidence on the model predictions. This permits to assess both the performance of competing models given a set of experimental observations based on a given experimental method, and the performance of competing experimental methods given a predicting model. The Bayesian approach departs from standard deterministic calibrations (i.e. least squares) by populating "all" the likely combinations of parameters of a predicting model suitable to represent the mean of the process of interest (i.e. fit of a given set of experimental observations), as opposed to proposing a single parameters combination (i.e. the optimal, which may not be unique). As a result, it is then possible to generate a full probabilistic description of the model parameters in the form of marginal probability density functions pdf (i.e. each model parameter is represented by its own pdf), and a full probabilistic description of the parameters' correlation structure (when taken two at the time).

It should also be noted that the concepts of "confidence interval" and "hypothesis testing" in frequentists' regression and Bayesian inference are different. As an illustration, when in interpreting the results of a frequentists' regression approach, the confidence interval for a parameter is reported as 90%, it means that if the exact same experiment is repeated several times, and for each time the confidence interval is obtained, then 90% of the obtained intervals include the parameter. It does not mean that there is 90% chance that the parameter is within the confidence interval. On the other hand, when a Bayesian approach reports a 90% confidence interval (or as typically called: the "credible interval" in the Bayesian inference) for a parameter, that means there is 90% chance that the credible interval contains the parameter.

7.4.1. *Motivation*

One main objective of TAMU-Erosion (Chapter 5) is to assimilate information collected from a broad range of erodibility tests and correlating those results with primary soil geotechnical properties through statistical modeling. However, regardless of the level of model sophistication, broadness of experimental observations, or accuracy of expert's judgement, there is a finite amount of uncertainty associated with every mathematical representation – none of the modeling results is capable of predicting the property of interest with complete confidence. This is due to several practical limitations:

- The effect of 'missing data' from the database may introduce bias on the proper model calibration;
- The proposed empirical models do not capture the 'mean of the process of interest';
- One single model selection 'the optimal' may represent only one single fit of possibly millions of likely combinations that may produce the same degree of 'curve fitting' (i.e. the regression analysis is an ill-posed problem);

Understanding this varying evidence condition motivates a specialized calibration that points to systematic and transparent assessment of prediction confidence based on all available evidence.

7.4.2. *Hypotheses*

The foregoing regression analysis has selected several groups of experimental observations and corresponding statistical models that showed satisfying model/observation comparisons. Herein, the proposed Probabilistic (Bayesian) Calibration Method (Medina-Cetina, 2006) is

introduced to complement the previous deterministic regression approach. Several hypotheses are proposed and intent to be thoroughly discussed in the following chapter:

- The probabilistic approach allows a full characterization of sources and propagation of model uncertainty, and their relative probabilities, through systematic assimilation of available evidences (i.e. experimental observations, model prediction and expert's judgment).
- Varying estimation confidence levels of parameters can exhibit in the parametric space.
- Varying correlation structures among parameters can be shown in the calibration results, which will help reveals the model nature.
- The probabilistic characteristics of the proposed models will be depicted in multi-dimensional 'physical domains' (comprised of model independent variables), the goodness of modeling does not solely depend on capturing each available observation (erodibility test results), but also on the confidence levels of estimations.

7.4.3. *Methodology*

7.4.3.1. Uncertainty quantification framework

The uncertainty quantification (UQ) of an inverse problem aims to identify, characterize and simulate the various sources of uncertainty inherently participating in the physical process of interest (Medina-Cetina, 2006). The expected output of the true process is represented by a set of random vectors d which based on the definition of the physical process at prescribed control points. In practice, experimental observations, d_{obs}, can be retrieved from lab or field measurements, and compared to predicting outcomes of the same process, d_{pred}. These are quantifiable vectors formed as a-priori information used to approximate the true process, d. Accordingly, the uncertainty quantification framework in terms of d, d_{obs} and d_{pred} can be summarized by:

$$d = d_{obs} + \Delta d_{obs}$$

$$d = d_{pred} + \Delta d_{pred}$$

$$d_{obs} - d_{pred} = \Delta d_{obs} - \Delta d_{pred} \tag{72}$$

Eq. (72) illustrates the tradeoff between the scientific evidence d_{obs} and d_{pred} through the gradients, Δd. The involved uncertainty incorporates random vectors both in experimental observations and theoretical predictions. Herein, d_{pred} is comprised of mathematical predictions stemming from a forward model $g(\theta)$, which is governed or characterized by a set of parameters, θ. Noticed that θ can represent geometric and statistical properties, such as shape parameters or linear/power parameters in this case. Similarly, the uncertainty involved in the calibration of vectors θ can be defined as:

$$\theta = \hat{\theta} + \Delta\theta \tag{73}$$

Where $\hat{\theta}$ denotes mean of parameters and $\Delta\theta$ represent the uncertainty component. Other than the deterministic methodology, the probabilistic calibration allows for an exhaustive exploration of all potential combinations of the model parameters that best resemble the experimental observations. As a result, the correlation structures of model parameters are populated, which ultimately be translated in a better understanding of uncertainty inherent to model nature (Δd_{pred}) with respect to the experimental observations. Noticed that in this work, the model prediction assumed to be unbiased with respect to process of interest, which implies $E\left(\Delta d_{obs} - \Delta d_{pred}\right) = 0$.

7.4.3.2.Bayesian probabilistic calibration

The proposed UQ framework requires assessment of plausible solutions of model parameters $\boldsymbol{\theta}$ conditioned on the data, d_{obs}, which generates the need of a mathematical mapping regarding this inverse problem. From a deterministic standpoint, this can be accomplished by selecting an 'optimal' set of model parameters, which maximize the likelihood of fitting d_{obs}. However, the proposed calibration can be an ill-posed inverse problem, since many combinations of the model parameters can lead to the same experimental response. To tackle this problem, the proposed probabilistic calibration method follows a Bayesian approach, which accounts for the full probabilistic description of the model parameters through probability maps. This starts from an expert's belief setting up the prior ($\pi(\theta)$) about model parameters θ before the experimental evidence is presented to the mechanical model (forward model). This prior knowledge ideally facilitates calibration of model parameters by limiting and defining plausible values in the form of probability distribution, which later updated systematically via quantifying likelihood ($p(d_{obs}|\theta)$) between available observations d_{pobs} and model parameters θ. From the basic definition of Bayes theorem:

$$\pi(\theta|d_{obs}) = \frac{p\big(d_{obs}|g(\theta),\theta\big)\pi(\theta)}{\int_{\Theta} p\big(d_{obs}|g(\theta),\theta\big)\pi(\theta)d\theta} \propto p(d_{obs}|g(\theta),\theta)\pi(\theta) \tag{74}$$

The posterior $\pi(\theta|d_{obs})$ is the probability proportional to the prior $\pi(\theta)$ and the likelihood, $p(d_{obs}|\theta)$. This is because of the integral of denominator is a normalizing constant over the parametric space Θ so that the integral of the posterior $\pi(\theta|d_{obs})$ can be 1.

One important note about implementing Bayesian inference is that the computations often involve very complex integrations that cannot be handled analytically. Also, the posterior distribution hardly is in explicit form and requires simulations in order to be achieved. Markov Chain Monte Carlo (MCMC) sampling methods are typically used to solve for complex posterior

models. The most typical MCMC sampling method is the Metropolis-Hasting (MH) (Metropolis et al., 1953; Hasting, 1970). This sampling method follows an algorithm that generates values from a posterior distribution and converge to a pre-determined target distribution. Further information on MCMC and its algorithm can be found in Hastings (1970). When any MCMC sampling method is used to approximate the posterior distributions, verifying its convergence becomes a vital step in the Bayesian inference approach. In this study, the sampling of the posterior is based on a Markov Chain Monte Carlo approach coupled with Metropolis Hastings criteria (MCMC- MH), which makes it possible to draw samples from a proposing distribution to infer the target posterior distributions.

7.4.4. *Probabilistic calibration for varying data scenarios*

The probabilistic calibrations discussed in this section are conducted on the proposed model/data scenarios produced by the deterministic regression results populated in the previous section.

Table 82 to Table 86 list 'deterministic regression calibrations' with the highest goodness of fit for each erodibility variable (i.e., critical shear stress τ_c, critical velocity v_c, erosion category EC, velocity slope E_v, and shear stress slope E_τ respectively).

The results of the probabilistic calibrations for all of the equations presented in Tables 79 to 83 are presented in the Appendix E of the appendices report. However, in this section, one case is discussed to illustrate the applicability of the method, labeled with Group No. 132 (See Table 84). In Appendix E, the same type of results as the ones described in this section are generated for all of the selected equations.

Table 82. Selected models for critical shear stress τ_c

Group No.	Independent variables	Dataset/ No. of data	Model expression (parameter values given by deterministic regression)	R^2	Cross-validation score
124	γ, A, WC, S_u, PF, D50	EFA/Fine 44	$\tau_c = (158.06) \times \gamma^5 \times A^{-0.46} \times WC^{10.03} \times S_u^{1.83} \times PF^{-18.28} \times D50^{-4.21}$	0.94	0.66
77	C_u, γ, D50	EFA/Coarse 28	$\tau_c = (1.58) \times C_u^{-0.04} \times \gamma^{0.02} \times D50^{0.77}$	0.93	0.99
113	PC, γ, WC, S_u, D50	JET/Global 28	$\tau_c = -0.248 \times PC - 1.23 \times \gamma + 0.21 \times WC + 0.07 \times S_u - 36.89 \times D50 + 31.82$ $for\ D50 < 0.3\ mm$	0.50	0.10
19	PI, S_u, D50	HET/Global 21	$\tau_c = (25.07) \times PI^{0.27} \times S_u^{0.55} \times D50^{0.5}$ $for\ D50 < 0.3\ mm$	0.64	0.43

Table 83. Selected models for critical velocity v_c

Group No.	Independent variables	Dataset/ No. of data	Model expression (parameter values given by deterministic regression)	R^2	Cross-validation score
117	PC, WC, S_u, D50	EFA/Fine 46	$v_c = (2.518 \times 10^{-5}) \times PC^{0.2} \times WC^{2.06} \times S_u^{0.51} \times D50^{-0.13}$	0.80	0.80
44	PI, γ, VST, PF, D50	EFA/Coarse 10	$v_c = 0.002 \times PI - 0.1 \times \gamma + 0.01 \times VST - 0.09 \times PF - 13.6 \times D50 + 7.21$ $for\ 0.074 < D50 < 0.3$	0.93	0.67

Table 84. Selected models for erosion category EC

Group No.	Independent variables	Dataset/ No. of data	Model expression (parameter values given by deterministic regression)	R^2	Cross-validation score
132	A, WC, S_u, D50	EFA/Fine 44	$EC = (0.1933) \times A^{-0.06} \times WC^{0.51} \times S_u^{0.09} \times D50^{-0.12}$	0.55	0.53
117	PC, WC, S_u, D50	EFA/Fine 44	$EC = 0.023 \times PC + 0.03 \times WC + 0.0017 \times S_u - 1.845 \times D50 + 0.8566$	0.56	0.43
91	C_u, WC, VST, D50	EFA/Coarse 11	$EC = (1.12) \times C_u^{0.1} \times WC^{-0.28} \times VST^{0.02} \times D50^{-0.44}$ $for\ 0.074 < D50 < 0.3$	0.92	0.80
13	PI, γ, PF	JET/Fine 56	$EC = (0.00375) \times PI^{0.12} \times \gamma^{1.81} \times PF^{0.21}$	0.51	0.47
88	PL, S_u, D50	JET/Global 28	$EC = -0.022 \times PL + 0.0031 \times S_u - 5.5 \times D50 + 3.34$ $for\ D50 < 0.3\ mm$	0.70	0.58
12	PI, γ, S_u	HET/Fine 21	$EC = (1.67) \times PI^{0.04} \times \gamma^{0.15} \times S_u^{0.03}$	0.70	0.54

Table 85. Selected models for velocity slope E_v

Group No.	Independent variables	Dataset/ No. of data	Model expression (parameter values given by deterministic regression)	R^2	Cross-validation score
86	C_u, γ, WC, D50	EFA/Coarse 28	$E_v = (88969.4) \times C_u^{-1.77} \times \gamma^{-2.26} \times WC^{0.34} \times D50^{-1.69}$	0.86	0.64

Table 86. Selected models for shear stress slope E_τ

Group No.	Independent variables	Dataset/ No. of data	Model expression (parameter values given by deterministic regression)	R^2	Cross-validation score
77	C_u, γ, D50	EFA/Coarse 28	$E_\tau = (3228.7) \times C_u^{-2.8} \times \gamma^{-1.58} \times D50^{-2.91}$	0.91	0.64
40	γ, WC, PF, D50	HET/Coarse 62	$E_\tau = (2.951) \times \gamma^{26.08} \times WC^{-7.48} \times PF^{-19.96} \times D50^{-5.32}$	0.86	0.55

7.4.4.1. Power model for erosion category EC, EFA/Fine dataset

The selected case is the power model created to predict erodibility parameter EC, for EFA/Fine dataset (group number 132). Four independent variables are considered: A, WC, Su, and D50 which denote soil activity, water content, undrained shear strength, and mean particle size, respectively. A total of 44 data observations are available where each consist of 4 geotechnical properties as input, and *EC* as the erodibility property or output. Table 84 provides optimization result of model parameters through non-linear regression. Taking these parameter values, the generated model predictions, along with observed data plotted along each variable domain as shown in Figure 263. It is shown that the vector of experimental observations is scattered along each variable domain, and that the proposed model overall captures the mean of the process.

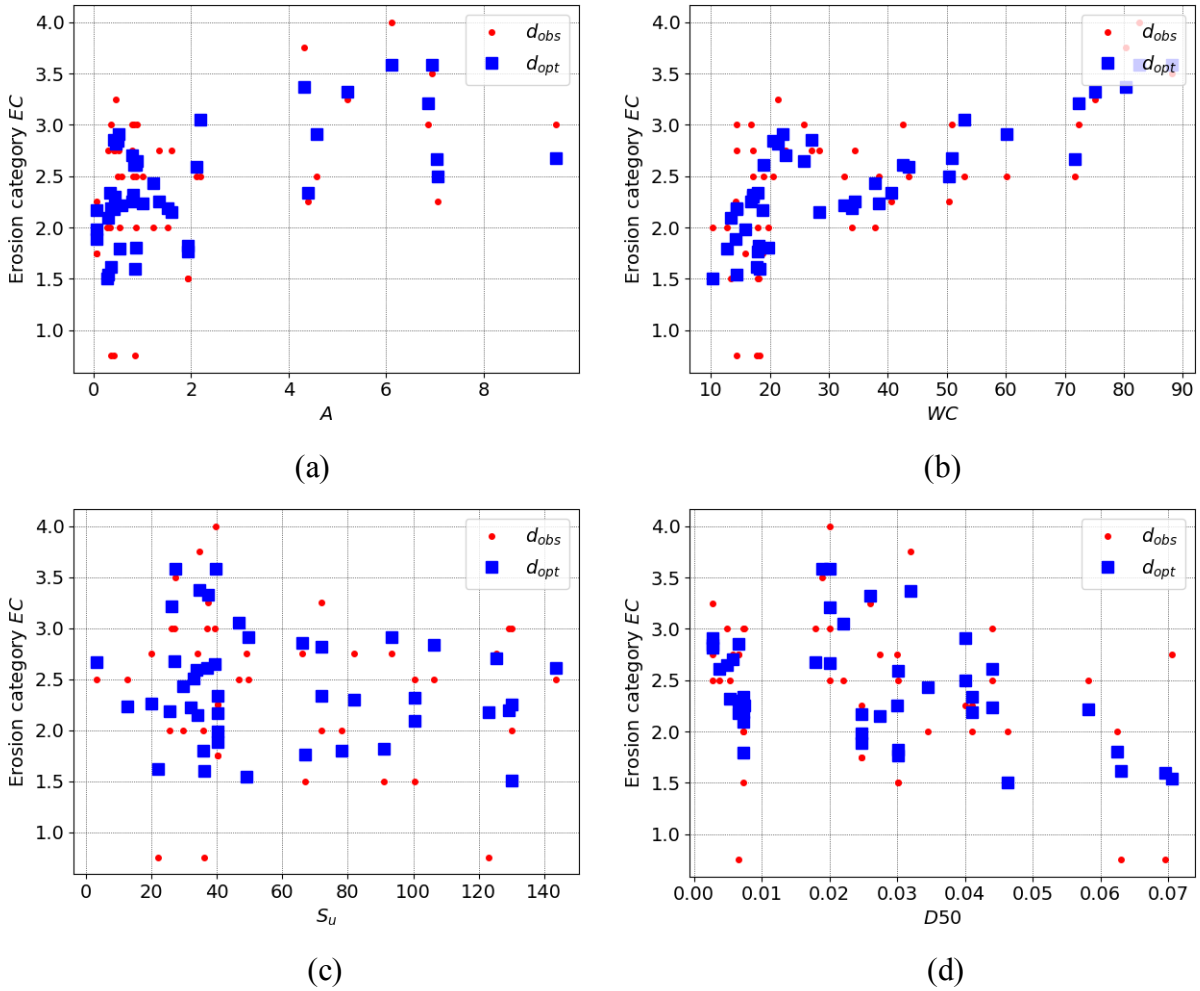

Figure 263. Experimental observations and model predictions along variable domains, (a) soil activity, (b) water content, (c) undrained shear strength, (d) mean particle size.

Step1. Optimization

In the proposed probabilistic calibration framework, the optimization result are not only able to provide the initial guess of random parameter values (as presented in Figure 263), but it also can retrieve the shape of the error between model predictions and observations, which leads to the selection of the probability function to be considered for the likelihood. Figure 264 (a) shows histogram and kernel density estimate of residuals of model prediction, a nominal Gaussian distribution of mean around zero seemingly a reasonable fit of empirical distribution, which

indicates also that unbiased character of the proposed model. However, the change of bin size and starting position of histogram may result in a variation to its shape. Even though the kernel density estimate can eliminate the effect of starting position of plot, one still needs to determine the kernel width for which there is not a systematic approach in practice. Figure 264 (b) indicates a better solution to the problem. By plotting empirical cumulative density function (eCDF) of error, a monotonic increase of probability is able to provide a unique description of error distribution. A Gaussian distribution presents a suitable approximation of error distribution, thus it is adopted as the likelihood function and used into the Bayesian formulation. A non-informative distribution is considered as a prior for the Bayesian formulation.

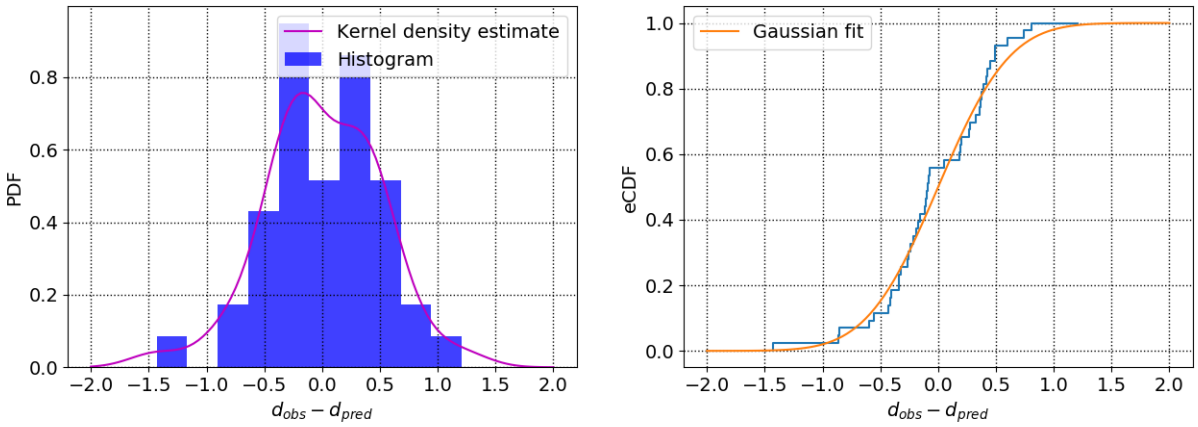

(a) (b)

Figure 264. (a) Histogram and kernel density estimate of error (b) eCDF and Gaussian fit of error

Step 2. Probabilistic calibration and convergence diagnose

For the sake of a better presentation of the calibration results for the group number 132 (Table 84), each model parameter is named following the variable it serves to, that is β_0, β_A, β_{WC},

and β_{S_u}. Where, β_0 refers to the scaling factor at the beginning of the equation. The selected prior for all parameters are vague Gaussian prior, with mean equals zero and standard deviation of 10^6.

Figure 265 present MCMC sample sequences of each parameter for 100,000 iterations. A stationary state was achieved for each parameter as illustrated by Figure 266 and Figure 267 are cumulative mean and cumulative standard deviations of sample sequences for each parameter. These plots are used to validate the convergence of MCMC achieved at a stationary condition, and to define the 'burn-in' point after which statistics about the model performance are computed. As the principle of stationary should be achieved for both cumulative mean and standard deviation plots, the burn-in point was set as 40,000.

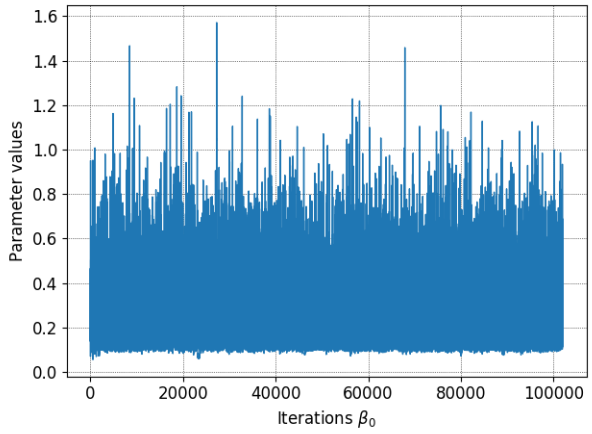

(a)

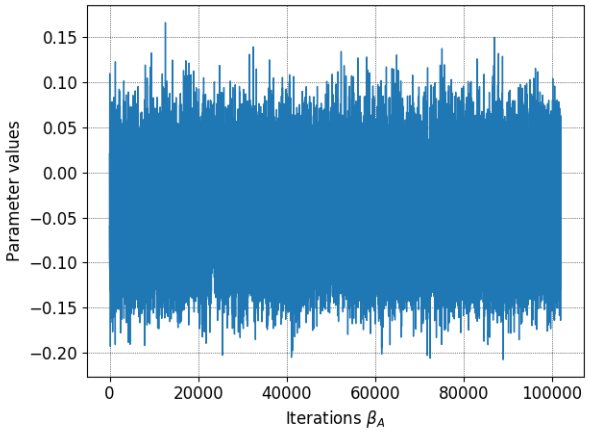

(b)

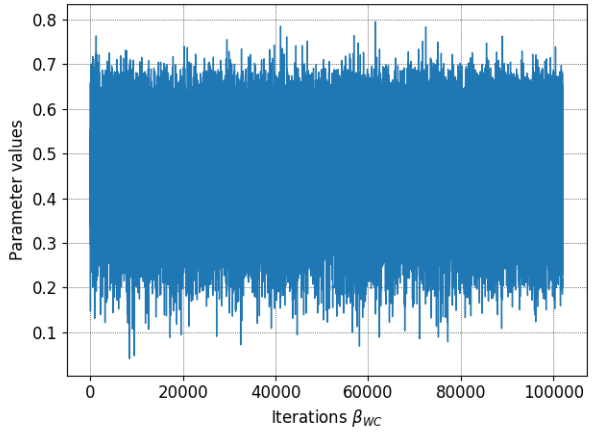

(b)

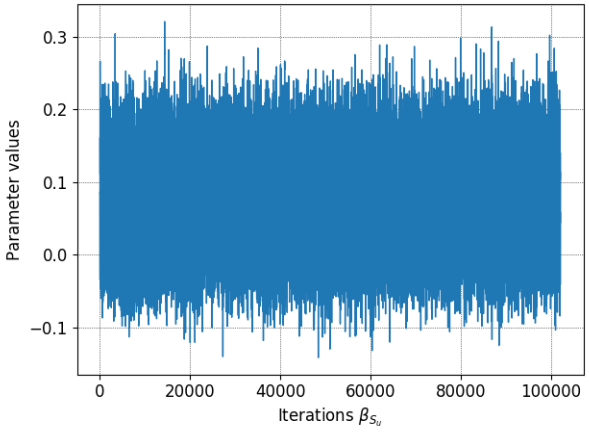

(d)

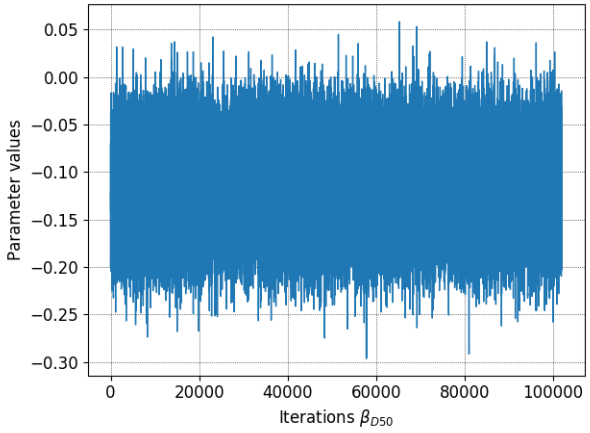

(e)

Figure 265. Random samples of model parameters, (a) $\boldsymbol{\beta_0}$, (b) $\boldsymbol{\beta_A}$, (c) $\boldsymbol{\beta_{WC}}$, (d) $\boldsymbol{\beta_{S_u}}$, (e)$\boldsymbol{\beta_{D50}}$

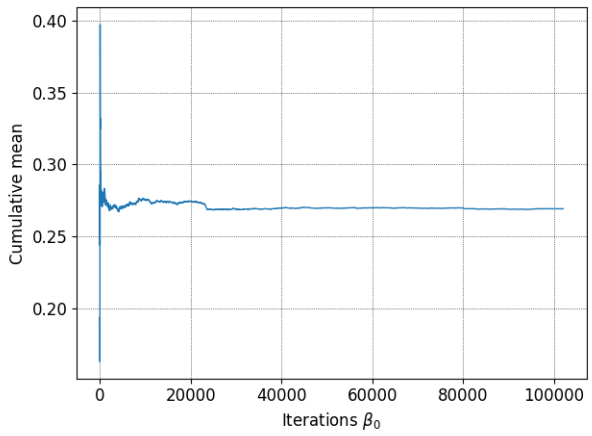

(a)

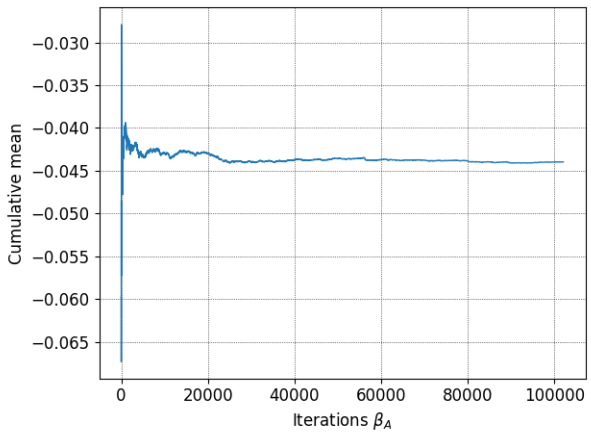

(b)

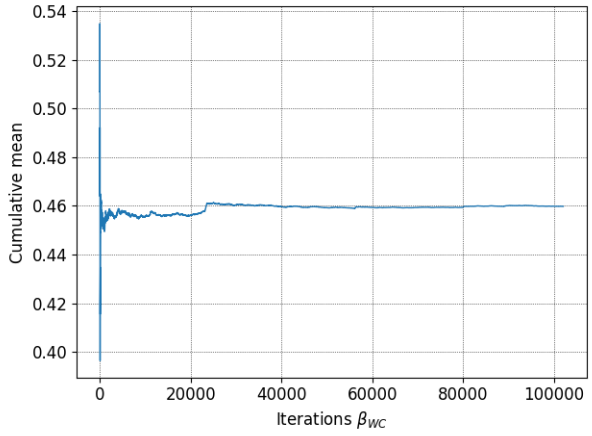

(a)

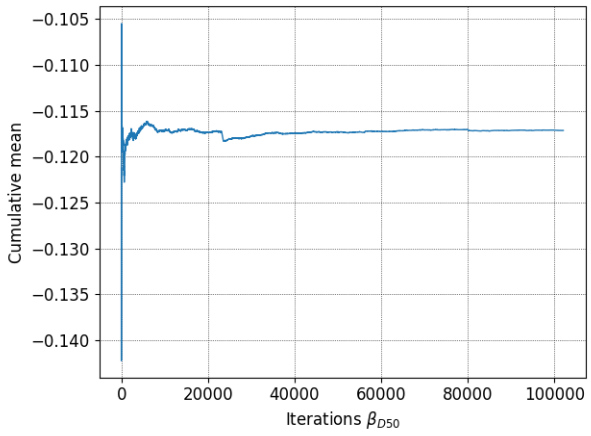

(d)

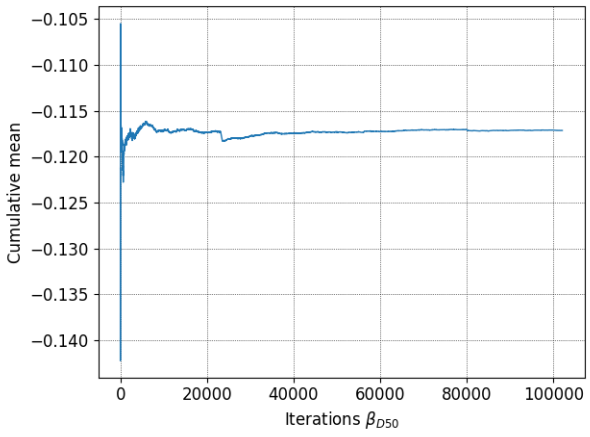

(e)

Figure 266. Cumulative mean of sample sequences for each parameter, (a) $\boldsymbol{\beta_0}$, (b) $\boldsymbol{\beta_A}$, (c) $\boldsymbol{\beta_{WC}}$, (d) $\boldsymbol{\beta_{S_u}}$, (e) $\boldsymbol{\beta_{D50}}$

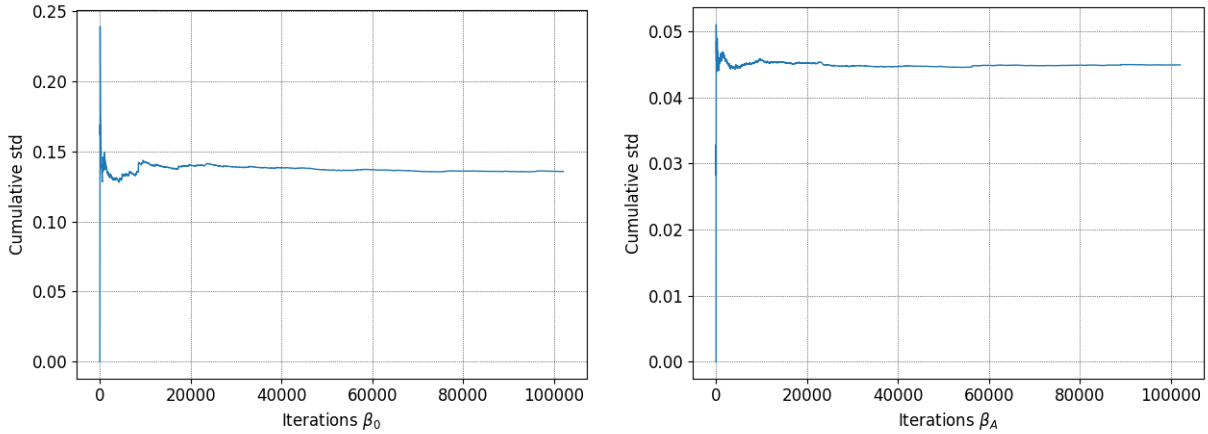

(a)

(b)

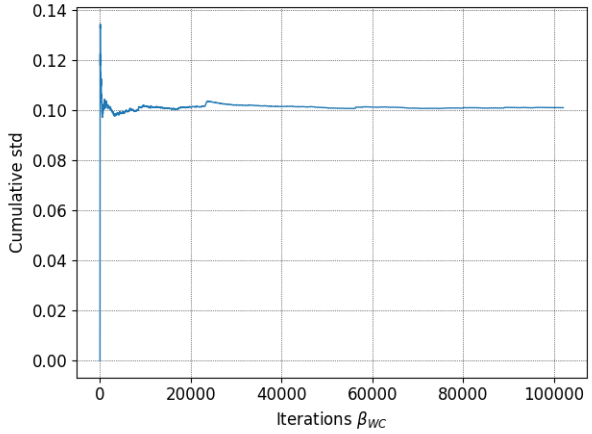

(b)

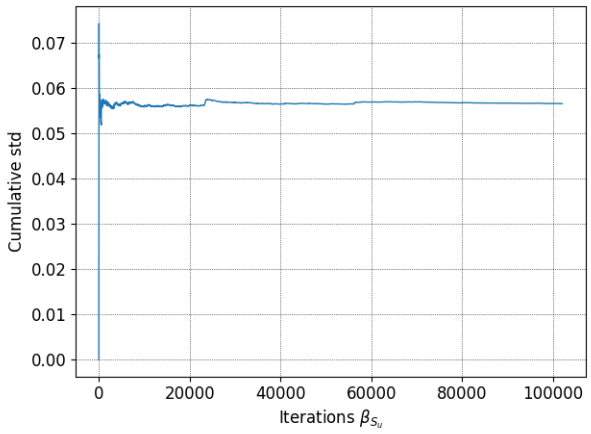

(d)

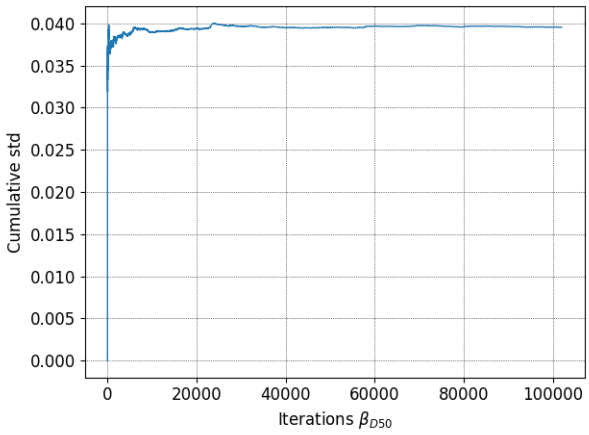

(e)

Figure 267. Cumulative standard deviation of sample sequences for each parameter, (a) $\boldsymbol{\beta_0}$, (b) $\boldsymbol{\beta_A}$, (c) $\boldsymbol{\beta_{WC}}$, (d) $\boldsymbol{\beta_{S_u}}$, (e) $\boldsymbol{\beta_{D50}}$

Step3. Posterior statistics

Once the MCMC posterior sampling reached a stationary state, statistical inferences can be generated. Figure 268 shows a depiction of the joint relative frequency histograms across all model parameters, as well as the marginal pdfs of each parameter presented along the figures' matrix diagonal. Most probability distributions indicate an asymptotic normality in its shape. The validity of this rests on the central limit theorem. Table 87 gives posterior statistics in terms of mean, standard deviation, coefficient of variation, mode, and 95% highest posterior density (HPD) region. The mean values are close to what has been obtained from regression analysis, but one should adopt these with caution. For instance, the distribution of β_0 is not symmetric and skew to the right (i.e., positive skewness), which yields its mean value bigger than the mode. A more rational choice would be the latter as it represents higher probability by the probabilistic calibration. Lower triangular plots in Figure 268 are the parameters cross-correlation investigations, with two at a time. Since β_0's pdf is asymmetric, non-linear correlation structure observed between β_0 and other parameters. A significant negative correlation is shown between β_A and β_{WC}, indicating the strong association of soil's water content and activity in predicting erosion category. The scatter plots of posterior samples and Pearson correlation coefficients are given in the upper triangular matrix, which provide direct delineations of correlation type and degree among various parameter combinations.

It is worth noting that in Table 87, the coefficients of variation are given as complementary information of parameter variability. Additionally, a 95% HPD region is given for each parameter which denotes the 'credible range where a given parameter exhibits higher probability of occurrence.

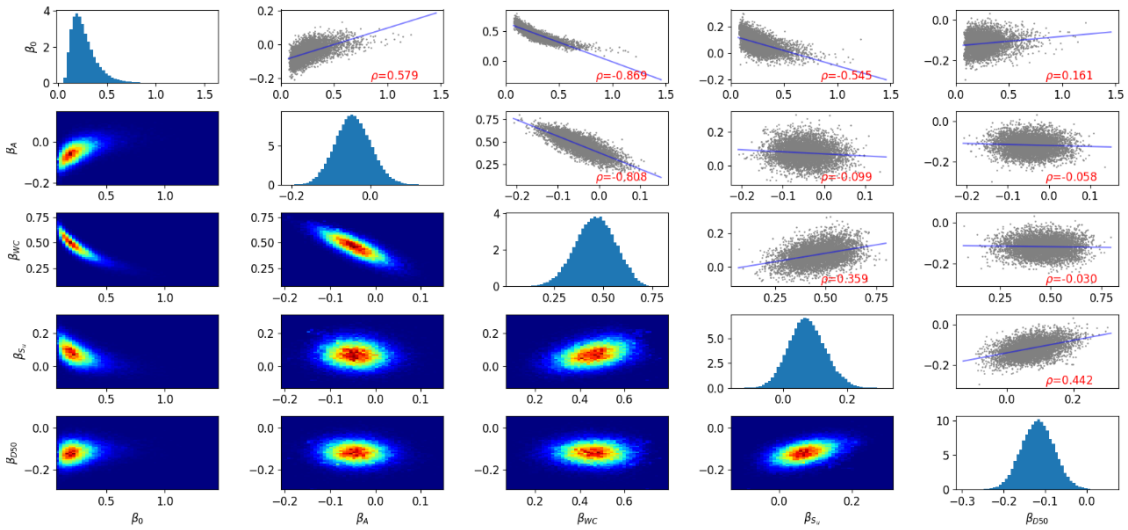

Figure 268. Joint relative frequency histogram of model parameters, two at a time.

Table 87. Statistics of probabilistic calibrated model parameters

Parameters	Mean	SD	CoV	mode	95% HPD region (lower and upper bound)	
β_0	0.27	0.13	0.50	0.19	0.07	0.53
β_A	-0.04	0.05	-1.02	-0.04	-0.13	0.05
β_{WC}	0.46	0.10	0.22	0.49	0.27	0.66
β_{S_u}	0.07	0.06	0.77	0.07	-0.03	0.19
β_{D50}	-0.12	0.04	-0.34	-0.12	-0.19	-0.04

Step4. Probabilistic realizations and assessment of model performance

Finally, the probabilistic calibration approach allows to produce a metric of the model performance. Once the posterior distribution is populated, likely realizations of the model predictions can be computed by sampling random parameter combinations from it. These model responses provide numerical evidence to estimate first and second order statistics in regards to model performance.

To achieve this goal, it is required to compose a multi-dimensional mesh grid retrieved across all independent variables, enabling the assessment if the model prediction along each

domain of all independent variables vs. the dependent variable or erodibility parameter. Each domain range is decided by minimum and maximum values retrieved from experimental observations, besides 10 uniform discretization steps was chosen for each variable to ensure computational efficiency and sufficiency on the inferences at the same time. For example, for the case of group No. 132 there are 4 independent variables and the mesh grid is discretized with 10 steps, meaning $10^4 = 10{,}000$ 'points' where the hyper-surface produced by the model will be repeatedly evaluated for different parameters' combinations. That is, from the posterior, 1000 random parameter samples are taken after the burn-in point which produce ensemble of model predictions (10^7 model predictions along the mesh grid).

Probabilistic and deterministic model realizations along each independent variable domain are shown in Figure 269. Once the ensemble of model predictions is plotted along each variable domain, a one-to-n mapping is then possible where multiple model outputs can correspond to one prescribed variable value, as it shown in Figure 269. This shows 1,000 probabilistic realizations as opposed to 1 deterministic realization. The progress of model realizations along A and D50 domains shows a distinct trend compared to WC and Su. This is due to the mean of parameters retrieved from posterior are positive for β_{WC} and β_{S_u}, whereas negative for β_A and β_{D50}.

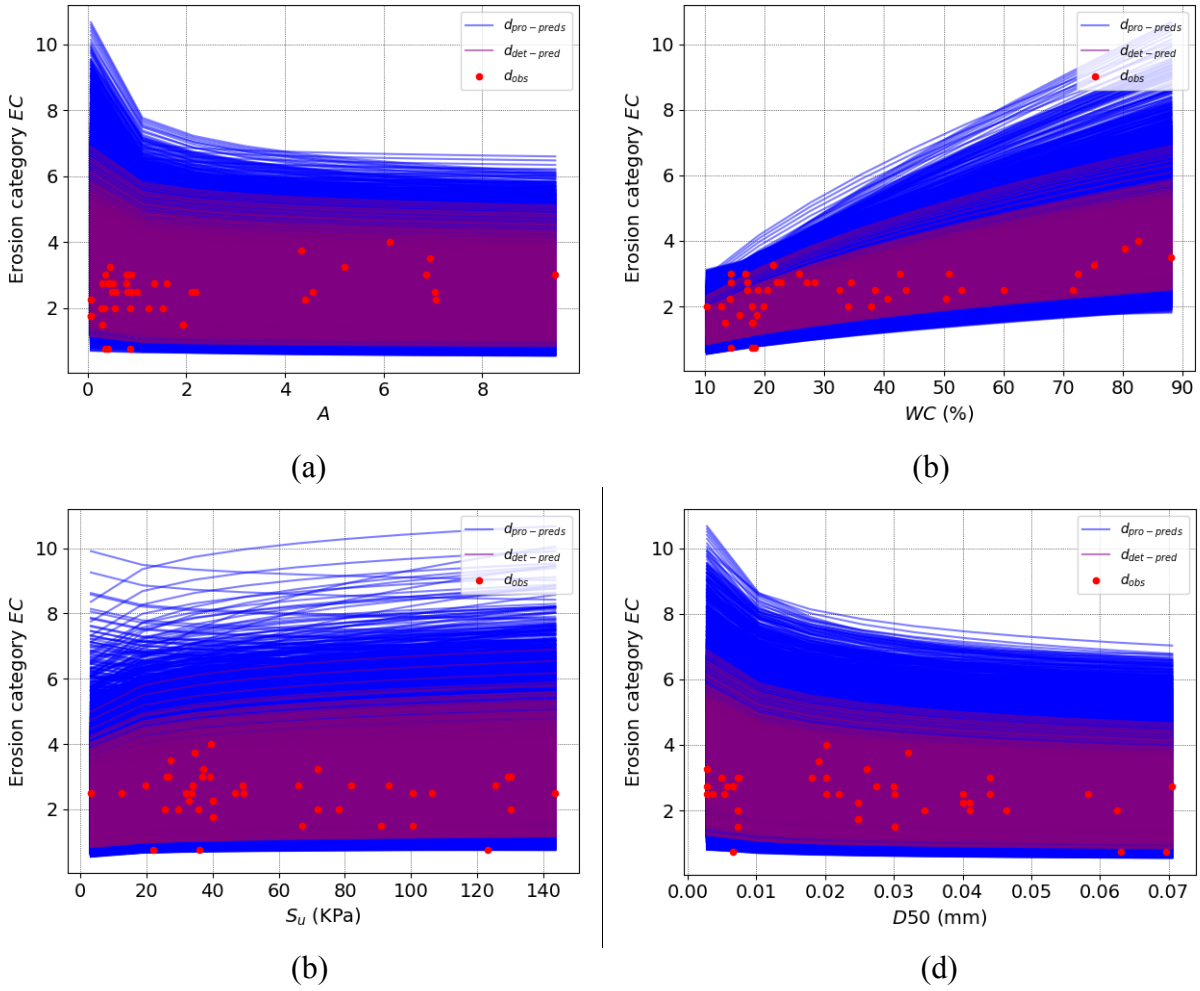

Figure 269. Model realizations coupling with observed dataset along each variable domain, (a) soil activity, (b) water content, (c) undrained shear strength, (d) mean particle size.

First order statistics for this model can be computed along the domain of each independent variable (physical domain) as presented in Figure 270, which show that the mean computed from the ensemble of simulations produced by the posterior, converges to the 'optimal' estimate produced by the deterministic calibration. However, a heteroscedastic condition is shown, or variance variability along each domain of all independent variables. This is a reflection of non-Gaussian nature of the variation of the mean of the EC process. Figure 270 shows larger HPD interval areas above the mean of the model predictions, which indicates that the EC predictions

are skewed to the upper side for all independent variables. It is very important to notice that these first and second order statistics correspond to the given model realizations (Group No. 132) which represent the credibility of the 'mean', not of the whole population. The yellow and red curves represent the mean of the probabilistic calibration and optimal model predictions at each independent variable. The mean produced from the probabilistic calibration stemmed from an exhaustive sampling process across all the parametric space (MCMC) as opposed to a limited sampling to assess the deterministic calibration to produce the 'optimal' vector of the model parameters. Figure 270 (b) presents the least overall uncertainty among the four independent variables, which shows WC as the best predictor for this group number.

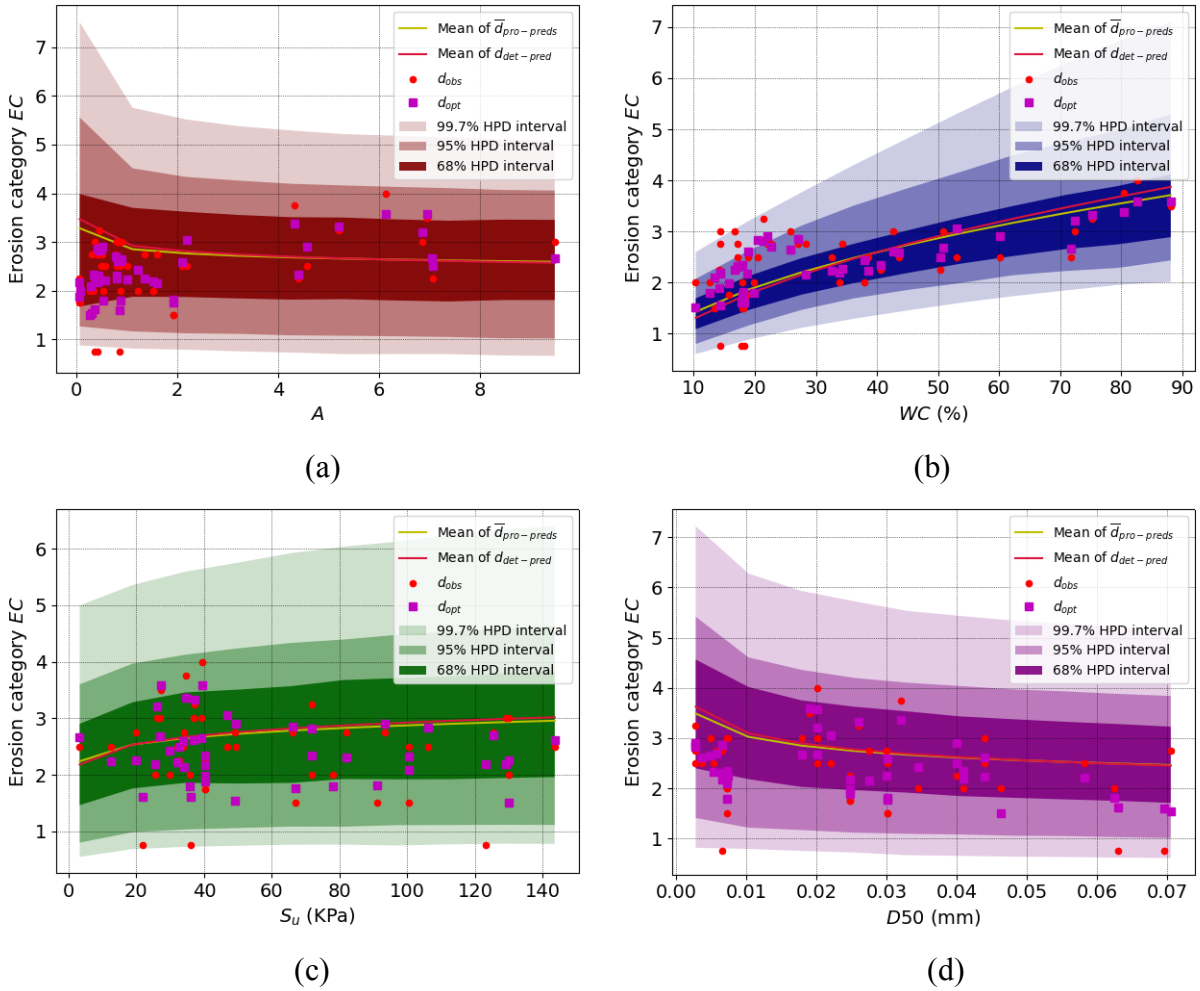

Figure 270. Mean and standard deviations of model predictions vs. observed data, (a) soil activity, (b) water content, (c) undrained shear strength, (d) mean particle size.

Similar to the POU/POO analyses performed based on the deterministic regression results, it is also possible to associate the correction factors with confidence levels with respect to the probabilistic results. Figure 271 presents the measured EC versus predicted EC in an equal aspect ratio context, where results laying along the 45-degree line means a perfect fit. Similar to the 1,000-posterior ensemble of realizations, this figure shows 1,000 model predictions at the same location of the available experimental EC observations. Boxplots at each of these points are presented to indicate the model variation or variation of the mean of the EC process. From the same 1,000

realizations, the correction factors (θ) are computed to produce POU levels as shown in Figure 272 (a). Figure 272 (b) presents the mean and HPD intervals for the same realizations, showing a growing uncertainty inherent in POU with the increase of the correction factor. This is a significant improvement over the previous deterministic plots, since these add a confidence metric on the assessment of the correction factors associated with every POU values.

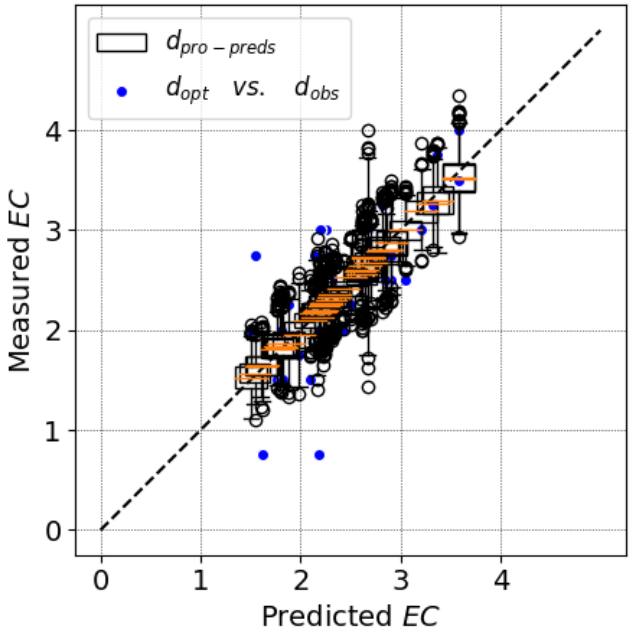

Figure 271. Measured EC vs. Predicted EC, based on optimization and probabilistic calibration results

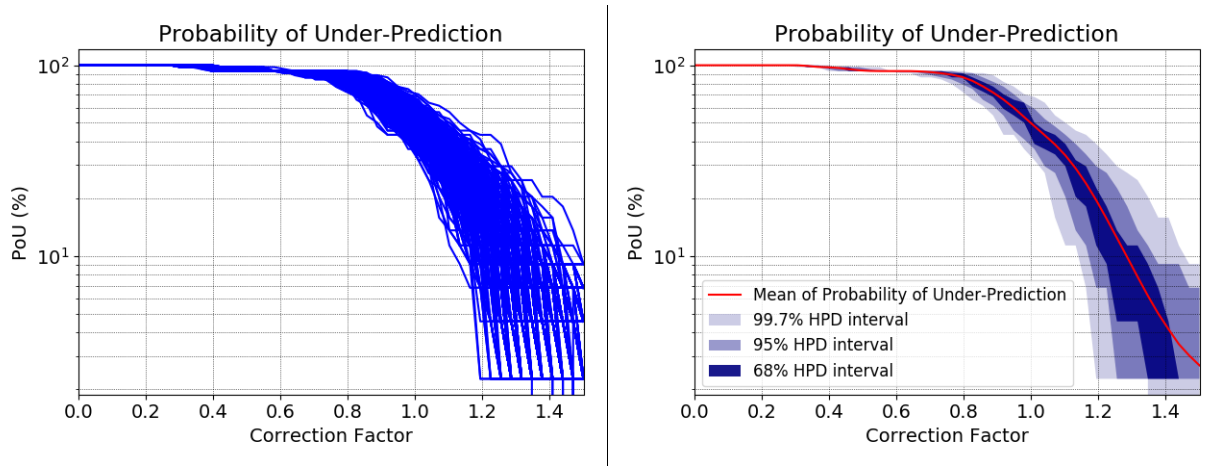

(a) (b)

Figure 272. (a) 1,000 realizations of POU vs. correction factor, (b) Mean and HPD intervals of POU

7.4.4.2.Linear model for erosion category EC, EFA/Fine dataset

A second probabilistic calibration is presented for the linear model for erodibility parameter EC, EFA/Fine dataset (Group No. 117). The main difference between the two cases discussed here is the proposed regression model used to predict the erosion category EC. Both first and second order statistics for each model parameter are evaluated. Only results after 'step 2' of the probabilistic calibration will be presented for this model since convergence of the MCMC posterior sample was also achieved. The matrix of plots presenting the posterior's joint relative frequency histograms of this model parameters is introduced in Figure 273. A uniform negative correlation between intercept β_0 and other parameters is presented at the bottom row, with correlation coefficients range from -0.491 to -0.841. In contrast with power model, all marginal pdfs along the diagonal are following Gaussian shape without skewness, which results from free boundary of possible EC parameter values in linear model (negative values of β_0 in the power model are by default not sampled during MCMC). Higher CoV values of β_{D50} and β_{S_u} are expected

to cause bigger variations along D50 and S_u domains which will be examined through realizations and statistical analysis in each variable domain.

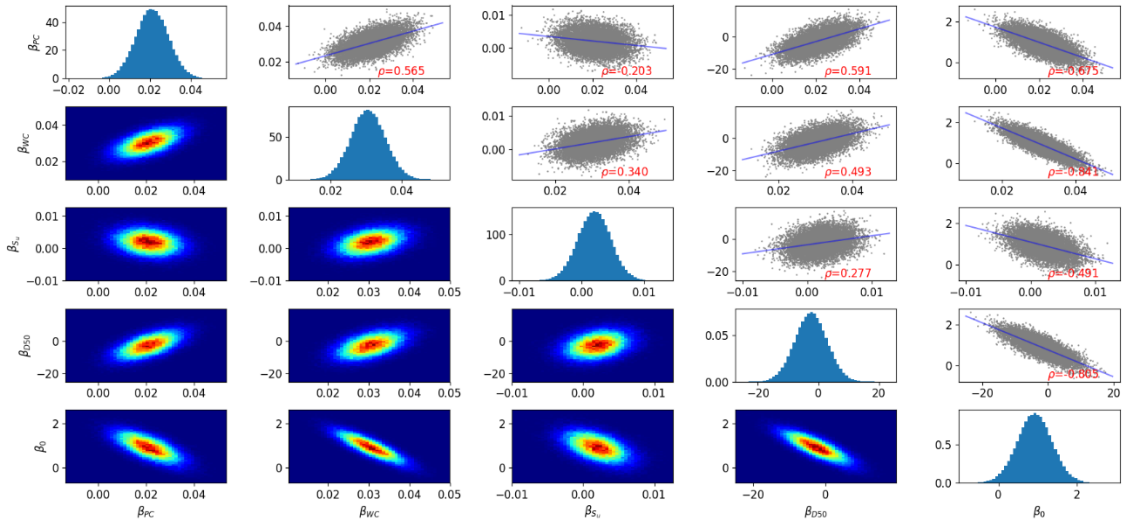

Figure 273. Joint relative frequency histogram of model parameters, two at a time

Table 88. Model characteristics and optimization result

Group No.	Independent variables	Dataset/ No. of data	Model expression (parameter values given by deterministic regression)	R^2	Cross-validation score
117	PC, WC, S_u, D50	EFA/Fine 44	$EC = 0.023 \times PC + 0.03 \times WC + 0.0017 \times S_u - 1.845 \times D50 + 0.8566$	0.56	0.43

Table 89. Statistics of probabilistic calibrated model parameters

Parameters	Mean	SD	CoV	mode	95% HPD region (lower and upper bound)	
β_{PC}	0.021	0.008	0.378	0.021	0.006	0.037
β_{WC}	0.031	0.005	0.160	0.030	0.021	0.040
β_{S_u}	0.002	0.003	1.313	0.002	-0.003	0.007
β_{D50}	-2.396	5.349	-2.232	-1.137	-12.858	8.083
β_0	0.922	0.440	0.477	1.004	0.053	1.770

Figure 274 and Figure 275 display 1,000 model realizations from the sampling of the posterior and its corresponding first and second order statistics along each domain of the independent variables. The mean of the EC process produced by the probabilistic calibration and the optimal realization produced by the deterministic regression show a significant agreement. In addition, comparison of HPD intervals for linear and power models indicates uncertainty is more uniformly distributed in both domains and co-domains for the former, and also quantitatively smaller. However, it is worth noticing that by using the linear model, it may yield negative values of EC that might not make sense in reality. A rational choice in such case would be power model instead or to further restrict the variation of EC during the MCMC sampling process of the posterior.

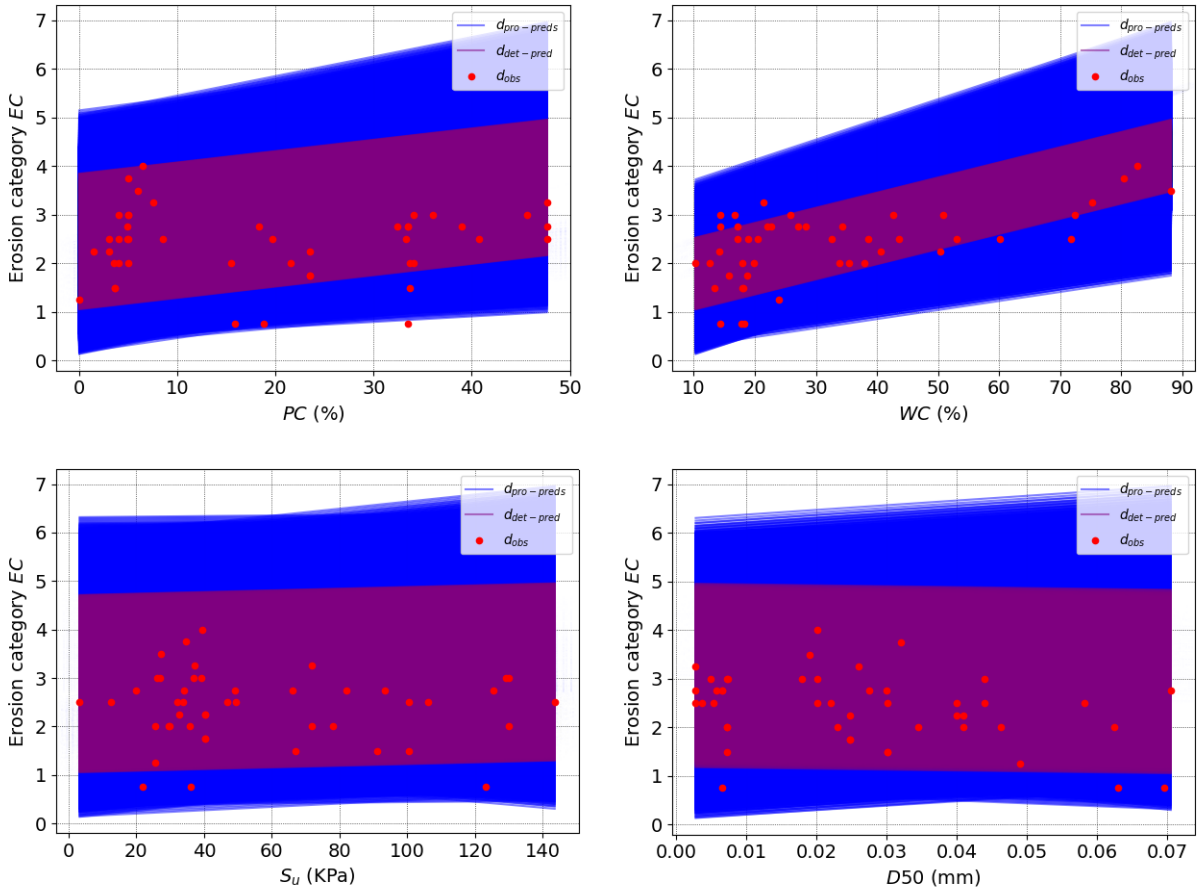

Figure 274. Model realizations coupling with observed dataset along each variable domain, (a) percent clay, (b) water content, (c) undrained shear strength, (d) mean particle size

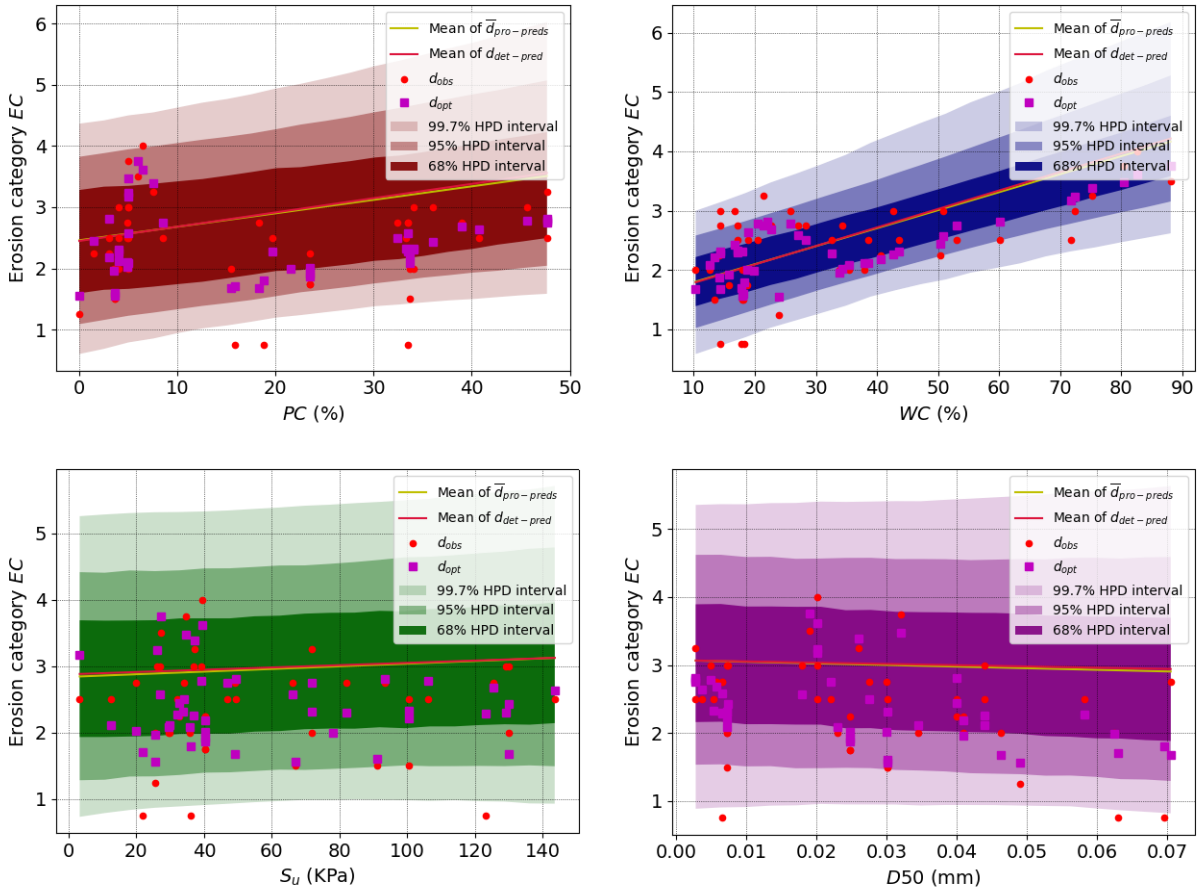

Figure 275. Mean and standard deviations of model predictions vs. observed data, (a) percent clay, (b) water content, (c) undrained shear strength, (d) mean particle size

Finally, a reliability-based analysis is conducted to assess the model performance. Even though both linear and power models show a good capacity to capture the mean of the EC process, a more uniform prediction variations is presented for the linear model (Figure 276), which is consistent with the findings in Figure 275. In regards to the plots of "POU vs. θ", results are similar for both models. For instance, seeking 90% confidence that the predicted EC is smaller than the actual EC, the predicted value should be multiplied by a correction factor equals to 0.80 for both scenarios.

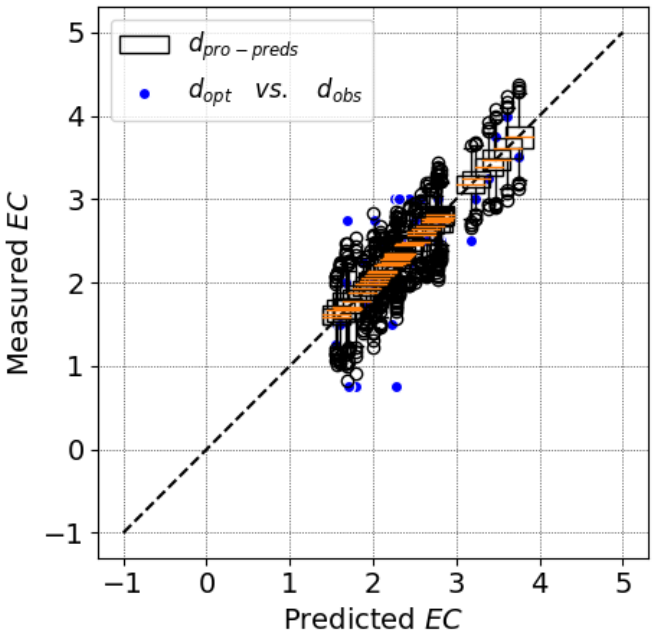

Figure 276. Measured EC vs. Predicted EC, based on optimization and probabilistic calibration results

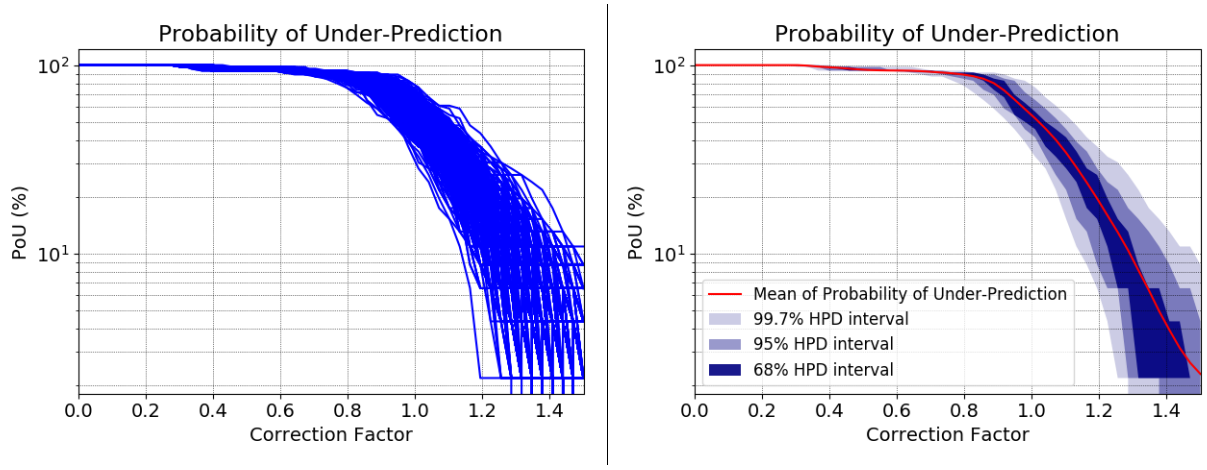

(a) (b)

Figure 277. (a) 1,000 realizations of POU vs. correction factor, (b) Mean and HPD intervals of POU

8. MOST ROBUST CORRELATION EQUATIONS

As discussed in the previous chapter, two statistical approaches, deterministic frequentists' regression and the probabilistic (Bayesian) inference, were carried out to identify the best correlation equations between the erodibility parameters and the geotechnical properties. In this chapter, the selected models are repeated and tabulated in order to make it easier for practitioners to use them. It should be noted that the erodibility parameters are predicted using different equations depending on what erosion test data (EFA, JET, or HET) are used to develop them. Therefore, the knowledge on the strength points/limitations of each test is a vital step prior to choosing an equation. Before presenting the most robust correlation equations, a summary of the advantages and disadvantages of each test is put together in Section 8.1 by the authors. Section 8.1 helps the readers identify and understand the differences between the erosion tests. The engineer is free to select the best equation according to his/her objective and considering the differences between the equations.

Sections 8.2 and 8.3 are a summary of the findings in the previous chapter. Section 8.2 presents the selected correlation equations generated using the deterministic frequentists' regression approach in a tabulated format. Section 8.3 also provides a look at the aforementioned equations using the Bayesian inference approach.

8.1. Differences between the EFA, the JET, and the HET

In this section, a list of advantages and disadvantages associated with the EFA, the JET, and the HET, as well as the applications of each erosion test are presented. It should be noted that the information provided here are the recommendations made by the authors based on decades of

experience in erosion testing, and according to the various challenges confronted in conducting hundreds of erosion tests during this project.

The proposed equations in Section 8.2 are developed based on the data obtained in different erosion tests; therefore, a good knowledge of each test is very useful in order to choose the best equation. Chapter 2 discussed all major differences between each erosion test. Additionally, the advantages and drawbacks of many different erosion tests were discussed; however, as mentioned earlier, the regression study performed in this project focused on the three major erosion tests namely: EFA, JET, and HET. In order to facilitate the use of the proposed equations, the advantages and drawbacks of these three tests are summarized in this section.

Table 90 shows a list of advantages, disadvantages, and applications for the EFA, the JET, and the HET. The content of this table should be studied carefully before using the proposed equations in Section 8.2.

Table 90. Comparison of the EFA, the JET, and the HET

Erosion Test	Advantages	Drawbacks	Applications
EFA	1) Minimize the sample disturbance effect, as it takes the un-extruded sample directly from the field using Shelby tubes. 2) Can be used for natural samples as well as human made samples 3) Gives all five erodibility parameters (i.e. v_c, τ_c, E_v, E_τ, and EC). Can give the erosion function directly. 4) Can monitor the erosion rate in real-time rather than interpolating or extrapolating using indirect equations. 5) EFA test results are directly used as input to the TAMU-SCOUR method for bridge scour depth predictions (Chapter 6 of HEC-18). 6) EFA can test the erodibility of the soil at any depth as long as a sample can be recovered. 7) Gives the erosion function which is a fundamental measure of erodibility at the element level. 8) Can be used to test very soft to very hard soils. Very broad applications. The velocity range is from 0.2 m/s up to 6 m/s.	1) Shear stress is indirectly measured from velocity using Moody charts which might not be accurate. Also, the average flow velocity is used in the calculation. 2) In some cases, obtaining samples is difficult and costly. The test needs to be done on the sample before the sample is affected by long periods of storage. 3) Particles larger than about 40 mm in size cannot be tested with confidence as the diameter of the sampling tube is 75 mm. 4) The EFA device is fairly expensive (around $50k in 2018).	1) Bridge scour 2) Meander migration 3) Levee overtopping 4) Soil improvement 5) Internal erosion of dams
JET	1) Can be run both in the field and in the lab. 2) The latest version of the JET, the mini-JET, is simple, quick, and inexpensive compared to other types of erosion test. 3) Can be performed on any surface vertical, horizontal, and inclined. 4) Very good as an index erodibility test.	1) Particles larger than 30 mm in size cannot be tested with confidence because of the small size of the sample. 2) Coarse grained soils tend to fall back into the open hole during the jet erosion process thereby making the readings dubious. 3) Very small-scale test application. 4) Typically used for manmade samples. Natural are more difficult to test	1) Agriculture erosion 2) Levees

Table 90 (Continued). Comparison of the EFA, the JET, and the HET

Erosion Test	Advantages	Drawbacks	Applications
JET		5) The flow within the eroded hole and at the soil boundary is complex and difficult to analyze. 6) Only gives three of the erodibility parameters (τ_c, E_τ, and EC) out of the five possible parameters. 7) The elements of erosion are inferred rather than measured directly. 8) There are multiple interpretation techniques to predict the critical shear stress which give significantly different results.	
HET	1) Direct similitude with piping erosion in earth dams. 2) Can apply to a wide range of pressure heads and therefore wide range of hydraulic shear stress at the soil-water interface.	1) The sample needs to be cohesive and strong enough to stand under its own weight. Therefore, the test cannot be run on loose cohesion-less soils or soft cohesive soils. 2) Very difficult to run on intact samples in Shelby tubes from the field. Only good for remolded re-compacted samples in the lab. 3) Difficult and time-consuming preparation of the test. 4) No direct monitoring of the erosion process. The erosion rate needs to be inferred and extrapolated. 5) The hydraulic shear stress is inferred, and not directly measured. 6) The data reduction process is quite subjective. 7) Only gives three of the erodibility parameters (τ_c, E_τ, and EC) out of the five possible parameters. 8) The flow within the eroded hole and at the soil boundary is complex.	1) Internal erosion of earth dams 2) Suffusion 3) Levee breach 4) Soil improvement

8.2. Deterministic (Frequentists' Regression) Analysis

The best models as discussed in the previous chapter are selected for each erodibility parameter and for each erosion test. The results are shown in the following tables. The first column from left shows the erosion test data used to develop the equations. The second column from left indicates the accepted mean particle size (D_{50}) range for the proposed equations. The third column from left shows the model, and the "probability of under/over-predicting (POU/POO)" plots for the model. For further information on the use of these plots, please refer to the Section 7.3.3.3 of this report. Finally, the last column from left presents some remarks on the proposed equation. It also presents the correction factor to reach a 90% confidence in under/over-predicting of the measured erodibility parameter. It should be noted that the units used for each parameter are indicated in Appendix D as well as in Table 47.

Table 91 shows the proposed correlation equations to predict the critical shear stress (τ_c) based on the EFA test. This table presents the recommended correlation equations to predict critical shear stress in different D_{50} ranges. It should be noted that alongside with each proposed equation, these tables often give two plots showing the POU (or POO, where applicable) vs. correction factor, as well as the "predicted" vs. "measured". Such plots provide great insight on using each equation. Also, a column containing some remarks is provided on the right side of each equation. This column includes the values of R^2 and the cross-validation score (named as C.V in the tables). Table 92 and Table 93 also show the proposed correlation equations to predict the critical shear stress (τ_c) based on the JET and HET, respectively.

Table 91. Proposed equations for critical shear stress (τ_c) based on the EFA Test data

EFA	$D50 > 0.3\ mm$	$\tau_c = D50$	
	$0.074\ mm < D50 < 0.3\ mm$	$\tau_c = (1.58) \times C_u^{-0.04} \times \gamma^{0.02} \times D50^{0.77}$ 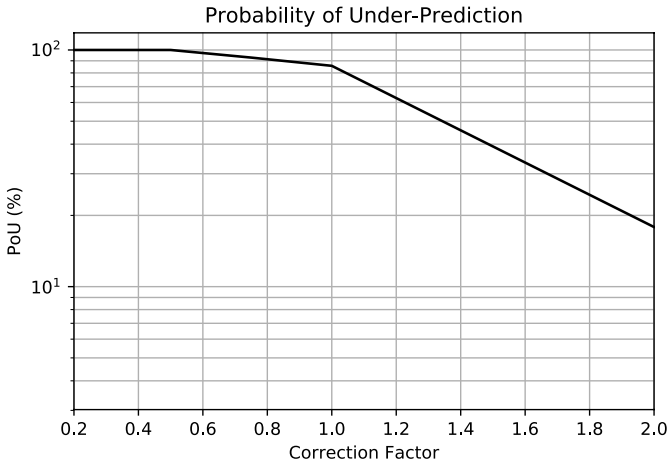 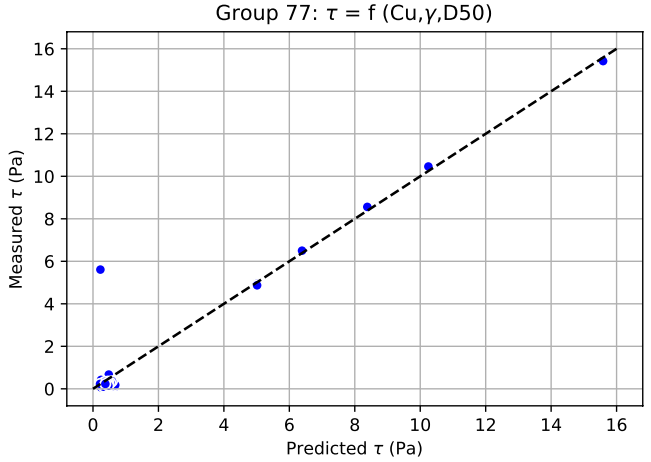	**Remarks** $R^2 = 0.93$ C.V Score = 0.99 1- Refer to the Group 77 in Table 50 for further information on the statistical significance of the proposed equation. 2- The "POU vs. Correction Factor" plot is based on the data used to develop the proposed equation. 3- In order to reach a 90% confidence that the predicted τ_c is smaller than the actual τ_c, the predicted value should be multiplied by 0.82. (with 0.3 Pa offset).

Table 91 (Continued). Proposed equations for critical shear stress (τ_c) based on the EFA Test data

EFA	$D50 > 0.3\ mm$	$\tau_c = D50$	
	$0.074\ mm < D50 < 0.3\ mm$	$\tau_c = (1.58) \times C_u^{-0.04} \times \gamma^{0.02} \times D50^{0.77}$ 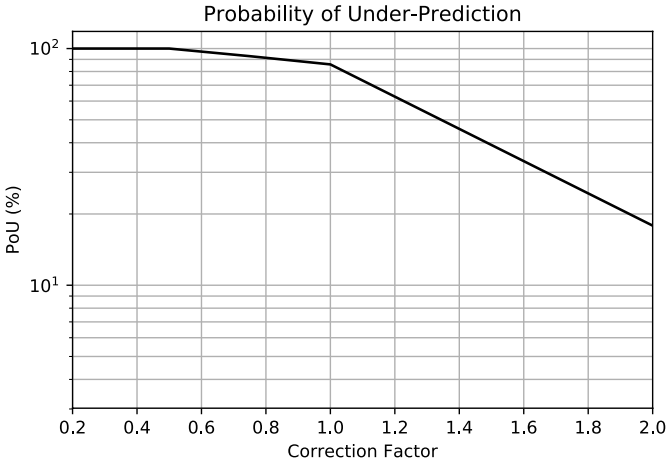 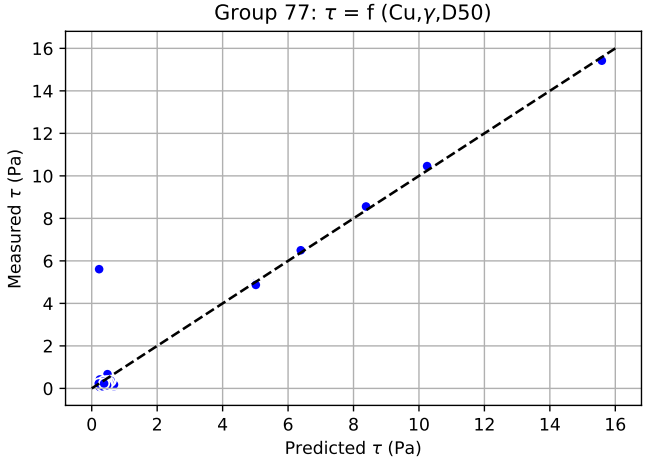	**Remarks** $R^2 = 0.93$ C.V Score = 0.99 1- Refer to the Group 77 in Table 50 for further information on the statistical significance of the proposed equation. 2- The "POU vs. Correction Factor" plot is based on the data used to develop the proposed equation. 3- In order to reach a 90% confidence that the predicted τ_c is smaller than the actual τ_c, the predicted value should be multiplied by 0.82. (with 0.3 Pa offset).

Table 92. Proposed equations for critical shear stress (τ_c) based on the JET data

JET	$D50 < 0.3\ mm$	$\tau_c = -0.248 \times PC - 1.23 \times \gamma + 0.21 \times WC + 0.07 \times S_u - 36.89 \times D50 + 31.82$ 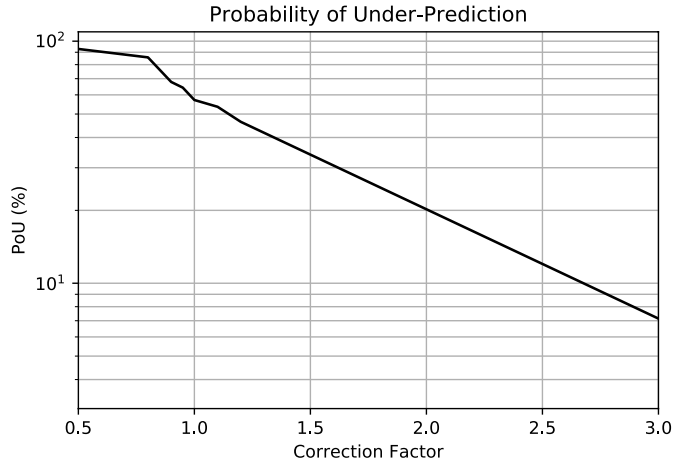 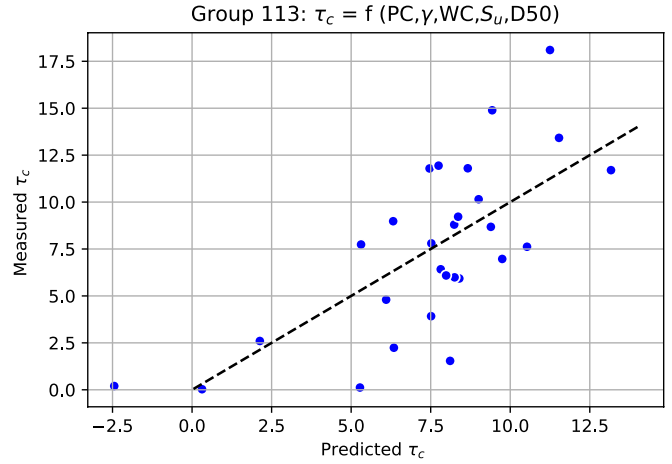	**Remarks** $R^2 = 0.50$ C.V Score = 0.10 1- Refer to the Group 113 in Table 51 for further information on the statistical significance of the proposed equation. 2- The "POU vs. Correction Factor" plot is based on the data used to develop the proposed equation. 3- In order to reach a 90% confidence that the predicted τ_c is smaller than the actual τ_c, the predicted value should be multiplied by 0.6 (with 1 Pa offset).

Table 93. Proposed equations for critical shear stress (τ_c) based on the HET data

HET	$D50 < 0.3\ mm$	$\tau_c = (25.07) \times PI^{0.27} \times S_u^{0.55} \times D50^{0.5}$ 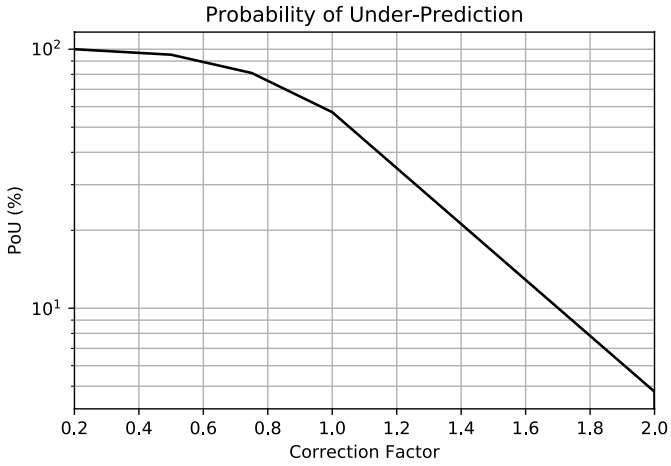 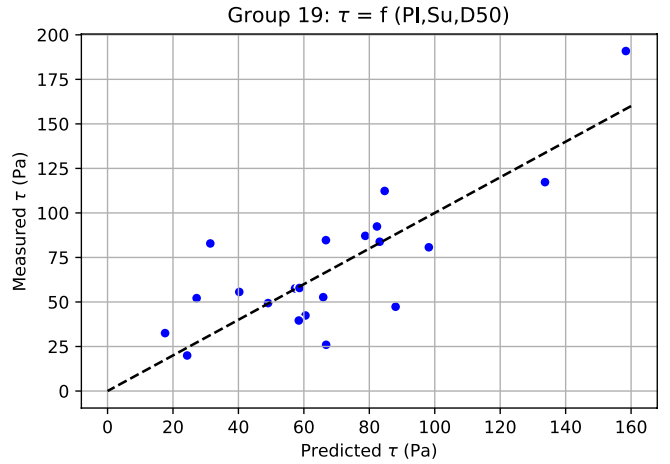	**Remarks** $R^2 = 0.64$ C.V Score = 0.43 1- Refer to the Group 19 in Table 54 for further information on the statistical significance of the proposed equation. 2- The "POU vs. Correction Factor" plot is based on the data used to develop the proposed equation. 3- In order to reach a 90% confidence that the predicted τ_c is smaller than the actual τ_c, the predicted value should be multiplied by 0.6 (with 1 Pa offset).

Table 94 shows the proposed correlation equations to predict the critical velocity (v_c) based on the EFA test. It is noteworthy that since the HET and the JET do not report the critical velocity as an output erodibility parameter, the critical velocity equations are proposed only based on the EFA Test.

Table 95 shows the proposed correlation equations to predict the initial linear slope of shear stress-erosion rate plot (E_τ) based on the EFA test. Table 96 and Table 97 also show the proposed correlation equations to predict E_τ based on the JET and HET, respectively.

Table 98 shows the proposed correlation equations to predict the initial linear slope of velocity-erosion rate plot (E_v) based on the EFA test. It is noteworthy that since the HET and the JET do not report E_v as an output erodibility parameter, the equations are proposed only based on the EFA Test.

Table 99 shows the proposed correlation equations to predict the erosion category (EC) based on the EFA test. Table 100 and Table 101 also show the proposed correlation equations to predict EC based on the JET and HET, respectively.

Table 94. Proposed equations for critical velocity (v_c) based on the EFA Test data

EFA	$D50 > 0.3\,mm$	$v_c = 0.315 \times (D50)^{0.5}$	
	$0.074\,mm < D50$	$v_c = (3 \times 10^{-15}) \times PI^{1.24} \times \gamma^{8.11} \times WC^{0.54} \times D50^{-2.35}$ 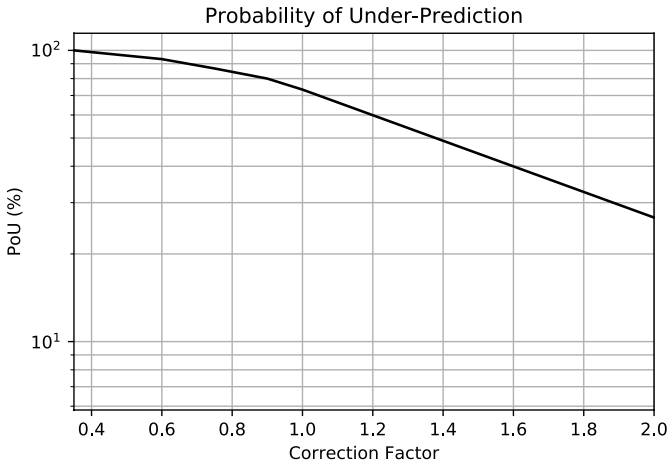 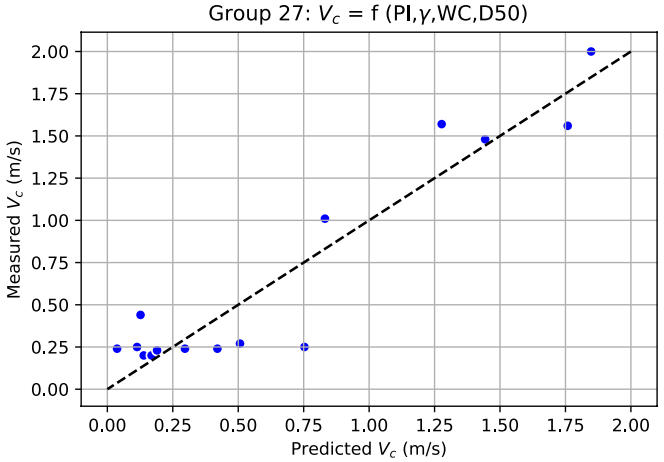	**Remarks** $R^2 = 0.88$ C.V Score = 0.72 1- Refer to the Group 27 in Table 58 for further information on the statistical significance of the proposed equation. 2- The "POU vs. Correction Factor" plot is based on the data used to develop the proposed equation. 3- In order to reach a 90% confidence that the predicted v_c is smaller than the actual v_c, the predicted value should be multiplied by 0.7 (with 0.1 m/s offset).

Table 94 (Continued). Proposed equations for critical velocity (v_c) based on the EFA Test data

EFA	$D50 < 0.074\ mm$	$v_c = (2.518 \times 10^{-5}) \times PC^{0.2} \times WC^{2.06} \times S_u^{0.51} \times D50^{-0.13}$ 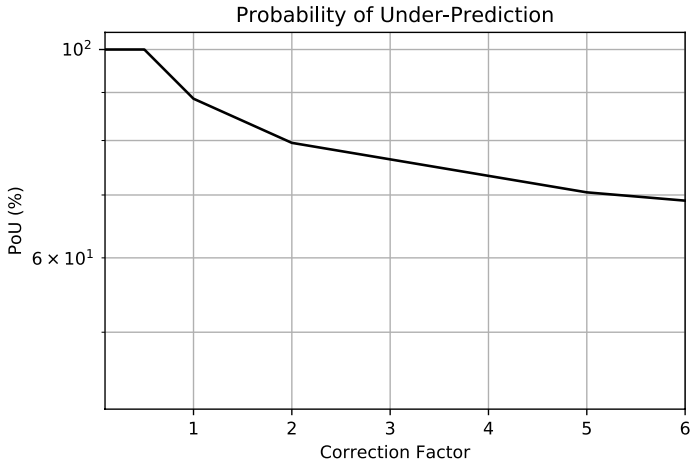 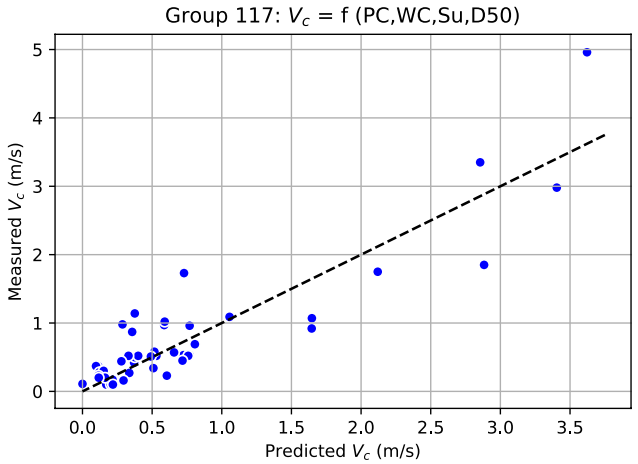	**Remarks** $R^2 = 0.80$ C.V Score = 0.80 1- Refer to the Group 117 in Table 56 for further information on the statistical significance of the proposed equation. 2- The "POU vs. Correction Factor" plot is based on the data used to develop the proposed equation. 3- In order to reach a 90% confidence that the predicted v_c is smaller than the actual v_c, the predicted value should be multiplied by 0.8 (with 0.2 m/s offset).

Table 95. Proposed equations for shear stress slope (E_τ) based on the EFA Test data

EFA	$D50 > 0.074$ mm	$E_\tau = (3228.7) \times C_u^{-2.8} \times \gamma^{-1.58} \times D50^{-2.91}$ 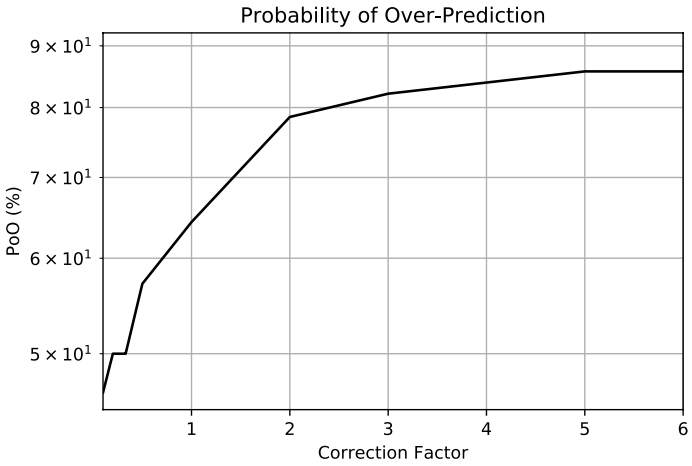 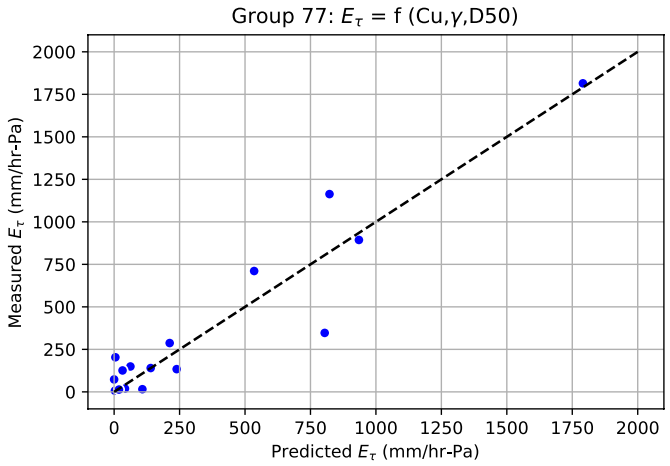	**Remarks** $R^2 = 0.91$ C.V Score = 0.64 1- Refer to the Group 77 in Table 61 for further information on the statistical significance of the proposed equation. 2- The "POO vs. Correction Factor" plot is based on the data used to develop the proposed equation. 3- In order to reach a 80% confidence that the predicted E_τ is greater than the actual E_τ, the predicted value should be multiplied by 2.5 (with 15 mm/hr-Pa offset).

Table 95 (Continued). Proposed equations for shear stress slope (E_τ) based on the EFA Test data

EFA	$D50 < 0.074\ mm$	$E_\tau = (1.429078 \times 10^{13}) \times A^{-0.47} \times \gamma^{-10.43} \times PF^{6.14} \times D50^{7.52}$ 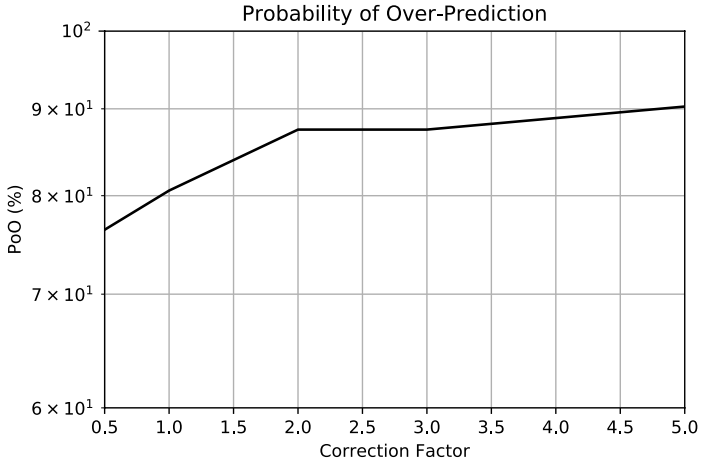 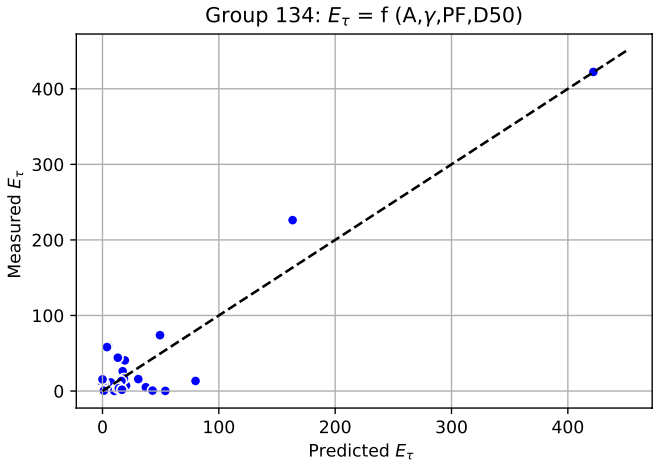	**Remarks** $R^2 = 0.90$ C.V Score = 0.51 1- Refer to the Group 134 in Table 59 for further information on the statistical significance of the proposed equation. 2- The "POO vs. Correction Factor" plot is based on the data used to develop the proposed equation. 3- In order to reach a 87% confidence that the predicted E_τ is greater than the actual E_τ, the predicted value should be multiplied by 2 (with 4 mm/hr-Pa offset).

Table 96. Proposed equations for shear stress slope (E_τ) based on the JET data

JET	$D50 > 0.074$ mm	$E_\tau = (55637006351614) \times PI^{-0.19} \times \gamma^{-6.39} \times WC^{-3.67}$ 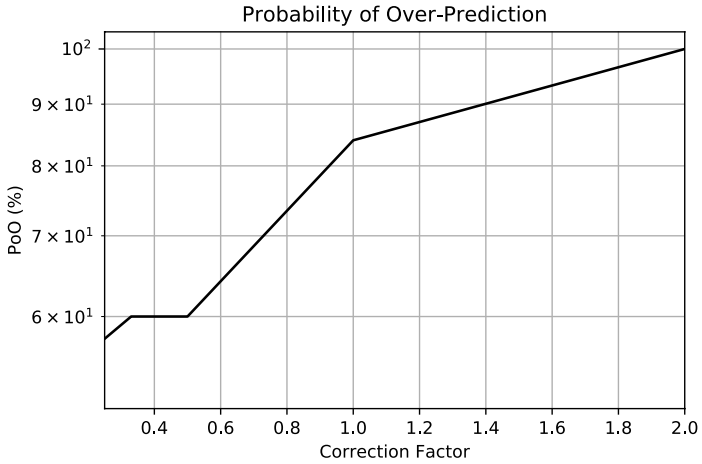 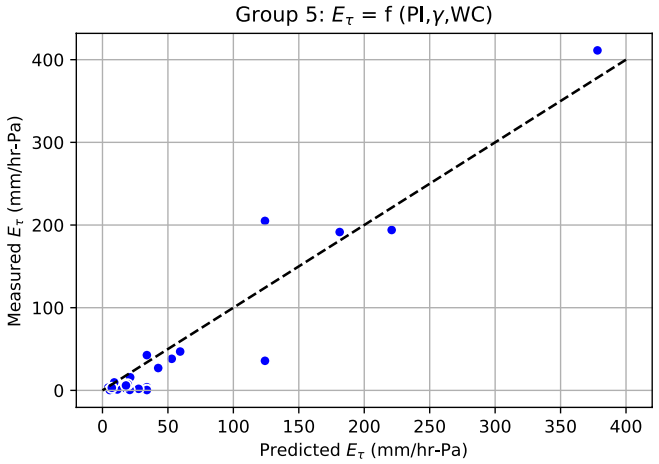	**Remarks** $R^2 = 0.90$ C.V Score = 0.67 1- Refer to the Group 5 in Table 65 for further information on the statistical significance of the proposed equation. 2- The "POO vs. Correction Factor" plot is based on the data used to develop the proposed equation. 3- In order to reach a 90% confidence that the predicted E_τ is greater than the actual E_τ, the predicted value should be multiplied by 1.4 (with 5 mm/hr-Pa offset).

Table 96 (Continued). Proposed equations for shear stress slope (E_τ) based on the JET data

JET	$D50 < 0.074\ mm$	$E_\tau = (396599.6) \times PI^{-2.54} \times WC^{4.58} \times S_u^{-4.91}$ 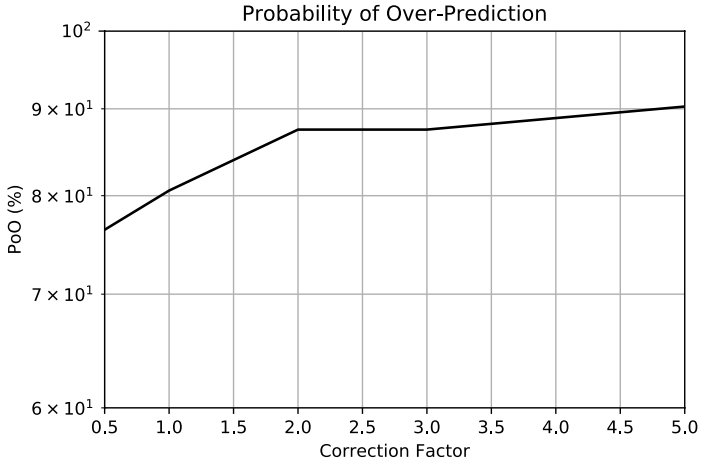 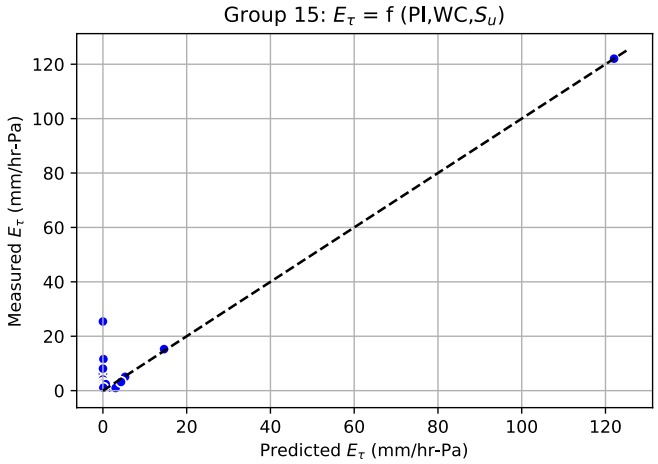	**Remarks** $R^2 = 0.93$ C.V Score = 0.23 1- Refer to the Group 15 in Table 63 for further information on the statistical significance of the proposed equation. 2- The "POO vs. Correction Factor" plot is based on the data used to develop the proposed equation. 3- In order to reach a 88% confidence that the predicted E_τ is greater than the actual E_τ, the predicted value should be multiplied by 2 (with 6 mm/hr-Pa offset).

Table 97. Proposed equations for shear stress slope (E_τ) based on the HET data

HET	$D50 > 0.074$ mm	$E_\tau = (2.951) \times \gamma^{26.08} \times WC^{-7.48} \times PF^{-19.96} \times D50^{-5.32}$ 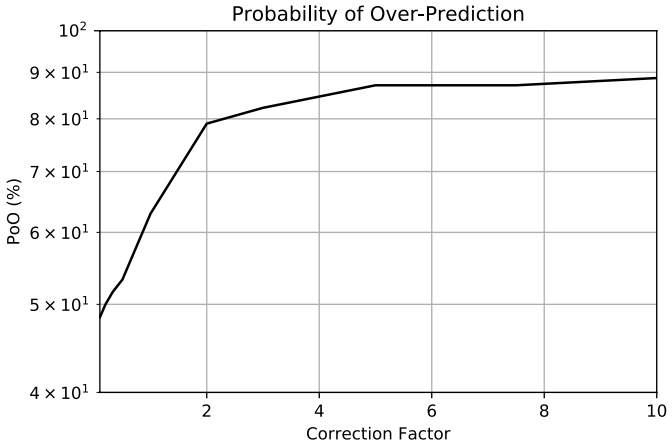 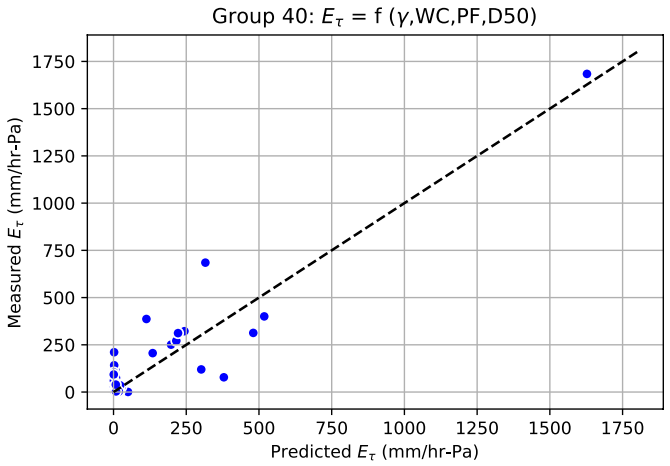	**Remarks** $R^2 = 0.86$ C.V Score = 0.55 1- Refer to the Group 40 in Table 66 for further information on the statistical significance of the proposed equation. 2- The "POO vs. Correction Factor" plot is based on the data used to develop the proposed equation. 3- In order to reach a 80% confidence that the predicted E_τ is greater than the actual E_τ, the predicted value should be multiplied by 2 (with 10 mm/hr-Pa offset).

Table 97 (Continued). Proposed equations for shear stress slope (E_τ) based on the HET data

HET	$D50 < 0.074\ mm$	$E_\tau = (9 \times 10^{-6}) \times LL^{-0.35} \times PL^{1.59} \times \gamma^{3.3} \times PC^{-0.48} \times S_u^{-0.19}$ 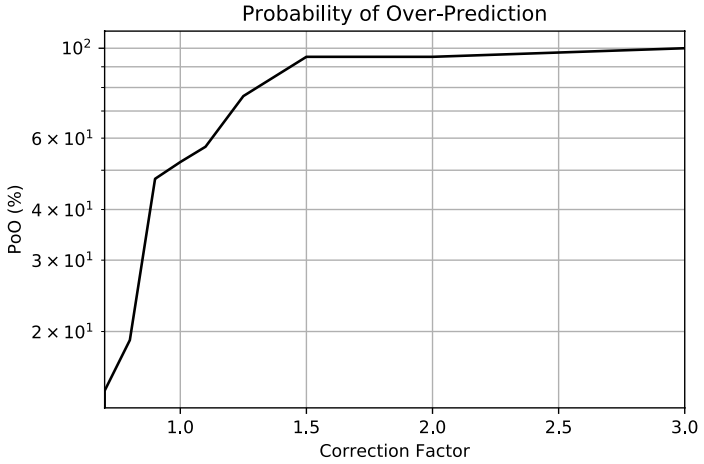 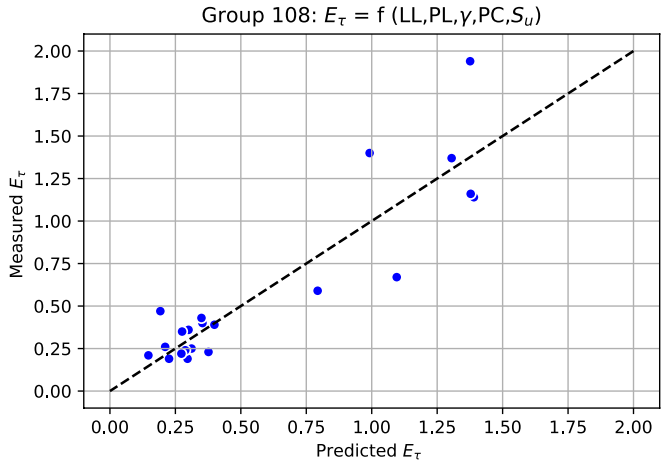	**Remarks** $R^2 = 0.81$ C.V Score = 0.55 1- Refer to the Group 108 in Table 68 for further information on the statistical significance of the proposed equation. 2- The "POO vs. Correction Factor" plot is based on the data used to develop the proposed equation. 3- In order to reach a 90% confidence that the predicted E_τ is greater than the actual E_τ, the predicted value should be multiplied by 1.45 (with 0 mm/hr-Pa offset).

Table 98. Proposed equations for velocity slope (E_v) based on the EFA Test data

EFA	$D50 > 0.074$ mm	$E_v = (88969.4) \times C_u^{-1.77} \times \gamma^{-2.26} \times WC^{0.34} \times D50^{-1.69}$ 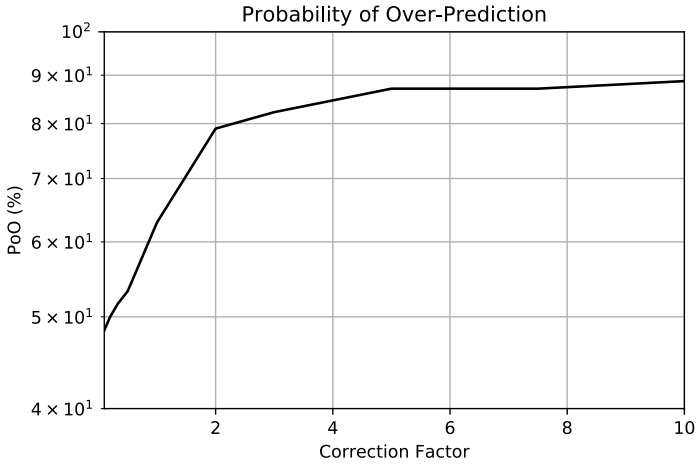 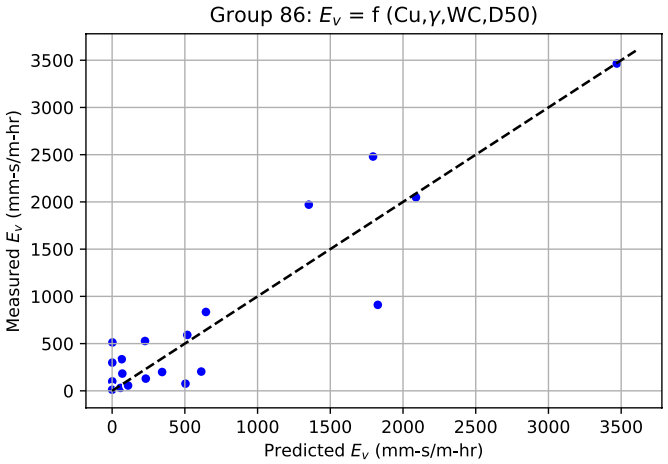	**Remarks** $R^2 = 0.86$ C.V Score = 0.64 1- Refer to the Group 86 in Table 71 for further information on the statistical significance of the proposed equation. 2- The "POO vs. Correction Factor" plot is based on the data used to develop the proposed equation. 3- In order to reach a 80% confidence that the predicted E_v is greater than the actual E_v, the predicted value should be multiplied by 5 (with 10 mm-s/m-hr offset).

Table 98 (Continued). Proposed equations for velocity slope (E_v) based on the EFA Test data

EFA	$D50 < 0.074\ mm$	$E_v = (1.682339 \times 10^{13}) \times D50^{5.10} \times \gamma^{-9.20} \times WC^{-1.13} \times PF^{4.69} \times A^{-0.01}$ 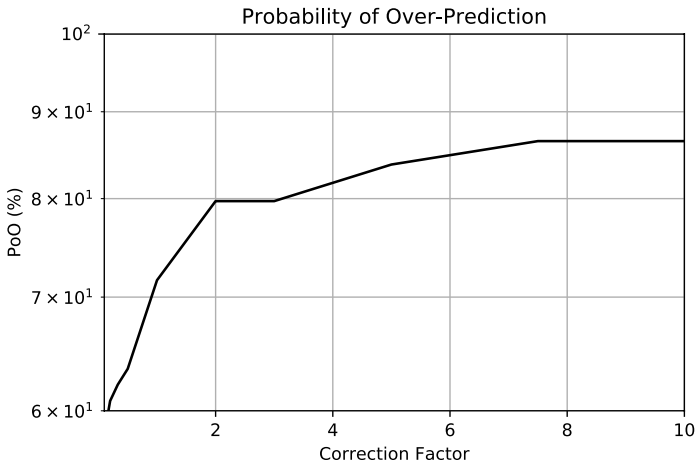 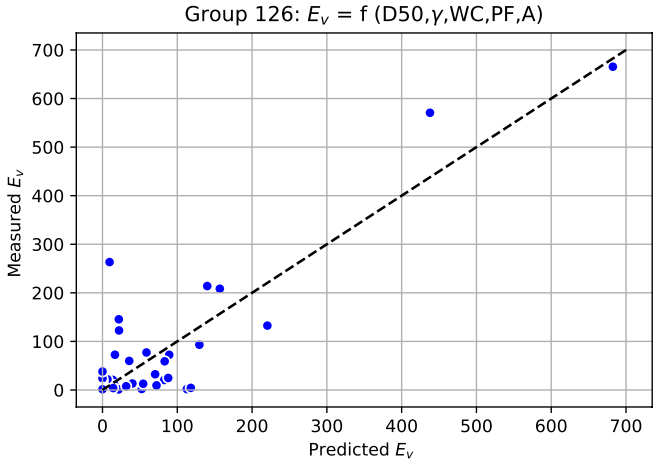	**Remarks** $R^2 = 0.79$ C.V Score = 0.52 1- Refer to the Group 126 in Table 69 for further information on the statistical significance of the proposed equation. 2- The "POO vs. Correction Factor" plot is based on the data used to develop the proposed equation. 3- In order to reach a 80% confidence that the predicted E_v is greater than the actual E_v, the predicted value should be multiplied by 2 (with 10 mm-s/m-hr offset).

Table 99. Proposed equations for erosion category (EC) based on the EFA Test data

EFA	$0.3\ mm > D50 > 0.074$ mm	$EC = (1.12) \times C_u^{0.1} \times WC^{-0.28} \times VST^{0.02} \times D50^{-0.44}$ 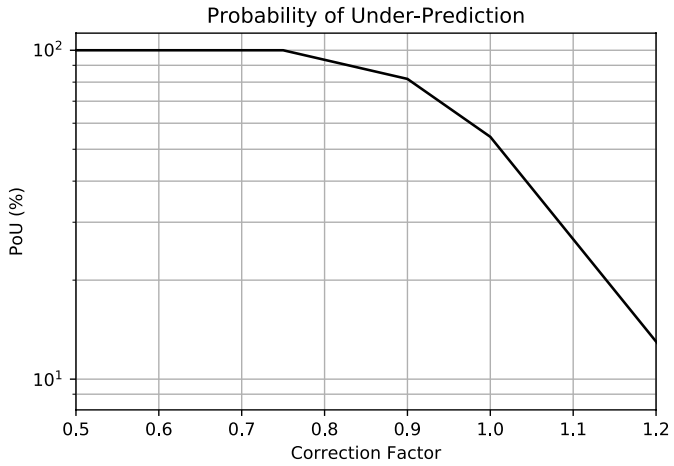 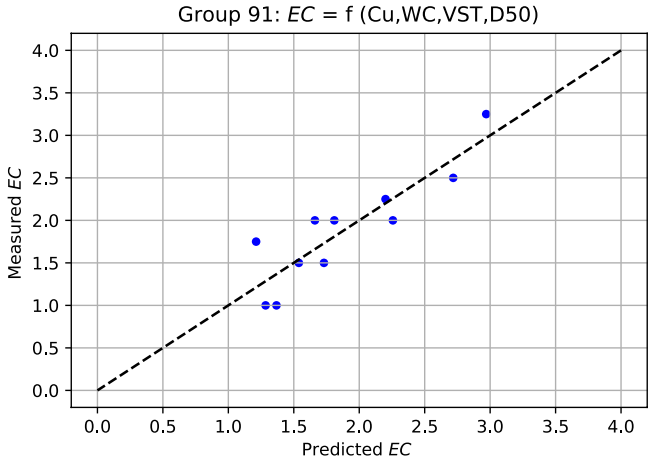	**Remarks** $R^2 = 0.92$ C.V Score = 0.80 1- Refer to the Group 91 in Table 75 for further information on the statistical significance of the proposed equation. 2- The "POU vs. Correction Factor" plot is based on the data used to develop the proposed equation. 3- In order to reach a 90% confidence that the predicted EC is smaller than the actual EC, the predicted value should be multiplied by 0.84.

Table 99 (Continued). Proposed equations for erosion category (EC) based on the EFA Test data

EFA	$D50 < 0.074\ mm$	$EC = (0.1933) \times A^{-0.06} \times WC^{0.51} \times S_u^{0.09} \times D50^{-0.12}$ 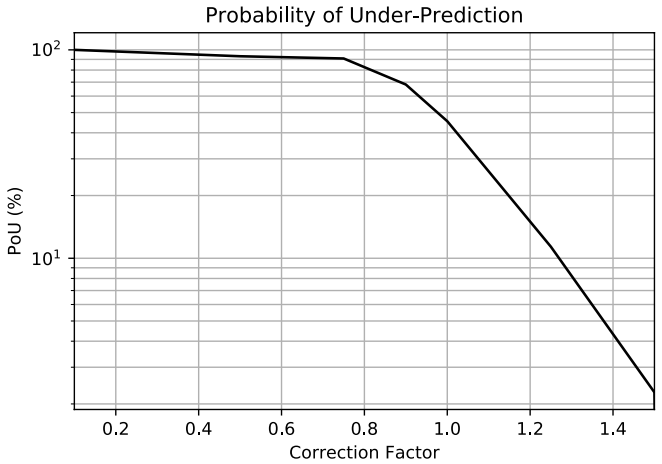 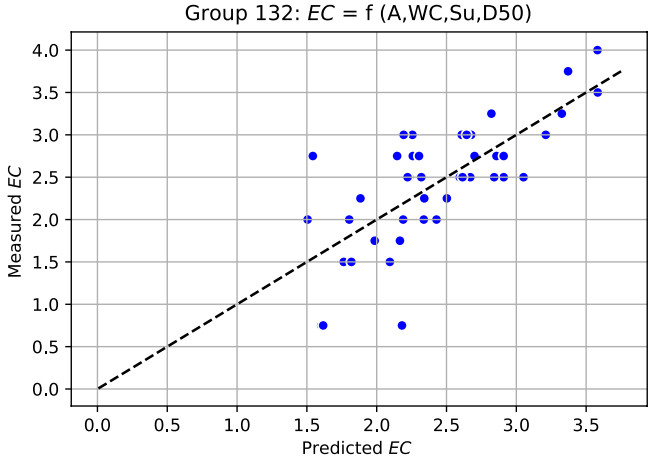	**Remarks** $R^2 = 0.55$ C.V Score = 0.53 1- Refer to the Group 132 in Table 73 for further information on the statistical significance of the proposed equation. 2- The "POU vs. Correction Factor" plot is based on the data used to develop the proposed equation. 3- In order to reach a 90% confidence that the predicted EC is smaller than the actual EC, the predicted value should be multiplied by 0.75.

Table 100. Proposed equations for erosion category (EC) based on the JET data

JET	$D50 < 0.3\ mm$	$EC = -0.022 \times PL + 0.0031 \times S_u - 5.5 \times D50 + 3.34$ 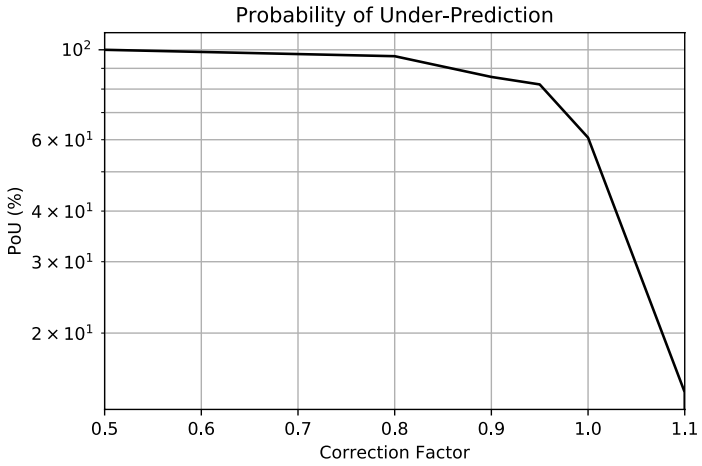 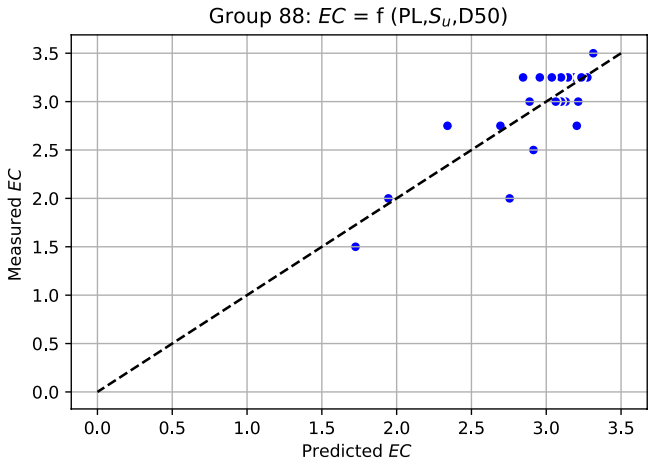	**Remarks** $R^2 = 0.70$ C.V Score = 0.58 1- Refer to the Group 88 in Table 76 for further information on the statistical significance of the proposed equation. 2- The "POU vs. Correction Factor" plot is based on the data used to develop the proposed equation. 3- In order to reach a 90% confidence that the predicted EC is smaller than the actual EC, the predicted value should be multiplied by 0.85.

Table 101. Proposed equations for erosion category (EC) based on the HET data

HET	$0.3\ mm > D50 > 0.074$ mm	$EC = (1.045) \times C_c^{-0.25} \times \gamma^{0.45} \times WC^{-0.04}$ 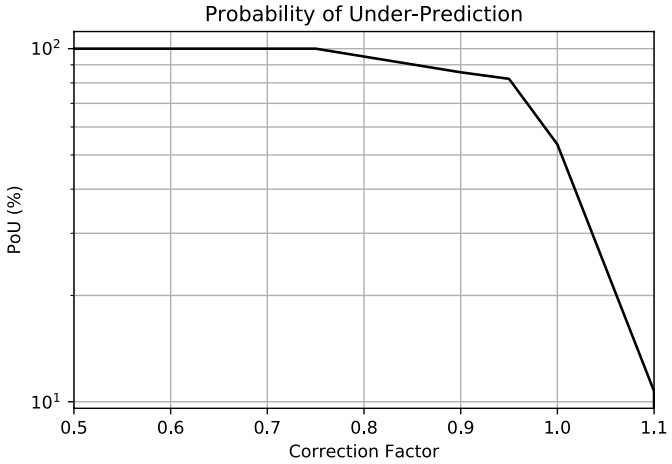 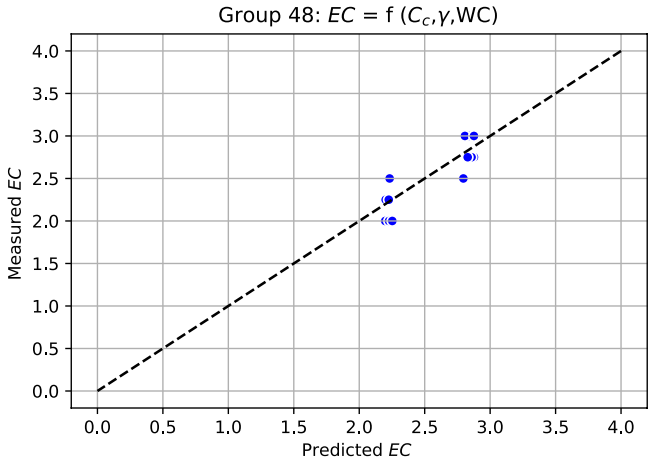	**Remarks** $R^2 = 0.77$ C.V Score = 0.78 1- Refer to the Group 48 in Table 81 for further information on the statistical significance of the proposed equation. 2- The "POU vs. Correction Factor" plot is based on the data used to develop the proposed equation. 3- In order to reach a 90% confidence that the predicted EC is smaller than the actual EC, the predicted value should be multiplied by 0.85.

Table 101 (Continued). Proposed equations for erosion category (EC) based on the HET data

HET	$D50 < 0.074\ mm$	$EC = (1.67) \times PI^{0.04} \times \gamma^{0.15} \times S_u^{0.03}$ 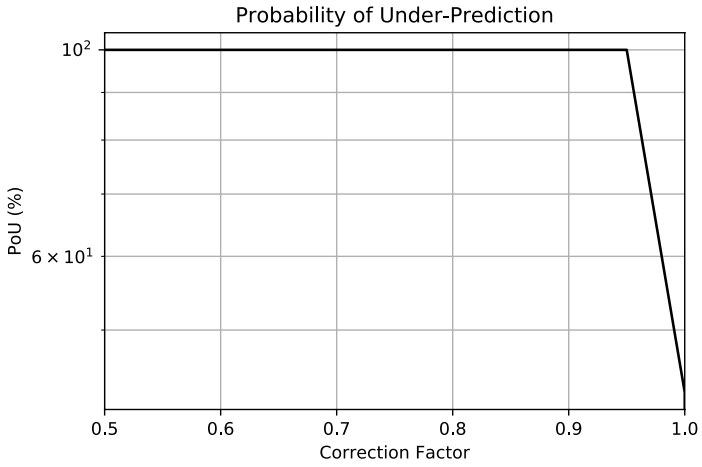 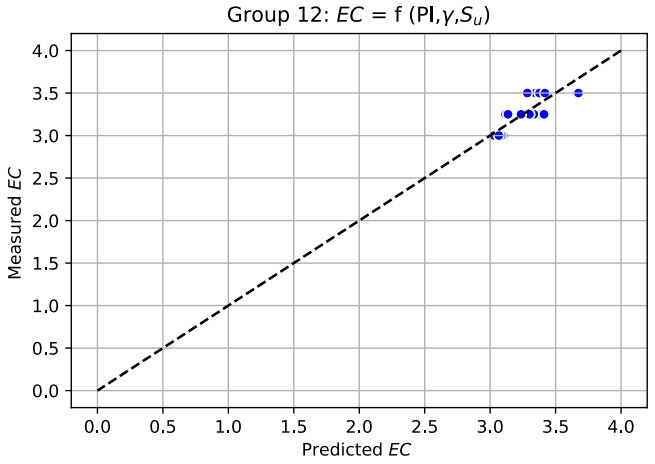	**Remarks** $R^2 = 0.70$ C.V Score = 0.54 1- Refer to the Group 12 in Table 79 for further information on the statistical significance of the proposed equation. 2- The "POU vs. Correction Factor" plot is based on the data used to develop the proposed equation. 3- In order to reach a 100% confidence that the predicted EC is smaller than the actual EC, the predicted value should be multiplied by 0.95.

9. CONCLUSIONS AND RECOMMENDATIONS

The goal of this project is to develop equations quantifying the erodibility of soils based on soil properties. Different soils exhibit different erodibility (sand, clay) therefore erodibility is tied to soil properties. On the other hand, many researchers have attempted to develop such equations without much success. One problem is that erodibility is not a single number but a relationship between the erosion rate and the water velocity or the hydraulic shear stress. This erosion function is a curve and it is difficult to correlate a curve to soil properties. Another problem that needs to be solved is associated with the availability of several erosion testing devices. In the laboratory, they include many erosion tests such as the pinhole test, the hole erosion test, the jet erosion test, the rotating cylinder test, the erosion function apparatus test. In the field, they include the jet erosion test, the NC State in situ scour evaluation probe test, the TAMU borehole erosion test and pocket erodometer test, and etc. All these tests measure the soil erodibility but give different results. It is important to give the DOT engineers options so that she or he can choose one test or another. Therefore, it would be helpful if all these tests could give the same answer. Indeed, the soil does not know the difference and the erosion function is a fundamental property of the soil. Experimental and numerical efforts were made to advance in this direction.

The major objective of this study was to develop equations which optimize the balance between reliability and simplicity. The reliability must consider the accuracy required for highway projects while the simplicity must consider the economic aspects of highway projects. The summary of the findings for each chapter is discussed below.

9.1. Chapter 1 - Introduction

This chapter was divided into two halves. The first half presented a definition for the erosion phenomenon and introduced different types of erosion. The general parameters to quantify the soil erodibility and the constitutive models for erosion were briefly discussed. The second half of this chapter presented the research approach. The project tasks were described one by one, and a summary of how and where within the report each one of the tasks are addressed was provided.

9.2. Chapter 2 - Existing Erosion Tests

This chapter presented a comprehensive literature review on different soil erosion tests. The tests developed all over the world in the last few decades were discussed in terms of their application in the lab or in the field, as well as their application in surface erosion or internal erosion problems. Advantages and disadvantages of the most important tests were explained, and a summary table about selected tests was provided at the end of this chapter. The advantages, the disadvantages, and the applications of the three major erosion tests (i.e. EFA, JET, HET) that are used in this study were presented in Table 90.

9.3. Chapter 3 – Existing Correlations between Soil Erodibility and Soil Properties

This chapter provided a literature review of the existing correlations between soil erodibility and soil properties. The observations and correlation equations proposed by various researchers in the last century were summarized. The influence factors on erosion including the less-easily-obtained engineering properties were presented and discussed in detail. A summary of these influencing parameters was presented in Table 10, which is also repeated below.

Table 10 (REPEATED). Influencing soil and water properties in erosion resistance of soils

More typically obtained properties:	Less typically obtained properties:
• Plasticity index • Liquidity Index • Unit weight • Water content • Undrained shear strength • Percent passing sieve #200 • Percent clay particles • Percent silt particles • Mean grain size • Coefficient of uniformity • Percent compaction (for man-made soils only) • Soil swell potential • Soil void ratio	• Specific gravity of solids • Soil dispersion ratio • pH (flowing water and pore water) • Salinity of eroding fluid • Organic content • Soil cation exchange cap • Soil clay minerals • Soil sodium adsorption ratio • Soil activity • Soil temperature • Density of cracks

9.4. Chapter 4 – Erosion Experiments

This chapter started by describing the soil erosion laboratory at Texas A&M University. The erosion testing devices built as part of this research project as well as the refurnished and armored Erosion Function Apparatus were presented. The test plan matrix proposed for this project

was presented and discussed. Next, the results of the hundreds of erosion tests performed within the Tasks 6 and 7 of this project were presented and discussed. Finally, the geotechnical engineering properties associated with each tested sample were obtained at Texas A&M University and presented in the form of a soil geotechnical properties spreadsheet for each sample. It should be noted that Appendix A and B of this report contain the erosion spreadsheets as well as the geotechnical properties spreadsheets for all tested samples in this project.

9.5. Chapter 5 – Organization and Interpretation of the Data

This chapter was largely dedicated to the organization and description of the erosion spreadsheet developed for this project and named "TAMU-Erosion". TAMU-Erosion includes nearly 1000 erosion tests with the geotechnical properties of each sample and is comprised of the two hundred erosion tests performed as part of this project as well as eight hundred erosion tests collected from all over the world. The compilation and collection process of erosion test data from all over the world was explained, and the contact people and organization who helped gather the information were mentioned. In TAMU-Erosion, all the erosion data are analyzed according to the procedures described in the report for the five erodibility parameters: 1) critical shear stress (τ_c), 2) critical velocity (v_c), 3) initial slope of velocity (E_v), 4) initial slope of shear stress (E_τ), and 5) erosion category (EC). TAMU-Erosion includes 50 columns and nearly 1000 rows. The column contents were discussed in detail. Finally, an inquiry operation manual explained how to search for specific data within TAMU-Erosion.

9.6. Chapter 6 – Comparison of Selected Soil Erosion Tests by Numerical Simulations

This chapter presented the comparison of selected soil erosion tests (i.e. EFA, HET, JET, and BET) with the use of numerical simulations software. This chapter was divided into two sections: 1) numerical simulations on non-erodible soils, 2) numerical simulations including the erosion process. The first part of the chapter dealt with the evolution of hydraulic shear stress and velocity profile with the assumption that the soil is not erodible. It was observed that there is a discrepancy between the Moody chart predictions and the numerical simulations, and that the Moody charts generally overestimate the shear stress. This discrepancy was more pronounced in higher shear stress values (up to 100% difference between the Moody chart prediction and the numerical simulation in one cases). In the second part, the erosion function was assigned to the water-soil interface, and the erosion was numerically simulated with a moving boundary for selected erosion tests. The results of numerical simulations were compared with the actual observations for each test. The findings showed that the erosion function obtained from the EFA test for each sample can be reasonably used to produce a similar "scour versus time" plot to what the JET, the HET, and the BET experiments would result. However, the variety of interpretation techniques that are used for each test to obtain the shear stress in the soil-water interface leads to different erosion functions. Therefore, one must be aware of the interpretation techniques that each test uses to obtain the erosion function (erosion rate versus shear stress).

9.7. Chapter 7 – Correlation Equation Development

This chapter was dedicated to the main goal of this study which is the development of correlation equations. This chapter was divided into four major parts. The first part presented a

preliminary and quick method to determine the erosion resistance of a soil using only the Unified Soil Classification System (USCS) of the soil and associated erosion categories. The plot of erosion rate vs. velocity based on the USCS categories is shown in Figure 145, which is also repeated below. The width of each box, that is associated with a USCS category, represents the zone in which 90% of the EFA results performed on such samples would fall in the Erosion Category Chart. For instance, if the soil type of a location in an arbitrary geotechnical site is classified as SM (silty sand) according to the USCS, it would most likely (with close to 90% confidence based on the EFA results compiled in the TAMU-Erosion) fall into the Category II (high erodibility).

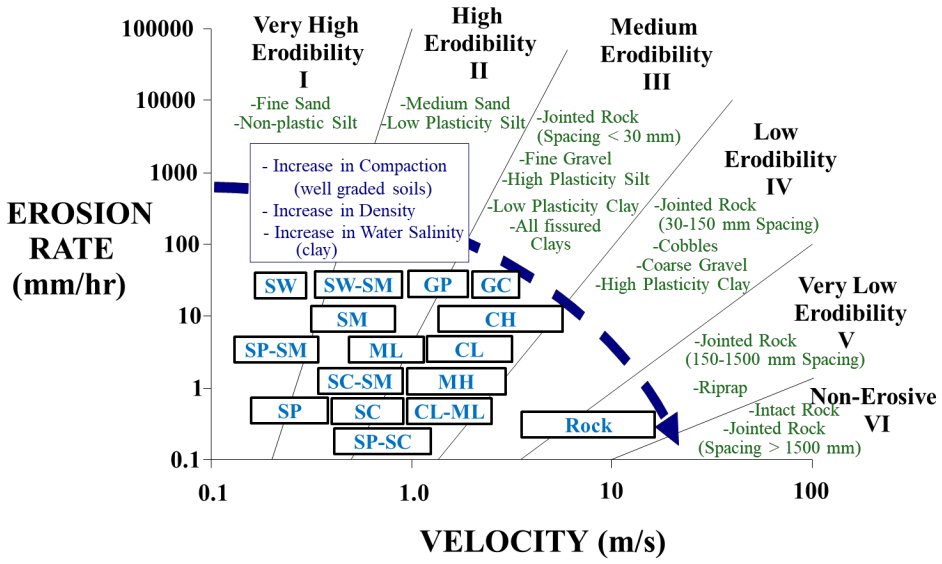

Figure 145 (REPEATED). Erosion Category Charts with the USCS Symbols

The second part of Chapter 7 dealt with improving existing plots of the critical velocity/critical shear stress versus the mean particle size. It was observed that for soils with mean particle size larger than 0.3 mm, following relationships exist between the critical velocity/shear stress and mean particle size: $v_c(m/s) = 0.315\left(D_{50}(mm)\right)^{0.5}$ and $\tau_c(Pa) = D_{50}(mm)$. It was also

concluded that for fine-grained soils there is no direct relationship between critical velocity/shear stress and the mean particle size. However, the data could be bracketed with an upper bound and a lower bound equation.

The third part of this chapter presented the "Frequentists' Regression" technique. The step-by-step procedure for implementing the frequentists' regression technique, the experimental design, and the model selection process were discussed, and the results of the regressions were presented. The best correlations equations were selected after passing through a four-filter process including: 1) R^2, 2) mean squared error (MSE), 3) statistical F-test, and 4) the cross-validation test. Plots of the "Probability of Over-Predicting" and "Under-Predicting" were also presented for the selected equations. Table 102 to Table 106 show the selected equations for each erodibility parameter and for each dataset.

Table 102. Selected models for critical shear stress τ_c

Group No.	Independent variables	Dataset/ No. of data	Model expression (parameter values given by deterministic regression)	R^2	Cross-validation score
124	γ, A, WC, S_u, PF, D50	EFA/Fine 44	$\tau_c = (158.06) \times \gamma^5 \times A^{-0.46} \times WC^{10.03} \times S_u^{1.83} \times PF^{-18.28} \times D50^{-4.21}$	0.94	0.66
77	C_u, γ, D50	EFA/Coarse 28	$\tau_c = (1.58) \times C_u^{-0.04} \times \gamma^{0.02} \times D50^{0.77}$	0.93	0.99
113	PC, γ, WC, S_u, D50	JET/Global 28	$\tau_c = -0.248 \times PC - 1.23 \times \gamma + 0.21 \times WC + 0.07 \times S_u - 36.89 \times D50 + 31.82$	0.50	0.10
19	PI, S_u, D50	HET/Global 21	$\tau_c = (25.07) \times PI^{0.27} \times S_u^{0.55} \times D50^{0.5}$	0.64	0.43

Table 103. Selected models for critical velocity v_c

Group No.	Independent variables	Dataset/ No. of data	Model expression (parameter values given by deterministic regression)	R^2	Cross-validation score
117	PC, WC, S_u, D50	EFA/Fine 46	$v_c = (2.518 \times 10^{-5}) \times PC^{0.2} \times WC^{2.06} \times S_u^{0.51} \times D50^{-0.13}$	0.80	0.80
27	PI, γ, WC, D50	EFA/Coarse 15	$v_c = (3 \times 10^{-15}) \times PI^{1.24} \times \gamma^{8.11} \times WC^{0.54} \times D50^{-2.35}$	0.88	0.72

Table 104. Selected models for erosion category EC

Group No.	Independent variables	Dataset/ No. of data	Model expression (parameter values given by deterministic regression)	R^2	Cross-validation score
132	A, WC, S_u, D50	EFA/Fine 44	$EC = (0.1933) \times A^{-0.06} \times WC^{0.51} \times S_u^{0.09} \times D50^{-0.12}$	0.55	0.53
91	C_u, WC, VST, D50	EFA/Coarse 11	$EC = (1.12) \times C_u^{0.1} \times WC^{-0.28} \times VST^{0.02} \times D50^{-0.44}$ for $0.074 < D50 < 0.3$	0.92	0.80
88	PL, S_u, D50	JET/Global 28	$EC = -0.022 \times PL + 0.0031 \times S_u - 5.5 \times D50 + 3.34$	0.70	0.58
12	PI, γ, S_u	HET/Fine 21	$EC = (1.67) \times PI^{0.04} \times \gamma^{0.15} \times S_u^{0.03}$	0.70	0.54
48	C_c, γ, WC	HET/Coarse 28	$EC = (1.045) \times C_c^{-0.25} \times \gamma^{0.45} \times WC^{-0.04}$	0.77	0.78

Table 105. Selected models for velocity slope E_v

Group No.	Independent variables	Dataset/ No. of data	Model expression (parameter values given by deterministic regression)	R^2	Cross-validation score
86	C_u, γ, WC, D50	EFA/Coarse 28	$E_v = (88969.4) \times C_u^{-1.77} \times \gamma^{-2.26} \times WC^{0.34} \times D50^{-1.69}$	0.86	0.64
126	D50, γ, WC, PF, A	EFA/Fine 74	$E_v = (1.682339 \times 10^{13}) \times D50^{5.10} \times \gamma^{-9.20} \times WC^{-1.13} \times PF^{4.69} \times A^{-0.01}$	0.79	0.52

Table 106. Selected models for shear stress slope E_τ

Group No.	Independent variables	Dataset/ No. of data	Model expression (parameter values given by deterministic regression)	R^2	Cross-validation score
77	C_u, γ, D50	EFA/Coarse 28	$E_\tau = (3228.7) \times C_u^{-2.8} \times \gamma^{-1.58} \times D50^{-2.91}$	0.91	0.64
134	A, γ, PF, D50	EFA/Fine 72	$E_\tau = (1.429078 \times 10^{13}) \times A^{-0.47} \times \gamma^{-10.43} \times PF^{6.14} \times D50^{7.52}$	0.90	0.51
40	γ, WC, PF, D50	HET/Coarse 62	$E_\tau = (2.951) \times \gamma^{26.08} \times WC^{-7.48} \times PF^{-19.96} \times D50^{-5.32}$	0.86	0.55
108	LL, PL, γ, PC, S_u	HET/Fine 21	$E_\tau = (9 \times 10^{-6}) \times LL^{-0.35} \times PL^{1.59} \times \gamma^{3.3} \times PC^{-0.48} \times S_u^{-0.19}$	0.81	0.51
5	PI, γ, WC	JET/Coarse 25	$E_\tau = (55637006351614) \times PI^{-0.19} \times \gamma^{-6.39} \times WC^{-3.67}$	0.90	0.67
15	PI, WC, S_u	JET/Fine 24	$E_\tau = (396599.6) \times PI^{-2.54} \times WC^{4.58} \times S_u^{-4.91}$	0.93	0.23

The last part of this chapter dealt with a probabilistic approach as opposed to the deterministic approach presented in the previous section. The probabilistic approach was based on the "Bayesian inference" method. The methodology of the Bayesian inference method and its results were presented in Section 7.4 as well as in the Appendix E of the appendices report.

9.8. Chapter 8 – Most Robust Correlation Equations

This chapter focused on the recommended correlation equations (Table 102 to Table 106) based on the work presented in Chapter 7, and provided instructions on how best to use them. Table 100, which is also repeated below, shows an example of the proposed equation charts for erosion category based on the JET data. This table presents the recommended correlation equations to predict erosion category in different D_{50} ranges. It should be noted that alongside with each proposed equation, these tables often give two plots showing the POU (or POO, where applicable) vs. correction factor, as well as the "predicted" vs. "measured". Such plots provide great insight on using each equation. Also, a column containing some remarks is provided on the right side of each equation. This column includes the values of R^2 and the cross-validation score (named as C.V in the tables). Same sort of tables was proposed for different erodibility parameters and different erosion tests.

Table 100 (REPEATED). Proposed equations for erosion category (EC) based on the JET data

JET	$D50 < 0.3\ mm$	$EC = -0.022 \times PL + 0.0031 \times S_u - 5.5 \times D50 + 3.34$ 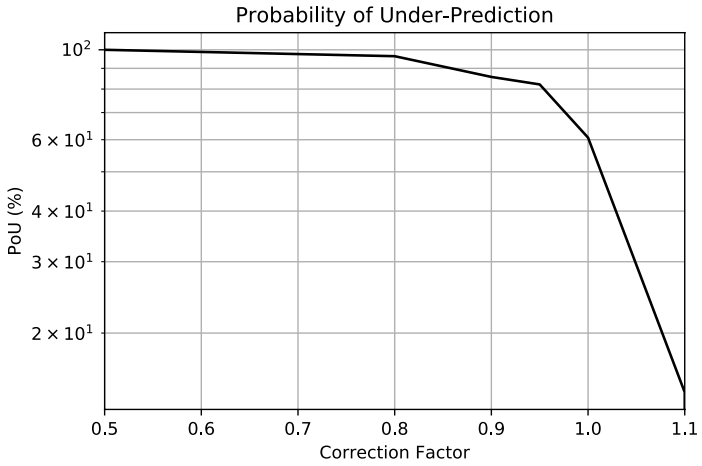 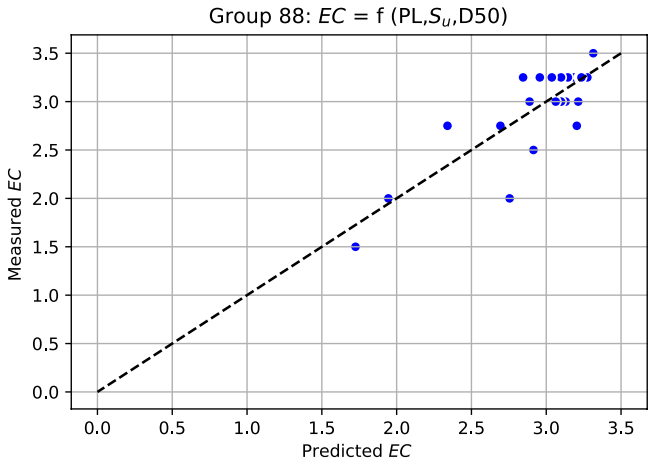	**Remarks** $R^2 = 0.70$ C.V Score = 0.58 1- Refer to the Group 88 in Table 76 for further information on the statistical significance of the proposed equation. 2- The "POU vs. Correction Factor" plot is based on the data used to develop the proposed equation. 3- In order to reach a 90% confidence that the predicted EC is smaller than the actual EC, the predicted value should be multiplied by 0.85.

9.9. Recommendations on How to Approach the Erosion-Related Design Problems

One of the key missions of this project was to provide the engineers in charge of erosion problems with a set of correlation equations to predict erosion parameters without having to perform multiple and costly erosion tests. In this section, a step-by-step approach is presented. It must be noted that each step can stand alone by itself, and help solve the problem; however, a combination of all four steps would lead to the most accurate results. While steps 1 and 2 yield more preliminary estimates of the erodibility parameters, steps 3 and 4 provide more detailed insights in obtaining the erodibility parameters. It is recommended that the engineer considers all four steps prior to making a final decision.

9.9.1. *Step 1- Probe the TAMU-Erosion*

Chapter 5 of this report discussed the development of the TAMU-Erosion database. This global spreadsheet is a searchable tool, and allows the engineer to filter the data based on multiple criteria. The first preliminary approach to evaluate the erodibility of a desired site is through probing TAMU-Erosion. The engineer can use as many geotechnical properties' information as possible from the site (i.e. the USCS category, the AASHTO classification, the Atterberg limits, the unit weight, etc.), and filter the TAMU-Erosion based on those criteria with the goal of finding the soil samples that are similar to the target soil. After filtering, the obtained soil samples might be tested with more than one erosion test (i.e. EFA, BET, JET, HET, etc.). The engineer then can see for his/herself that what erodibility parameters he/she must expect from the soil without the need to conduct different erosion tests. Probing the TAMU-Erosion also helps the engineer to compare the results of these different erosion test on the similar soil samples.

9.9.2. *Step 2- Use the USCS-Erosion Charts to estimate the erosion resistance*

Section 7.1 showed that the erosion functions for soils with a given USCS category do not generally fall distinctly into a single erosion category but rather seem to plot approximately across two categories. Figure 145 summarized all results into the erosion category charts. Figure 145 can be used as another preliminary tool to estimate the erodibility of any sample, using only the USCS category. In this figure, the width of each box, that is associated with a USCS category, represents the zone in which 90% of the EFA results performed on such samples would fall in the Erosion Category Chart. For instance, if the soil type of a location in an arbitrary geotechnical site is classified as SM (silty sand) according to the USCS, it would most likely (with close to 90% confidence based on the EFA results compiled in the TAMU-Erosion) fall into the Category II (high erodibility) on Figure 145. Similarly, a soil classified as CH (fat clay) would most likely fall into the Category III (medium erodibility), and a SP (poorly graded sand) would fall within the Categories I and II (very high to high erodibility). The wider the box is for a USCS category, the more the variability of the erosion category (EC) is for that particular soil type. Knowledge of the erosion category of a soil can lead to many useful information about the erosion resistance of that soil; however, it should be noted that such results are not accurate enough for design purposes.

9.9.3. *Step 3- Use the deterministic regression results*

Section 7.3 presented a comprehensive deterministic approach to select the best correlation equations between the geotechnical properties and the erodibility parameters. The most robust equations were repeated and tabulated in Section 8.2. The proposed equations are developed based on the data obtained in different erosion tests (the EFA, the JET, and the HET); therefore, the in-advance knowledge on each test is extremely useful in order to choose the best equation. Table 90

showed a list of advantages, disadvantages, and application for the EFA, the JET, and the HET. The content of this table should be studied carefully before using the proposed equations in Section 8.2. Plots of "probability of under/over-predicting" (POU/POO) were presented with the best equations. These plots help the engineer find the correction factor needed to reach a certain confidence that the predicted value is under/over predicted. They can be very useful for design purposes.

9.9.4. *Step 4- Use the Bayesian inference results*

One of the issues with conventional deterministic approaches is that they fail to capture the uncertainty by only accounting for the mean value of the unknown parameter. Therefore, Section 7.4 was dedicated to perform a probabilistic analysis using the Bayesian inference approach. The comprehensive deterministic frequentists' regression analysis performed in Section 7.3 was the foundation of the Bayesian inference analysis performed in Section 7.4. The selected correlation equations using the deterministic approach were analyzed using the Bayesian inference. The engineer can evaluate the sensitivity of the predicted value with regard to one or more model parameters. All possible values that an erodibility parameter can get for each selected equation are presented in the form of a probability distribution. Examples of the Bayesian inference analysis were presented in Section 7.4. Appendix E of the appendices report presents the entire results of the Bayesian inference analysis.

9.10. General Observations on the Effect of Geotechnical Properties on Soil Erodibility

Out of all the findings of this study, the correlation matrices (such as Figure 154), alongside with the proposed equations in Chapter 8, may be the best measures to understand the effect of each geotechnical property on each soil erodibility parameter. Appendix C of the Appendices Report presents all of the correlation matrices for the 12 groups shown in Figure 148. As discussed in Section 7.3.2, the correlation matrices also show the Pearson's Correlation Coefficient (PCC) for each plot. PCC was used to reflect the linear dependency between two variables, with +1 showing a strong positive relationship, -1 indicating a solid negative relationship, and 0 referring to no relationship at all.

In general, the geotechnical properties that, by increasing, lead to an increase of the critical shear stress (τ_c), the critical velocity (v_c), and the erosion category (EC), and to a decrease in the shear stress slope (E_τ) and the velocity slope (E_v) are considered as parameters that have a positive impact on the erosion resistance. On the other hand, those geotechnical properties that, by increasing, lead to a decrease of τ_c, v_c, EC, and and to an increase in E_τ and E_v are considered as parameters that have a negative impact on the soil erosion resistance. The following observations were made regarding the effect of each soil property on the erodibility of soils:

- An increase in the mean particle size (D_{50}) leads to an increase in the erosion resistance for soils with D_{50} larger than 0.3 mm. On the other hand, regardless of the erosion test type, an increase in D_{50} leads to a decrease of the erosion resistance of soils with D_{50} smaller than 0.3 mm.
- In fine grained soils (D_{50} < 0.074 mm), a decrease in the coefficient of curvature or coefficient of uniformity (C_c and C_u) leads to an increase in the soil erosion resistance.

- In both fine and coarse-grained soils, an increase in percent clay leads to an increase in the erosion resistance of the soil.
- An increase in the plasticity index (PI) in general leads to an increase in the erosion resistance in both coarse-grained and fine-grained soils (especially soils with D_{50} smaller than 0.3 mm); however, there are a few exceptions to this statement.
- An increase in the plastic limit (PL) leads to an increase in the erosion resistance in fine-grained soils. This influence was found to be more pronounced in the EFA dataset than in the JET and the HET datasets.
- In many cases, the wet unit weight (γ) and the undrained shear strength (S_u) for fine-grained soils) showed to be directly proportional to the erosion resistance of a soil with D_{50} smaller than 0.3 mm.
- The water content (WC) seemed to have a positive impact on the erosion resistance of finer soils in general. However, WC showed a negative effect on the erosion resistance of coarse-grained soils in the EFA test. It appears that the water content alone is poorly correlated with the erosion resistance.

Overall, the geotechnical properties were found to have a mixed and complex relationship with the erosion resistance in general. Nevertheless, the aforementioned observations as well as the proposed equations can be used as a first step to estimate the erosion resistance of many soils. If by using such relationships the erosion issue is clearly not a problem it is unlikely that further effort is necessary. However, if the use of such equations leads to uncertainty, it is desirable to run erosion tests on site specific samples.

REFERENCES

1. Al-Madhhachi, A.T., Hanson, G.J., Fox, G.A., Tyagi, A.K., Bulut, R. 2013. Measuring soil erodibility using a laboratory mini jet. American Society of Agricultural and Biological Engineers. Vol. 56(3), pp. 901-910.
2. Arulanandan, K. and Perry, E.B. 1983. Erosion in relation to filter design criteria in earth dams. Journal of the Geotechnical Engineering Division, ASCE. 109(GT5), pp. 682-698.
3. Arulanandan, K., Sargunam, A., Loganathan, P. and Krone, R.B. 1973. Application of chemical and electrical parameters to prediction of erodibility. In Soil Erosion: Causes and Mechanisms; Prevention and Control. Special Report 135, Highway Research Board, pp 42-51.
4. ASTM D854-14. 2014. Standard test methods for specific gravity of soil solids by water pycnometer. ASTM International, West Conshohocken, PA, 2014.
5. ASTM D1587 / D1587M-15. 2015. Standard practive for thin-walled tube sampling of fine-grained soils for geotechnical purposes. ASTM International, West Conshohocken, PA, 2015.
6. ASTM D2216-10. 2010. Standard test methods for laboratory determination of water (moisture) content of soil and rock by mass. ASTM International, West Conshohocken, PA, 2010.
7. ASTM D2487-17. 2017. Standard practice for classification of soils for engineering purposes (unified soil classification system). ASTM International, West Conshohocken, PA, 2017.
8. ASTM D422-63. 2007. Standard test method for particle-size analysis of soils. ASTM International, West Conshohocken, PA, 2007.

9. ASTM D4318-17e1. 2017. Standard test methods for liquid limit, plastic limit, and plasticity indexof soils. ASTM International, West Conshohocken, PA, 2017.
10. ASTM D4647 / D4647M-13. 2013. Standard test methods for identification and classification of dispersive clay soils by the pinhole test. ASTM International, West Conshohocken, PA, 2013.
11. ASTM D4648. 2016. Standard test methods for laboratory miniature vane shear test for saturated fine-grained clayey soil. ASTM International, West Conshohocken, PA, 2016
12. ASTM D5852. 2007. Standard test method for erodibility determination of soil in the field or in the laboratory by the jet index method (withdrawn 2016). ASTM International, West Conshohocken, PA, 2007.
13. ASTM D7263-09. 2018. Standard test methods for laboratory determination of density (unit weight) of soil speciments. ASTM International, West Conshohocken, PA, 2018.
14. ASTM D7928-17. 2017. Standard test method for particle-size distribution (gradation) of fine-grained soils using sedimentation (hydrometer) analysis. ASTM International, West Conshohocken, PA, 2017.
15. Benedict, S. T., Deshpande, N., Aziz, N. M. Conrads, P. A. 2006. Trends of abutment-scour prediction equations applied to 144 field sites in South Carolina: U.S. Geological Survey Open-File Report 2003-295, 150 p., available online at http://pubs.waterusgs.gov/ofr03-295/.
16. Bloomquist, D., Sheppard, D.M., Schofield, S., Crowley, R.W. 2012. The rotating erosion testing apparatus (RETA): A laboratory device for measuring erosion rates versus shear stresses of rock and cohesive materials. Geotechnical Testing Journal, Vol. 35(4). Paper ID GTJ104221

17. Bogdanov, V.I., Smirnov, R.A. Vlaznost gruntov zony aeratcii v usloviyah zastroyki. In a book : Problemy prognozirovaniay povysheniya urovny gruntovyh vod na zastroennyh territoriayh I borba s ih podtopleniyem, Belgorod, 1972. (Богданов В.И., Смирнов Р.А. Влажность грунтов зоны аэрации в условиях застройки. В кн.: Проблемы прогнозирования повышения уровня грунтовых вод на застроенных территориях и борьба с их подтоплением (материалы совещания), Белгород, 1972)
18. Briaud, J. L. 2008. Case histories in soil and rock erosion: Woodrow Wilson Bridge, Brazos River Meander, Normandy Cliffs, and New Orleans Levees, The 9th Ralph B. Peck Lecture, Journal of Geotechnical and Geoenvironmental Engineering, Vol. 134(10), ASCE, Reston Virginia, USA.
19. Briaud, J. L. 2013. Geotechnical engineering: unsaturated and saturated soils, John Wiley and Sons, New York, USA.
20. Briaud, J. L. 2015. Scour depth at bridges: Method including soil properties. I: Maximum scour depth prediction. J. Geotech. Geoenviron. Eng., 141(2): 04014104. ISSN 1090-0241/04014104(13).
21. Briaud, J. L., Bernhardt, M., Leclair, M. 2012. The pocket erodometer test: development and preliminary results. Geotechnical Testing Journal, Vol. 35, No. 2, Paper ID GTJ102889.
22. Briaud, J. L., Chen, H. C., Kwak, K., Han, S., Ting, F. 2001. Multiflood and multilayer method for scour rate prediction at bridge piers, Journal of Geotechnical and Geoenvironmental Engineering, Vol. 127(2), pp. 114-125, Feb. 2001, ASCE, Reston, Virginia.
23. Briaud, J. L., Chen, H. C., Li, Y., Nurtjahyo, P., Wang, J. 2005. SRCIOS-EFA method for contraction scour in fin-grained soils. Journal of Geotechnical and Geoenvironmental Engineering. Vol. 131, No. 10, ISSN 1090-0241/2005/10-1283-1294.

24. Briaud, J. L., Gardoni, P., Yao, C. 2014. Statistical, risk, and reliability analysis of bridge scour, J. Geotech. Geoenviron. Eng., 140(2), 04013011, ASCE
25. Briaud, J. L., Ting, F. C. K., Chen, H. C., Gudavalli, R., Perugu, S., Wei, G. 1999. SRICOS: Prediction of scour rate in cohesive soils at bridge piers, Journal of Geotechnical and Geoenvironmental Engineering, Vol. 125(4), pp. 237-246, April 1999, ASCE, Reston, Virginia.
26. Briaud, J. L., Ting, F., Chen, H.C., Cao, Y., Han, S.-W., Kwak, K., 2001, Erosion function apparatus for scour rate predictions, Journal of Geotechnical and Geoenvironmental Engineering, Vol. 127(2), pp. 105-113, Feb. 2001, ASCE, Reston, Virginia.
27. Briaud, J.-L. 2013. Geotechnical Engineering: Unsaturated and Saturated Soils. College Station: WILEY.
28. CDC, 1994. Addressing emerging infectious disease threats: a prevention strategy for the United States. Atlanta, GA: US Department of Health and Human Services, Public Health Service.
29. CFGB, 1997. Internal erosion: typology, detection, repair, Bulletin du Comite Francais des Grande Barrages FRCOLD NEWS. No. 6 – Special Cingress CIGB Florence.
30. Chapius, R. P. 1986. Quantitative measurement of the scour resistance of natural solid clays. Canadian Geotechnical Journal. 23, pp. 132-141.
31. Chapius, R. P. and Gatien, T. 1986. An improved rotating cylinder technique for quantitative measurements of the scour resistance of clays. Canadian Geotechnical Journal. 23. pp 83-87.
32. Chapuis, R. P. 1986. Use of rotational erosion device on cohesive soils. Transportation Research Record 1089.

33. Chapuis, R., Gatien, T. 1986. An improved rotating cylinder technique for quantitative measurements of the scour resistance of clays. Can. Geotech. J., pp. 83-87.
34. Chedid, M., Shafii, I., Briaud, J. L., 2018. Erosion Tests on the Teton Dam Soils. The 9th International Conference on Scour and Erosion, Taipei, Taiwan.
35. Chen, Y.H, Anderson, B.A. 1987. Methodology for Estimating Embankment Damage Caused by Flood Overtopping. Transportation Research Record. Issue 1151, pp. 1-15.
36. Chow, V.T. 1959. Open-channel hydraulics. New York, McGraw-Hill Book Co., Inc.
37. Clark, L.A., Wynn, T.M. 2007. Methods for Determining Streambank Critical Shear Stress and Soil Erodibility: Implications for Erosion Rate Predictions. Transactions of the ASAE. Vol. 50(1), pp. 95-106.
38. Croad, R.N. 1981. Physics of Erosion of Cohesive Soils, PhD Thesis, Department of Civil Engineering, University of Auckland, NZ.
39. Decker, R. S. and Dunnigan, L. P. 1977. Development and use of the soil conservation service dispersion test. In Dispersive Clays, Related Piping, and Erosion in Geotechnical Projects, ASTM STP 623, Eds. Sherard, J. L. and Decker, R.S., American Society for Testing and Materials, 1977, pp. 94-109.
40. Dunn, I. S. 1959. Tractive resistance of cohesive channels. Journal of Soil Mechanics and Foundations Division, ASCE, pp. 1–24.
41. Gabr, M., Caruso, C., Key, A., Kayser, M. 2013. Assessment of in situ scour profile in sand using a jet probe. Geotechnical Testing Journal, Vol. 36(2).
42. Ghebreiyessus, Y. T., Gantzer, C. J., Alberts, E. E., Lentz, R. W. 1994. Soil erosion by concentrated flow: shear stress and bulk density. Transactions of the ASAE. Vol. 37(6), pp. 1791-1797.

43. Gibbs, H. J. 1962. A study of erosion and tractive force characteristics in relation to soil mechanics properties. US Department of the Interior, Bureau of Reclamation, Division of Engineering Laboratories, Soils Engineering Report No. EM-643.
44. Grishanin K.V. 1969. Dynamics of River Flows. Gidrometeoizdat, Leningrad. (In Russian).
45. Hanson, G. J. 1990. Surface erodibility of earthern channels at high stresses. Part I – Open channel testing. Transactions of the ASAE, Vol. 33, Issue 1, pp. 127-131.
46. Hanson, G. J. 1990. Surface erodibility of earthern channels at high stresses. Part II – Developing an in situ testing device. Transactions of the ASAE, Vol. 33, Issue 1, pp. 132-137.
47. Hanson, G. J. 1991. Development of a jet index to characterize erosion resistance of soils in earthen spillways. Trans. ASAE. General Edition, Vol. 34(5), pp. 2015-2020. ISSN 00012351.
48. Hanson, G. J., Cook, K. R. 2004. Apparatus, test procedures, and analytical methods to measure soil erodibility in situ. Applied Engineering in Agriculture. American Society of Agricultural Engineers. ISSN 0883-8542. Vol. 20(4), pp. 455-462.
49. Hanson, G. J., Hunt, S. L. 2007. Lessons learned using laboratory JET method to measure soil erodibility of compacted soils. Applied Engineering in Agriculture. American Society of Agricultural and Biological Engineers ISSN 0883-8542. Vol. 23(3), pp 305-312.
50. Hanson, G. J., Robinson, K. M., Cook, K. R. 2002. Scour below an overfall: Part II. Prediction. Transactions of the ASAE. American Society of Agricultural Engineers, Vol. 45(4), pp. 957-964. ISSN 0001-2351.
51. Hanson, G. J., Robinson, K. M., Temple, D. M. 1990. Hydraulic Engineering – Proceedings of the 1990 National Conference. pp. 525-530. ISBN 0872627748.

52. Hanson, G. J., Simon, A., Cook, K. R. 2002. Non-vertical jet testing of cohesive streambank materials. ASAE Annual International Meeting / CIGR XVth World Congress. Paper Number: 022119.

53. Hanson, G.J., and Simon, A. 2001. Erodibility of cohesive streambeds in the loess area of the Midwestern USA, Hydrological Processes, Vol. 15(1), pp. 23-38.

54. Hanson, G.J., and Simon, A. 2001. Erodibility of cohesive streambeds in the loess area of the Midwestern USA, Hydrological Processes, Vol. 15(1), pp. 23-38.

55. Hofland, B., Battjes, J.A., Booij, R. 2005. Measurement of fluctuating pressures on coarse bed material, Journal of Hydraulic Engineering, Vol. 131(9), pp.770-781.

56. Julian, J.P., and Torres, R. 2006. Hydraulic erosion of cohesive riverbanks, Geomorphology, 76 (1-2), pp. 193-206.

57. Julien, P.Y. 1995. Erosion and Sedimentation. Cambridge University Press.

58. Justin, J. D. The Design of Earth Dams, Trans. ASCE 87, pp. 1-61, 1923

59. Kandiah, A., Arulanandan, K. 1974. Hydraulic erosion of cohesive soils. Transportation Research Record No. 497.

60. Lefebvre, G., Rohan, K., Douville, S. 1985. Erosivity of natural intact structured clay: Evaluation. Canadian Geotechnical Journal. Vol. 22, pp. 508-517.

61. Lomtadze V.D. 1977. Engineering geology. Engineering geodynamics. Moscow, Nedra (in Russian)

62. Lyle, W. M., Smerdon, E. T. 1965. Relation of compaction and other soil properties to erosion resistance of soils. Transactions of the ASAE. Vol. 8(3), pp. 419-422. 284-298.

63. Masch, F. D., Jr., Espey, W. H., Jr., and Moore, W. L. 1963. Measurements of the shear resistance of cohesive sediments. Proceedings of the Federal Inter-Agency Sedimentation

Conference, Agricultural Research Service, Publication No. 970, Washington, D.C., pp. 151-155.

64. Maslov, N. N. 1968. Osnovy mechaniki gruntov i injenernayay geologiya. Vyshayay skola.
65. McNeil, J., Taylor, C., Lick, W. 1996. Measurements of Erosion of Undisturbed Bottom Sediments with Depth. Journal of Hydraulic Engineering. June 1996. Vol. 122 (6), pp. 316-324.
66. Mirzhulava, Z.E. 1967. Razmyv rusla I metodika ocenki ego ustoichivosti. Kolos. Moskva
67. Moody L.F. 1944. Friction Factors for Pipe Flow. Transaction of the American Society of Civil Engineers, Vol. 66.
68. Moore, W. L., Masch, F. D., Jr. 1962. Experiments on the scour resistance of cohesive sediments. Journal of Geophysical Research, Vol. 67(4), pp. 1437-1449.
69. Mostafa, T.S., Imran, J., Chaudhry, M.H., Kahn, I.B. 2008. Erosion Resistance of Cohesive Soils. Journal of Hydraulic Research. Vol. 46(6), pp. 777-787.
70. Neill, C.R. 1967. Mean-velocity criterion for scour of coarse uniform bed-material, International Association for Hydraulic Research, Vol. 3, pp. 46-54.
71. Osipov V.I., Sokolov V.N., Rumyanzeva E.M. 1989. Microstructure of clayey soils. Moscow, Nedra, (in Russian)
72. Reddi, L. N., Lee, I., Bonala, M. V. S. 2000. Comparison of internal and surface erosion using flow pump test on a sand-kaolinite mixture, Geotechnical Testing Journal. Vol. 23, pp. 116–122.
73. Roberts, J.D., Jepsen, R.A., James, S.C. 2003. Measurement of Sediment Erosion and Transport with the Adjustable Shear Stress Erosion and Transport Flume. Journal of Hydraulic Engineering. Nov. 2003. Vol. 129(11), pp. 862-871.

74. Sanchez, R. L., Strutynsky, A. I. and Silver, M. L. 1983. Evaluation of the erosion potential of embankment core materials using the laboratory triaxial erosion rest procedure. Geotechnical Laboratory, U.S. Army Engineer Waterways Experiment Station, Technical Report GL-83-4.
75. Sargunan, A. 1977. Concept of critical shear stress in relation to characterization of dispersive clays. In Dispersive Clays, Related Piping, and Erosion in Geotechnical Projects. Symposium, Seventy-ninth Annual Meeting, American Society for Testing and Materials, ASTM Special Technical Publication 623, Sherard, J.L. and Decker R.S. eds., pp. 390-397.
76. Shafii, I., Briaud, J. L., Chen, H. C., and Shidlovskaya, A., 2016. Relationship between Soil Erodibility and Engineering Properties. The 8th International Conference on Scour and Erosion, Oxford, U.K.
77. Shafii, I., Zhang, Z., Briaud, J. L., 2018. Measurement of Hydrodynamic Forces on Gravel Particles in the Erosion Function Apparatus. The 9th International Conference on Scour and Erosion, Taipei, Taiwan.
78. Shaikh, A., Ruff, J. F., Charlie, W.A. and Abt, S.R. 1988. Erosion rate of dispersive and nondispersive clays. Journal of Geotechnical Engineering. Vol. 114(5), pp. 589-600.
79. Shaikh, A., Ruff, J.F., Abt, S. R. 1988. Erosion rate of compacted NA-montmorillonite soils. Journal of Geotechnical Engineering, ASCE. Vol. 114(3), pp. 296-305.
80. Shan, H., Shen, J., Kilgore, R., Kerenyi, K. 2015. Scour in cohesive soils. US Department of Transportation, Federal Highway Administration. Publication No. FHWA-HRT-15-033
81. Sheppard, D.M., Bloomquist, D., Slagle, P.M. 2006. Rate of erosion properties of rock and clay. Developed for the Florida Department of Transportation. UF Project 00030890 (4554013-12)

82. Sheppard, D.M., Odeh, M., Glasser, T. 2004. Large scale clear-water local pier scour experiments. Journal of Hydraulic Engineering. Vol. 130, No. 10. ISSN 0733-9429/2004/10-957

83. Sherard, J. L. 1984. Discussions and closure on 'Erosion in relation to filter design criteria in earth dams' by Arulanandan, K. and Perry, E.B. Journal of the Geotechnical Engineering Division, ASCE. Vol. 110(7), pp. 996-1005.

84. Sherard, J. L. 1985. Hydraulic fracturing in embankment dams. Symposium on Seepage and Leakage from Dams and Impoundments, ASCE, Eds. Volpe, R.L. and Kelly, W.E., pp. 115-141.

85. Sherard, J. L. Dunningan, L. P. 1989. Critical filters for impervious soils. Journal of Geotechnical Engineering. Vol. 115(7), pp. 927-947.

86. Sherard, J. L., Decker, R. S., Ryker, N. L. 1972. Piping in earth dams of dispersive clay. Conference on Performance of Earth and Earth-supported Structures, ASCE, 1972. Vol. 1(1), pp. 589-626.

87. Sherard, J. L., Dunnigan, L. P., Decker, R. S. 1976. Identification and nature of dispersive soils. Journal of Geotechnical Engineering Division, ASCE. 102, pp. 298-312.

88. Sherard, J. L., Dunnigan, L. P., Decker, R. S. and Steele, E. F. 1976. Pinhole test for identifying dispersive soils. Journal of Geotechnical Engineering Division, ASCE. Vol. 102, pp. 69-85.

89. Sherard, J. L., Dunnigan, L. P., Talbot, J. R. 1984. Filters for silts and clays. Journal of the Geotechnical Engineering Division, ASCE. Vol. 110(6), pp. 684-699.

90. Sherard, J. L.1973. Embankment dam cracking. in embankment dam engineering, Eds. Hirschfeld, R.C. and Poulos, S.J., pp. 271-353.

91. Shidlovskaya, A.V., Briaud, J.-L. Chedid, M., Keshavarz M. Erodibility of soil above the groundwater level: some test results. Proceedings of the 3-rd European Conference on Unsaturated Soils. 12-14 September 2016. Paris. France.
92. Skempton, A.W. 1953. The colloidal "activity" of clays. 3rd International Conference on Soil Mechanics and Foundation Engineering, Switzerland, 1953, Vol. 1, pp.57–61.
93. Skempton, A.W. 1953. The colloidal "activity" of clays. 3rd International Conference on Soil Mechanics and Foundation Engineering, Switzerland, 1953, Vol. 1, pp.57–61.
94. Smerdon, E. T., Beasley, R. P. 1961. Critical tractive forces in cohesive soils, Journal of Agricultural Engineering. Vol. 42(1), pp. 26-29.
95. SPSS Inc. 2014. IBM SPSS Statistics 23 core system user's guide. Chicago, IL.
96. Straub, T. D., Over, T. M., Domanski, M. M. 2013. Ultimate pier and contraction scour prediction in cohesive soils at selected bridges in Illinois. A report of the findings of ICT-R27-105 Bridge Scour Estimation at Sites with Cohesive Soils, Illinois Center for Transportation. Research Report No. FHWA-ICT-13-025. ISSN: 0197-9191.
97. Straub, T. D., Over, T. M. 2010. Pier and contraction scour prediction in cohesive soils at selected bridges in Illinois. A report of the findings of ICT-R27-19 Pier and Contraction Scour Prediction in Cohesive Soils, Illinois Center for Transportation, Research Report ICT-10-074. ISSN: 0197-9191.
98. Terzaghi, K., Peck, R. B. 1967. Soil Mechanics in Engineering Practice. 2st Ed. John Wiley and Sons, New York.
99. Thoman, R. W., Niezgoda, S. L. 2008. Determining erodibility, critical shear stress, and allowable discharge estimates for cohesive channels: Case study in the Powder River Basin of

Wyoming. Journal of Hydraulic Engineering. Vol. 134(12), ISSN 0733-9429/2008/12-1677-1687.

100. Trammell, M. 2004. Laboratory apparatus and methodology for determining water erosion rates of erodible rock and cohesive sediments. MS thesis to the University of Florida.

101. USSD. 2011. 21st Century Dam Design-Advances and Adaptations. 31st Annual USSD Conference, pp. 1023-1032.

102. Utley, B., Wynn, T. 2008. Cohesive soil erosion: theory and practice. World Environmental and Water Resources Congress.

103. V.T. Trofimov. Moscow. KDU, 2011. Engineering geology of Russia. Vol. 2. (In Russian).

104. Wahl, T. L. 2010. A comparison of the hole erosion test and jet erosion test. Joint Federal Interagency Conference on Sedimentation and Hydrologic Modeling, Las Vegas, NV.

105. Wahl, T. L. 2014. Measuring erodibility of gravelly fine-grained soils. Hydraulic Laboratory Report HL-2014-05.

106. Wahl, T. L., Regazzoni, P. L., Erdogan, Z. 2009. Practical improvements for the Hole Erosion Test. 33rd IAHR Congress, Vancouver, BC, Canada.

107. Wahl, T., Hanson, G., Regazzoni, P. 2009. Quantifying erodibility of embankment materials for the modeling of dam breach processes. ASDSO Dam Safety 2009.

108. Wahl, T.L., and Erdogan, Z. 2008. Erosion indices of soils used in ARS piping breach tests. U.S. Dept. of the Interior, Bureau of Reclamation, Hydraulic Laboratory Report HL-2008-04, pp. 142.

109. Wan, C. F., Fell, R. 2002. Investigation of internal erosion and piping of soils in embankment dams by the slot erosion test and the hole erosion test. UNICIV Report R-412. The University of New South Wales.

110. Wan, C. F., Fell, R. 2004. Investigation of rate of erosion of soils in embankment dams. Journal of Geotechnical and Geoenvironmental Engineering. Vol. 130(4), pp. 373-380.

111. Wan, C. F., Fell, R. 2004. Laboratory tests on the rate of piping erosion of soils in embankment dams. ASTM Geotechnical Testing Journal. Vol. 27(3), pp. 295-303.

112. Winterwep, J.C., Van Kesteren, W.G.M. 2004. Introduction to the Physics of Cohesive Sediment in the Marine Environment. Development in Sedimentology Series No. 56. ISBN 0444515534.

113. Wynn, T.M., Mostaghimi, S., Alphin, E.A. 2004. The Effects of Vegetation on Stream Bank Erosion. ASAE/CSAE Annual International Meeting Sponsered by ASAE/CSAE.

114. Zimon, A.D. 1976. Adhesion of Dust and Powder. Moscow.

115. Zvonkov V.V. 1962. Water and Wind Erosion. Isd. Akad. Nauk SSSR, Moscow. (In Russian).

APPENDIX A

EROSION TEST RESULTS SPREADSHEETS

Clay Samples - EFA

Velocity	Equiva Rough	Reyso Numb	Friction	Shear Factor	Shear Stres	Erosic Readi	Test Time	Erosion
m/sec	mm	R_e	Moody	R_a hart		mm	sec	mm/hr
0.49	0 0.002	2974	30.024	0.7	20	0	120	0 0.0
0.97	0 0.500	5891	40.035	4.1	19	0	120	0 0.0
1.97	0 0.500	11958	40.035	16.9	72	6	120	0 18.0
2.99	5 0.500	18182	80.035	39.2	39	5.5	60	0 33.0

Velocity (m/s				
Shear stress				
Erosion Rate				

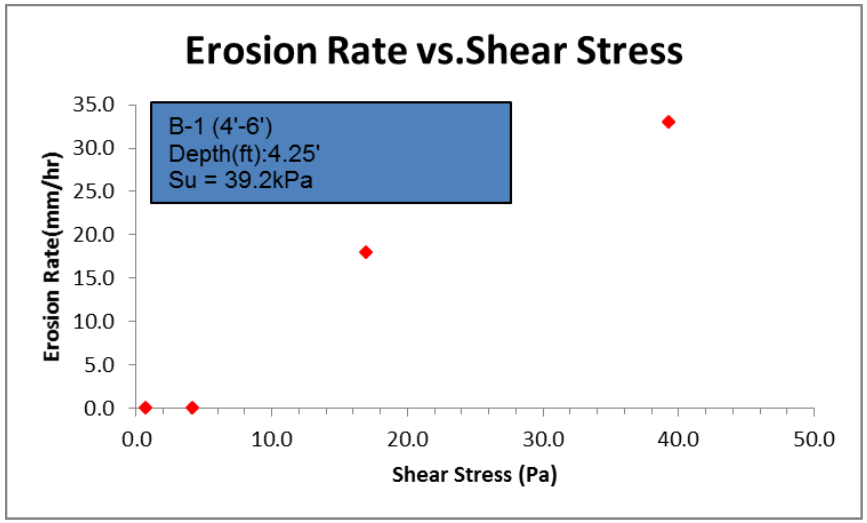

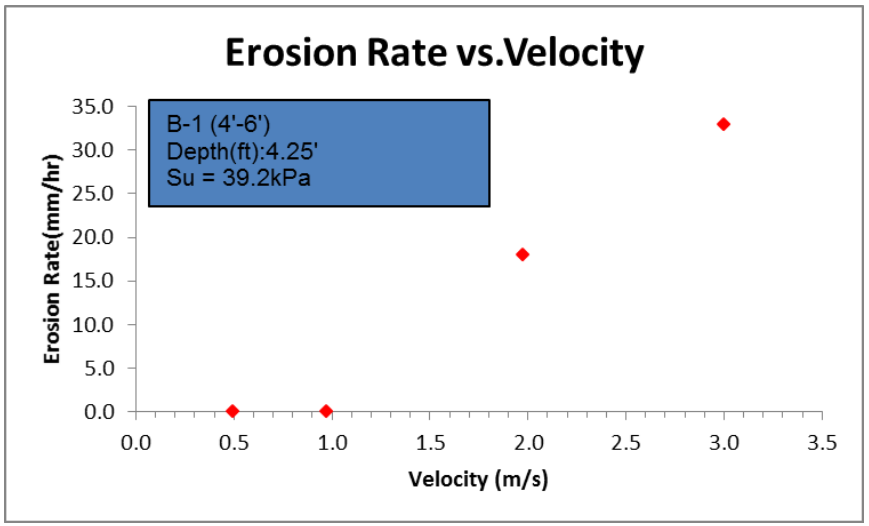

Figure A-1. B-1 (4'-6') Beaumont Formation

Velocity	Equiva Rough	Reyso Numb	Friction	Shear Factor Stres	Erosic Readi	Test Time	Erosion
m/sec	mm	R_e	Moody	Chart	mm	sec	mm/hr
0.50	30.003	3053	90.023	0.72	7 0	120	0 0.0
1.11	12.000	6745	20.057	8.794	1	123	0 2.9
1.91	02.000	11594	60.057	25.9	85 2	121	5 5.9

Velocity (m/s			
Shear stress a			
Erosion Rate			

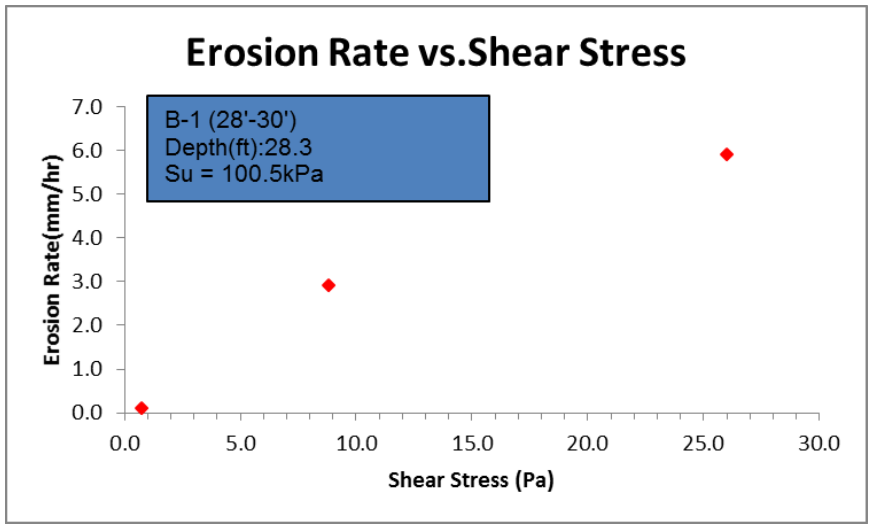

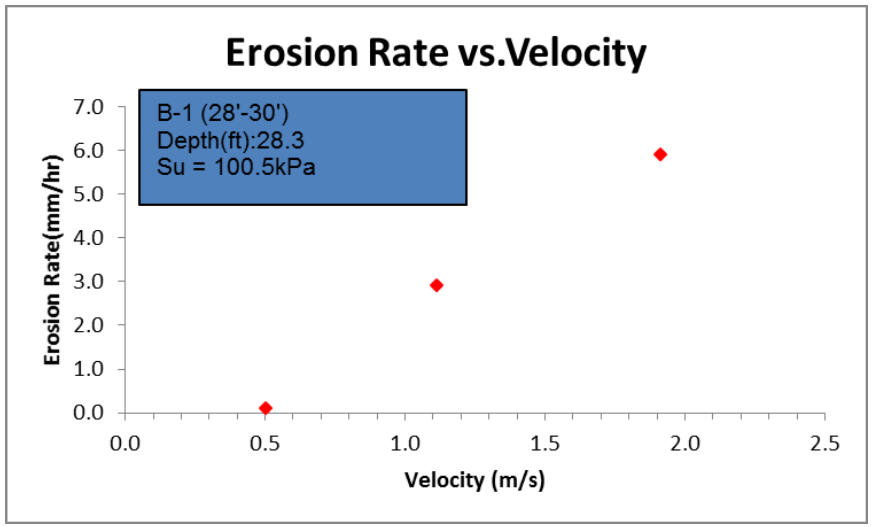

Figure A-2. B-1 (28'-30') Beaumont Formation

Velocity	Equiva Rough	Reyso Numb	Friction	Shear Factor Stres	Erosic Readi	Test Time	Erosion
m/sec	mm	R_e	Moody	$R_a$hart	mm	sec	mm/hr
0.51	20.002	23110	80.023	0.755	1	1339.8	2.6
0.99	70.002	26051	70.020	2.484	2	1020	7.0
1.43	50.002	28712	90.019	4.891	3	126	0 8.5
2.62	70.002	215950	80.017	14.67	2	90	0 8.0
3.97	60.002	241388	60.015	29.38	1	24	0 15.0

Velocity (m/s					
Shear stress					
Erosion Rate					

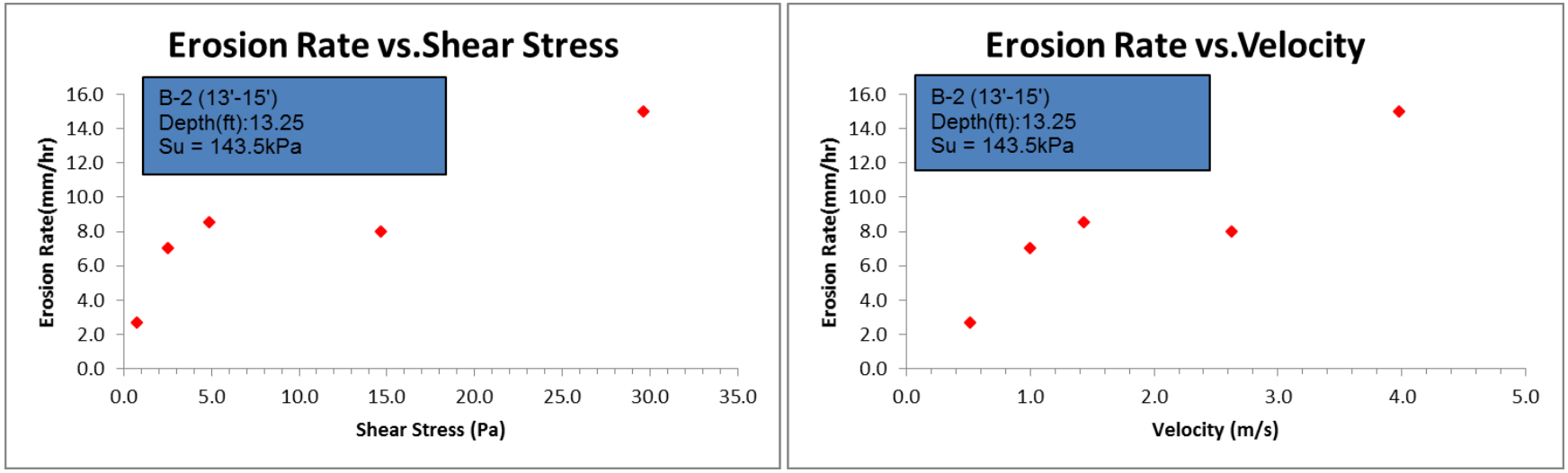

Figure A-3. B-2 (13'-15') Beaumont Formation

Velocity	Equiva Rough	Reyso Numb	Friction	Shear Factor Stres	Erosic s Readi	Test Time	Erosion
m/sec	mm	R_e	Moody	$R_a$hart	mm	sec	mm/hr
0.52	40.004	3181	20.023	0.789	0	1201.	0020.0
1.52	60.500	9266	60.035	10.1	92 0.5	114	3 1.5
2.48	31.000	15074	00.044	33.9	03 1	1153.	0023.1
3.55	41.000	21579	90.044	69.4	83 1.5	99	0 5.4
4.49	71.000	27301	10.044	111.2	10 2	108	0 6.6

Velocity (m/s					
Shear stress					
Erosion Rate					

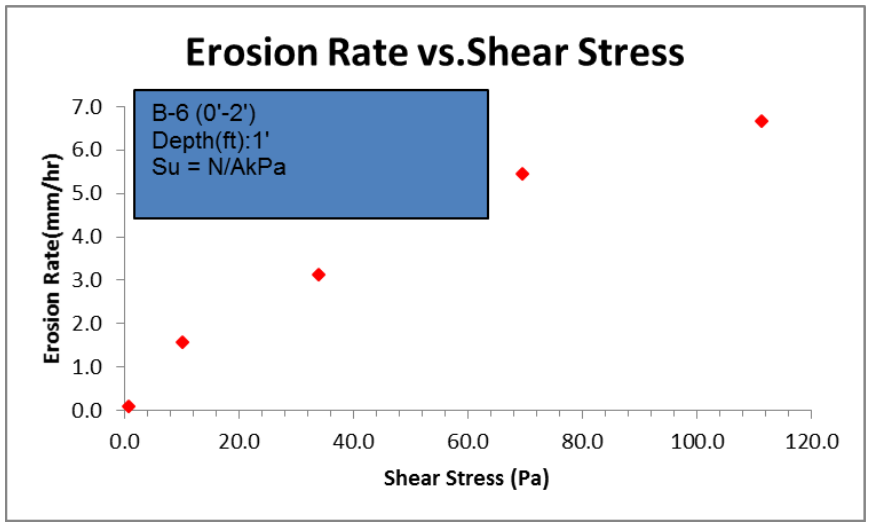

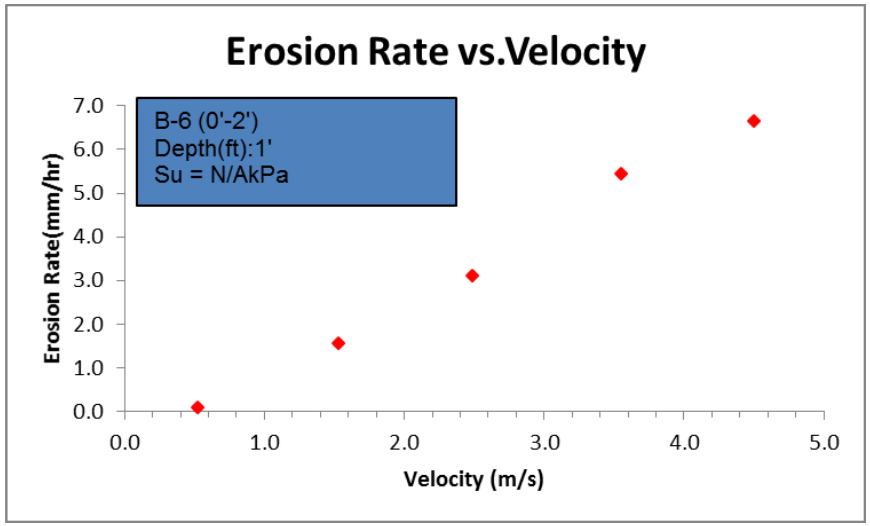

Figure A-4. B-6 (0'-2') Beaumont Formation

Velocity	Equiva Rough	Reyso Numb	Friction	Shear Factor	Erosic Stres Readi	Test Time	Erosion
m/sec	mm	R_e	Moody	$R_a$hart	mm	sec	mm/hr
0.52	90.003	3209	10.023	0.803	0	101	1 0.0
1.04	80.003	6363	10.020	2.746	1	123	0 2.9
2.03	60.500	12362	80.035	18.140	2	129	6 5.5
3.05	31.000	18534	60.044	51.257	3	1624.002	6.6
4.05	91.000	24645	10.044	90.624	3	120	0 9.0

Velocity (m/s					
Shear stress					
Erosion Rate					

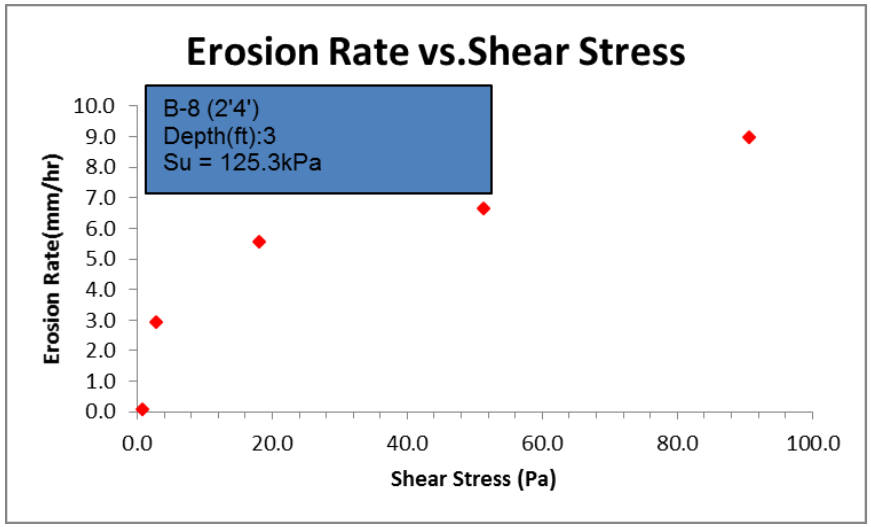

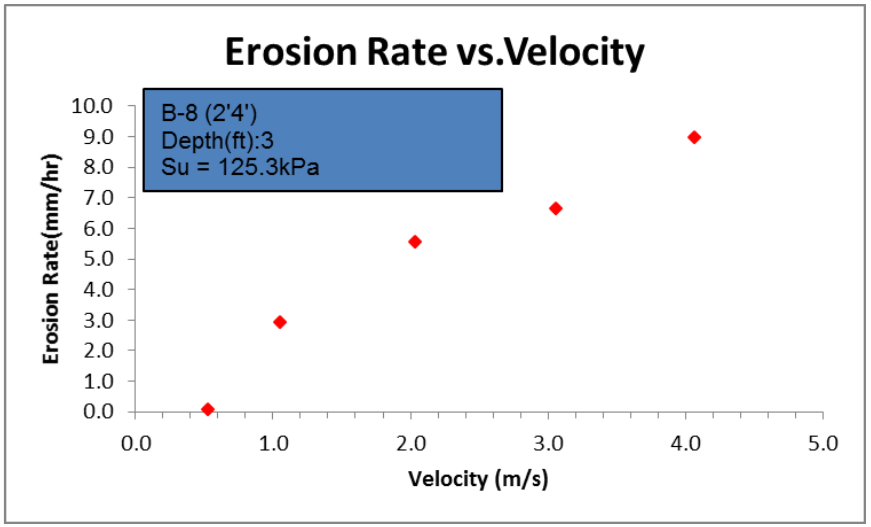

Figure A-5. B-8 (2'-4') 5694 Alluvium

Velocity	Equiva Rough	Reyso Numb	Friction	Shear Factor	Erosic Stres Readi	Test Time	Erosion
m/sec	mm	R_e	Moody	$R_a$hart	mm	sec	mm/hr
0.46	81.000	02838	80.045	1.230	0	45	0 0.0
0.98	41.000	05974	40.044	5.326	0	48	0 0.0
1.48	91.000	09039	30.044	12.191	0	114	0 0.0
2.03	11.000	12331	40.044	22.688	2	120	0 6.0
2.96	01.000	17973	10.044	48.198	7	265	.2 95.0

Velocity (m/s					
Shear stress (a					
Erosion Rate					

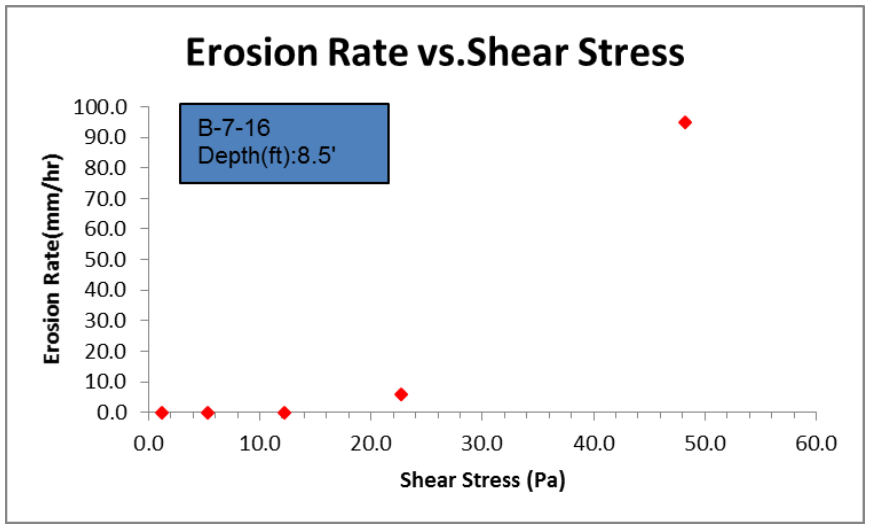

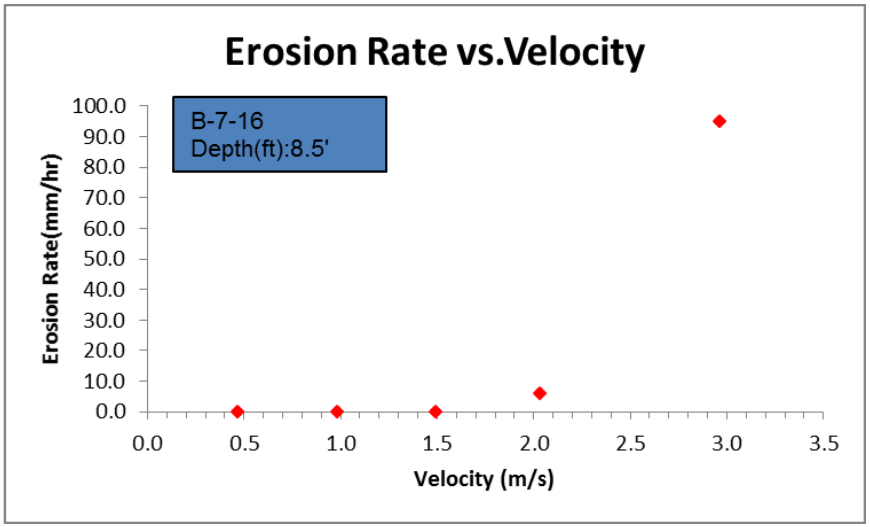

Figure A-7. B-7-16 (8'-10.5') Top

Velocity	Equiva Rough	Reyso Numb	Friction	Shear Factor Stres	Erosic Readi	Test Time	Erosion
m/sec	mm	R_e	Moody	$R_a$hart	mm	sec	mm/hr
0.51	90.003	3151	00.023	0.774	0	180	0 0.0
1.01	60.003	6170	10.020	2.582	1	180	0 2.0
1.97	50.500	11988	60.035	17.058	3	180	0 6.0
3.05	51.000	18548	30.044	51.32	6	180	0 12.0
4.05	91.000	24642	40.044	90.604	4	1390	.02 10.3
5.06	51.000	30749	80.044	141.080	8	162	0 17.7

Velocity (m/s						
Shear stress						
Erosion Rate						

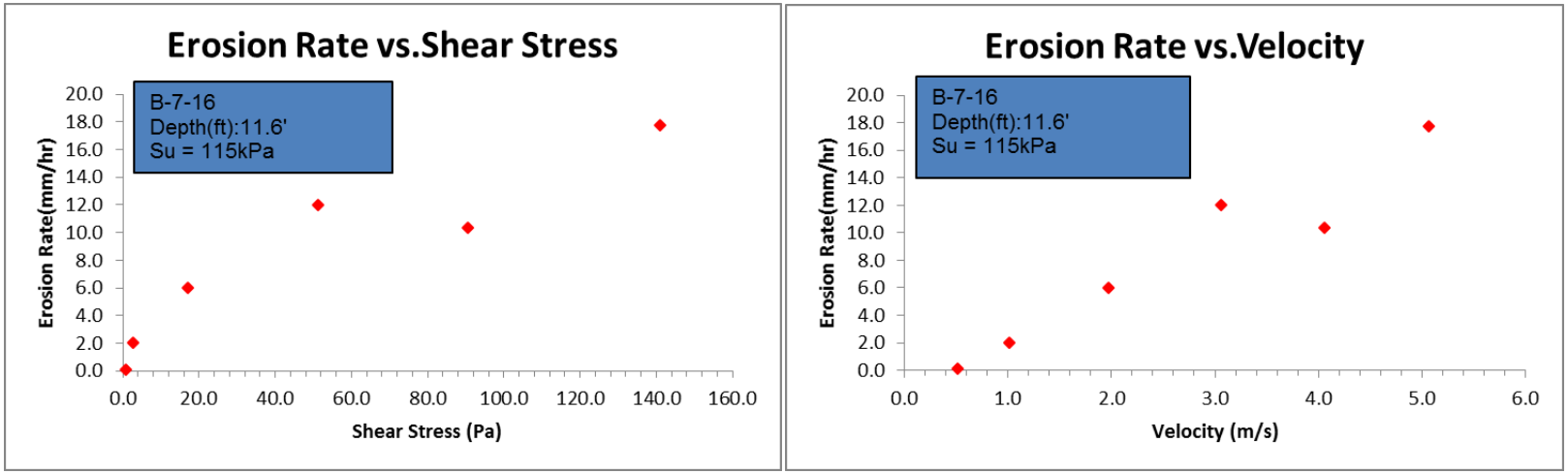

Figure A-8. B-7-16 (10.5'-13') Bottom

Velocity	Equiva Rough	Reyso Numb	Friction	Shear Factor Stres	Erosic Readi	Test Time	Erosion
m/sec	mm	R_e	Moody	$R_a$hart	mm	sec	mm/hr
0.44	20.003	2681	00.024	0.5	850	126	0 0.0
1.06	30.003	6455	90.020	2.8	27 1.5	120	0 4.5
2.09	80.003	12736	80.017	9.3	52 2.5	90	0 10.0
3.12	40.003	18967	20.016	19.5	193	102	0 10.5
4.01	30.003	24366	30.015	30.1	993	90	0 12.0
5.20	60.003	31610	30.015	50.8	254	90	0 16.0

Velocity(m/s						
Shear stress						
Erosion Rate						

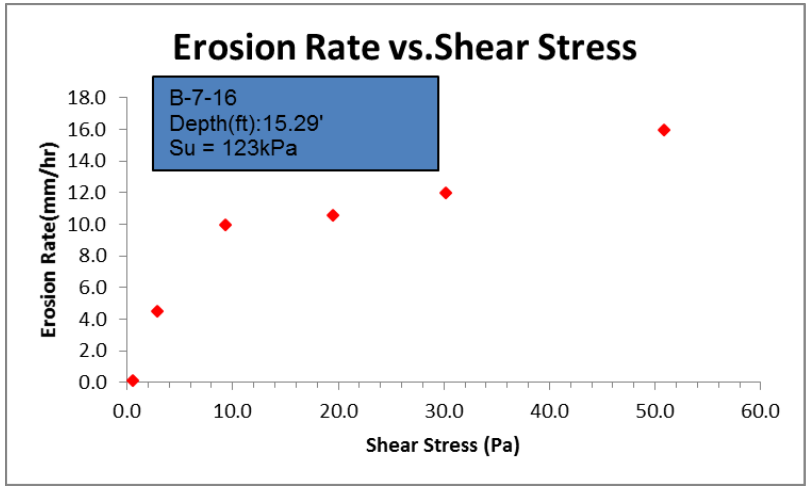

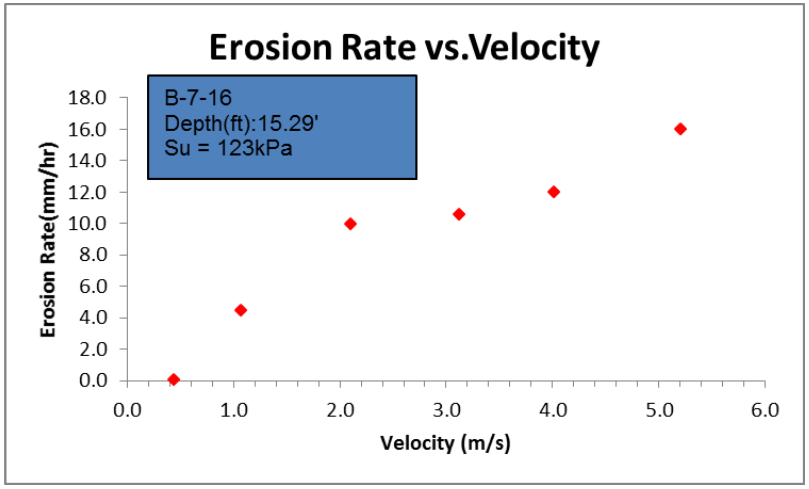

Figure A-9. B-7-16 (13'-15.5') Bottom

Velocity	Equiva Rough	Reyso Numb	Friction	Shear Factor Stres	Erosic Readi	Test Time	Erosion
m/sec	mm	R_e	Moody	$R_a$hart	mm	sec	mm/hr
0.52	10.003	3165	30.023	0.78	10	1210.	0020.0
1.07	40.003	6519	10.020	2.88	22	117	0 6.1
2.08	60.003	12666	40.017	9.24	94	138	0 10.4
2.97	90.003	18084	40.016	17.7	44 4.5	108	0 15.0
4.01	60.003	24384	00.015	30.2	43 11	78	0 50.7

Velocity (m/s					
Shear stress a					
Erosion Rate					

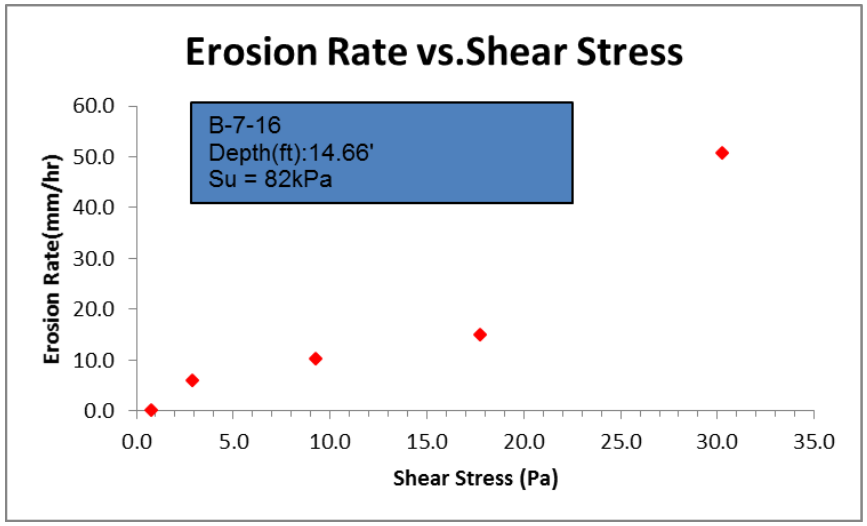

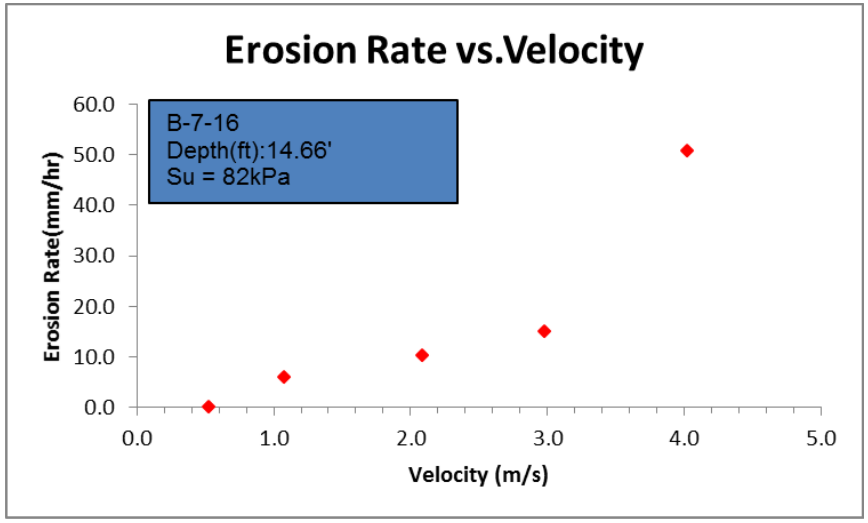

Figure A-10. B-7-16 (13'-15.5') Middle

Velocity	Equiva Rough	Reyso Numb	Friction	Factor	Shear Stres	Erosic Readi	Test Time	Erosion
m/sec	mm	R_e	Moody	$C_a$hart		mm	sec	mm/hr
0.51	60.003	3132	90.023	0.7	66	0	180	0 0.0
0.98	70.003	5993	80.020	2.4	36	5	1105.	00216.2
2.01	70.003	12249	00.018	9.1	58	10	132	0 27.2
3.12	60.003	18982	00.016	19.5	49	15	114	0 47.3
4.13	70.003	25117	50.015	32.0	90	2	138	0 5.2
5.08	40.003	30869	80.015	48.4	72	3	114	0 9.4

Velocity (m/s							
Shear stres a							
Erosion Rate							

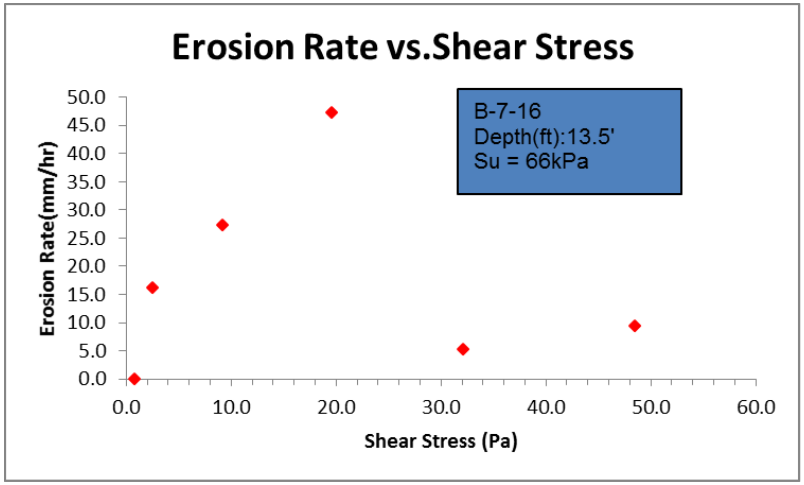

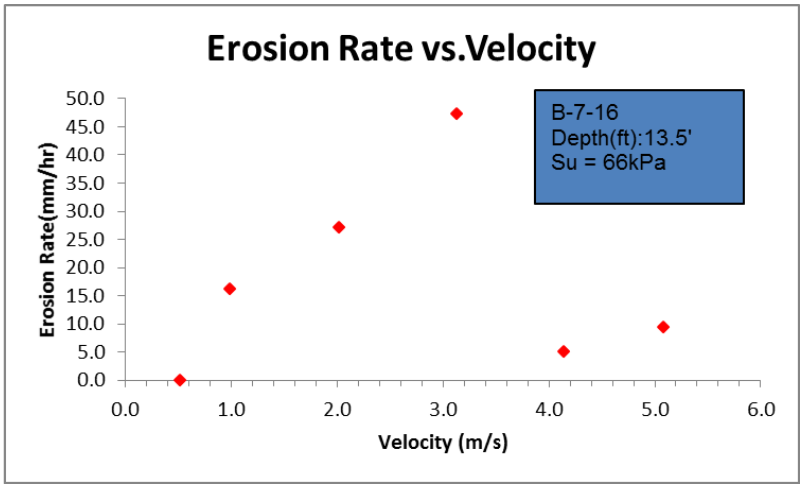

Figure A-11. B-7-16 (13'-15.5') Top

Velocity	Equiva Rough	Reyso Numb	Friction	Shear Factor	Shear Stres	Erosic Readi	Test Time	Erosion
m/sec	mm	R_e	Moody	Chart		mm	sec	mm/hr
0.43	0 0.500	0 2610	7 0.037	0.8	55	2	90	0 8.0
1.01	0 1.000	0 6132	1 0.044	5.6	11	5	90	0 20.0
1.54	0 1.000	0 9350	0 0.044	13.0	44	8	1060.	00227.1
2.40	0 0.500	0 14571	40.035	25.2	00	5	745.0	00224.1

Velocity (m/s				
Shear stress				
Erosion Rate				

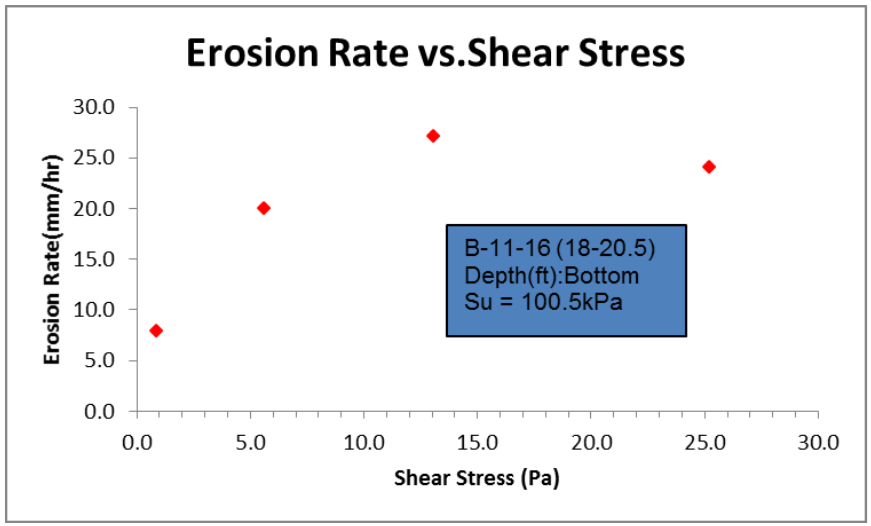

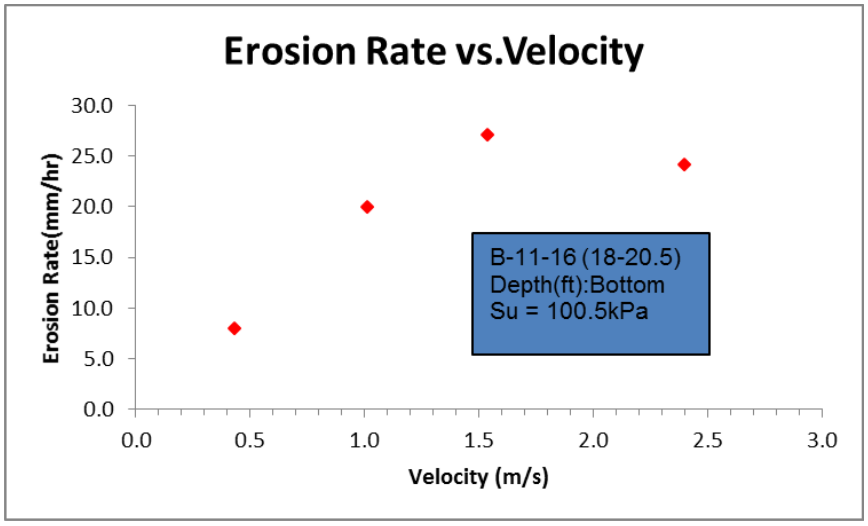

Figure A-12. B-11-16 (18'- 20.5') Bottom

Velocity	Equiva Rough	Reyso Numb	Friction	Shear Factor Stres	Erosic Readi	Test Time	Erosion
m/sec	mm	R_e	Moody	$R_a$hart	mm	sec	mm/hr
0.36	01.000	02185	70.045	0.729	1	1339.8	2.6
0.69	01.000	04189	30.044	2.619	2	760.002	9.4
1.21	01.000	07346	40.044	8.053	12	1170	36.9
1.53	01.000	09289	30.044	12.875	6	15	0 144.0

Velocity (m/s				
Shear stress				
Erosion Rate				

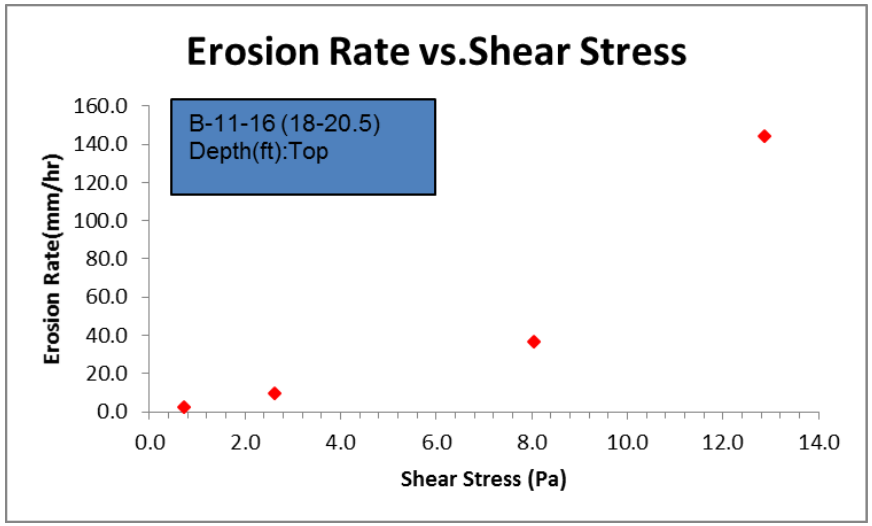

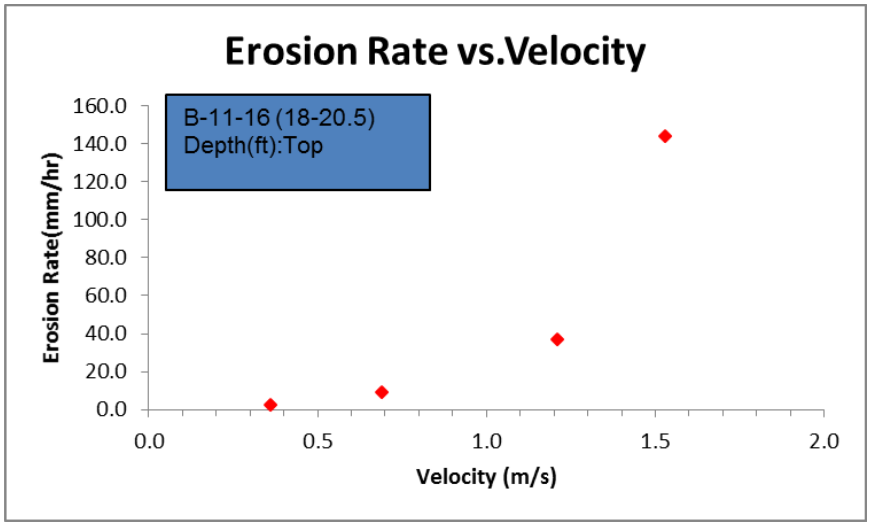

Figure A-13. B-11-16 (18'- 20.5') Top

Velocity	Equiva Rough	Reyso Numb	Friction	Shear Factor Stres	Erosic Readi	Test Time	Erosion
m/sec	mm	R_e	Moody	$R_a$hart	mm	sec	mm/hr
0.45	20.001	2741	90.024	0.6	12 0	121	2 0.0
0.98	50.001	5981	50.020	2.4	26 1	150	0 2.4
2.08	10.001	12634	10.017	9.2	02 2	138	0 5.2
3.00	60.001	18249	90.016	18.0	70 3	1399.	9987.7
3.99	00.001	24228	00.015	29.8	58 4	114	0 12.6

Velocity (m/s					
Shear stress (a					
Erosion Rate					

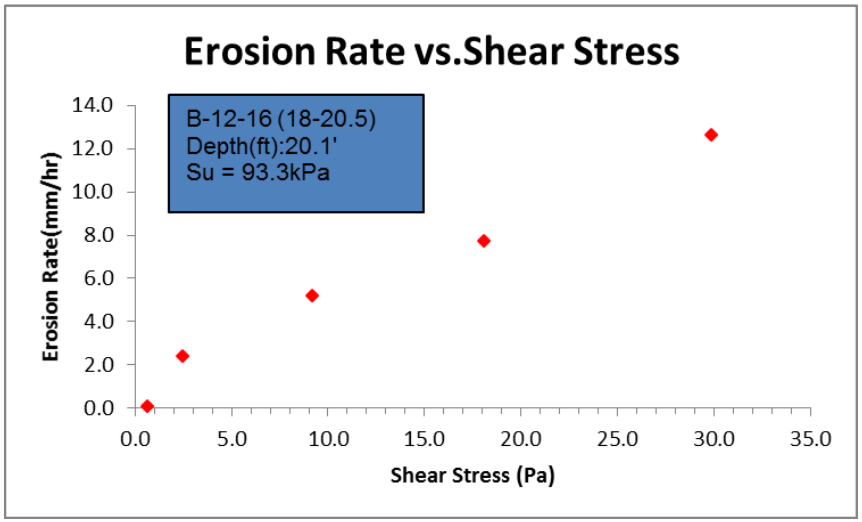

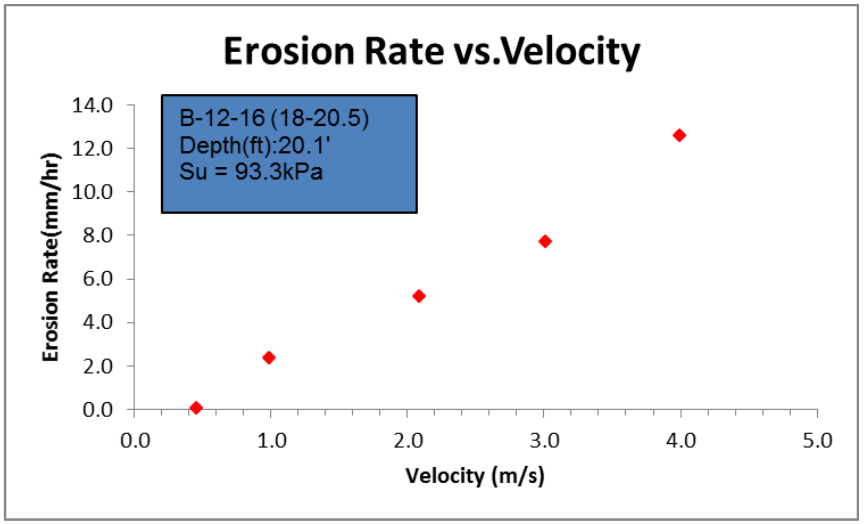

Figure A-14. B-12-16 (18'- 20.5') Bottom

Velocity	Equiva Rough	Reyso Numb	Friction	Shear Stres	Erosic Readi	Test Time	Erosion
m/sec	mm	R_e	Moody	τ_a hart	mm	sec	mm/hr
0.56	60.001	3435	70.023	0.92	10	90	0 0.0
1.06	00.001	6433	50.020	2.80	71	150	0 2.4
1.97	70.001	12003	30.017	8.30	61.5	150	0 3.6
3.00	30.001	18231	20.016	18.0	341.5	152	7 3.5
4.08	80.001	24821	40.015	31.3	382	133	5 5.3
5.16	50.001	31357	50.015	50.0	153	198	0 5.4

Velocity (m/s						
Shear stress						
Erosion Rate						

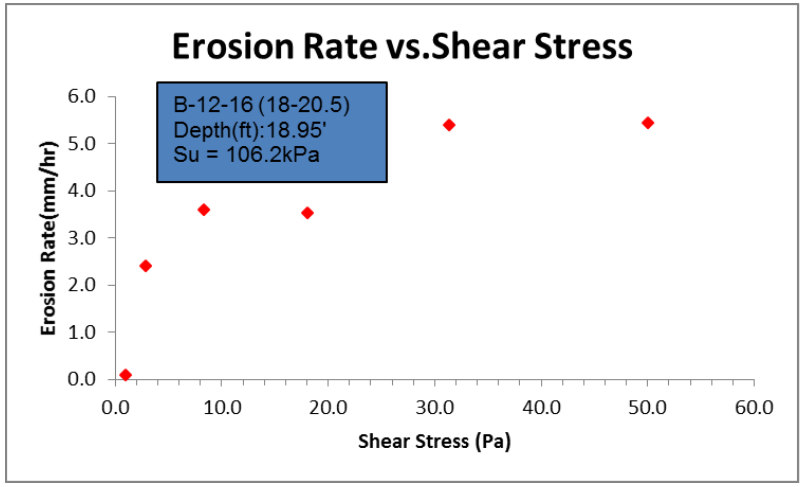

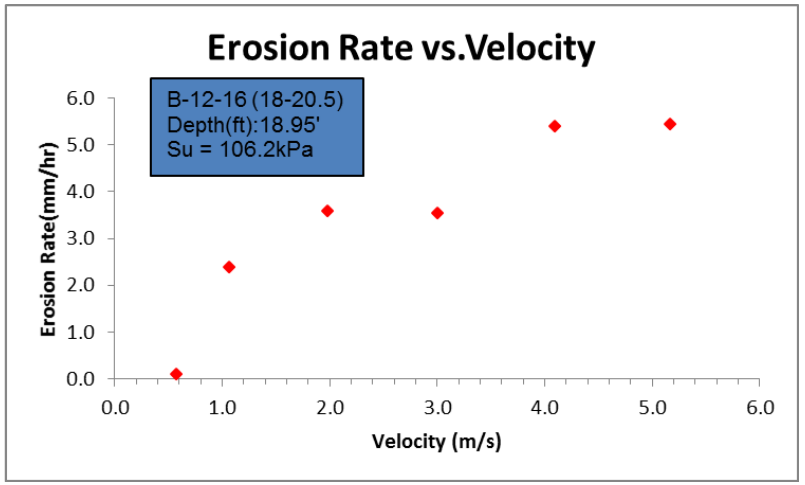

Figure A-16. B-12-16 (18'- 20.5') Middle

Velocity	Equiva Rough	Reyso Numb	Friction	Shear Factor Stres	Erosic Readi	Test Time	Erosion
m/sec	mm	R_e	Moody	$R_a$hart	mm	sec	mm/hr
0.43	50.001	2639	30.024	0.567	0	132	0 0.0
1.02	00.001	6194	10.020	2.602	0	1579.	998 0.0
2.06	30.001	12527	40.017	9.047	1	170	1 2.1
3.09	90.001	18814	60.016	19.206	2	171	0 4.2
4.09	10.001	24840	30.015	31.386	2	1200	.96 5.9
5.05	11.000	30669	60.044	140.345	7	72	0 35.0

Velocity(m/s						
Shear stress						
Erosion Rate						

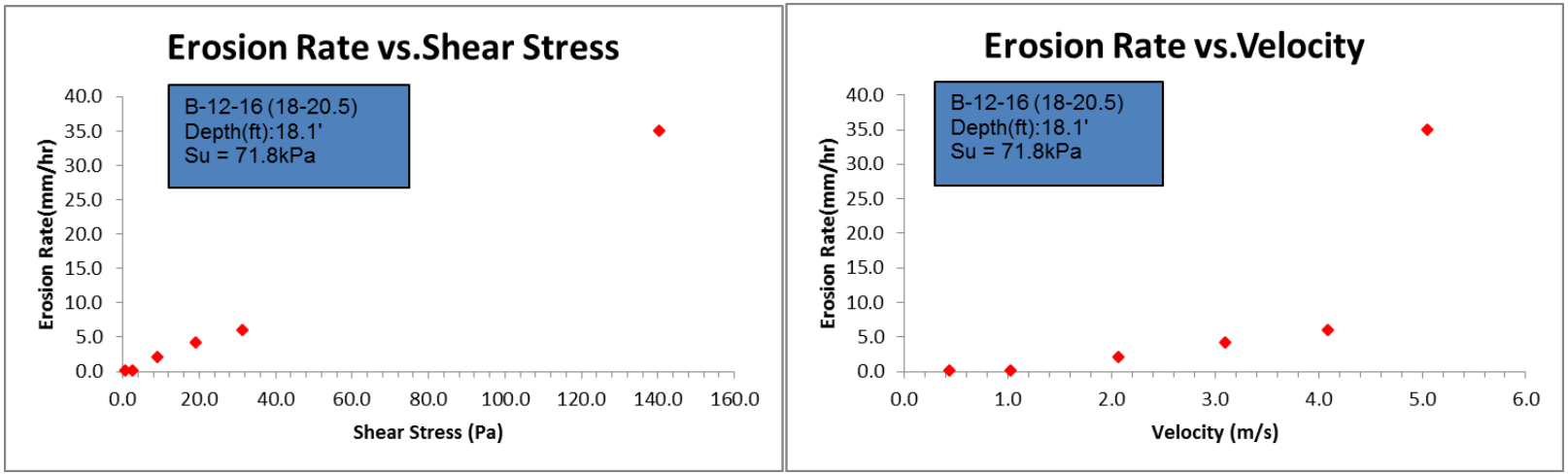

Figure A-17. B-12-16 (18'- 20.5') Top

Velocity	Equiva Rough	Reyso Numb	Friction	Shear Factor Stres	Erosic Readi	Test Time	Erosion
m/sec	mm	R_e	Moody	$R_a$hart	mm	sec	mm/hr
0.46	10.004	2799	00.024	0.6	380	1477.998	0.0
0.98	40.004	5974	50.020	2.4	210	150	0.0
1.58	90.004	9646	60.018	5.6	800	0.5 180	1.0
2.46	00.004	14936	50.017	12.8	611	1.5 156	3.4

Velocity (m/s				
Shear stress				
Erosion Rate				

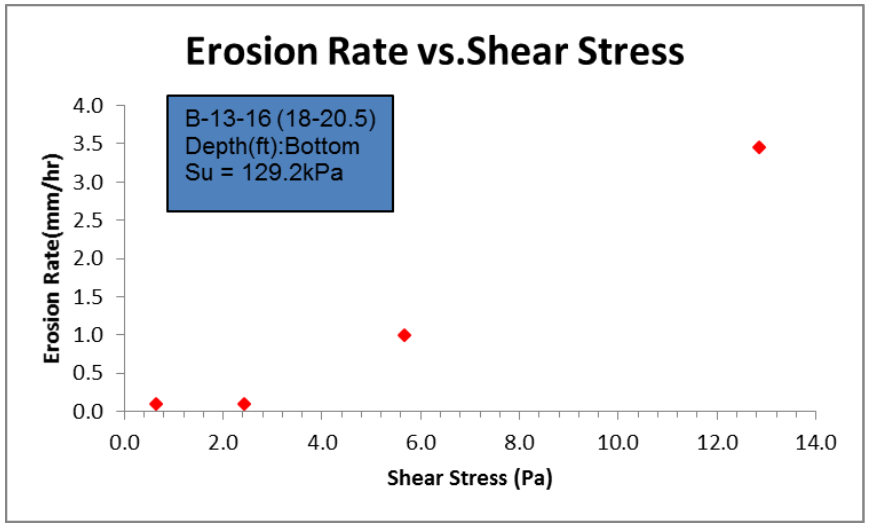

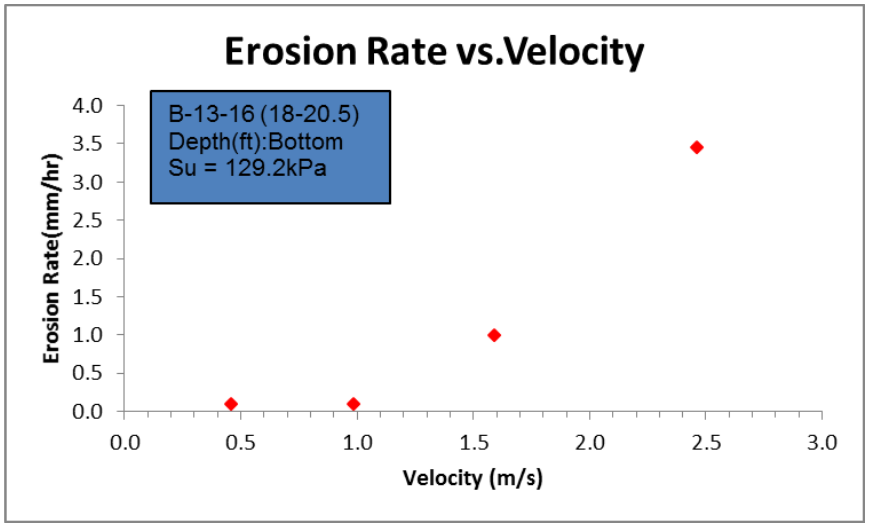

Figure A-18. B-13-16 (18'- 20.5') Bottom

Velocity	Equiva Rough	Reyso Numb	Friction	Shear Factor Stres	Erosic Readi	Test Time	Erosion
m/sec	mm	R_e	Moody	$R_a$hart	mm	sec	mm/hr
0.32	0 0.004	1942	90.026	0.33	1	180	0 2.0
0.70	0 0.004	4250	00.022	1.34	3	60	0 18.0
0.93	0 0.004	5646	40.021	2.27	2	93	0 7.7
1.56	0 0.004	9471	40.018	5.47	2	150	0 4.8
2.54	0 0.004	15421	40.017	13.7	2	123	0 5.8

Velocity (m/s					
Shear stress					
Erosion Rate					

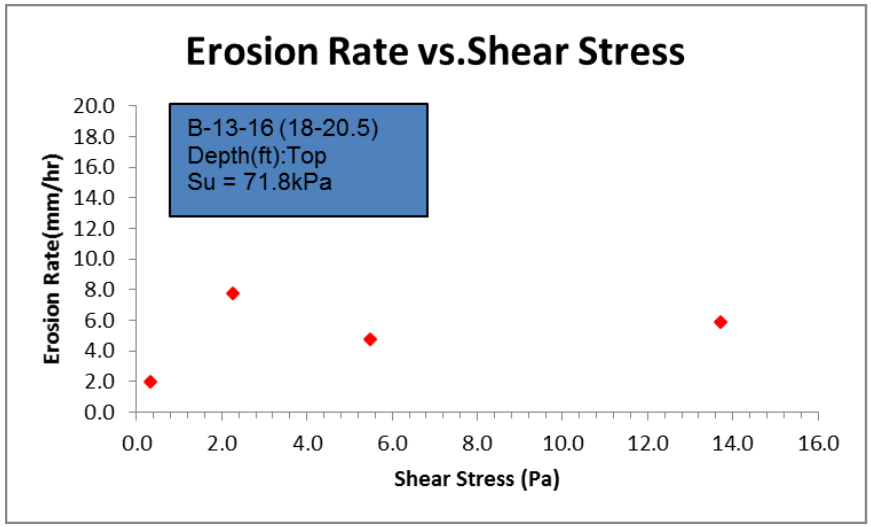

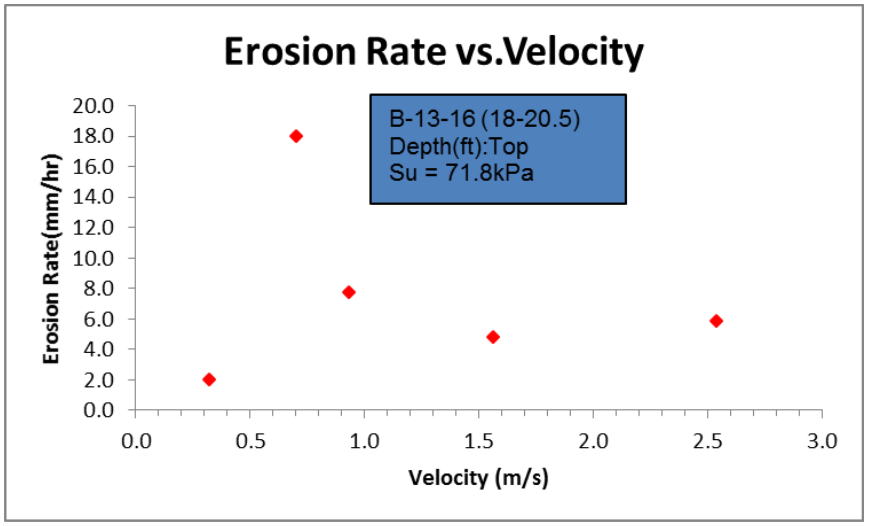

Figure A-19. B-13-16 (18'- 20.5') Top

Velocity	Equiva Rough	Reyso Numb	Friction	Shear Stres	Erosic Readi	Test Time	Erosion
m/sec	mm	R_e	Moody	τ_a hart	mm	sec	mm/hr
0.44	61.000	02707	00.045	1.1	18 1	96	0 3.7
1.10	12.000	06681	80.057	8.6	30 3	90	0 12.0
2.18	72.000	13280	40.057	34.0	90 6	117	0 18.4
3.59	02.000	21796	60.057	91.8	29 4.5	78	0 20.7
4.67	32.000	28374	40.057	155.6	17 5.5	78	0 25.3

Velocity (m/s					
Shear stress					
Erosion Rate					

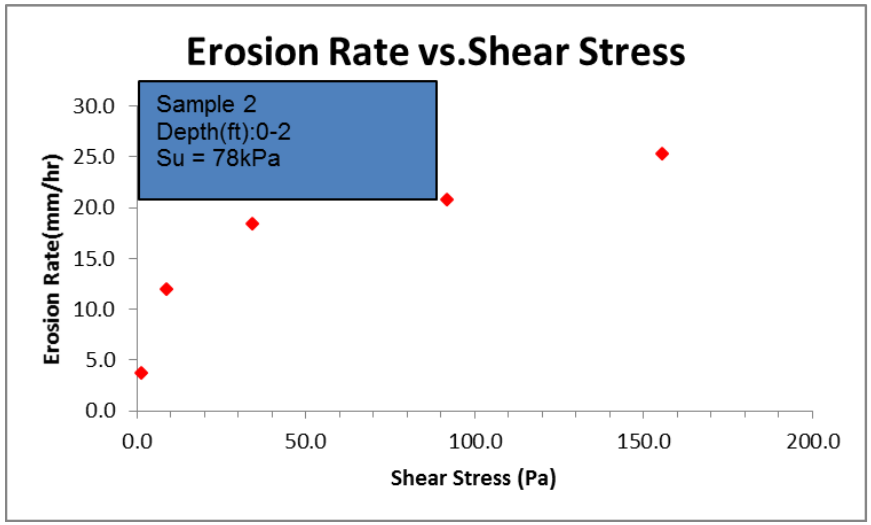

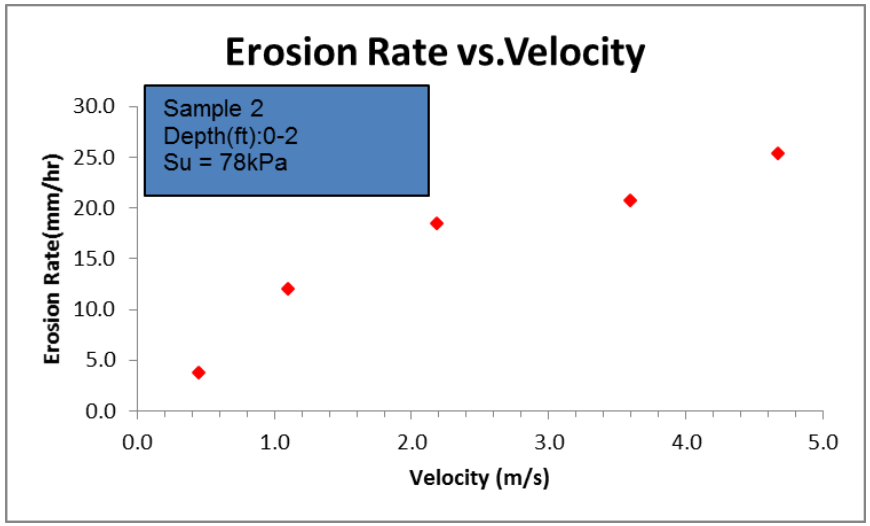

Figure A-20. GEER Sample #2

Velocity	Equiva Rough	Reyso Numb	Friction	Shear Factor Stres	Erosic Readi	Test Time	Erosion
m/sec	mm	R_e	Moody	$R_a$hart	mm	sec	mm/hr
0.32	90.029	1994	70.027	0.364	0	91	50.0
0.57	70.029	3501	90.024	0.998	0	94	50.0
1.22	20.029	7421	80.021	3.923	1.5	1060.9	9985.0
2.07	20.029	12580	00.019	10.196	3.5	1270.02	9.9
3.44	40.029	20911	80.018	26.692	6	105	0 20.5

Velocity (m/s	[illegible]	[illegible]	[illegible]	[illegible]	[illegible]
Shear stress (a	[illegible]	[illegible]	[illegible]	[illegible]	[illegible]
Erosion Rate	[illegible]	[illegible]	[illegible]	[illegible]	[illegible]

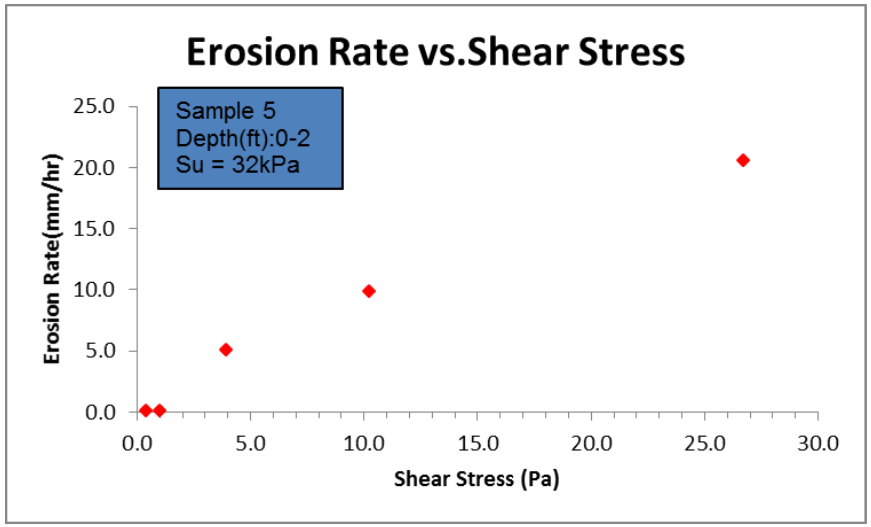

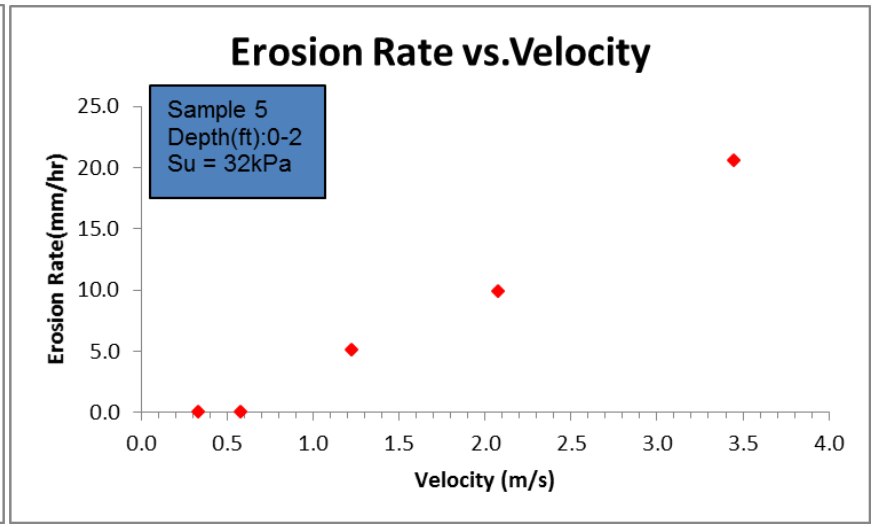

Figure A-21. GEER Sample #5

Velocity	Equiva Rough	Reyso Numb	Friction	Shear Factor	Erosic Stres Readi	Test Time	Erosion
m/sec	mm	R_e	Moody	Chart	mm	sec	mm/hr
0.26	11.000	1585	00.046	0.392	0	87	0 0.0
0.50	82.000	3086	20.058	1.873	0	790.00	00020.0
1.16	71.000	7082	90.044	7.485	1	132	0 2.7
2.17	21.000	13189	20.044	25.955	2	1420.9	9985.0
3.50	91.000	21305	00.044	67.724	3	1201.	0028.9
4.91	31.000	29829	70.044	132.764	3	631.00	0021 7.1

Velocity(m/s						
Shear stress						
Erosion Rate						

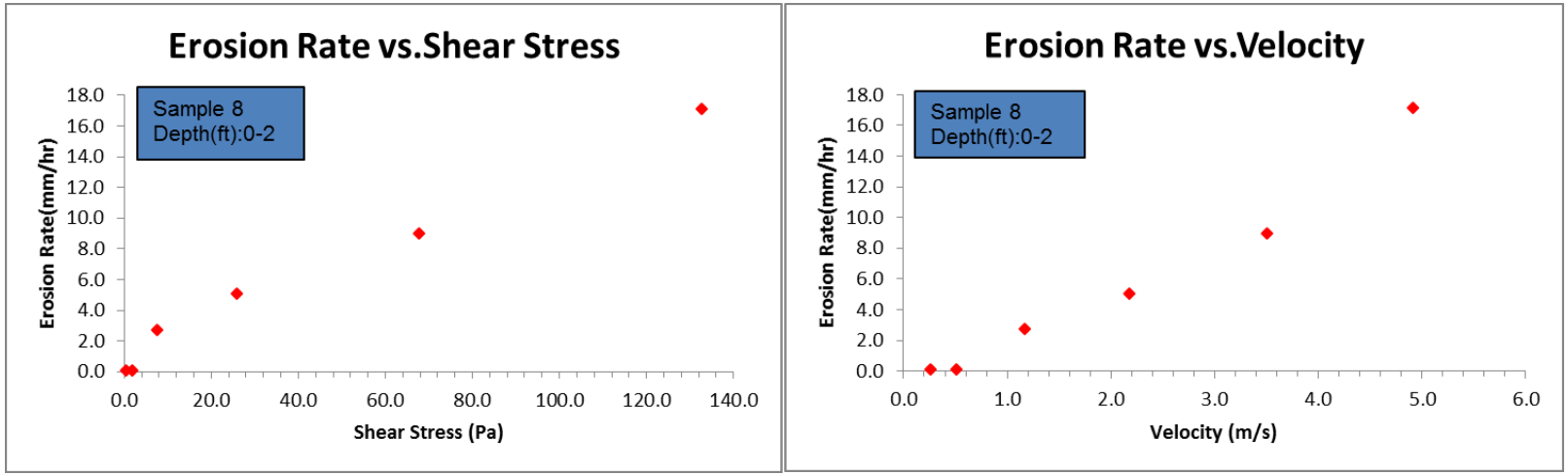

Figure A-22. GEER Sample #8

Velocity	Equiva Rough	Reyso Numb	Friction	Shear Factor	Shear Stres	Erosic Readi	Test Time	Erosion
m/sec	mm	R_e	Moody	$R_a$hart		mm	sec	mm/hr
0.25	51.000	01546	30.046	0.37	3	6	69	0 31.3
0.46	22.000	02804	90.058	1.54	7	22	529.9	98149.4
1.17	03.000	07103	40.068	11.6	35	41	24	0 615.0
1.79	23.000	010877	00.068	27.2	81	27	12	0 810.0

Velocity(m/s				
Shear stress				
Erosion Rate				

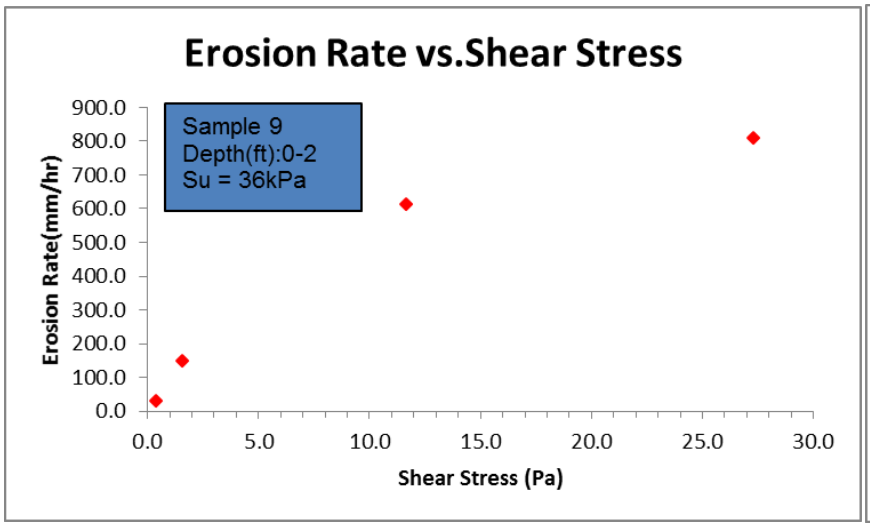

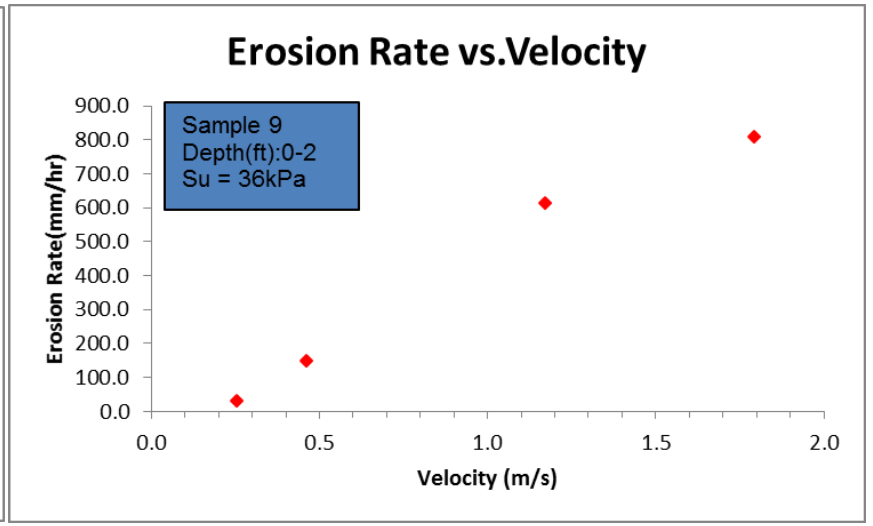

Figure A-23. GEER Sample #9

Silt Samples - EFA

Velocity	Equiva Rough	Reyso Numb	Friction	Shear Factor	Erosic Stres Readi	Test Time	Erosion
m/sec	mm	R_e	Moody	Chart	mm	sec	mm/hr
0.29	10.022	1764	10.027	0.285	0	949.9	98 0.0
0.45	20.022	2744	60.025	0.639	1	159	0 2.2
0.92	60.022	5620	80.022	2.357	4	769.9	98 18.7

Velocity (m/s			
Shear stress			
Erosion Rate			

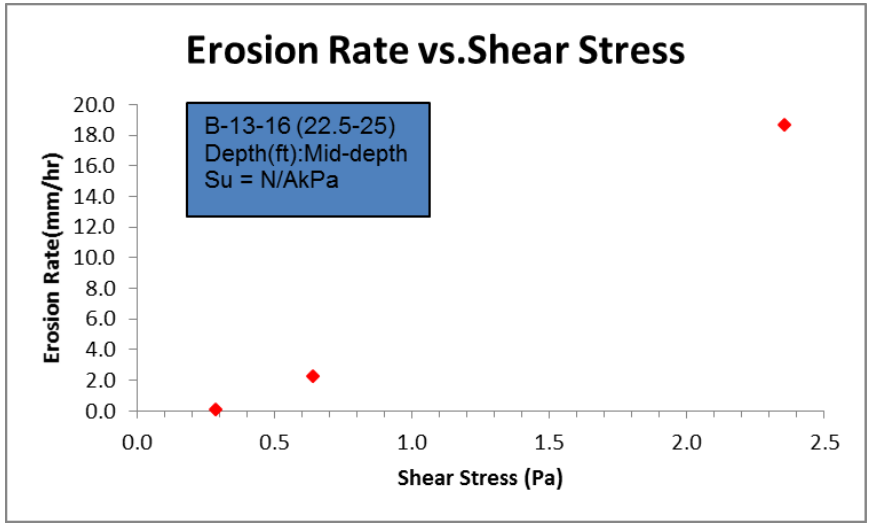

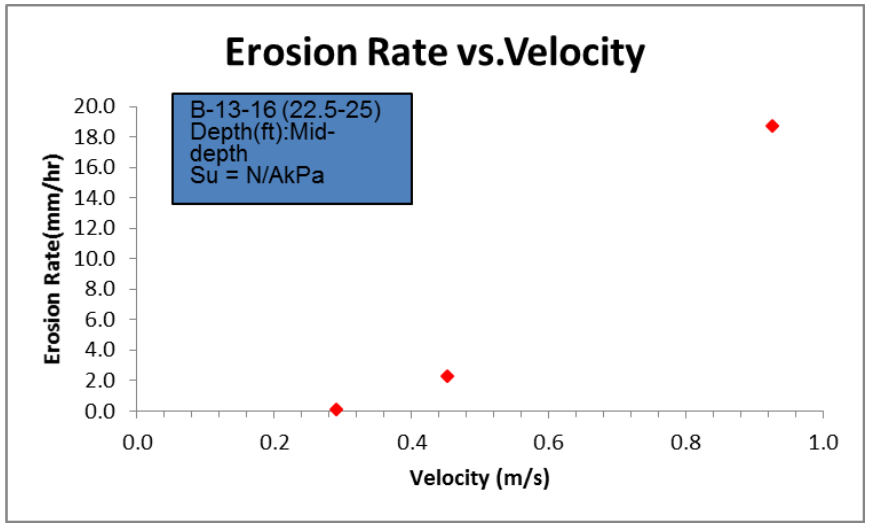

Figure A-24. B-13-16 (22.5'-25')

Velocity	Equiva Rough	Reyso Numb	Friction	Shear Factor	Erosic Stres Readi	Test Time	Erosion
m/sec	mm	R_e	Moody	$R_a$hart	mm	sec	mm/hr
0.36	80.012	2234	40.026	0.44	401	36	0 10.0
0.60	40.012	3667	50.023	1.04	98	63	0 45.7
1.10	20.012	6689	00.020	3.03	410	47	1 76.4
1.84	10.012	11179	60.019	8.05	312	31	5 137.1

Velocity (m/s				
Shear stress				
Erosion Rate				

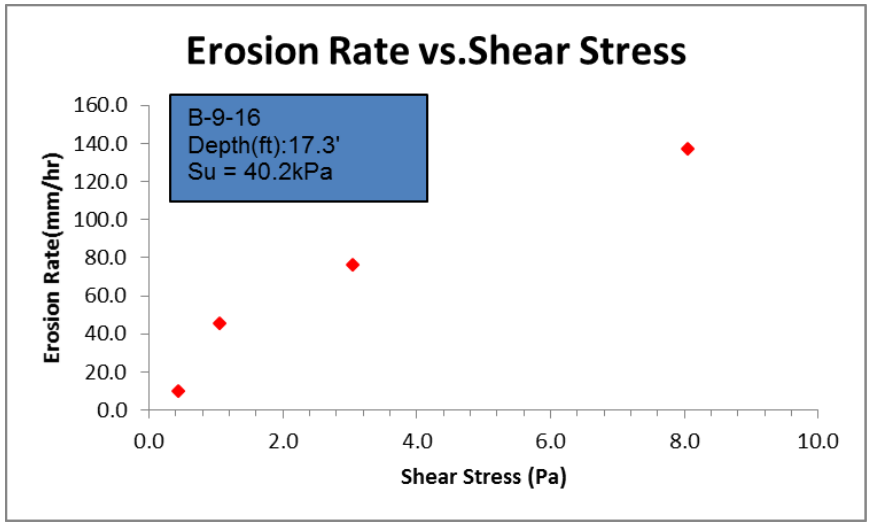

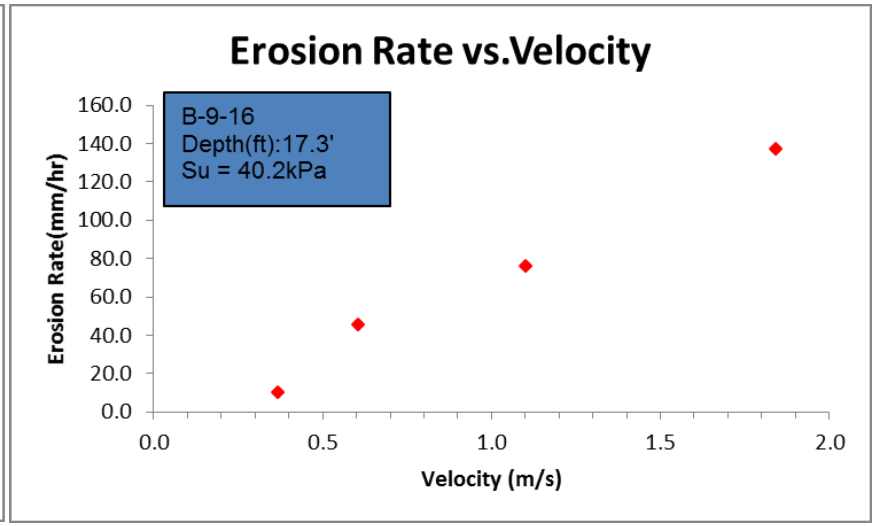

Figure A-25. B-9-16 (16'-17.5') Bottom

Velocity	Equiva Rough	Reyso Numb	Friction	Shear Factor	Erosic Stres Readi	Test Time	Erosion
m/sec	mm	R_e	Moody	$R_a$hart	mm	sec	mm/hr
0.17	40.012	1058	80.031	0.1	18 0	36	0 0.0
0.56	50.012	3431	90.023	0.9	19 4	30	0 48.0
0.93	60.012	5685	70.021	2.3	02 12	241.0	0021 79.2
1.56	10.012	9475	60.019	5.7	85 20	184.99	9938 89.1

Velocity (m/s				
Shear stress a				
Erosion Rate				

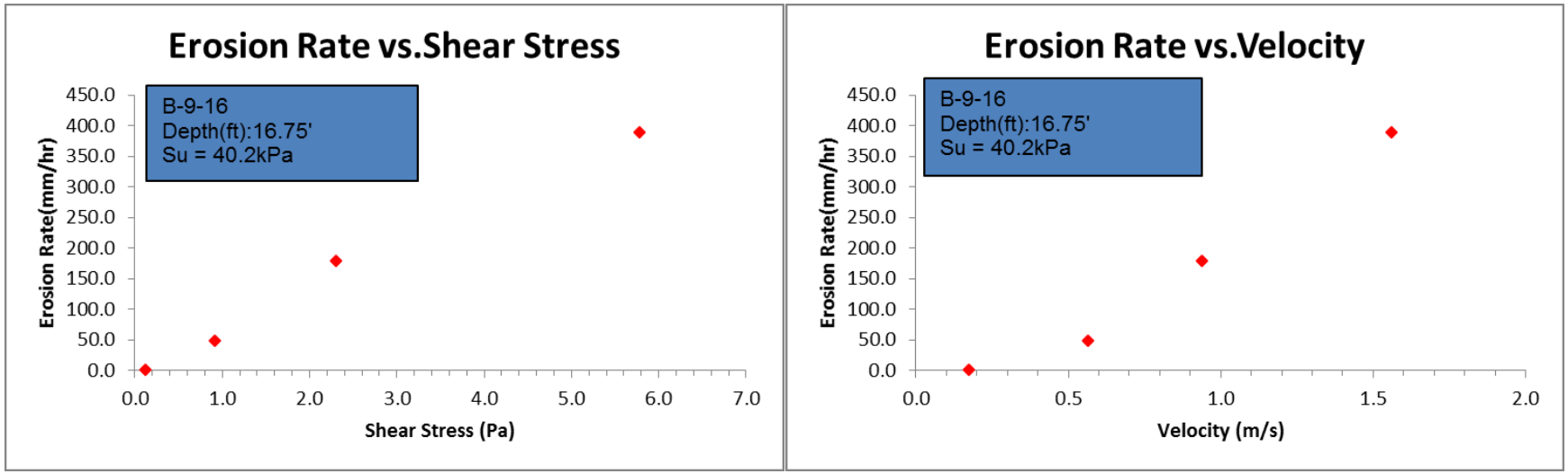

Figure A-26. B-9-16 (16'-17.5') Middle

Velocity	Equiva Rough	Reyso Numb	Friction	Shear Factor Stres	Erosic s Readi	Test Time	Erosion
m/sec	mm	R_e	Moody	$R_a$hart	mm	sec	mm/hr
0.27	80.012	1689	70.027	0.26	10	90	0 0.0
0.53	10.012	3222	40.024	0.84	50.5	721.0	002 2.4
1.13	30.012	6877	30.020	3.20	81.5	661.0	02 8.1
1.70	70.012	10363	50.019	6.92	02	81	0 8.8
2.83	10.012	17188	30.017	17.0	318	120	0 24.0
3.94	20.012	23933	50.017	33.0	216	940.0	00222.9

Velocity (m/s						
Shear stress						
Erosion Rate						

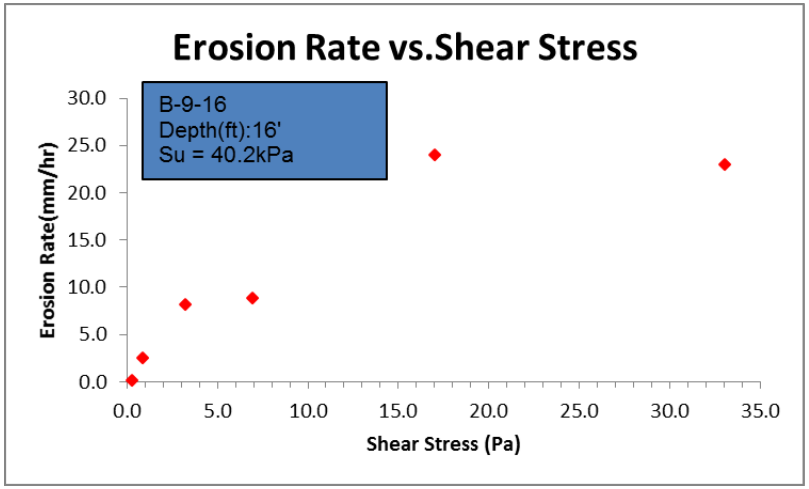

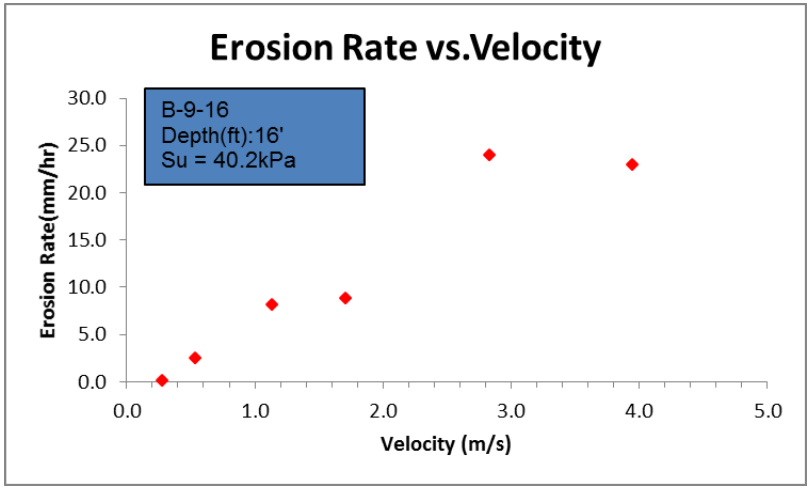

Figure A-27. B-9-16 (16'-17.5') Top

Velocity	Equiva Rough	Reyso Numb	Friction	Shear Factor	Shear Stres	Erosic Readi	Test Time	Erosion
m/se	c m m	R_e	Moody	charPrt	$_a$	m m	sec	m m/h
0.36	71.0000	2225	90.045	0.756	0	120	0	0.0
1.03	11.0000	6260	10.044	5.847	1	120	0	3.0
1.97	41.0000	11984	50.044	21.43	2	146	4	4.9
3.08	91.0000	18753	00.044	52.47	3	111	0	9.7
3.91	91.0000	23792	80.044	84.46	8	117	0	24.6

Velocity(m/s					
Shear stres					
Erosion Rate					

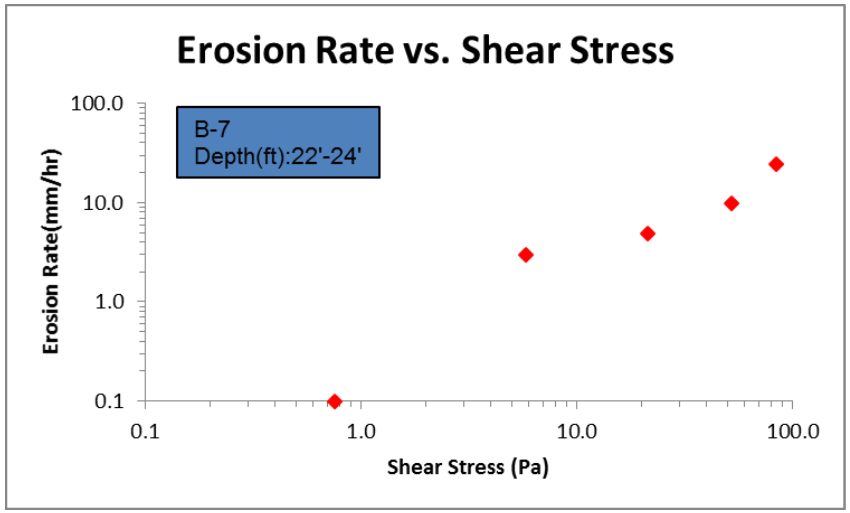

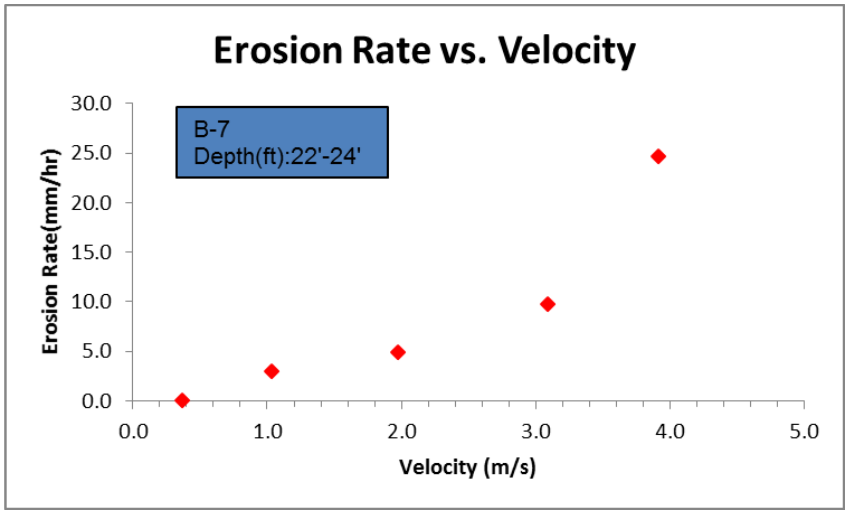

Figure A-28. B-7 (22'-24') Tittabawsee River

Velocity	Equiva Rough	Reyso Numb	Friction	Shear Factors	Shear Stres	Erosic Readi	Test Time	Erosion
m/se	c m m	R_e	Moody	char	P_a	m m	sec	m m/hr
0.44	0 1.000	2671	40.045	1.089	2	1390	.02	5.1
1.00	0 1.000	6071	40.044	5.500	8	604.	02	47.6
1.46	0 1.000	8864	30.044	11.724	9	319	.8	101.3
1.91	0 1.000	11596	40.044	20.065	18	60	0	108.0
2.69	0 1.000	16332	10.044	39.799	17	319	.8	191.3

Velocity (m/s					
Shear stress					
Erosion Rate					

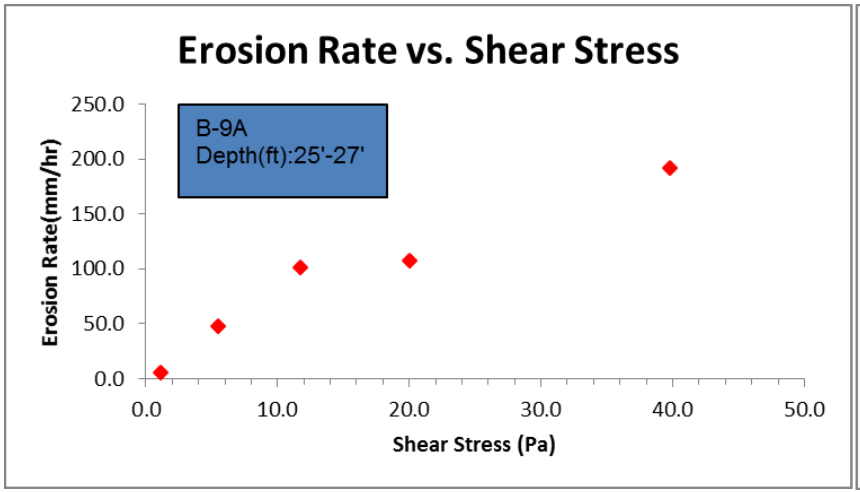

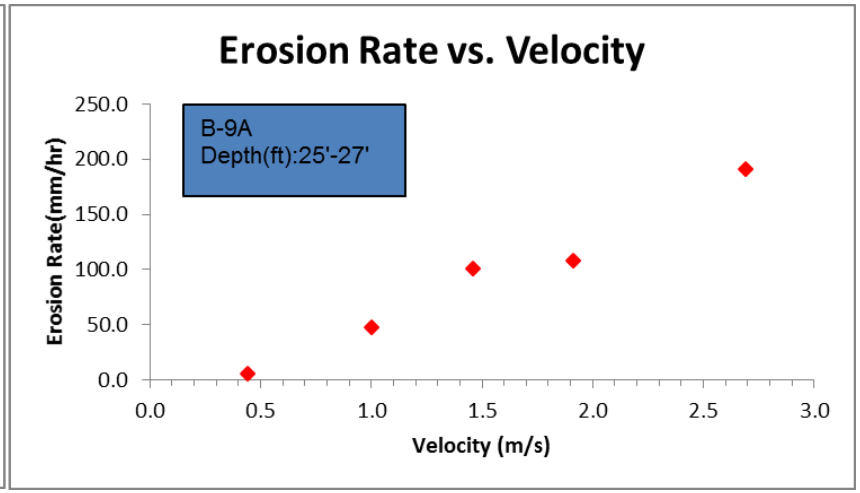

Figure A-29. B-9A (25'-27') Tittabawsee River

Velocity	Equiva Rough	Reyso Numb	Friction	Shear Factor Stres	Erosic Readi	Test Time	Erosion
m/sec	mm	R_e	Moody	$R_a$hart	mm	sec	mm/hr
0.35	0 0.003	2125	60.026	0.398	0	1504.8	0.0
0.98	7 0.003	5995	10.020	2.438	1	1504.062	2.3
1.96	2 0.003	11910	20.018	8.658	2	137 1	5.2
3.02	1 0.003	18342	40.016	18.254	4	120 0	12.0
4.21	7 0.003	25602	50.015	33.341	9	919.98	35.2

Velocity (m/s					
Shear stress (a					
Erosion Rate					

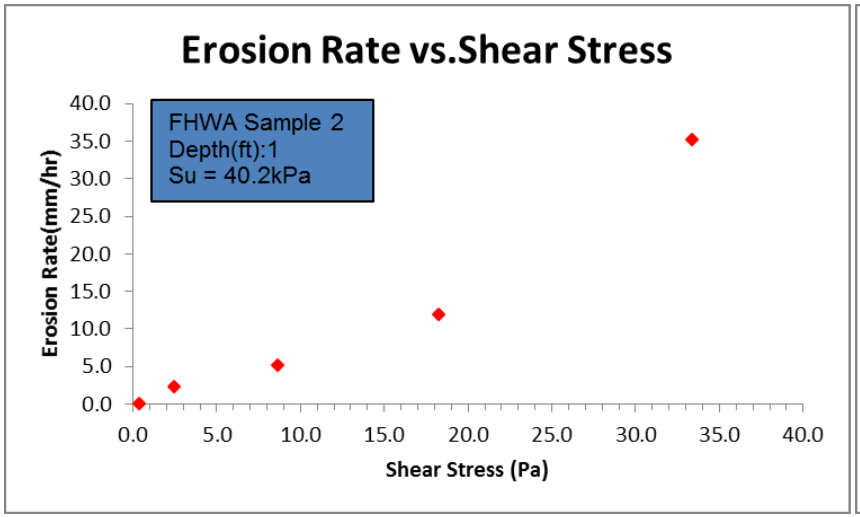

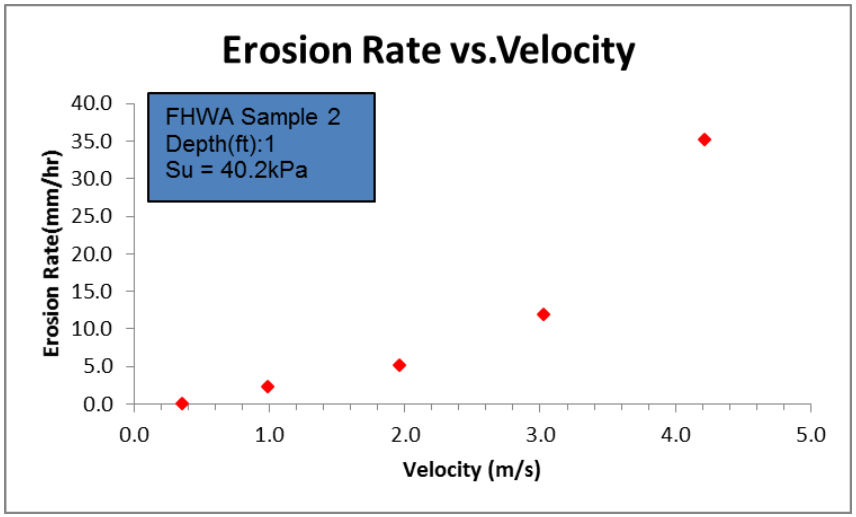

Figure A-30. FHWA Sample #2

Velocity	Equiva Rough	Reyso Numb	Friction	Shear Stres	Erosic Readi	Test Time	Erosion
m/sec	mm	R_e	Moody	Chart	mm	sec	mm/hr
0.30	80.032	1870	20.027	0.32	06	30	072.0
0.51	92.000	3151	40.058	1.95	20	340.0	0022 11.7
0.99	43.000	6035	40.068	8.39	35	121.0	06120 41.

Velocity (m/s			
Shear stress			
Erosion Rate			

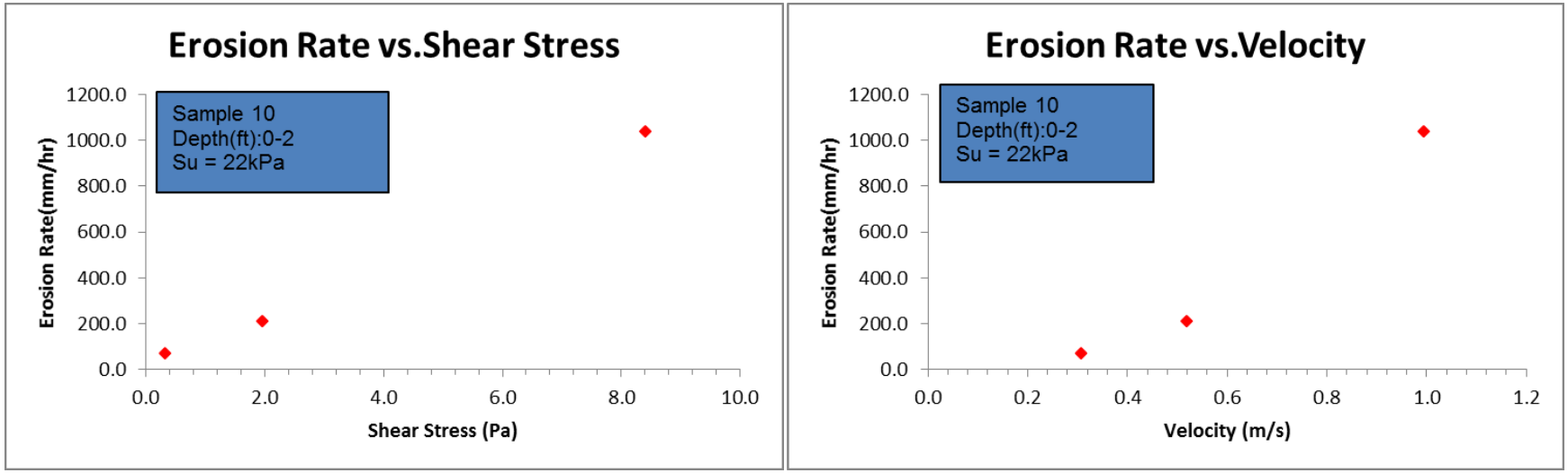

Figure A-31. GEER Sample #10

Sand Samples - EFA

Velocity	Equiva Rough	Reyso Numb	Friction	Shear Stres	Erosic Readi	Test Time	Erosion
m/sec	mm	R_e	Moody	τ_a hart	mm	sec	mm/hr
0.24	40.500	1481	70.039	0.290	0	111	0 0.0
0.42	83.000	2597	50.069	1.579	11	42	0 94.2
0.80	12.000	4860	50.057	4.566	11	340.0	0 21 16.4
1.53	92.000	9345	20.057	16.80	11	30	0 132.0
1.86	92.000	11346	50.057	24.85	24	157.9	9854 6.8

Velocity (m/s	[illegible]	[illegible]	[illegible]	[illegible]	[illegible]
Shear stress (τ_a)	[illegible]	[illegible]	[illegible]	[illegible]	[illegible]
Erosion Rate	[illegible]	[illegible]	[illegible]	[illegible]	[illegible]

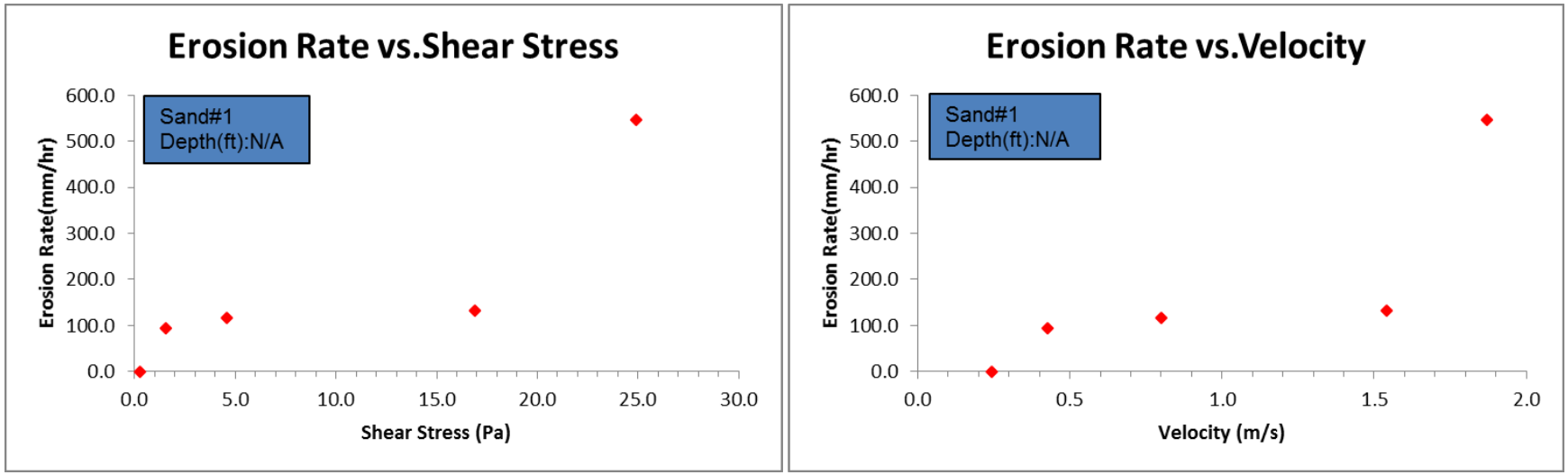

Figure A-32. Sand #1

Velocity	Equiva Rough	Reyso Numb	Friction	Shear Factor Stres	Erosic Readi	Test Time	Erosion
m/sec	mm	R_e	Moody	$R_a$hart	mm	sec	mm/hr
0.24	40.123	1481	90.031	0.2	31 0	90	0 0.0
0.63	30.500	3842	40.036	1.8	02 2.5	1201.	002 7.4
1.27	61.000	7749	40.044	8.9	60 4.5	120	0 13.5
2.05	91.000	12499	30.044	23.3	11 8	102	0 28.2
3.13	01.000	19005	30.044	53.8	93 9	90	0 36.0

Velocity (m/s					
Shear stress (Pa)					
Erosion Rate					

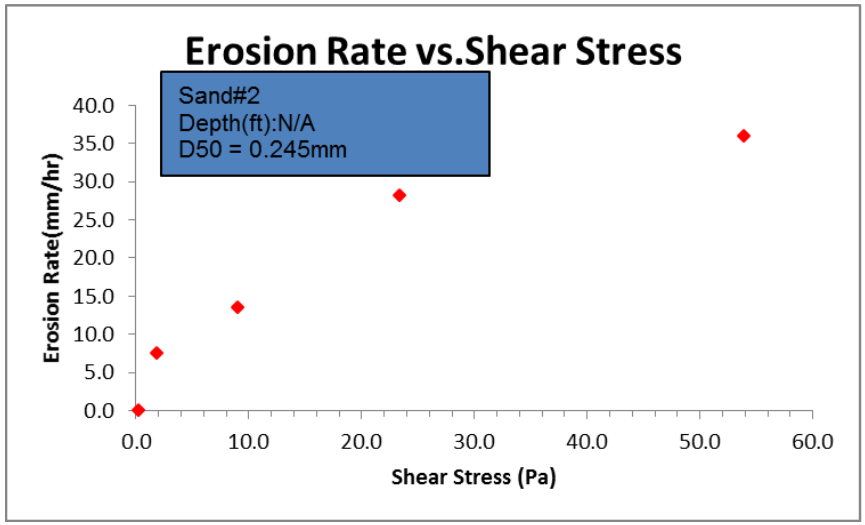

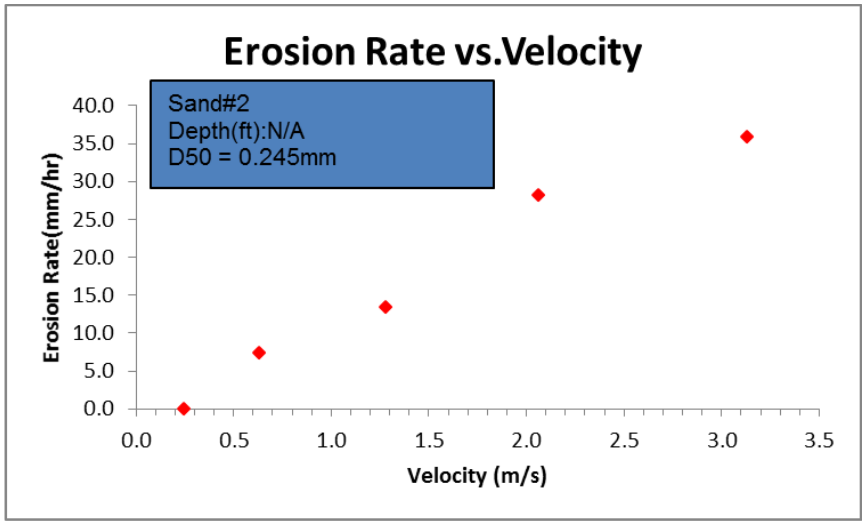

Figure A-33. Sand #2

Velocity	Equiva Rough	Reyso Numb	Friction	Shear Factor Stres	Erosic Readi	Test Time	Erosion
m/sec	mm	R_e	Moody	$R_a$hart	mm	sec	mm/hr
0.26	50.500	1608	30.038	0.3	33 0.5	120	0 1.5
0.50	41.000	3062	40.045	1.4	31 5.5	120	0 16.5
1.02	11.000	6198	80.044	5.7	33 8	120	0 24.0
1.99	00.500	12080	40.035	17.3	21 10.5	123	0 30.7
3.03	10.500	18403	10.035	40.1	95 11.5	931.9	98 44.4
4.09	30.500	24850	60.035	73.2	94 12	556.0	00 27 7.6

Velocity(m/s						
Shear stress						
Erosion Rate						

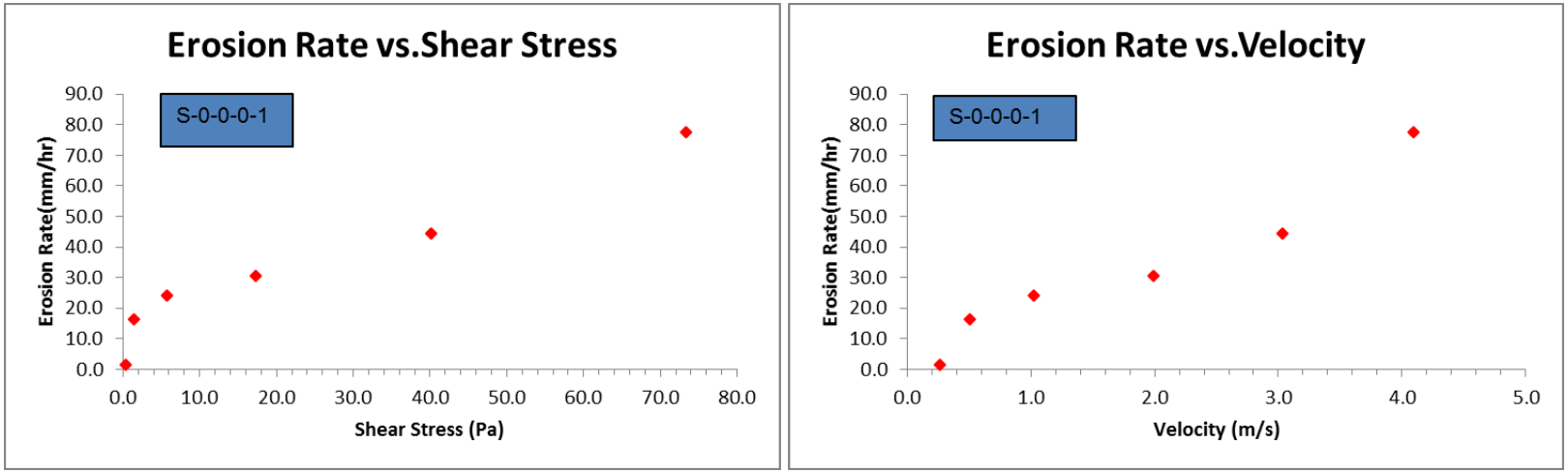

Figure A-34. S-0-0-0

Velocity	Equiva Rough	Reyso Numb	Friction	Shear Factor	Shear Stres	Erosic Readi	Test Time	Erosion
m/se	c m m	R_e	Moody	char	Pa	m m	sec	m m/h
0.49	0 1.000	2975	0 0.045	1.35	1	1	146	1 2.4
1.01	0 1.000	6132	1 0.044	5.6	1	2	90	0 8.0
2.00	0 1.000	12142	90.044	22.0	0	3	111	0 9.7
2.53	0 1.000	15360	70.044	35.2	0	4	139	5 10.3
3.42	0 1.000	20764	30.044	64.3	3	4	61	5 23.4

Velocity (m/s					
Shear stress					
Erosion Rate					

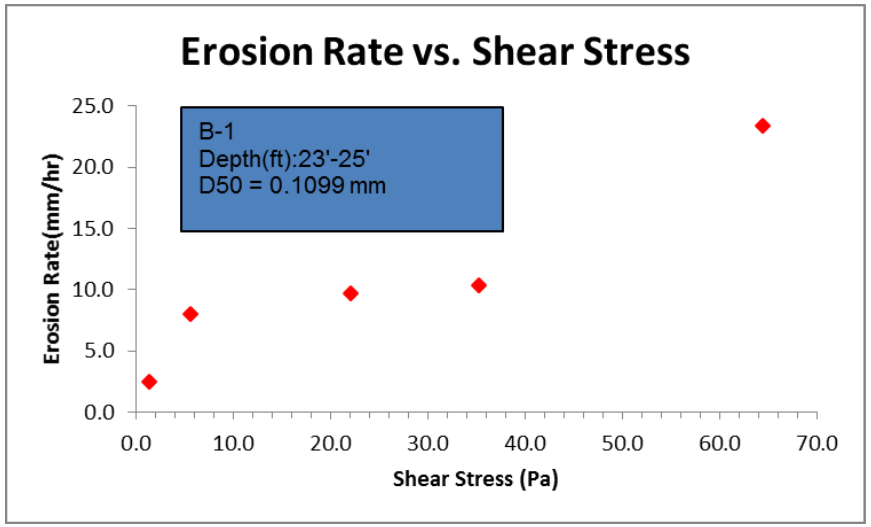

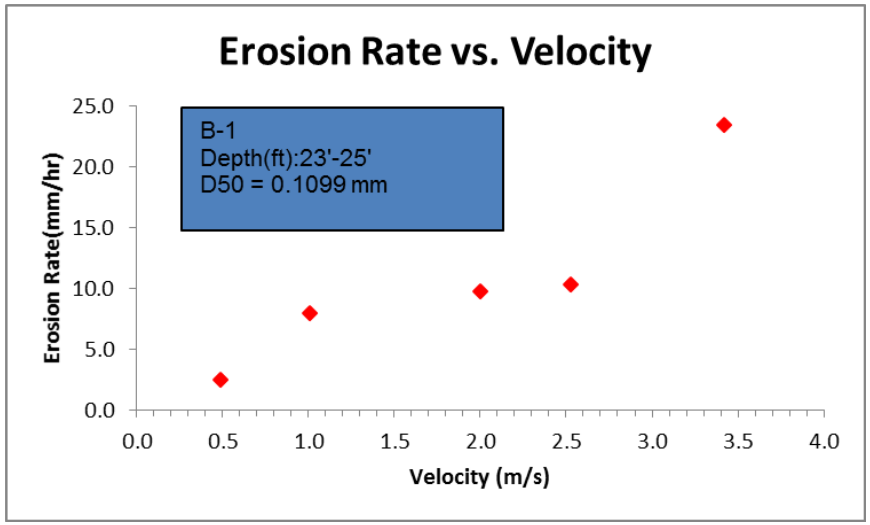

Figure A-35. B-1 (23'-25') Tittabawsee River

Velocity	Equiva Rough	Reyso Numb	Friction	Shear Factor	Erosic Stress	Readi	Test Time	Erosion
m/se	c m m	R_e	Moody	char	P_a	m m	sec	m m/h
0.52	0 1.000	0 3157	10.045	1.52	1	0	90	0 0.0
1.01	0 1.000	0 6132	10.044	5.6	1	0	180	0 0.0
1.86	0 1.000	0 11292	90.044	19.0	28	0.5	150	0 1.2
2.52	0 1.000	0 15300	00.044	34.9	27	1	1540	.2 2.3
3.52	0 1.000	0 21371	40.044	68.1	47	1.5	117	0 4.6
5.02	0 1.000	0 30478	60.044	138.6	02	3.5	121	8 10.3

Velocity(m/s							
Shear stress							
Erosion Rate							

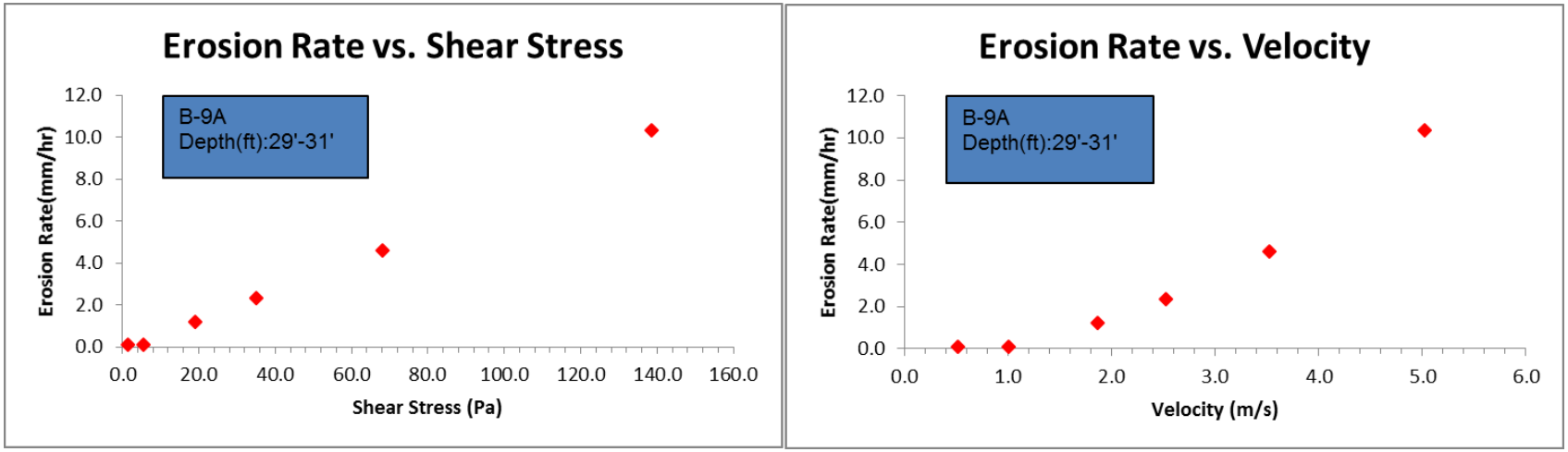

Figure A-36. B-9A (29'-31') Tittabawsee River

Velocity	Equiva Rough	Reyso Numb	Friction	Factor	Shear Stres	Erosic Readi	Test Time	Erosion
m/sec	mm	R_e	Moody	Chart		mm	sec	mm/hr
0.32	80.100	1992	70.029	0.39	1	9	90	0 36.0
0.46	90.100	2849	90.027	0.74	4	25	30	0 300.0
0.96	00.100	5825	90.025	2.87	7	48	12	0 1440.

Velocity(m/s			
Shear stress			
Erosion Rate			

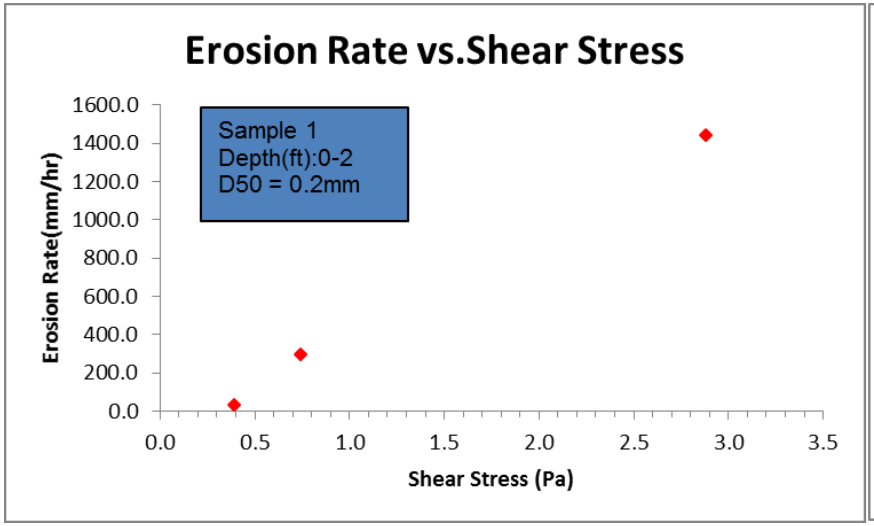

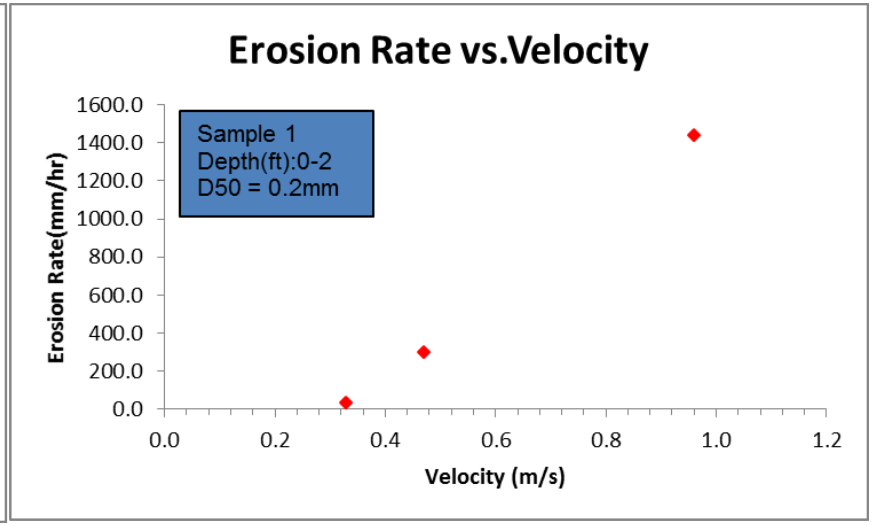

Figure A-37. GEER Sample #1

Velocity	Equiva Rough	Reyso Numb	Friction	Shear Factor Stres	Erosic Readi	Test Time	Erosion
m/sec	mm	R_e	Moody	$R_a$hart	mm	sec	mm/hr
0.23	21.000	01407	60.047	0.316	0	69	0 0.0
0.68	61.000	04166	30.044	2.590	1	66	0 5.4
1.27	71.000	07751	40.044	8.965	2	66	0 10.9
2.08	01.000	12627	20.044	23.790	3	69	0 15.6
3.34	61.000	20315	20.044	61.578	5	850.0	00221.1

Velocity(m/s					
Shear stress					
Erosion Rate					

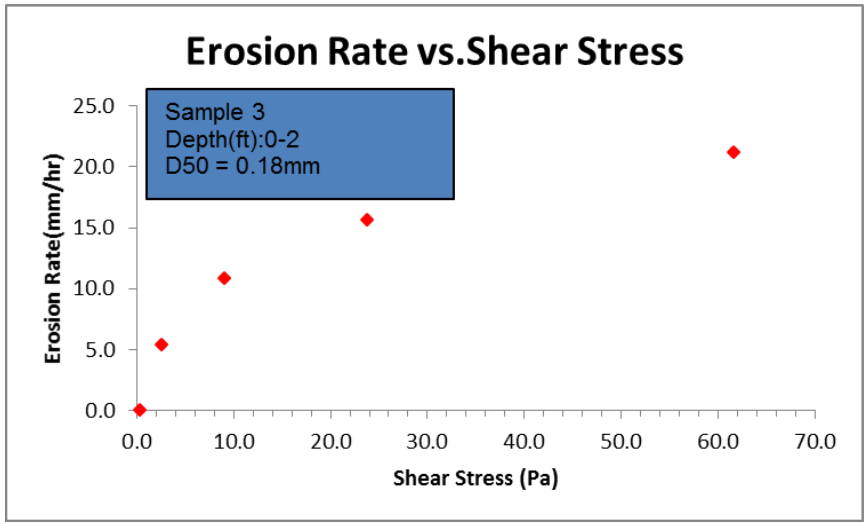

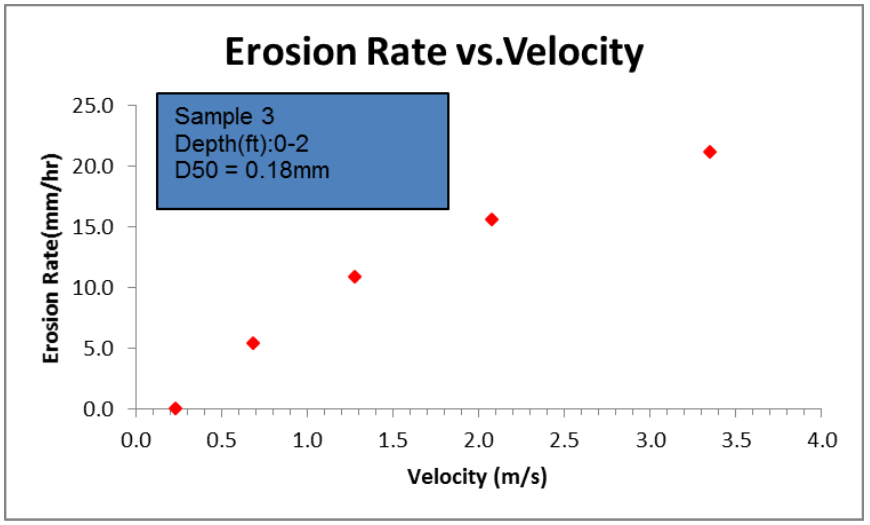

Figure A-38. GEER Sample #3

Velocity	Equiva Rough	Reyso Numb	Friction	Shear Factor	Shear Stres	Erosic Readi	Test Time	Erosion
m/sec	mm	R_e	Moody	Chart		mm	sec	mm/hr
0.25	30.043	1535	20.029	0.2	32	0	48	0 0.0
0.49	11.000	2982	40.045	1.3	57	1	48	0 7.5
1.17	02.000	7102	40.057	9.7	50	15	400.0	0 0 21 3 5.
2.08	32.000	12647	00.057	30.9	16	47	280.0	0 0 26 0 4.

Velocity (m/s				
Shear stress				
Erosion Rate				

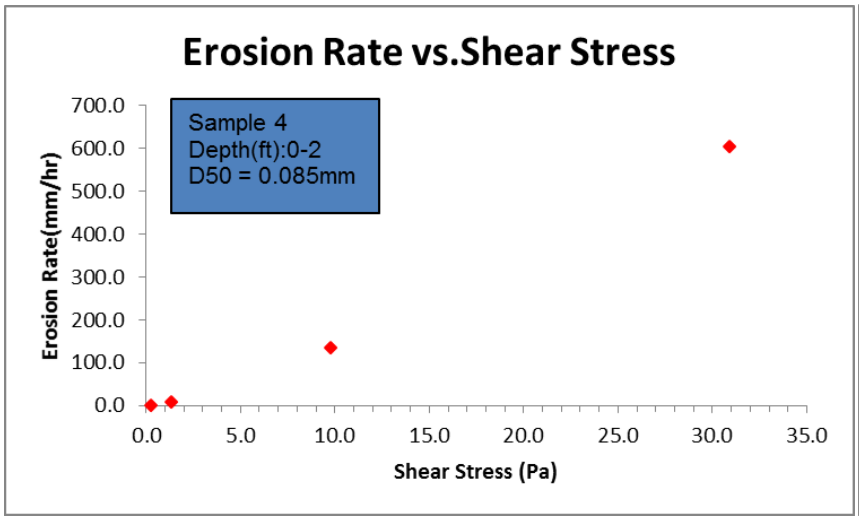

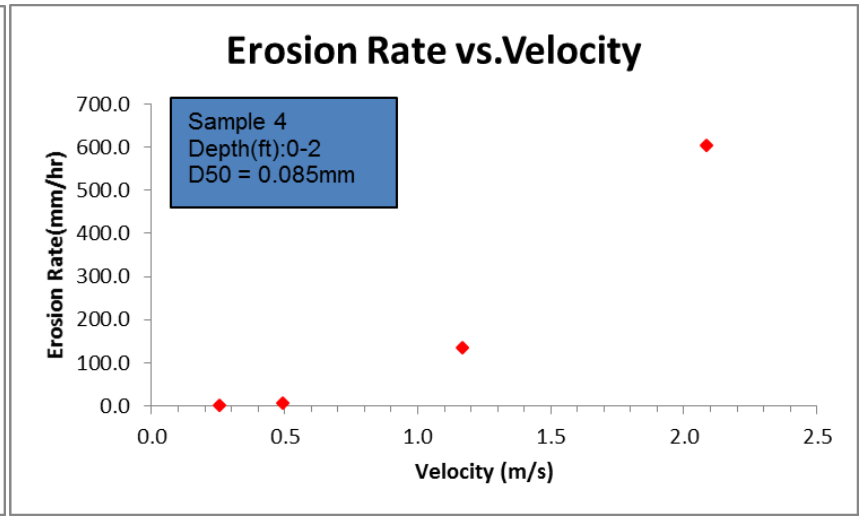

Figure A-39. GEER Sample #4

Velocity	Equiva Rough	Reyso Numb	Friction	Shear Stres	Erosic Readi	Test Time	Erosion
m/sec	mm	R_e	Moody	Chart	mm	sec	mm/hr
0.30	60.100	1856	50.029	0.33	915	39	0 138.4
0.44	10.100	2679	70.027	0.65	738	27	0 506.6
0.57	40.100	3484	40.026	1.07	038	12	0 1140.

Velocity(m/s			
Shear stress			
Erosion Rate			

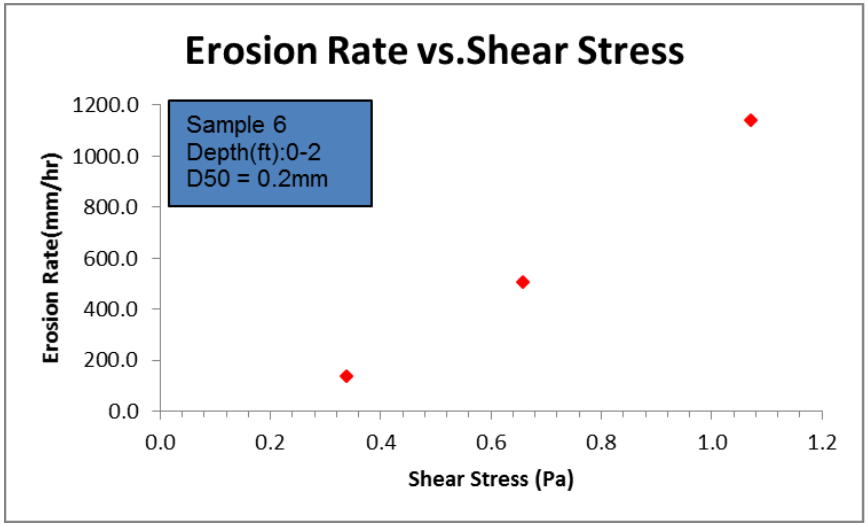

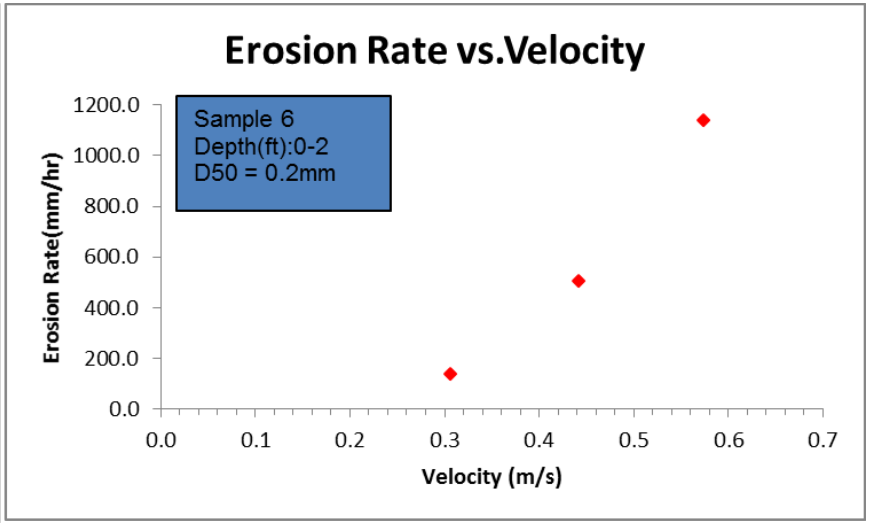

Figure A-40. GEER Sample #6

Velocity	Equiva Rough	Reyso Numb	Friction	Shear Factor	Erosic Stres Readi	Test Time	Erosion
m/sec	mm	R_e	Moody	Chart	mm	sec	mm/hr
0.25	80.105	1565	30.030	0.249	7	730.0	00234.5
0.47	60.105	2889	30.027	0.764	18	298.00	00221 7.4
0.81	40.105	4944	50.025	2.073	48	12	6 1371.

Velocity(m/s			
Shear stress			
Erosion Rate			

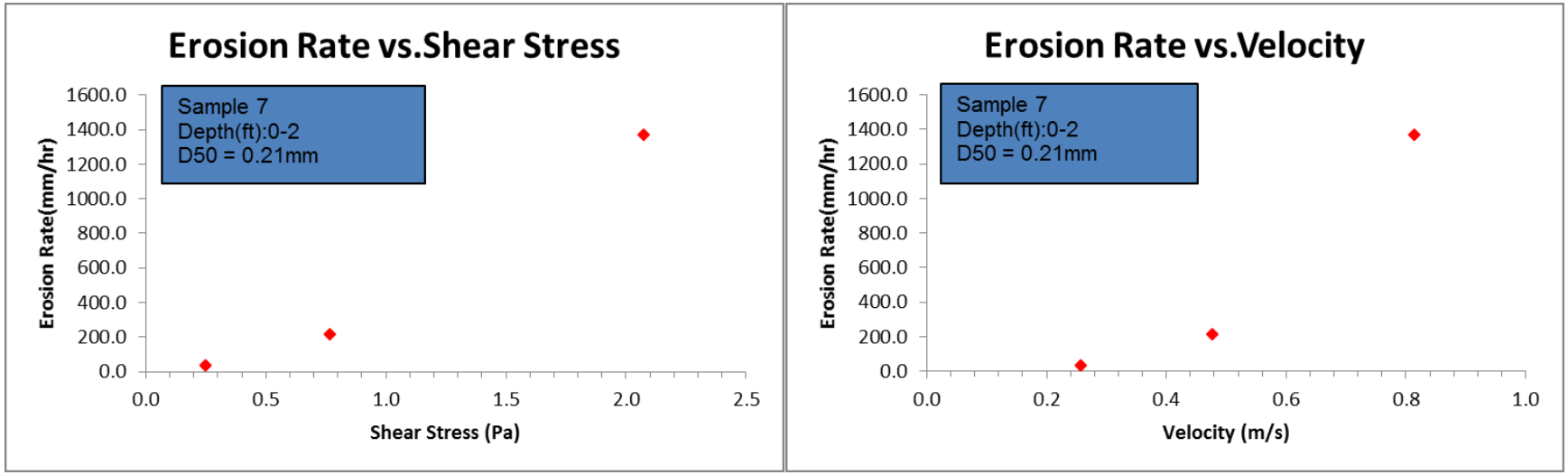

Figure A-41. GEER Sample #7

Gravel Samples - EFA

Velocity	Equiva Rough	Reyso Numb	Friction	Shear Factor Stres	Erosic Readi	Test Time	Erosion
m/sec	mm	R_e	Moody	$R_a$hart	mm	sec	mm/hr
0.25	24.250	1529	10.081	0.642	0	1399	.98 0.0
0.40	74.250	2469	60.080	1.654	0	78	0 0.0
0.92	54.250	5616	60.080	8.558	0	74	1 0.0
1.25	34.250	7608	90.080	15.706	18	66	0 98.1
1.62	24.250	9845	90.080	26.299	52	27	0 693.3

Velocity (m/s					
Shear stress					
Erosion Rate					

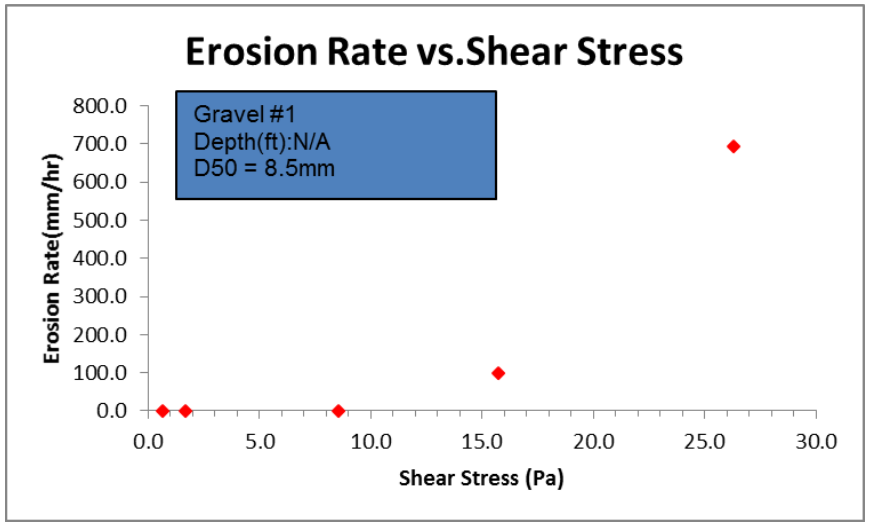

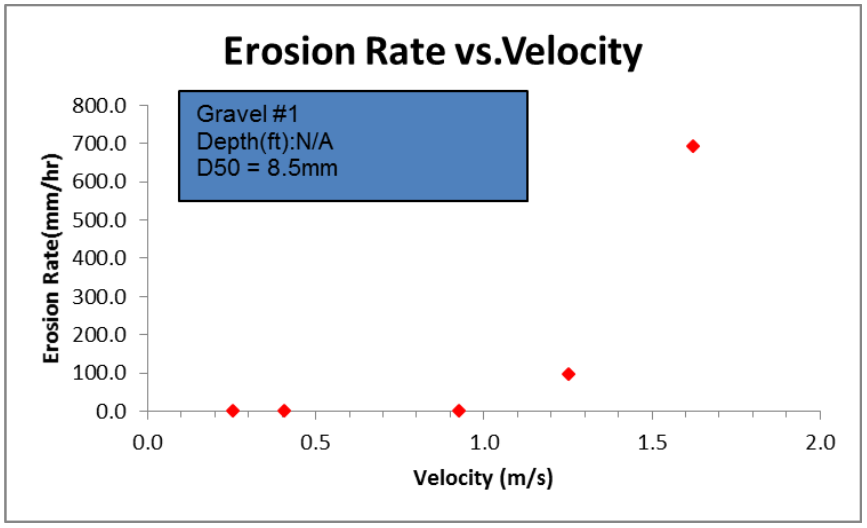

Figure A-42. Gravel #1

Velocity	Equiva Rough	Reyso Numb	Friction	Shear Factor Stres	Erosic Readi	Test Time	Erosion
m/sec	mm	R_e	Moody	Chart	mm	sec	mm/hr
0.18	59.500	1121	60.125	0.53	30	66	0 0.0
0.46	99.500	2845	70.124	3.405	0	72	0 0.0
0.99	89.500	6056	70.124	15.4	250	751.0	002 0.0
1.27	59.500	7738	60.124	25.1	816	69	0 31.3
1.84	69.500	11207	40.124	52.8	1558	190.9	9918093.

Velocity (m/s					
Shear stress (a					
Erosion Rate					

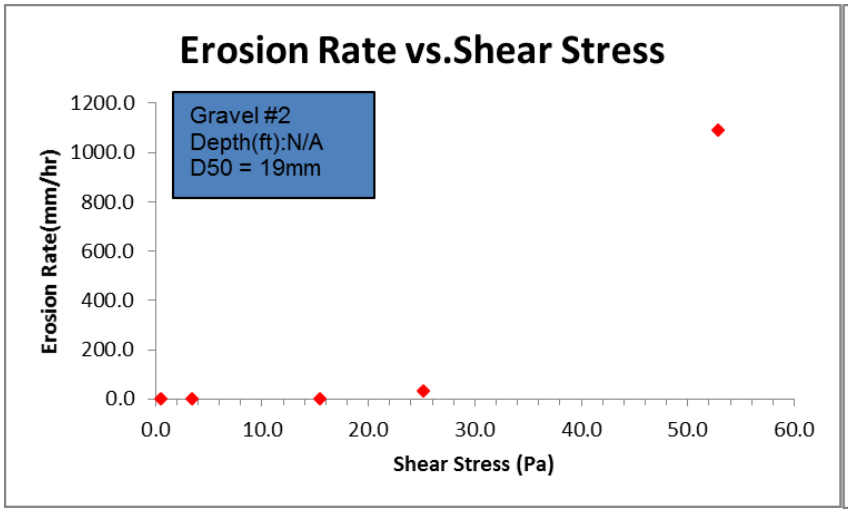

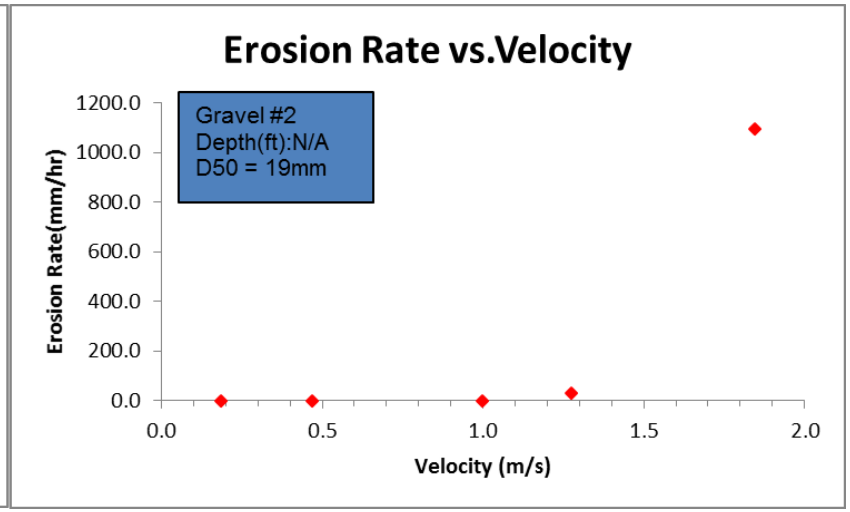

Figure A-43. Gravel #2

Velocity	Equiva Rough	Reyso Numb	Friction	Shear Factor Stres	Erosic Readi	Test Time	Erosion
m/sec	mm	R_e	Moody	Chart	mm	sec	mm/hr
0.29	73.000	1801	10.069	0.759	0	1030.0	0020.0
0.49	93.000	3031	50.068	2.119	0	511.00	0020.0
0.87	53.000	5310	10.068	6.502	0	51	0 0.0
1.17	33.000	7124	70.068	11.705	3	72	0 15.0
1.52	83.000	9277	50.068	19.847	78	370.00	0 0 0725 8.9

Velocity (m/s					
Shear stress (a					
Erosion Rate					

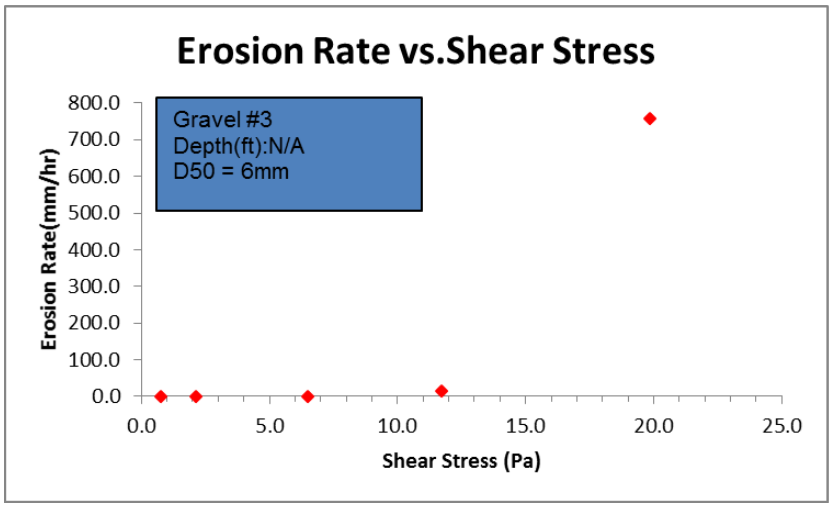

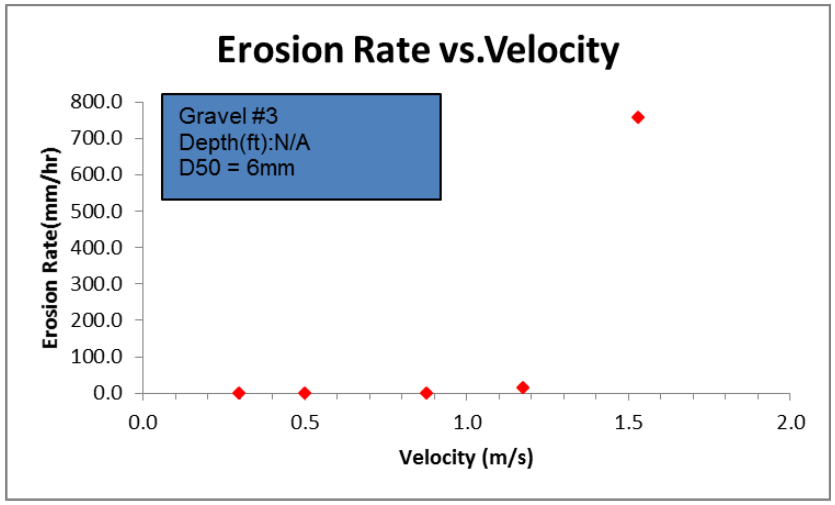

Figure A-44. Gravel #3

Velocity	Equiva Rough	Reyso Numb	Friction	Shear Factor Stres	Erosic Readi	Test Time	Erosion
m/sec	mm	R_e	Moody	Chart	mm	sec	mm/hr
0.27	55.500	1668	00.092	0.868	0	1429.9	9980.0
0.53	65.500	3254	90.091	3.269	0	1084.9	9980.0
0.95	95.500	5821	40.091	10.458	0	649.9	9980.0
1.17	75.500	7143	40.091	15.746	6	985.00	0022 1.9
1.76	25.500	10697	10.091	35.310	38	12	0 1140.

Velocity (m/s					
Shear stress (a					
Erosion Rate					

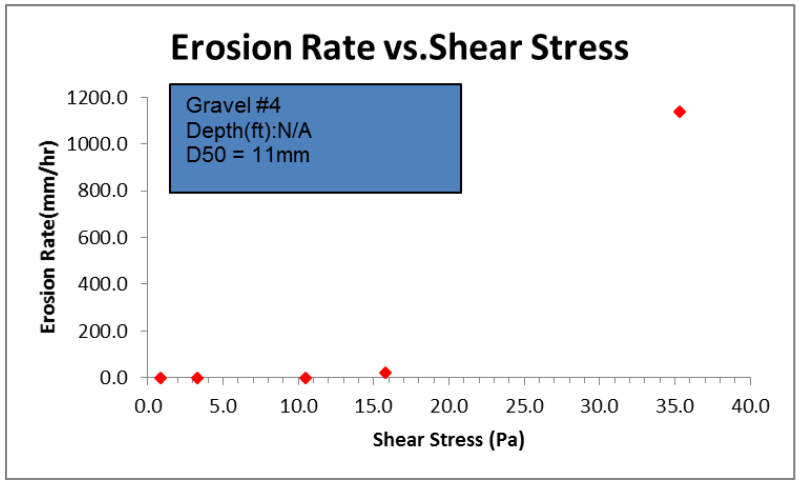

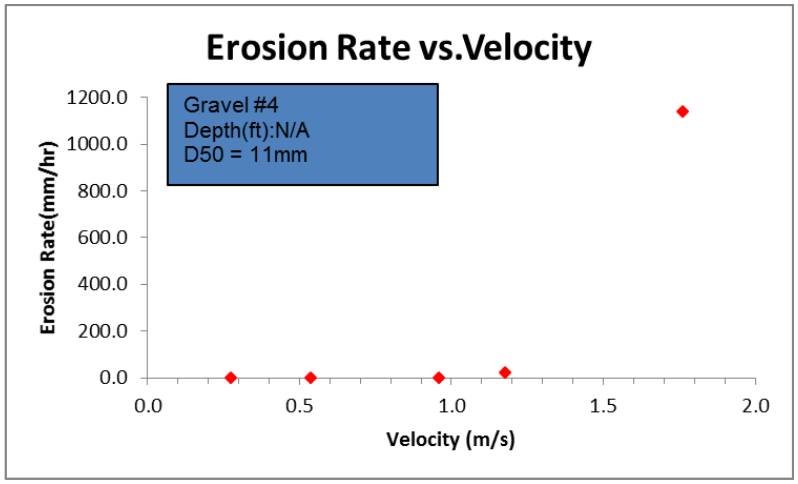

Figure A-45. Gravel #4

Clay Samples – JET

Site:	Beamunt Forma
Date:	4/2/2017
Test #:	B-1 (2'-4')
JET #:	1
Operator:	Iman
Test Location:	A&M Erosion L

Pt Gage Reading at N	4
Ref. Pt Gage Reading	0.9869 Nozzle
Nozzle Diam:	0.125
Nozzle Height (ft):	0.1181

Initial guess (Pt Gage)	1
Initial guess (Scour)	1

Scour Depth Readings

Time (min)	Diff Time (min)	Pt Gage Reading (mm)	Depth Pt Gage (ft)	Pt Gage Reading (ft)	Max Scour Depth (ft)	Head S Time (min)	Head
0	0	40	0.131	0.869	0.000	0	45.1
0.25	0.25	40	0.131	0.869	0.000	0.25	45.1
0.5	0.25	40	0.131	0.869	0.000	0.5	45.1
1	0.5	41	0.135	0.865	0.003	1	45.1
1.5	0.5	41	0.135	0.865	0.003	1.5	45.1
2	0.5	42	0.138	0.862	0.007	2	45.1
2.5	0.5	42	0.138	0.862	0.007	2.5	45.1
3	0.5	43	0.141	0.859	0.010	3	45.1
4	1	43	0.141	0.859	0.010	4	45.1
5	1	43	0.141	0.859	0.010	5	45.1
6	1	43	0.141	0.859	0.010	6	45.1
8	2	43.5	0.143	0.857	0.011	8	45.1
10	2	44	0.144	0.856	0.013	10	45.1
12	2	44	0.144	0.856	0.013	12	45.1
15	3	44	0.144	0.856	0.013	15	45.1
18	3	44	0.144	0.856	0.013	18	45.1
23	5	45	0.148	0.852	0.016	23	45.1
28	5	45.5	0.149	0.851	0.018	28	45.1
33	5	46	0.151	0.849	0.020	33	45.1
38	5	46	0.151	0.849	0.020	38	45.1
43	5	46	0.151	0.849	0.020	43	45.1

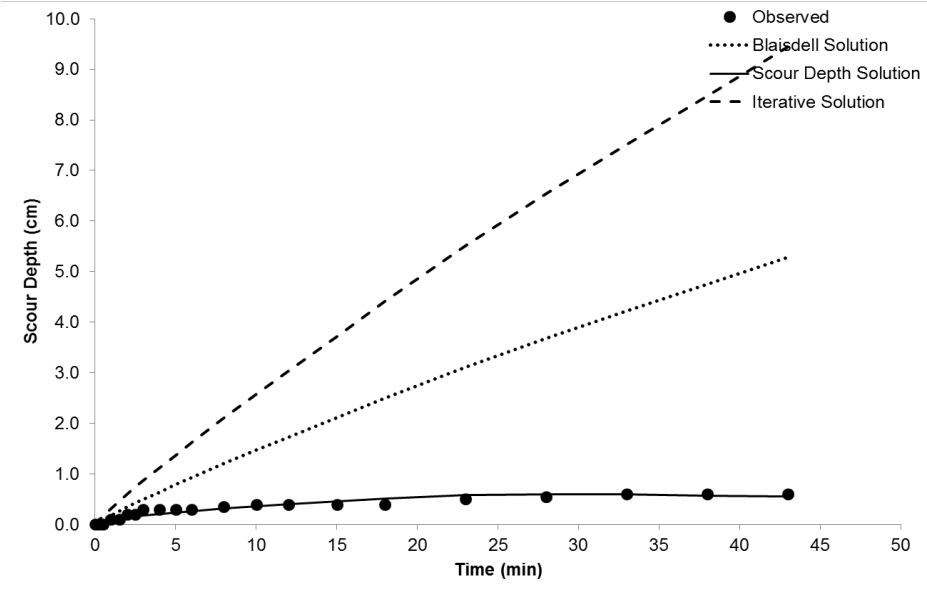

Figure A-46. B-1 (2'-4') Beaumont Formation

Site:	Beamunt Forma
Date:	7/29/2017
Test #:	B-1 (4'-6')
JET #:	1
Operator:	Iman
Test Location:	A&M Erosion L

Pt Gage Reading at Nozzle	4
Ref. Pt Gage Reading at Nozzle	0.869
Nozzle Diameter	0.125
Nozzle Height (ft):	0.984

Initial guess for τ_c (Pa)	1
Initial guess for k_d (cm³/N-s)	1

Scour Depth Readings					
Time (min)	Diff Time (min)	Pt Gage Reading (mm)	Depth Pt Gage Reading (ft)	Depth (ft)	Maximum Depth (ft)
0	0	34	0.112	0.888	0.000
0.25	0.25	34	0.112	0.888	0.000
0.5	0.25	34	0.112	0.888	0.000
1	0.5	34	0.112	0.888	0.000
2	1	35	0.115	0.885	0.003
3	1	35	0.115	0.885	0.003
4	1	35.5	0.116	0.884	0.005
5	1	36	0.118	0.882	0.007
6	1	36	0.118	0.882	0.007
8	2	36.5	0.120	0.880	0.008
10	2	36.5	0.120	0.880	0.008
12	2	37	0.121	0.879	0.010
14	2	37	0.121	0.879	0.010
19	5	38	0.125	0.875	0.013
24	5	39	0.128	0.872	0.016
29	5	40	0.131	0.869	0.020
34	5	40.5	0.133	0.867	0.021
39	5	41	0.135	0.865	0.023
44	5	41.5	0.136	0.864	0.025
49	5	42	0.138	0.862	0.026
54	5	43	0.141	0.859	0.030
59	5	44	0.144	0.856	0.033
64	5	44.5	0.146	0.854	0.034
69	5	44.5	0.146	0.854	0.034

Head S	
Time (min)	Head (in)
0	45.1
0.25	45.1
0.5	45.1
1	45.1
2	45.1
3	45.1
4	45.1
5	45.1
6	45.1
8	45.1
10	45.1
12	45.1
14	45.1
19	45.1
24	45.1
29	45.1
34	45.1
39	45.1
44	45.1
49	45.1
54	45.1
59	45.1
64	45.1
69	45.1

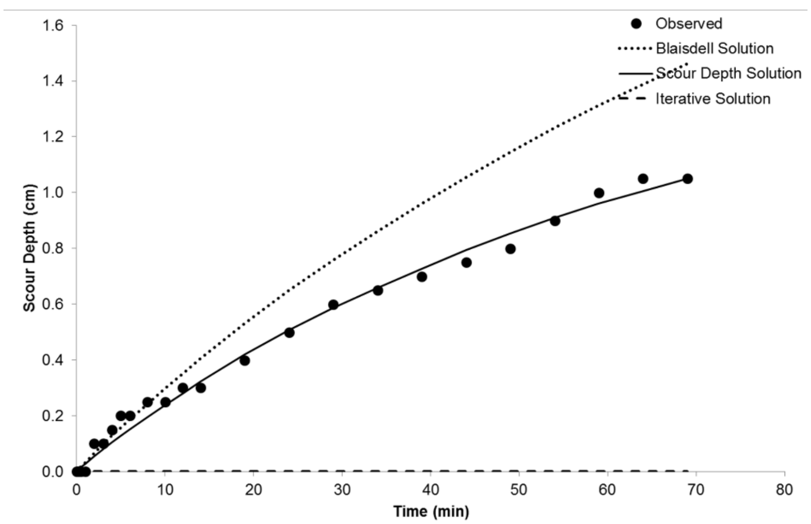

Figure A-47. B-1 (4'-6') Beaumont Formation

Site:	Beamunt Forma
Date:	3/31/2017
Test #:	B-1 (8'-10')
JET #:	1
Operator:	Iman
Test Lo	A&M Erosion L

Pt Gage Reading	4
Ref. Pt Gage Read	0.9
Nozzle Dia	0.125
Nozzle He	0.67

Initial gues	1
Initial gues	1

Scour Depth Readings						Head S
Time (min)	Diff Time (min)	Pnt Gage Read (mm)	Dep Pnt Gage Read (ft)	Pnt Gage Read (ft)	Maximum Depth (ft)	Time (min)
0	0	40	0.131	0.869	0.000	0
0.25	0.25	41	0.135	0.865	0.003	0.25
0.5	0.25	41	0.135	0.865	0.003	0.5
1	0.5	41	0.135	0.865	0.003	1
2	1	42	0.138	0.862	0.007	2
3	1	42	0.138	0.862	0.007	3
4	1	42	0.138	0.862	0.007	4
5	1	42	0.138	0.862	0.007	5
7	2	42	0.138	0.862	0.007	7
10	3	43	0.141	0.859	0.010	10
13	3	43	0.141	0.859	0.010	13
16	3	44	0.144	0.856	0.013	16
20	4	44	0.144	0.856	0.013	20
24	4	45	0.148	0.852	0.016	24
28	4	45	0.148	0.852	0.016	28
33	5	46	0.151	0.849	0.020	33
38	5	47	0.154	0.846	0.023	38
43	5	47	0.154	0.846	0.023	43
48	5	47	0.154	0.846	0.023	48
53	5	48	0.157	0.843	0.026	53
58	5	49	0.161	0.839	0.030	58
63	5	49.5	0.162	0.838	0.031	63
68	5	49.5	0.162	0.838	0.031	68

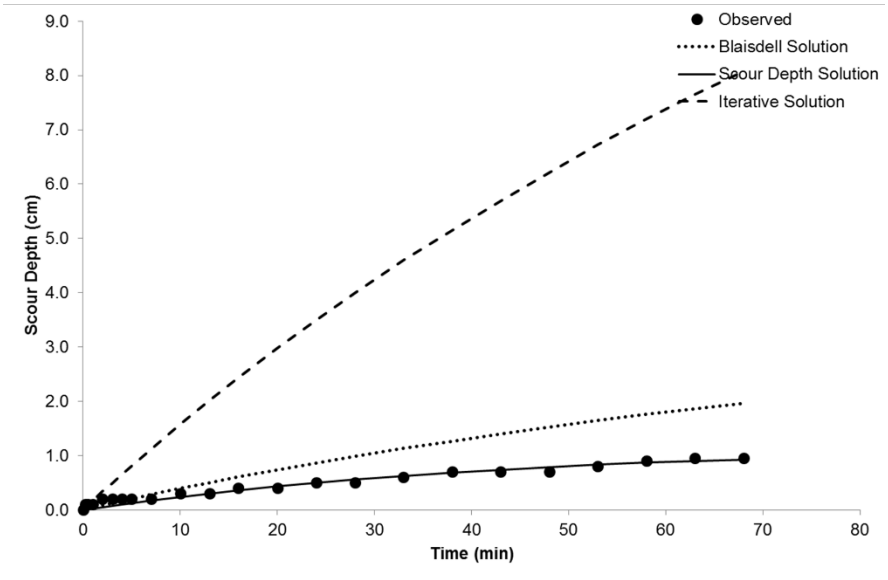

Figure A-48. B-1 (8'-10') Beaumont Formation

Site:	Beaumont Form
Date:	4/19/2017
Test #:	B-1 (10'-12')
JET #:	1
Operator:	Iman Shafii
Test Location:	A&M Erosion L

Pt Gage Reading at Nozzle	4
Ref. Pt Gage Reading at Nozzle	0.9869
Nozzle Diameter	0.125
Nozzle Height (ft):	0.0984

Initial guess for τ_c (Pa)	1
Initial guess for k_d (cm^3/N-s)	1

Scour Depth Readings					
Time (min)	Diff Time (min)	Pt Gage Reading (mm)	Depth Pt Gage (ft)	Pt Gage Reading (ft)	Maximum Depth (ft)
0	0	34	0.112	0.888	0.000
0.25	0.25	34	0.112	0.888	0.000
0.5	0.25	34	0.112	0.888	0.000
1	0.5	34	0.112	0.888	0.000
2	1	35	0.115	0.885	0.003
3	1	35	0.115	0.885	0.003
4	1	35	0.115	0.885	0.003
6	2	35	0.115	0.885	0.003
8	2	35	0.115	0.885	0.003
11	3	36	0.118	0.882	0.007
14	3	37	0.121	0.879	0.010
17	3	37	0.121	0.879	0.010
20	3	38	0.125	0.875	0.013
23	3	38	0.125	0.875	0.013
28	5	39	0.128	0.872	0.016
33	5	39.5	0.130	0.870	0.018
38	5	40	0.131	0.869	0.020
43	5	41	0.135	0.865	0.023
48	5	41	0.135	0.865	0.023
53	5	41.5	0.136	0.864	0.025
58	5	42	0.138	0.862	0.026
63	5	42.5	0.139	0.861	0.028
68	5	43	0.141	0.859	0.030
73	5	43	0.141	0.859	0.030

Head S	
Time (min)	Head (in)
0	45.0
0.25	45.0
0.5	45.0
1	45.0
2	45.0
3	45.0
4	45.0
6	45.0
8	45.0
11	45.0
14	45.0
17	45.0
20	45.0
23	45.0
28	45.0
33	45.0
38	45.0
43	45.0
48	45.0
53	45.0
58	45.0
63	45.0
68	45.0
73	45.0

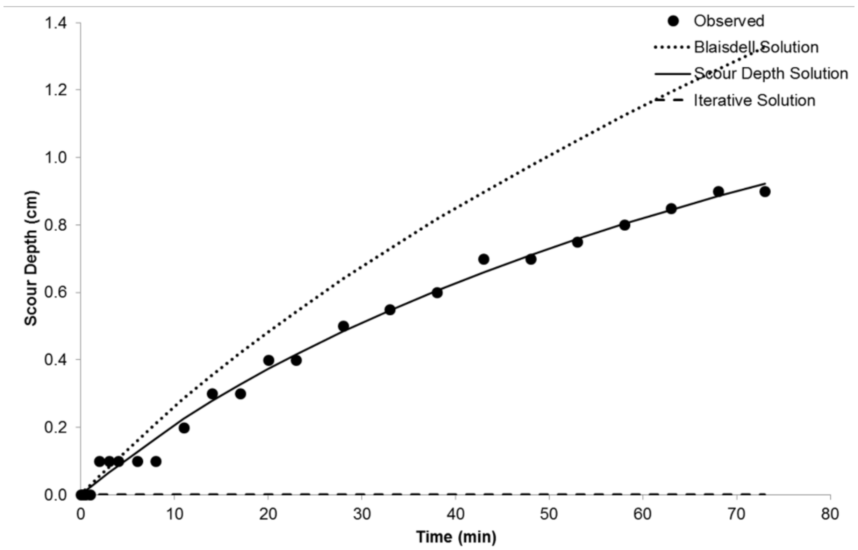

Figure A-49. B-1 (10'-12') Beaumont Formation

Site:	Beaumont Formation
Date:	3/29/2017
Test #:	B-1 (13'-15')
JET #:	1
Operator:	Iman
Test Location	A&M Erosion Lab

Pt Gage Reading at Nozzle	4
Ref. Pt Gage Reading at Nozzle	0.986
Nozzle Diameter	0.125
Nozzle Height (ft):	0.167

Initial guess (z_o) (ft)	1
Initial guess (z_o) (mm)	1

Scour Depth Readings						Head S
Time (min)	Diff Time (min)	Pointer Gage Reading (mm)	Deepest Pntr Depth (ft)	Gage Reading Maximum Depth (ft)		ST (min)
0	0	35	0.115	0.885	0.000	0
0.25	0.25	50	0.164	0.836	0.049	0.25
0.5	0.25	53	0.174	0.826	0.059	0.5
0.75	0.25	56	0.184	0.816	0.069	0.75
1	0.25	57	0.187	0.813	0.072	1
1.25	0.25	58	0.190	0.810	0.075	1.25
1.75	0.5	59	0.194	0.806	0.079	1.75
2	0.25	60	0.197	0.803	0.082	2
3	1	67	0.220	0.780	0.105	3
3.5	0.5	71	0.233	0.767	0.118	3.5
4	0.5	72	0.236	0.764	0.121	4
4.5	0.5	74	0.243	0.757	0.128	4.5
5	0.5	75	0.246	0.754	0.131	5
5.5	0.5	75	0.246	0.754	0.131	5.5
6	0.5	76	0.249	0.751	0.135	6
6.5	0.5	77	0.253	0.747	0.138	6.5
7	0.5	78	0.256	0.744	0.141	7
7.5	0.5	80	0.262	0.738	0.148	7.5
8	0.5	81	0.266	0.734	0.151	8
8.5	0.5	85	0.279	0.721	0.164	8.5
9	0.5	89	0.292	0.708	0.177	9
9.5	0.5	91	0.299	0.701	0.184	9.5
10	0.5	92	0.302	0.698	0.187	10
10.5	0.5	93	0.305	0.695	0.190	10.5
11	0.5	93	0.305	0.695	0.190	11
11.5	0.5	93	0.305	0.695	0.190	11.5
12.5	1	93	0.305	0.695	0.190	12.5
14	1.5	93	0.305	0.695	0.190	14
16	2	93	0.305	0.695	0.190	16
20	4	93	0.305	0.695	0.190	20

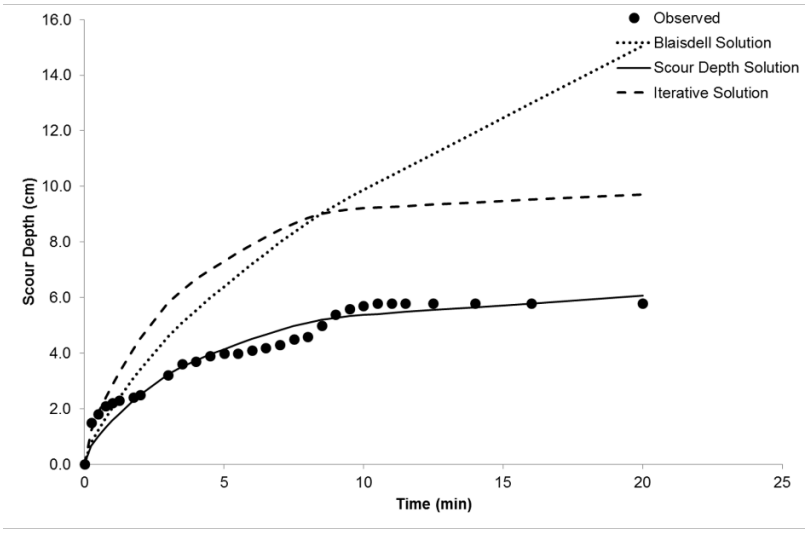

Figure A-50. B-1 (13'-15') Beaumont Formation

Site:	Beaumont Formation
Date:	4/2/2017
Test #:	B-1 (18'-20')
JET #:	1
Operator:	Iman
Test Location	A&M Erosion Lab

Pt Gage Reading at Nozzle	4
Ref. Pt Gage Reading at Nozzle	0.988 ft
Nozzle Diameter	0.125 in
Nozzle Height (ft):	0.988 ft

Initial guess (Pt)	1
Initial guess (Min)	1

Scour Depth Readings						Head S
Time (min)	Diff Time (min)	Pnt Gage Reading (mm)	Deepest Pnt Gage Reading (ft)	Max Scour Depth (ft)		ST (min)
0	0	34	0.112	0.888	0.000	0
0.25	0.25	34	0.112	0.888	0.000	0.25
0.5	0.25	35	0.115	0.885	0.003	0.5
1	0.5	35	0.115	0.885	0.003	1
2	1	35	0.115	0.885	0.003	2
3	1	36	0.118	0.882	0.007	3
4	1	36	0.118	0.882	0.007	4
6	2	36	0.118	0.882	0.007	6
8	2	37	0.121	0.879	0.010	8
10	2	37	0.121	0.879	0.010	10
12	2	38	0.125	0.875	0.013	12
14	2	39	0.128	0.872	0.016	14
16	2	40	0.131	0.869	0.020	16
18	2	41	0.135	0.865	0.023	18
20	2	41	0.135	0.865	0.023	20
22	2	42	0.138	0.862	0.026	22
24	2	42	0.138	0.862	0.026	24
26	2	43	0.141	0.859	0.030	26
28	2	43	0.141	0.859	0.030	28
30	2	44	0.144	0.856	0.033	30
32	2	45	0.148	0.852	0.036	32
34	2	46	0.151	0.849	0.039	34
36	2	46	0.151	0.849	0.039	36
38	2	47	0.154	0.846	0.043	38
40	2	47	0.154	0.846	0.043	40
43	3	49	0.161	0.839	0.049	43
46	3	50	0.164	0.836	0.052	46
49	3	50.5	0.166	0.834	0.054	49
52	3	51	0.167	0.833	0.056	52
55	3	52	0.171	0.829	0.059	55
58	3	52	0.171	0.829	0.059	58
63	5	52	0.171	0.829	0.059	63
68	5	52	0.171	0.829	0.059	68

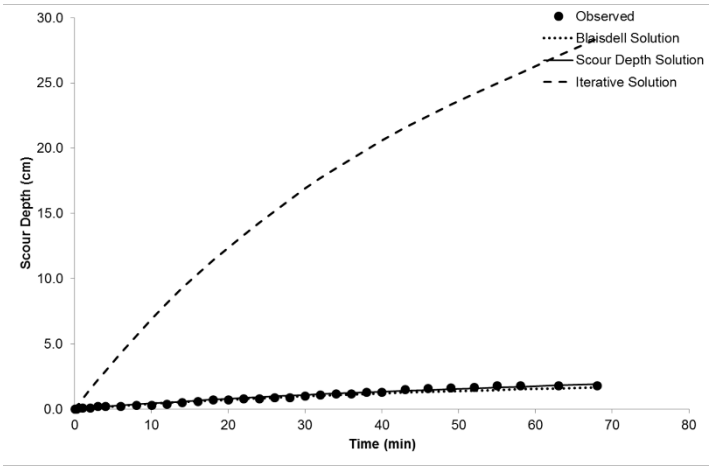

Figure A-51. B-1 (18'-20') Beaumont Formation

Site:	Beamunt Forma
Date:	8/2/2017
Test #:	B-1 (28'-30')
JET #:	1
Operator:	Iman
Test Location:	A&M Erosion L

Pt Gage Reading at Nozzle	4
Ref. Pt Gage Reading at Nozzle	0.9869
Nozzle Diameter	0.125
Nozzle Height (ft):	0.0951

Initial guess for τ_c (Pa)	1
Initial guess for k_d (cm³/N-s)	1

Scour Depth Readings					
Time (min)	Diff Time (min)	Point Gage Reading (mm)	Depth (ft)	Point Gage Reading (ft)	Maximum Depth (ft)
0	0	33	0.108	0.892	0.000
0.25	0.25	33	0.108	0.892	0.000
0.5	0.25	33	0.108	0.892	0.000
1	0.5	33.5	0.110	0.890	0.002
2	1	33.5	0.110	0.890	0.002
3	1	33.5	0.110	0.890	0.002
5	2	34	0.112	0.888	0.003
7	2	34	0.112	0.888	0.003
10	3	34	0.112	0.888	0.003
13	3	34.5	0.113	0.887	0.005
16	3	35	0.115	0.885	0.007
19	3	35	0.115	0.885	0.007
24	5	36	0.118	0.882	0.010
29	5	36.5	0.120	0.880	0.011
34	5	37	0.121	0.879	0.013
39	5	37.5	0.123	0.877	0.015
44	5	38	0.125	0.875	0.016
49	5	38	0.125	0.875	0.016

Head Sc	
Time (min)	Scour Rea (in)
0	45.1
0.25	45.1
0.5	45.1
1	45.1
2	45.1
3	45.1
5	45.1
7	45.1
10	45.1
13	45.1
16	45.1
19	45.1
24	45.1
29	45.1
34	45.1
39	45.1
44	45.1
49	45.1

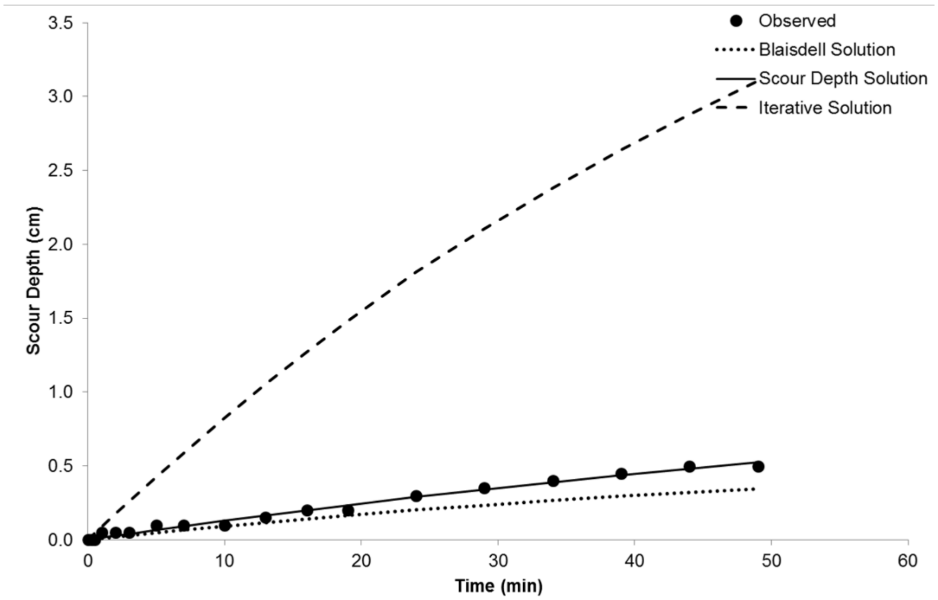

Figure A-52. B-1 (28’-30’) Beaumont Formation

Site:	Beaumont Formation
Date:	3/26/2017
Test #:	B-2 (2'-4')
JET #:	1
Operator:	Iman
Test Location:	A&M Erosion Lab

Pt Gage Reading at Nozzle	4
Ref. Pt Gage Reading at Nozzle	0.9875
Nozzle Diameter	0.125
Nozzle Height (ft):	0.1875

Initial guess (ft) for d_s:	1
Initial guess (ft) for $d_{s,max}$:	1

Scour Depth Readings						Head Sc	
Time (min)	Diff Time (min)	Pointer Gage Reading (mm)	Depth Pointer Gage Reading (ft)	Maximum Depth (ft)		Scour Head (min)	Scour Head (in)
0	0	37	0.121	0.879	0.000	0	45.1
0.5	0.5	38	0.125	0.875	0.003	0.5	45.1
1	0.5	38	0.125	0.875	0.003	1	45.1
2	1	39	0.128	0.872	0.007	2	45.1
3	1	40	0.131	0.869	0.010	3	45.1
4	1	40	0.131	0.869	0.010	4	45.1
6	2	41	0.135	0.865	0.013	6	45.1
8	2	42	0.138	0.862	0.016	8	45.1
11	3	43	0.141	0.859	0.020	11	45.1
14	3	44	0.144	0.856	0.023	14	45.1
17	3	44	0.144	0.856	0.023	17	45.1
20	3	45	0.148	0.852	0.026	20	45.1
23	3	46	0.151	0.849	0.030	23	45.1
26	3	47	0.154	0.846	0.033	26	45.1
29	3	47	0.154	0.846	0.033	29	45.1
34	5	48	0.157	0.843	0.036	34	45.1
39	5	49	0.161	0.839	0.039	39	45.1
44	5	50	0.164	0.836	0.043	44	45.1
49	5	50	0.164	0.836	0.043	49	45.1
54	5	51	0.167	0.833	0.046	54	45.1
59	5	51	0.167	0.833	0.046	59	45.1
64	5	52	0.171	0.829	0.049	64	45.1
70	6	53	0.174	0.826	0.052	70	45.1
76	6	53	0.174	0.826	0.052	76	45.1

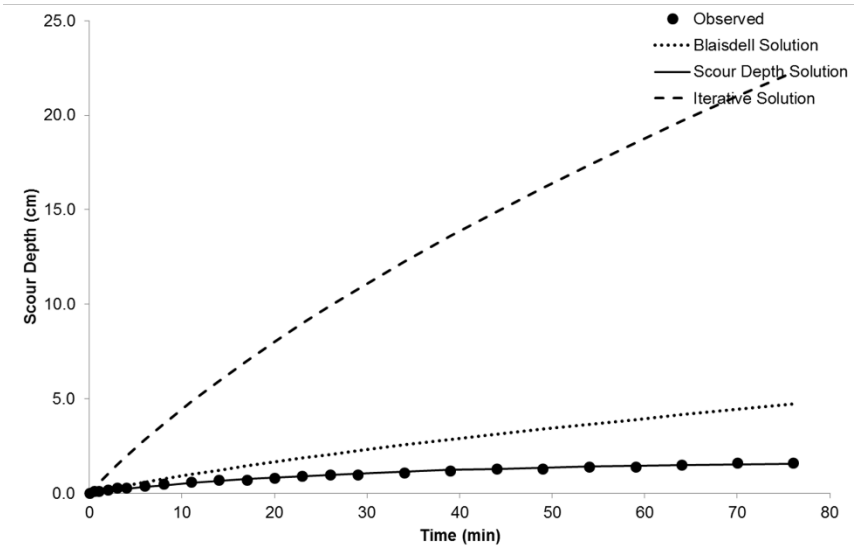

Figure A-53. B-2 (2'-4') Beaumont Formation

Site:	Lissie Formatic
Date:	5/20/2017
Test #:	B-2 (8'-10')
JET #:	1
Operator:	Iman
Test Location:	A&M Erosion L

Pt Gage Reading at N	4
Ref. Pt Gage Reading	0.9875 Nozzle
Nozzle Diam	0.125
Nozzle Height (ft):	0.0729

Initial guess (ft) for	1
Initial guess (mm) for	1

Scour Depth Readings						Head S
Time (min)	Diff Time (min)	Point Gage Reading (mm)	Depth Ptg (ft)	Gage Reading (ft)	Maximum Depth (ft)	ST cum Hea (min) (in)
0	0	33	0.108	0.892	0.000	0 45.0
0.25	0.25	33	0.108	0.892	0.000	0.25 45.0
0.5	0.25	33	0.108	0.892	0.000	0.5 45.0
1	0.5	35	0.115	0.885	0.007	1 45.0
1.5	0.5	35.5	0.116	0.884	0.008	1.5 45.0
2	0.5	35.5	0.116	0.884	0.008	2 45.0
3	1	36	0.118	0.882	0.010	3 45.0
4	1	37	0.121	0.879	0.013	4 45.0
5	1	37	0.121	0.879	0.013	5 45.0
6	1	38	0.125	0.875	0.016	6 45.0
7	1	38	0.125	0.875	0.016	7 45.0
8	1	38	0.125	0.875	0.016	8 45.0
10	2	39	0.128	0.872	0.020	10 45.0
12	2	39	0.128	0.872	0.020	12 45.0
15	3	39.5	0.130	0.870	0.021	15 45.0
20	5	40.5	0.133	0.867	0.025	20 45.0
25	5	42	0.138	0.862	0.030	25 45.0
30	5	42	0.138	0.862	0.030	30 45.0
35	5	43	0.141	0.859	0.033	35 45.0
40	5	43	0.141	0.859	0.033	40 45.0
45	5	43	0.141	0.859	0.033	45 45.0

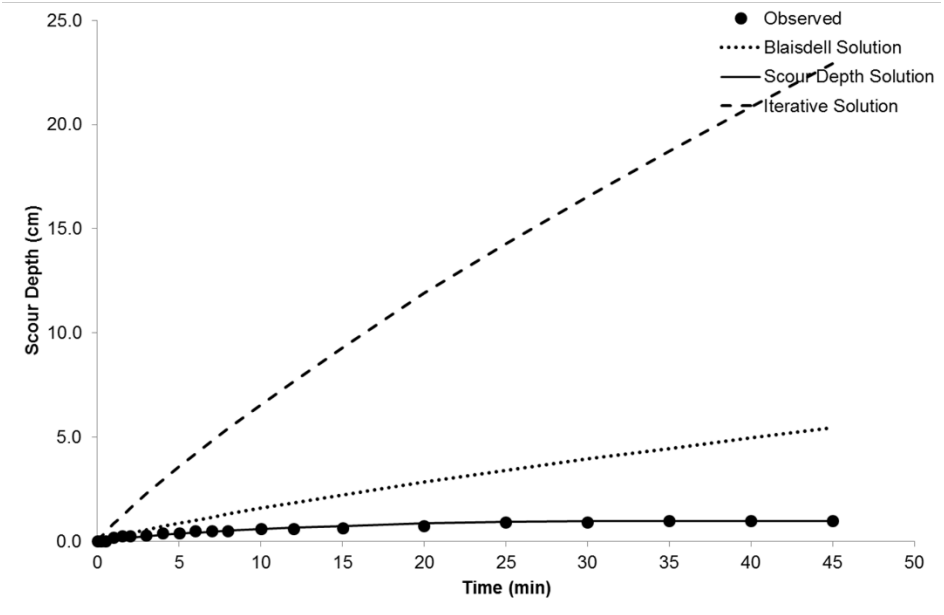

Figure A-54. B-2 (8'-10') Lissie Formation

Site:	Beamunt Forma
Date:	3/26/2017
Test #:	B-2 (13'-15')
JET #:	1
Operator:	Iman
Test Location:	A&M Erosion L

Pt Gage Reading	4
Ref. Pt Gage Read	0.9 8a6t9N ozzle
Nozzle Diar	0.125
Nozzle He	0ig1h0t1(ft):

Initial gues	1
Initial gues	1

Scour Depth Readings

Time (min)	Diff Time (min)	Pnt Gage Read (mm)	Depth Pnt Gage (ft)	Reading (ft)	Maximum Depth (ft)
0	0	35	0.115	0.885	0.000
0.25	0.25	35	0.115	0.885	0.000
0.5	0.25	35	0.115	0.885	0.000
1	0.5	36	0.118	0.882	0.003
2	1	36	0.118	0.882	0.003
3	1	36	0.118	0.882	0.003
5	2	37	0.121	0.879	0.007
7	2	37	0.121	0.879	0.007
10	3	38	0.125	0.875	0.010
13	3	38	0.125	0.875	0.010
18	5	39	0.128	0.872	0.013
23	5	40	0.131	0.869	0.016
28	5	40	0.131	0.869	0.016
33	5	40	0.131	0.869	0.016

Head S

ST	Cumulative (min)	Area (in)
0	45.0	
0.25	45.0	
0.5	45.0	
1	45.0	
2	45.0	
3	45.0	
5	45.0	
7	45.0	
10	45.0	
13	45.0	
18	45.0	
23	45.0	
28	45.0	
33	45.0	

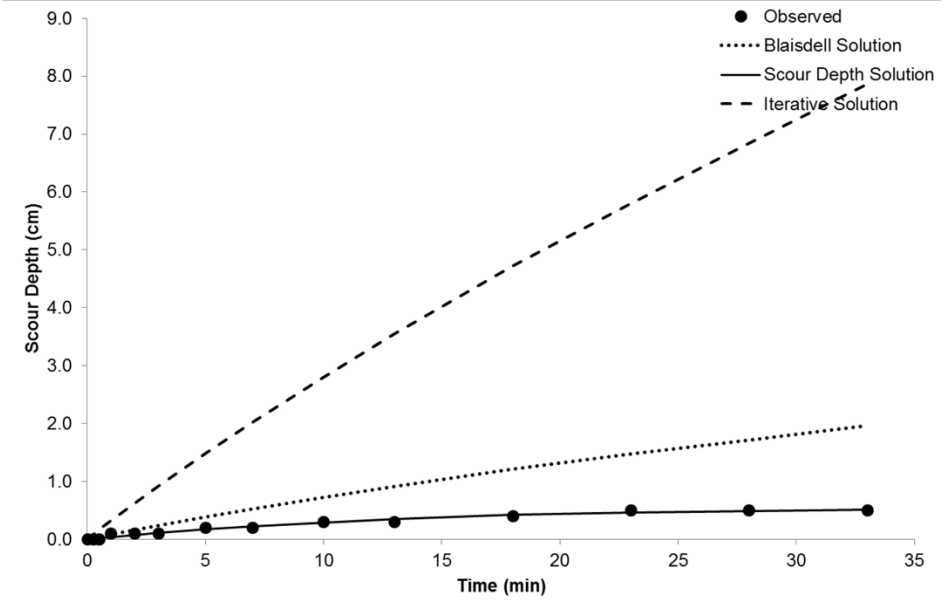

Figure A-55. B-2 (13'-15') Beaumont Formation

Site:	Beaumont Form
Date:	3/25/2017
Test #:	B-4 (8'-10')
JET #:	1
Operator:	Iman
Test Location:	A&M Erosion L

Pt Gage Reading at N	4
Ref. Pt Gage Reading	0.9 8 6 9 Nozzle
Nozzle Diameter	0.1 2 5
Nozzle Height (ft):	0.5

Initial guess (ft/hr)	1
Initial guess (mm/hr)	1

Scour Depth Readings						Head S
Time (min)	Diff Time (min)	Pointer Gage Reading (mm)	Depth Ptr Gage Reading (ft)	Ptr Gage Reading Minus Initial (ft)	Maximum Depth (ft)	STime (min)
0	0	3 8	0.1 2 5	0.8 7 5	0.0 0 0	0
0.2 5	0.2 5	4 0	0.1 3 1	0.8 6 9	0.0 0 7	0.2 5
0.5	0.2 5	4 1	0.1 3 5	0.8 6 5	0.0 1 0	0.5
1	0.5	4 3	0.1 4 1	0.8 5 9	0.0 1 6	1
1.5	0.5	4 4	0.1 4 4	0.8 5 6	0.0 2 0	1.5
2	0.5	4 5	0.1 4 8	0.8 5 2	0.0 2 3	2
2.5	0.5	4 6	0.1 5 1	0.8 4 9	0.0 2 6	2.5
3.5	1	4 7	0.1 5 4	0.8 4 6	0.0 3 0	3.5
4	0.5	4 8	0.1 5 7	0.8 4 3	0.0 3 3	4
5	1	4 9	0.1 6 1	0.8 3 9	0.0 3 6	5
6	1	5 0	0.1 6 4	0.8 3 6	0.0 3 9	6
7	1	5 0	0.1 6 4	0.8 3 6	0.0 3 9	7
8	1	5 0	0.1 6 4	0.8 3 6	0.0 3 9	8
9	1	5 1	0.1 6 7	0.8 3 3	0.0 4 3	9
1 1	2	5 2	0.1 7 1	0.8 2 9	0.0 4 6	1 1
1 3	2	5 2	0.1 7 1	0.8 2 9	0.0 4 6	1 3
1 6	3	5 3	0.1 7 4	0.8 2 6	0.0 4 9	1 6
1 9	3	5 3	0.1 7 4	0.8 2 6	0.0 4 9	1 9
2 4	5	5 4	0.1 7 7	0.8 2 3	0.0 5 2	2 4
3 0	6	5 6	0.1 8 4	0.8 1 6	0.0 5 9	3 0
3 5	5	5 8	0.1 9 0	0.8 1 0	0.0 6 6	3 5
4 0	5	5 8	0.1 9 0	0.8 1 0	0.0 6 6	4 0

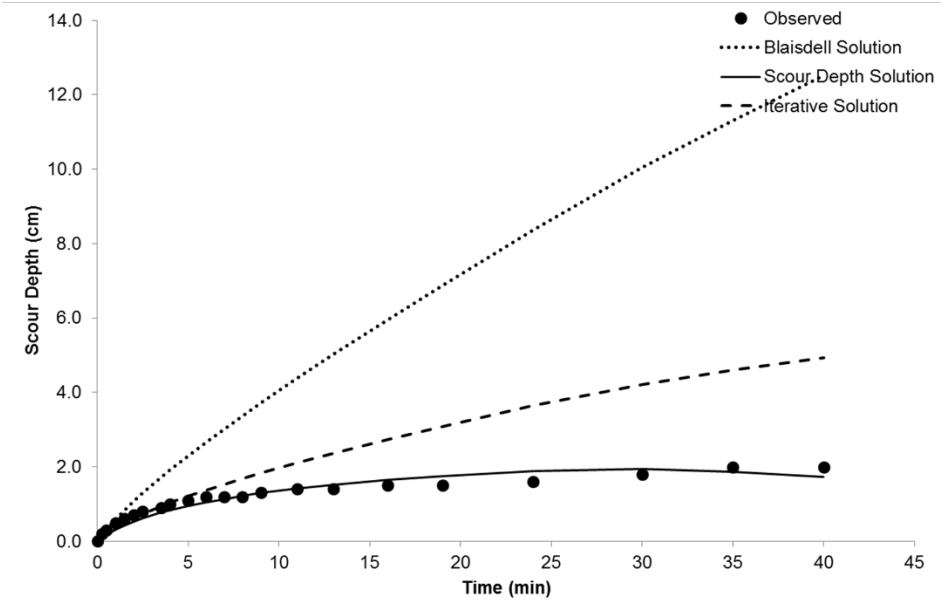

Figure A-56. B-4 (8'-10') Beaumont Formation

Site:	Beaumont Form
Date:	5/18/2017
Test #:	B-5 (4'-6')
JET #:	1
Operator:	Iman
Test Location	A&M Erosion L

Pt Gage Reading at N	4
Ref. Pt Gage Reading at Nozzle	0.986
Nozzle Diameter:	0.125
Nozzle Height (ft):	0.021

Initial guess (S^*)	1
Initial guess (S_{max})	1

Scour Depth Readings						Head S
Time (min)	Diff Time (min)	Pnt Gage Reading (mm)	Depth Pnt Gage Reading (ft)	Max Depth Pnt Gage Reading (ft)	Maximum Depth (ft)	ST Cumulative Time (min)
0	0	35	0.115	0.885	0.000	0
0.25	0.25	35	0.115	0.885	0.000	0.25
0.5	0.25	35	0.115	0.885	0.000	0.5
1	0.5	35	0.115	0.885	0.000	1
2	1	35	0.115	0.885	0.000	2
4	2	35	0.115	0.885	0.000	4
9	5	35.5	0.116	0.884	0.002	9
14	5	36	0.118	0.882	0.003	14
19	5	36	0.118	0.882	0.003	19
24	5	36.5	0.120	0.880	0.005	24
29	5	37	0.121	0.879	0.007	29
34	5	37.5	0.123	0.877	0.008	34
39	5	37.5	0.123	0.877	0.008	39
44	5	38	0.125	0.875	0.010	44
49	5	38	0.125	0.875	0.010	49
54	5	38	0.125	0.875	0.010	54

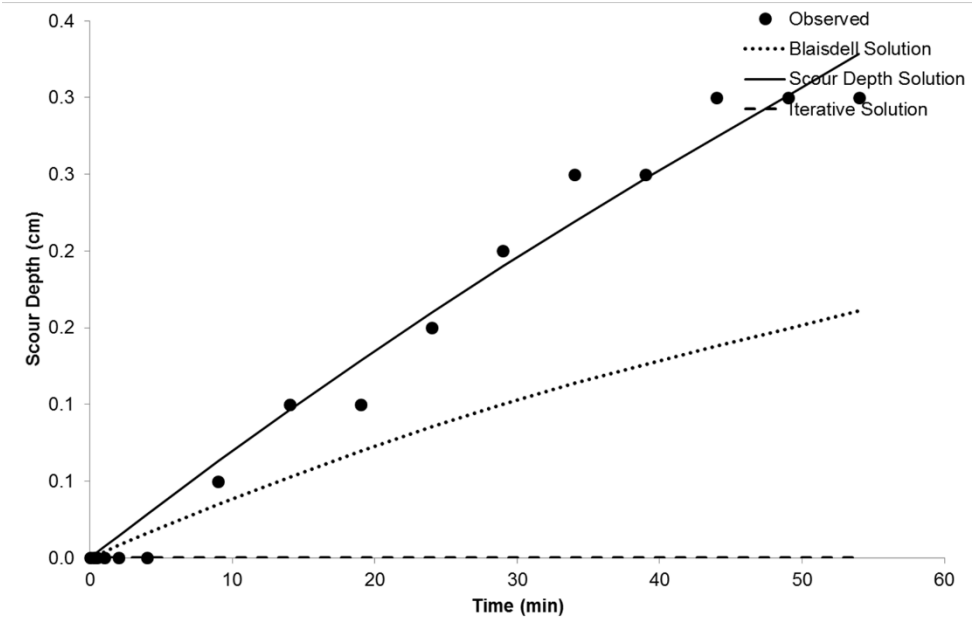

Figure A-57. B-5 (4'-6') Beaumont Formation

Site:	Beaumont Formation
Date:	3/29/2017
Test #:	B-5 (6'-8')
JET #:	1
Operator:	Iman
Test Location	A&M Erosion Lab

Pt Gage Reading at N	4
Ref. Pt Gage Reading	0.986
Nozzle Diameter	0.125
Nozzle Height (ft):	0.667

Initial guess (Pitcher)	1
Initial guess (Simons)	1

Scour Depth Readings						Head S
Time (min)	Diff Time (min)	Gage Reading (mm)	Depth Pt Gage (ft)	Gage Reading (ft)	Maximum Depth (ft)	Time (min)
0	0	37	0.121	0.879	0.000	0
0.5	0.5	37	0.121	0.879	0.000	0.5
1	0.5	38	0.125	0.875	0.003	1
2	1	38	0.125	0.875	0.003	2
3	1	38	0.125	0.875	0.003	3
4	1	38	0.125	0.875	0.003	4
6	2	39	0.128	0.872	0.007	6
8	2	39	0.128	0.872	0.007	8
10	2	40	0.131	0.869	0.010	10
13	3	40	0.131	0.869	0.010	13
16	3	41	0.135	0.865	0.013	16
19	3	41	0.135	0.865	0.013	19
22	3	41	0.135	0.865	0.013	22
27	5	42	0.138	0.862	0.016	27
32	5	42	0.138	0.862	0.016	32
37	5	43	0.141	0.859	0.020	37
42	5	43	0.141	0.859	0.020	42
47	5	44	0.144	0.856	0.023	47
52	5	44	0.144	0.856	0.023	52
57	5	44	0.144	0.856	0.023	57

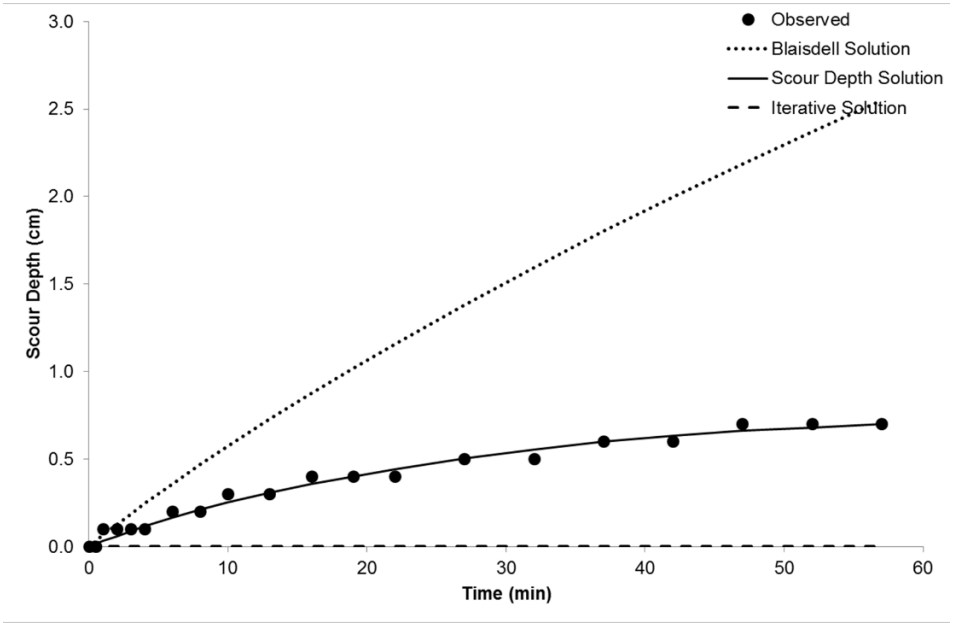

Figure A-58. B-5 (6'-8') Beaumont Formation

Site:	Beaumont Form
Date:	4/19/2017
Test #:	B-6 (0'-2')
JET #:	1
Operator:	Iman Shafii
Test Location:	A&M Erosion L

Pt Gage Reading at N	4
Ref. Pt Gage Reading	0.9875
Nozzle Diam	0.125
Nozzle Height (ft):	0.1667

Initial guess (Pt Gage)	1
Initial guess (Scour)	1

Scour Depth Readings

Time (min)	Diff Time (min)	Pnt Gage Reading (mm)	Depth Pnt Gage (ft)	Gage Reading (ft)	Maximum Depth (ft)
0	0	35	0.115	0.885	0.000
0.25	0.25	35	0.115	0.885	0.000
0.5	0.25	35	0.115	0.885	0.000
1	0.5	35	0.115	0.885	0.000
2	1	35	0.115	0.885	0.000
3	1	35.5	0.116	0.884	0.002
5	2	35.5	0.116	0.884	0.002
7	2	35.5	0.116	0.884	0.002
10	3	36	0.118	0.882	0.003
13	3	36.5	0.120	0.880	0.005
16	3	36.5	0.120	0.880	0.005
19	3	36.5	0.120	0.880	0.005
24	5	37	0.121	0.879	0.007
29	5	37	0.121	0.879	0.007
34	5	37	0.121	0.879	0.007
39	5	37	0.121	0.879	0.007

Head S

Time (min)	Cumulative Area (in)
0	45.0
0.25	45.0
0.5	45.0
1	45.0
2	45.0
3	45.0
5	45.0
7	45.0
10	45.0
13	45.0
16	45.0
19	45.0
24	45.0
29	45.0
34	45.0
39	45.0

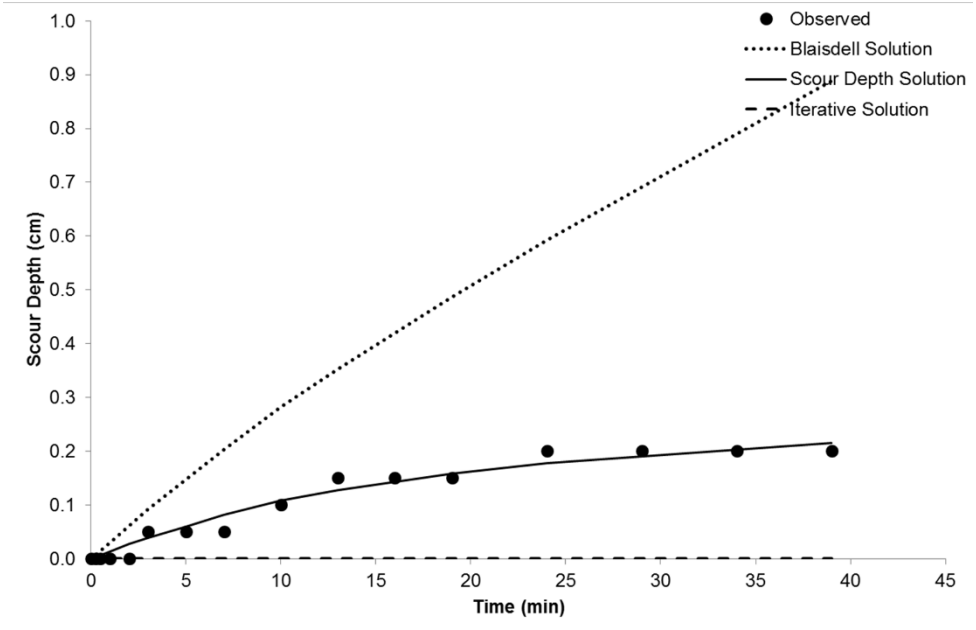

Figure A-59. B-6 (0'-2') Beaumont Formation

Site:	Alluvium Forma
Date:	4/20/2017
Test #:	B-8 (2'-4')
JET #:	1
Operator:	Iman Shafii
Test Location:	A&M Erosion L

Pt Gage Reading at N	4
Ref. Pt Gage Reading	0.9875
Nozzle Diameter	0.125
Nozzle Height (ft):	0.167

Initial guess (Pt Gage)	1
Initial guess (Scour)	1

Scour Depth Readings						Head S
Time (min)	Diff Time (min)	Pointer Gage Reading (mm)	Depth Pointer Gage Reading (ft)	Water Depth Pointer Gage Reading (ft)	Maximum Depth (ft)	ST (min)
0	0	35	0.115	0.885	0.000	0
0.25	0.25	35.5	0.116	0.884	0.002	0.25
0.5	0.25	35.5	0.116	0.884	0.002	0.5
1	0.5	35.5	0.116	0.884	0.002	1
1.5	0.5	36	0.118	0.882	0.003	1.5
2	0.5	36.5	0.120	0.880	0.005	2
2.5	0.5	36.5	0.120	0.880	0.005	2.5
3	0.5	36.5	0.120	0.880	0.005	3
4	1	36.5	0.120	0.880	0.005	4
5	1	37	0.121	0.879	0.007	5
6	1	37	0.121	0.879	0.007	6
7	1	37	0.121	0.879	0.007	7
9	2	37.5	0.123	0.877	0.008	9
11	2	37.5	0.123	0.877	0.008	11
13	2	38	0.125	0.875	0.010	13
15	2	38	0.125	0.875	0.010	15
17	2	38.5	0.126	0.874	0.011	17
20	3	39	0.128	0.872	0.013	20
23	3	39.5	0.130	0.870	0.015	23
26	3	40	0.131	0.869	0.016	26
29	3	40	0.131	0.869	0.016	29
32	3	40	0.131	0.869	0.016	32
37	5	41	0.135	0.865	0.020	37
42	5	41.5	0.136	0.864	0.021	42
47	5	42	0.138	0.862	0.023	47
52	5	42.5	0.139	0.861	0.025	52
57	5	43	0.141	0.859	0.026	57
62	5	43	0.141	0.859	0.026	62
67	5	43.5	0.143	0.857	0.028	67
72	5	43.5	0.143	0.857	0.028	72

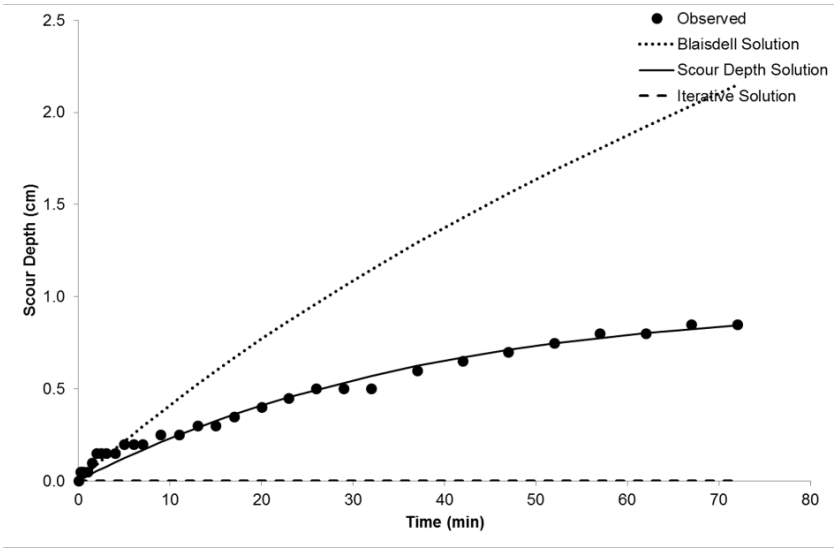

Figure A-60. B-8 (2'-4') 5694 Alluvium

Site:	Alluvium Freepo
Date:	6/8/2017
Test #:	B-13 (18'-20') B
JET #:	1
Operator:	Iman Shafii
Test Location	A&M Erosion L

Pt Gage Reading at N	4
Ref. Pt Gage Reading	0.98
Nozzle Diameter	0.125
Nozzle Height (ft):	0.5

Initial guess (Pa)	1
Initial guess (m)	1

Scour Depth Readings						Head S
Time (min)	Diff Time (min)	Gage Reading (mm)	Depth Ptg (ft)	Gage Reading (ft)	Maximum Depth (ft)	(min)
0	0	38	0.125	0.875	0.000	0
0.25	0.25	38	0.125	0.875	0.000	0.25
0.5	0.25	38	0.125	0.875	0.000	0.5
1	0.5	38.5	0.126	0.874	0.002	1
2	1	39	0.128	0.872	0.003	2
3	1	39	0.128	0.872	0.003	3
4	1	39	0.128	0.872	0.003	4
6	2	39.5	0.130	0.870	0.005	6
8	2	39.5	0.130	0.870	0.005	8
10	2	40	0.131	0.869	0.007	10
13	3	40.5	0.133	0.867	0.008	13
16	3	40.5	0.133	0.867	0.008	16
21	5	41	0.135	0.865	0.010	21
26	5	42	0.138	0.862	0.013	26
31	5	42.5	0.139	0.861	0.015	31
36	5	43	0.141	0.859	0.016	36
41	5	43.5	0.143	0.857	0.018	41
46	5	44.5	0.146	0.854	0.021	46
51	5	45	0.148	0.852	0.023	51
56	5	46	0.151	0.849	0.026	56
61	5	46	0.151	0.849	0.026	61
66	5	46	0.151	0.849	0.026	66

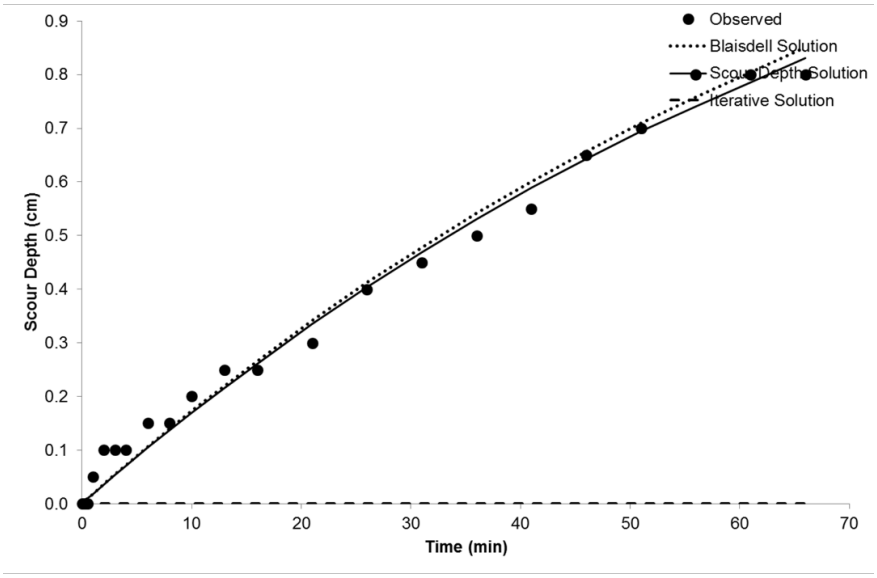

Figure A-61. B-13 (18'-20') Bottom Alluvium

Site:	Alluvium Freepo
Date:	5/11/2017
Test #:	B-13 (18'-20') T
JET #:	1
Operator:	Iman Shafii
Test Location	A&M Erosion L

Pt Gage Reading at N	4
Ref. Pt Gage Reading	0.9875
Nozzle Diameter	0.125
Nozzle Height (ft):	0.0104

Initial guess (Pfister)	1
Initial guess (Sumer)	1

Scour Depth Readings						Head S
Time (min)	Diff Time (min)	Pointer Gage Reading (mm)	Deepest Ptg Gage Reading (ft)	Shallowest Ptg Gage Reading (ft)	Maximum Depth (ft)	STime (min)
0	0	37	0.121	0.879	0.000	0
0.25	0.25	37	0.121	0.879	0.000	0.25
0.5	0.25	37.5	0.123	0.877	0.002	0.5
1	0.5	38	0.125	0.875	0.003	1
2	1	38	0.125	0.875	0.003	2
3	1	38.5	0.126	0.874	0.005	3
4	1	39	0.128	0.872	0.007	4
5	1	39	0.128	0.872	0.007	5
6	1	39	0.128	0.872	0.007	6
8	2	39.5	0.130	0.870	0.008	8
10	2	40	0.131	0.869	0.010	10
12	2	40.5	0.133	0.867	0.011	12
14	2	41	0.135	0.865	0.013	14
16	2	41	0.135	0.865	0.013	16
18	2	41.5	0.136	0.864	0.015	18
20	2	42	0.138	0.862	0.016	20
23	3	43	0.141	0.859	0.020	23
26	3	43.5	0.143	0.857	0.021	26
29	3	43.5	0.143	0.857	0.021	29
34	5	44	0.144	0.856	0.023	34
39	5	45	0.148	0.852	0.026	39
44	5	46	0.151	0.849	0.030	44
49	5	46	0.151	0.849	0.030	49

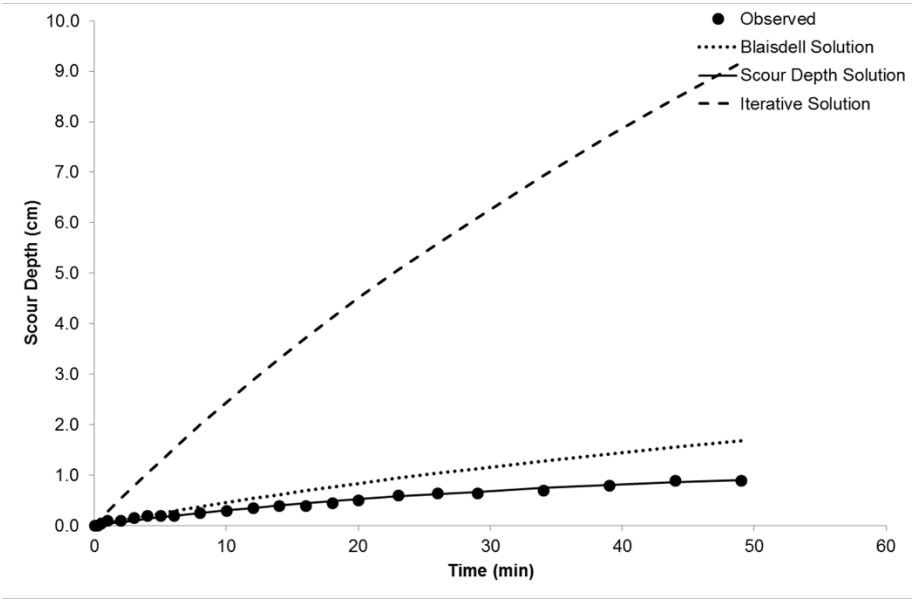

Figure A-62. B-13 (18'-20') Top Alluvium

Site:	Bay City Bridg
Date:	9/20/2017
Test #	Sample #2 - Bay
JET #:	1
Operator:	Iman Shafii
Test Location	A&M Erosion L

Pt Gage Reading	4
Ref. Pt Gage Reading	0.9869
Nozzle Diam	0.125
Nozzle Height (ft):	0.869

Initial guess (Pt Gage)	1
Initial guess (smooth)	1

Scour Depth Readings

Time (min)	Diff Time (min)	Pt Gage Reading (mm)	Depth Pt Gage (ft)	Gage Reading (ft)	Maximum Depth (ft)
0	0	30.5	0.100	0.900	0.000
0.5	0.5	30.5	0.100	0.900	0.000
1	0.5	31	0.102	0.898	0.002
1.5	0.5	31	0.102	0.898	0.002
2	0.5	31	0.102	0.898	0.002
3	1	31.5	0.103	0.897	0.003
4	1	31.5	0.103	0.897	0.003
5	1	32	0.105	0.895	0.005
6	1	32.5	0.107	0.893	0.007
7	1	33	0.108	0.892	0.008
8	1	33.5	0.110	0.890	0.010
9	1	33.5	0.110	0.890	0.010
10	1	33.5	0.110	0.890	0.010
12	2	34	0.112	0.888	0.011
14	2	34	0.112	0.888	0.011
16	2	34.5	0.113	0.887	0.013
18	2	35	0.115	0.885	0.015
20	2	35.5	0.116	0.884	0.016
22	2	36	0.118	0.882	0.018
24	2	36	0.118	0.882	0.018
26	2	36.5	0.120	0.880	0.020
28	2	37	0.121	0.879	0.021
30	2	37.5	0.123	0.877	0.023
32	2	37.5	0.123	0.877	0.023
34	2	37.5	0.123	0.877	0.023
39	5	38	0.125	0.875	0.025
44	5	39	0.128	0.872	0.028
49	5	40	0.131	0.869	0.031
54	5	41	0.135	0.865	0.034
59	5	41	0.135	0.865	0.034
64	5	41	0.135	0.865	0.034
69	5	41	0.135	0.865	0.034

Head S

Time (min)	Head (in)
0	45.1
0.5	45.1
1	45.1
1.5	45.1
2	45.1
3	45.1
4	45.1
5	45.1
6	45.1
7	45.1
8	45.1
9	45.1
10	45.1
12	45.1
14	45.1
16	45.1
18	45.1
20	45.1
22	45.1
24	45.1
26	45.1
28	45.1
30	45.1
32	45.1
34	45.1
39	45.1
44	45.1
49	45.1
54	45.1
59	45.1
64	45.1
69	45.1

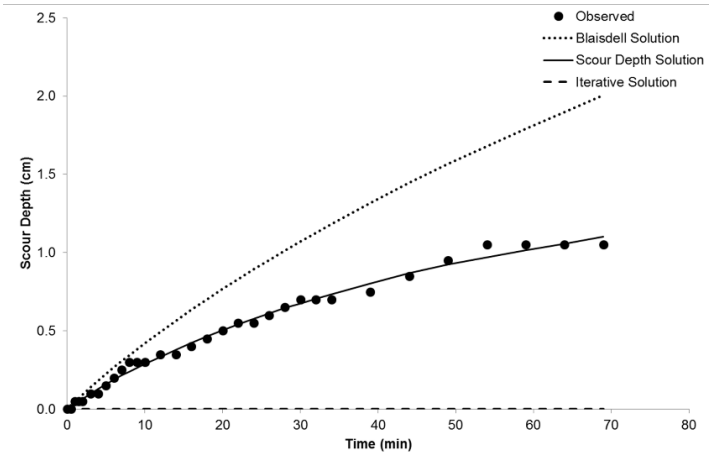

Figure A-63. GEER Sample #2

Silt Samples – JET

Site	M-20 Bridge on Titt
Date:	5/17/2017
Test #:	B-1 (23'-25')
JET #:	1
Operator:	Iman
Test Location	A&M Erosion L

Pt Gage Reading	4
Ref. Pt Gage Read	0n.g 8a6t 9N ozzle
Nozzle Diam	0.125
Nozzle He	0ig0h9 5(ft):

Initial gues	1
Initial gues	1

Scour Depth Readings						Head S	
Time (min)	Diff Time (min)	Point Gage Reading (mm)	Deepest Point Gage Reading (ft)	Maximum Depth (ft)		ST time (min)	Area (in)
0	0	33	0.108	0.892	0.000	0	45.0
0.25	0.25	33	0.108	0.892	0.000	0.25	45.0
0.5	0.25	33.5	0.110	0.890	0.002	0.5	45.0
1	0.5	34	0.112	0.888	0.003	1	45.0
1.5	0.5	34	0.112	0.888	0.003	1.5	45.0
2	0.5	34.5	0.113	0.887	0.005	2	45.0
3	1	35	0.115	0.885	0.007	3	45.0
4	1	35	0.115	0.885	0.007	4	45.0
5	1	35	0.115	0.885	0.007	5	45.0
7	2	36	0.118	0.882	0.010	7	45.0
9	2	36	0.118	0.882	0.010	9	45.0
11	2	37	0.121	0.879	0.013	11	45.0
13	2	37	0.121	0.879	0.013	13	45.0
15	2	37	0.121	0.879	0.013	15	45.0
17	2	37.5	0.123	0.877	0.015	17	45.0
20	3	38	0.125	0.875	0.016	20	45.0
23	3	38.5	0.126	0.874	0.018	23	45.0
26	3	38.5	0.126	0.874	0.018	26	45.0
31	5	40	0.131	0.869	0.023	31	45.0
36	5	41	0.135	0.865	0.026	36	45.0
41	5	42	0.138	0.862	0.030	41	45.0
46	5	43	0.141	0.859	0.033	46	45.0
51	5	44	0.144	0.856	0.036	51	45.0
56	5	44	0.144	0.856	0.036	56	45.0
61	5	45	0.148	0.852	0.039	61	45.0
66	5	45	0.148	0.852	0.039	66	45.0

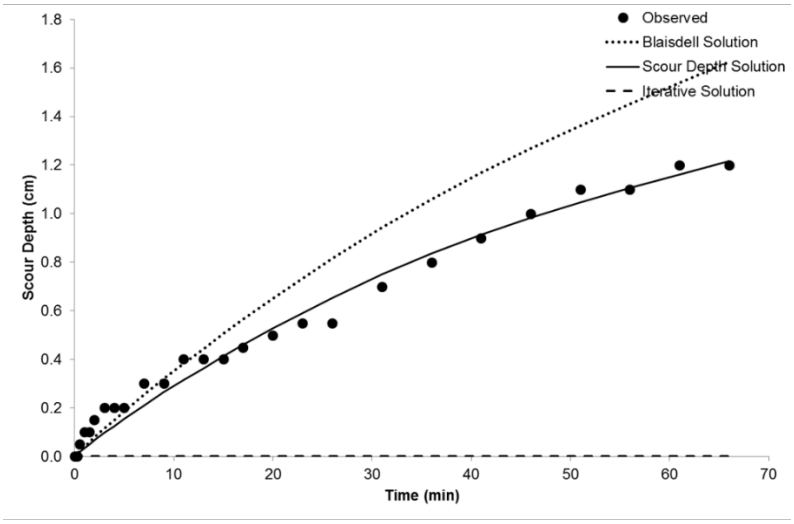

Figure A-64. B-1 (23'-25') Tittabawsee River

Site:	Baumont Formation
Date:	6/15/2017
Test #:	B-3 (8'-10') 548
JET #:	1
Operator:	Iman Shafii
Test Location	A&M Erosion Lab

Pt Gage Reading at N	4
Ref. Pt Gage Reading	0.986
Nozzle Diameter	0.125
Nozzle Height (ft):	0.0938

Initial guess (Pritchard)	1
Initial guess (Melville)	1

Scour Depth Readings

Time (min)	Diff Time (min)	Gage Reading (mm)	Depth (ft)	Gage Reading (ft)	Maximum Depth (ft)
0	0	32	0.105	0.895	0.000
0.25	0.25	34	0.112	0.888	0.007
0.5	0.25	36	0.118	0.882	0.013
0.75	0.25	38.5	0.126	0.874	0.021
1	0.25	40.5	0.133	0.867	0.028
1.5	0.5	41	0.135	0.865	0.030
2	0.5	43	0.141	0.859	0.036
2.5	0.5	46	0.151	0.849	0.046
3	0.5	48	0.157	0.843	0.052
3.5	0.5	49.5	0.162	0.838	0.057
4	0.5	51	0.167	0.833	0.062
4.5	0.5	51.5	0.169	0.831	0.064
5	0.5	52	0.171	0.829	0.066
6	1	53	0.174	0.826	0.069
7	1	54	0.177	0.823	0.072
8	1	55.5	0.182	0.818	0.077
9	1	57	0.187	0.813	0.082
10	1	58.5	0.192	0.808	0.087
11	1	59	0.194	0.806	0.089

Head S

Time (min)	Incremental Increa (in)
0	45.0
0.25	45.0
0.5	45.0
0.75	45.0
1	45.0
1.5	45.0
2	45.0
2.5	45.0
3	45.0
3.5	45.0
4	45.0
4.5	45.0
5	45.0
6	45.0
7	45.0
8	45.0
9	45.0
10	45.0
11	45.0

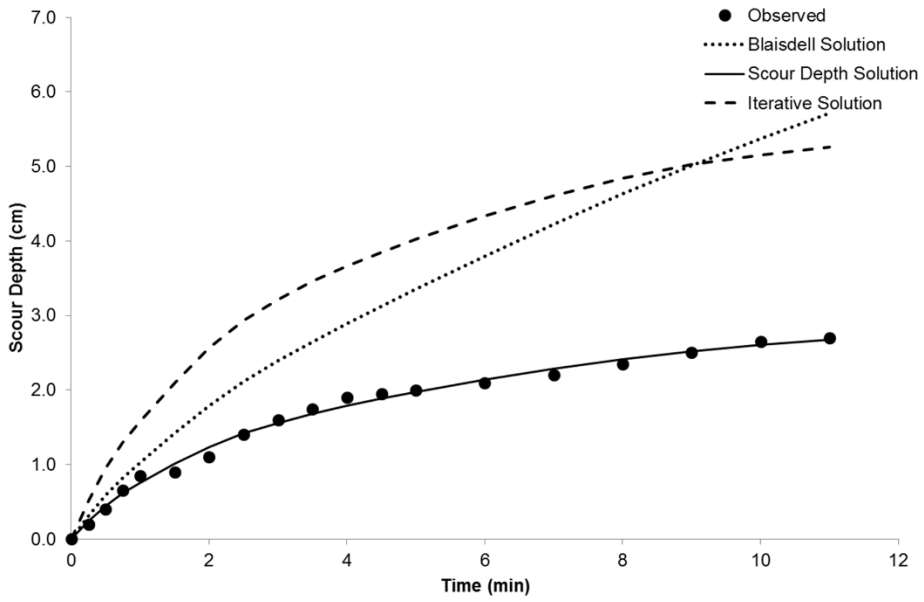

Figure A-65. B-3 (8'-10') Beaumont Formation

Site:	Tittabawsee Ri
Date:	6/9/2017
Test #:	B-7 (22'-24')
JET #:	1
Operator:	Iman Shafii
Test Location:	A&M Erosion L

Pt Gage Reading	4
Ref. Pt Gage Read	0.9 8 6 9
Nozzle Dia	0.1 2 5
Nozzle He	0 1 1 6

Nozzle

Initial gues	1
Initial gues	1

Scour Depth Readings						Head S
Time (min)	Diff Time (min)	Pnt Gage Read (mm)	Depth Pnt Gage (ft)	Gage Reading (ft)	Max Depth (ft)	ST Cum Head (min)
0	0	39.5	0.130	0.870	0.000	0
0.25	0.25	40	0.131	0.869	0.002	0.25
0.5	0.25	40.5	0.133	0.867	0.003	0.5
1	0.5	41	0.135	0.865	0.005	1
1.5	0.5	41.5	0.136	0.864	0.007	1.5
2	0.5	42	0.138	0.862	0.008	2
3	1	42	0.138	0.862	0.008	3
4	1	42.5	0.139	0.861	0.010	4
5	1	42.5	0.139	0.861	0.010	5
6	1	43	0.141	0.859	0.011	6
8	2	43.5	0.143	0.857	0.013	8
10	2	44	0.144	0.856	0.015	10
12	2	44	0.144	0.856	0.015	12
15	3	45	0.148	0.852	0.018	15
18	3	45	0.148	0.852	0.018	18
23	5	46	0.151	0.849	0.021	23
28	5	47.5	0.156	0.844	0.026	28
33	5	48	0.157	0.843	0.028	33
38	5	49	0.161	0.839	0.031	38
43	5	49.5	0.162	0.838	0.033	43
48	5	50	0.164	0.836	0.034	48
53	5	50.5	0.166	0.834	0.036	53
58	5	50.5	0.166	0.834	0.036	58

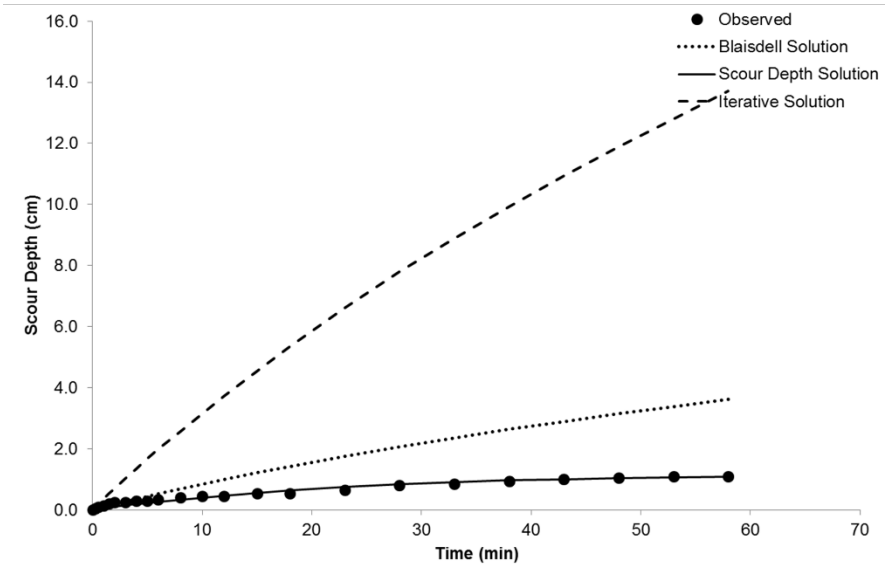

Figure A-66. B-7 (22'-24') Tittabawsee River

Site:	Tittabawsee Ri
Date:	5/10/2017
Test #:	B-9A (25-27)
JET #:	1
Operator:	Iman Shafii
Test Location:	A&M Erosion L

Pt Gage Reading at	4
Ref. Pt Gage Reading	0.98
Nozzle Diam	0.125
Nozzle Height (ft):	0.078

Initial guess (Pt gage)	1
Initial guess (scour)	1

Scour Depth Readings						Head S
Time (min)	Diff Time (min)	Pt Gage Reading (mm)	Deepest Pt gage Reading (ft)	Pt gage Reading (ft)	Maximum Depth (ft)	ST Time (min)
0	0	28	0.092	0.908	0.000	0
0.25	0.25	31	0.102	0.898	0.010	0.25
0.5	0.25	31	0.102	0.898	0.010	0.5
1	0.5	33	0.108	0.892	0.016	1
1.5	0.5	34	0.112	0.888	0.020	1.5
2	0.5	34.5	0.113	0.887	0.021	2
2.5	0.5	35	0.115	0.885	0.023	2.5
3	0.5	35	0.115	0.885	0.023	3
3.5	0.5	36	0.118	0.882	0.026	3.5
4	0.5	36.5	0.120	0.880	0.028	4
4.5	0.5	36.5	0.120	0.880	0.028	4.5
5.5	1	37	0.121	0.879	0.030	5.5
6	0.5	37	0.121	0.879	0.030	6
6.5	0.5	37	0.121	0.879	0.030	6.5
7	0.5	37.5	0.123	0.877	0.031	7
8	1	38	0.125	0.875	0.033	8
9	1	38	0.125	0.875	0.033	9
10	1	38.5	0.126	0.874	0.034	10
11	1	39.5	0.130	0.870	0.038	11
12	1	39.5	0.130	0.870	0.038	12
13	1	40	0.131	0.869	0.039	13
14	1	40.5	0.133	0.867	0.041	14
15	1	41	0.135	0.865	0.043	15
16	1	41	0.135	0.865	0.043	16
17	1	42	0.138	0.862	0.046	17
18	1	42	0.138	0.862	0.046	18
19	1	42.5	0.139	0.861	0.048	19
20	1	43	0.141	0.859	0.049	20
21	1	43	0.141	0.859	0.049	21
22	1	43.5	0.143	0.857	0.051	22
24	2	44	0.144	0.856	0.052	24
26	2	44	0.144	0.856	0.052	26
30	4	45	0.148	0.852	0.056	30
34	4	45	0.148	0.852	0.056	34
38	4	45.5	0.149	0.851	0.057	38
42	4	46	0.151	0.849	0.059	42
46	4	46	0.151	0.849	0.059	46

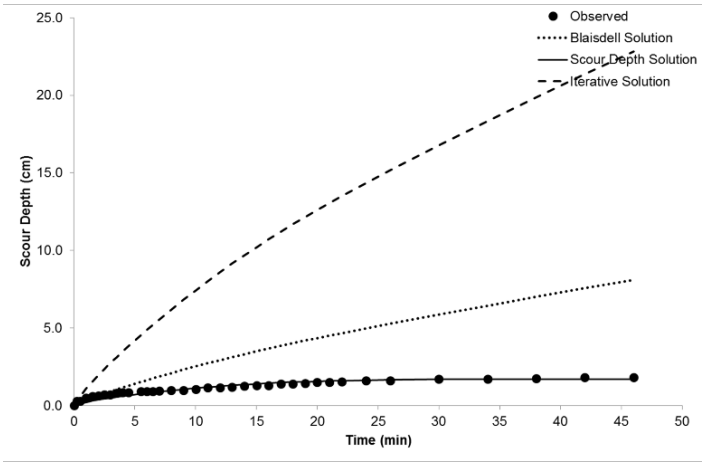

Figure A-67. B-9A (25'-27') Middle Tittabawsee River

Site:	Tittabawsee Ri
Date:	6/7/2017
Test #:	B-9A (25'-27') T
JET #:	1
Operator:	Iman Shafii
Test Location:	A&M Erosion L

Pt Gage Reading at N	4
Ref. Pt Gage Reading	0.98619 Nozzle
Nozzle Diam	0.125
Nozzle Height (ft):	0.0208

Initial guess (Pt Gage)	1
Initial guess (mm)	1

Scour Depth Readings						Head S	
Time (min)	Diff Time (min)	Pt Gage Reading (mm)	Depth Pt Gage (ft)	Gage Reading (ft)	Maximum Depth (ft)	Time (min)	Area (in)
0	0	31	0.102	0.898	0.000	0	45.0
0.25	0.25	31	0.102	0.898	0.000	0.25	45.0
0.5	0.25	31.5	0.103	0.897	0.002	0.5	45.0
1	0.5	31.5	0.103	0.897	0.002	1	45.0
2	1	32	0.105	0.895	0.003	2	45.0
3	1	32	0.105	0.895	0.003	3	45.0
4	1	32	0.105	0.895	0.003	4	45.0
6	2	32.5	0.107	0.893	0.005	6	45.0
8	2	33	0.108	0.892	0.007	8	45.0
10	2	33.5	0.110	0.890	0.008	10	45.0
12	2	33.5	0.110	0.890	0.008	12	45.0
14	2	34	0.112	0.888	0.010	14	45.0
16	2	34.5	0.113	0.887	0.011	16	45.0
18	2	35	0.115	0.885	0.013	18	45.0
20	2	35.5	0.116	0.884	0.015	20	45.0
22	2	36	0.118	0.882	0.016	22	45.0
24	2	37	0.121	0.879	0.020	24	45.0
27	3	37.5	0.123	0.877	0.021	27	45.0
30	3	38	0.125	0.875	0.023	30	45.0
33	3	38	0.125	0.875	0.023	33	45.0
38	5	38.5	0.126	0.874	0.025	38	45.0
43	5	40	0.131	0.869	0.030	43	45.0
48	5	40.5	0.133	0.867	0.031	48	45.0
53	5	40.5	0.133	0.867	0.031	53	45.0
58	5	40.5	0.133	0.867	0.031	58	45.0

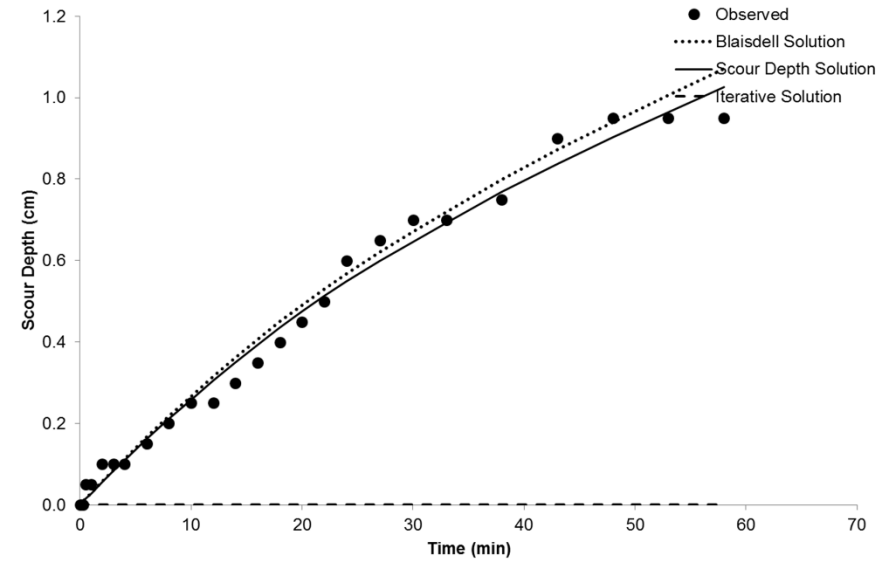

Figure A-68. B-9A (25'-27') Top Tittabawsee River

Site:	FHWA Erosion
Date:	7/27/2017
Test #:	Sample 2
JET #:	1
Operator:	Iman Shafii
Test Location	A&M Erosion L

Pt Gage Reading	4
Ref. Pt Gage Reading	0.9
Nozzle Diam	0.125
Nozzle Height (ft):	0.9

Initial guess (s*)	1
Initial guess (s=y/D)	1

Scour Depth Readings

Time (min)	Diff Time (min)	Pnt Gage Read (mm)	Depth Pnt Gage (ft)	Depth Pnt Gage (ft)	Max Scour Depth (ft)
0	0	34	0.112	0.888	0.000
0.25	0.25	34	0.112	0.888	0.000
0.5	0.25	34	0.112	0.888	0.000
1	0.5	35	0.115	0.885	0.003
2	1	36.5	0.120	0.880	0.008
3	1	37	0.121	0.879	0.010
4	1	37.5	0.123	0.877	0.011
5	1	39	0.128	0.872	0.016
6	1	40	0.131	0.869	0.020
7	1	40	0.131	0.869	0.020
8	1	40	0.131	0.869	0.020
10	2	41	0.135	0.865	0.023
12	2	42	0.138	0.862	0.026
14	2	43	0.141	0.859	0.030
16	2	44	0.144	0.856	0.033
18	2	45	0.148	0.852	0.036
20	2	45.5	0.149	0.851	0.038
22	2	46	0.151	0.849	0.039
24	2	47	0.154	0.846	0.043
26	2	47	0.154	0.846	0.043
31	5	48	0.157	0.843	0.046
36	5	50	0.164	0.836	0.052
41	5	51	0.167	0.833	0.056
46	5	52	0.171	0.829	0.059
51	5	53	0.174	0.826	0.062
56	5	54.5	0.179	0.821	0.067
61	5	55	0.180	0.820	0.069
66	5	56.5	0.185	0.815	0.074
71	5	57.5	0.189	0.811	0.077
76	5	58	0.190	0.810	0.079
81	5	58.5	0.192	0.808	0.080
86	5	59	0.194	0.806	0.082
91	5	59	0.194	0.806	0.082

Head S

STime (min)	Area (in)
0	45.0
0.25	45.0
0.5	45.0
1	45.0
2	45.0
3	45.0
4	45.0
5	45.0
6	45.0
7	45.0
8	45.0
10	45.0
12	45.0
14	45.0
16	45.0
18	45.0
20	45.0
22	45.0
24	45.0
26	45.0
31	45.0
36	45.0
41	45.0
46	45.0
51	45.0
56	45.0
61	45.0
66	45.0
71	45.0
76	45.0
81	45.0
86	45.0
91	45.0

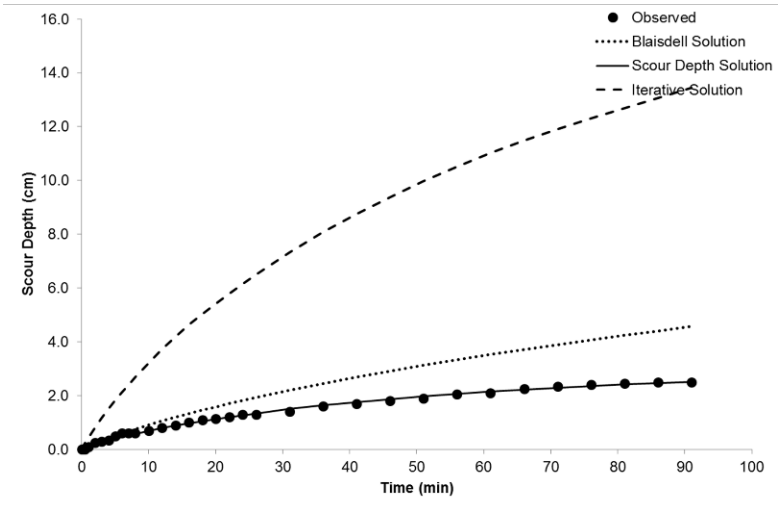

Figure A-69. FHWA Sample 2

Site:	Teton Dam
Date:	7/12/2017
Test #:	Left Core
JET #:	1
Operator:	Mabeland Ima
Test Lo: ation	A&M Erosion L

Pt Gage Reading	4
Ref. Pt Gage Read	0.98
Nozzle Diar	0.125
Nozzle He	0

Nozzle
ig 1h 1: 8 (ft):

Initial gues	1
Initial gues	1

Scour Depth Readings						Head S	
Time (min)	Diff Time (min)	Pnt Gage R (mm)	Dep Pnt (ft)	Gage Rea (ft)	Max Depth (ft)	STem (min)	Hea (in)
0	0	40	0.131	0.869	0.000	0	45.0
0.25	0.25	52	0.171	0.829	0.039	0.25	45.0
0.5	0.25	62	0.203	0.797	0.072	0.5	45.0
0.75	0.25	66	0.217	0.783	0.085	0.75	45.0
1	0.25	72	0.236	0.764	0.105	1	45.0
1.5	0.5	78	0.256	0.744	0.125	1.5	45.0
2	0.5	83	0.272	0.728	0.141	2	45.0
2.5	0.5	86	0.282	0.718	0.151	2.5	45.0
3	0.5	93	0.305	0.695	0.174	3	45.0
3.5	0.5	93	0.305	0.695	0.174	3.5	45.0
4	0.5	93	0.305	0.695	0.174	4	45.0
5	1	99	0.325	0.675	0.194	5	45.0
6	1	102	0.335	0.665	0.203	6	45.0
7.5	1.5	103	0.338	0.662	0.207	7.5	45.0
8	0.5	103	0.338	0.662	0.207	8	45.0
9	1	104	0.341	0.659	0.210	9	45.0
12	3	104	0.341	0.659	0.210	12	45.0
15	3	106	0.348	0.652	0.217	15	45.0
18	3	107	0.351	0.649	0.220	18	45.0
23	5	112	0.367	0.633	0.236	23	45.0
28	5	119	0.390	0.610	0.259	28	45.0

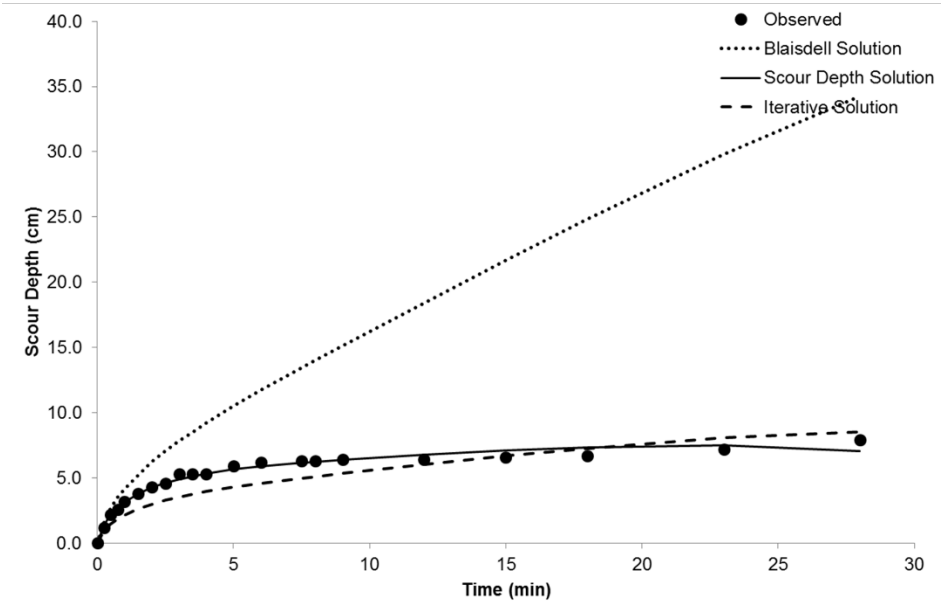

Figure A-70. Teton Dam Left Core

Sand Samples – JET

Site:	FHWA Erosion
Date:	11/16/2017
Test #:	Sand #1
JET #:	1
Operator:	Iman Shafii
Test Location	A&M Erosion L

Pt Gage Reading	4
Ref. Pt Gage Reading	0.98
Nozzle Dia	0.125
Nozzle Height	0.5

Initial guess (Pt Gage)	1
Initial guess (Scour)	1

Scour Depth Readings						Head S
Time (min)	Diff Time (min)	Gage Reading (mm)	Depth (ft)	Pt Gage Reading (ft)	Maximum Depth (ft)	ST (min)
0	0	45	0.148	0.852	0.000	0
0.25	0.25	46	0.151	0.849	0.003	0.25
0.5	0.25	47	0.154	0.846	0.007	0.5
0.75	0.25	48	0.157	0.843	0.010	0.75
1	0.25	48.5	0.159	0.841	0.011	1
1.5	0.5	50	0.164	0.836	0.016	1.5
2	0.5	51	0.167	0.833	0.020	2
2.5	0.5	53	0.174	0.826	0.026	2.5
3	0.5	54.5	0.179	0.821	0.031	3
3.5	0.5	56	0.184	0.816	0.036	3.5
4	0.5	58	0.190	0.810	0.043	4
4.5	0.5	60	0.197	0.803	0.049	4.5
5	0.5	62.5	0.205	0.795	0.057	5
5.5	0.5	64	0.210	0.790	0.062	5.5
6	0.5	65	0.213	0.787	0.066	6
6.5	0.5	66.5	0.218	0.782	0.071	6.5
7	0.5	68.5	0.225	0.775	0.077	7
7.5	0.5	70	0.230	0.770	0.082	7.5
8	0.5	71	0.233	0.767	0.085	8
8.5	0.5	72.5	0.238	0.762	0.090	8.5
9	0.5	74	0.243	0.757	0.095	9
9.5	0.5	75	0.246	0.754	0.098	9.5
10	0.5	76	0.249	0.751	0.102	10
10.5	0.5	77	0.253	0.747	0.105	10.5
11	0.5	78	0.256	0.744	0.108	11
11.5	0.5	78.5	0.258	0.742	0.110	11.5
12	0.5	78.5	0.258	0.742	0.110	12
12.5	0.5	79	0.259	0.741	0.112	12.5
13	0.5	80	0.262	0.738	0.115	13
13.5	0.5	80.5	0.264	0.736	0.116	13.5
14	0.5	80.5	0.264	0.736	0.116	14
14.5	0.5	80.5	0.264	0.736	0.116	14.5
15	0.5	81.5	0.267	0.733	0.120	15
15.5	0.5	82.5	0.271	0.729	0.123	15.5
16	0.5	83.5	0.274	0.726	0.126	16
16.5	0.5	84	0.276	0.724	0.128	16.5
17	0.5	85	0.279	0.721	0.131	17
17.5	0.5	85	0.279	0.721	0.131	17.5
18	0.5	85.5	0.281	0.719	0.133	18
18.5	0.5	85.5	0.281	0.719	0.133	18.5
19	0.5	85.5	0.281	0.719	0.133	19
20	1	86	0.282	0.718	0.135	20
21	1	86	0.282	0.718	0.135	21

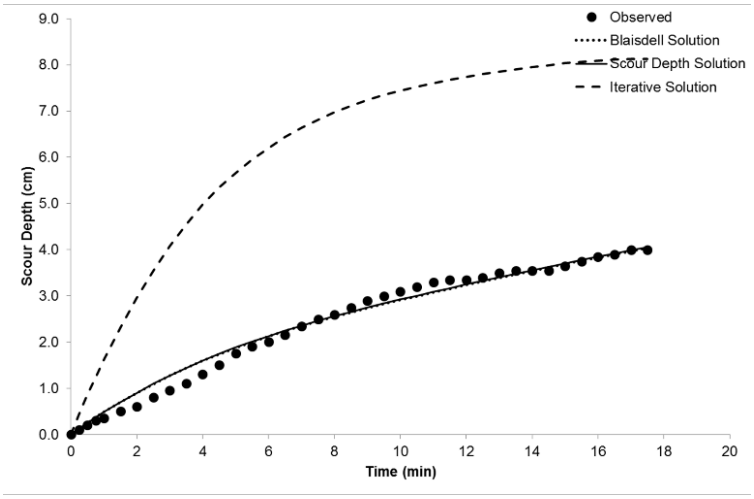

Figure A-71. Sand #1

Site:	FHWA Erosion
Date:	11/16/2017
Test #:	Sand #2
JET #:	1
Operator:	Iman Shafii
Test Location:	A&M Erosion L

Pt Gage Reading	4
Ref. Pt Gage Reading	0.988
Nozzle Dia:	0.125
Nozzle Height (ft):	0.104

Initial guess (d_c) (ft):	1
Initial guess (d_{ss}) (ft):	1

Scour Depth Readings						Head S
Time (min)	Diff Time (min)	Point Gage Reading (mm)	Deepest Point Gage Reading (ft)	Maximum Depth (ft)		ST Time (min)
0	0	34.5	0.113	0.887	0.000	0
0.5	0.5	35	0.115	0.885	0.002	0.5
1	0.5	36	0.118	0.882	0.005	1
1.5	0.5	37	0.121	0.879	0.008	1.5
2	0.5	38	0.125	0.875	0.011	2
2.5	0.5	38	0.125	0.875	0.011	2.5
3	0.5	39	0.128	0.872	0.015	3
3.5	0.5	39	0.128	0.872	0.015	3.5
4	0.5	39	0.128	0.872	0.015	4
5	1	40	0.131	0.869	0.018	5
6	1	40.5	0.133	0.867	0.020	6
7	1	41	0.135	0.865	0.021	7
8	1	42	0.138	0.862	0.025	8
9	1	42	0.138	0.862	0.025	9
10	1	43	0.141	0.859	0.028	10
11	1	43.5	0.143	0.857	0.030	11
12	1	45	0.148	0.852	0.034	12
13	1	45.5	0.149	0.851	0.036	13
14	1	46.5	0.153	0.847	0.039	14
15	1	47.5	0.156	0.844	0.043	15
16	1	47.5	0.156	0.844	0.043	16
17	1	48	0.157	0.843	0.044	17
18	1	48.5	0.159	0.841	0.046	18
19	1	49.5	0.162	0.838	0.049	19
20	1	50	0.164	0.836	0.051	20
21	1	50.5	0.166	0.834	0.052	21
22	1	51	0.167	0.833	0.054	22
23	1	51	0.167	0.833	0.054	23
24	1	52	0.171	0.829	0.057	24
26	2	53	0.174	0.826	0.061	26
28	2	53.5	0.176	0.824	0.062	28
30	2	54	0.177	0.823	0.064	30
32	2	55	0.180	0.820	0.067	32
34	2	55	0.180	0.820	0.067	34
36	2	56	0.184	0.816	0.071	36
38	2	56	0.184	0.816	0.071	38
40	2	57	0.187	0.813	0.074	40
42	2	57.5	0.189	0.811	0.075	42
44	2	58	0.190	0.810	0.077	44
46	2	58.5	0.192	0.808	0.079	46
48	2	59	0.194	0.806	0.080	48
50	2	59	0.194	0.806	0.080	50
52	2	60	0.197	0.803	0.084	52

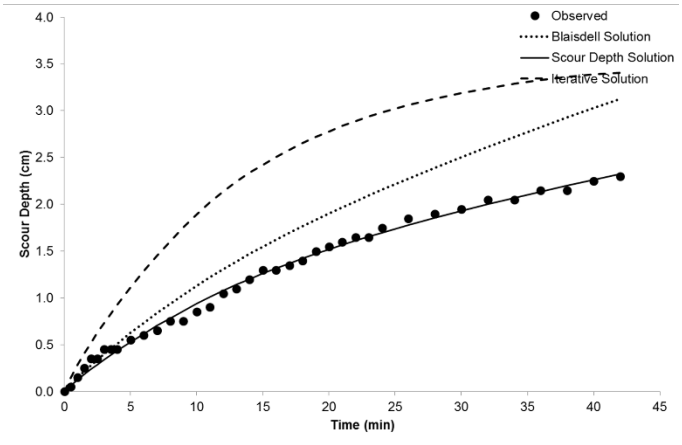

Figure A-72. Sand #2

Site:	Man-made at A&
Date:	7/28/2017
Test #:	S-0-0-0
JET #:	1
Operator:	Iman Shafii
Test Location:	A&M Erosion L

Pt Gage Reading at N	4
Ref. Pt Gage Reading at Nozzle	0.9869
Nozzle Diameter	0.125
Nozzle Height (ft):	0.1411

Initial guess τ_c (Pa) for	1
Initial guess k_d (cm³/N-s) for	1

Scour Depth Readings					
Time (min)	Diff Time (min)	Pt Gage Reading (mm)	Depth (ft)	Pt Gage Reading (ft)	Maximum Depth (ft)
0	0	47	0.154	0.846	0.000
0.25	0.25	48	0.157	0.843	0.003
0.5	0.25	48	0.157	0.843	0.003
1	0.5	48	0.157	0.843	0.003
2	1	49	0.161	0.839	0.007
3	1	50	0.164	0.836	0.010
4	1	50.5	0.166	0.834	0.011
5	1	51	0.167	0.833	0.013
6	1	52	0.171	0.829	0.016
7	1	52	0.171	0.829	0.016
9	2	54	0.177	0.823	0.023
11	2	54.5	0.179	0.821	0.025
13	2	55.5	0.182	0.818	0.028
15	2	57	0.187	0.813	0.033
17	2	58	0.190	0.810	0.036
19	2	58	0.190	0.810	0.036
24	5	60	0.197	0.803	0.043
29	5	61.5	0.202	0.798	0.048
34	5	62.5	0.205	0.795	0.051
39	5	63.5	0.208	0.792	0.054
44	5	65	0.213	0.787	0.059
49	5	67	0.220	0.780	0.066
54	5	69	0.226	0.774	0.072
59	5	72	0.236	0.764	0.082
64	5	72	0.236	0.764	0.082

Head S	
Time (min)	Head (in)
0	45.1
0.25	45.1
0.5	45.1
1	45.1
2	45.1
3	45.1
4	45.1
5	45.1
6	45.1
7	45.1
9	45.1
11	45.1
13	45.1
15	45.1
17	45.1
19	45.1
24	45.1
29	45.1
34	45.1
39	45.1
44	45.1
49	45.1
54	45.1
59	45.1
64	45.1

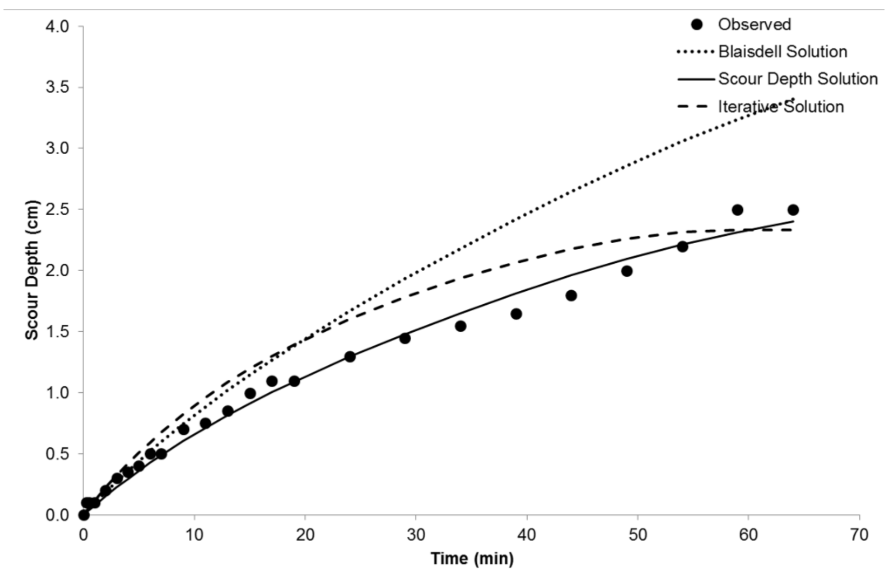

Figure A-73. S-0-0-0

Site:	Lissie Formatio
Date:	6/6/2017
Test #:	B-3 (10'-12')
JET #:	1
Operator:	Iman Shafii
Test Location:	A&M Erosion L

Pt Gage Reading at Nozzle	4
Ref. Pt Gage Reading at Nozzle	0.9869
Nozzle Diameter	0.125
Nozzle Height (ft):	0.984

Initial guess (τ_c) (Pa)	1
Initial guess (k_d) (cm^3/N-s)	1

Scour Depth Readings					
Time (min)	Diff Time (min)	Pt Gage Reading (mm)	Depth (ft)	Pt Gage Reading (ft)	Maximum Depth (ft)
0	0	34	0.112	0.888	0.000
0.25	0.25	35	0.115	0.885	0.003
0.5	0.25	36	0.118	0.882	0.007
1	0.5	39	0.128	0.872	0.016
1.5	0.5	40	0.131	0.869	0.020
2	0.5	41	0.135	0.865	0.023
2.5	0.5	42	0.138	0.862	0.026
3	0.5	42.5	0.139	0.861	0.028
3.5	0.5	43	0.141	0.859	0.030
4	0.5	43.5	0.143	0.857	0.031
4.5	0.5	43.5	0.143	0.857	0.031
5	0.5	44	0.144	0.856	0.033
6	1	44.5	0.146	0.854	0.034
7	1	45.5	0.149	0.851	0.038
8	1	46	0.151	0.849	0.039
10	2	49	0.161	0.839	0.049
11	1	49.5	0.162	0.838	0.051
12	1	50	0.164	0.836	0.052
13	1	51	0.167	0.833	0.056
14	1	51	0.167	0.833	0.056
16	2	52	0.171	0.829	0.059
18	2	55	0.180	0.820	0.069
20	2	57	0.187	0.813	0.075
22	2	58	0.190	0.810	0.079
24	2	60	0.197	0.803	0.085
26	2	60	0.197	0.803	0.085
29	3	61	0.200	0.800	0.089
32	3	62	0.203	0.797	0.092
35	3	64	0.210	0.790	0.098
38	3	65	0.213	0.787	0.102
41	3	65	0.213	0.787	0.102
46	5	65	0.213	0.787	0.102

Head S	
Time (min)	Head (in)
0	45.0
0.25	45.0
0.5	45.0
1	45.0
1.5	45.0
2	45.0
2.5	45.0
3	45.0
3.5	45.0
4	45.0
4.5	45.0
5	45.0
6	45.0
7	45.0
8	45.0
10	45.0
11	45.0
12	45.0
13	45.0
14	45.0
16	45.0
18	45.0
20	45.0
22	45.0
24	45.0
26	45.0
29	45.0
32	45.0
35	45.0
38	45.0
41	45.0
46	45.0

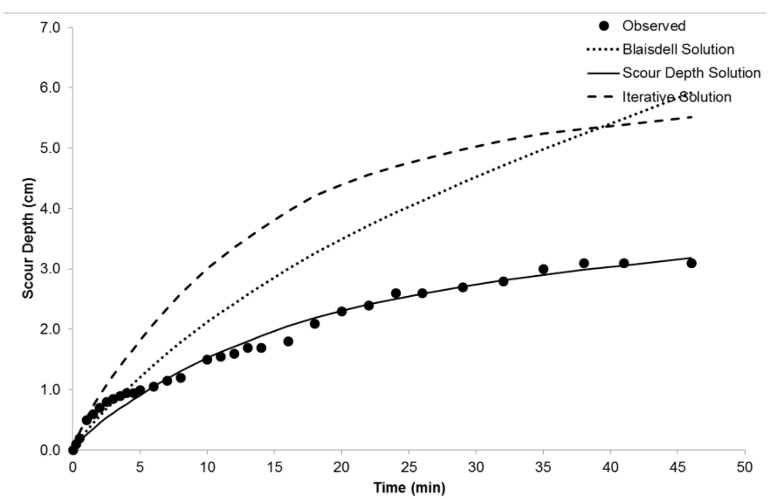

Figure A-74. B-3 (10’-12’) Lissie Formation

Clay Samples – HET

Time	Time	Flow rate		U/S Tube Pressure	D/S Tube Pressure			Sample length	Gradient	Flow rate	Friction Factor		Hole diameter		Reynold's No.		Diameter
											If Laminar	If Turbulent	If Laminar	If Turbulent	If Laminar	If Turbulent	
(mins)	(s)	(gpm)	(l/min)	(in)	(in)	(in)	(mm)	L (mm)	S	Q (m^3/s)	$f_{\bar{D}}$	f_P	$D_{\bar{D}}$	D_P	Re(l)	Re(t)	D (m)
0.00	0	0.86	3.26	23.5	5.0	18.5	470	115	4.086	5.64925578E-05	3015.272	16.2963	0.006000	0.006000	101015	9.185159	0.18050 6
0.50	30	0.86	3.26	23.5	5.0	18.5	470	115	4.086	5.64925578E-05	30.52171E+00	1.091270E+00	0.006180	2.700620	140682	9.412079	1.26000 6 2 0 4
1.00	60	0.92	3.48	23.5	5.0	18.5	470	115	4.086	5.68905473E-05	30.31611E+00	2.021245E+00	0.010649	9.700655	191801	9.160918	9.10306559
2.00	120	0.92	3.48	23.5	5.0	18.5	470	115	4.086	5.68905473E-05	40.35051E+00	2.081193E+00	0.010682	6.400687	180249	2.074139	4.90706878
3.00	180	0.92	3.48	23.5	5.0	18.5	470	115	4.086	5.68905473E-05	40.89406E+00	3.041141E+00	0.010712	4.400714	160705	3.130222	3.30607146
4.00	240	1.08	4.09	23.5	5.0	18.5	470	115	4.086	6.68915377E-05	50.48292E+00	4.001089E+00	0.010780	5.700786	180877	2.120485	6.30307868
5.00	300	1.11	4.20	24.0	5.0	19.0	483	115	4.196	5.21703390E-05	60.67191E+00	4.061037E+00	0.010807	7.700813	150269	8.455222	8.10108135
6.00	360	1.27	4.81	24.5	5.0	19.5	495	115	4.306	5.86512225E-05	60.66608E+00	5.011986E+00	0.010863	8.200875	111044	6.315298	7.30008751
8.00	480	1.37	5.19	24.5	5.0	19.5	495	115	4.306	5.86542324E-05	70.83887E+00	6.031882E+00	0.010935	8.300939	119194	0.314636	9.80909399
9.00	540	1.46	5.53	25.0	5.0	20.0	508	115	4.417	5.91231014E-05	80.52766E+00	6.091830E+00	0.010970	5.100976	151971	2.212363	9.28000976
10.00	600	1.49	5.64	25.0	5.0	20.0	508	115	4.417	5.91430044E-05	90.61655E+00	7.051778E+00	0.010999	3.601000	181060	7.196591	1.02910007
11.00	660	1.52	5.75	25.0	5.0	20.0	508	115	4.417	5.91538094E-05	90.60555E+00	8.011727E+00	0.011027	4.701024	111754	7.319254	6.40310241
12.00	720	1.59	6.02	25.0	5.0	20.0	508	115	4.417	5.91030341E-05	100.4194E+00	8.072675E+00	0.011063	9.001057	151463	5.414570	5.40031057
14.00	840	1.74	6.59	25.0	5.0	20.0	508	115	4.417	5.91039748E-05	100.4372E+00	9.092571E+00	0.011137	0.501124	161391	3.915204	5.92081124
17.00	1020	2.32	8.78	25.0	5.0	20.0	508	115	4.417	5.91436347E-05	100.3139E+00	1.012742E+00	0.021313	2.001304	103875	4.433850	6.60113040
18.00	1080	2.66	10.07	26.0	5.0	21.0	533	115	4.638	6.06877822E-05	100.3728E+00	1.022336E+00	0.021372	1.901377	155709	2.155033	2.20613775
19.00	1140	2.92	11.05	26.0	5.2	20.8	528	115	4.594	6.68945272E-05	100.4317E+00	1.022931E+00	0.021440	0.601446	125378	6.315597	1.23081446
20.00	1200	3.13	11.85	26.0	5.5	20.5	521	115	4.527	8.69078477E-05	100.4906E+00	1.032526E+00	0.021500	9.701505	176723	5.118919	4.20815047
21.00	1260	3.33	12.61	26.0	6.0	20.0	508	115	4.417	9.21130049E-05	100.5495E+00	1.042121E+00	0.021565	0.301563	156556	5.317658	1.25021563
22.00	1320	3.6	13.63	26.0	6.5	19.5	495	115	4.306	9.26257212E-05	100.6084E+00	1.042716E+00	0.021640	1.201634	177008	8.316731	4.66916347
23.00	1380	3.92	14.84	26.0	6.8	19.2	488	115	4.240	6.92546753 21	100.6673E+00	1.052311E+00	0.021716	0.401711	117079	4.157846	4.10617100
24.00	1440	4.28	16.20	26.0	7.0	19.0	483	115	4.196	5.21770393 E-05	100.7262E+00	1.052905E+00	0.021794	0.801788	158657	0.115630	9.40317885
25.00	1500	4.76	18.02	26.0	7.0	19.0	483	115	4.196	5.21703391 E-05	100.7851E+00	1.062500E+00	0.021880	0.001880	109071	2.116977	1.06071880

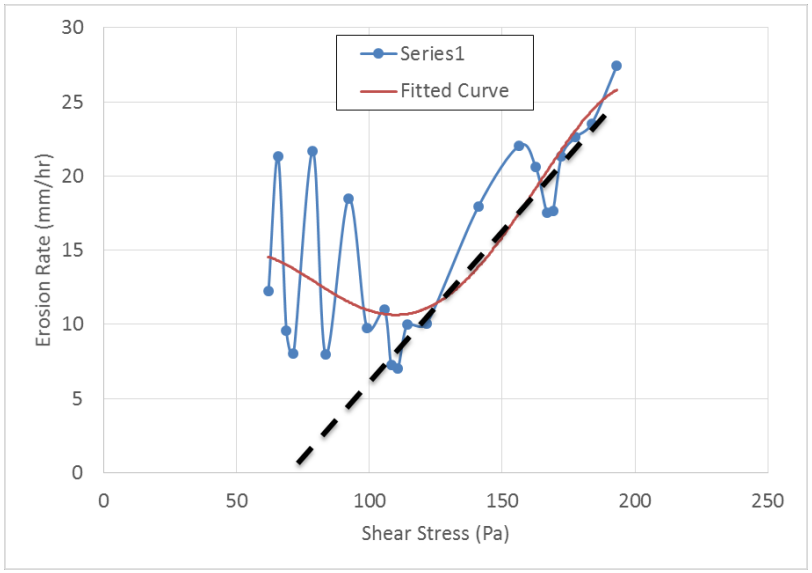

Figure A-75. Clay #1

Time	Time	Flow rate		U/S Tube Pressure	D/S Tube Pressure		Sample length	Gradient	Flow rate	Friction Factor		Hole diameter		Reynold's No.		Diameter
										If Laminar	If Turbulent	If Laminar	If Turbulent	If Laminar	If Turbulent	
(mins)	(s)	(gpm)	(l/min)	in	in	(in)	(mm)	L (mm)	S	Q (m3/s)	$f_{\bar{D}}$	f_P	$D_{\bar{D}}$	D_P	Re(l)	Re(t)	D (m)
0.00	0	1.08	4.09	26.0	5.0	21.0	533	115	4.638	6.088E-07	-2085.267	11.7297	0.00600	0.00600	1040.013	1640.013	0.00600
0.50	30	1.19	4.50	26.5	5.0	21.5	546	115	4.748	7.556E-07	-30.6003	1.03103	0.00627	0.00634	1741.771	1435.961	0.00906
1.00	60	1.24	4.69	26.5	5.0	21.5	546	115	4.748	7.586E-07	-30.5738	1.04147	0.00647	0.00658	1244.900	1435.661	0.00906
2.00	120	1.24	4.69	27.0	5.0	22.0	559	115	4.859	7.084E-07	-30.5209	1.07122	0.00665	0.00678	1440.504	1462.301	0.01000
3.00	180	1.27	4.81	27.0	5.0	22.0	559	115	4.859	7.004E-07	-30.8681	1.09197	0.00692	0.00705	1449.282	1462.301	0.01000
4.00	240	1.30	4.92	27.5	5.0	22.5	572	115	4.969	6.522E-07	-40.2152	1.02172	0.00710	0.00727	1443.203	1034.913	0.00940
5.00	300	1.36	5.15	27.8	5.0	22.8	578	115	5.024	8.256E-07	-40.5623	1.05146	0.00740	0.00756	1141.308	2184.903	0.00803
6.00	360	1.39	5.26	27.5	5.0	22.5	572	115	4.969	6.572E-07	-40.9094	1.08121	0.00766	0.00780	1245.115	2195.869	0.00650
8.00	480	1.65	6.25	27.5	6.0	21.5	546	115	4.748	9.506E-07	-60.4036	3.03171	0.00861	0.00873	1843.914	4642.700	0.00508
10.00	600	2.03	7.68	27.5	6.5	21.0	533	115	4.638	1.602E-06	-60.4979	3.09120	0.00967	0.00983	1069.341	8155.076	0.01070
12.00	720	2.41	9.12	27.5	6.5	21.0	533	115	4.638	1.905E-06	-60.8921	4.04170	0.01060	0.01080	1972.694	7713.583	0.00501
14.00	840	2.82	10.67	27.5	6.5	21.0	533	115	4.638	2.078E-06	-70.4863	5.00119	0.01153	0.01178	1093.038	2195.937	0.00403
16.00	960	3.33	12.61	27.5	6.5	21.0	533	115	4.638	2.018E-06	-80.3806	5.05169	0.01254	0.01285	2406.652	2207.168	0.00601
18.00	1080	3.96	14.99	27.5	7.5	20.0	508	115	4.417	2.143E-06	-90.0748	6.01118	0.01387	0.01417	2626.224	2417.477	0.00910
20.00	1200	4.38	16.58	27.5	8.0	19.5	495	115	4.306	2.676E-06	-90.7690	6.06168	0.01482	0.01509	2222.997	2625.794	0.00602
22.00	1320	4.76	18.02	27.5	8.5	19.0	483	115	4.196	2.107E-06	-100.463	7.02216	0.01573	0.01593	2435.532	2612.566	0.00602
24.00	1440	5.01	18.96	27.3	8.5	18.8	476	115	4.141	2.041E-06	-100.158	7.07267	0.01642	0.01654	2834.750	2935.704	0.00306
26.00	1560	5.3	20.06	28.0	9.0	19.0	483	115	4.196	2.137E-06	-100.485	8.03216	0.01699	0.01711	2247.273	2341.122	0.00681
28.00	1680	5.55	21.01	28.0	9.5	18.5	470	115	4.086	3.659E-06	-102.455	8.08266	0.01775	0.01775	2040.343	3224.543	0.00205

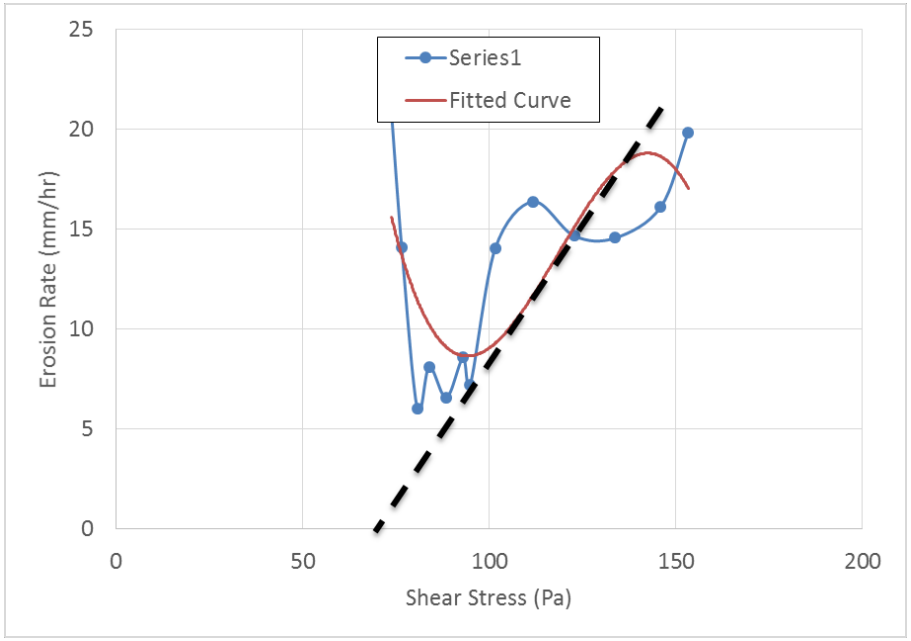

Figure A-76. Clay #2

Time	Time	Flow rate		U/S Tube Pressure Di	Db/S Tube Pressure Di			Sample length	Gradient	Flow rate	Friction Factor		Hole diameter		Reynold's No.		Diamete
											If Laminar	If Turbulent	If Laminar	If Turbulent	If Laminar	If Turbulent	
(mins)	(s)	(gpm)	(l/min)	in	in	(in)	(mm)	L (mm)	S	Q (m3/s)	$f_{\bar{D}}$	f_p	$D_{\bar{D}}$	D_p	Re(l)	Re(t)	D (m)
0.00	0	0.70	2.65	26.0	5.0	21.0	533	115	4.63826	4.04817E-03	4035.61200	27.92150	0.00600	0.00600	90008.309	97083.009	0.07006
1.00	60	0.98	3.71	29.0	5.0	24.0	610	115	5.30088	6.91586E-03	50.63888E-3	3.05137E-02	0.00106	0.00700	161732.5	172789.2	0.07007006
2.00	120	1.01	3.82	29.5	5.0	24.5	622	115	5.41136	6.43374E-03	50.31164E-3	4.02179E-02	0.00107	0.00703	171315.6	170971.6	0.06030733
3.00	180	1.11	4.20	30.0	5.0	25.0	635	115	5.52173	7.90103E-03	60.59411E-3	5.00129E-02	0.00107	0.00783	161152.2	191202.8	0.06070783
4.00	240	1.17	4.43	30.0	5.0	25.0	635	115	5.52173	7.93183E-03	70.67117E-3	5.07165E-02	0.00107	0.00783	161952.4	0.0	0.07008226
5.00	300	1.30	4.92	30.3	5.0	25.3	641	115	5.57692	8.62502E-03	70.53493E-3	6.05110E-02	0.00108	0.00877	142304.8	215153.4	0.07040877
6.00	360	1.40	5.30	31.0	5.5	25.5	648	115	5.63217	8.38931E-03	80.52269E-3	7.02153E-02	0.00108	0.00921	172735.0	211283.4	0.08060921
8.00	480	1.65	6.25	31.0	6.8	24.3	616	115	5.35608	8.60945E-03	90.47822E-3	8.07140E-02	0.00109	0.01032	211228.9	218264.6	0.09031032
10.00	600	2.25	8.52	31.0	7.0	24.0	610	115	5.30088	6.94516E-03	10.41137E-3	1.00228E-02	0.00215	0.01208	125513.1	184149.8	0.05021208
12.00	720	2.89	10.94	31.0	8.0	23.0	584	115	5.08	1.82336E-02	10.24936E-3	1.01271E-02	0.00213	0.01383	196996.6	216425.7	0.07091383
14.00	840	3.62	13.70	31.0	10.0	21.0	533	115	4.63826	2.02887E-02	10.43848E-3	1.03220E-02	0.00215	0.01579	158748.0	177583.4	0.06011579
16.00	960	4.19	15.86	31.0	12.5	18.5	470	115	4.08602	2.66945E-02	10.52036E-3	1.04269E-02	0.00217	0.01754	178893.1	178458.9	0.07017547
18.00	1080	4.60	17.41	29.5	13.0	16.5	419	115	3.64433	2.79802E-02	10.65588E-3	1.06217E-02	0.00219	0.01900	108084.9	151849.0	0.0501 19

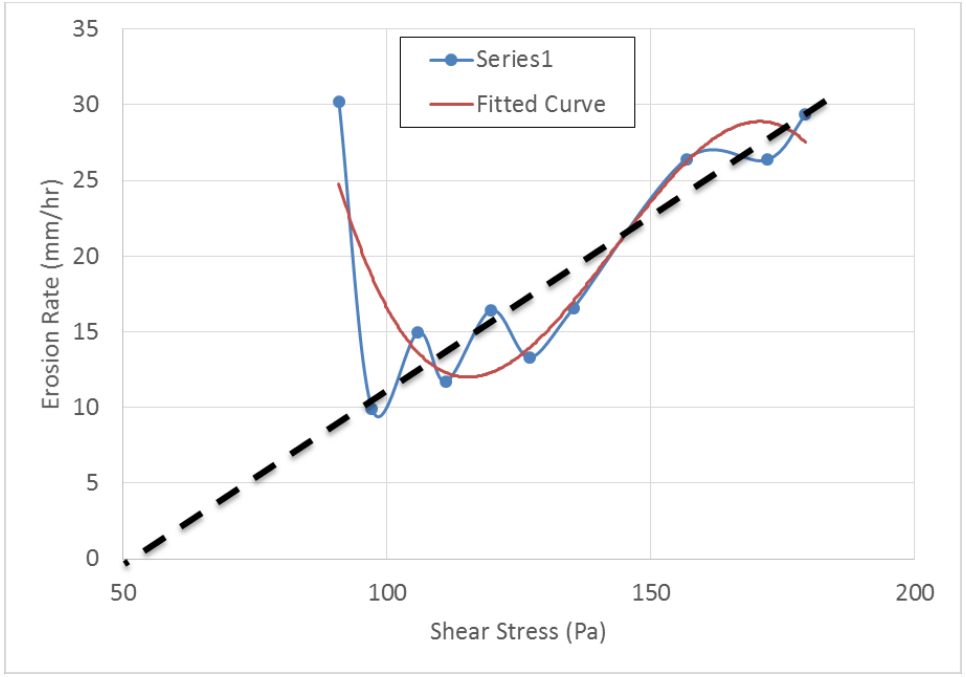

Figure A-77. Clay #3

Time	Time	Flowrate		U/S Tube	D/S Tube	Pressure Di	
(mins)	(s)	(gpm)	(l/min)	in	in	(in)	(mm)
0.00	0	0.73	2.76	12.0	5.0	7.0	178
1.00	60	0.76	2.88	12.8	5.0	7.8	197
3.00	180	0.82	3.10	12.8	5.0	7.8	197
5.00	300	0.89	3.37	13.5	5.0	8.5	216
7.00	420	1.05	3.97	14.3	5.0	9.3	235
9.00	540	1.14	4.32	14.5	5.3	9.3	235
11.00	660	1.33	5.03	15.0	6.0	9.0	229
13.00	780	1.43	5.41	15.0	6.5	8.5	216
15.00	900	1.62	6.13	15.5	7.0	8.5	216
17.00	1020	1.81	6.85	16.5	7.5	9.0	229
19.00	1140	2.06	7.80	17.0	7.5	9.5	241
21.00	1260	2.15	8.14	17.0	7.5	9.5	241
23.00	1380	2.32	8.78	17.0	7.5	9.5	241
25.00	1500	2.51	9.50	17	7.5	9.5	241.3
27.00	1620	2.73	10.33	17	7.25	9.75	247.65
29.00	1740	2.9	10.98	17	7.25	9.75	247.65
31.00	1860	2.95	11.17	17	7.25	9.75	247.65
33.00	1980	3.11	11.77	17.25	9.5	7.75	196.85
36.00	2160	3.29	12.45	17.25	10	7.25	184.15
39.00	2340	3.46	13.10	17.25	10.5	6.75	171.45
42.00	2520	3.55	13.44	17.25	10.5	6.75	171.45
45.00	2700	3.68	13.93	17	11.25	5.75	146.05
48.00	2880	3.96	14.99	17.25	12	5.25	133.35

Sample length	Gradient	Flow rate	Friction Factor		Hole diameter		Reynold's No.		Diameter
			If Laminar	If Turbulent	If Laminar	If Turbulent	If Laminar	If Turbulent	Turbulent
L (mm)	S	Q (m3/s)	$f_{\tilde{O}}$	f_P	$D_{\tilde{O}}$	D_P	Re(l)	Re(t)	D (m)
115	1.5460	[illegible]	[illegible]	12.7696	0.00650	[illegible]	[illegible]	[illegible]	[illegible]
115	1.7117	[illegible]	[illegible]	[illegible]	[illegible]	[illegible]	[illegible]	[illegible]	[illegible]
115	1.7117	[illegible]	[illegible]	[illegible]	[illegible]	[illegible]	[illegible]	[illegible]	[illegible]
115	1.8773	[illegible]	[illegible]	[illegible]	[illegible]	[illegible]	[illegible]	[illegible]	[illegible]
115	2.0430	[illegible]	[illegible]	[illegible]	[illegible]	[illegible]	[illegible]	[illegible]	[illegible]
115	2.0430	[illegible]	[illegible]	[illegible]	[illegible]	[illegible]	[illegible]	[illegible]	[illegible]
115	1.9878	[illegible]	[illegible]	[illegible]	[illegible]	[illegible]	[illegible]	[illegible]	[illegible]
115	1.8773	[illegible]	[illegible]	[illegible]	[illegible]	[illegible]	[illegible]	[illegible]	[illegible]
115	1.8773	[illegible]	[illegible]	[illegible]	[illegible]	[illegible]	[illegible]	[illegible]	[illegible]
115	1.9878	[illegible]	[illegible]	[illegible]	[illegible]	[illegible]	[illegible]	[illegible]	[illegible]
115	2.0982	[illegible]	[illegible]	[illegible]	[illegible]	[illegible]	[illegible]	[illegible]	[illegible]
115	2.0982	[illegible]	[illegible]	[illegible]	[illegible]	[illegible]	[illegible]	[illegible]	[illegible]
115	2.0982	[illegible]	[illegible]	[illegible]	[illegible]	[illegible]	[illegible]	[illegible]	[illegible]
115	2.0982	[illegible]	[illegible]	[illegible]	[illegible]	[illegible]	[illegible]	[illegible]	[illegible]
115	2.1534	[illegible]	[illegible]	[illegible]	[illegible]	[illegible]	[illegible]	[illegible]	[illegible]
115	2.1534	[illegible]	[illegible]	[illegible]	[illegible]	[illegible]	[illegible]	[illegible]	[illegible]
115	2.1534	[illegible]	[illegible]	[illegible]	[illegible]	[illegible]	[illegible]	[illegible]	[illegible]
115	1.7117	[illegible]	[illegible]	[illegible]	[illegible]	[illegible]	[illegible]	[illegible]	[illegible]
115	1.6013	[illegible]	[illegible]	[illegible]	[illegible]	[illegible]	[illegible]	[illegible]	[illegible]
115	1.4908	[illegible]	[illegible]	[illegible]	[illegible]	[illegible]	[illegible]	[illegible]	[illegible]
115	1.4908	[illegible]	[illegible]	[illegible]	[illegible]	[illegible]	[illegible]	[illegible]	[illegible]
115	1.27	[illegible]	[illegible]	[illegible]	[illegible]	[illegible]	[illegible]	[illegible]	[illegible]
115	1.1595	[illegible]	[illegible]	[illegible]	[illegible]	0.0192	[illegible]	[illegible]	[illegible]

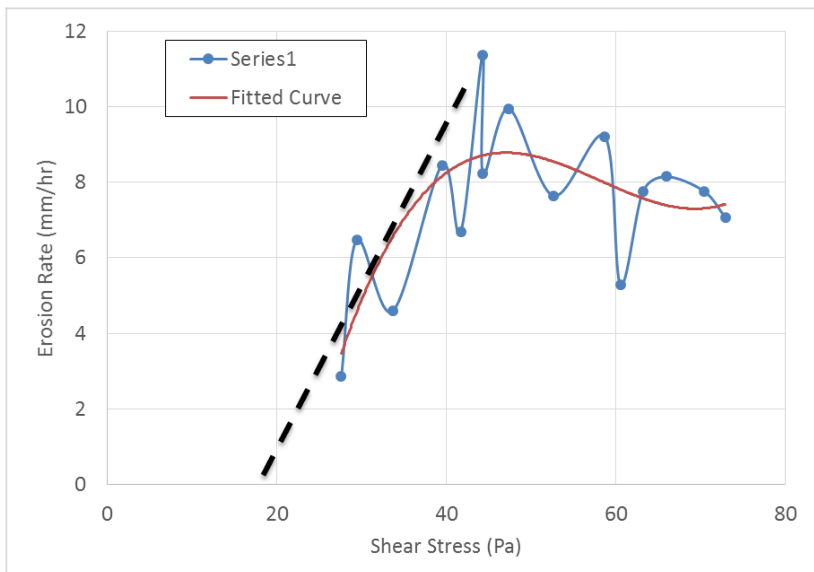

Figure A-78. Clay #4

Time	Time	Flow rate		U/S Tube	D/S Tube	Pressure Di	
(min)	(s)	(gpm)	(l/min)	in	in	(in)	(mm)
0.00	0	0.60	2.27	18.0	5.0	13.0	330
0.50	30	0.79	2.99	18.5	5.0	13.5	343
1.00	60	0.92	3.48	18.5	5.0	13.5	343
1.50	90	0.98	3.71	19.0	5.0	14.0	356
2.00	120	1.01	3.82	19.3	5.0	14.3	362
3.00	180	1.11	4.20	19.5	5.3	14.3	362
4.00	240	1.24	4.69	19.5	5.5	14.0	356
5.00	300	1.34	5.07	19.5	5.5	14.0	356
6.00	360	1.50	5.68	19.8	5.8	14.0	356
7.00	420	1.77	6.70	20.0	6.0	14.0	356
8.00	480	1.99	7.53	20.5	6.3	14.3	362
9.00	540	2.29	8.67	20.0	6.3	13.8	349
10.00	600	2.61	9.88	21.5	7.3	14.3	362
11.00	660	2.91	11.02	22.5	7.75	14.75	374.65
12.00	720	3.33	12.61	22.0	8	14	355.6
13.00	780	3.51	13.29	22.0	9	13	330.2
14.00	840	3.89	14.73	23.5	10	13.5	342.9

Sample length	Gradient	Flow rate	Friction Factor		Hole diameter		Reynold's No.		Diameter
			If Laminar	If Turbulent	If Laminar	If Turbulent	If Laminar	If Turbulent	
L (mm)	S	Q (m3/s)	$f_{\tilde{O}}$	f_P	$D_{\tilde{O}}$	D_P	Re (l)	Re (t)	D (m)
115	2.87130	3.47384584 E-30	15.49 76	23.5264	0.0060000	0.006000	70708 5.4	7785.4	0.8006
115	2.98173	4.991834 1 E-30	.6 0 94 E-2	.0912 9 6 E-0	0.0010679	0.5.0069 4	95075 0.6	3285 5.1	8 6 0 0 6 9 4 5
115	2.98173	5.981034 3 E-40	.6 6 91 E-3	.0510 6 6 E-0	0.0010744	01.2 0 0 7 6 5	92632 5.7	9136 0.0	7 2 0 0 7 6 5 2
115	3.09217	6.3198123 8 E-40	.5 2 88 E-4	.0018 3 6 E-0	0.0010778	00.6 0 0 8 0 3	92830 6.0	8 9849 8.8	2 8 0 0 8 0 3 2
115	3.14739	6.1337024 1 E-40	.9 8 84 E-4	.0616 0 6 E-0	0.0010806	08.9 0 0 8 3 1	98704 5.2	6 9045 3.3	3 8 0 0 8 3 1 8
115	3.14739	7.1030034 0 E-50	.9 0 78 E-5	.0811 4 5 E-0	0.0010880	09.8 0 0 9 0 2	99800 9.3	7 9457 1.3	0 1 0 0 9 0 2 8
115	3.09217	7.3892133 2 E-60	.8 2 71 E-6	.0916 8 5 E-0	0.0010964	09.4 0 0 9 8 2	10060 0 4.7	9780 3 0.3	2 8 0 0 9 8 2 0
115	3.09217	8.3495143 1 E-70	.7 4 64 E-8	.0112 2 4 E-0	0.0011032	08.0 0 1 0 4 4	15031 0 1.2	9928 7.7	6 2 0 1 0 4 4 5
115	3.09217	9.3496133 5 E-80	.6 6 58 E-9	.0217 6 4 E-0	0.0011113	02.2 0 1 1 2 2	11064 9 0.5	1006 4 0 6.9	0 0 2 1 1 2 2 1
115	3.09217	1.3191163 7 E-90	.5 8 51 E-1	.0014 3 0 E-0	0.0021216	05.7 0 1 2 2 7	14123 2 7.1	1614 2 2 7.0	0 7 0 8 1 2 2 7 4
115	3.14739	1.1235054 5 E-10	.0 5 04 E-1	.0125 8 4 E-0	0.0021296	05.6 0 1 3 0 8	19149 4 9.3	1608 3 6.3	0 4 0 8 1 3 0 8 9
115	3.03695	1.6454242 8 E-10	.4 4 24 E-1	.0227 3 8 E-0	0.0021413	09.6 0 1 4 2 1	12236 0 9.0	1726 5 4 4.5	9 0 6 1 4 2 1 2
115	3.14739	1.1634064 7 E-10	.2 3 43 E-1	.0328 9 2 E-0	0.0021497	06.4 0 1 5 1 2	19325 6 8.0	1938 4 3 1.0	0 4 0 6 1 5 1 2 9
115	3.25782	0.6000807 1 8	3 1 5 3 9 2 2 6 2 4	8 6 6 6 84 6 2	1 0 4 0 7 1 1 5 7 2	0 4.0 0 6 1 8 5 9 4	164042048.3	1 2 4 0 2 0 0 8 7.7	0 6 0 7 1 9 5 9 9 4 6
115	3.09217	0.3090103 2 1	0 1 0 4 9 1.8 1 8	1 9 2 20 0 1	7 0 5 6 1 4 7 1 1	0 3.5 0 0 1 8 7 2 5	1953144 9.2	1 2 5 6 0 3 2 5 1.2	0 2 0 3 1 6 7 6 2 5 9
115	2.87130	0.4030408 2 2	1 1 4 5 4 1 6 0 1 1	5 7 8 55 4 1 3	0 6 0 5 1 6 8 2 2	0 9.7 0 6 1 2 8 1 3	1747939 0.3	1 3 5 6 0 4 6 8 6.3	0 9 0 8 1 4 8 3 1 3 7
115	2.98173	3.9010302 4 5	1 4 6 2 0 1 2 0 4	9 6 6 5 90 8 0	9 0 7.0 4 1 9 9	0.019	15939.7	1 4 5 1 9 3 3 1 9.7	0 4 0 1 1 3 9 1

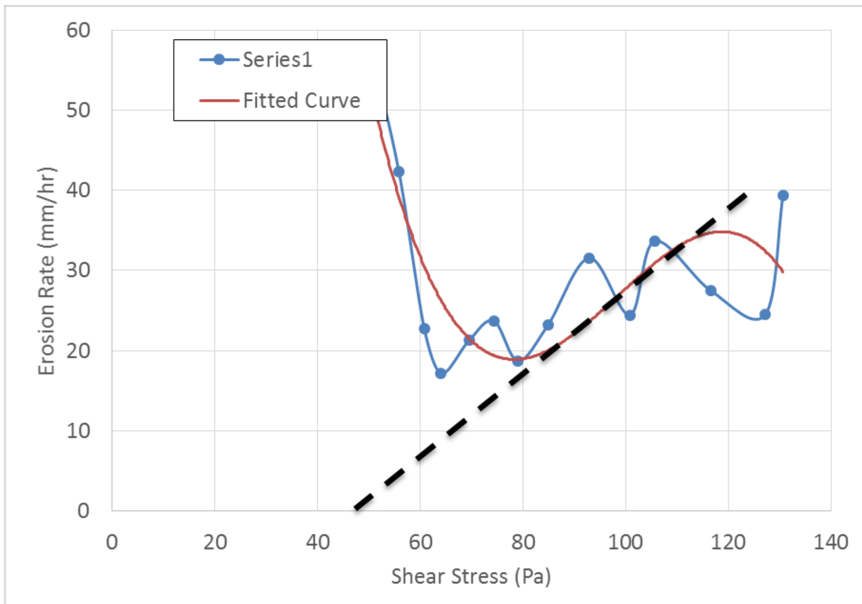

Figure A-79. Clay #5

Flow rate		U/S Tube	Db/S Tube	Pressure Di		Sample length	Gradient	Flow rate	Friction Factor		Hole diameter		Reynold's No.		Diameter
						If Laminar	If Turbulent	If Laminar	If Turbulent						
(gpm)	(l/min)	in	in	(in)	(mm)	L (mm)	S	Q (m3/s)	f_Q	f_P	D_Q	D_P	Re(l)	Re(t)	D (m)
1.27	4.81	43.0	5.5	37.5	953	115	8.282606	8.06192E-05	40	25.92521	15.14744	0.006000	0.006000	1060479.	2661479.	0.006106	
1.46	5.53	43.0	5.5	37.5	953	115	8.282606	9.26191E-05	40.68015	1.081994	0.006466	0.006631	1217857.	3071791.	0.006637		
1.40	5.30	44.0	5.5	38.5	978	115	8.503478	8.82362E-05	50.66777	2.021840	0.006490	0.006731	1176078.	3176217.	0.006906		
1.36	5.15	43.5	5.5	38.0	965	115	8.393048	8.54870E-05	50.84293	3.001532	0.006677	0.007071	1155863.	3134963.	0.006807		
1.46	5.53	43.5	6.0	37.5	953	115	8.282606	9.26191E-05	70.59321	4.051916	0.006753	0.007911	1195508.	3174935.	0.006792		
1.68	6.36	43.5	6.0	37.5	953	115	8.282606	1.06599E-04	80.84366	6.011301	0.006841	0.008871	1552548.	4147737.	0.006808		
2.12	8.03	43.2	6.5	36.7	931	115	8.098551	1.03732E-04	10.64944	7.062685	0.006966	0.010231	1277085.	3416912.	0.006611		
2.79	10.56	45.0	7.5	37.5	953	115	8.282606	1.87690E-04	10.20444	9.022070	0.006111	0.011791	1391744.	3718418.	0.006505		
3.77	14.27	45.0	10.0	35.0	889	115	7.730432	2.43788E-04	10.35955	1.002745	0.006212	0.013912	2023651.	5412818.	0.006410		
4.85	18.36	43.0	14.0	29.0	737	115	6.405213	3.70359E-04	10.51455	1.022284	0.006215	0.016402	2749275.	7293013.	0.006071		
5.23	19.80	36.0	16.0	20.0	508	115	4.417393	3.12390E-04	10.66955	1.032822	0.006218	0.018652	2010832.	5314832.	0.006418		

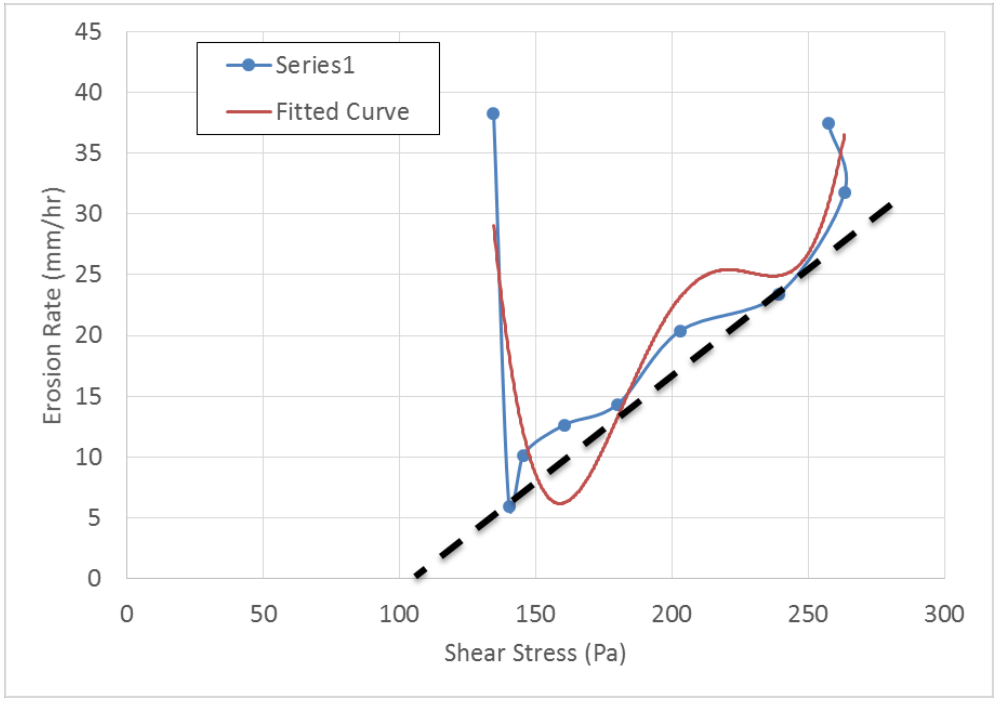

Figure A-80. Clay #6

Time	Time	Flow rate		U/S Tube	D/S Tube	Pressure Di		Sample length	Gradient	Flow rate	Friction Factor		Hole diameter		Reynold's No.		Diameter
											If Laminar	If Turbulent			If Laminar	If Turbulent	
(mins)	(s)	(gpm)	(l/min)	in	in	(in)	(mm)	L (mm)	S	Q (m3/s)	$f_{\bar{D}}$	f_D	$D_{\bar{D}}$	D_D	Re(l)	Re(t)	D (m)
0.00	0	0.89	3.37	18.0	5.0	13.0	330	115	2.871365	4.46E-05	2015.234	10.6925	0.006000	0.006000	1010548.4	1515548.4	0.050906
1.00	60	0.89	3.37	18.0	5.0	13.0	330	115	2.871365	4.46E-05	20.28485	1.021752	0.001061	0.006211	51126.93	151548.4	0.770306
2.00	120	0.89	3.37	18.0	5.0	13.0	330	115	2.871365	4.46E-05	20.44621	1.041811	0.001062	0.006401	41001.63	121908.1	0.940306
4.00	240	0.92	3.48	18.0	5.0	13.0	330	115	2.871365	4.83E-05	20.36911	1.081929	0.001066	0.006815	50880.63	150508.1	0.810681
6.00	360	0.95	3.60	17.8	5.0	12.8	324	115	2.816056	4.99E-05	30.69191	2.031047	0.001069	0.007205	49015.73	213259.6	0.900407
8.00	480	0.98	3.71	17.8	5.0	12.8	324	115	2.816056	5.19E-05	30.45147	2.071165	0.001073	0.007541	43034.43	181814.6	0.880754
11.00	660	1.02	3.86	17.8	5.0	12.8	324	115	2.816056	5.49E-05	30.59891	3.031342	0.001077	0.007986	45062.61	239244.4	0.930079
14.00	840	1.11	4.20	18.5	5.0	13.5	343	115	2.981737	5.90E-05	40.58311	3.091520	0.001081	0.008442	48086.42	311042.8	0.970608
17.00	1020	1.17	4.43	19.0	5.0	14.0	356	115	3.092173	6.39E-05	40.86737	4.051697	0.001084	0.008881	48057.73	371083.2	0.940608
20.00	1200	1.27	4.81	19.0	5.0	14.0	356	115	3.092173	6.93E-05	50.55165	5.011874	0.001089	0.009346	46160.25	391585.7	0.760409
26.00	1560	1.40	5.30	19.0	5.0	14.0	356	115	3.092173	7.63E-05	60.52006	6.041229	0.001097	0.010141	42141.30	391927.4	0.670110
30.00	1800	1.49	5.64	19.0	6.0	13.0	330	115	2.871365	8.04E-05	60.95656	7.021465	0.001105	0.010811	41103.95	411087.9	0.810811
35.00	2100	1.71	6.47	19.0	7.0	12.0	305	115	2.650431	9.25E-05	70.47266	8.021760	0.001118	0.011921	40152.76	421916.8	0.900119
40.00	2400	2.09	7.91	19.5	7.3	12.3	311	115	2.705651	1.13E-04	80.47976	9.031056	0.001129	0.013166	48295.58	512436.1	0.660213
45.00	2700	2.47	9.35	19.5	7.5	12.0	305	115	2.650431	1.34E-04	90.38677	10.01335	0.001214	0.014436	46395.30	571382.0	0.730414
50.00	3000	3.04	11.51	18.8	8.5	10.3	260	115	2.263911	1.66E-04	100.4194	11.01236	0.002165	0.016500	40403.44	711543.4	0.650316

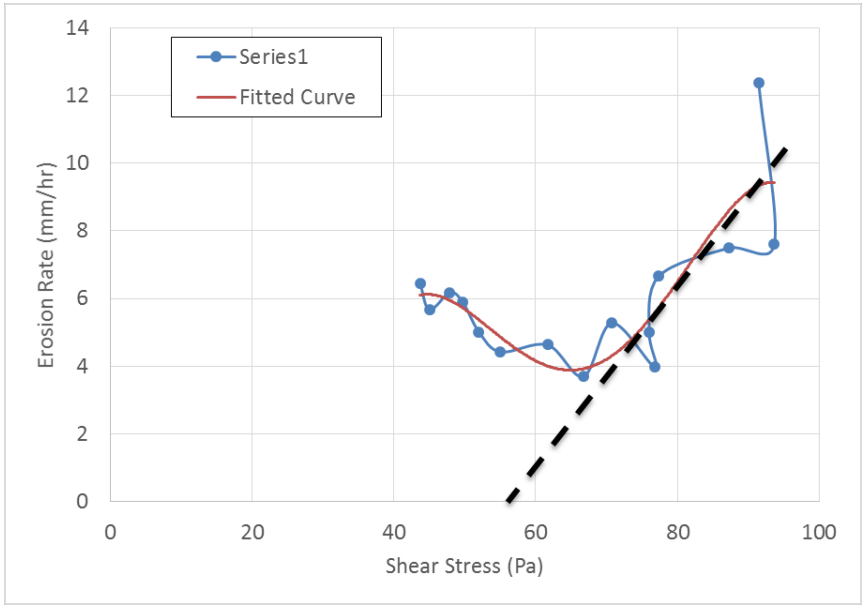

Figure A-81. Clay #7

Time	Time	Flow rate		U/S Tube Pressure	Dn/S Tube Pressure	Pressure Di		Sample length	Gradient	Flow rate	Friction Factor		Hole diameter		Reynold's No.		Diameter
											If Laminar	If Turbulent	If Laminar	If Turbulent	If Laminar	If Turbulent	
(mins)	(s)	(gpm)	(l/min)	in	in	(in)	(mm)	L (mm)	S	Q (m3/s)	f_D	f_P	D_D	D_P	Re(l)	Re(t)	D (m)
0.00	0	0.54	2.04	13.8	5.0	8.8	222	115	1.93260	3.84609669E-05	2035.55559	19.54955	0.000600	0.000600	70000	6.93	7000	6.93	0.00006
0.50	30	0.57	2.16	13.8	5.0	8.8	222	115	1.93260	3.85599661E-05	2048.13374E-01	2.001374E-01	0.000615	0.000618	72210	5.74	7441	8.38	0.00006182
1.00	60	0.60	2.27	13.8	5.0	8.8	222	115	1.93260	3.87689564E-05	2057.10E-01	2.011199E-01	0.000631	0.000636	70359	7.91	7384	4.22	0.00006360
2.00	120	0.63	2.38	13.8	5.0	8.8	222	115	1.93260	3.89679467E-05	2058.64E-01	2.021849E-01	0.000651	0.000658	73582	7.17	7649	9.00	0.00006583
3.00	180	0.65	2.46	13.8	5.0	8.8	222	115	1.93260	3.81609069E-05	2053.01E-01	2.041498E-01	0.000668	0.000676	70527	4.57	7748	5.80	0.00006760
4.00	240	0.68	2.57	13.8	5.0	8.8	222	115	1.93260	3.82699061E-05	2058.17E-01	2.061148E-01	0.000687	0.000697	73669	7.87	7591	6.93	0.00006973
5.00	300	0.70	2.65	14.5	5.0	9.5	241	115	2.09826	4.04817663E-05	2059.32E-01	2.071798E-01	0.000684	0.000702	75935	8.92	7757	4.93	0.00007025
8.00	480	0.75	2.84	14.8	5.3	9.5	241	115	2.09826	4.07837188E-05	3021787E-01	3.021746E-01	0.000727	0.000746	82042	9.23	7818	4.60	0.00007462
10.00	600	0.85	3.22	14.8	5.3	9.5	241	115	2.09826	5.03867277E-05	3050955E-01	3.061046E-01	0.000775	0.000799	87563	2.38	8927	4.51	0.00007997
12.00	720	0.96	3.63	14.8	5.3	9.5	241	115	2.09826	6.00857677E-05	3034003E-01	3.091345E-01	0.000825	0.000854	95005	9.03	8374	6.75	0.00008544
14.00	840	1.03	3.90	15.5	5.3	10.3	260	115	2.26391	6.34094833E-05	3059711E-01	4.021644E-01	0.000840	0.000879	96594	5.37	7911	5.74	0.00008796
16.00	960	1.15	4.35	15.8	5.8	10.0	254	115	2.20869	7.52655524E-05	4052018E-01	4.051943E-01	0.000895	0.000937	97969	8.80	9154	7.53	0.00009377
18.00	1080	1.27	4.81	15.8	5.8	10.0	254	115	2.20869	8.50615225E-05	4053226E-01	4.091243E-01	0.000942	0.000989	13074	94.1	9919	3.80	0.00009893
20.00	1200	1.46	5.53	16.0	6.0	10.0	254	115	2.20869	9.52615122E-05	4066334E-01	5.021542E-01	0.001003	0.001059	17173	23.1	1517	25.1	0.00105971
22.00	1320	1.65	6.25	16.0	6.5	9.5	241	115	2.09826	6.00847106E-05	4089423E-01	5.051841E-01	0.001080	0.001138	11178	84.1	1102	86.5	0.00113811
24.00	1440	1.88	7.12	16.0	6.8	9.3	235	115	2.04304	4.31487681E-05	5042506E-01	5.091140E-01	0.001156	0.001219	14296	53.7	1250	2.20	0.00121944
26.00	1560	2.28	8.63	16.0	7.0	9.0	229	115	1.98782	2.64038875E-05	5035576E-01	6.021440E-01	0.001126	0.001339	10420	51.6	1237	256.	0.00133906
28.00	1680	2.42	9.16	15.8	7.0	8.8	222	115	1.93260	1.85529668E-05	5058656E-01	6.051739E-01	0.001131	0.001393	13442	82.1	1393	15.2	0.00107139
30.00	1800	2.61	9.88	15.8	7.5	8.3	210	115	1.82211	1.36941637E-05	5048173E-01	6.091038E-01	0.001139	0.001467	14415	31.1	1536	84.7	0.00151467
32.00	1920	2.82	10.67	15.8	7.5	8.3	210	115	1.82211	1.37971931E-05	6044815E-01	7.021337E-01	0.001453	0.001527	17541	03.3	1743	70.9	0.00152777
34.00	2040	2.98	11.28	15.8	8.0	7.8	197	115	1.71173	3.98183011E-05	6027897E-01	7.051637E-01	0.001530	0.001595	16561	55.3	1645	39.3	0.00159556
36.00	2160	3.11	11.77	15.8	8.5	7.3	184	115	1.60130	1.49364281E-05	6050965E-01	7.081936E-01	0.001606	0.001659	10550	68.2	1542	94.3	0.00165902
38.00	2280	3.17	12.00	15.8	8.5	7.3	184	115	1.60130	2.44030480E-05	6074045E-01	8.021235E-01	0.001636	0.001685	15530	85.2	2346	42.2	0.00168552
40.00	2400	3.20	12.11	15.0	9.0	6.0	152	115	1.32522	2.70319819E-05	6087125E-01	8.051534E-01	0.001767	0.001771	10430	93.2	2147	06.7	0.00177102
42.00	2520	3.27	12.38	15.0	9.0	6.0	152	115	1.32522	2.70369310E-05	7020202E-01	8.081834E-01	0.001800	0.001801	10401	43.3	3148	43.6	0.00180181

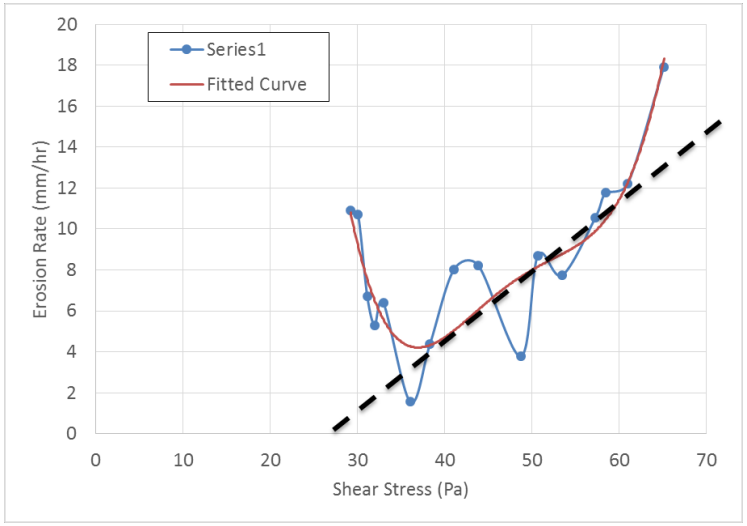

Figure A-82. Clay #8

Time	Time	Flow rate		U/S Tube	D/S Tube	Pressure Di	
(mins)	(s)	(gpm)	(l/min)	in	in	(in)	(mm)
0.00	0	0.44	1.67	27.8	5.0	22.8	578
0.50	30	0.60	2.27	28.0	5.0	23.0	584
1.00	60	0.73	2.76	28.0	5.0	23.0	584
2.00	120	0.89	3.37	28.0	5.0	23.0	584
3.00	180	0.95	3.60	28.0	5.0	23.0	584
4.00	240	1.01	3.82	28.5	5.3	23.3	591
5.00	300	1.08	4.09	29.0	5.3	23.8	603
6.00	360	1.17	4.43	28.8	5.3	23.5	597
7.00	420	1.30	4.92	29.0	5.5	23.5	597
8.00	480	1.43	5.41	29.0	6.3	22.8	578
9.00	540	1.62	6.13	29.0	6.3	22.8	578
10.50	630	1.87	7.08	29.5	6.5	23.0	584
11.00	660	1.98	7.50	29.5	6.5	23.0	584
12.00	720	2.28	8.63	29.5	6.8	22.8	578
13.00	780	2.58	9.77	29.5	7.0	22.5	572
15.00	900	3.04	11.51	29.5	7.5	22.0	559
16.00	960	3.23	12.23	29.5	7.5	22.0	559
17.00	1020	3.48	13.17	29.5	9.0	20.5	521
18.00	1080	3.69	13.97	29.5	9.5	20.0	508
19.00	1140	3.81	14.42	28.0	10.0	18.0	457
20.00	1200	3.96	14.99	27.0	10.5	16.5	419
21.00	1260	4.00	15.14	25.0	11.0	14.0	356

Sample length	Gradie	Flow rat	Friction	Factor	Hole diameter		Reynold's No.		Diameter
			If Laminar	If Turbul	If Laminar	If Turbul	If Laminar	If Turbul	ulent
L (mm)	S	Q (m3/s)	$f_{\tilde{O}}$	f_P	$D_{\tilde{O}}$	D_P	Re(l)	Re(t)	D (m)
115	5.0247	8 2276709 0 E	-7055.1646	76.5582	0.006000	0.0.0060 0	050700 9.3	550709.3	500006
115	5.08	3.7854 E	-70.5952 E	7+.0517 13 E	-0.0010662	0.3.10067	672075 3.0	660907.4	70000676 2
115	5.08	4.6056 E	-70.5740 E	7+.0418 68 E	-0.0010706	0.3.80072	988014 5.8	07587.4	7040072 98
115	5.08	5.6150 E	-70.5315 E	7+.0311 79 E	-0.0010753	01.90078	694129 9.6	83810.8	88007864
115	5.08	5.9936 E	-70.5890 E	7+.0114 89 E	-0.0010768	02.80080	394652 7.0	19205.5	33008034
115	5.1352	16733792 11 E	-70.5465 E	6+.0917 99 E	-0.0010779	08.00081	716080 83.	79811 6.6	590081 76
115	5.2456	652811734 7 E	-70.5040 E	6+.0811 10 E	-0.0010790	02.50083	212046 40.	0170 7103.	2070908322
115	5.1904	37437881 35 E	-70.2616 E	6+.0614 20 E	-0.0010812	09.00085	618122 05.	51200 631.	20050856 8
115	5.1904	384270813 7 E	-70.2191 E	6+.0417 30 E	-0.0010840	03.20088	911210 44.	4131583.	40805088 91
115	5.0247	89206201 99 E	-70.5766 E	6+.0310 41 E	-0.0010875	01.50092	417267 21.	516240 39.	01060924 7
115	5.0247	81206202 91 E	-70.4341 E	6+.0113 51 E	-0.0010910	05.00096	618318 52.	21138045.	40206096 68
115	5.08	1.1798 E	-70.0704 E	5+.0818 16 E	-0.0010948	03.00101	311523 44.	4154370.	307051013 1
115	5.08	1.2492 E	-70.0492 E	5+.0719 71 E	-0.0010966	00.80103	315559 56.	41441914.	8050210335
115	5.0247	81246308 95 E	-70.0067 E	5+.0612 82 E	-0.0011014	02.50108	914785 01.	5106629 2.	99001089 4
115	4.9695	61562217 77 E	-60.9642 E	5+.0415 92 E	-0.0011058	06.70114	012869 73.	4147161 5.	6806114 02
115	4.8591	31094137 59 E	-60.8792 E	5+.0112 13 E	-0.0011121	09.80120	725160 94.	8159699.	70402120 75
115	4.8591	32004337 58 E	-60.8367 E	4+.0915 23 E	-0.0011142	05.30122	829230 10.	02901462.	60409122 89
115	4.5278	22610985 75 E	-60.7943 E	4+.0718 33 E	-0.0011196	06.80127	522256 40.	4281624 5.	60202127 52
115	4.4173	92133208 40 E	-60.7518 E	4+.0611 44 E	-0.0011227	08.00130	225353 98.	2272055.	40901130 25
115	3.9756	52241073 47 E	-60.7093 E	4+.0414 54 E	-0.0011282	06.20133	724311 26.	52521179.	10402133 74
115	3.6443	42748928 64 E	-60.6668 E	4+.0217 64 E	-0.0011334	06.50137	124301 00.	12228480.	97001371 4
115	3.0921	72359213 36 E	-60.6243 E	4+.0110 74 E	-0.0011411	05.00141	125200 62.	92920062.	99001411 5

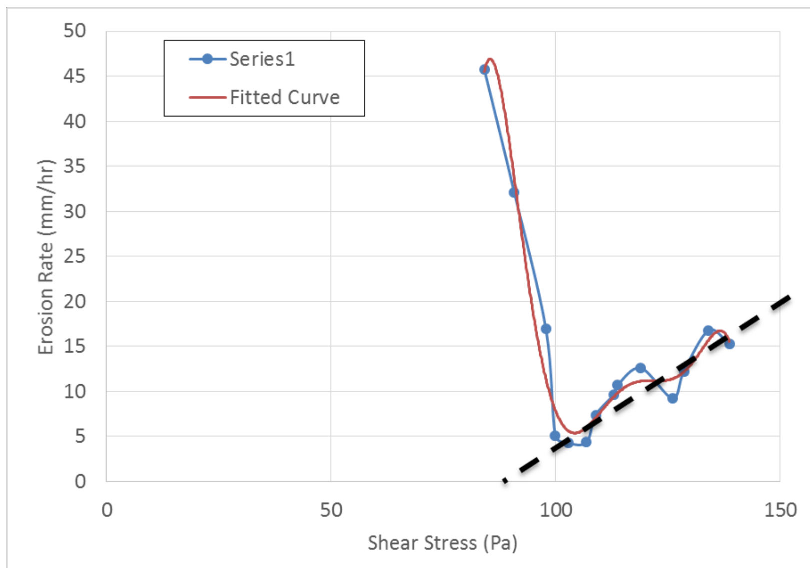

Figure A-83. Clay #9

Time	Time	Flow rate		U/S Tube Pressure	D/S Tube Pressure		
(mins)	(s)	(gpm)	(l/min)	(in)	(in)	(in)	(mm)
0.00	0	1.01	3.82	27.5	5.0	22.5	572
0.50	30	1.05	3.97	27.5	5.0	22.5	572
1.00	60	1.08	4.09	27.5	5.0	22.5	572
2.00	120	1.20	4.54	27.8	5.0	22.8	578
3.00	180	1.36	5.15	27.5	5.3	22.3	565
4.00	240	1.51	5.72	27.5	5.3	22.3	565
5.00	300	1.59	6.02	27.5	5.3	22.3	565
6.00	360	1.81	6.85	27.0	6.5	20.5	521
7.00	420	2.09	7.91	27.0	7.0	20.0	508
8.00	480	2.22	8.40	26.5	7.0	19.5	495
9.00	540	2.66	10.07	27.5	8.0	19.5	495
10.00	600	2.82	10.67	27.5	8.0	19.5	495
11.00	660	2.90	10.98	27.0	7.5	19.5	495
12.00	720	2.92	11.05	27.0	8.0	19.0	483

Sample length	Gradient	Flow rate	Friction Factor		Hole diameter		Reynold's No.		Diameter
			If Laminar	If Turbulent	If Laminar	If Turbulent	If Laminar	If Turbulent	
L (mm)	S	Q (m3/s)	$f_{\bar{O}}$	f_P	$D_{\bar{O}}$	D_P	Re(l)	Re(t)	D (m)
115	4.969	6.532712E-05	3025.385	14.36999	0.006000	0.006000	1030105.3	1534105.9	0.00596406
115	4.969	6.562214E-05	3025.707	14.37240	0.006000	0.006000	1030271.1	1534257.8	0.00596406
115	4.969	6.582113E-05	3025.929	14.37109	0.006000	0.006000	1030384.2	1534063.4	0.00596406
115	5.024	7.256709E-05	3025.674	14.37849	0.006000	0.006000	1030243.9	1534947.0	0.00596698
115	4.914	4.758826E-05	3026.318	14.39159	0.006000	0.006000	1030599.2	1536902.0	0.00597206
115	4.914	4.758226E-05	3026.318	14.39159	0.006000	0.006000	1030599.2	1536902.0	0.00597206
115	4.914	4.708023E-05	3026.318	14.39159	0.006000	0.006000	1030599.2	1536902.0	0.00597206
115	4.527	2.610481E-05	3026.318	14.39159	0.006000	0.006000	1030599.2	1536902.0	0.00597206
115	4.417	1.133108E-05	3026.318	14.39159	0.006000	0.006000	1030599.2	1536902.0	0.00597206
115	4.306	1.645020E-05	3026.318	14.39159	0.006000	0.006000	1030599.2	1536902.0	0.00597206
115	4.306	1.665728E-05	3026.318	14.39159	0.006000	0.006000	1030599.2	1536902.0	0.00597206
115	4.306	1.675729E-05	3026.318	14.39159	0.006000	0.006000	1030599.2	1536902.0	0.00597206
115	4.306	1.685229E-05	3026.318	14.39159	0.006000	0.006000	1030599.2	1536902.0	0.00597206
115	4.196	2.187432E-05	3026.318	14.39159	0.006000	0.006000	1030599.2	1536902.0	0.00597206

Reynold's No.	Diameter
Re(t)	Turbulent
	D (m)
1534105.9	0.00596406
1534257.8	0.00596406
1534063.4	0.00596406
1534947.0	0.00596698
1536902.0	0.00597206
1536902.0	0.00597206
1536902.0	0.00597206
1536902.0	0.00597206
1536902.0	0.00597206
1536902.0	0.00597206
1536902.0	0.00597206
1536902.0	0.00597206
1536902.0	0.00597206

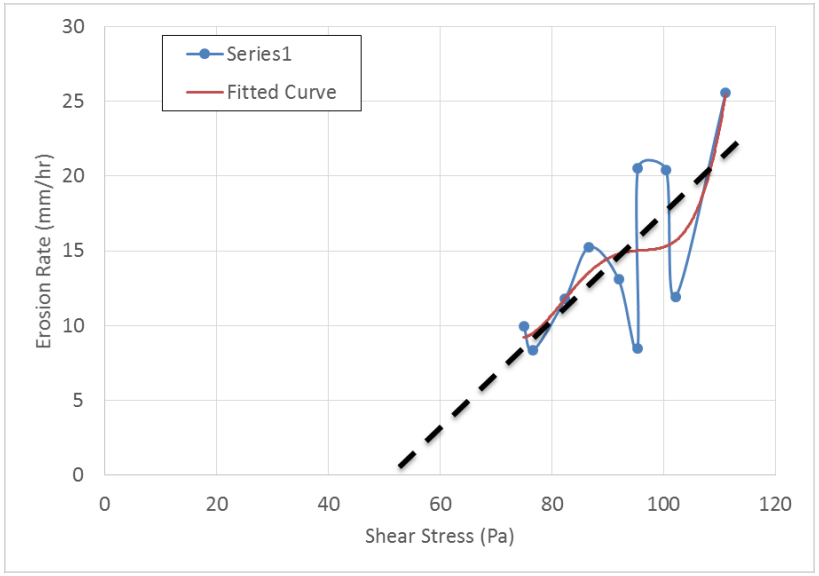

Figure A-84. Clay #10

Time	Time	Flow rate		U/S Tube	Dn/S Tube	Pressure Di		Sample length	Gradient	Flow rate	Friction Factor		Hole diameter		Reynold's No.		Diameter
											If Laminar	If Turbulent	If Laminar	If Turbulent	If Laminar	If Turbulent	
(mins)	(s)	(gpm)	(l/min)	in	in	(in)	(mm)	L (mm)	S	Q (m3/s)	f_{δ}	f_P	D_{δ}	D_P	Re (l)	Re (t)	D (m)
0.00	0	0.73	2.76	17.0	5.0	12.0	305	115	2.650424	4.467085E-06	2035.8970	14.6707	0.000600	0.000600	90407.23	914.723	0.00100
1.00	60	0.76	2.88	17.0	5.0	12.0	305	115	2.650424	4.477984E-06	20.67706	1.061922	0.006315	0.006279	94316.87	954.308	0.00100
2.00	120	0.76	2.88	17.0	5.0	12.0	305	115	2.650424	4.477984E-06	20.96435	1.091174	0.006530	0.006439	92085.57	931.981	0.00100
4.00	240	0.79	2.99	17.5	5.0	12.5	318	115	2.760844	4.995864E-06	30.53906	2.031678	0.006920	0.006758	89837.95	909.299	0.00100
6.00	360	0.80	3.03	18.0	6.0	12.0	305	115	2.650424	5.407487E-06	40.51136	2.081181	0.007410	0.007098	81480.11	837.824	0.00100
7.00	420	1.33	5.03	39.5	7.0	32.5	826	115	7.178266	9.038971E-06	40.50091	3.001433	0.006440	0.007231	116006.8	1240.19	0.00100
8.00	480	1.74	6.59	43.5	7.0	36.5	927	115	8.061738	1.190193E-05	40.46883	3.021685	0.006920	0.007971	119956.2	1295.76	0.00100
9.00	540	1.97	7.46	43.0	7.5	35.5	902	115	7.840886	1.092546E-05	40.47560	3.041936	0.007430	0.008542	126006.4	1178.46	0.00100
10.00	600	2.35	8.90	43.0	7.5	35.5	902	115	7.840886	1.945862E-05	50.42629	3.071188	0.008020	0.009286	126207.8	1697.02	0.00100
11.00	660	2.73	10.33	42.5	8.5	34.0	864	115	7.509556	1.572212E-05	50.45502	3.091440	0.008710	0.010062	122493.8	1521.40	0.00100
12.00	720	3.11	11.77	39.0	10.0	29.0	737	115	6.405211	1.793692E-05	50.43755	4.011691	0.009760	0.011066	126438.4	1791.87	0.00100
13.50	810	3.21	12.15	30.0	10.0	20.0	508	115	4.417329	2.103205E-05	60.42685	4.051069	0.011430	0.012266	121485.6	2206.82	0.00100
14.50	870	3.17	12.00	25.0	10.0	15.0	381	115	3.313024	2.304070E-05	60.45558	4.071321	0.011270	0.013041	119924.0	2413.09	0.00100
16.00	960	3.22	12.19	23.0	10.0	13.0	330	115	2.871302	2.403418E-05	60.48668	5.001698E	0.011370	0.013700	108029.8	2184.29	0.00100

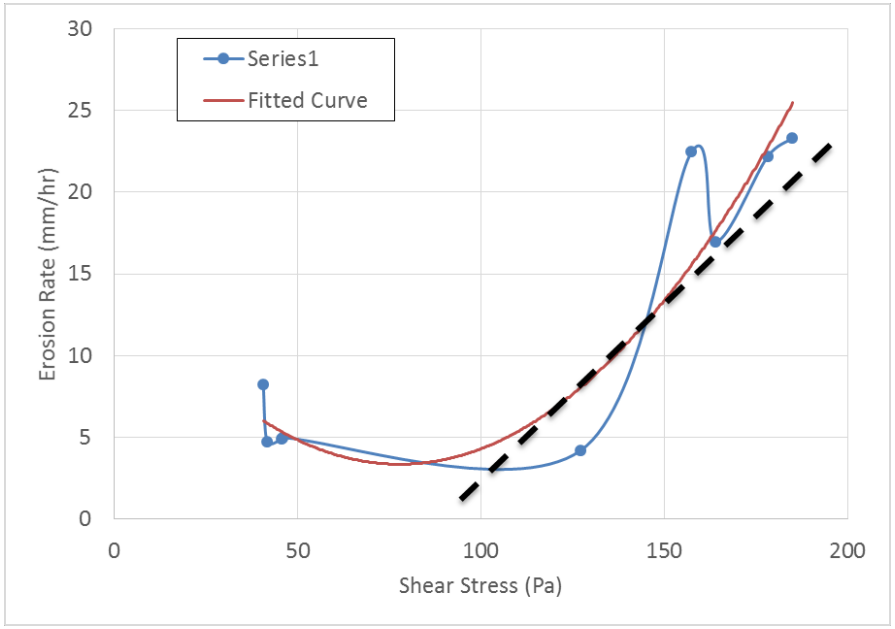

Figure A-85. Clay #11

Time	Time	Flow rate		U/S Tube	Dn/S Tube Pressure Di		Sample length	Gradient	Flow rate	Friction Factor		Hole diameter		Reynolds No	Diameter
										If Laminar	If Turbulent	If Laminar	If Turbulent	If Laminar	If Turbulent
(mins)	(s)	(gpm)	(l/min)	in	in	(in)	(mm)	L (mm)	S	Q (m3/s)	$f_{Ō}$	f_p	$D_{Ō}$	D_p	Re(l)	Re(t)	D (m)
0.00	0	1.21	4.58	41.5	5.0	36.5	927	115	8.061737	3.961333E-4	035.85523	16.24191	0.000600	0.000600	1050700.	715700.	010306
0.50	30	1.33	5.03	43.0	5.0	38.0	965	115	8.393044	4.334971E-4	50.56401E-3	1.011374E-4	0.001066	04.20705	1153655.	1045840.	0.040807051
1.00	60	1.40	5.30	43.0	5.3	37.8	959	115	8.337828	4.668038E-4	60.34285E-3	4.061507E-4	0.001071	89.10779	1752161.	1399780.	0.091080779
1.50	90	1.55	5.87	43.0	5.3	37.8	959	115	8.337828	4.667897E-4	70.92166E-3	6.011640E-4	0.001078	407.5085	1159377.	1448045.	0.101080859
2.00	120	1.65	6.25	43.0	5.5	37.5	953	115	8.282606	4.980649160E-4	90.40044E-3	7.061772E-4	0.001084	100.6092	1175127.	1430937.	0.101070921
3.00	180	1.71	6.47	43.0	6.0	37.0	940	115	8.172171	5.307183838E-4	10.44458E-3	1.002704E-4	0.002092	301.9100	1942420.	1332870.	0.401007019
4.00	240	1.87	7.08	43.0	6.5	36.5	927	115	8.061737	5.911739838E-4	10.38816E-3	1.032730E-4	0.002101	609.4109	1441316.	1303102.	0.501091944
5.00	300	2.00	7.57	42.5	7.0	35.5	902	115	7.840866	6.925661586E-4	10.46173E-3	1.062757E-4	0.002110	602.0117	1445075.	1631235.	0.701411764
6.00	360	2.19	8.29	42.5	7.5	35.0	889	115	7.730434	7.437881137E-4	10.85315E-3	1.092783E-4	0.002119	803.0126	1741222.	1723548.	0.801012647
7.00	420	2.51	9.50	42.5	7.5	35.0	889	115	7.730434	8.145788336E-4	20.48882E-3	2.022810E-4	0.002130	506.5137	1149966.	3144220.	0.601413741
8.00	480	2.85	10.79	42.5	7.5	35.0	889	115	7.730434	8.477988831E-4	20.32466E-3	2.052836E-4	0.002141	105.0148	2135171.	2547968.	0.501481423
9.00	540	3.33	12.61	42.5	9.0	33.5	851	115	7.399132	1.014030359E-3	20.56604E-3	2.082863E-4	0.002155	709.0162	1066640.	7552934.	0.001316270
10.00	600	4.03	15.26	42.5	11.0	31.5	800	115	6.957392	1.215340245E-3	20.49611E-3	3.012889E-4	0.002174	501.8181	1677878.	3177299.	0.401811366
11.00	660	4.63	17.53	42.0	14.5	27.5	699	115	6.073912	1.390241431E-3	30.63191E-3	3.042916E-4	0.002196	407.6200	1084346.	3769691.	0.501920060
12.00	720	5.26	19.91	40.0	16.5	23.5	597	115	5.190437	1.437188835E-3	30.26766E-3	3.072942E-4	0.002221	500.0221	1080488.	3183488.	0.301032215

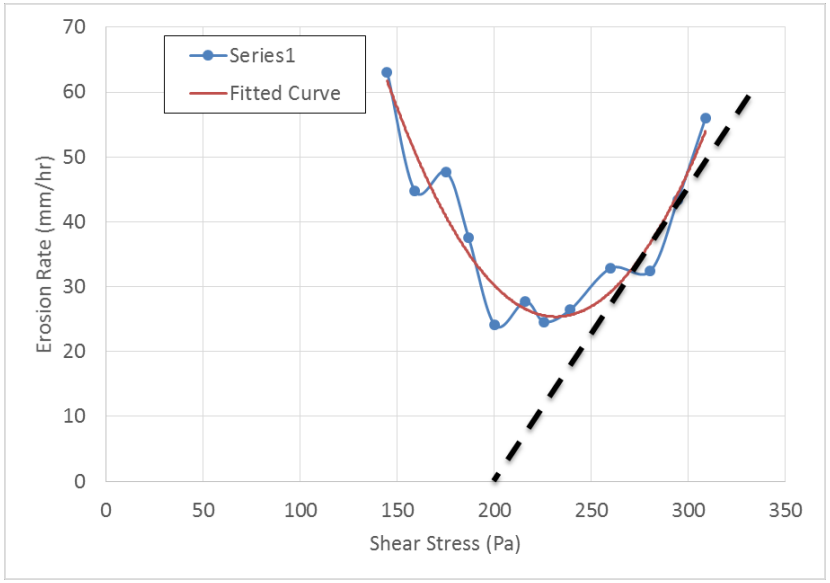

Figure A-86. Clay #12

Time	Time	Flow rate		U/S Tube Pressure Di	Db/S Tube Pressure Di			Sample length	Gradient	Flow rate	Friction Factor		Hole diameter		Reynold's No.		Diameter
											If Laminar	If Turbulent	If Laminar	If Turbulent	If Laminar	If Turbulent	
(mins)	(s)	(gpm)	(l/min)	in	in	(in)	(mm)	L (mm)	S	Q (m3/s)	$f_{\bar{0}}$	f_p	$D_{\bar{0}}$	D_p	Re(l)	Re(t)	D (m)
0.00	0	1.01	3.82	42.5	5.0	37.5	953	115	8.282666	6.836792E-61	5035.9752	23.94999	0.006000	0.006000	10301	5.3	5.3
0.50	30	1.13	4.28	42.5	5.0	37.5	953	115	8.282667	7.816299E-62	50.45987	2.051179	0.001062	0.007503	18470	36.9	14.3
1.00	60	1.21	4.58	42.5	5.0	37.5	953	115	8.282667	7.866393E-69	50.59981	2.061408	0.001064	0.011006	16496	02.3	18.4
2.00	120	1.43	5.41	42.5	5.0	37.5	953	115	8.282669	9.806291E-69	50.80211	2.081865	0.001069	0.016007	17671	31.2	16.5
3.00	180	1.65	6.25	42.8	5.5	37.3	946	115	8.227391	1.034014E-60	60.40443	3.011323	0.001073	0.030771	14755	05.3	15.5
4.00	240	1.84	6.97	42.8	6.5	36.3	921	115	8.006521	1.176309E-60	60.20677	3.031780	0.001077	0.060445	15864	49.7	16.4
5.00	300	2.16	8.18	42.8	7.0	35.8	908	115	7.896081	1.396527E-60	60.40896	3.061238	0.001083	0.072089	12902	21.9	13.8
6.50	390	2.83	10.71	42.8	7.0	35.8	908	115	7.896081	1.679855E-60	60.71244	3.091925	0.001092	0.102401	12135	83.8	12.9
7.00	420	3.08	11.66	42.8	7.0	35.8	908	115	7.896081	1.699453E-60	60.81356	4.011153	0.001095	0.104105	24520	97.5	23.2
8.00	480	3.08	11.66	30.5	7.5	23.0	584	115	5.08	1.943E-70	60.61588	4.031611	0.001111	0.065116	21104	55.2	20.7
10.00	600	3.08	11.66	24.0	7.5	16.5	419	115	3.644347	4.798423E-62	70.42046	4.081526	0.001127	0.001272	10808	51.8	12.8

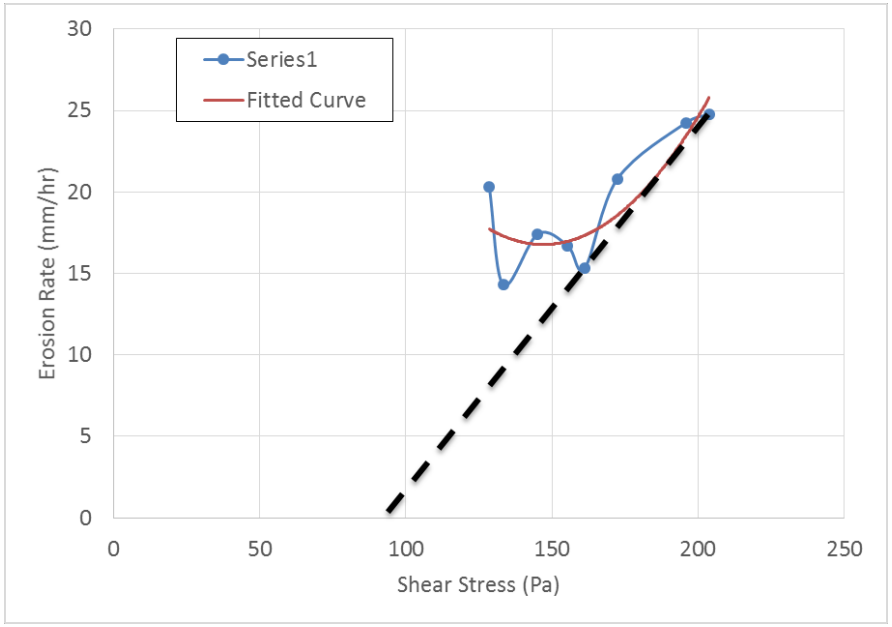

Figure A-87. Clay #13

Time	Time	Flow rate		U/S Tube	D/S Tube	Pressure Di		Sample length	Gradient	Flow rate	Friction Factor		Hole diameter		Reynolds No.		Diameter
											If Laminar	If Turbulent	If Laminar	If Turbulent	If Laminar	If Turbulent	If Turbulent
(mins)	(s)	(gpm)	(l/min)	in	in	(in)	(mm)	L (mm)	S	Q (m3/s)	$f_{Ō}$	f_P	$D_Ō$	D_P	Re(l)	Re(t)	D (m)
0.00	0	0.87	3.29	42.5	5.0	37.5	953	115	8.282665846898868E	6025.660900	32.278100	0.010600	0.010600	10102.884	3432.884	0.940306	
0.50	30	0.95	3.60	42.5	5.0	37.5	953	115	8.282665898699366E	5530.071853	31.011852E	0.010619	0.010619	18149.481	3510.322	0.947020	6198
1.00	60	1.01	3.82	42.5	5.0	37.5	953	115	8.282665836792615E	5353.011426E	31.011426E	0.010632	0.010632	15204.241	11294.122	0.949030	6335
2.00	120	1.21	4.58	42.5	5.0	37.5	953	115	8.282667866393695E	4604.001573E	31.001573E	0.010674	0.010677	12349.631	7183.909	0.947006	7722
3.00	180	1.43	5.41	42.8	5.5	37.3	946	115	8.227391010320149E	4573.621721E	31.021721E	0.010717	0.010720	19525.184	11504.430	0.943007	2095
4.00	240	1.65	6.25	42.8	6.5	36.3	921	115	8.000652107431900E	4427.681868E	31.021868E	0.010762	0.010763	11618.574	6853.333	0.938007	6310
5.00	300	2.01	7.61	42.8	7.0	35.8	908	115	7.896081629658771E	4119.611016E	31.021016E	0.010820	0.010823	11940.722	7194.011	0.936508	2310
6.50	390	2.63	9.96	42.8	7.0	35.8	908	115	7.896081669559573E	4156.611737E	31.021737E	0.010902	0.010908	20276.984	12175.481	0.936809	0800
7.00	420	2.98	11.28	42.8	7.0	35.8	908	115	7.896081689850771E	4502.611311E	31.021311E	0.010942	0.010951	12544.627	7204.682	0.936809	5155
7.50	450	3.35	12.68	42.5	7.5	35.0	889	115	7.730431417183355E	4848.518855E	31.018855E	0.010988	0.010998	21623.933	12561.305	0.952709	9814
9.00	540	4.22	15.97	42.5	8.0	34.5	876	115	7.62	2.662464E	4.416066E	0.011077	0.011086	37074.833	21012.314	0.946010	8667
10.00	600	5.06	19.15	41.5	9.5	32.0	813	115	7.067826109827474E	4.317754E	0.011178	0.011178	30304.411	18654.411	0.960511	1778	

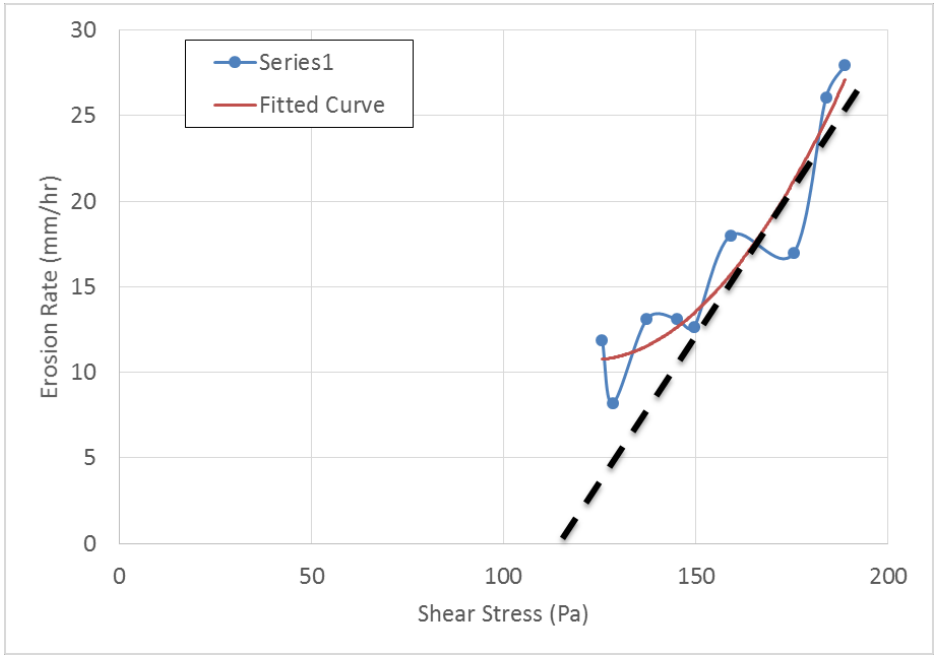

Figure A-88. Clay #14

Silt Samples – HET

Time	Time	Flow rate		U/S Tube	Dn/S Tube	Pressure Di		Sample length	Gradient	Flow rate	Friction Factor		Hole diameter		Reynold's No.		Diameter
											If Laminar	If Turbulent	If Laminar	If Turbulent	If Laminar	If Turbulent	If Turbulent
(mins)	(s)	(gpm)	(l/min)	in	in	(in)	(mm)	L (mm)	S	Q (m3/s)	$f_Ō$	f_P	$D_Ō$	D_P	Re(l)	Re(t)	D (m)
0.00	0	0.69	2.61	20.0	5.5	14.5	368	115	3.202626	4.83659362E-3	085.841	29.6071	0.006500	0.006508	0206	4.5	42645.5	0.040065
0.50	30	0.76	2.88	20.0	5.5	14.5	368	115	3.202626	4.87699469E-3	0.905	4E2.091	0.006720	5.006748	5709	8.4	3772.3	0.040067	44
1.00	60	0.82	3.10	20.0	5.5	14.5	368	115	3.202626	5.81679364E-3	0.952	7E2.091	1.20E-6	0.006949	1263	8.8	4896.9	0.050069	41
2.00	120	0.90	3.41	20.0	5.5	14.5	368	115	3.202626	5.86679861E-3	0.969	3E2.081	6.32E-6	0.007150	3.5	0.007189	0769	5.0	7758.0	0.070071	80
3.00	180	0.96	3.63	20.0	6.0	14.0	356	115	3.092176	5.30951637E-3	0.611	9E2.081	1.45E-6	0.007420	1.5	0.007391	4090	7 0.	3801	07.	0.080107394
4.00	240	1.28	4.85	20.0	6.0	14.0	356	115	3.092176	7.30971535E-3	0.654	6E2.071	6.57E-6	0.008197	7.2	0.008261	7281	5 7.	1102	9 5 3.	0.100208267
5.00	300	1.71	6.47	19.9	6.3	13.7	347	115	3.014864	9.05768558E-3	0.697	2E2.071	1.70E-6	0.009130	6.3	0.009291	7435	7 1.	1547	3 1 9.	0.150409297
6.00	360	2.08	7.87	19.8	6.8	13.0	330	115	2.871301	1.04334283E-2	0.743	8E2.061	6.83E-6	0.009940	6.9	0.010111	7602	8 0.	1856	0 0 6.	0.170010116
7.00	420	2.66	10.07	19.5	7.5	12.0	305	115	2.650431	1.46778832E-2	0.824	2E2.061	1.95E-6	0.011120	6.7	0.011301	1836	1 2.	3165	3 2 4.	0.190611301
7.50	450	3.05	11.55	19.8	7.8	12.0	305	115	2.650431	1.49728433E-2	0.842	0E2.051	9.51E-6	0.011166	6.6	0.011912	4073	5 5.	3129	4 9 2 9.	0.210211914
8.50	510	3.91	14.80	19.0	8.0	11.0	279	115	2.429562	2.54261678E-2	0.842	4E2.051	4.64E-6	0.011308	9.5	0.013332	9372	5 6.	2242	8 2 0.	0.300813339
9.50	570	4.14	15.67	19.0	8.0	11.0	279	115	2.429562	2.56211179E-2	0.828	9E2.041	9.77E-6	0.011338	6.7	0.013592	5450	7 9.	2253	7 0 7.	0.290113595
10.50	630	4.40	16.66	19.0	8.3	10.8	273	115	2.374342	2.77872660E-2	0.831	6E2.041	4.89E-6	0.011381	0.8	0.013942	0408	0 3.	2214	6 5 7 3.	0.380813939
12.00	720	4.96	18.78	18.8	8.5	10.3	260	115	2.263931	3.10249332E-2	0.839	5E2.031	7.58E-6	0.011467	5.0	0.014672	5603	1 4.	2169	3 1 4.	0.410914675

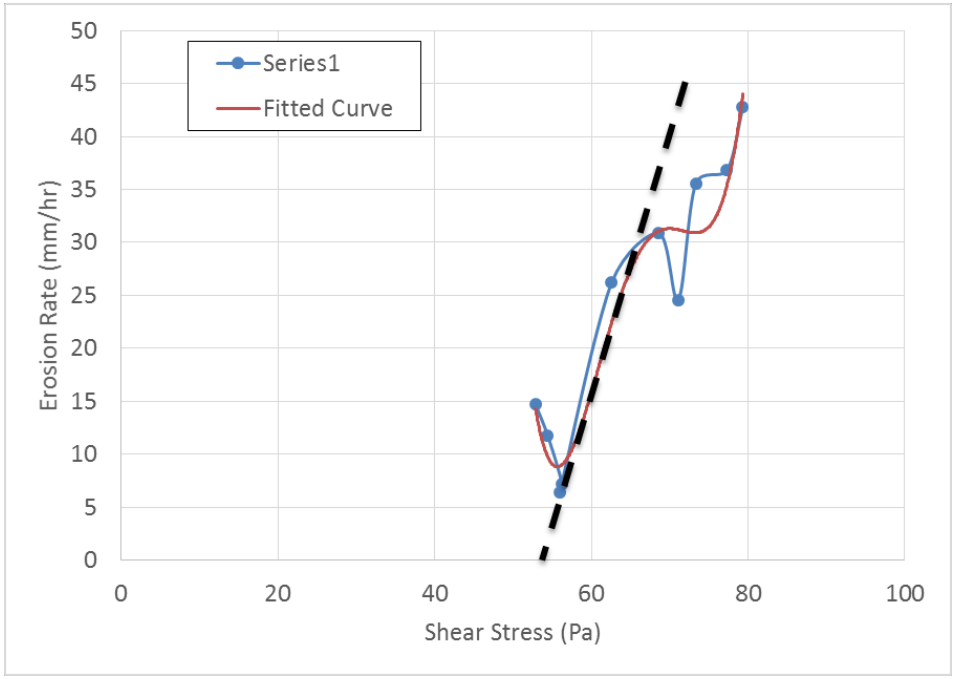

Figure A-89. Silt #1

Time	Time	Flow rate		U/S Tube Pressure Di	Db/S Tube Pressure Di			Sample length	Gradient	Flow rate	Friction Factor		Hole diameter		Reynold's No		Diameter
											If Laminar	If Turbulent	If Laminar	If Turbulent	If Laminar	If Turbulent	If Turbulent
(mins)	(s)	(gpm)	(l/min)	in	in	(in)	(mm)	L (mm)	S	Q (m3/s)	f_D	f_P	D_D	D_P	Re(l)	Re(t)	D (m)
0.00	0	0.68	2.57	22.0	5.5	16.5	419	115	3.644343	4.72892061E-05	3055.274478	23.24788	0.000600	0.000600	808023.5	8182354	0.01006
1.00	60	0.88	3.33	22.0	5.5	16.5	419	115	3.644343	5.75852169E-05	30.51112E+00	2.041251E+00	0.010665	0.010670	1802302.4	1607213.0	0.010106708
2.00	120	1.01	3.82	22.0	5.5	16.5	419	115	3.644343	6.73872261E-05	30.89499E+00	2.051253E+00	0.010707	0.010714	1610113.1	1713003.7	0.010607146
3.00	180	1.09	4.13	21.8	5.5	16.3	413	115	3.589135	7.08473658E-05	40.67787E+00	2.061256E+00	0.010740	0.010744	1716455.7	1817394.5	0.010407447
4.00	240	1.33	5.03	21.8	6.0	15.8	400	115	3.478693	8.53695120E-05	40.26244E+00	2.071259E+00	0.010811	0.010817	1623756.7	1902364.3	0.010708176
5.00	300	1.45	5.49	21.8	6.0	15.8	400	115	3.478693	9.51645821E-05	40.54622E+00	2.081262E+00	0.010847	0.010852	1531324.1	1934241.9	0.010708525
6.00	360	1.77	6.70	21.5	6.3	15.3	387	115	3.368226	1.01817677E-04	40.62999E+00	2.091265E+00	0.010927	0.010935	1748854.1	1914972.6	0.010609357
7.00	420	2.30	8.71	21.5	6.5	15.0	381	115	3.313043	1.34457181E-04	40.81365E+00	2.001268E+00	0.011031	0.012404	1673364.1	1747059.8	0.010902104
8.00	480	2.85	10.79	21.5	7.5	14.0	356	115	3.092171	1.37991831E-04	40.89974E+00	2.011271E+00	0.011147	0.011676	1190333.3	1595011.1	0.010704116
9.00	540	3.49	13.21	21.3	8.0	13.3	337	115	2.926521	2.12703198E-04	50.48111E+00	2.021273E+00	0.011265	0.011287	1271346.7	1251600.2	0.010081287
10.00	600	3.98	15.07	20.9	8.0	12.9	328	115	2.849212	2.75319110E-04	50.36499E+00	2.031276E+00	0.011349	0.011372	1282795.5	1212557.0	0.010401372
11.25	675	4.59	17.38	20.5	8.3	12.3	311	115	2.705652	3.28197548E-04	50.45945E+00	2.041530E+00	0.011460	0.011479	1244646.9	1254615.4	0.010514794
12.00	720	5.03	19.04	20.3	8.5	11.8	298	115	2.595213	3.71379314E-04	50.47324E+00	2.051282E+00	0.011539	0.011554	1215744.3	1245897.3	0.010607155
13.00	780	5.34	20.21	20.0	9.0	11.0	279	115	2.429563	4.53261970E-04	50.48161E+00	2.061285E+00	0.011622	0.011622	1205063.1	1255631.9	0.010816222

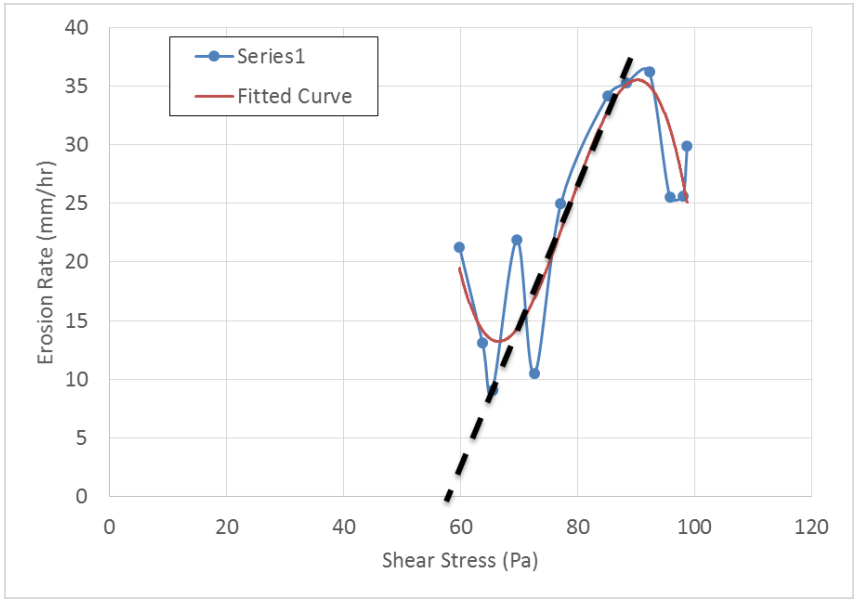

Figure A-90. Silt #2

Time	Time	Flow rate		U/S Tube	Db/S Tube	Pressure Di		Sample length	Gradient	Flow rate	Friction Factor		Hole diameter		Reynold's No.		Diameter
								If Laminar	If Turbulent		If Laminar	If Turbulent	If Laminar	If Turbulent	If Laminar	If Turbulent	
(mins)	(s)	(gpm)	(l/min)	in	in	(in)	(mm)	L (mm)	S	Q (m3/s)	$f_{Õ}$	f_p	$D_{Õ}$	D_p	Re(l)	Re(t)	D (m)
0.00	0	0.75	2.84	24.0	5.5	18.5	470	115	4.086	8.67935178E-3	55.8588	21.4272	0.006000	0.006009	90703	1831.8	0.07006
0.50	30	0.99	3.75	24.0	5.5	18.5	470	115	4.086	8.62945579E-3	30.8213E+0	2.02168E+0	0.010672	0.010678	111546	1365	0.060678
1.00	60	1.12	4.24	24.0	5.5	18.5	470	115	4.086	8.60965671E-3	40.6568E+0	2.03198E+0	0.010714	0.010720	112720	2.1	1521	1107.8	0.060720
1.50	90	1.22	4.62	24.0	5.5	18.5	470	115	4.086	8.66995770E-3	40.9923E+0	2.05119 3E	0.010749	0.010752	118296	77.3	1528	615.7	0.060752
2.00	120	1.41	5.34	24.0	5.8	18.3	464	115	4.030	8.69859657E-3	40.5278E+0	2.06144 8E	0.010804	0.010807	117366	53.2	1345	90.1	0.060807
2.50	150	1.57	5.94	24.0	6.3	17.8	451	115	3.920	9.49708532E-3	40.3632E+0	2.07170 3E	0.010855	0.010858	118442	88.7	1543	282.0	0.060858
3.00	180	1.80	6.81	24.0	6.8	17.3	438	115	3.81	1.13566E-2	40.8987E+0	2.08195 8E	0.010918	0.010917	125225	56.4	1502	278.0	0.060917
3.50	210	2.00	7.57	24.3	7.0	17.3	438	115	3.81	1.26185E-2	50.2342E+0	3.00121 4E	0.010966	0.010964	186611	17.4	1358	138.1	0.060964
4.00	240	2.25	8.52	24.5	7.5	17.0	432	115	3.754	1.24610995E-2	50.4696E+0	3.01146 9E	0.011024	0.011022	167509	6.7	1671	29.3	0.061022
5.00	300	2.77	10.49	24.0	8.0	16.0	406	115	3.533	1.37044736E-2	50.8406E+0	3.03197 9E	0.011151	0.011142	138072	3.1	1558	87.9	0.061142
6.00	360	3.32	12.57	24.0	8.3	15.8	400	115	3.478	1.50695426E-2	60.4115E+0	3.06149 0E	0.011261	0.011249	260948	7.2	2405	83.4	0.061249
6.50	390	3.91	14.80	25.3	8.5	16.8	425	115	3.699	1.54261678E-2	60.6470E+0	3.07174 5E	0.011321	0.011326	283104	3.2	2269	43.2	0.061326
7.00	420	4.21	15.94	25.3	8.8	16.5	419	115	3.644	1.57685266E-2	60.8825E+0	3.09100 0E	0.011376	0.011379	273480	8.2	2036	75.5	0.061379
7.50	450	4.66	17.64	25.0	9.0	16.0	406	115	3.533	1.63904430E-2	70.4179E+0	4.00125 5E	0.011455	0.011455	204093	4.2	1529	34.9	0.061455

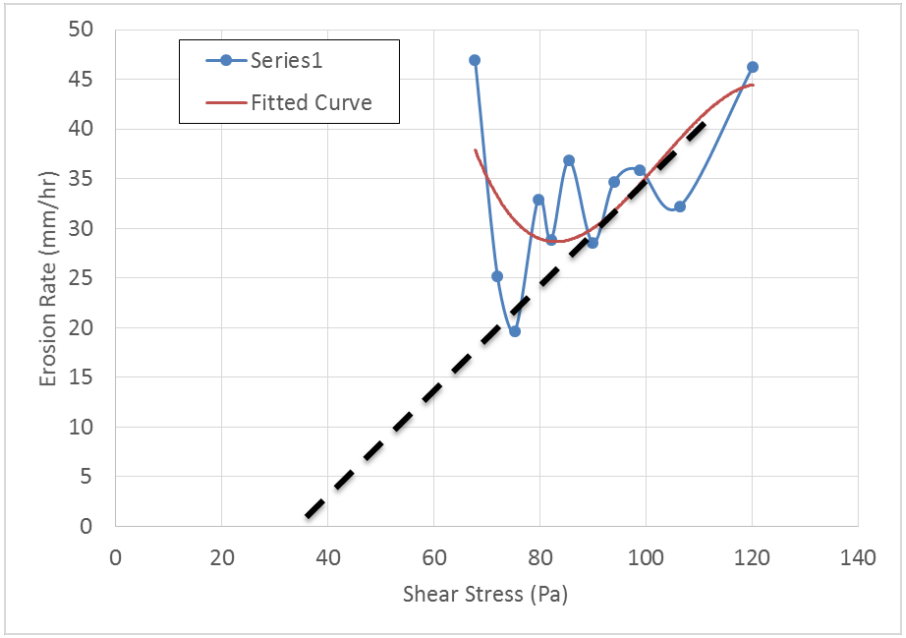

Figure A-91. Silt #3

Time	Time	Flow ra		U/S T	D/S Tu	Pressure Di	
(min)	(s)	(gpm)	(l/min)	in	in	(in)	(mm)
0.00	0	0.89	3.37	26.00	5.0	21.0	533
0.50	30	1.14	4.32	26.00	5.0	21.0	533
1.00	60	1.26	4.77	26.00	5.3	20.8	527
1.50	90	1.36	5.15	26.00	5.5	20.5	521
2.00	120	1.51	5.72	26.00	5.8	20.3	514
3.00	180	1.69	6.40	26.00	6.3	19.8	502
4.00	240	1.94	7.34	26.00	6.5	19.5	495
5.00	300	2.12	8.03	26.25	6.8	19.5	495
6.00	360	2.39	9.05	26.50	7.0	19.5	495
7.00	420	2.84	10.75	26.00	7.5	18.5	470
8.00	480	3.54	13.40	26.00	7.8	18.3	464
8.50	510	4.08	15.44	27.00	8.0	19.0	483
9.00	540	4.59	17.38	28.00	9.3	18.8	476
11.00	660	4.96	18.78	28.25	10.0	18.3	464

Sample length	Gradient	Flow rate	Friction	Factor	Hole diameter (m)		Reynold's No.		Diameter
			If Laminar	If Turbulent	If Laminar	If Turbulent	If Laminar	If Turbulent	Turbulent
L (mm)	S	Q (m3/s)	$f_{\tilde{O}}$	f_P	$D_{\tilde{O}}$	D_P	Re (l)	Re (t)	D (m)
115	4.63826	506817 50 E-30	45.3016	17.2725	0.006000	0.006000	10105 48.4	15 9548.4	0 50906
115	4.63826	701 8972 3 E-30	.5331 E-1	.0716 20 E-0	0010658	0.70066 5	11304 87.	1 0 3 6 3 4 4.5	9 8040 6650
115	4.58304	7 39 44 79 84 E-30	.6361 E-1	.0719 67 E-0	0010689	06.90069 6	16442 23.3	1 9 4 9 0 8 1.5	9 3070 6966
115	4.52782	3 65 08 80 73 E-30	.7391 E-1	.0813 14 E-0	0010716	09.80072 2	17457 67.8	1 8 4 3 6 4 9.9	9 600 07227
115	4.47260	9 85 62 96 66 E-30	.8420 E-1	.0816 61 E-0	0010752	02.50075 8	13536 27.9	1 2 5 0 5 0 2.5	9 4030 7583
115	4.36217	1 30 96 16 32 E-40	.0480 E-1	.0913 55 E-0	0010801	03.90080 3	10694 18.3	1 4 6 8 3 8 3.4	0 4010 8030
115	4.30695	1 62 52 23 29 E-40	.2539 E-2	.0010 49 E-0	0010856	07.30085 6	18746 29.6	1 9 7 9 6 2 7.3	9 6020 8568
115	4.30695	1 63 53 27 25 E-40	.4599 E-2	.0017 43 E-0	0010896	04.60089 3	18864 11.5	1 4 8 7 4 6 5.1	0 000 08938
115	4.30695	1 65 50 27 29 E-40	.6658 E-2	.0114 37 E-0	0010947	01.50094 3	19966 45.5	1 0 9 8 7 1 1.9	9 7010 9439
115	4.08608	1 67 99 51 78 E-40	.8718 E-2	.0211 31 E-0	0011035	07.80102 8	26143 46.9	2 8 1 5 4 9 5.2	0 2051 0286
115	4.03086	2 92 53 63 54 E-50	.0777 E-2	.0218 25 E-0	0011135	03.40113 3	24442 75.2	2 1 4 4 3 1 5.8	0 2001 1334
115	4.19652	2 15 77 34 91 E-50	.4807 E-2	.0311 72 E-0	0011182	03.70119 3	26648 65.2	2 9 6 3 6 1 1.5	9 7011 1936
115	4.14130	2 48 39 45 88 E-50	.2836 E-2	.0315 19 E-0	0011243	02.90125 8	22887 42.6	2 4 8 3 2 4 0 0.1	0 3011 2582
115	4.03086	3 91 52 69 53 E-50	.6955 E-2	.0419 07 E-0	0011320	00.00132 0	20902 54.5	2 2 9 2 2 5 4.5	9 2021 32

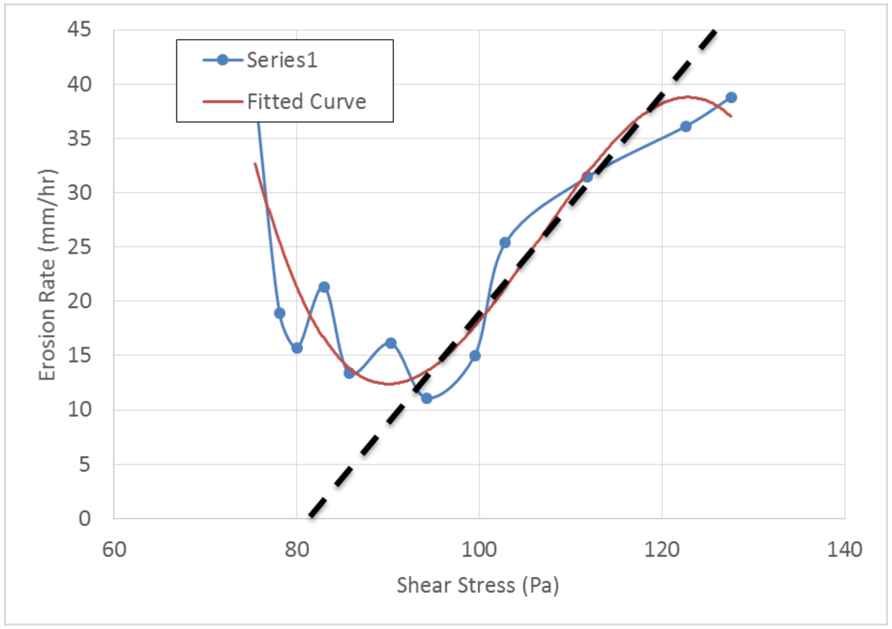

Figure A-92. Silt #4

Time	Time	Flow rate		U/S Tube	Dn/S Tube	Pressure Di		Sample length	Gradient	Flow rate	Friction Factor If Laminar	Friction Factor If Turbulent	Hole diameter If Laminar	Hole diameter If Turbulent	Reynold's No. If Laminar	Reynold's No. If Turbulent	Diameter
(mins)	(s)	(gpm)	(l/min)	in	in	(in)	(mm)	L (mm)	S	Q (m3/s)	f_{D_H}	f_D	D_{H_L}	D_{H_T}	Re(l)	Re(t)	D (m)
0.00	0	1.03	3.90	23.50	5.5	18.0	457	115	3.975651	5.24197843E-04	45.702020	4.4423	0.000500	0.000500	10600.38	1864.38	0.080405
0.50	30	1.21	4.58	23.50	5.5	18.0	457	115	3.975651	7.26137349E-04	10.660445	5.051350E	0.000549	0.000557	12751.46	2269.05	0.160105572
1.00	60	1.35	5.11	23.50	5.5	18.0	457	115	3.975651	8.25177742E-04	10.855076	6.061277E	0.000590	0.000603	15767.89	2734.14	0.200603 5
2.00	120	1.52	5.75	23.50	5.5	18.0	457	115	3.975651	9.25187947E-04	20.231126	8.081131E	0.000654	0.000670	10800.89	1576.62	0.480806700
2.50	150	1.65	6.25	23.50	5.5	18.0	457	115	3.975651	1.20147140E-03	20.421146	9.091058E	0.000690	0.000708	17845.93	2811.25	0.240507087
3.00	180	1.78	6.74	23.50	5.5	18.0	457	115	3.975651	1.21127340E-03	20.611176	1.001999E	0.001072	0.000746	10920.70	1435.76	0.190307460
3.50	210	1.96	7.42	23.50	5.5	18.0	457	115	3.975651	1.22137646E-03	20.801901	1.021091E	0.001076	0.000790	11958.64	1693.12	0.170407901
4.00	240	2.14	8.10	23.75	6.0	17.8	451	115	3.920431	1.43758031E-03	20.892221	1.031184E	0.001081	0.001083	20035.10	2819.52	0.440108350
4.50	270	2.36	8.93	24.00	6.5	17.5	445	115	3.865217	1.74389819E-03	30.482246	1.041277E	0.001086	0.001088	28113.46	2357.65	0.700708848
5.00	300	2.59	9.80	23.50	6.3	17.3	438	115	3.81	1.6340E-03	30.372266	1.051369E	0.001090	0.001093	26281.70	2185.73	0.650409346
6.00	360	3.09	11.70	23.50	7.0	16.5	419	115	3.644347	1.79842965E-03	30.745311E	1.071555E	0.001101	0.001039	22387.11	1820.81	0.810610392
7.00	420	3.56	13.48	24.00	8.8	15.3	387	115	3.368226	2.02847601E-03	40.433661	1.091740E	0.001127	0.001143	28445.79	2343.23	0.970711438
8.00	480	3.89	14.73	21.00	9.0	12.0	305	115	2.650432	2.44758432E-03	40.511411E	2.011926E	0.001129	0.001269	27303.77	2263.52	0.440612697
9.00	540	4.06	15.37	25.50	11.0	14.5	368	115	3.202602	2.85569165E-03	40.894646E	2.041111E	0.001267	0.001267	25409.38	2948.38	0.900812675

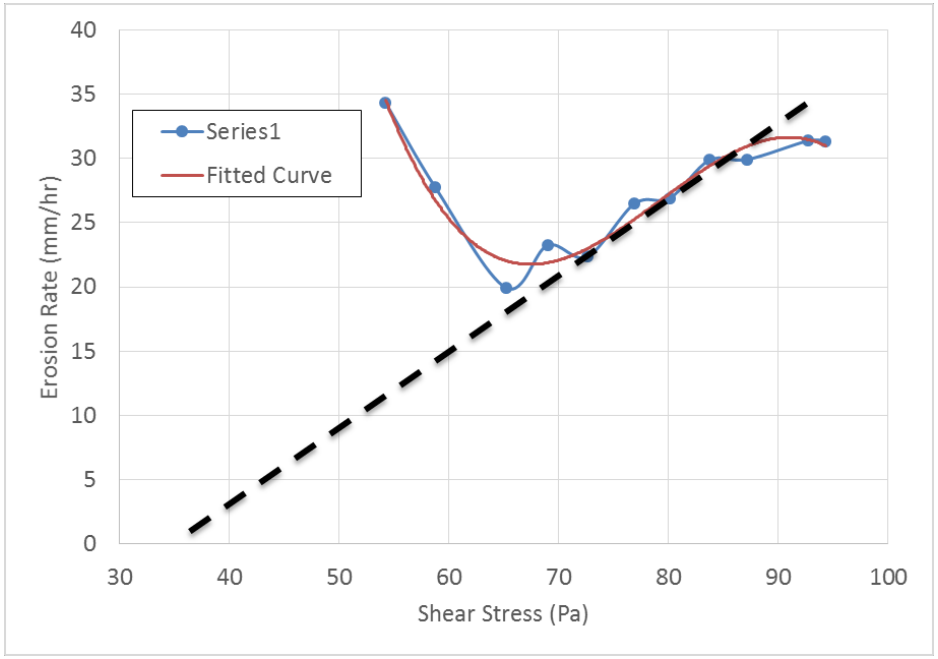

Figure A-93. Silt #5

Time	Time	Flow rate		U/S Tube Pressure	Dn/S Tube Pressure	Pressure Di	
(mins)	(s)	(gpm)	(l/min)	in	in	(in)	(mm)
0.00	0	0.63	2.38	22.25	5.5	16.8	425
0.50	30	0.81	3.07	22.25	5.5	16.8	425
1.00	60	1.02	3.86	22.25	5.5	16.8	425
1.50	90	1.16	4.39	22.25	5.5	16.8	425
2.00	120	1.30	4.92	22.25	5.5	16.8	425
3.00	180	1.40	5.30	22.25	5.8	16.5	419
4.00	240	1.53	5.79	22.25	5.8	16.5	419
5.00	300	1.64	6.21	22.50	5.8	16.8	425
6.00	360	1.81	6.85	22.75	6.0	16.8	425
7.00	420	2.06	7.80	23.25	6.3	17.0	432
8.00	480	2.33	8.82	23.50	6.8	16.8	425
9.00	540	2.65	10.03	23.00	7.3	15.8	400
10.00	600	3.11	11.77	23.00	8.3	14.8	375
11.00	660	3.51	13.29	23.75	10.3	13.5	343

Sample length	Gradient	Flow rate	Friction Factor		Hole diameter		Reynold's No.		Diameter
			If Laminar	If Turbulent	If Laminar	If Turbulent	If Laminar	If Turbulent	Turbulent
L (mm)	S	Q (m^3/s)	$f_{\bar{D}}$	f_p	$D_{\bar{D}}$	D_p	Re(l)	Re(t)	D (m)
115	3.699563	5.92714E-05	2095.771	17.7953	0.005500	0.005508	80901.79	8917.91	0.010055
115	3.699563	5.51211E-05	2.94949E-02	2.001936E-02	0.010618	0.006284	12061.93	12037.00	0.020628
115	3.699563	5.42315E-05	1.28E-02	2.041076E-02	0.010688	0.007084	14175.27	12081.93	0.020850
115	3.699563	5.32118E-05	5.93061E-03	2.071216E-02	0.010739	0.007643	13292.11	11951.81	0.020907
115	3.699563	5.22017E-05	2.48545E-03	2.001356E-02	0.010788	0.008172	17208.38	12233.77	0.021058
115	3.644343	4.78832E-05	8.42E-04	2.061636E-02	0.010850	0.008772	12218.11	11623.25	0.021304
115	3.644343	4.76852E-05	5.19826E-04	2.021917E-02	0.010912	0.009381	11350.49	11426.97	0.021040
115	3.699563	5.02314E-05	4.55555E-04	2.091197E-02	0.010963	0.009884	13302.46	12491.92	0.021988
115	3.699563	5.12417E-05	3.49125E-04	2.051478E-02	0.011029	0.010531	10386.91	11538.81	0.021910
115	3.754781	5.22699E-05	2.42699E-04	2.011758E-02	0.011101	0.011291	17405.57	11481.96	0.021411
115	3.699563	5.42710E-05	1.62626E-04	2.081038E-02	0.011185	0.012131	15553.00	11549.47	0.021907
115	3.478691	5.56751E-05	1.06983E-04	2.041319E-02	0.011295	0.013116	15539.24	11456.71	0.021603
115	3.257821	5.69068E-05	7.33401E-05	2.001599E-02	0.011430	0.014445	13679.32	11387.51	0.021603
115	2.981732	5.92134E-05	4.86977E-05	2.061879E-02	0.011567	0.015671	15704.33	11704.33	0.021001

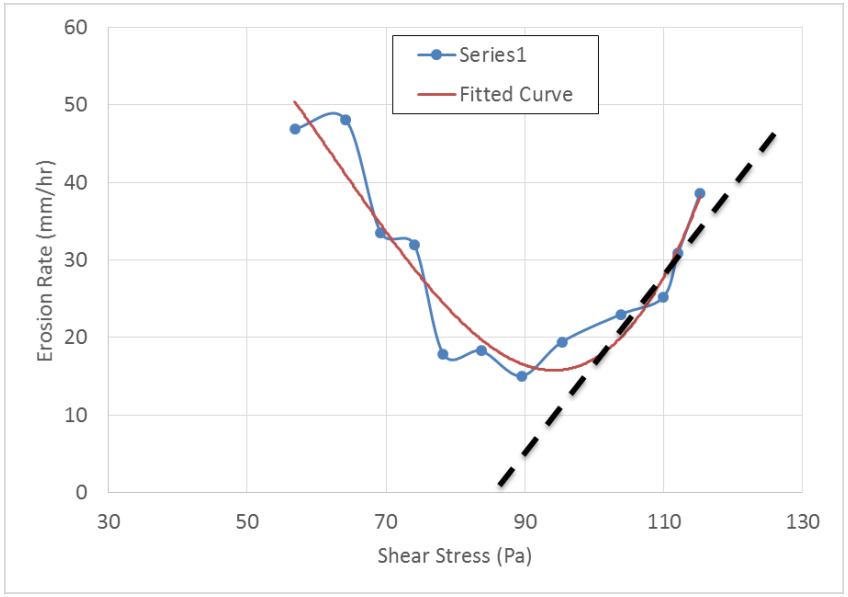

Figure A-94. Silt #6

Time	Time	Flow rate		U/S Tube	Db/S Tube	Pressure Di		Sample length	Gradient	Flow rate	Friction Factor		Hole diameter		Reynold's No.		Diameter
											If Laminar	If Turbulent	If Laminar	If Turbulent	If Laminar	If Turbulent	
(mins)	(s)	(gpm)	(l/min)	in	in	(in)	(mm)	L (mm)	S	Q (m3/s)	f_D	f_p	D_D	D_p	Re(l)	Re(t)	D (m)
0.00	0	0.73	2.76	24.00	5.5	18.5	470	115	4.08608	4.66905576E-06	30	65.8412	22.6173	0.00600	0.00600	90407	2.3	3147	2.3	0.00600	
0.50	30	0.85	3.22	23.50	5.5	18.0	457	115	3.97565	5.23167247E-06	30	8.24	0E+00	2.03113	5E+00	0.00644	0.00644	100726	0.2	16002	74.7	0.00644	0
1.00	60	0.96	3.63	23.00	5.5	17.5	445	115	3.86521	6.70359617E-06	30	9.64	0E+00	2.03165	3E+00	0.00686	0.00683	100489	2.1	13019	42.3	0.00683	0
1.50	90	1.02	3.86	22.50	5.5	17.0	432	115	3.75478	8.24630592E-06	30	40.5	039E+00	2.04117	0E+00	0.00715	0.00702	191310	3.1	18023	33.3	0.00702	0.00
2.00	120	1.13	4.28	22.50	5.8	16.8	425	115	3.69957	9.51221972E-06	30	40.2	438E+00	2.04168	8E+00	0.00752	0.00741	181169	7.1	21785	9.6	0.00741	0.00
2.50	150	1.24	4.69	22.50	6.0	16.5	419	115	3.64433	1.07882362E-05	30	40.5	837E+00	2.05120	5E+00	0.00788	0.00775	142224	9.3	16224	49.9	0.00775	0.00
3.00	180	1.37	5.19	22.50	6.5	16.0	406	115	3.53391	1.36044334E-05	30	40.5	236E+00	2.05172	3E+00	0.00831	0.00815	122682	2.9	14233	83.1	0.00815	0.00
3.50	210	1.49	5.64	22.25	6.5	15.8	400	115	3.47869	1.54605024E-05	30	40.6	635E+00	2.06124	1E+00	0.00868	0.00849	113435	3.3	13356	61.2	0.00849	0.00
4.00	240	1.63	6.17	22.75	6.5	16.3	413	115	3.58913	1.30042385E-05	30	40.8	035E+00	2.06175	8E+00	0.00894	0.00878	114418	5.7	19431	51.3	0.00878	0.00
4.50	270	2.00	7.57	23.00	6.5	16.5	419	115	3.64433	4.72862168E-06	30	40.8	434E+00	2.07127	6E+00	0.00962	0.00953	176618	5.3	15038	25.8	0.00953	0.00
5.00	300	2.39	9.05	23.50	7.5	16.0	406	115	3.53391	1.35047439E-05	30	50.4	833E+00	2.07179	4E+00	0.01041	0.01034	147187	3.3	18749	88.3	0.01034	0.00
5.50	330	2.71	10.26	23.50	8.0	15.5	394	115	3.42347	1.87206917E-05	30	50.2	232E+00	2.08131	1E+00	0.01107	0.01098	179105	7.3	19203	107.1	0.01098	0.00
6.00	360	3.16	11.96	23.25	8.5	14.8	375	115	3.25782	2.69098376E-05	30	50.3	631E+00	2.08182	9E+00	0.01195	0.01184	220758	4.7	20874	100.5	0.01184	0.00
6.50	390	3.78	14.31	24.00	9.0	15.0	381	115	3.31304	2.33487488E-05	30	50.5	031E+00	2.09134	6E+00	0.01272	0.01272	253012	6.2	29912	99.0	0.01272	0.00

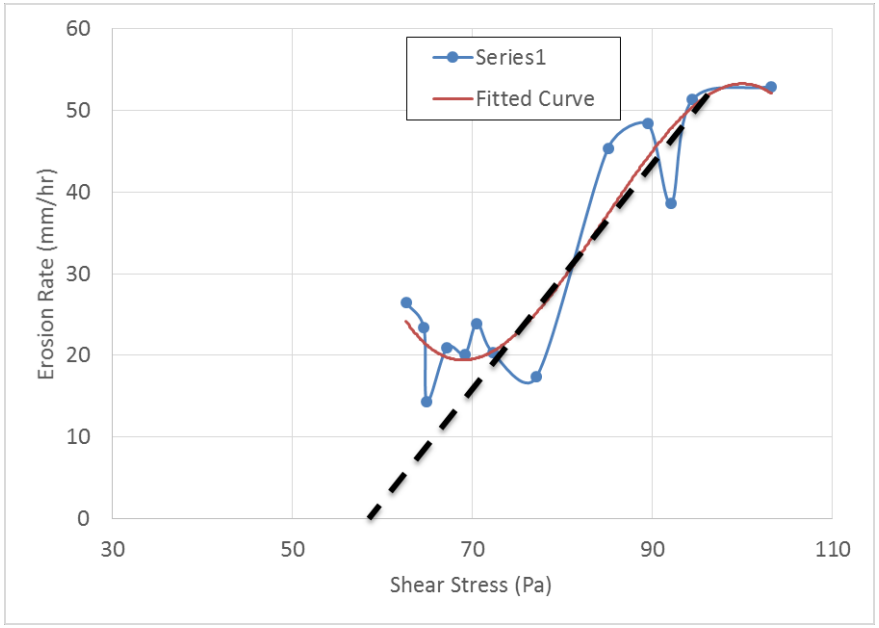

Figure A-95. Silt #7

Time	Flow rate		U/S Tube Diameter	D/S Tube Diameter	Pressure Differential		Sample length	Gradient	Flow rate	Friction Factor		Hole diameter		Reynold's No.		Diameter
										If Laminar	If Turbulent	If Laminar	If Turbulent	If Laminar	If Turbulent	
(s)	(gpm)	(l/min)	in	in	(in)	(mm)	L (mm)	S	Q (m3/s)	$f_{\bar{O}}$	f_P	$D_{\bar{O}}$	D_P	Re(l)	Re(t)	D (m)
0	0.71	2.69	14.3	5.00	9.3	236	115	2.054084	8.4975974E-05	1095.041912	12.01944	0.006000	0.006000	902012.8	9512.8	0.00506
15	0.79	2.99	14.3	5.00	9.3	236	115	2.054084	9.4985471E-05	40.95446E+00	1.011919E+00	0.002085	0.005709	771697.2	8172.078	0.000990
30	0.86	3.26	14.3	5.25	9.1	230	115	1.998867	9.4526558E-05	70.95850E+00	2.021636E+00	0.002104	0.008011	766453.0	8147.459	0.001011
45	1.12	4.24	14.3	5.25	9.1	230	115	1.998867	9.9566651E-05	40.50255E+00	3.032353E+00	0.002126	0.006401	761898.5	8196.596	0.001014
60	1.49	5.64	14.3	5.50	8.8	224	115	1.943692	9.2410704E-05	40.50666E+00	4.042070E+00	0.002152	0.006771	771661.2	8601.669	0.001016
75	2.00	7.57	14.3	5.75	8.5	216	115	1.887739	9.1236014E-05	40.47106E+00	5.042787E+00	0.002181	0.007198	784517.8	8793.462	0.001019
90	2.51	9.50	14.3	6.75	7.5	191	115	1.656521	7.5783396E-05	20.64147E+00	6.052504E+00	0.002215	0.007230	993006.4	9184.621	0.001026
105	3.00	11.36	15.5	8.75	6.8	171	115	1.490816	6.9859625E-05	20.43187E+00	7.062221E+00	0.002248	0.007302	1097490.5	8994.612	0.001029
120	3.66	13.85	16.5	10.50	6.0	152	115	1.325212	6.2733099E-05	20.46228E+00	8.062939E+00	0.002287	0.008297	1194981.0	9158.944	0.001029
180	4.51	17.07	18.0	12.00	6.0	152	115	1.325212	7.8349514E-05	30.83896E+00	1.022981E+00	0.003500	0.003500	1000032.1	14040.32	0.001043

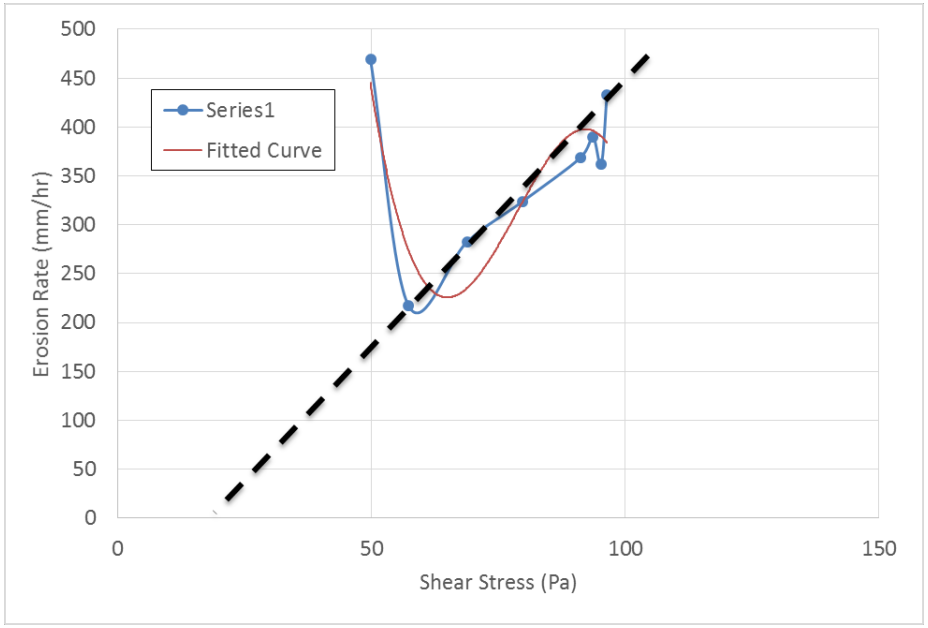

Figure A-96. Teton Dam Left Core

APPENDIX B

GEOTECHNICAL PROPERTIES SPREADSHEETS

Clay Samples - EFA

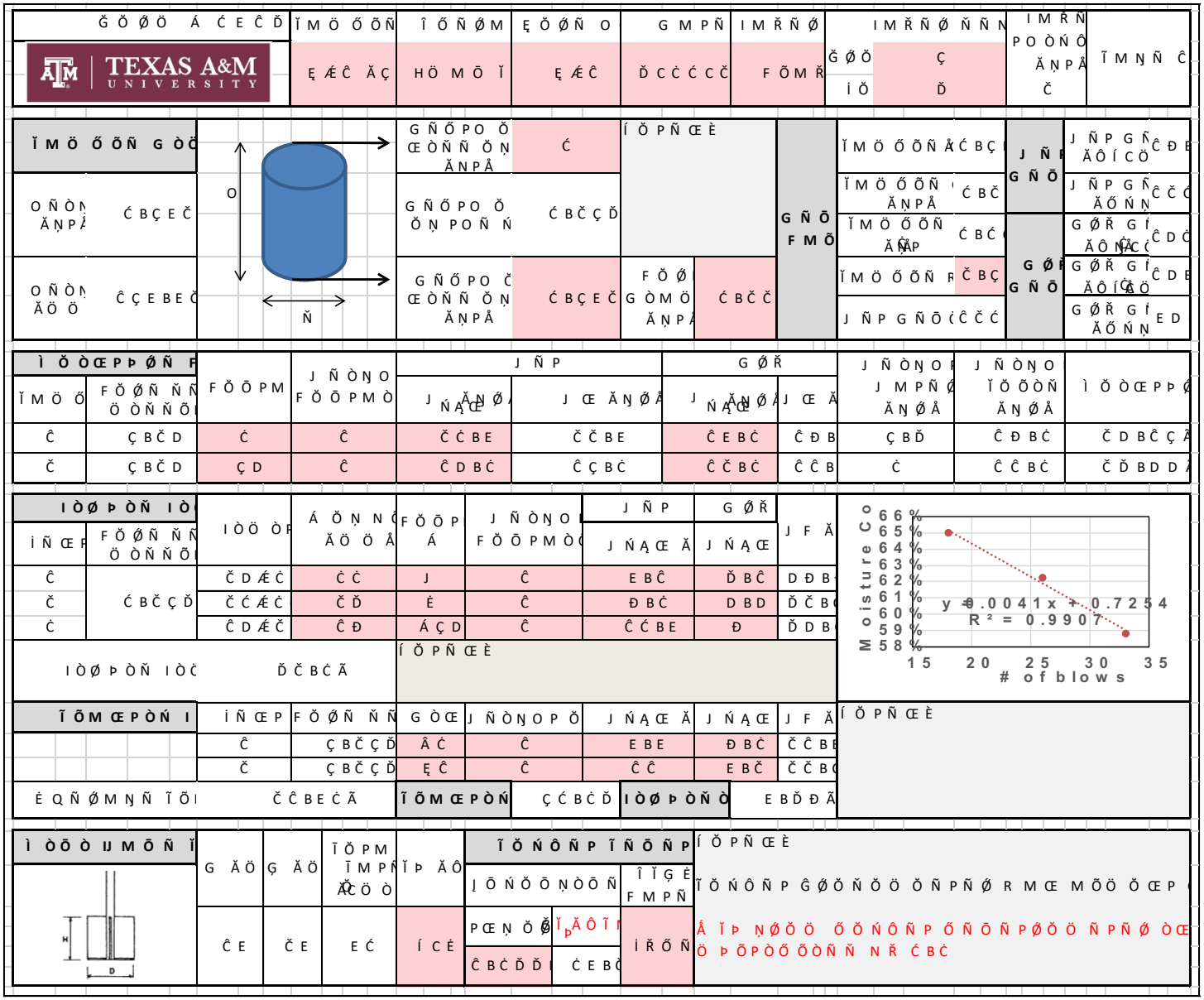

Figure B-1. B-1 (4’-6’) Beaumont Formation - Page 1

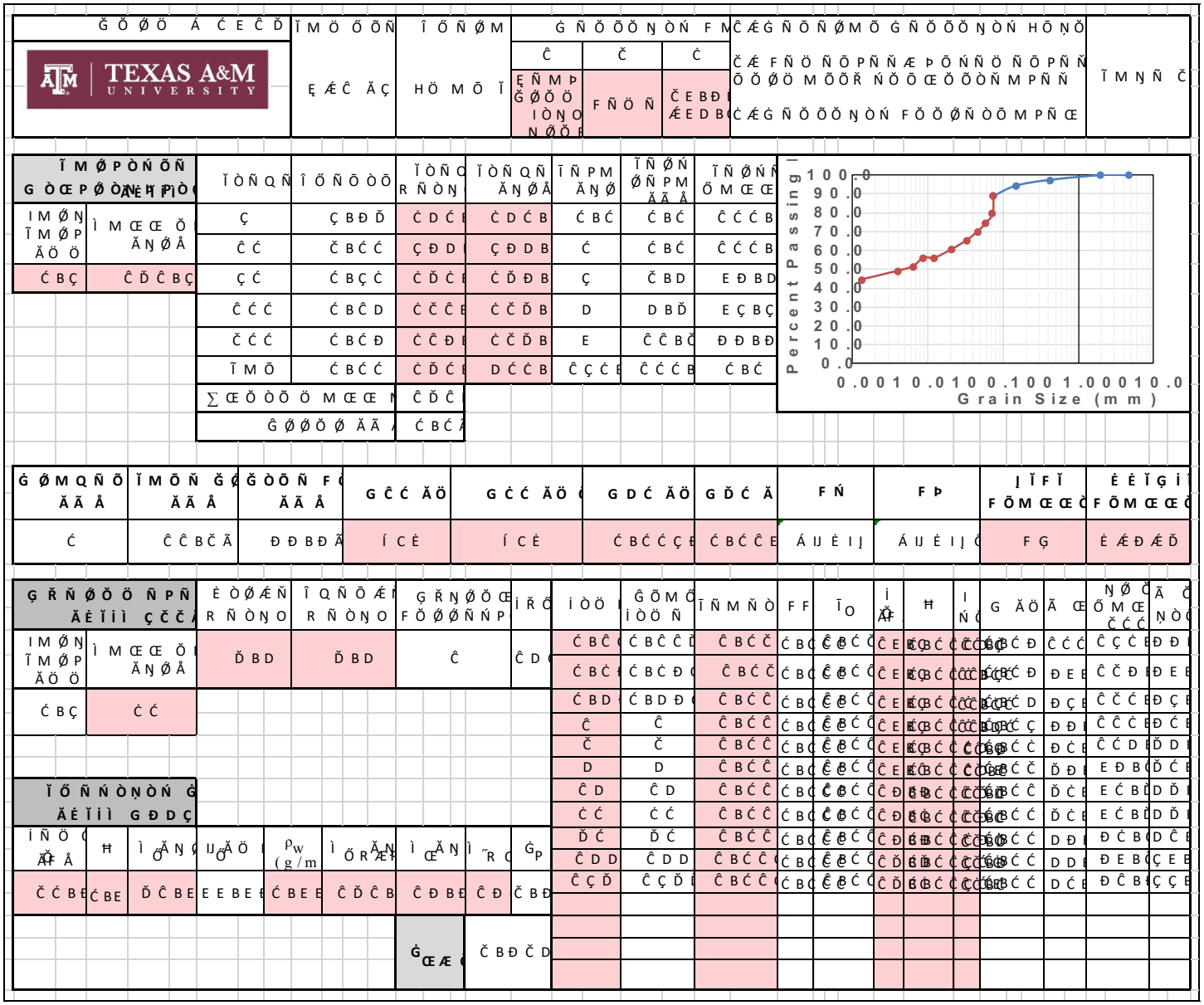

Figure B-2. B-1 (4’-6’) Beaumont Formation - Page 2

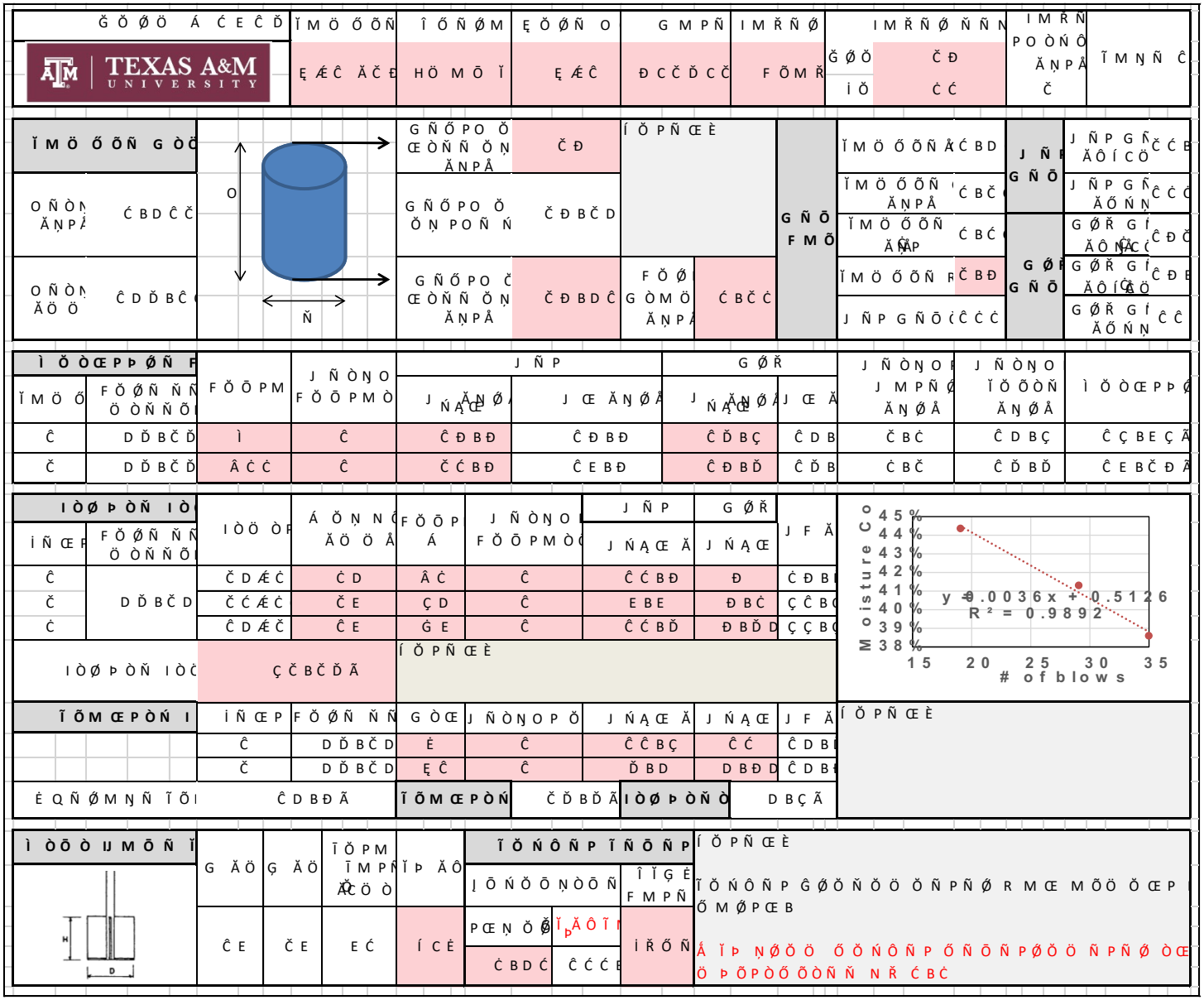

Figure B-3. B-1 (28’-30’) Beaumont Formation - Page 1

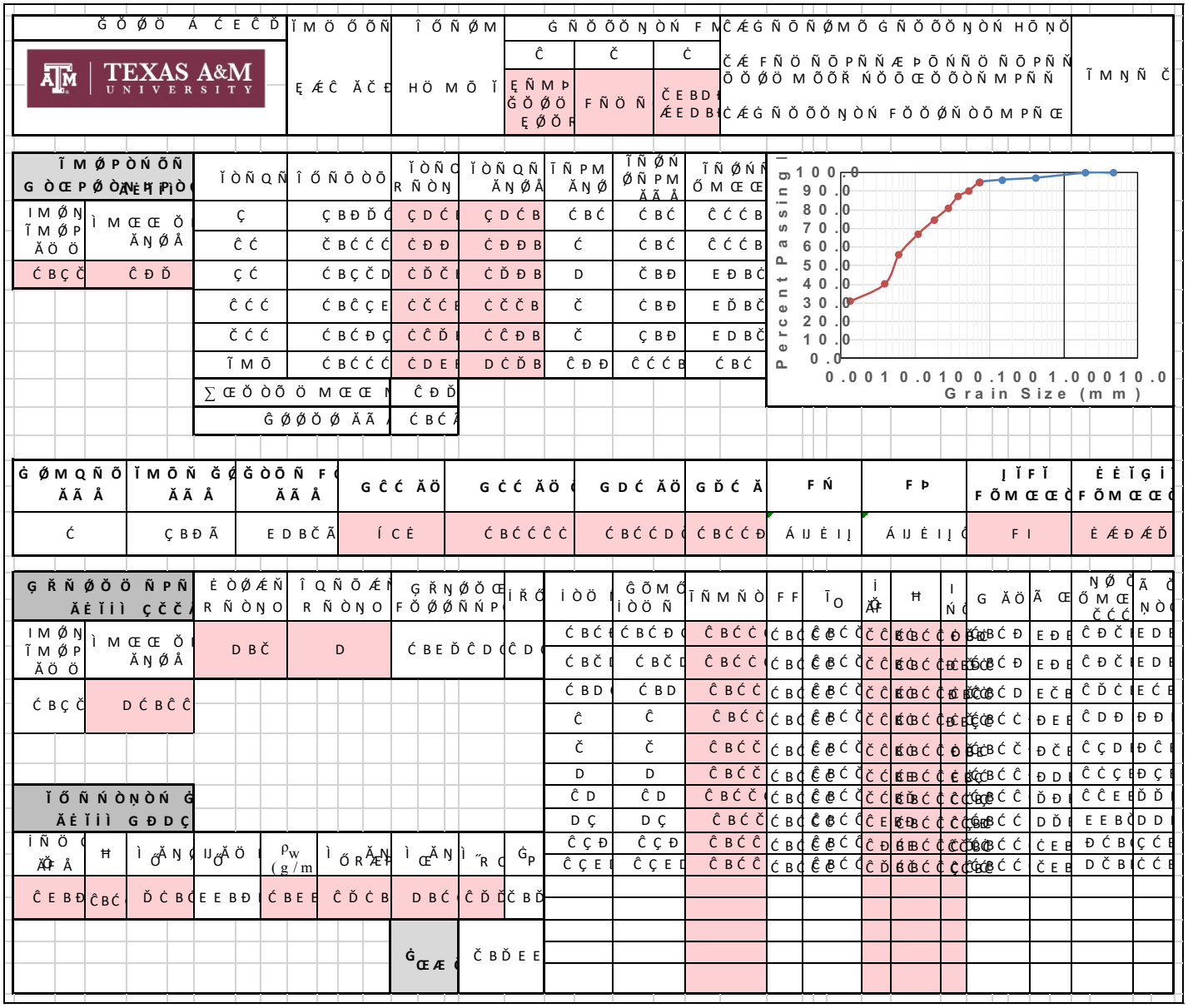

Figure B-4. B-1 (28’-30’) Beaumont Formation - Page 2

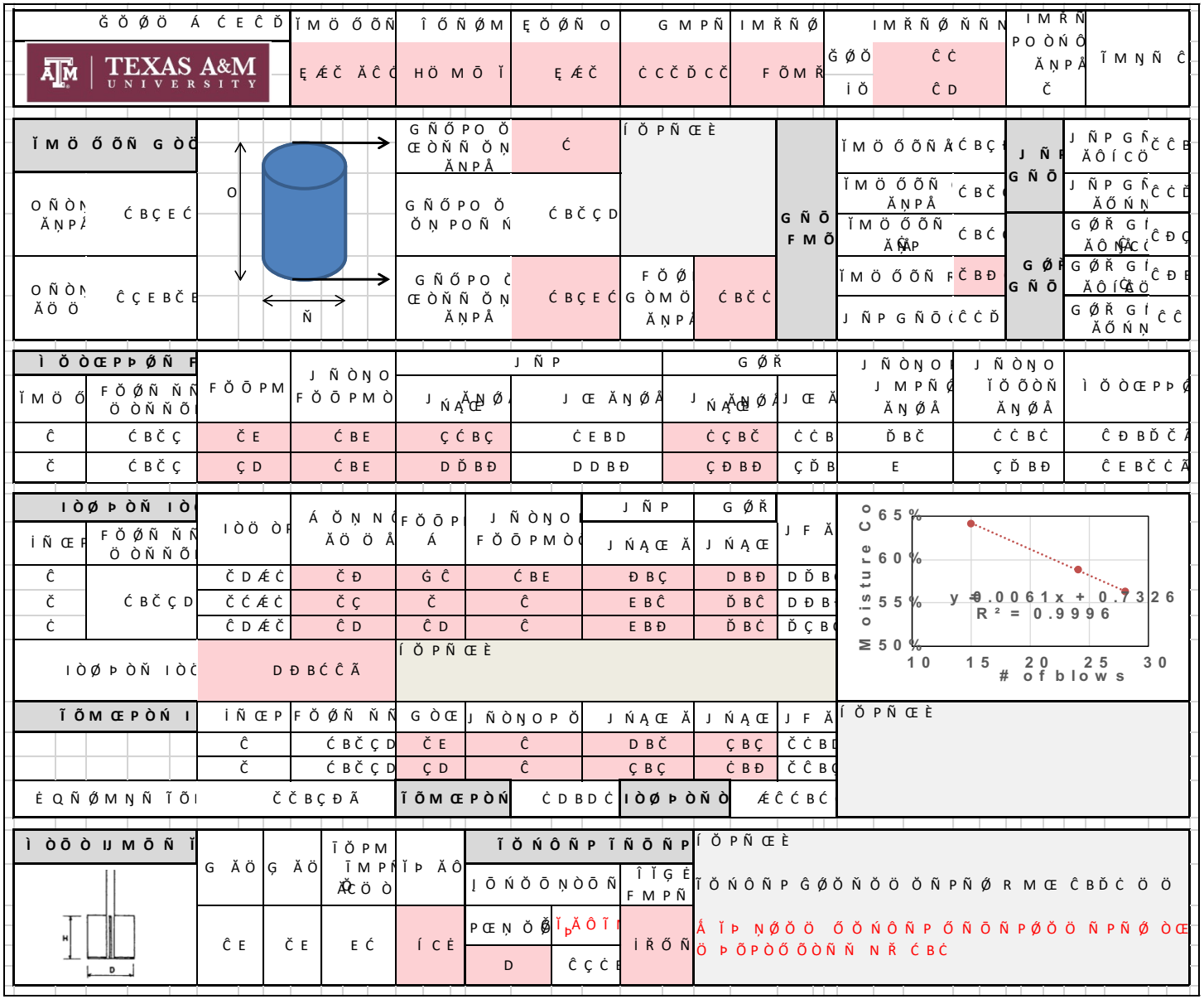

Figure B-5. B-2 (13'-15') Beaumont Formation - Page 1

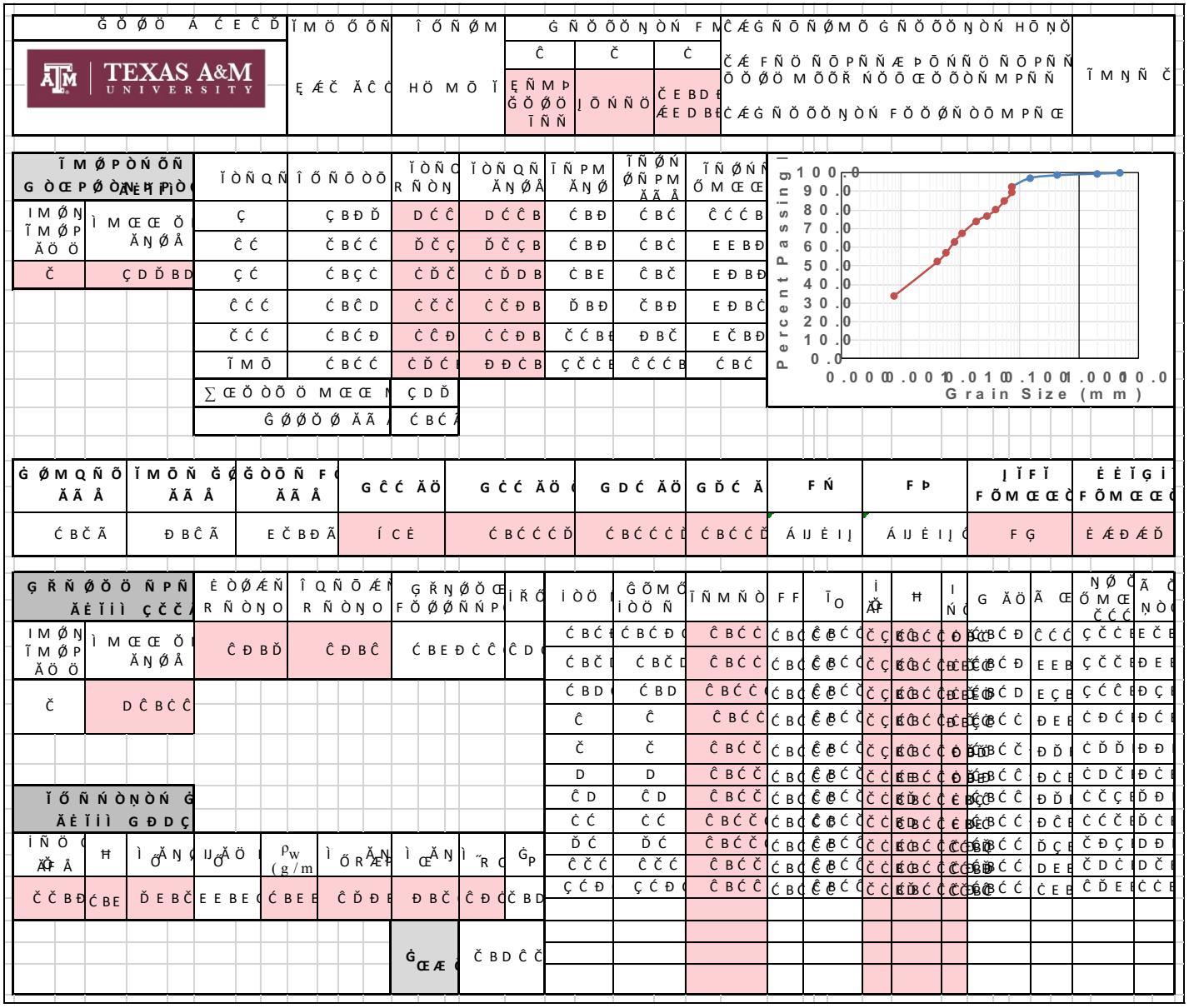

Figure B-6. B-2 (13'-15') Beaumont Formation - Page 2

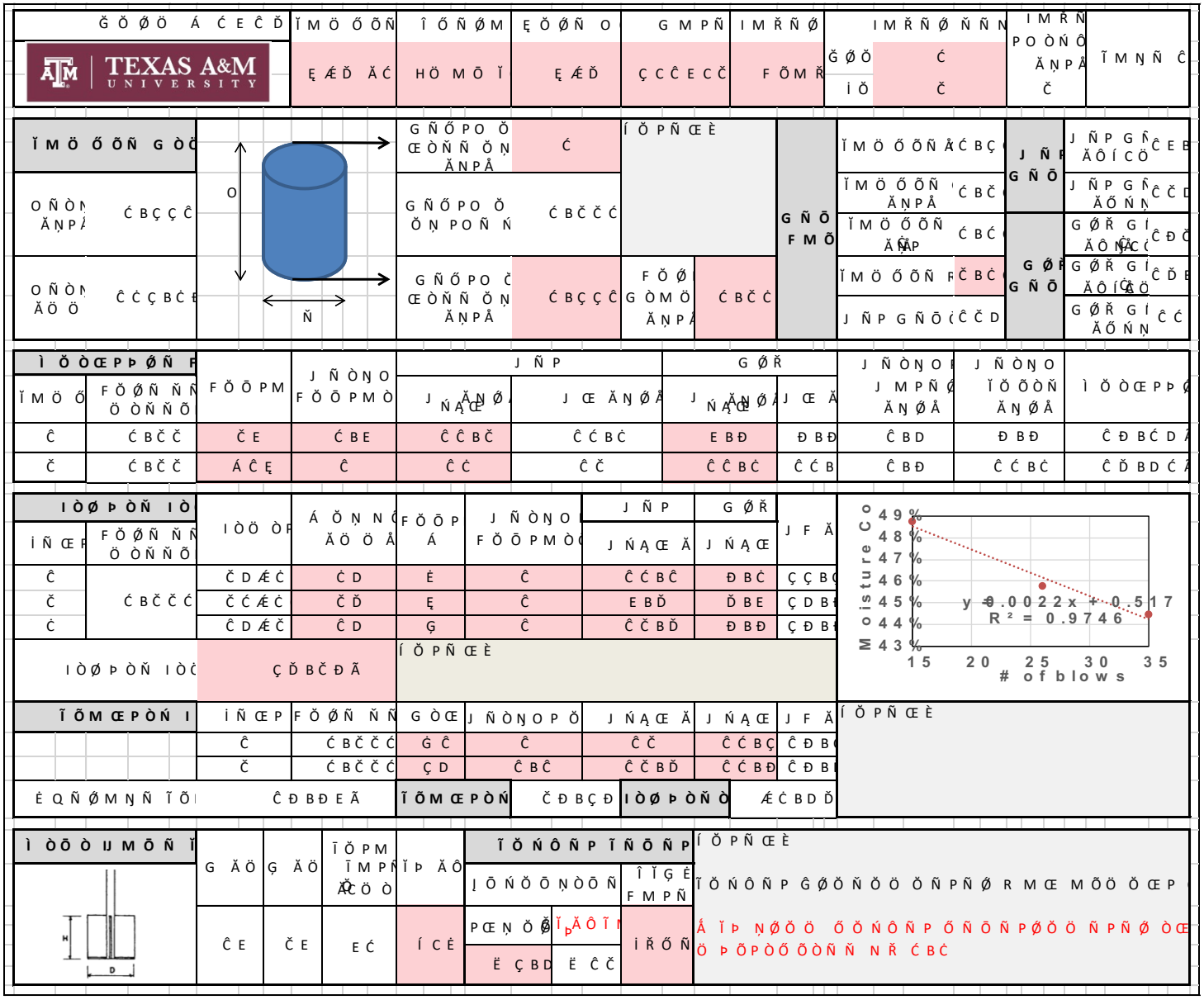

Figure B-7. B-6 (0'-2') Beaumont Formation - Page 1

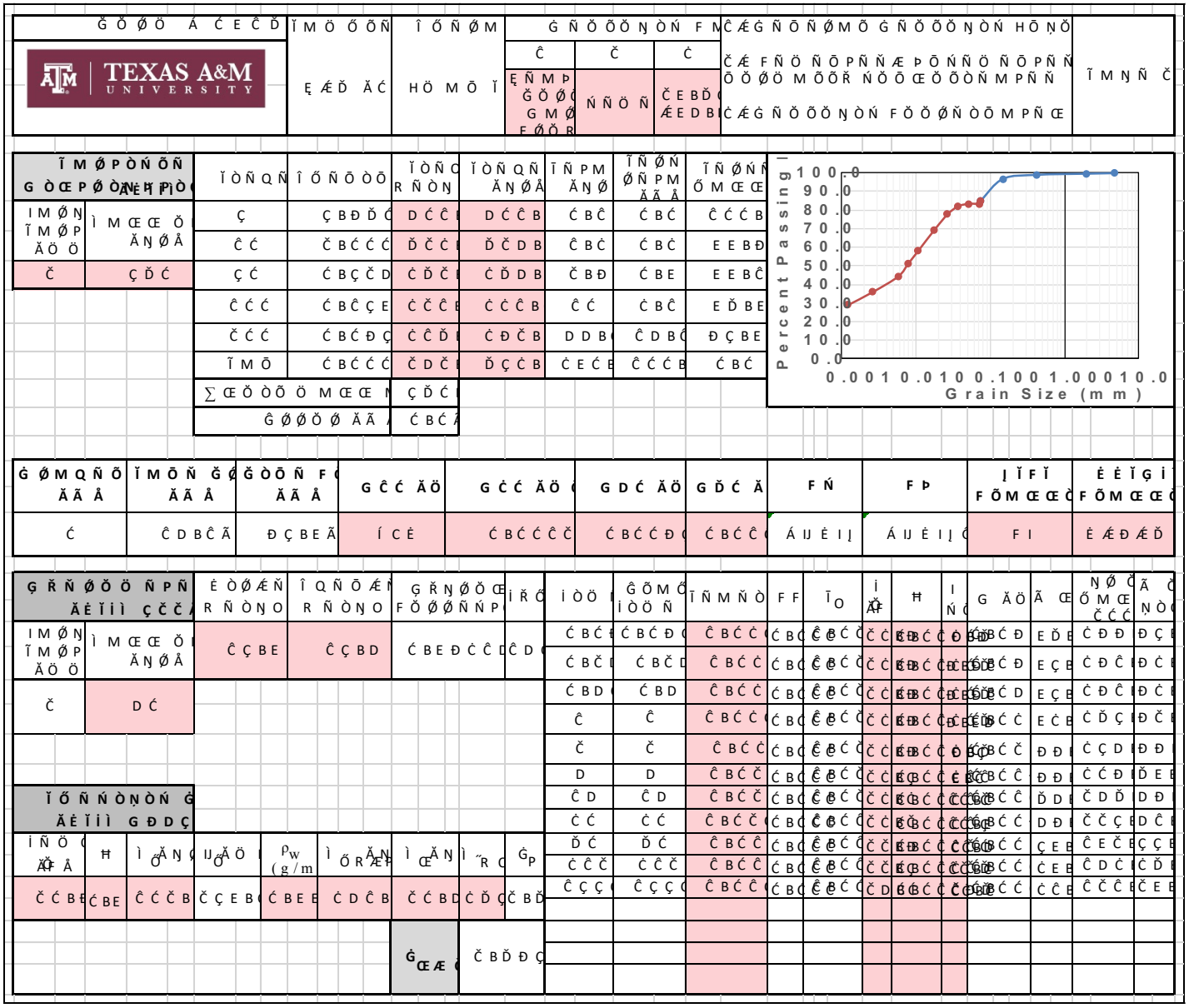

Figure B-8. B-6 (0'-2') Beaumont Formation - Page 2

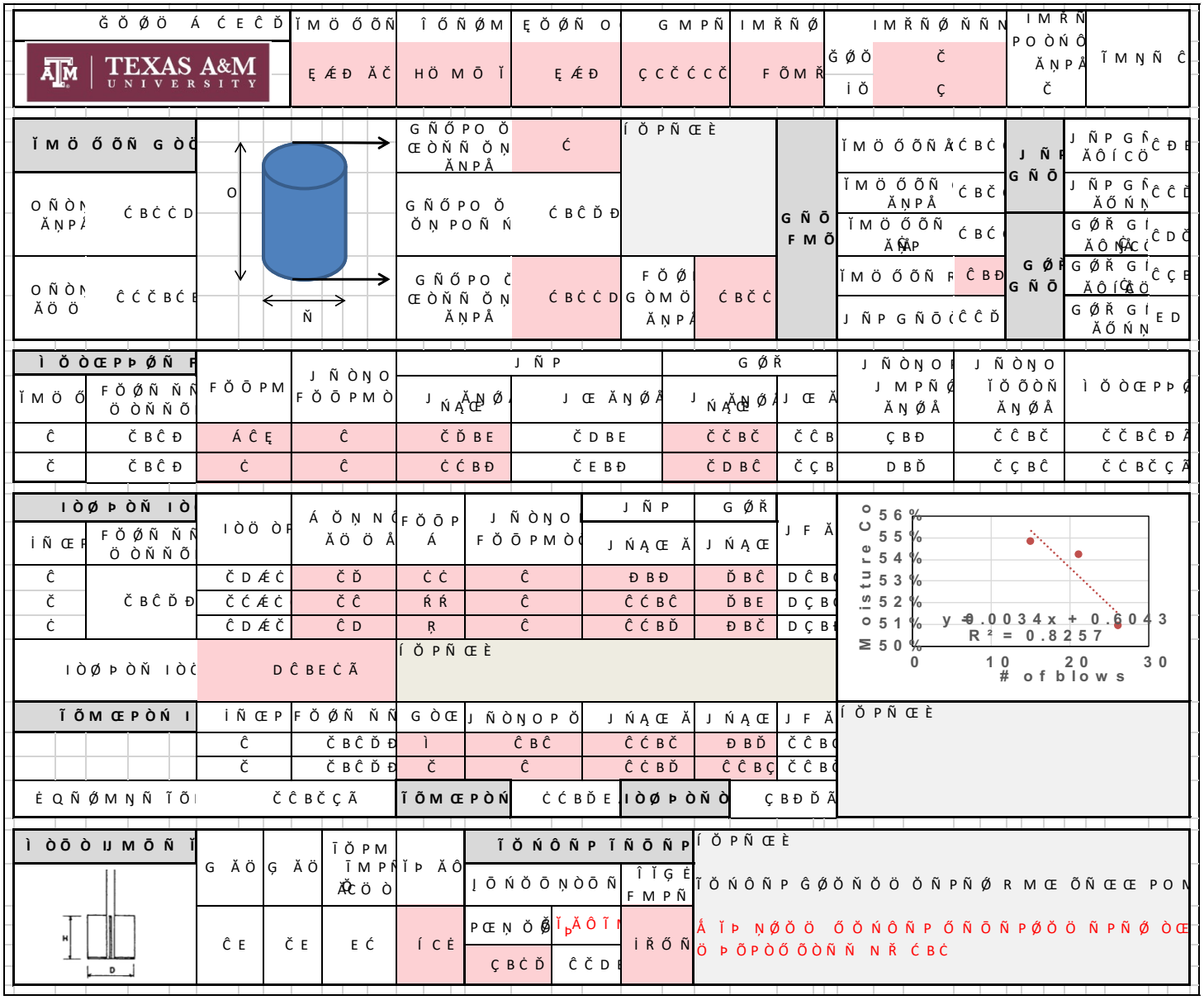

Figure B-9. B-8 (2'-4') 5694 Alluvium - Page 1

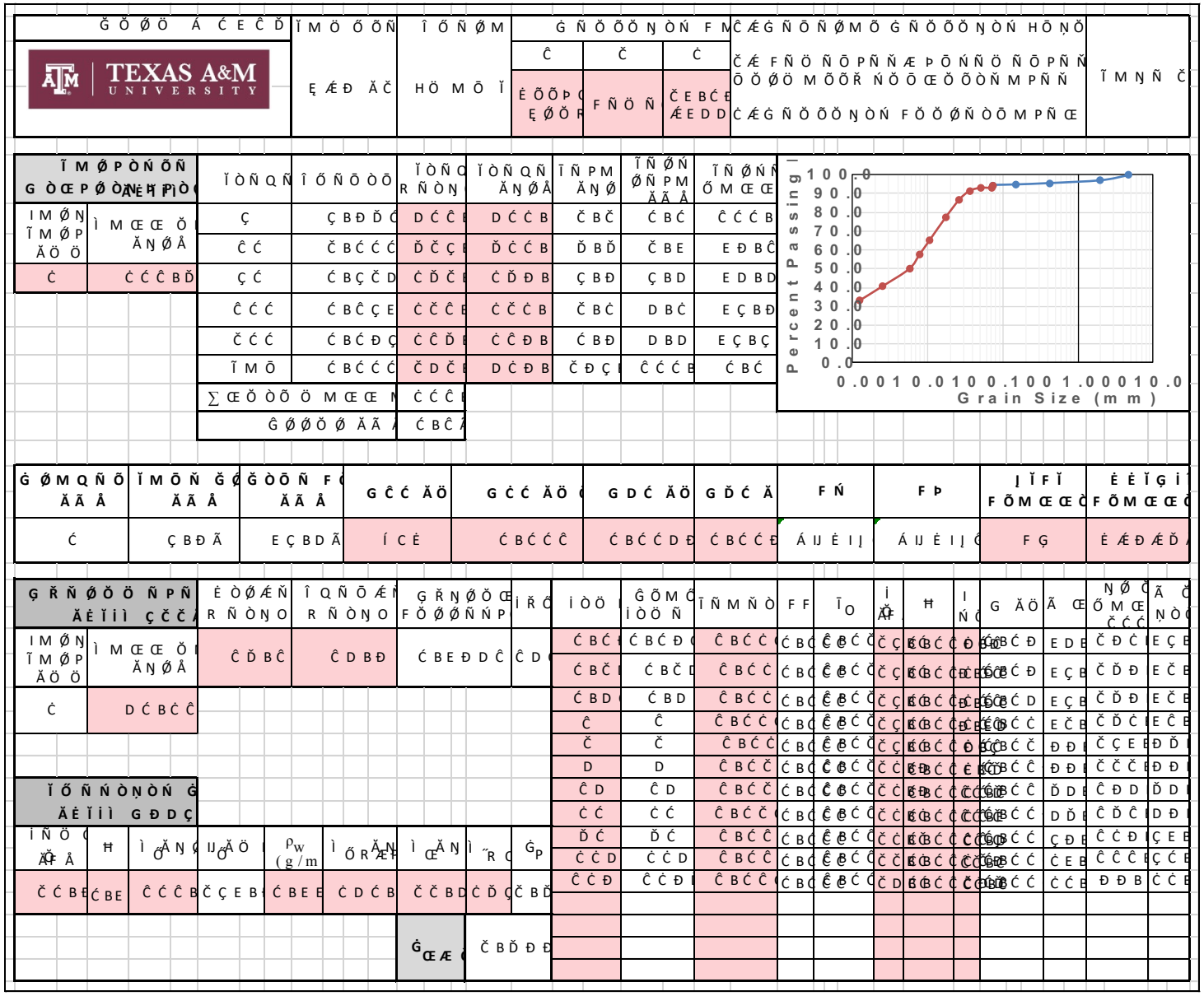

Figure B-10. B-8 (2'-4') 5694 Alluvium - Page 2

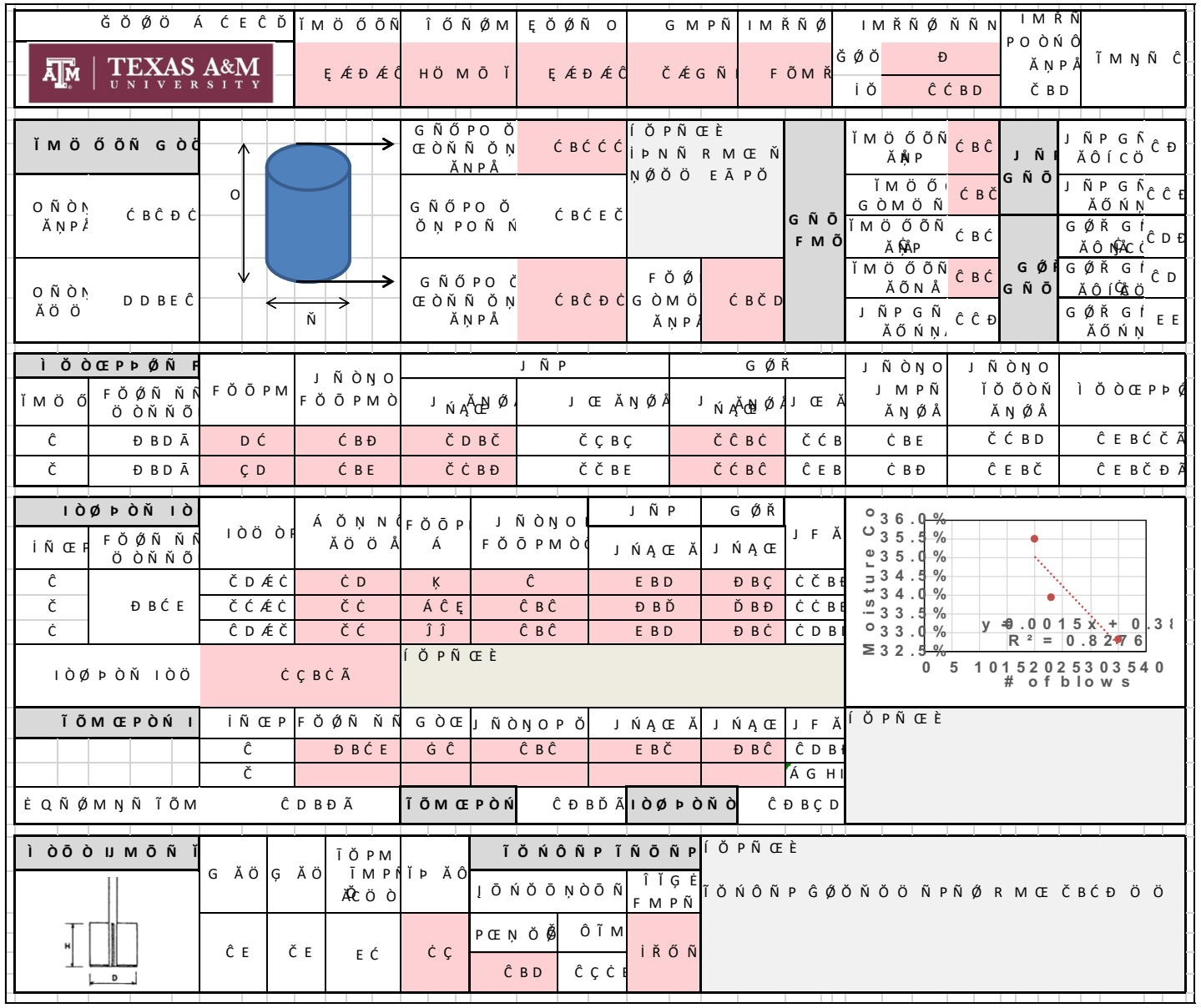

Figure B-11. B-7-16 (8’-10.5’) Top - Page 1

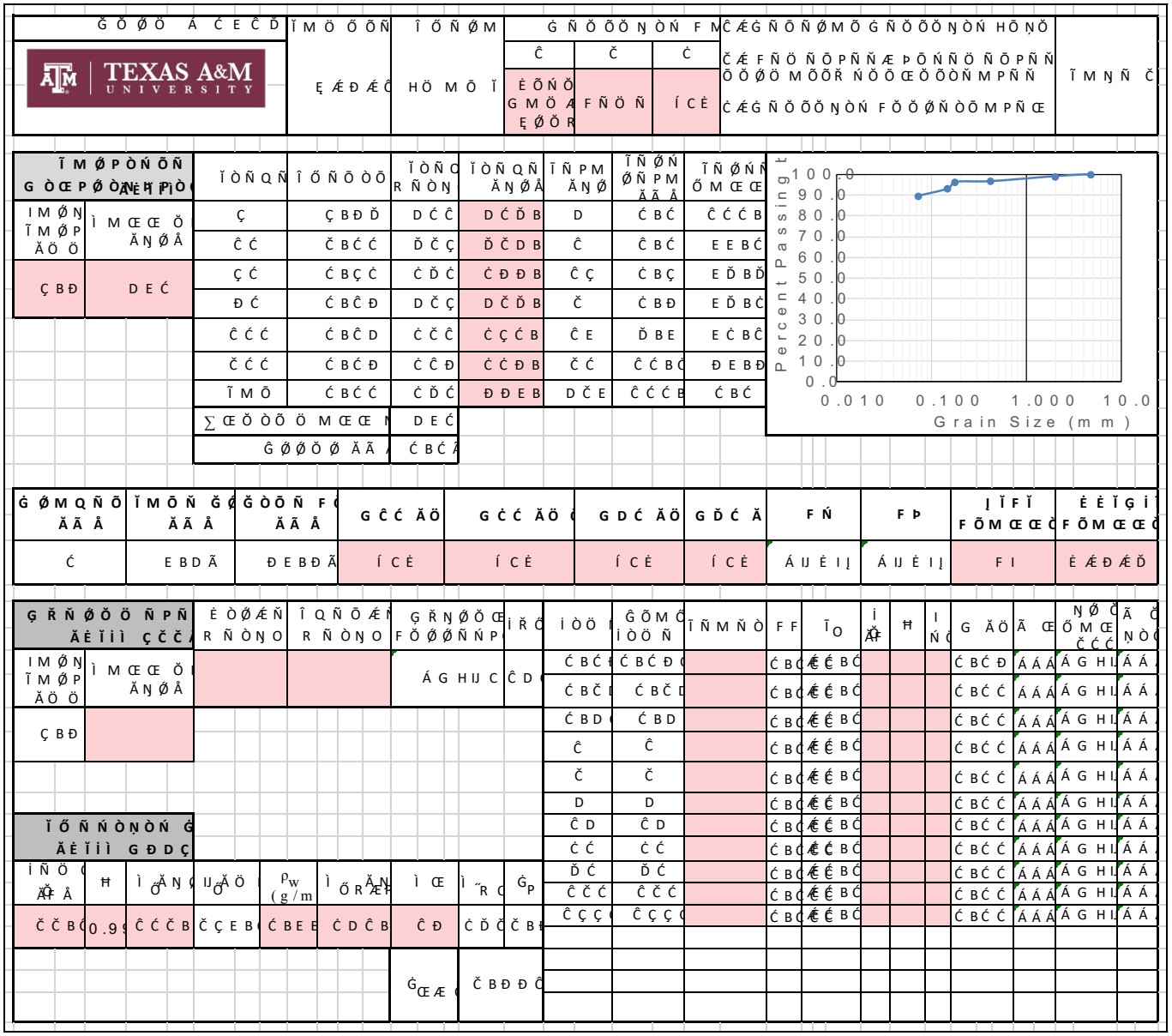

Figure B-12. B-7-16 (8’-10.5’) Top - Page 2

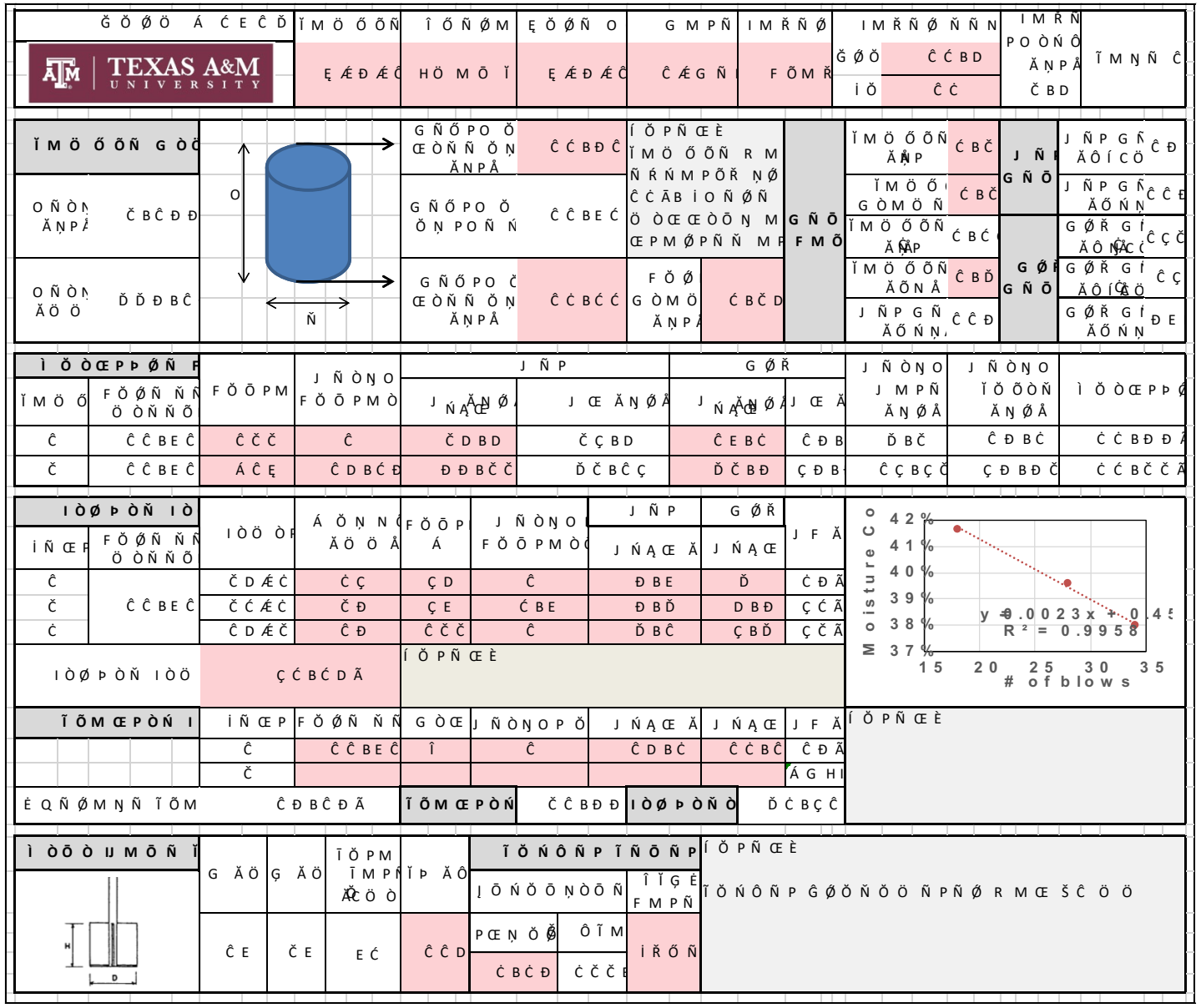

Figure B-13. B-7-16 (10.5'-13') Bottom - Page 1

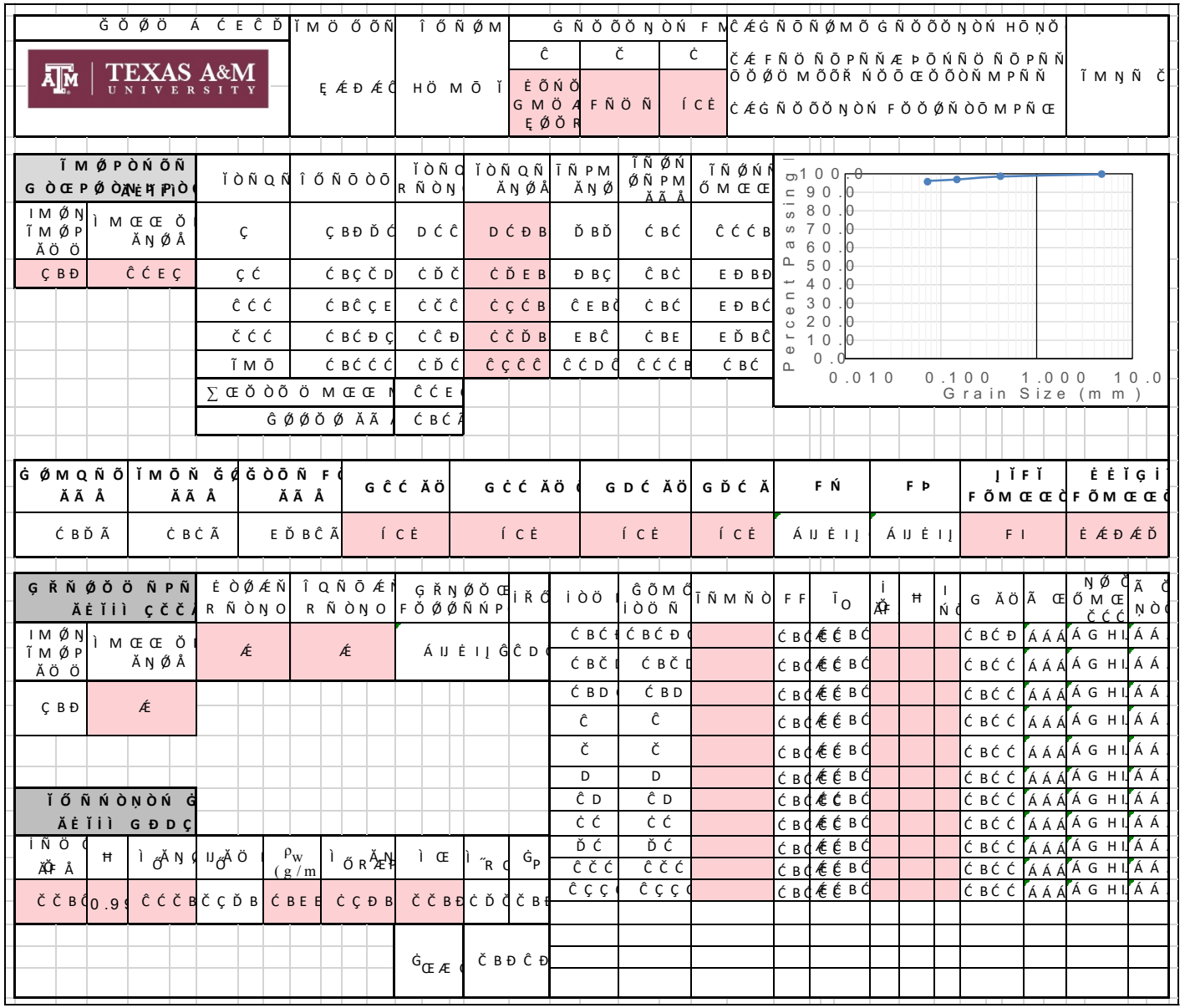

Figure B-14. B-7-16 (10.5’-13’) Bottom - Page 2

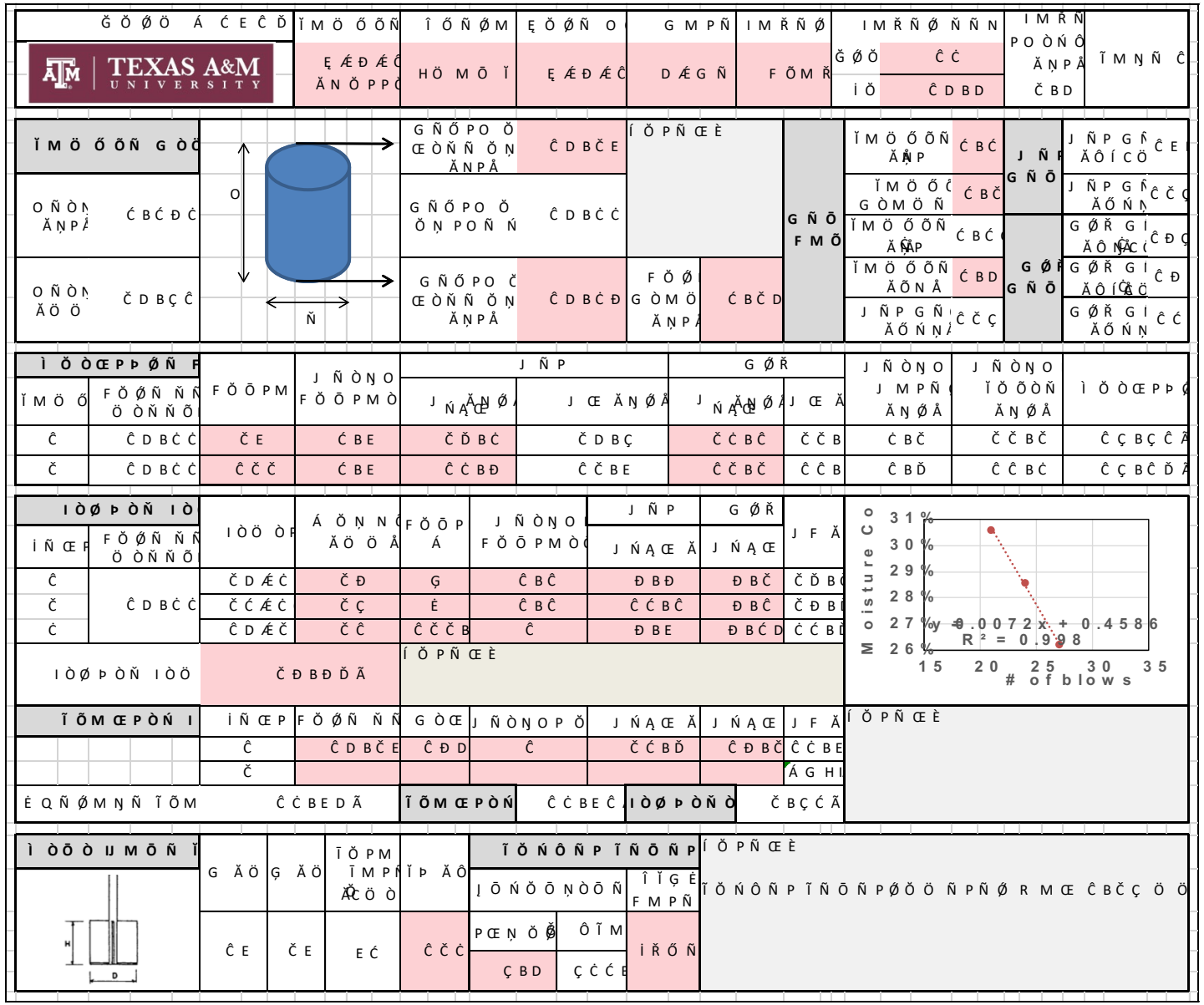

Figure B-15. B-7-16 (13'-15.5') Bottom - Page 1

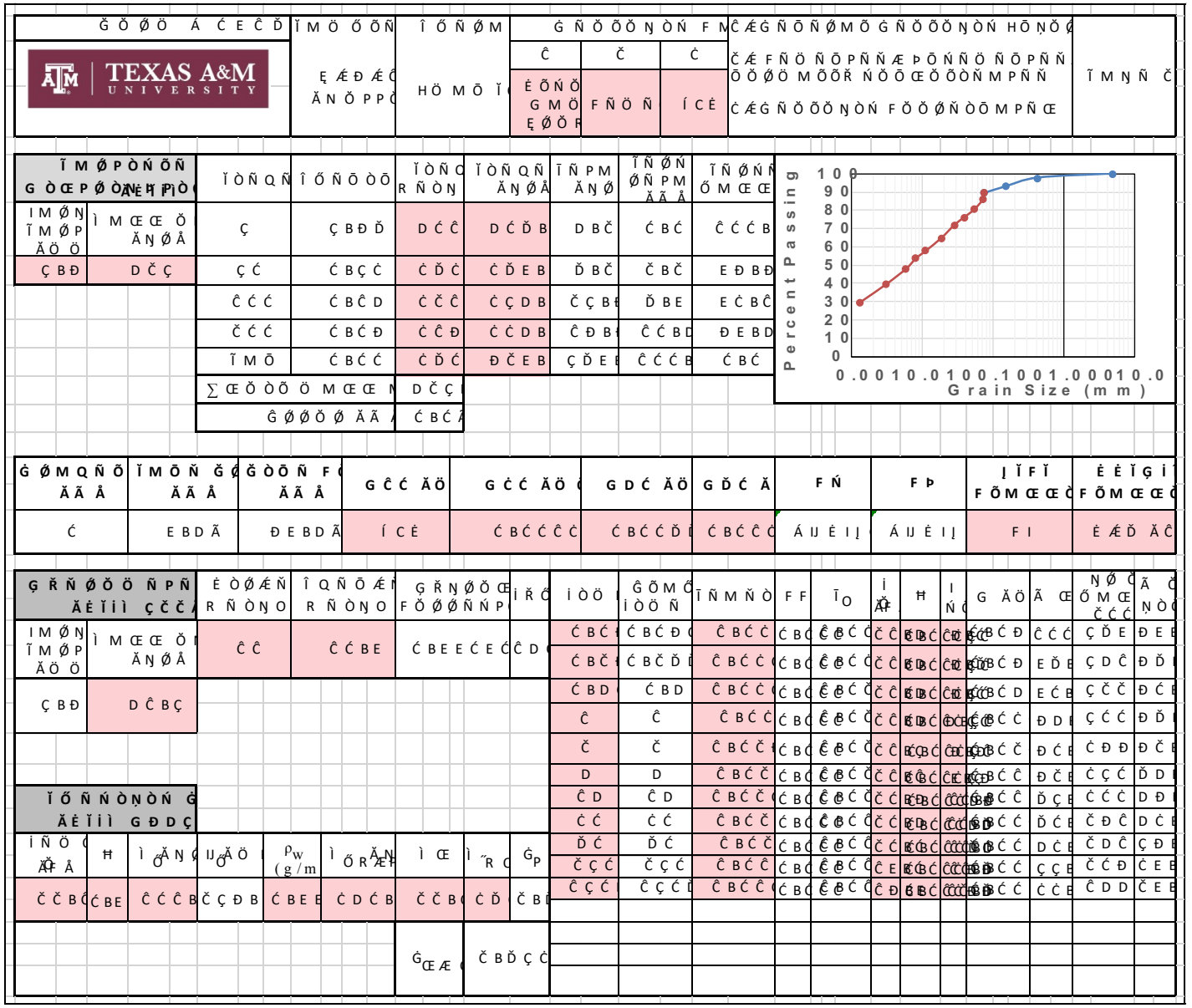

Figure B-16. B-7-16 (13'-15.5') Bottom - Page 2

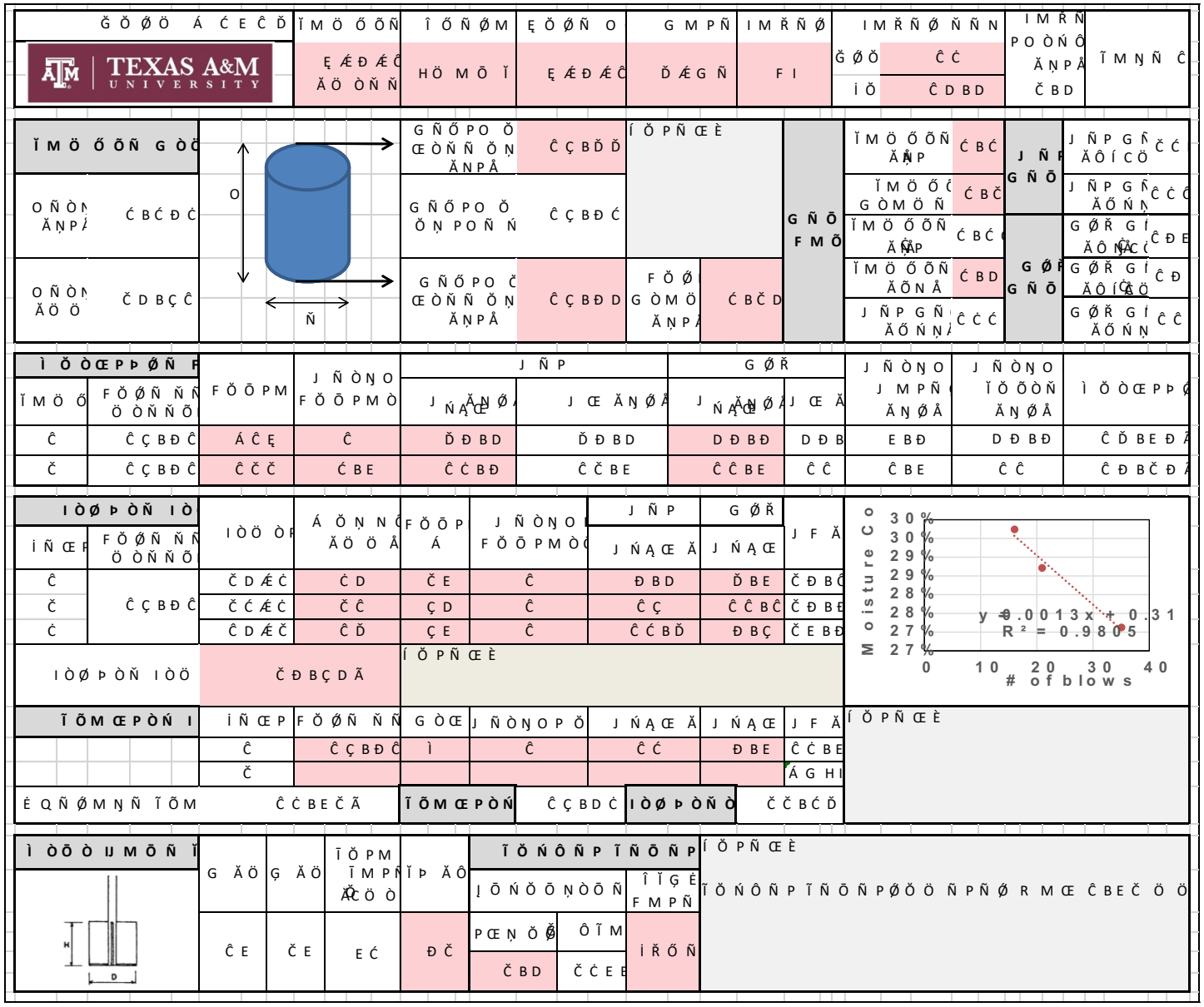

Figure B-17. B-7-16 (13’-15.5’) Middle - Page 1

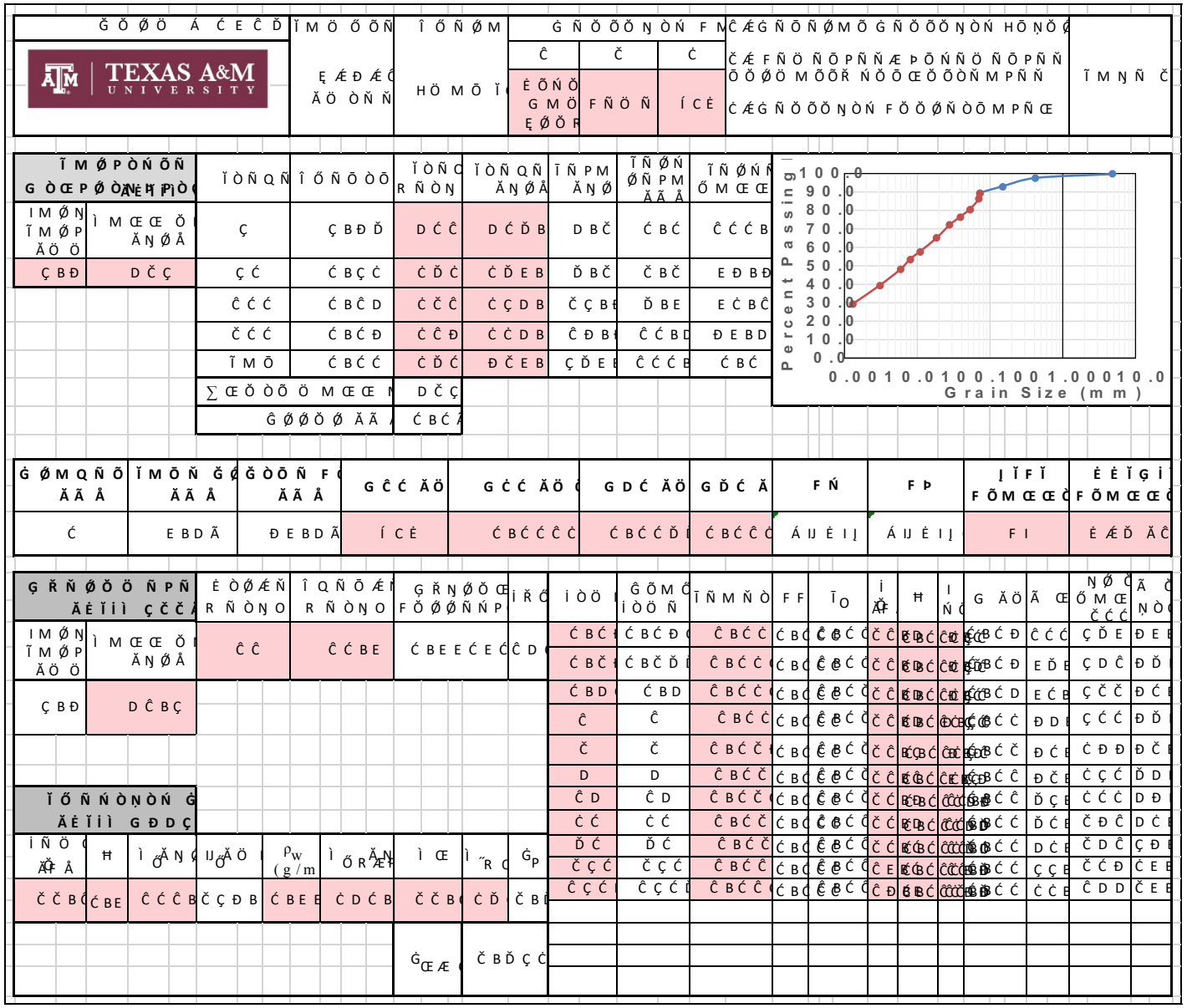

Figure B-18. B-7-16 (13'-15.5') Middle - Page 2

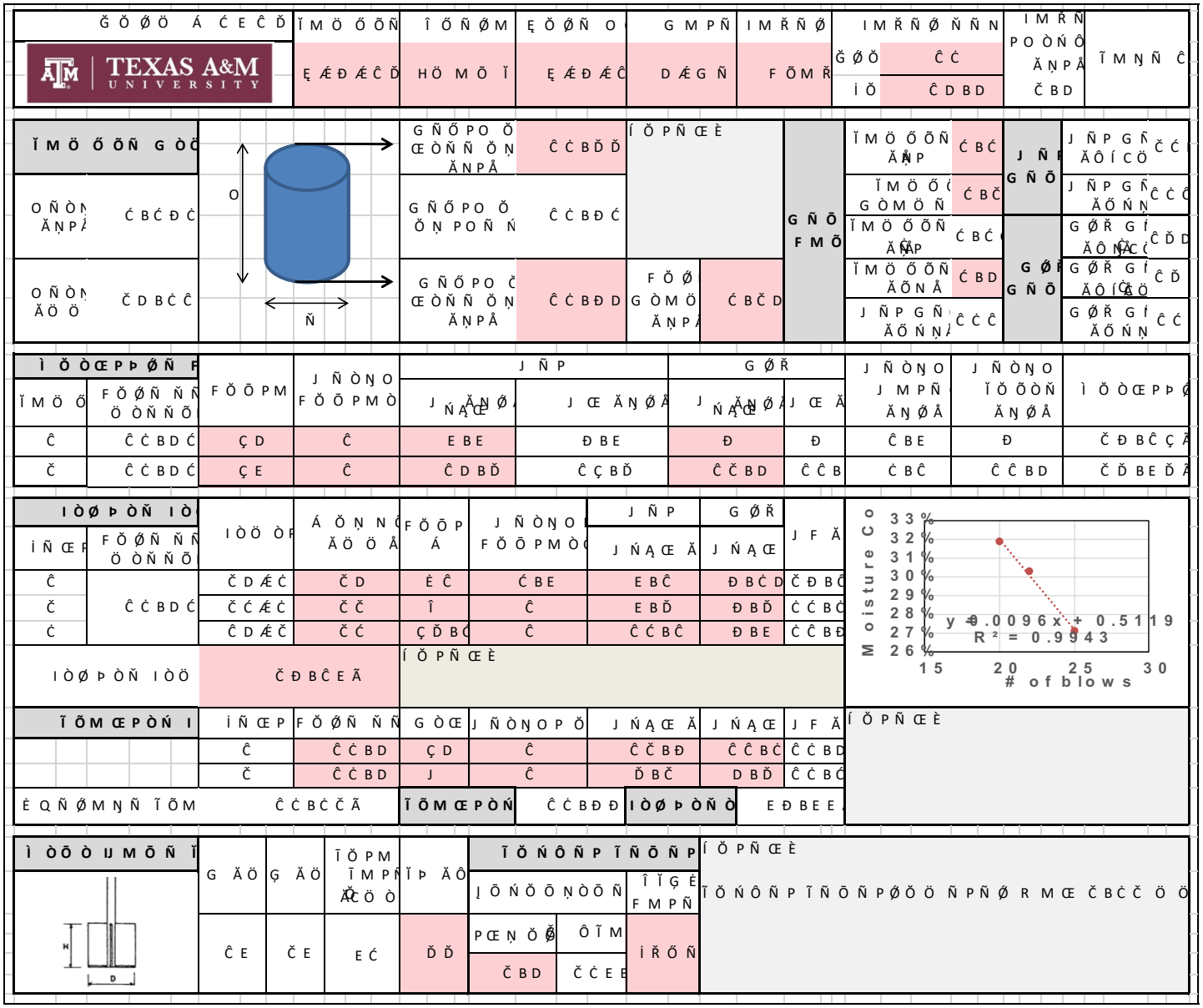

Figure B-19. B-7-16 (13'-15.5') Top - Page 1

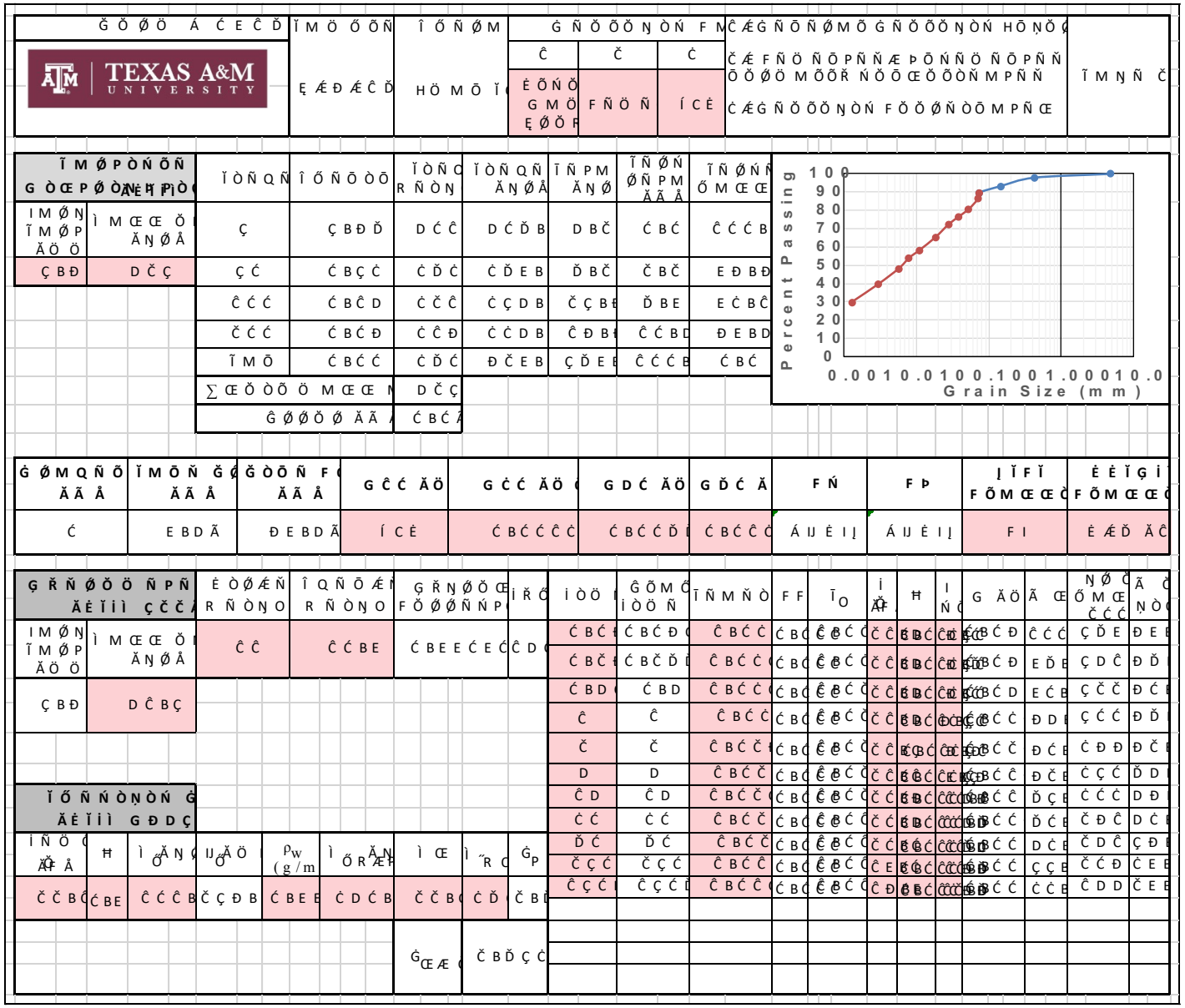

Figure B-20. B-7-16 (13'-15.5') Top - Page 2

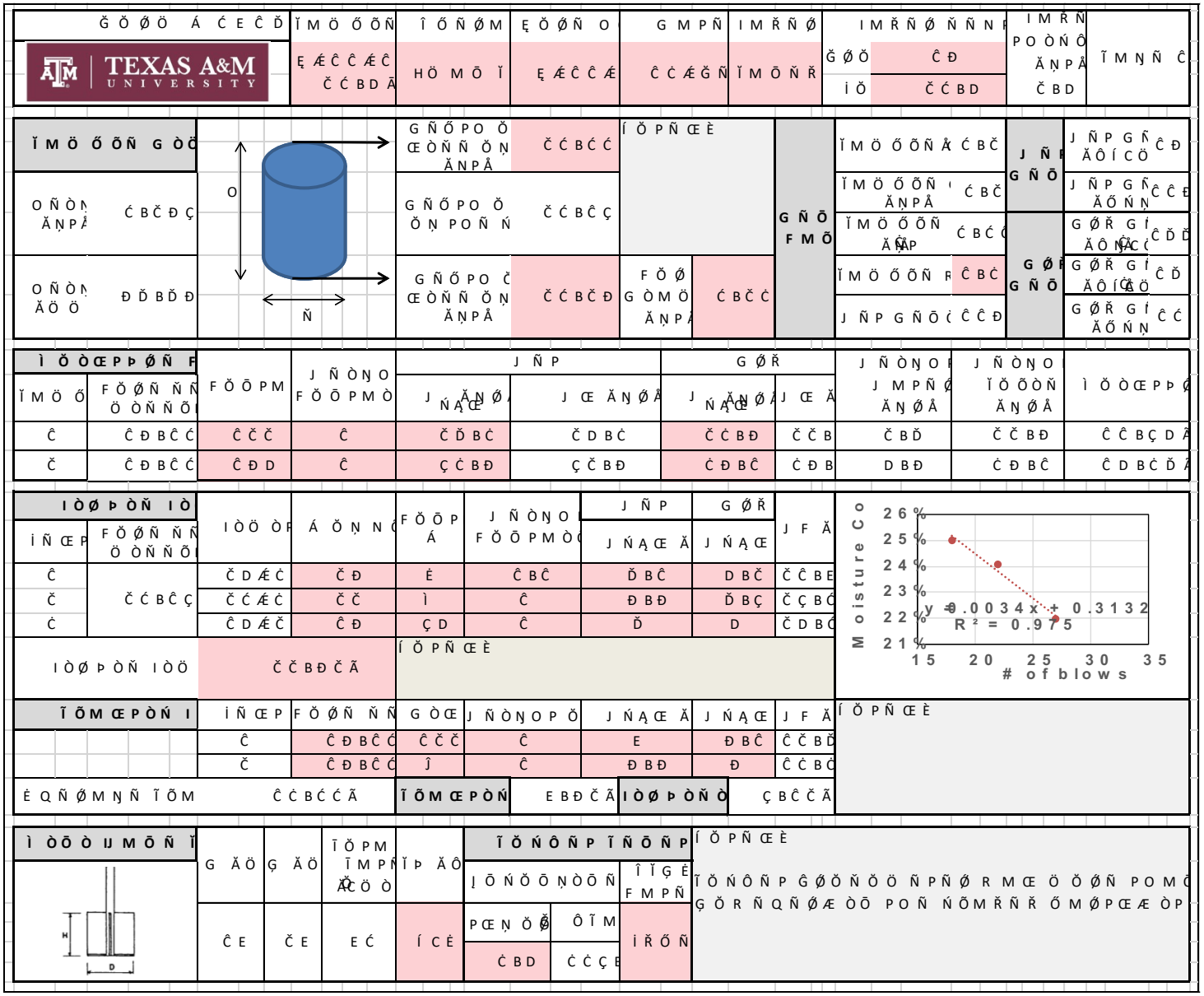

Figure B-21. B-11-16 (18'-20.5') Bottom - Page 1

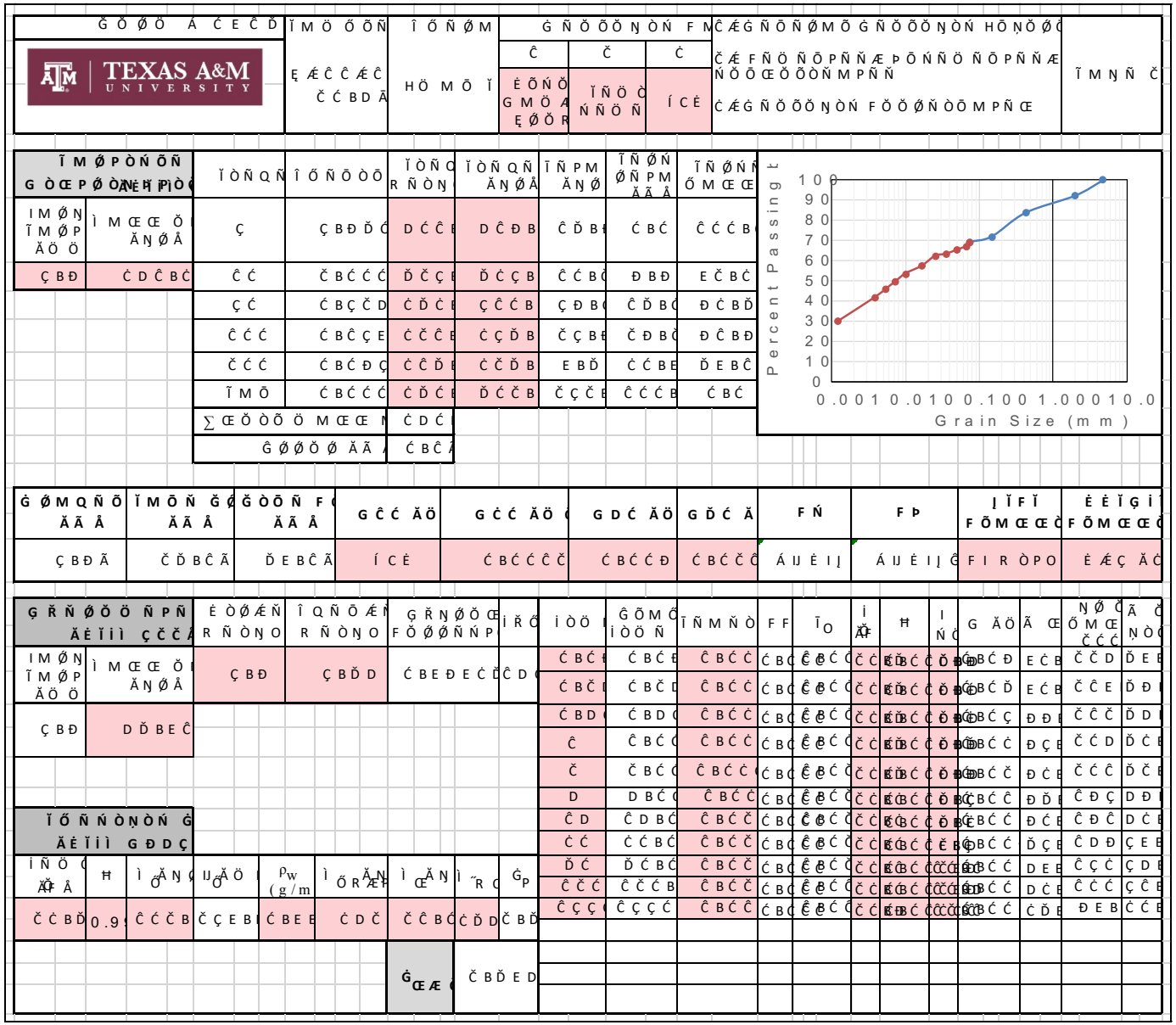

Figure B-22. B-11-16 (18'-20.5') Bottom - Page 2

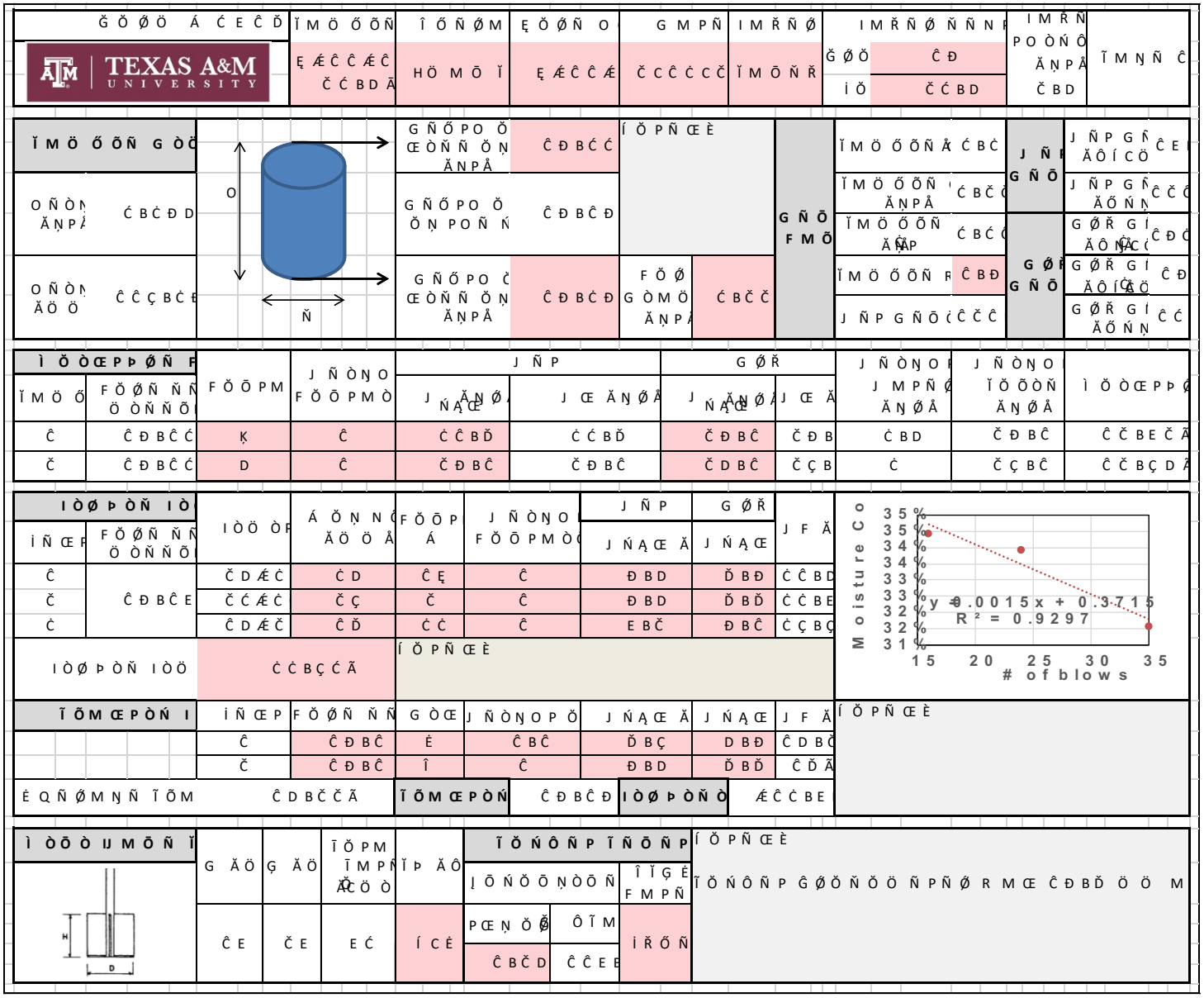

Figure B-23. B-11-16 (18'-20.5') Top - Page 1

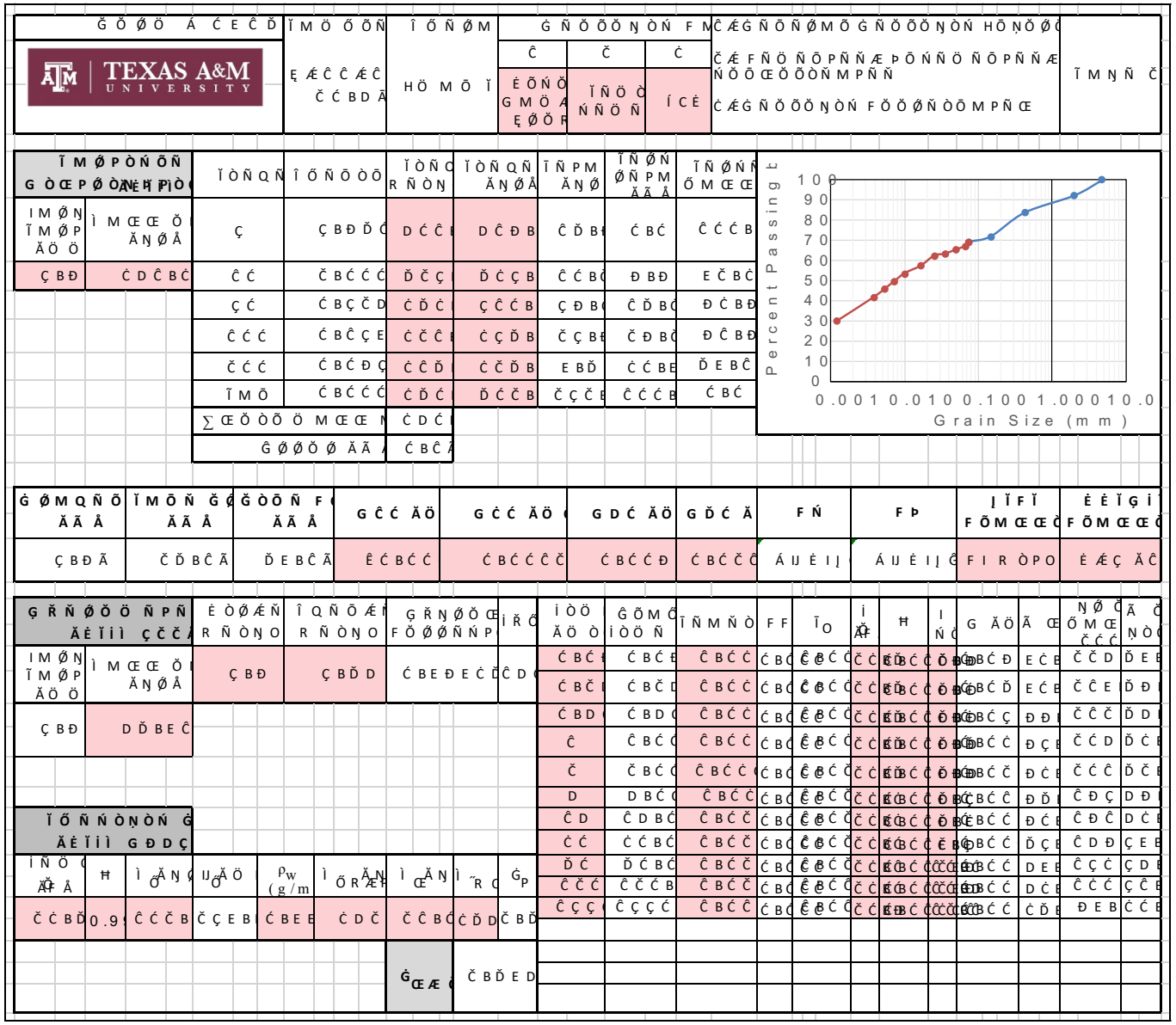

Figure B-24. B-11-16 (18'-20.5') Top - Page 2

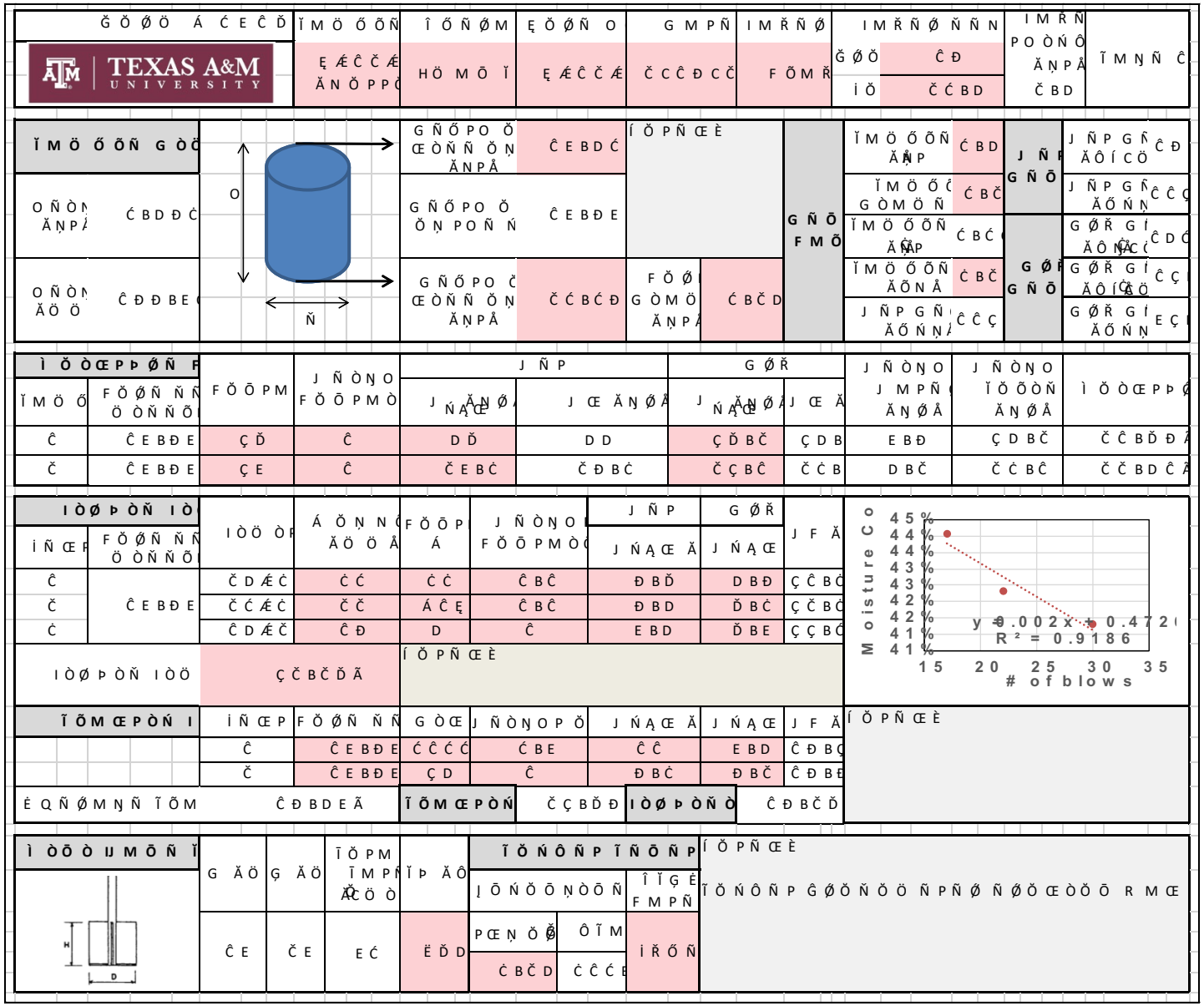

Figure B-25. B-12-16 (18’-20.5’) Bottom - Page 1

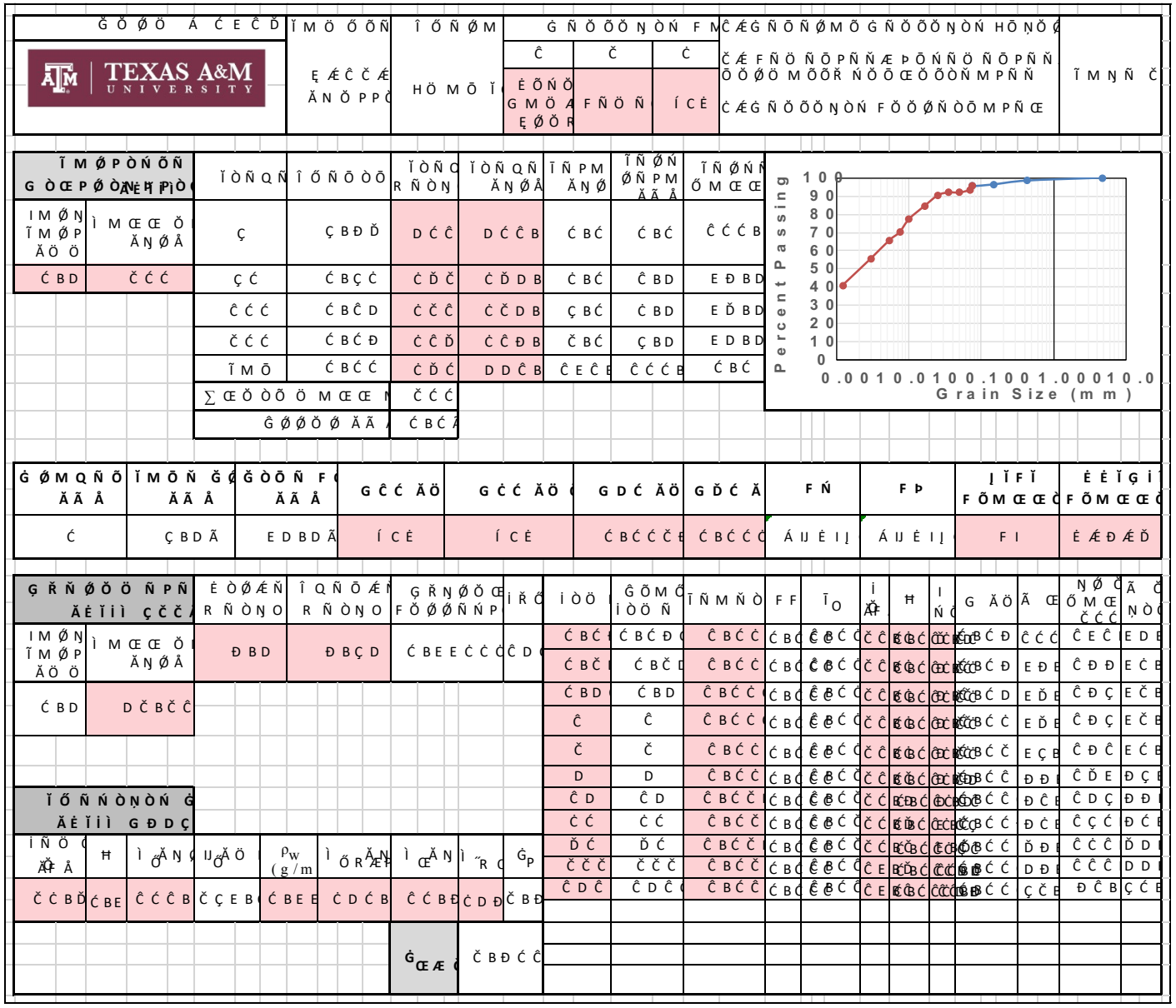

Figure B-26. B-12-16 (18'-20.5') Bottom - Page 2

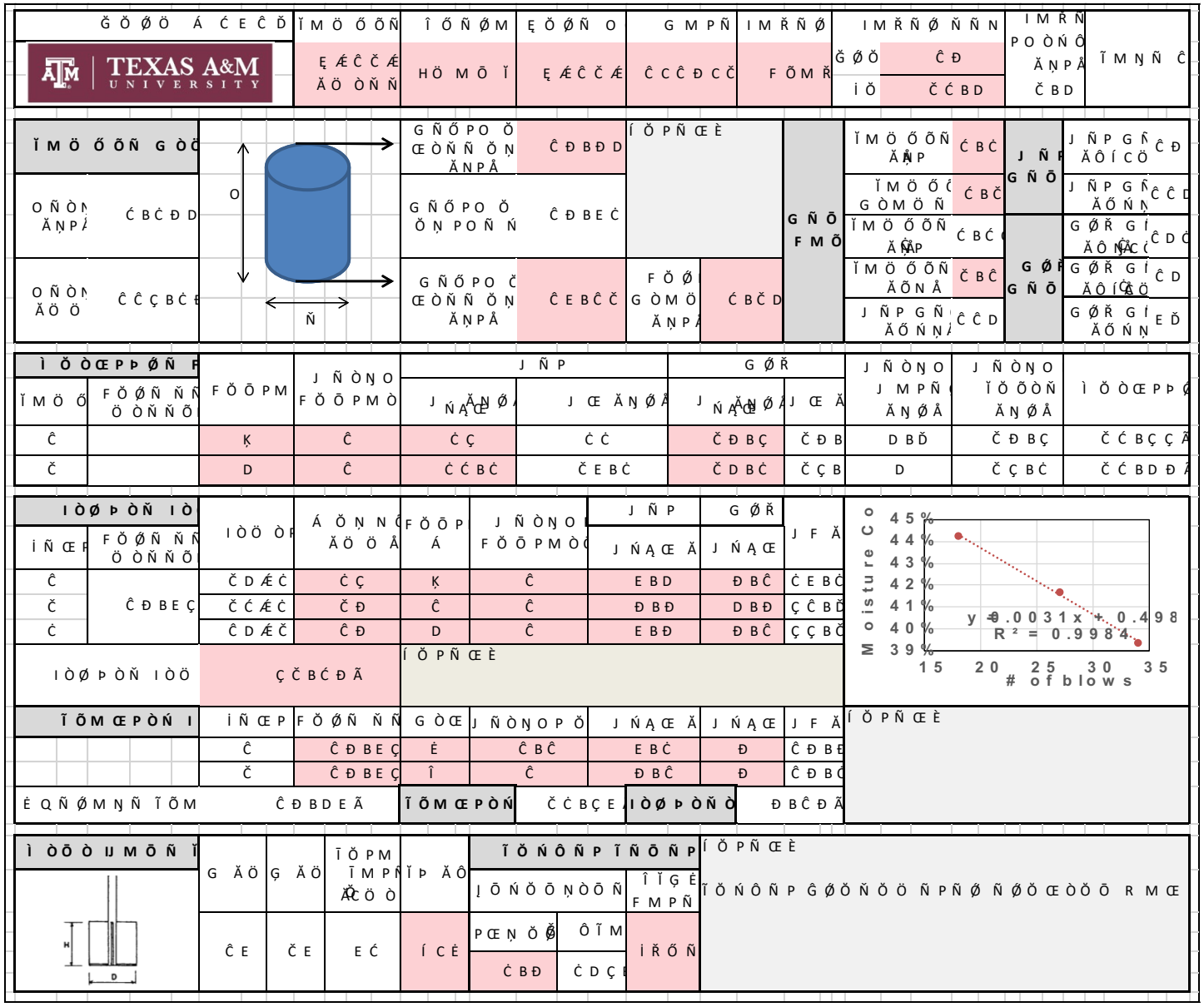

Figure B-27. B-12-16 (18'-20.5') Middle - Page 1

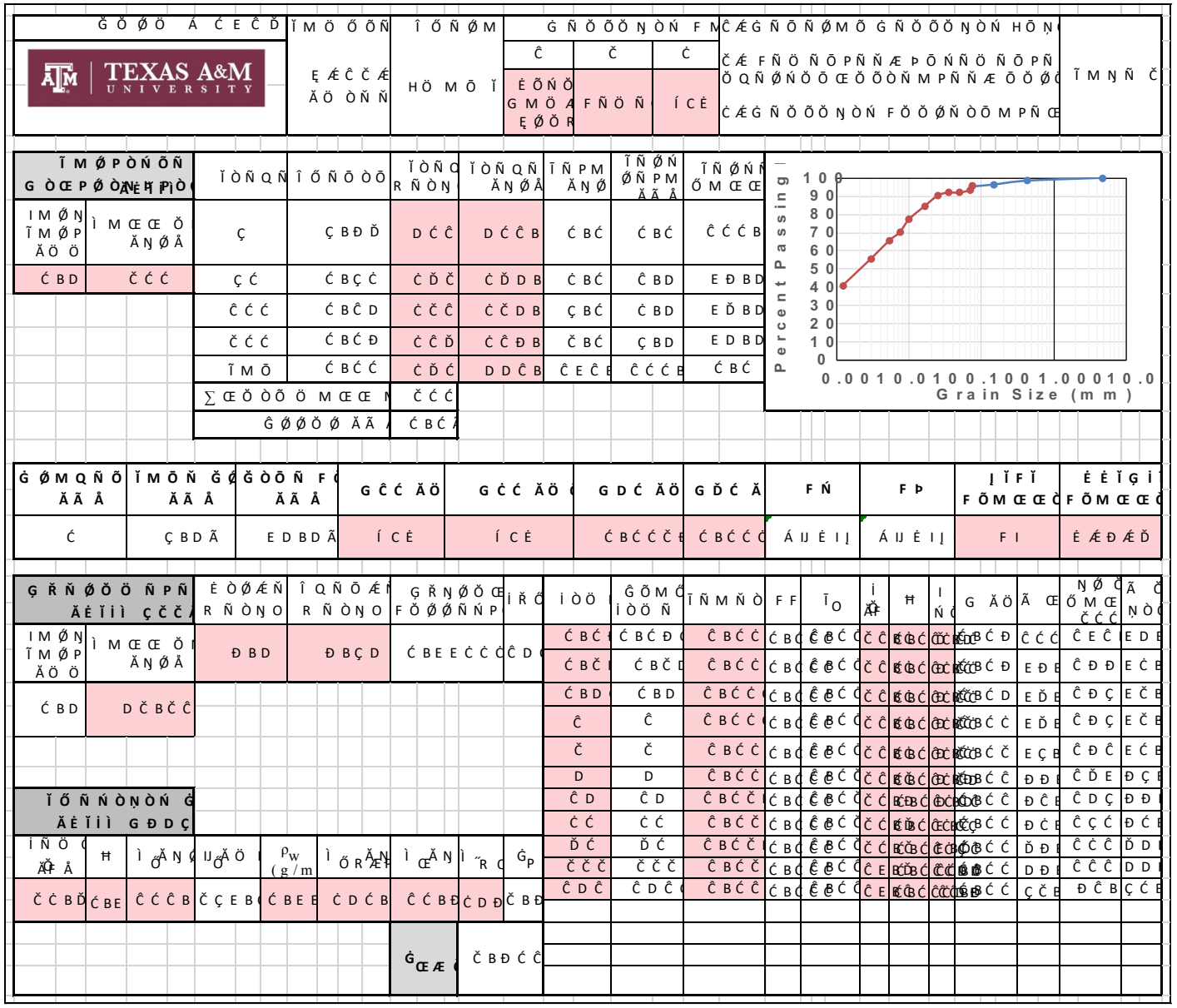

Figure B-28. B-12-16 (18'-20.5') Middle - Page 2

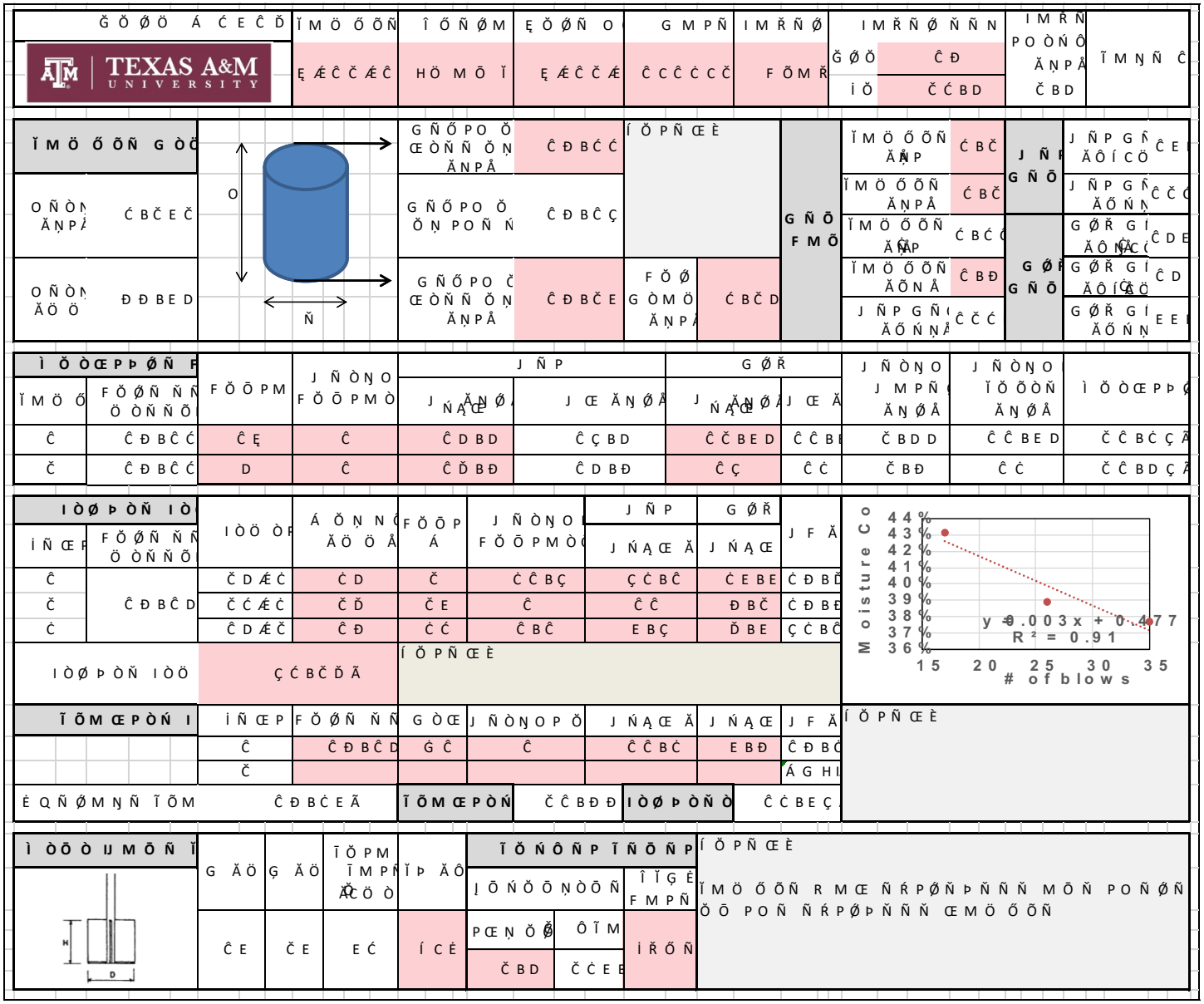

Figure B-29. B-12-16 (18'-20.5') Top - Page 1

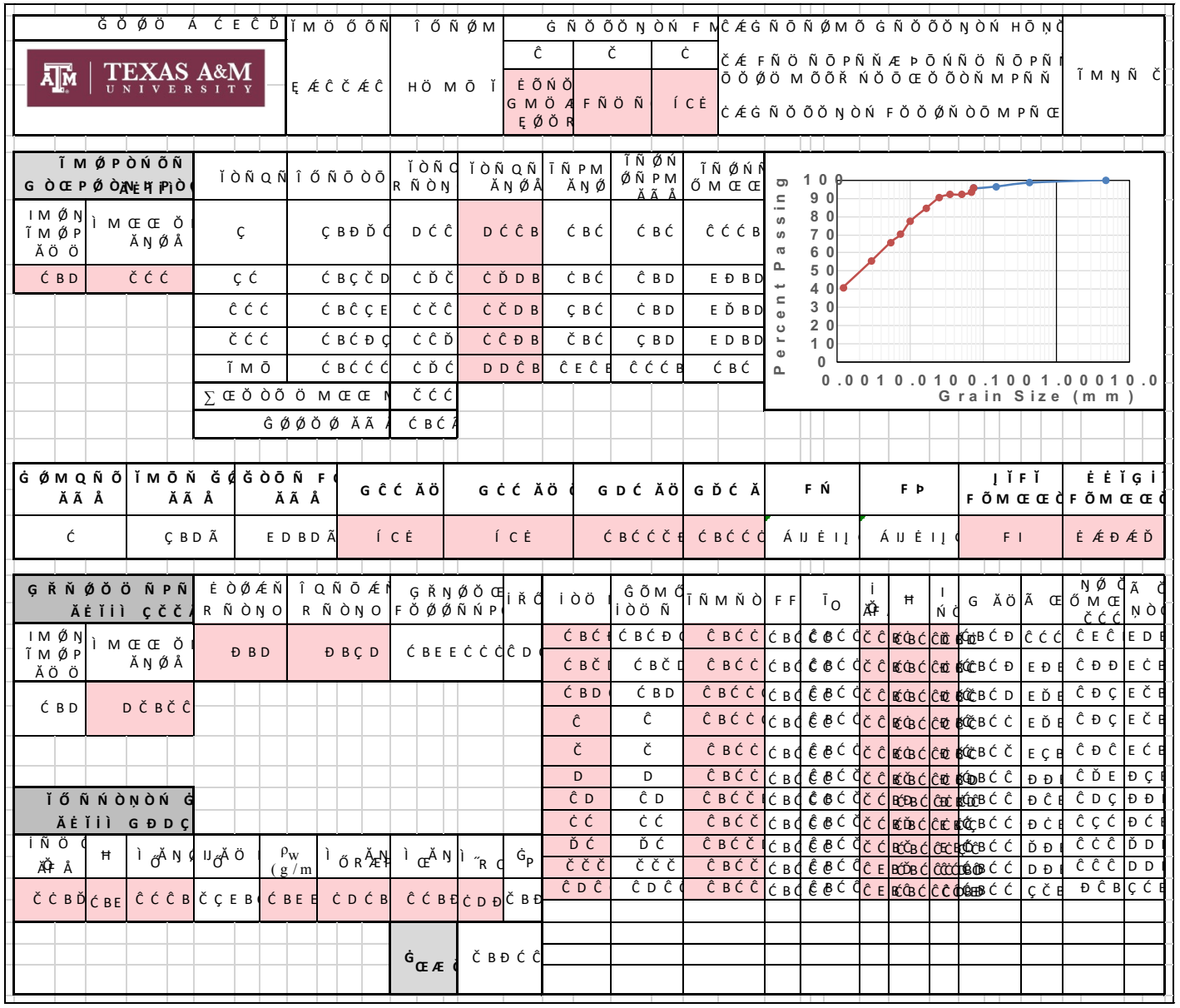

Figure B-30. B-12-16 (18'-20.5') Top - Page 2

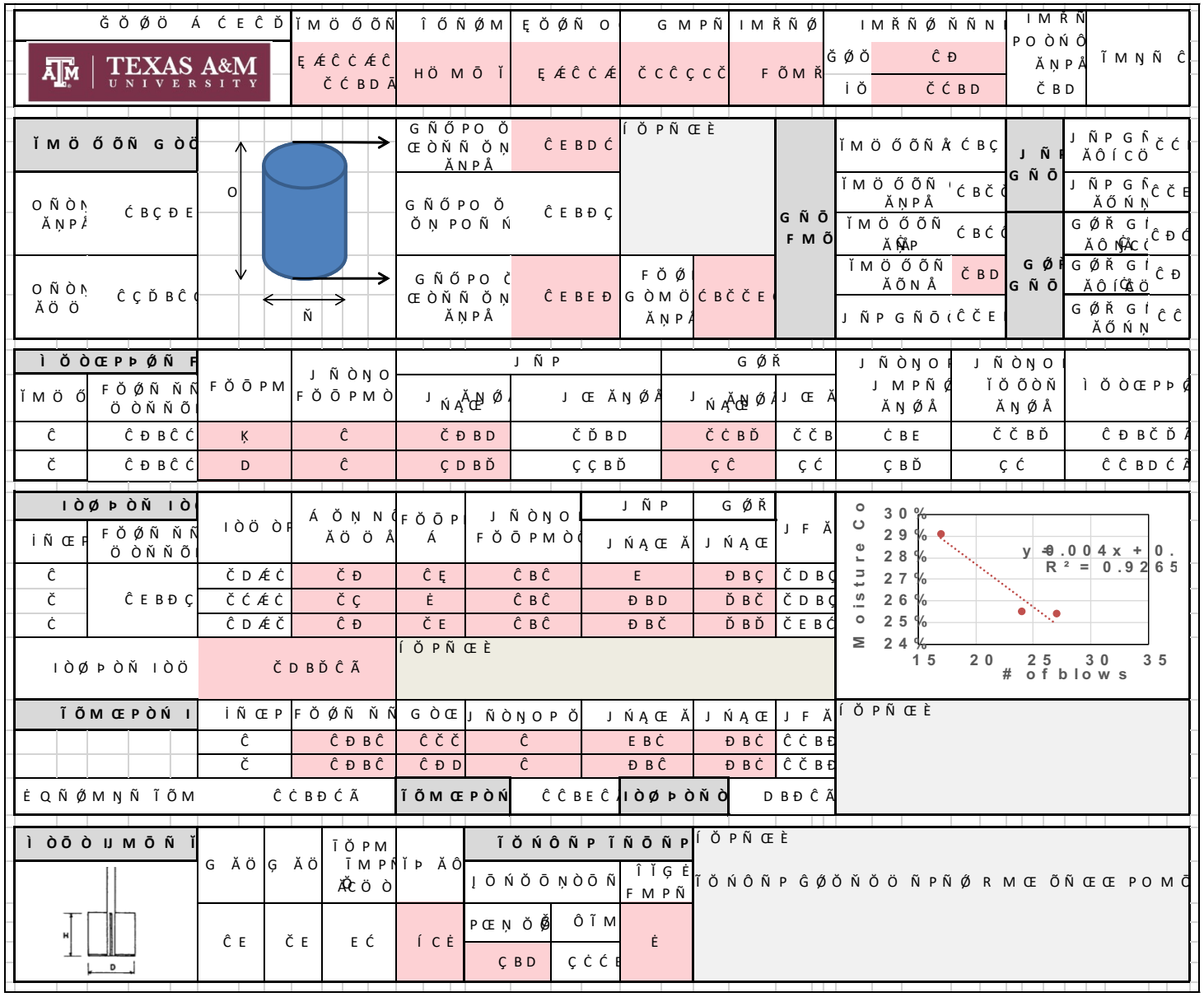

Figure B-31. B-13-16 (18'-20.5') Bottom - Page 1

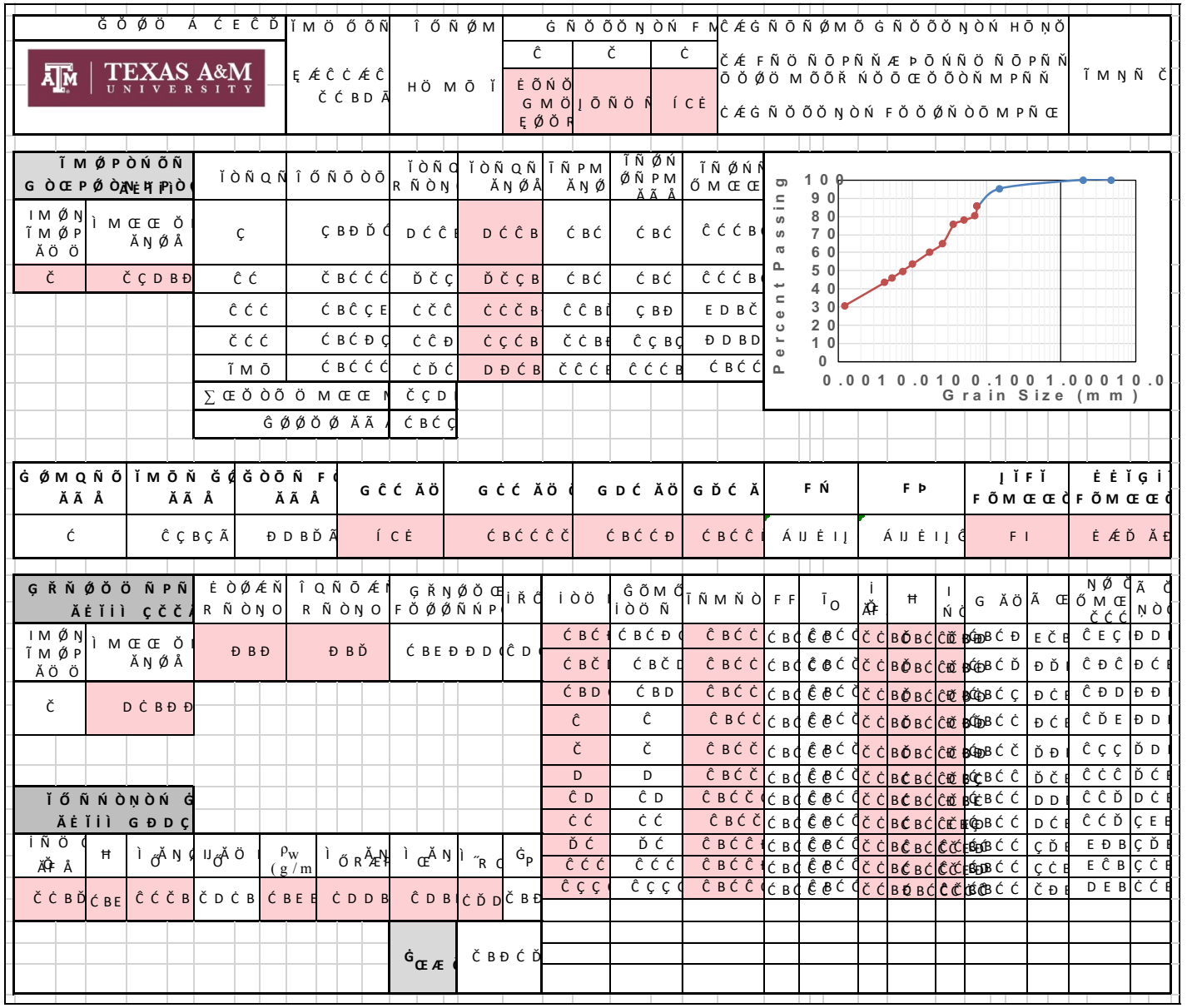

Figure B-32. B-13-16 (18'-20.5') Bottom - Page 2

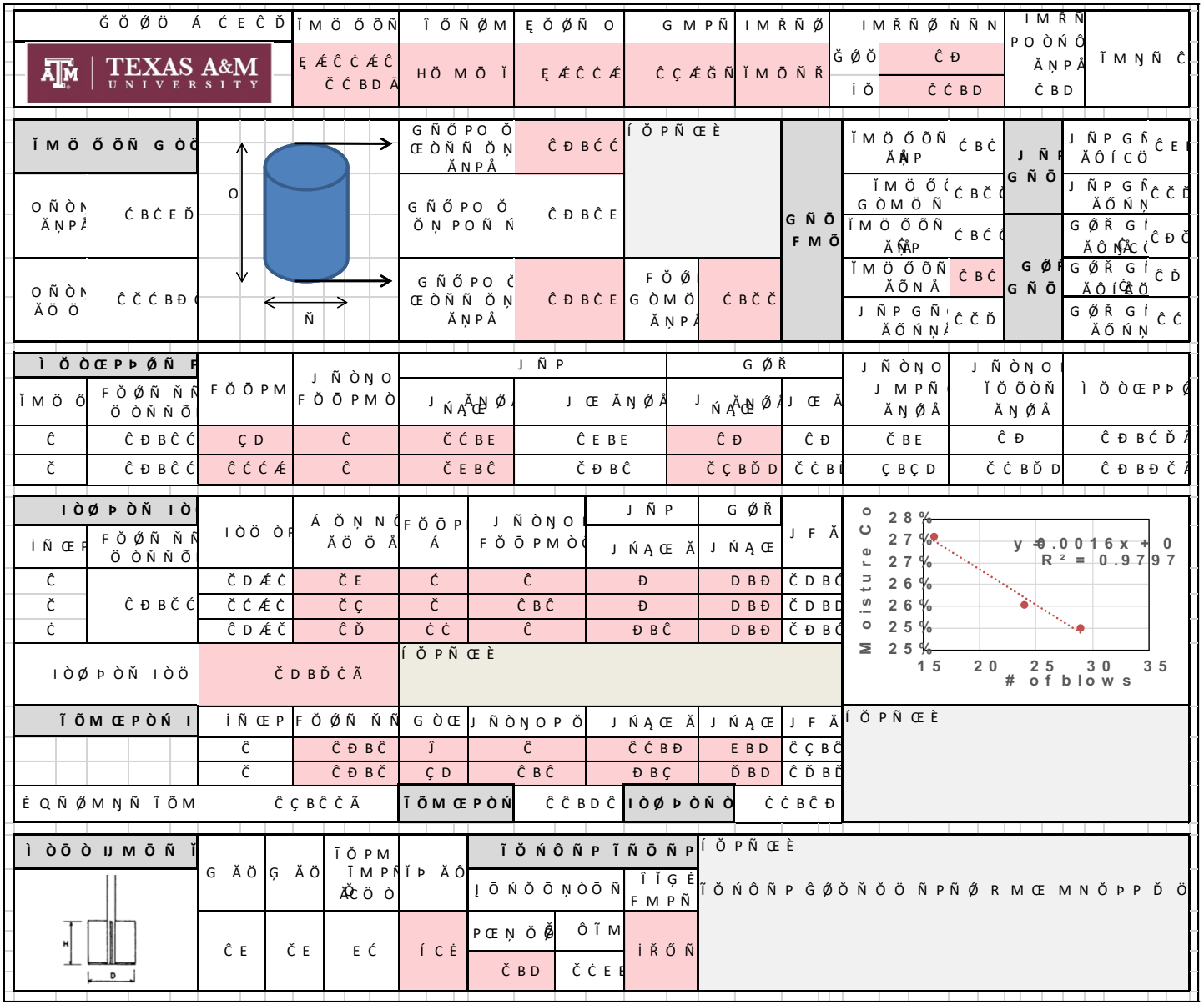

Figure B-33. B-13-16 (18'-20.5') Top - Page 1

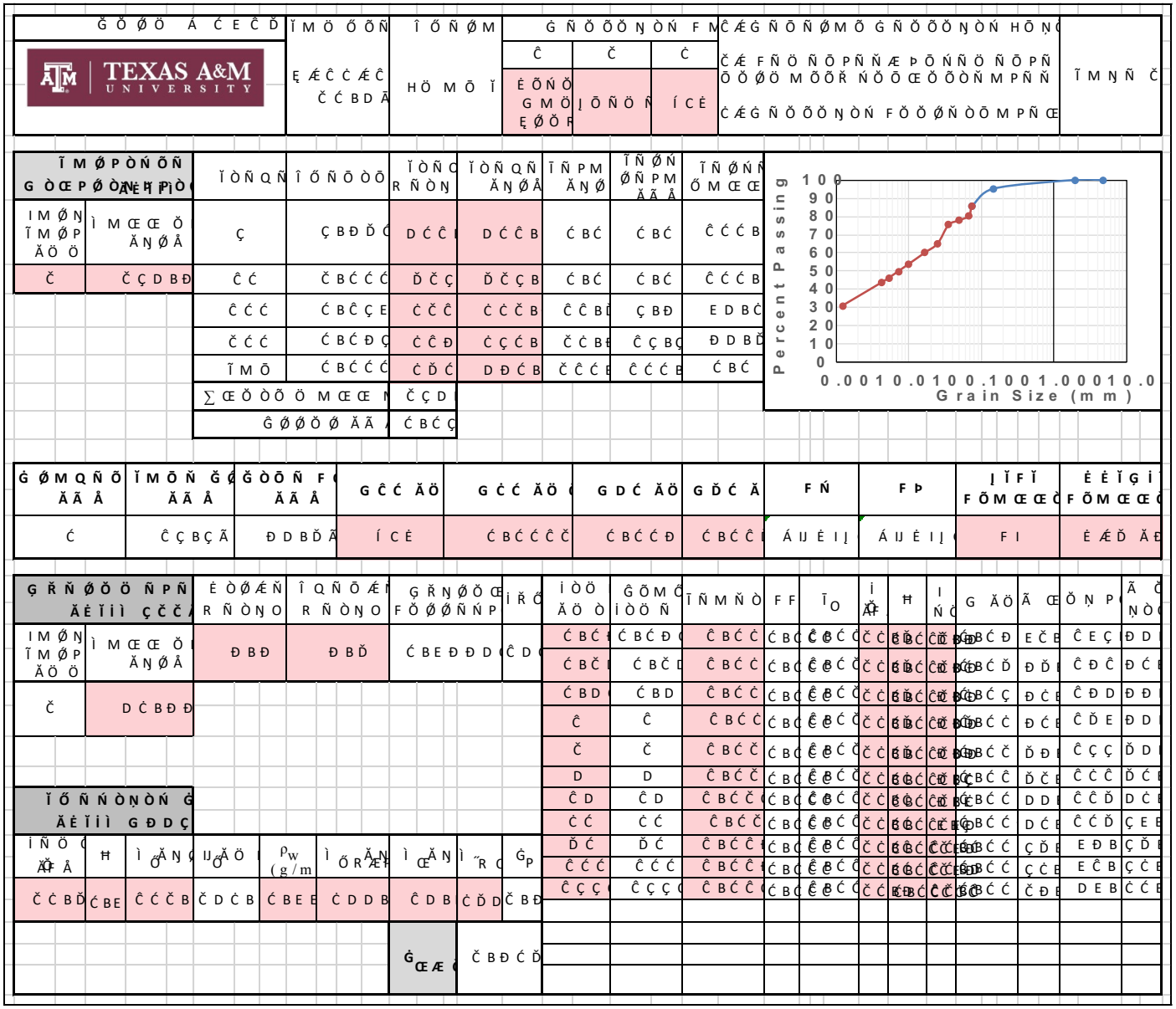

Figure B-34. B-13-16 (18’-20.5’) Top - Page 2

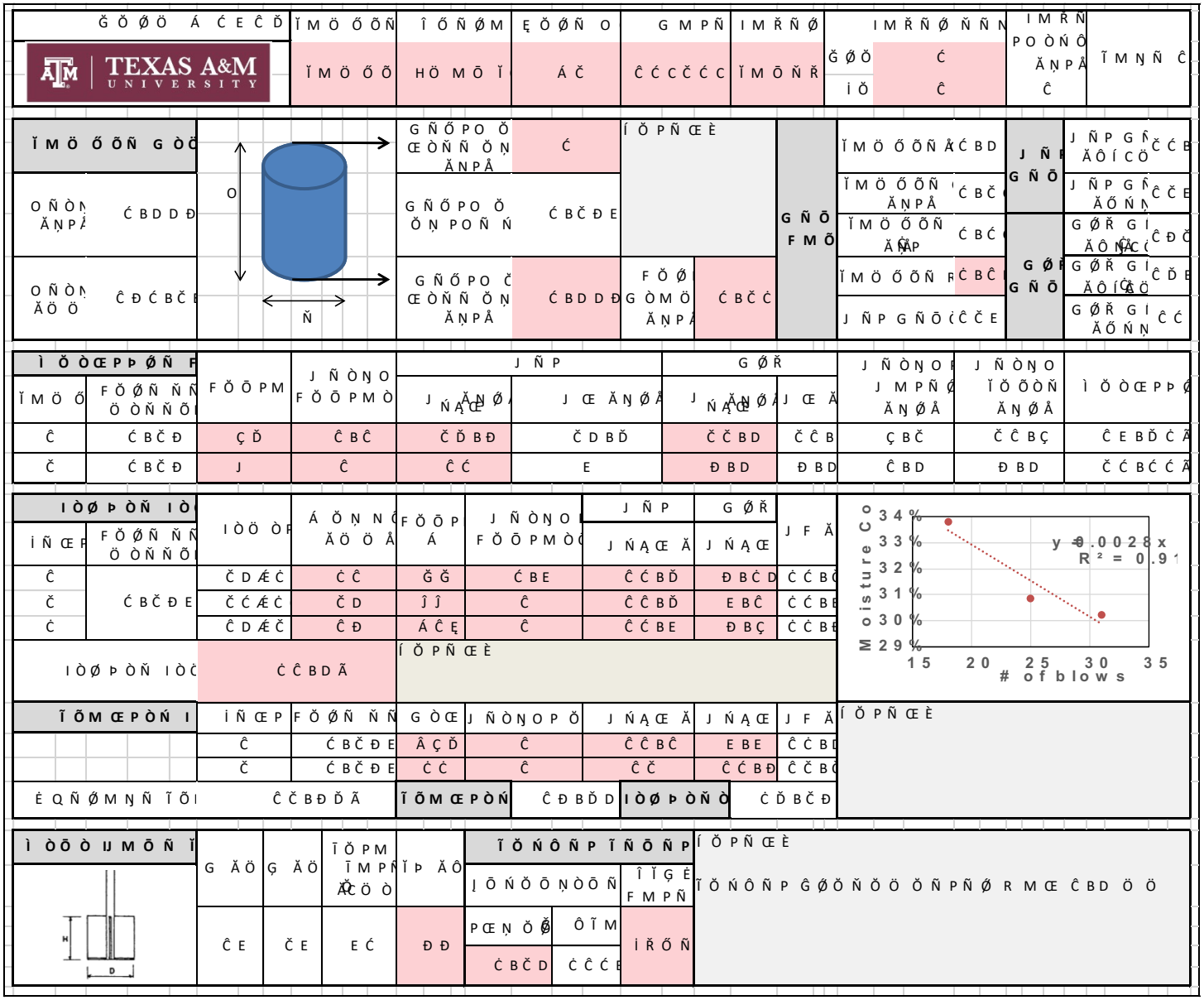

Figure B-35. GEER Sample #2 - Page 1

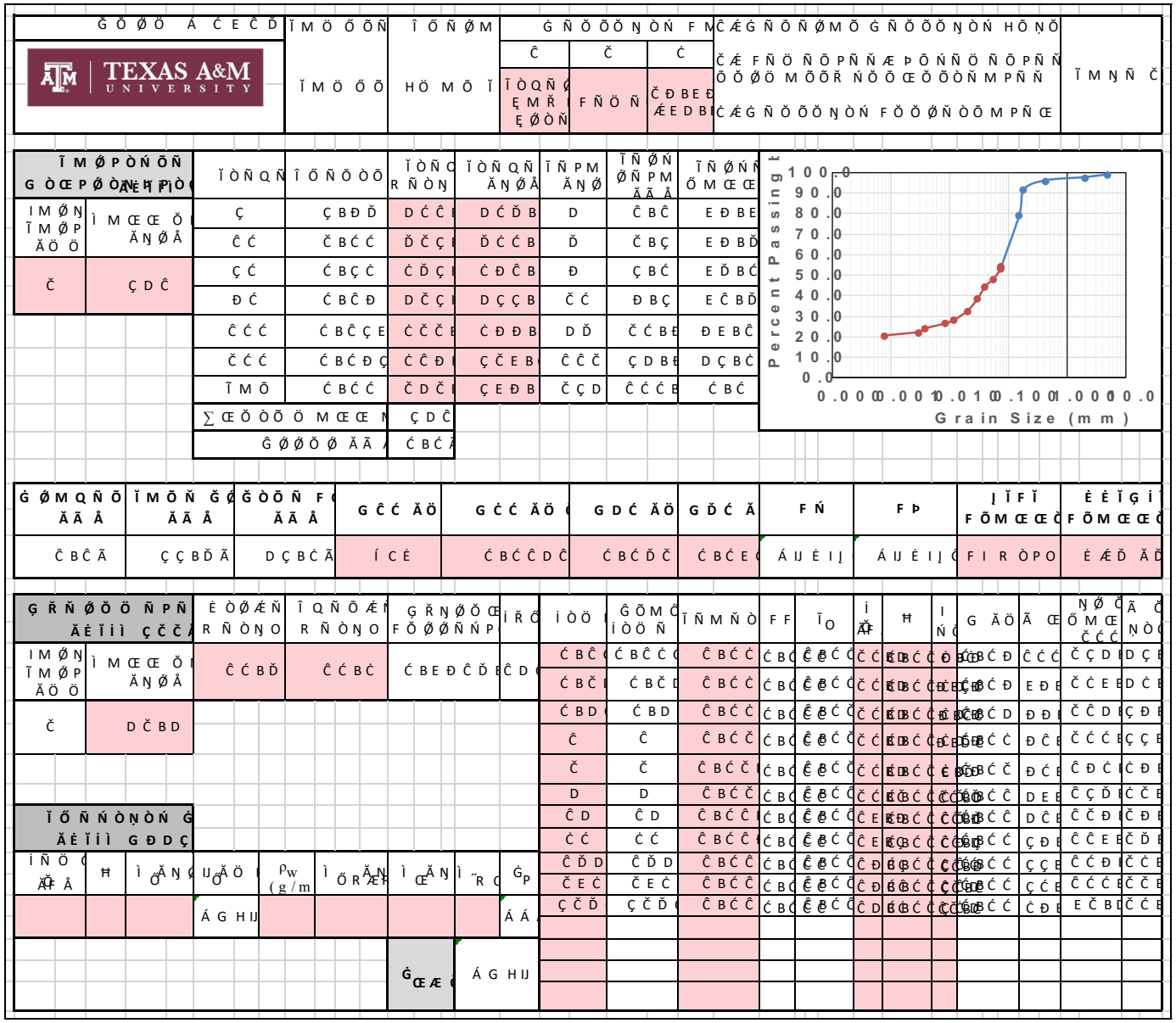

Figure B-36. GEER Sample #2 – Page 2

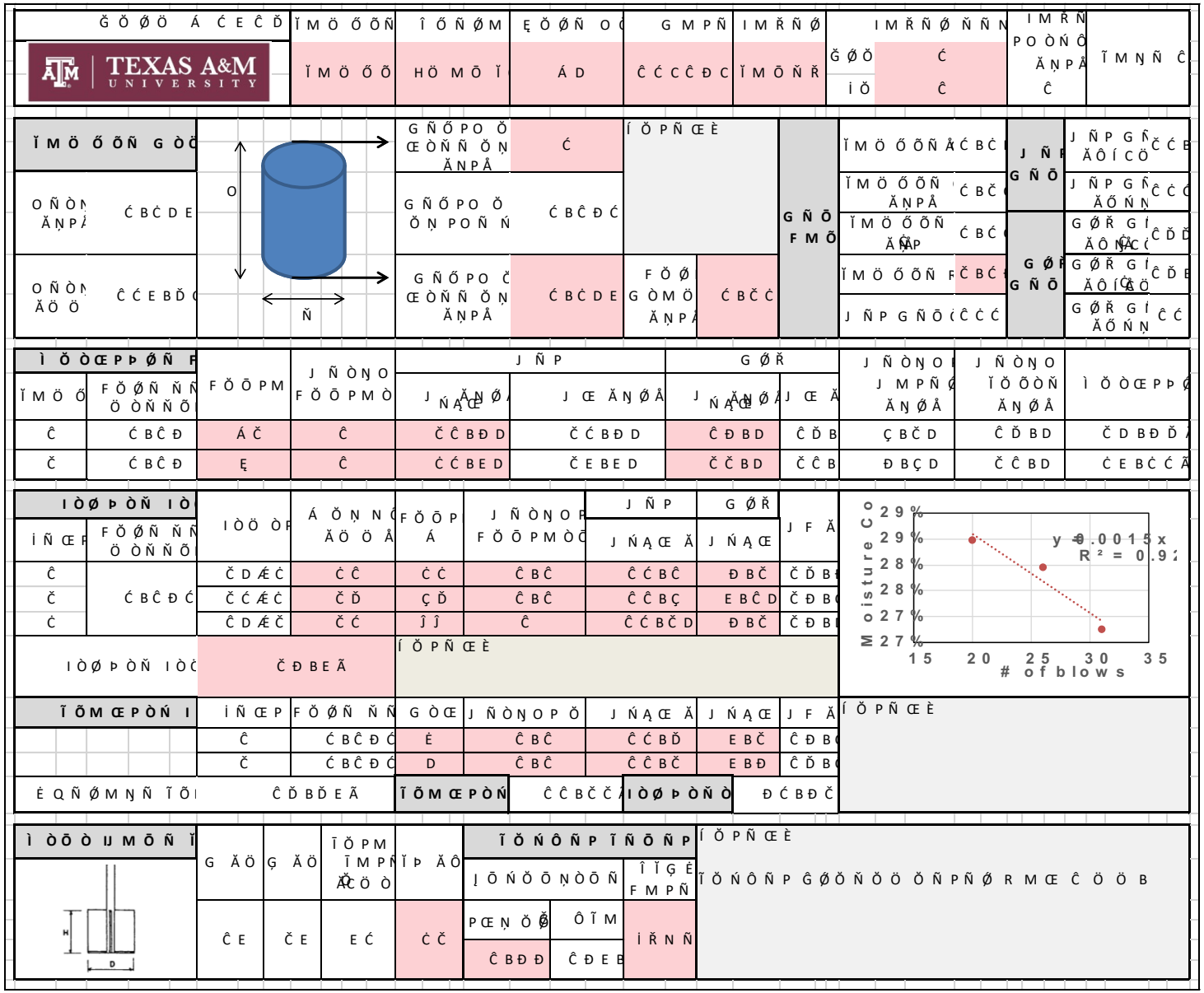

Figure B-37. GEER Sample #5 - Page 1

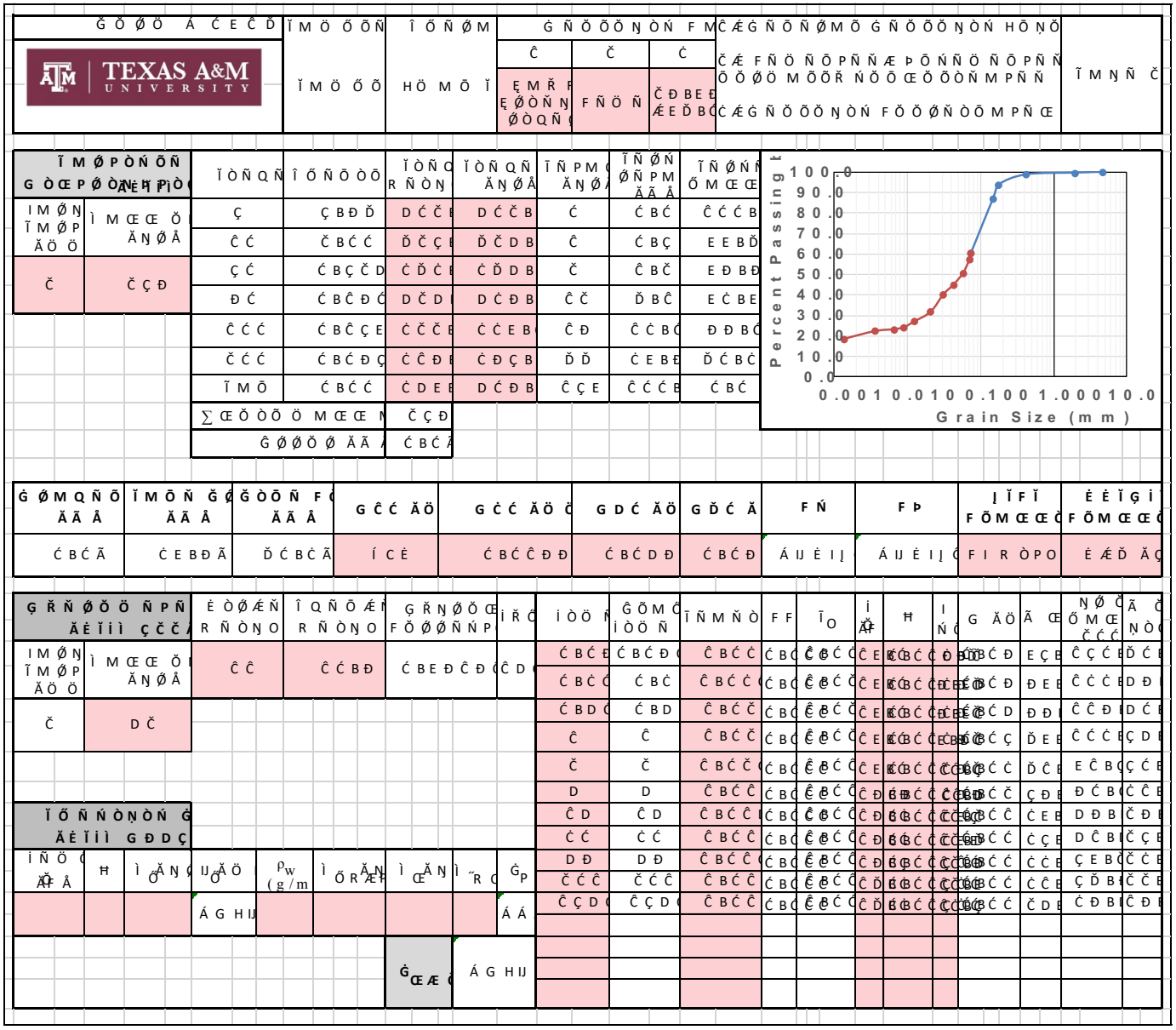

Figure B-38. GEER Sample #5 - Page 2

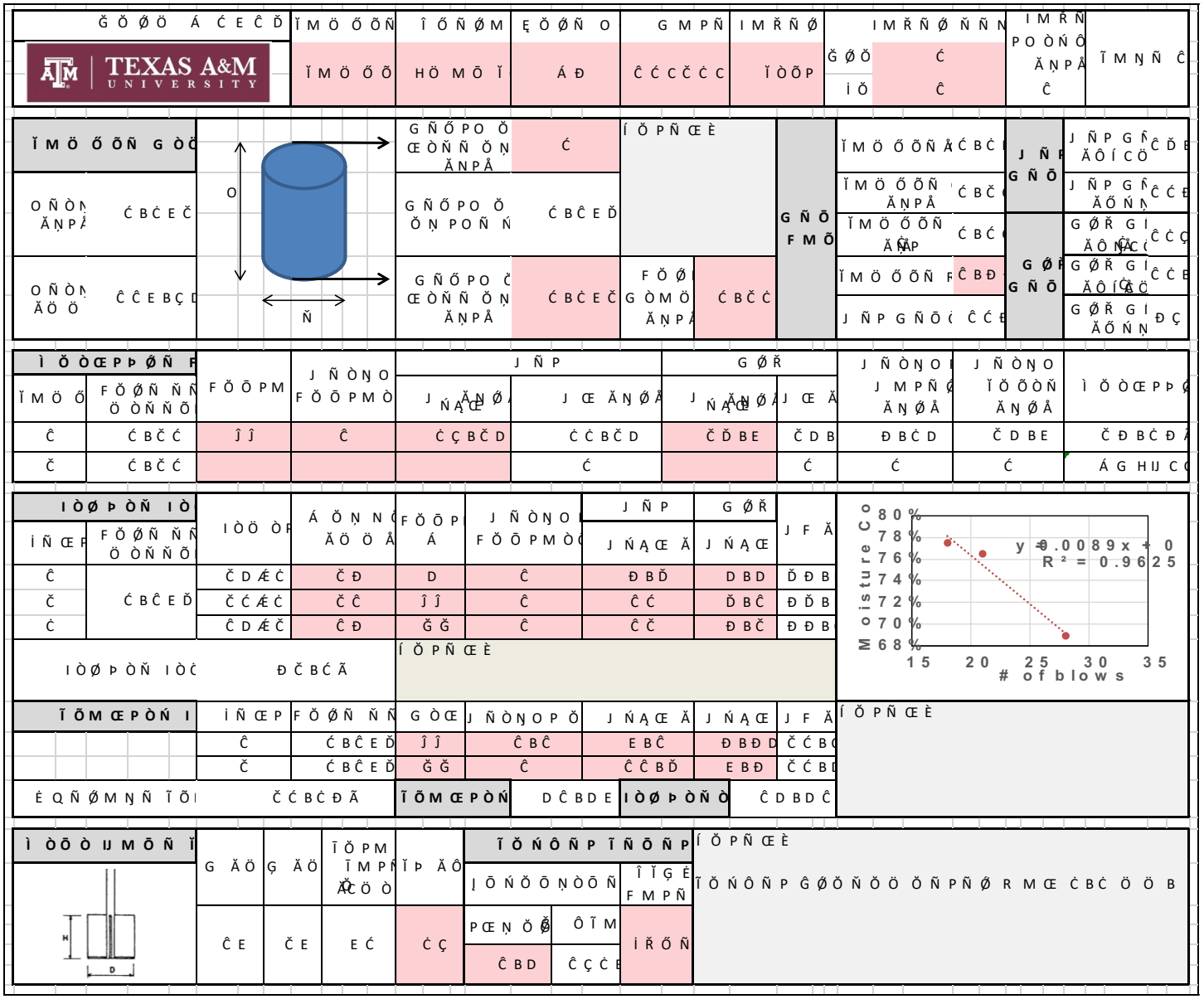

Figure B-39. GEER Sample #8 - Page 1

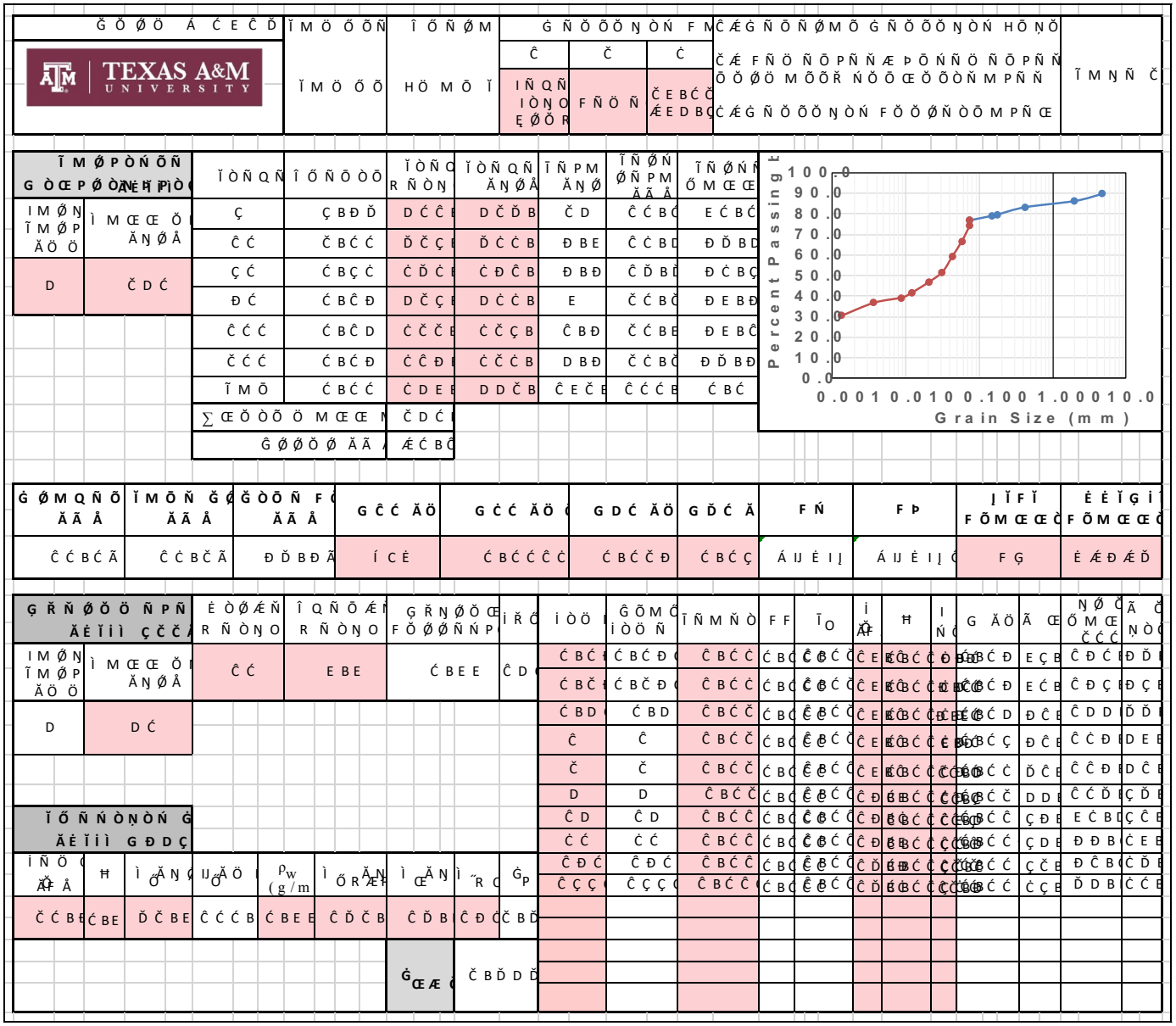

Figure B-40. GEER Sample #8 - Page 2

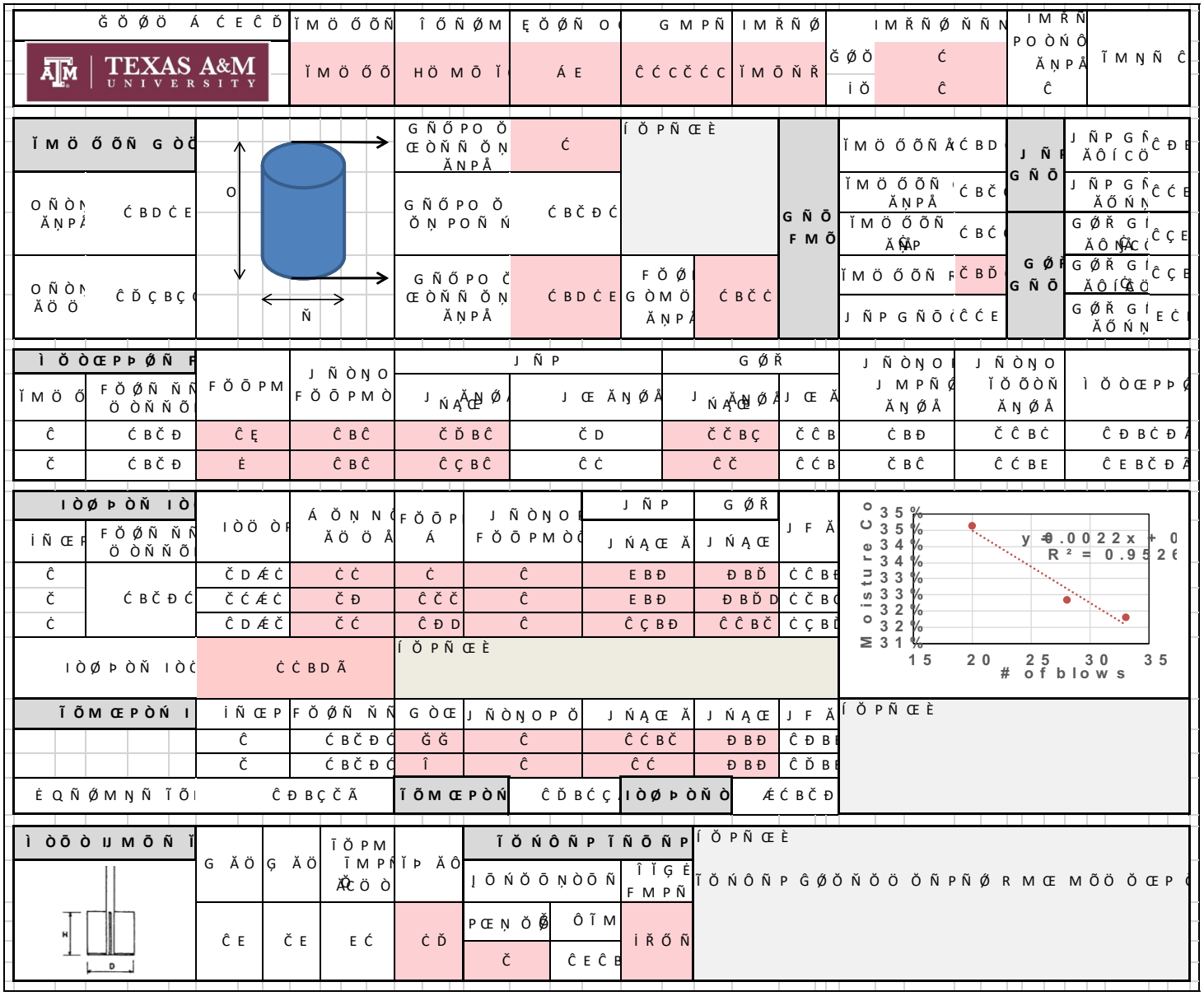

Figure B-41. GEER Sample #9 - Page 1

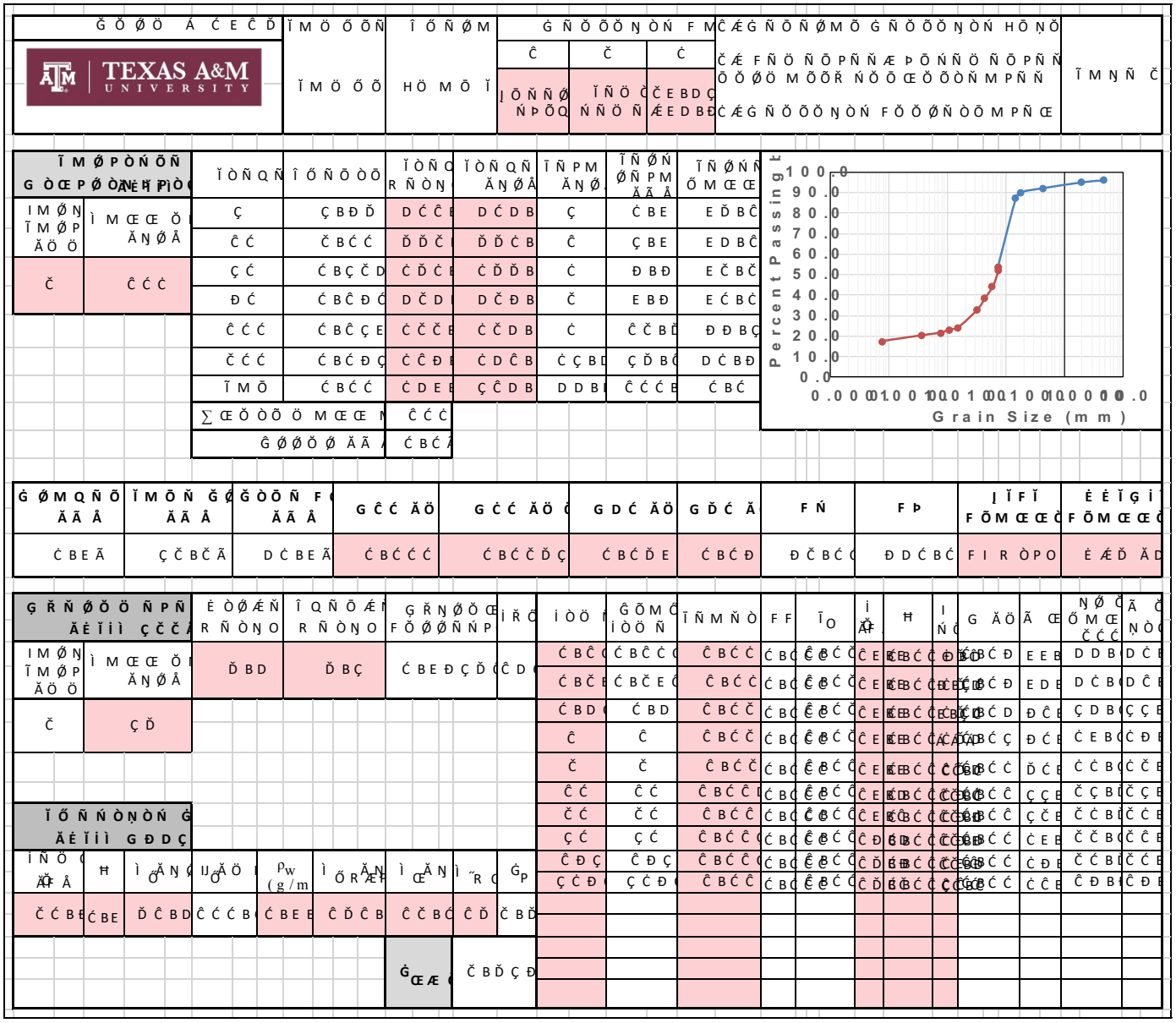

Figure B-42. GEER Sample #9 - Page 2

Silt Samples - EFA

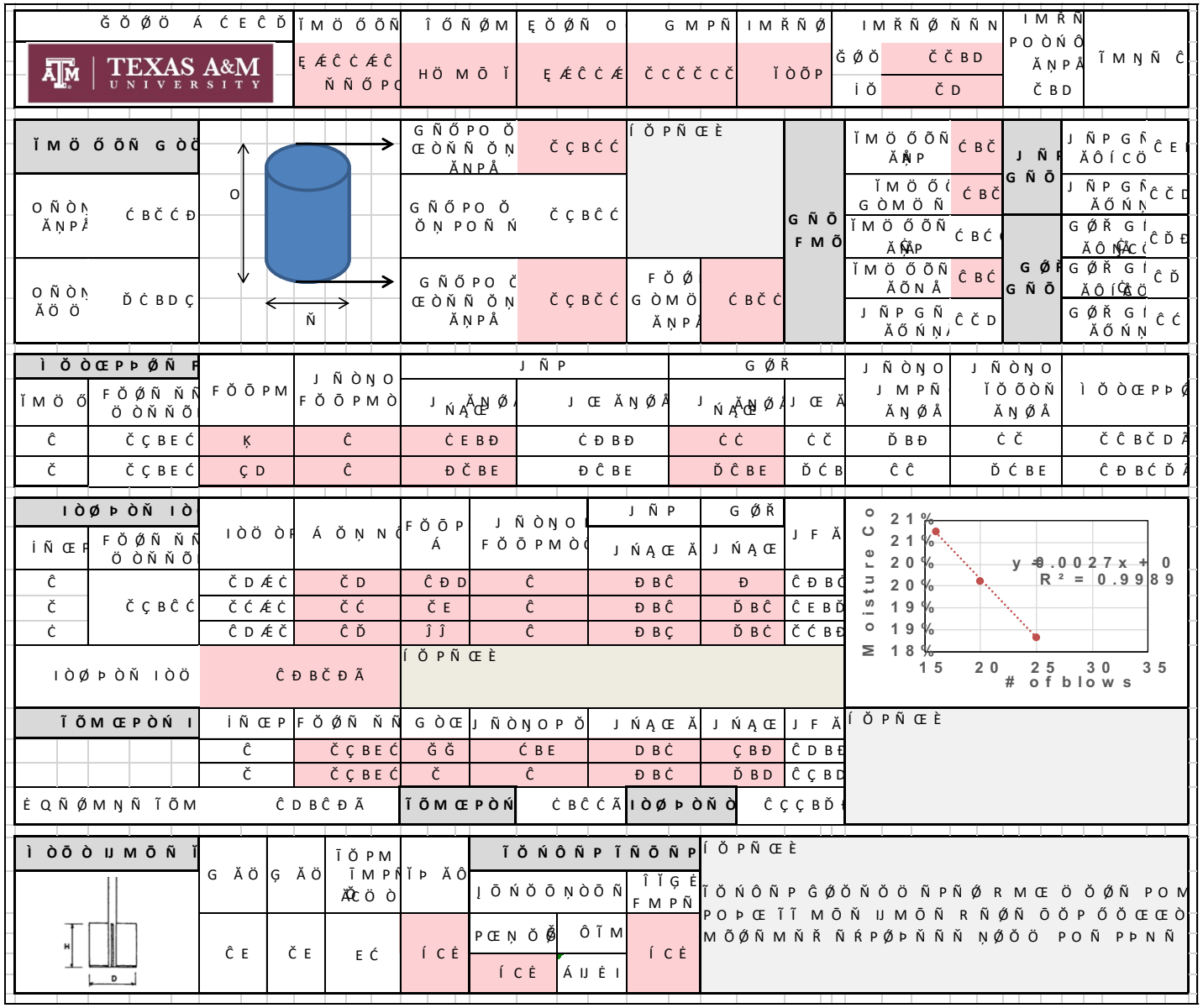

Figure B-43. B-13-16 (22.5'-25') - Page 1

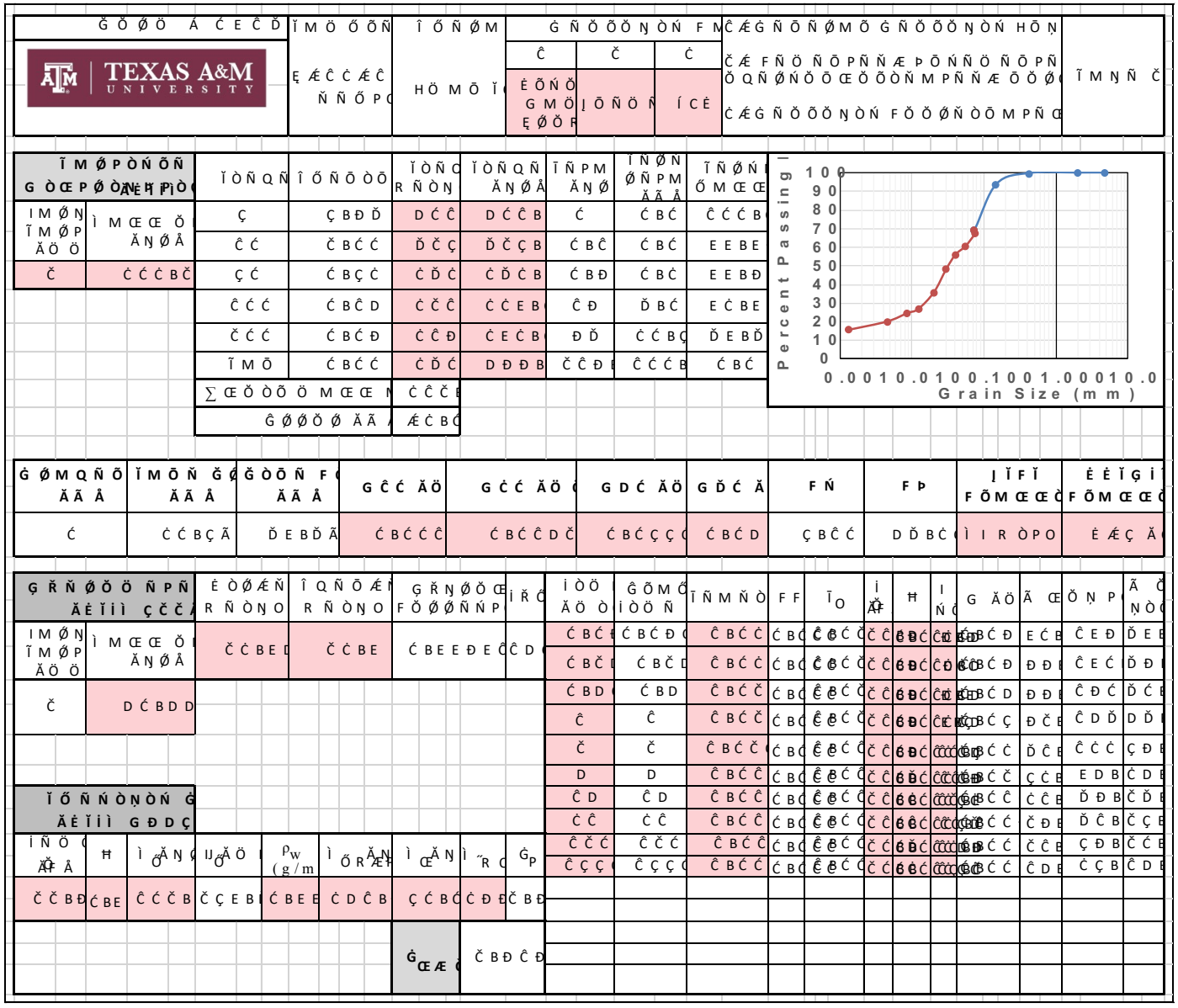

Figure B-44. B-13-16 (22.5'-25') - Page 2

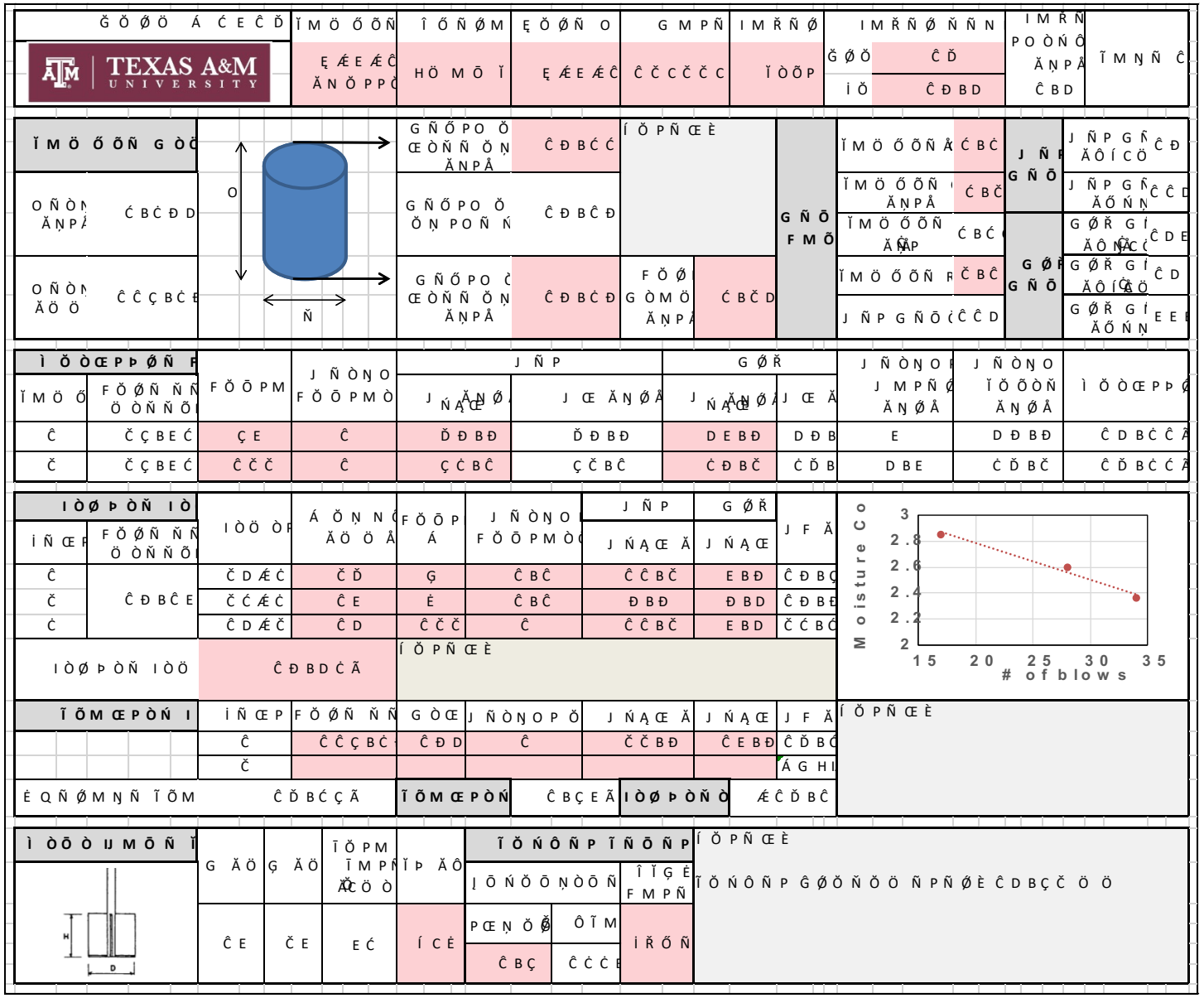

Figure B-45. B-9-16 (16'-17.5') Bottom – Page 1

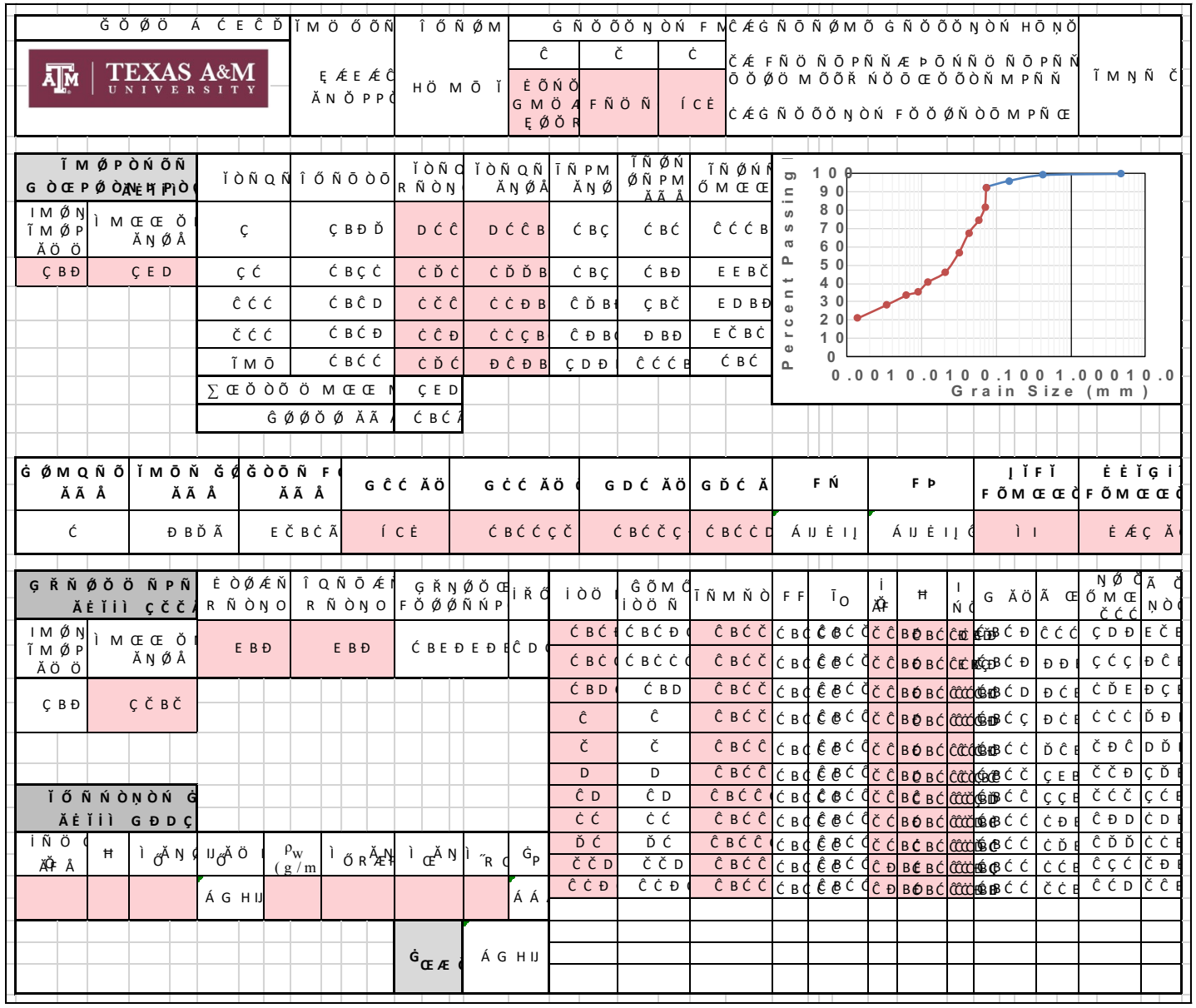

Figure B-46. B-9-16 (16'-17.5') Bottom – Page 2

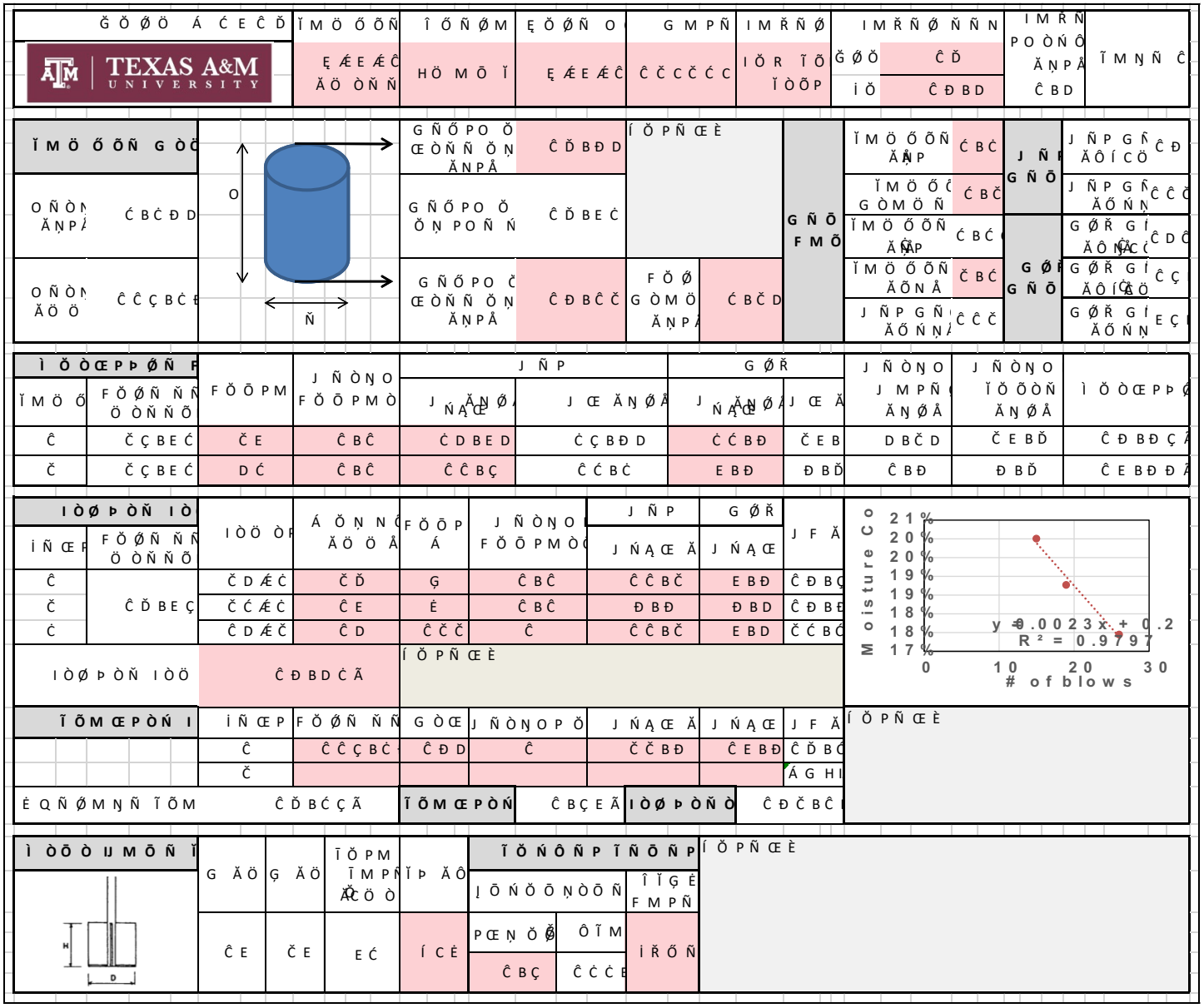

Figure B-47. B-9-16 (16'-17.5') Middle – Page 1

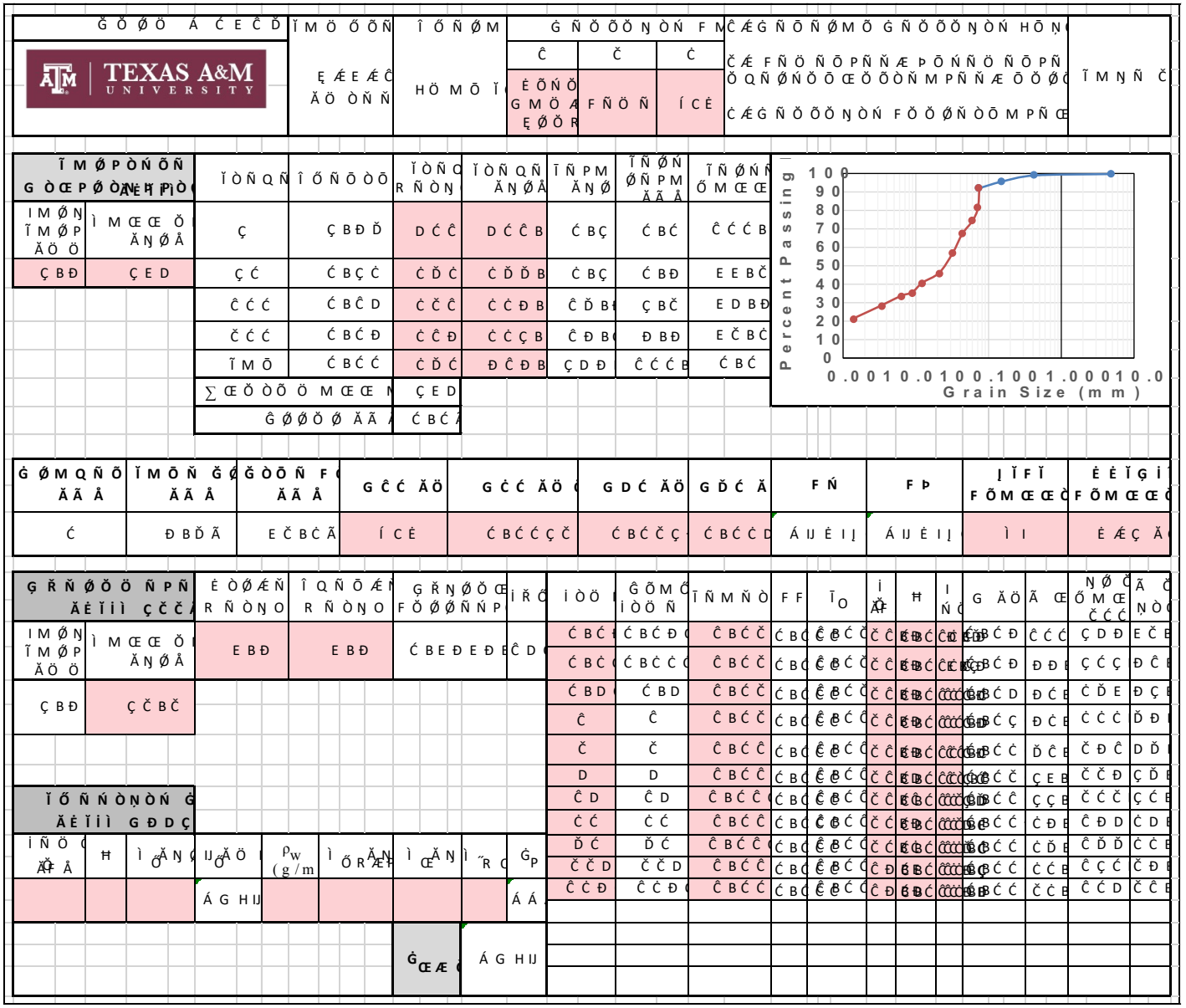

Figure B-48. B-9-16 (16'-17.5') Middle – Page 2

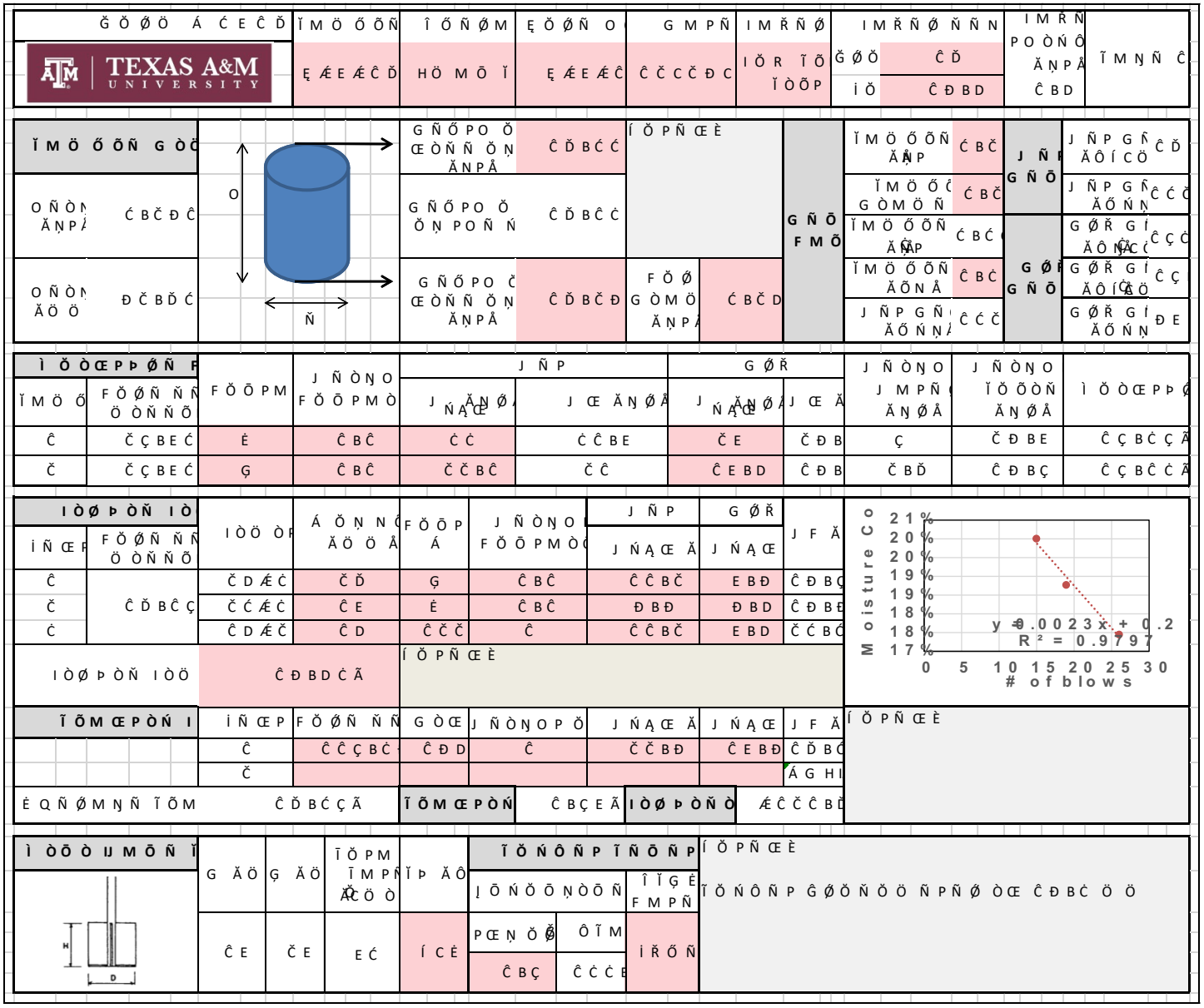

Figure B-49. B-9-16 (16'-17.5') Top – Page 1

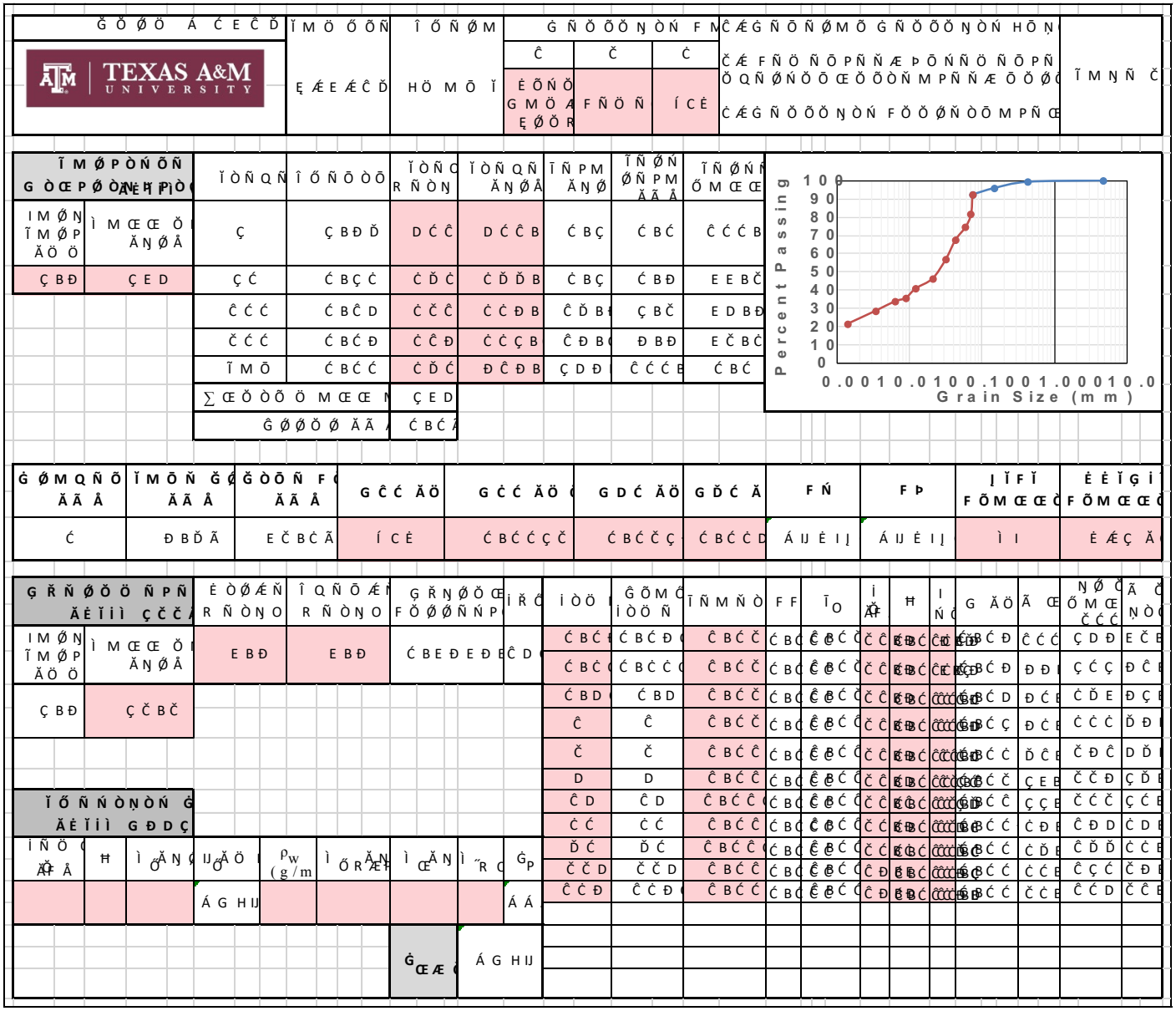

Figure B-50. B-9-16 (16'-17.5') Top – Page 2

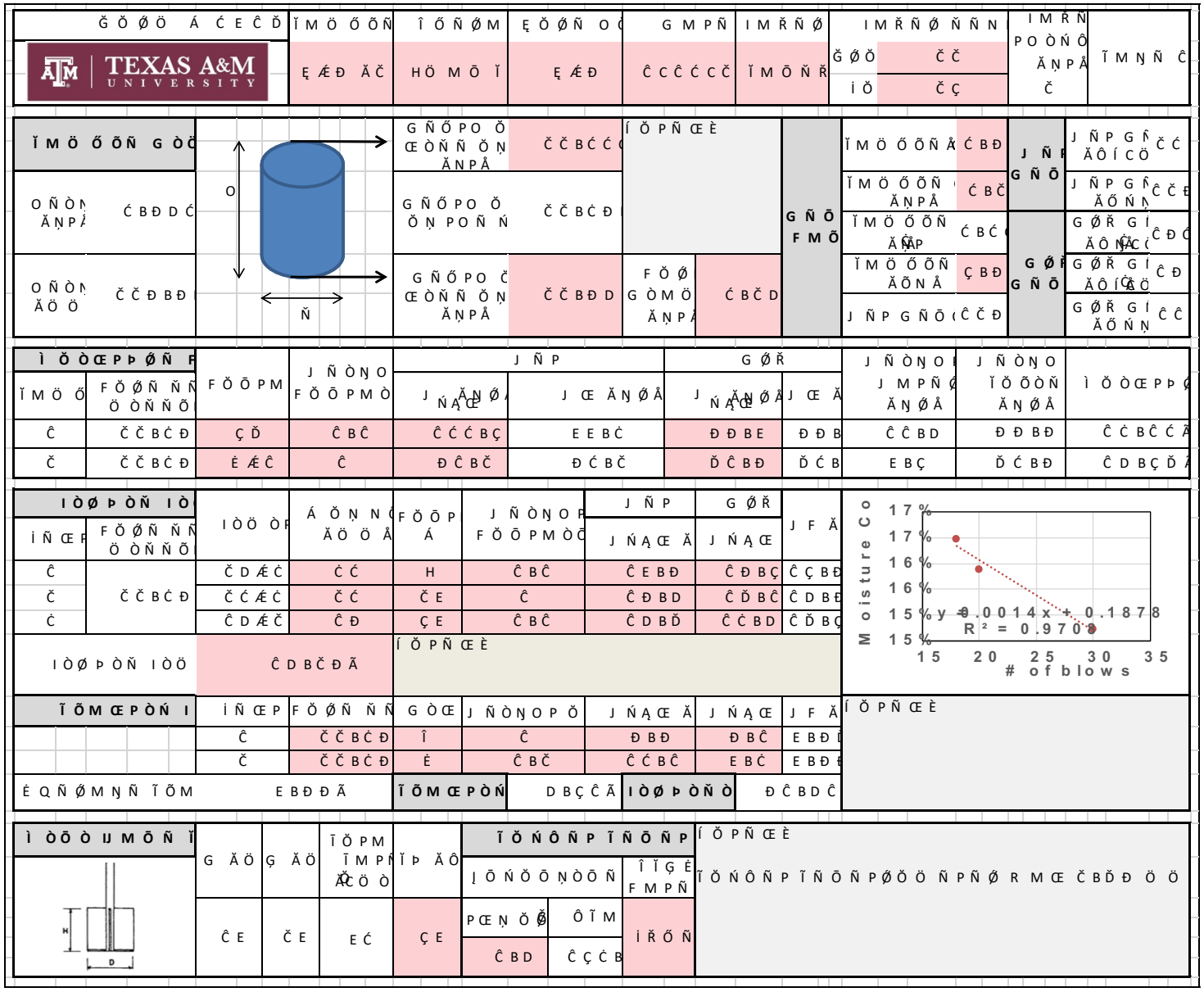

Figure B-51. B-7 (22'-24') Tittabawsee River – Page 1

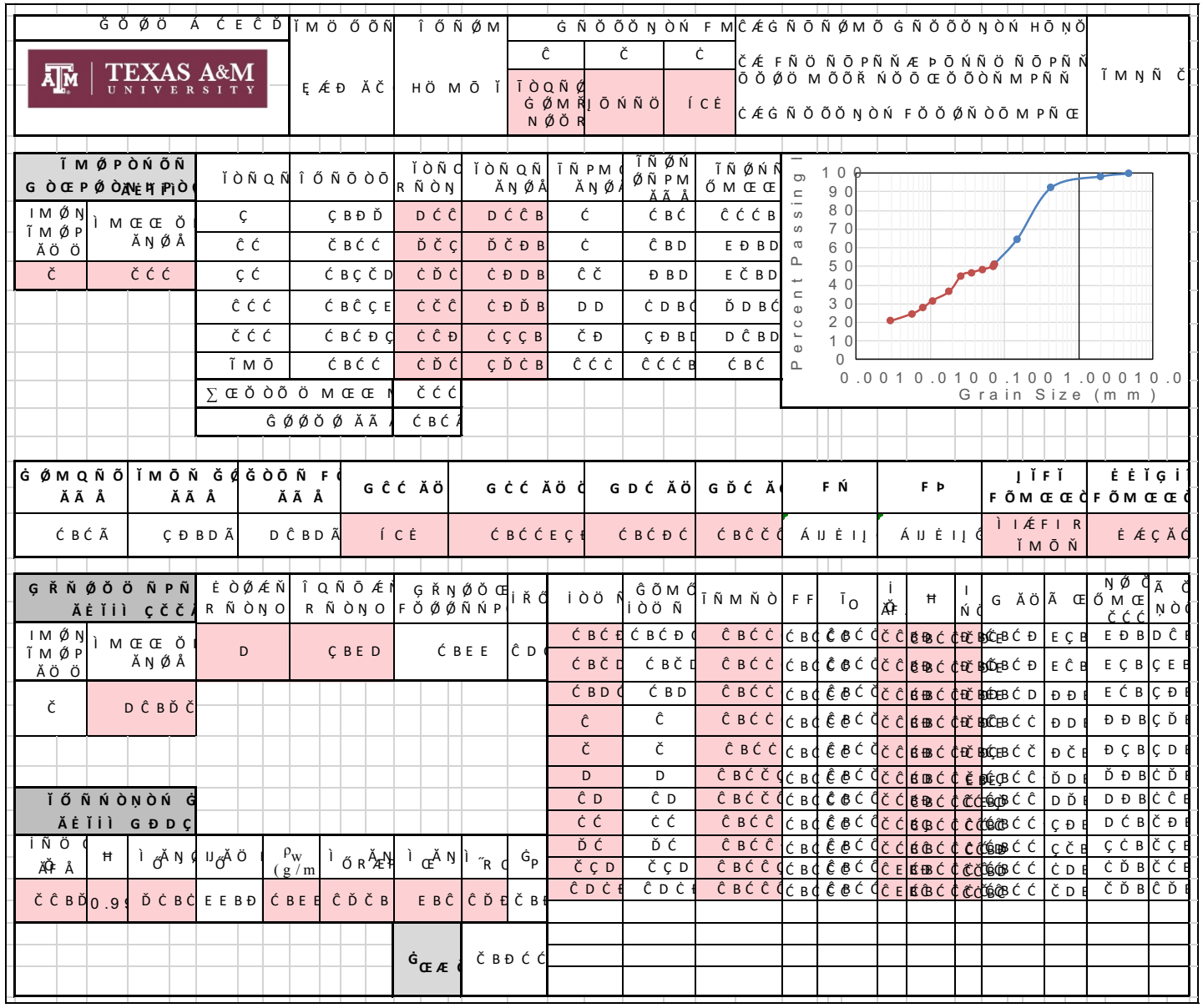

Figure B-52. B-7 (22'-24') Tittabawsee River – Page 2

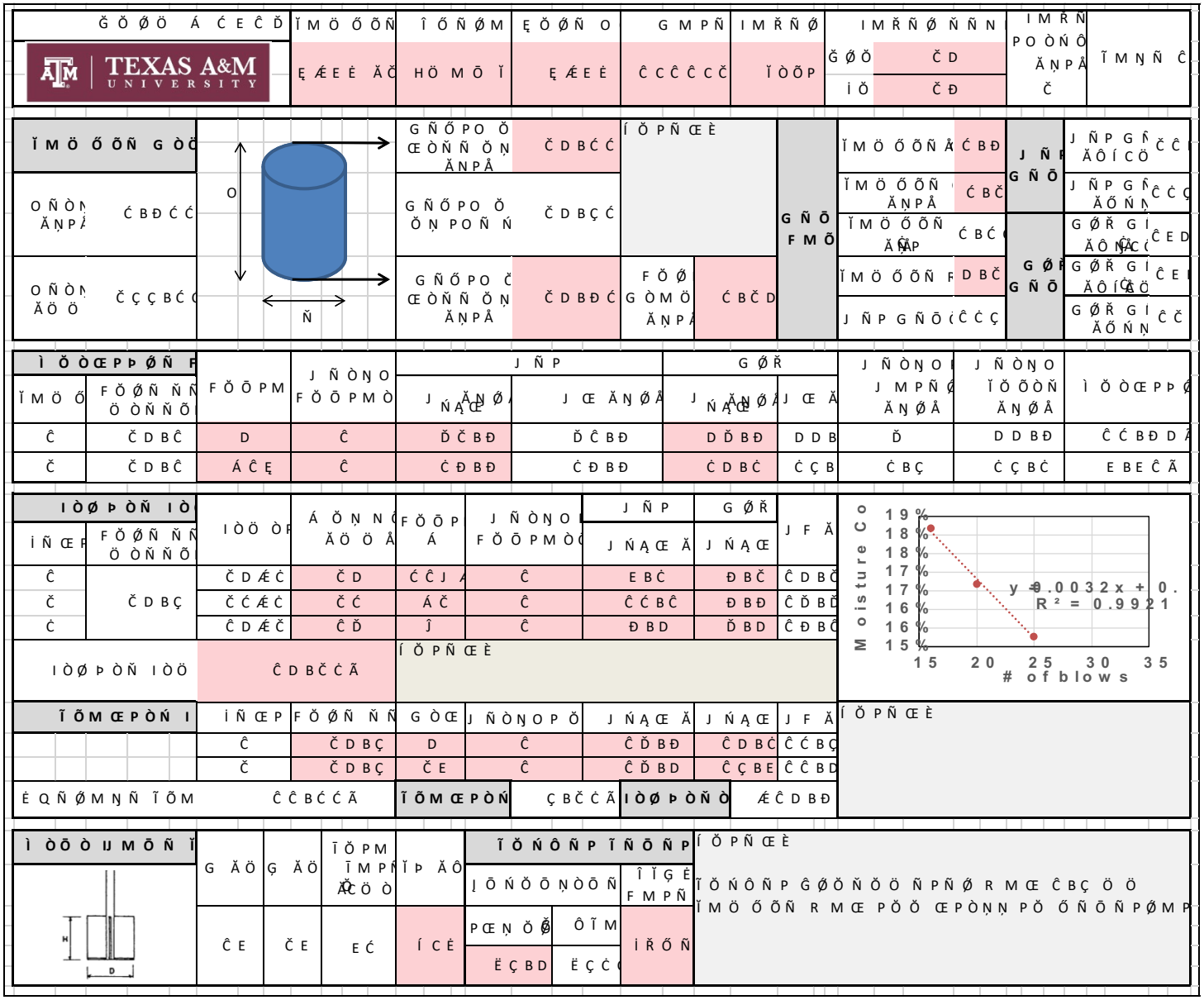

Figure B-53. B-9A (25’-27’) Tittabawsee River – Page 1

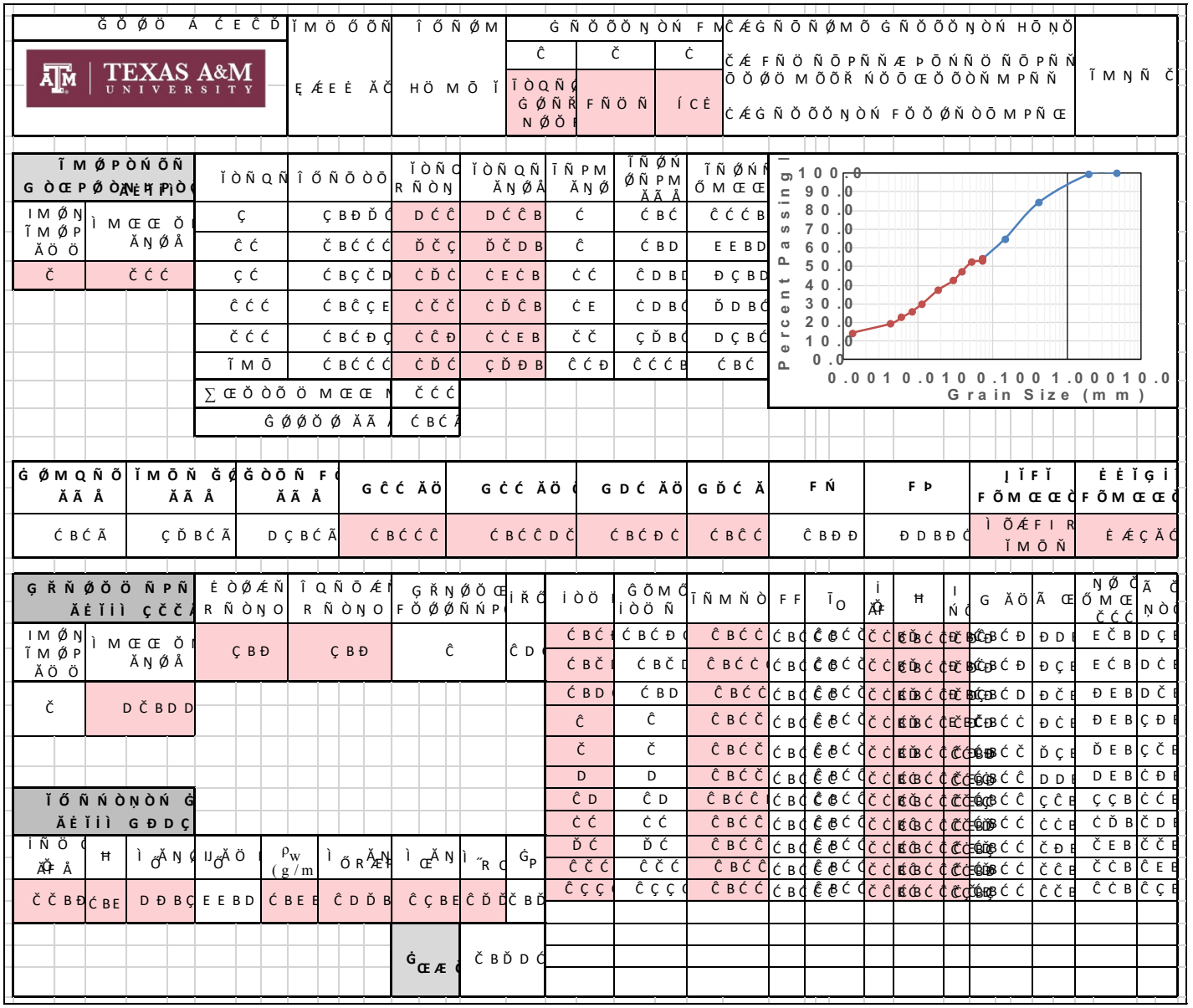

Figure B-54. B-9A (25'-27') Tittabawsee River – Page 2

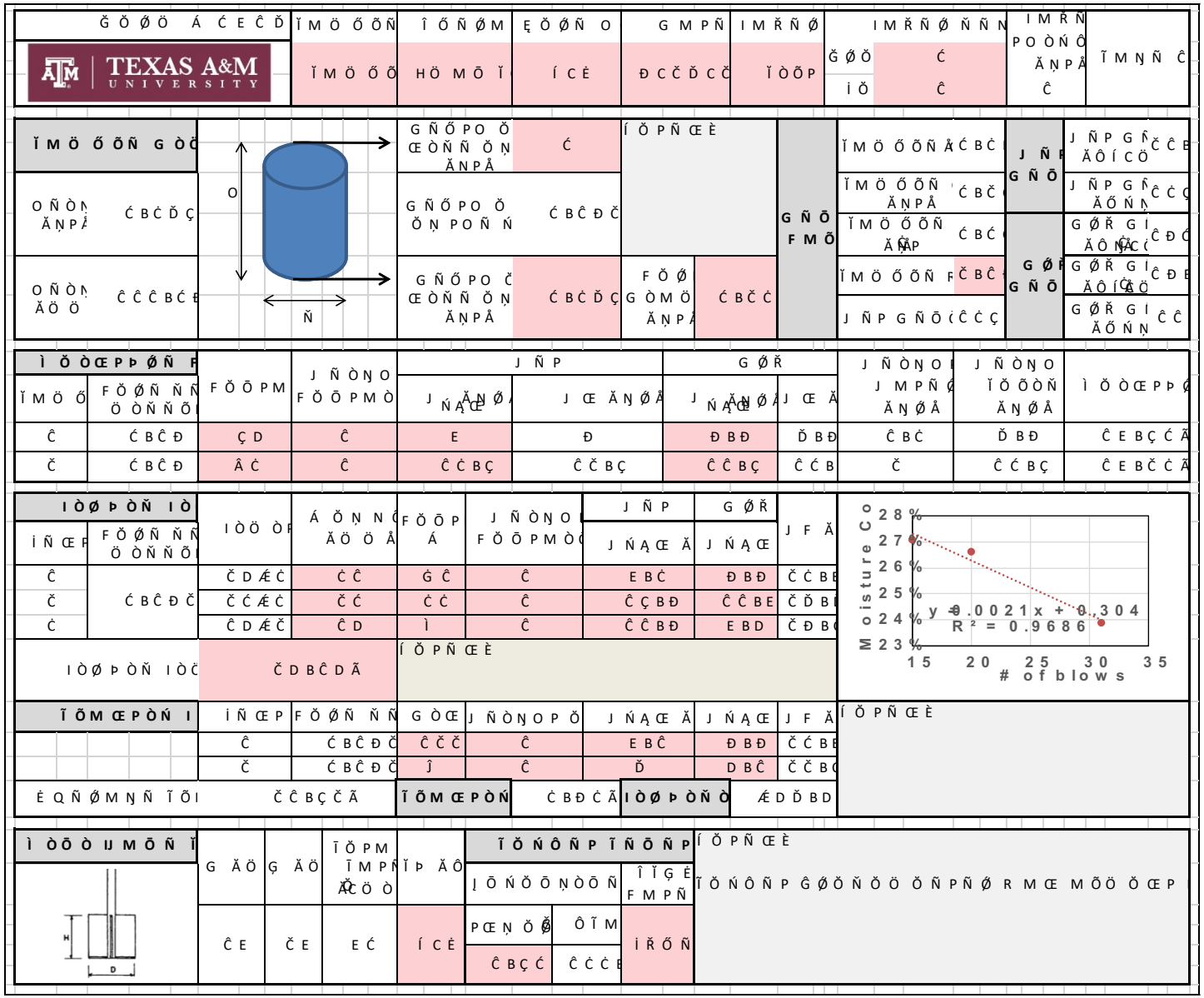

Figure B-55. FHWA Sample 2 – Page 1

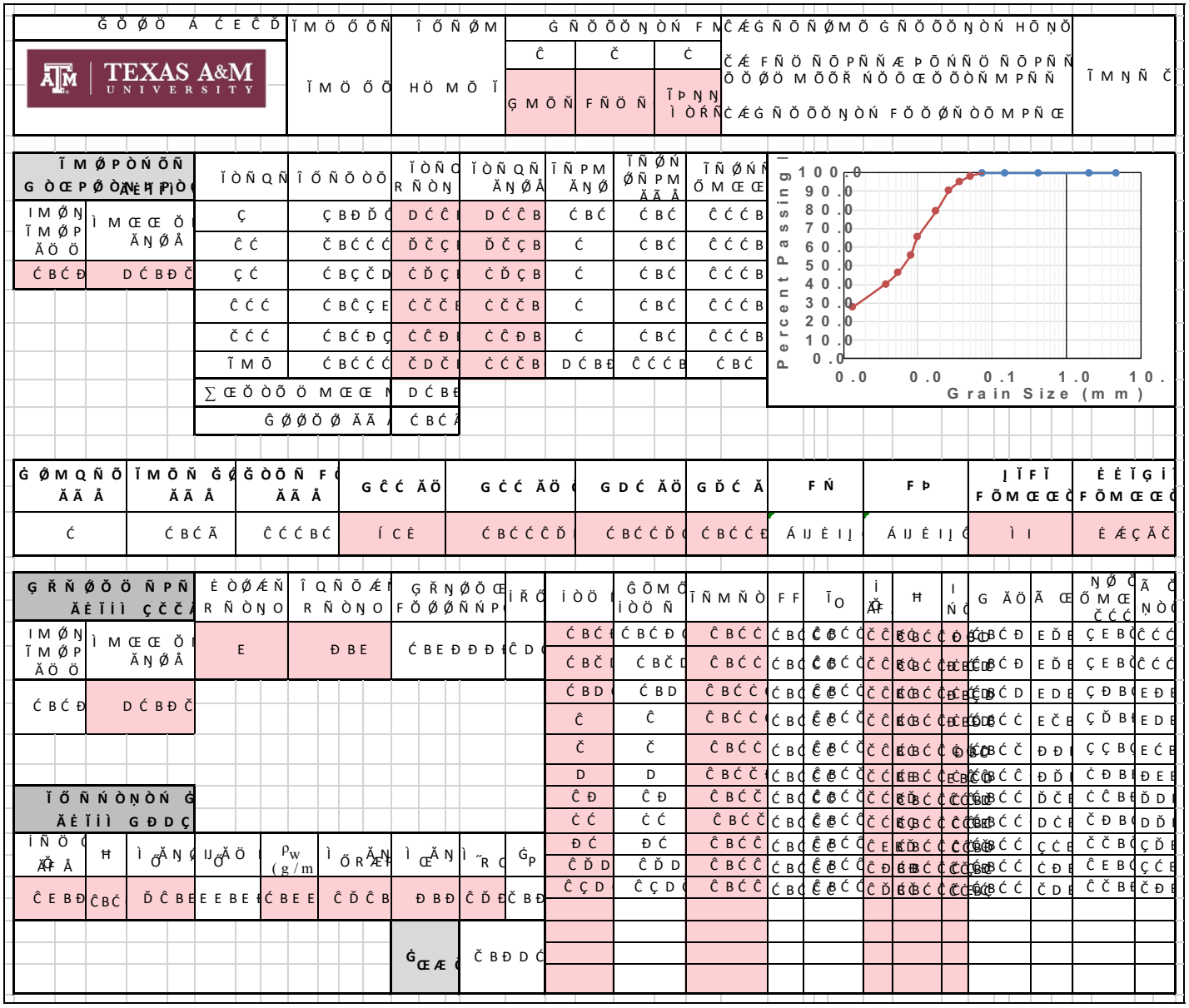

Figure B-56. FHWA Sample 2 – Page 2

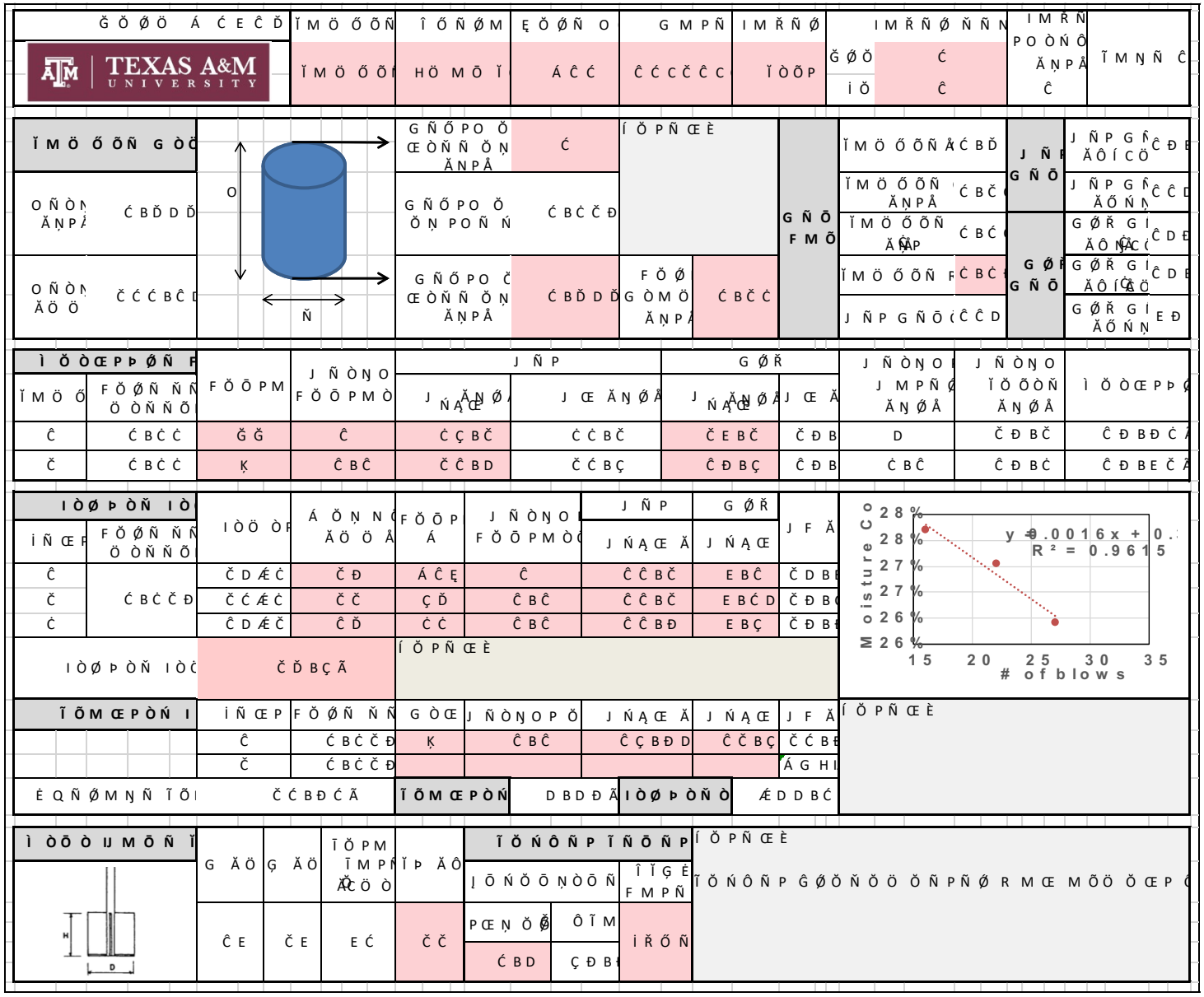

Figure B-57. GEER Sample 10 – Page 1

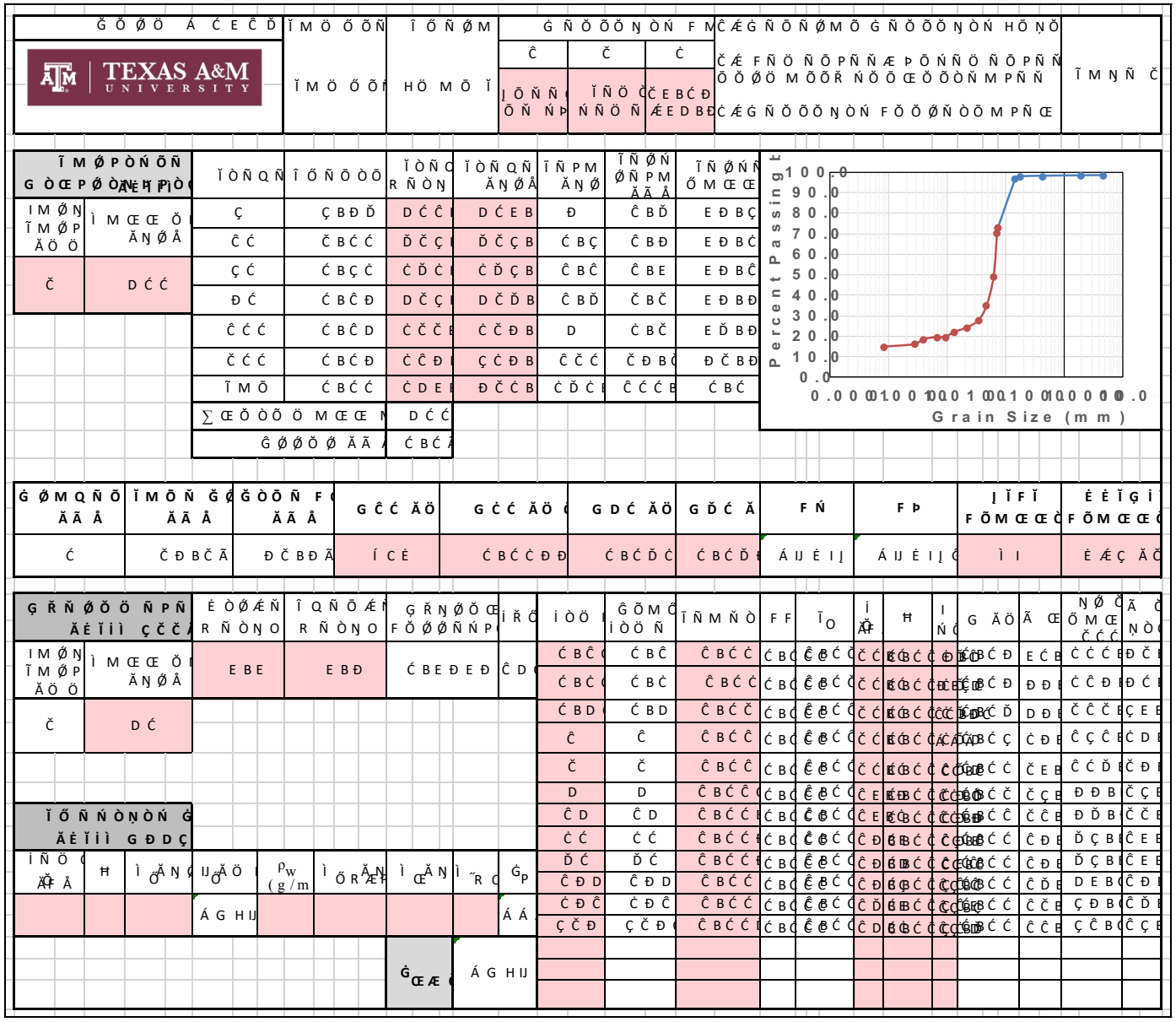

Figure B-58. GEER Sample 10 – Page 2

Sand Samples - EFA

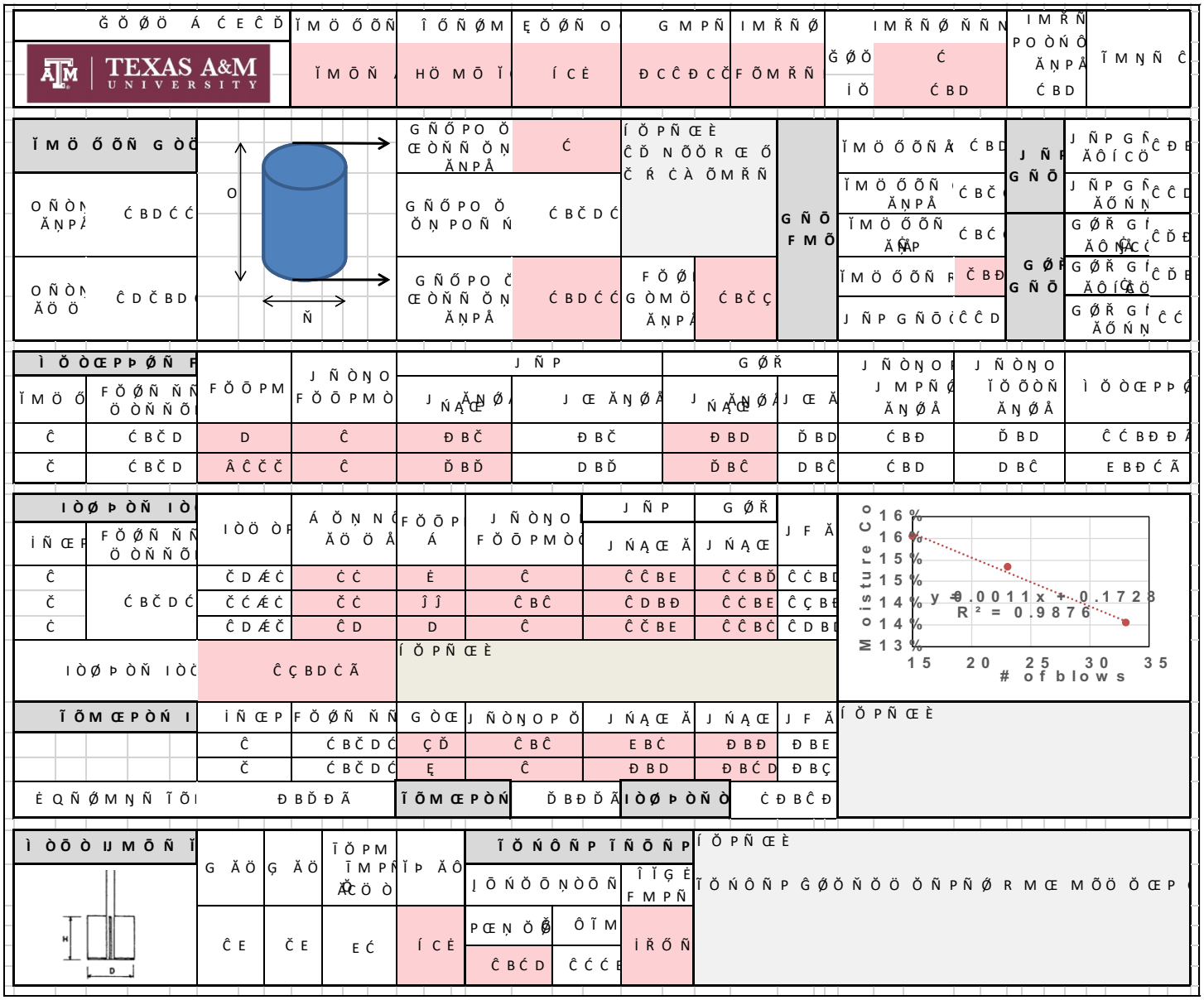

Figure B-59. Sand #1 – Page 1

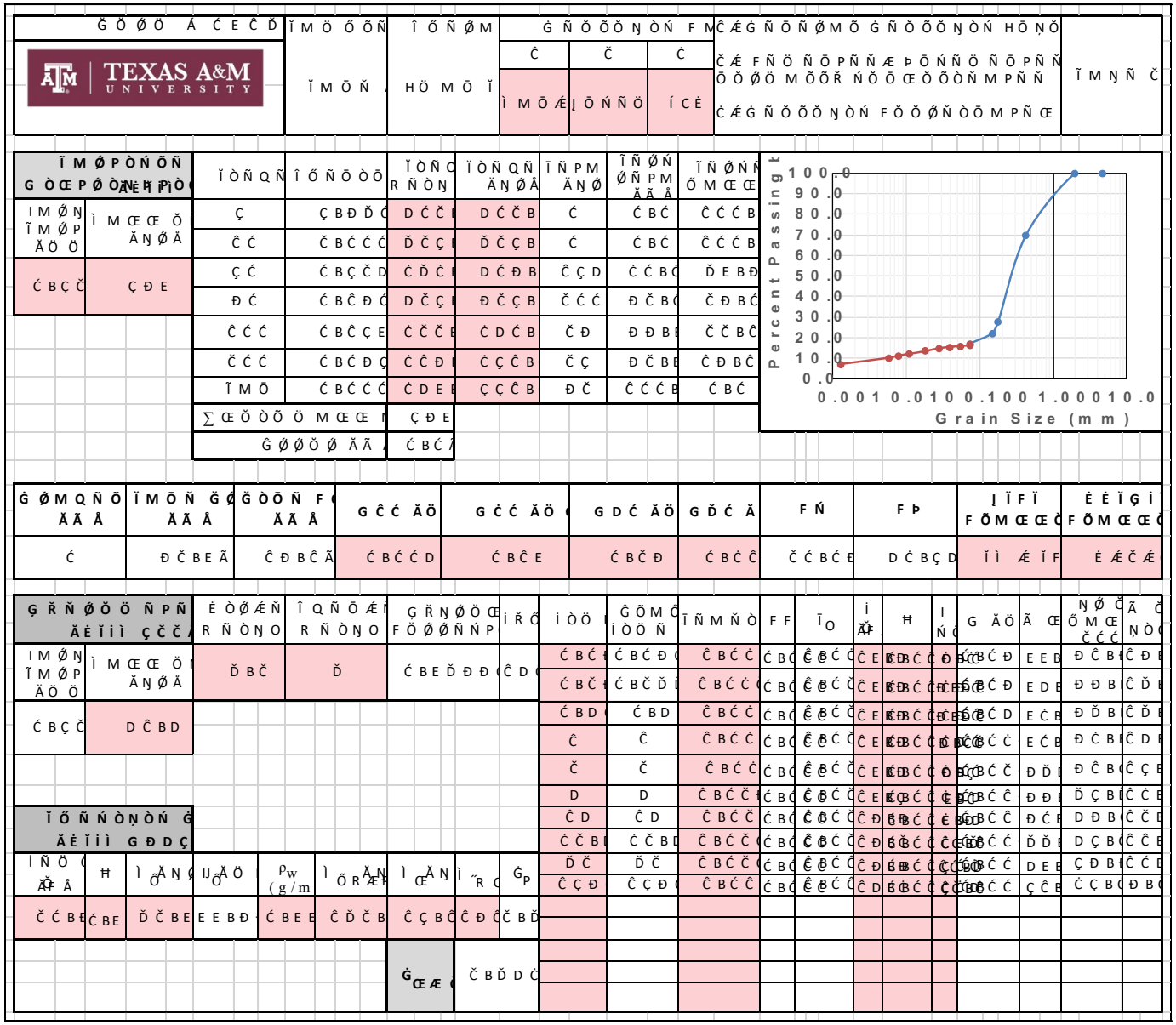

Figure B-60. Sand #1 – Page 2

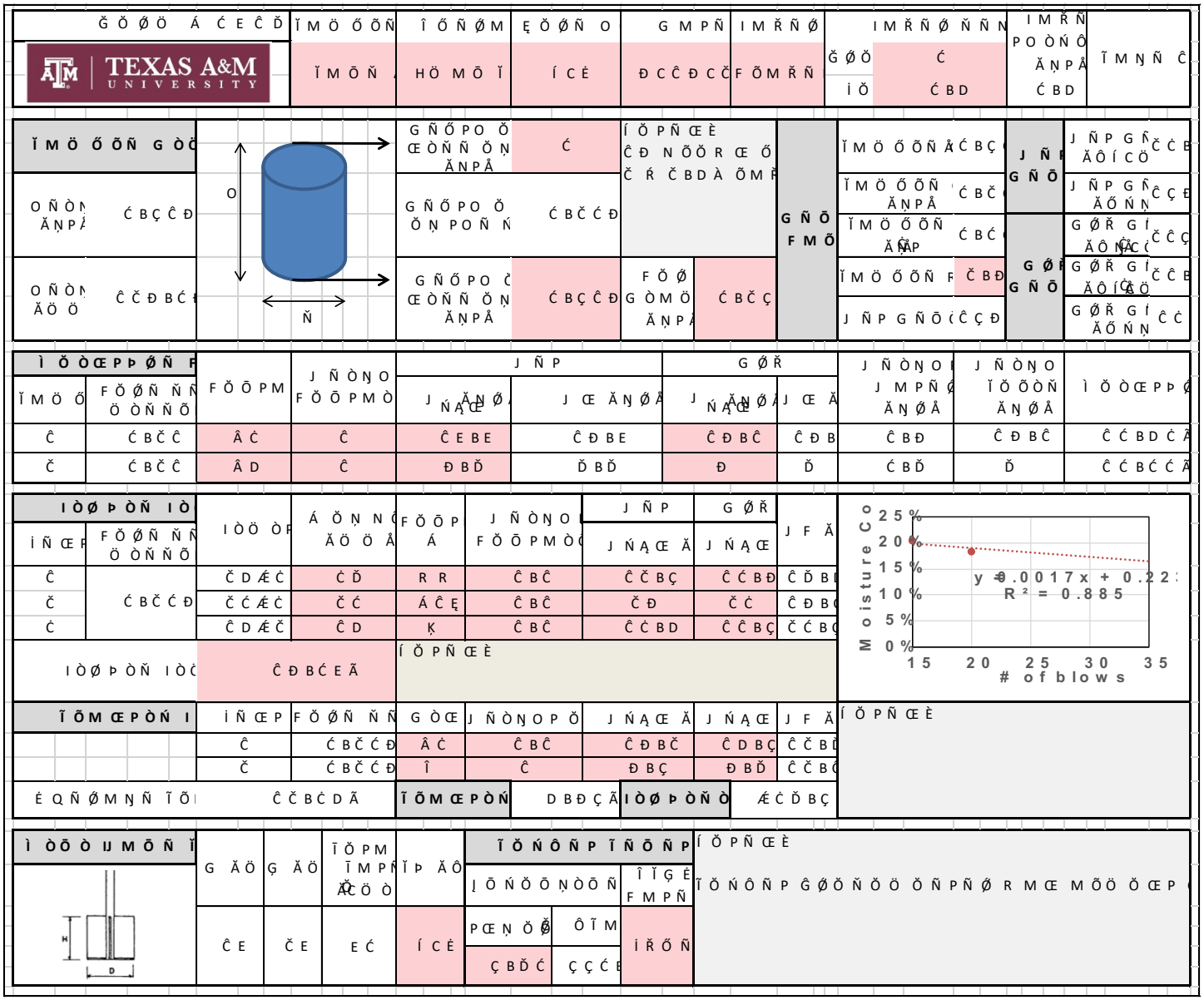

Figure B-61. Sand #2 – Page 1

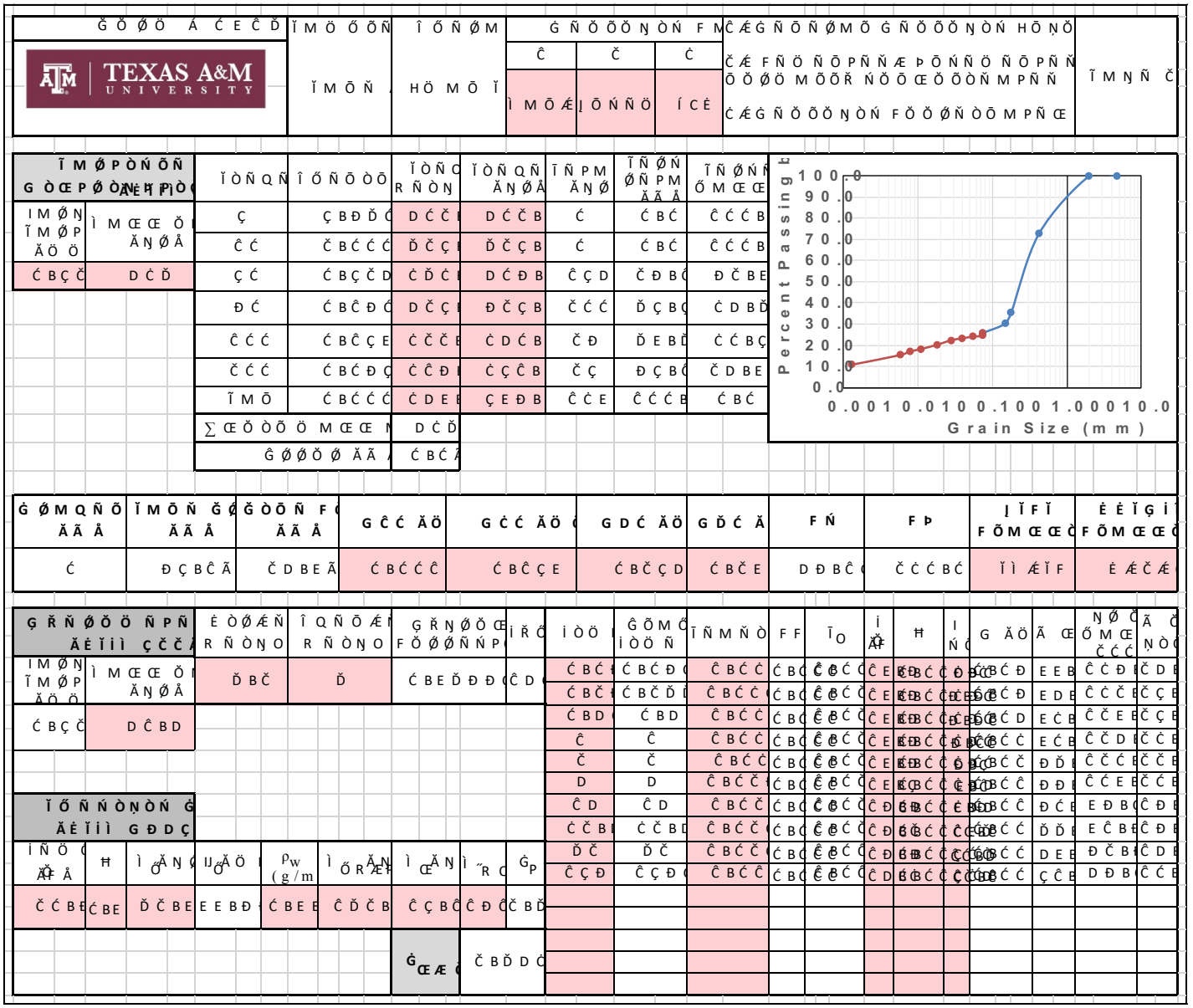

Figure B-62. Sand #2 – Page 2

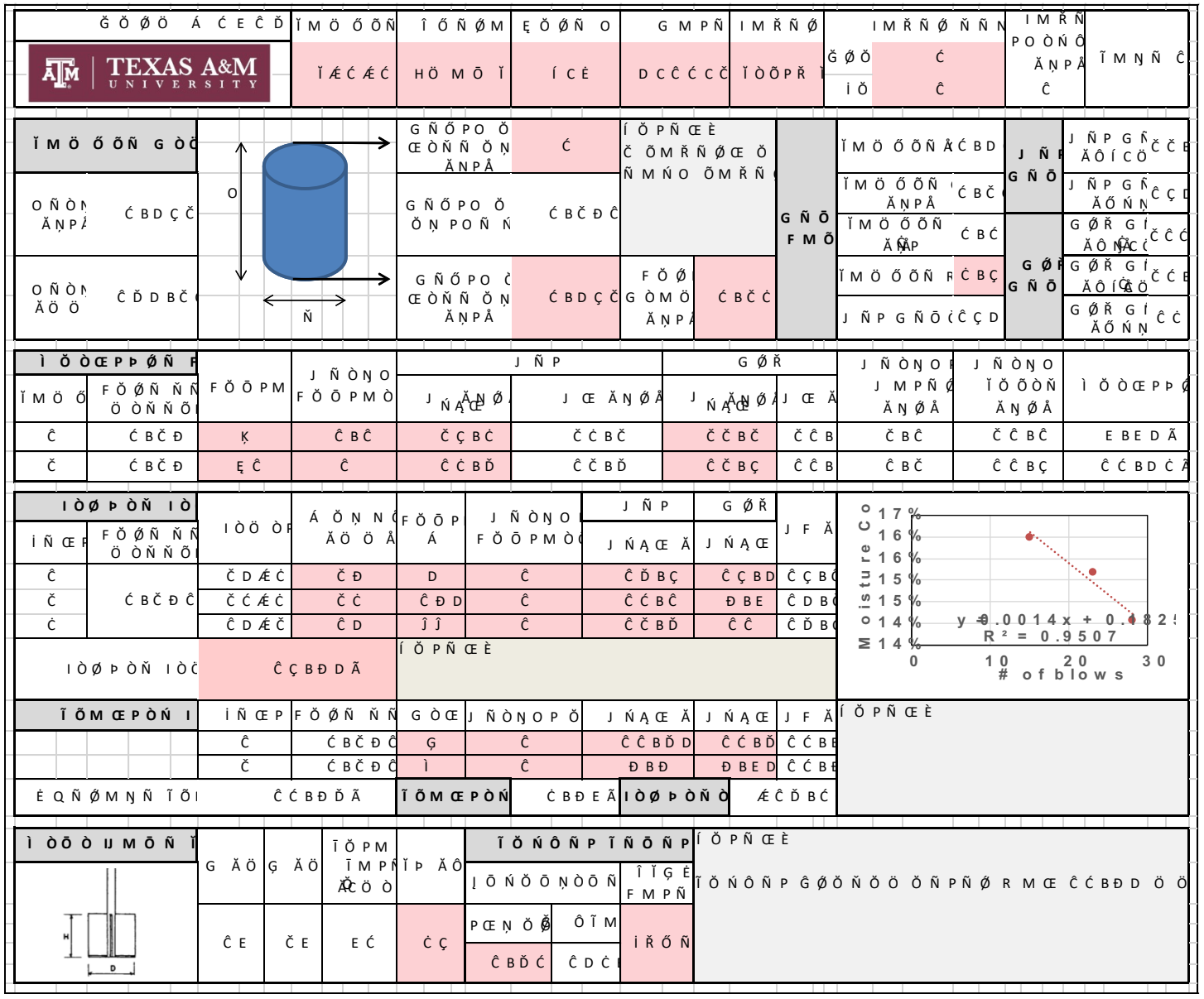

Figure B-63. S-0-0-0 – Page 1

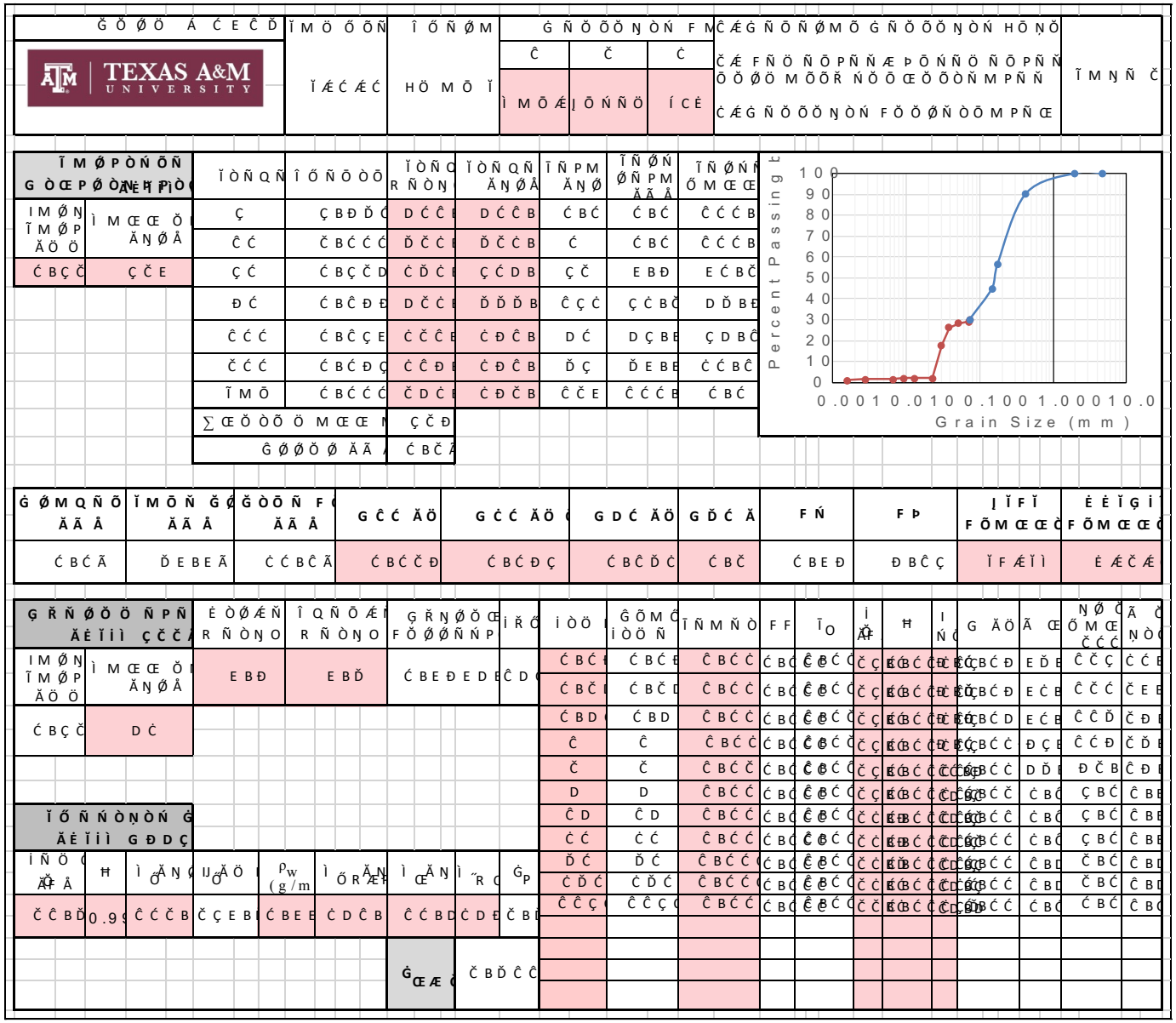

Figure B-64. S-0-0-0 – Page 2

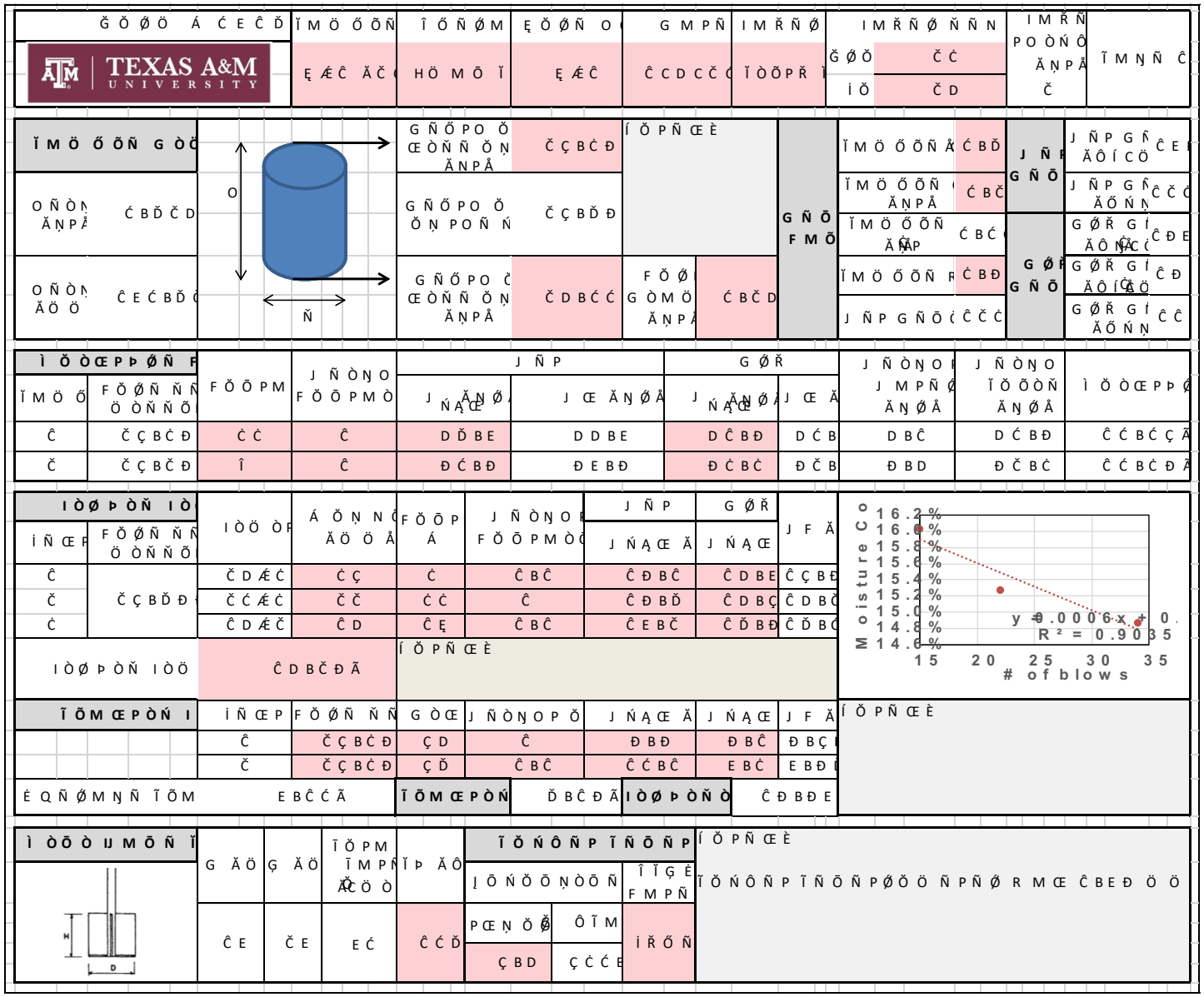

Figure B-65. B-1 (23'-25') Tittabawsee River – Page 1

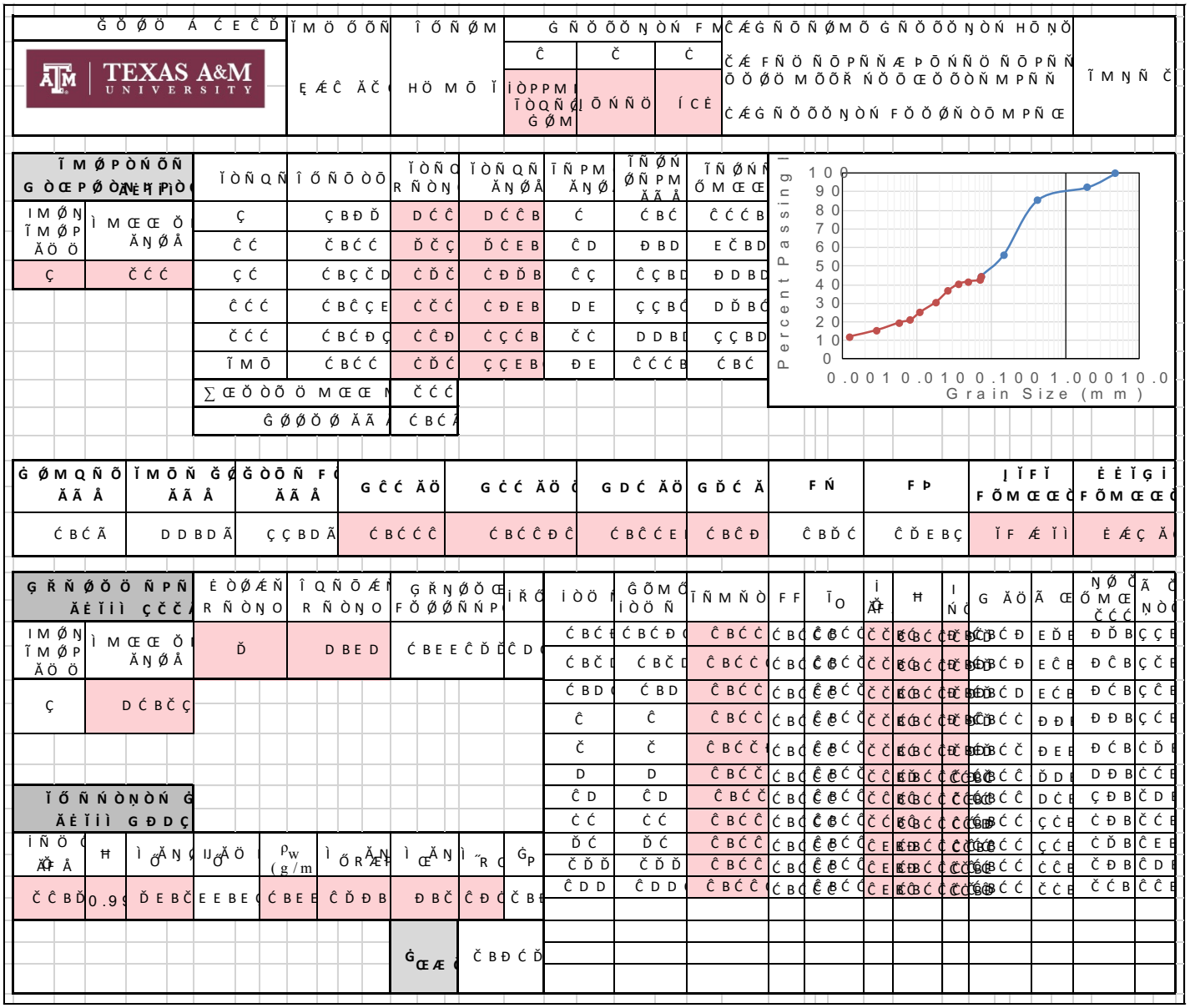

Figure B-66. B-1 (23’-25’) Tittabawsee River – Page 2

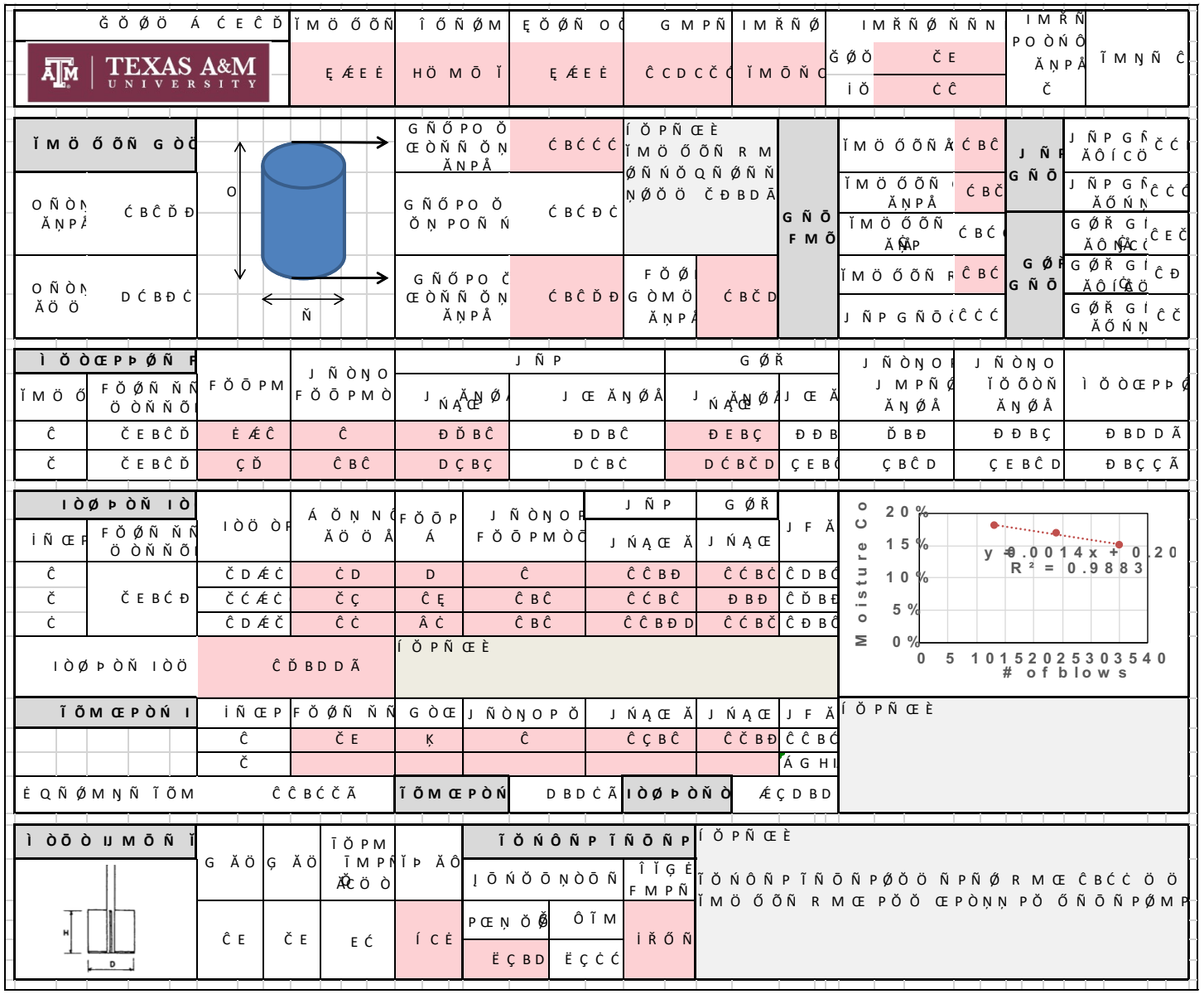

Figure B-67. B-9A (29’-31’) Tittabawsee River – Page 1

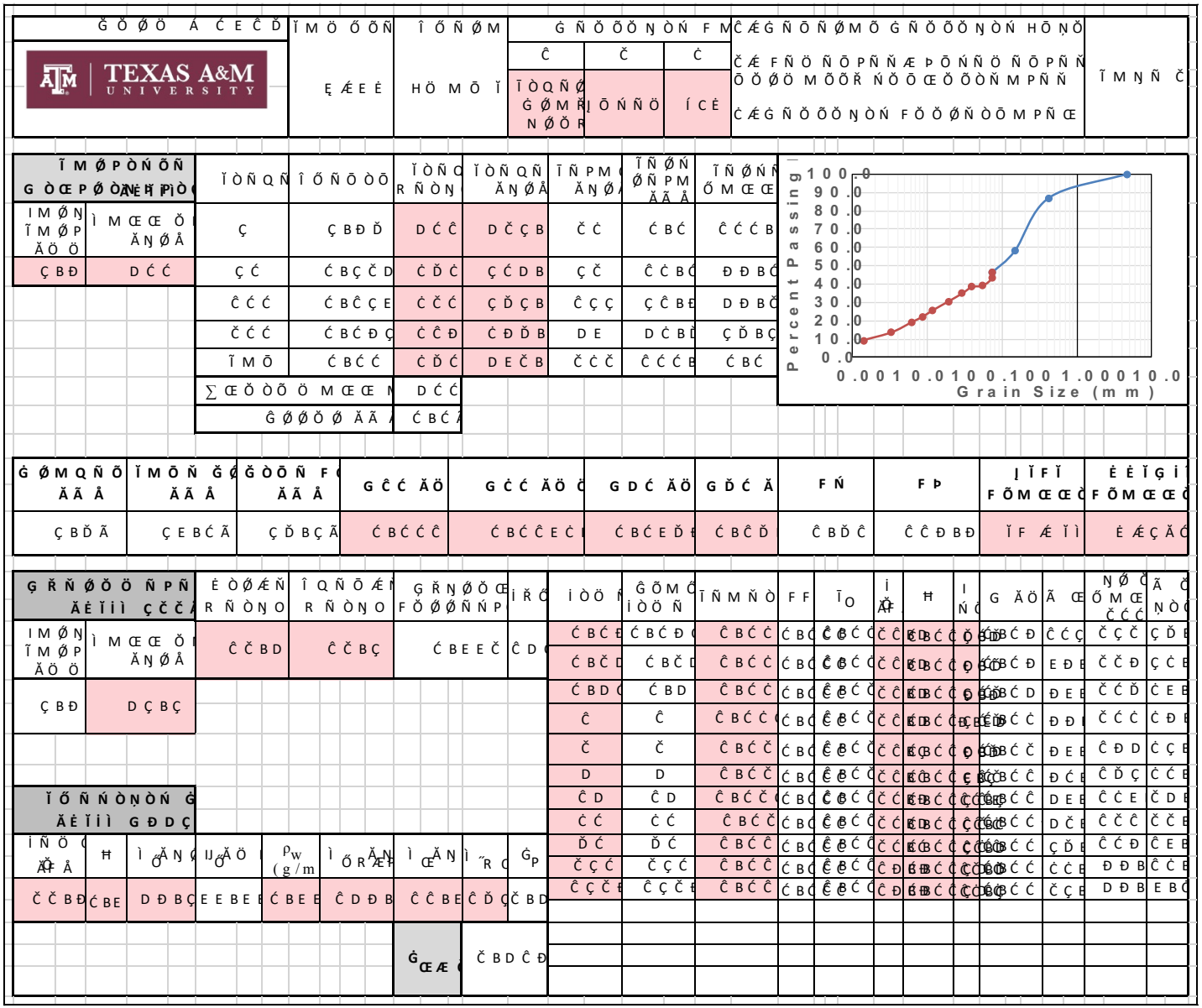

Figure B-68. B-9A (29’-31’) Tittabawsee River – Page 2

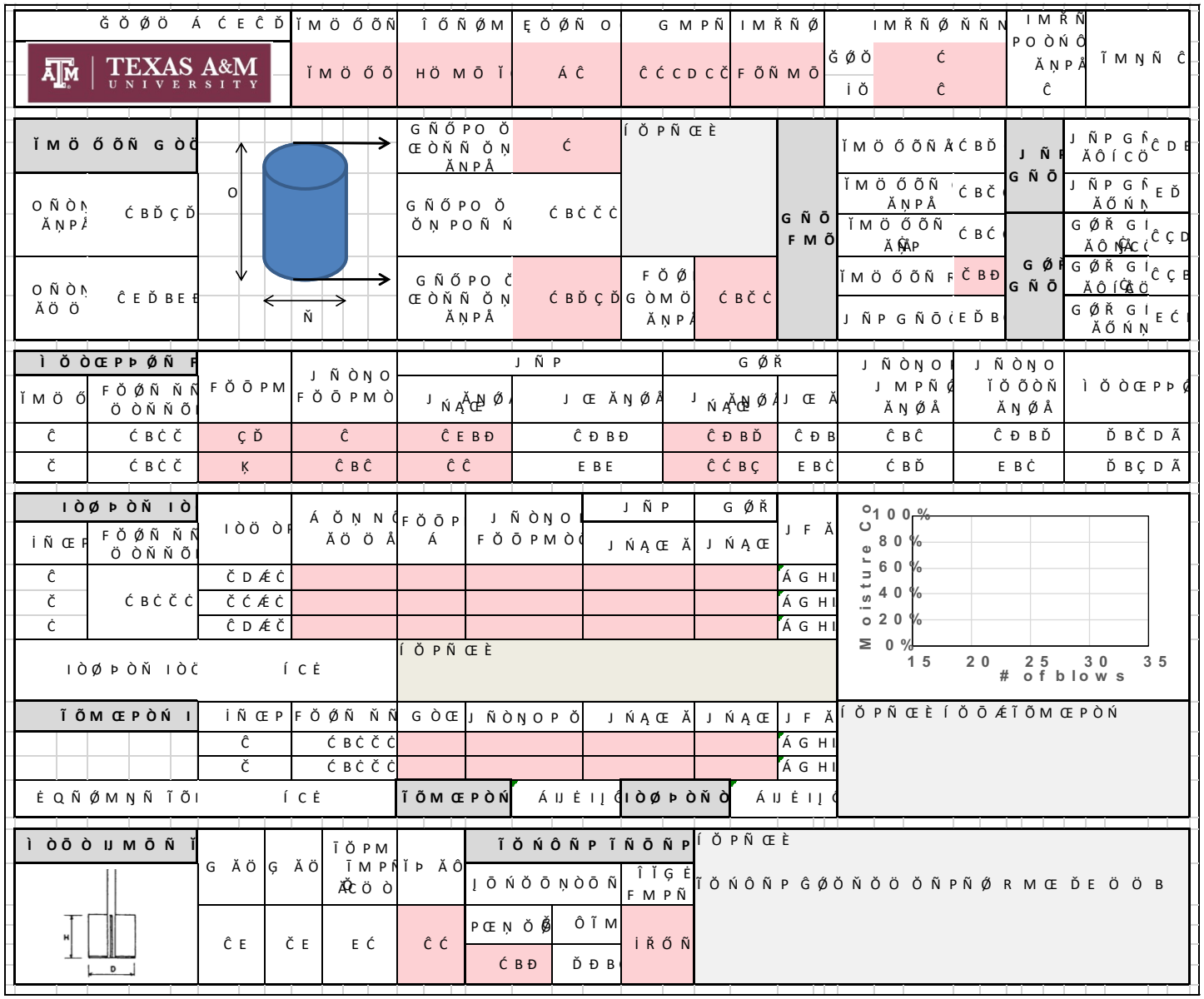

Figure B-69. GEER Sample #1 – Page 1

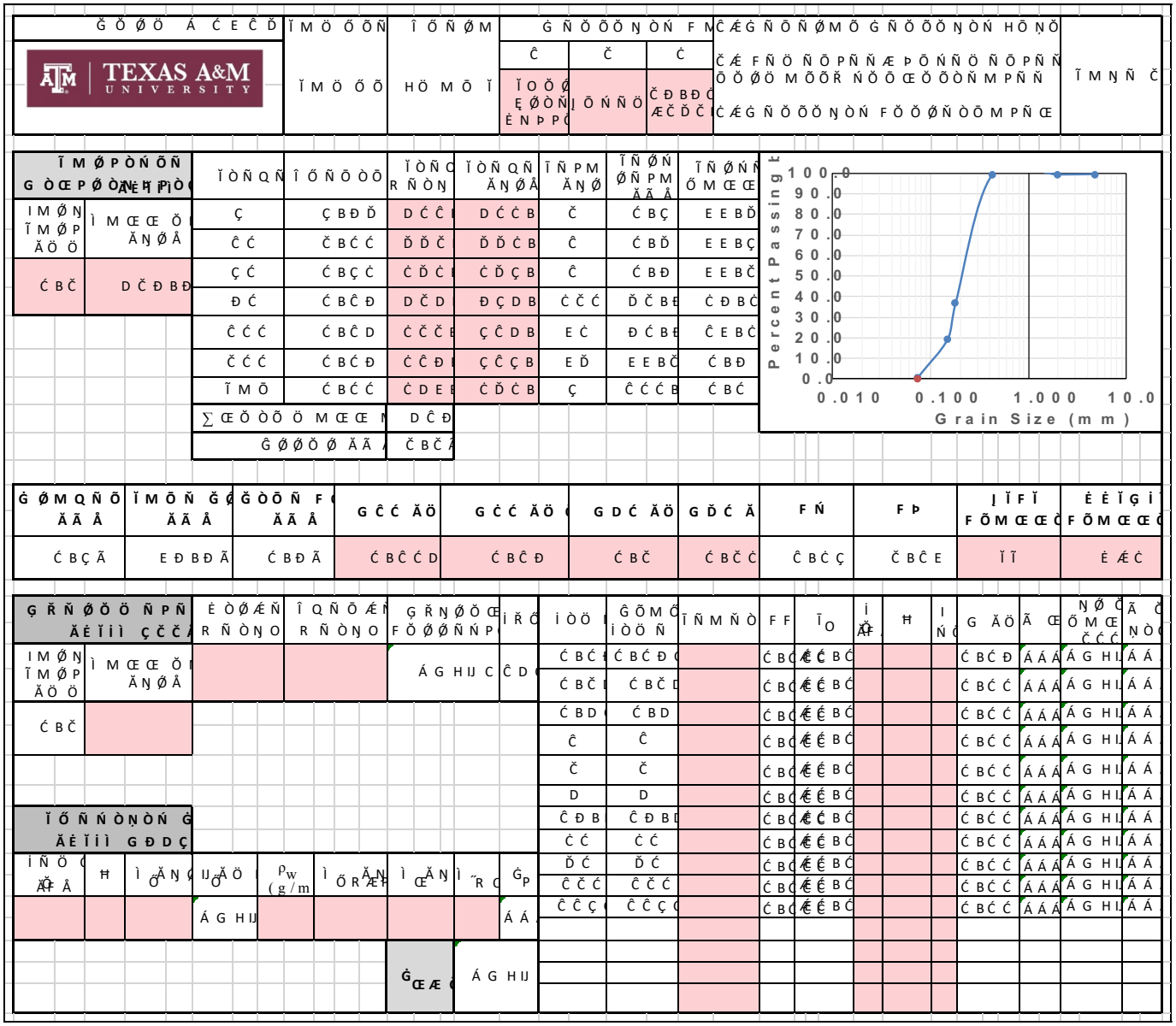

Figure B-70. GEER Sample #1 – Page 2

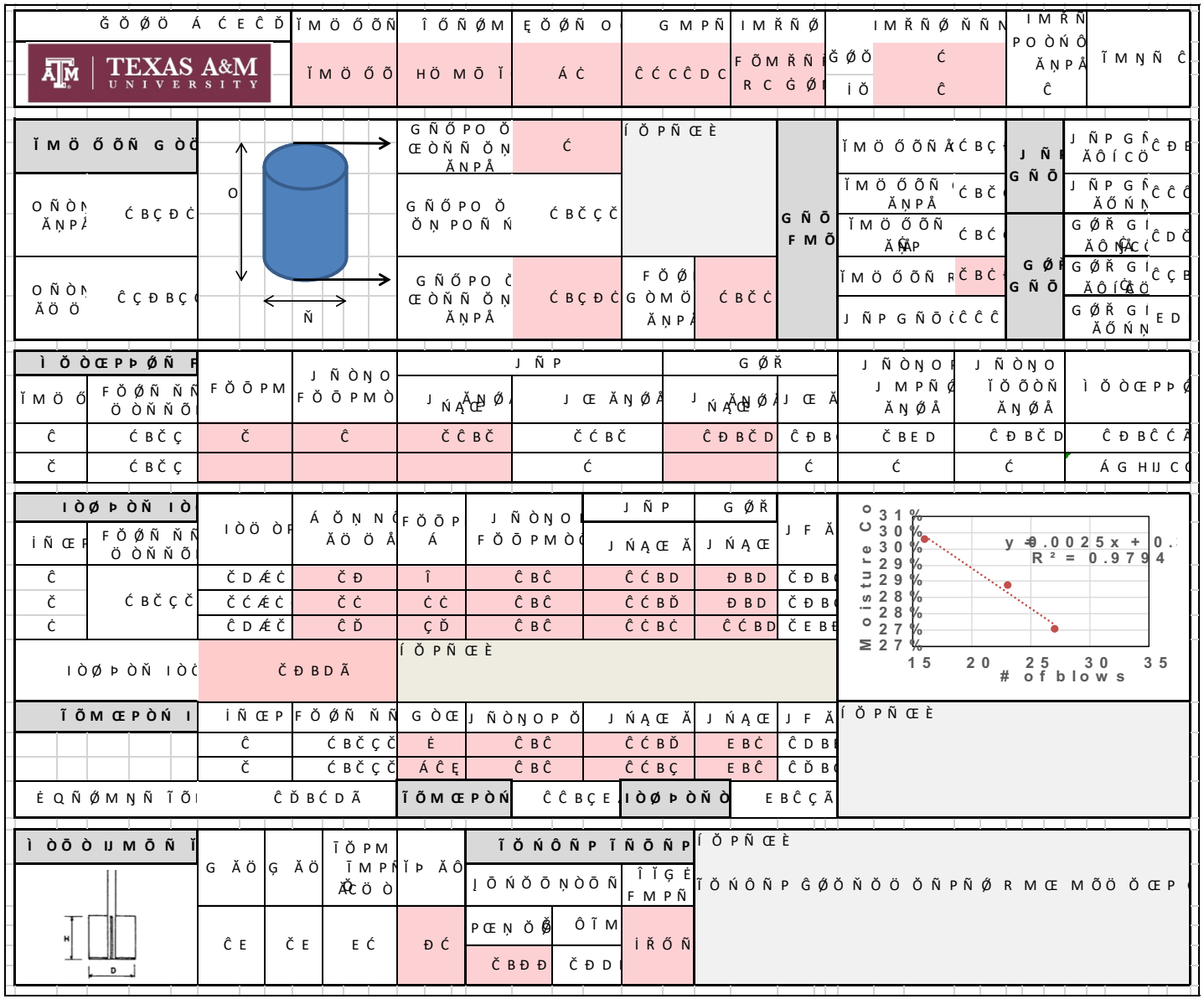

Figure B-71. GEER Sample #3 – Page 1

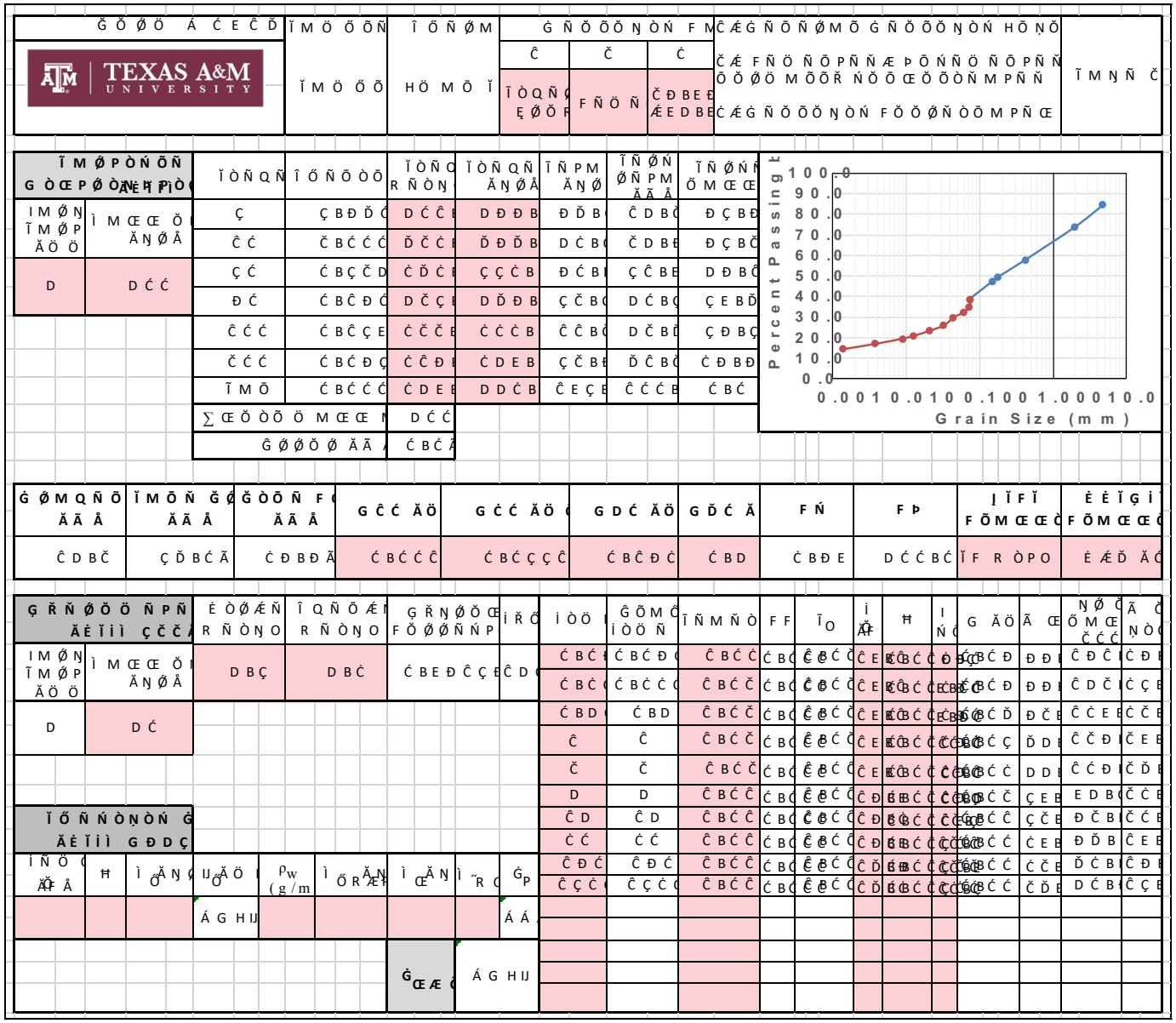

Figure B-72. GEER Sample #3 – Page 2

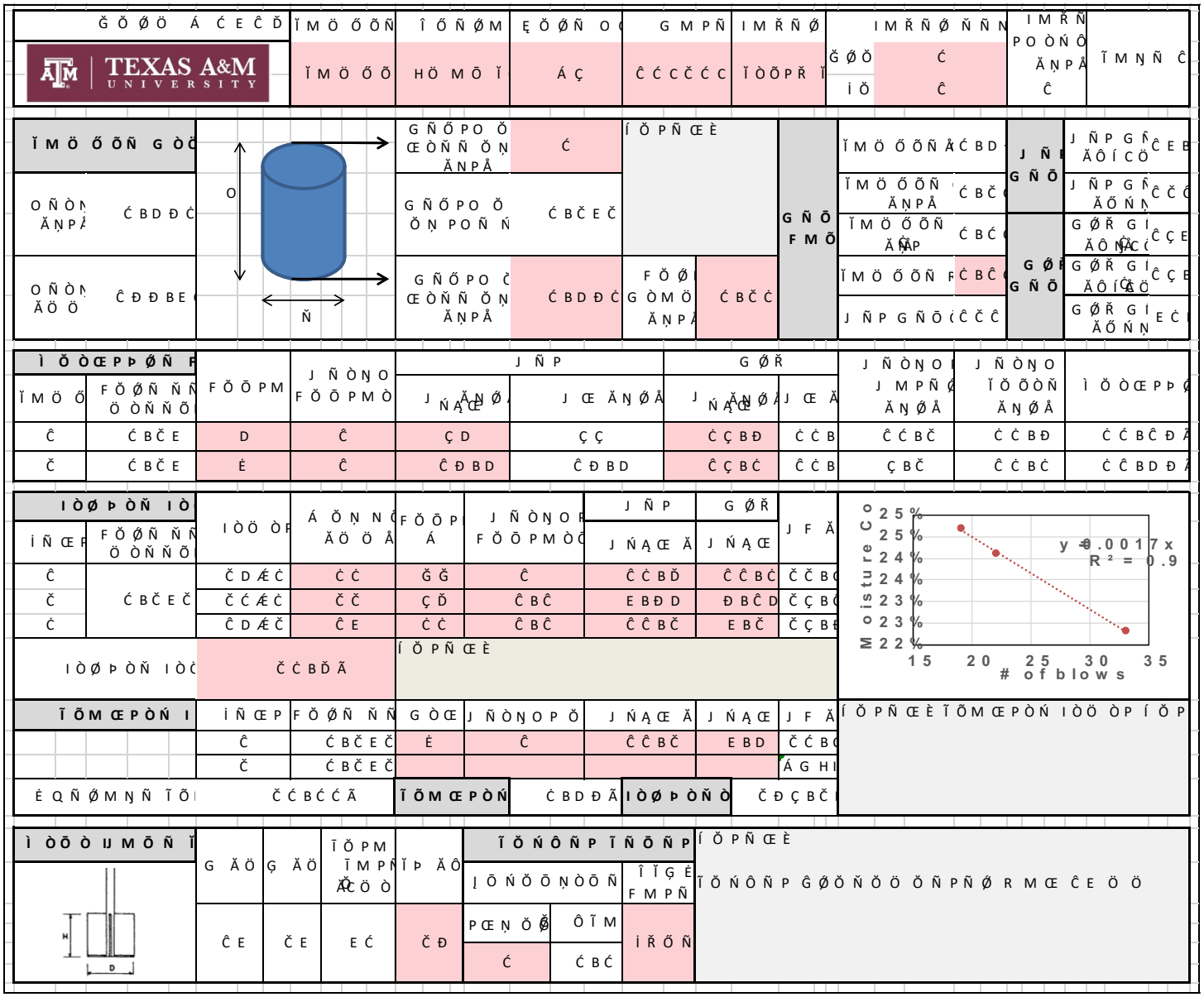

Figure B-73. GEER Sample #4 – Page 1

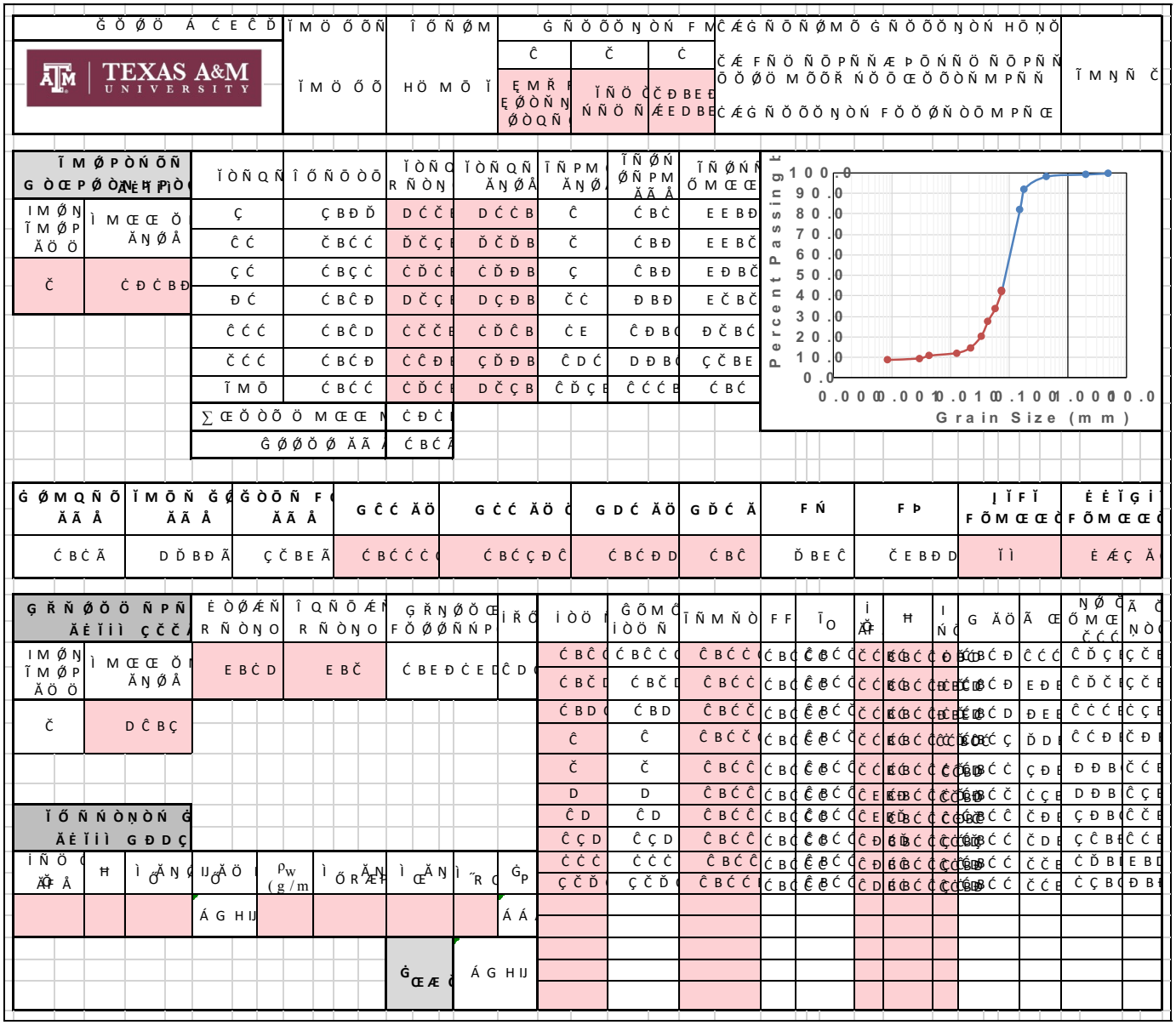

Figure B-74. GEER Sample #4 – Page 2

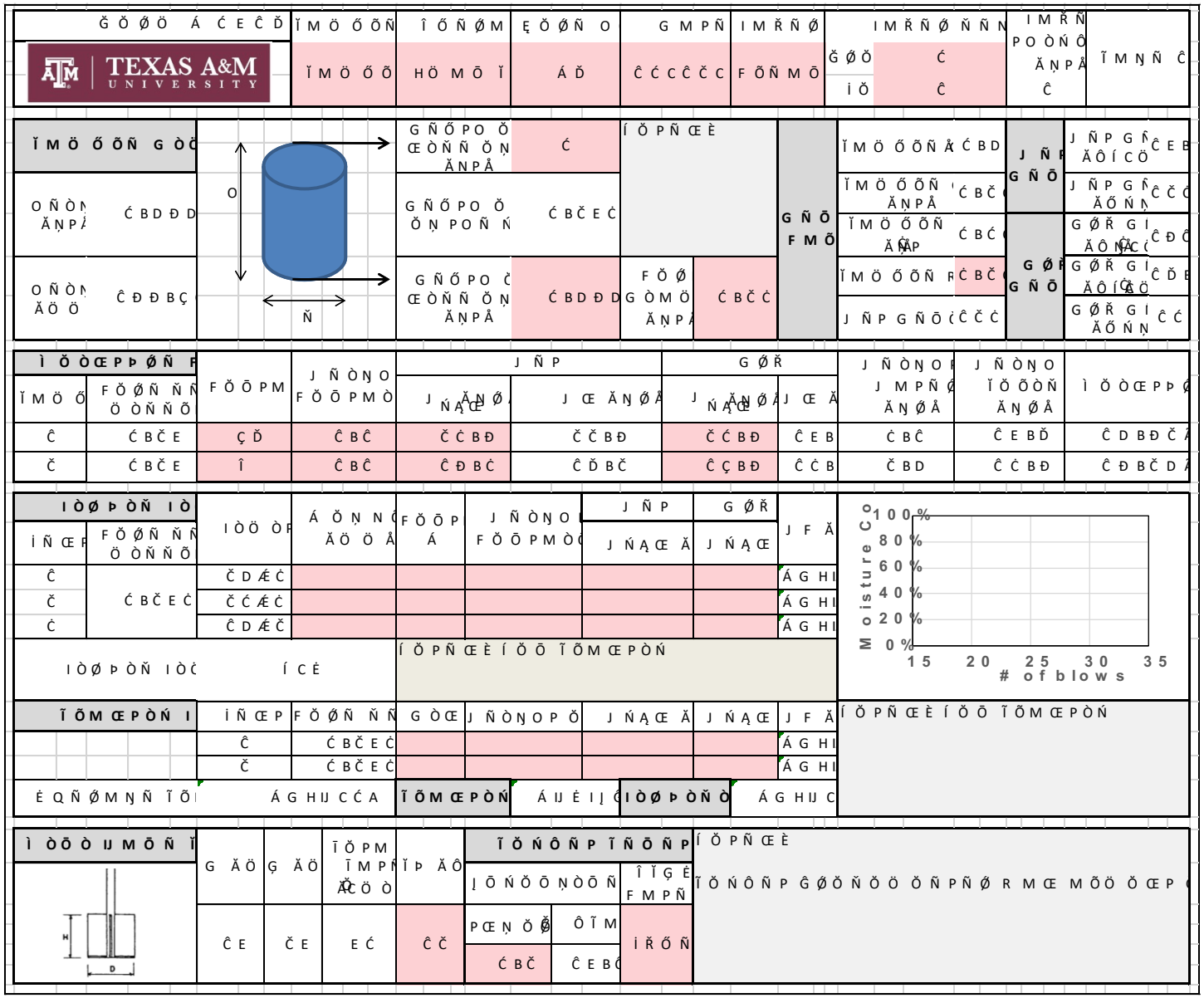

Figure B-75. GEER Sample #6 – Page 1

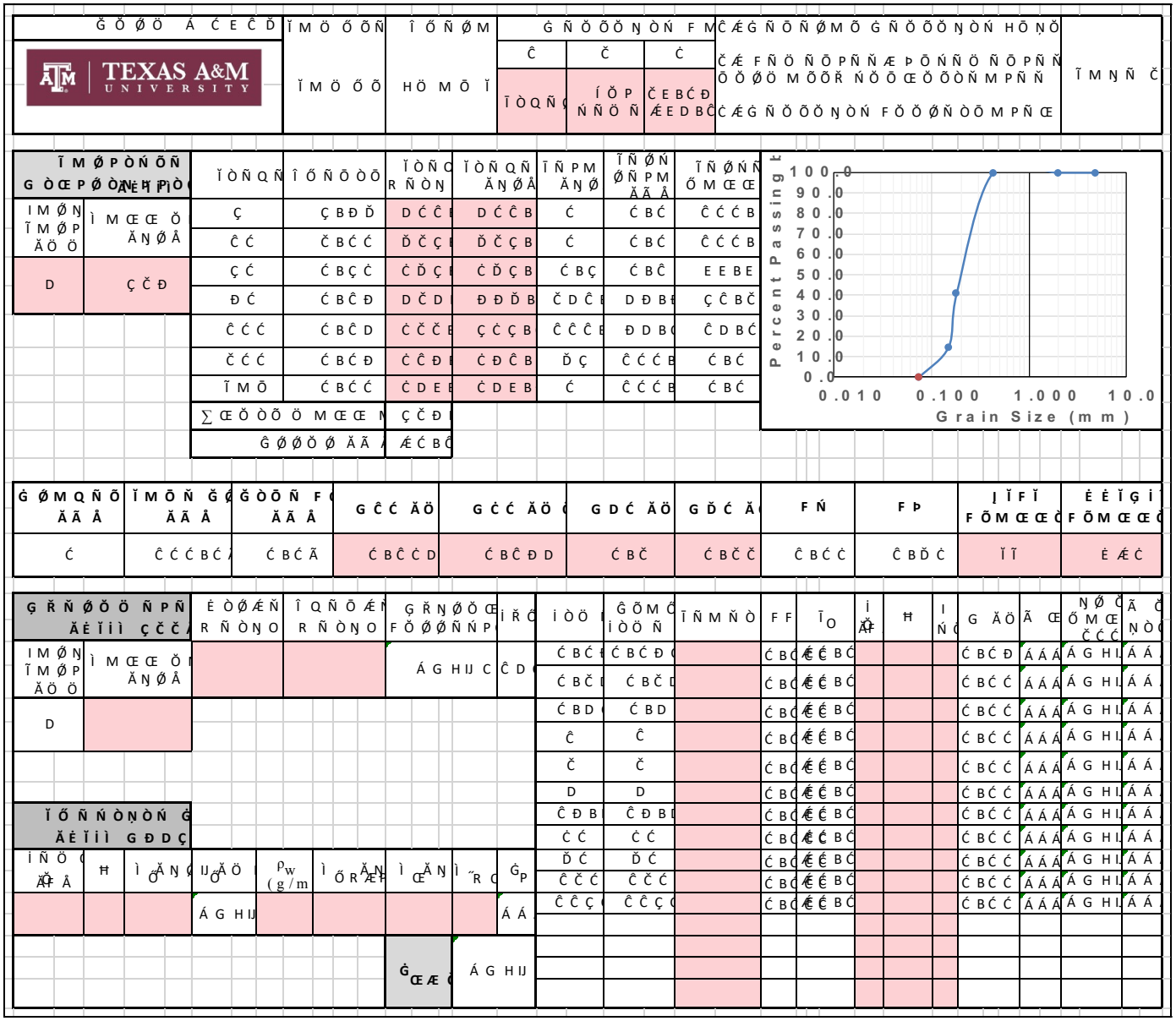

Figure B-76. GEER Sample #6 – Page 2

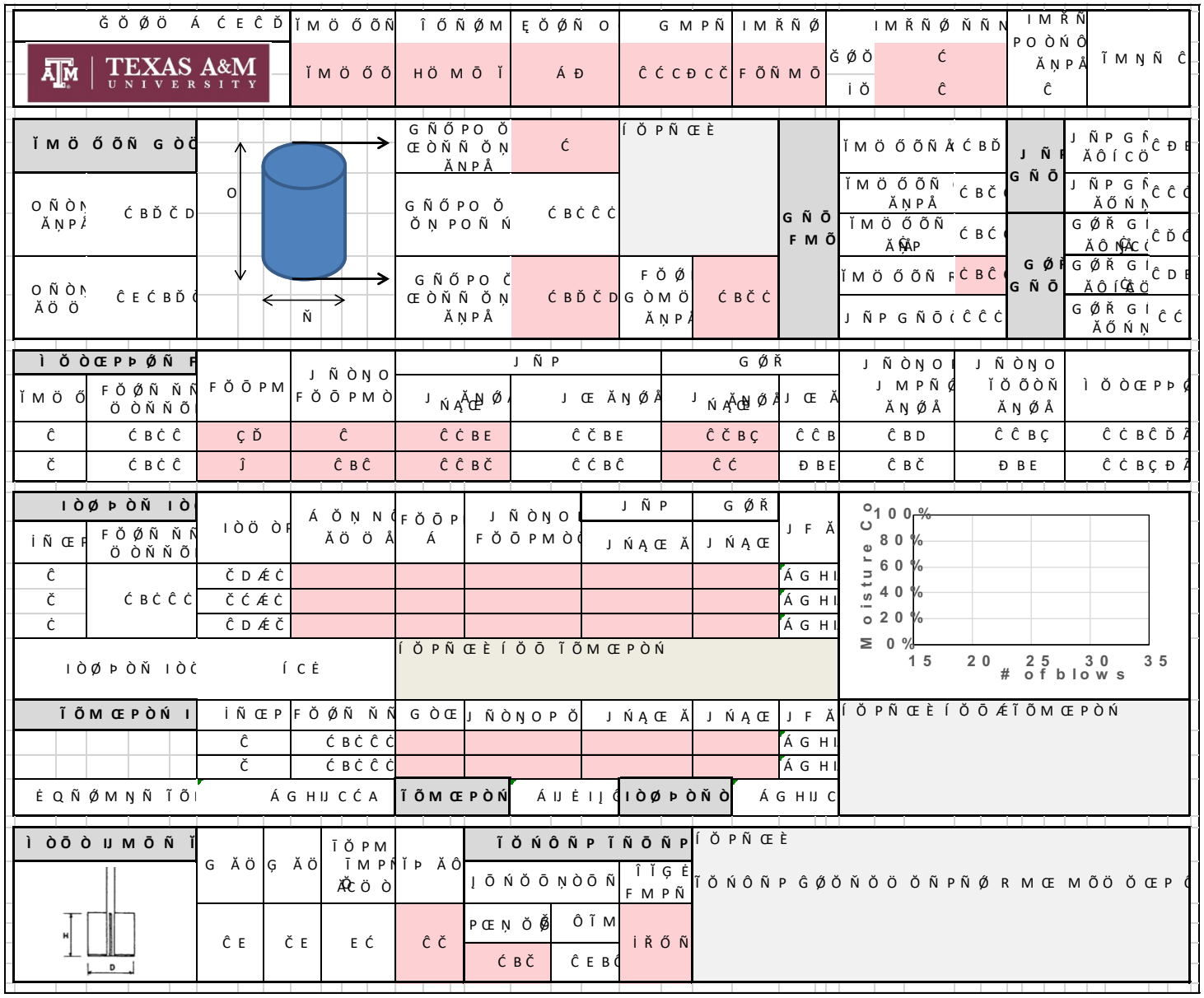

Figure B-77. GEER Sample #7 – Page 1

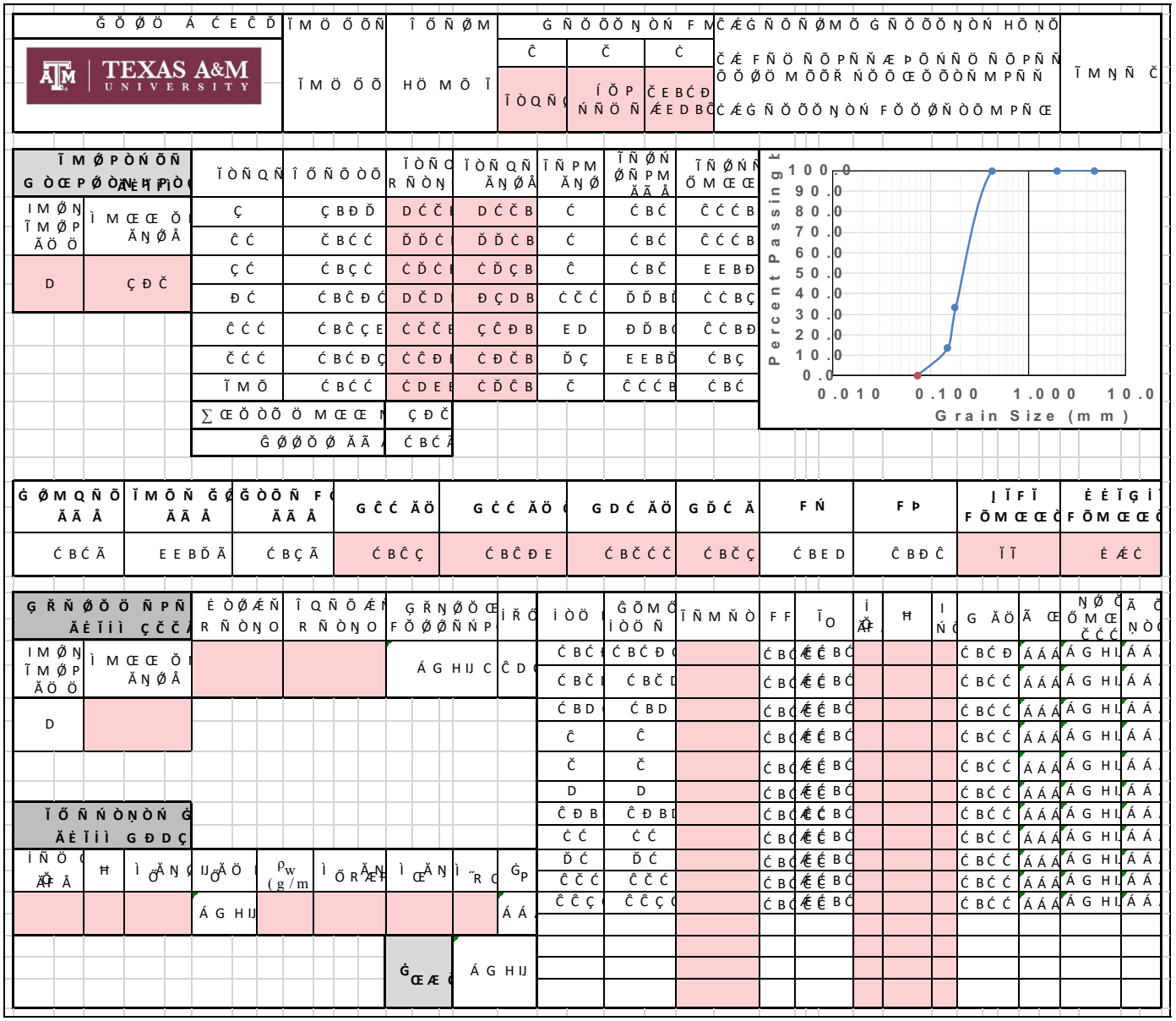

Figure B-78. GEER Sample #7 – Page 2

Gravel Samples - EFA

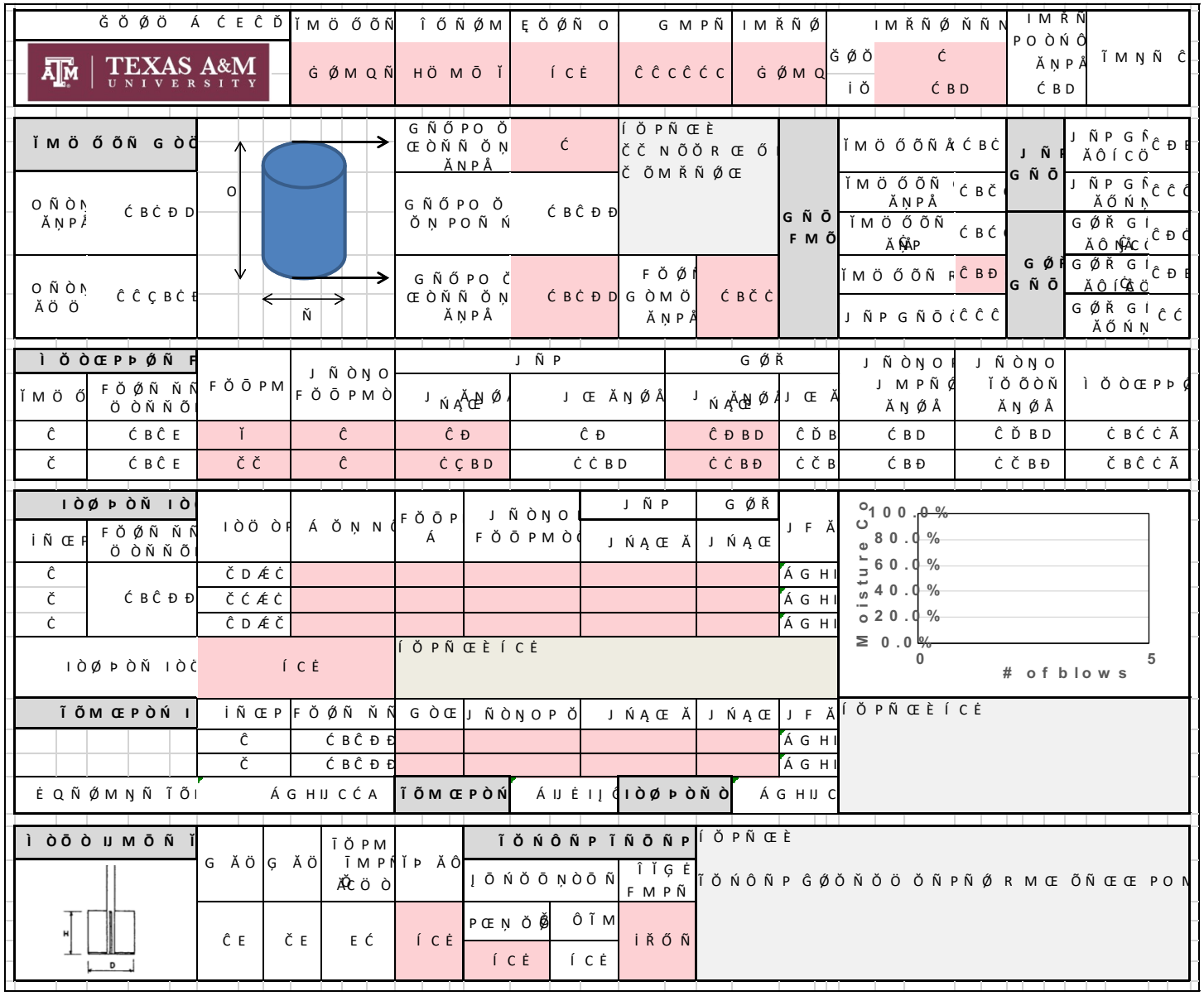

Figure B-79. Gravel #1 – Page 1

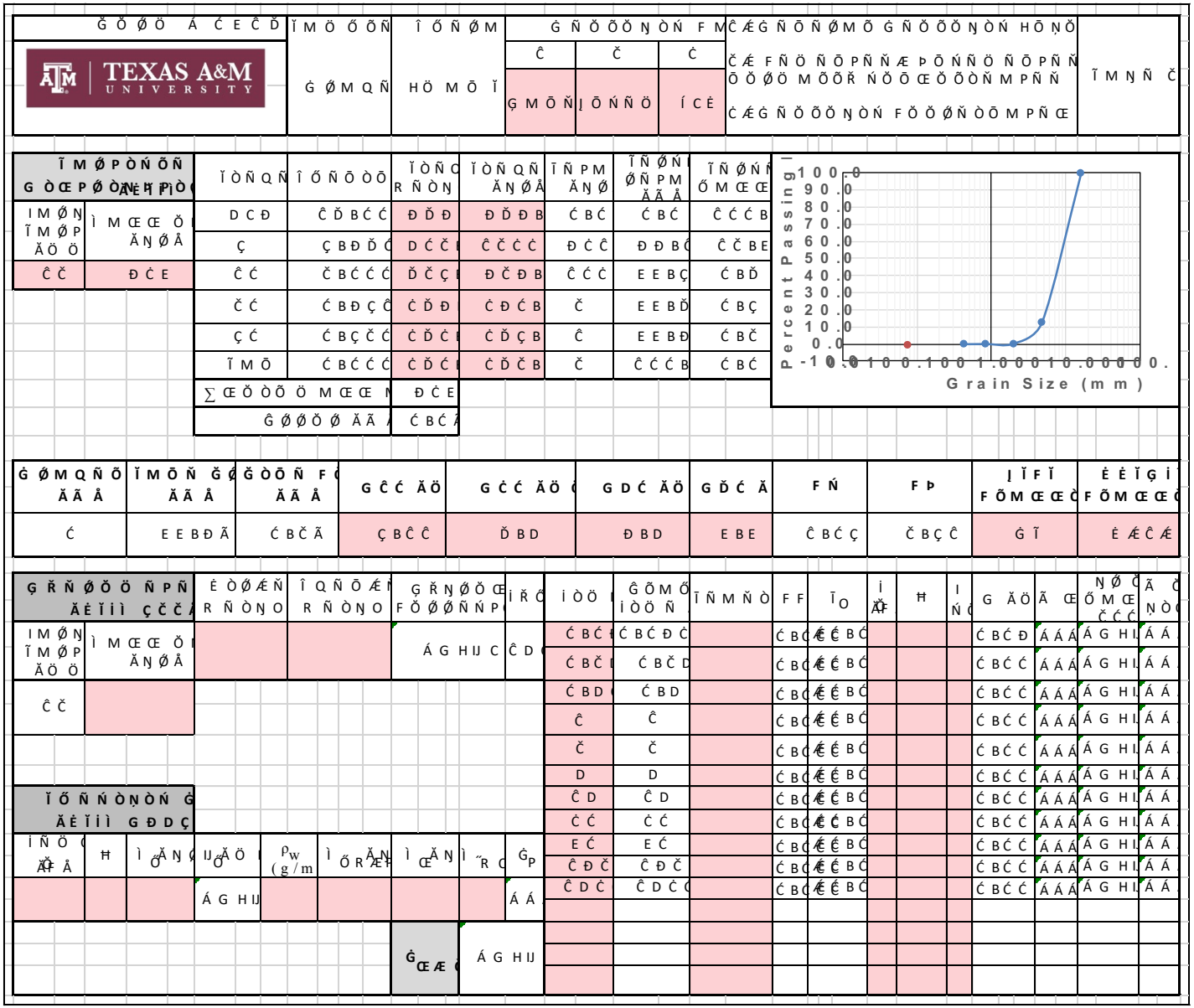

Figure B-80. Gravel #1 – Page 2

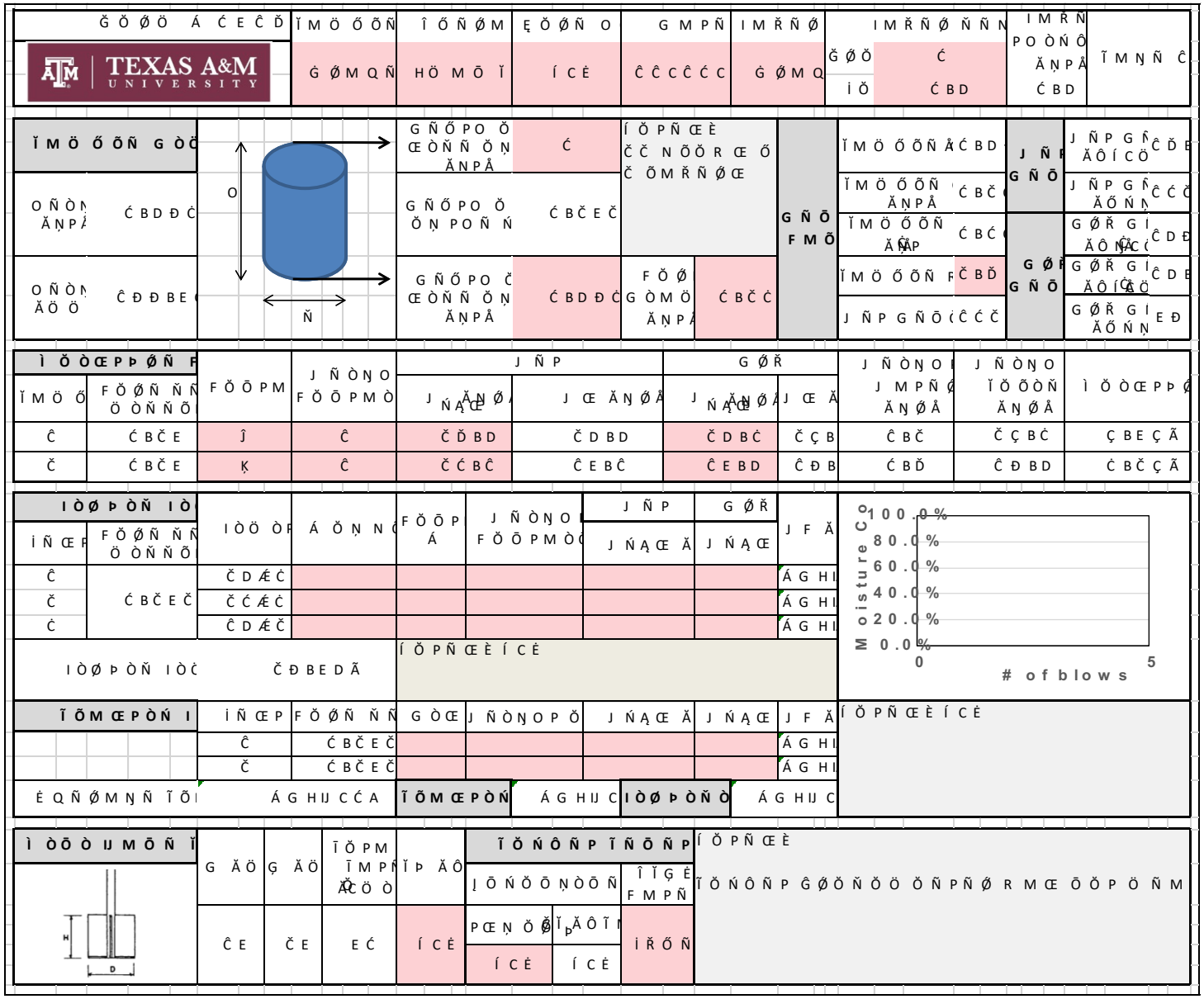

Figure B-81. Gravel #2 – Page 1

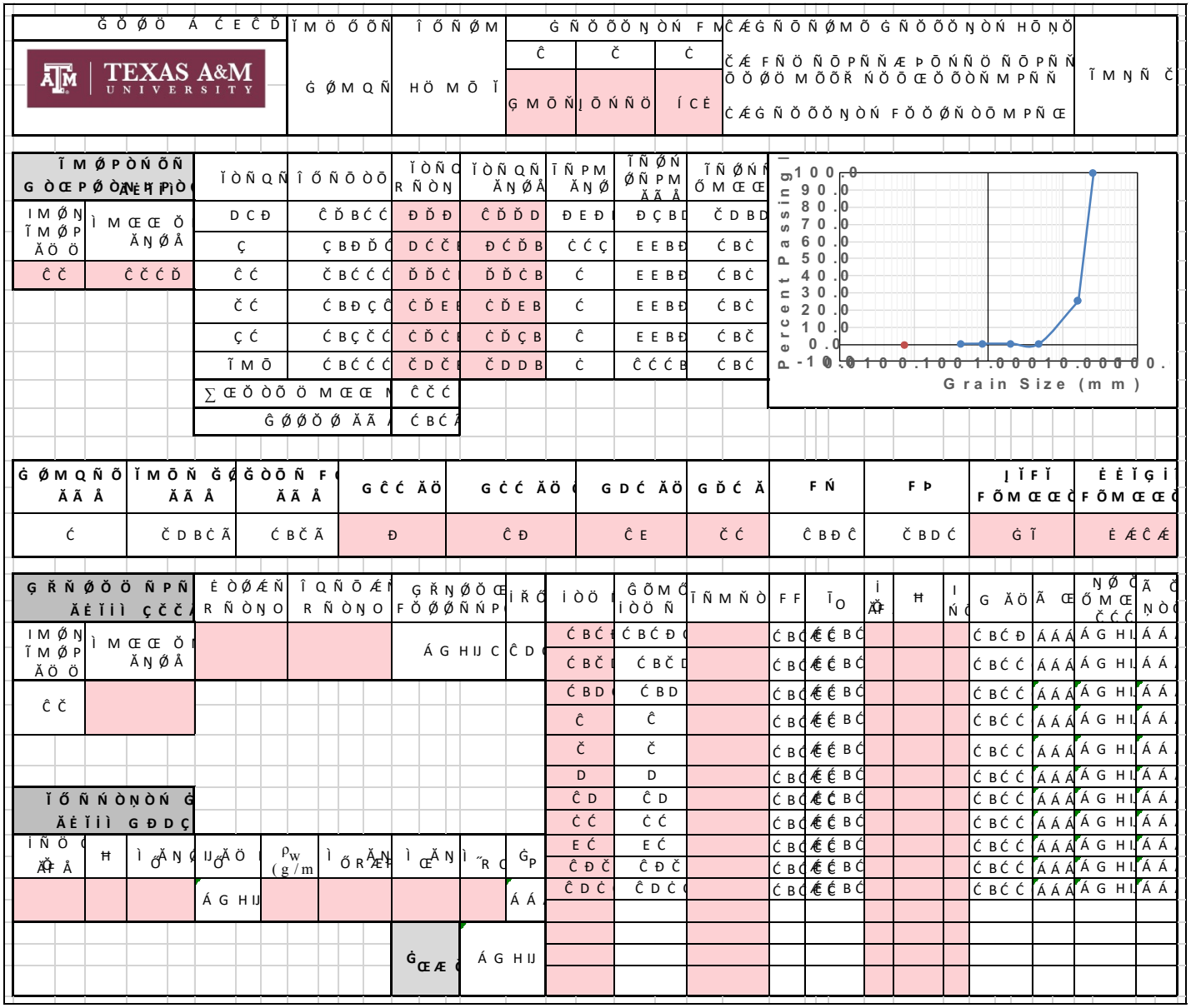

Figure B-82. Gravel #2 – Page 2

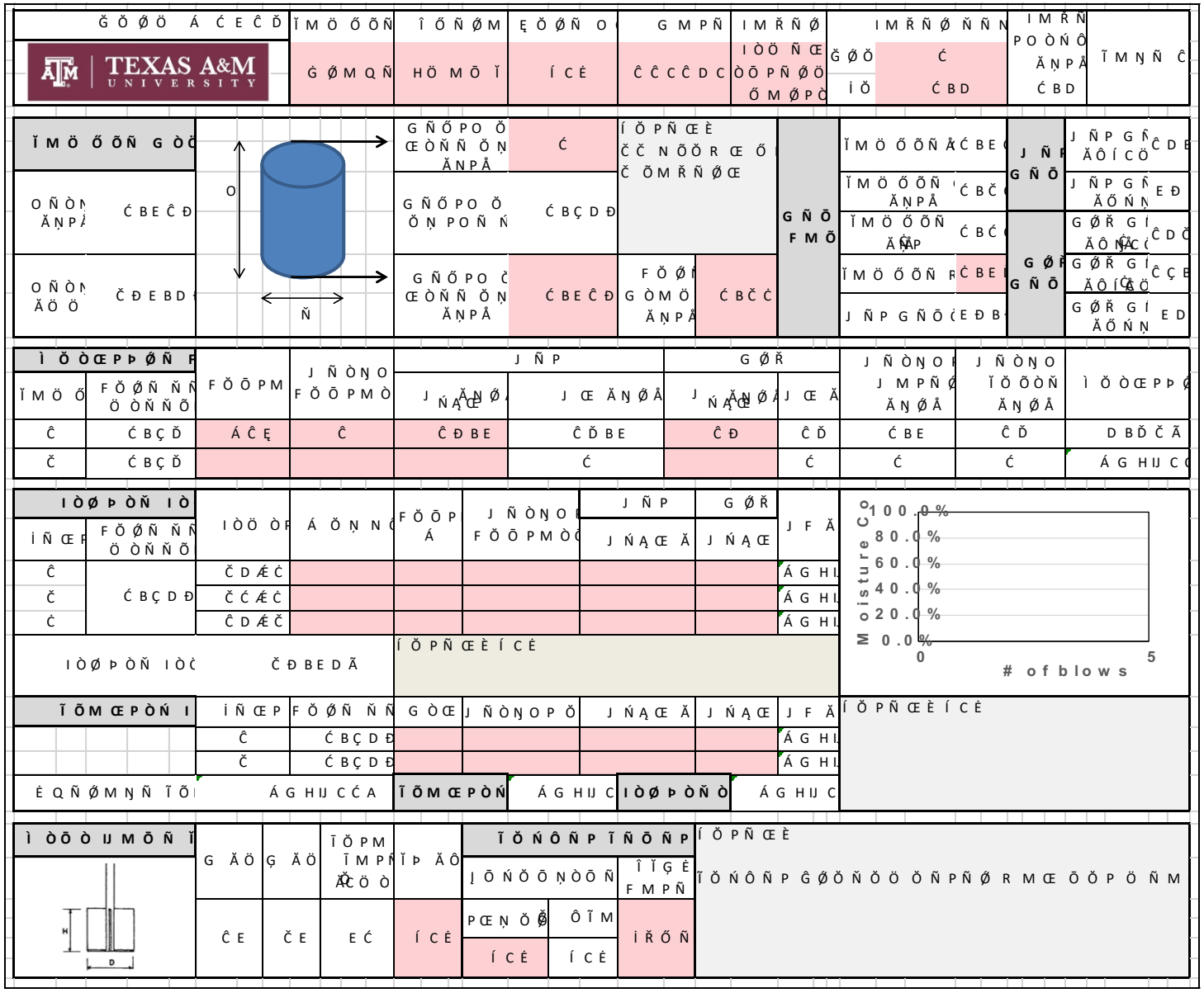

Figure B-83. Gravel #3 – Page 1

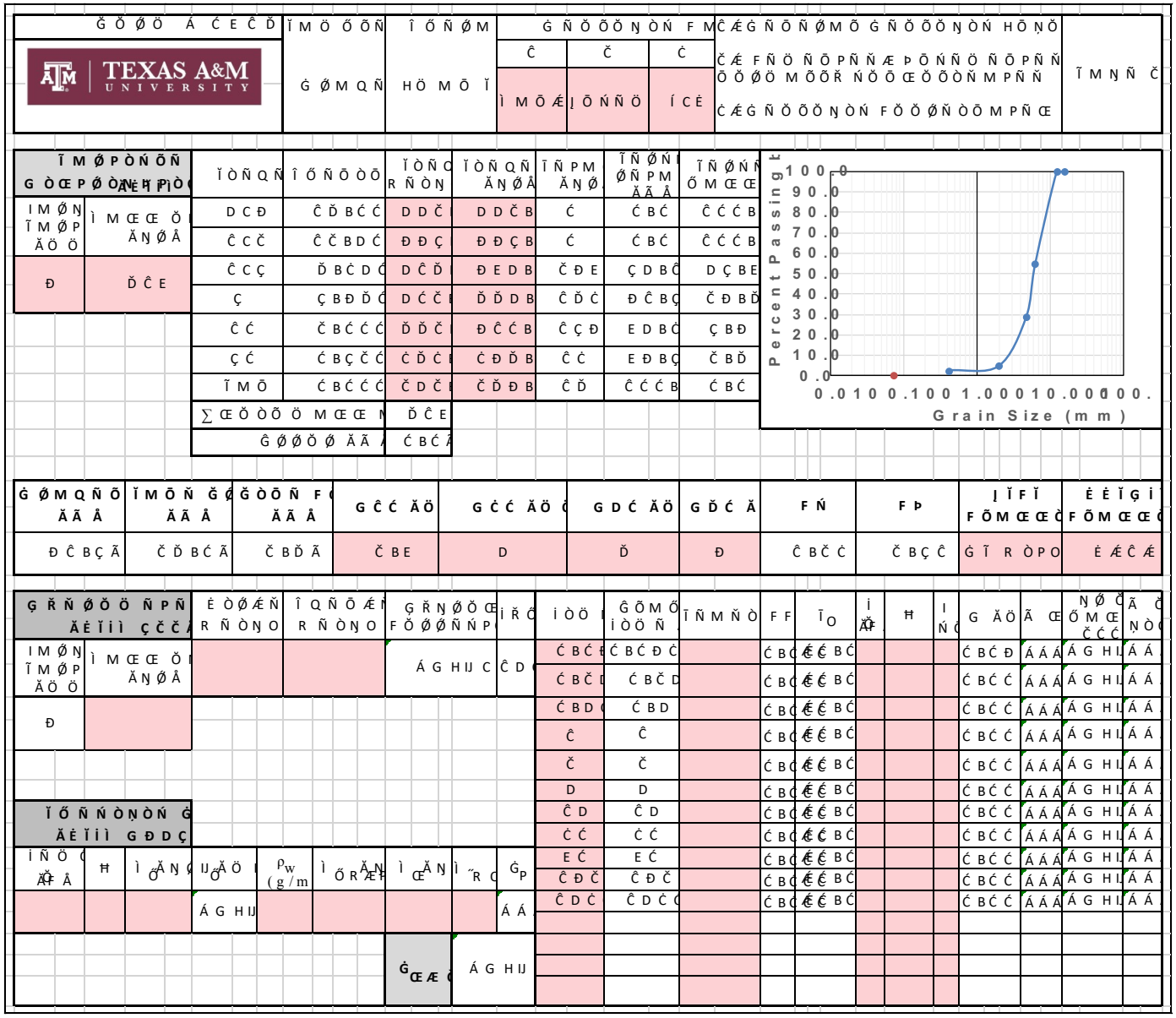

Figure B-84. Gravel #3 – Page 2

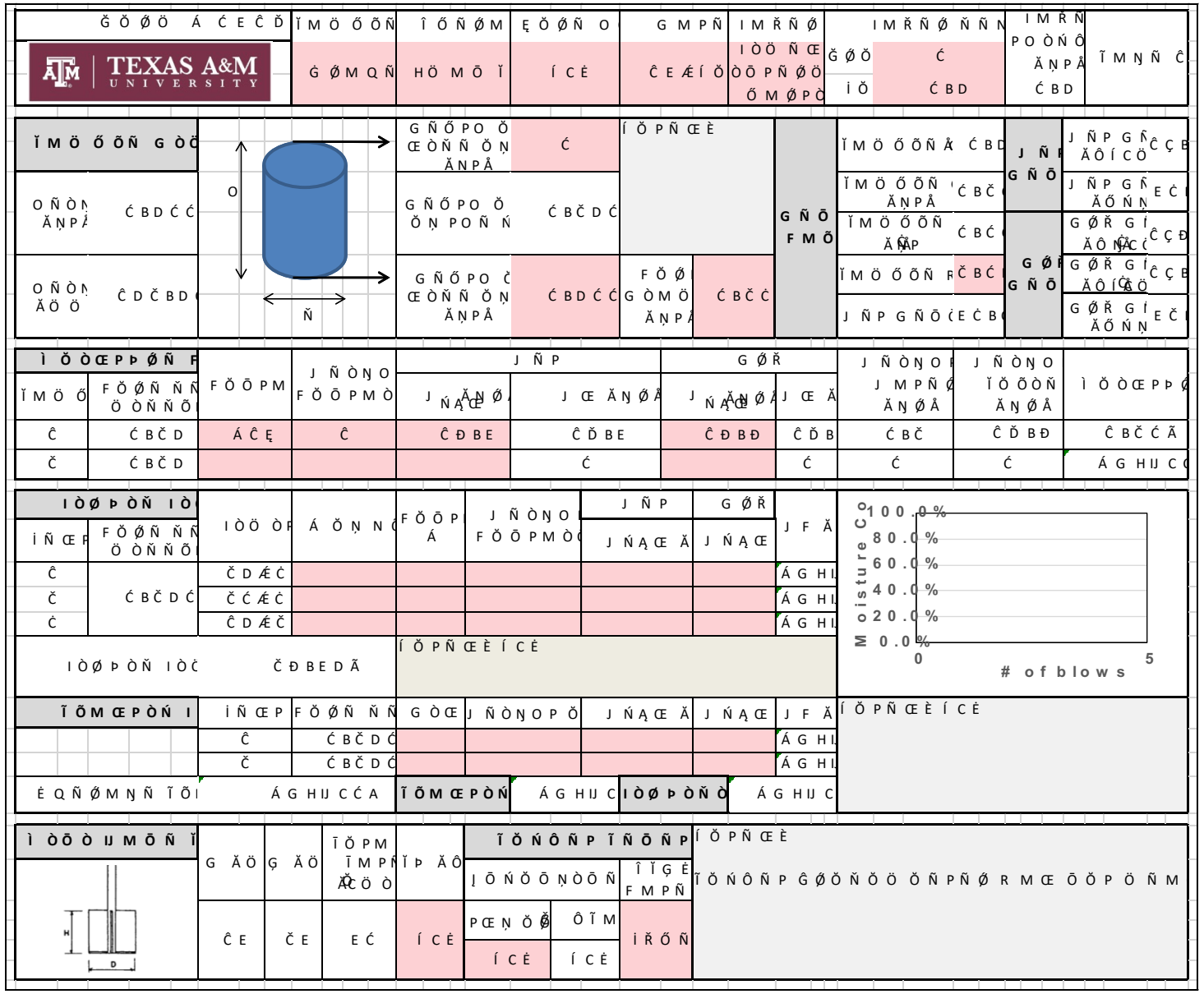

Figure B-85. Gravel #4 – Page 1

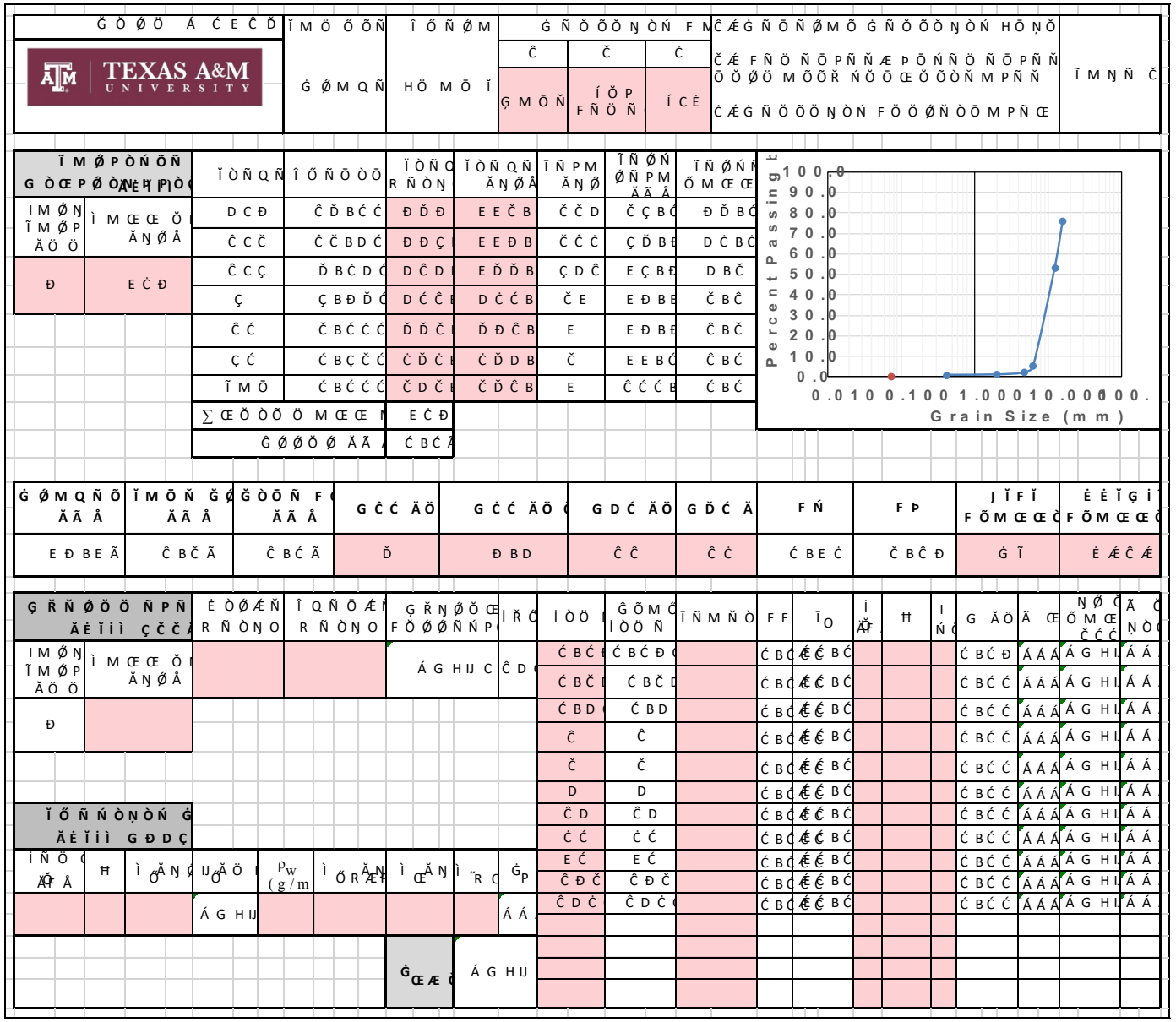

Figure B-86. Gravel #4 – Page 2

Clay Samples - JET

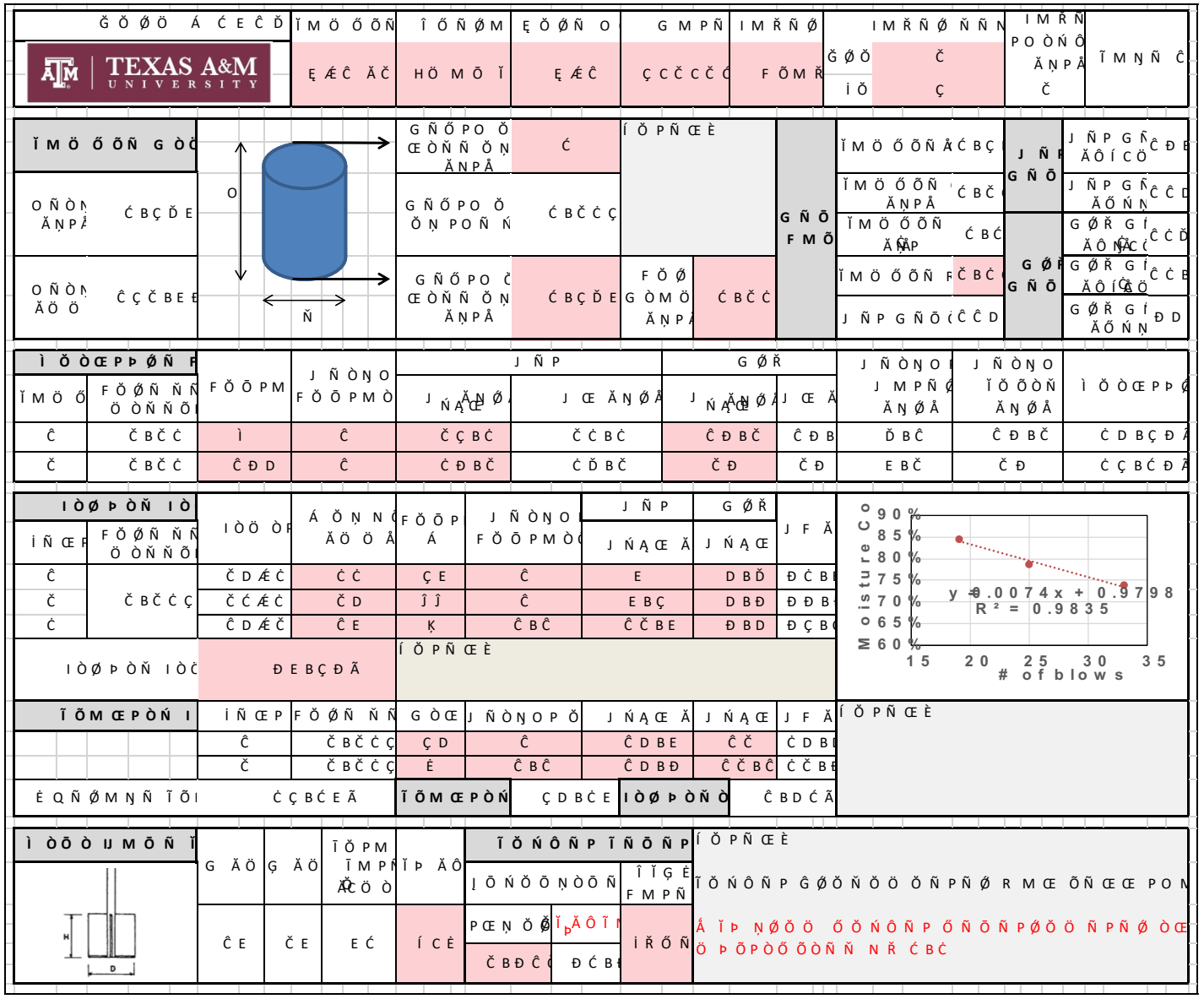

Figure B-87. B-1 (2'-4') Beaumont Formation – Page 1

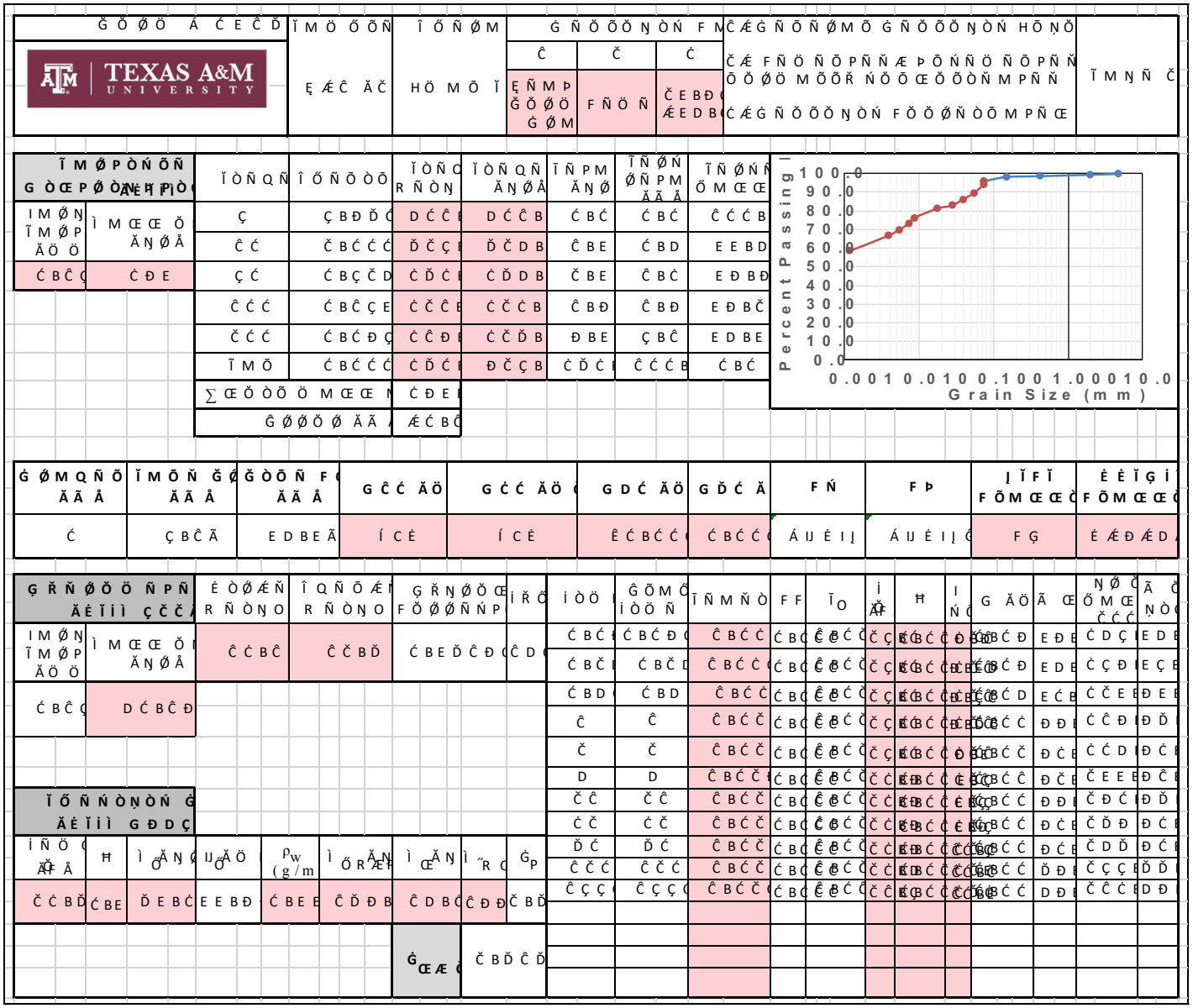

Figure B-88. B-1 (2'-4') Beaumont Formation – Page 2

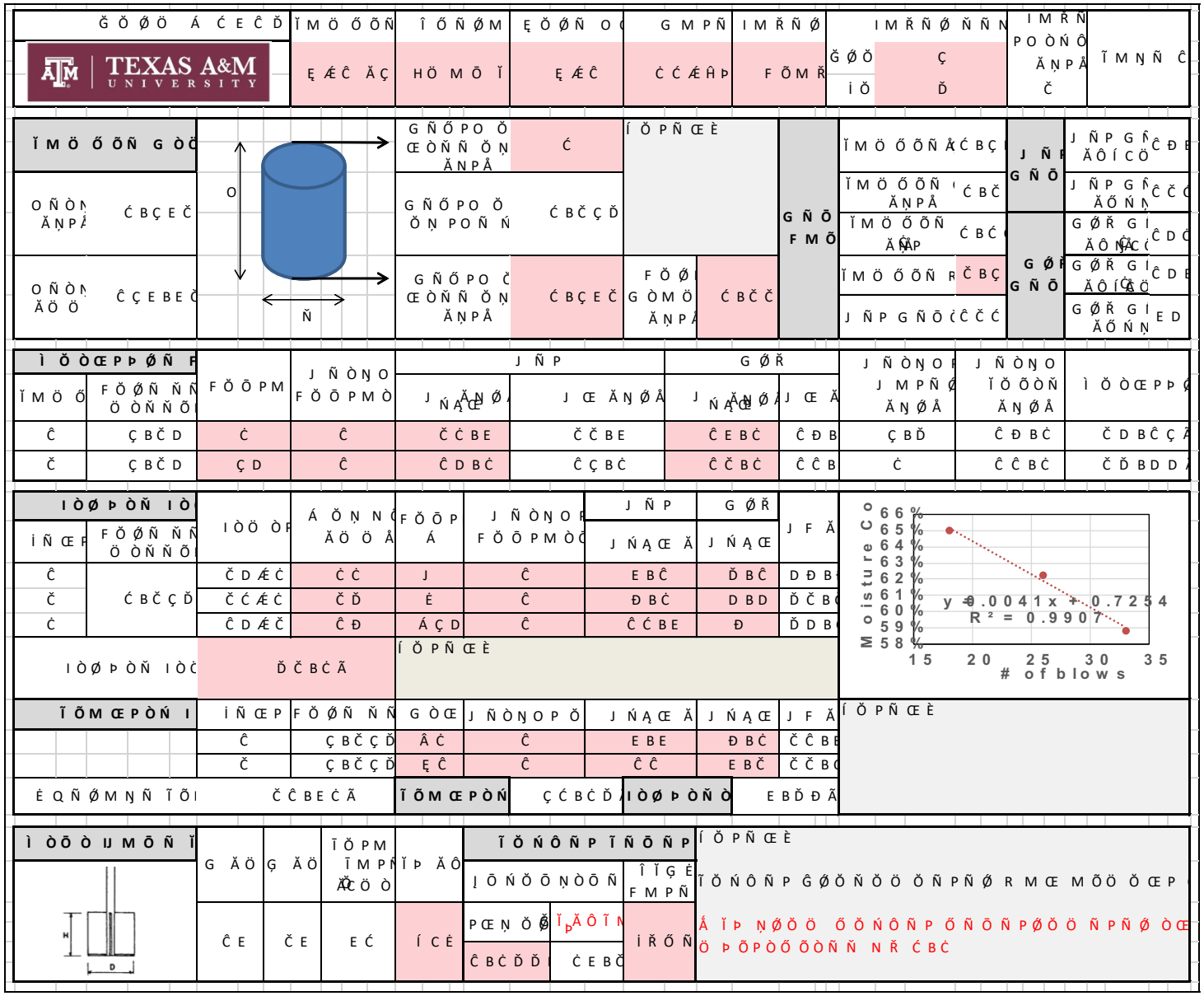

Figure B-89. B-1 (4'-6') Beaumont Formation – Page 1

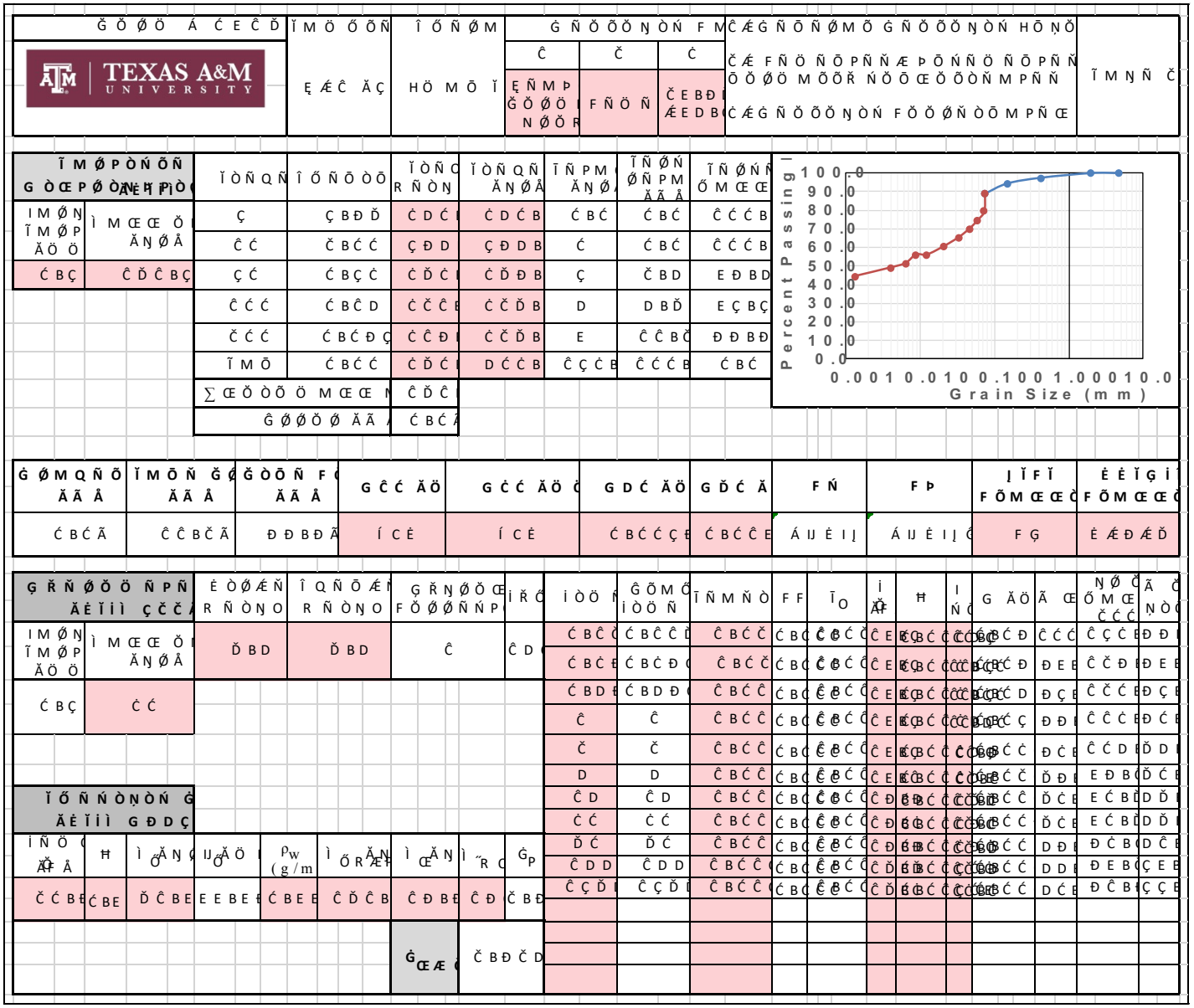

Figure B-90. B-1 (4’-6’) Beaumont Formation – Page 2

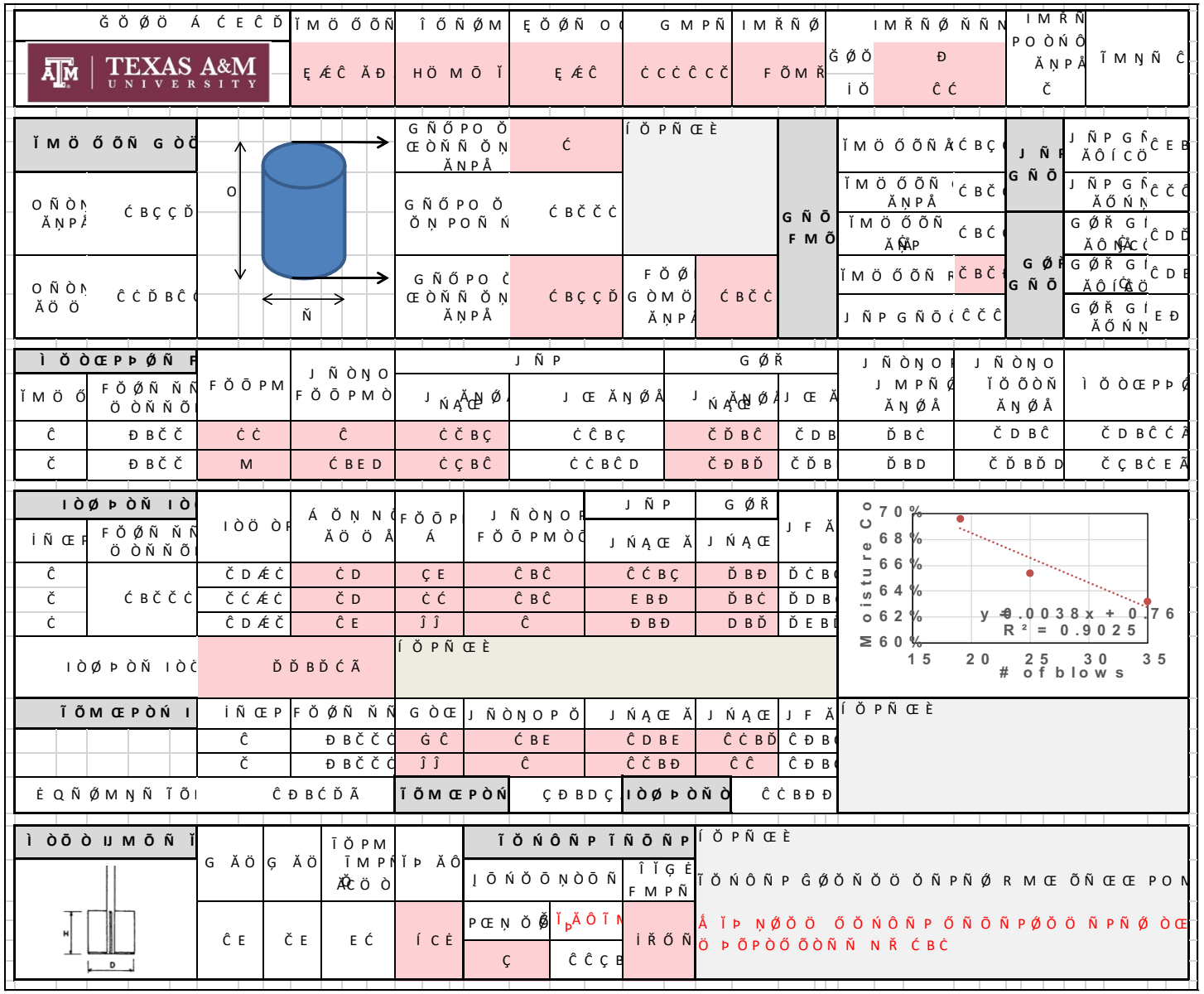

Figure B-91. B-1 (8’-10’) Beaumont Formation – Page 1

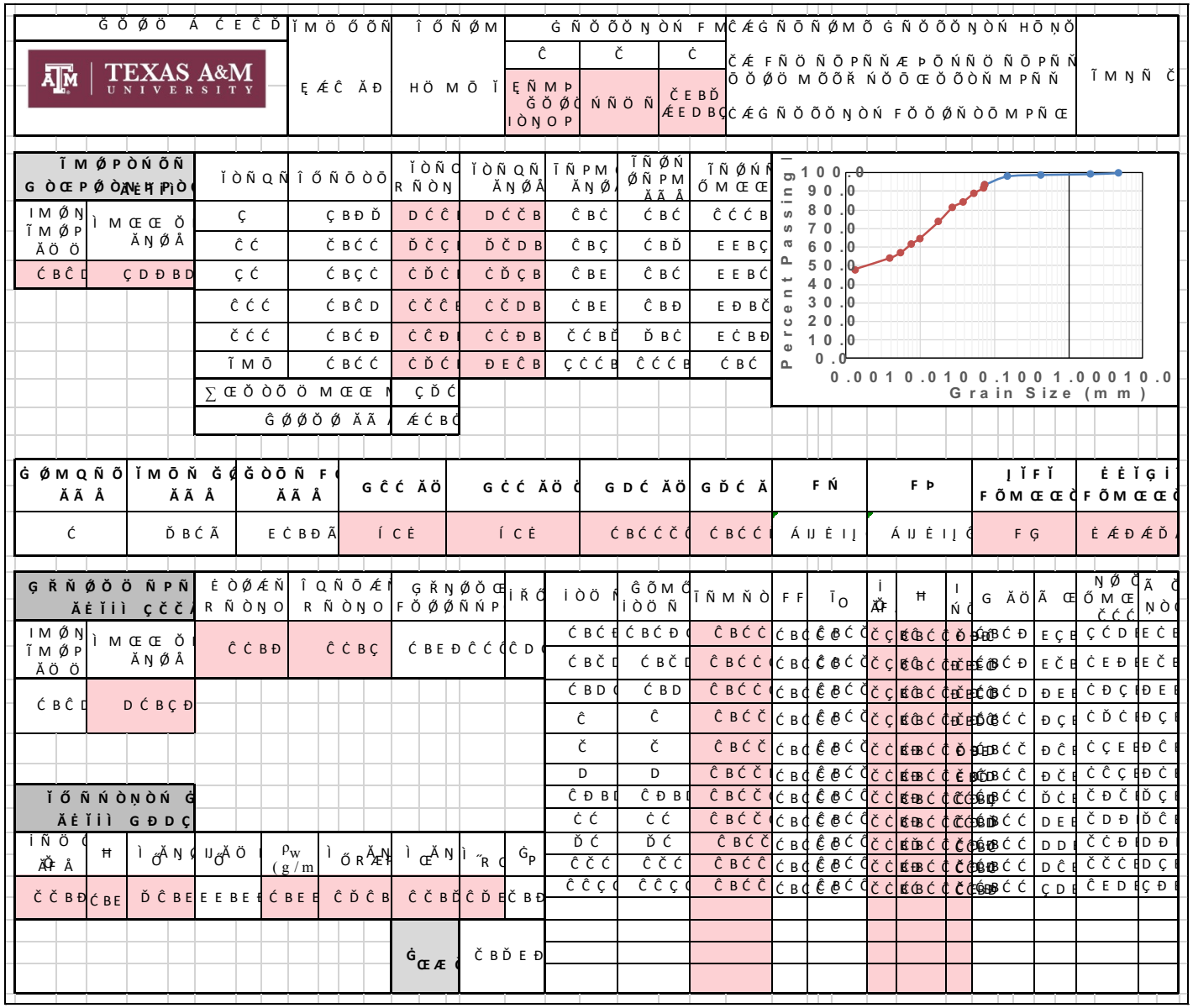

Figure B-92. B-1 (8’-10’) Beaumont Formation – Page 2

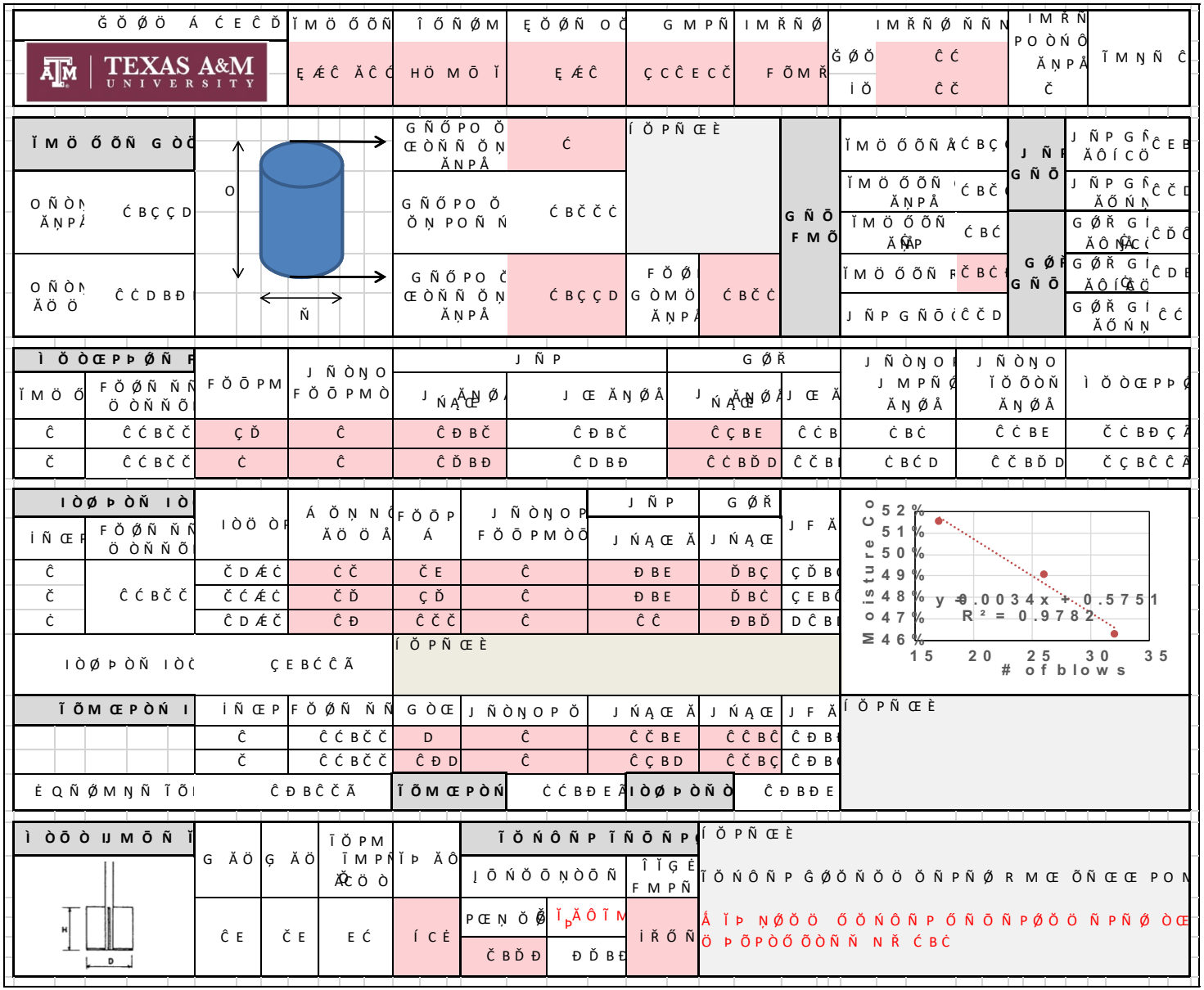

Figure B-93. B-1 (10’-12’) Beaumont Formation – Page 1

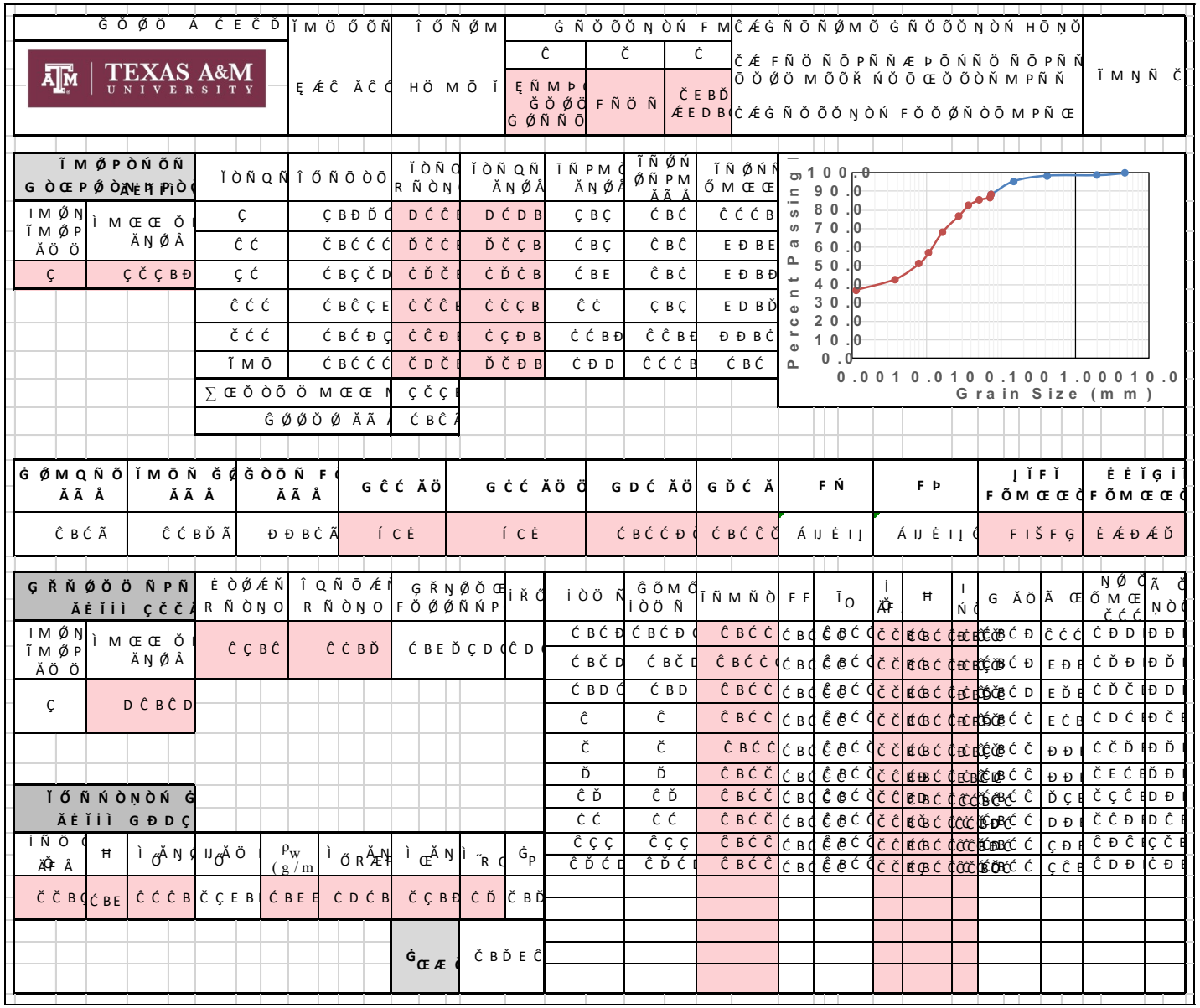

Figure B-94. B-1 (10’-12’) Beaumont Formation – Page 2

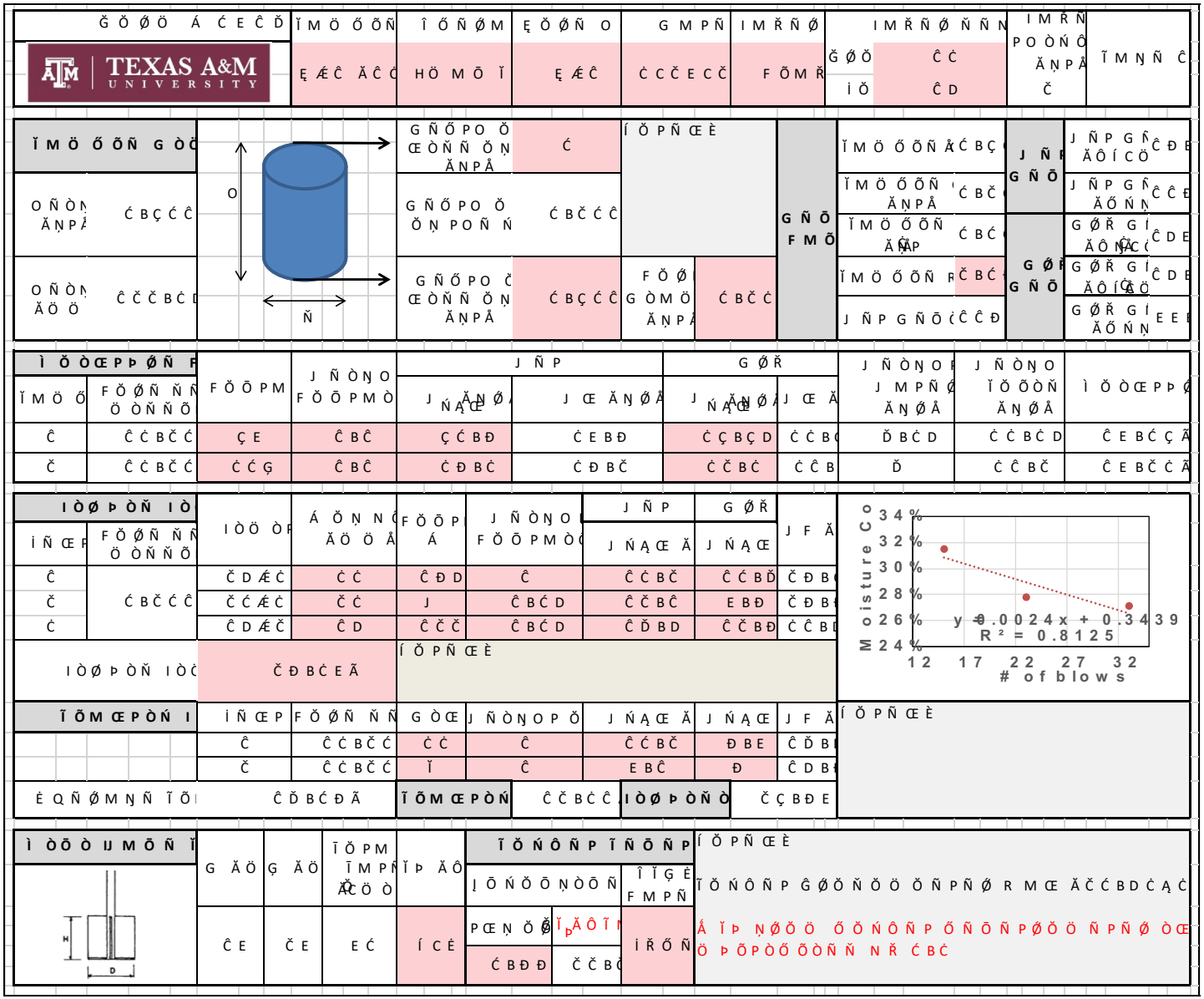

Figure B-95. B-1 (13'-15') Beaumont Formation – Page 1

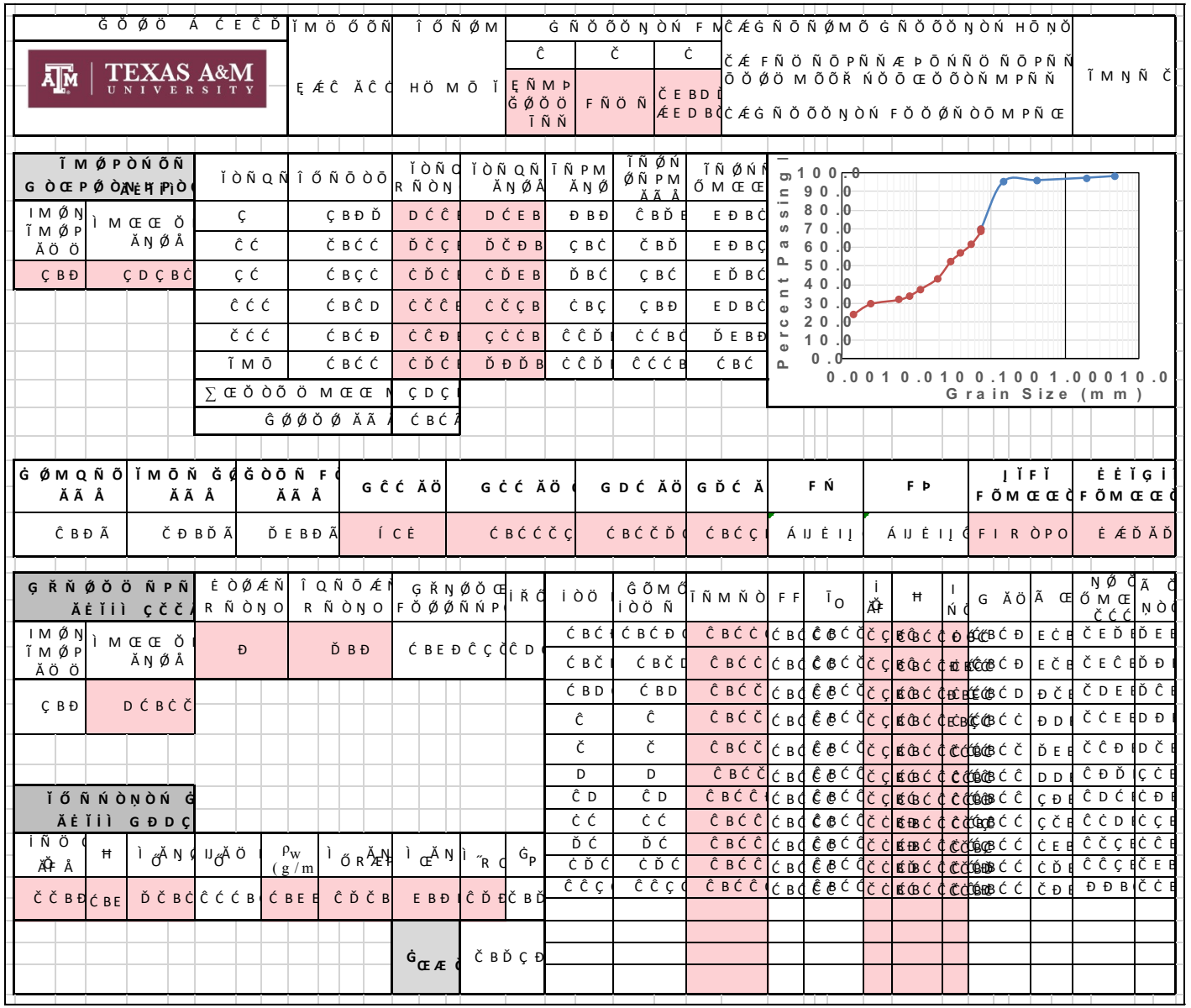

Figure B-96. B-1 (13'-15') Beaumont Formation – Page 2

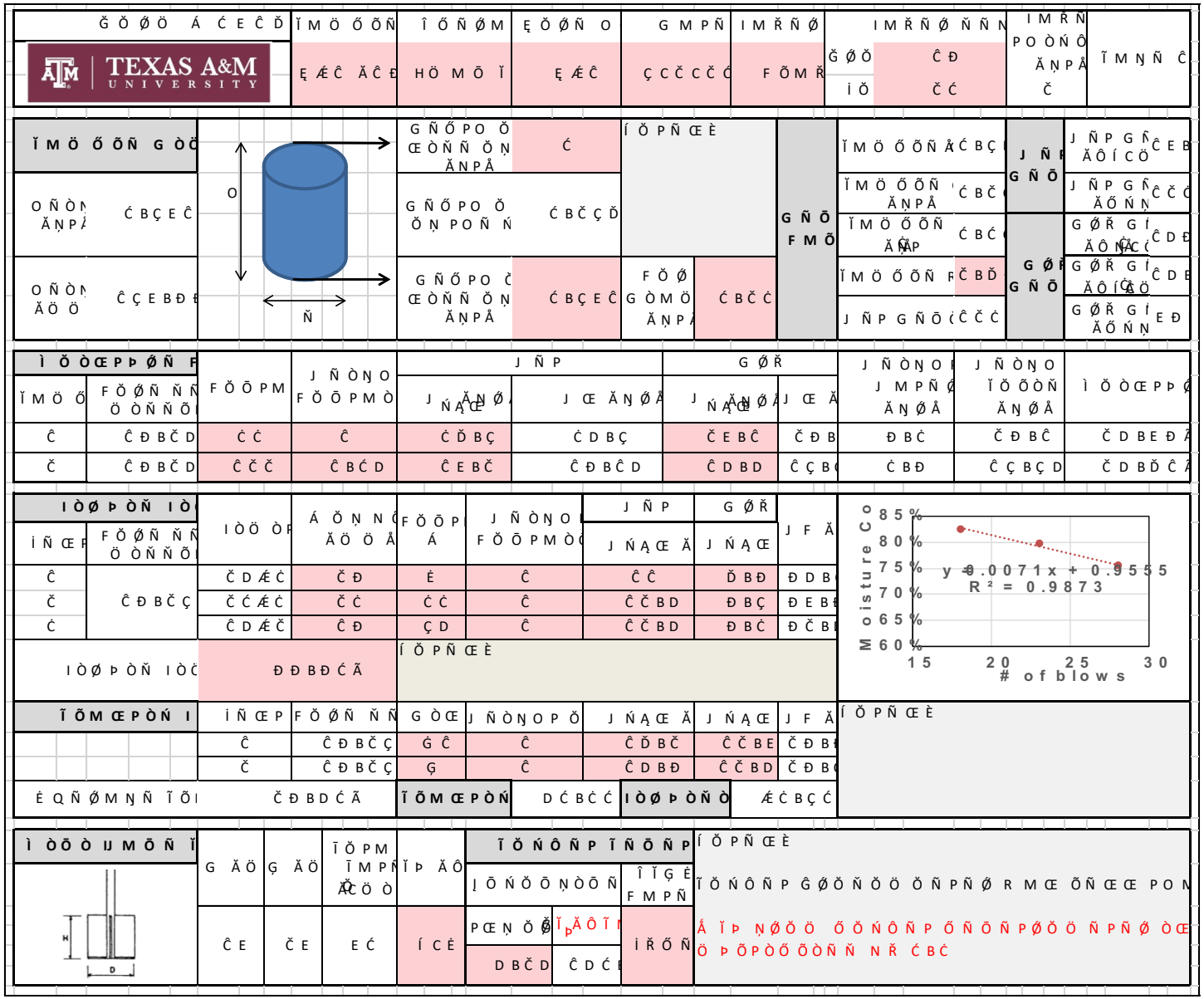

Figure B-97. B-1 (18'-20') Beaumont Formation – Page 1

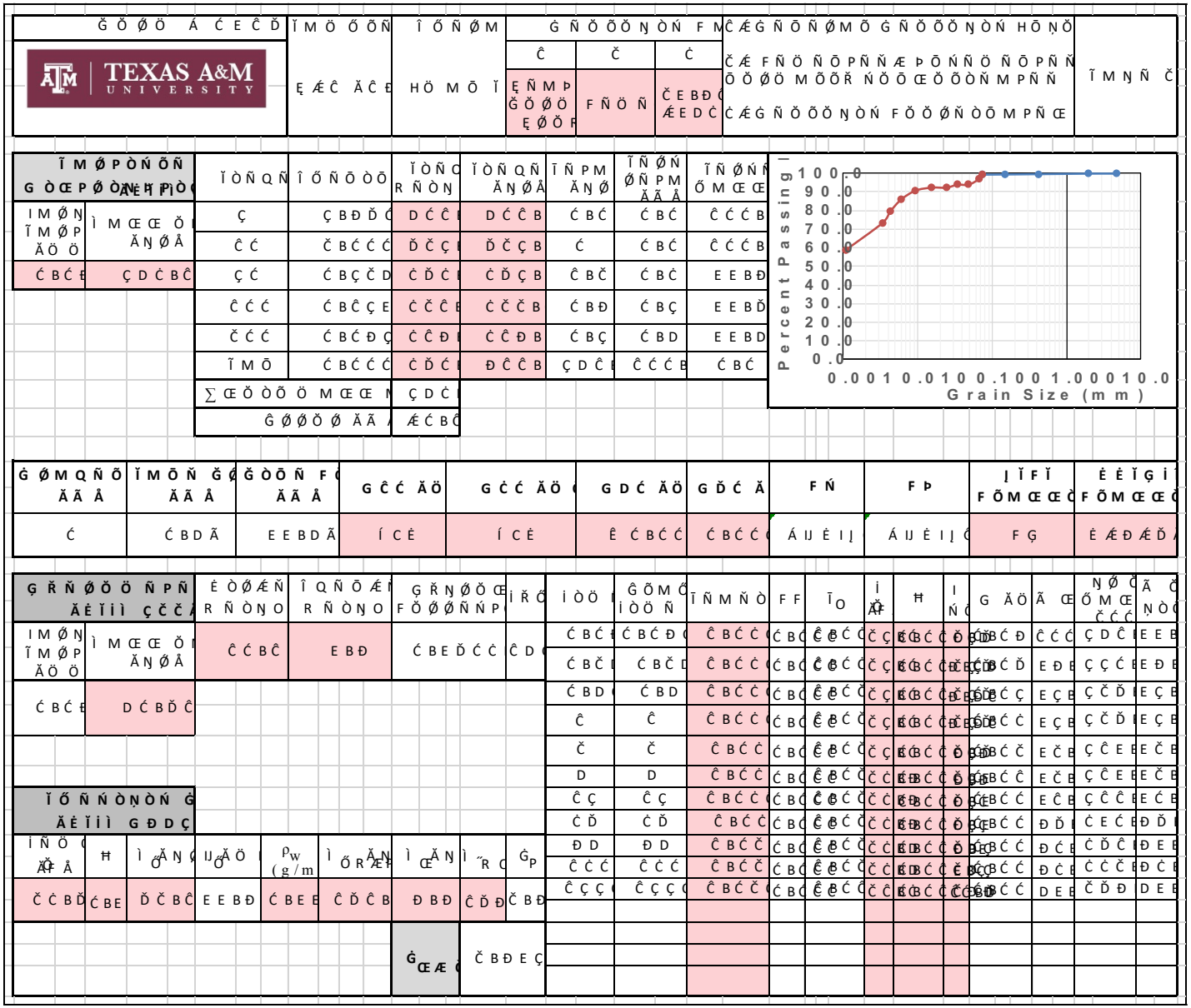

Figure B-98. B-1 (18’-20’) Beaumont Formation – Page 2

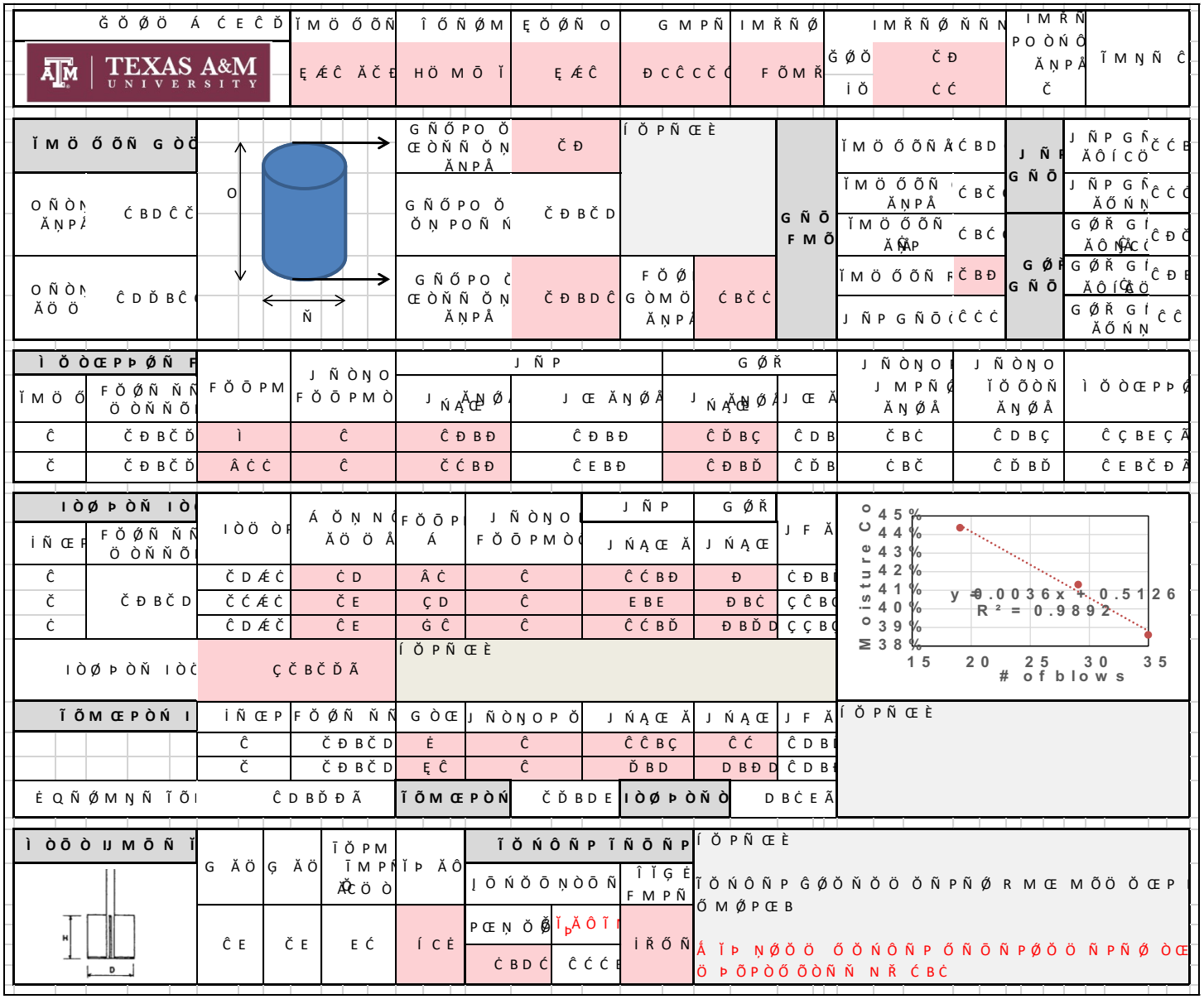

Figure B-99. B-1 (28’-30’) Beaumont Formation – Page 1

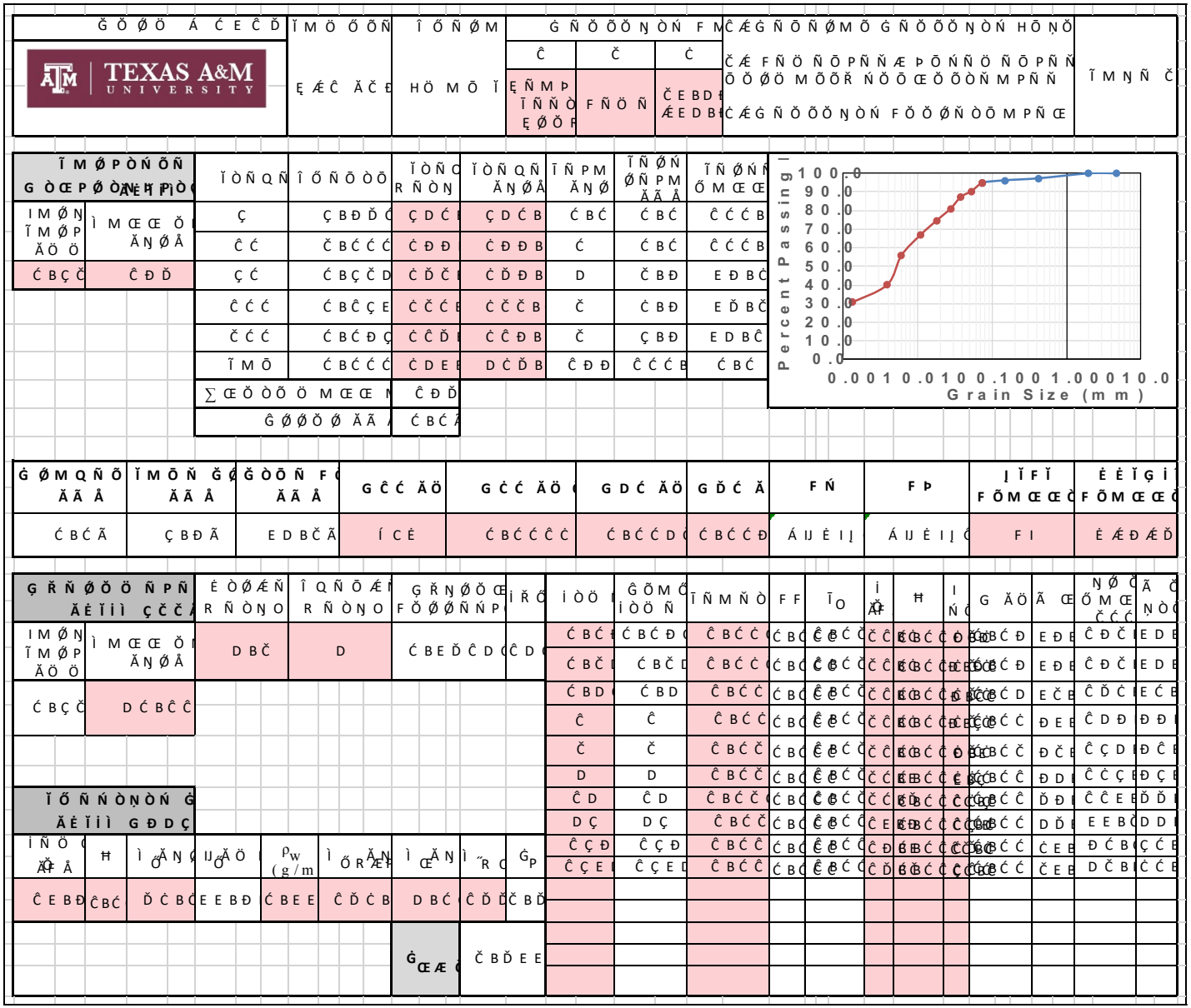

Figure B-100. B-1 (28’-30’) Beaumont Formation – Page 2

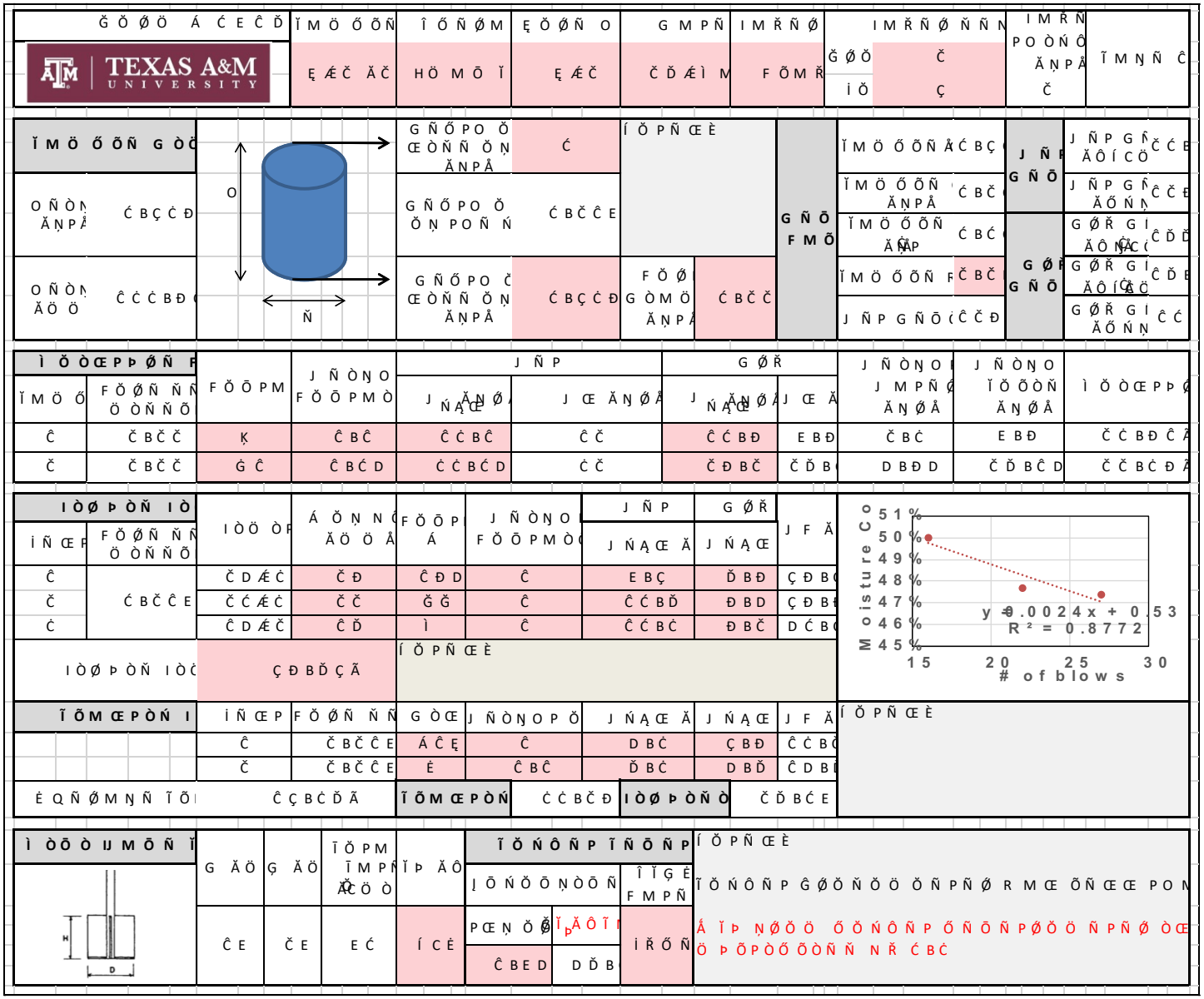

Figure B-101. B-2 (2'-4') Beaumont Formation – Page 1

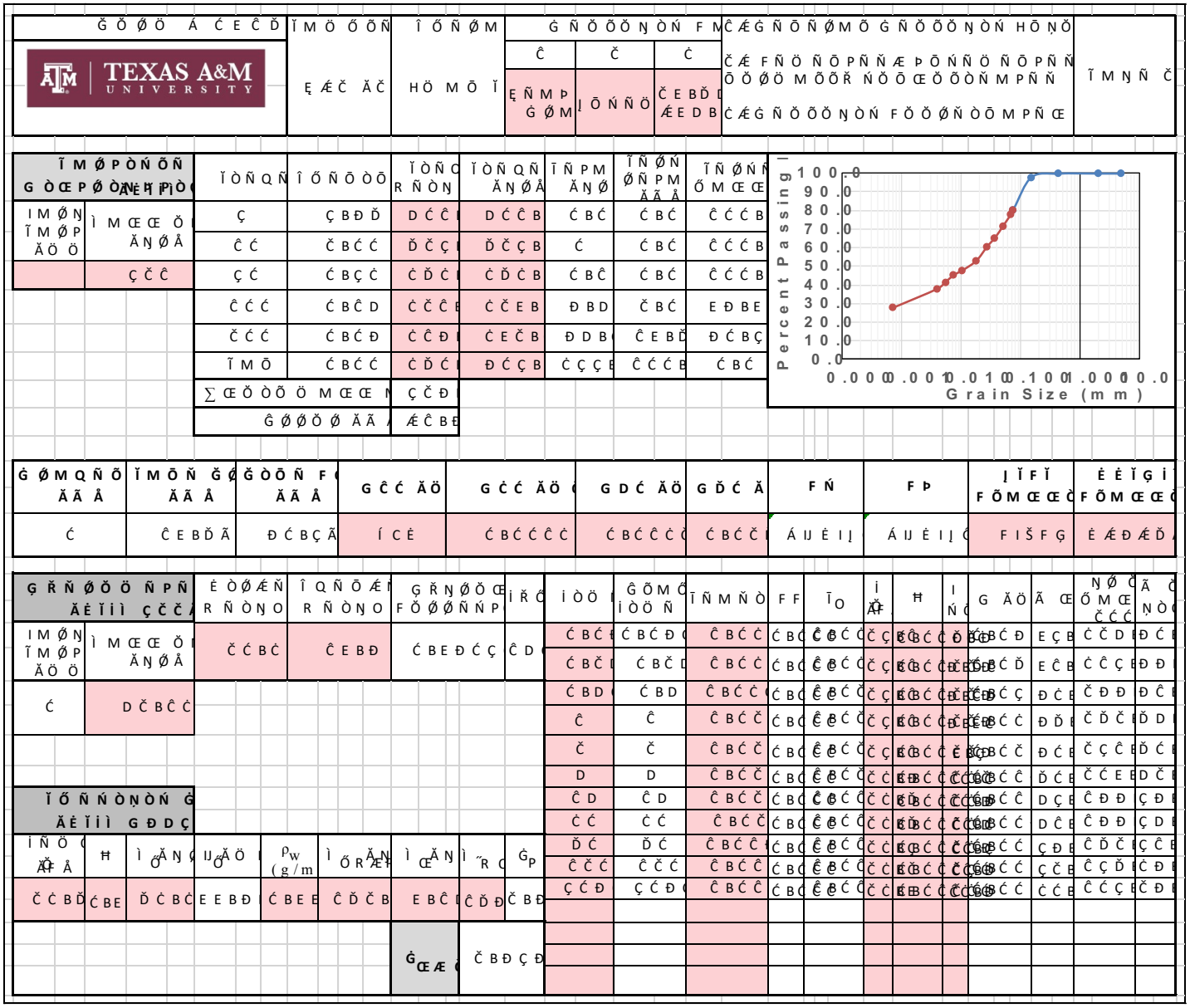

Figure B-102. B-2 (2'-4') Beaumont Formation – Page 2

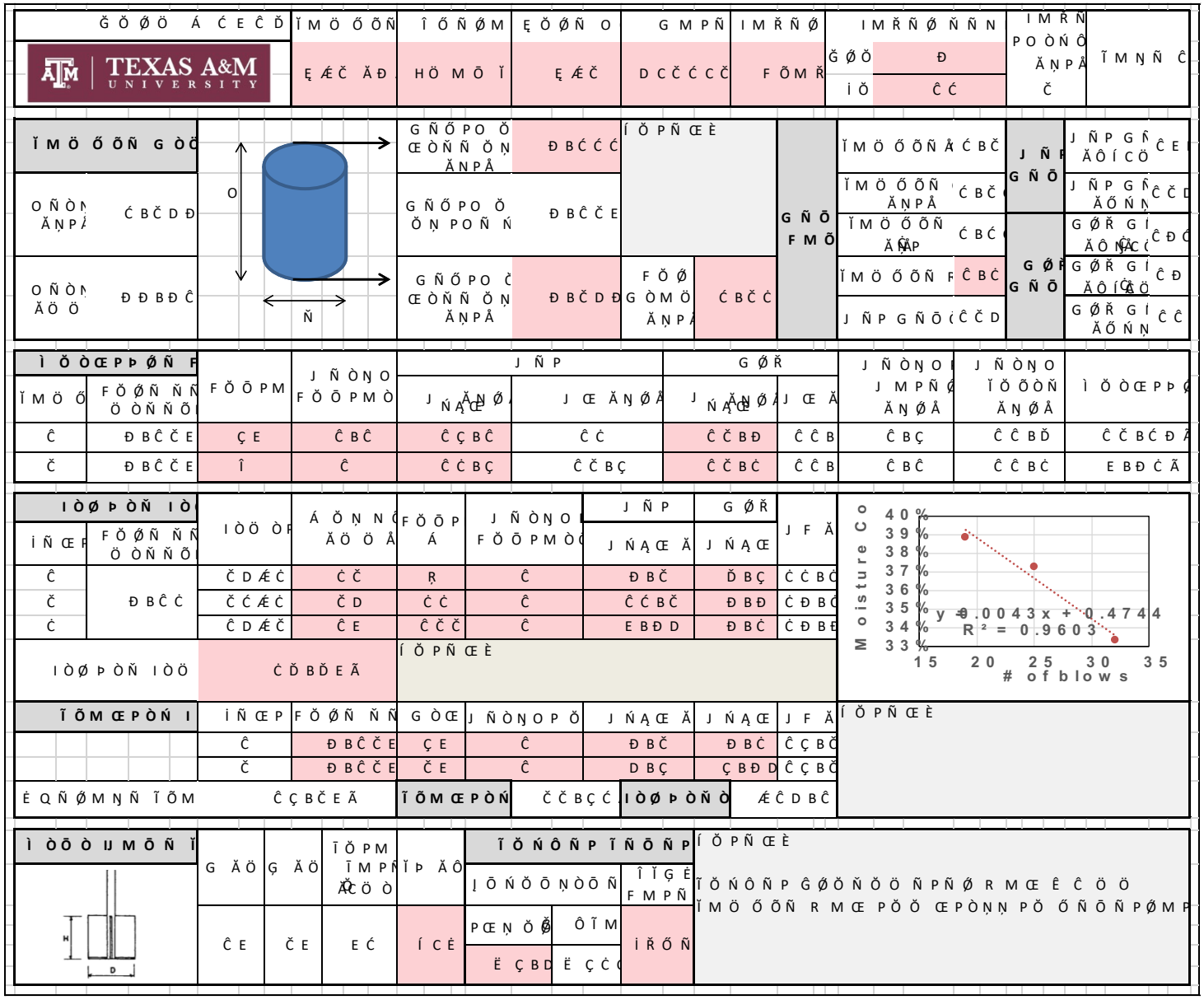

Figure B-103. B-2 (8'-10') Lissie Formation – Page 1

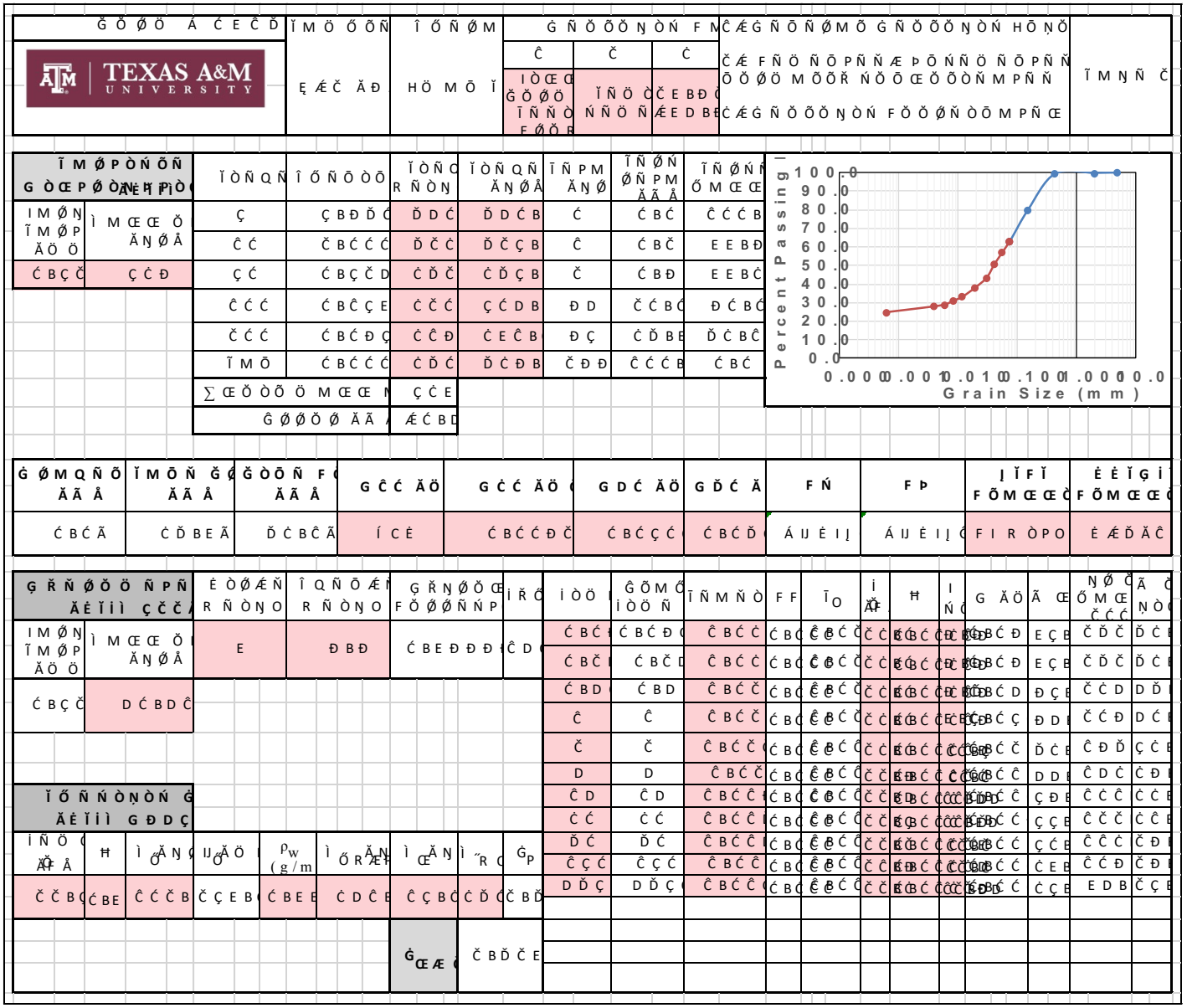

Figure B-104. B-2 (8’-10’) Lissie Formation – Page 2

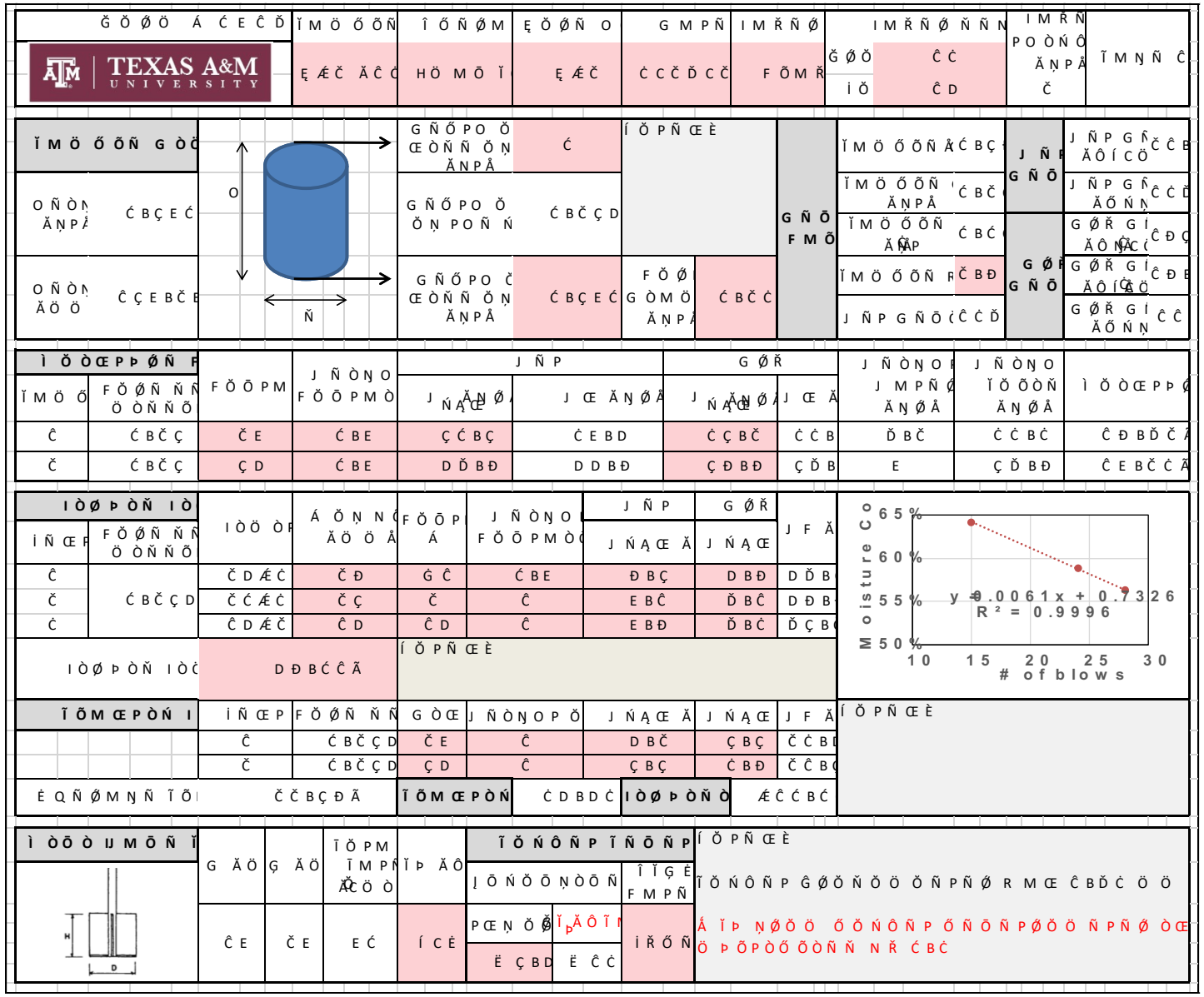

Figure B-105. B-2 (13'-15') Beaumont Formation – Page 1

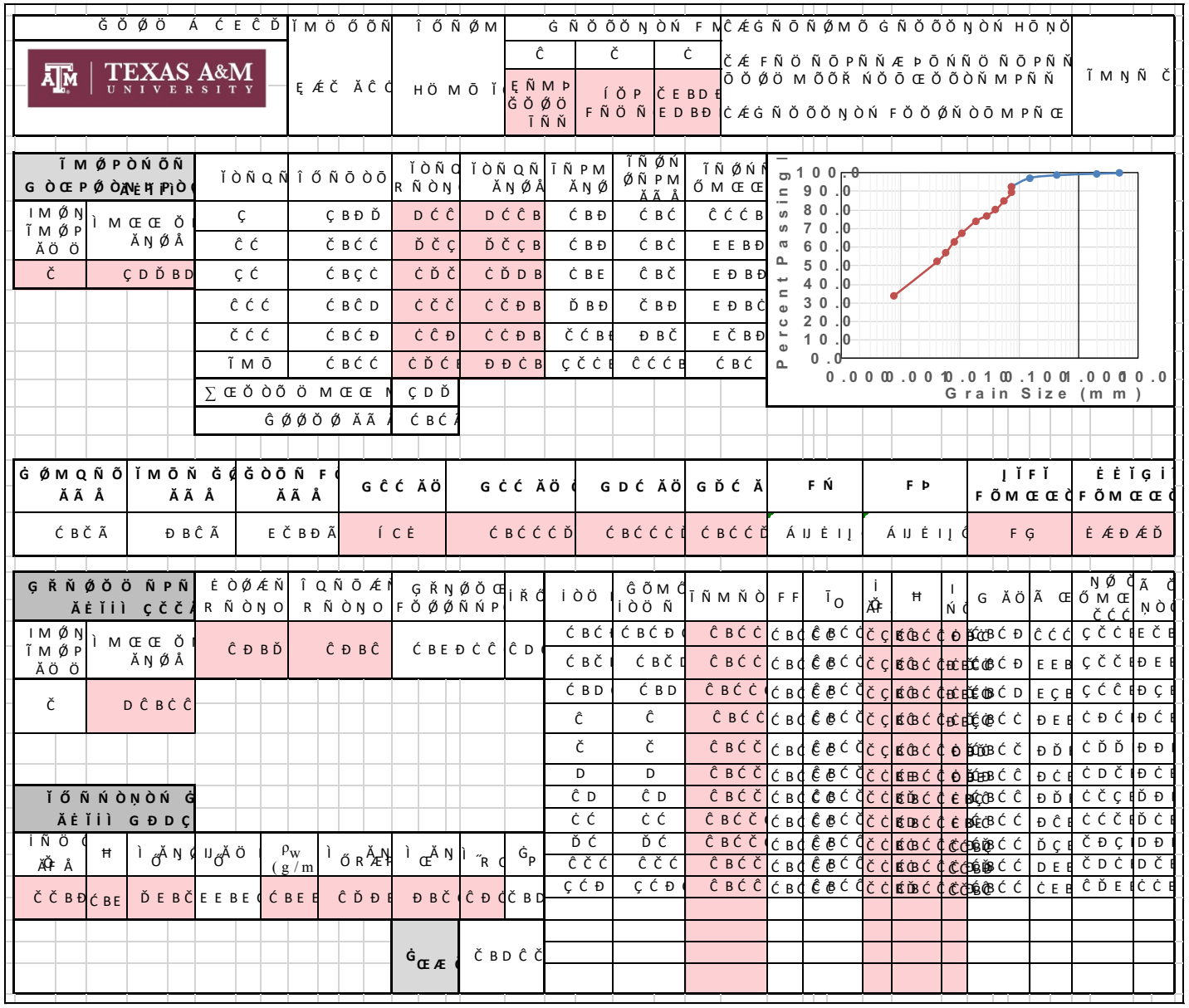

Figure B-106. B-2 (13'-15') Beaumont Formation – Page 2

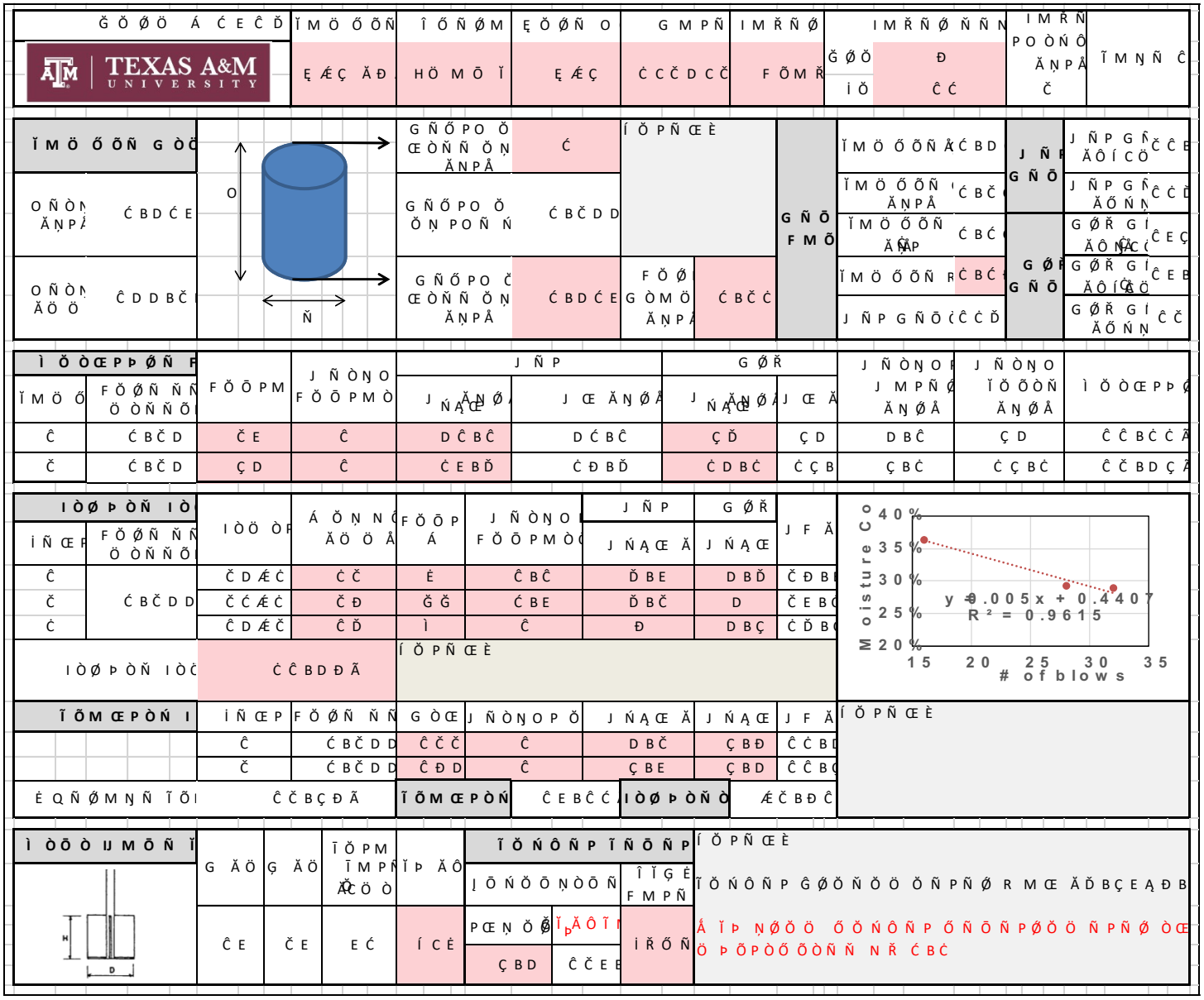

Figure B-107. B-4 (8’-10’) Beaumont Formation – Page 1

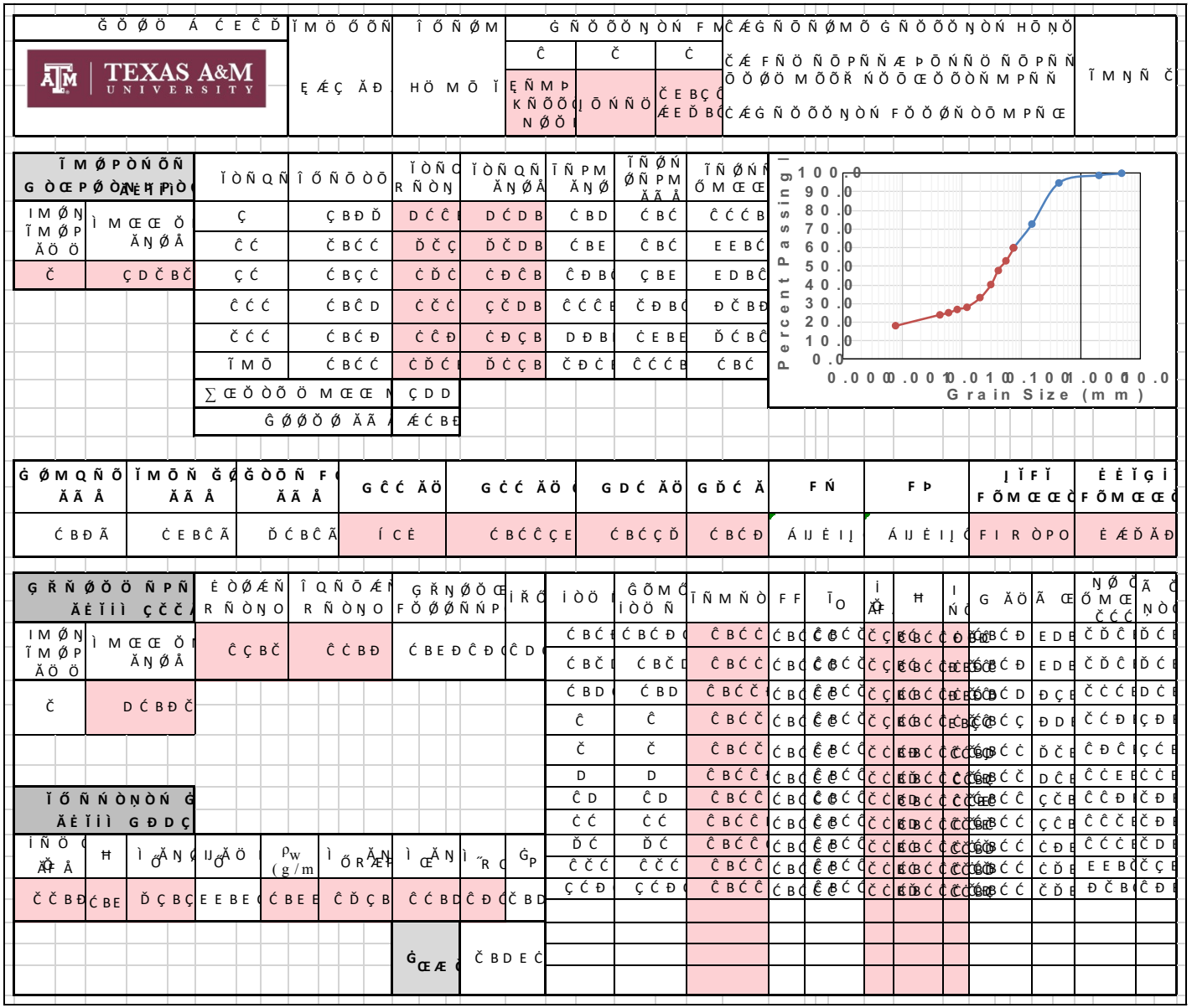

Figure B-108. B-4 (8’-10’) Beaumont Formation – Page 2

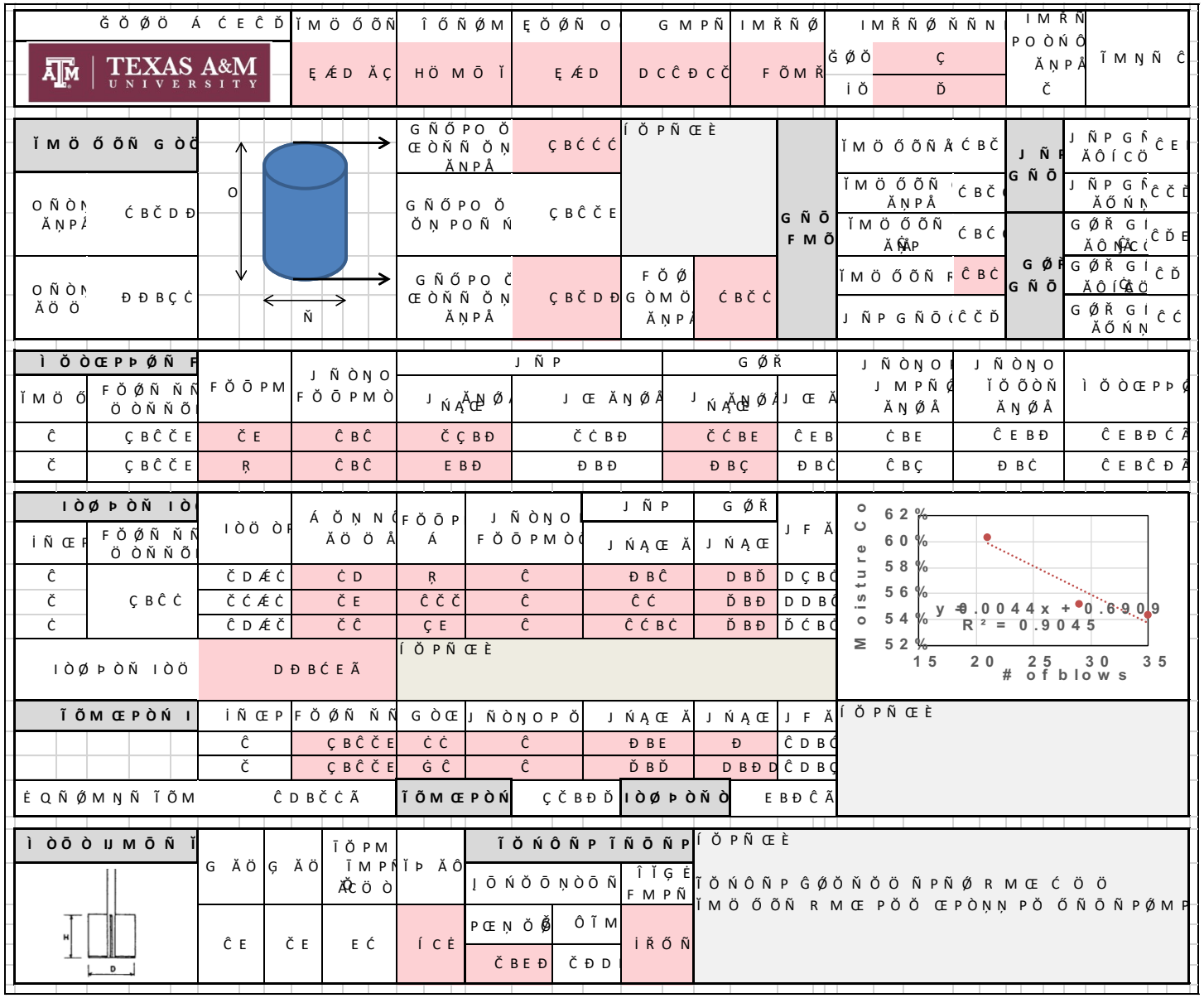

Figure B-109. B-5 (4'-6') Beaumont Formation – Page 1

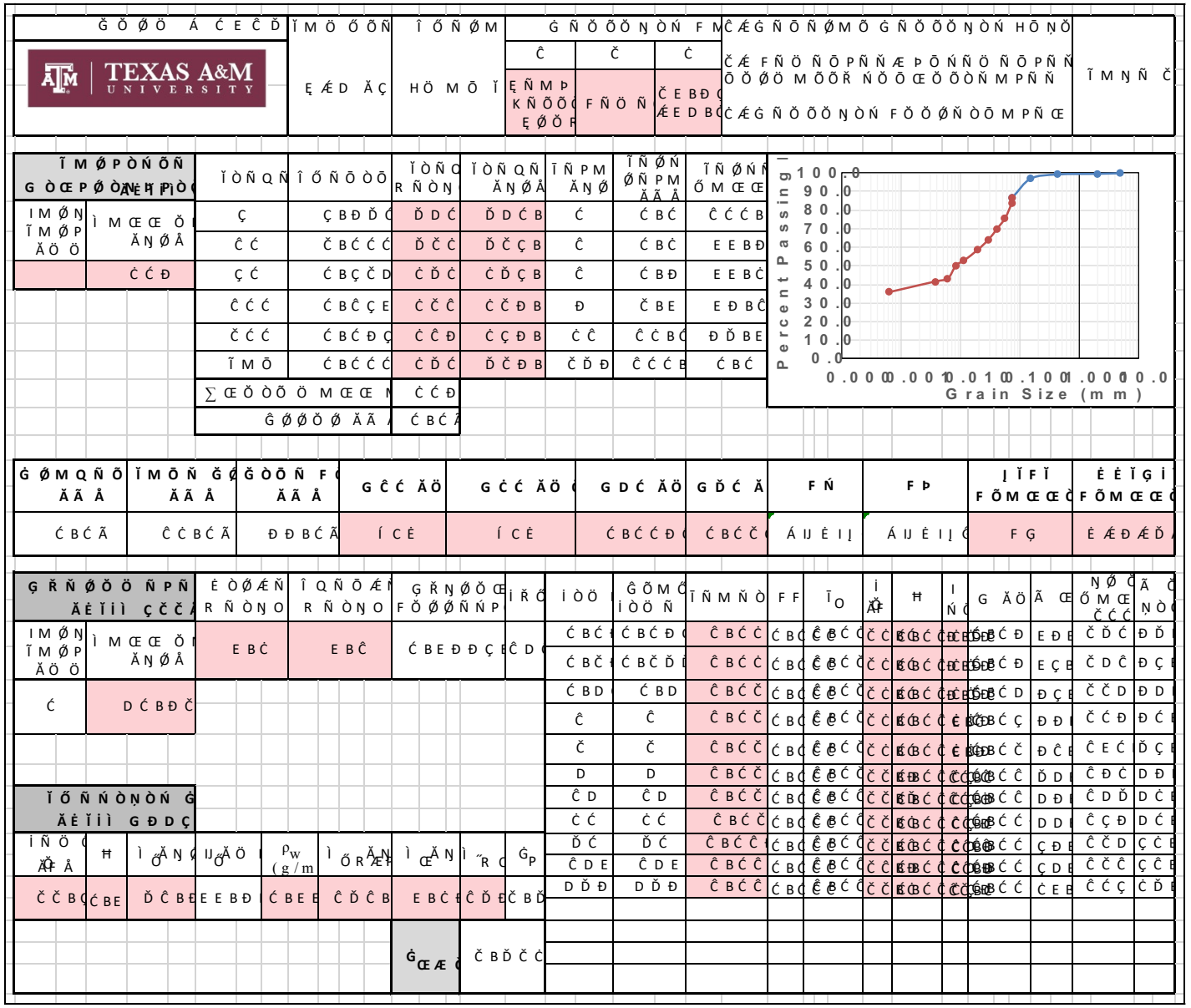

Figure B-110. B-5 (4'-6') Beaumont Formation – Page 2

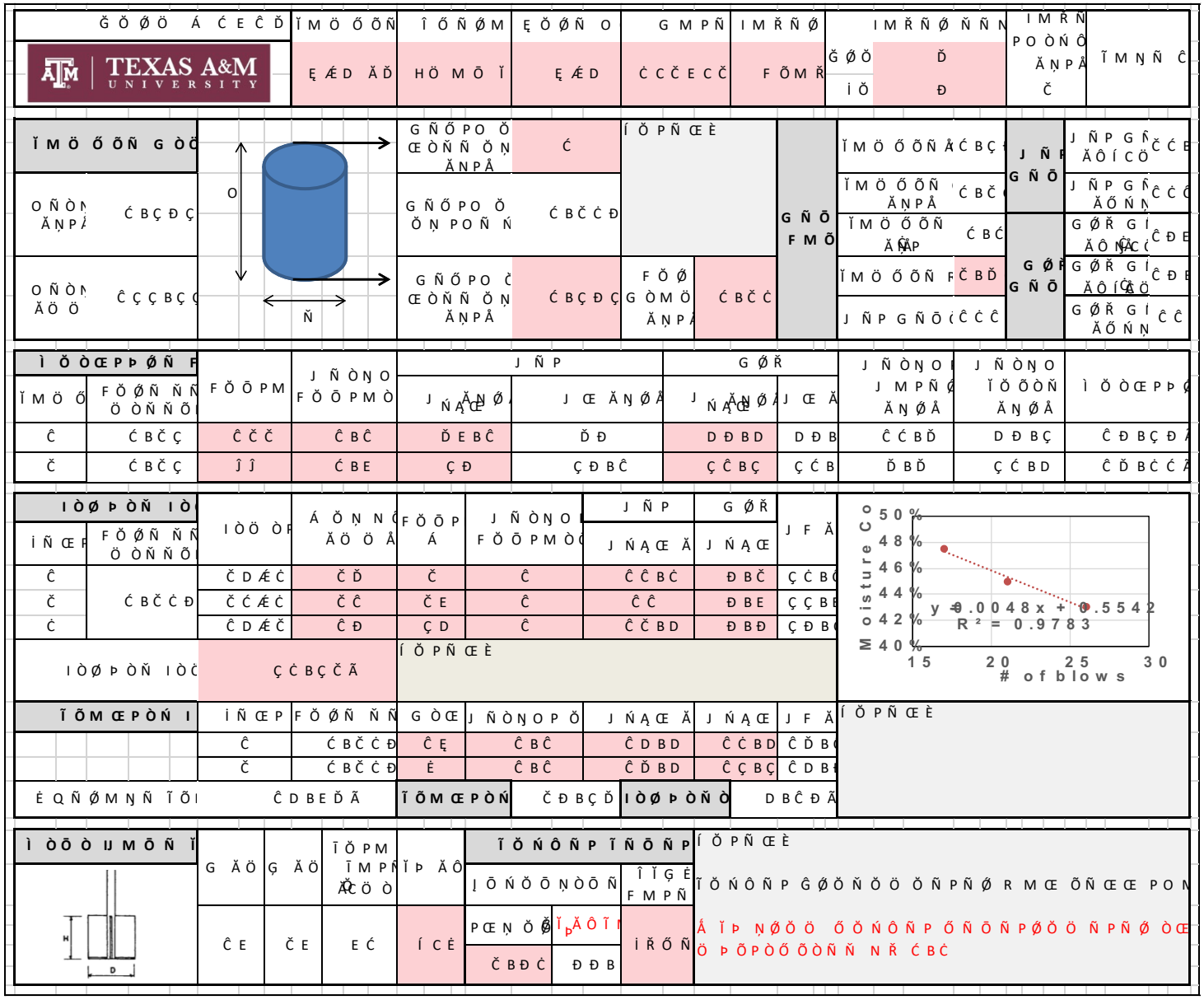

Figure B-111. B-5 (6’-8’) Beaumont Formation – Page 1

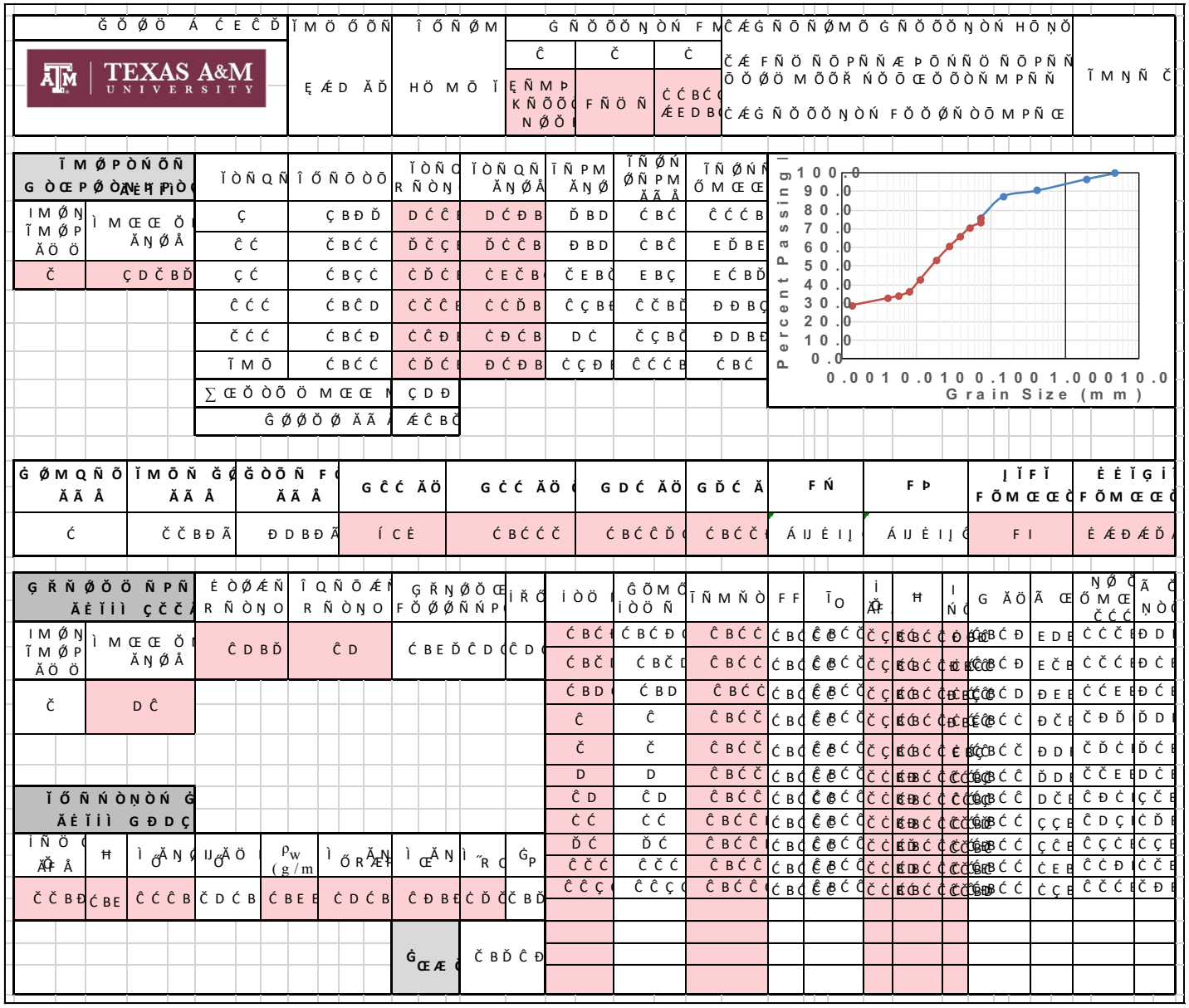

Figure B-112. B-5 (6’-8’) Beaumont Formation – Page 2

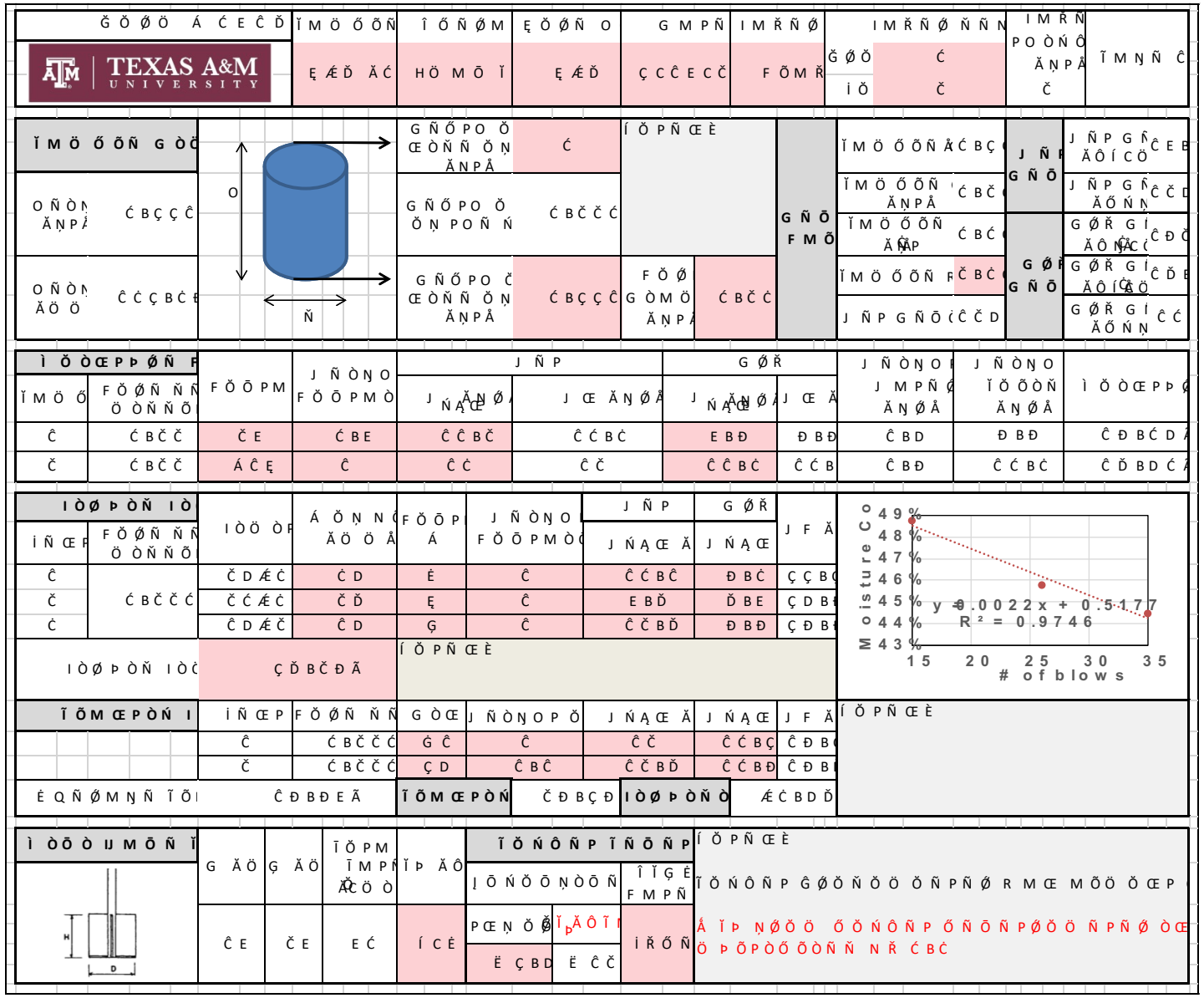

Figure B-113. B-6 (0'-2') Beaumont Formation – Page 1

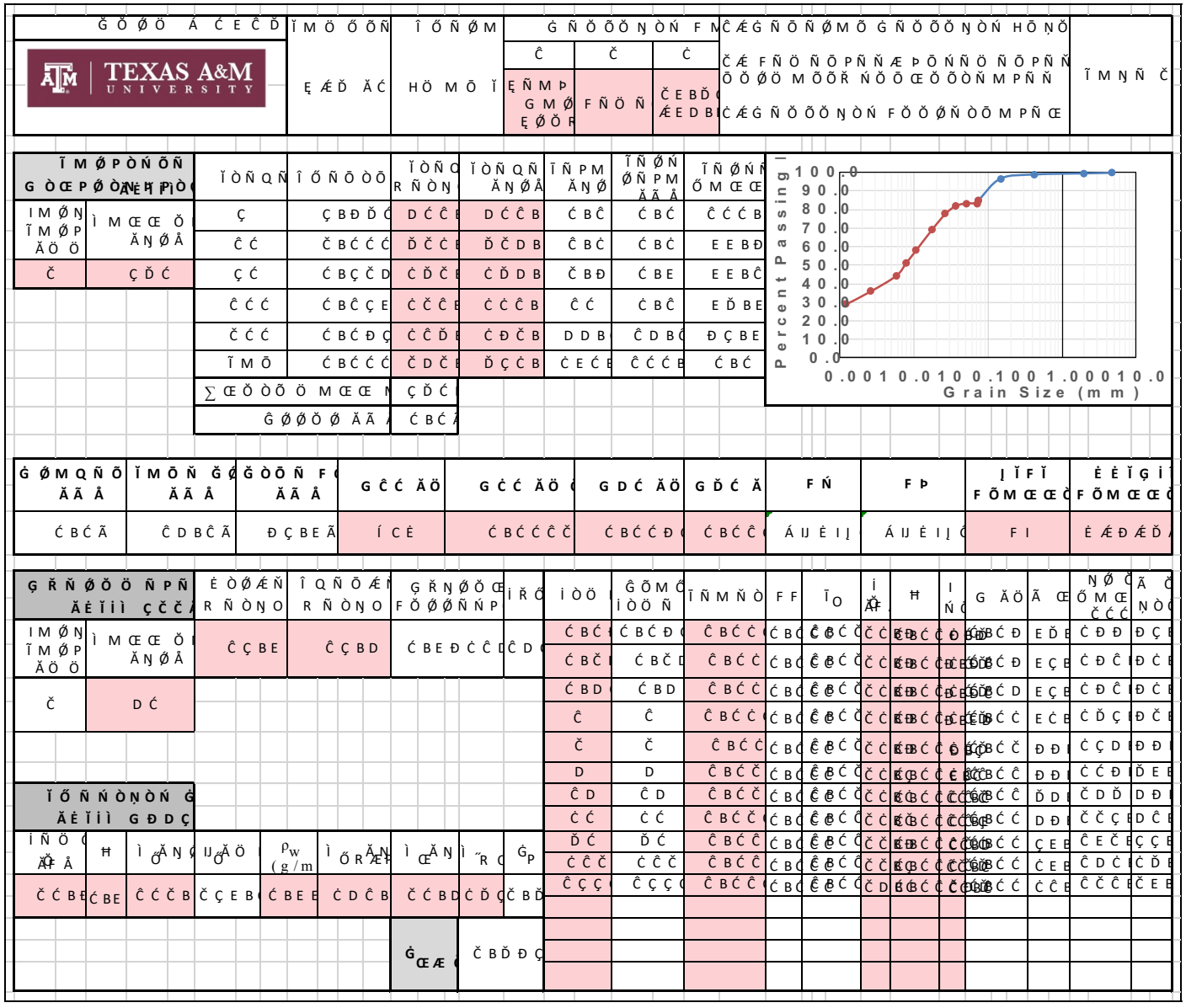

Figure B-114. B-6 (0'-2') Beaumont Formation – Page 2

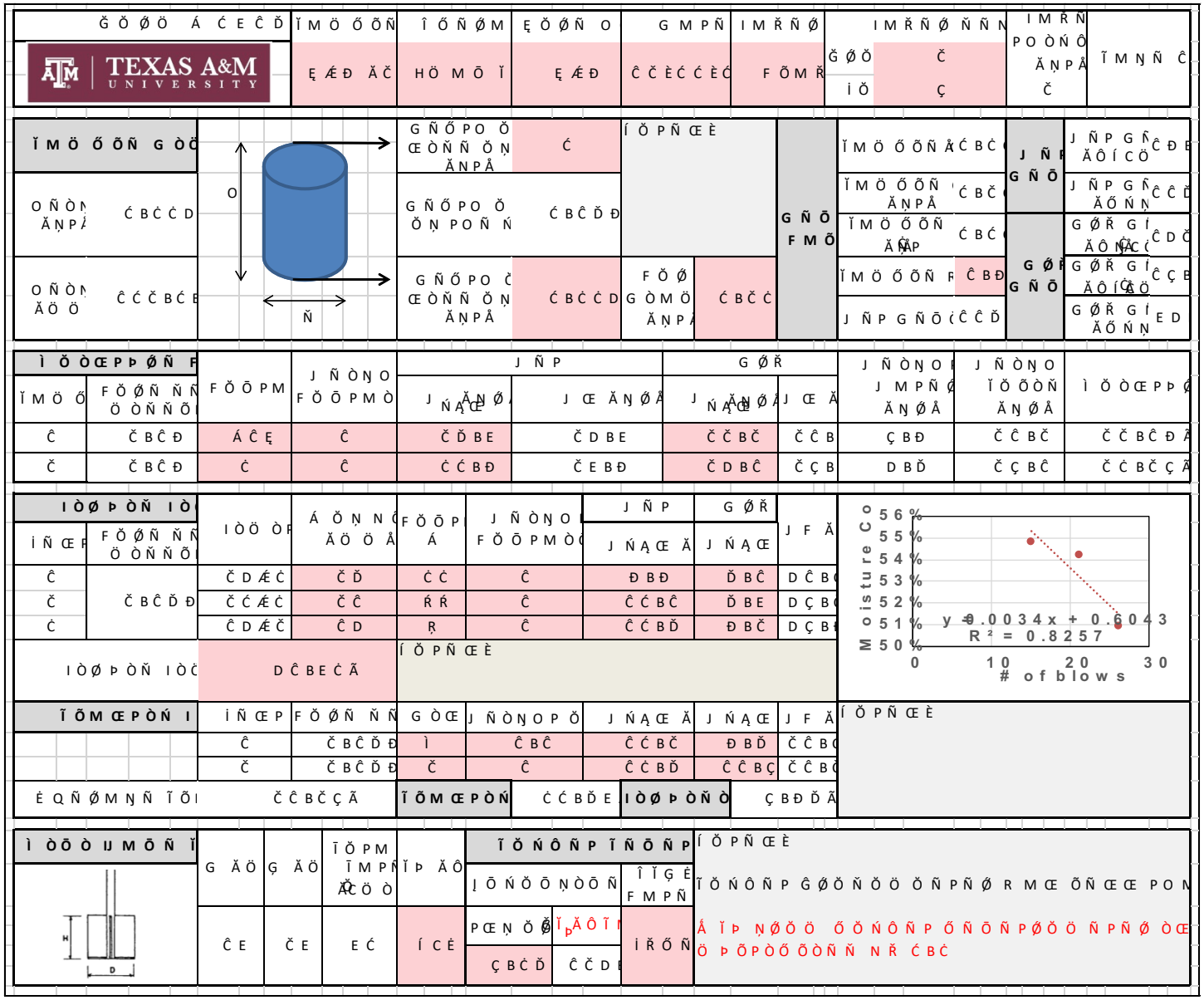

Figure B-115. B-8 (2'-4') Alluvium Formation – Page 1

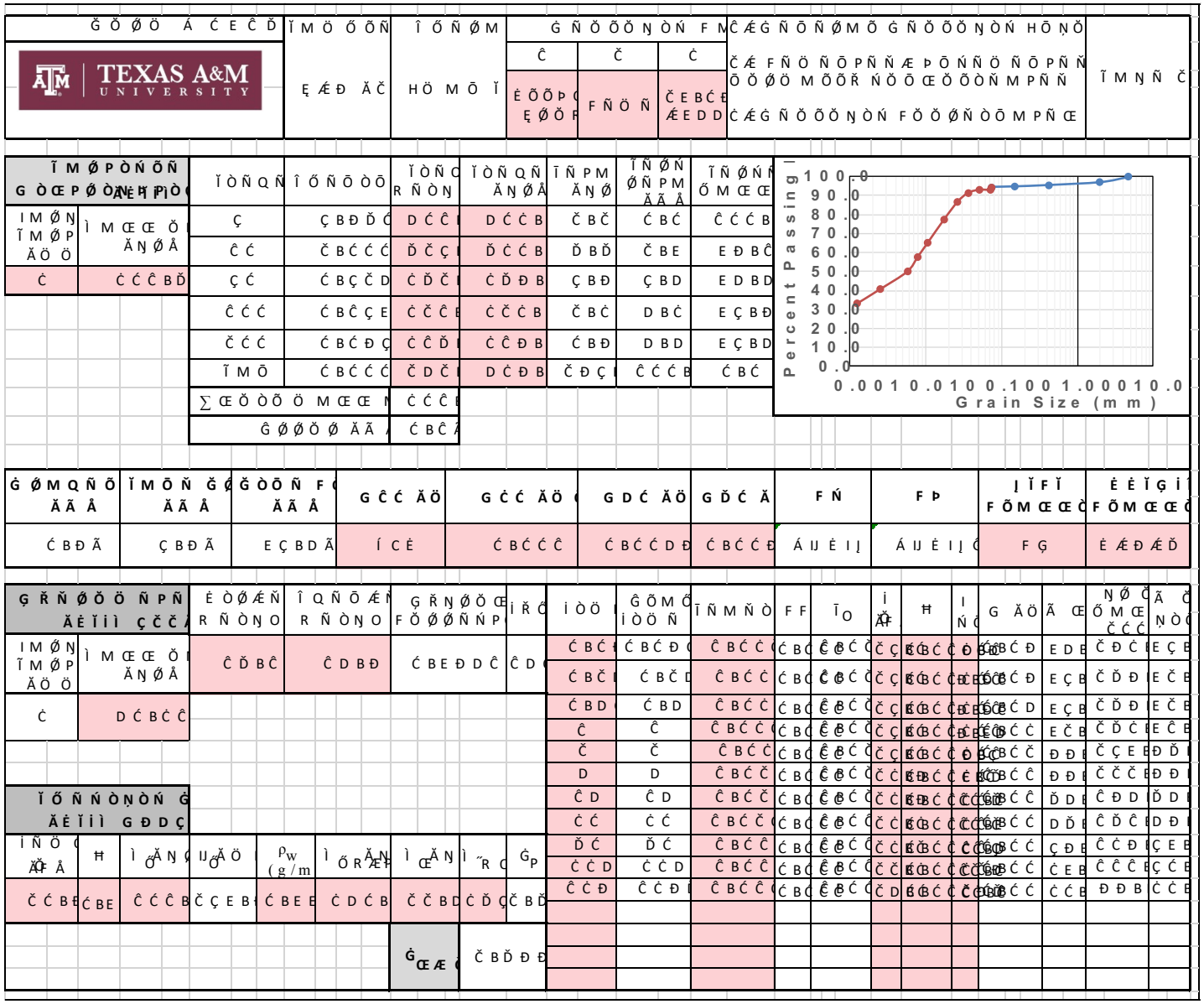

Figure B-116. B-8 (2'-4') Alluvium Formation – Page 2

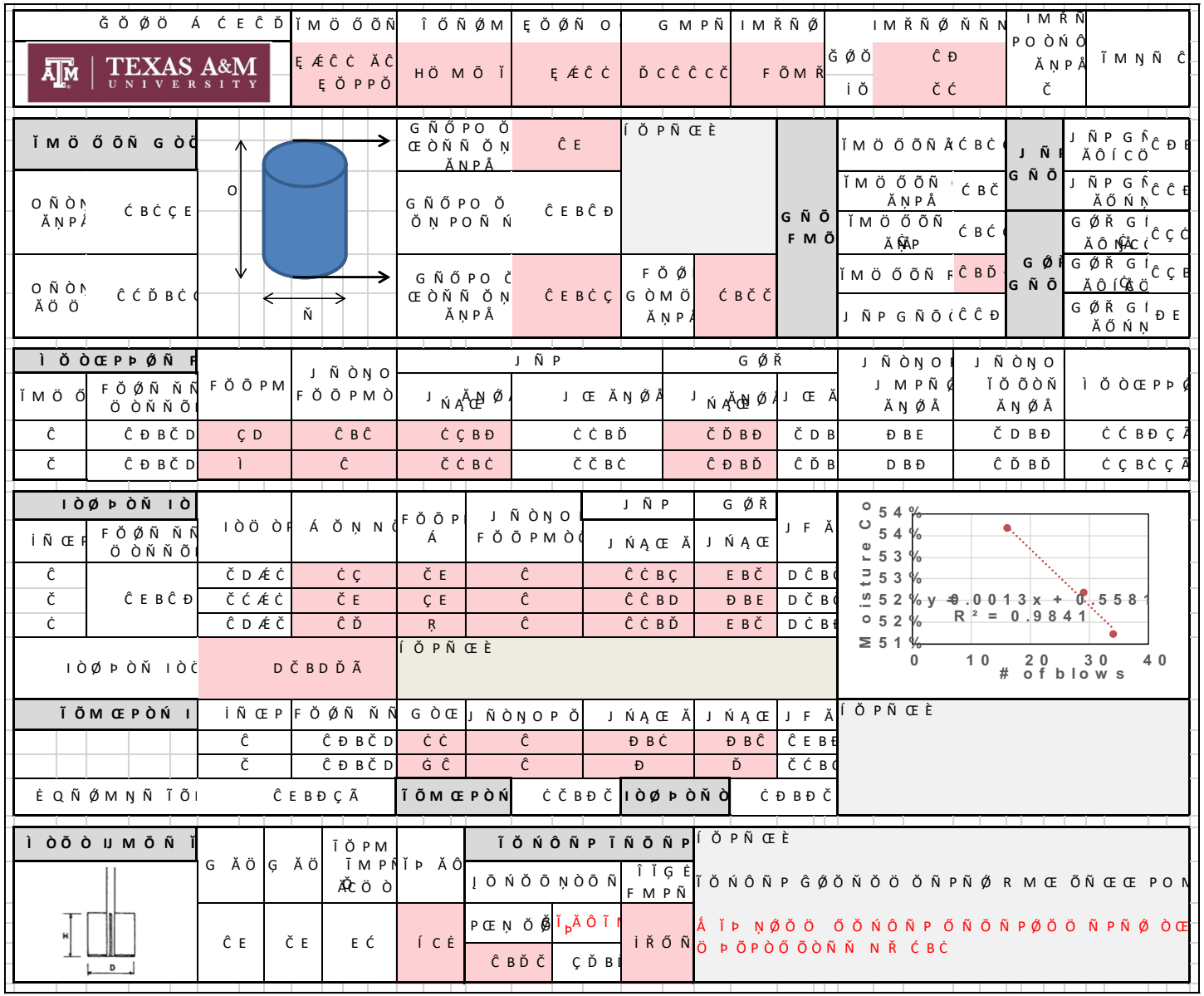

Figure B-117. B-13 (18'-20') Bottom Alluvium Formation – Page 1

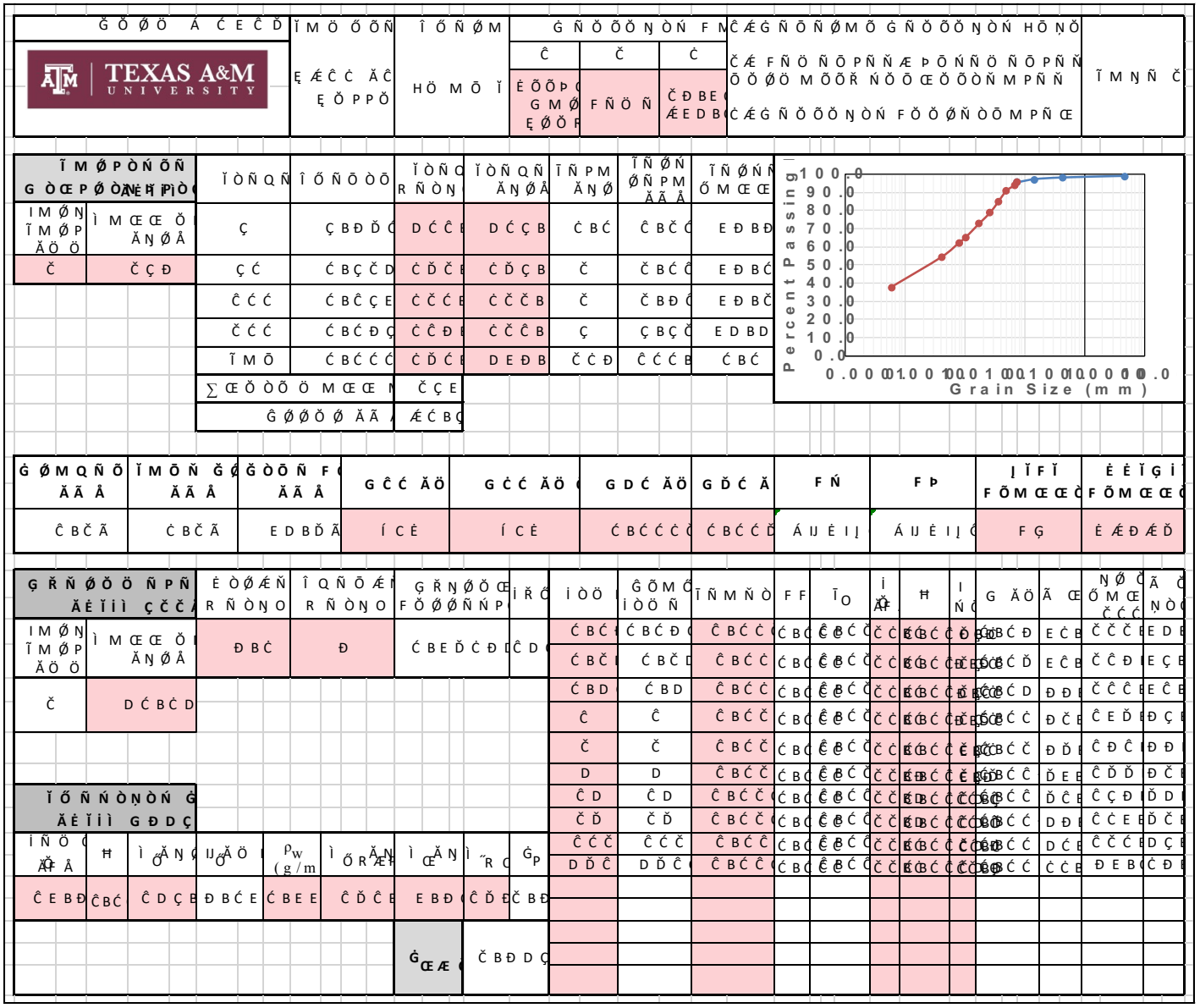

Figure B-118. B-13 (18'-20') Bottom Alluvium Formation – Page 2

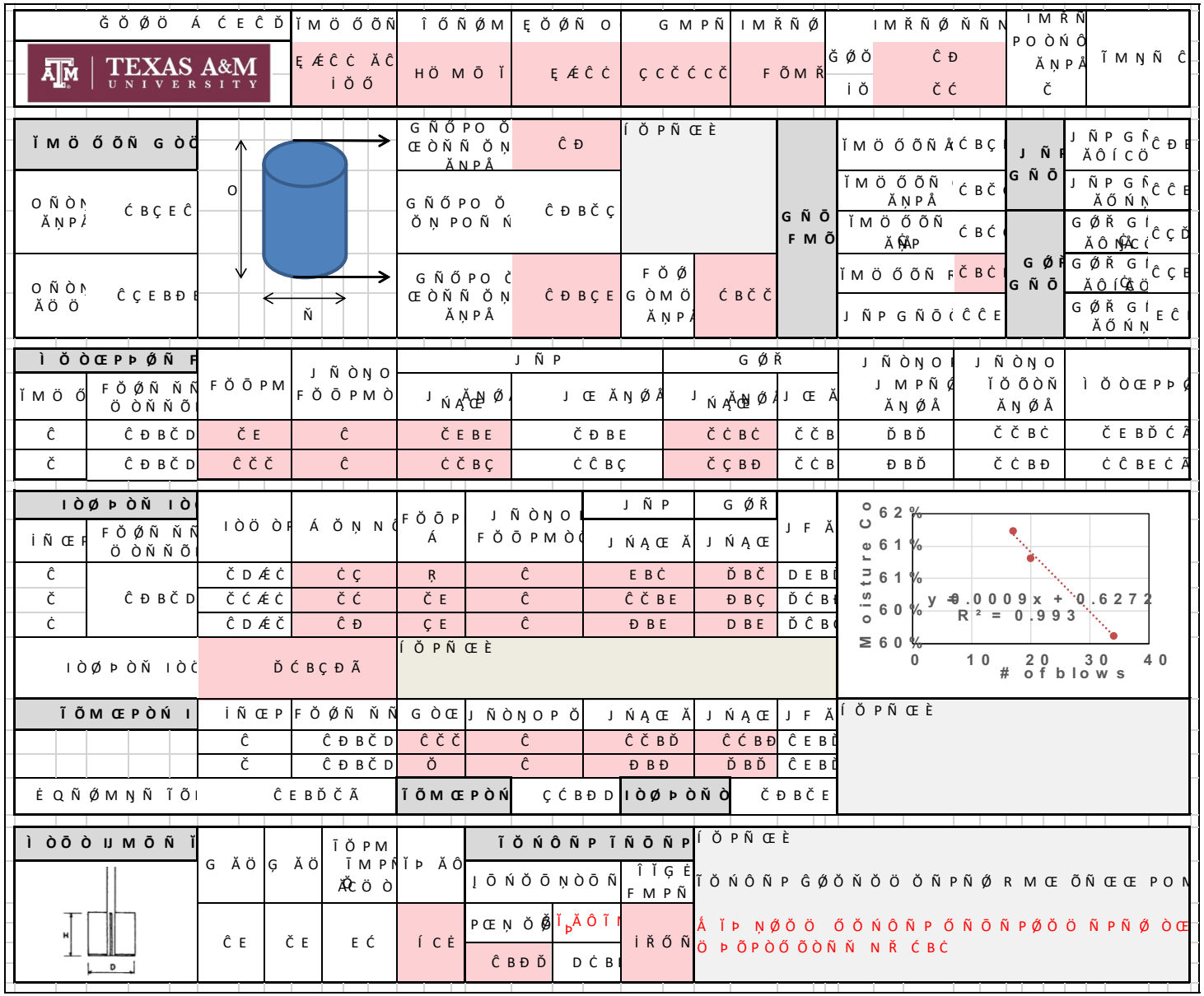

Figure B-119. B-13 (18'-20') Top Alluvium Formation – Page 1

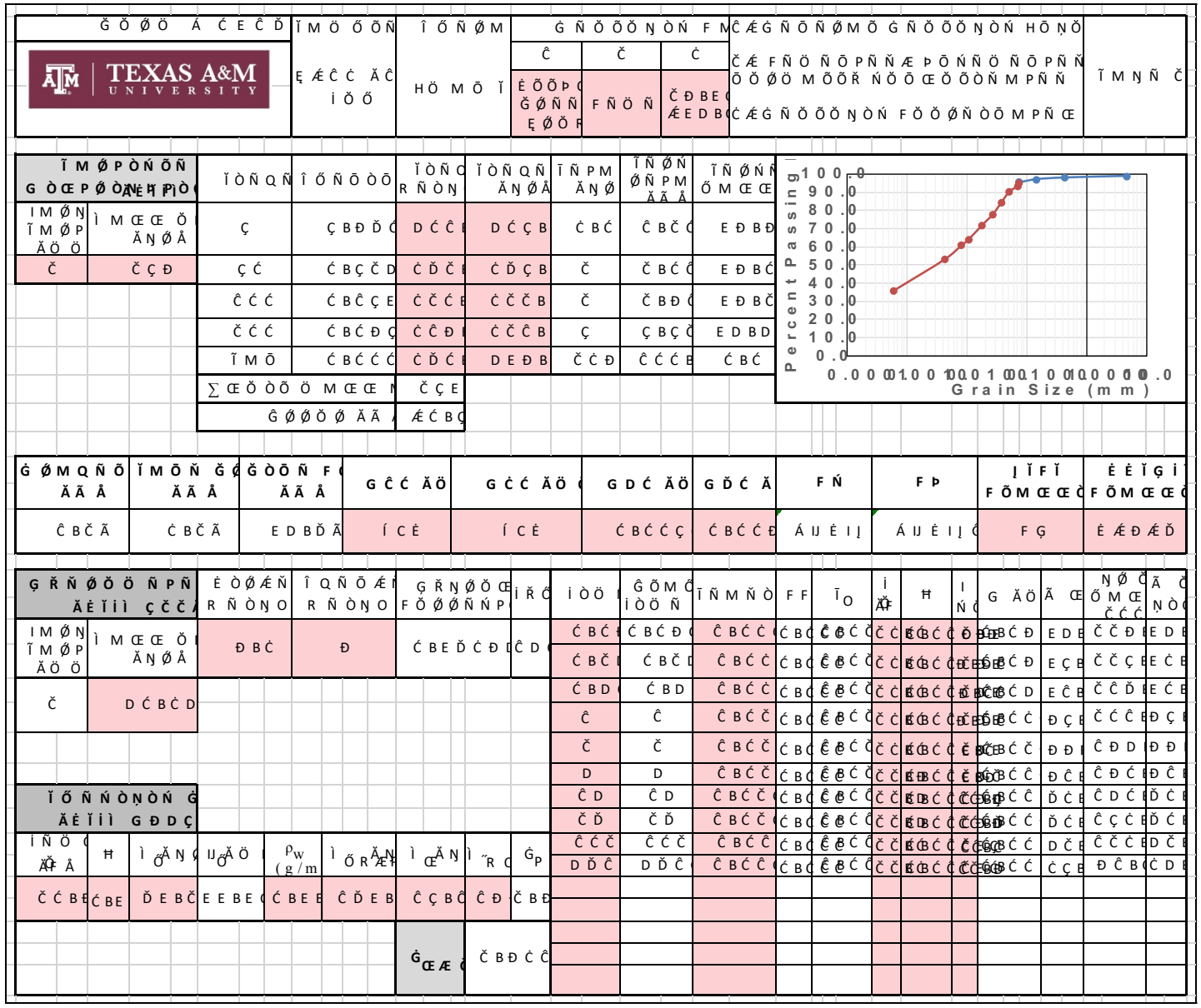

Figure B-120. B-13 (18'-20') Top Alluvium Formation – Page 2

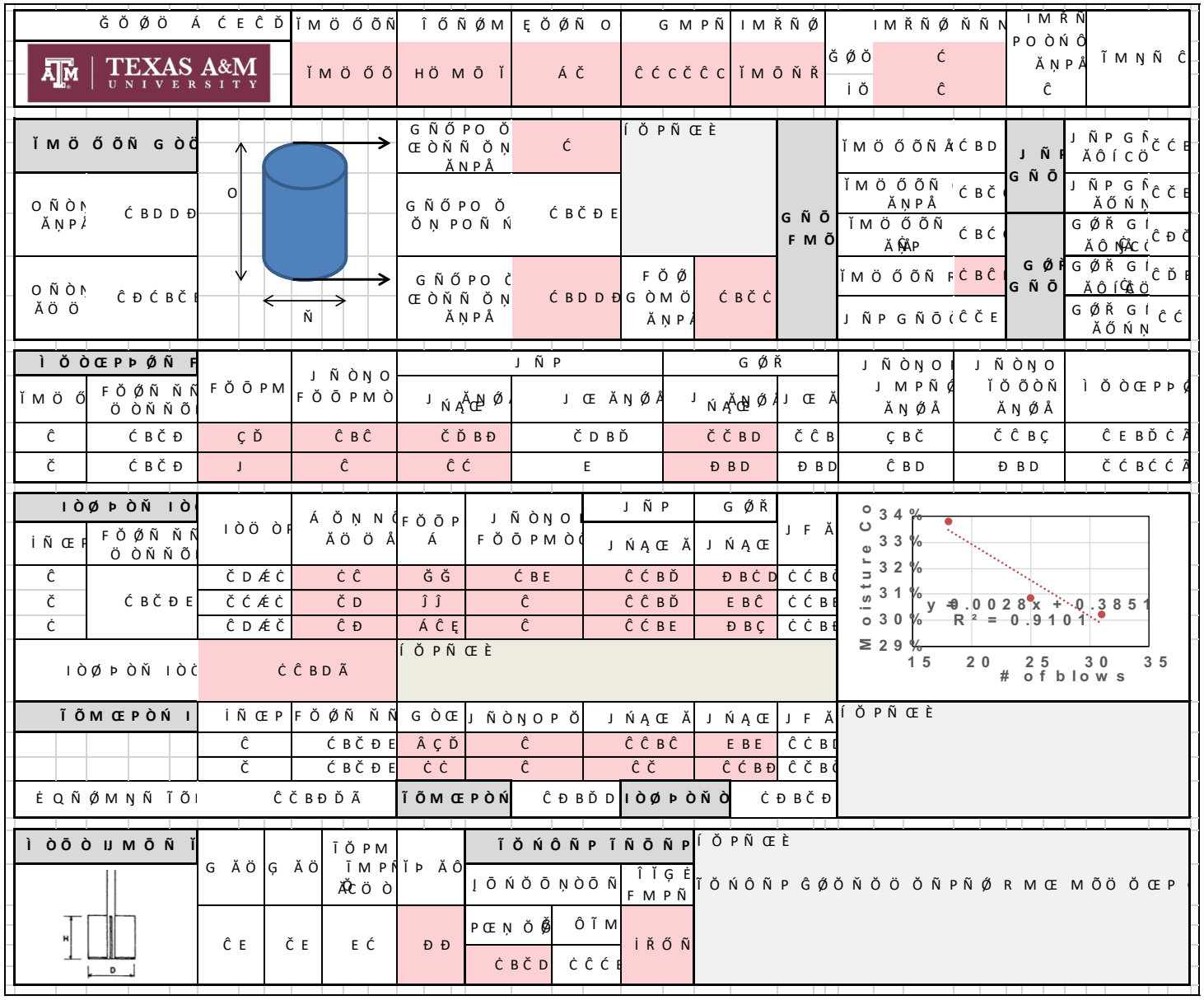

Figure B-121. GEER Sample #2 – Page 1

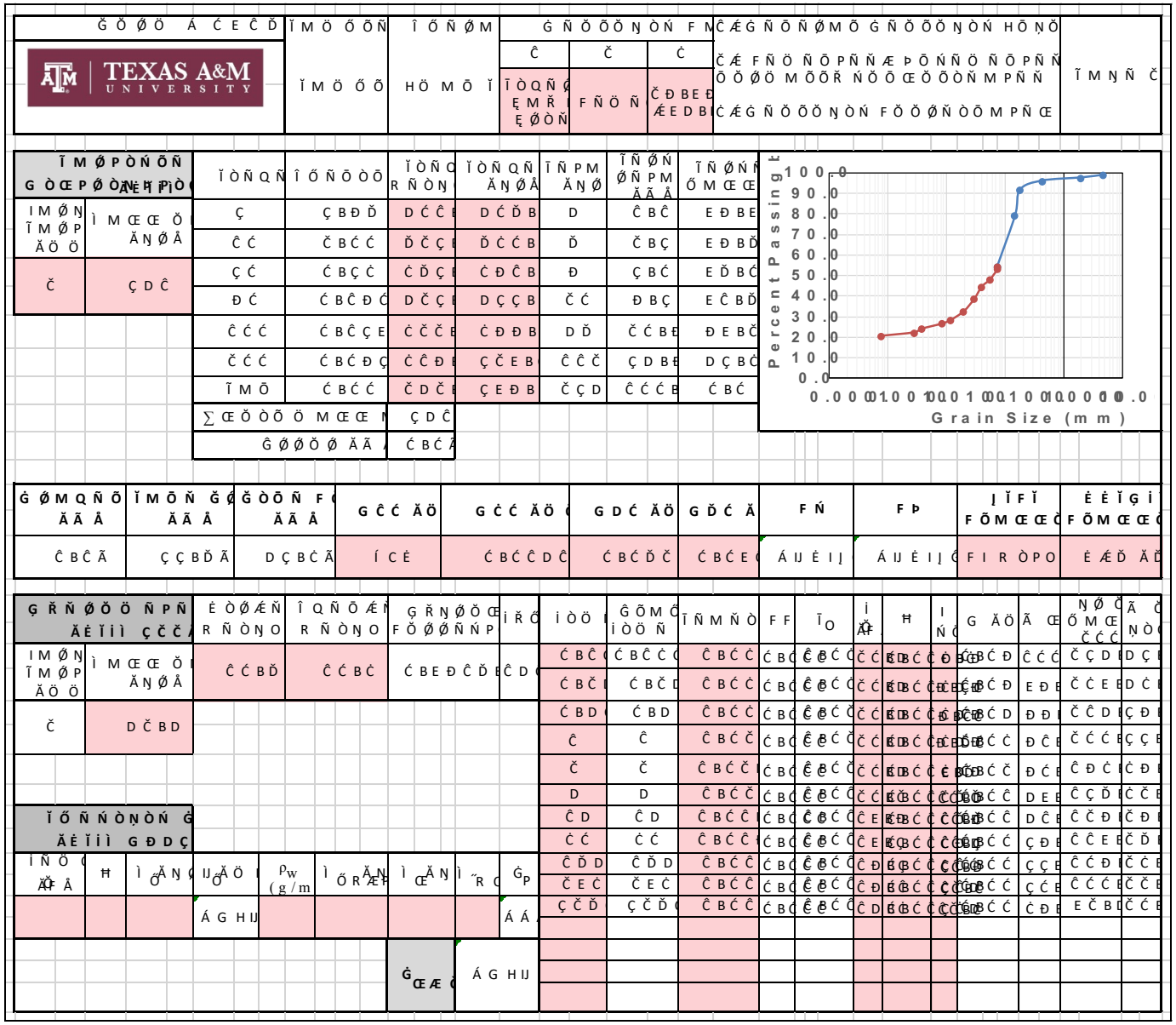

Figure B-122. GEER Sample #2 – Page 2

Silt Samples - JET

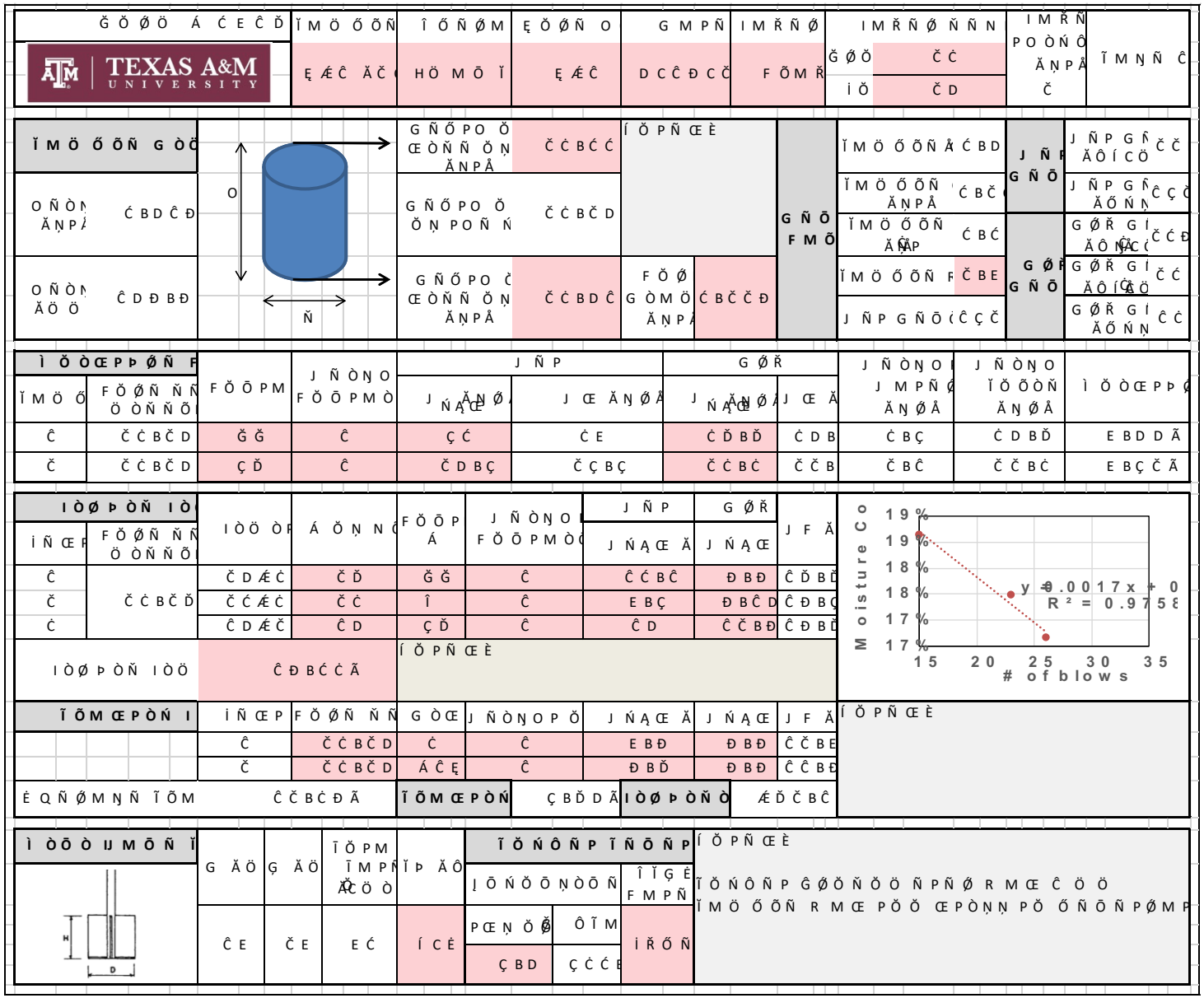

Figure B-123. B-1 (23’-25’) Tittabawsee River – Page 1

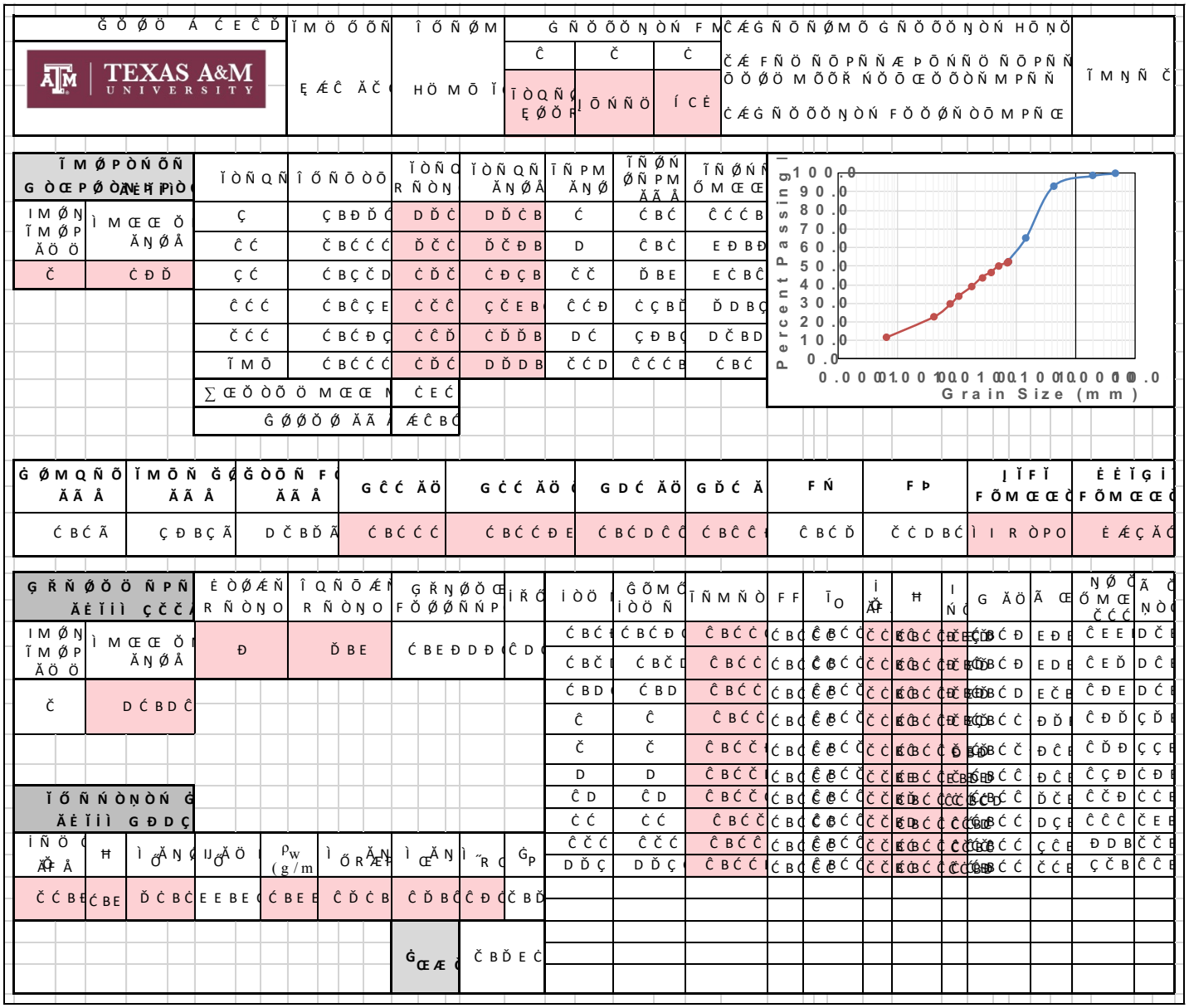

Figure B-124. B-1 (23’-25’) Tittabawsee River – Page 2

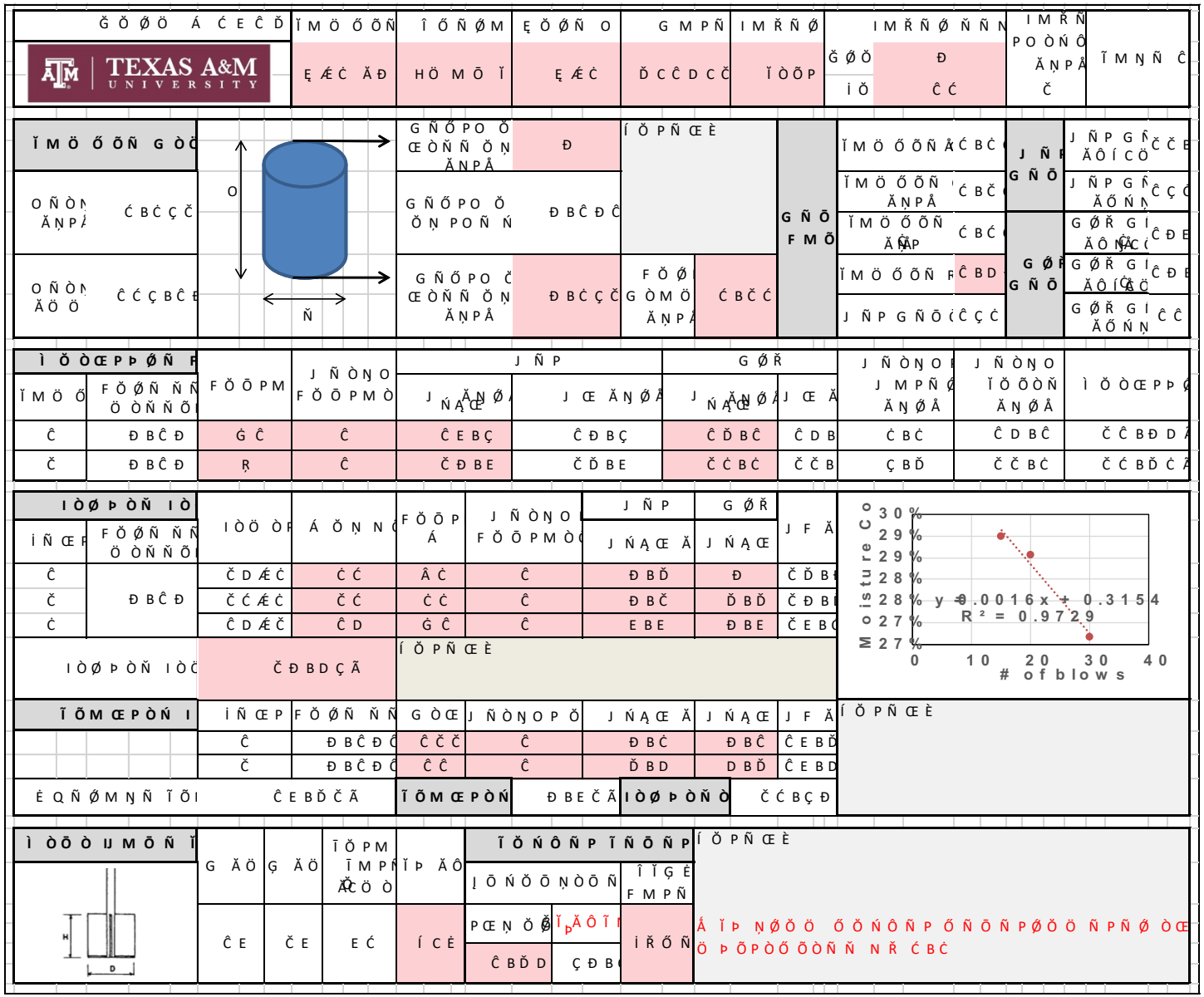

Figure B-125. B-3 (8’-10’) Beaumont Formation – Page 1

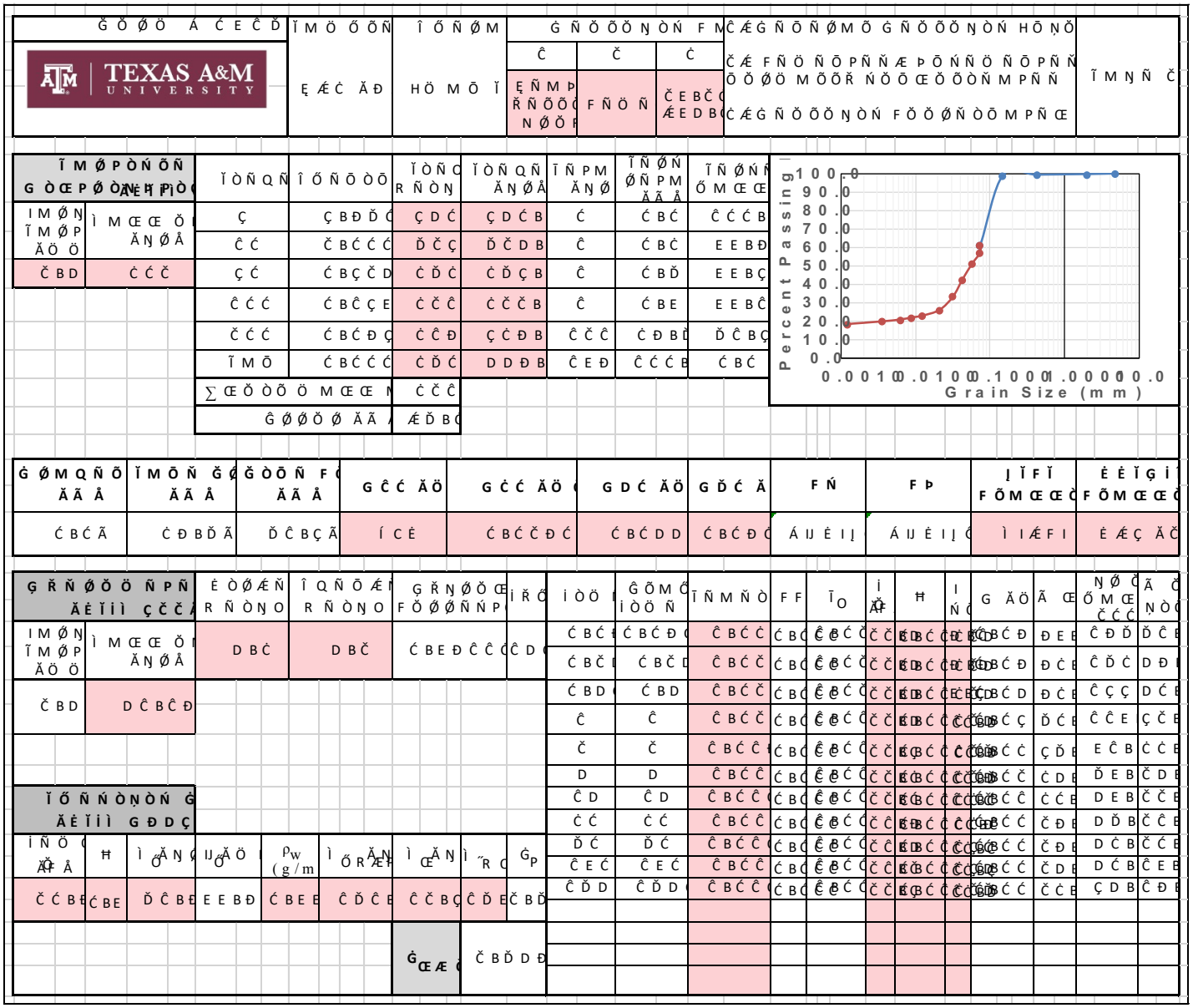

Figure B-126. B-3 (8’-10’) Beaumont Formation – Page 2

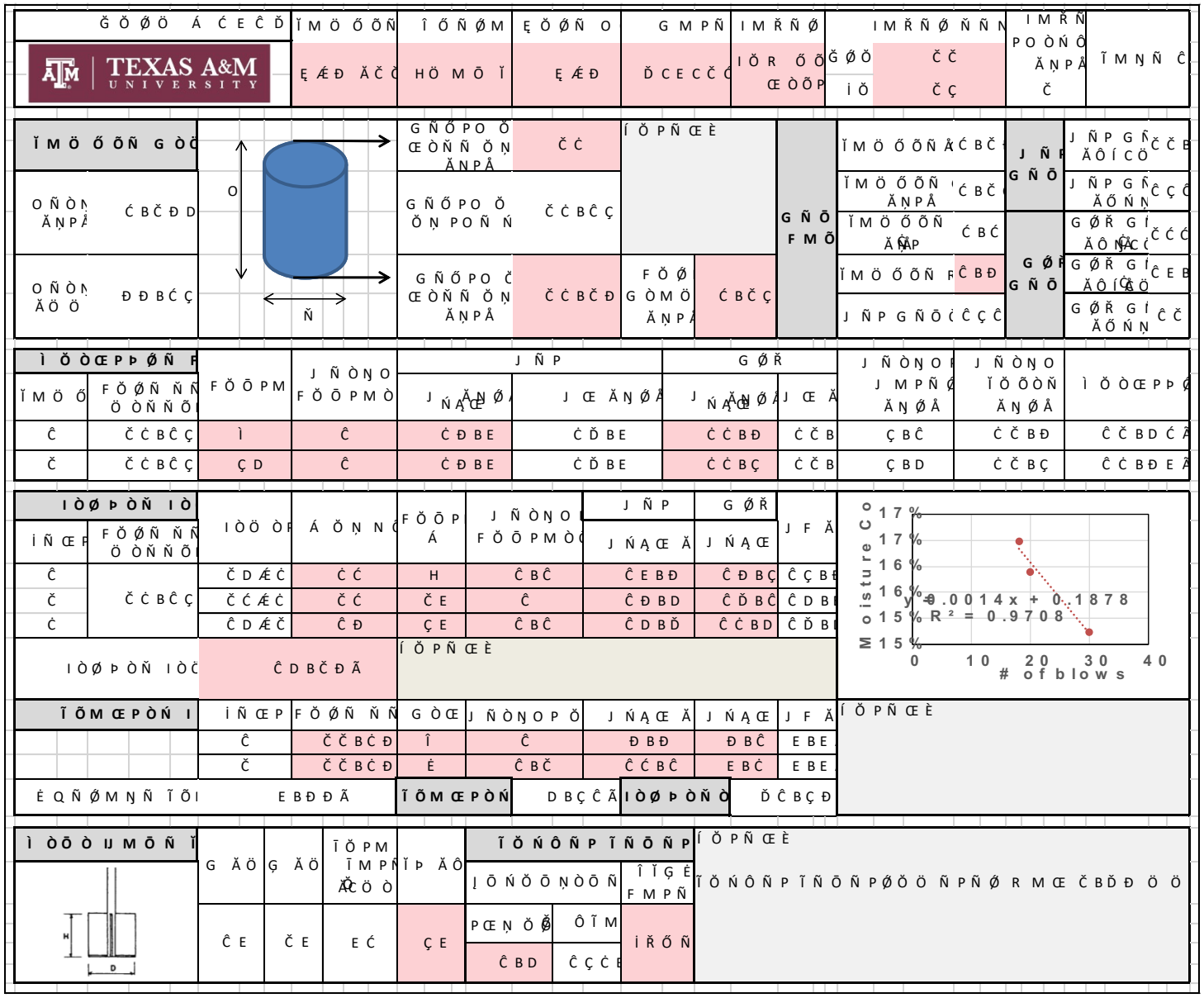

Figure B-127. B-7 (22'-24') Tittabawsee River – Page 1

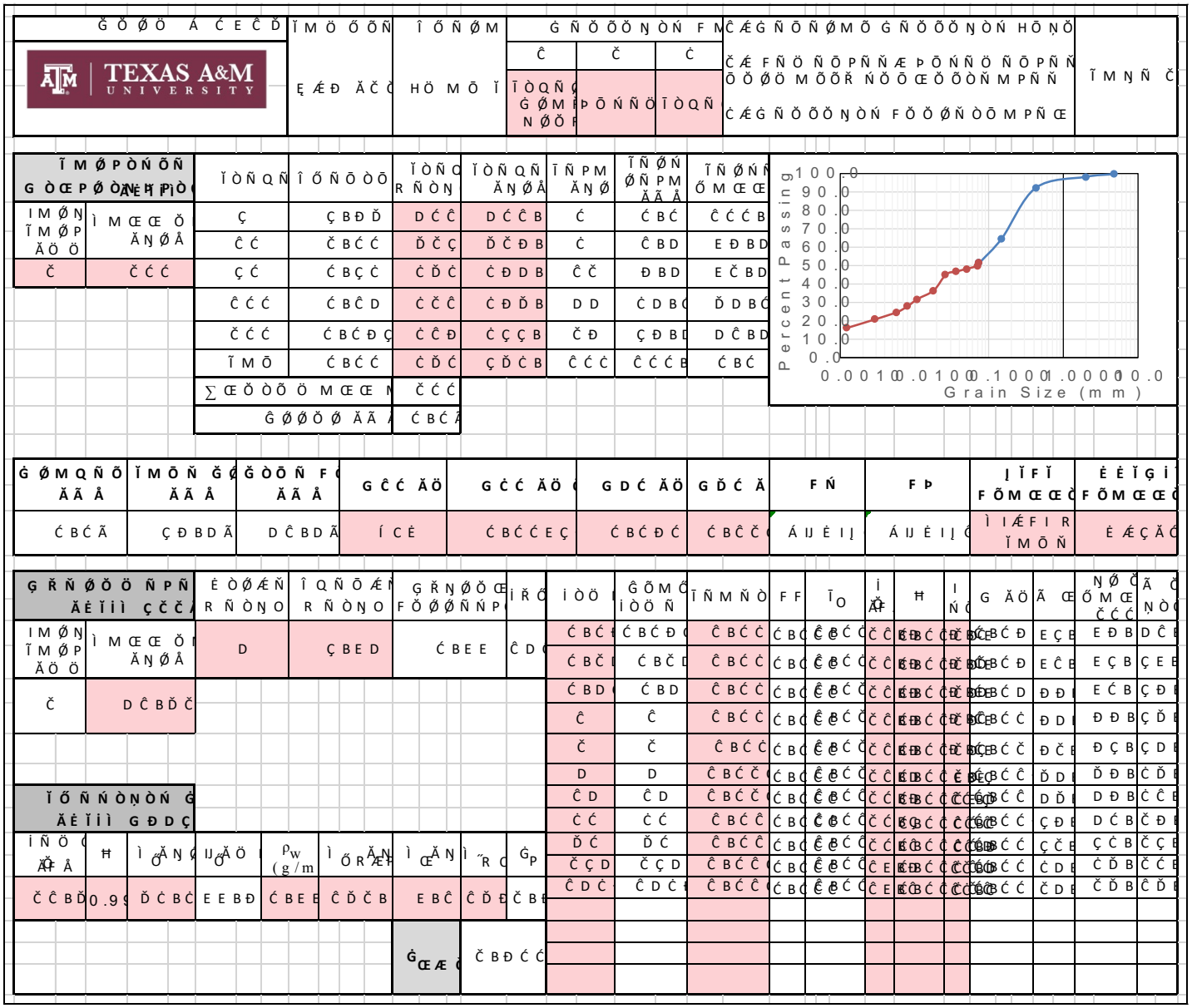

Figure B-128. B-7 (22'-24') Tittabawsee River – Page 2

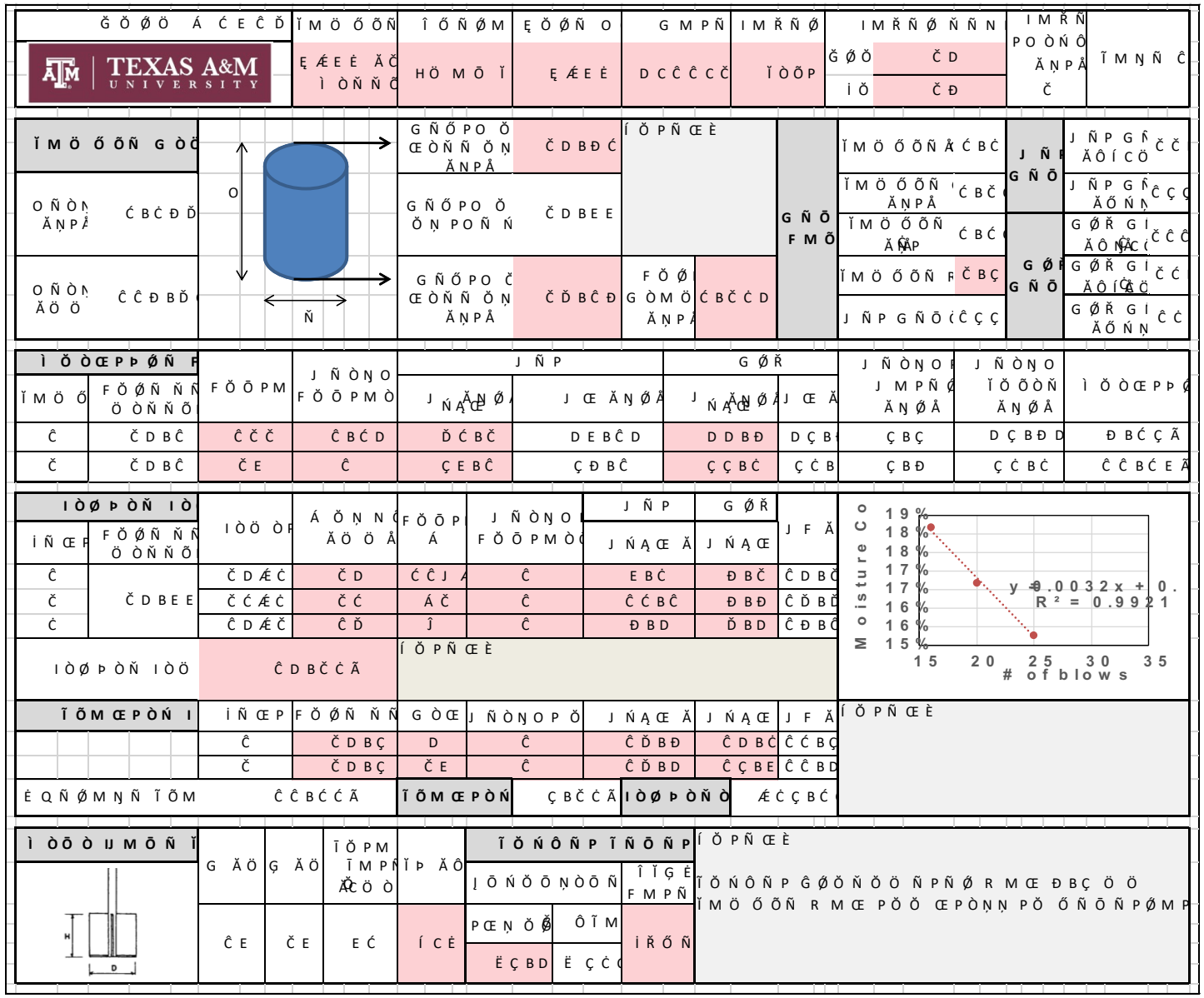

Figure B-129. B-9A (25’-27’) Middle Tittabawsee River – Page 1

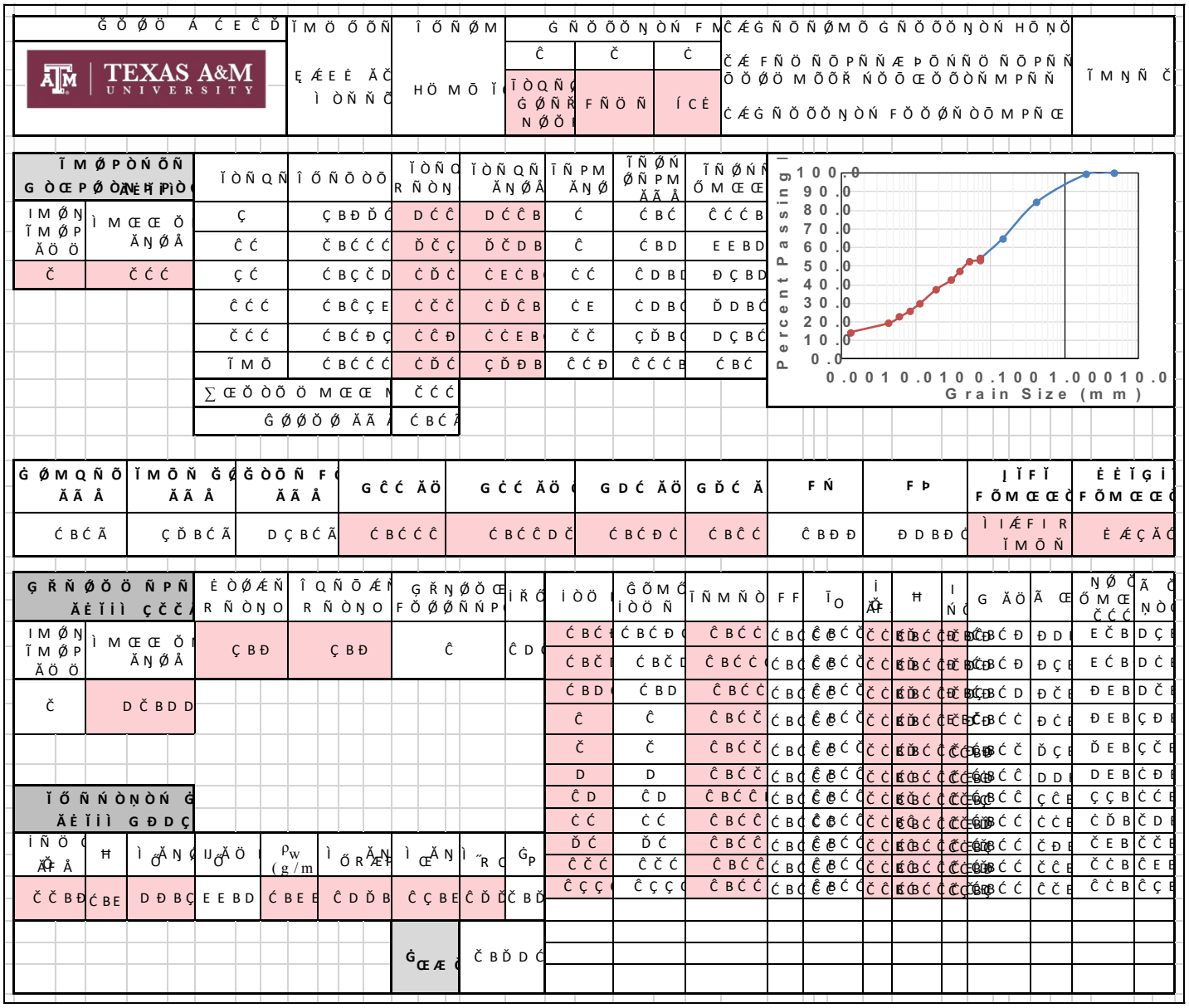

Figure B-130. B-9A (25’-27’) Middle Tittabawsee River – Page 2

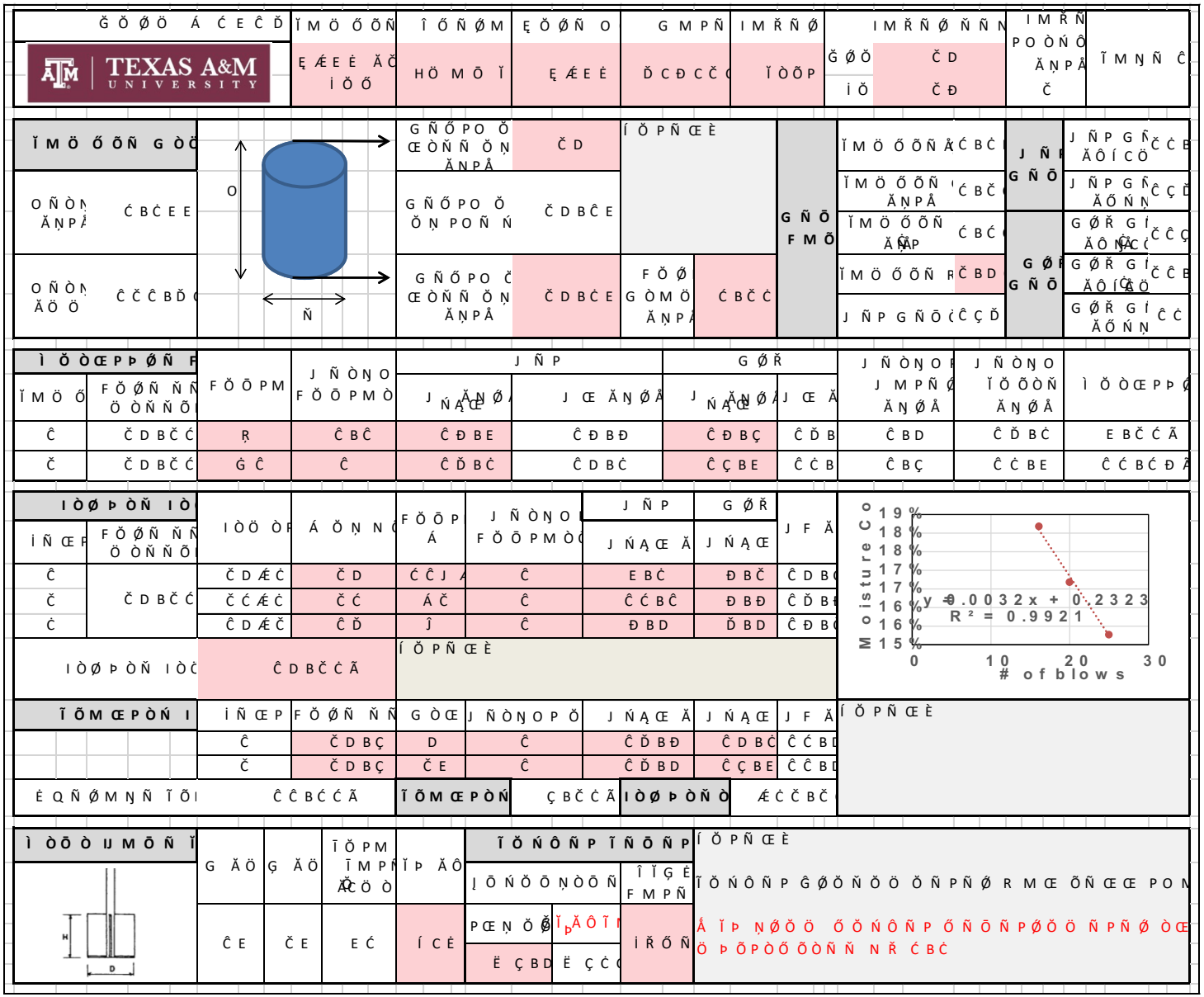

Figure B-131. B-9A (25’-27’) Top Tittabawsee River – Page 1

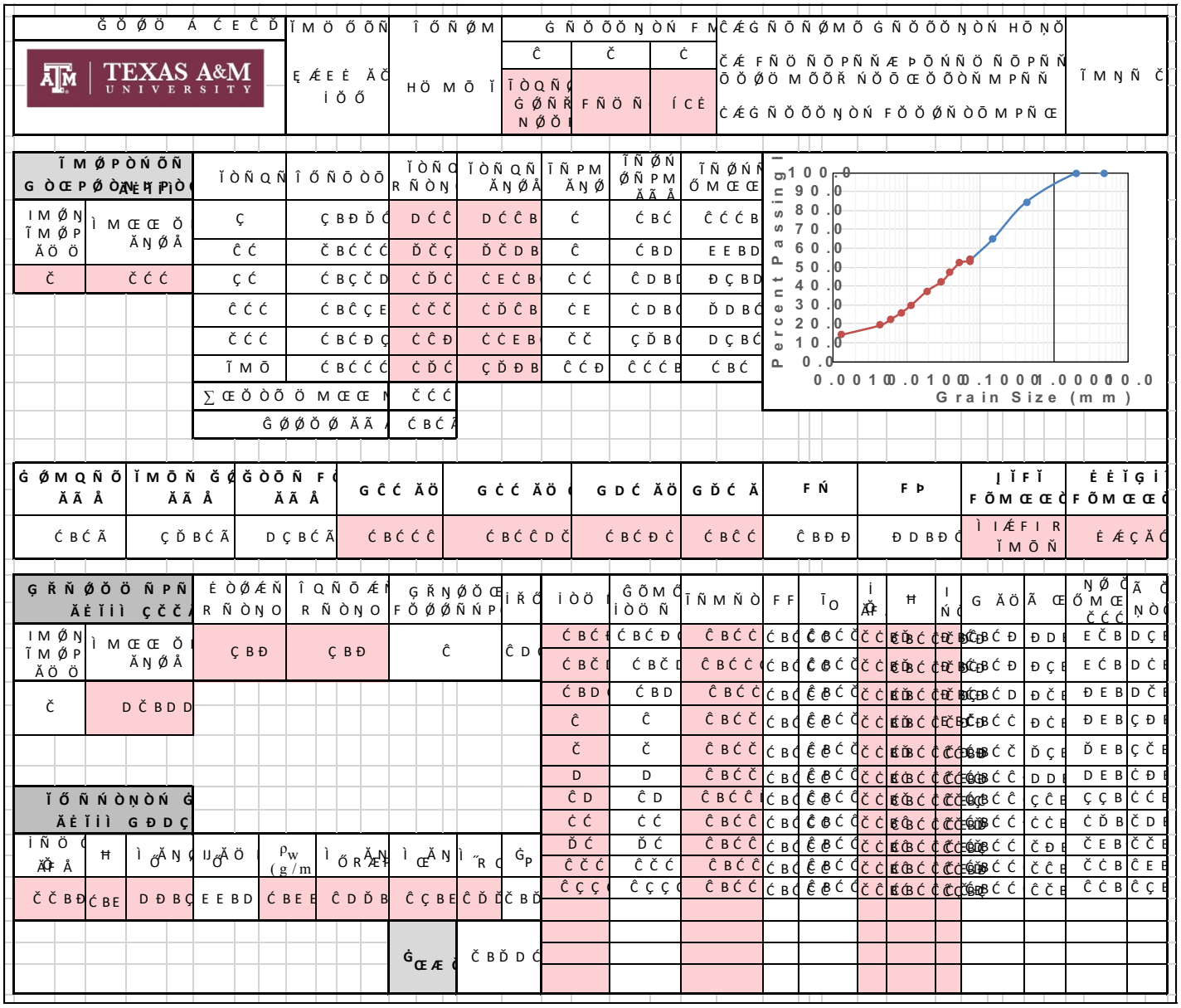

Figure B-132. B-9A (25’-27’) Top Tittabawsee River – Page 2

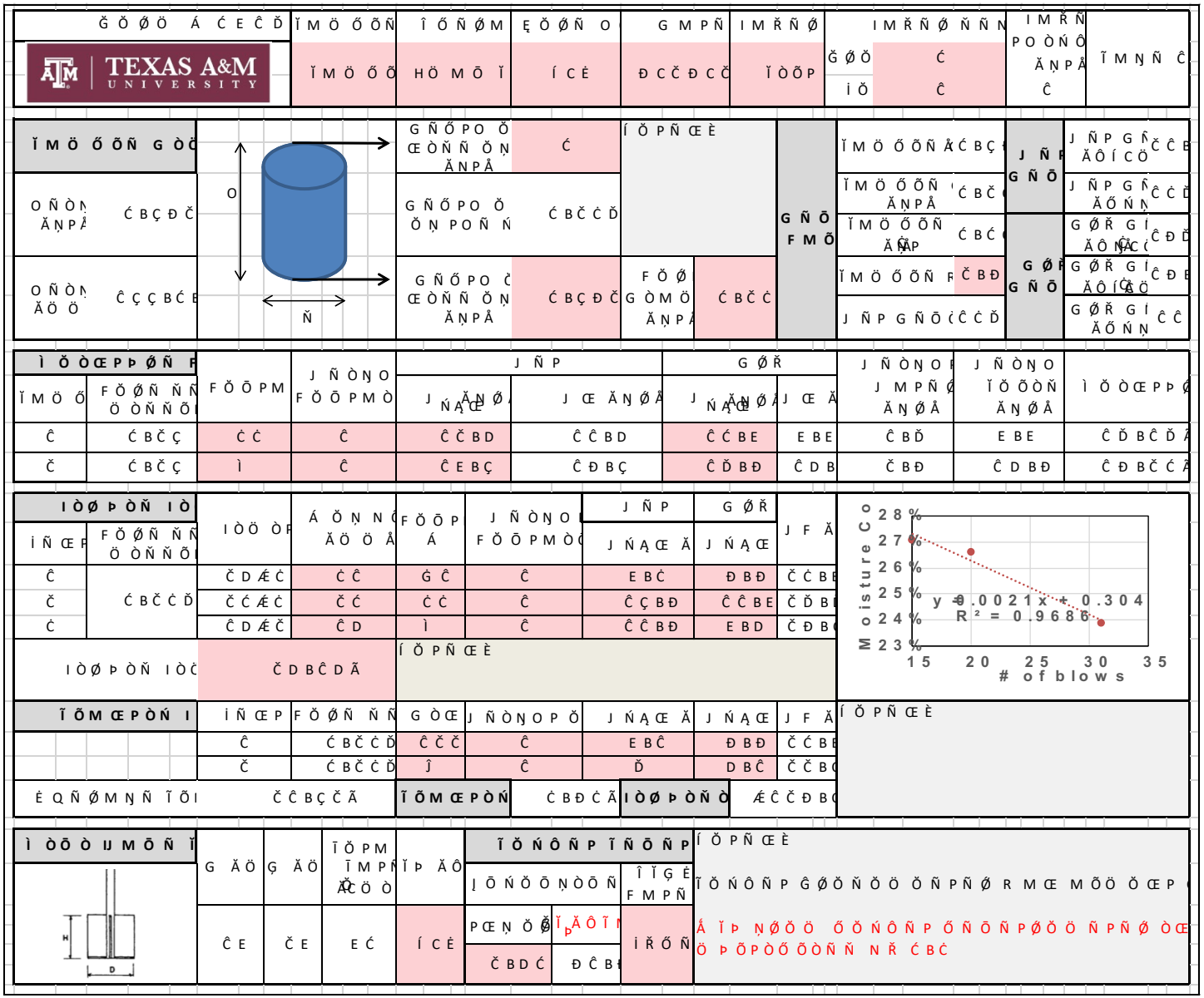

Figure B-133. FHWA Sample 2 – Page 1

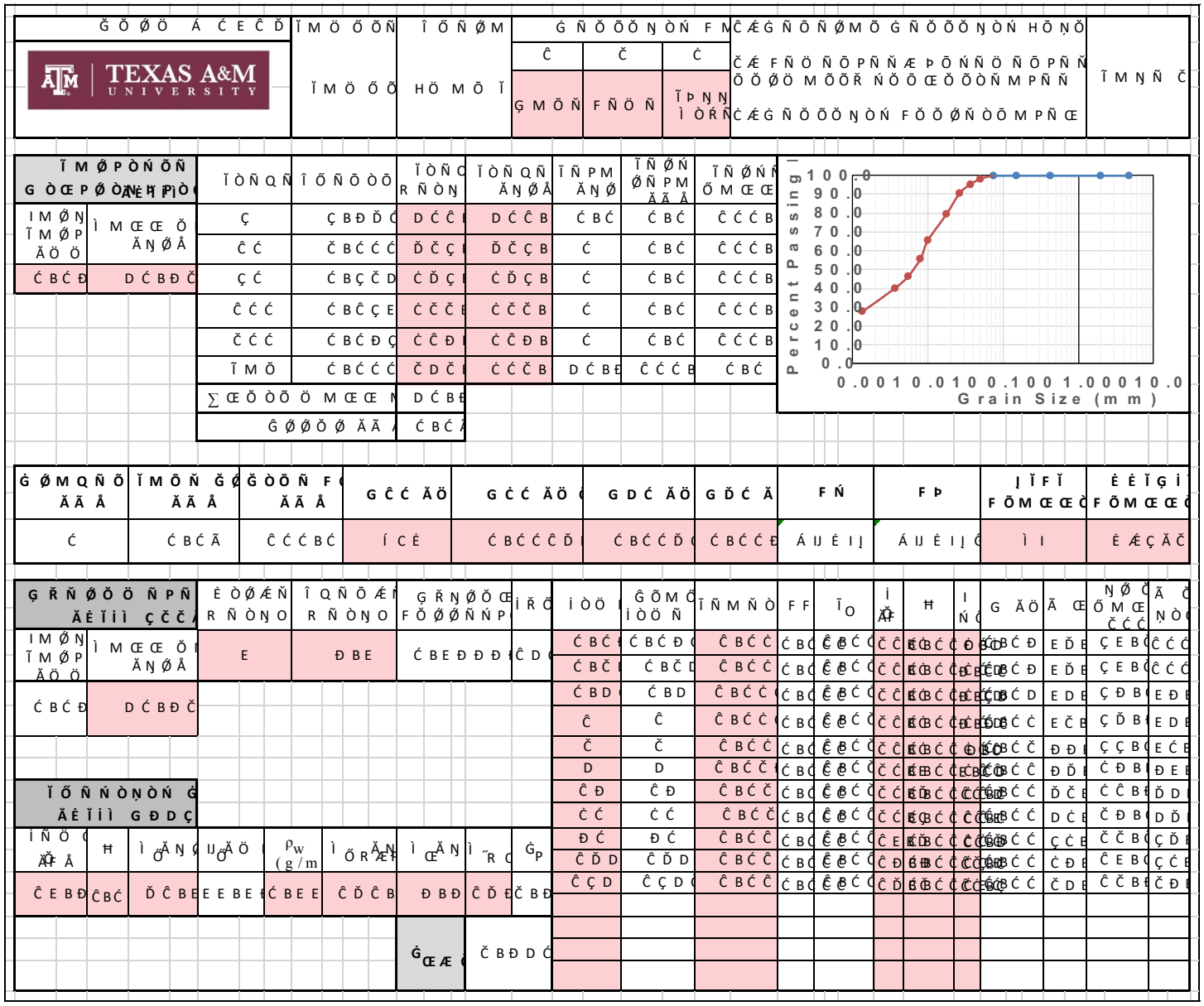

Figure B-134. FHWA Sample 2 – Page 2

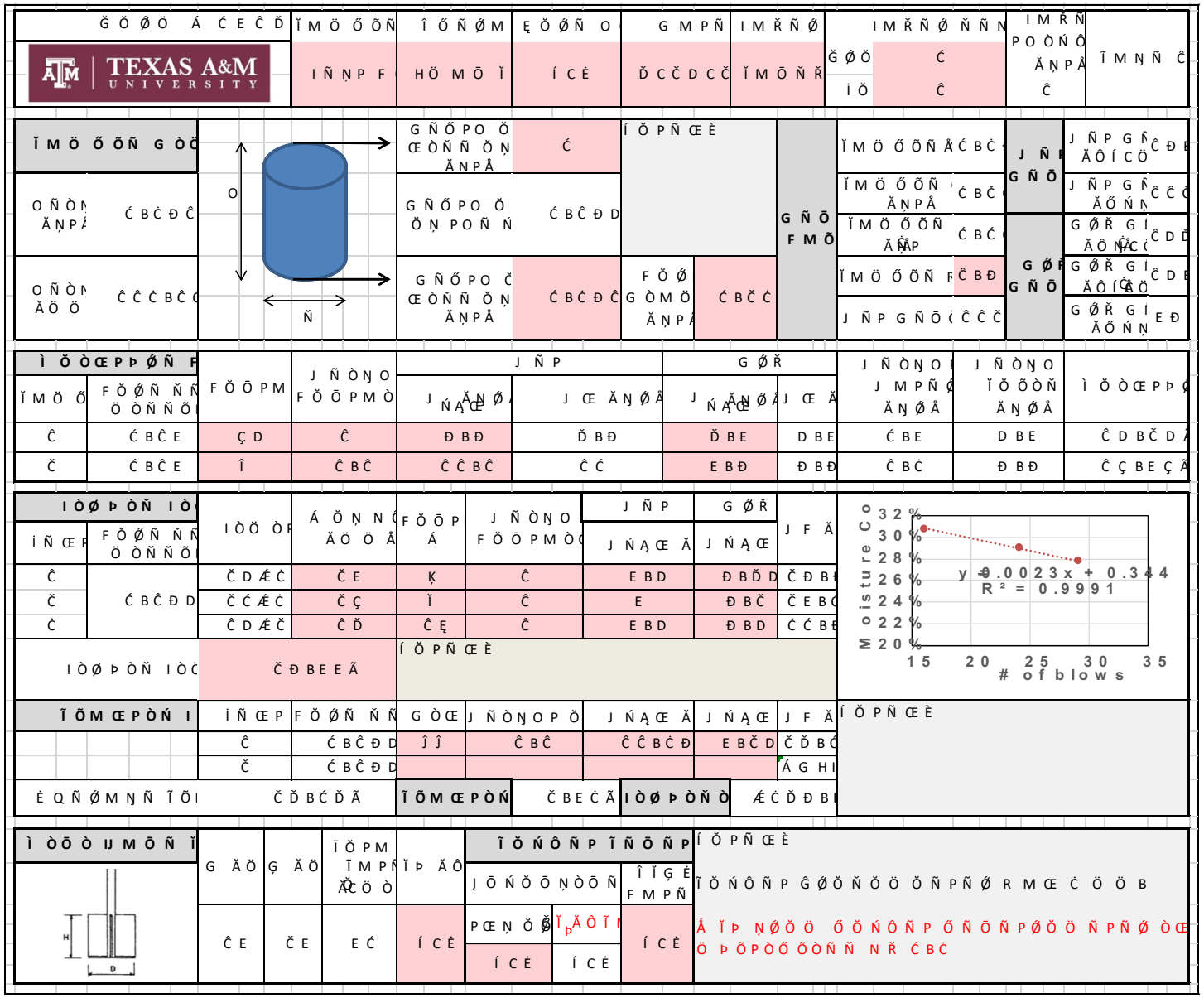

Figure B-135. Teton Dam Left Core – Page 1

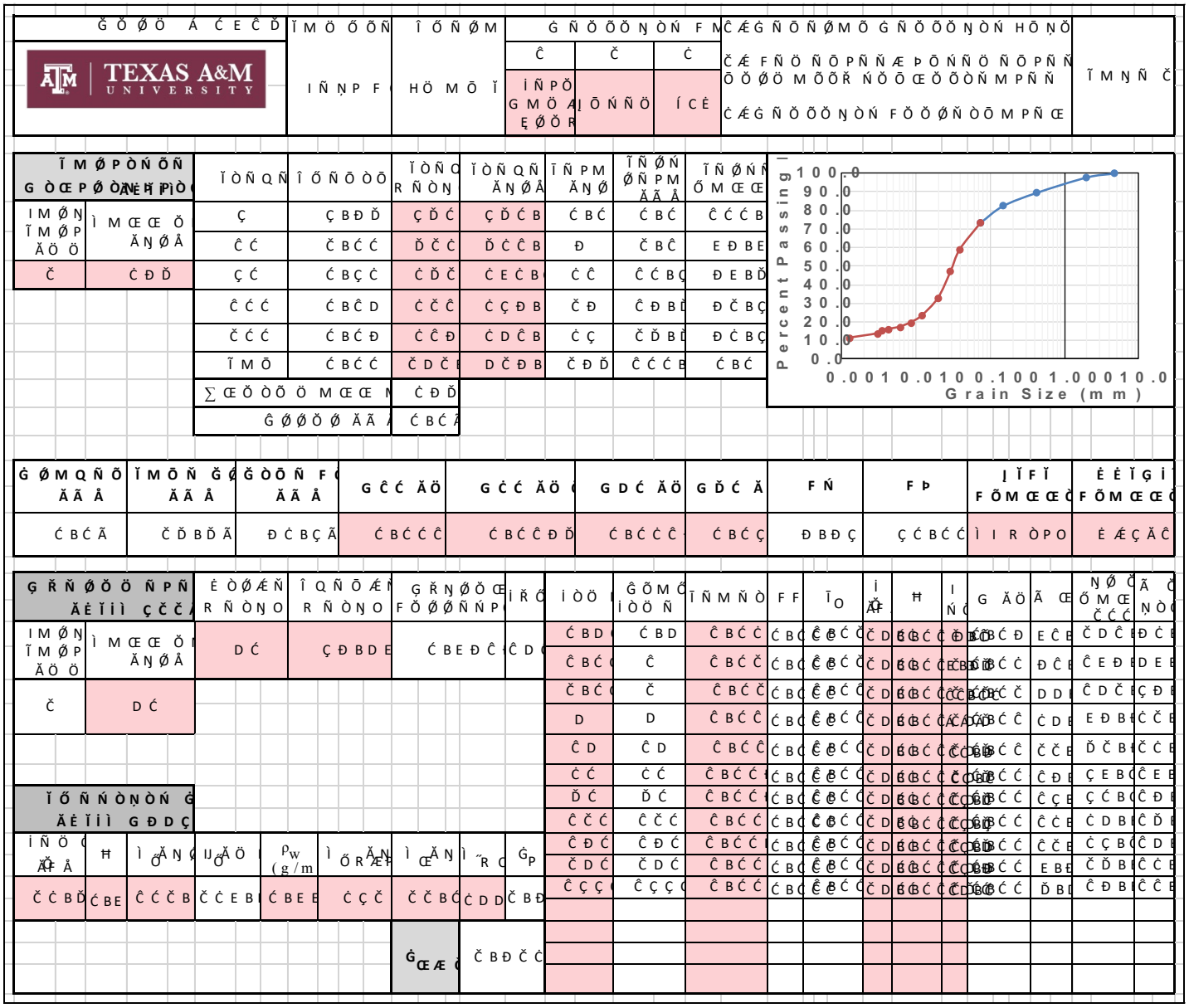

Figure B-136. Teton Dam Left Core – Page 2

Sand Samples - JET

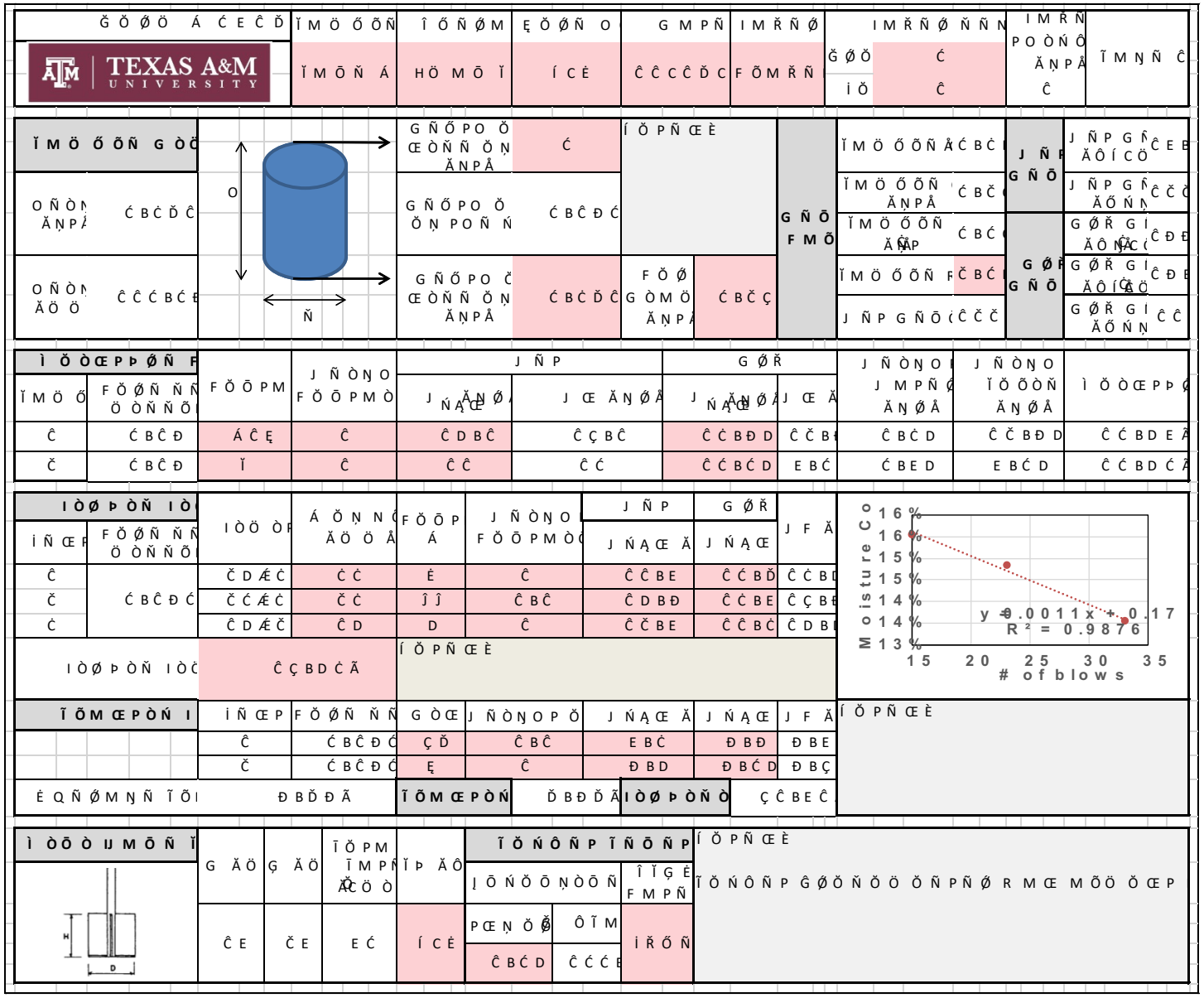

Figure B-137. Sand #1 – Page 1

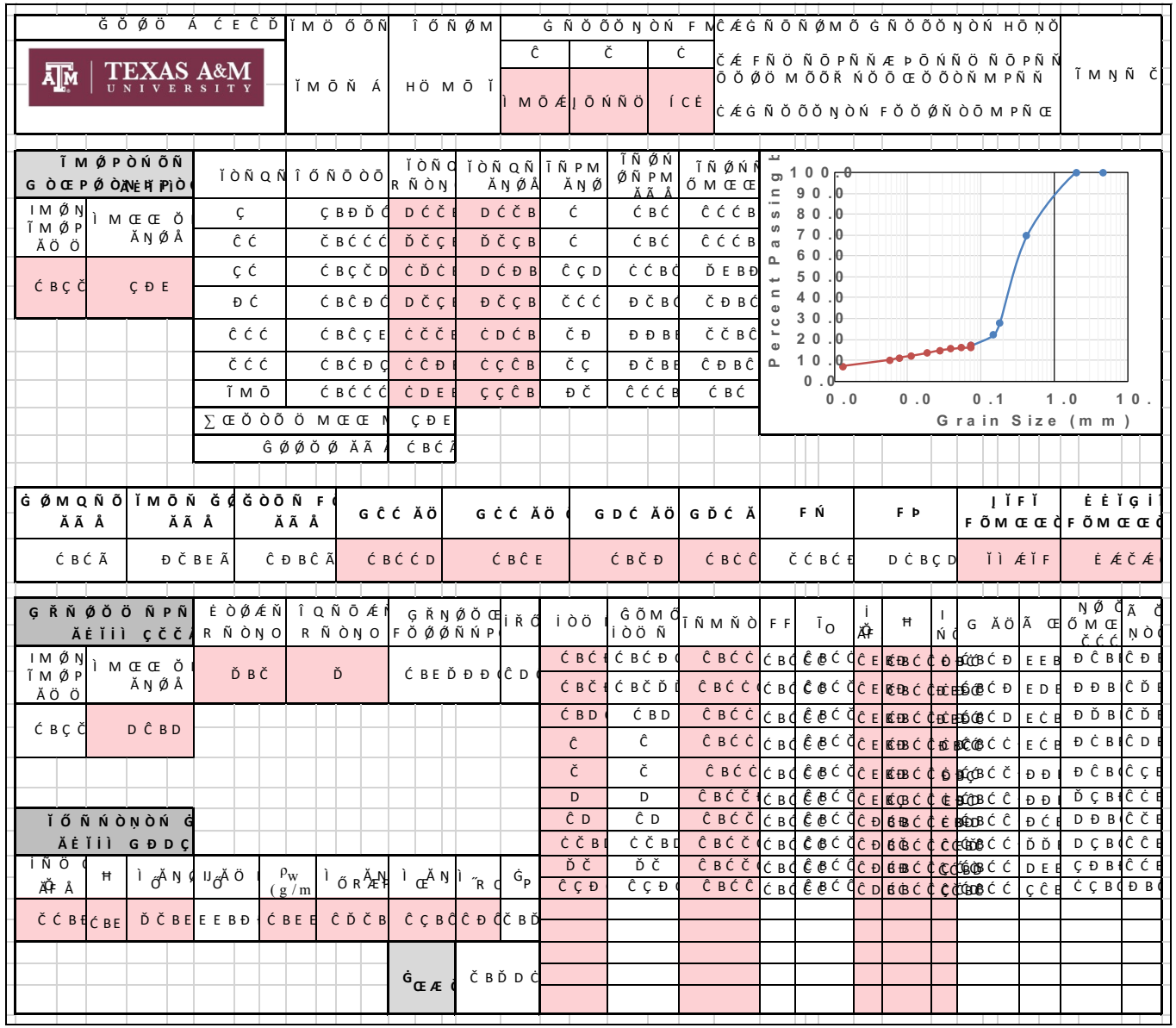

Figure B-138. Sand #1 – Page 2

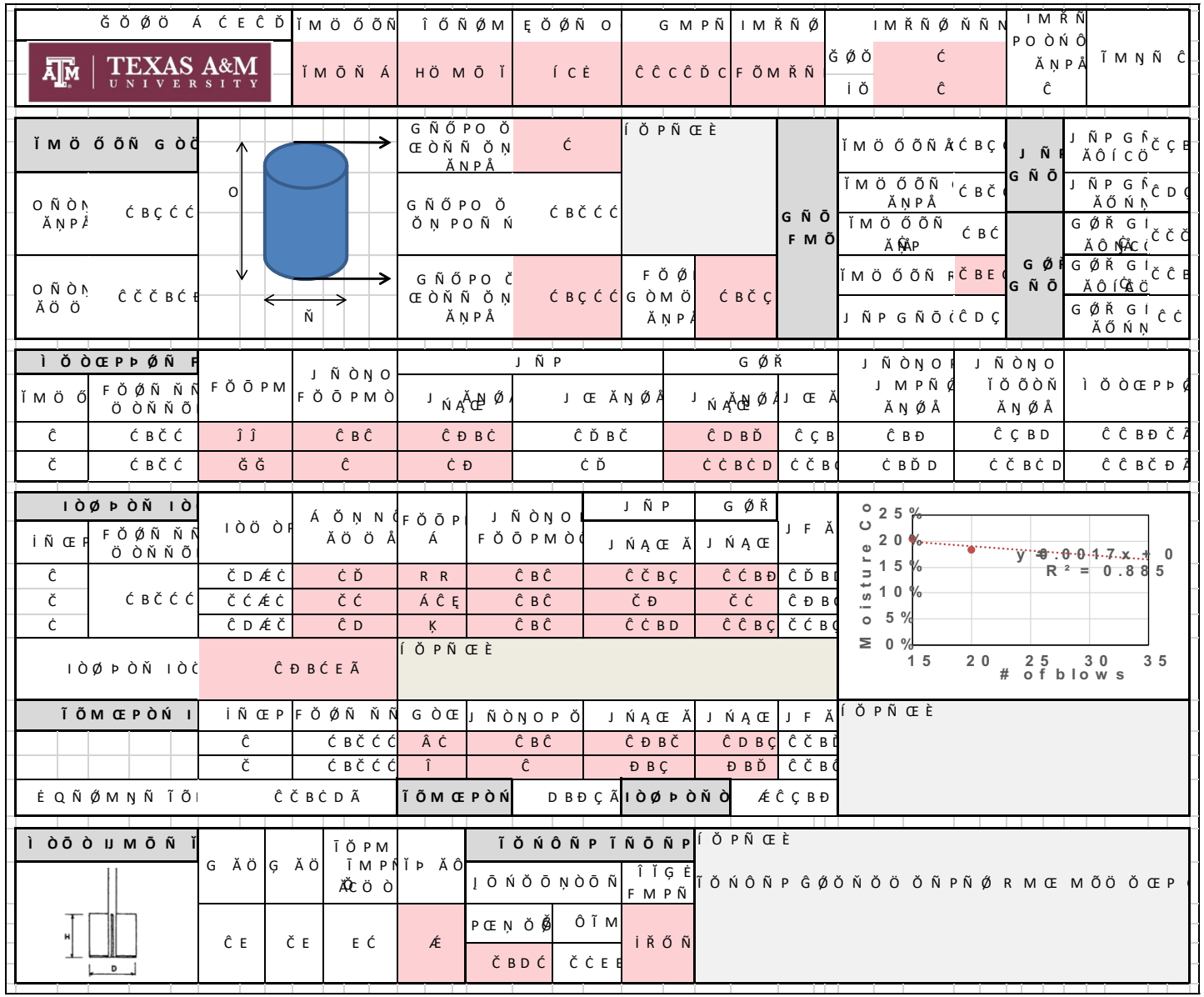

Figure B-139. Sand #2 – Page 1

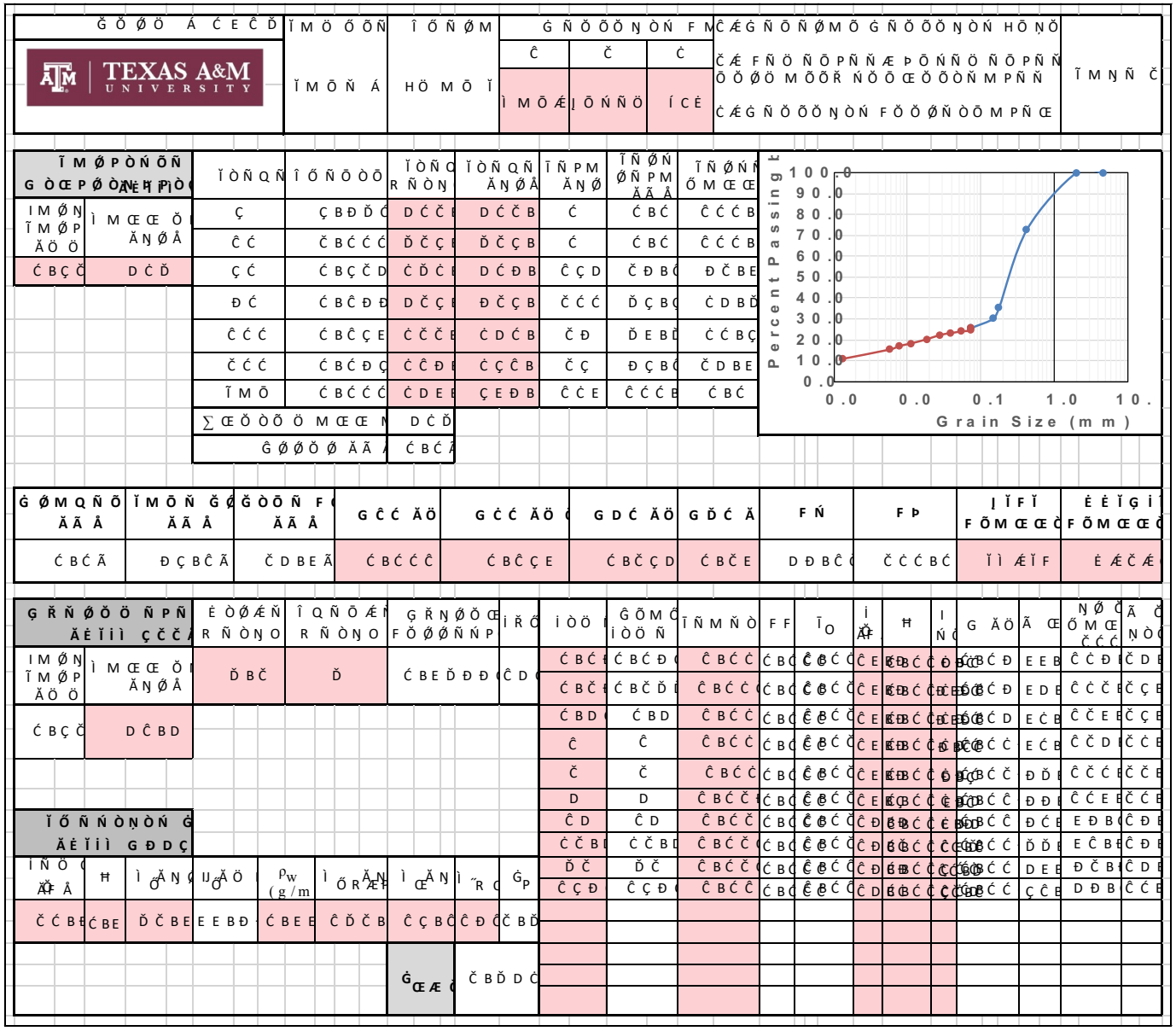

Figure B-140. Sand #2 – Page 2

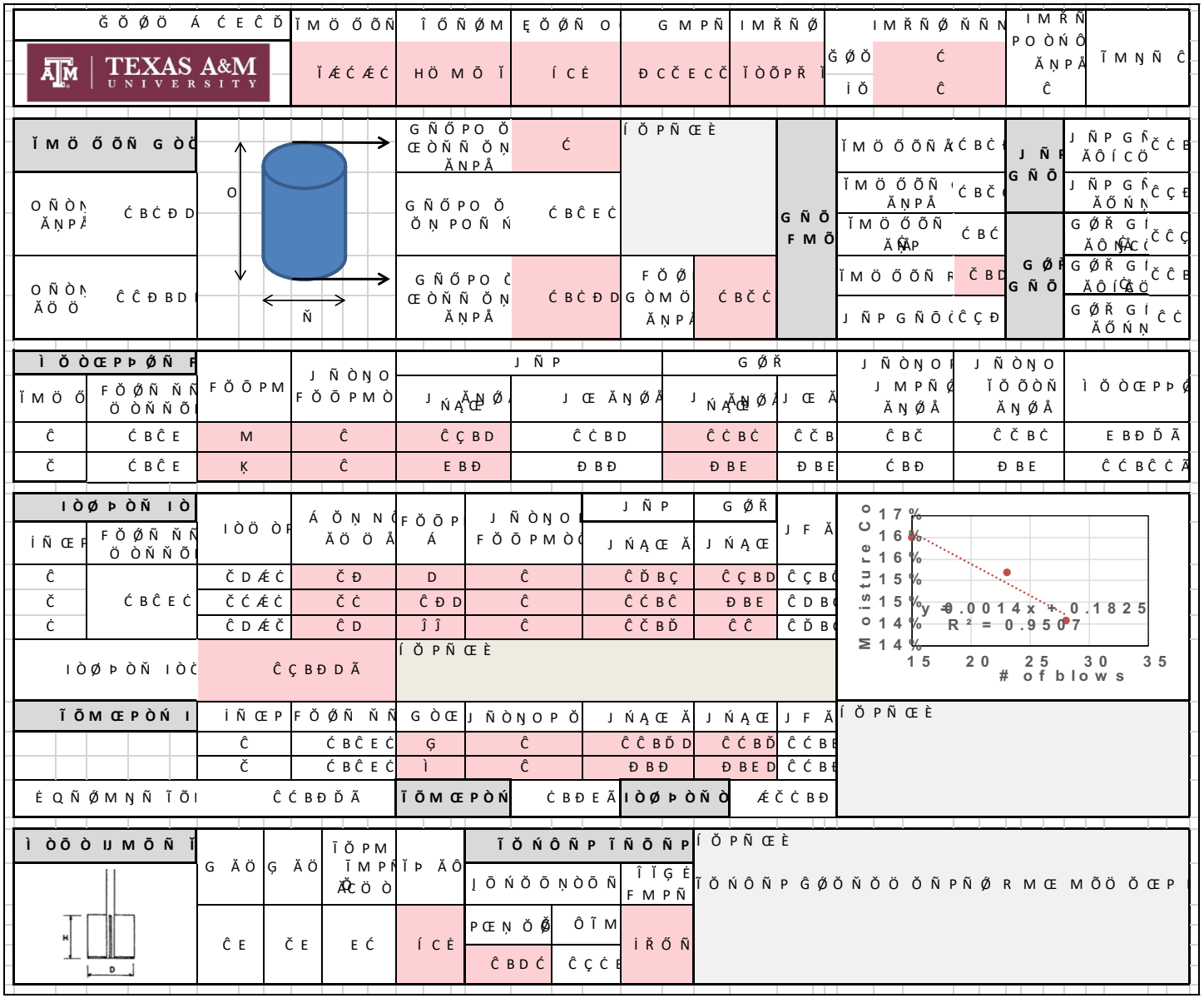

Figure B-141. S-0-0-0 – Page 1

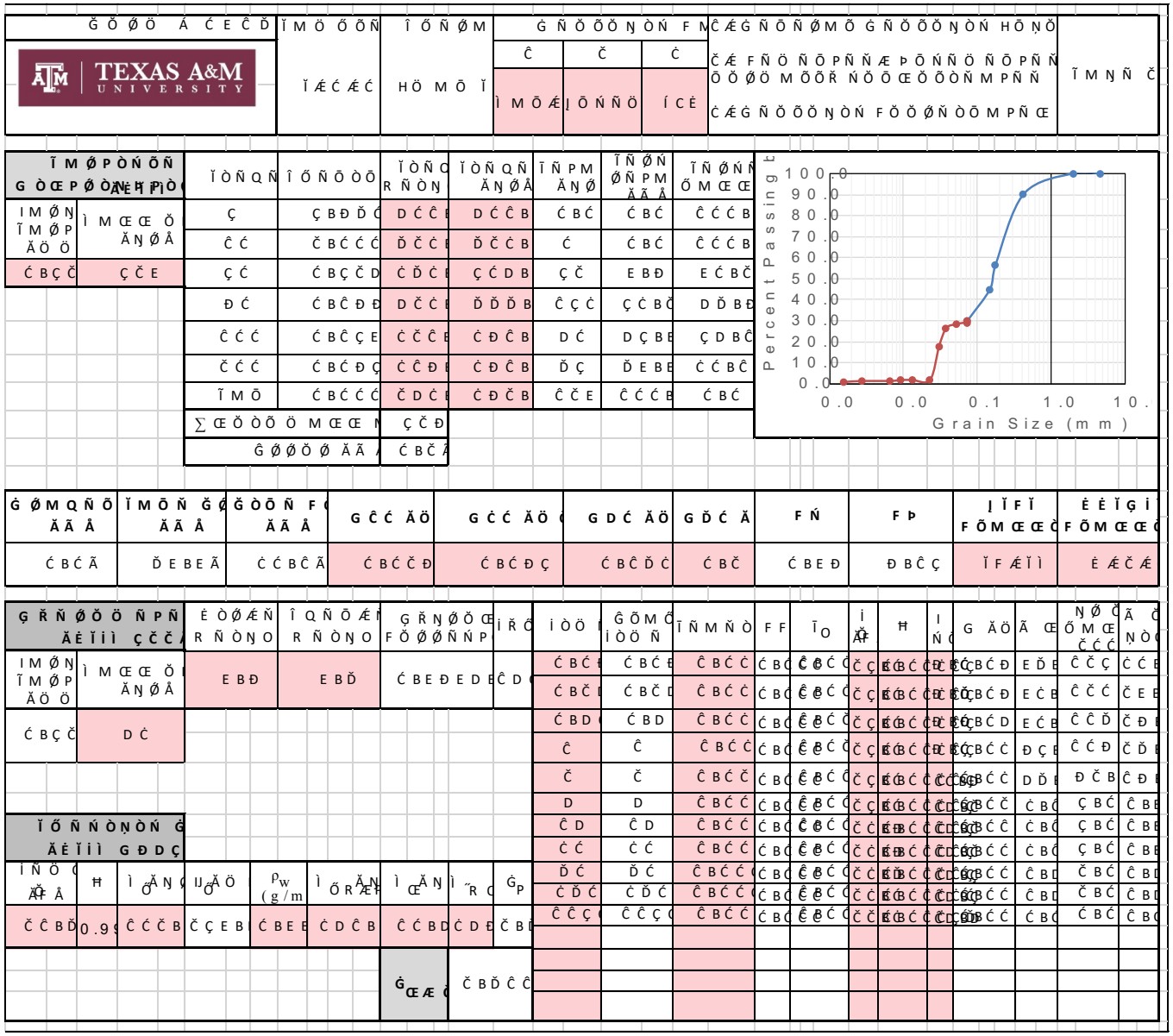

Figure B-142. S-0-0-0 – Page 2

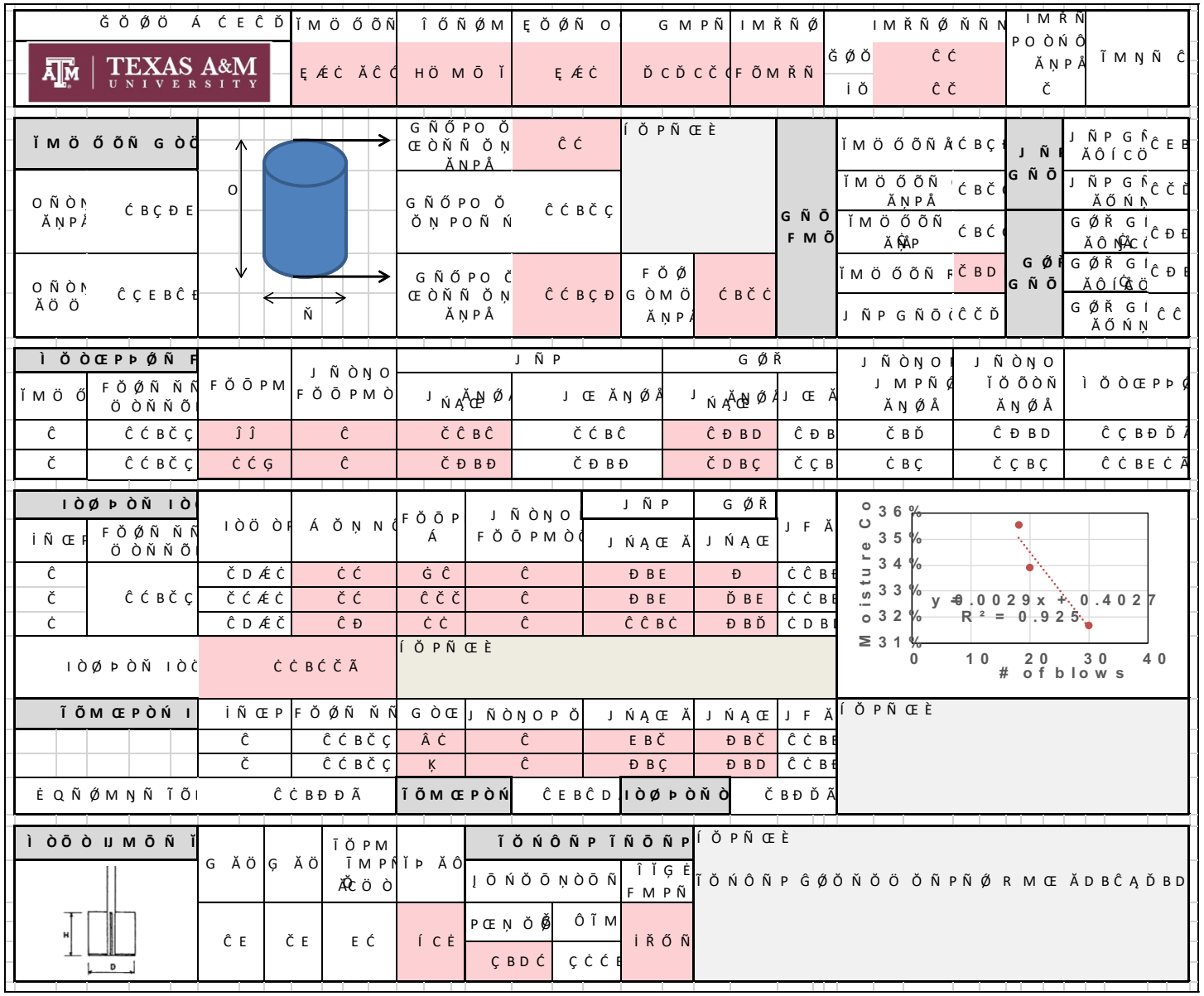

Figure B-143. B-3 (10'-12') Lissie Formation – Page 1

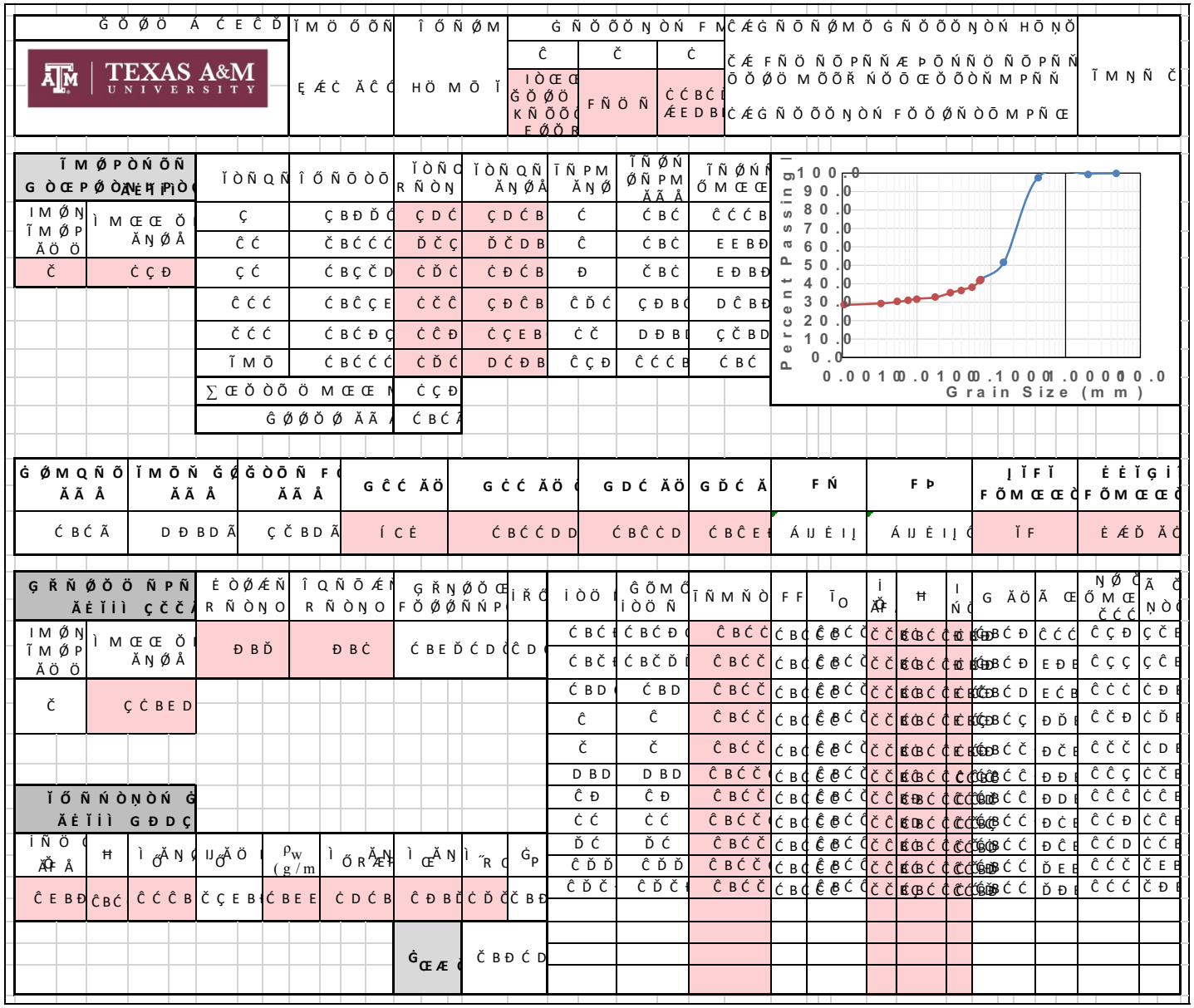

Figure B-144. B-3 (10'-12') Lissie Formation – Page 2

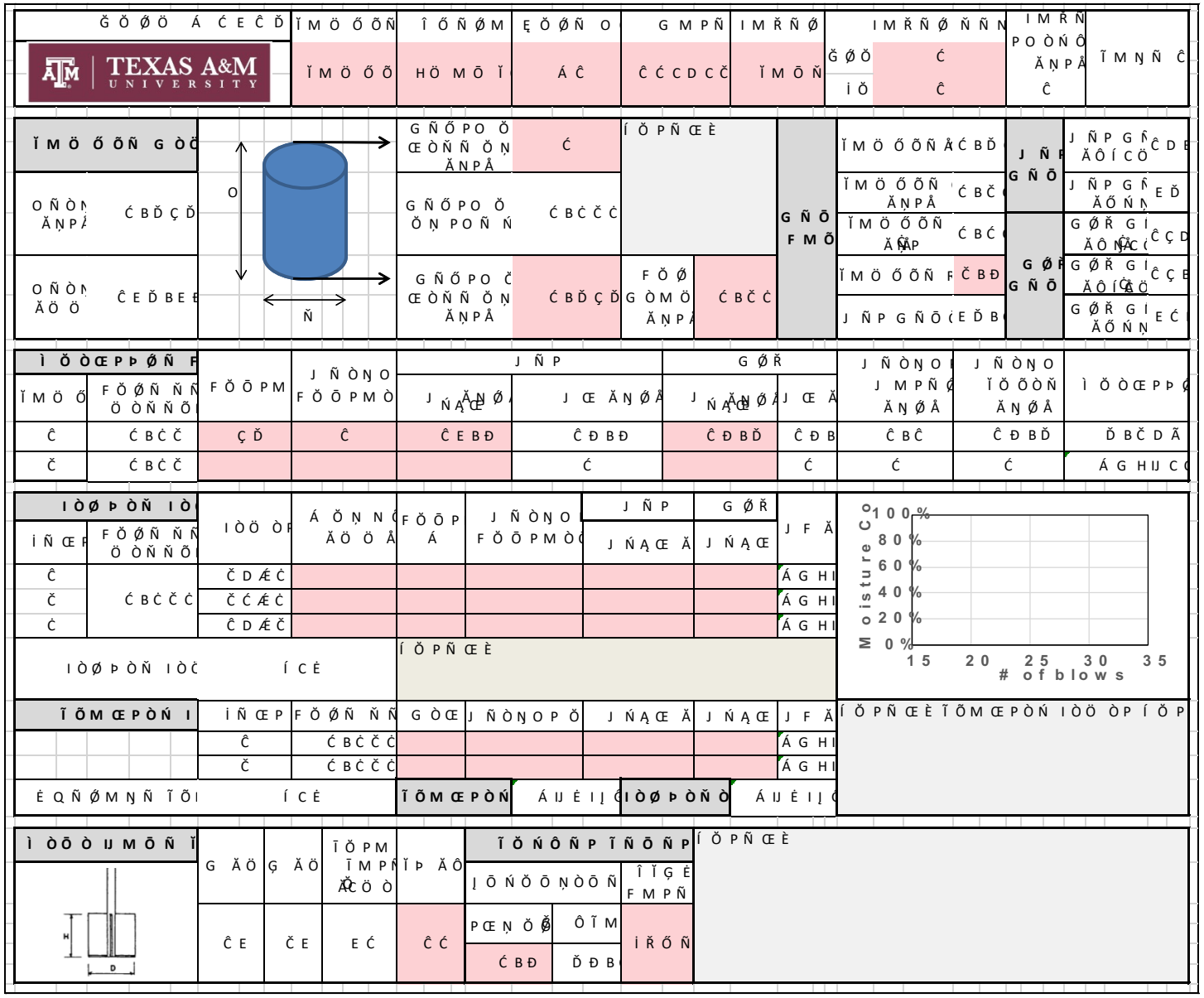

Figure B-145. GEER Sample #1 – Page 1

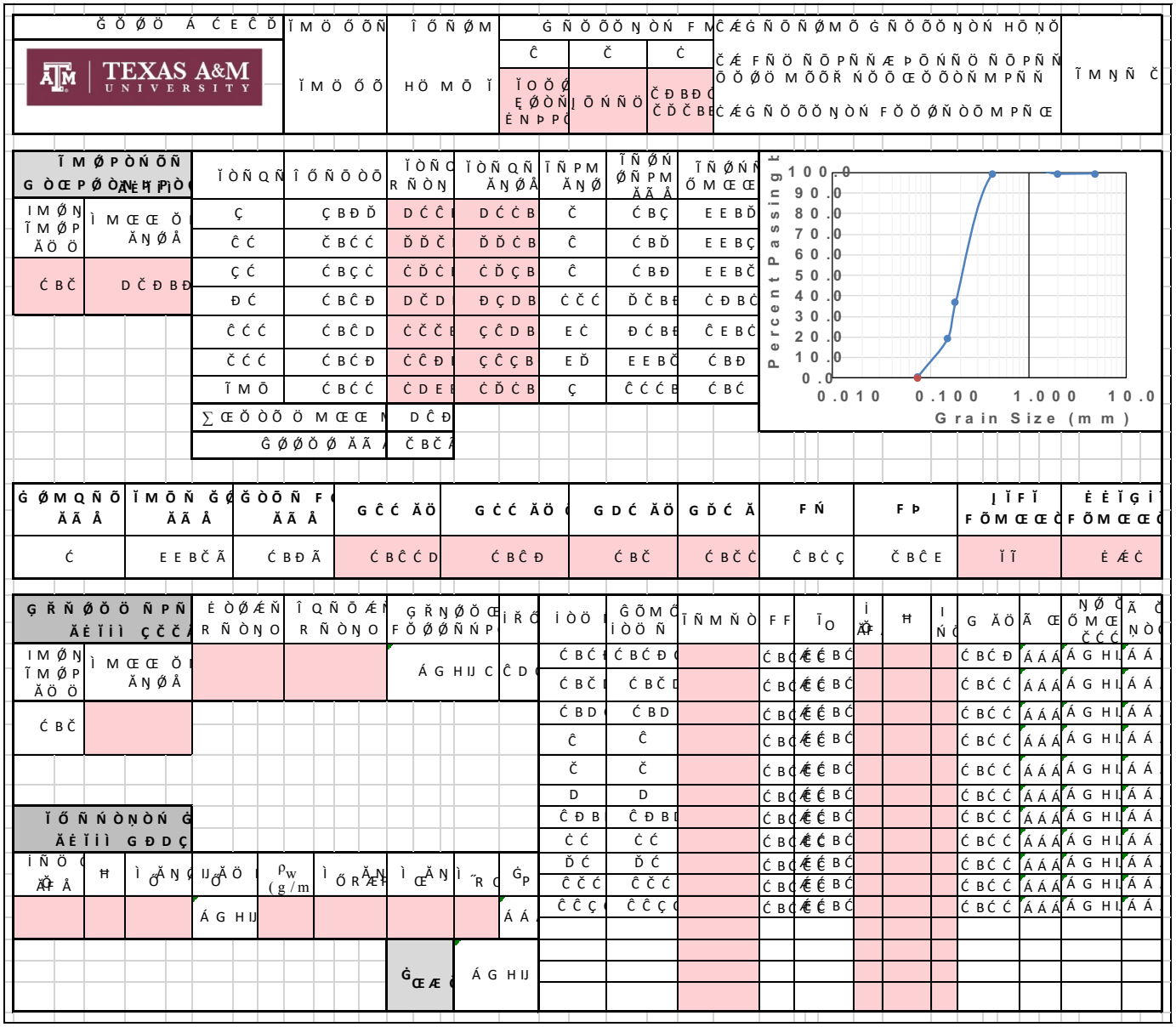

Figure B-146. GEER Sample #1 – Page 2

Clay Samples - HET

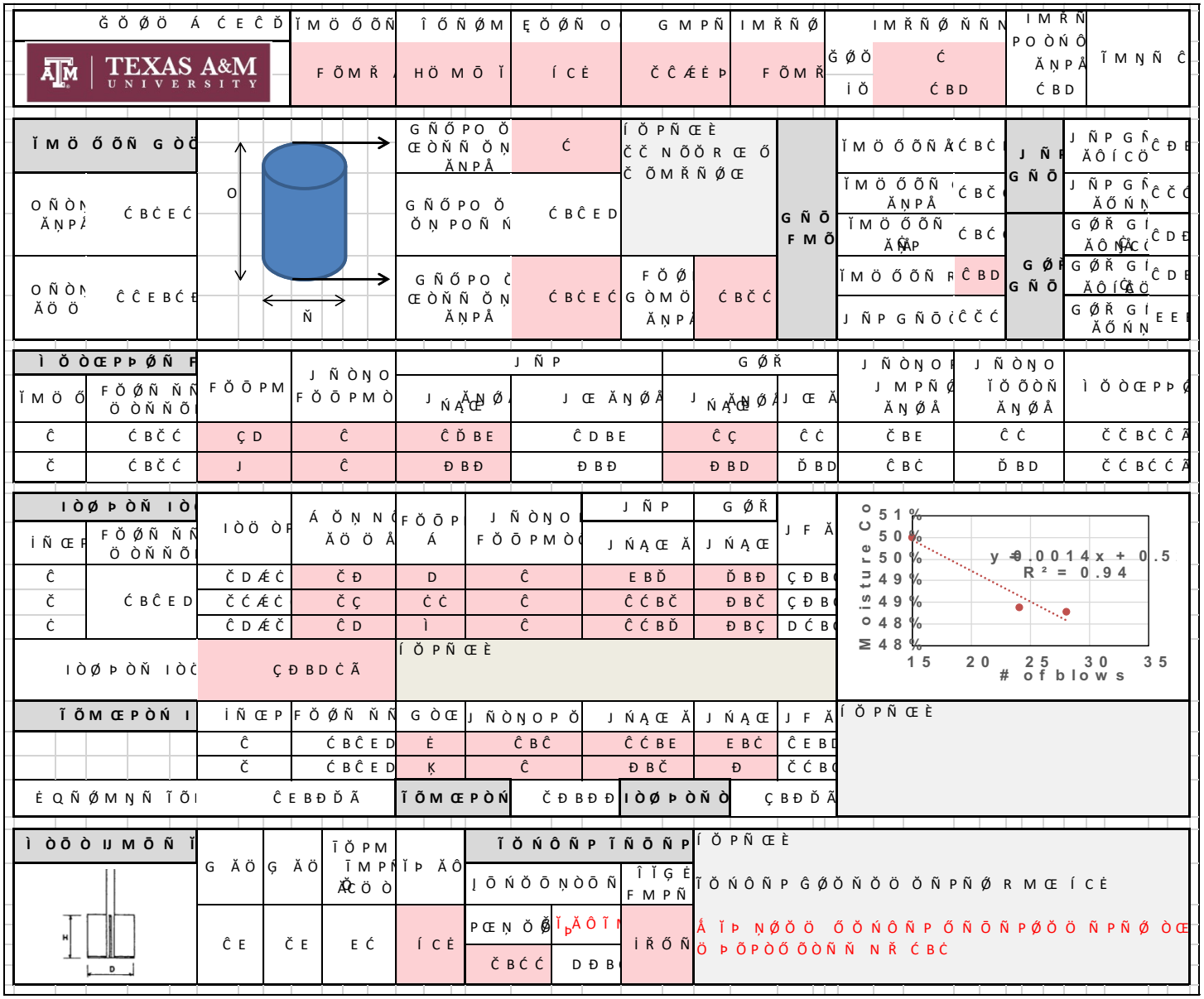

Figure B-147. Clay #1 – Page 1

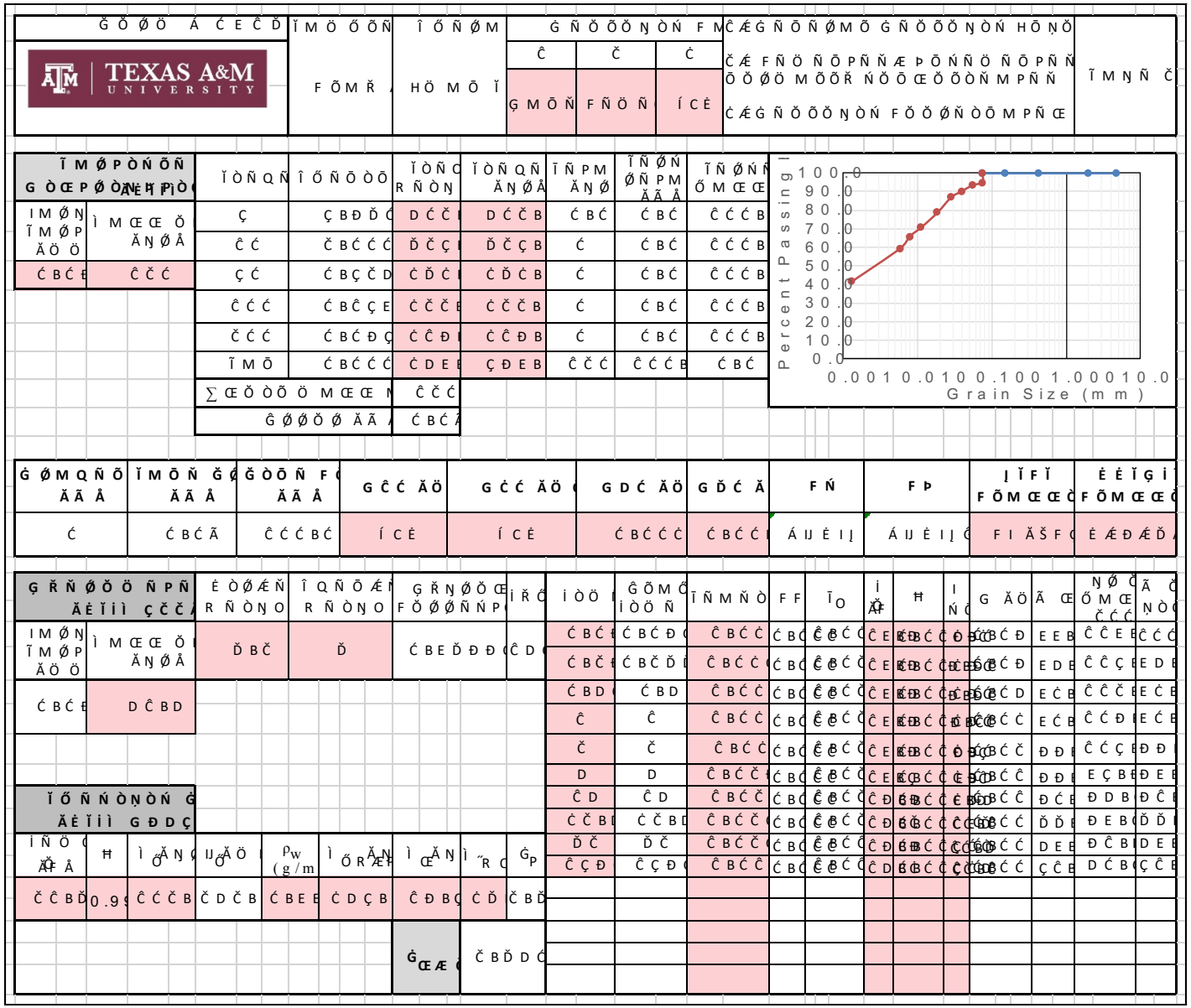

Figure B-148. Clay #1 – Page 2

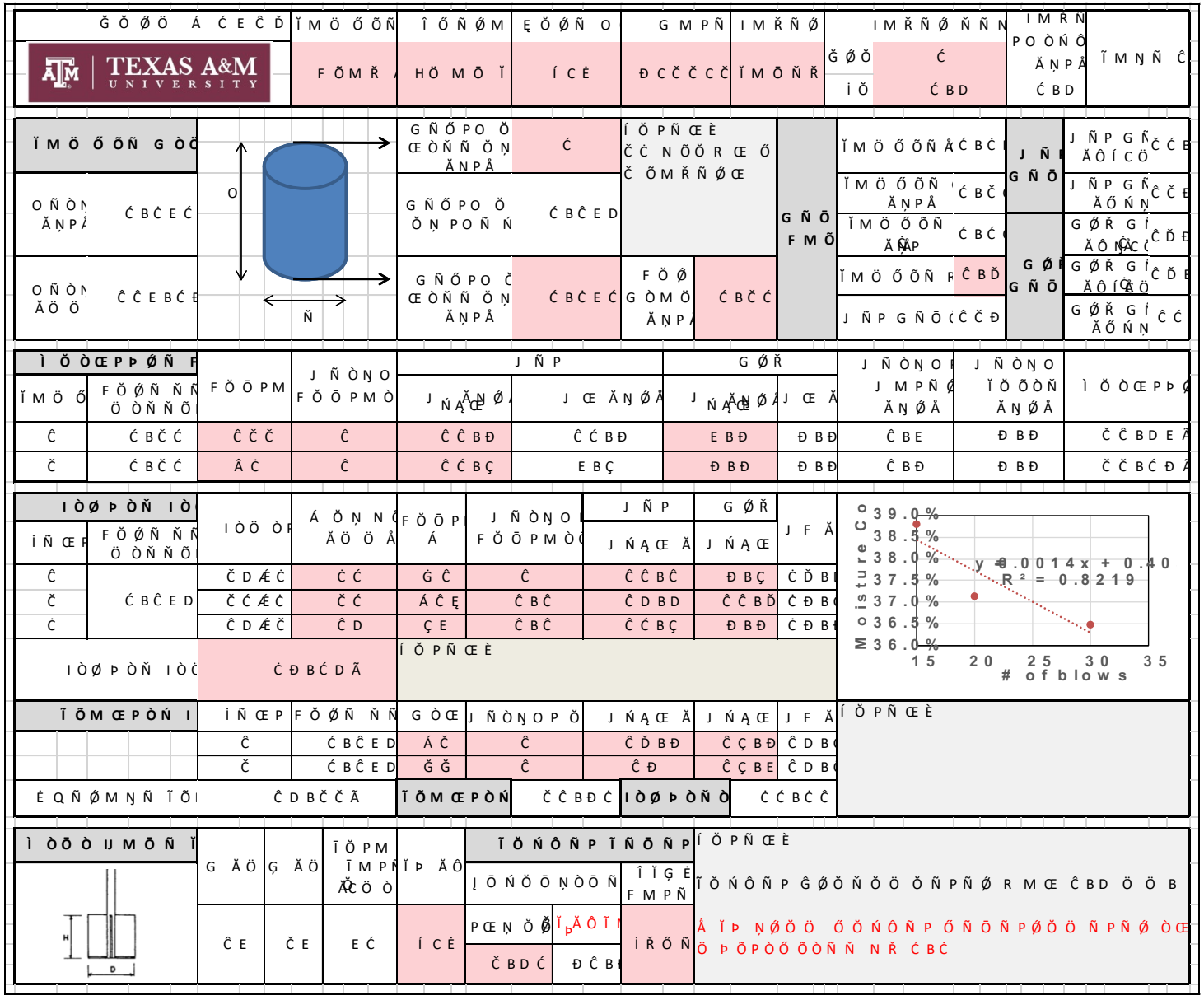

Figure B-149. Clay #2 – Page 1

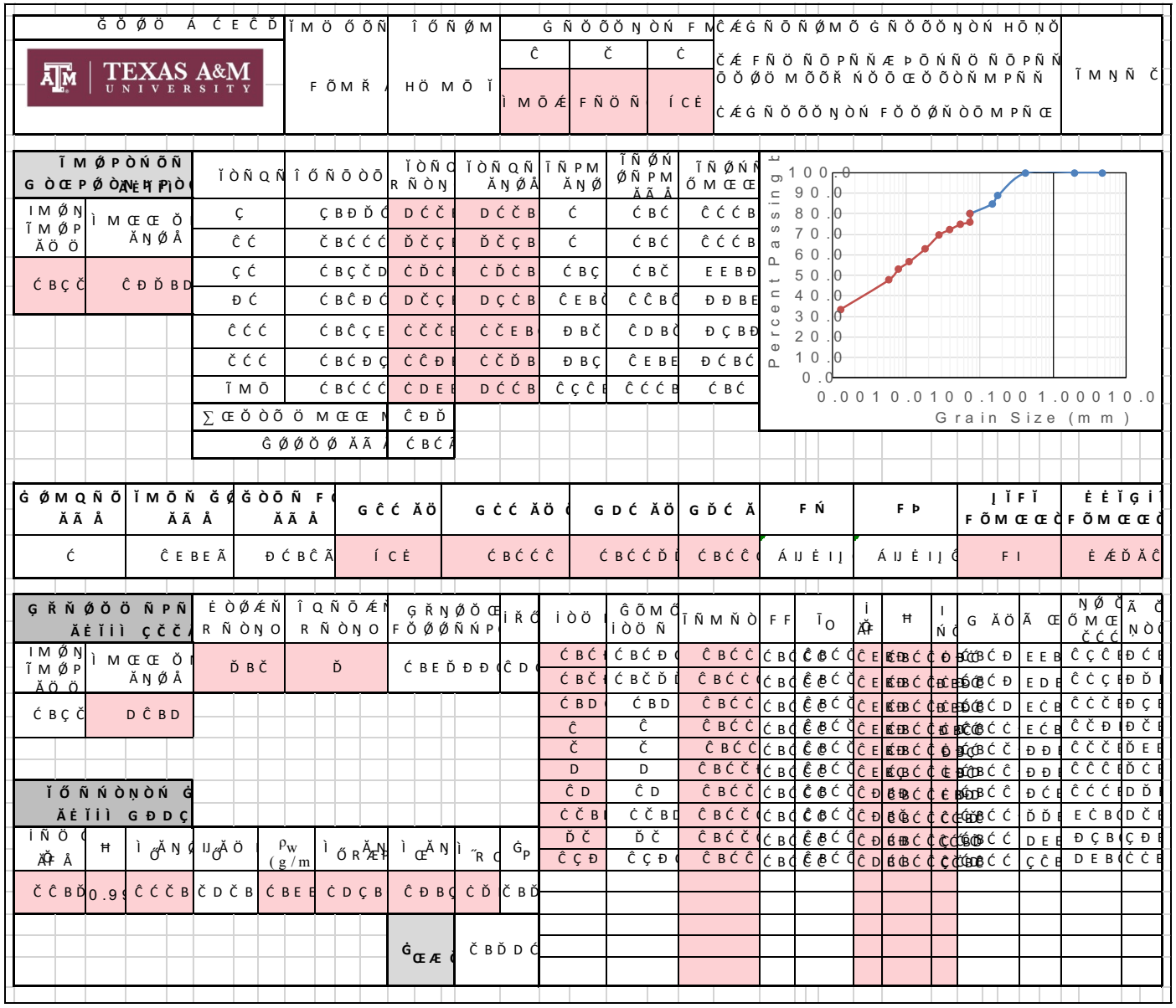

Figure B-150. Clay #2 – Page 2

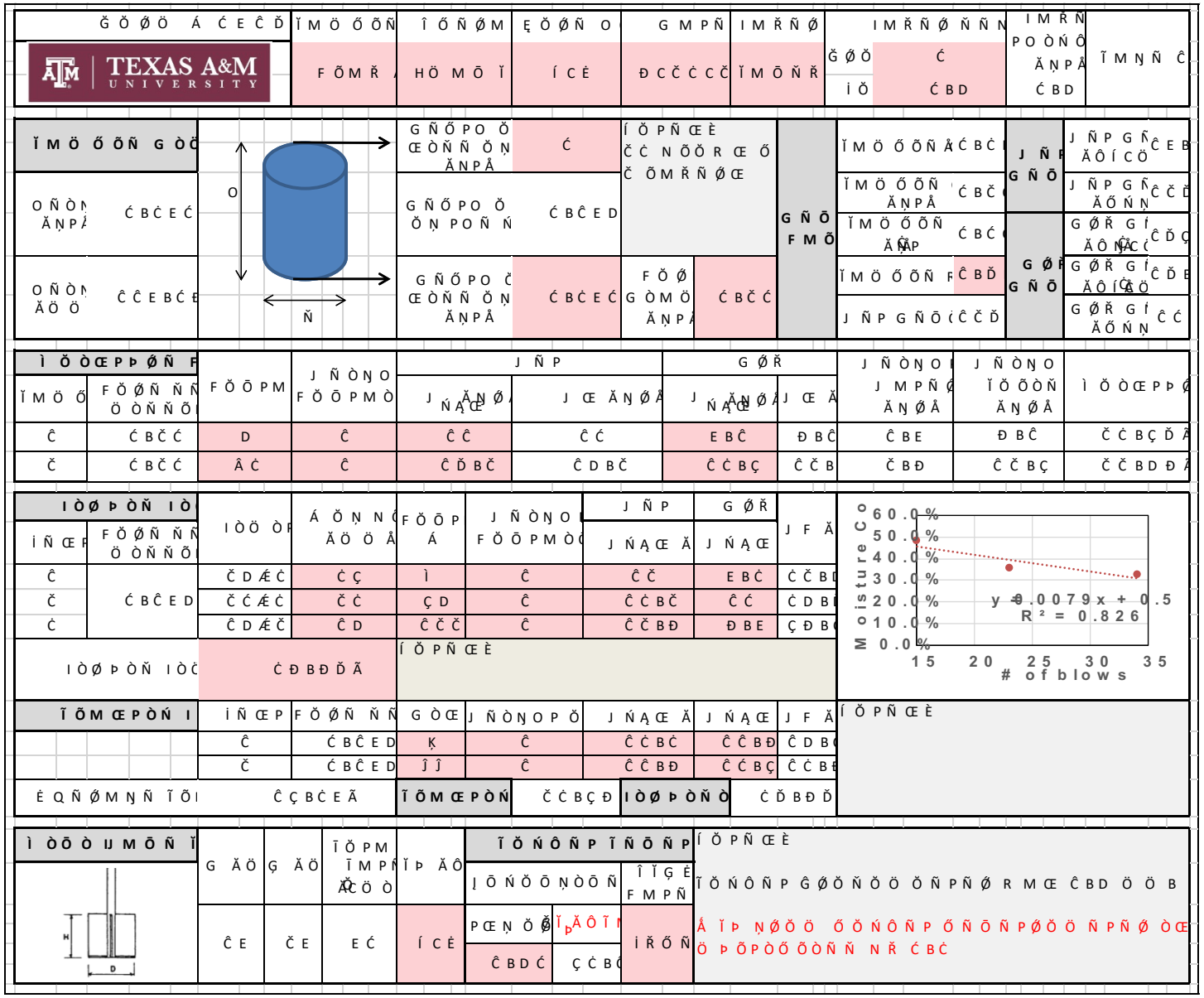

Figure B-151. Clay #3 – Page 1

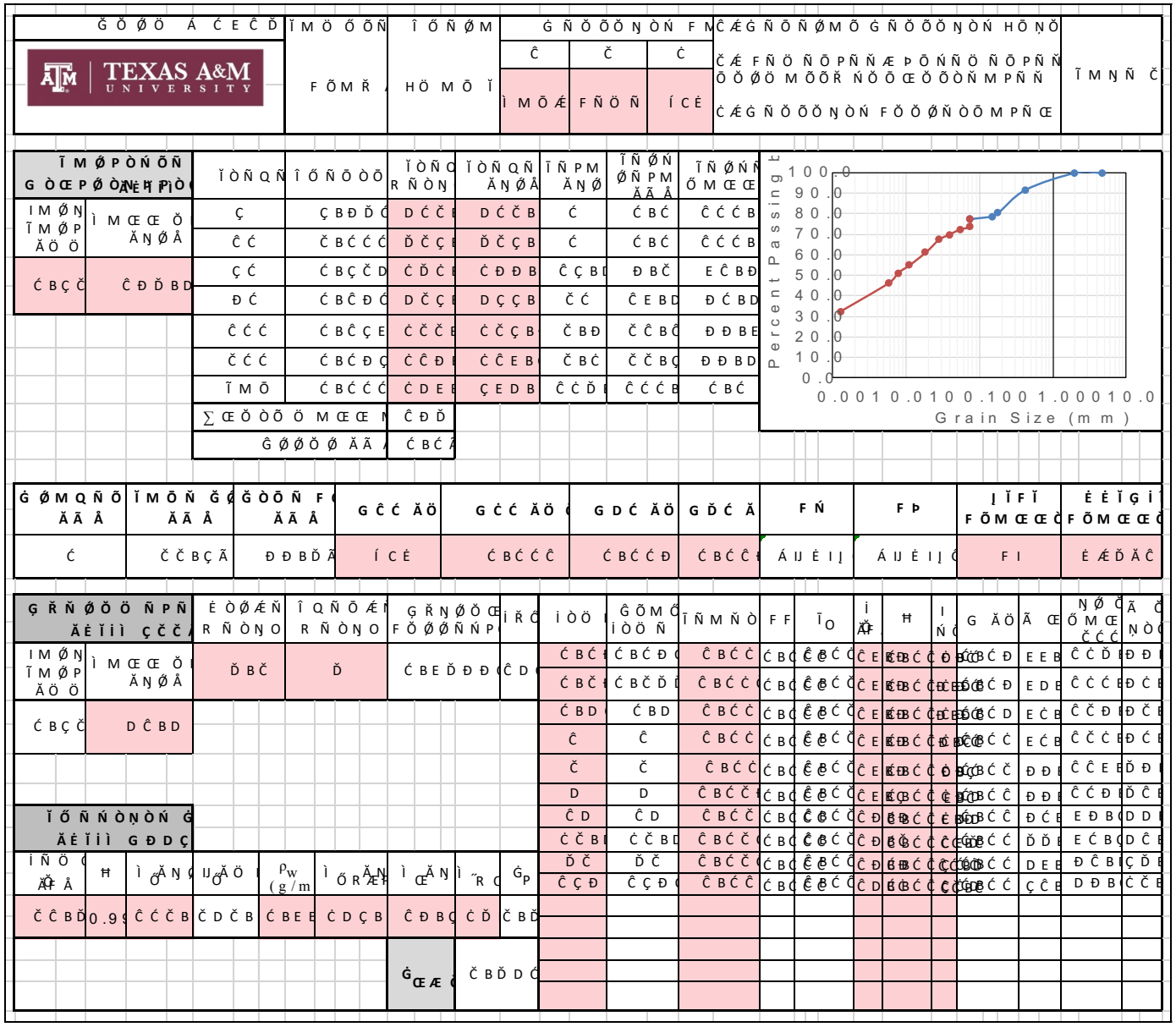

Figure B-152. Clay #3 – Page 2

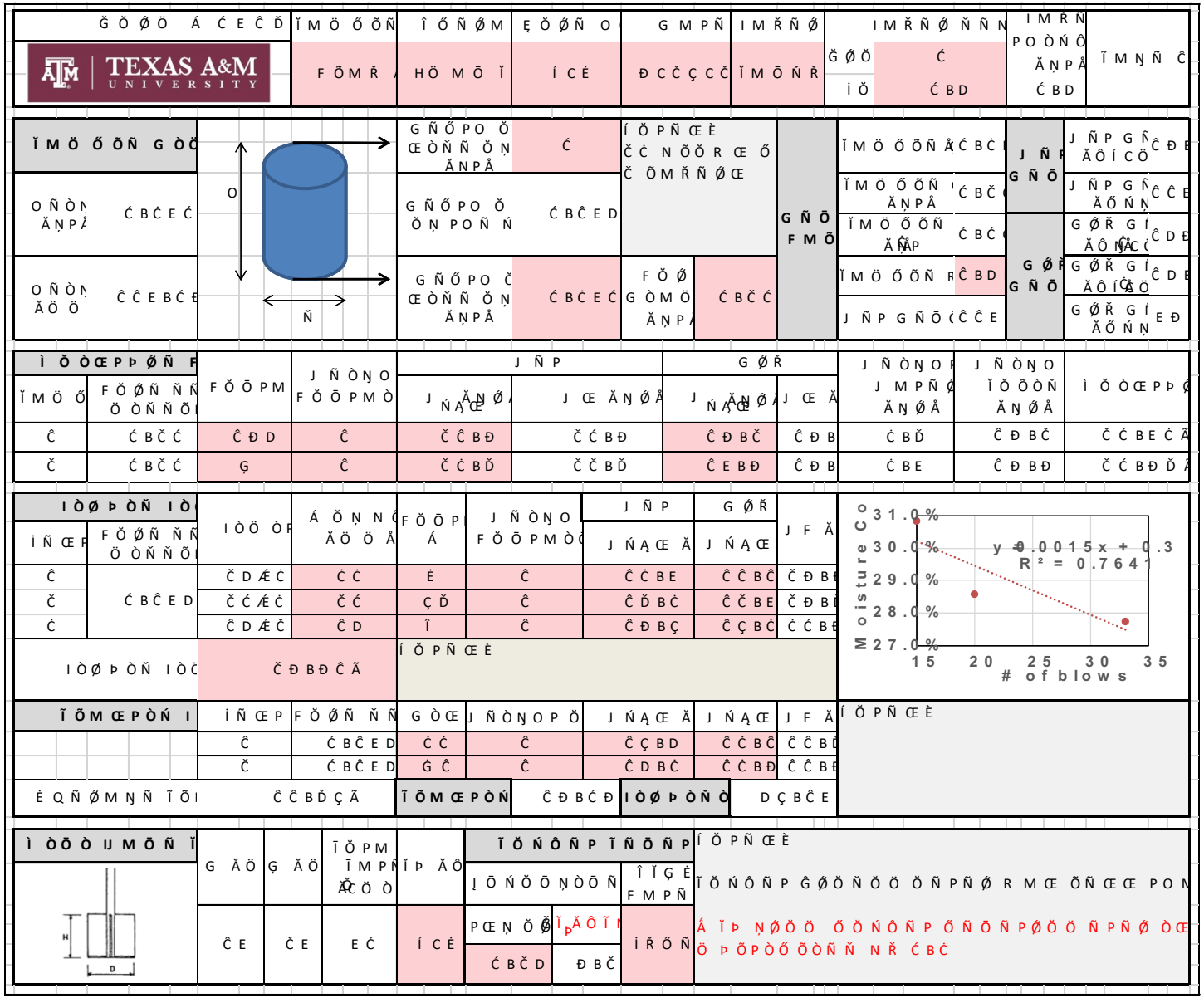

Figure B-153. Clay #4 – Page 1

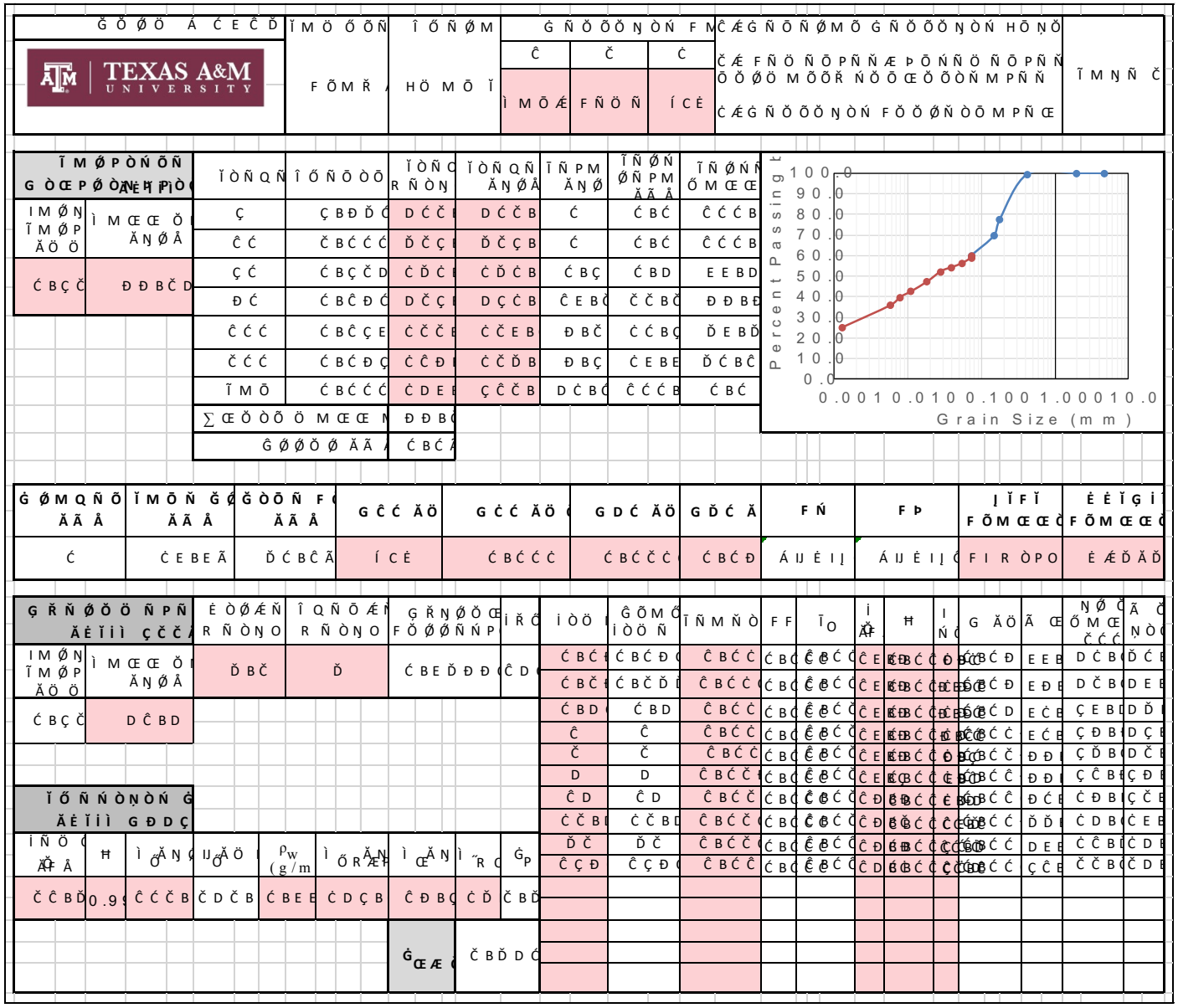

Figure B-154. Clay #4 – Page 2

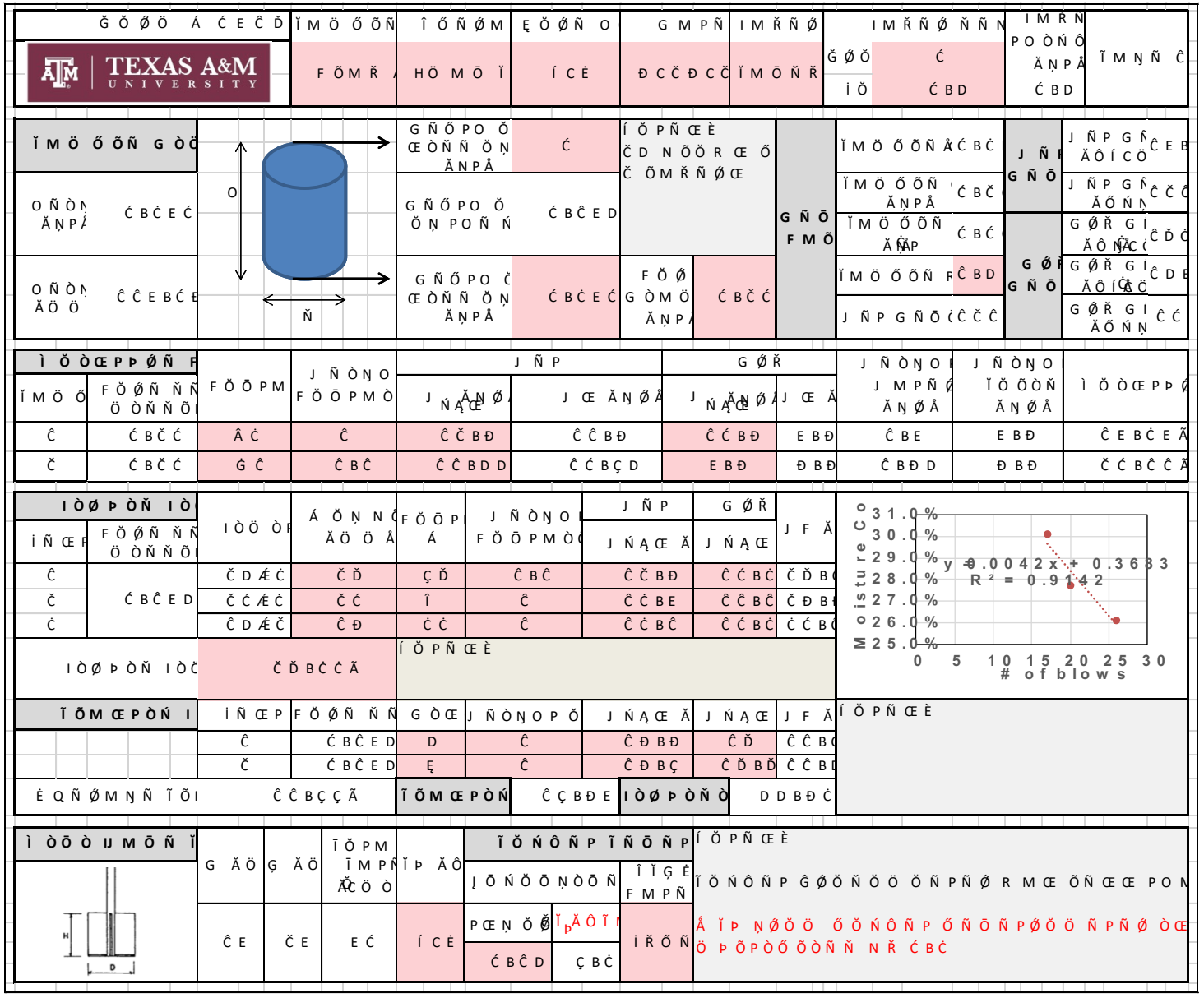

Figure B-155. Clay #5 – Page 1

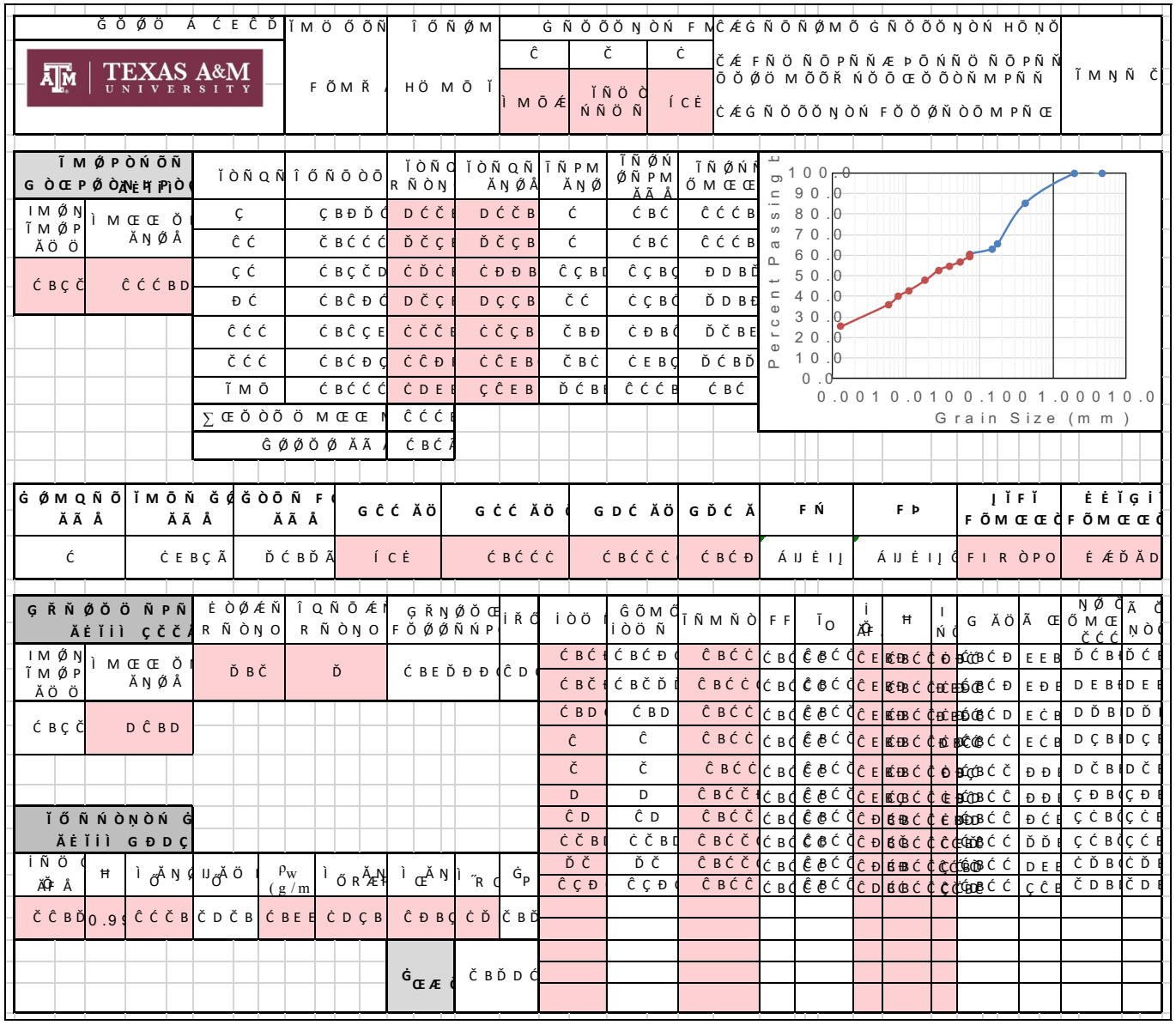

Figure B-156. Clay #5 – Page 2

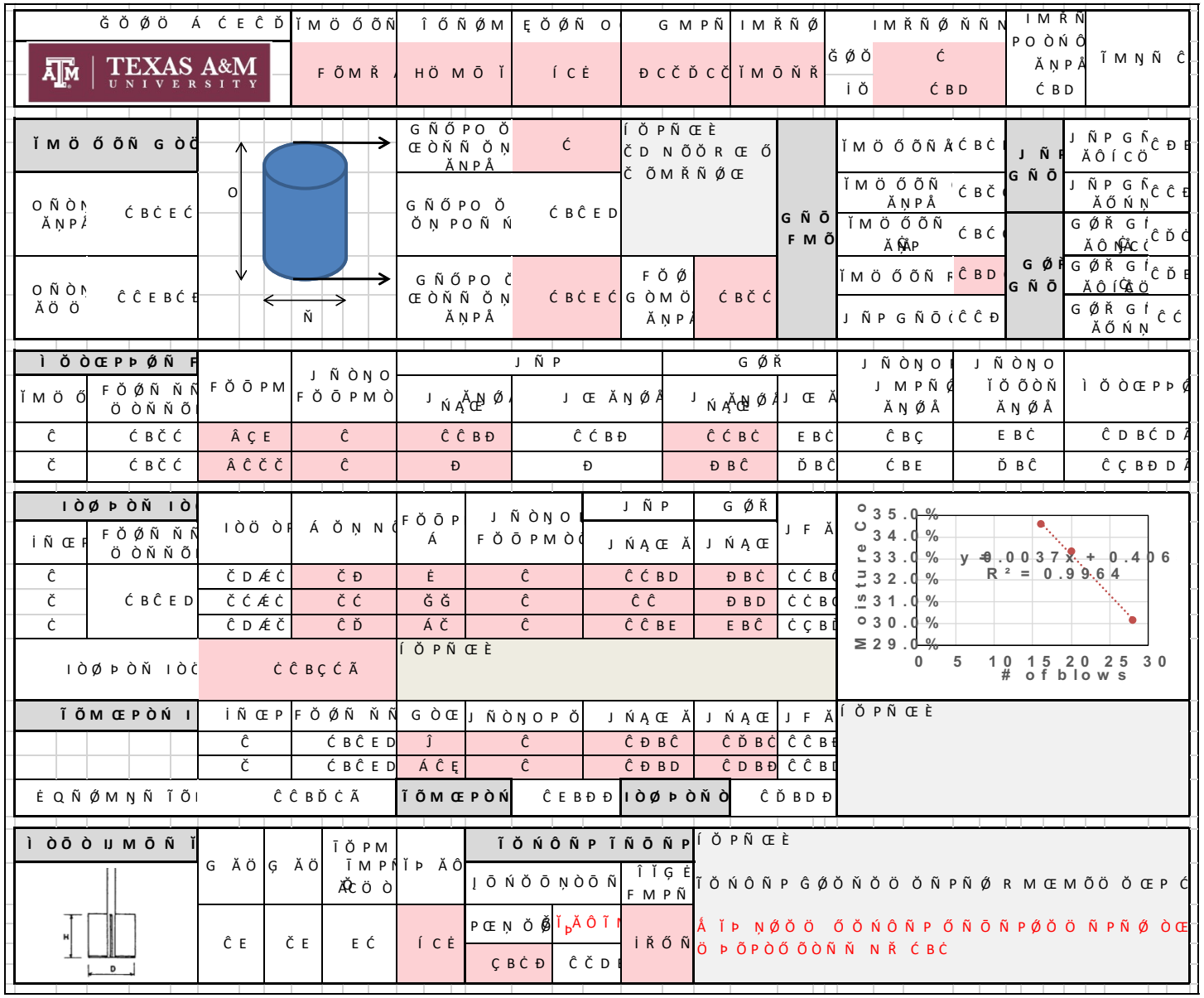

Figure B-157. Clay #6 – Page 1

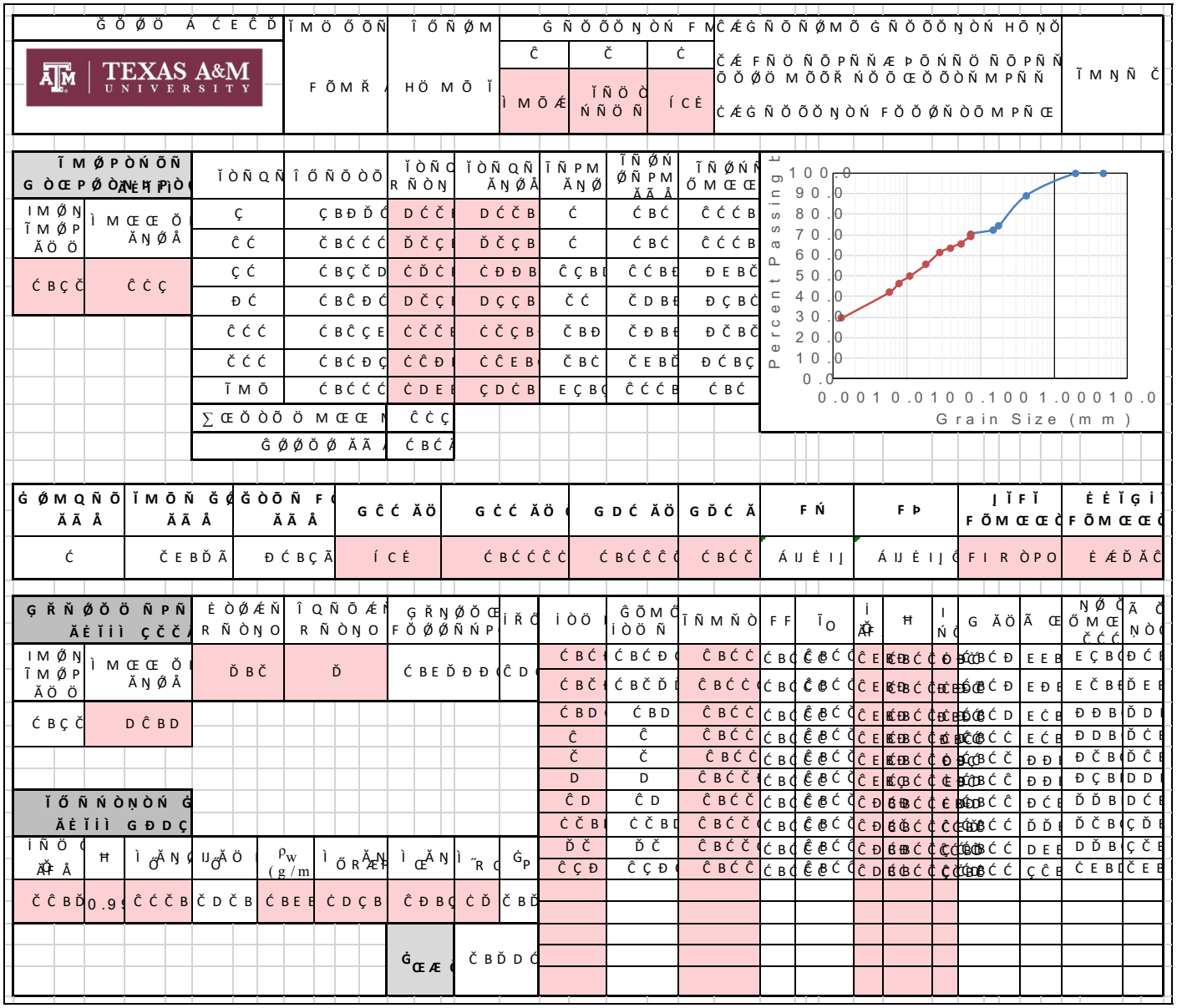

Figure B-158. Clay #6 – Page 2

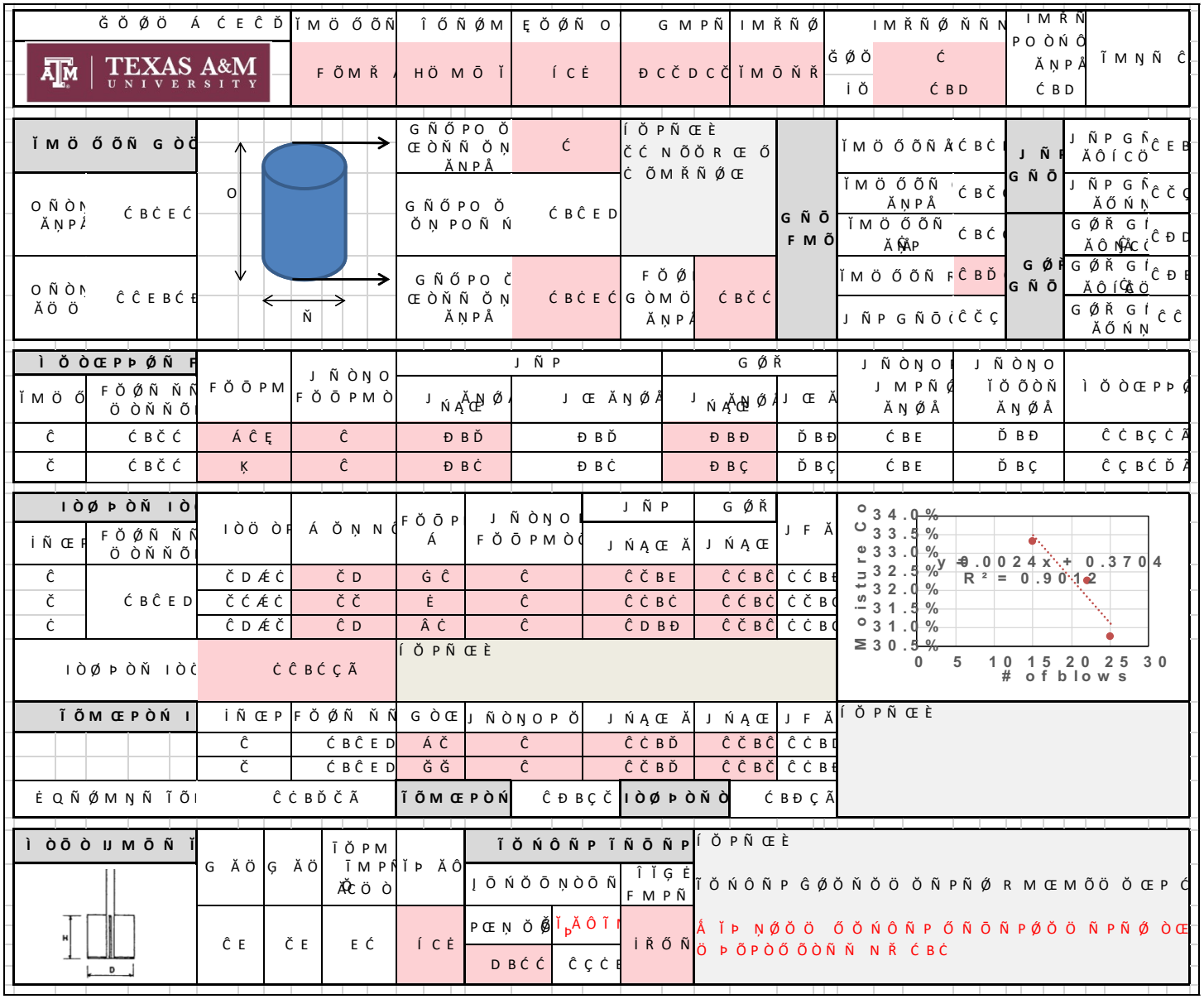

Figure B-159. Clay #7 – Page 1

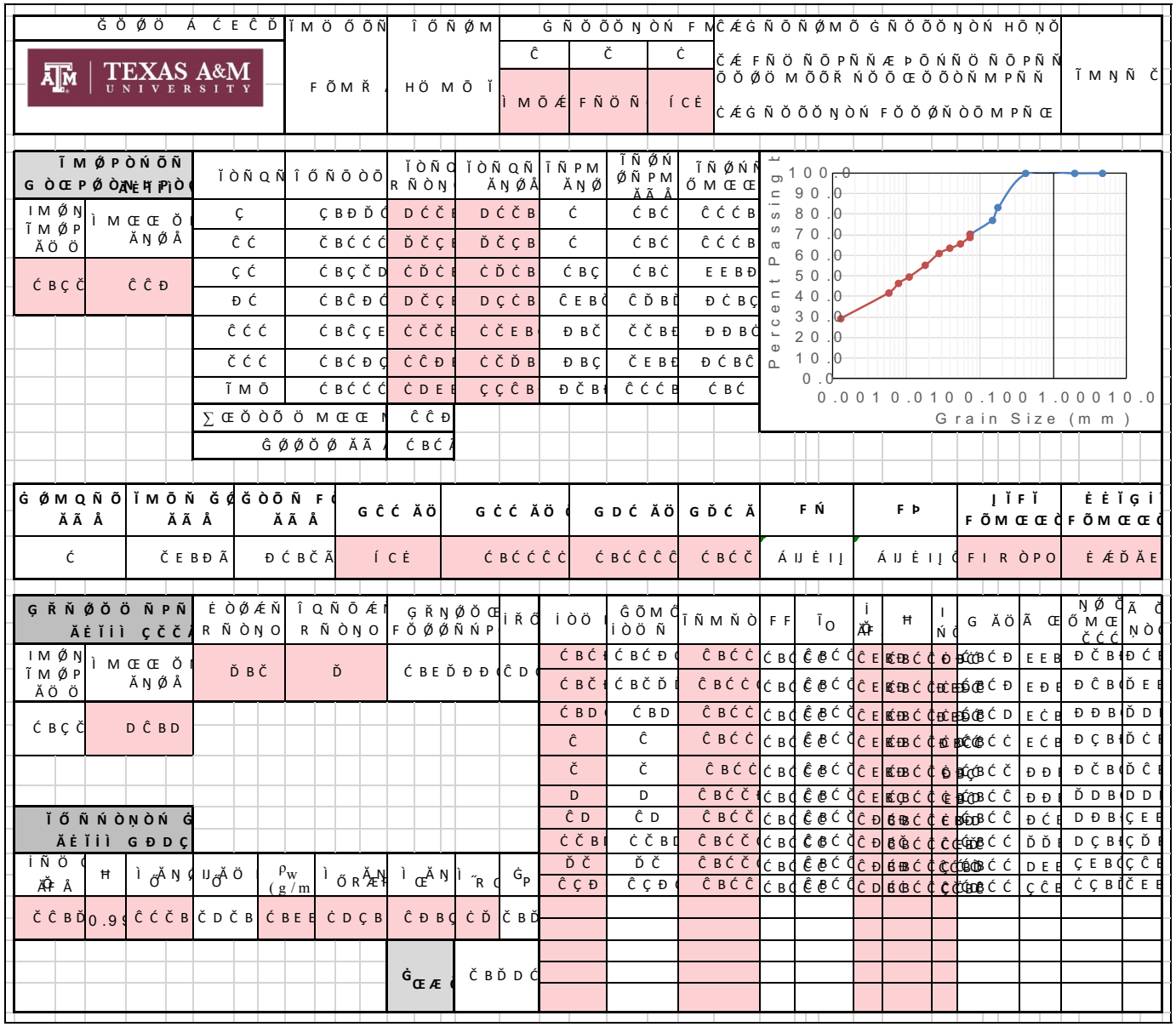

Figure B-160. Clay #7 – Page 2

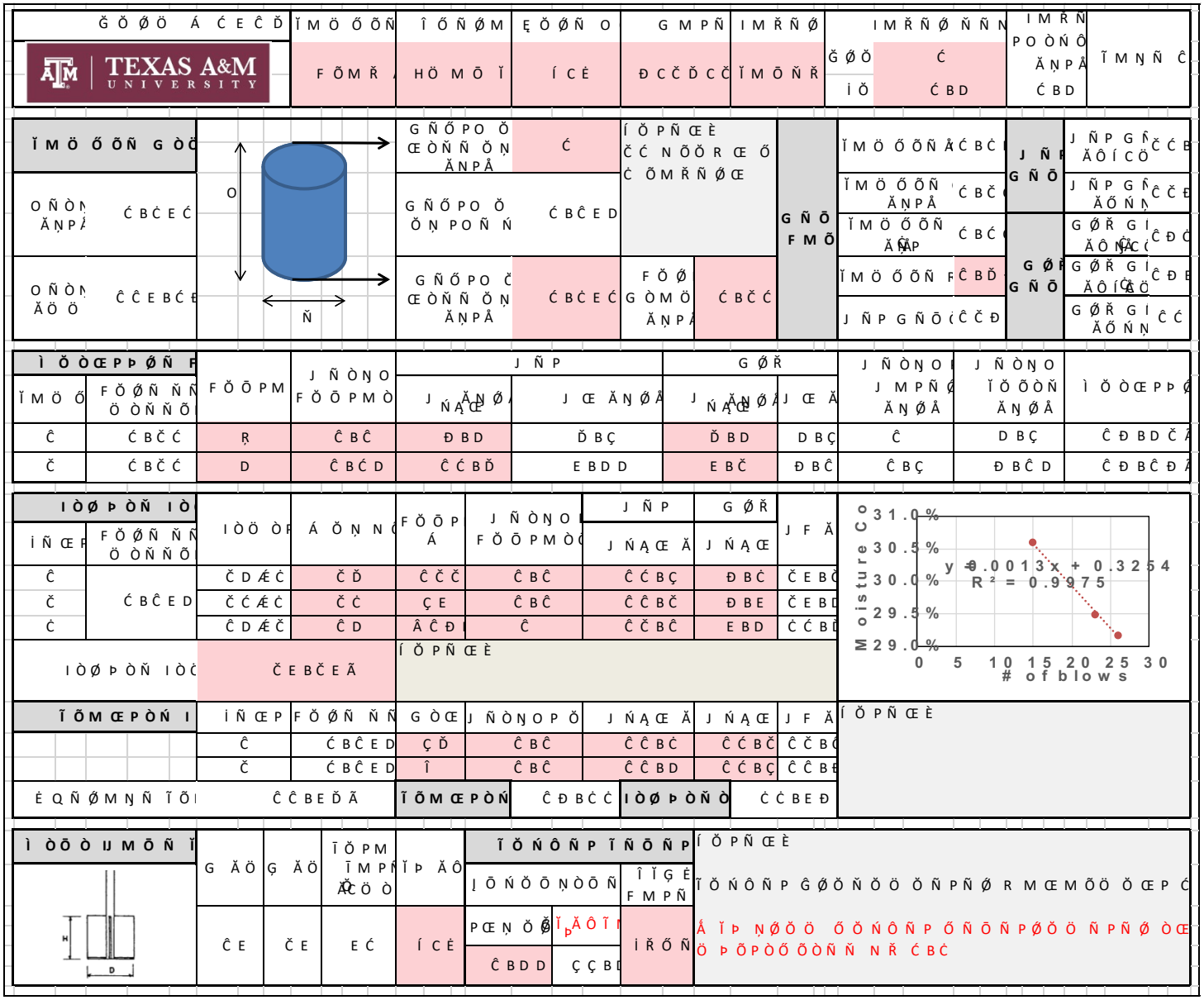

Figure B-161. Clay #8 – Page 1

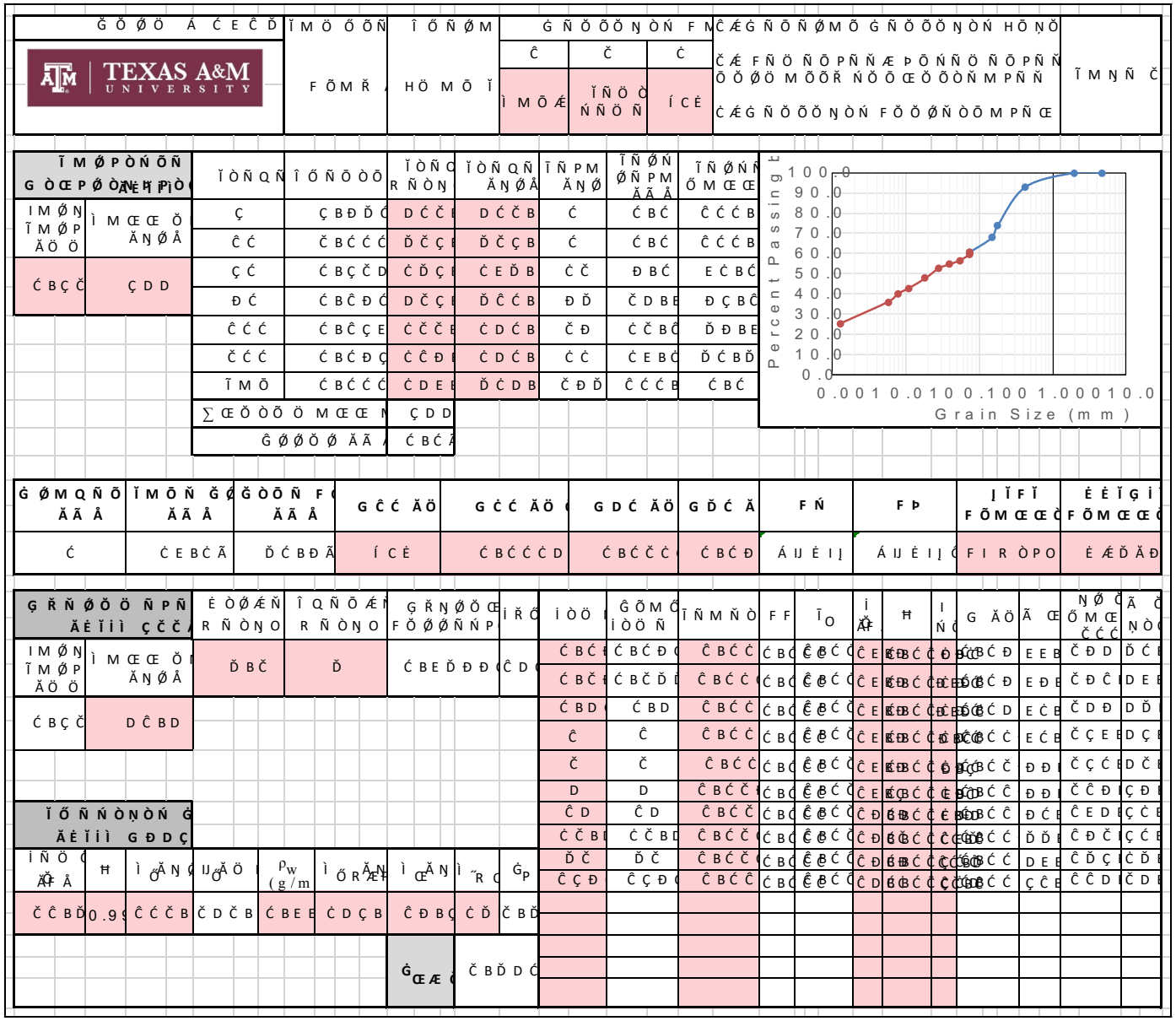

Figure B-162. Clay #8 – Page 2

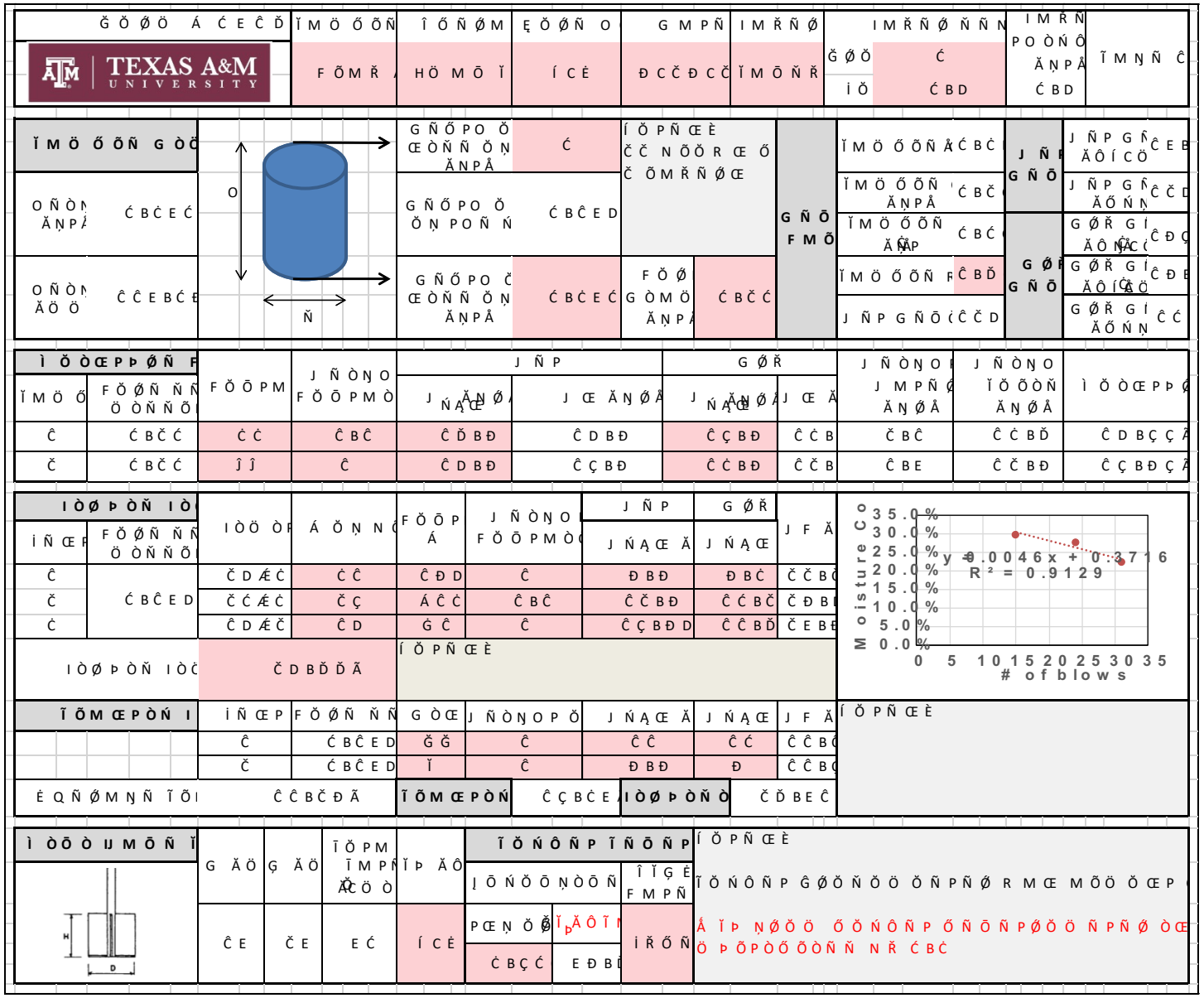

Figure B-163. Clay #9 – Page 1

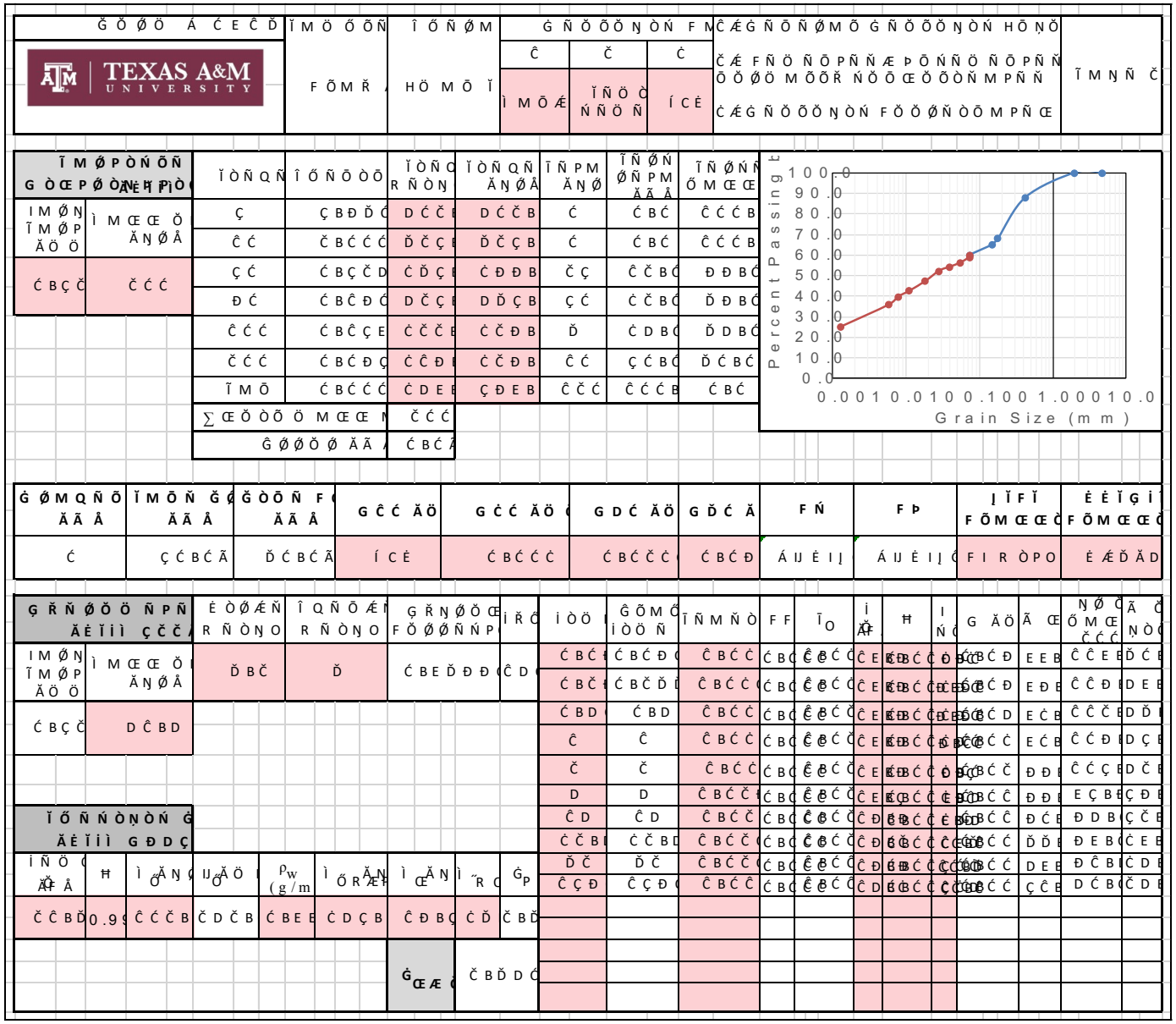

Figure B-164. Clay #9 – Page 2

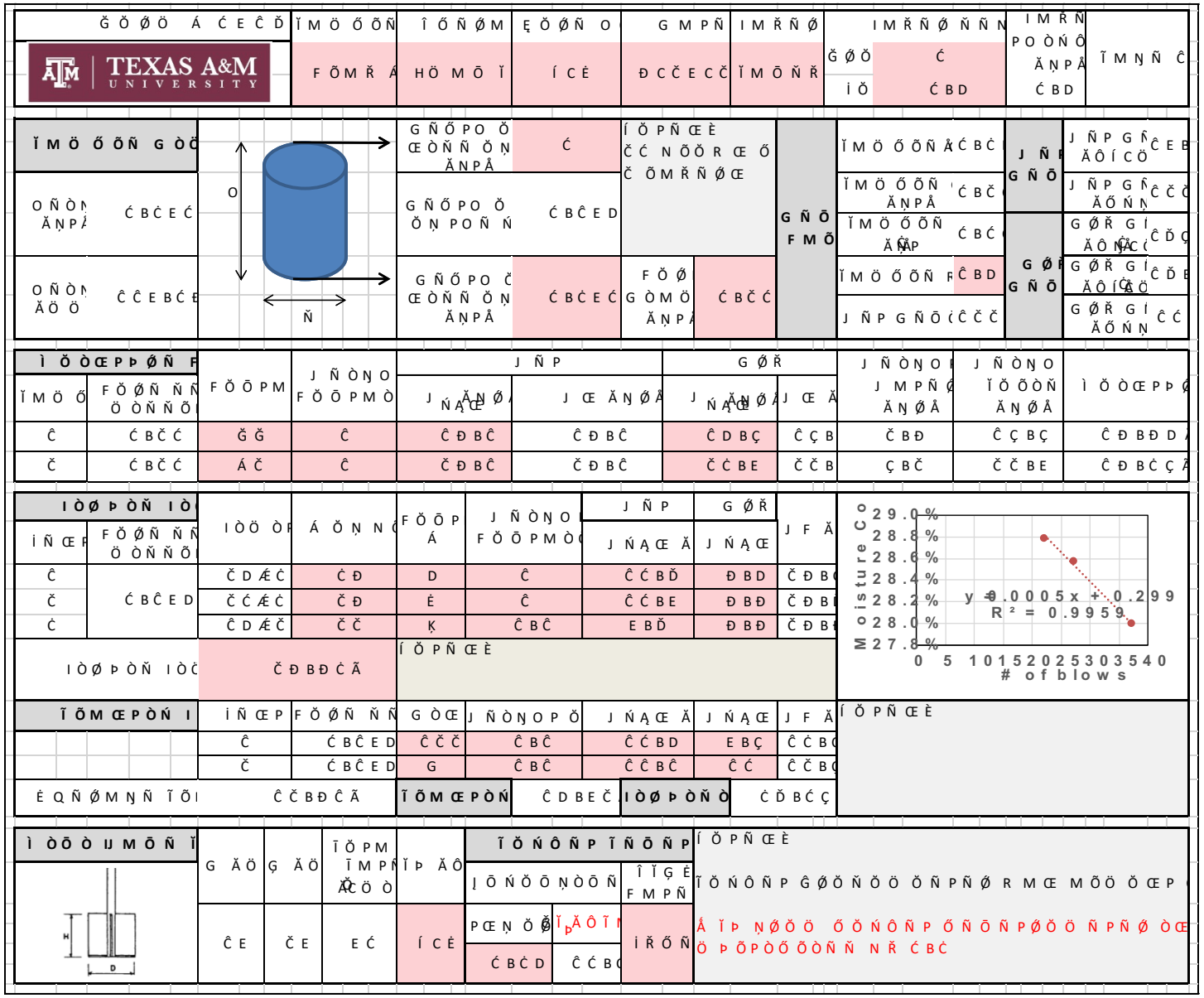

Figure B-165. Clay #10 – Page 1

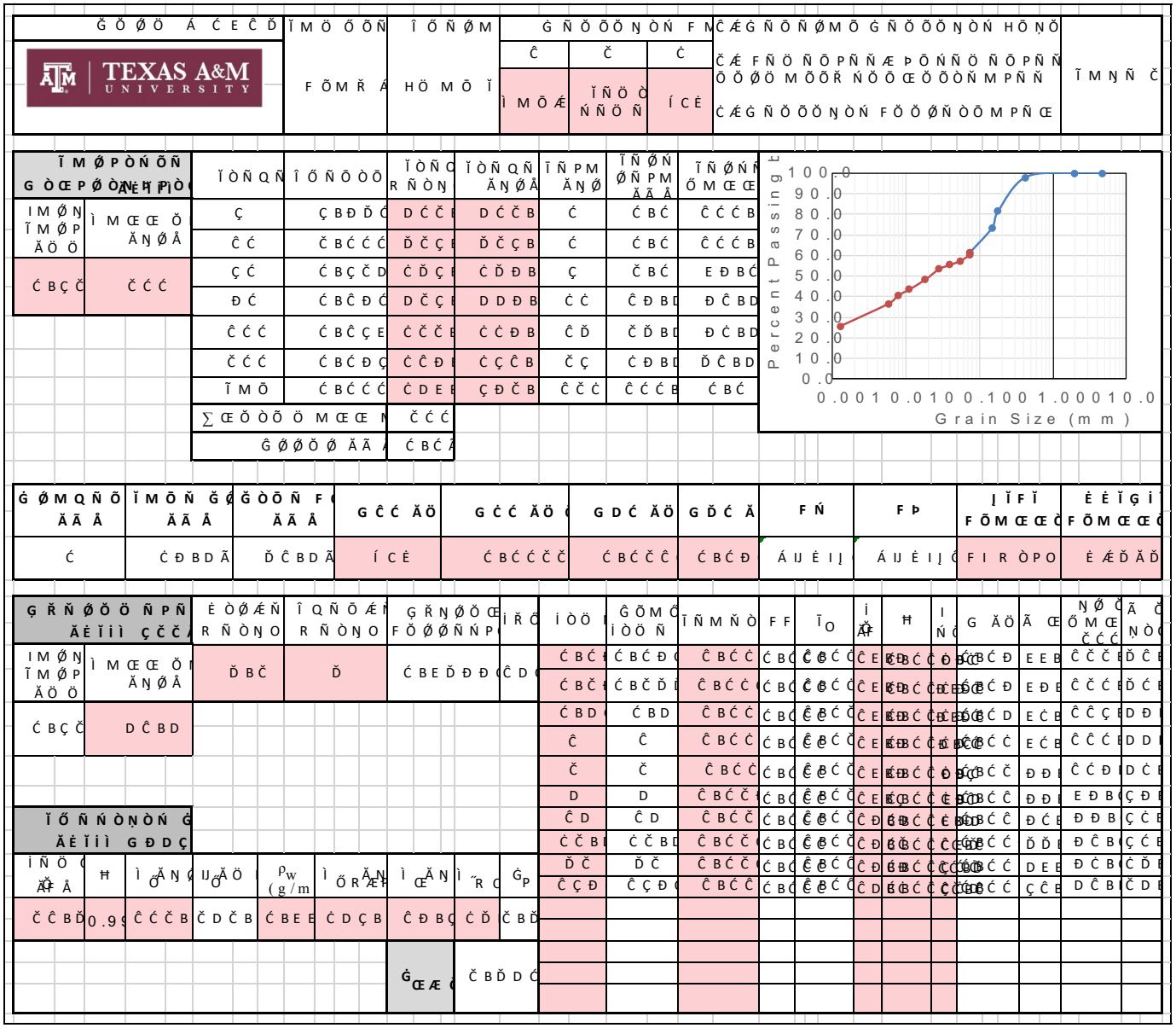

Figure B-166. Clay #10 – Page 2

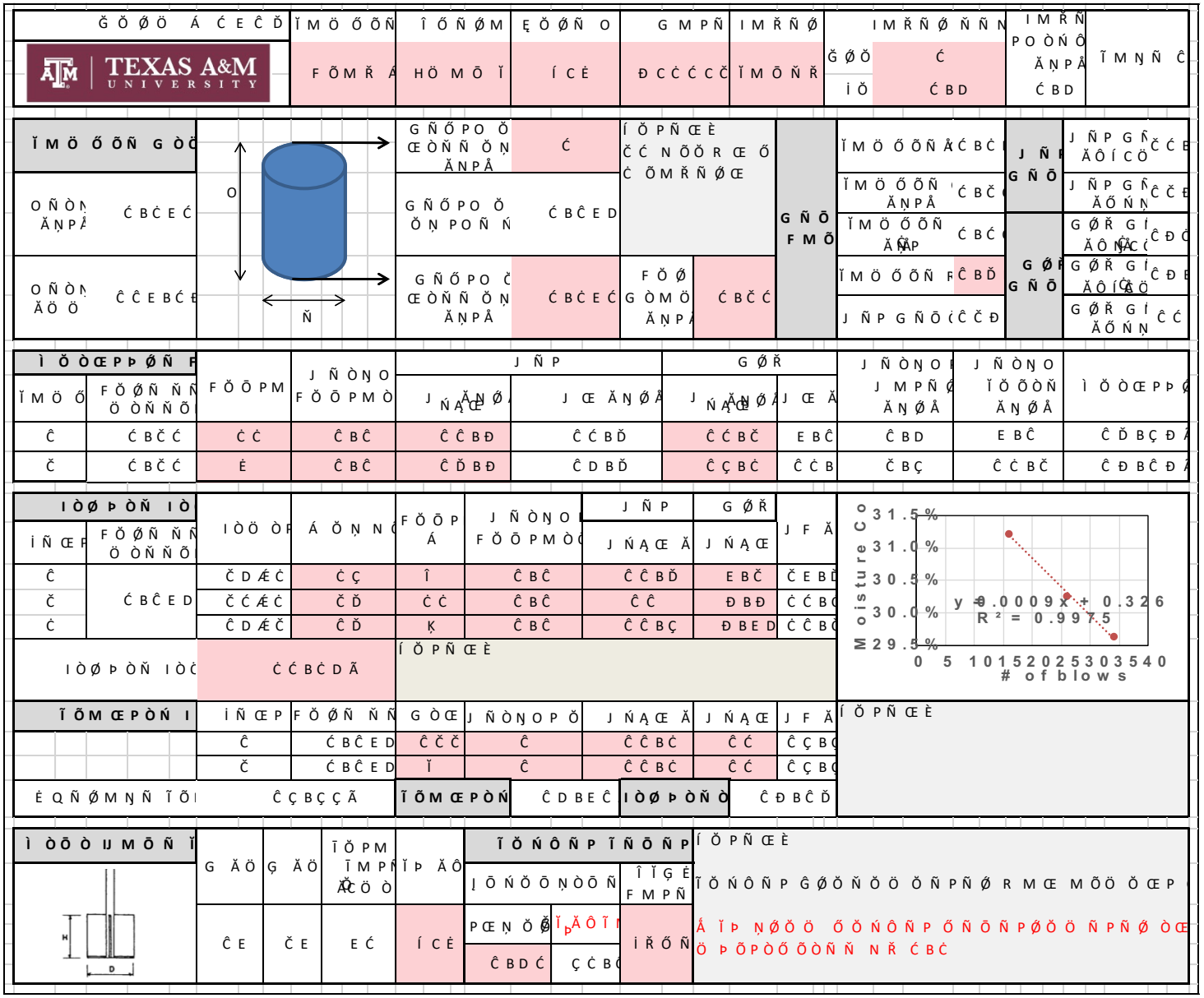

Figure B-167. Clay #11 – Page 1

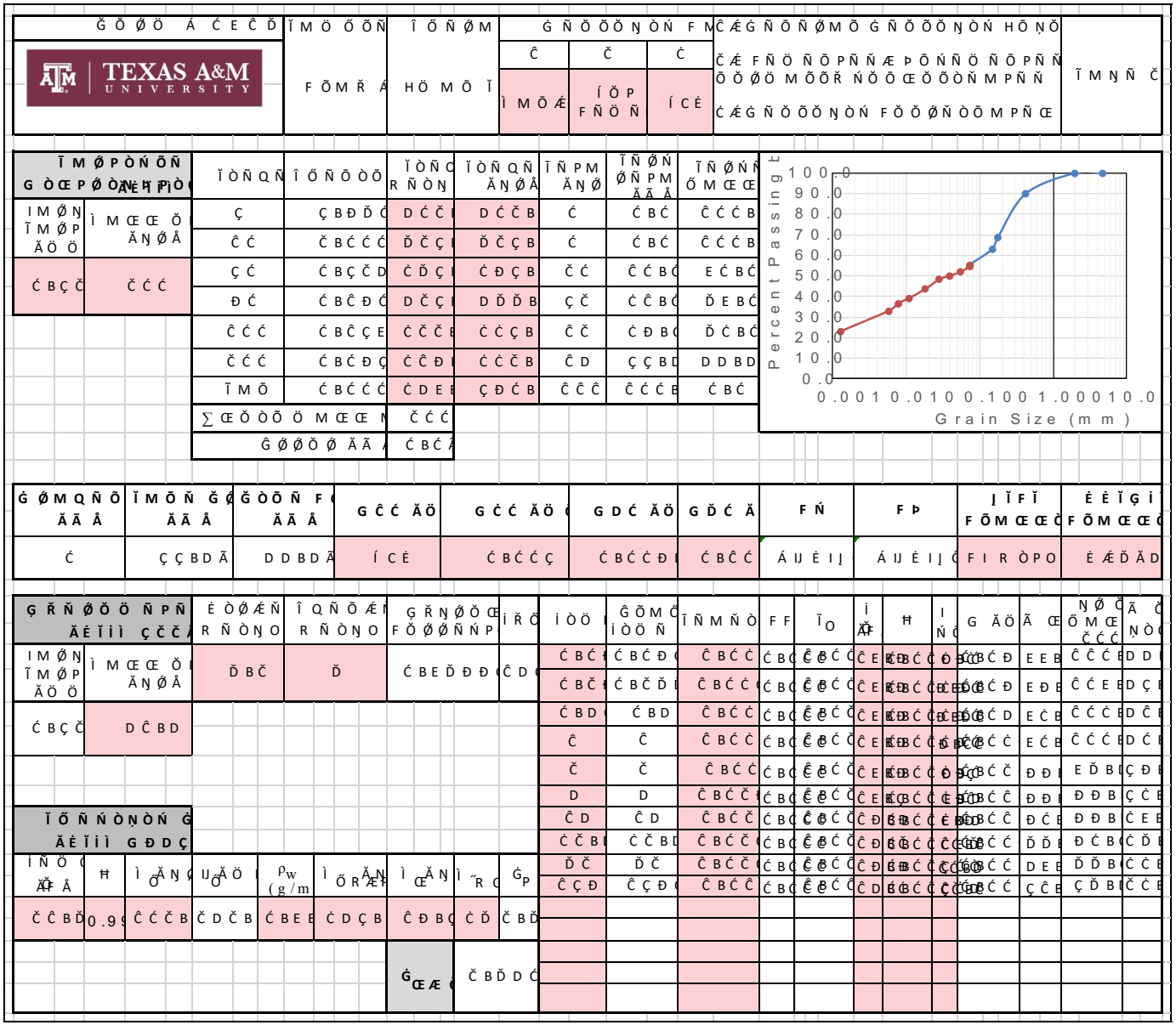

Figure B-168. Clay #11 – Page 2

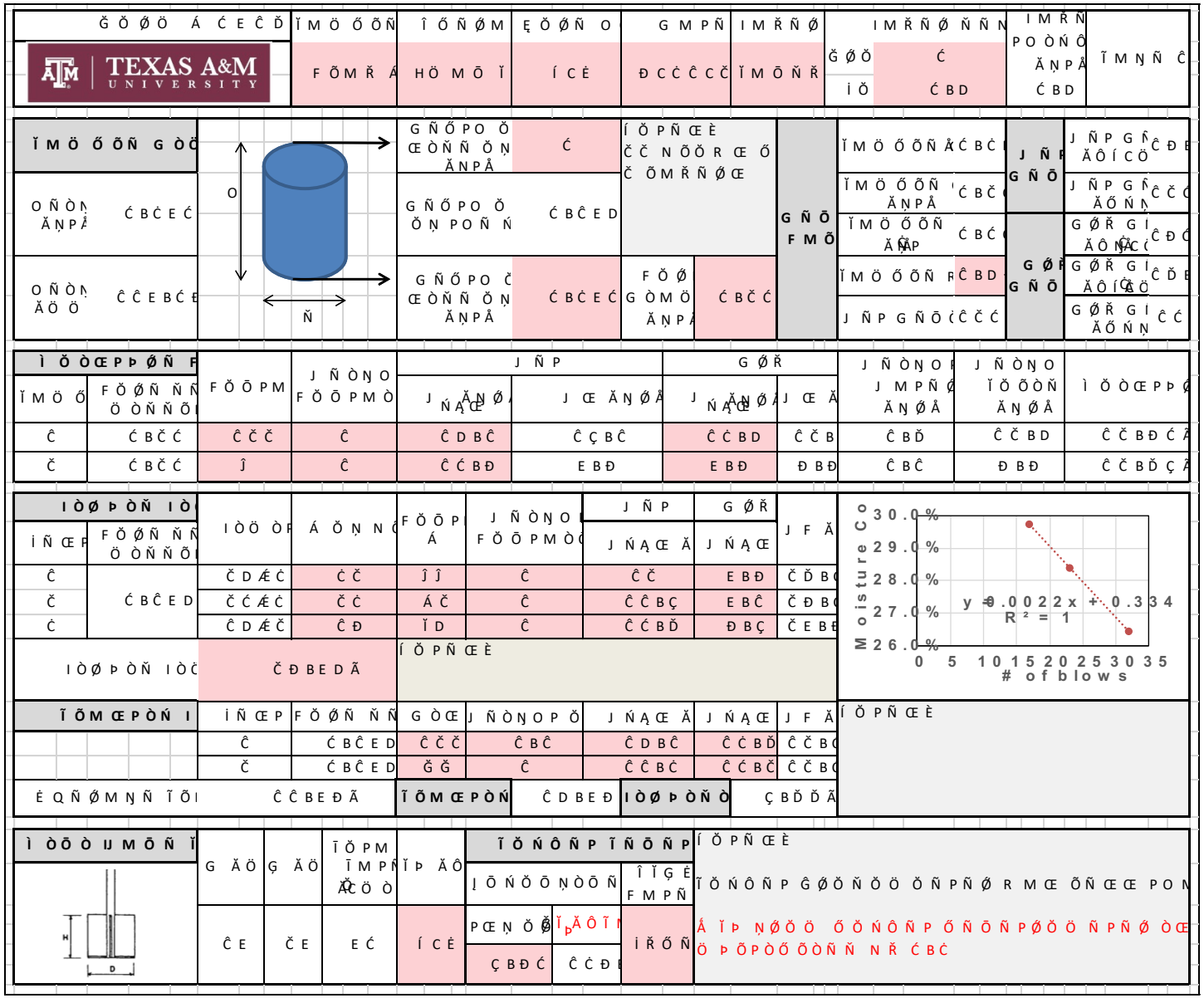

Figure B-169. Clay #12 – Page 1

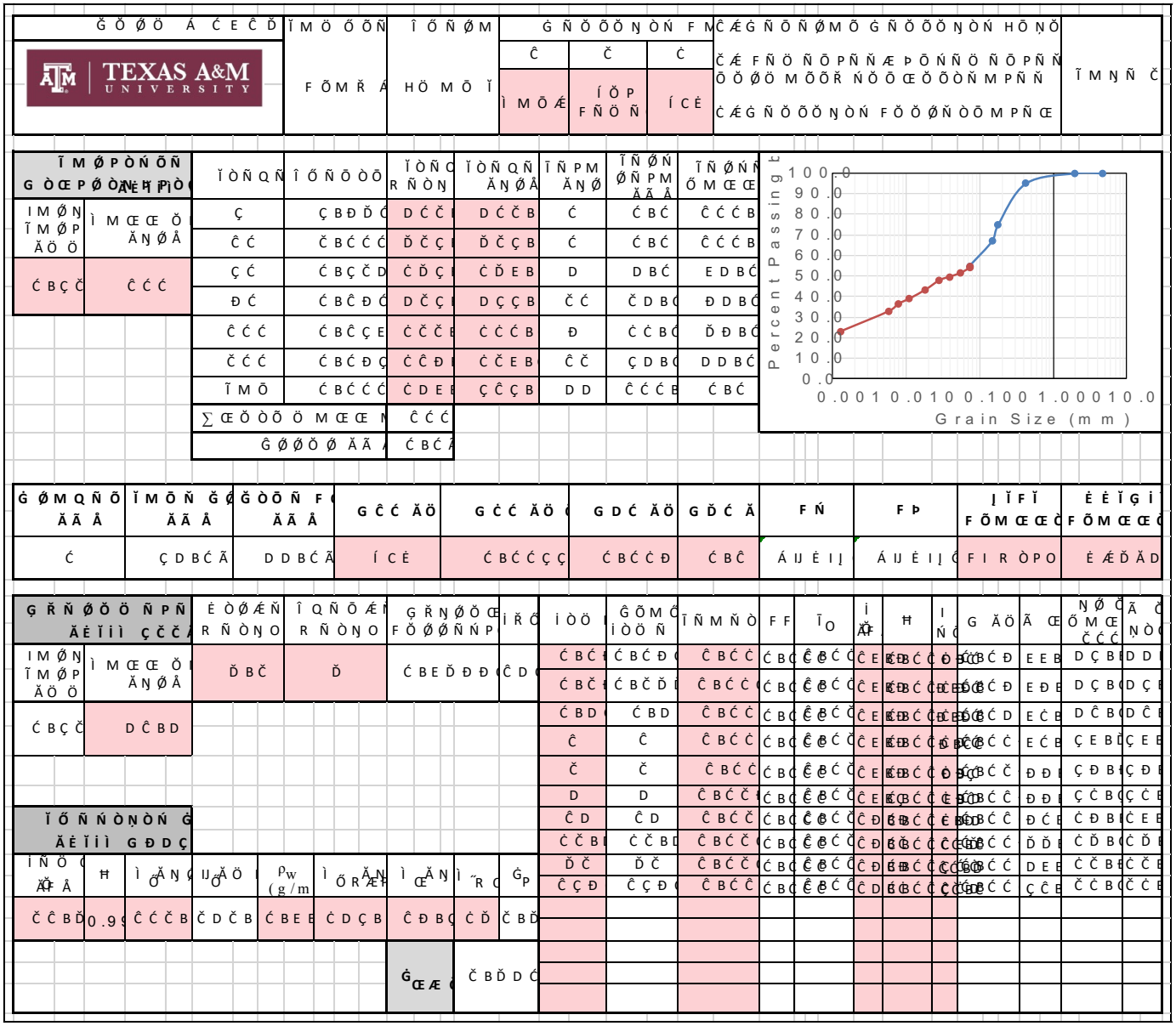

Figure B-170. Clay #12 – Page 2

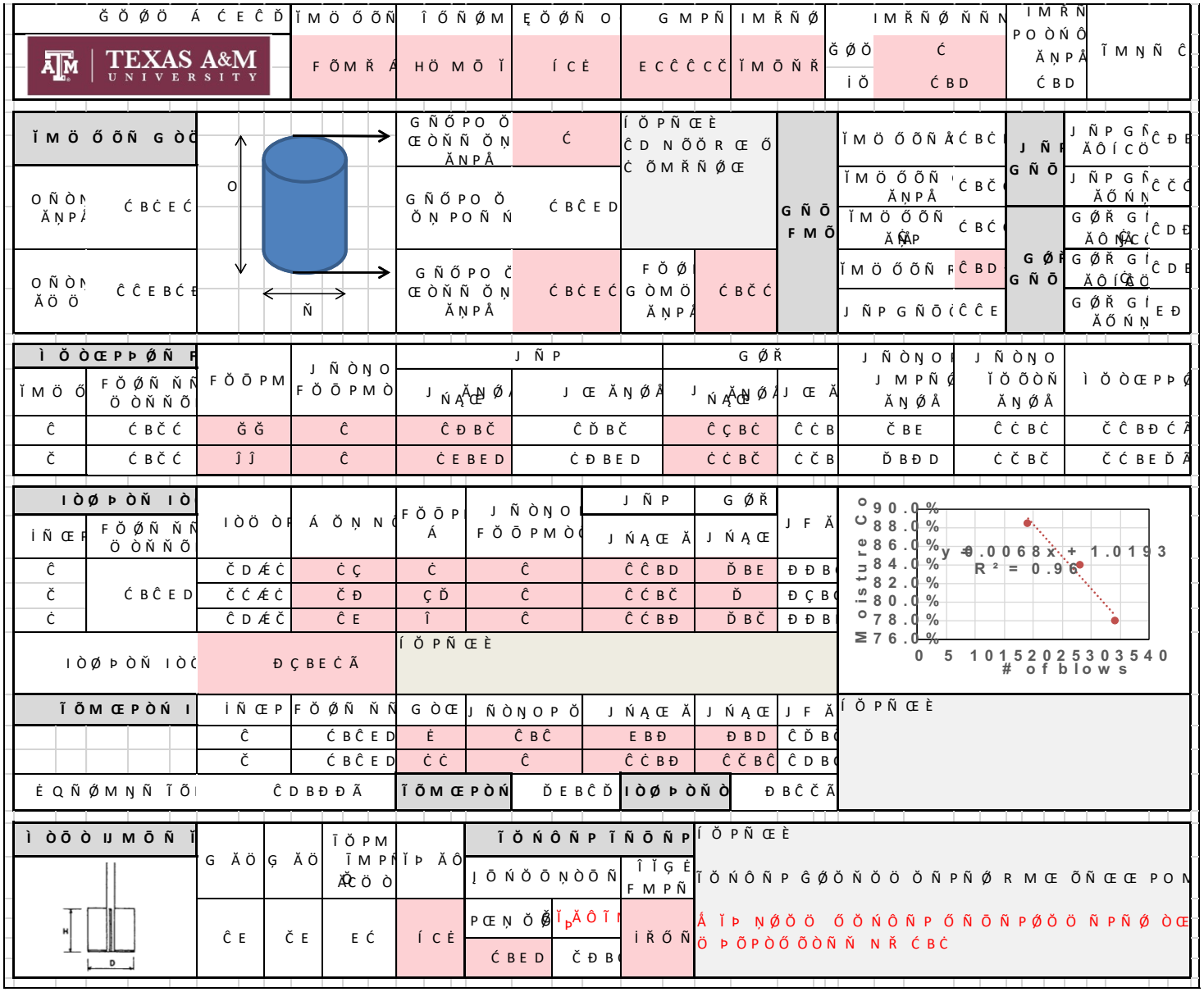

Figure B-171. Clay #13 – Page 1

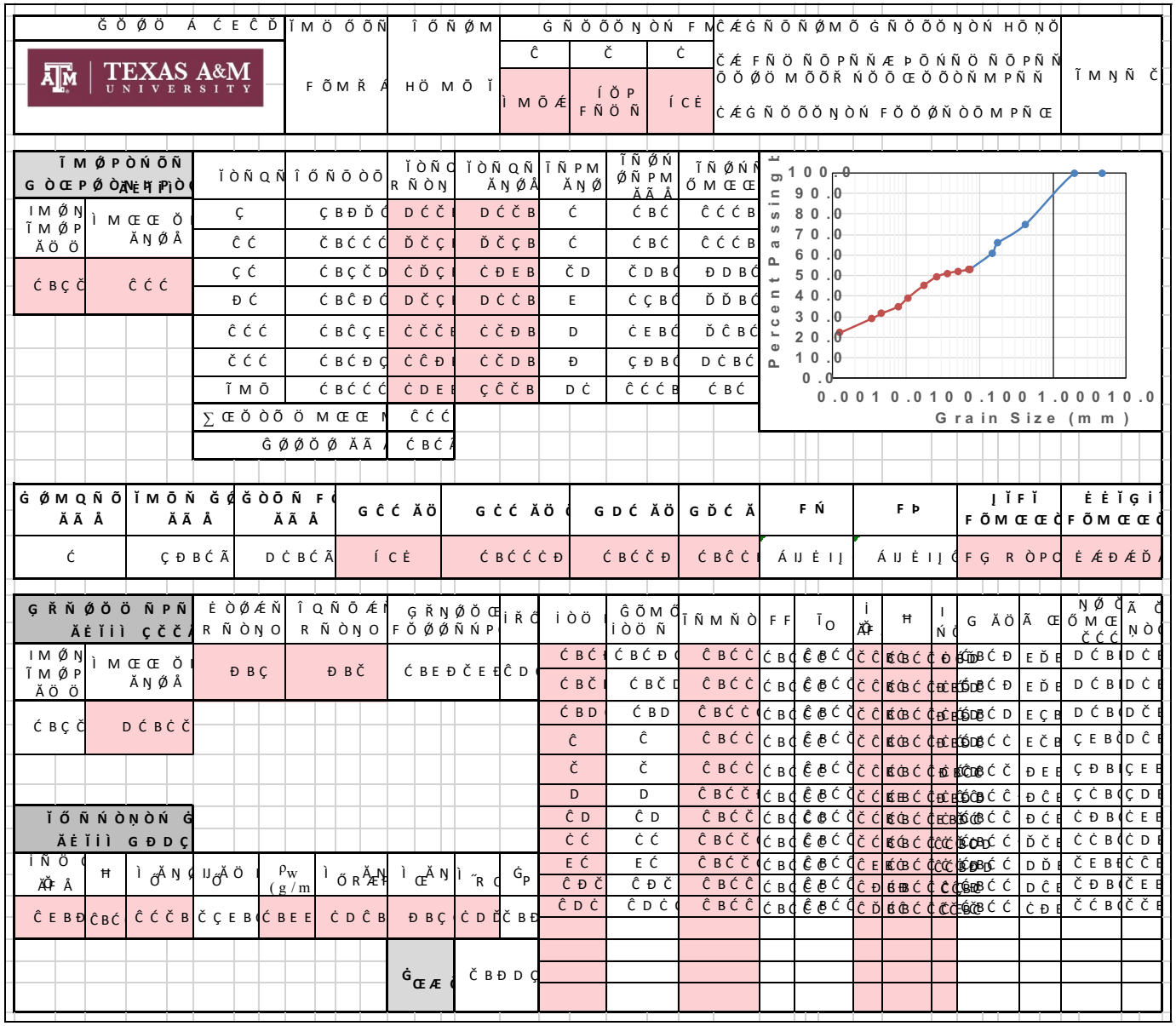

Figure B-172. Clay #13 – Page 2

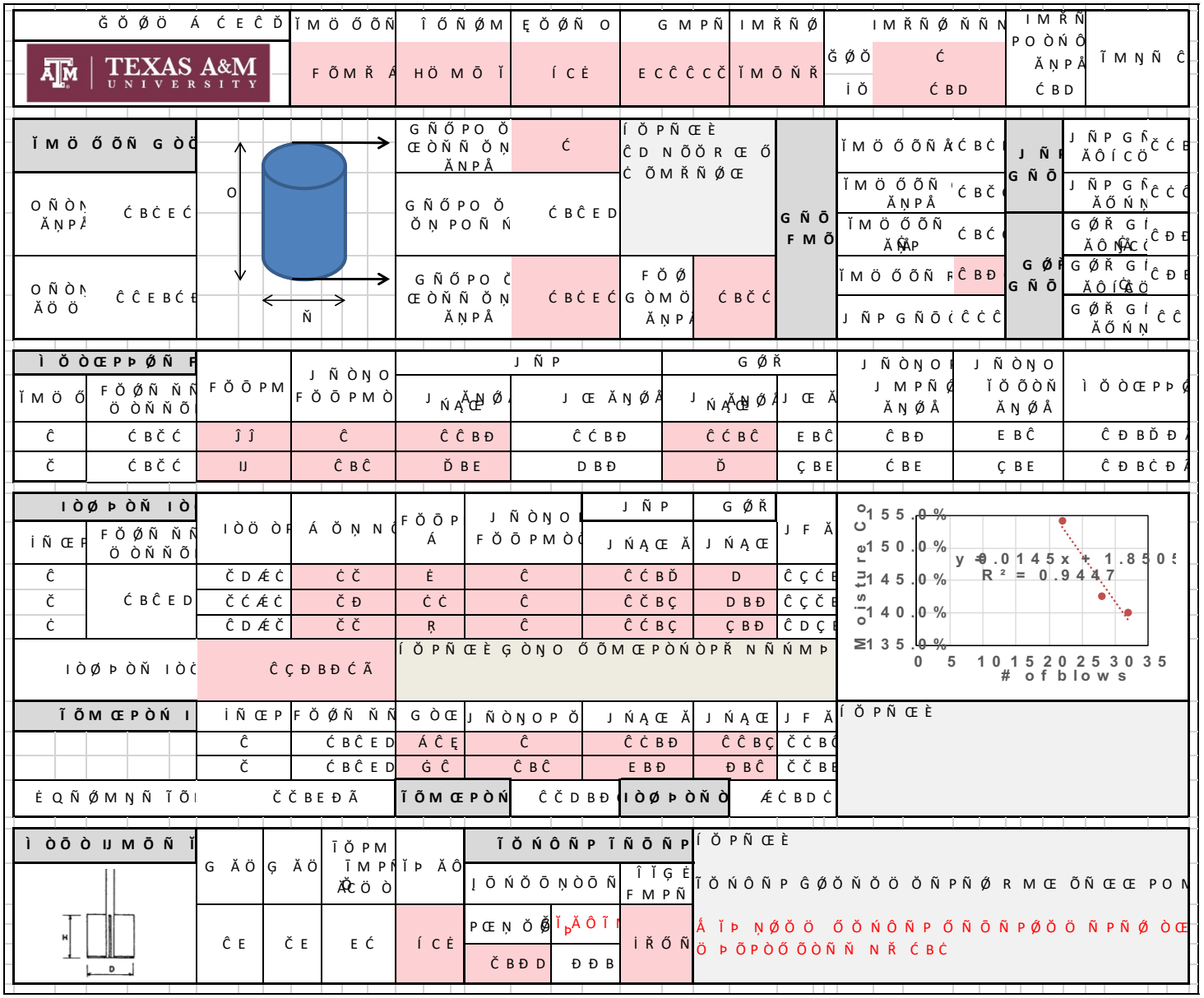

Figure B-173. Clay #14 – Page 1

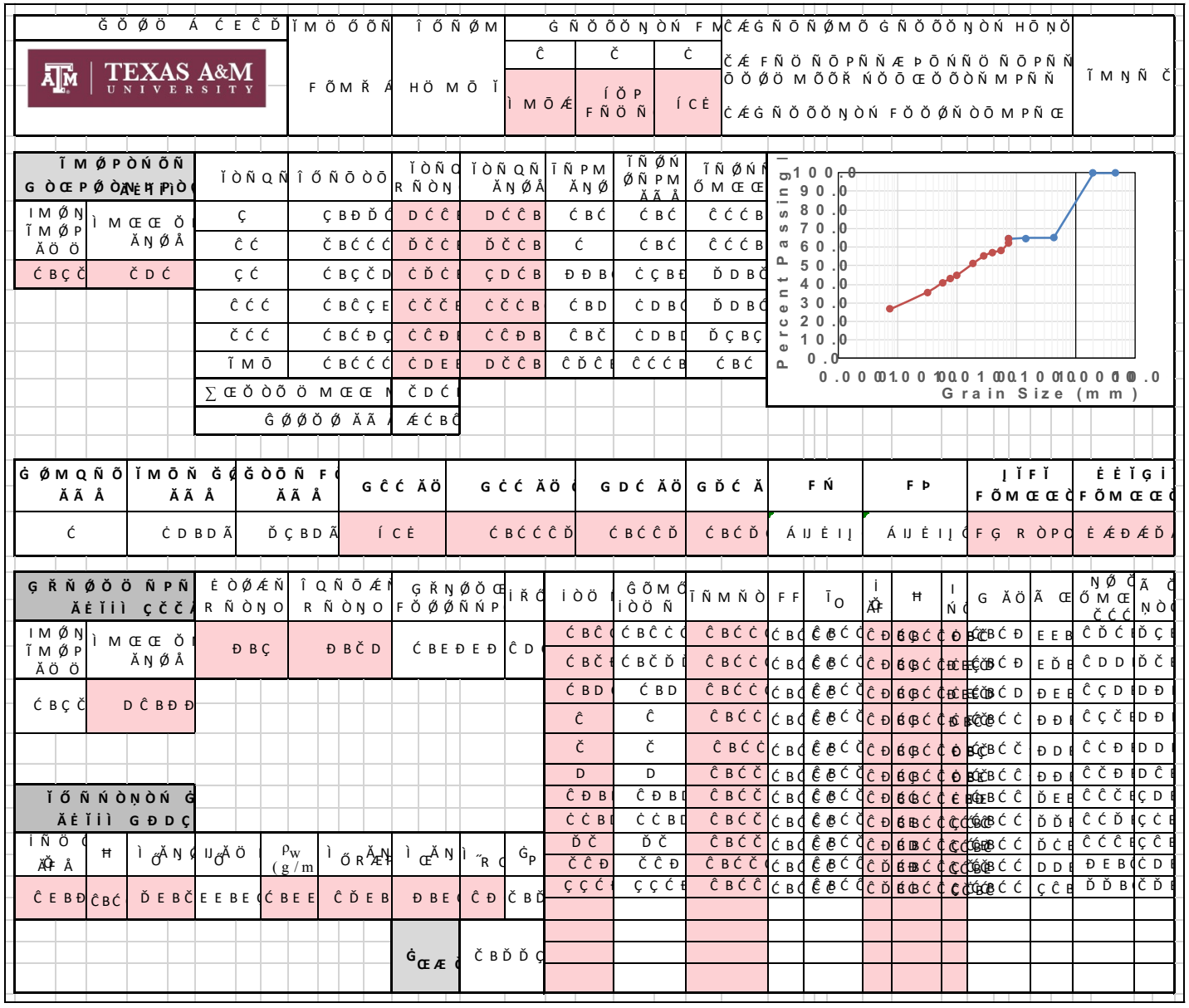

Figure B-174. Clay #14 – Page 2

Silt Samples - HET

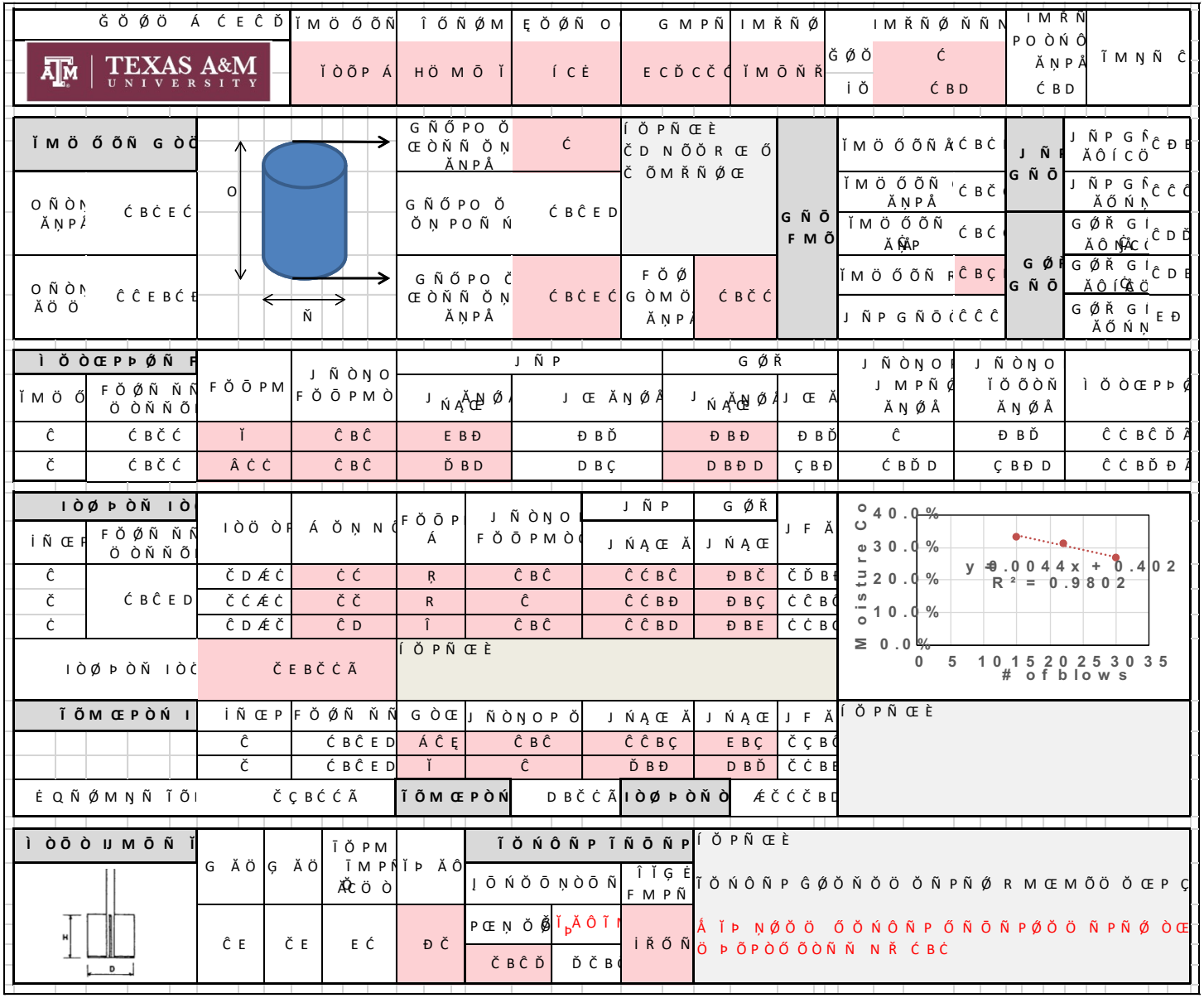

Figure B-175. Silt #1 – Page 1

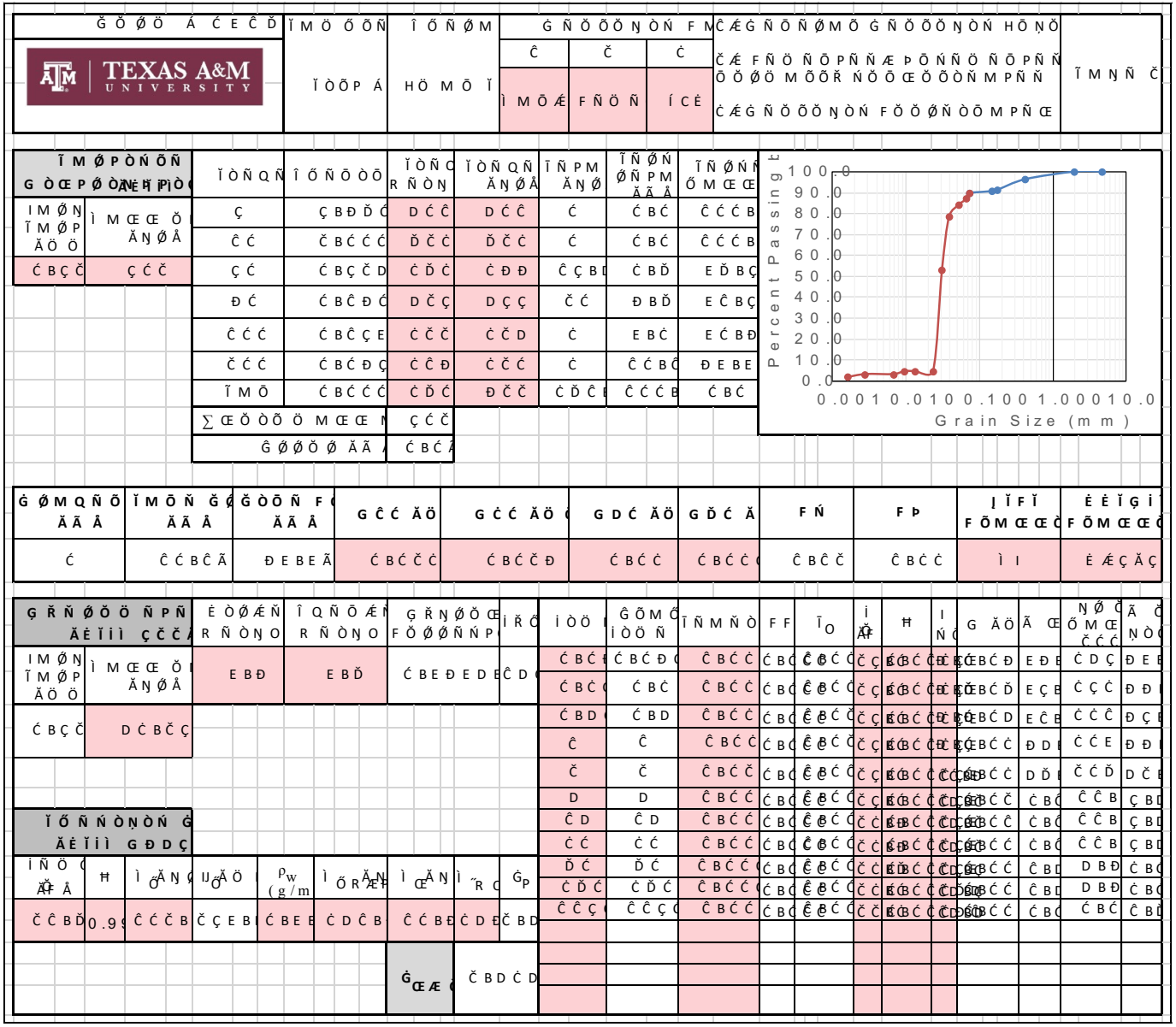

Figure B-176. Silt #1 – Page 2

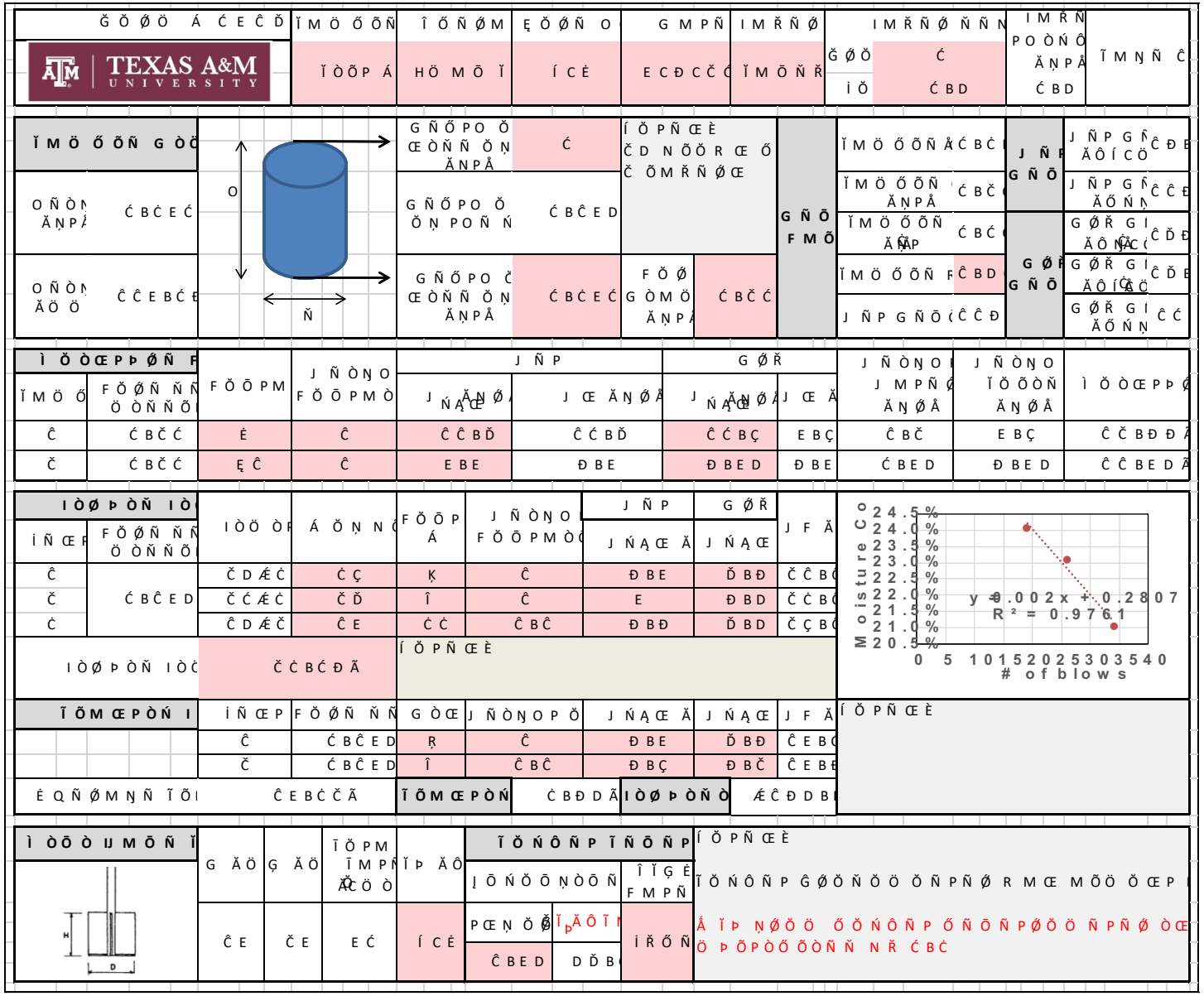

Figure B-177. Silt #2 – Page 1

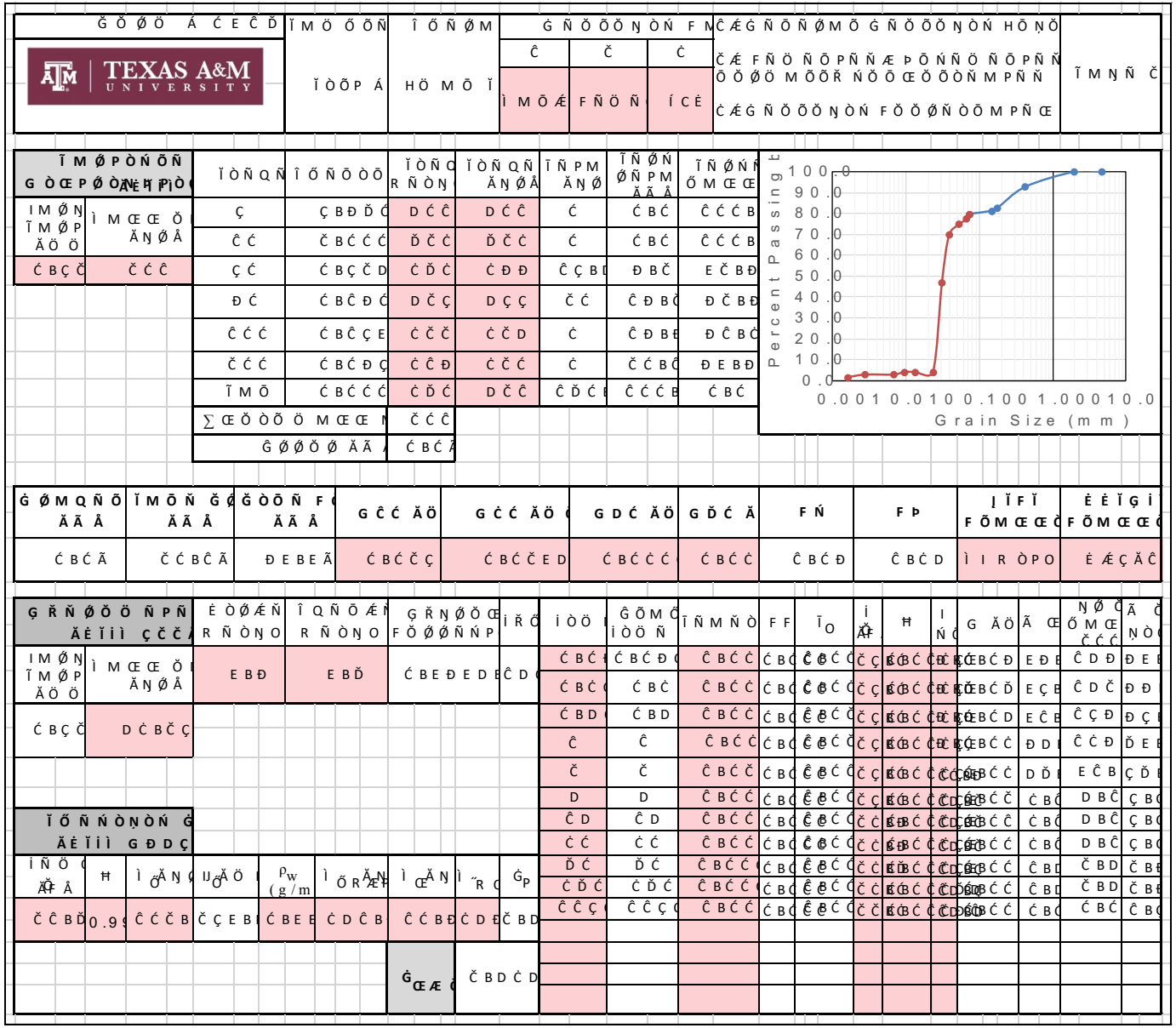

Figure B-178. Silt #2 – Page 2

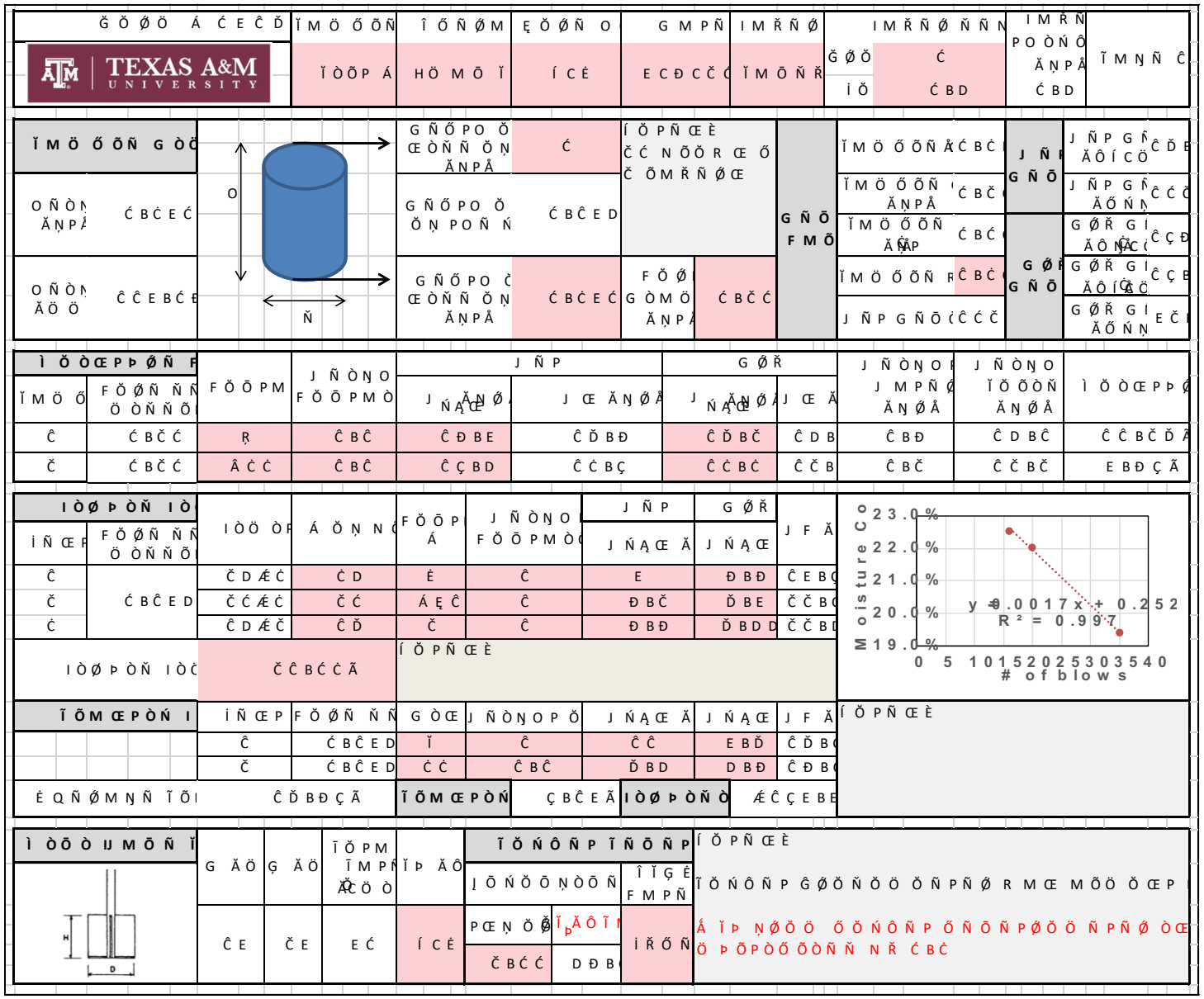

Figure B-179. Silt #3 – Page 1

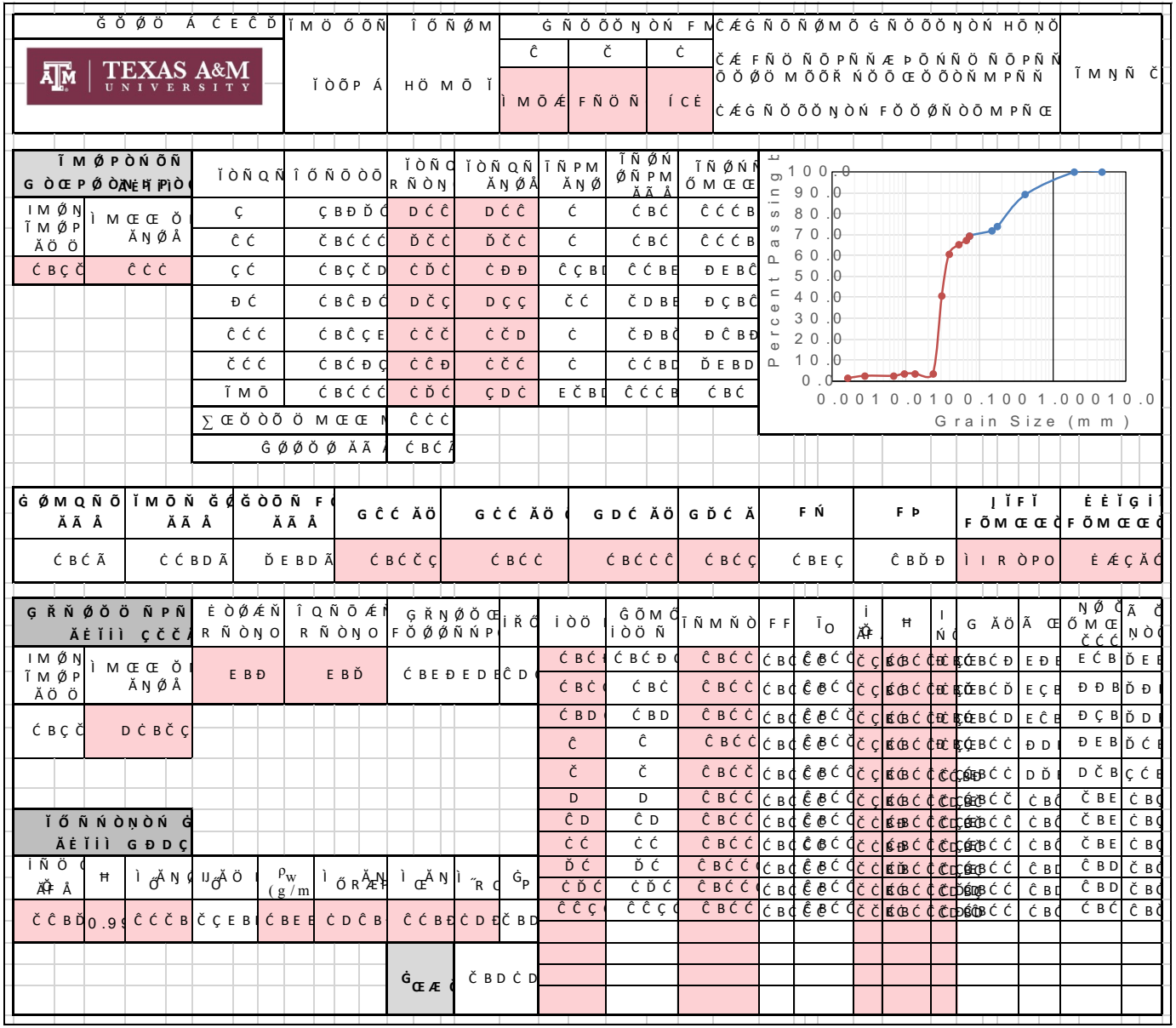

Figure B-180. Silt #3 – Page 2

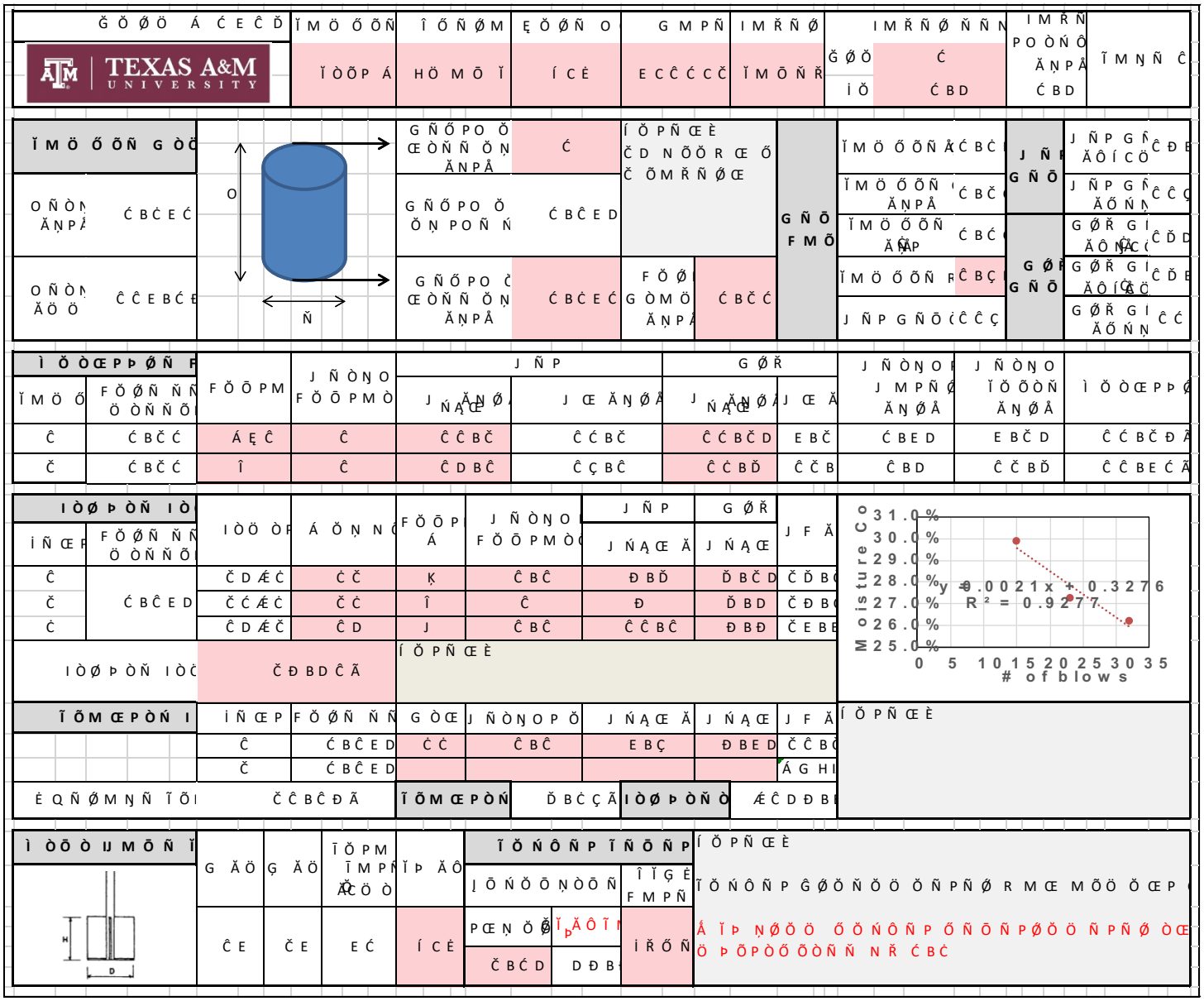

Figure B-181. Silt #4 – Page 1

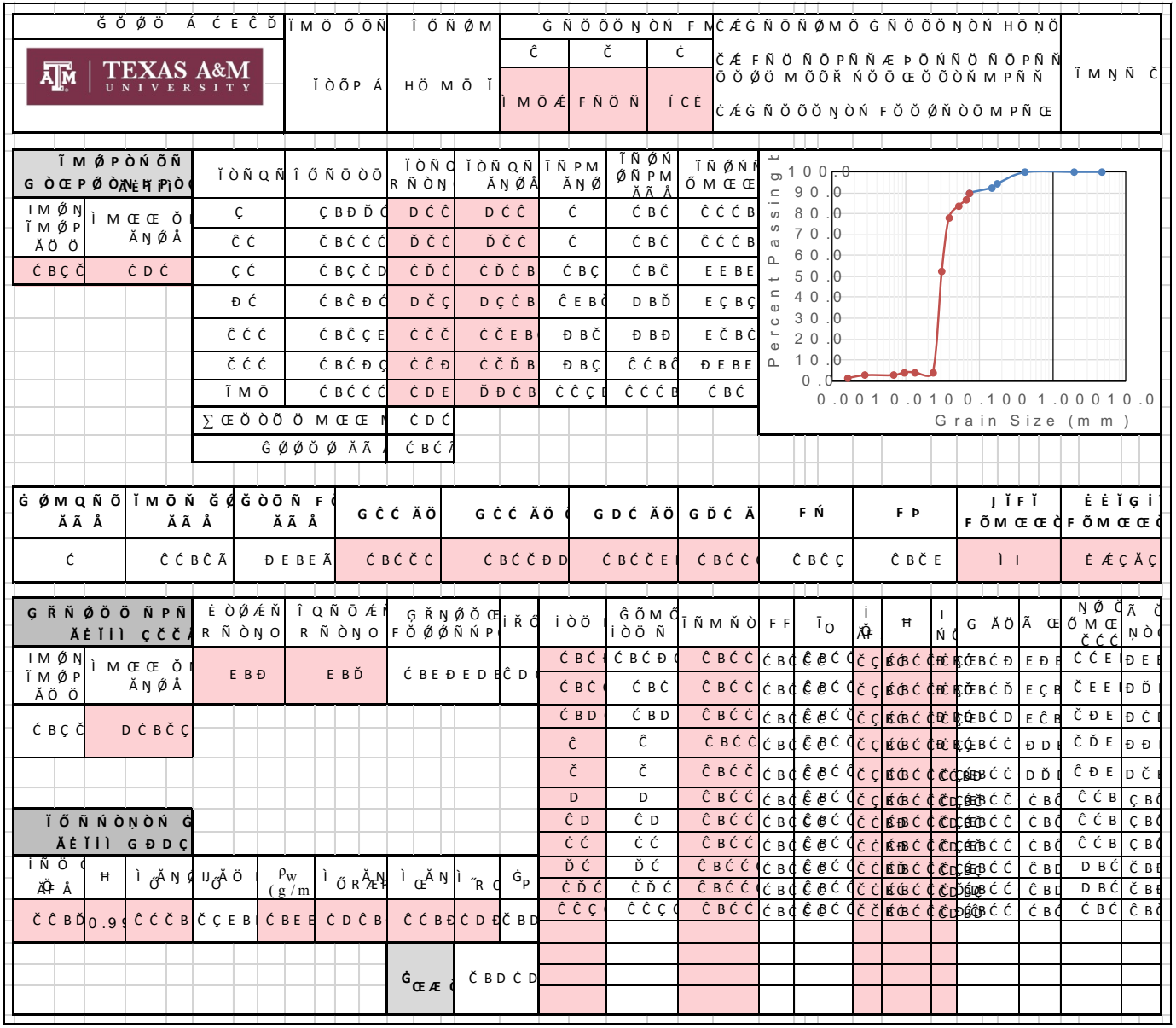

Figure B-182. Silt #4 – Page 2

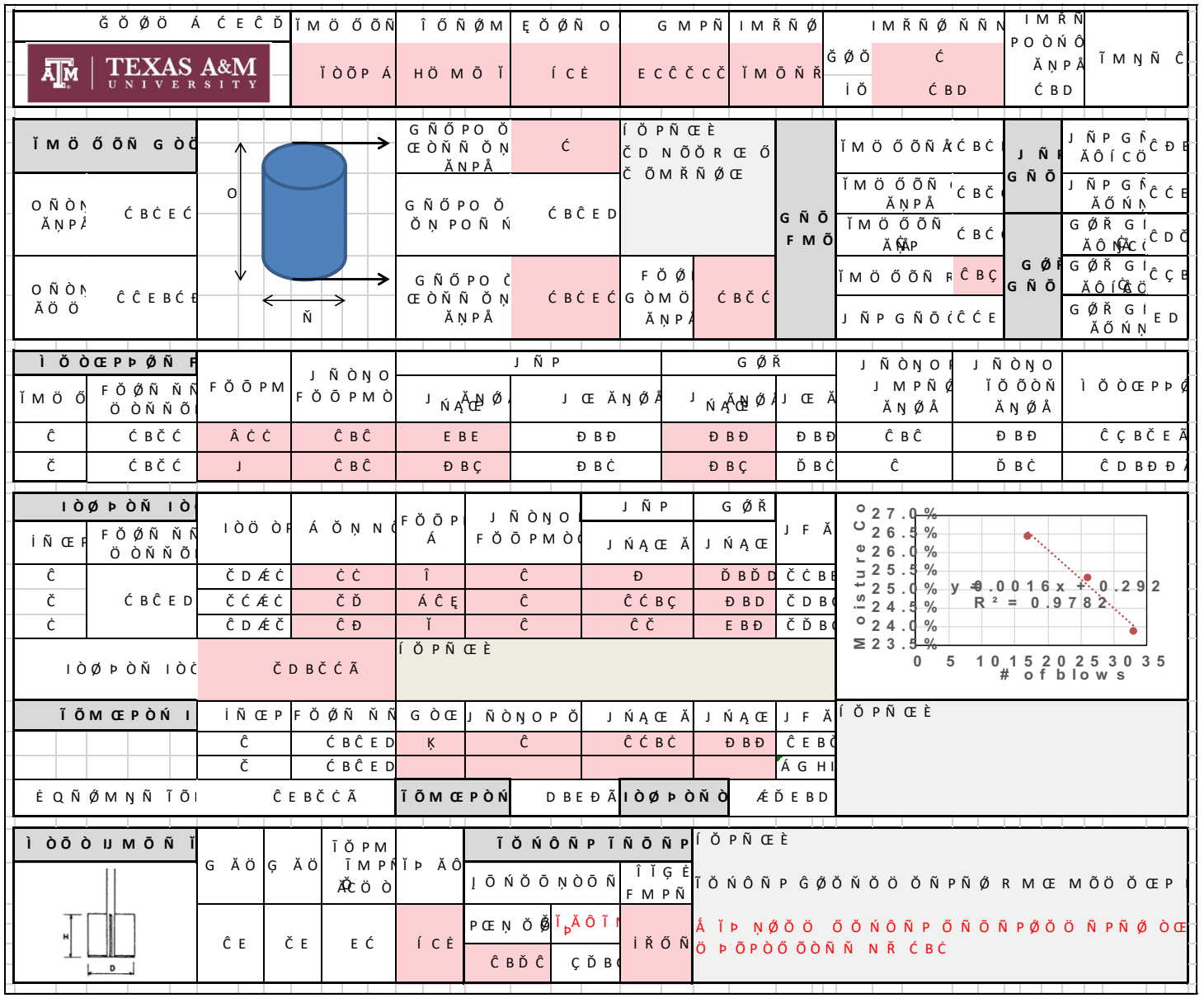

Figure B-183. Silt #5 – Page 1

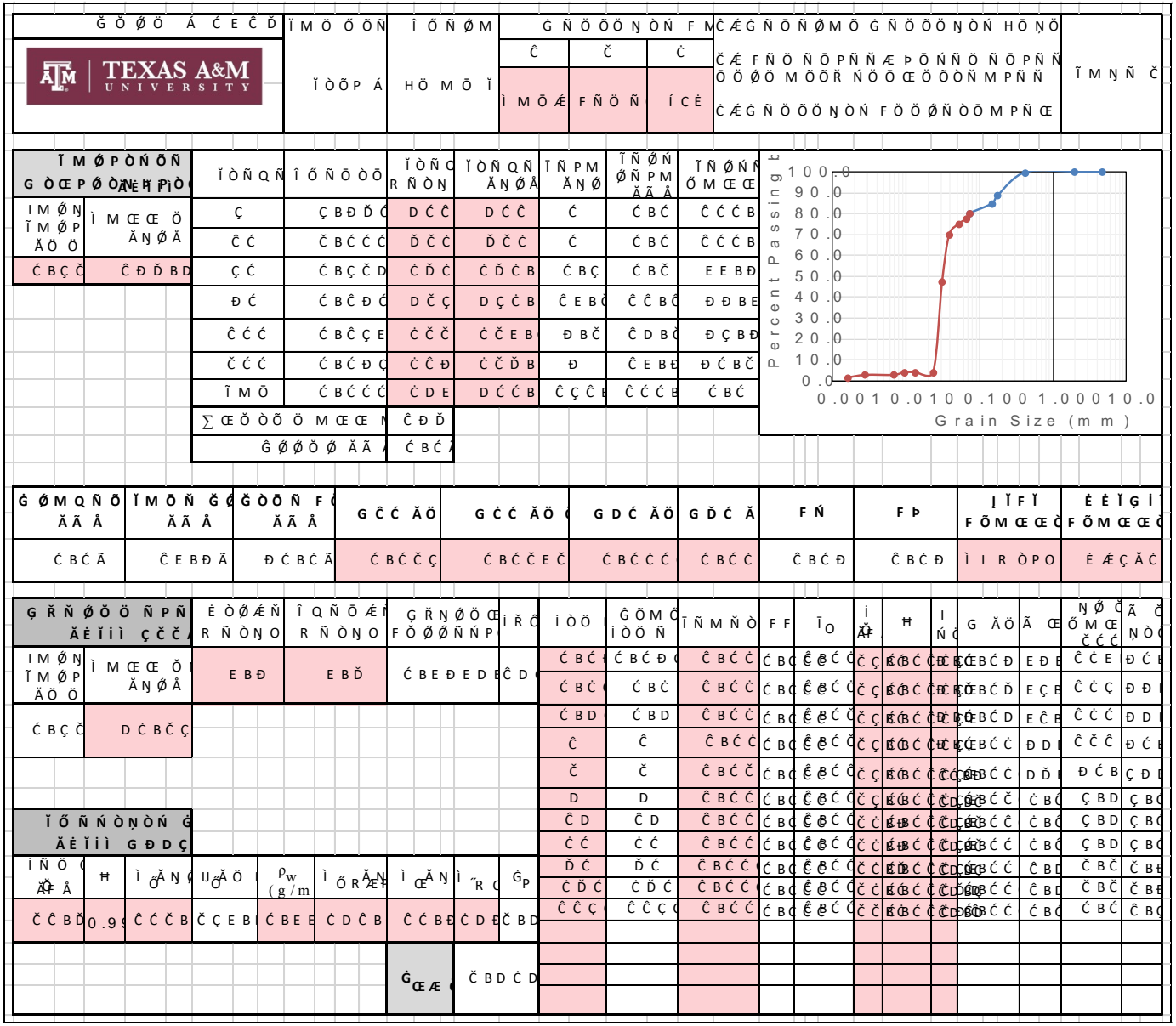

Figure B-184. Silt #5 – Page 2

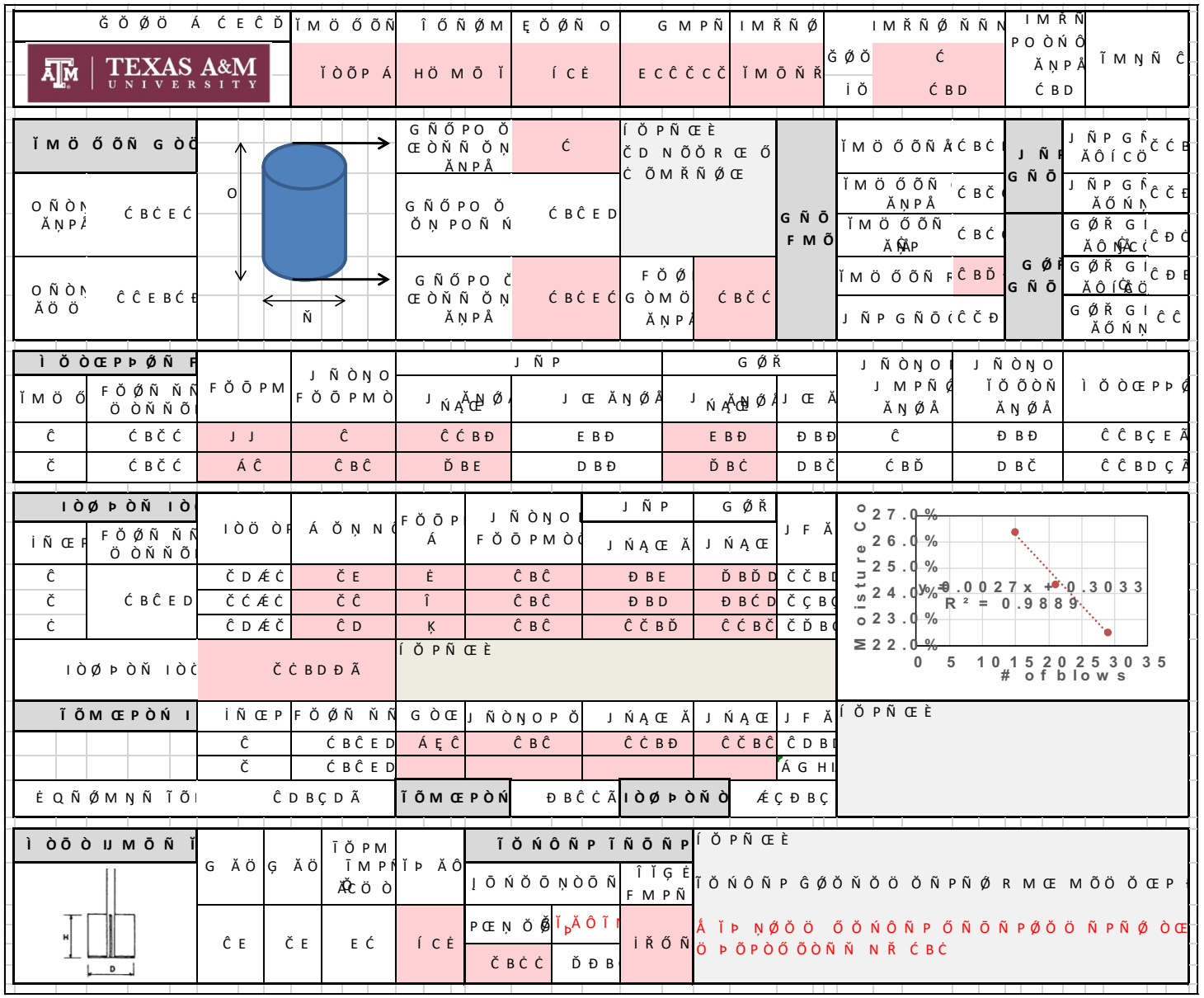

Figure B-185. Silt #6 – Page 1

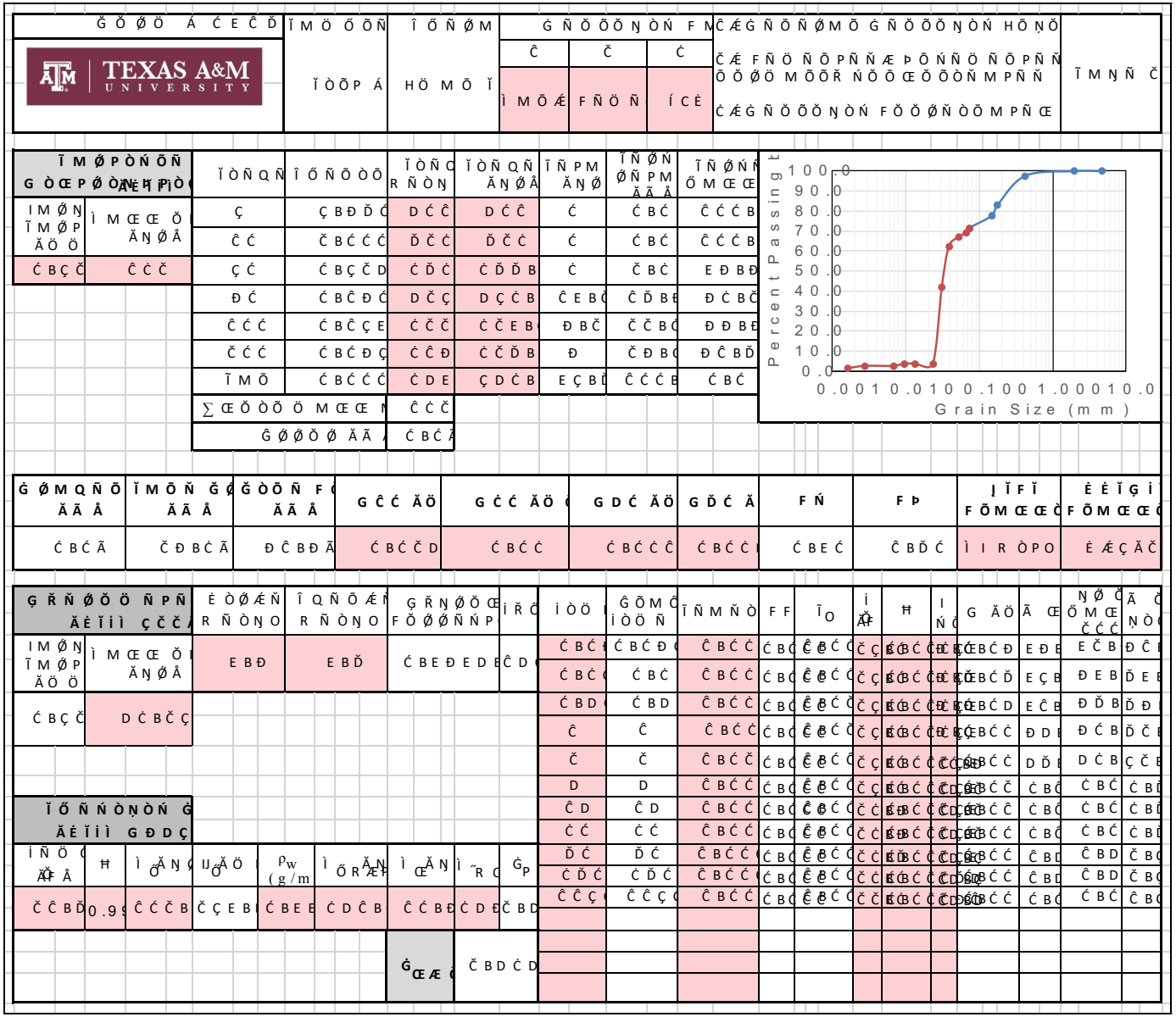

Figure B-186. Silt #6 – Page 2

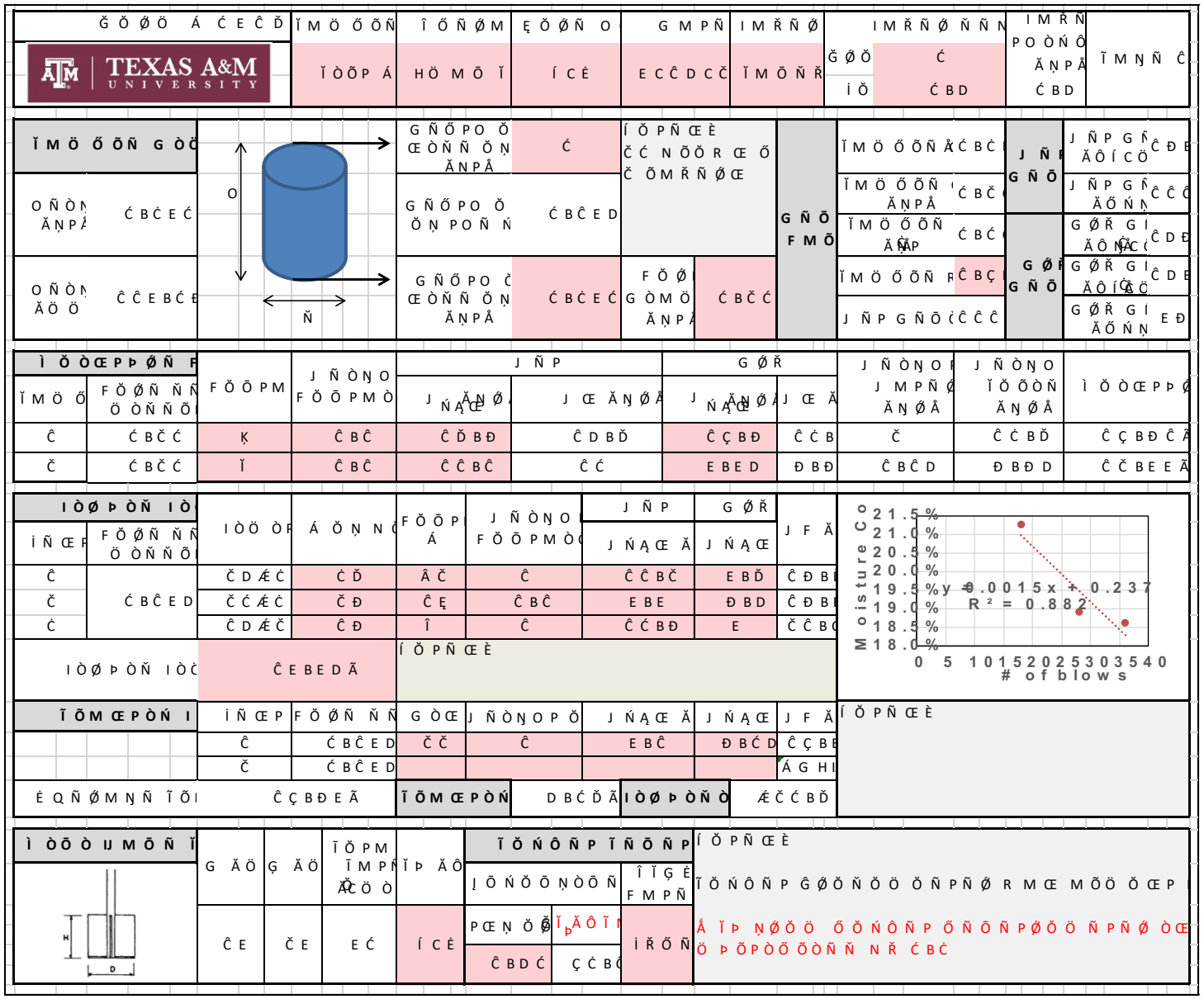

Figure B-187. Silt #7 – Page 1

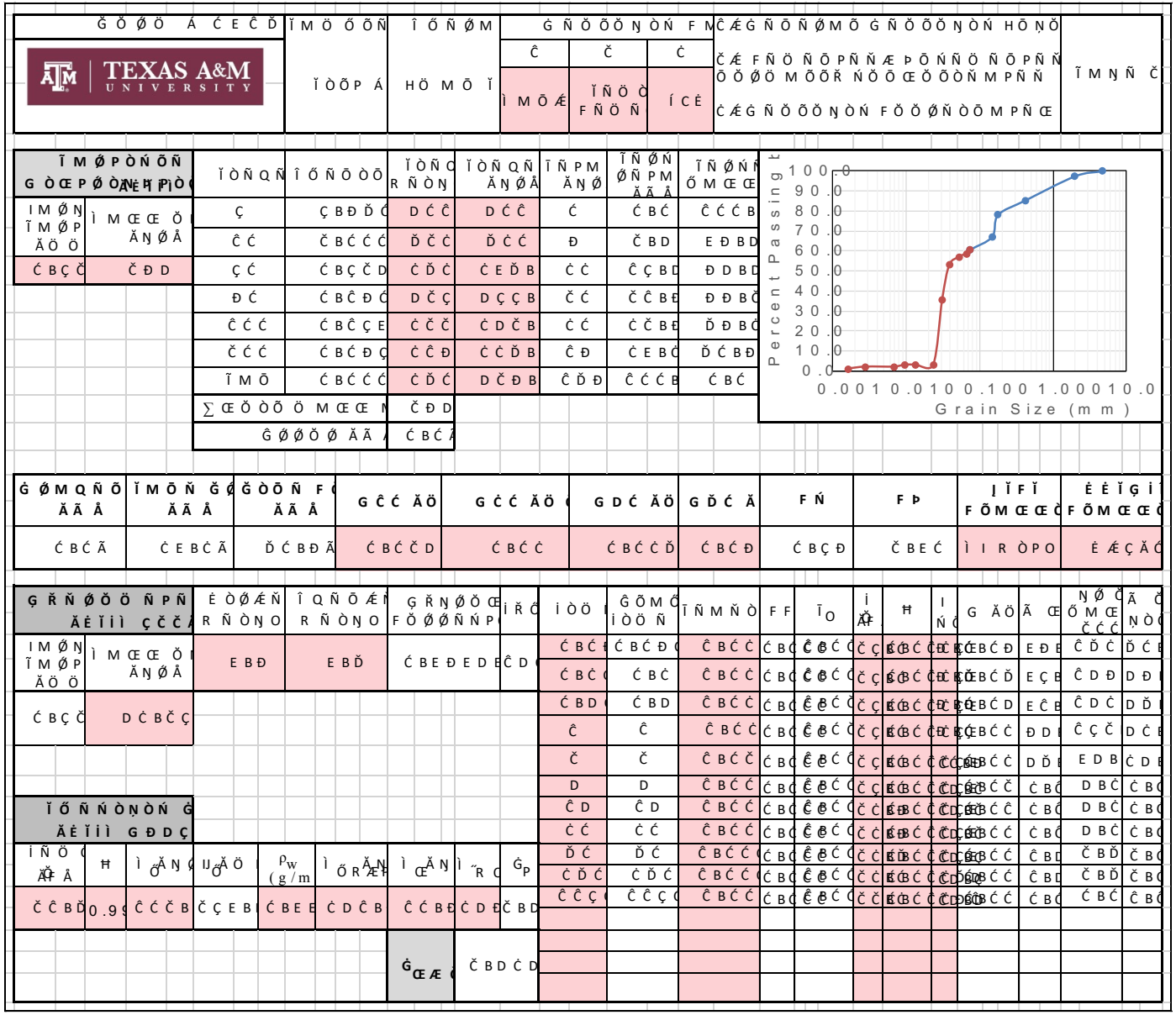

Figure B-188. Silt #7 – Page 2

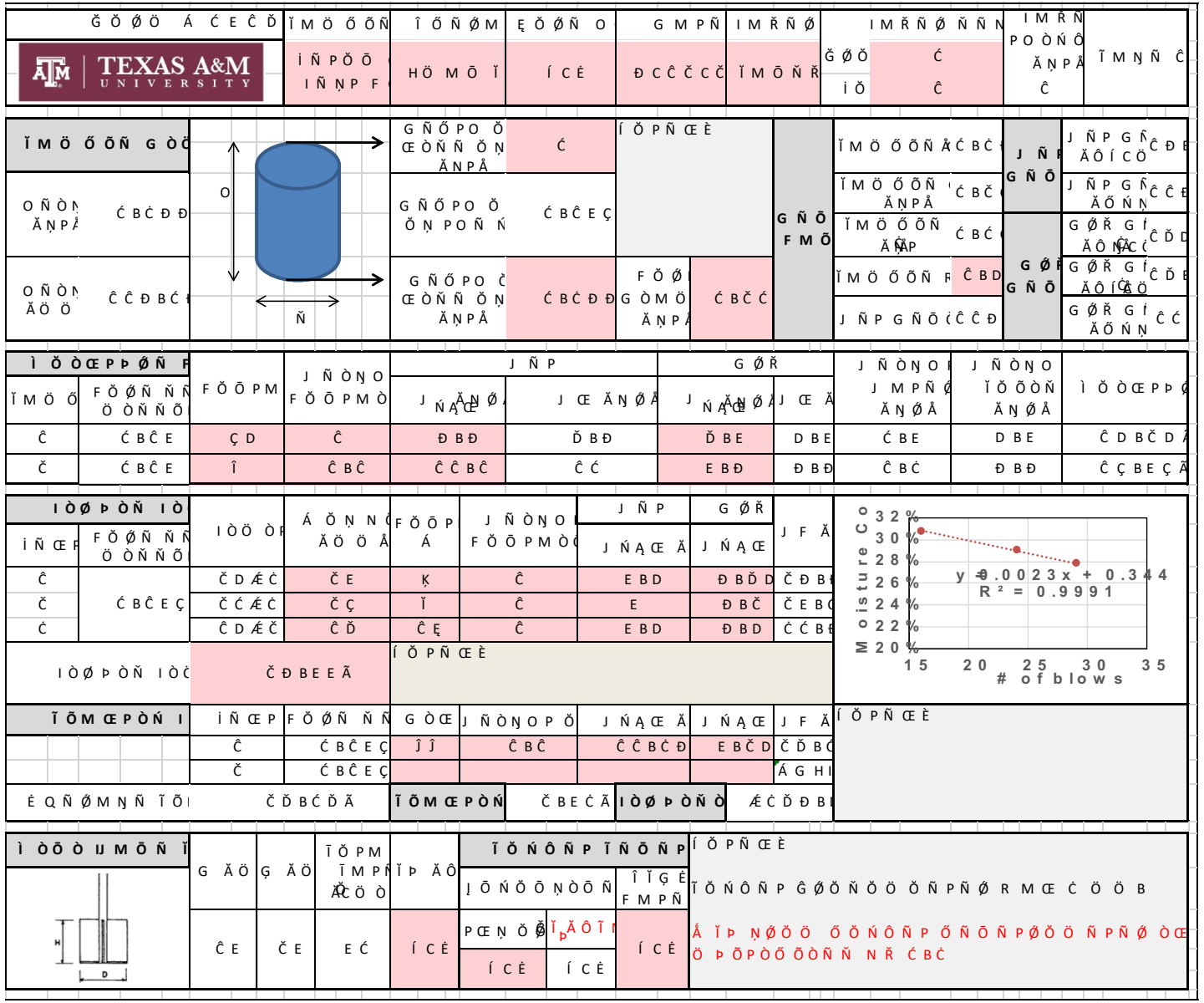

Figure B-189. Teton Dam Left Core – Page 1

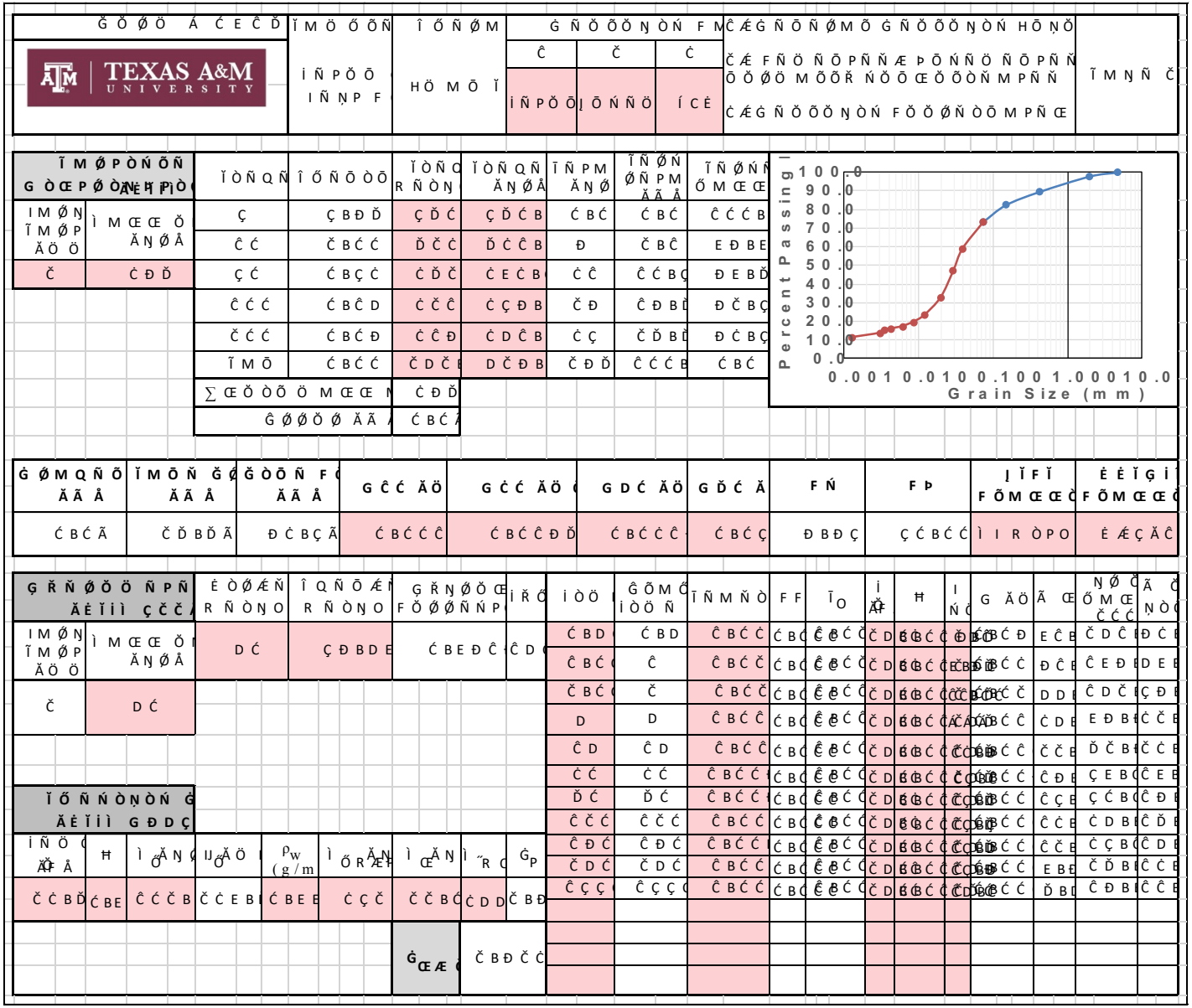

Figure B-190. Teton Dam Left Core – Page 2

APPENDIX C

FIRST AND SECOND ORDER STASTICAL ANALYSES RESULTS

First Order Statistics of the Erodibility Parameters

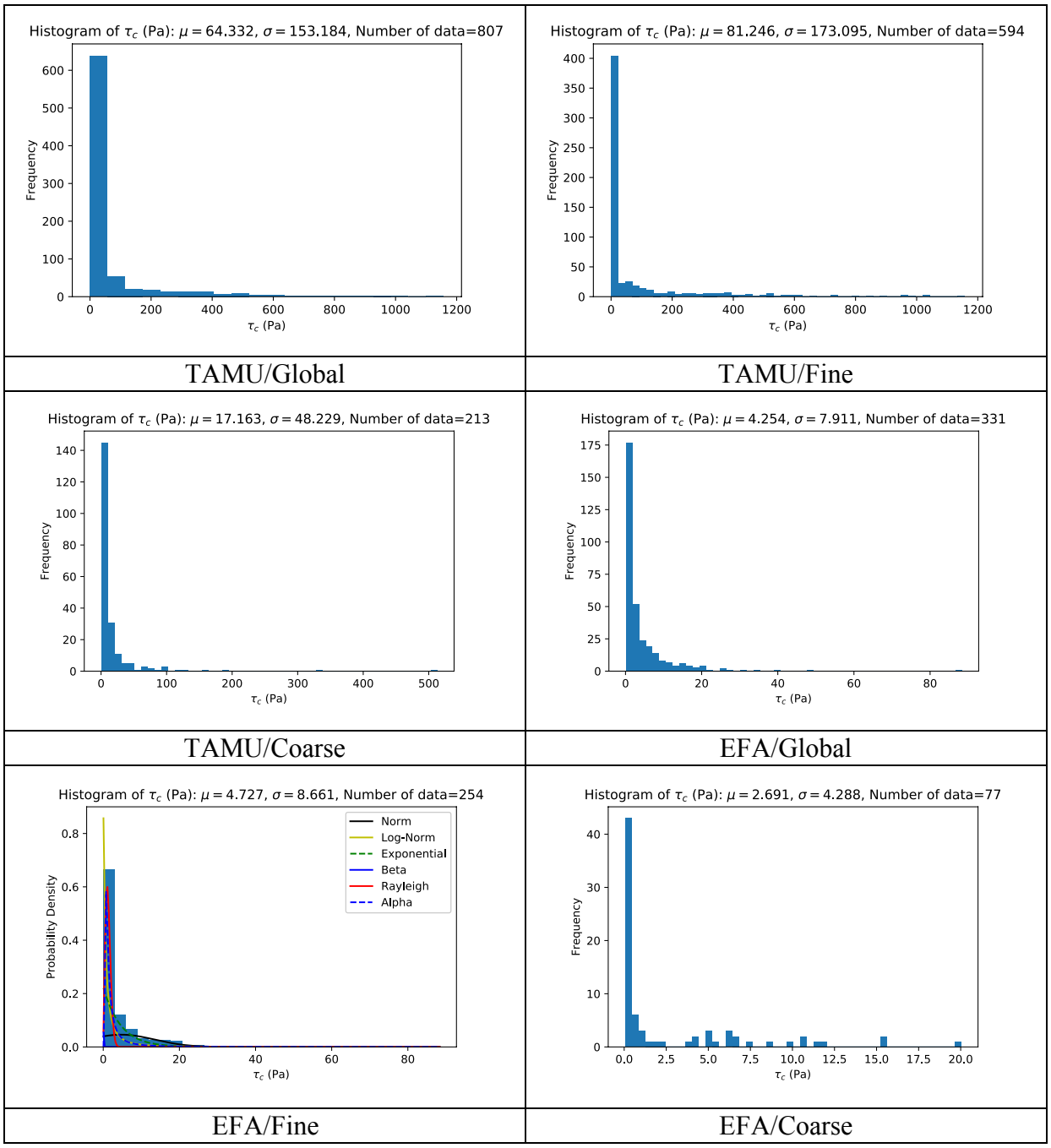

Figure C-1. a) Critical Shear Stress (τ_c) Histograms

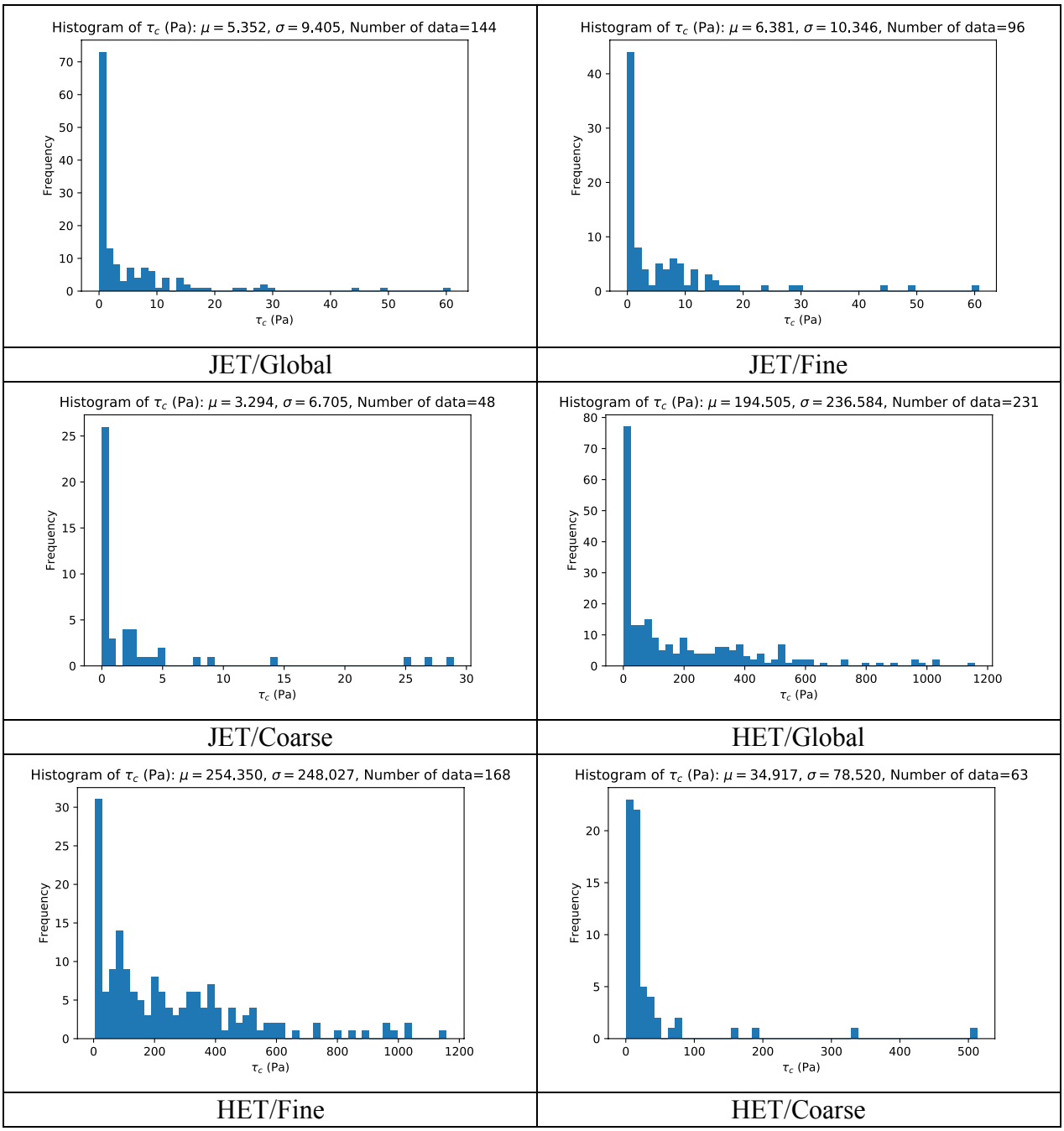

Figure C-1. b) Critical Shear Stress (τ_c) Histograms

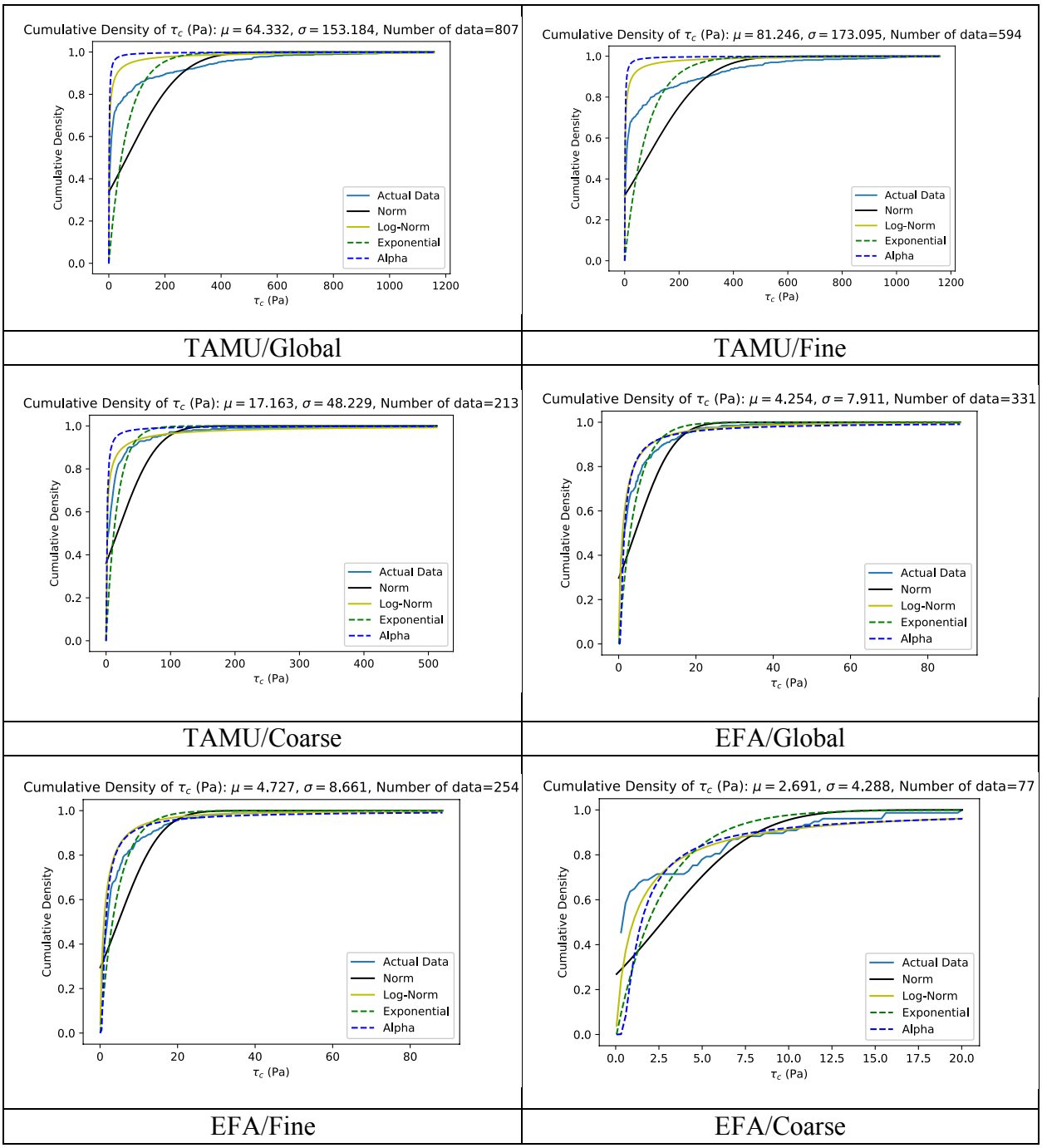

Figure C-2. a) Critical Shear Stress (τ_c) Empirical Cumulative Density Functions (ECDFs)

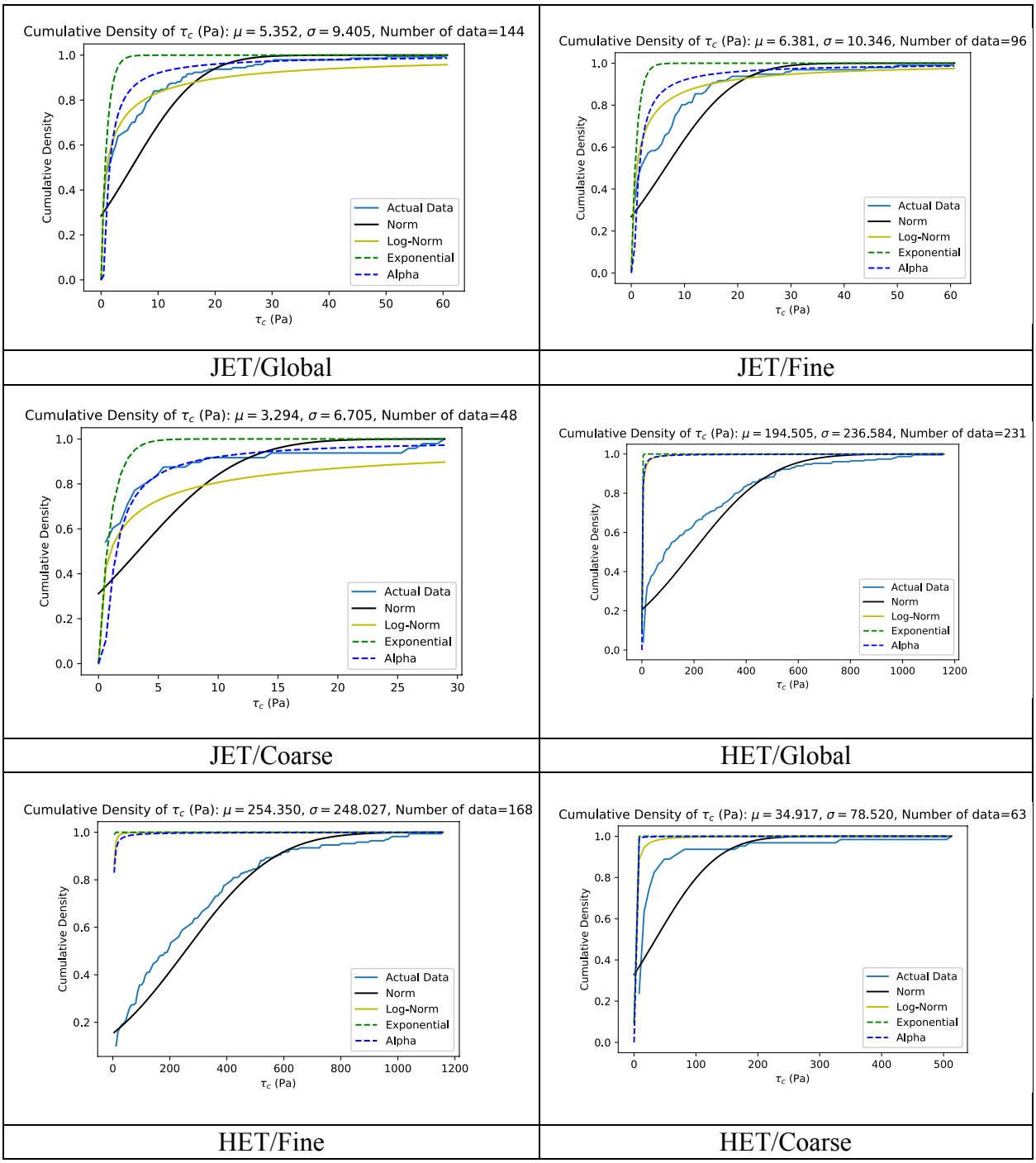

Figure C-2. a) Critical Shear Stress (τ_c) Empirical Cumulative Density Functions (ECDFs)

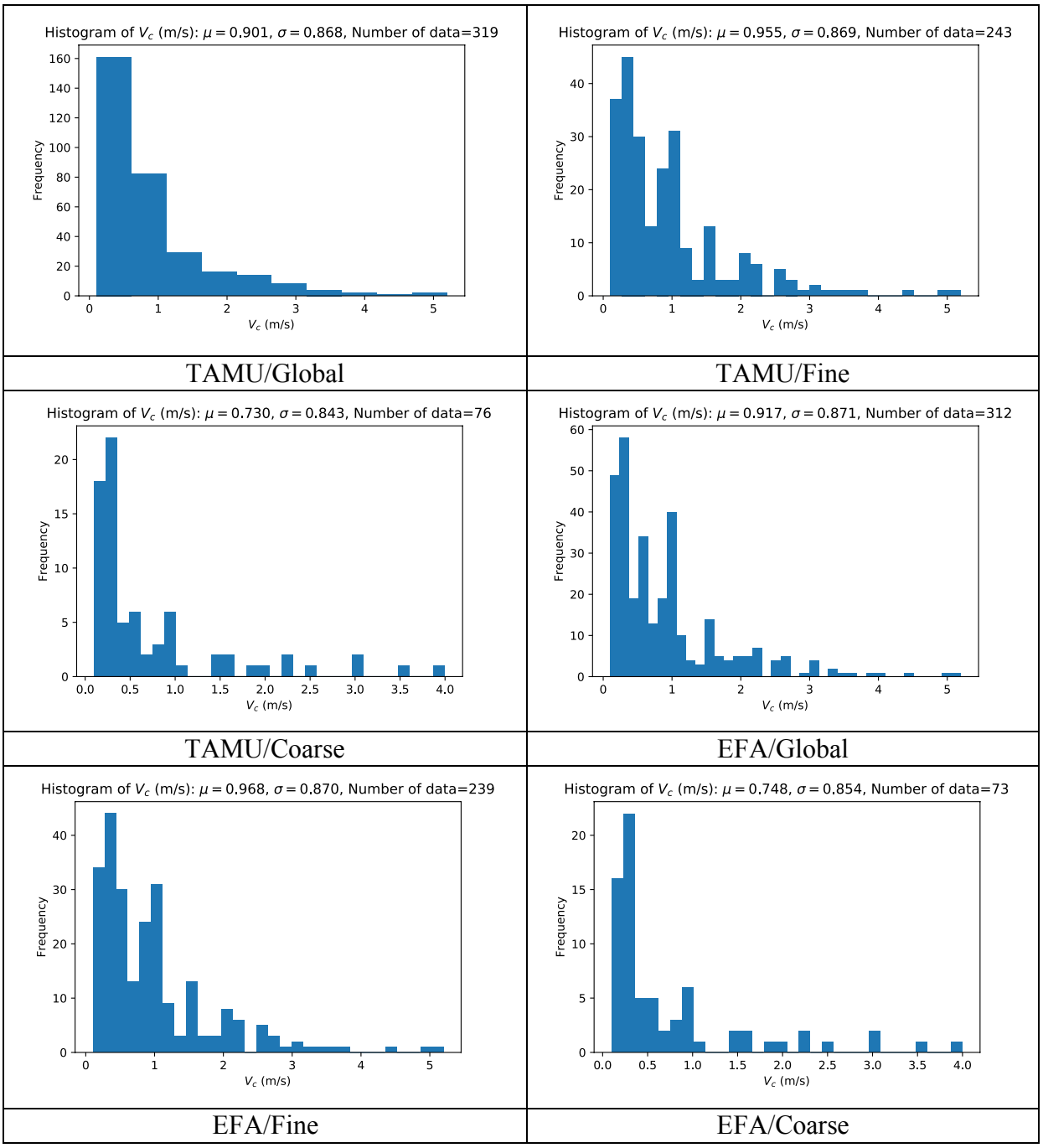

Figure C-3. Critical Velocity (v_c) Histograms

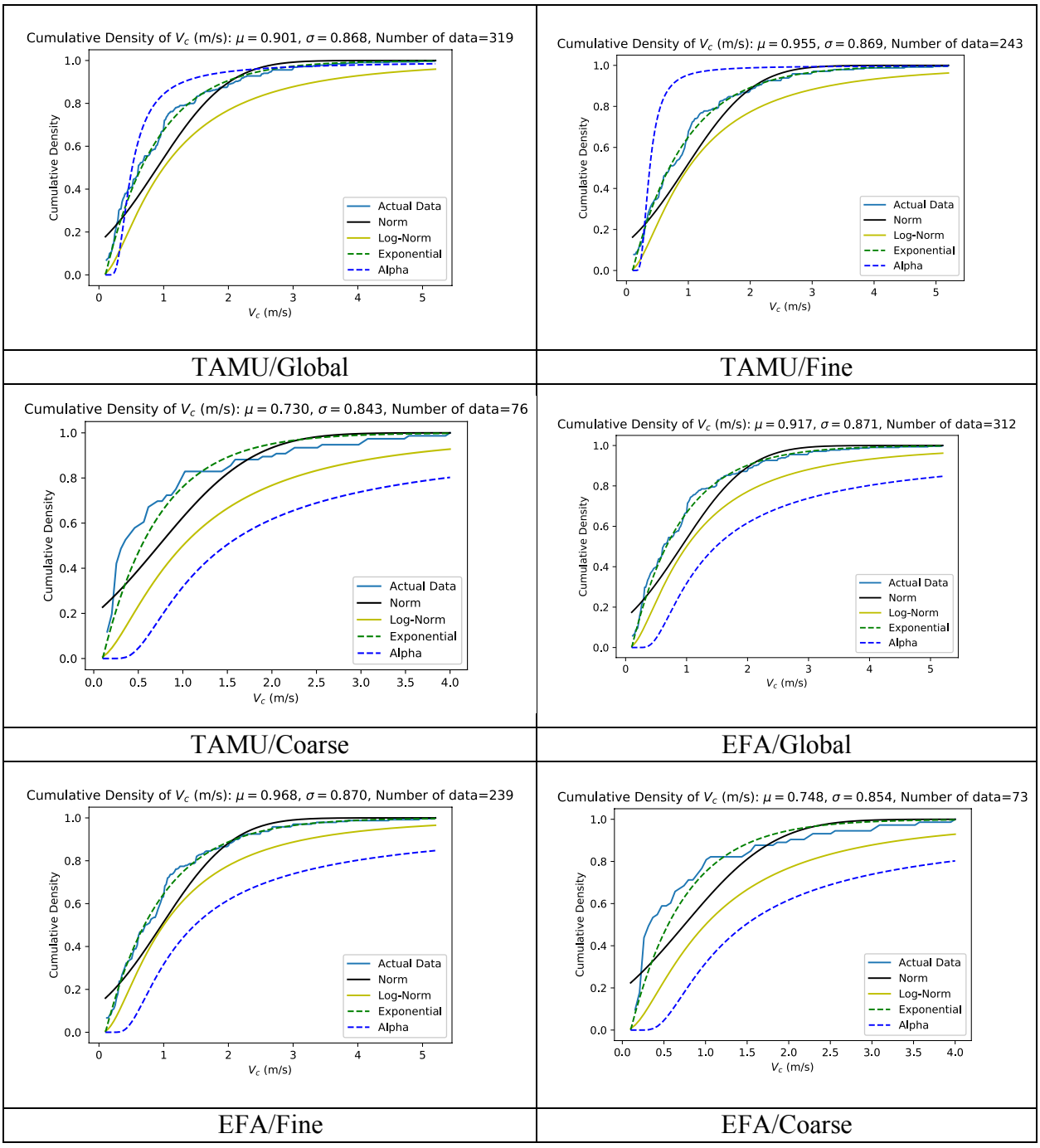

Figure C-4. Critical Velocity (v_c) Empirical Cumulative Density Functions (ECDFs)

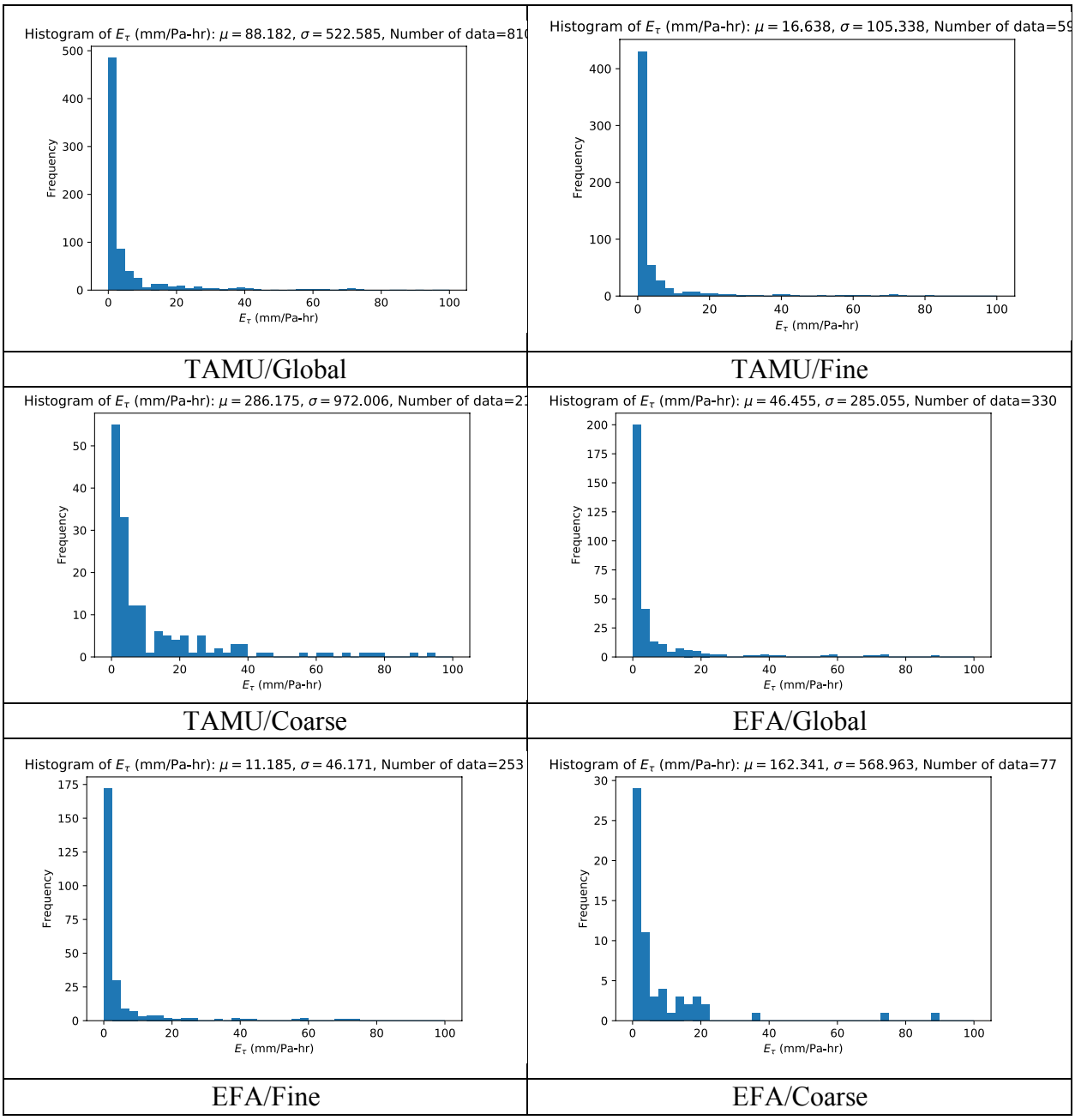

Figure C-5. a) Shear Stress Slope (E_τ) Histograms

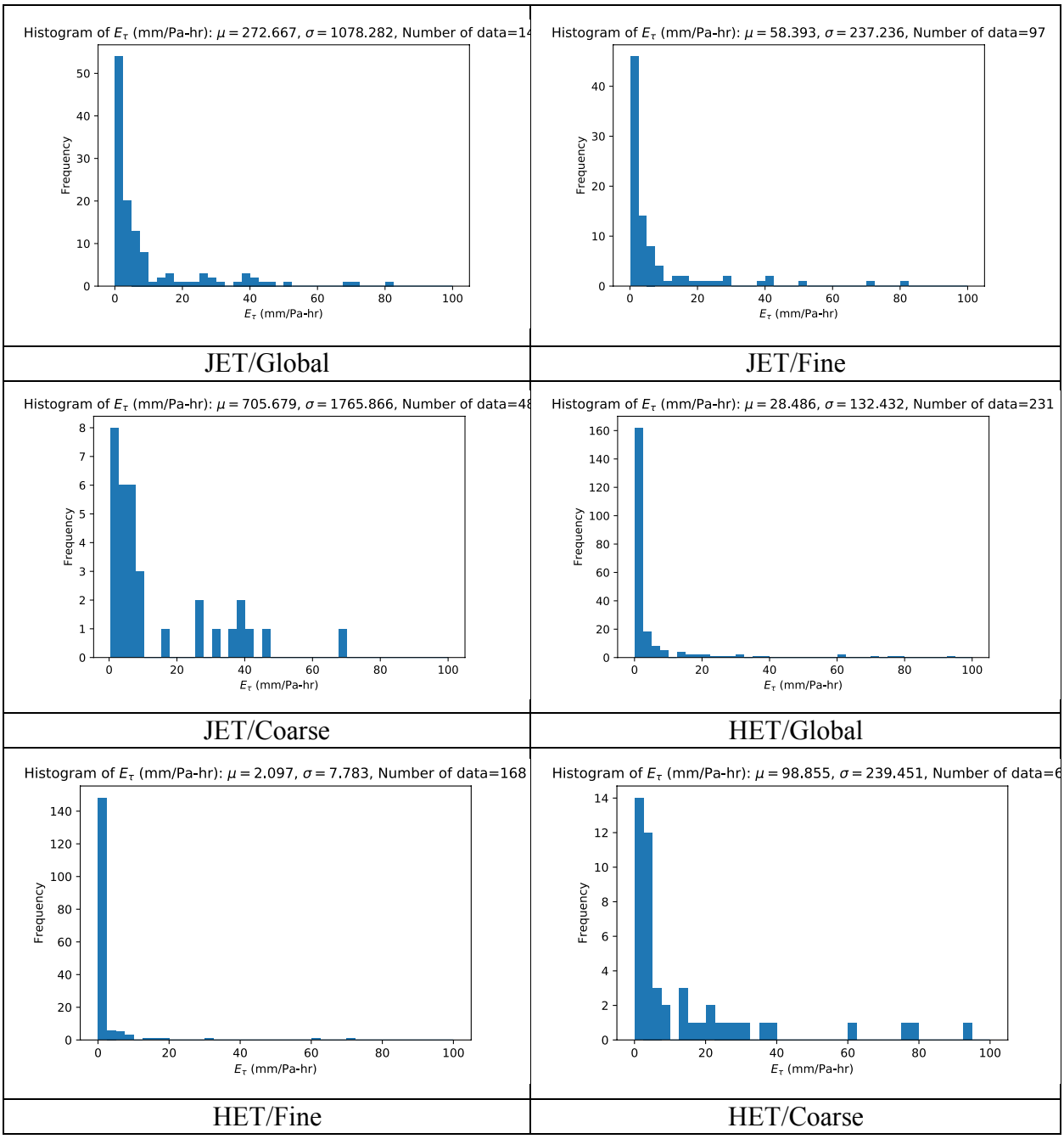

Figure C-5. b) Shear Stress Slope (E_τ) Histograms

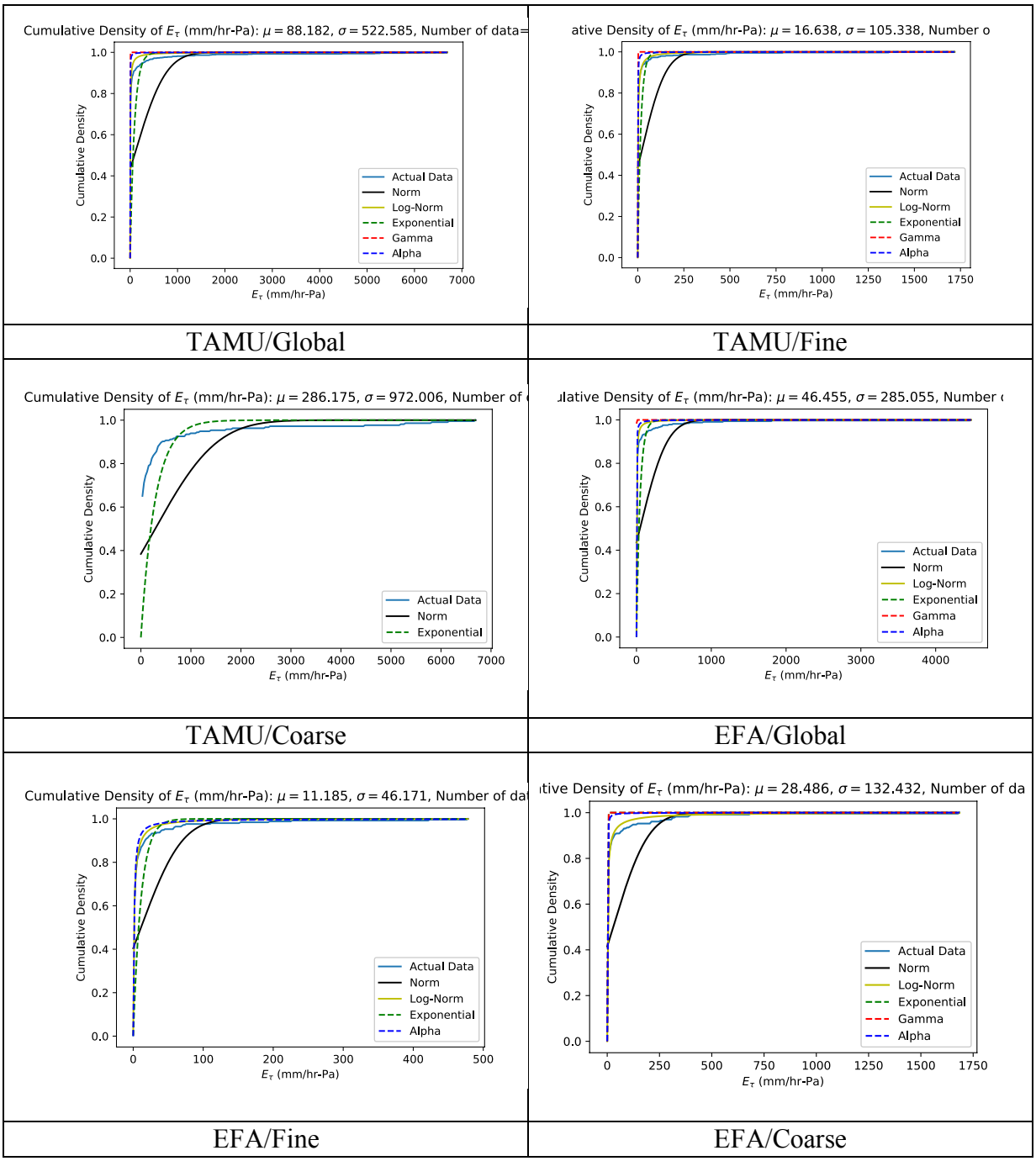

Figure C-6. a) Shear Stress Slope (E_τ) Empirical Cumulative Density Functions (ECDFs)

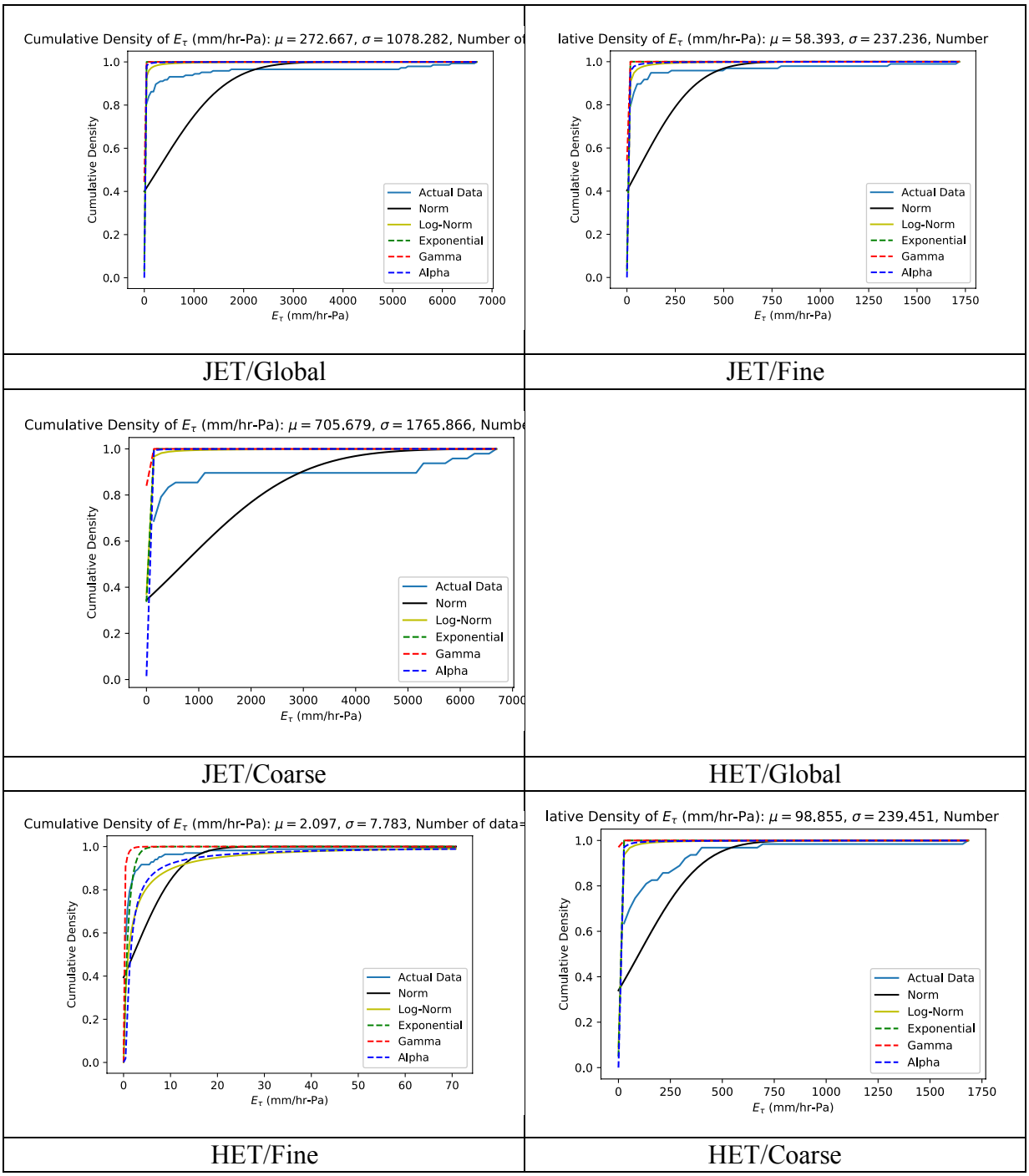

Figure C-6. b) Shear Stress Slope (E_τ) Empirical Cumulative Density Functions (ECDFs)

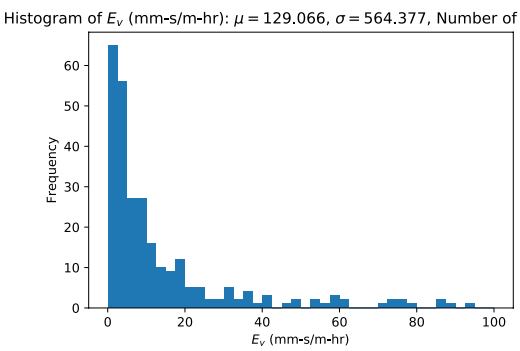

TAMU/Global

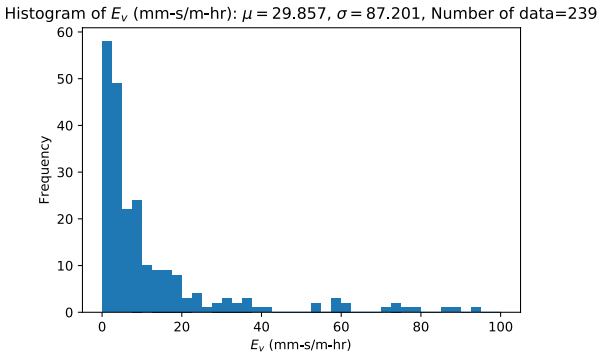

TAMU/Fine

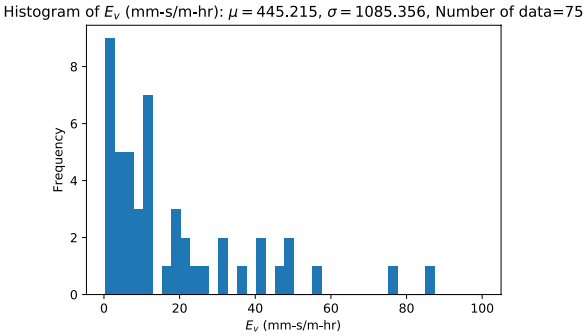

TAMU/Coarse

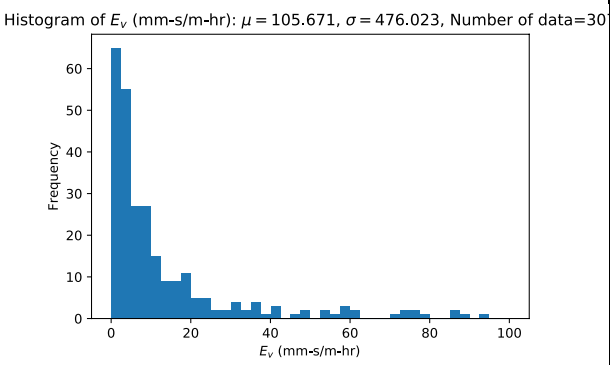

EFA/Global

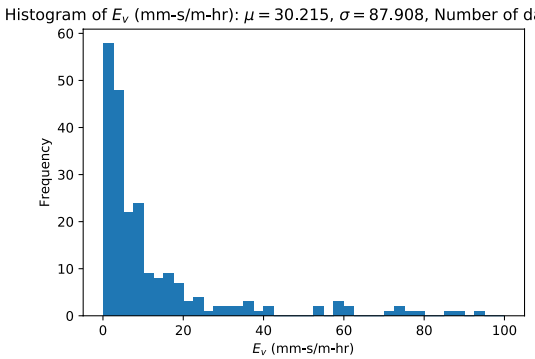

EFA/Fine

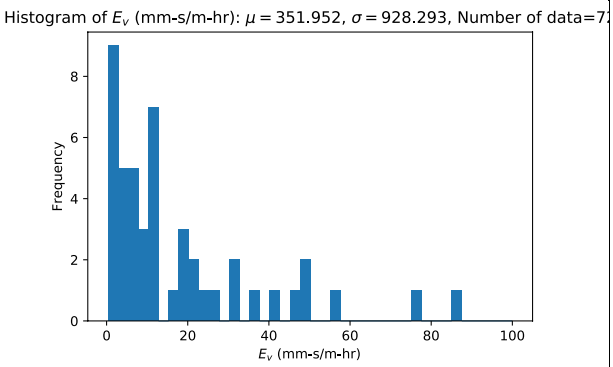

EFA/Coarse

Figure C-7. Velocity Slope (E_v) Histograms

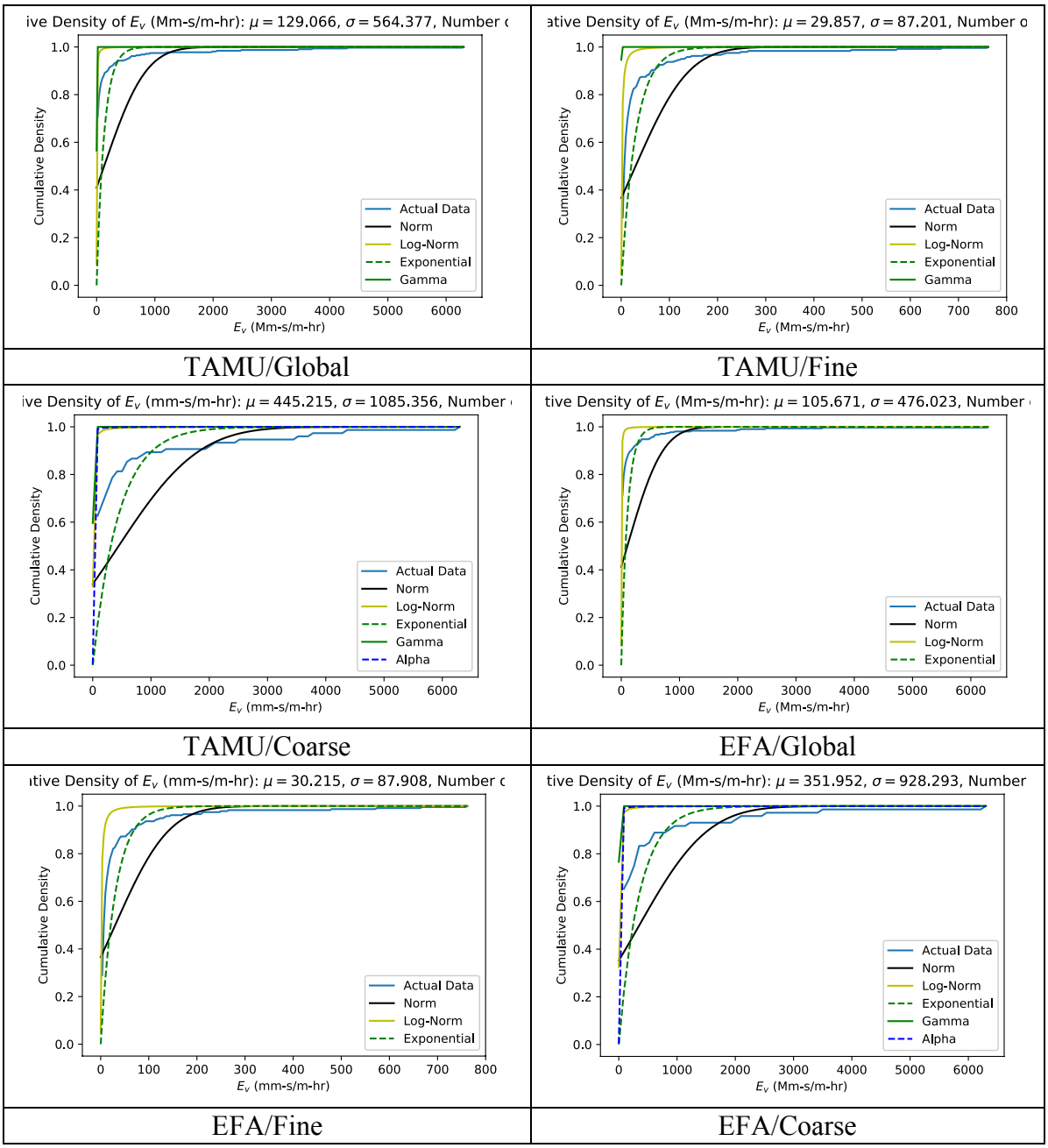

Figure C-8. Velocity Slope (E_v) Empirical Cumulative Density Functions (ECDFs)

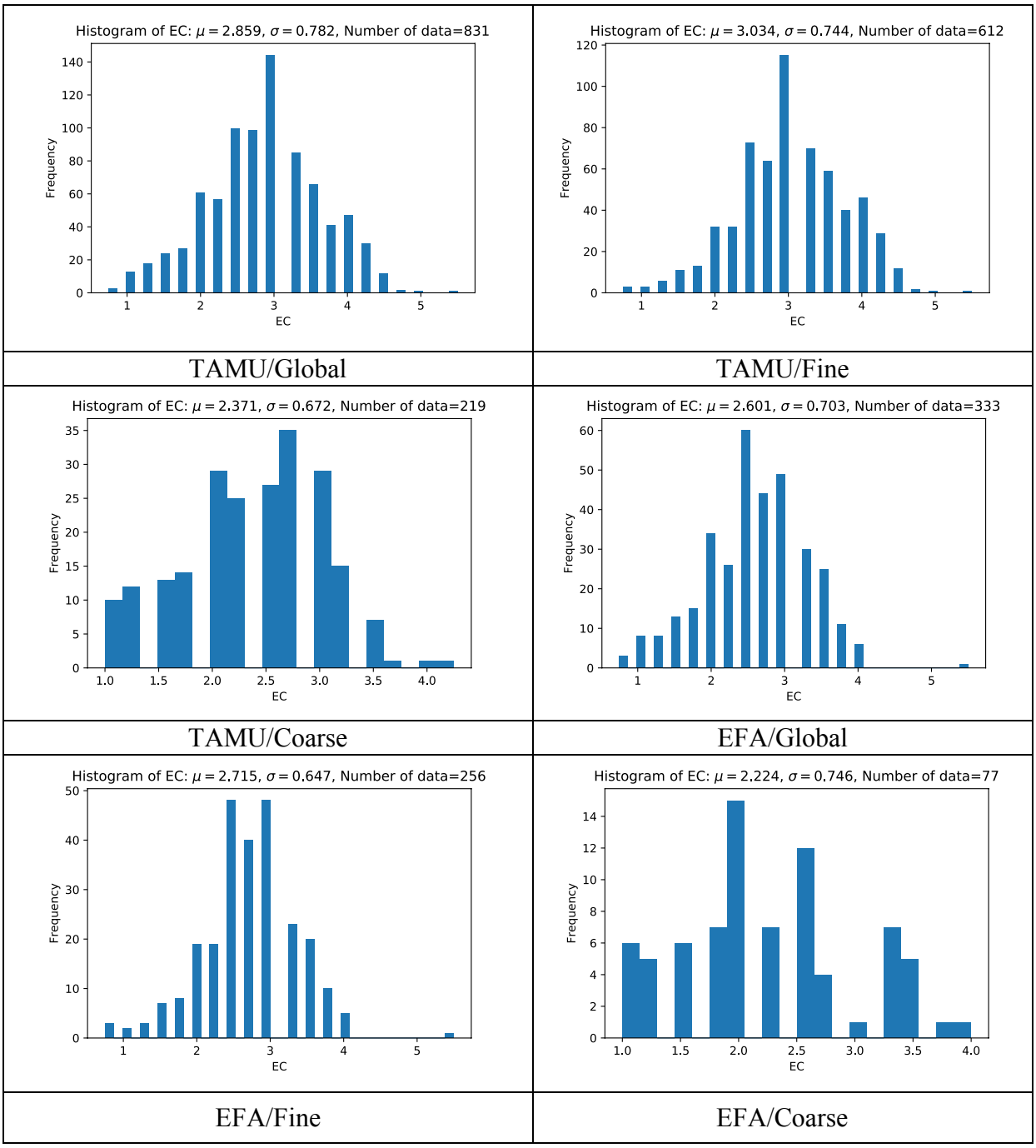

Figure C-9. a) Erosion Category (EC) Histograms

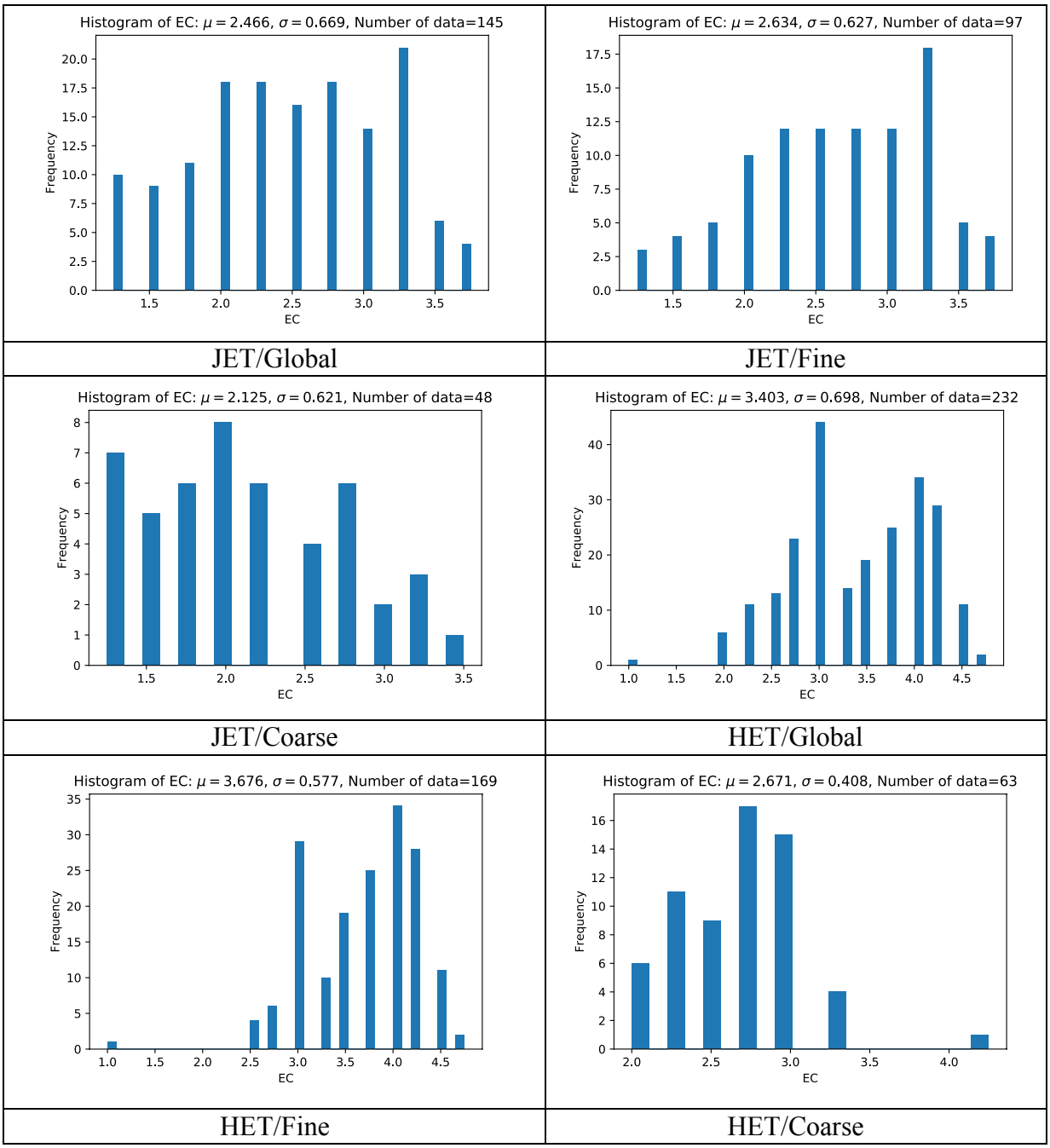

Figure C-9. b) Erosion Category (EC) Histograms

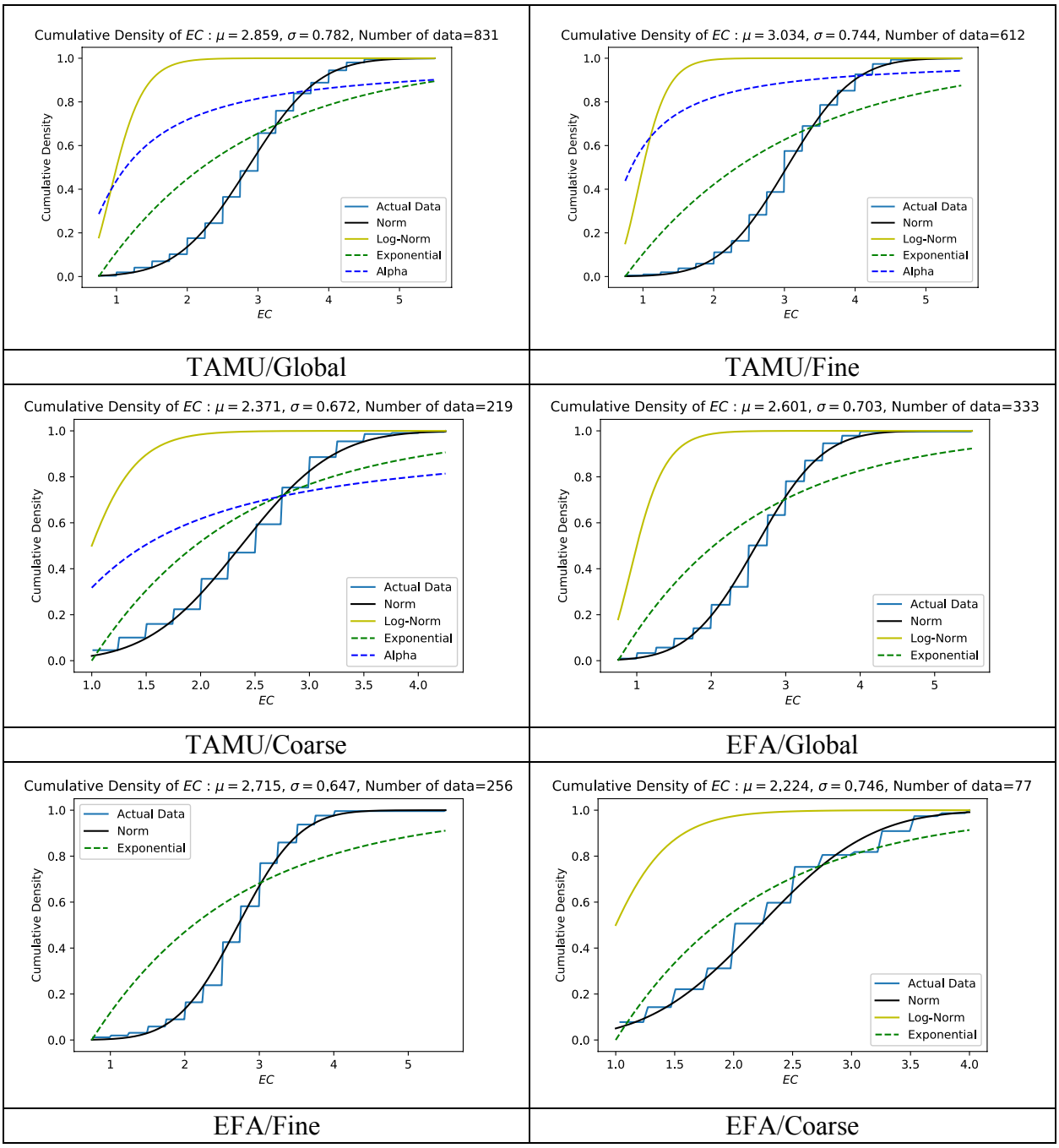

Figure C-10. a) Erosion Category (EC) Empirical Cumulative Density Functions (ECDFs)

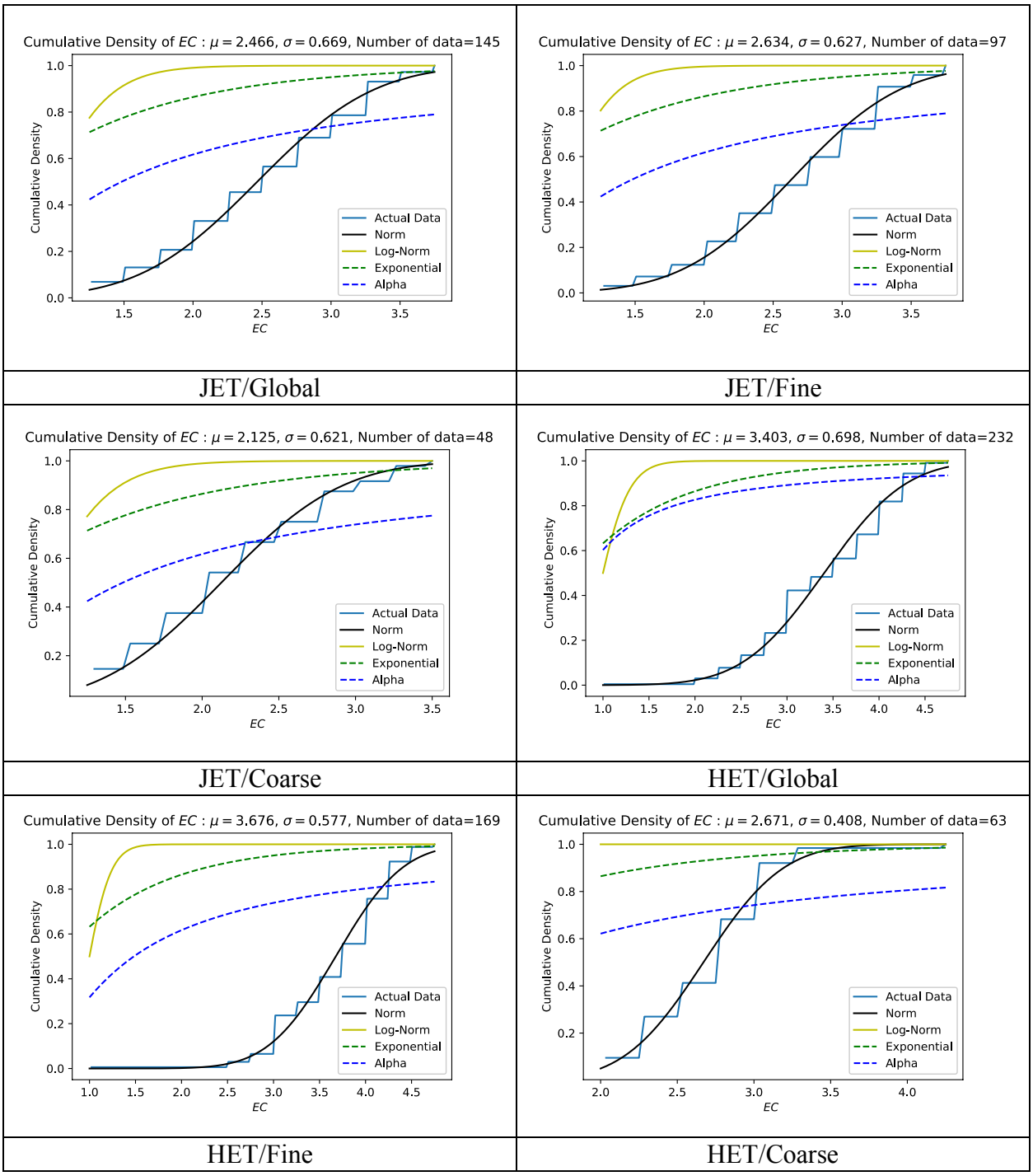

Figure C-10. b) Erosion Category (EC) Empirical Cumulative Density Functions (ECDFs)

Second Order Statistics of the Erodibility Parameters

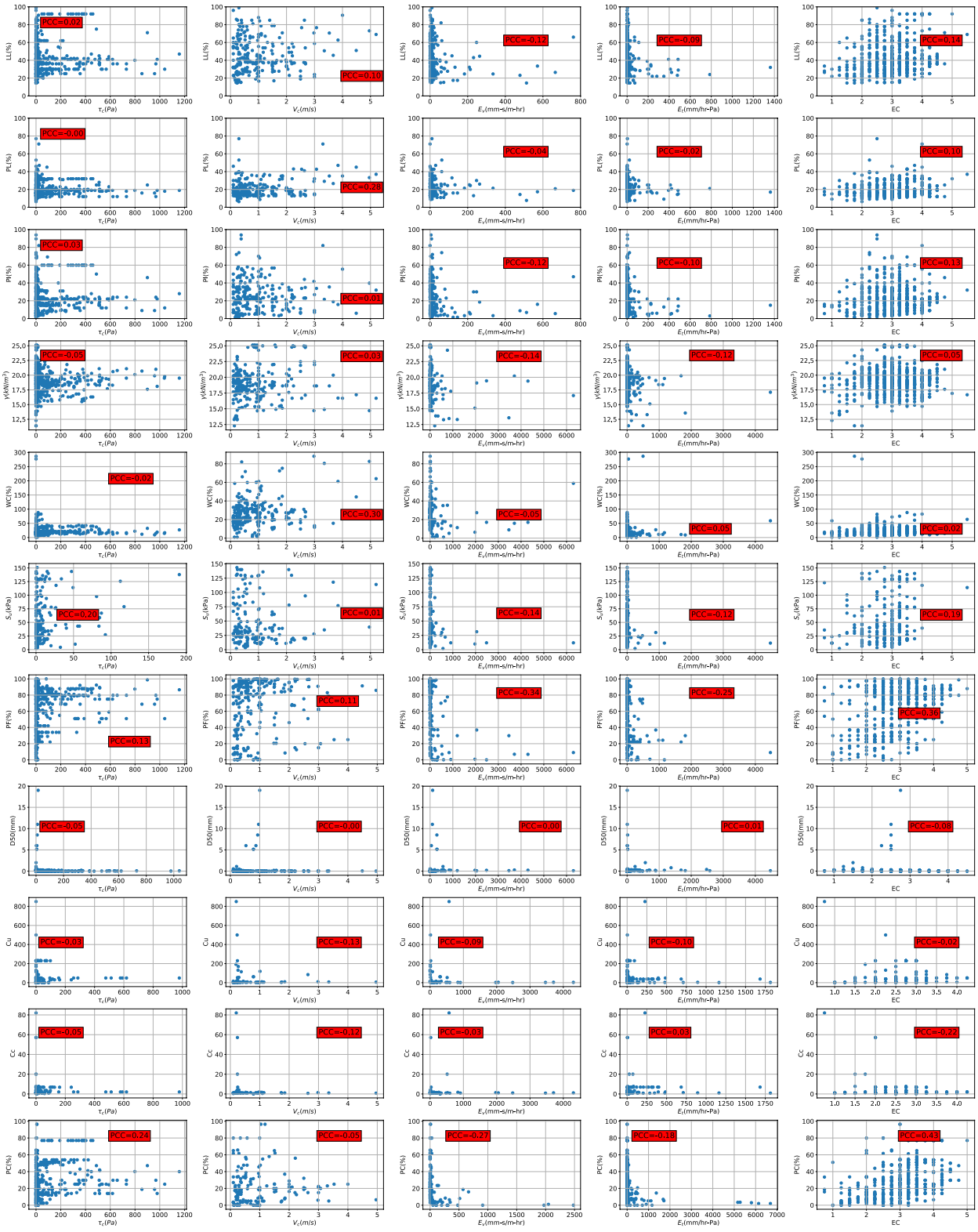

Figure C-11. Correlation Matrix for TAMU/Global

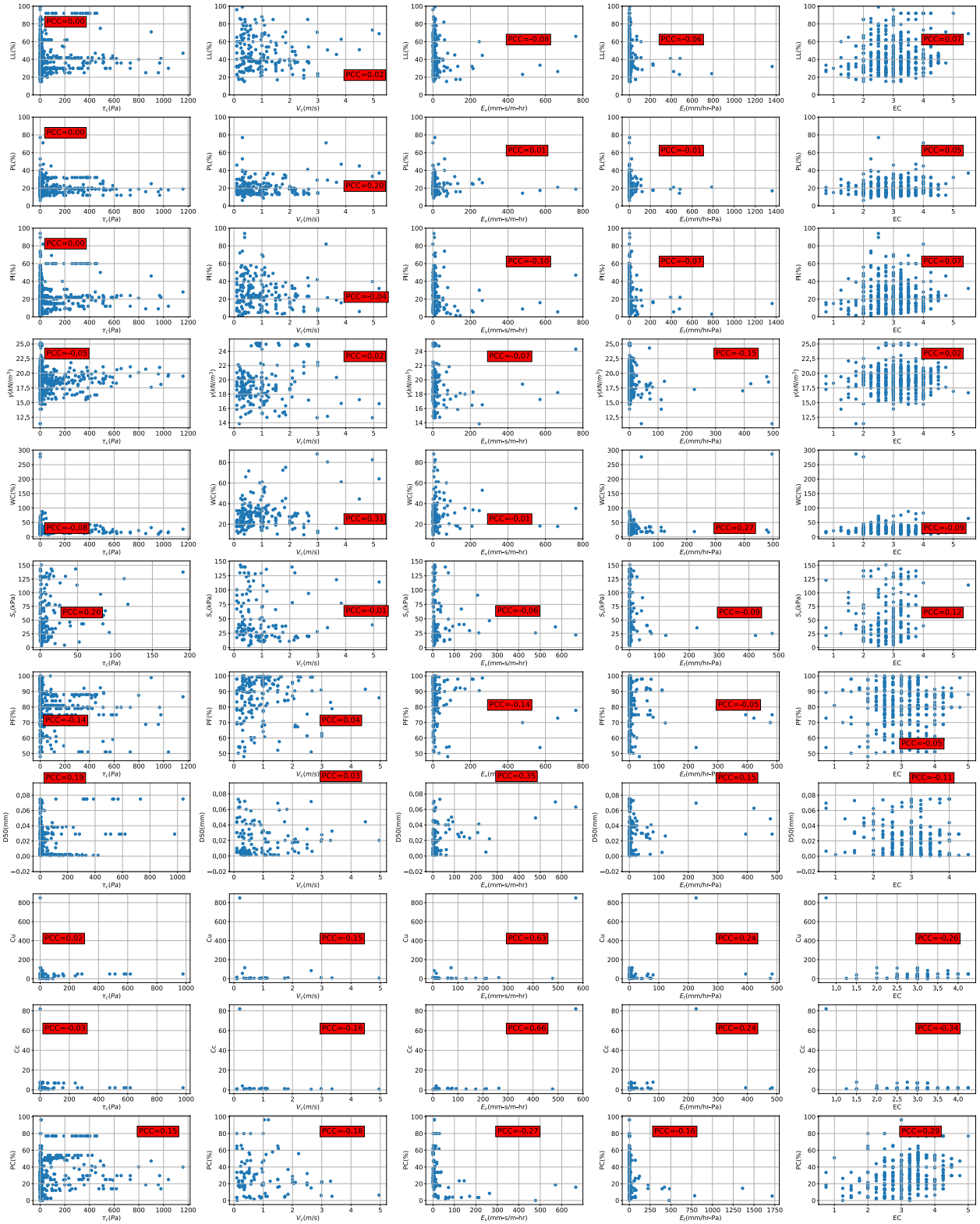

Figure C-12. Correlation Matrix for TAMU/Fine

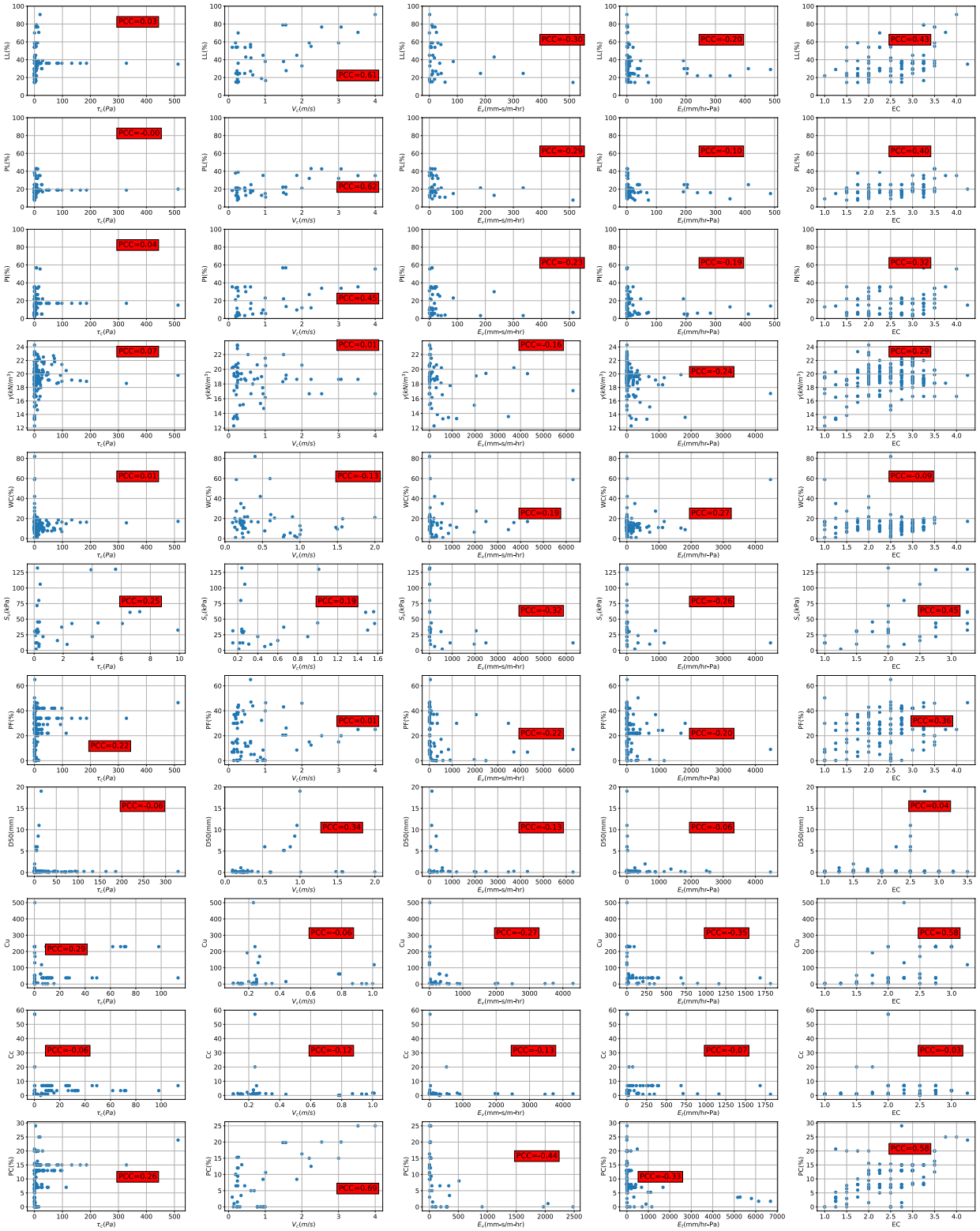

Figure C-13. Correlation Matrix for TAMU/Coarse

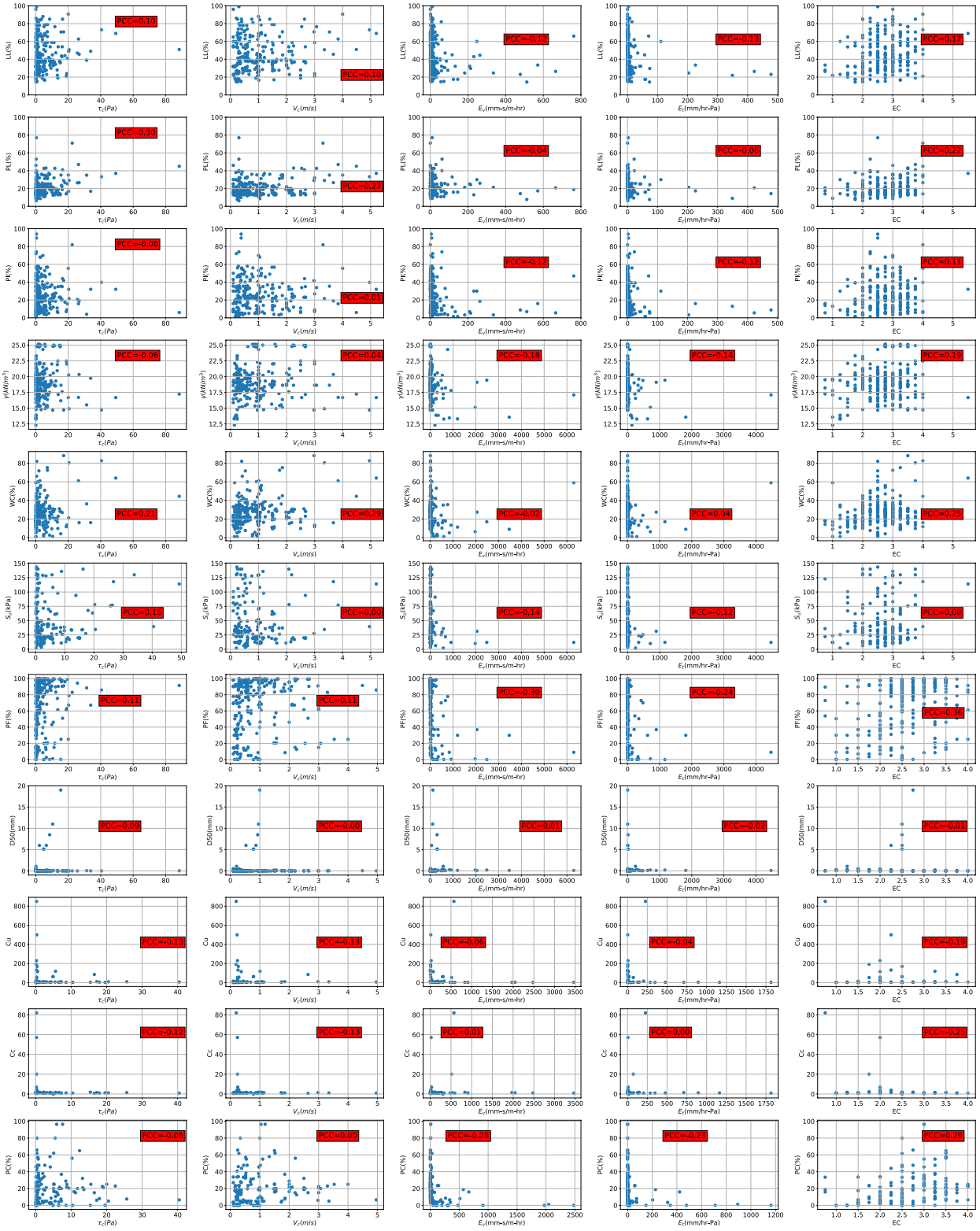

Figure C-14. Correlation Matrix for EFA/Global

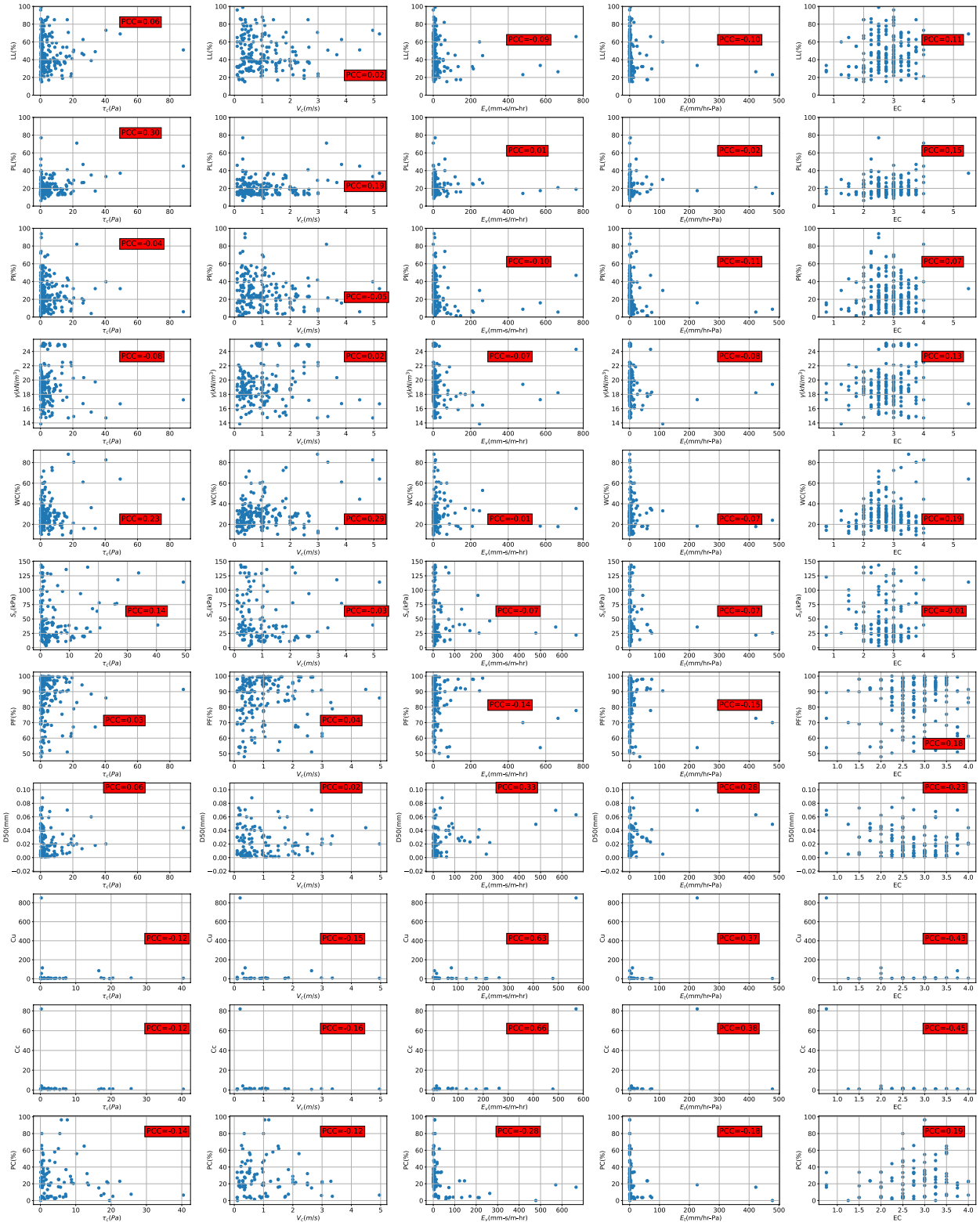

Figure C-15. Correlation Matrix for EFA/Fine

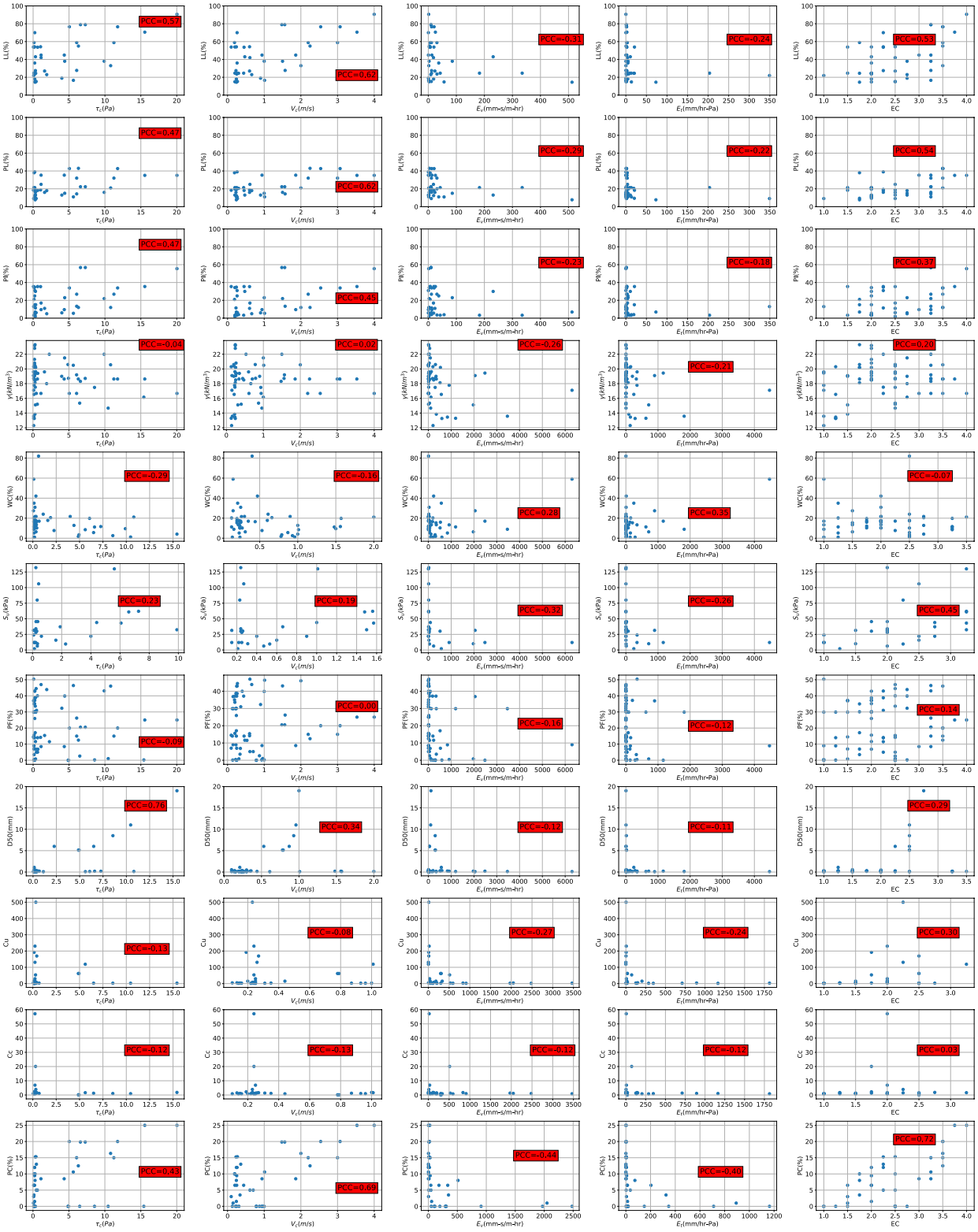

Figure C-16. Correlation Matrix for EFA/Coarse

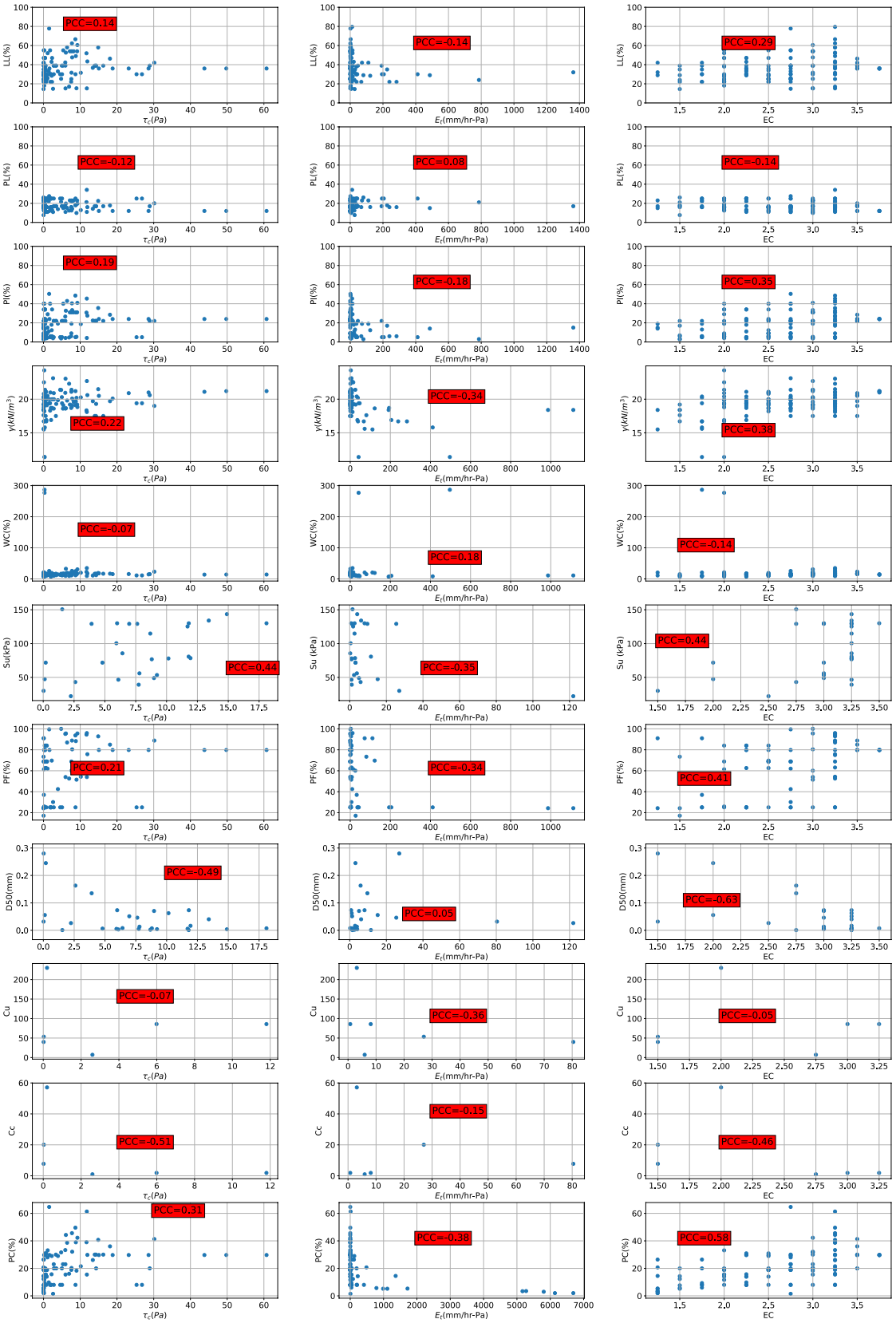

Figure C-17. Correlation Matrix for JET/Global

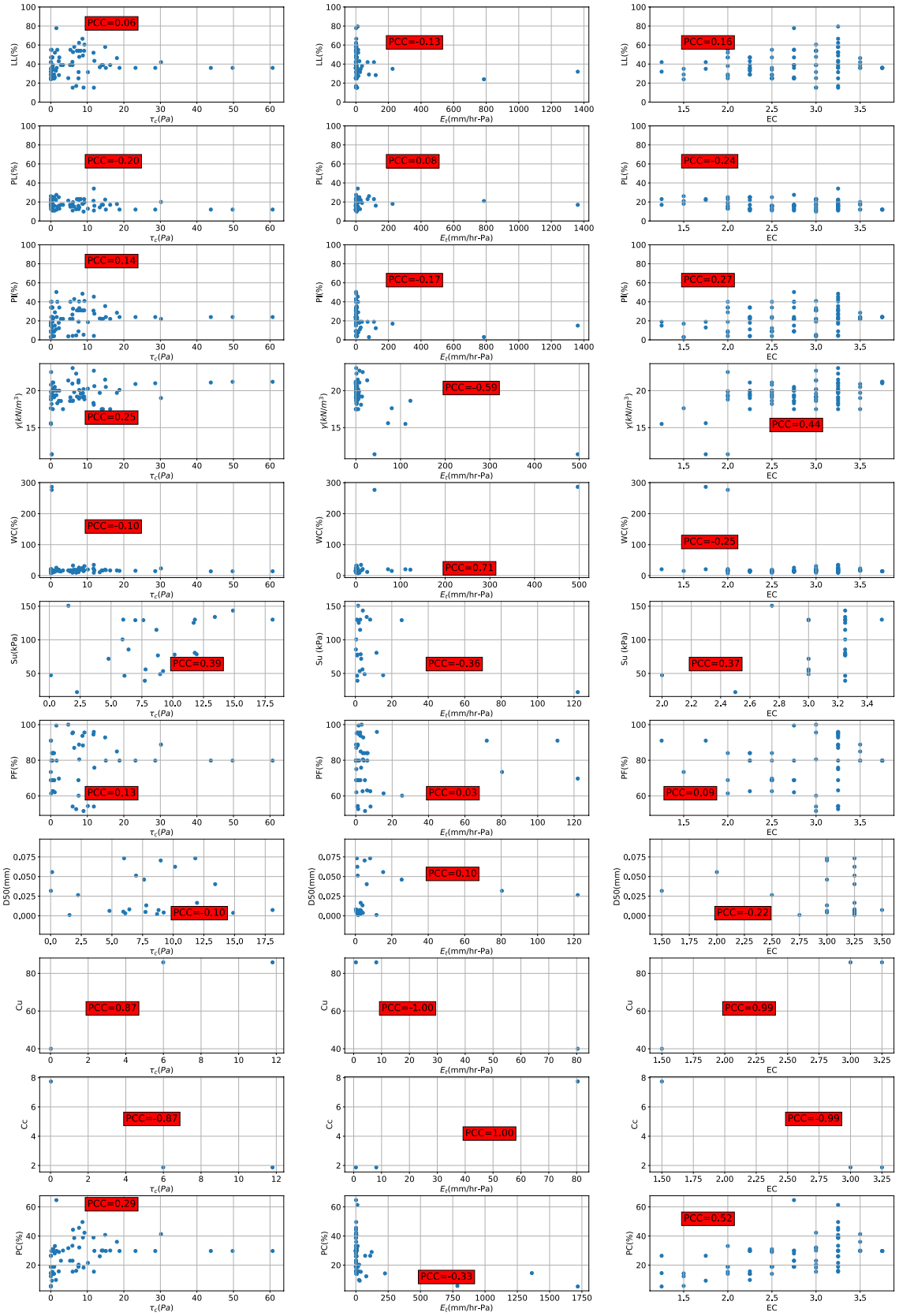

Figure C-18. Correlation Matrix for JET/Fine

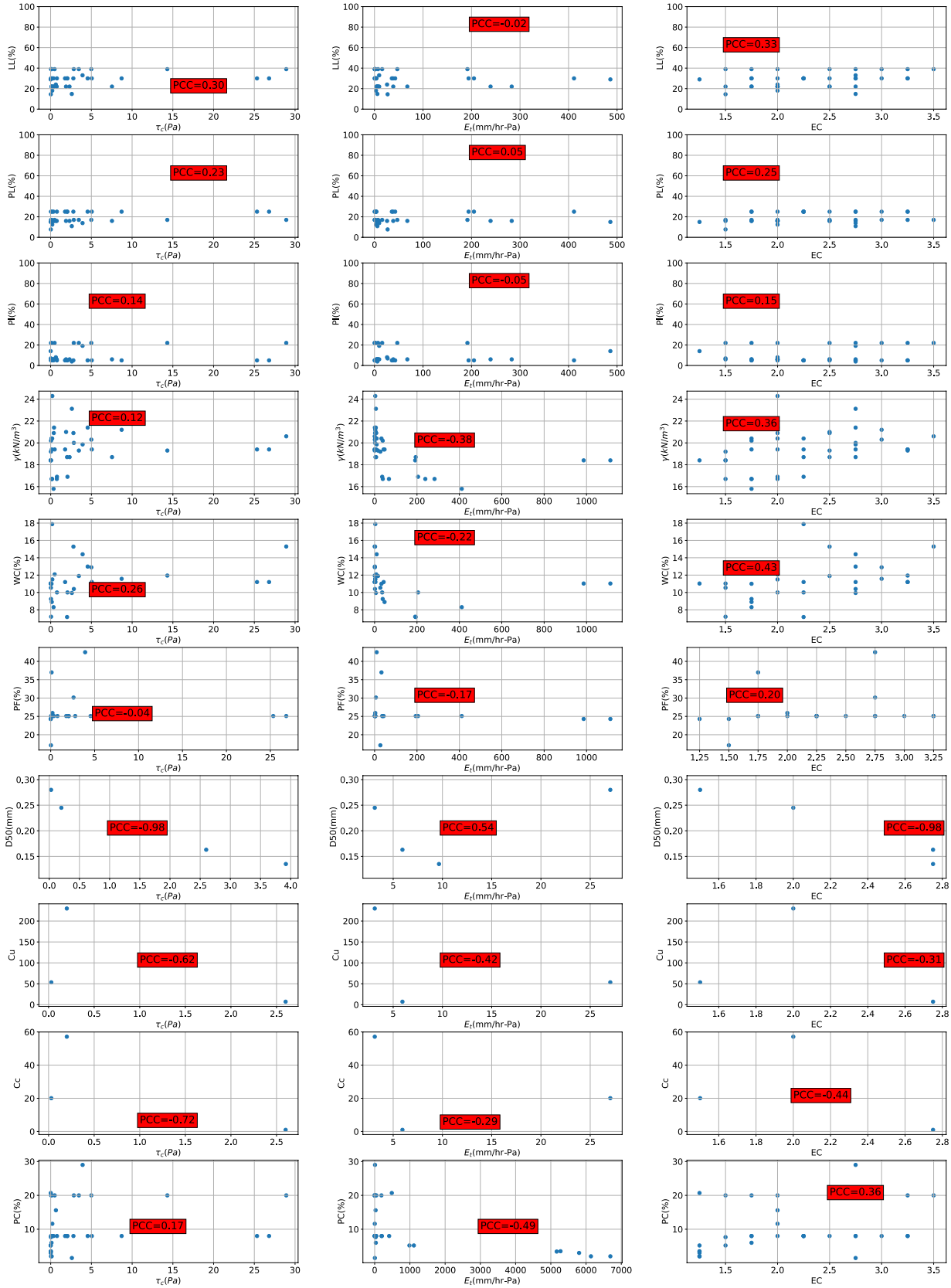

Figure C-19. Correlation Matrix for JET/Coarse

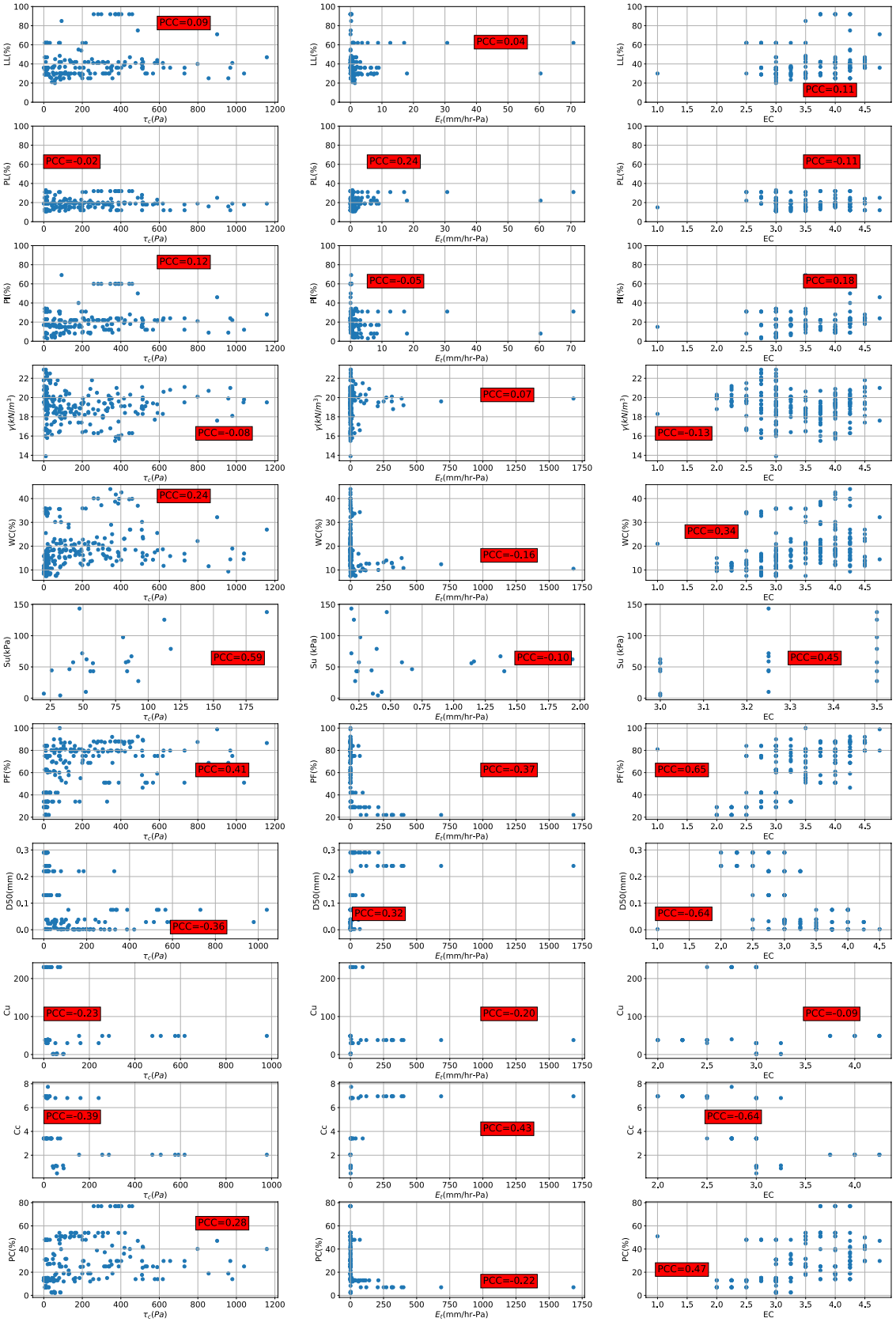

Figure C-20. Correlation Matrix for HET/Global

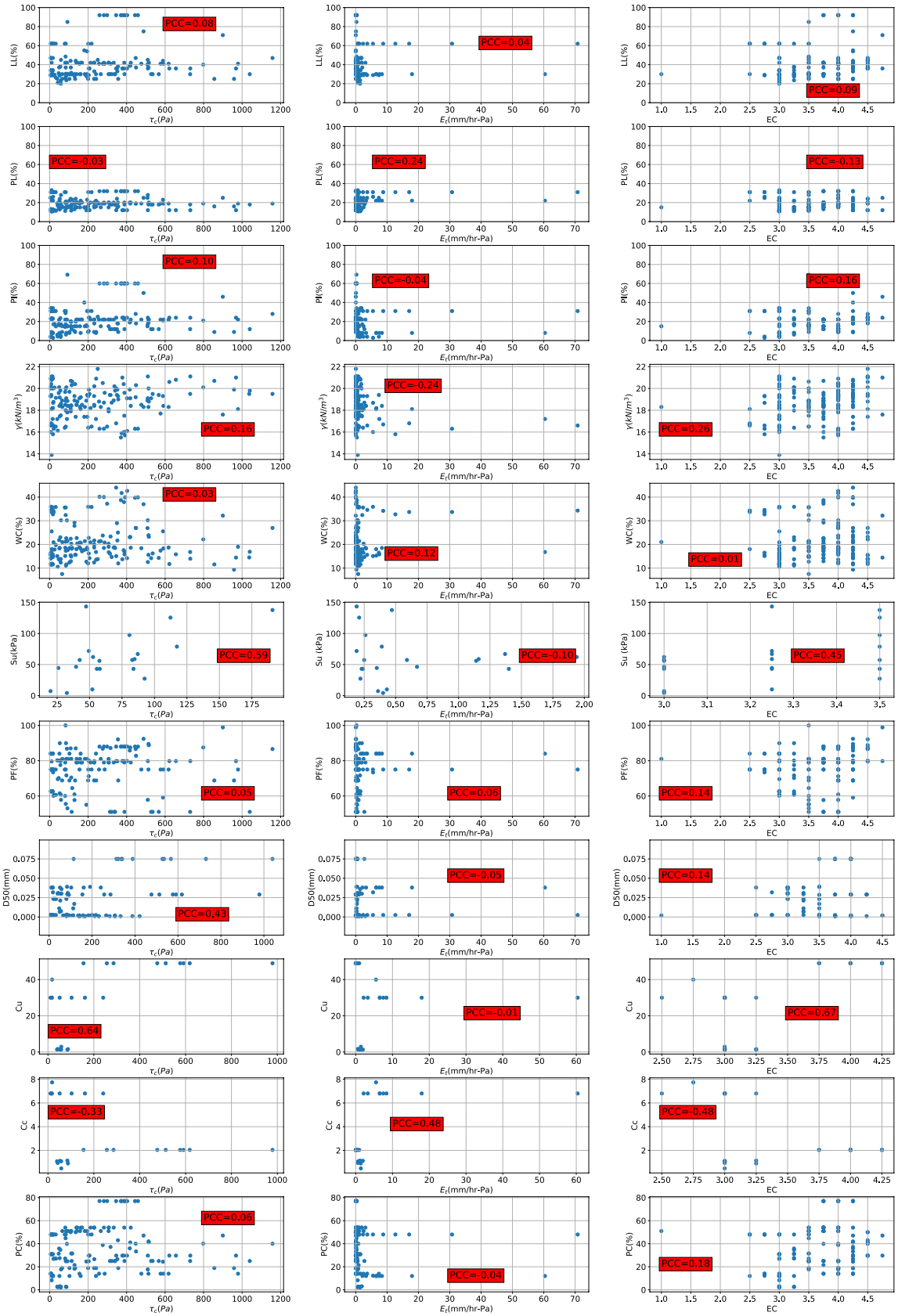

Figure C-21. Correlation Matrix for HET/Fine

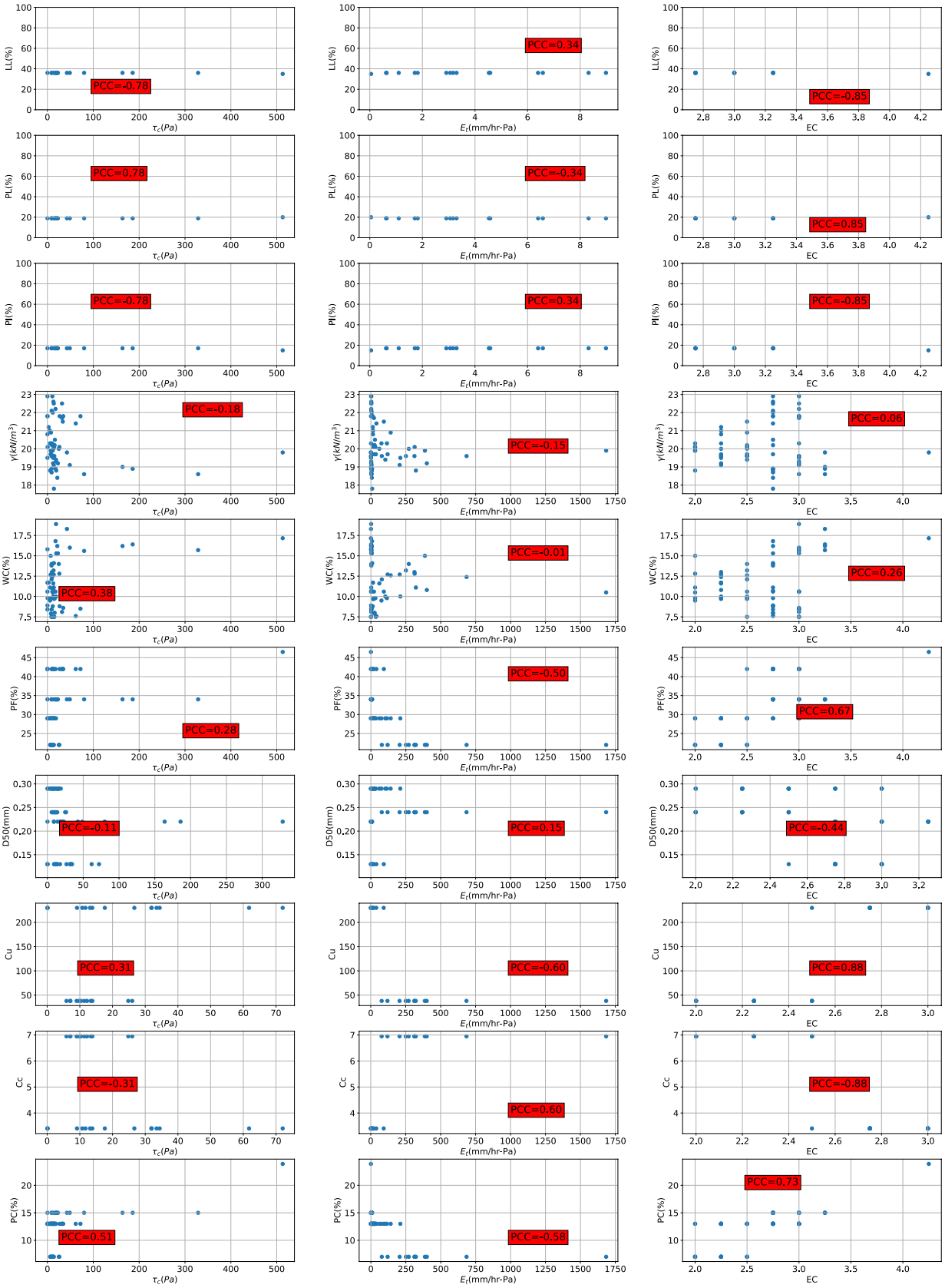

Figure C-22. Correlation Matrix for HET/Coarse

APPENDIX D

DETERMINISTIC FREQUENTISTS' REGRESSION ANALYSIS

Table D-1. Units of the Parameters Used in Regression Analyses

Parameter	Description	Unit
τ_c	Critical Shear Stress	Pa
C_c	Coefficient of Curvature	-
C_u	Coefficient of Uniformity	-
D50	Mean Particle Size	mm
EC	Erosion Category	-
E_v	Slope of Velocity-Erosion Rate	mm-s/m-hr
E_τ	Slope of Shear-Erosion Rate	Mm/hr-Pa
LL	Liquid Limit	%
PC	Clay Percentage (<0.002 mm)	%
PF	Percent Finer than Sieve #200	%
PI	Plasticity Index	%
PL	Plastic Limit	%
PP	Pocket Penetrometer Strength	kPa
S_u	Undrained Shear Strength	kPa
V_c	Critical Velcoity	m/s
VST	Vane Shear Strength	kPa
WC	Water Content	%
γ	Unit weight	kN/m^3

List of the Soil Parameter Combination Groups

List f Combination Groups for Global and Fine Datasets:

1- LL, PL, γ
2- LL, PL
3- LL, γ
4- LL, PL, γ, WC
5- LL, PL, γ, WC, S_u
6- LL, PF
7- PI, PF
8- PI, D50
9- PI, S_u
10- PI, WC
11- PI, γ, WC
12- PI, γ, S_u
13- PI, γ, PF
14- PI, γ, D50
15- PI, WC, S_u
16- PI, WC, PF
17- PI, WC, D50
18- PI, S_u, PF
19- PI, S_u, D50
20- γ, WC, S_u
21- γ, WC, PF
22- γ, WC, D50
23- WC, S_u, PF
24- WC, S_u, D50
25- S_u, γ, PF
26- S_u, γ, D50
27- PF, PI, D50
28- PF, γ, D50
29- PF, WC, D50
30- PF, S_u, D50
31- PI, γ, WC, S_u
32- PI, γ, WC, PF
33- PI, γ, WC, D50
34- PI, γ, S_u, PF
35- PI, γ, S_u, D50
36- PI, γ, PF, D50
37- PI, WC, S_u, PF
38- PI, WC, S_u, D50
39- PI, WC, PF, D50
40- PI, S_u, PF, D50
41- γ, WC, S_u, PF
42- γ, WC, S_u, D50
43- γ, S_u, PF, D50
44- WC, S_u, PF, D50

45- PI, S_u, PF, D50
46- γ, WC, PF, D50
47- PI, γ, WC, S_u, PF
48- PI, γ, WC, S_u, D50
49- γ, WC, S_u, PF, D50
50- PI, γ, S_u, PF, D50
51- PI, γ, WC, PF, D50
52- PI, WC, S_u, PF, D50
53- PI, γ, WC, S_u, PF, D50
54- LL, γ, WC
55- LL, γ, S_u
56- LL, γ, PF
57- LL, γ, D50
58- LL, WC, S_u
59- LL, WC, PF
60- LL, WC, D50
61- LL, S_u, PF
62- LL, S_u, D50
63- PF, LL, D50
64- LL, γ, WC, S_u
65- LL, γ, WC, PF
66- LL, γ, WC, D50
67- LL, γ, S_u, PF
68- LL, γ, S_u, D50
69- LL, γ, PF, D50
70- LL, WC, S_u, PF
71- LL, WC, S_u, D50
72- LL, WC, PF, D50
73- LL, S_u, PF, D50
74- LL, γ, WC, S_u, PF
75- LL, γ, WC, S_u, D50
76- LL, γ, S_u, PF, D50
77- LL, γ, WC, PF, D50
78- LL, WC, S_u, PF, D50
79- LL, γ, WC, S_u, PF, D50
80- PL, γ, WC
81- PL, γ, S_u
82- PL, γ, PF
83- PL, γ, D50
84- PL, WC, S_u
85- PL, WC, PF
86- PL, WC, D50
87- PL, S_u, PF
88- PL, S_u, D50
89- PF, PL, D50
90- PL, γ, WC, S_u

91- PL, γ, WC, PF
92- PL, γ, WC, D50
93- PL, γ, S_u, PF
94- PL, γ, S_u, D50
95- PL, γ, PF, D50
96- PL, WC, S_u, PF
97- PL, WC, S_u, D50
98- PL, WC, PF, D50
99- PL, S_u, PF, D50
100-PL, γ, WC, S_u, PF
101-PL, γ, WC, S_u, D50
102-PL, γ, S_u, PF, D50
103-PL, γ, WC, PF, D50
104-PL, WC, S_u, PF, D50
105-PL, γ, WC, S_u, PF, D50
106-PC, PL, γ
107-LL, PC
108-LL, PL, γ, PC, S_u
109-PC, γ, WC, S_u, PF, D50
110-PC, WC, S_u, PF, D50
111-PC, γ, WC, PF, D50
112-PC, γ, S_u, PF, D50
113-PC, γ, WC, S_u, D50
114-PC, γ, WC, S_u, PF
115-PC, S_u, PF, D50
116-PC, WC, PF, D50
117-PC, WC, S_u, D50
118-PC, WC, S_u, PF
119-PC, γ, PF, D50
120-PC, WC, D50
121-WC, A, γ
122-A, WC
123-A, PL, γ, WC, S_u
124-γ, A, WC, S_u, PF, D50
125-γ, WC, S_u, PF, A
126-D50, γ, WC, PF, A
127-D50, γ, S_u, PF, A
128-D50, γ, WC, S_u, A
129-LL, γ, A, S_u, PF
130-D50, S_u, PF, A
131-D50, WC, PF, A
132-A, WC, S_u, D50
133-A, WC, Su, PF
134-A, γ, PF, D50
135-A, WC, D50

List f Combination Groups for Coarse Datasets:

1- PI, PF
2- PI, D50
3- PI, VST
4- PI, WC
5- PI, γ, WC
6- PI, γ, VST
7- PI, γ, PF
8- PI, γ, D50
9- PI, WC, VST
10- PI, WC, PF
11- PI, WC, D50
12- PI, VST, PF
13- PI, VST, D50
14- γ, WC, VST
15- γ, WC, PF
16- γ, WC, D50
17- WC, VST, PF
18- WC, VST, D50
19- VST, γ, PF
20- VST, γ, D50
21- PF, PI, D50
22- PF, γ, D50
23- PF, WC, D50
24- PF, VST, D50
25- PI, γ, WC, VST
26- PI, γ, WC, PF
27- PI, γ, WC, D50
28- PI, γ, VST, PF
29- PI, γ, VST, D50
30- PI, γ, PF, D50
31- PI, WC, VST, PF
32- PI, WC, VST, D50
33- PI, WC, PF, D50
34- PI, VST, PF, D50
35- γ, WC, VST, PF
36- γ, WC, VST, D50
37- γ, VST, PF, D50
38- WC, VST, PF, D50
39- PI, VST, PF, D50
40- γ, WC, PF, D50
41- PI, γ, WC, VST, PF
42- PI, γ, WC, VST, D50
43- γ, WC, VST, PF, D50
44- PI, γ, VST, PF, D50

45- PI, γ, WC, PF, D50
46- PI, WC, VST, PF, D50
47- PI, γ, WC, VST, PF, D50
48- C_c, γ, WC
49- C_c, γ, VST
50- C_c, γ, PF
51- C_c, γ, D50
52- C_c, WC, VST
53- C_c, WC, PF
54- C_c, WC, D50
55- C_c, VST, PF
56- C_c, VST, D50
57- PF, C_c, D50
58- C_c, γ, WC, VST
59- C_c, γ, WC, PF
60- C_c, γ, WC, D50
61- C_c, γ, VST, PF
62- C_c, γ, VST, D50
63- C_c, γ, PF, D50
64- C_c, WC, VST, PF
65- C_c, WC, VST, D50
66- C_c, WC, PF, D50
67- C_c, VST, PF, D50
68- C_c, γ, WC, VST, PF
69- C_c, γ, WC, VST, D50
70- C_c, γ, VST, PF, D50
71- C_c, γ, WC, PF, D50
72- C_c, WC, VST, PF, D50
73- C_c, γ, WC, VST, PF, D50
74- C_u, γ, WC
75- C_u, γ, VST
76- C_u, γ, PF
77- C_u, γ, D50
78- C_u, WC, VST
79- C_u, WC, PF
80- C_u, WC, D50
81- C_u, VST, PF
82- C_u, VST, D50
83- PF, C_u, D50
84- C_u, γ, WC, VST
85- C_u, γ, WC, PF
86- C_u, γ, WC, D50
87- C_u, γ, VST, PF
88- C_u, γ, VST, D50
89- C_u, γ, PF, D50
90- C_u, WC, VST, PF

91- C_u, WC, VST, D50
92- C_u, WC, PF, D50
93- C_u, VST, PF, D50
94- C_u, γ, WC, VST, PF
95- C_u, γ, WC, VST, D50
96- C_u, γ, VST, PF, D50
97- C_u, γ, WC, PF, D50
98- C_u, WC, VST, PF, D50
99- C_u, γ, WC, VST, PF, D50
100- C_c, C_u
101- C_c, C_u, PI
102- C_c, C_u, γ
103- C_c, C_u, WC
104- C_c, C_u, VST
105- C_c, C_u, PF

“Predicted vs. Measured” Plots for the Selected Correlation Equations

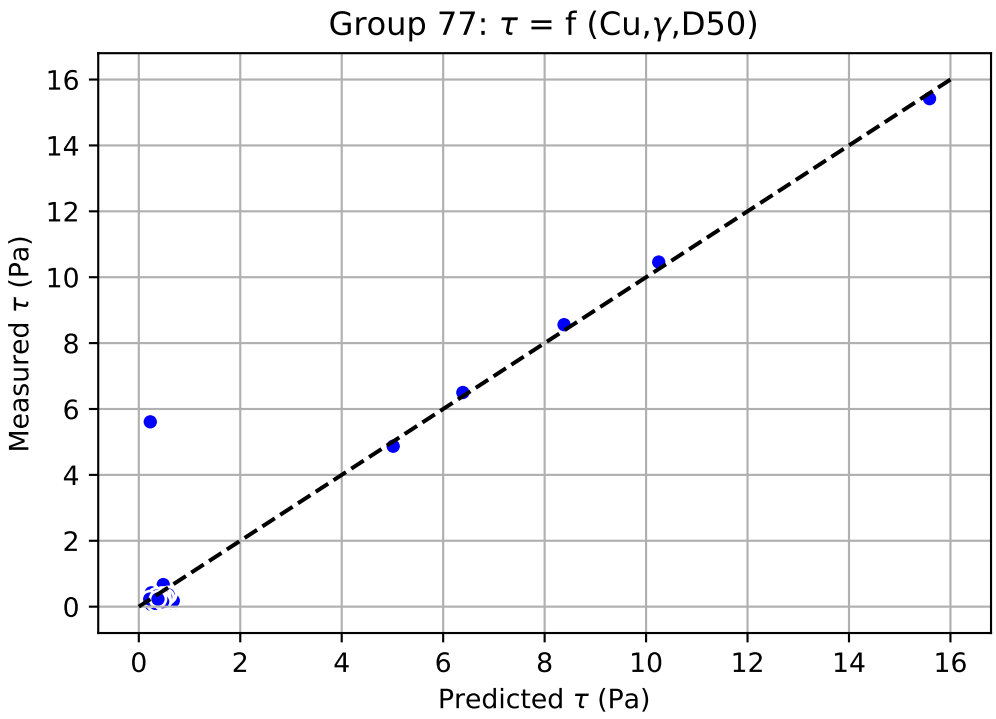

Figure D-1. Group 77 in Table 50

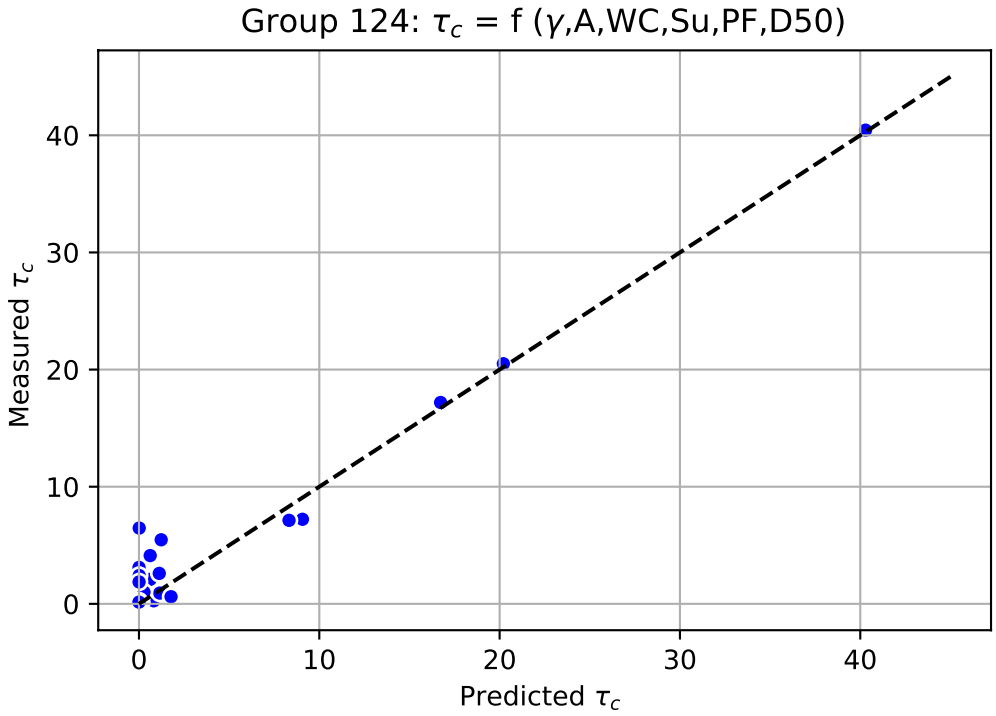

Figure D-2. Group 124 in Table 48

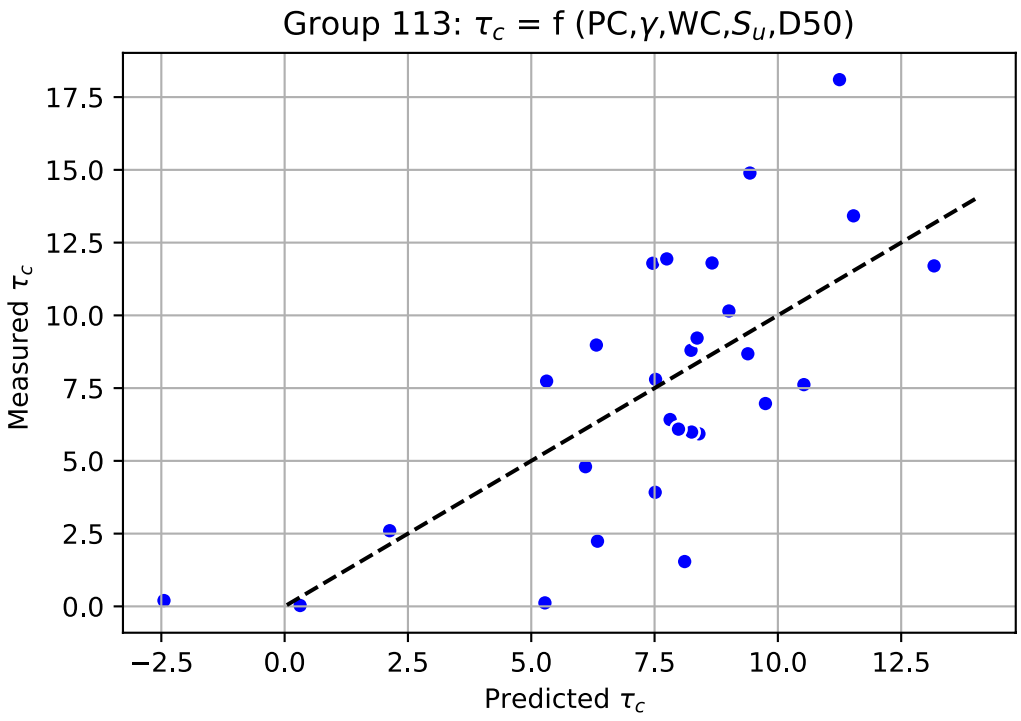

Figure D-3. Group 113 in Table 51

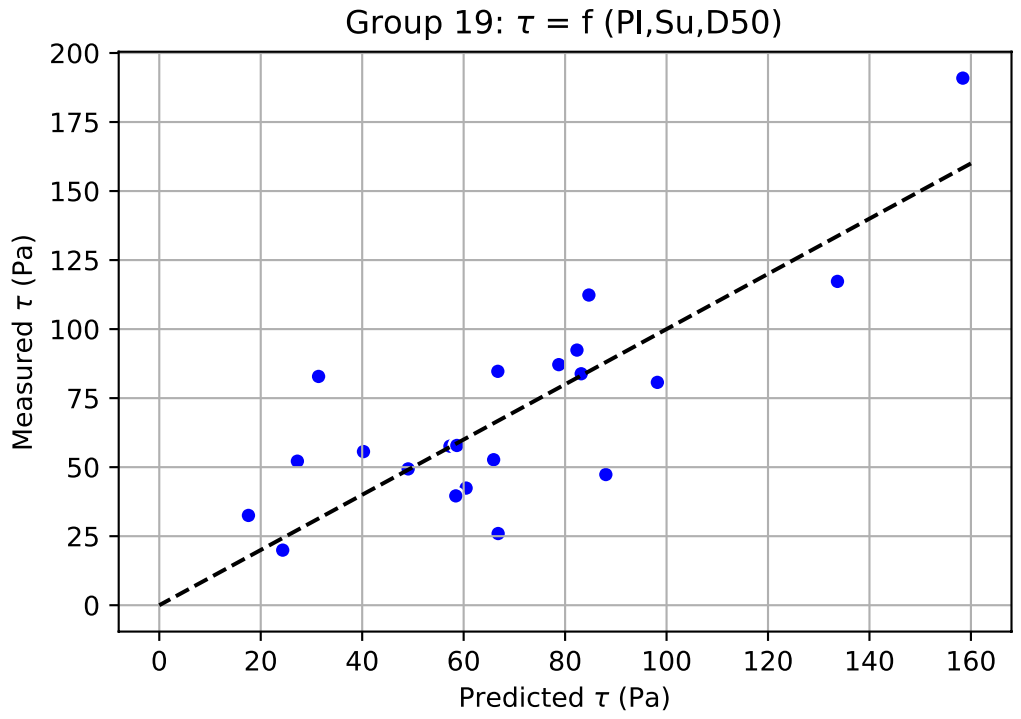

Figure D-4. Group 19 in Table 54

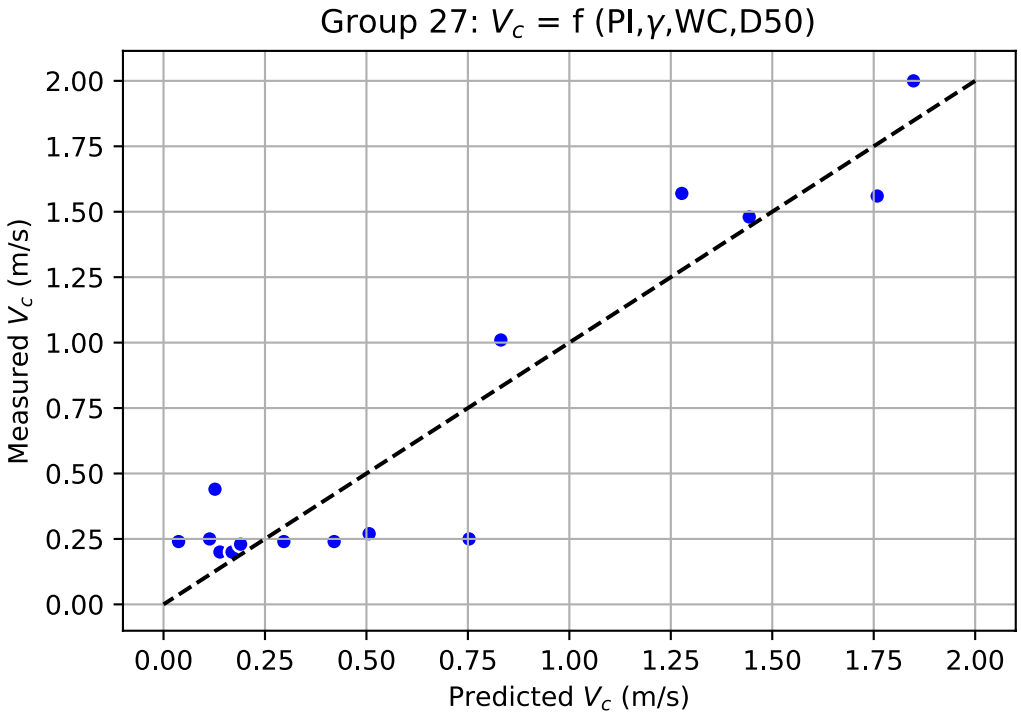

Figure D-5. Group 27 in Table 58

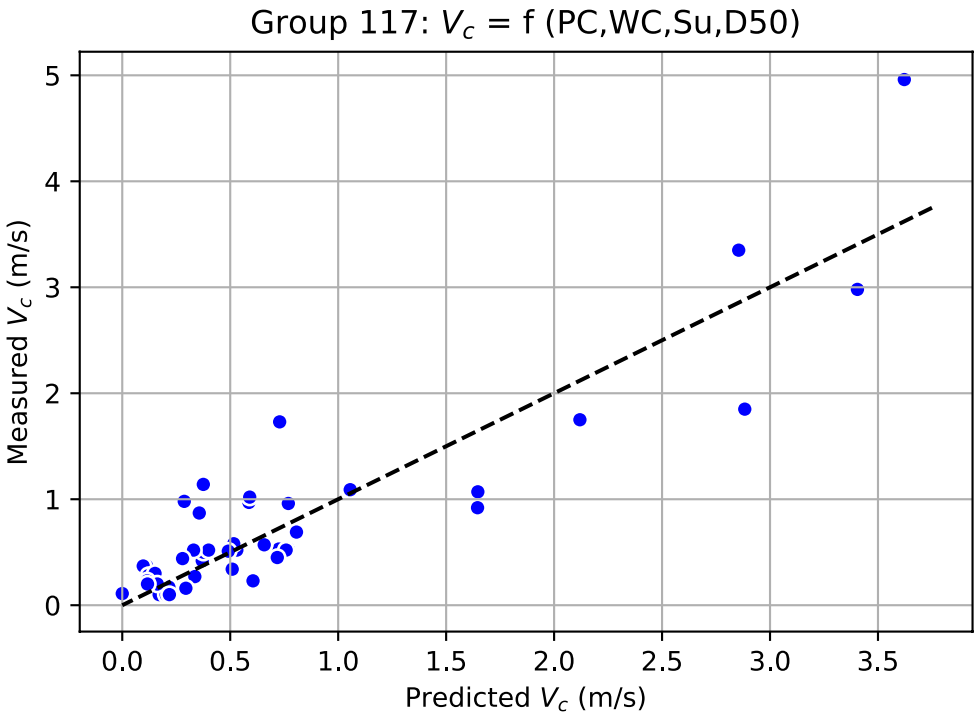

Figure D-6. Group 117 in Table 56

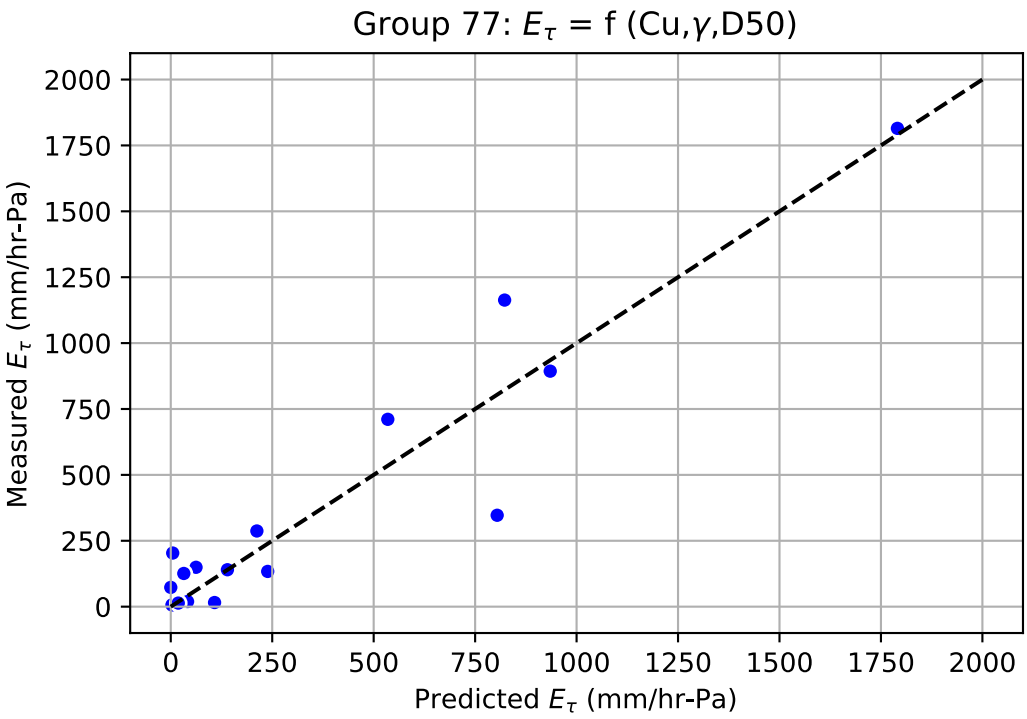

Figure D-7. Group 77 in Table 61

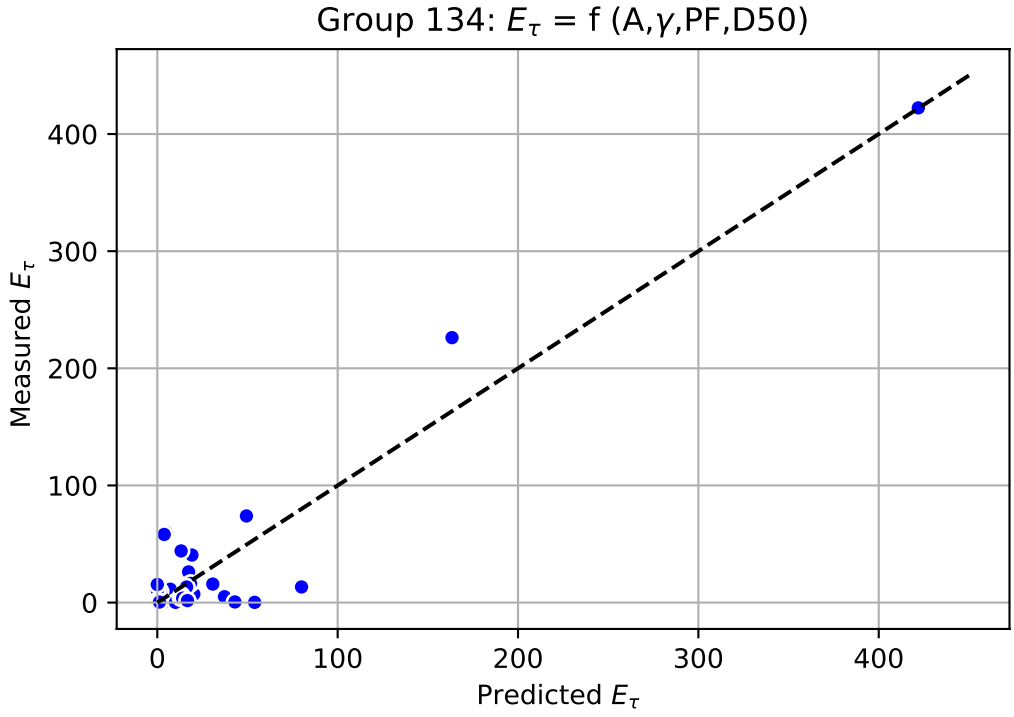

Figure D-8. Group 134 in Table 59

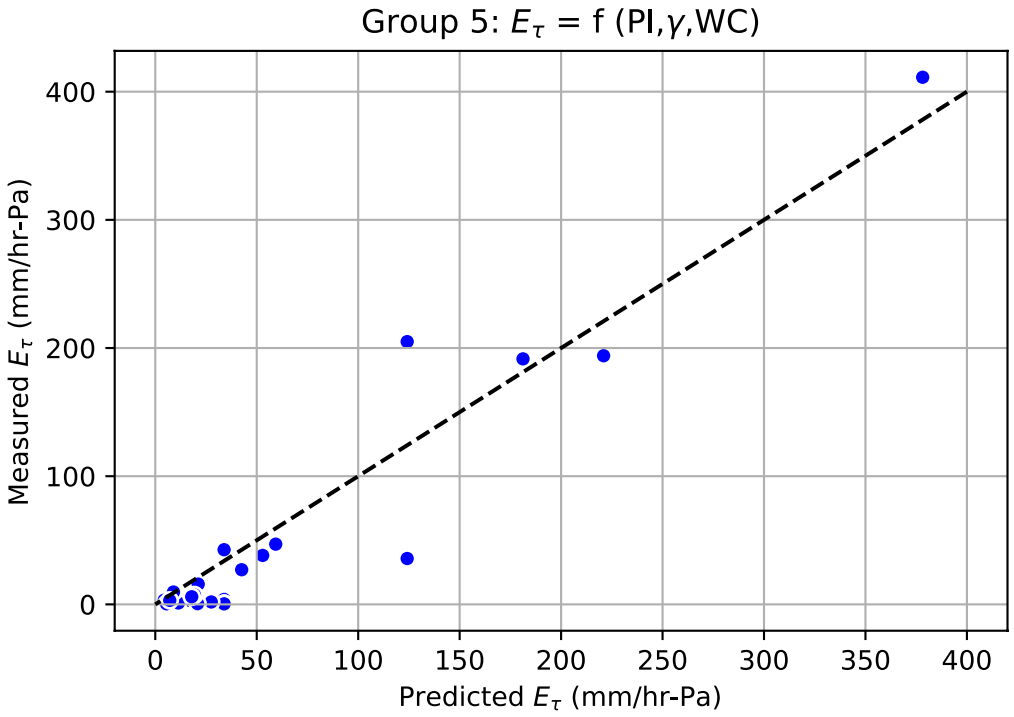

Figure D-9. Group 5 in Table 65

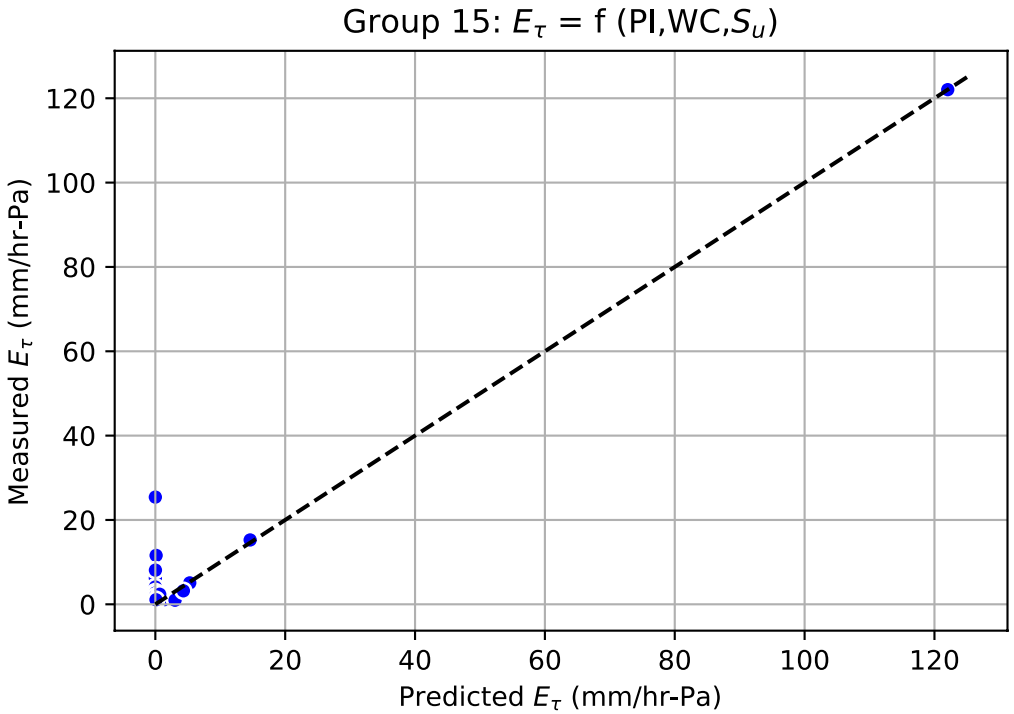

Figure D-10. Group 15 in Table 63

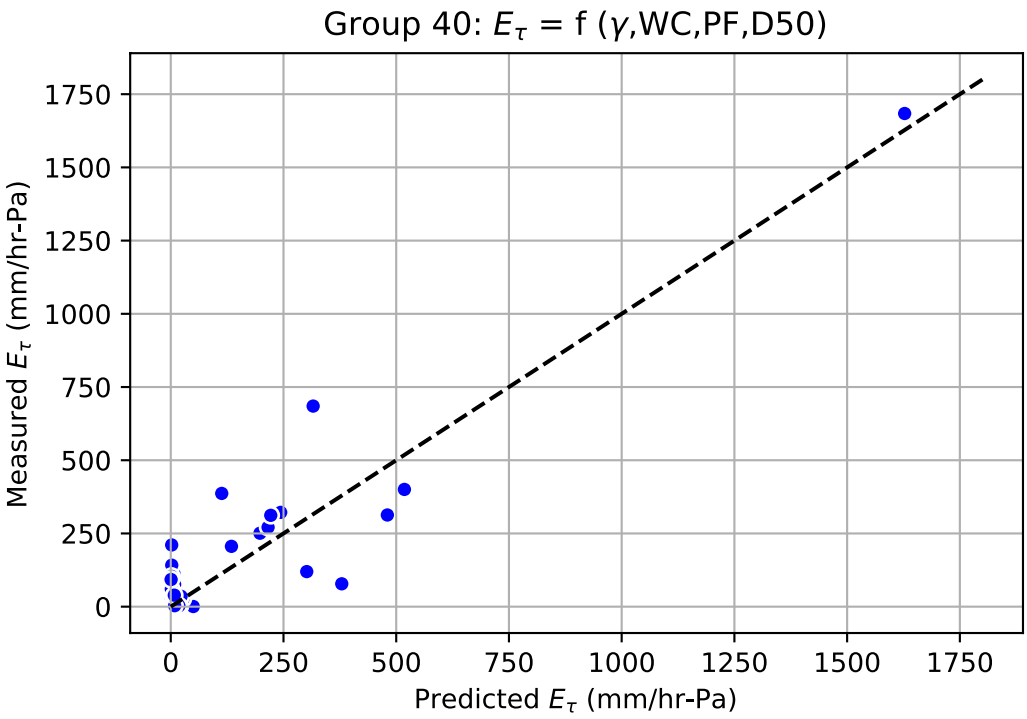

Figure D-11. Group 40 in Table 66

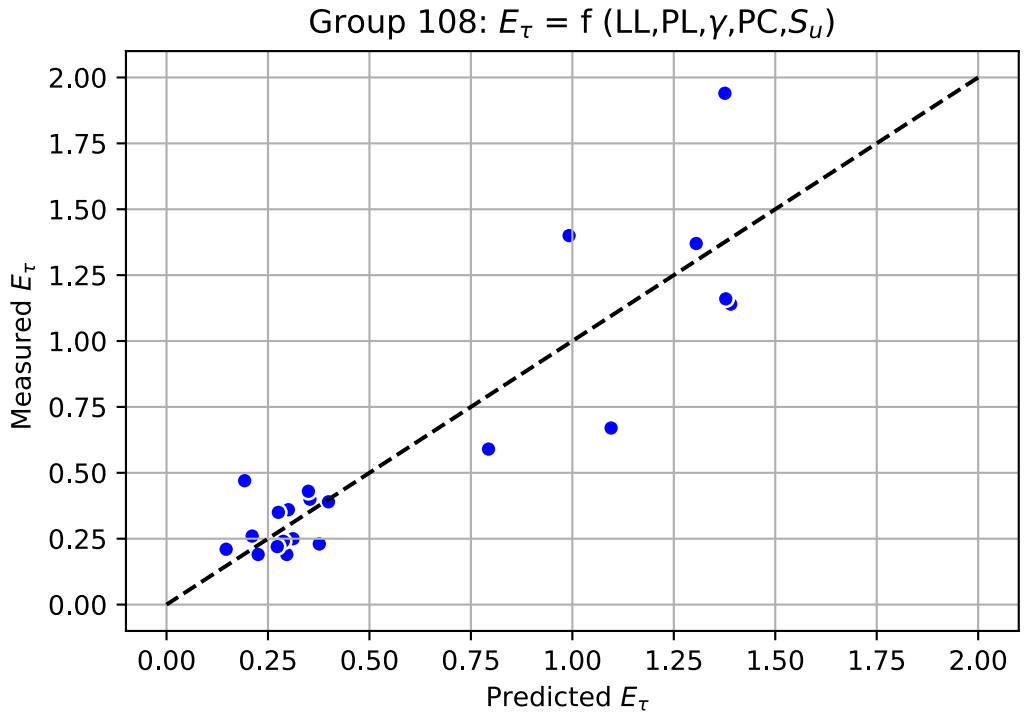

Figure D-12. Group 108 in Table 68

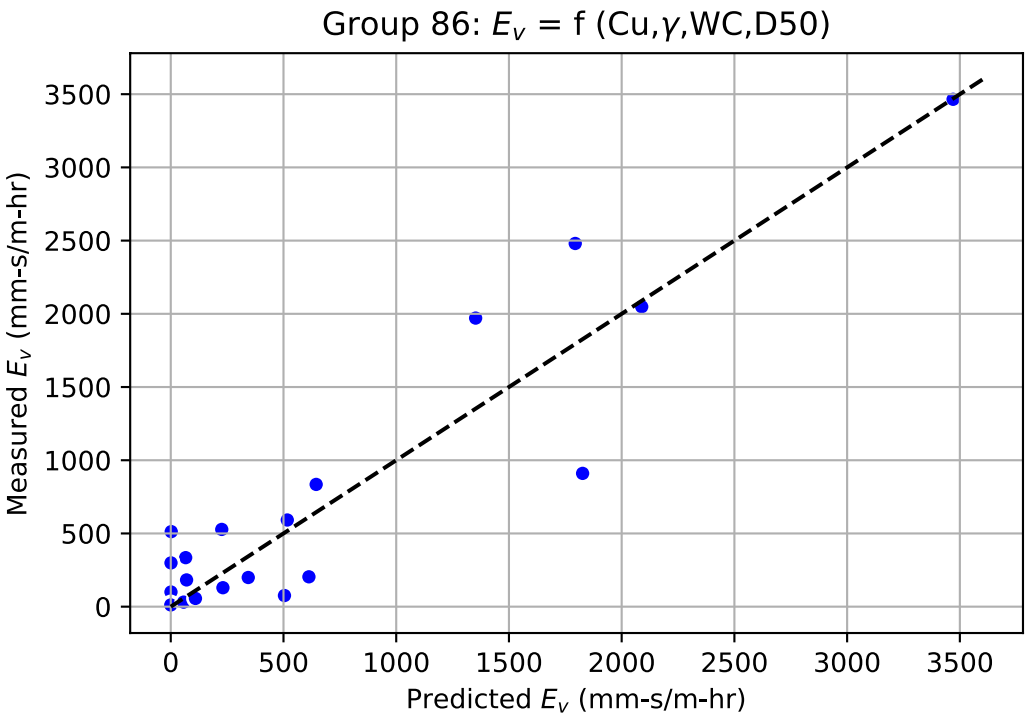

Figure D-13. Group 86 in Table 71

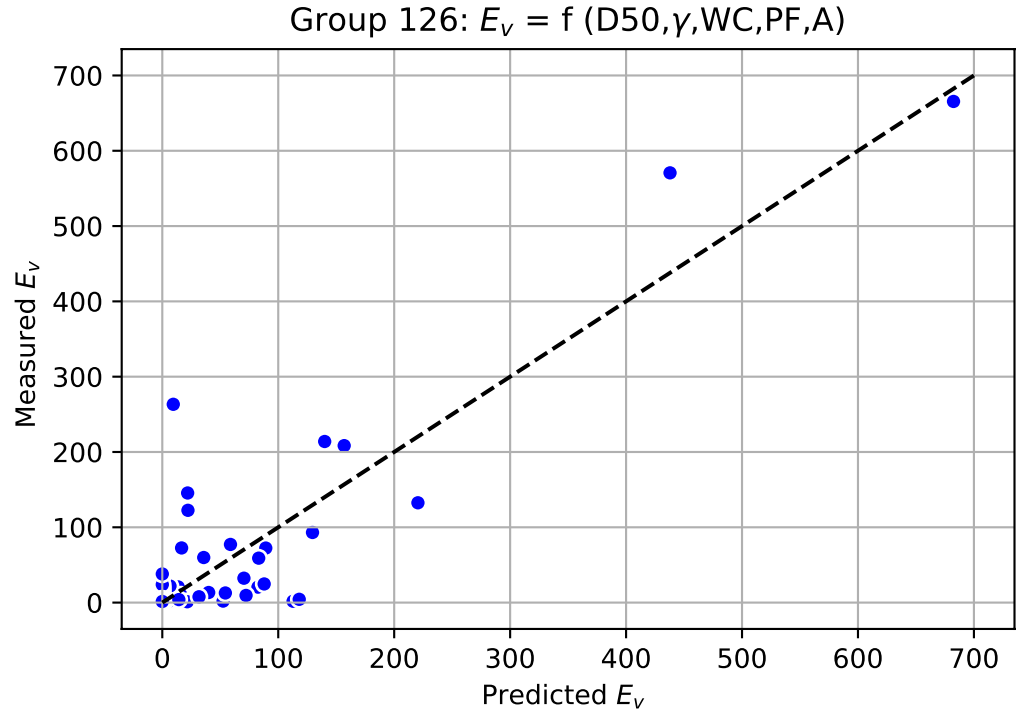

Figure D-14. Group 126 in Table 69

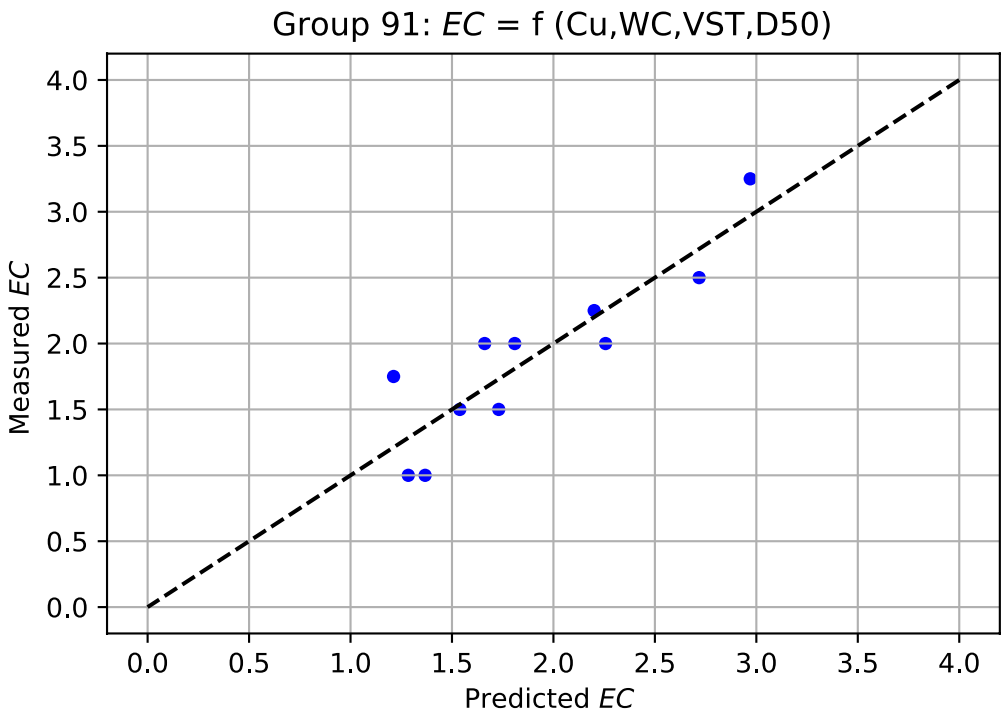

Figure D-15. Group 91 in Table 75

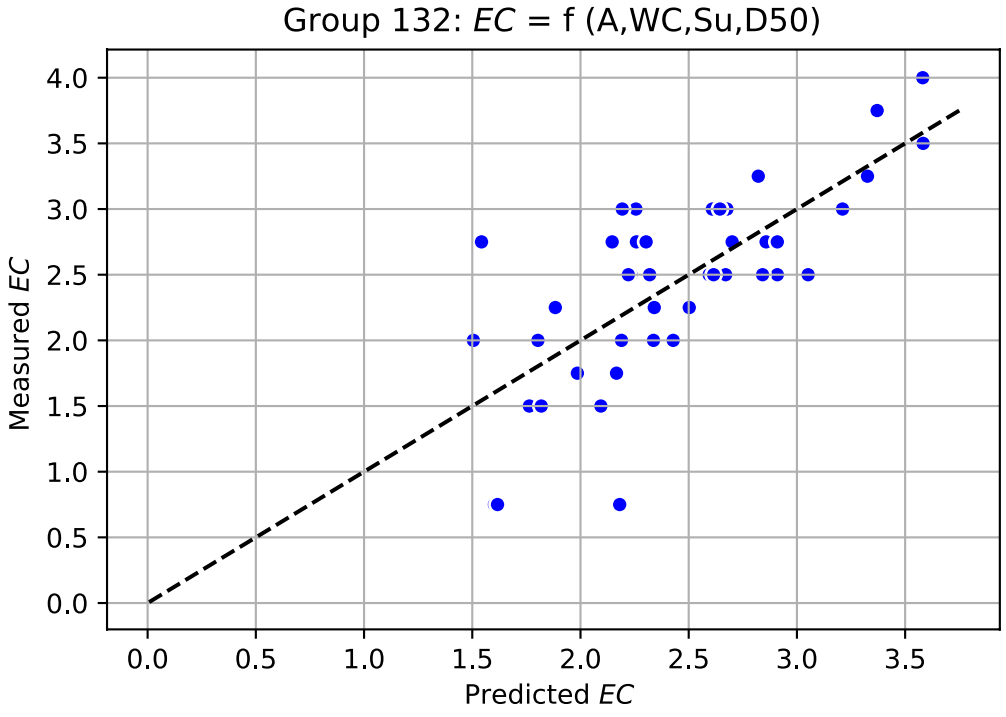

Figure D-16. Group 132 in Table 73

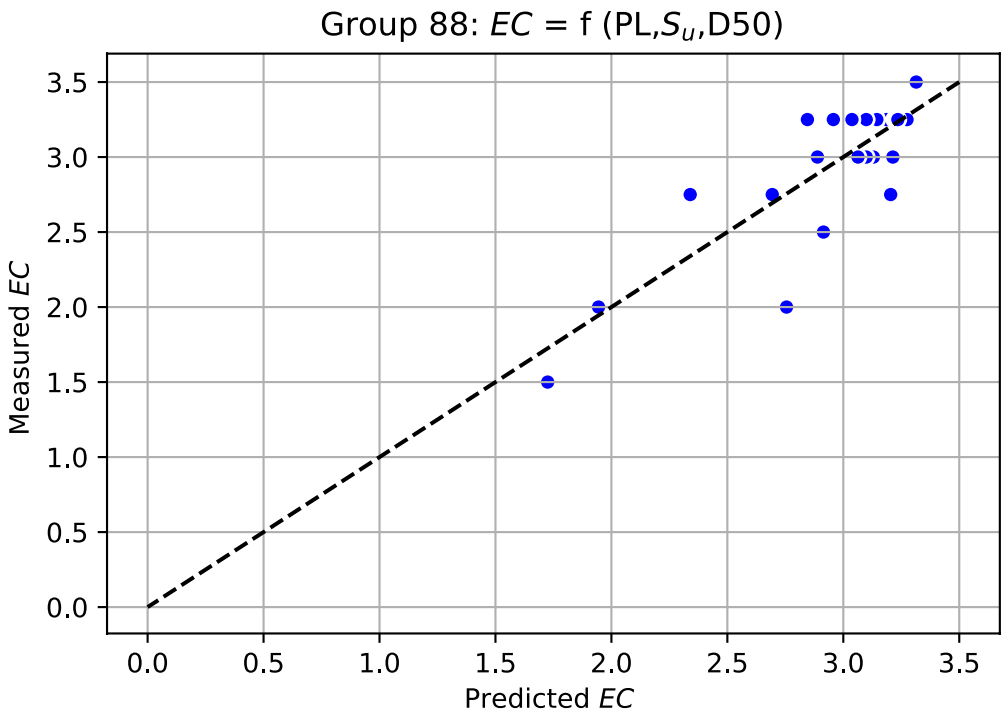

Figure D-17. Group 88 in Table 76

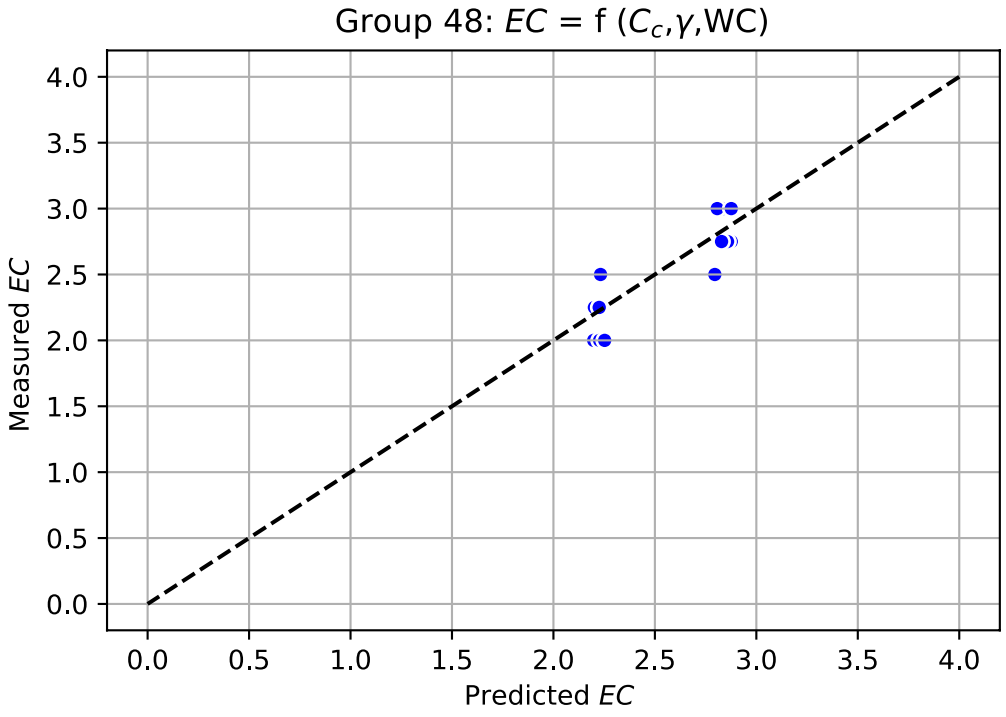

Figure D-18. Group 48 in Table 81

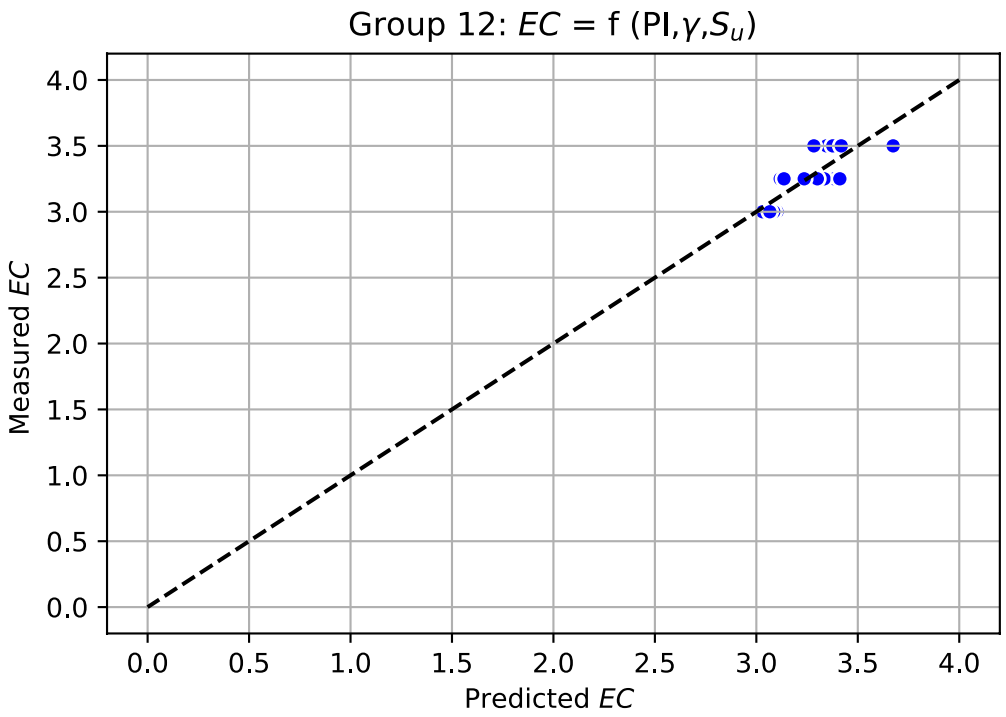

Figure D-19. Group 12 in Table 79

APPENDIX E

PROBABILISTIC CALIBRATION RESULTS

Models for critical shear stress τ_c in EFA/Fine dataset:

(1) Model characteristics:

Group No.	Independent variables	Dataset/ No. of data	Model expression (parameter values given by deterministic regression)	R^2	Cross-validation score
124	γ, A, WC, S_u, PF, D50	EFA/Fine 44	$\tau_c = (158.06) \times \gamma^5 \times A^{-0.46} \times WC^{10.03} \times S_u^{1.83} \times PF^{-18.28} \times D50^{-4.21}$	0.94	0.66

(2) Statistics of marginal posterior distribution:

Parameters	Mean	SD	CoV	mode	95% HPD region (lower and upper bound)	
β_0	810371.44	605863.97	0.75	10257.49	9736.49	1969077.88
β_γ	6.94	3.29	0.47	15.29	0.75	13.79
β_A	7.79	2.57	0.33	13.65	2.66	13.08
β_{WC}	14.40	2.64	0.18	21.13	9.57	20.00
β_{S_u}	3.52	0.54	0.15	4.34	2.43	4.56
β_{PF}	-25.53	4.79	-0.19	-36.94	-35.70	-16.85
β_{D50}	1.31	1.58	1.20	4.12	-1.90	4.23

(3) Joint relative frequency histogram:

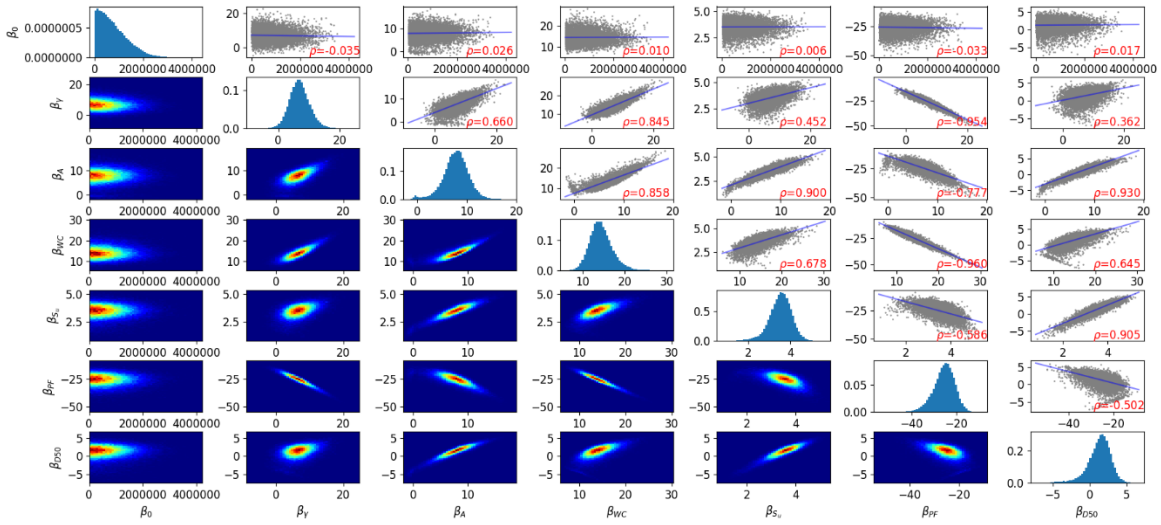

(4) Model realizations and first order statistics of model predictions:

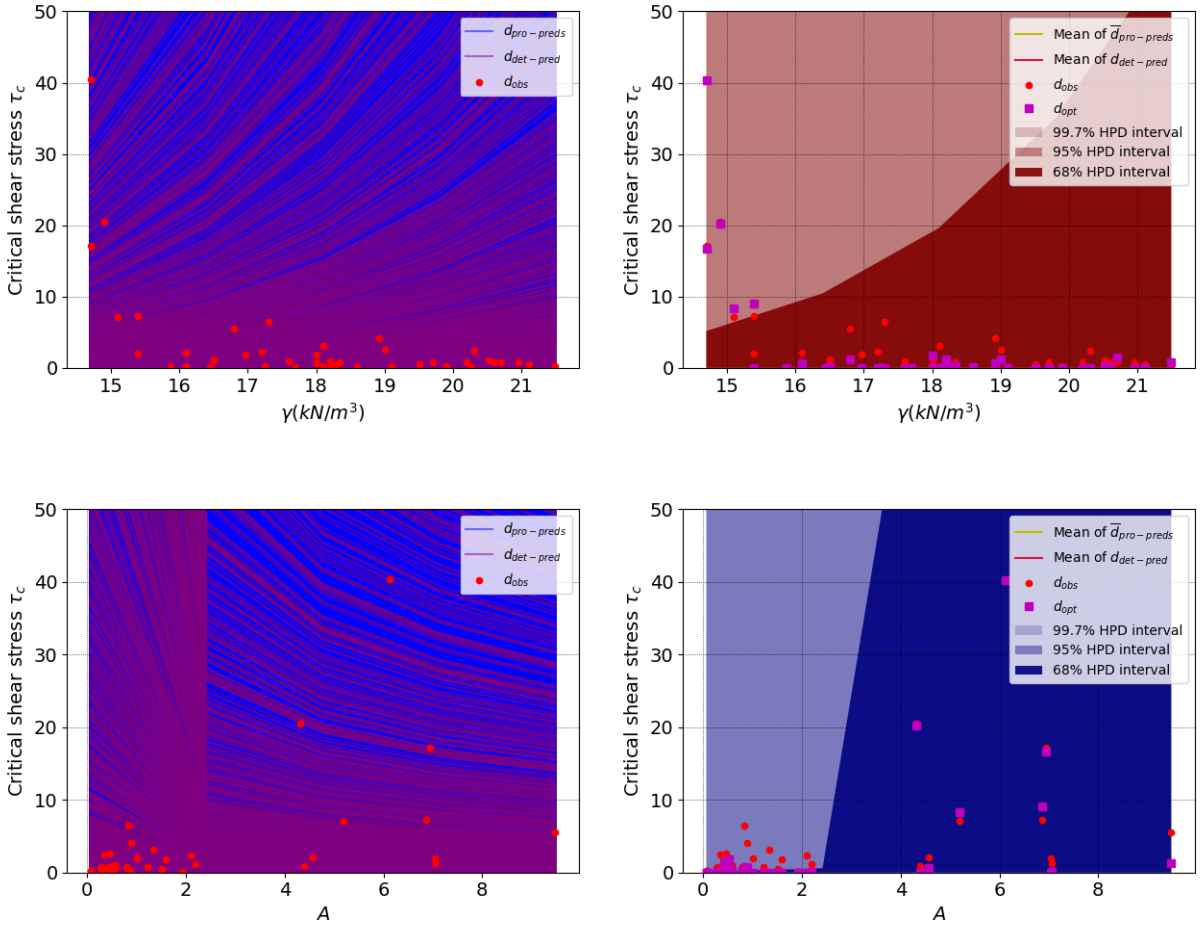

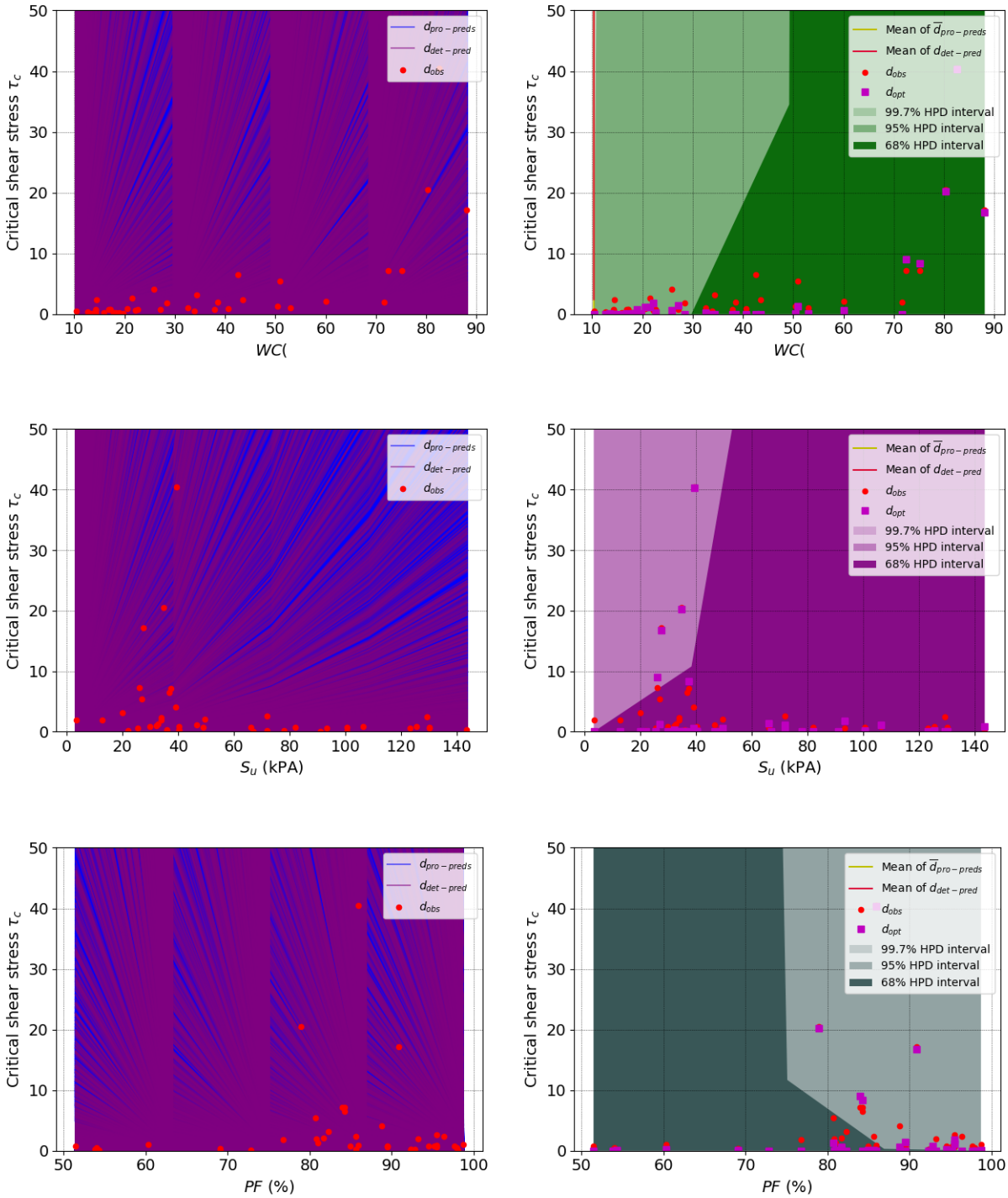
Critical shear stress τ_c
$WC($
S_u (kPA)
PF (%)
$d_{pro-preds}$
$d_{det-pred}$
d_{obs}
Mean of $\overline{d}_{pro-preds}$
Mean of $d_{det-pred}$
d_{opt}
99.7% HPD interval
95% HPD interval
68% HPD interval

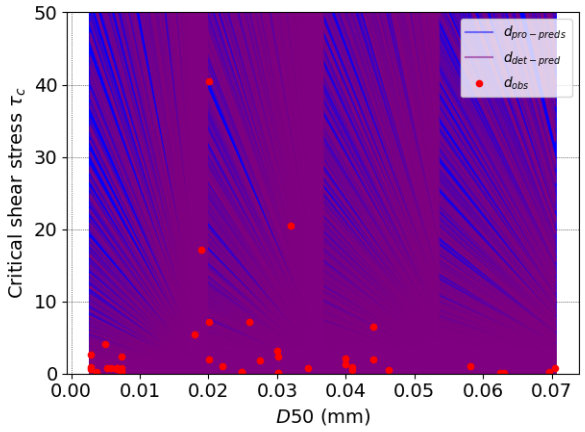
Critical shear stress τ_c
$D50$ (mm)
$d_{pro-preds}$
$d_{det-pred}$
d_{obs}

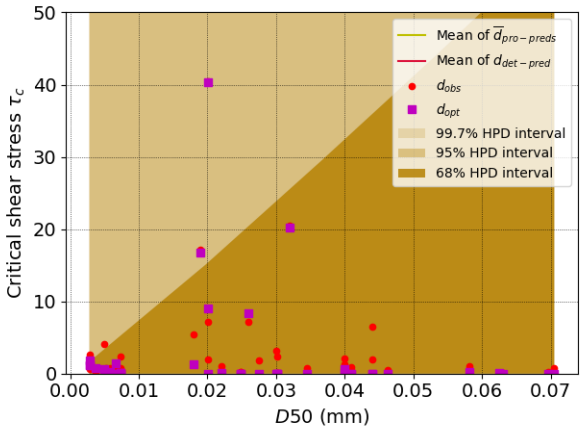
Critical shear stress τ_c
$D50$ (mm)
Mean of $\overline{d}_{pro-preds}$
Mean of $d_{det-pred}$
d_{obs}
d_{opt}
99.7% HPD interval
95% HPD interval
68% HPD interval

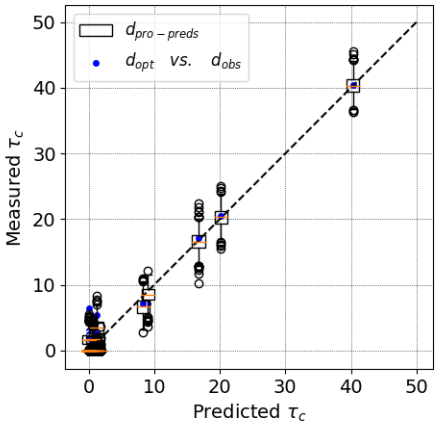
Measured τ_c
Predicted τ_c
$d_{pro-preds}$
d_{opt} vs. d_{obs}

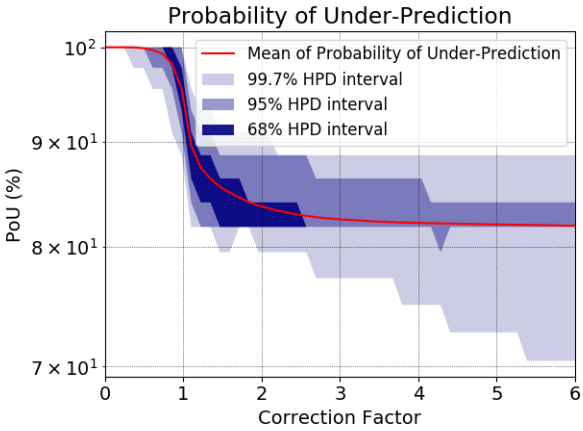
Probability of Under-Prediction
PoU (%)
Correction Factor
Mean of Probability of Under-Prediction
99.7% HPD interval
95% HPD interval
68% HPD interval

Models for critical shear stress $\boldsymbol{\tau_c}$ in EFA/Coarse dataset:

(1) Model characteristics:

Group No.	Independent variables	Dataset/ No. of data	Model expression (parameter values given by deterministic regression)	R^2	Cross-validation score
77	C_u, γ, D50	EFA/Coarse 28	$\tau_c = (1.58) \times C_u^{-0.04} \times \gamma^{0.02} \times D50^{0.77}$	0.93	0.99

(2) Statistics of marginal posterior distribution:

Parameters	Mean	SD	CoV	mode	95% HPD region (lower and upper bound)	
β_0	0.002	0.019	7.764	0.001	0.000	0.006
β_{C_u}	-0.239	0.081	-0.337	-0.231	-0.396	-0.080
β_γ	3.727	1.126	0.302	3.451	1.605	6.007
β_{D50}	0.932	0.116	0.125	0.901	0.715	1.165

(3) Joint relative frequency histogram:

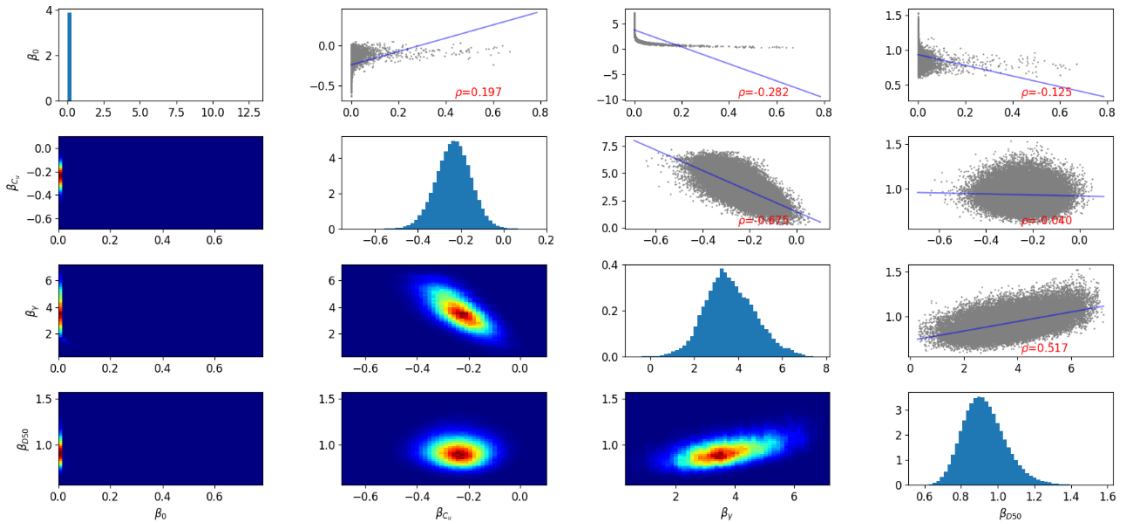

(4) Model realizations and first order statistics of model predictions:

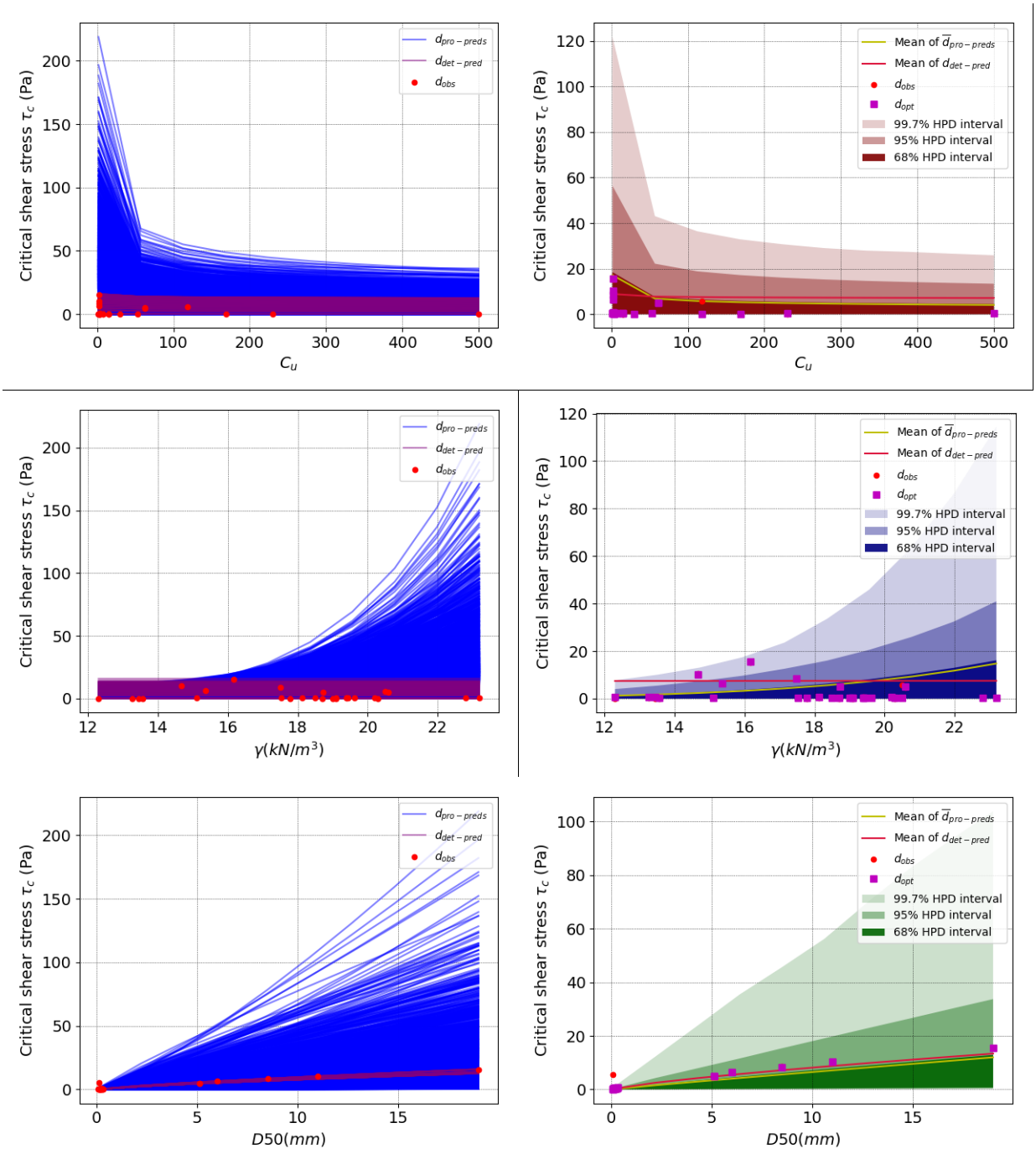
Critical shear stress τ_c (Pa)
C_u
$\gamma(kN/m^3)$
$D50(mm)$
$d_{pro-preds}$
$d_{det-pred}$
d_{obs}
Mean of $\overline{d}_{pro-preds}$
Mean of $d_{det-pred}$
d_{opt}
99.7% HPD interval
95% HPD interval
68% HPD interval

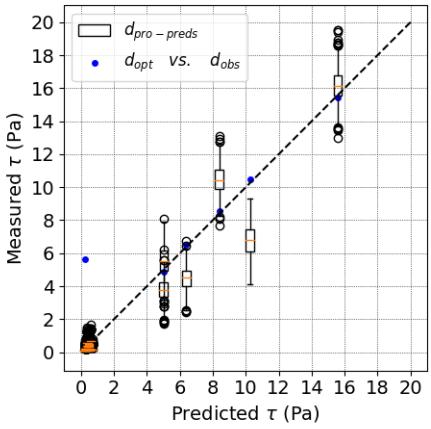
$d_{pro-preds}$
d_{opt} vs. d_{obs}
Measured τ (Pa)
Predicted τ (Pa)
0 2 4 6 8 10 12 14 16 18 20

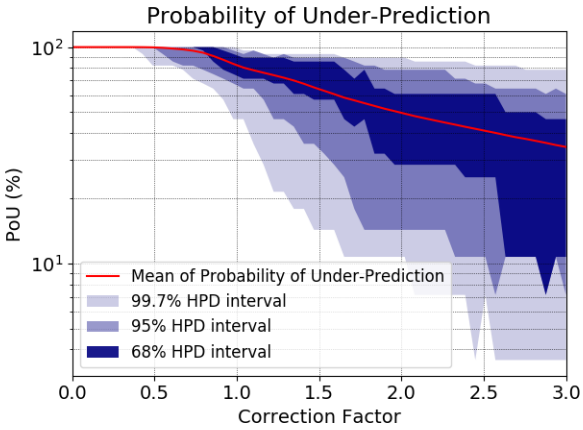
Probability of Under-Prediction
PoU (%)
10^2
10^1
Mean of Probability of Under-Prediction
99.7% HPD interval
95% HPD interval
68% HPD interval
0.0 0.5 1.0 1.5 2.0 2.5 3.0
Correction Factor

Models for critical shear stress $\boldsymbol{\tau_c}$ in JET/Global dataset:

(1) Model characteristics:

Group No.	Independent variables	Dataset/ No. of data	Model expression (parameter values given by deterministic regression)	R^2	Cross-validation score
113	PC, γ, WC, S_u, D50	JET/Global 28	$\tau_c = -0.248 \times PC - 1.23 \times \gamma + 0.21 \times WC + 0.07 \times S_u - 36.89 \times D50 + 31.82$ $for\ D50 < 0.3\ mm$	0.50	0.10

(2) Statistics of marginal posterior distribution:

Parameters	Mean	SD	CoV	mode	95% HPD region (lower and upper bound)	
β_{PC}	-0.346	0.130	-0.377	-0.350	-0.608	-0.100
β_{γ}	-1.372	0.569	-0.414	-1.390	-2.455	-0.242
β_{WC}	0.390	0.244	0.625	0.420	-0.078	0.859
β_{S_u}	0.089	0.027	0.300	0.090	0.036	0.141
β_{D50}	-36.925	12.178	-0.330	-33.790	-60.861	-13.071
β_0	32.871	12.838	0.391	35.230	7.832	58.231

(3) Joint relative frequency histogram:

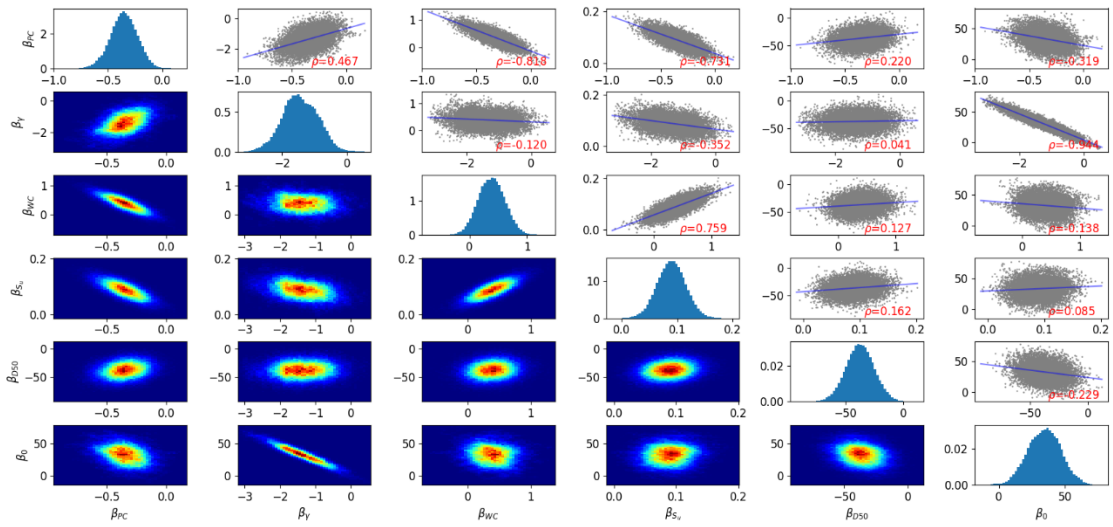

(4) Model realizations and first order statistics of model predictions:

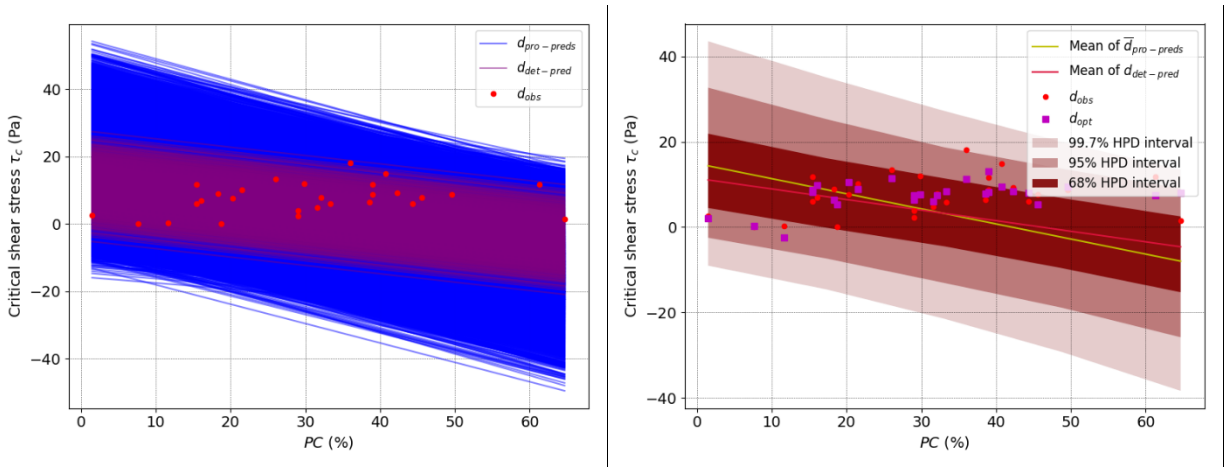

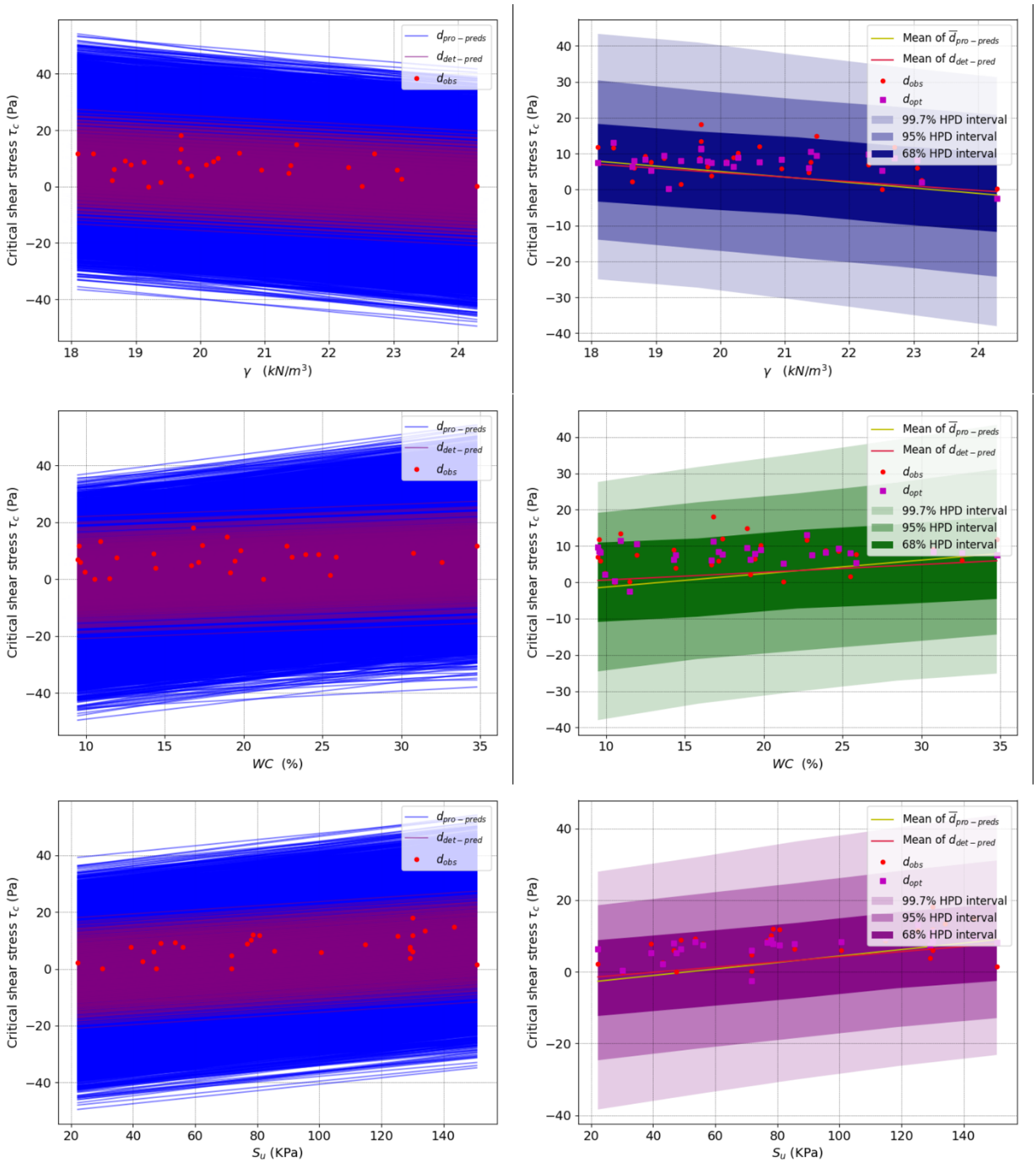
Critical shear stress τ_c (Pa)
γ (kN/m^3)
WC (%)
S_u (KPa)
$d_{pro-preds}$
$d_{det-pred}$
d_{obs}
d_{opt}
Mean of $\overline{d}_{pro-preds}$
Mean of $d_{det-pred}$
99.7% HPD interval
95% HPD interval
68% HPD interval

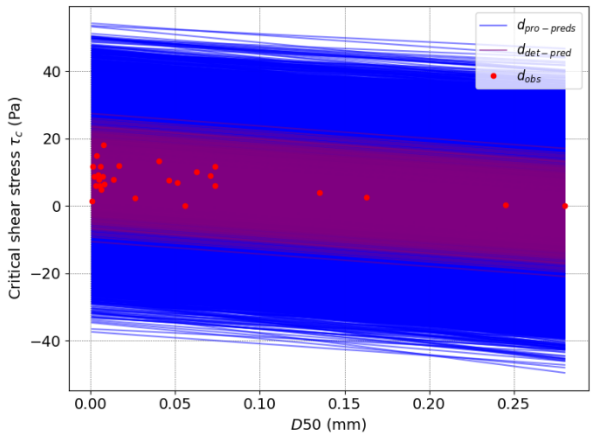
$d_{pro-preds}$
$d_{det-pred}$
d_{obs}
Critical shear stress τ_c (Pa)
$D50$ (mm)

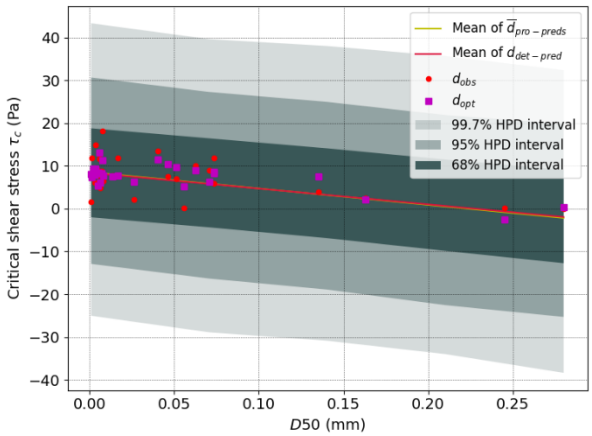
Mean of $\overline{d}_{pro-preds}$
Mean of $d_{det-pred}$
d_{obs}
d_{opt}
99.7% HPD interval
95% HPD interval
68% HPD interval
Critical shear stress τ_c (Pa)
$D50$ (mm)

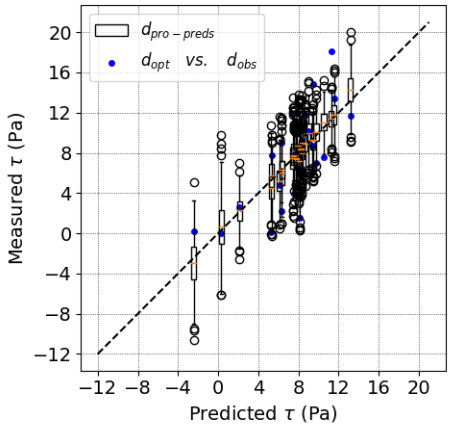
$d_{pro-preds}$
d_{opt} vs. d_{obs}
Measured τ (Pa)
Predicted τ (Pa)

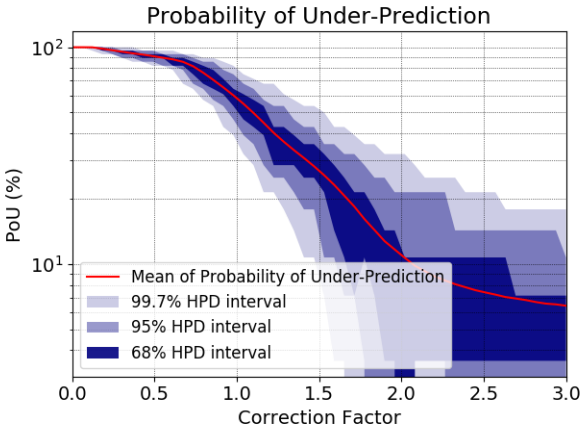
Probability of Under-Prediction
Mean of Probability of Under-Prediction
99.7% HPD interval
95% HPD interval
68% HPD interval
PoU (%)
Correction Factor

Models for critical shear stress $\boldsymbol{\tau_c}$ in HET/Global dataset:

(1) Model characteristics:

Group No.	Independent variables	Dataset/ No. of data	Model expression (parameter values given by deterministic regression)	R^2	Cross-validation score
19	PI, S_u, D50	HET/Global 21	$\tau_c = (25.07) \times PI^{0.27} \times S_u^{0.55} \times D50^{0.5}$ $for\ D50 < 0.3\ mm$	0.64	0.43

(2) Statistics of marginal posterior distribution:

Parameters	Mean	SD	CoV	mode	95% HPD region (lower and upper bound)	
β_0	171.146	447.669	2.616	22.827	2.111	580.280
β_{PI}	0.368	0.088	0.238	0.360	0.198	0.543
β_{S_u}	0.655	0.131	0.201	0.647	0.399	0.911
β_{D50}	1.032	0.295	0.286	0.936	0.485	1.627

(3) Joint relative frequency histogram:

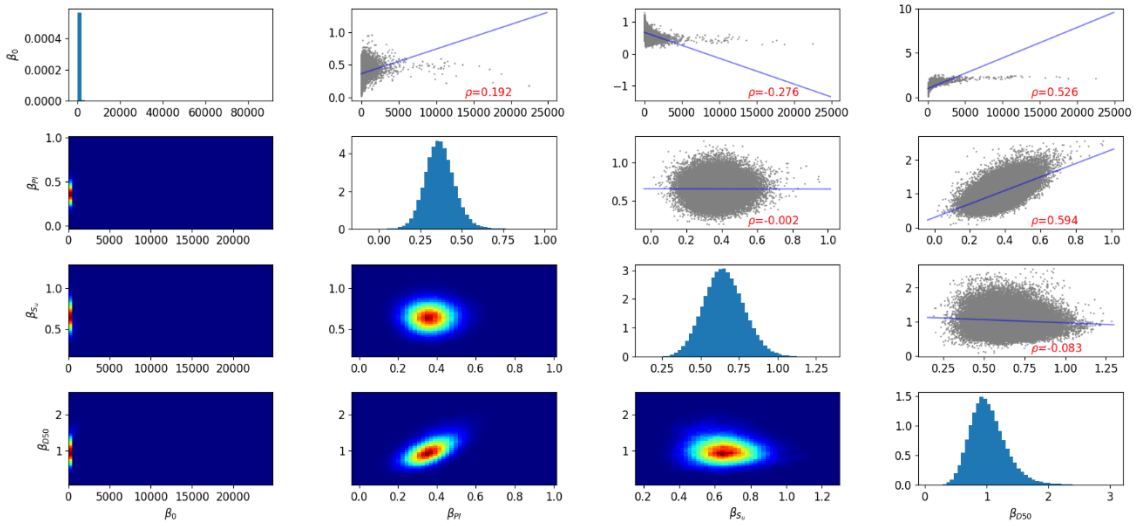

(4) Model realizations and first order statistics of model predictions:

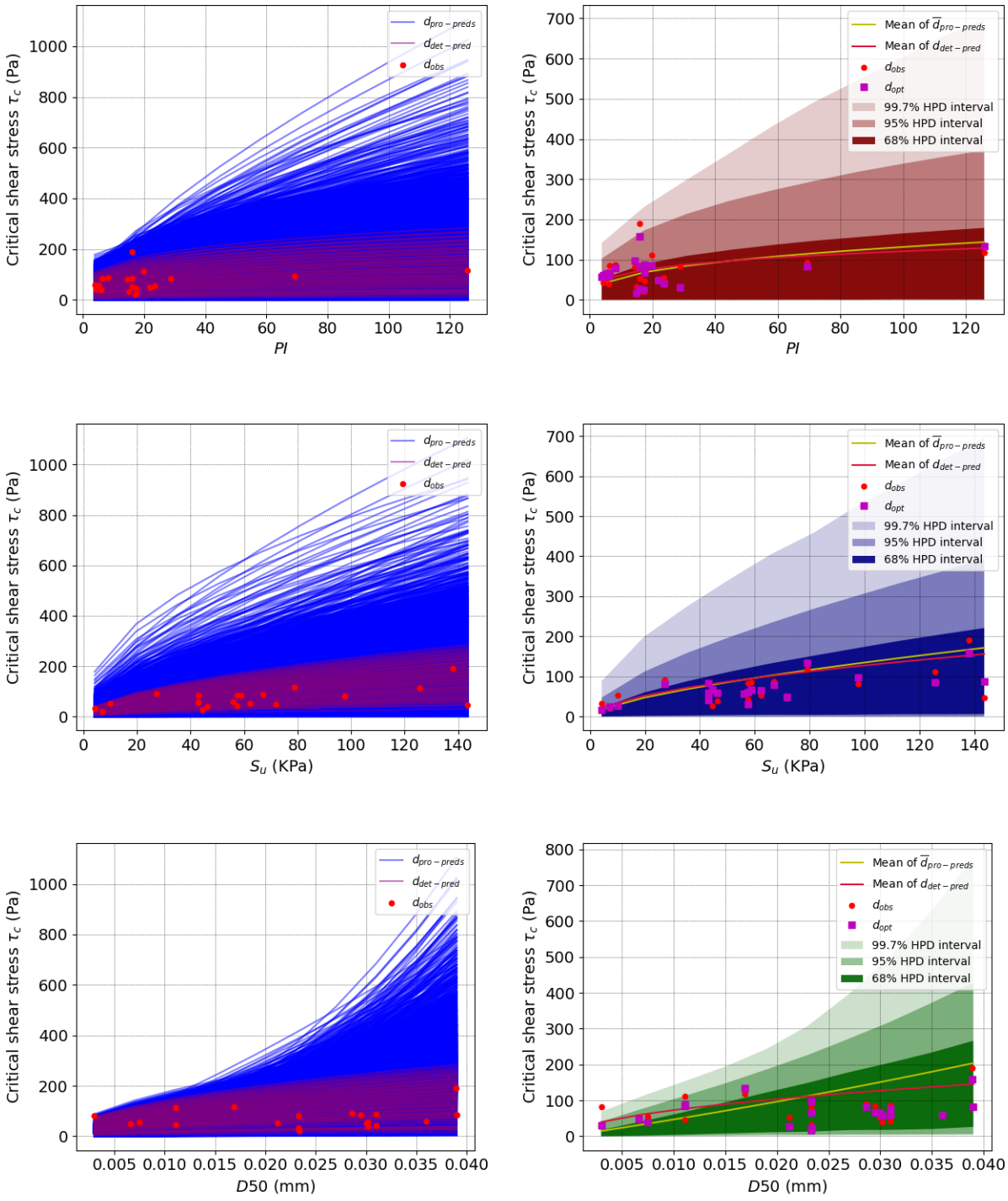

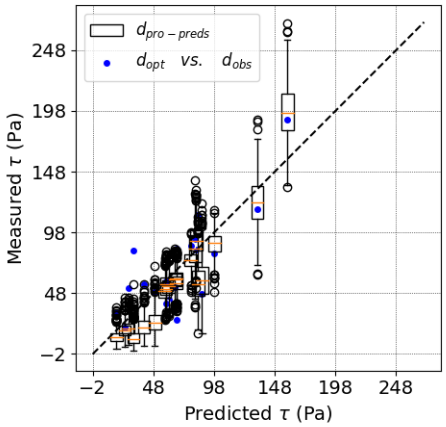
$d_{pro-preds}$
d_{opt} vs. d_{obs}
248
198
148
98
48
−2
Measured τ (Pa)
−2
48
98
148
198
248
Predicted τ (Pa)

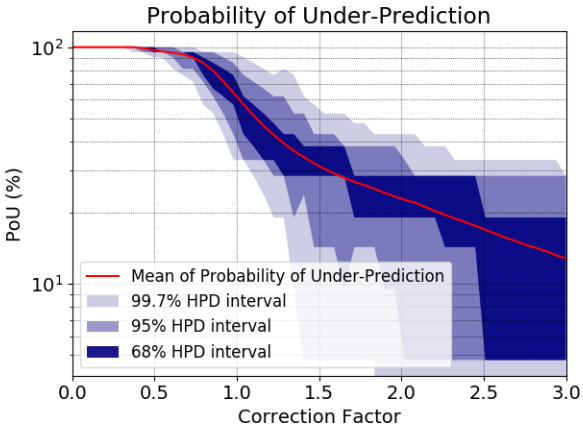
Probability of Under-Prediction
10^2
10^1
PoU (%)
Mean of Probability of Under-Prediction
99.7% HPD interval
95% HPD interval
68% HPD interval
0.0
0.5
1.0
1.5
2.0
2.5
3.0
Correction Factor

Models for critical velcoity $\boldsymbol{v_c}$ in EFA/Fine:

(1) Model characteristics:

Group No.	Independent variables	Dataset/ No. of data	Model expression (parameter values given by deterministic regression)	R^2	Cross-validation score
117	PC, WC, S_u, D50	EFA/Fine 46	$v_c = (2.518 \times 10^{-5}) \times PC^{0.2} \times WC^{2.06} \times S_u^{0.51} \times D50^{-0.13}$	0.80	0.80

(2) Statistics of marginal posterior distribution:

Parameters	Mean	SD	CoV	mode	95% HPD region (lower and upper bound)	
β_0	0.0002	0.0002	1.2303	0.0000	0.0000	0.0006
β_{PC}	0.2250	0.1260	0.5600	0.2135	0.0000	0.4496
β_{WC}	1.8904	0.1601	0.0847	2.1470	1.5718	2.1905
β_{S_u}	0.3968	0.1249	0.3148	0.5533	0.1579	0.6407
β_{D50}	-0.0130	0.1446	-11.1215	-0.0724	-0.3128	0.2518

(3) Joint relative frequency histogram:

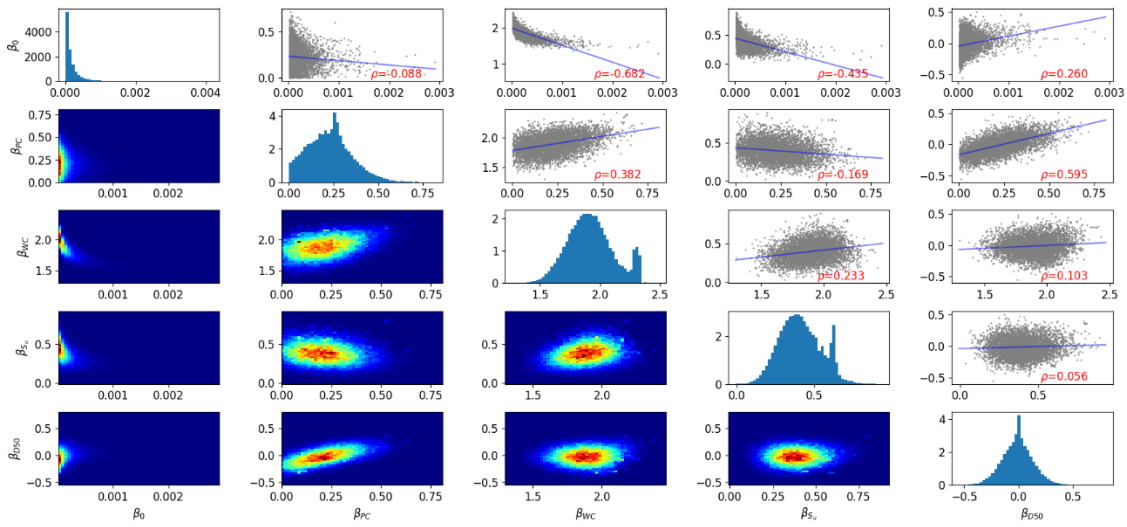

(4) Model realizations and first order statistics of model predictions:

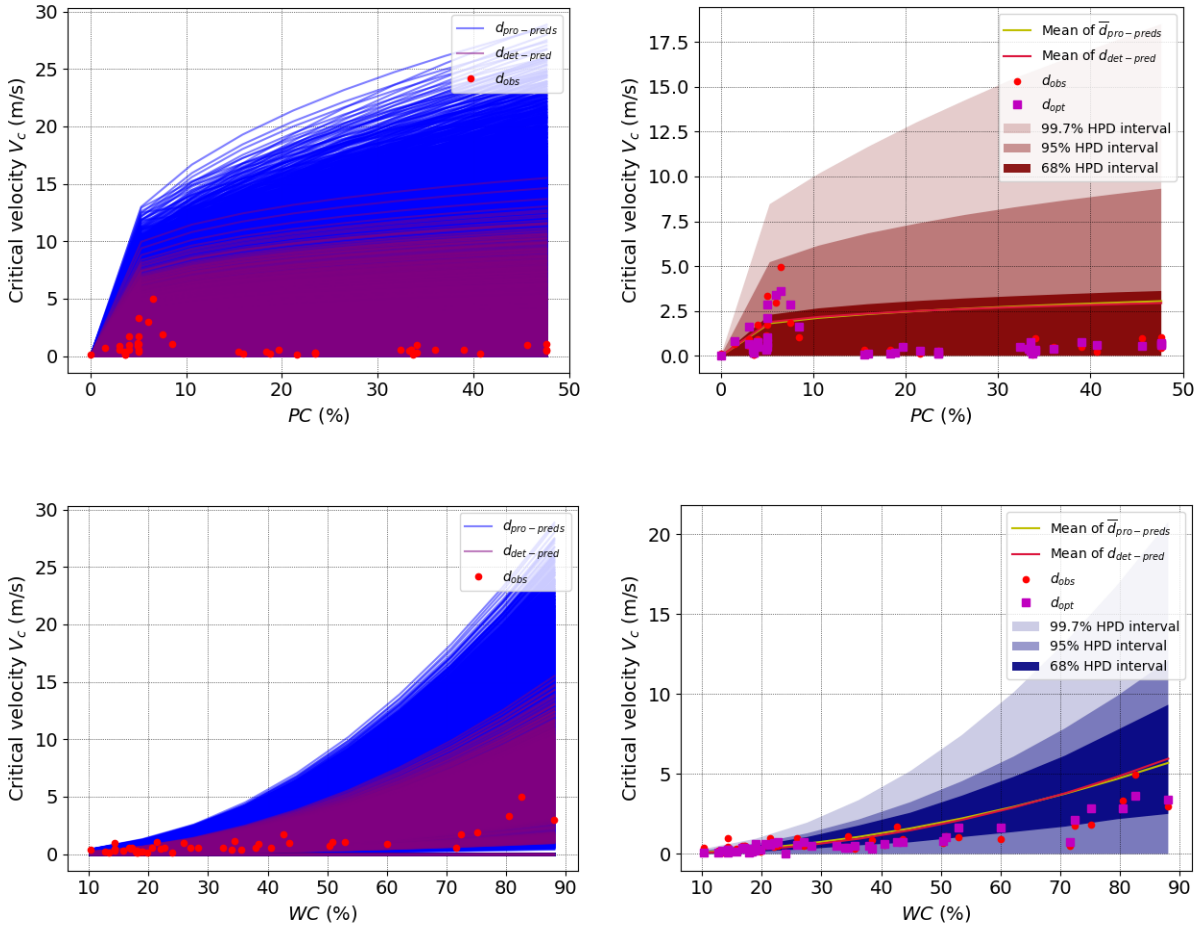

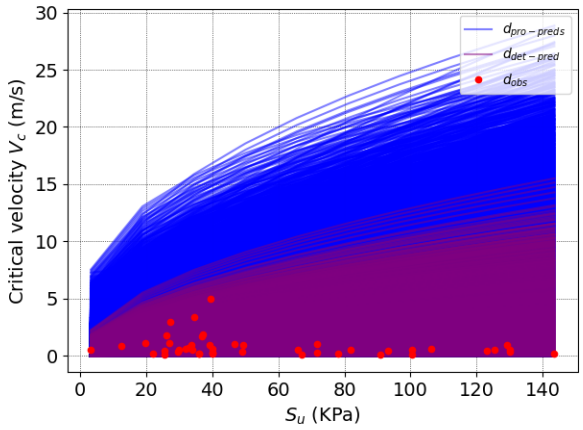
$d_{pro-preds}$
$d_{det-pred}$
d_{obs}
Critical velocity V_c (m/s)
S_u (KPa)

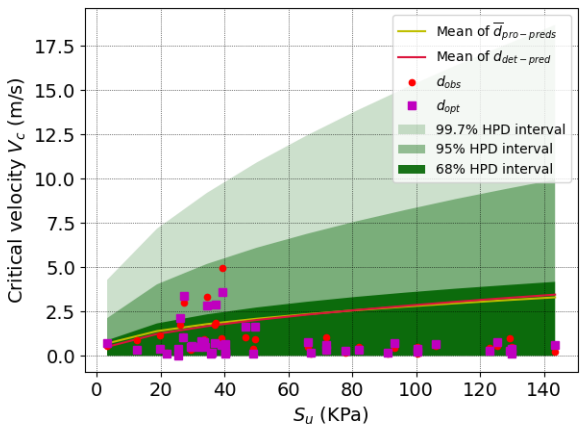
Mean of $\overline{d}_{pro-preds}$
Mean of $d_{det-pred}$
d_{obs}
d_{opt}
99.7% HPD interval
95% HPD interval
68% HPD interval
Critical velocity V_c (m/s)
S_u (KPa)

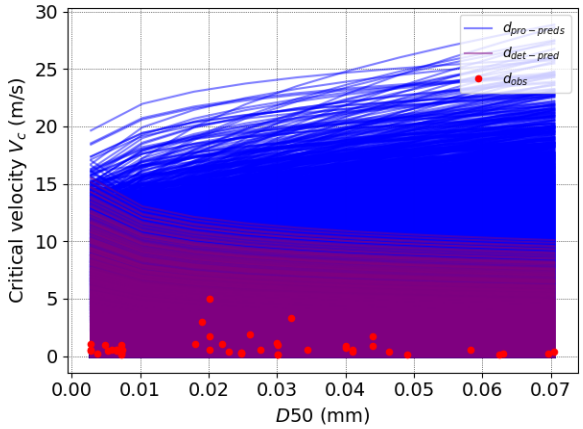
$d_{pro-preds}$
$d_{det-pred}$
d_{obs}
Critical velocity V_c (m/s)
$D50$ (mm)

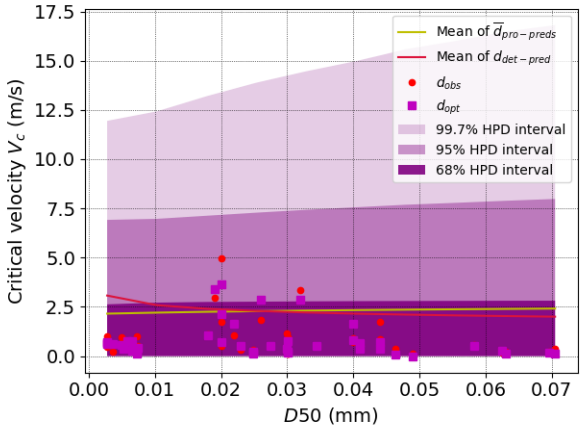
Mean of $\overline{d}_{pro-preds}$
Mean of $d_{det-pred}$
d_{obs}
d_{opt}
99.7% HPD interval
95% HPD interval
68% HPD interval
Critical velocity V_c (m/s)
$D50$ (mm)

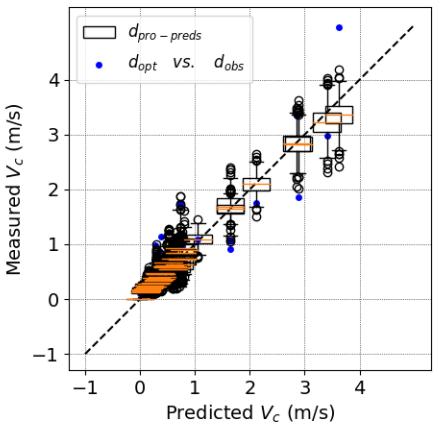
$d_{pro-preds}$
d_{opt} vs. d_{obs}
Measured V_c (m/s)
Predicted V_c (m/s)

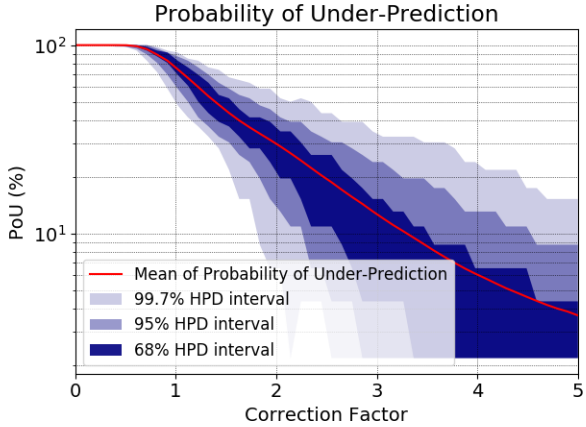
Probability of Under-Prediction
Mean of Probability of Under-Prediction
99.7% HPD interval
95% HPD interval
68% HPD interval
PoU (%)
Correction Factor

Models for critical velcoity $\boldsymbol{v_c}$ in EFA/Coarse dataset:

(1) Model characteristics:

Group No.	Independent variables	Dataset/ No. of data	Model expression (parameter values given by deterministic regression)	R^2	Cross-validation score
44	PI, γ, VST, PF, D50	EFA/Coarse 10	$v_c = 0.002 \times PI - 0.1 \times \gamma + 0.01 \times VST - 0.09 \times PF - 13.6 \times D50 + 7.21$ $for\ 0.074 < D50 < 0.3$	0.93	0.67

(2) Statistics of marginal posterior distribution:

Parameters	Mean	SD	CoV	mode	95% HPD region (lower and upper bound)	
β_{PI}	0.001	0.004	3.655	0.000	-0.007	0.009
β_{γ}	-0.114	0.036	-0.313	-0.120	-0.184	-0.044
β_{VST}	0.010	0.002	0.198	0.010	0.006	0.014
β_{PF}	-0.095	0.014	-0.146	-0.090	-0.123	-0.069
β_{D50}	-13.810	1.783	-0.129	-13.850	-17.227	-10.271
β_0	7.496	1.136	0.152	7.650	5.321	9.755

(3) Joint relative frequency histogram:

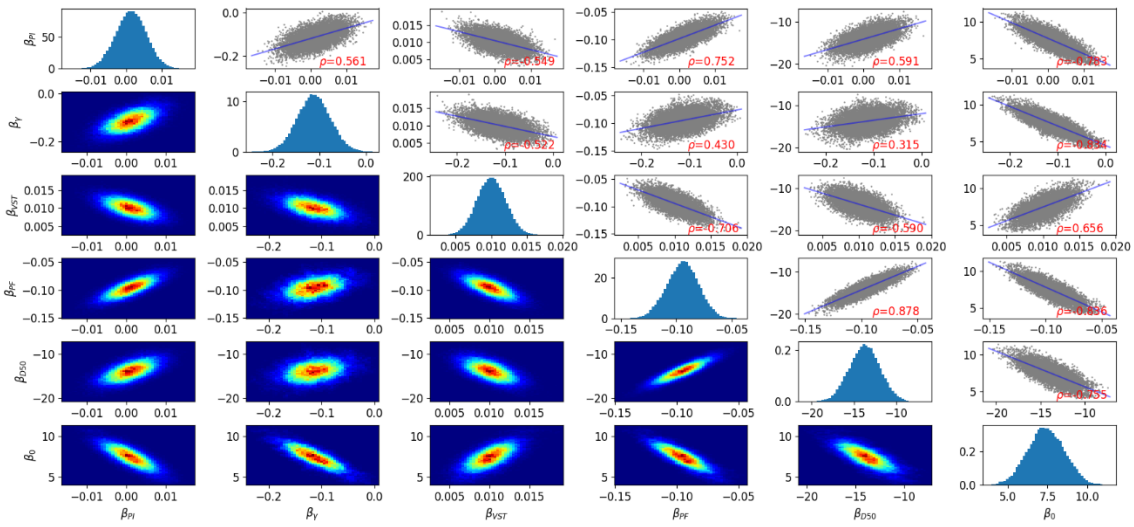

(4) Model realizations and first order statistics of model predictions:

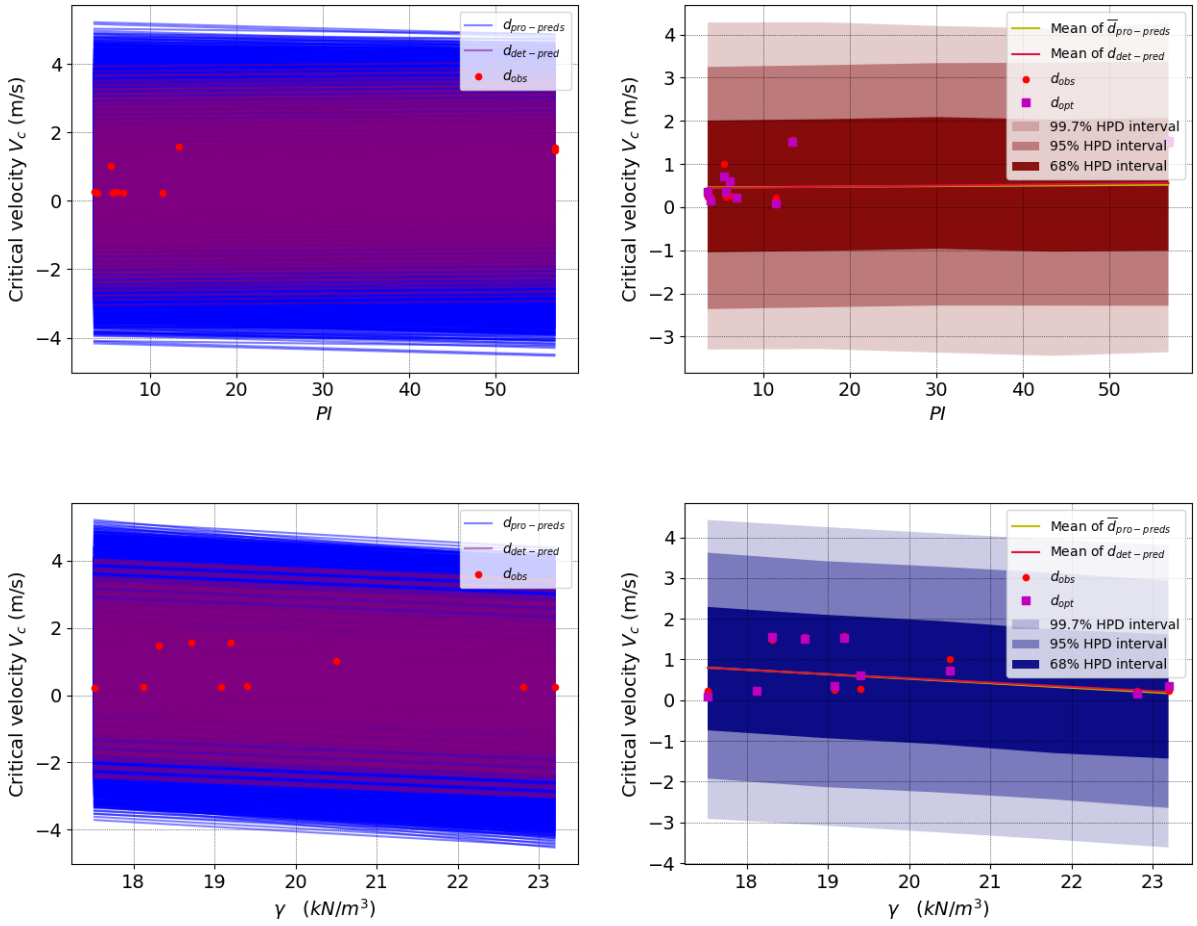

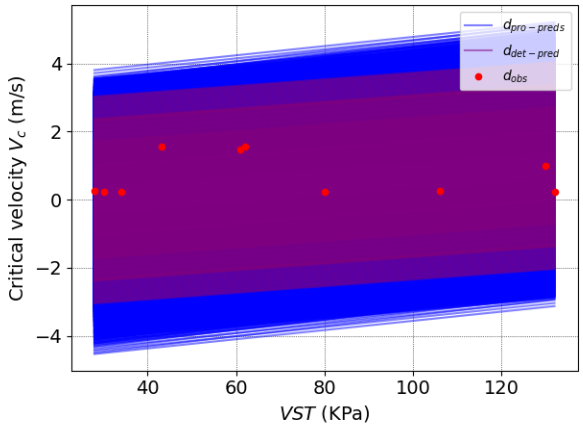
$d_{pro-preds}$
$d_{det-pred}$
d_{obs}
Critical velocity V_c (m/s)
VST (KPa)

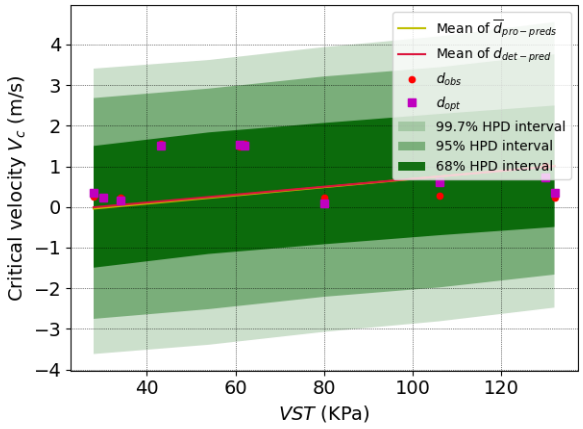
Mean of $\overline{d}_{pro-preds}$
Mean of $d_{det-pred}$
d_{obs}
d_{opt}
99.7% HPD interval
95% HPD interval
68% HPD interval
Critical velocity V_c (m/s)
VST (KPa)

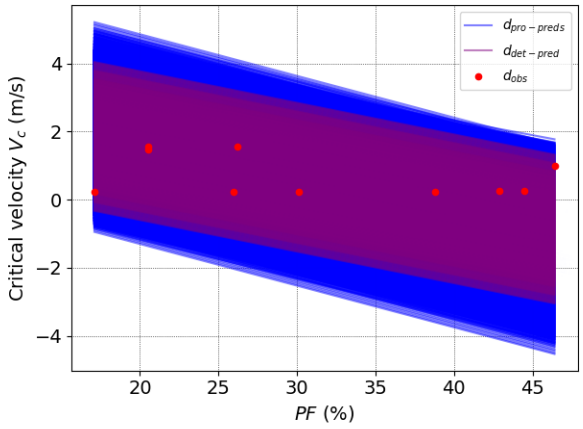
$d_{pro-preds}$
$d_{det-pred}$
d_{obs}
Critical velocity V_c (m/s)
PF (%)

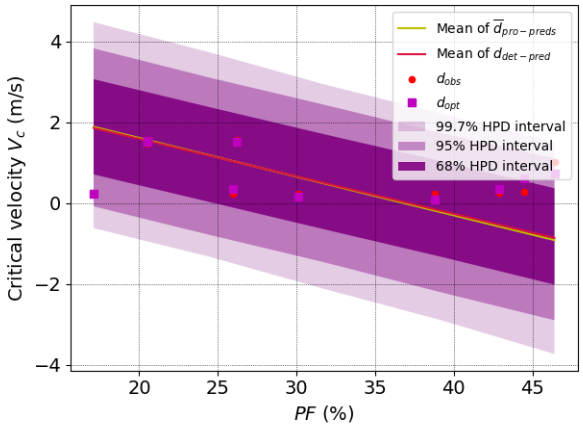
Mean of $\overline{d}_{pro-preds}$
Mean of $d_{det-pred}$
d_{obs}
d_{opt}
99.7% HPD interval
95% HPD interval
68% HPD interval
Critical velocity V_c (m/s)
PF (%)

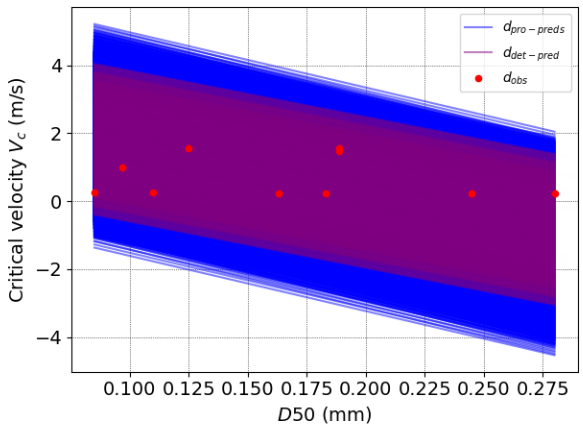
$d_{pro-preds}$
$d_{det-pred}$
d_{obs}
Critical velocity V_c (m/s)
*D*50 (mm)

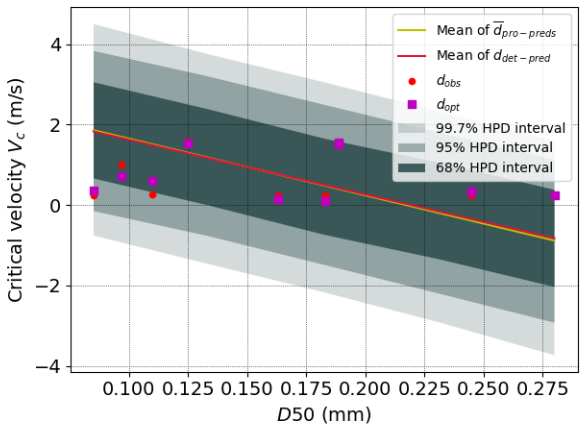
Mean of $\overline{d}_{pro-preds}$
Mean of $d_{det-pred}$
d_{obs}
d_{opt}
99.7% HPD interval
95% HPD interval
68% HPD interval
Critical velocity V_c (m/s)
*D*50 (mm)

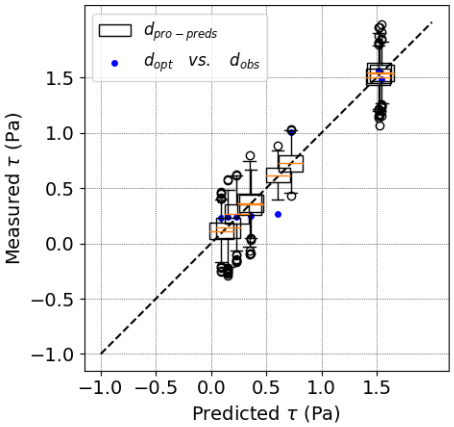
$d_{pro-preds}$
d_{opt} vs. d_{obs}
Measured τ (Pa)
Predicted τ (Pa)
1.5
1.0
0.5
0.0
−0.5
−1.0
−1.0 −0.5 0.0 0.5 1.0 1.5

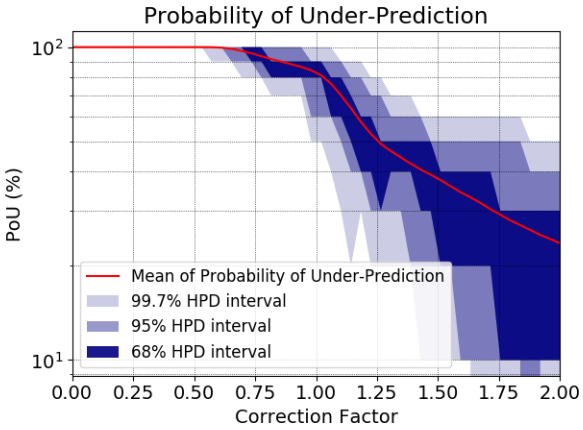
Probability of Under-Prediction
PoU (%)
10^2
10^1
Mean of Probability of Under-Prediction
99.7% HPD interval
95% HPD interval
68% HPD interval
0.00 0.25 0.50 0.75 1.00 1.25 1.50 1.75 2.00
Correction Factor

Models for Erosion Category EC in EFA/Fine dataset:

(1) Model characteristics:

Group No.	Independent variables	Dataset/ No. of data	Model expression (parameter values given by deterministic regression)	R^2	Cross-validation score
132	A, WC, S_u, D50	EFA/Fine 44	$EC = (0.1933) \times A^{-0.06} \times WC^{0.51} \times S_u^{0.09} \times D50^{-0.12}$	0.55	0.53

(2) Statistics of marginal posterior distribution:

Parameters	Mean	SD	CoV	mode	95% HPD region (lower and upper bound)	
β_0	0.27	0.13	0.50	0.19	0.07	0.53
β_A	-0.04	0.05	-1.02	-0.04	-0.13	0.05
β_{WC}	0.46	0.10	0.22	0.49	0.27	0.66
β_{S_u}	0.07	0.06	0.77	0.07	-0.03	0.19
β_{D50}	-0.12	0.04	-0.34	-0.12	-0.19	-0.04

(3) Joint relative frequency histogram:

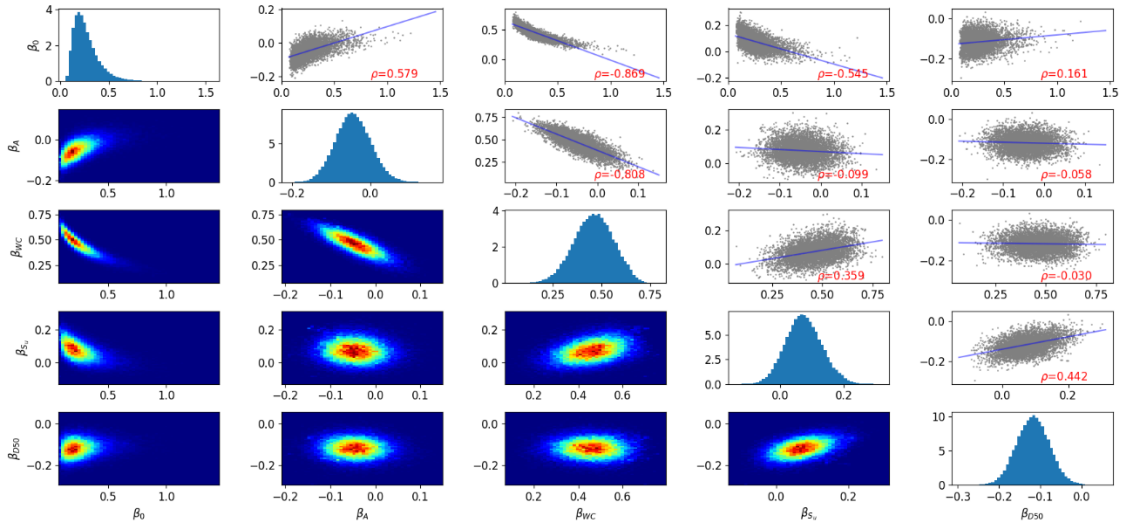

(4) Model realizations and first order statistics of model predictions:

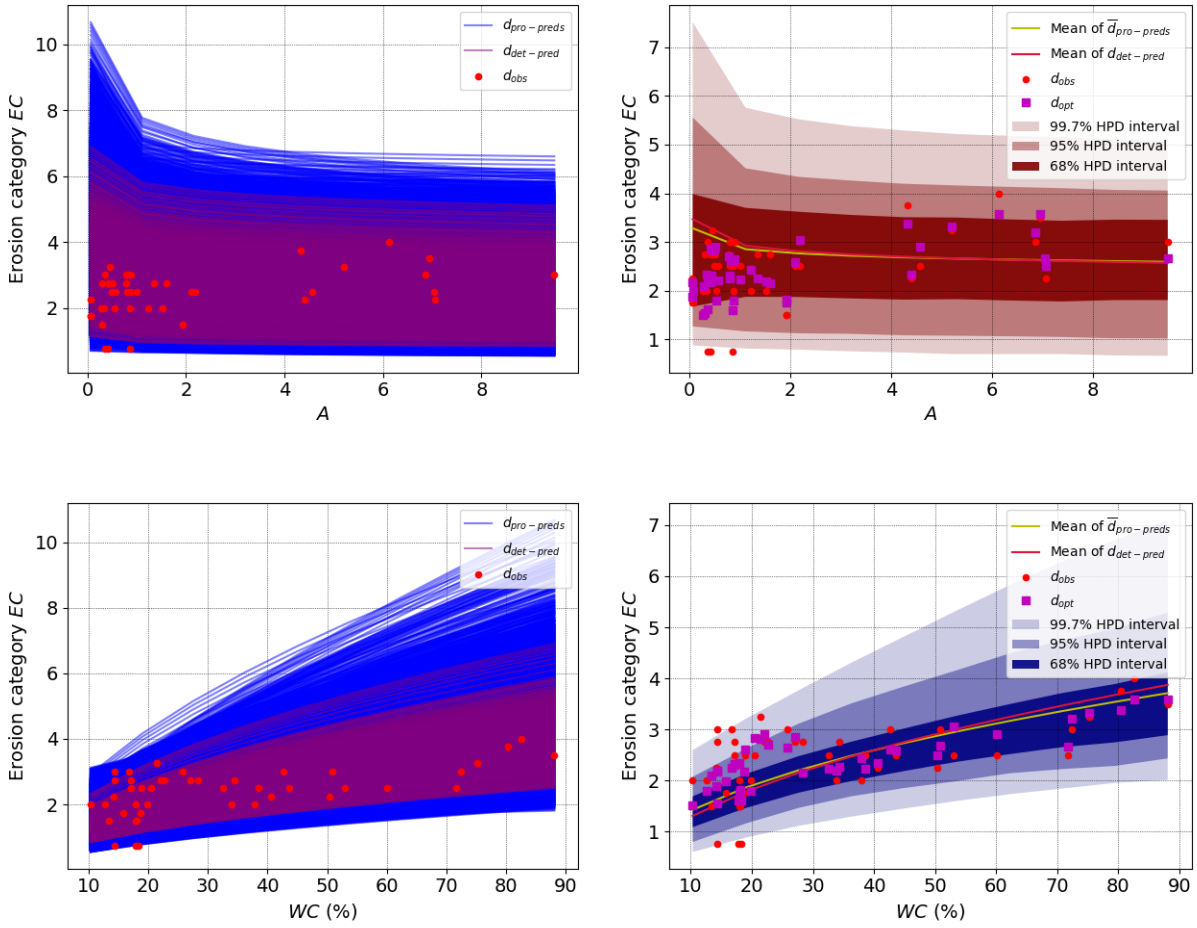

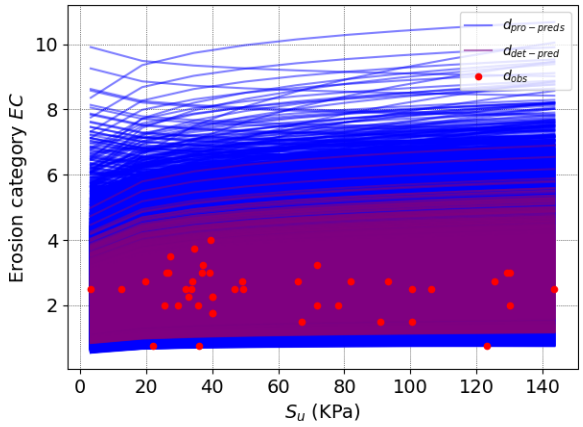
$d_{pro-preds}$
$d_{det-pred}$
d_{obs}
Erosion category EC
S_u (KPa)

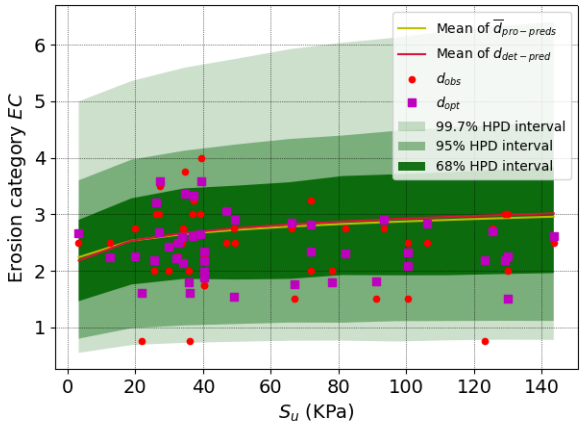
Mean of $\overline{d}_{pro-preds}$
Mean of $d_{det-pred}$
d_{obs}
d_{opt}
99.7% HPD interval
95% HPD interval
68% HPD interval
Erosion category EC
S_u (KPa)

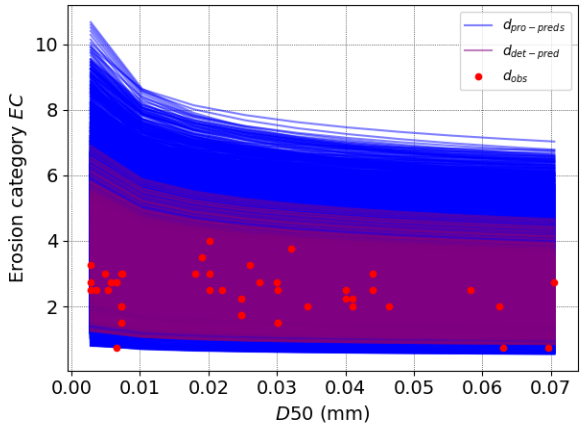
$d_{pro-preds}$
$d_{det-pred}$
d_{obs}
Erosion category EC
$D50$ (mm)

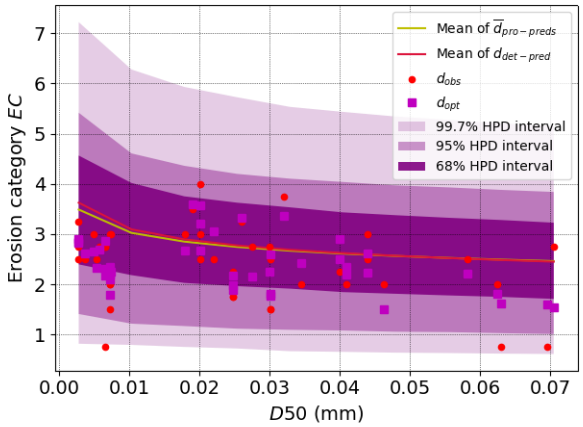
Mean of $\overline{d}_{pro-preds}$
Mean of $d_{det-pred}$
d_{obs}
d_{opt}
99.7% HPD interval
95% HPD interval
68% HPD interval
Erosion category EC
$D50$ (mm)

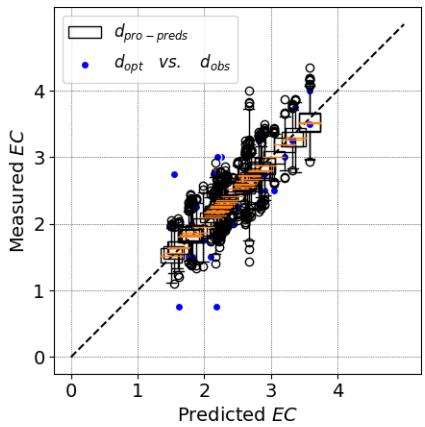
$d_{pro-preds}$
d_{opt} vs. d_{obs}
Measured EC
Predicted EC

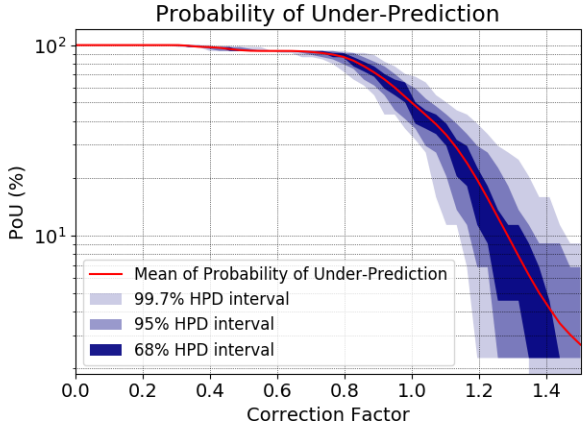
Probability of Under-Prediction
PoU (%)
Mean of Probability of Under-Prediction
99.7% HPD interval
95% HPD interval
68% HPD interval
Correction Factor

Models for Erosion Category EC in EFA/Fine dataset:

(1) Model characteristics:

Group No.	Independent variables	Dataset/ No. of data	Model expression (parameter values given by deterministic regression)	R^2	Cross-validation score
117	PC, WC, S_u, D50	EFA/Fine 44	$EC = 0.023 \times PC + 0.03 \times WC + 0.0017 \times S_u - 1.845 \times D50 + 0.8566$	0.56	0.43

(2) Statistics of marginal posterior distribution:

Parameters	Mean	SD	CoV	mode	95% HPD region (lower and upper bound)	
β_{PC}	0.021	0.008	0.378	0.021	0.006	0.037
β_{WC}	0.031	0.005	0.160	0.030	0.021	0.040
β_{S_u}	0.002	0.003	1.313	0.002	-0.003	0.007
β_{D50}	-2.396	5.349	-2.232	-1.137	-12.858	8.083
β_0	0.922	0.440	0.477	1.004	0.053	1.770

(3) Joint relative frequency histogram:

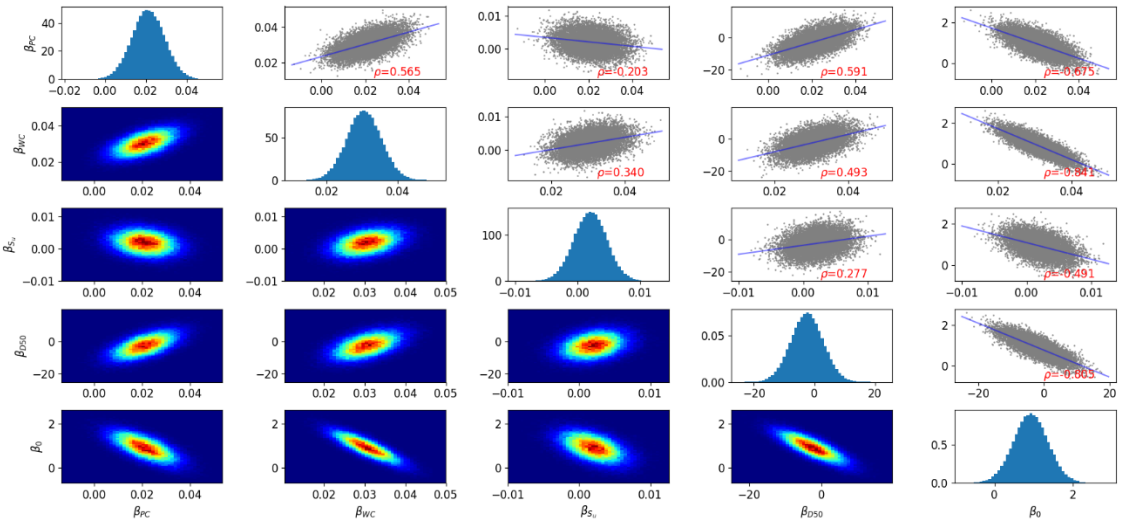

(4) Model realizations and first order statistics of model predictions:

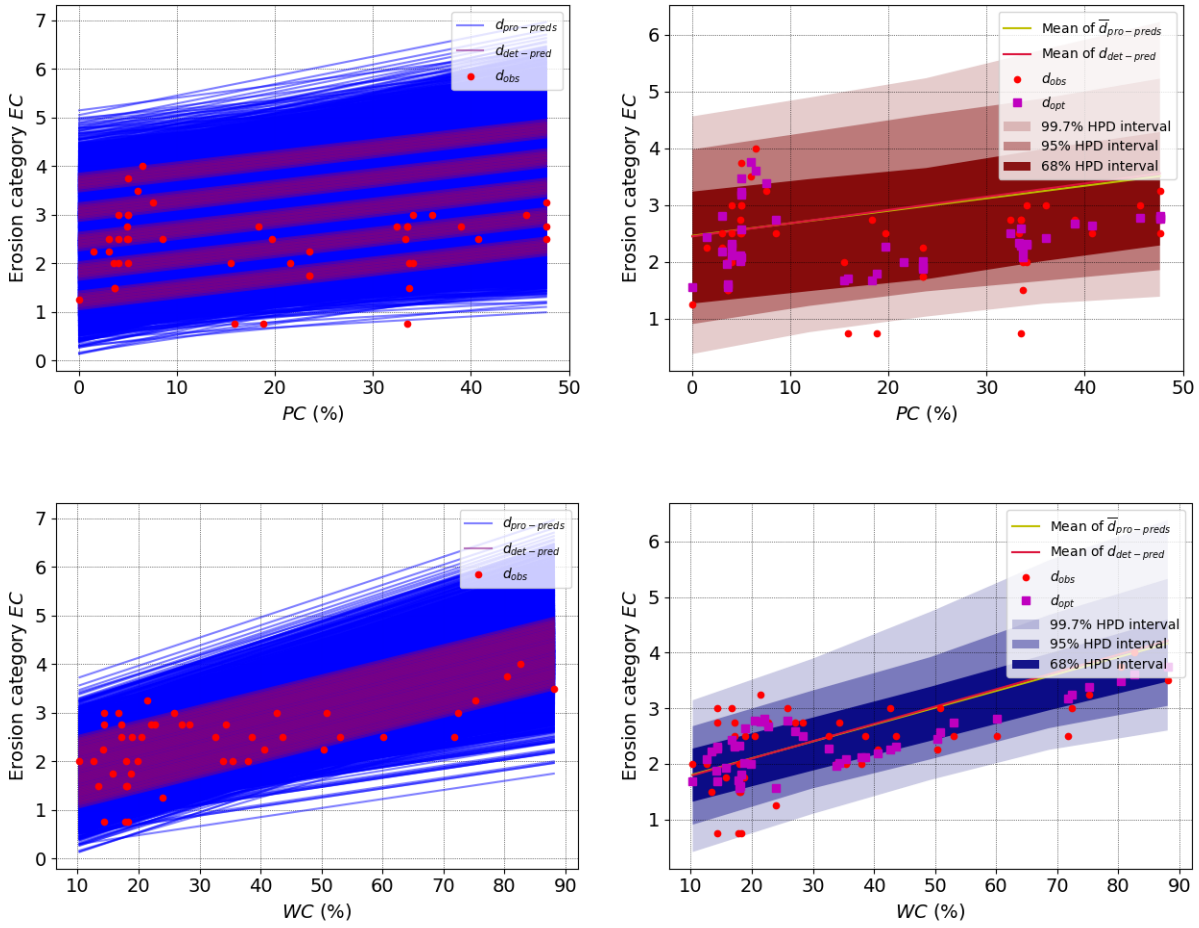

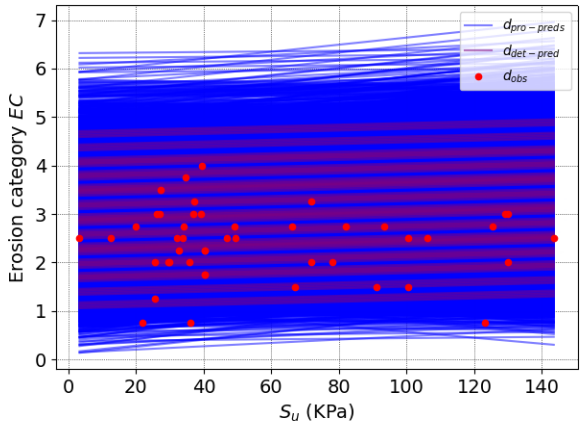
$d_{pro-preds}$
$d_{det-pred}$
d_{obs}
Erosion category EC
S_u (KPa)

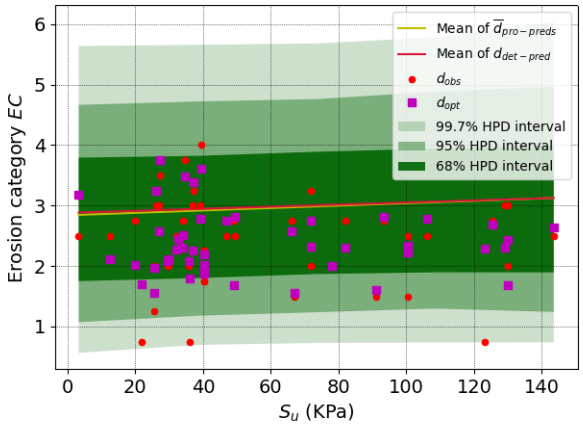
Mean of $\overline{d}_{pro-preds}$
Mean of $d_{det-pred}$
d_{obs}
d_{opt}
99.7% HPD interval
95% HPD interval
68% HPD interval
Erosion category EC
S_u (KPa)

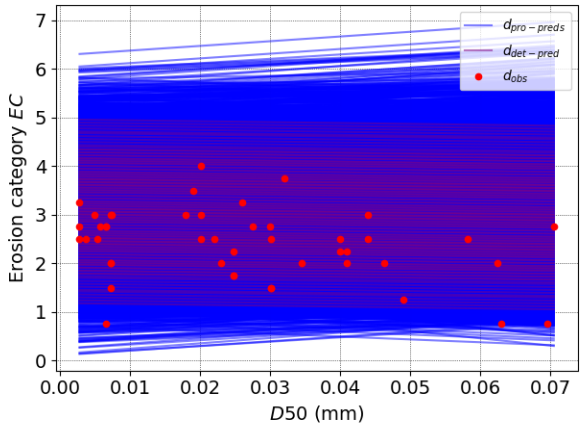
$d_{pro-preds}$
$d_{det-pred}$
d_{obs}
Erosion category EC
$D50$ (mm)

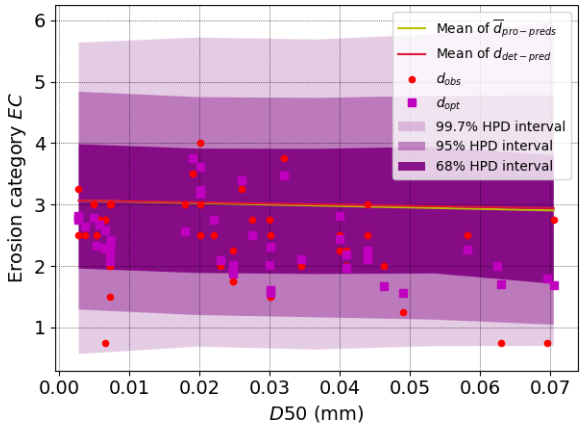
Mean of $\overline{d}_{pro-preds}$
Mean of $d_{det-pred}$
d_{obs}
d_{opt}
99.7% HPD interval
95% HPD interval
68% HPD interval
Erosion category EC
$D50$ (mm)

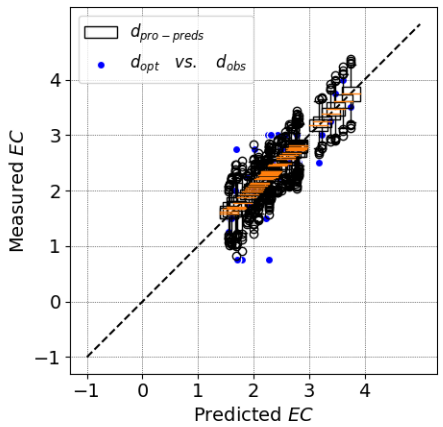
$d_{pro-preds}$
d_{opt} vs. d_{obs}
Measured EC
Predicted EC

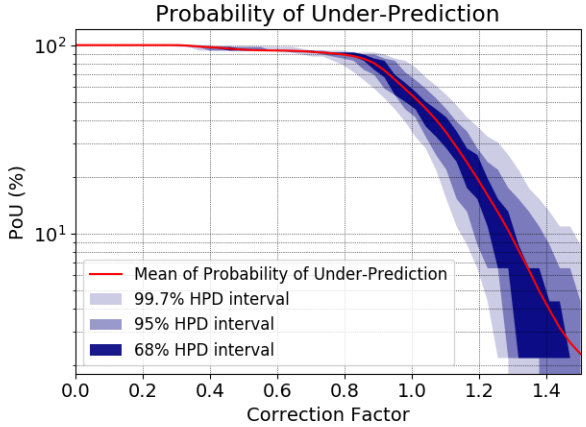
Probability of Under-Prediction
Mean of Probability of Under-Prediction
99.7% HPD interval
95% HPD interval
68% HPD interval
PoU (%)
Correction Factor

Models for Erosion Category EC in EFA/Coarse dataset:

(1) Model characteristics:

Group No.	Independent variables	Dataset/ No. of data	Model expression (parameter values given by deterministic regression)	R^2	Cross-validation score
91	C_u, WC, VST, D50	EFA/Coarse 11	$EC = (1.12) \times C_u^{0.1} \times WC^{-0.28} \times VST^{0.02} \times D50^{-0.44}$ $for\ 0.074 < D50 < 0.3$	0.92	0.80

(2) Statistics of marginal posterior distribution:

Parameters	Mean	SD	CoV	mode	95% HPD region (lower and upper bound)	
β_0	1.264	0.375	0.297	0.979	0.577	1.997
β_{C_u}	0.110	0.038	0.347	0.108	0.035	0.184
β_{WC}	-0.304	0.077	-0.254	-0.323	-0.454	-0.150
β_{VST}	0.000	0.088	1453.277	-0.010	-0.175	0.170
β_{D50}	-0.451	0.089	-0.197	-0.442	-0.624	-0.274

(3) Joint relative frequency histogram:

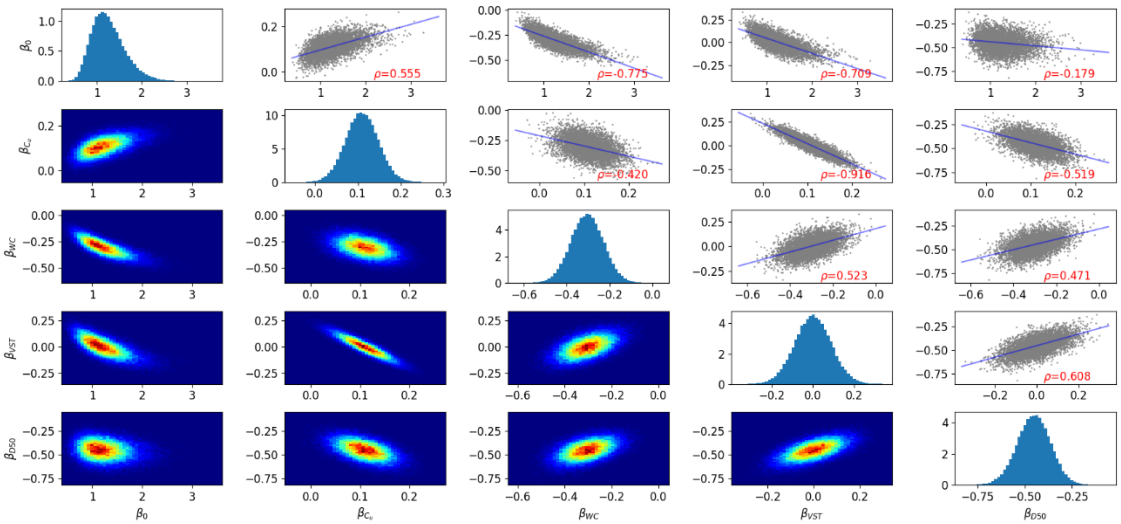

(4) Model realizations and first order statistics of model predictions:

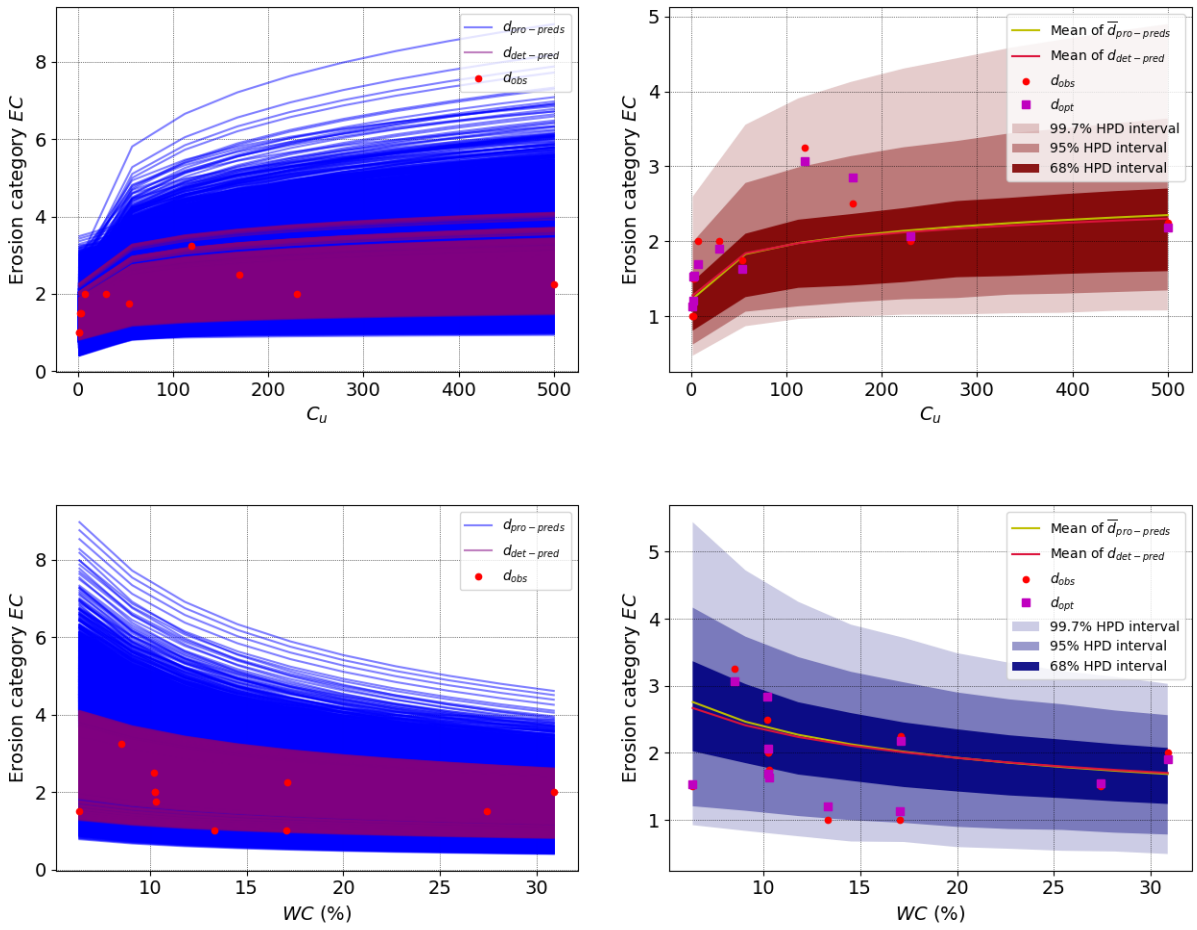

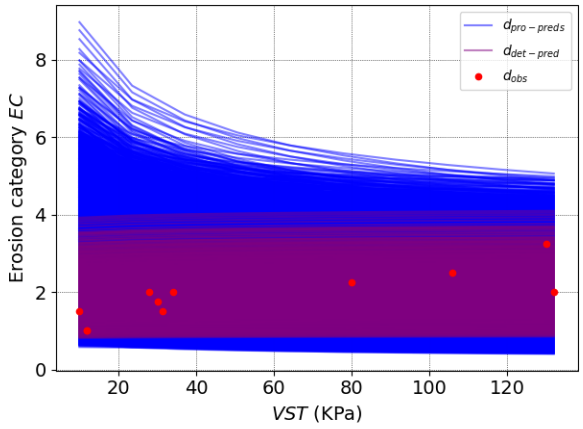
$d_{pro-preds}$
$d_{det-pred}$
d_{obs}
Erosion category *EC*
VST (KPa)

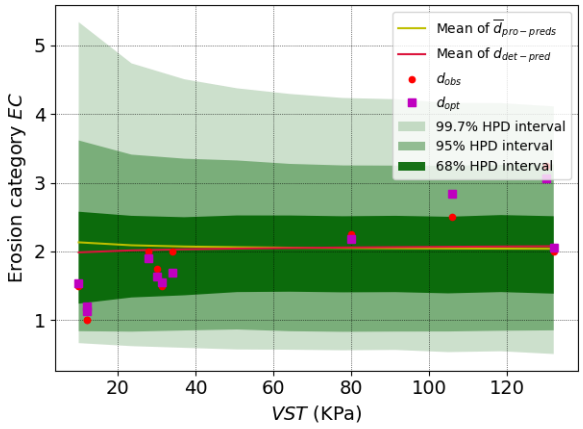
Mean of $\overline{d}_{pro-preds}$
Mean of $d_{det-pred}$
d_{obs}
d_{opt}
99.7% HPD interval
95% HPD interval
68% HPD interval
Erosion category *EC*
VST (KPa)

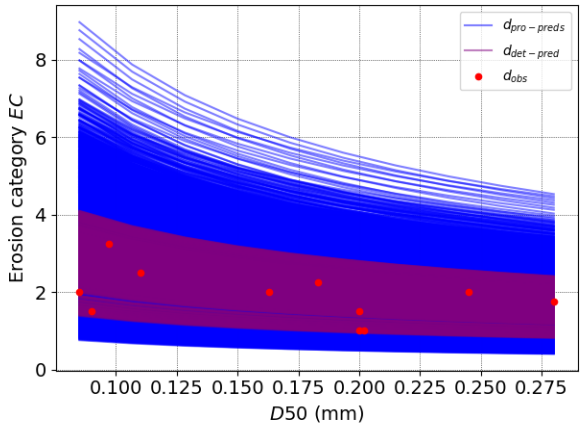
$d_{pro-preds}$
$d_{det-pred}$
d_{obs}
Erosion category *EC*
*D*50 (mm)

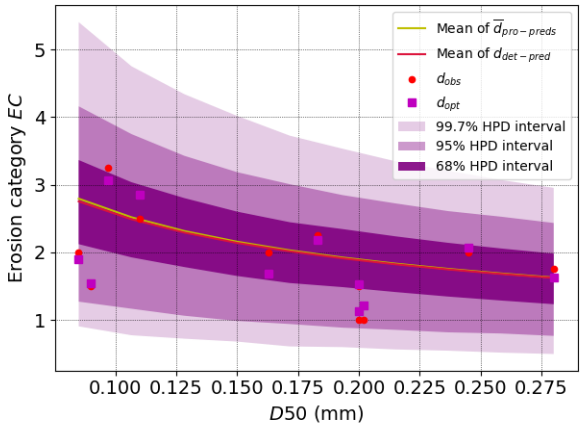
Mean of $\overline{d}_{pro-preds}$
Mean of $d_{det-pred}$
d_{obs}
d_{opt}
99.7% HPD interval
95% HPD interval
68% HPD interval
Erosion category *EC*
*D*50 (mm)

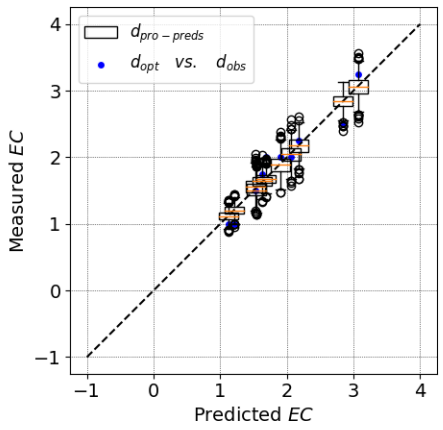
$d_{pro-preds}$
d_{opt} *vs.* d_{obs}
Measured *EC*
Predicted *EC*

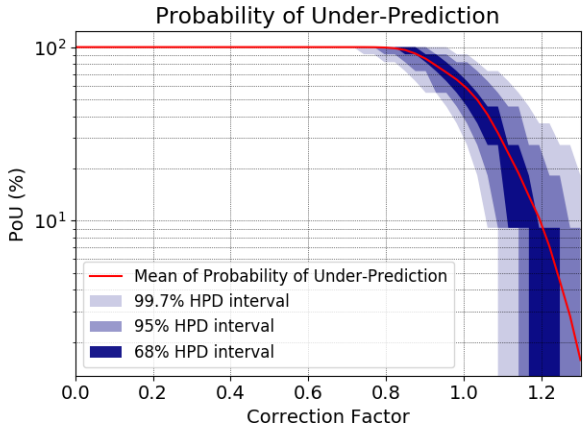
Probability of Under-Prediction
Mean of Probability of Under-Prediction
99.7% HPD interval
95% HPD interval
68% HPD interval
PoU (%)
Correction Factor

Models for Erosion Category EC in JET/Fine dataset:

(1) Model characteristics:

Group No.	Independent variables	Dataset/ No. of data	Model expression (parameter values given by deterministic regression)	R^2	Cross-validation score
13	PI, γ, PF	JET/Fine 56	$EC = (0.00375) \times PI^{0.12} \times \gamma^{1.81} \times PF^{0.21}$	0.51	0.47

(2) Statistics of marginal posterior distribution:

Parameters	Mean	SD	CoV	mode	95% HPD region (lower and upper bound)	
β_0	0.052	0.077	1.493	0.006	0.004	0.189
β_{PI}	0.127	0.029	0.232	0.120	0.070	0.184
β_γ	1.368	0.261	0.191	1.494	0.884	1.881
β_{PF}	0.042	0.126	3.016	0.071	-0.215	0.277

(3) Joint relative frequency histogram:

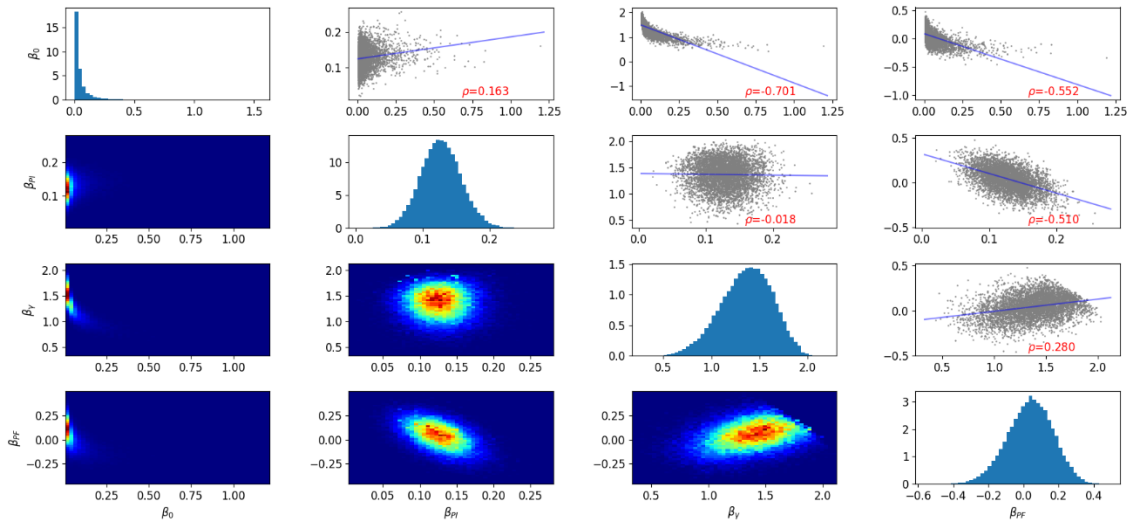

(4) Model realizations and first order statistics of model predictions:

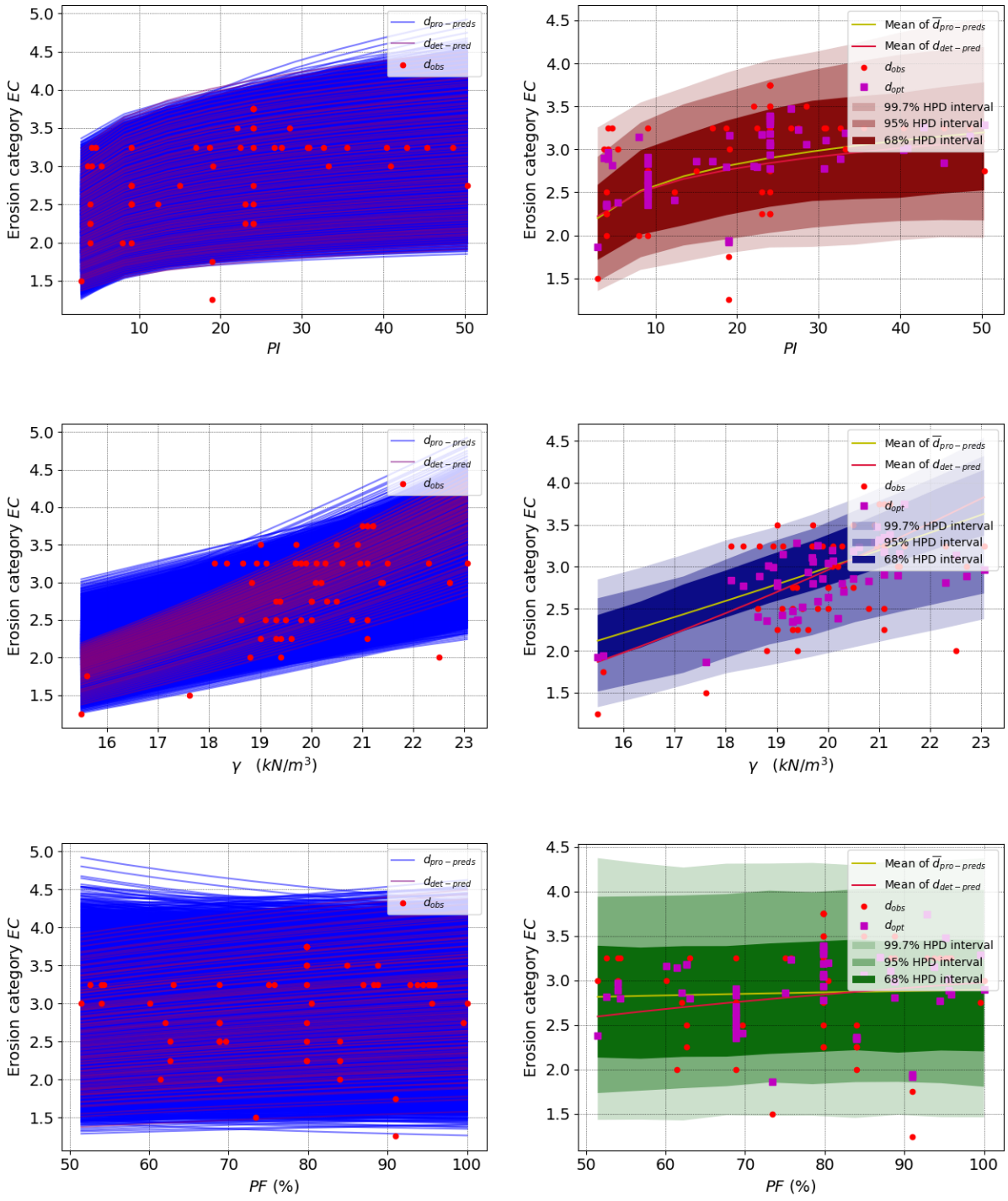

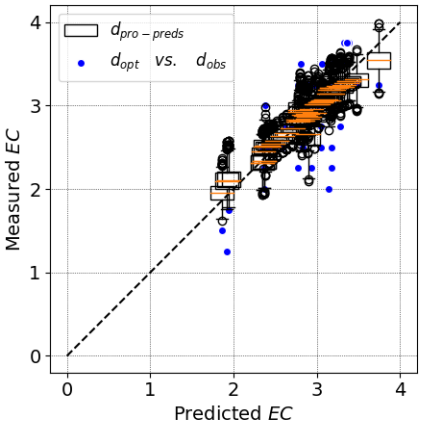
$d_{pro-preds}$
d_{opt} vs. d_{obs}
Measured *EC*
Predicted *EC*
0
1
2
3
4

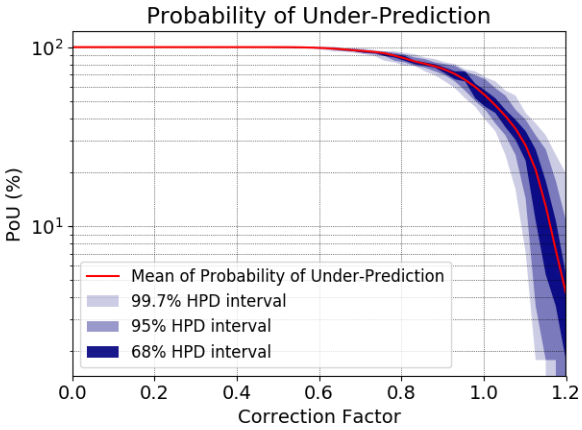
Probability of Under-Prediction
PoU (%)
10^2
10^1
Mean of Probability of Under-Prediction
99.7% HPD interval
95% HPD interval
68% HPD interval
0.0
0.2
0.4
0.6
0.8
1.0
1.2
Correction Factor

Models for Erosion Category EC in JET/Global:

(1) Model characteristics:

Group No.	Independent variables	Dataset/ No. of data	Model expression (parameter values given by deterministic regression)	R^2	Cross-validation score
88	PL, S_u, D50	JET/Global 28	$EC = -0.022 \times PL + 0.0031 \times S_u - 5.5 \times D50 + 3.34$ $for\ D50 < 0.3\ mm$	0.70	0.58

(2) Statistics of marginal posterior distribution:

Parameters	Mean	SD	CoV	mode	95% HPD region (lower and upper bound)	
β_{PL}	-0.026	0.011	-0.417	-0.024	-0.047	-0.005
β_{S_u}	0.003	0.001	0.399	0.003	0.001	0.005
β_{D50}	-5.644	0.851	-0.151	-5.464	-7.294	-3.951
β_0	3.417	0.248	0.073	3.420	2.927	3.901

(3) Joint relative frequency histogram:

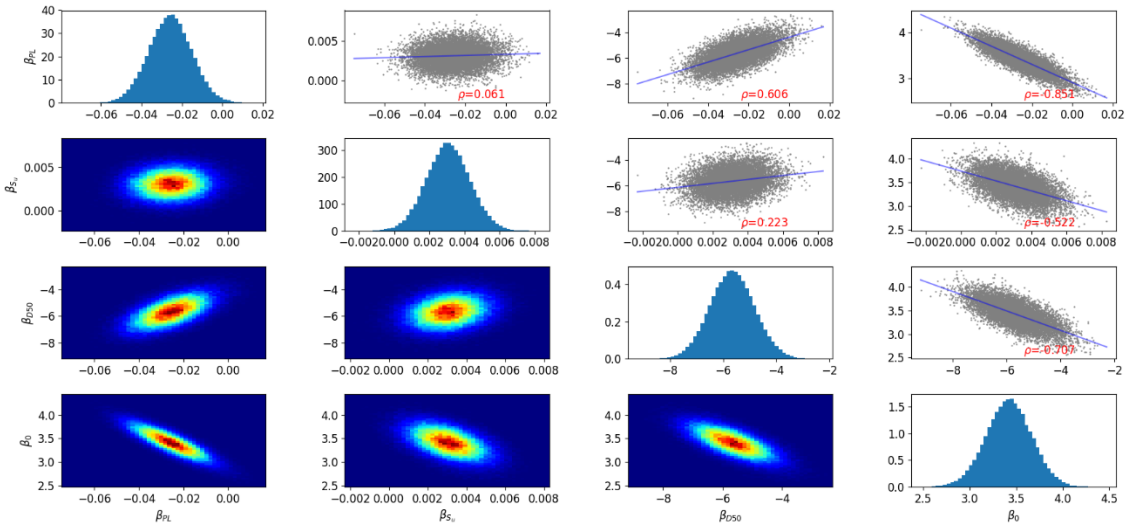

(4) Model realizations and first order statistics of model predictions:

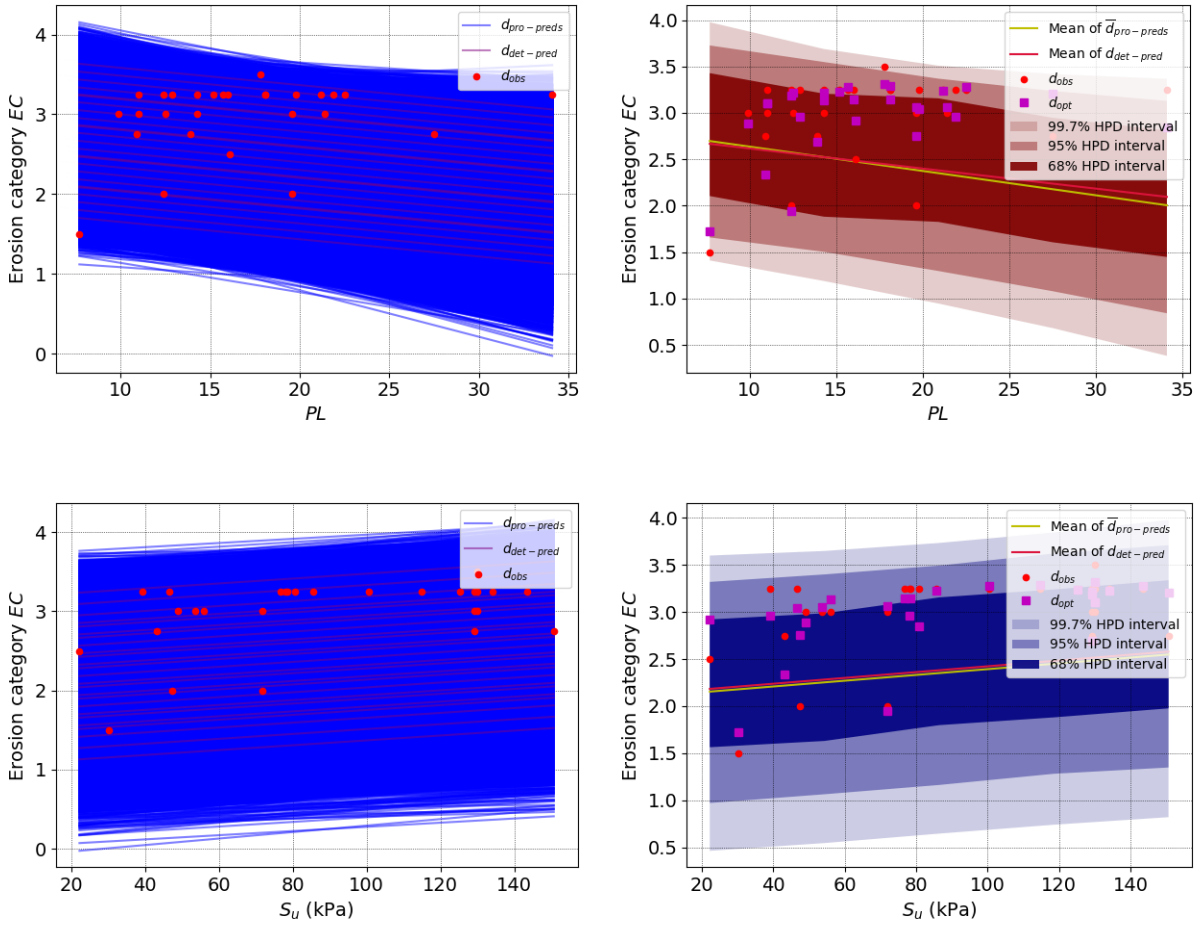

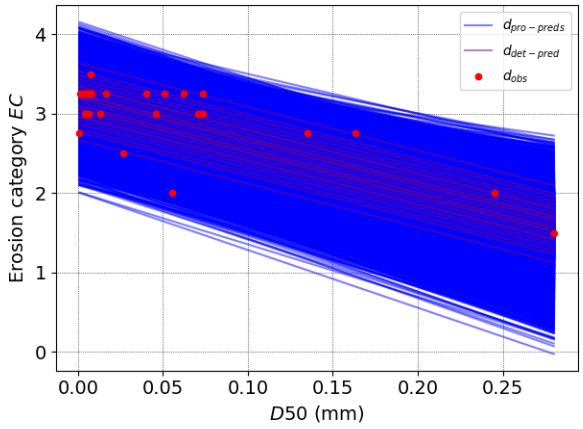
$d_{pro-preds}$
$d_{det-pred}$
d_{obs}
Erosion category *EC*
*D*50 (mm)

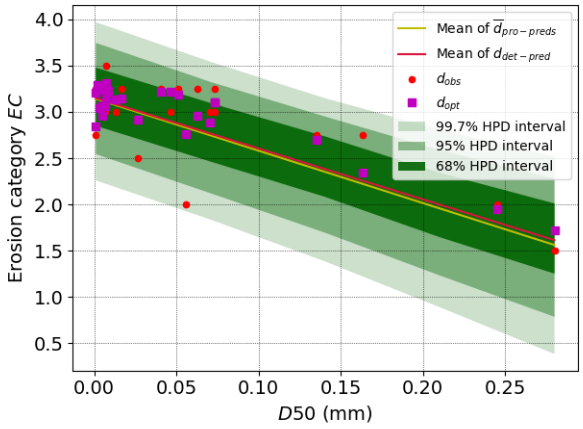
Mean of $\overline{d}_{pro-preds}$
Mean of $d_{det-pred}$
d_{obs}
d_{opt}
99.7% HPD interval
95% HPD interval
68% HPD interval
Erosion category *EC*
*D*50 (mm)

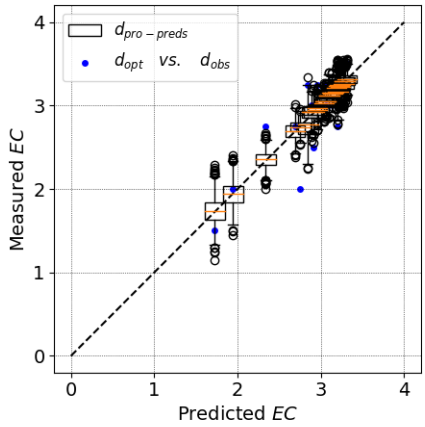
$d_{pro-preds}$
d_{opt} *vs.* d_{obs}
Measured *EC*
Predicted *EC*

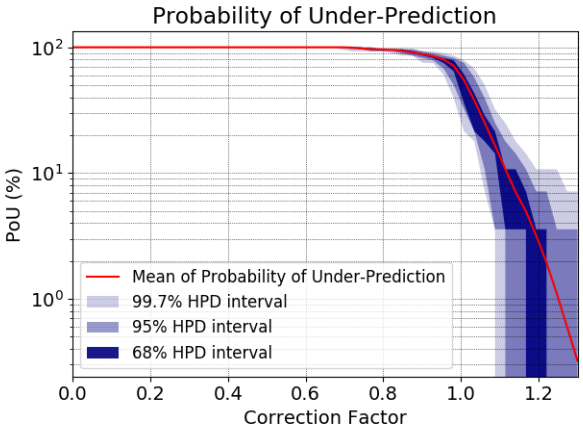
Probability of Under-Prediction
Mean of Probability of Under-Prediction
99.7% HPD interval
95% HPD interval
68% HPD interval
PoU (%)
Correction Factor

Models for Erosion Category EC in HET/Fina dataset:

(1) Model characteristics:

Group No.	Independent variables	Dataset/ No. of data	Model expression (parameter values given by deterministic regression)	R^2	Cross-validation score
12	PI, γ, S_u	HET/Fine 21	$EC = (1.67) \times PI^{0.04} \times \gamma^{0.15} \times S_u^{0.03}$	0.70	0.54

(2) Statistics of marginal posterior distribution:

Parameters	Mean	SD	CoV	mode	95% HPD region (lower and upper bound)	
β_0	2.410	1.143	0.474	0.932	0.892	4.631
β_{PI}	0.047	0.011	0.235	0.049	0.026	0.069
β_γ	0.051	0.154	3.010	0.112	-0.232	0.347
β_{S_u}	0.031	0.009	0.286	0.031	0.014	0.049

(3) Joint relative frequency histogram:

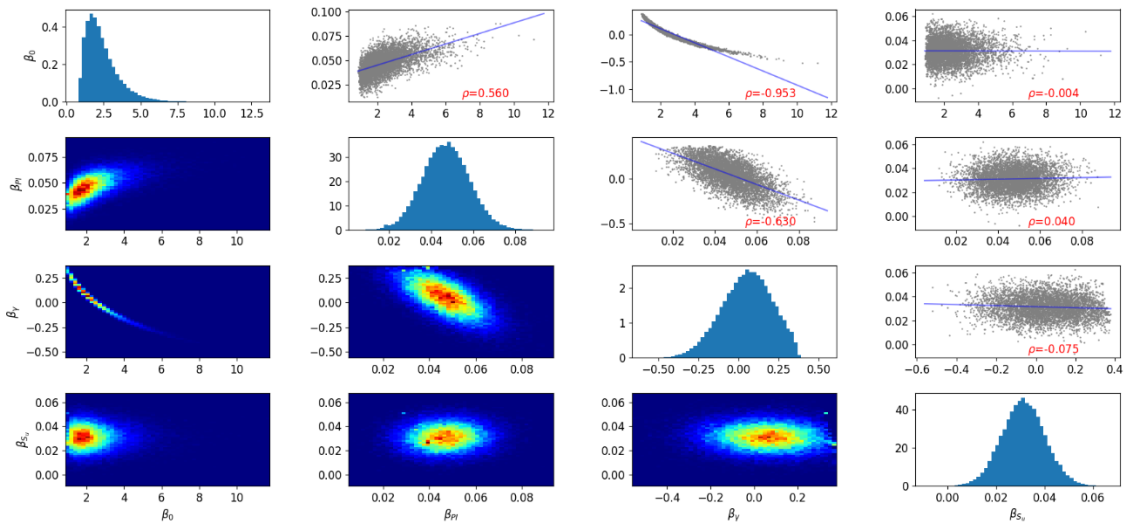

(4) Model realizations and first order statistics of model predictions:

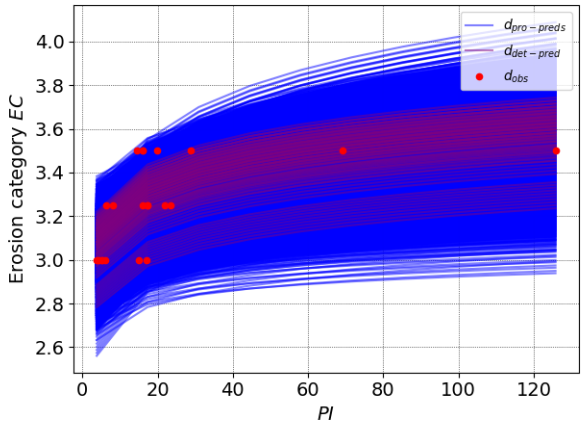
$d_{pro-preds}$
$d_{det-pred}$
d_{obs}
Erosion category EC
PI

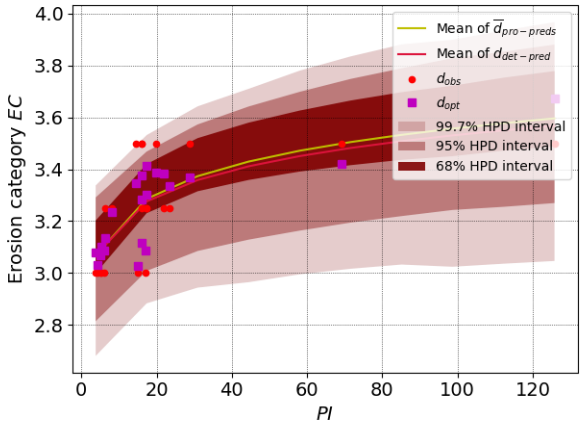
Mean of $\overline{d}_{pro-preds}$
Mean of $d_{det-pred}$
d_{obs}
d_{opt}
99.7% HPD interval
95% HPD interval
68% HPD interval
Erosion category EC
PI

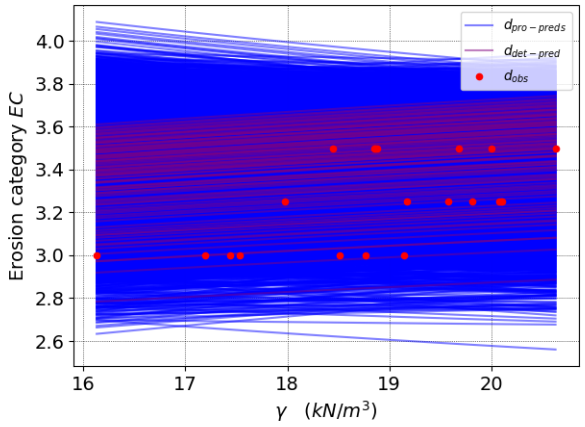
$d_{pro-preds}$
$d_{det-pred}$
d_{obs}
Erosion category EC
γ (kN/m^3)

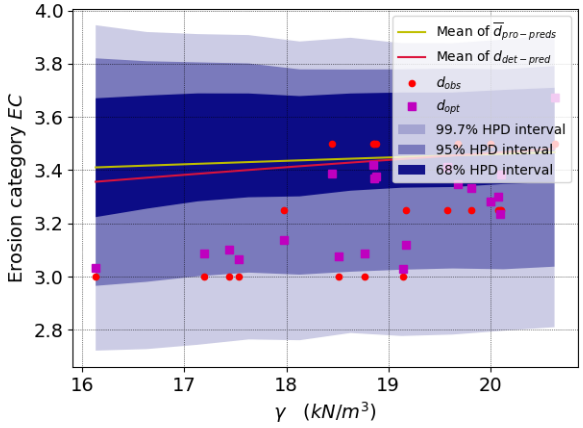
Mean of $\overline{d}_{pro-preds}$
Mean of $d_{det-pred}$
d_{obs}
d_{opt}
99.7% HPD interval
95% HPD interval
68% HPD interval
Erosion category EC
γ (kN/m^3)

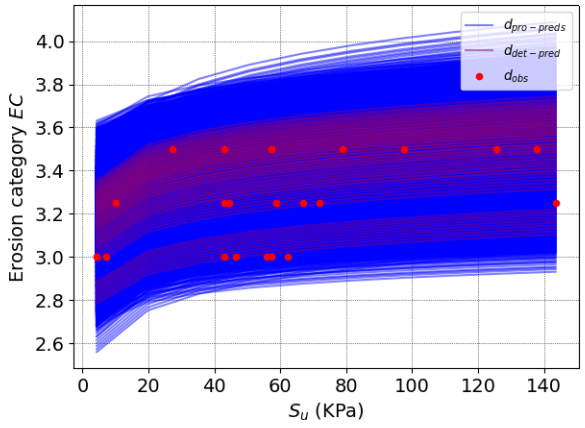
$d_{pro-preds}$
$d_{det-pred}$
d_{obs}
Erosion category EC
S_u (KPa)

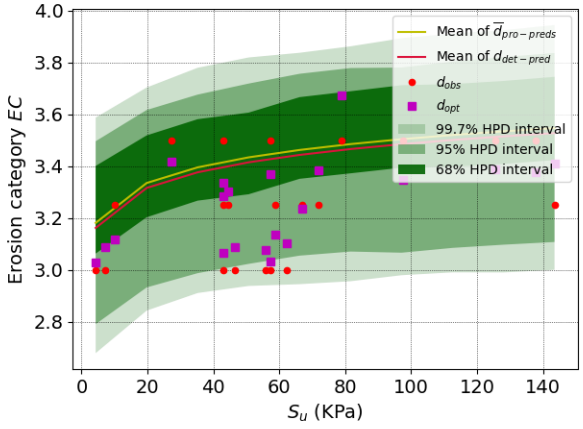
Mean of $\overline{d}_{pro-preds}$
Mean of $d_{det-pred}$
d_{obs}
d_{opt}
99.7% HPD interval
95% HPD interval
68% HPD interval
Erosion category EC
S_u (KPa)

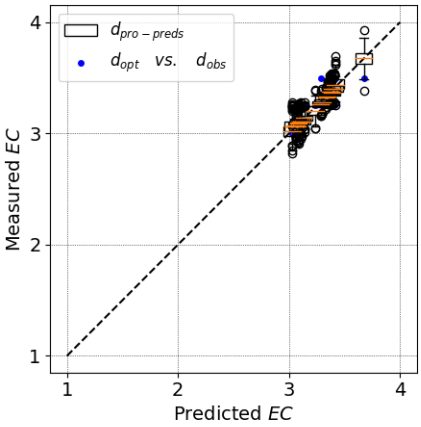
$d_{pro-preds}$
d_{opt} vs. d_{obs}
Measured *EC*
Predicted *EC*
1
2
3
4

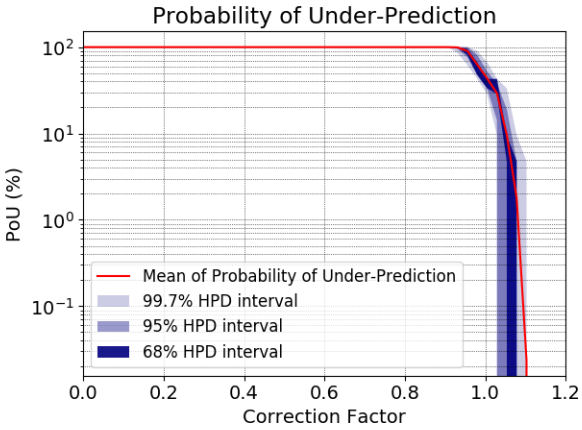
Probability of Under-Prediction
PoU (%)
10^{2}
10^{1}
10^{0}
10^{-1}
Mean of Probability of Under-Prediction
99.7% HPD interval
95% HPD interval
68% HPD interval
0.0
0.2
0.4
0.6
0.8
1.0
1.2
Correction Factor

Models for Velocity Slope $\boldsymbol{E_v}$ in EFA/Coarse dataset:

(1) Model characteristics:

Group No.	Independent variables	Dataset/ No. of data	Model expression (parameter values given by deterministic regression)	R^2	Cross-validation score
86	C_u, γ, WC, D50	EFA/Coarse 28	$E_v = (88969.4) \times C_u^{-1.77} \times \gamma^{-2.26} \times WC^{0.34} \times D50^{-1.69}$	0.86	0.64

(2) Statistics of marginal posterior distribution:

Parameters	Mean	SD	CoV	mode	95% HPD region (lower and upper bound)	
β_0	776485.449	554061.565	0.714	91446.538	67920.060	1856186.853
β_{C_u}	-1.794	0.391	-0.218	-2.331	-2.541	-1.087
β_γ	-3.017	0.340	-0.113	-2.265	-3.605	-2.322
β_{WC}	0.551	0.171	0.310	0.379	0.212	0.874
β_{D50}	-1.522	0.331	-0.218	-1.920	-2.215	-0.938

(3) Joint relative frequency histogram:

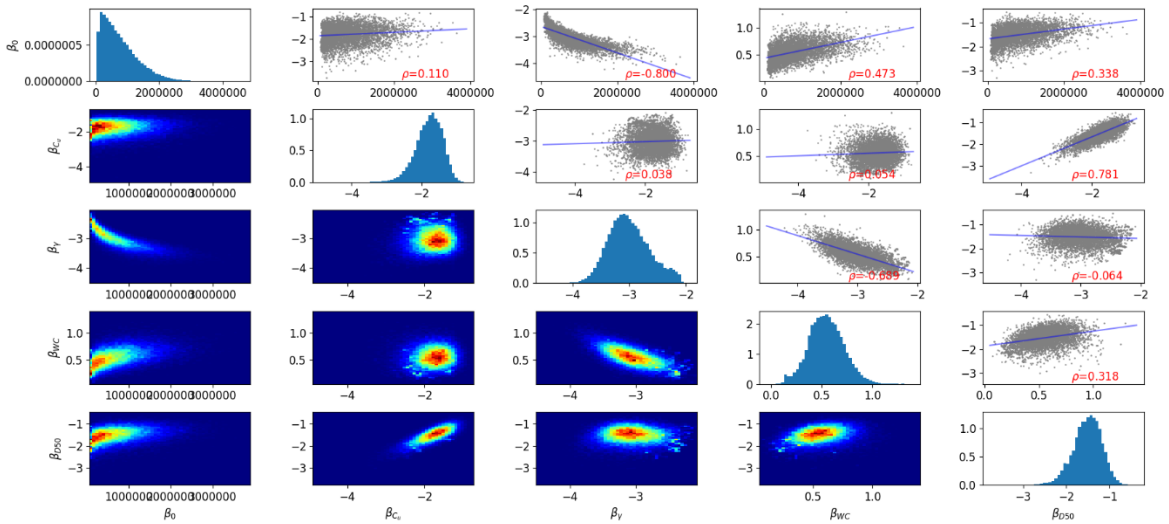

(4) Model realizations and first order statistics of model predictions:

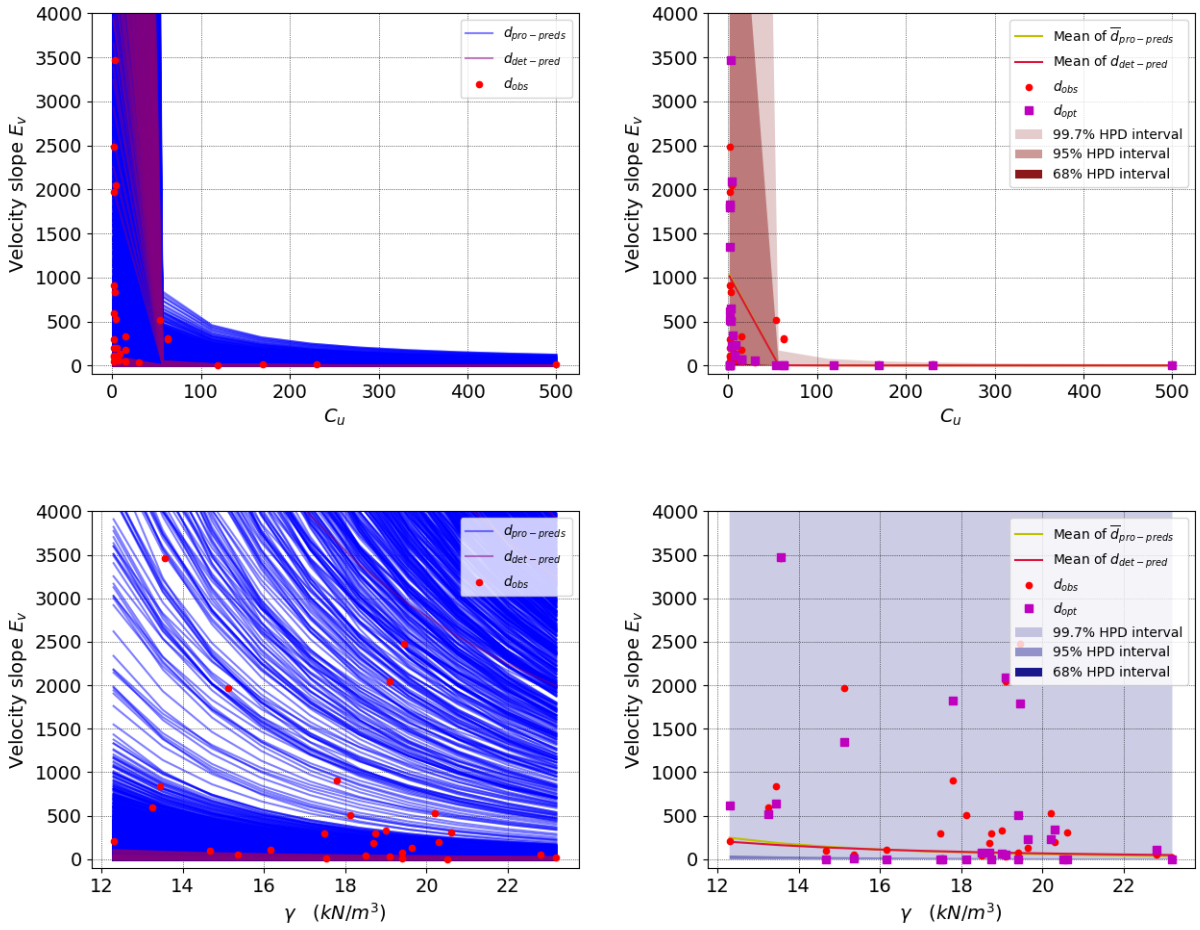

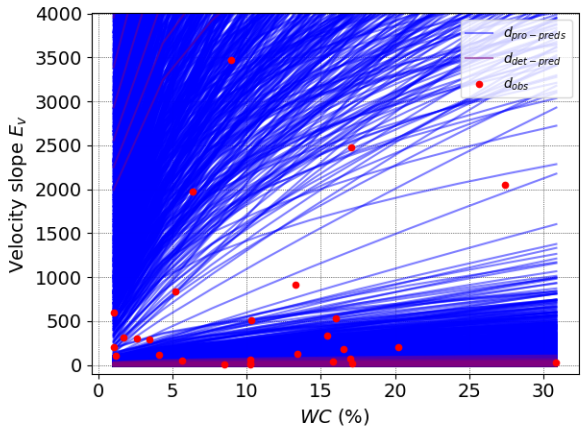
$d_{pro-preds}$
$d_{det-pred}$
d_{obs}
Velocity slope E_v
WC (%)

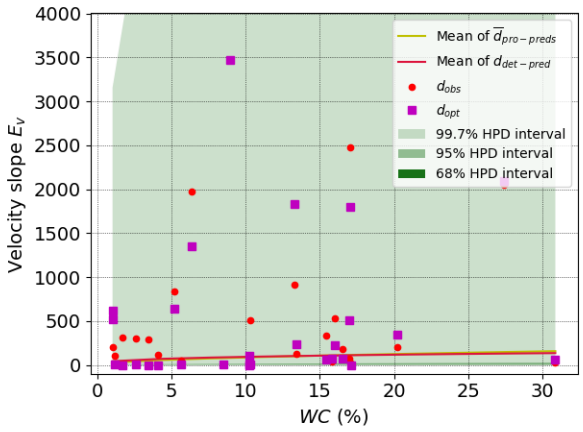
Mean of $\overline{d}_{pro-preds}$
Mean of $d_{det-pred}$
d_{obs}
d_{opt}
99.7% HPD interval
95% HPD interval
68% HPD interval
Velocity slope E_v
WC (%)

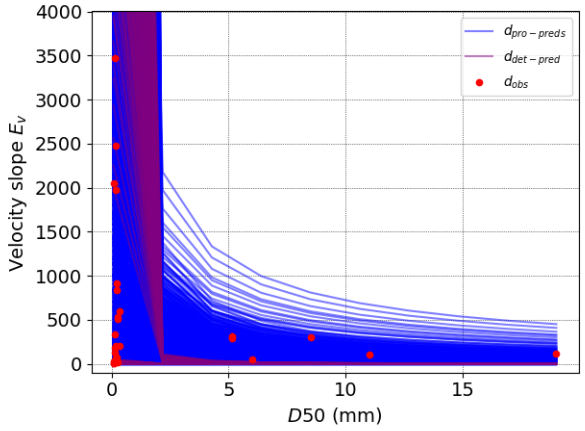
$d_{pro-preds}$
$d_{det-pred}$
d_{obs}
Velocity slope E_v
$D50$ (mm)

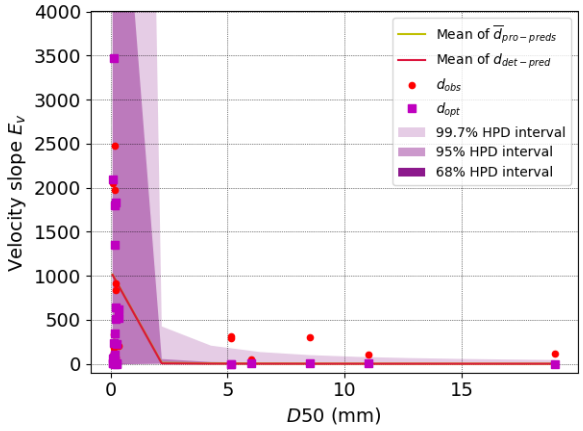
Mean of $\overline{d}_{pro-preds}$
Mean of $d_{det-pred}$
d_{obs}
d_{opt}
99.7% HPD interval
95% HPD interval
68% HPD interval
Velocity slope E_v
$D50$ (mm)

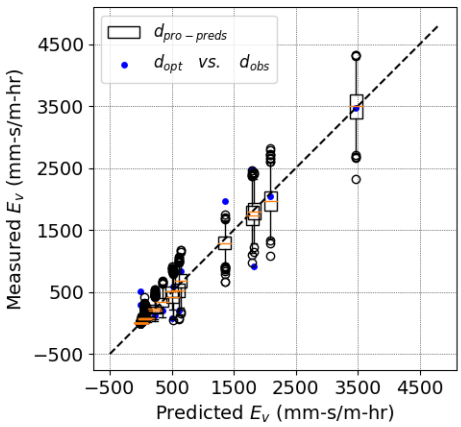
$d_{pro-preds}$
d_{opt} vs. d_{obs}
Measured E_v (mm-s/m-hr)
Predicted E_v (mm-s/m-hr)

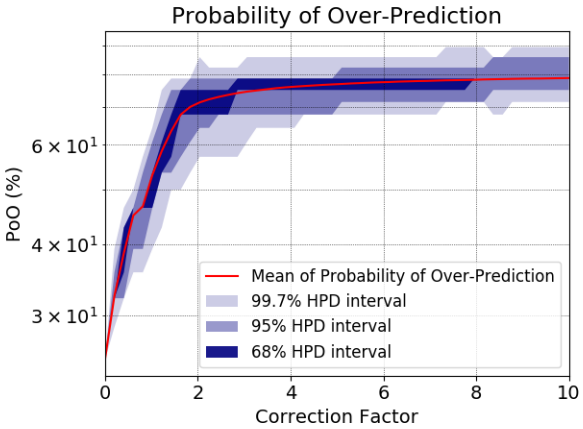
Probability of Over-Prediction
Mean of Probability of Over-Prediction
99.7% HPD interval
95% HPD interval
68% HPD interval
PoO (%)
Correction Factor

Models for Shear Stress Slope $\boldsymbol{E_\tau}$ in EFA/Coarse dataset:

(1) Model characteristics:

Group No.	Independent variables	Dataset/ No. of data	Model expression (parameter values given by deterministic regression)	R^2	Cross-validation score
77	C_u, γ, D50	EFA/Coarse 28	$E_\tau = (3228.7) \times C_u^{-2.8} \times \gamma^{-1.58} \times D50^{-2.91}$	0.91	0.64

(2) Statistics of marginal posterior distribution:

Parameters	Mean	SD	CoV	mode	95% HPD region (lower and upper bound)	
β_0	3181.776	3823.996	1.202	1067.800	21.313	9335.370
β_{C_u}	-2.040	0.308	-0.151	-2.000	-2.647	-1.443
β_γ	-1.193	0.320	-0.268	-1.200	-1.809	-0.556
β_{D50}	-2.249	0.241	-0.107	-2.200	-2.737	-1.794

(3) Joint relative frequency histogram:

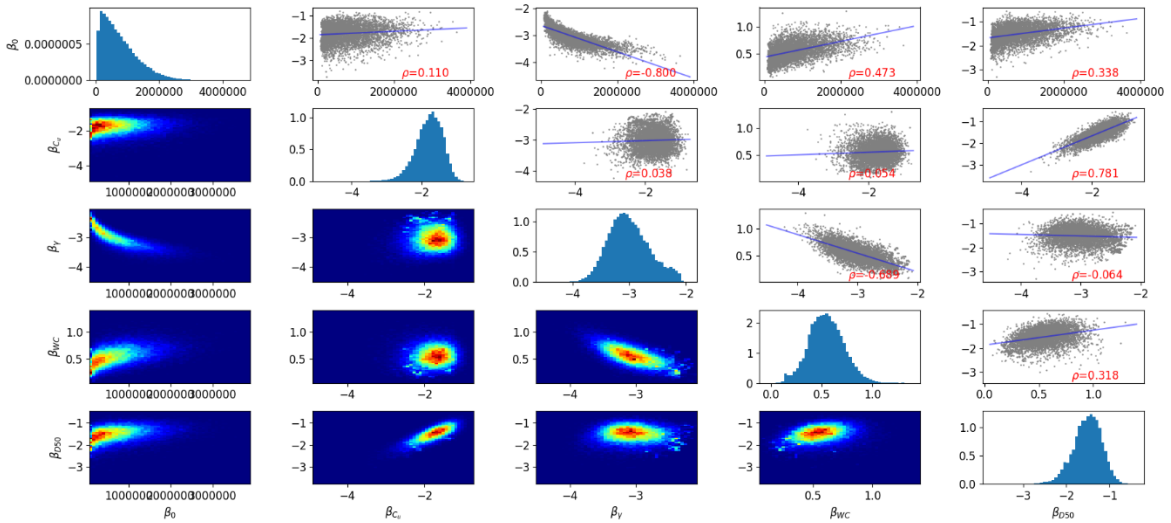

(4) Model realizations and first order statistics of model predictions:

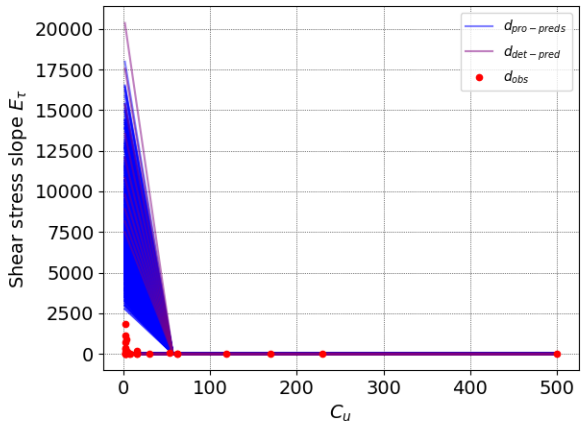
Shear stress slope E_τ
C_u
$d_{pro-preds}$
$d_{det-pred}$
d_{obs}

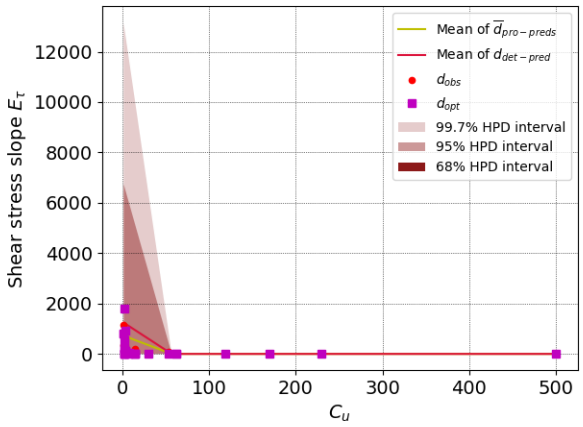
Shear stress slope E_τ
C_u
Mean of $\overline{d}_{pro-preds}$
Mean of $d_{det-pred}$
d_{obs}
d_{opt}
99.7% HPD interval
95% HPD interval
68% HPD interval

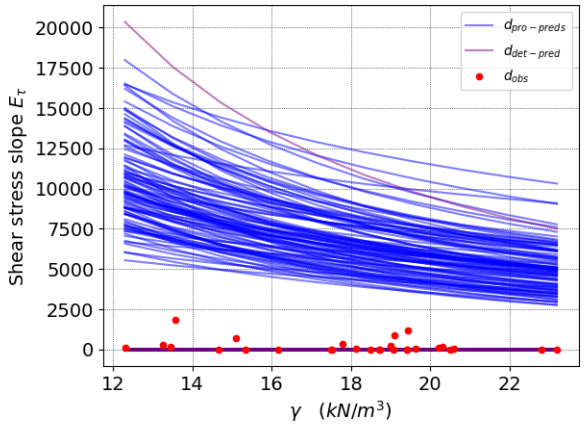
Shear stress slope E_τ
γ (kN/m^3)
$d_{pro-preds}$
$d_{det-pred}$
d_{obs}

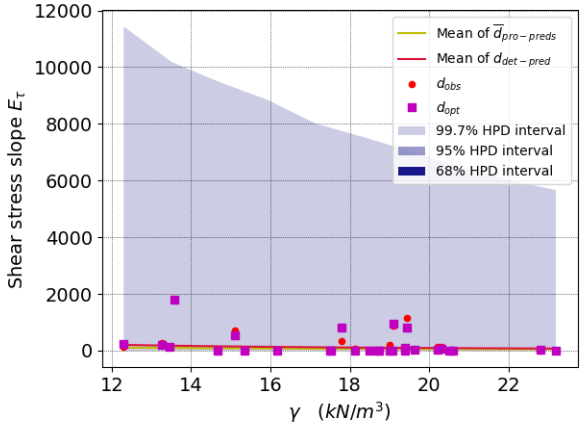
Shear stress slope E_τ
γ (kN/m^3)
Mean of $\overline{d}_{pro-preds}$
Mean of $d_{det-pred}$
d_{obs}
d_{opt}
99.7% HPD interval
95% HPD interval
68% HPD interval

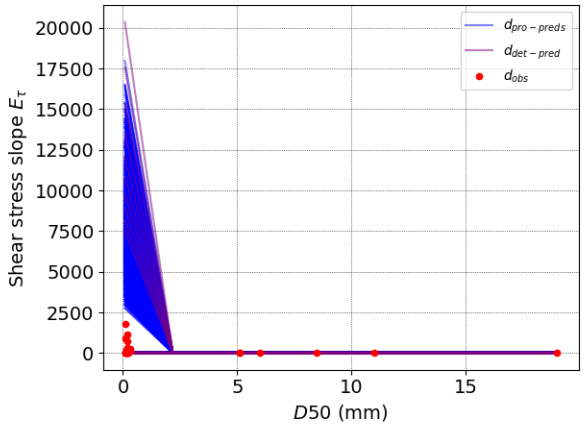
Shear stress slope E_τ
$D50$ (mm)
$d_{pro-preds}$
$d_{det-pred}$
d_{obs}

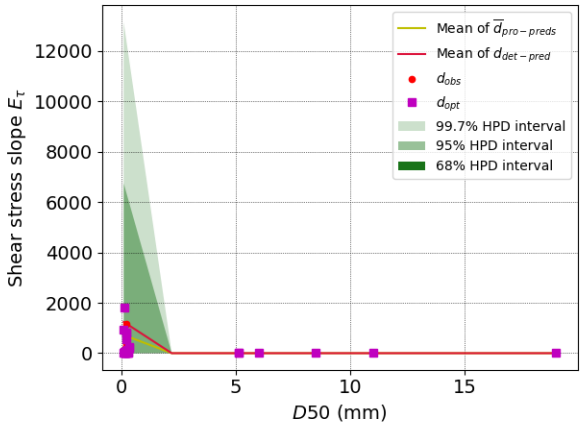
Shear stress slope E_τ
$D50$ (mm)
Mean of $\overline{d}_{pro-preds}$
Mean of $d_{det-pred}$
d_{obs}
d_{opt}
99.7% HPD interval
95% HPD interval
68% HPD interval

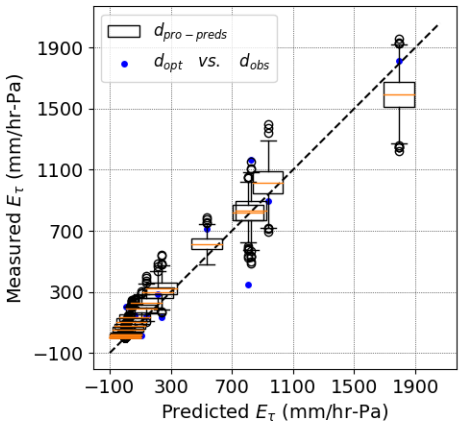
$d_{pro-preds}$
d_{opt} vs. d_{obs}
1900
1500
1100
700
300
−100
−100 300 700 1100 1500 1900
Measured E_τ (mm/hr-Pa)
Predicted E_τ (mm/hr-Pa)

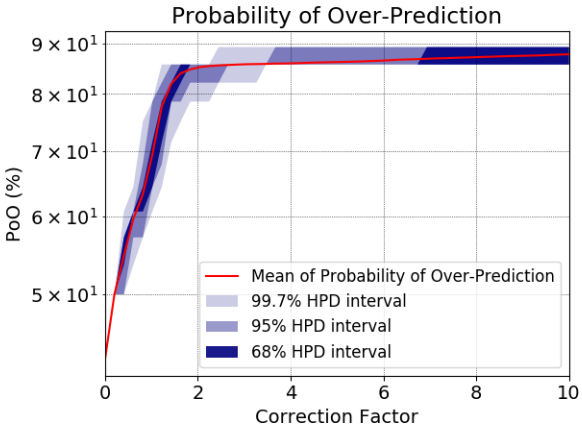
Probability of Over-Prediction
9×10^1
8×10^1
7×10^1
6×10^1
5×10^1
PoO (%)
Mean of Probability of Over-Prediction
99.7% HPD interval
95% HPD interval
68% HPD interval
0 2 4 6 8 10
Correction Factor

Models for Shear Stress Slope $\boldsymbol{E_\tau}$ in HET/Coarse dataset:

(1) Model characteristics:

Group No.	Independent variables	Dataset/ No. of data	Model expression (parameter values given by deterministic regression)	R^2	Cross-validation score
40	γ, WC, PF, D50	HET/Coarse 62	$E_\tau = (2.951) \times \gamma^{26.08} \times WC^{-7.48} \times PF^{-19.96} \times D50^{-5.32}$	0.86	0.55

(2) Statistics of marginal posterior distribution:

Parameters	Mean	SD	CoV	mode	95% HPD region (lower and upper bound)	
β_0	829973.740	605826.039	0.730	14235.580	14235.580	1993148.732
β_γ	28.075	3.667	0.131	26.940	21.203	35.423
β_{WC}	-7.508	0.632	-0.084	-7.206	-8.782	-6.310
β_{PF}	-27.489	5.471	-0.199	-28.886	-38.634	-18.538
β_{D50}	-8.953	7.805	-0.872	-16.508	-24.489	4.691

(3) Joint relative frequency histogram:

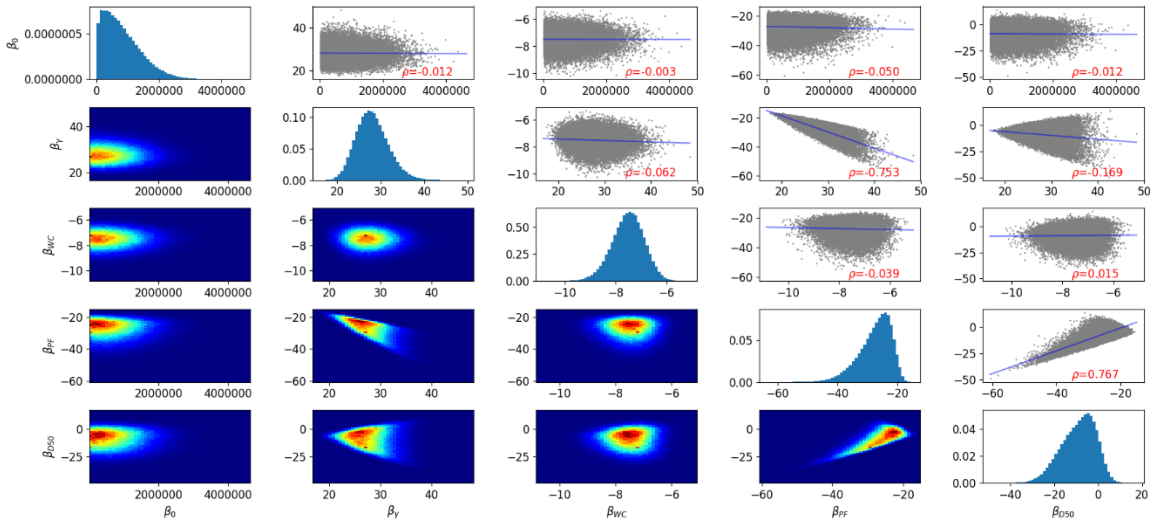

(4) Model realizations and first order statistics of model predictions:

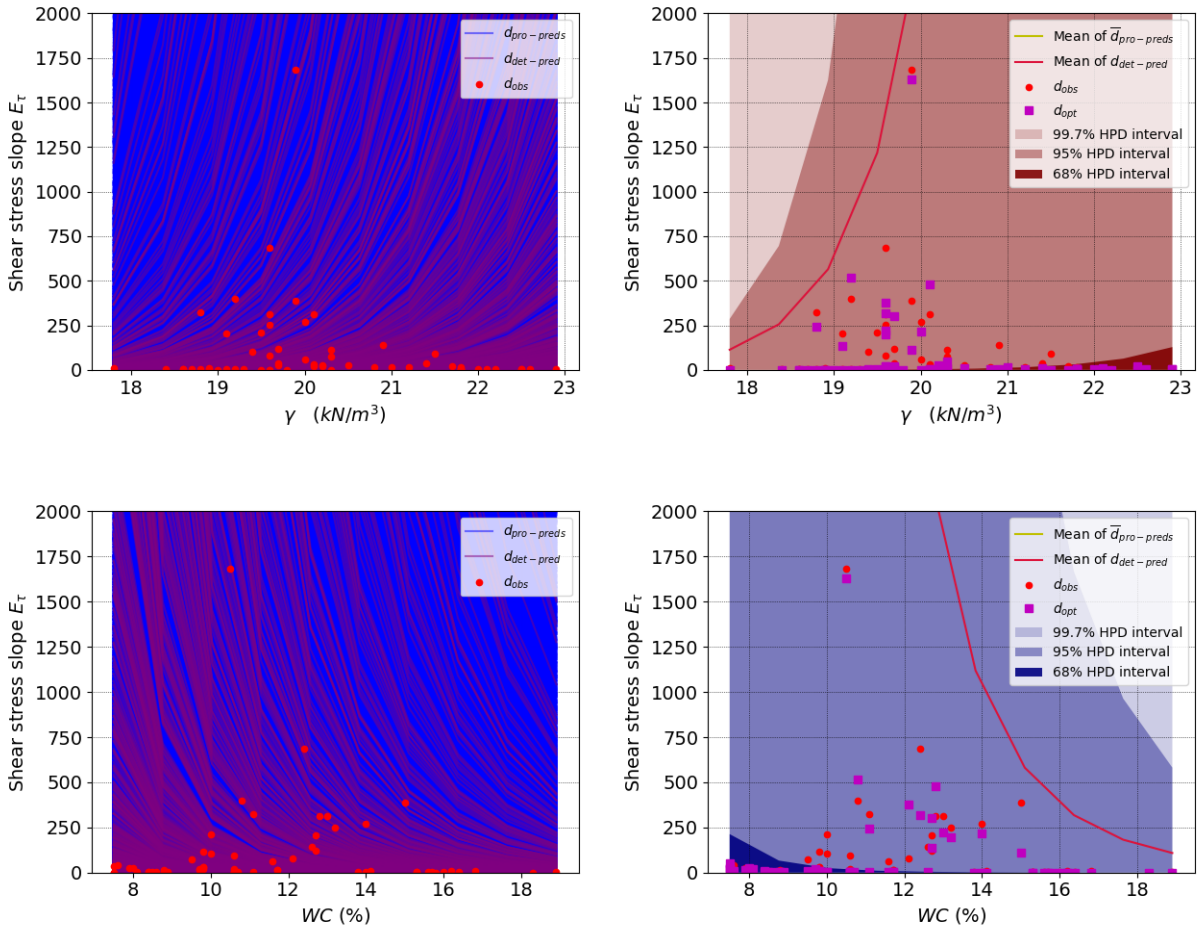

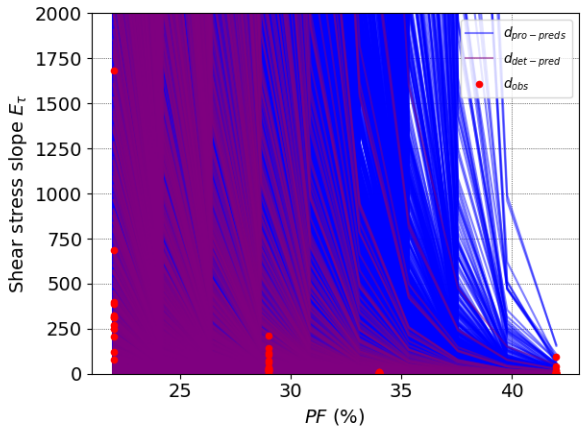
Shear stress slope E_τ
PF (%)
$d_{pro-preds}$
$d_{det-pred}$
d_{obs}

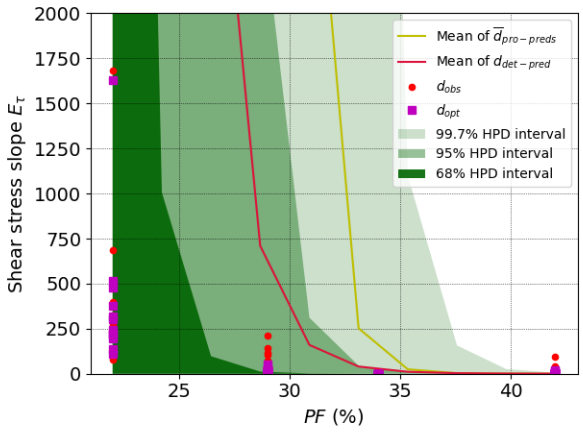
Shear stress slope E_τ
PF (%)
Mean of $\overline{d}_{pro-preds}$
Mean of $d_{det-pred}$
d_{obs}
d_{opt}
99.7% HPD interval
95% HPD interval
68% HPD interval

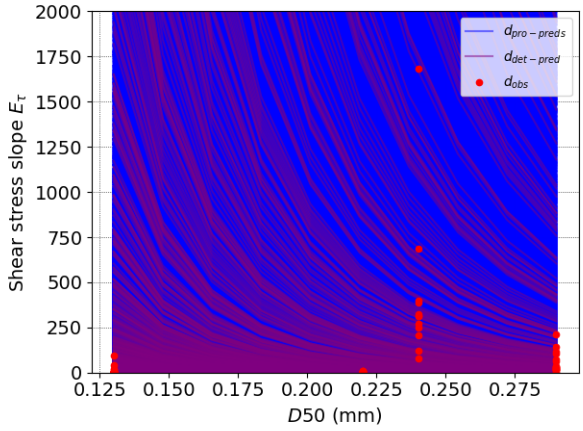
Shear stress slope E_τ
$D50$ (mm)
$d_{pro-preds}$
$d_{det-pred}$
d_{obs}

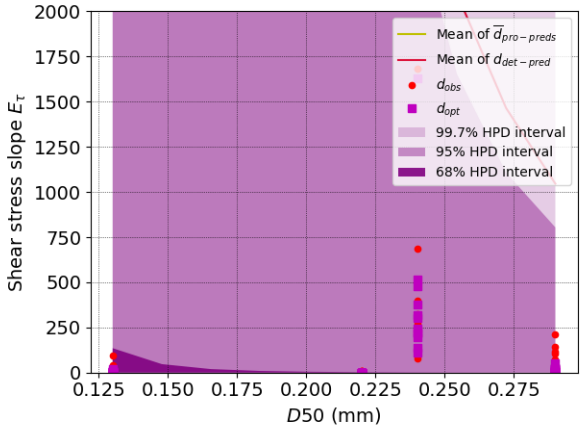
Shear stress slope E_τ
$D50$ (mm)
Mean of $\overline{d}_{pro-preds}$
Mean of $d_{det-pred}$
d_{obs}
d_{opt}
99.7% HPD interval
95% HPD interval
68% HPD interval

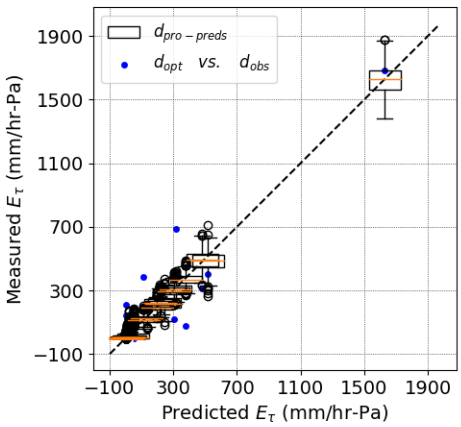
Measured E_τ (mm/hr-Pa)
Predicted E_τ (mm/hr-Pa)
$d_{pro-preds}$
d_{opt} vs. d_{obs}

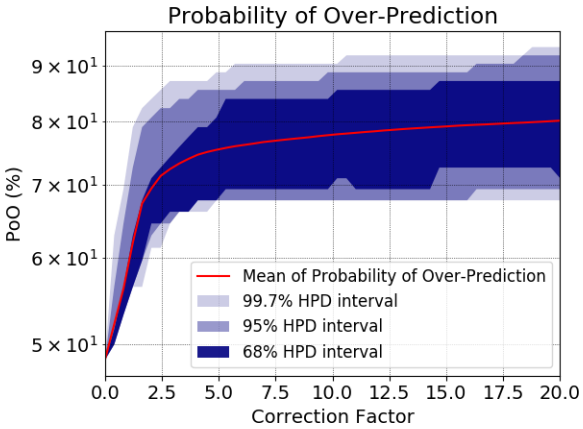
Probability of Over-Prediction
PoO (%)
Correction Factor
Mean of Probability of Over-Prediction
99.7% HPD interval
95% HPD interval
68% HPD interval